



BOOK OF ABSTRACTS

*Congresso Nazionale GRICU2022,
ISCHIA, 3-6 Luglio, 2022*

Guest Editor: Maurizio Masi

ISBN: 978-88-95608-04-4



9 788895 608044

DOI: 10.3303/BOA2201

Pubblicato da:



Associazione Italiana di Ingegneria Chimica
Via Giuseppe Colombo, 81/A
20133 Milano, Italy
Phone: +39-02-70608276;
e-mail: gricu2022@aidic.it

<https://www.aidic.it/gricu2022/>

Disclaimer

While any effort is made by the publisher and editorial board to see that no inaccurate or misleading data, opinion or statement appears in this volume, they wish to make clear that the data and opinions appearing in the articles herein are the sole responsibility of the contributor concerned. Accordingly, the publisher, the copy, the editorial board and editors and their respective employees, officers and agents accept no responsibility or liability whatsoever for the consequences of any inaccurate or misleading data, opinion or statement.

The Publisher

In order to make this volume available as economically and as rapidly as possible the typescript has been reproduced in its original form. This method unfortunately has its typographical limitations but it is hoped that they in no way distract the reader.

Indice

Bnvenuti a GRICU2022	i
Paper Index	iii
Author Index	xix
PAPERS	1



Benvenuto a GRICU 2022

A nome del Gruppo Italiano di Ingegneria Chimica dell'Università, GRICU, vi porgiamo un cordiale benvenuto al Convegno Nazionale:

GRICU 2022: Centralità dell'Ingegneria Chimica in un Mondo che cambia

in svolgimento dal 3 al 6 Luglio 2022 nell'isola di ISCHIA.

Siamo lieti di aprire con voi GRICU2022 e di condividere con voi l'atmosfera unica di questo evento, che offre oltre ad un programma molto interessante anche l'opportunità di scambiare idee con colleghi di tutti i settori e condividere la presentazione delle ultime innovazioni chiave all'interno dell'ingegneria chimica.

L'evento è organizzato da **AIDIC**, Associazione Italiana di Ingegneria Chimica.

L'organizzazione di questo Convegno Internazionale è stata possibile grazie all'aiuto e alla cura di molti colleghi: ringraziamo il contributo degli Autori dei manoscritti e dei Membri dei Comitati.

A nome dei Comitati del Convegno vi auguriamo giornate stimolanti e produttive, nonché un affascinante soggiorno nell'isola di ISCHIA.

A nome degli Organizzatori

Maurizio Masi
Presidente GRICU

Organizzato da



Associazione Italiana di Ingegneria Chimica
Via Giuseppe Colombo, 81/A
20133 Milano, Italy
Phone: +39-02-70608276;
e-mail: gricu2022@aidic.it

<https://www.aidic.it/gricu2022/>

PAPER INDEX

PROCESSES & TECHNOLOGY

Exergy Analysis of a Green Dimethyl Ether Production Plant <i>Marcello De Falco, Mauro Capocelli, Gianluca Natrella, Marco Facchino</i>	1
Supercritical CO₂ Assisted Process for the Production of Nano-niosomes <i>Lucia Baldino, Ernesto Reverchon</i>	3
Catalytic Assisted non Thermal Plasma Process for Degradation of Acid Orange 7 Dye in Aqueous Solution <i>Giuseppina Iervolino, Vincenzo Vaiano, Vincenzo Palma</i>	5
Rational Scale-up in Multiphase Apis Syntheses <i>Filippo Nanto, Paolo Canu, Dario Ciato</i>	8
Reaping Chemical Engineering Heritage by Leveraging Green Solvents: Opportunities and Issues <i>Vittoria Sapone, Alessio Mazzelli, Marco Valentini, Agnese Cicci, Marco Bravi</i>	10
Liquid Pyrolysis of Mixed Plastic Waste for the Co-production of Lubricants and Hydrogen: the Plasbreaker™ Process <i>Francesco Negri, Francesco Gallo, Flavio Manenti</i>	16
Sustainable Hydrogen Production from Corn Stover Hydrothermal Liquefaction Aqueous Phase <i>Giuseppe Pipitone, Giulia Zoppi, Samir Bensaid, Raffaele Pirone</i>	18
Sorption-enhanced Gasification in Dual Interconnected Fluidised Beds – Behaviour of Limestone-based Sorbents <i>Antonio Coppola, Fabio Montagnaro, Piero Salatino, Fabrizio Scala</i>	20
The Virtchem Project: the Virtual Immersive Education for Chemistry and Chemical Engineering <i>Carlo Pirola, Alessandro Pedretti, Claude Jolival, Arefi Farzaneh, Mika Ludek, Petr Smejkal</i>	22
Deep Learning-based Non-intrusive Detection of Instabilities in Formulated Liquids <i>Maurizio De Micco, Diego Gagnaniello, Fabio Zonfrilli, Massimiliano Maria Villone, Giovanni Poggi, Luisa Verdoliva, Vincenzo Guida</i>	24
Technical and Economic Analysis of the Decarbonization of Steelmaking Using Green Hydrogen <i>Antonio Trinca, Giorgio Vilardi</i>	30
The Colors of Hydrogen: a Process Simulation-based Comparison of Different Production Processes <i>Elena Barbera, Andrea Mio, Marco Disnan, Alessandro Massi Pavan, Alberto Bertucco, Maurizio Fermeglia</i>	34

Valuable C-based Chemical Intermediates and Biochar from “end of Life” Olive Stone Waste: Analysis in Thermal Pyrolytic Conditions	37
<i>Sina Ebrahim Atakoohi, Elena Spennati, Alessandro Alberto Casazza, Paola Riani, Gabriella Garbarino</i>	
A Study on the Adsorption on Activated Carbons as Upgrading Technology for Kraft Lignin Pyrolytic Gas	39
<i>Matteo Borella, Alessandro Alberto Casazza, Gabriella Garbarino, Paola Riani, Guido Busca</i>	
Analyzing the Production of Pure K₂SO₄ via Rigorous Process Simulation to Overcome Lack of Literature and Experimental Data	41
<i>Marco Vaccari, Livia Di Plama, Leonardo Tognotti, Giovanni Papa, Elisabetta Brunazzi</i>	
Artificial Intelligence Applied to Chemical Engineering	45
<i>Luigi Piero Di Bonito, Lelio Campanile, Mauro Iacono, Francesco Di Natale</i>	
Automated Machine Learning Framework for Surrogate Model Generation: Application to the Aspen Hysys Process Simulator	49
<i>Andrea Galeazzi, Kristiano Prifti, Flavio Manenti</i>	
Generalized Framework for the Simultaneous Capex/opex Robust Optimization (coro) of Production Processes Using Commercial Simulation Suites	53
<i>Kristiano Prifti, Andrea Galeazzi, Flavio Manenti</i>	
Hydrooil, the Opportunity to Save Leather	55
<i>Omar Salmi, Giacomo Pacchi, Massimiliano Franceschi, Maurizio Maraviglia, Roberto Lupi, Maurizio Masi</i>	
Scale-up of Electrodialysis with Bipolar Membrane (edbm) Unit for Valorisation of Waste Brine by Experimental Analysis	61
<i>Calogero Cassaro, Andrea Culcasi, Andrea Cipollina, Alessandro Tamburini, Giorgio Micale</i>	
THERMODYNAMICS AND TRANSPORT PHENOMENA	
Detailed Understanding of Transport Mechanisms During Sr²⁺ and Cs⁺ Adsorption Onto Cryogels via Application of Rigorous Diffusion Models	63
<i>Alzhan Baimenov, Marco Balsamo, Vassilis Inglezakis, Fabio Montagnaro</i>	
CO₂ Sorption and Diffusion in Fluorinated Polymers for Carbon Transport Application	65
<i>Virginia Signorini, Marco Giacinti Baschetti, Matteo Minelli</i>	
CFD Simulation and Convolutional Neural Networks Modelling for Flow and Transport in Porous Media	67
<i>Agnese Marcato, Gianluca Boccardo, Daniele Marchisio</i>	
Simulation of a Methane-based Poly(3-hydroxybutyrate) Production Process: the Effect of Internal Gas Recycling	71
<i>Claudia Amabile, Teresa Abate, Simeone Chianese, Dino Musmarra</i>	
Multiscale Modeling Approaches to Describe Complex Chemical Engineering Systems	75
<i>Petrosino Francesco, Giorgio De Luca, Javier Luque Di Salvo, Chakraborty Sudip, Stefano Curcio</i>	

Design and Development of a Microfluidic Platform for Extracellular Vesicles Engineering <i>Caterina Piunti, Sara Micheli, Elisa Cimetta</i>	79
Steady and Unsteady Reactive Flows in an X-microreactor <i>Sara Tomasi Masoni, Matteo Antognoli, Roberto Mauri, Chiara Galletti, Elisabetta Brunazzi</i>	83
Phase Field Modeling of Phase Separation in a Binary Mixture in Presence of External Forces <i>Roberto Mauri, Antonio Bertei</i>	87
One-way Vs Two-way Coupling Approach for Predicting Brownian-sieving Hydrodynamic Chromatography Separation Performance <i>Claudia Venditti, Stefano Cerbelli, Alessandra Adrover</i>	89
Validation Study of Windtrax Backward Lagrangian Model: Critical Discussion on Model Reliability and Its Optimisation <i>Francesca Tagliaferri, Marzio Invernizzi, Selena Sironi</i>	91
Influence of Cross-flows on the Performance of Open-channel Liquid Chromatography <i>Alessandra Adrover, Valentina Biagioni, Claudia Venditti, Stefano Cerbelli</i>	102
Influence of Side Injection Position on the Mixing Process in a Tubular Reactor Equipped with Sulzer Static Mixers <i>Jody Albertazzi, Valentina Busini, Federico Florit, Renato Rota</i>	104
Flow Features in a T-microchannel with Cylindrical Obstacles Mixing Water and Ethanol <i>Matteo Antognoli, Sara Tomasi Masoni, Roberto Mauri, Chiara Galletti, Elisabetta Brunazzi</i>	112
Using Dissipative Particle Dynamics as a Computational Rheological Tool: Simulation of High Schmidt Number Fluids <i>Nunzia Lauriello, Antonio Buffo, Gianluca Boccardo, Daniele Marchisio, Martin Lisal</i>	116
Open-cell Foams Modeling: Workflows for Geometry Generation and CFD Simulations for Pressure Drops and Mass Transport <i>Enrico Agostini, Maxime Moreaud, Yacine Haroun, Gianluca Boccardo, Daniele Marchisio</i>	122
Fractionation of Three-particles Mixture by Brownian Sieving Mechanism <i>Valentina Biagioni, Alessandra Adrover, Stefano Cerbelli</i>	128
Modeling Flux Reduction in Multiphase Gas Barrier Materials Trough 3D CFD Approach <i>Lorenzo Merlonghi, Marco Giacinti Baschetti, Maria Grazia De Angelis</i>	130
Slippage at the Solid-liquid Interfaces: Implications for Colloidal Transport in Confined Geometries <i>Giuseppe Procopio, Massimiliano Giona</i>	132
Non-brownian Suspensions: Frequency-dependent Irreversibility Threshold <i>Simona Moliterno, Johanna Vargas Clavijo, Claudia Carotenuto, Mario Minale</i>	134

Thermodynamic Characterization of Liquid-vapor Equilibria of Propionic Acid-water at Atmospheric Pressure	140
<i>Leone Mazzeo, Vincenzo Piemonte</i>	
 INNOVATIVE MATERIALS	
Organic Coatings from Vegetable Oils for Corrosion Protection	148
<i>Leonardo Iannucci, Camilla Noè, Valeria Gozzano, Marco Sangermano, Emma Angelini, Sabrina Grassini</i>	
Soot Coatings Wettability with Different Liquids. Preliminary Results.	150
<i>Raffaella Griffò, Arianna Parisi, Gianluigi De Falco, Mariano Sirignano, Francesco Di Natale, Mario Minale, Claudia Carotenuto</i>	
Biodegradability Evaluation of Waste-derived Polyhydroxyalkanoates	156
<i>Laura Lorini, Marco Santini, Sara Alfano, Francesco Valentino, Andrea Martinelli, Marianna Villano, Mauro Majone</i>	
Tuning the Molecular Architecture of 2D Go-based Nanocomposites for Gas Separation Application	158
<i>Giacomo Foli, Vincenzo Palermo, Matteo Minelli</i>	
Investigation of the Effect of Aeration Time, Storage and Heating on the Microstructure of Oil-continuous Foams with X-ray Tomography and Radiography	160
<i>Lorenzo Metilli, Malte Storm, Shashidhara Marathe, Aris Lazidis, Stephanie Marty-Terrade, Elena Simone</i>	
Fused Filament Fabrication of Pla: the Role of Interlayer Adhesion on the Mechanical Performances	164
<i>Sara Liparoti, Vittorio Alfieri, Annalaura Fabbricatore, Fabrizia Caiazzo, Roberto Pantani</i>	
Rheological and Viscoelastic Characterization of Hdpe/Ildpe Blends	168
<i>Francesca Gentile, Sara Liparoti, Valentina Volpe, Roberto Pantani</i>	
Biphasic Porous Structures Formed by Monomer/water Interface Stabilization with Colloidal Nanoparticles	174
<i>Fabio Pizzetti, Giovanna Massobrio, Valeria Vanoli, Franca Castiglione, Filippo Rossi</i>	
Functionalized Magnetite Nanoparticles for the Recovery of Vfas from a Water Solution	176
<i>Elisa Lacroce, Giovanna Massobrio, Filippo Rossi, Maurizio Masi</i>	
Comparative Study on the Effect of Leucine and Citric Acid on Calcium Carbonate Precipitation	179
<i>Giuseppe Mazziotti Di Celso, Marina Prisciandaro, Despina Karatza, Dino Musmarra, Amedeo Lancia</i>	
Multiscale Modeling of Solubility in Semi-crystalline Polymers: Bridging Molecular Dynamics Simulations with Lattice Fluid Theory	182
<i>Omar Atiq, Eleonora Ricci Ricci, Maria Grazia De Angelis, Marco Giacinti Baschetti</i>	
Geopolymer-zeolite Composite Materials for Carbon Capture Applications: Adsorption Tests and Modelling of Thermal Effects	186
<i>Mattia Boscherini</i>	

Effect of Flow Induced Crystallization on the Flow Length of Injection Molded Polypropylene <i>Rita Salomone, Vito Speranza, Sara Liparoti, Roberto Pantani</i>	192
 ENVIRONMENTAL SUSTAINABILITY & CIRCULAR ECONOMY	
Microwave-assisted Hydrothermal Preparation of Photocatalytic Fibrous Membranes for Water Treatment <i>Carlo Boaretti, Yin Jiayi, Michele Modesti, Alessandra Lorenzetti, Alessandro Martucci, Martina Roso</i>	195
Phosphorous Removal and Recovery from Wastewater by Adsorption Using an Innovative Calcined Pyroaurite <i>Dario Frascari, Carla Maggetti, Tommaso Tabanelli, Davide Pinelli</i>	198
Recycling of Automotive Waste for the Recovery of Precious and Critical Metals: Treasure Horizon 2020 Project <i>Nicolò Maria Ippolito, Marco Passadoro, Svetlana Borisovna Zueva, Francesco Vegliò</i>	202
Multiscale Modeling for the Estimation of Economic, Energy and Environmental Indicators <i>Andrea Mio, Elena Barbera, Alessandro Massi Pavan, Alberto Bertucco, Maurizio Fermeglia</i>	203
Techno-economic and Life Cycle Assessment for the Industrial Implementation of Hydrothermal Liquefaction Coupling with Aqueous Phase Reforming <i>Edoardo Tito, Giulia Zoppi, Giuseppe Pipitone, Edoardo Miliotti, Arturo Di Fraia, Andrea Maria Rizzo, Samir Bensaid, Raffaele Pirone, David Chiaramonti</i>	209
Energy Valorisation of Municipal Sewage Sludge for the Production of Renewable Liquid Fuels Through the Hydrothermal Liquefaction Process <i>Francesca Di Lauro, Marco Balsamo, Roberto Solimene, Piero Salatino, Fabio Montagnaro</i>	211
Hydrothermal Liquefaction of Sewage Sludge: Towards the Effects of Transition Metals in the Presence of Homogeneous Hydrogen Producers <i>Claudia Prestigiacomo, Joscha Zimmermann, Ursel Hornung, Nicolaus Dahmen, Onofrio Scialdone, Alessandro Galia, Klaus Raffelt</i>	213
Synthetic and Natural Surfactants for Environmental Applications Using Sear Technology: Process Study by Column Continuous Test <i>Berardino Barbati, Neda Amanat, Marco Bellagamba, Marco Buccolini, Marco Petrangeli Papini</i>	215
Combustion of a Biomass-derived Syngas to Decarbonize a Tissue Paper Plant: Impact of the Turbulence-chemistry Interaction Treatment on Numerical Simulations <i>Chiara Galletti, Lorenzo Giuntini, Linari Luca, Saccomano Pietro, Mainardi Davice, Leonardo Tognotti, Rachele Lamioni</i>	219
Electronic Nose for Real-time Monitoring of Odour Emissions at a Wastewater Treatment Plant <i>Stefano Prudenza, Carmen Bax, Laura Capelli</i>	223
Upcycling of Pu Waste via Microwave-assisted Chemolysis Process <i>Riccardo Donadini, Carlo Boaretti, Alessandra Lorenzetti, Michele Modesti</i>	235
Ammonia Fuel Cells Onboard Zero-emission Ships: a Comparison of Different Solutions	

<i>Roberta Russo, Tommaso Coppola, Luca Micoli</i>	241
Hydrodynamic Cavitation as a Treatment for the Removal of Methylene Blue from Synthetic Textile Wastewaters	
<i>Valentina Innocenzi, Marina Prisciandaro</i>	249
Removal and Recovery of Ammonium from Municipal Wastewater by Adsorption/ion Exchange on an Innovative Potassium Based Geopolymer Adsorbent	
<i>Carla Maggetti, Valentina Medri, Elettra Papa, Elena Landi, Davide Pinelli, Dario Frascari</i>	253
A Novel Integrated Technology to Recover High-valuable Minerals from Seawater Through a Circular Economy Approach	
<i>Carmelo Morgante, Fabrizio Vassallo, Andrea Cipollina, Alessandro Tamburini, Giorgio Micale</i>	257
Olive Mill Wastewater Treatment by a Continuous-flow Anaerobic Co-digestion Process with Municipal Sewage Sludge	
<i>Davide Pinelli, Dario Frascari, Alessandro Ragini, Francesco Avolio, Giannicola Scarcella, Sara Bovina</i>	259
Benchmark on Literature Data Processes for Precious Metals Recovery from Spent Auto-catalyst, Waste Printed Circuit Boards and Photovoltaic Panel	
<i>Ionela Birloaga, Pietro Romano, Francesco Vegliò</i>	263
Eco-sustainable Design of Hybrid Redox-active Materials to Remove (micro)plastics from Water	
<i>Paola Amato, Marica Muscetta, Claudio Imparato, Aurelio Bifulco, Mariacristina Cocca, Raffaele Marotta, Giuseppe Vitiello, Antonio Aronne</i>	264
A Multi-objective Optimization Approach for Preliminary Design of Economical and Environmentally Sustainable CO₂ Transport Pipelines	
<i>Francesco Zanobetti, Haroun Mahgerefteh, Sergey Martynov, Valerio Cozzani</i>	266
Assessment of Wastewater Plant Serving a Paper Industry: Performances Evaluation and Proposal Treatment for the Reduction of Freshwater Consumption	
<i>Nicolò Maria Ippolito, Giovanni Del Re</i>	268
Experimental Study on Voc's Production During High Monomer Content Emulsion Polymerizations	
<i>Marco Barozzi, Luca Leopardi, Carlo Bottinelli, Jacopo Ghezzi, Anita Barni, Sabrina Copelli</i>	269
BIOTECHNOLOGIES FOR CHEMICAL ENGINEERING APPLICATIONS	
Managing the Operative Conditions in Photobioreactors to Improve Photoconversion Efficiency: Led Applied to Microalgae Cultivation	
<i>Lisa Borella, Elena Barbera, Nicola Trivellin, Eleonora Sforza</i>	273
A Circular Economy Approach for Olive Oil Industry: from Olive Pomace to Microalgal Biomass	
<i>Alessandro Alberto Casazza, Patrizia Perego, Attilio Converti</i>	277
Medium Chain Fatty Acids Production via Biological Chain Elongation	
<i>Federico Battista, David Bolzonella</i>	279

Bioactive Substances from Hazelnut Processing Residues via Soxhlet Extraction: set Up, Mass Balances and Yield	283
<i>Michele Miccio, Marcello Casa, Michela Fraganza, Zainutdinova Aisylu, Paola Brachi, Giovanna Ferrari</i>	
A New Methodology for the Selection of a Methanogen-free Acetogen Inoculum from Mixed Sludge	291
<i>Jacopo Ferretti, Marianna Villano, Mauro Majone, Marco Zeppilli</i>	
Categorical Multifactor Design to Evaluate Different Operative Parameters During the Bioremediation of Hydrocarbon-polluted Soil in Early Experimental Stages.	294
<i>David Javier Castro Rodriguez, Omar Gutiérrez Benítez, Enmanuel Casals Pérez, Micaela Demichela, Alberto Godio, Fulvia Chiampo</i>	
Advancements of Scale-up Methods for Stirred Aerobic Fermenters	297
<i>Federico Alberini, Francesco Maluta, Giuseppina Montante, Alessandro Paglianti</i>	
Caratterizzazione Di Un Processo Di Co-digestione Anaerobica Di Biomasse Residuali	299
<i>Giuseppe Cristian Piso, Piero Bareschino, Erasmo Mancusi, Francesco Pepe</i>	
Empowered Parameter Identification Procedure for Anaerobic Digestion Models Stability and Reliability	304
<i>Federico Moretta, Federico Rocca, Flavio Manenti, Giulia Bozzano</i>	
Biological Conversion of Agricultural Wastes Into Microbial Proteins for Aquaculture Feed	306
<i>Giovanna Pesante, Anna Zuliani, David Bolzonella, Nicola Frison</i>	
Protein-rich Biomass Production Exploiting Biological Nitrogen Fixation: Respirometry as a Tool to Investigate Diazotrophic Cyanobacteria Cultivation	312
<i>Veronica Lucato, Elena Barbera, Eleonora Sforza</i>	
Mixotrophic Cultivation of Phaeodactylum Tricornutum and Value-added Compounds Extraction Through a Biorefinery Concept	316
<i>Caterina Celi, Debora Fino, Francesco Savorani</i>	
A Stochastic Approach for Modeling Cell Mass Distribution of Microalgae Culture	320
<i>Stefania Tronci, Schaum Alexander</i>	
A Circular Economy Approach for Cupriavidus Necator Dsm 545 Biosynthesis of Poly Hydroxybutyrate	322
<i>Silvia Bellini, Tonia Tommasi, Debora Fino</i>	
Monitoring and Control of a Bioreactor for Yeast Fermentation	325
<i>Silvia Lisci, Massimiliano Grosso, Stefania Tronci</i>	
From N₂ to Cyanophycin: High-value Compound Production Through Biological Nitrogen Fixation in Continuous Systems	327
<i>Giulia Trentin, Boris Zorin, Inna Khozin-Goldberg, Alberto Bertucco, Eleonora Sforza</i>	
Stabilization and Characterization of Microbial Strains in Liquid Formulation	

<i>Chiara Bufalini, Roberta Campardelli, Pier Francesco Ferrari, Domenico Palombo, Patrizia Perego</i>	331
Comparison of Kinetic Models for <i>Chlorella Vulgaris</i> Growth in Mixotrophic Culture <i>Shabnam Mirizadeh, Alessandro Alberto Casazza, Attilio Converti</i>	335
Electrochemically-steered Processes for Polyhydroxyalkanoates Production with Mixed Microbial Cultures <i>Gaia Salvatori, Matteo Di Luzio, Angela Marchetti, Ottavia Giampaoli, Fabio Sciubba, Alfredo Micchelli, Marianna Villano</i>	337
Scale Up of a Dechlorinating Microbial Consortium Based on Chemostat Approach <i>Edoardo Dell'Armi, Marco Zeppilli, Mauro Majone, Marco Petrangeli Papini</i>	339
3D Bioprinting for the Production of a Perfusable Vascularized Model of a Cancer Niche <i>Federico Maggiotto, Lorenzo Bova, Elisa Cimetta</i>	341
Modelling of the Growth of <i>Nannochloropsis Gaditana</i> in Different Reactor Geometries, Experimental Kinetic Parameters from Batch Cultures and Biochemical Analysis of the Obtained Biomass <i>Luca Schembri, Serena Lima, Alberto Brucato, Giuseppe Caputo, Silvia La Scala, Francesca Scargiali</i>	345
CHEMICAL ENGINEERING FOR FOOD & BIOMEDICALS APPLICATIONS	
Nife Alloy Based Electrochemical Sensor for Sugars Detection in Food <i>Francesca Mazzara, Bernardo Patella, Michele Russo, Alan O'Riordan, Giuseppe Aiello, Claudia Torino, Antonio Vilasi, Rosalinda Inguanta</i>	346
A Data-driven Approach to Assess the Rheological Properties of Durum Wheat Dough by Indirect Ftir Measurements <i>Fabio Fanari, Francesco Desogus, Massimiliano Grosso, Manfred Wilhelm</i>	349
Calibration of a Lyophilization Model in the Presence of Limited Industrial Data for Product Transfer Applications <i>Margherita Geremia, Gabriele Bano, Emanuele Tomba, Massimiliano Barolo, Fabrizio Bezzo</i>	351
Data-driven Optimization of a Freeze-drying Unit Using Design of Dynamic Experiments <i>Christopher Castaldello, Pierantonio Facco, Fabrizio Bezzo, Christos Georgakis, Massimiliano Barolo</i>	353
Carrier/curcumin Microparticles Obtained by Supercritical Antisolvent Precipitation <i>Iolanda De Marco</i>	355
Boosting Butyrate and Hydrogen Production in Acidogenic Fermentation of Food Waste and Sewage Sludge Mixture <i>Francesco Valentino, Hojjat Borhany, Michele Rasera, Alessio Dell'Olivo, Paolo Pavan, Marco Gottardo</i>	357
Electrochemical Detection of Human Immunoglobulin-g Using Immunosensor Based on ZnO Nanorods <i>Nadia Moukri, Bernardo Patella, Gaia Regalbuto, Giuseppe Aiello, Chiara Cipollina, Elisabetta Pace, Serena Di Vincenzo, Alan O'Riordan, Rosalinda Inguanta</i>	361
Monoclonal Antibody Controlled and Targeted Delivery: the Atherosclerosis Case Study	

<i>Roberta Campardelli, Pier Francesco Ferrari, Giulia De Negri Atanasio, Domenico Palombo, Patrizia Perego</i>	365
Integration and Digitalization in the Manufacturing of Therapeutic Proteins <i>Mattia Sponchioni, Tae Keun Kim, Ismaele Fioretti, Massimo Morbidelli</i>	368
Development of Model-based Strategies to Accelerate the Experimental Campaign for the Production of Oral Solid Dosage Through Direct Compression <i>Francesca Cenci, Gabriele Bano, Charalampos Christodoulou, Yuliya Vueva, Simeone Zomer, Pierantonio Facco</i>	369
Accelerating Cell Lines Selection in Biopharmaceutical Process Development Through Machine Learning on Process and Metabolomic Dynamics <i>Gianmarco Barberi, Antonio Benedetti, Paloma Diaz-Fernandez, Daniel C. Sévin, Johanna Vappiani, Gary Finka, Fabrizio Bezzo, Massimiliano Barolo, Pierantonio Facco</i>	371
Crystal Engineering as a Tool for Rational Design of Novel Sustainable Food, Agrochemical and Pharmaceutical Formulations <i>Panayiotis Klitou, Lorenzo Metilli, Elena Simone</i>	373
Cancer Viscoelasticity: a Dynamic Compression Assay for Tumor Spheroids Characterization <i>Rosalia Ferraro, Sergio Caserta</i>	377
Cfd-dem Simulations of Shear-activated Nanotherapeutic Particles <i>Giuliano Lorenzo Vasquez, Graziano Frungieri, Antonio Buffo, Marco Vanni</i>	380
Advanced Logistic in the Food Industry: a System Engineering Approach for a Multi-layered Solution <i>Maria Teresa Gaudio, Chakraborty Sudip, Stefano Curcio</i>	384
Wearable Sensor for Real-time Monitoring of Oxidative Stress <i>Maria Giuseppina Bruno, Bernardo Patella, Giuseppe Aiello, Francesco Lopresti, Vincenzo La Carrubba, Claudia Torino, Antonio Vilasi, Chiara Cipollina, Serena Di Vincenzo, Elisabetta Pace, Alan O'Riordan, Rosalinda Inguanta</i>	388
Preliminary Investigations on an Experimental Setup for Nuclear Graphite Dissolution in the Respiratory Tract <i>Martina Mazzi, Alessandro Antonio Porta, Fabrizio Campi, Marco Derudi</i>	390
Micro-channel Arrays by Two Photon Lithography for Cancer Cell Migration Studies <i>Sara Micheli, Elisa Varaschin, Caterina Piunti, Elisa Cimetta</i>	392
Using Machine Learning Tools for Residual Moisture Monitoring in Freeze-drying Processes for Pharmaceutical Applications <i>Ambra Massei, Serena Bobba, Nunzio Zinfullino, Davide Fissore</i>	396
Design and in Vivo Applications of Decorated Nanogels for Selective Drug Delivery in Spinal Cord Injury <i>Filippo Pinelli, Filippo Rossi</i>	404
Development of Active Food Packaging with Thermal Insulating Properties	

<i>Emanuela Drago, Roberta Campardelli, Antonio Barbucci, Patrizia Perego</i>	406
Pla-based Active Food Packaging Production with Antioxidant Properties <i>Maria Bolla, Margherita Pettinato, Roberta Campardelli, Giuseppe Firpo, Patrizia Perego</i>	408
Oil-in-water Nanoemulsions for Encapsulation of Lycopene from Tomato Waste <i>Junyang Li, Giulia De Negri Atanasio, Roberta Campardelli, Patrizia Perego</i>	410
Electrical Conductivity of Basil Based Sauces for Mef Processing <i>Oriana Casaburi, Aldo Romano, Cosimo Brondi, Francesco Marra</i>	414
Coupling of Experimental and Computational Approaches in the Study of Complex (nano)systems for Industrial and Biomedical Applications <i>Domenico Marson, Maria Russi, Erik Laurini, Sabrina Pricl</i>	418
Turboflux: a Mobile Transportable Unit to Produce Formulations for the Chemical and Health Sectors <i>Riccardo Bacci Di Capaci, Gabriele Pannocchia, Chiara Galletti, Elisabetta Brunazzi</i>	422
Engineered Small-diameter Vascular Prostheses: a Study in Bioreactor <i>Pier Francesco Ferrari, Giulia De Negri Atanasio, Jan Oscar Pralits, Domenico Palombo, Patrizia Perego</i>	427
Use of Hydrofluorocarbon Solvent for the Recovery of Lipid and Aqueous Extracts from Olive Pomace <i>Rosa Colucci Cante, Isidoro Garella, Alessandro Nigro, Elisabetta Iannone, Marianna Gallo, Roberto Nigro</i>	429
Injectable Polymer-nanoparticle Hydrogel with Ph and Thermo-responsive Drug Release <i>Elisa Lacroce, Filippo Rossi</i>	434
The Production Process of an Injectable Hyaluronic Acid Gel Solution for Regenerative Medicine Using Two Different Crosslinking Agents <i>Oystein Ovrebo, Zoe Giorgi, Giuseppe Perale, Håvard J. Haugen, Filippo Rossi</i>	437
LOW-CARBON CHEMICAL VECTORS	
Life Cycle Assessment of an Innovative Thermochemical Water-splitting Cycle for the Production of Green Hydrogen <i>Maria Beatrice Falasconi, Alice Bertino, Alberto Giaconia, Vincenzo Piemonte</i>	440
Simulation and Optimization of an Innovative Thermochemical Water-splitting Cycle for the Production of Green Hydrogen <i>Alice Bertino, Maria Beatrice Falasconi, Alberto Giaconia, Vincenzo Piemonte</i>	441
A Compendium of Behavioral Characterizations of Biomasses and Oxygen Carriers in the Clara (chemical Looping Gasification for Sustainable Production of Biofuels) Project <i>Andrea Di Giuliano, Stefania Lucantonio, Barbara Malsegna, Katia Gallucci</i>	442
Dynamic Simulation and Control of Ngl Recovery Plant <i>Marta Mandis, Roberto Baratti, Stefania Tronci, José A. Romagnoli</i>	458

Hydrogen Sulfide Mix Gas Permeation in Aquivion® Perfluorosulfonic Acid (pfsa) Ionomer Membranes for Natural Gas Sweetening	460
<i>Virginia Signorini, Marco Giacinti Baschetti, Diego Pizzi, Luca Merlo</i>	
Heterogeneous Catalysts for Hydrogen Storage Formates in Aqueous Solution	464
<i>Marcella Calabrese, Danilo Russo, Raffaele Marotta, Roberto Andreozzi, Almerinda Di Benedetto</i>	
Basing Offshore Energy Vectors Production on Optimized Energy Mixes: a Methanol Facility in the Adriatic Sea	466
<i>Mariasole Cipolletta, Valeria Casson Moreno, Valerio Cozzani</i>	
Biogas Upgrading by Adsorption: Experimental Performance of Commercial Zeolites and Comparison with Carbon-based Sorbents	468
<i>Fabrizio Rainone, Sabrina Mauro, Marco Balsamo, Amedeo Lancia, Alessandro Erto</i>	
Oxymethylene Ethers as the Next-generation Energy Carriers: Kinetic Model Development	472
<i>Alessandro Pegurri, Alessandro Stagni</i>	
Novel Process for Cyan Hydrogen Production	476
<i>Alessandra Di Nardo, Maria Portarapillo, Danilo Russo, Almerinda Di Benedetto, Giuseppina Luciani, Gianluca Landi, Giovanna Ruoppolo</i>	
A Comprehensive Chemical Kinetic Framework for the Thermo-catalytic Pyrolysis of Light Hydrocarbons for Value Added Carbon Solids and Turquoise Hydrogen Production.	478
<i>Matteo Pelucchi, Francesco Serse, Clarissa Giudici, Zhao-Bin Ding, Andrea Nobili, Davide Cafaro, Daniele Micale, Matteo Ferri, Mauro Bracconi, Matteo Maestri</i>	
SAFETY AND SECURITY IN CHEMICAL ENGINEERING	
Coupling Machine Learning and Engineering Judgment to Reduce the Cycle Time of an Industrial Batch Process	480
<i>Francesco Sartori, Federico Zuecco, Pierantonio Facco, Fabrizio Bezzo, Massimiliano Barolo</i>	
Feasibility Study of a Soft Sensor Predicting the Vapor Composition Inside a Flammable Liquid Storage Tank	482
<i>Gabriele Baldissone, Micaela Demichela, Davide Fissore</i>	
Identification of Cyber-risks Due to the Malicious Manipulation of Industrial Automation and Control Systems in Chemical and Process Facilities	486
<i>Matteo Iaiani, Alessandro Tugnoli, Valerio Cozzani</i>	
An Innovative Application of the Advanced Recursive Operability Analysis to the Bhopal Accident Reconstruction	488
<i>Federico Florit, Marco Barozzi, Martina Silvia Scotton, Sabrina Copelli</i>	
Risk of Major Accidents in Plants Producing Energy from Wastes	494
<i>Sabrina Copelli, Marco Barozzi, Martina Silvia Scotton, Vincenzo Torretta, Federico Florit</i>	
Investigation of the Bottom Corrosion of Atmospheric Storage Tanks for the Management of Safety	

<i>Maria Francesca Milazzo, Elpida Piperopoulos, Amani Khaskhoussi, Giuseppe Scionti, Paolo Bragatto, Edoardo Proverbio</i>	500
Multi-objective Optimization of a Carbon Capture and Sequestration Chain Under Seismic Risk Constraints	
<i>Daniel Cristiu, Federico D'amore, Paolo Mocellin, Fabrizio Bezzo</i>	504
Safe Operation of Reactors: an Investigation on the Thermal Stability of Hydroxylamine Solutions.	
<i>Paolo Mocellin, Gianmaria Pio, Chiara Vianello, Ernesto Salzano, Giuseppe Maschio</i>	506
Flashback Phenomenon in Domestic Condensing Boiler in H₂-enriched Admixtures	
<i>Rachele Lamioni, Filippo Fruzza, Leonardo Tognotti, Chiara Galletti</i>	509
A Comparative Analysis of Software Codes for the Consequence Assessment of CO₂ Leakage Scenarios from Onshore Facilities and Pipelines	
<i>Federica Tamburini, Sarah Bonvicini, Valerio Cozzani</i>	513
Assessment of Failure Frequencies of Pipelines Caused by Earthquakes in the Natech Risk Assessment Framework	
<i>Fabiola Amaducci, Alessio Misuri, Valerio Cozzani</i>	515
Emergency Response Management in the Risk Assessment of Cascading Events Caused by Natech Accidents	
<i>Federica Ricci, Ming Yang, Genserik Reniers, Valerio Cozzani</i>	519
CATALYSIS AND REACTION ENGINEERING	
Catalytic Activity of Si-modified Ni/al₂O₃ Catalysts for CO₂ Hydrogenation to Methane	
<i>Elena Spennati, Paola Riani, Guido Busca, Gabriella Garbarino</i>	521
Enhancing Fluidized Operations in Heterogeneous Catalysis Through Dynamically Structured Pulsed Reactors	
<i>Davide Cafaro, Daniele Micale, Riccardo Uglietti, Kaiqiao Wu, Mauro Bracconi, Marc-Olivier Coppens, Matteo Maestri</i>	523
Catalysis by Confinement: an Application to Diels-alder Reactions within Voids of Molecular Dimensions	
<i>Gabriele Contaldo, Zhao-Bin Ding, Matteo Maestri</i>	525
Optimization of the Lifetime of CeO₂-carrier Material over Consecutive Conversion Cycles of Methane for Hydrogen and Syngas Production	
<i>Matteo Minelli, Mattia Boscherini, Francesco Miccio, Elena Landi, Ferruccio Doghieri, Alba Storione</i>	528
Methane Cracking in Molten Tin to Produce Pure Hydrogen and Carbon.	
<i>Benedetta De Caprariis, Francesco Anania, Paolo De Filippis, Gaetano Iaquaniello</i>	534
3d-cfd Simulation of a Vessel with Inside Catalytic Filter Candles for Particulate Abatement and Tar Steam Reforming	
<i>Andrea Di Carlo, Elisa Savuto, Alessandra Tacconi, Alessandro Antonio Papa, Bora Aydin</i>	538

Study on Mesoporous-supported Catalysts for Simultaneous CO₂ and Steam Reforming of Biogas	548
<i>Camilla Galletti, Fabio Alessandro Deorsola, Samir Bensaid, Nunzio Russo, Debora Fino</i>	
Experimental Study of Sorption-enhanced Methanation in a Lab-scale Fluidized Bed System	550
<i>Fiorella Massa, Antonio Coppola, Fabrizio Scala</i>	
Core-shell Structures to Enhance the Formation of Gasoline Products via CO₂ Hydrogenation	558
<i>Elena Corrao, Fabio Salomone, Emanuele Giglio, Raffaele Pirone, Samir Bensaid</i>	
Evaluation of Transition Metal Heterogeneous Catalysts Deactivation in Green Chemistry Processes	560
<i>Gabriella Garbarino</i>	
Past, Present and Future of a Spouted Bed Reactor	562
<i>Cristina Moliner, Filippo Marchelli, Elisabetta Arato</i>	
CeO₂ and CeZr_{1-x}O₂ for the Direct Synthesis of Diethyl Carbonate from CO₂ and Ethanol in Presence of 2-cyanopyridine as Dehydrating Agent	565
<i>Mara Arduino, Fabio Alessandro Deorsola, Samir Bensaid</i>	
Comparative Study of Catalytic Methane Dry Reforming, with Microwave Heating Vs. Conventional Heating	567
<i>Francesco Esposito, Paolo Canu</i>	
Facile and Scalable Synthesis of Cu₂O-SnO₂ Catalyst for the Photoelectrochemical CO₂ Conversion	569
<i>Maddalena Zoli, Daniela Roldán, Hilmar Guzmán, Micaela Castellino, Angelica Chiodoni, Katarzyna Bejtka, Nunzio Russo, Simelys Hernández</i>	
Electrification of Methane Steam Reforming on Joule-heated Slic Foams Washcoated with a Rh/Al₂O₃ Catalyst	571
<i>Matteo Ambrosetti, Francesca Zaio, Lei Zheng, Alessandra Beretta, Gianpiero Groppi, Enrico Tronconi</i>	
Evaluating the Mass Transfer Properties of 3D Printed Catalyst Substrates with Catalytic H₂ Oxidation in Rich Conditions	573
<i>Federico Sascha Franchi, Matteo Ambrosetti, Mauro Braconi, Riccardo Balzarotti, Gianpiero Groppi, Enrico Tronconi</i>	
Experimental Campaigns and In-silico Assessment for the Conceptual Design of a Catalytic Splitting Process of Hydrogen Sulfide Into Hydrogen and Elemental Sulfur	575
<i>Anna Nova, Flavio Manenti</i>	
ELECTROCHEMICAL PROCESSES	
Nanostructured Nickel–zinc Alloy Electrodes for Hydrogen Evolution Reaction in Alkaline Electrolyzer	577
<i>Sonia Carbone, Francesco Bonafede, Fabrizio Ganci, Bernardo Patella, Giuseppe Aiello, Rosalinda Inguanta</i>	
Electrically Driven Sic-based Structured Catalysts for Hydrogen Production	

<i>Vincenzo Palma, Eugenio Meloni, Giuseppina Iervolino</i>	579
Design of an Offshore Renewable Energy-based Process for Hydrogen Production by Electrolysis	
<i>Leonardo Bozzoli, Valeria Casson Moreno, Valerio Cozzani</i>	583
Nanostructured Ni–fe Alloy Electrodes for Seawater Electrolyzer.	
<i>Francesco Bonafede, Sonia Carbone, Bernardo Patella, Fabrizio Ganci, Giuseppe Aiello, Rosalinda Inguanta, Giuseppe Inturri</i>	585
Physics-based Modeling Opportunities to Overcome Critical Challenges in Lithium-ion Batteries	
<i>Marco Lagnoni, Xuekun Lu, Antonio Bertei</i>	588
An Experimental Investigation on Ionic Shortcut Currents Reduction in Acid-base Flow Battery Systems	
<i>Alessandra Pellegrino, Andrea Culcasi, Alessandro Cosenza, Alessandro Tamburini, Andrea Cipollina, Giorgio Micale</i>	590
Scale Up of a Sequential Reductive/oxidative Bioelectrochemical Process for Chlorinated Aliphatic Hydrocarbons (cahs) Removal from Contaminated Groundwater	
<i>Marco Zeppilli, Edoardo Dell'Armi, Marco Petrangeli Papini, Mauro Majone</i>	592
Influence of the Morphology of the Precursors on the Electrochemical Capacity of Cathodes of Li-ion Batteries	
<i>Maria Para, Andrea Querio, Mohsen Shiea, Silvia Bodoardo, Daniele Marchisio</i>	594
Engineering the Electrochemical CO₂ Conversion to Chemicals and Fuels by Using Metal-oxide-based Catalysts and Optimized Cell Configurations	
<i>Simelys Hernández, Hilmar Guzmán, Samir Bensaid, Nunzio Russo</i>	598
Computational Modelling of the Solid Electrolyte Interface (sei) in Lithium-ion Batteries and Its Impact on Long-term Battery Aging	
<i>Luca Banetta, Graziano Frungieri, Agnese Marcato, Gianluca Boccardo, Silvia Bodoardo, Daniele Marchisio</i>	602
Hemp Fibers Modified with Graphite Oxide as a Sustainable System for Removal of Cationic Dyes from Wastewaters	
<i>Elena Lamberti, Gianluca Viscusi, Giuliana Gorrasi</i>	608
Understanding the Role of Imidazolium-based Ionic Liquids in the Electrochemical CO₂ Reduction Reaction: an Experimental and Theoretical Study	
<i>Alessia Fortunati, Simelys Hernández, Nunzio Russo, Giancarlo Cicero, Francesca Risplendi, Michele Re Fiorentin, Boyan Iliev, Thomas J.S. Schubert, Maria Jose Rubio</i>	612
Production of Acidic and Alkaline Solutions via Electrodialysis with Bipolar Membranes from Synthetic and Real Brines from Saltworks	
<i>Antonia Filingeri, Andrea Culcasi, Andrea Cipollina, Alessandro Tamburini, Giorgio Micale</i>	616
An Application of Reverse Electrodialysis: Energy Production from Produced Water.	
<i>Giovanni Campisi, Alessandro Cosenza, Andrea Cipollina, Alessandro Tamburini, Giorgio Micale</i>	618

Simulation-based Design of a Bipolar Membranes Electrodialysis Unit for Chemicals Production from Brines.	620
<i>Giovanni Virruso, Andrea Culcasi, Andrea Cipollina, Alessandro Tamburini, Giorgio Micale</i>	
Comprehensive Steady State Behavior Modeling of Polyelectrolyte Hydrogels	622
<i>Raffaella De Piano, Diego Caccavo, Anna Angela Barba, Gaetano Lamberti</i>	
Improved Electrochemical CO₂ Reduction to C₂+ Products on B-doped CuO Catalysts	626
<i>Hilmar Guzmán, Daniela Roldán, Federica Zammillo, Nunzio Russo, Simelys Hernández</i>	
Insight Into the Practical Challenges of Membrane-electrode Assembly for the CO₂ Electrochemical Reduction and Its Advantages	630
<i>Federica Zammillo, Hilmar Guzmán, Simelys Hernández</i>	
Electrochemical Sensor for H₂O₂ Released from Human Thp-1 Macrophages	632
<i>Astrid Sofia Fiorentino, Bernardo Patella, Maria Rita Giuffrè, Chiara Cipollina, Serena Di Vincenzo, Maria Ferraro, Elisabetta Pace, Giuseppe Aiello, Michele Russo, Rosalinda Inguanta</i>	
Technical and Economic Analysis of Most Promising Electrochemical Routes for the Conversion of CO₂ to Formic Acid	636
<i>Federica Proietto, Alessandro Galia, Onofrio Scialdone</i>	
Functionalized Cathodic Porous Transport Layers for Alkaline Water Electrolyzer	638
<i>Andrea Zaffora, Francesco Di Franco, Davide Pupillo, Barbara Seminara, Giada Tranchida, Monica Santamaria</i>	
Experimental Findings on the Application of Electric Fields to Enhance the Deposition Rate of Carbon Nanoparticle Films in Flame-synthesis	640
<i>Arianna Parisi, Gianluigi De Falco, Mariano Sirignano, Patrizia Minutolo, Mario Commodo, Claudia Carotenuto, Francesco Di Natale</i>	
2D Modelling of a Molten Carbonate Cell for Steam Electrolysis	644
<i>Maria Anna Murmura, Silvia Lo Conte, Luca Turchetti, Stefano Cerbelli, Maria Cristina Annesini</i>	
COVID PANDEMIC	
One Year of Surgical Mask Testing at the University of Bologna Labs	650
<i>Cristiana Boi, Martina Cappelletti, Maria Grazia De Angelis, Matteo Minelli, Alessandro Paglianti, Francesco Saverio Violante</i>	
An Electronic Nose for Covid-19 Detection by Means of Exhaled Breath Analysis	651
<i>Stefano Robbiani, Carmen Bax, Emanuela Zannin, Christian Ratti, Simone Bonetti, Luca Novelli, Federico Raimondi, Fabiano Di Marco, Raffaele Dellacà, Laura Capelli</i>	
From Reaction Safety Modelling Towards Covid-19 Pandemic Risk Early Detection	658
<i>Chiara Vianello, Fernanda Strozzi, Paolo Mocellin, Bruno Fabiano, Flavio Manenti, Giuseppe Maschio</i>	
GRICU EARLY CAREER AWARD	
Automation and Machine Learning in Chemical Engineering	662
<i>Danilo Russo</i>	

The Role of Safety for the Implementation of Cryogenic Systems <i>Gianmaria Pio</i>	663
Ottimizzazione Delle Condizioni Operative Di Processi Di Produzione Di Microalghe in Continuo Attraverso Modelli Matematici <i>Elena Barbera</i>	664
Single-atom Catalysts for a New Generation of Industrial Chemical Processes <i>Gianvito Vilé</i>	665
From Waste to New Products: Recovery and Applications of Bioactive Compounds from Agri-food Industry By-products <i>Margherita Pettinato</i>	666
Analysis of Technologies for CO₂ Capture from the Air <i>Grazia Leonzio, Nilay Shah</i>	667
Municipal Solid Waste and Circular Economy: Alternative Resource for the Production of Energy Vectors and Green Fine Chemicals <i>Giorgio Vilardi</i>	668
Composite Materials Based on Self-assembly Strategies and Fdm Techniques: Versatile Tools to Realize Innovative Hybrid Materials for Energetic, Environmental and Biomedical Applications <i>Massimiliano Gaeta</i>	669

AUTHOR INDEX

Baimenov Alzhan	63	Biagioni Valentina	102, 128
Abate Teresa	71	Bifulco Aurelio	264
Adrover Alessandra	89, 102, 128	Birloaga Ionela	263
Agostini Enrico	122	Boaretti Carlo	195, 235
Aiello Giuseppe	346, 361, 388, 577, 585, 632	Bobba Serena	396
Aisylu Zainutdinova	283	Boccardo Gianluca	67, 116, 122, 602
Alberini Federico	297	Bodoardo Silvia	594, 602
Albertazzi Jody	104	Boi Cristiana	650
Alexander Schaum	320	Bolla Maria	408
Alfano Sara	156	Bolzonella David	279, 306
Alfieri Vittorio	164	Bonafede Francesco	577, 585
Amabile Claudia	71	Bonetti Simone	651
Amaducci Fabiola	515	Bonvicini Sarah	513
Amanat Neda	215	Borella Lisa	273
Amato Paola	264	Borella Matteo	39
Ambrosetti Matteo	571, 573	Borhany Hojjat	357
Anania Francesco	534	Boscherini Mattia	186, 528
Andreozzi Roberto	464	Bottinelli Carlo	269
Angelini Emma	148	Bova Lorenzo	341
Annesini Maria Cristina	644	Bovina Sara	259
Antognoli Matteo	83, 112	Bozzano Giulia	304
Arato Elisabetta	562	Bozzoli Leonardo	583
Arduino Mara	565	Bracconi Mauro	478, 523, 573
Aronne Antonio	264	Brachi Paola	283
Atiq Omar	182	Bragatto Paolo	500
Avolio Francesco	259	Bravi Marco	10
Aydin Bora	538	Brondi Cosimo	414
Bacci Di Capaci Riccardo	422	Brucato Alberto	345
Baldino Lucia	3	Brunazzi Elisabetta	41, 83, 112, 422
Baldissoni Gabriele	482	Bruno Maria Giuseppina	388
Balsamo Marco	63, 211, 468	Buccolini Marco	215
Balzarotti Riccardo	573	Bufalini Chiara	331
Banetta Luca	602	Buffo Antonio	116, 380
Bano Gabriele	351, 369	Busca Guido	39, 521
Baratti Roberto	458	Busini Valentina	104
Barba Anna Angela	622	Caccavo Diego	622
Barbati Berardino	215	Cafaro Davide	478, 523
Barbera Elena	34, 203, 273, 312, 664	Caiazzo Fabrizia	164
Barberi Gianmarco	371	Calabrese Marcella	464
Barbucci Antonio	406	Campanile Lelio	45
Bareschino Piero	299	Campardelli Roberta	331, 365, 406, 408, 410
Barni Anita	269	Campi Fabrizio	390
Barolo Massimiliano	351, 353, 371, 480	Campisi Giovanni	618
Barozzi Marco	269, 488, 494	Canu Paolo	8, 567
Battista Federico	279	Capelli Laura	223, 651
Bax Carmen	223, 651	Capocelli Mauro	1
Bejtka Katarzyna	569	Cappelletti Martina	650
Bellagamba Marco	215	Caputo Giuseppe	345
Bellini Silvia	322	Carbone Sonia	577, 585
Benedetti Antonio	371	Carotenuto Claudia	134, 150, 640
Bensaid Samir	18, 209, 548, 558, 565, 598	Casa Marcello	283
Beretta Alessandra	571	Casaburi Oriana	414
Bertei Antonio	87, 588	Casals Pérez Enmanuel	294
Bertino Alice	440, 441	Casazza Alessandro Alberto	37, 39, 277, 335
Bertuccio Alberto	34, 203, 327	Caserta Sergio	377
Bezzo Fabrizio	351, 353, 371, 480, 504	Cassaro Calogero	61

Casson Moreno Valeria	466, 583	Di Bonito Luigi Piero	45
Castaldello Christopher	353	Di Carlo Andrea	538
Castellino Micaela	569	Di Fraia Arturo	209
Castiglione Franca	174	Di Franco Francesco	638
Castro Rodriguez David Javier	294	Di Giuliano Andrea	442
Celi Caterina	316	Di Lauro Francesca	211
Cenci Francesca	369	Di Luzio Matteo	337
Cerbelli Stefano	89, 102, 128, 644	Di Marco Fabiano	651
Chiampo Fulvia	294	Di Nardo Alessandra	476
Chianese Simeone	71	Di Natale Francesco	45, 150, 640
Chiaramonti David	209	Di Plama Livia	41
Chiodoni Angelica	569	Di Salvo Javier Luque	75
Christodoulou Charalampos	369	Di Vincenzo Serena	361, 388, 632
Ciato Dario	8	Diaz-Fernandez Paloma	371
Cicci Agnese	10	Ding Zhao-Bin	478, 525
Cicero Giancarlo	612	Disnan Marco	34
Cimetta Elisa	79, 341, 392	Doghieri Ferruccio	528
Cipolletta Mariasole	466	Donadini Riccardo	235
Cipollina Andrea	61, 257, 590, 616, 618, 620	Drago Emanuela	406
Cipollina Chiara	361, 388, 632	Ebrahim Atakoochi Sina	37
Cocca Mariacristina	264	Erto Alessandro	468
Colucci Cante Rosa	429	Esposito Francesco	567
Commodo Mario	640	Fabbricatore Annalaura	164
Contaldo Gabriele	525	Fabiano Bruno	658
Converti Attilio	277, 335	Facchino Marco	1
Copelli Sabrina	269, 488, 494	Facco Pierantonio	353, 369, 371, 480
Coppens Marc-Olivier	523	Falasconi Maria Beatrice	440, 441
Coppola Antonio	20, 550	Fanari Fabio	349
Coppola Tommaso	241	Farzaneh Arefi	22
Corrao Elena	558	Fermeglia Maurizio	34, 203
Cosenza Alessandro	590, 618	Ferrari Giovanna	283
	266, 466, 486, 513, 515, 519	Ferrari Pier Francesco	331, 365, 427
Cozzani Valerio	583	Ferraro Maria	632
Cristiu Daniel	504	Ferraro Rosalia	377
Culcasi Andrea	61, 590, 616, 620	Ferretti Jacopo	291
Curcio Stefano	75, 384	Ferri Matteo	478
D'amore Federico	504	Filingeri Antonia	616
Dahmen Nicolaus	213	Finka Gary	371
Davice Mainardi	219	Fino Debora	316, 322, 548
De Angelis Maria Grazia	130, 182, 650	Fiorentino Astrid Sofia	632
De Caprariis Benedetta	534	Fioretti Ismaele	368
De Falco Gianluigi	150, 640	Firpo Giuseppe	408
De Falco Marcello	1	Fissore Davide	396, 482
De Filippis Paolo	534	Florit Federico	104, 488, 494
De Luca Giorgio	75	Foli Giacomo	158
De Marco Iolanda	355	Fortunati Alessia	612
De Micco Maurizio	24	Fraganza Michela	283
De Negri Atanasio Giulia	365, 410, 427	Franceschi Massimiliano	55
De Piano Raffaella	622	Francesco Petrosino	75
Del Re Giovanni	268	Franchi Federico Sascha	573
Dellacà Raffaele	651	Frascardi Dario	198, 253, 259
Dell'Armi Edoardo	339, 592	Frison Nicola	306
Dell'Olivo Alessio	357	Frungieri Graziano	380, 602
Demichela Micaela	294, 482	Fruzza Filippo	509
Deorsola Fabio Alessandro	548, 565	Gaeta Massimiliano	669
Derudi Marco	390	Galeazzi Andrea	49, 53
Desogus Francesco	349	Galia Alessandro	213, 636
Di Benedetto Almerinda	464, 476	Galletti Camilla	548

Galletti Chiara	83, 112, 219, 422, 509	La Carrubba Vincenzo	388
Gallo Francesco	16	La Scala Silvia	345
Gallo Marianna	429	Lacroe Elisa	176, 434
Gallucci Katia	442	Lagnoni Marco	588
Ganci Fabrizio	577, 585	Lamberti Elena	608
Garbarino Gabriella	37, 39, 521, 560	Lamberti Gaetano	622
Garella Isidoro	429	Lamioni Rachele	219, 509
Gaudio Maria Teresa	384	Lancia Amedeo	179, 468
Gentile Francesca	168	Landi Elena	253, 528
Georgakis Christos	353	Landi Gianluca	476
Geremia Margherita	351	Lauriello Nunzia	116
Ghezzi Jacopo	269	Laurini Erik	418
Giacinti Baschetti Marco	65, 130, 182, 460	Lazidis Aris	160
Giaconia Alberto	440, 441	Leonzio Grazia	667
Giampaoli Ottavia	337	Leopardi Luca	269
Giglio Emanuele	558	Li Junyang	410
Giona Massimiliano	132	Lima Serena	345
Giorgi Zoe	437	Liparoti Sara	164, 168, 192
Giudici Clarissa	478	Lisal Martin	116
Giuffrè Maria Rita	632	Lisci Silvia	325
Giuntini Lorenzo	219	Lo Conte Silvia	644
Godio Alberto	294	Lopresti Francesco	388
Gorrasi Giuliana	608	Lorenzetti Alessandra	195, 235
Gottardo Marco	357	Lorini Laura	156
Gozzano Valeria	148	Lu Xuekun	588
Gragnaniello Diego	24	Luca Linari	219
Grassini Sabrina	148	Lucantonio Stefania	442
Griffo Raffaella	150	Lucato Veronica	312
Groppi Gianpiero	571, 573	Luciani Giuseppina	476
Grosso Massimiliano	325, 349	Ludek Mika	22
Guida Vincenzo	24	Lupi Roberto	55
Gutiérrez Benítez Omar	294	Maestri Matteo	478, 523, 525
Guzmán Hilmar	569, 598, 626, 630	Maggetti Carla	198, 253
Haroun Yacine	122	Maggiotto Federico	341
Haugen Håvard J.	437	Mahgereteh Haroun	266
Hernández Simelys	569, 598, 612, 626, 630	Majone Mauro	156, 291, 339, 592
Hornung Ursel	213	Malsegna Barbara	442
Iacono Mauro	45	Maluta Francesco	297
Iaiani Matteo	486	Mancusi Erasmo	299
Iannone Elisabetta	429	Mandis Marta	458
Iannucci Leonardo	148	Manenti Flavio	16, 49, 53, 304, 575, 658
Iaquaniello Gaetano	534	Marathe Shashidhara	160
Iervolino Giuseppina	5, 579	Maraviglia Maurizio	55
Iliev Boyan	612	Marcato Agnese	67, 602
Imparato Claudio	264	Marchelli Filippo	562
Inglezakis Vassilis	63	Marchetti Angela	337
Inguanta Rosalinda	346, 361, 388, 577, 585, 632	Marchisio Daniele	67, 116, 122, 594, 602
Innocenzi Valentina	249	Maria Rizzo Andrea	209
Inturri Giuseppe	585	Marotta Raffaele	264, 464
Invernizzi Marzio	91	Marra Francesco	414
Ippolito Nicolò Maria	202, 268	Marson Domenico	418
Jiayi Yin	195	Martinelli Andrea	156
Jolival Claude	22	Martucci Alessandro	195
Karatza Despina	179	Martynov Sergey	266
Khaskhoussi Amani	500	Marty-Terrade Stephanie	160
Khazin-Goldberg Inna	327	Maschio Giuseppe	506, 658
Kim Tae Keun	368	Masi Maurizio	55, 176
Klitou Panayiotis	373	Massa Fiorella	550

Massei Ambra	396	Palermo Vincenzo	158
Massi Pavan Alessandro	34, 203	Palma Vincenzo	5, 579
Massobrio Giovanna	174, 176	Palombo Domenico	331, 365, 427
Mauri Roberto	83, 87, 112	Pannocchia Gabriele	422
Mauro Sabrina	468	Pantani Roberto	164, 168, 192
Mazzara Francesca	346	Papa Alessandro Antonio	538
Mazzelli Alessio	10	Papa Elettra	253
Mazzeo Leone	140	Papa Giovanni	41
Mazzi Martina	390	Para Maria	594
Mazziotti Di Celso Giuseppe	179	Parisi Arianna	150, 640
Medri Valentina	253	Passadoro Marco	202
Meloni Eugenio	579	Patella Bernardo	346, 361, 388, 577, 585, 632
Merlo Luca	460	Pavan Paolo	357
Merlonghi Lorenzo	130	Pedretti Alessandro	22
Metilli Lorenzo	160, 373	Pegurri Alessandro	472
Micale Daniele	478, 523	Pellegrino Alessandra	590
Micale Giorgio	61, 257, 590, 616, 618, 620	Pelucchi Matteo	478
Micchelli Alfredo	337	Pepe Francesco	299
Miccio Francesco	528	Perale Giuseppe	437
Miccio Michele	283		277, 331, 365, 406, 408, 410,
Micheli Sara	79, 392	Perego Patrizia	427
Micoli Luca	241	Pesante Giovanna	306
Milazzo Maria Francesca	500	Petrangeli Papini Marco	215, 339, 592
Miliotti Edoardo	209	Pettinato Margherita	408, 666
Minale Mario	134, 150	Piemonte Vincenzo	140, 440, 441
Minelli Matteo	65, 158, 528, 650	Pietro Saccomano	219
Minutolo Patrizia	640	Pinelli Davide	198, 253, 259
Mio Andrea	34, 203	Pinelli Filippo	404
Mirizadeh Shabnam	335	Pio Gianmaria	506, 663
Misuri Alessio	515	Piperopoulos Elpida	500
Mocellin Paolo	504, 506, 658	Pipitone Giuseppe	18, 209
Modesti Michele	195, 235	Pirola Carlo	22
Moliner Cristina	562	Pirone Raffaele	18, 209, 558
Molitierno Simona	134	Piso Giuseppe Cristian	299
Montagnaro Fabio	20, 63, 211	Piunti Caterina	79, 392
Montante Giuseppina	297	Pizzetti Fabio	174
Morbidelli Massimo	368	Pizzi Diego	460
Moreaud Maxime	122	Poggi Giovanni	24
Moretta Federico	304	Porta Alessandro Antonio	390
Morgante Carmelo	257	Portarapillo Maria	476
Moukri Nadia	361	Pralits Jan Oscar	427
Murmura Maria Anna	644	Prestigiacomo Claudia	213
Muscetta Marica	264	Pricl Sabrina	418
Musmarra Dino	71, 179	Prifti Kristiano	49, 53
Nanto Filippo	8	Prisciandaro Marina	179, 249
Natrella Gianluca	1	Procopio Giuseppe	132
Negri Francesco	16	Proietto Federica	636
Nigro Alessandro	429	Proverbio Edoardo	500
Nigro Roberto	429	Prudenza Stefano	223
Nobili Andrea	478	Pupillo Davide	638
Noè Camilla	148	Querio Andrea	594
Nova Anna	575	Raffelt Klaus	213
Novelli Luca	651	Ragini Alessandro	259
O'Riordan Alan	346, 361, 388	Raimondi Federico	651
Ovrebø Oystein	437	Rainone Fabrizio	468
Pacchi Giacomo	55	Rasera Michele	357
Pace Elisabetta	361, 388, 632	Ratti Christian	651
Paglianti Alessandro	297, 650	Re Fiorentin Michele	612

Regalbuto Gaia	361	Speranza Vito	192
Reniers Genserik	519	Sponchioni Mattia	368
Reverchon Ernesto	3	Stagni Alessandro	472
Riani Paola	37, 39, 521	Storione Alba	528
Ricci Eleonora Ricci	182	Storm Malte	160
Ricci Federica	519	Strozzi Fernanda	658
Risplendi Francesca	612	Sudip Chakraborty	75, 384
Robbiani Stefano	651	Tabanelli Tommaso	198
Rocca Federico	304	Tacconi Alessandra	538
Roldán Daniela	569, 626	Tagliaferri Francesca	91
Romagnoli José A.	458	Tamburini Alessandro	61, 257, 590, 616, 618, 620
Romano Aldo	414	Tamburini Federica	513
Romano Pietro	263	Tito Edoardo	209
Roso Martina	195	Tognotti Leonardo	41, 219, 509
Rossi Filippo	174, 176, 404, 434, 437	Tomasi Masoni Sara	83, 112
Rota Renato	104	Tomba Emanuele	351
Rubio Maria Jose	612	Tommasi Tonia	322
Ruoppolo Giovanna	476	Torino Claudia	346, 388
Russi Maria	418	Torretta Vincenzo	494
Russo Danilo	464, 476, 662	Tranchida Giada	638
Russo Michele	346, 632	Trentin Giulia	327
Russo Nunzio	548, 569, 598, 612, 626	Trinca Antonio	30
Russo Roberta	241	Trivellin Nicola	273
Salatino Piero	20, 211	Tronci Stefania	320, 325, 458
Salmi Omar	55	Tronconi Enrico	571, 573
Salomone Fabio	558	Tugnoli Alessandro	486
Salomone Rita	192	Turchetti Luca	644
Salvatori Gaia	337	Uglietti Riccardo	523
Salzano Ernesto	506	Vaccari Marco	41
Sangermano Marco	148	Vaiano Vincenzo	5
Santamaria Monica	638	Valentini Marco	10
Santini Marco	156	Valentino Francesco	156, 357
Sapone Vittoria	10	Vanni Marco	380
Sartori Francesco	480	Vanoli Valeria	174
Savorani Francesco	316	Vappiani Johanna	371
Savuto Elisa	538	Varaschin Elisa	392
Scala Fabrizio	20, 550	Vargas Clavijo Johanna	134
Scarcella Giannicola	259	Vasquez Giuliano Lorenzo	380
Scargiali Francesca	345	Vassallo Fabrizio	257
Schembri Luca	345	Vegliò Francesco	202, 263
Schubert Thomas J.S.	612	Venditti Claudia	89, 102
Scialdone Onofrio	213, 636	Verdoliva Luisa	24
Scionti Giuseppe	500	Vianello Chiara	506, 658
Sciubba Fabio	337	Vilardi Giorgio	30, 668
Scotton Martina Silvia	488, 494	Vilasi Antonio	346, 388
Seminara Barbara	638	Vilé Gianvito	665
Serse Francesco	478	Villano Marianna	156, 291, 337
Sévin Daniel C.	371	Villone Massimiliano Maria	24
Sforza Eleonora	273, 312, 327	Violante Francesco Saverio	650
Shah Nilay	667	Virruso Giovanni	620
Shiea Mohsen	594	Viscusi Gianluca	608
Signorini Virginia	65, 460	Vitiello Giuseppe	264
Simone Elena	160, 373	Volpe Valentina	168
Sirignano Mariano	150, 640	Vueva Yuliya	369
Sironi Selena	91	Wilhelm Manfred	349
Smejkal Petr	22	Wu Kaiqiao	523
Solimene Roberto	211	Yang Ming	519
Spennati Elena	37, 521	Zaffora Andrea	638

Zaio Francesca	571	Zoli Maddalena	569
Zammillo Federica	626, 630	Zomer Simeone	369
Zannin Emanuela	651	Zonfrilli Fabio	24
Zanobetti Francesco	266	Zoppi Giulia	18, 209
Zeppilli Marco	291, 339, 592	Zorin Boris	327
Zheng Lei	571	Zuecco Federico	480
Zimmermann Joscha	213	Zueva Svetlana Borisovna	202
Zinfolino Nunzio	396	Zuliani Anna	306

Exergy Analysis of a green Dimethyl Ether production plant

Marcello De Falco^a, Gianluca Natrella^b, Mauro Capocelli^a

^a *Research Unit "Process Engineering", Faculty of Engineering, University of Rome "Campus Bio-Medico", Via Alvaro del Portillo 21, 00128 Rome, Italy.*

^b *University of Genoa, Via dell'Opera 11 A, 16145 Genoa, Italy.*

Corresponding author: m.defalco@unicampus.it; tel: +39 347 6809041

Abstract

CO₂ capture and utilization (CCU) is a promising approach to reduce GHG emissions. Many technologies in this field are recently attracting attention. However, since CO₂ is a very stable compound, its utilization as a reagent is energetic intensive. As a consequence, it is unclear whether CCU processes allows for a net reduction of environmental impacts from a life cycle perspective and whether these solutions are sustainable. Among the tools to apply for the quantification of the real environmental benefits of CCU technologies, exergy analysis is the most rigorous from a scientific point of view [1].

The exergy of a system is the maximum obtainable work during a process that brings the system into equilibrium with its reference environment through a series of reversible processes in which the system can only interact with such environment [2-4]. In other words, exergy is an "opportunity for doing work" and, in real processes, it is destroyed by entropy generation. Exergy-based analysis is useful to evaluate the thermodynamic inefficiencies of processes, to understand and locate the main consumption of fuels or primary energy, to provide an instrument for comparison among different process configurations and to detect solution to reduce the energy penalties of a process.

In this work, the exergy analysis of a process for the production of Dimethyl Ether (DME) from green hydrogen generated through an electrolysis unit and pure CO₂ captured from a flue gas is performed. The model simulates the behavior of all units composing the plant (electrolyzer, carbon capture section, DME synthesis reactor, purification step), with the scope to quantify the performance indices based on the II Law of Thermodynamics and to identify the entropy generation points. Then, a plant optimization strategy is proposed to maximize the exergy efficiency.

Keywords: Green DME production, Exergy Analysis, Energy Penalties, Exergy Efficiency

- [1] Bejan A, Tsatsaronis G, Moran MJ. Thermal Design and Optimization, John Wiley & Sons; 1996.
- [2] Moran MJ, Shapiro HN, Boettner DD, Bailey M. Fundamentals of engineering thermodynamics. John Wiley & Sons; 2010.
- [3] Kotas TJ. The exergy method of thermal plant analysis. Paragon Publishing; 2012.
- [4] Rocco MV, Colombo E, Sciubba E. Advances in exergy analysis: a novel assessment of the Extended Exergy Accounting method. Applied Energy 113 (2014) 1405–1420.

Supercritical CO₂ assisted process for the production of nano-niosomes

Lucia Baldino* and Ernesto Reverchon

Department of Industrial Engineering, University of Salerno, Via Giovanni Paolo II, 132, 84084, Fisciano (SA), Italy

**Corresponding author E-Mail: lbaldino@unisa.it*

1. Introduction

Niosomes are a kind of drug nanocarrier formed by non-ionic compounds, with a lipophilic tail and a hydrophilic head that tend to self-assemble in aqueous dispersions, producing vesicles [1,2]. They are characterized by a high biocompatibility and good physico-chemical stability at room temperature; moreover, the raw materials for their preparation are cheap and readily available [3]. The traditional techniques proposed for niosomes production, such as thin-film hydration, reverse phase evaporation, emulsion, microfluidization and freeze-drying [2,4] suffer from some limits: i.e., they are batch and time consuming [5,6], use organic solvents [7], and have a reduced control on size and shape of the obtained vesicles [8,9]. Supercritical CO₂ (SC-CO₂) assisted processes have been proposed as a green alternative to produce micro- and nanocapsules [10], liposomes [11] and, in some cases, niosomes [12-14]. The advantages of using a SC-CO₂ assisted process are mainly related to SC-CO₂ gas-like diffusivity and liquid-like density [12-14] that allow to obtain solvent-free nanometric particles, at high drug encapsulation efficiency and in a faster way [11]. Therefore, the aim of this work is the production of nanometric and stable niosomes, using a SC-CO₂ assisted process. Different Span® 80 and Tween® 80 formulations were tested and analyzed by dynamic light scattering and field emission scanning electron microscope, in order to determine the optimal ones to be used for a following loading of active pharmaceutical ingredients.

2. Methods

100 mL of ethanolic solution containing the surfactants (20 mg/mL total surfactant concentration) were prepared by magnetic stirring at 250 rpm, for 1 h and at room temperature. The formulations tested in this work were obtained at a Span® 80 to Tween® 80 weight ratio of: 100/0 (N01), 90/10 (N02), 80/20 (N03) and 70/30 (N04). The hydrophilic to lipophilic balance (HLB) of the surfactants' mixture was 4.30, 5.37, 6.44 and 7.51, respectively.

The apparatus used for niosomes production was a lab-scale high-pressure plant, formed by three feeding lines for the delivery, in the formation vessel, of CO₂, water and the ethanolic solution of surfactants. At the end of the experiment, the system was slowly depressurized and the mixture ethanol+CO₂ was removed using a separator downstream of the formation vessel; whereas the niosomal suspension was collected in a reservoir located at the bottom of this vessel. More details about this high-pressure plant and the experimental procedure are published elsewhere [14].

Niosomes suspension was characterized by dynamic light scattering (DLS, mod. Zetasizer Nano S, Worcestershire, United Kingdom) and field emission scanning electron microscope (FE-SEM, mod. LEO 1525, Carl Zeiss SMT AG, Oberkochen, Germany).

3. Results and discussion

This work is aimed at the identification of an optimal Span® 80 to Tween® 80 ratio for the preparation of niosomal formulations that produce nanometric and stable vesicles. The operative conditions adopted for the SC-CO₂ assisted process were: 100 bar pressure, 40 °C temperature, 7 mL/min water flow rate, 3.5 mL/min ethanolic solution flow rate and 6.5 g/min CO₂ flow rate.

DLS results showed that niosomes mean diameter varied from 120 ± 51 nm for N01 to 215 ± 80 nm for N04, increasing the amount of Tween® 80 from 0 to 30% in the starting ethanolic solution. The different Span® 80 to Tween® 80 ratio determined a variation of HLB parameter from 4.30 to 7.51, and the literature demonstrated that, when HLB value increases, a larger number of hydrophilic groups are present in the

vesicle structure [15] that increases the surface-free energy of the system, producing larger niosomes [16]. In all cases, PDI lower than 0.4 and ζ -potential larger than 20, in modulus, were measured. Figure 1 shows an example of the niosomes morphology observed by FE-SEM: spherical and regular niosomes were produced, with a mean dimension consistent with DLS results.

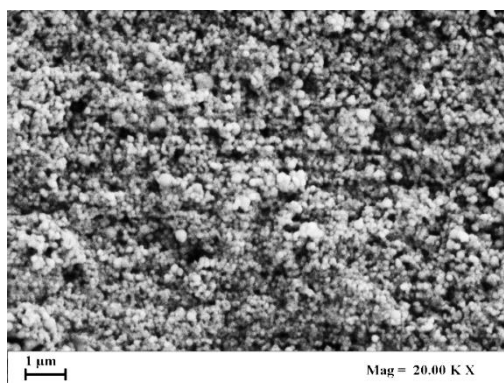


Figure 1. SEM images of N02 niosomes, produced at 100 bar and 40 °C.

N01 to N04 samples were analyzed by DLS after 2 and 4 months storage in Falcon tubes at 4 °C. These samples were stable over time since preserved the mean size: i.e., an increase in size of around 12% was detected only for N01 samples after 4 months from the production; whereas the other samples showed an increase in size lower than 8%, after the same time. This result is a consequence of the ζ -potential values detected up to 4 months from the niosomes production that ranged from a minimum of -37.0 mV for N02 after production to a maximum of -20 mV for N04 after 4 months storage.

4. Conclusions

The systematic study performed in this work on the niosomes mean dimension, morphology and stability over time demonstrated that the optimal formulations for the following encapsulation of active pharmaceutical ingredients were the vesicles prepared at a Span® 80 to Tween® 80 ratio of 90/10. Indeed, they were characterized by a mean diameter lower than 200 nm, spherical morphology and good stability up to 4 months storage.

References

- [1] Y. Kawabata, K. Wada, M. Nakatani, S. Yamada, S. Onoue, *Int. J. Pharm.* 420 (2011) 1-10.
- [2] G. Amoabediny, F. Haghirsadat, S. Naderinezhad, M.N. Helder, E.A. Kharanaghi, J.M. Arough, B. Zandieh-Doulabi, *Int. J. Polym. Mater. Polym. Biomater.* 67 (2018) 383-400.
- [3] A. Verma, A. Tiwari, S. Saraf, P.K. Panda, A. Jain, S.K. Jain, *Expert Opin. Drug Delivery* 18 (2021) 55-71.
- [4] N.B. Mahale, P.D. Thakkar, R.G. Mali, D.R. Walunj, S.R. Chaudhari, *Adv. Colloid Interface Sci.* 183-184 (2012) 46-54.
- [5] P. Shah, B. Goodyear, A. Haq, V. Puri, B. Michniak-Kohn, *Pharmaceutics* 12 (2020) 246-252.
- [6] M.M. El-Mahdy, E.-E.M. Mohamed, M.S. Saddik, M.F. Ali, A.M. El-Sayed, *J. Adv. Biomed. & Pharm. Sci.* 3 (2020) 116-126.
- [7] M. Fidan-Yardimci, S. Akay, F. Sharifi, C. Sevimli-Gur, G. Ongen, O. Yesil-Celiktas, *Food Chem.* 293 (2019) 57-65.
- [8] R. Ghafelehbashi, I. Akbarzadeh, M.T. Yarak, A. Lajevardi, M. Fatemizadeh, L.H. Saremi, *Int. J. Pharm.* 569 (2019) 118580.
- [9] D. Pando, M. Matos, G. Gutiérrez, C. Pazos, *Colloids Surf., B* 128 (2015) 398-404.
- [10] I. Palazzo, E.P. Lamparelli, M.C. Ciardulli, P. Scala, E. Reverchon, N. Forsyth, N. Maffulli, A. Santoro, G. Della Porta, *Int. J. Pharm.* 592 (2021) 120108.
- [11] M.A. Chaves, L. Baldino, S.C. Pinho, E. Reverchon, *J. Taiwan Inst. Chem. Eng.* 132 (2022) 104120.
- [12] A. Manosroi, R. Chutoprapat, M. Abe, J. Manosroi, *Int. J. Pharm.* 352 (2008) 248-255.
- [13] M.E. Wagner, K.A. Spoth, L.F. Kourkoutis, S.S.H. Rizvi, *J. Liposome Res.* 26 (2016) 261-268.
- [14] L. Baldino, E. Reverchon, *J. CO₂ Utiliz.* 52 (2021) 101669.
- [15] P. Bhardwaj, P. Tripathi, R. Gupta, S. Pandey, *J. Drug Delivery Sci. Technol.* 56 (2020) 101581.
- [16] Y. Zhang, Q. Jing, H. Hu, Z. He, T. Wu, T. Guo, N. Feng, *Int. J. Pharm.* 580 (2020) 119183.

Catalytic Assisted Non Thermal Plasma Process for Degradation of Acid Orange 7 Dye in Aqueous Solution

Giuseppina Iervolino*, Vincenzo Vaiano and Vincenzo Palma

Affiliation and address; 2 Affiliation and address

**Corresponding author E-Mail: giervolino@unisa.it*

1. Introduction

Non-thermal plasma is one of the most promising technologies used for the degradation of hazardous pollutants in wastewater. Recent studies evidenced that various operating parameters influence the yield of the Non-Thermal Plasma (NTP)-based processes. In particular, the presence of a catalyst, suitably placed in the NTP reactor, induces a significant increase in process performance with respect to NTP alone. For this purpose, several researchers have studied the ability of NTP coupled to catalysts for the removal of different kind of pollutants in aqueous solution. The most used method to create NTP is gas discharge in which the energy from the electric field is accumulated by the electrons through collision, and only a fraction of the energy will then be transferred to other molecules [1]. In order to induce NTP there are different types of reactors such as corona discharge, dielectric barrier discharge (DBD), plasma jet [25] or gliding arc [17]. Among these reactors, dielectric barrier discharge (DBD) presents, as advantages, a high removal rate for contaminants and a simple functioning, receiving for these reasons, more attention among the water treatment field in recent years [2]. However, some studies showed that sometimes the only use of non-thermal plasma (NTP) generated by the DBD does not guarantee the complete degradation of organic contaminants. Furthermore, without a catalytic material, it may be necessary to adopt operating conditions, requiring the use of very high voltages to induce NTP. For this reason, the synergistic effect of NTP with catalysts is certainly an interesting topic. In this work the aim is the optimization of the performance of the cold plasma technology coupled with a structured catalyst for the discoloration and mineralization of “acid orange 7” (AO7) azo dye.

2. Methods

The structured catalyst consists of Fe₂O₃ immobilized on glass spheres, and it was prepared by the “dip coating” method and characterized by different chemico-physical techniques. The experiments were carried out in a dielectric barrier discharge (DBD) reactor. It is a quartz cylindrical DBD reactor characterized by the presence of two electrodes: an inner electrode (a copper tube) and an outer one (stainless-steel mesh), placed at a specific distance between them. In the present study, the applied voltage between the two electrodes was lower, and it was equal to 12 kV. The aqueous solution to be treated is characterized by a specific initial concentration of AO7 dye (20 mg/L). During the tests the gas and liquid phase were analyzed.

3. Results and discussion

The effect of Fe₂O₃ amount immobilized on glass spheres (in the range 0.13 - 0.37 wt %), in terms of AO7 (20 mg/L) discoloration (a) and mineralization, (b) is shown in Figure 1.

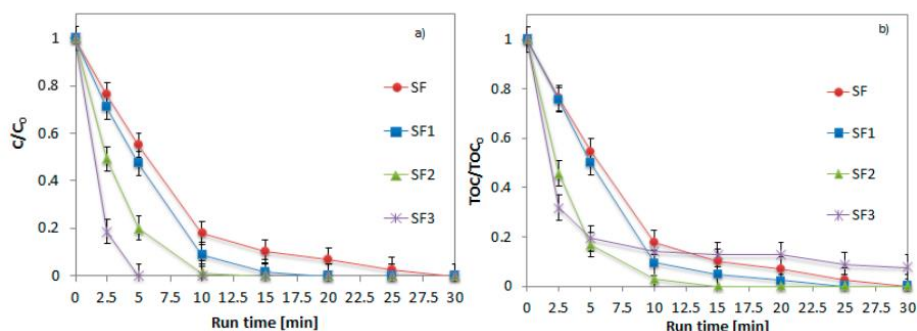


Figure 1. Influence of Fe_2O_3 amount on glass spheres in AO7 cold plasma degradation. Discoloration (a) and mineralization (b) behaviour during the run time. AO7 initial concentration: 20 mg/L. Glass spheres amount: 36 g. Applied voltage: 12 kV. O_2 flow rate: 0.18 NL/min.

During the tests, it was possible to note a progressive decrease of AO7 concentration, obtaining a discoloration equal to 53, 80 and 100% with the SF1, SF2 and SF3 samples (Figure 1a), respectively after only 5 minutes of reaction time; after the same treatment time, the mineralization was equal to 53, 80 and 78% for the identical samples (Figure 1b). This effect is due to the presence of iron oxide (Fe_2O_3) which acts as a photocatalyst, activated by the presence of UV light emitted by the ionized gas.

4. Conclusions

The efficiency of the catalytic assisted cold plasma process, in the removal of AO7 azo dye pollutant in aqueous solution, was demonstrated. Furthermore, through the dip coating method, it is possible to immobilize Fe_2O_3 on the glass spheres surface and use it as catalyst in the NTP process. The catalytic packed material (named SF2) improved the performance of the DBD reactor, reducing the time required for discoloration and mineralization. In particular, in presence of this catalyst, it was possible to observe a simultaneous discoloration and mineralization behaviour, confirming the absence of reaction by-products.

References

The reference format is provided below [1 – 3]. [Times New Roman 10].

- [1] Fridman, A. Plasma Chemistry; Cambridge University Press: Cambridge, UK, 2008
- [2] Chen, J.; Du, Y.; Shen, Z.; Lu, S.; Su, K.; Yuan, S.; Hu, Z.; Zhang, A.; Feng, J. Non-thermal plasma and $BiPO_4$ induced degradation of aqueous crystal violet. *Sep. Purif. Technol.* 2017, 179, 135–144

Rational scale-up in multiphase APIs syntheses

Filippo Nanto^{1*}, Dario Ciato², Paolo Canu¹

1 University of Padua, Department of Industrial Engineering, Via Marzolo 9, Padua, 35131, Italy;

2 Lundbeck Pharmaceuticals Italy, Quarta Strada 2, Padua, Italy.

**Corresponding author E-Mail: filippo.nanto@phd.unipd.it*

1. Introduction

In the pharmaceutical industry batch processes prevail, often involving the presence of solid phases, making the rate of mass transport and the multiphase flow controlling features, affecting their efficiency [2]. Solids can be found as catalysts, reagents, or products, where they could undergo dissolution, precipitation, and crystallization. Moreover, processes are brought to the industrial scale replicating conditions demonstrated at the laboratory scale, without rational scale-up and optimization [3]. The application of common procedures to manufacture large-scale batches may also overlook the impact of physical steps, such as the dissolution time of key reagents [4]. Quantitative tracking of composition in batch experiments (or industrial runs) is also routinely carried out by HPLC, measuring the product quality based on relative quantities, with methods such as the Liquid Chromatography Area Percentage (LCAP) [5,6]. This approach is convenient and swift when evaluating the product fraction, which often needs to be in a defined ratio, but it does not give an indication on the absolute quantity of single species, revealing the impact of mass-transfer limited processes, that selectively add and remove species from the liquid phase usually sampled. This work investigates the impact of LCAP in underestimating the interaction of reaction kinetics and dissolution rate of the key reactant, in representative synthetic step of a proprietary API.

2. Methods

The reaction has been investigated at 2 different scales (500 mL, 170 L, lab and pilot, respectively), batchwise. The synthetic cascade starts from an intermediate (M6), which undergoes two hydrogenation steps in methanol/acetic acid, supported by a Pd/C solid catalyst. Two different groups, say A and B, are reduced, leading to two competitive paths, where the reduction of A before B is alternative to the opposite sequence. One reduction step leads to isomers, so the final product is always a mixture of two stereoisomers, called R and S, in a fixed ratio of α . This hydrogenation is carried out at a pressure of 9 bar, where hydrogen is fed semi-batchwise, by sparger placed at the bottom, to keep the pressure constant. The quantification of species inside the liquid phase was carried out through HPLC analysis, using either LCAP or calibration lines, for absolute quantities estimation.

3. Results and discussion

Reagent M6 is charged inside the reactors, at the beginning of the process, as a solid powder. From the state of the art, developed inside the industrial facility, a complete dissolution of M6 in the solvent mixture was reported. During the first experiment in the pilot plant a LCAP method was adopted, to follow the species concentration over time. The profile for M6 showed an unusual plateau after 20 minutes, reported in Figure 1a. Instead, by analyzing the absolute quantities (calibration lines) for M6, the concentration in the liquid phase shows an increase during the first 50 minutes, suggesting that a dissolution process was affecting the kinetics of M6 consumption, being on a comparable characteristic time. This finding is in contrast with the established company knowledge of the process. In addition to delaying the conversion, a lower availability of M6 in the liquid phase may affect the selectivity, preferentially supporting one of the 2 reaction paths. The evidence of

dissolution, a physical process, affecting the overall process rate must be properly investigated in scaling-up, where fluid dynamics (thus reactor and impeller geometry) will become the key controlling factor.

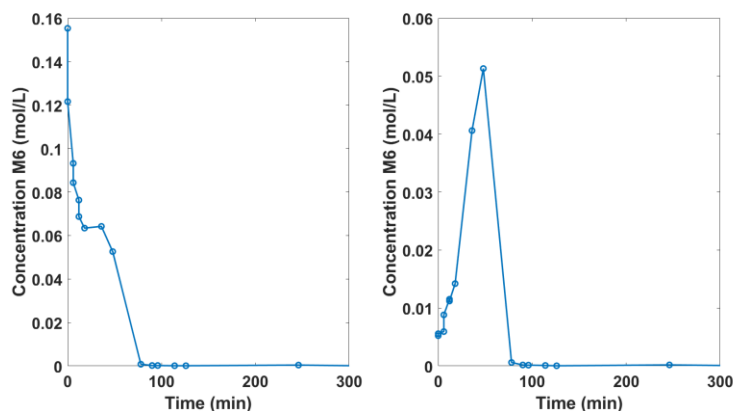


Figure 1. left, Concentration of M6 over time with LCAP method. Right, Concentration of over time M6 via HPLC absolute area

The finding calls for an investigation of the kinetics of dissolution. It was investigated at a laboratory scale, maintaining geometrical similarity and reactor operation as close as possible to the pilot. The M6 dissolution kinetics was measured and correlated with the Noyes-Whitney eq., estimating K_{LA} at a defined temperature, as shown in Figure 2. Combination of the dissolution rate with reaction kinetics allows to identify a quantitative kinetic model that more appropriately describe the chemistry of the synthesis, as shown in Figure 3.

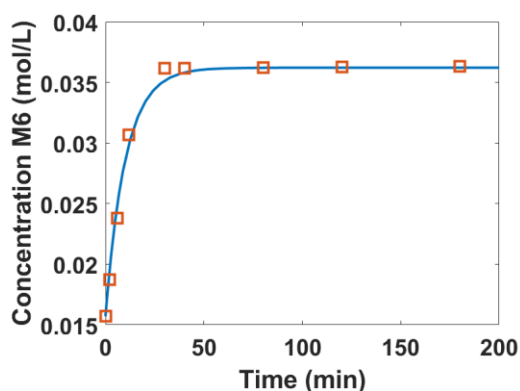


Figure 2. M6 dissolution profile at laboratory scale

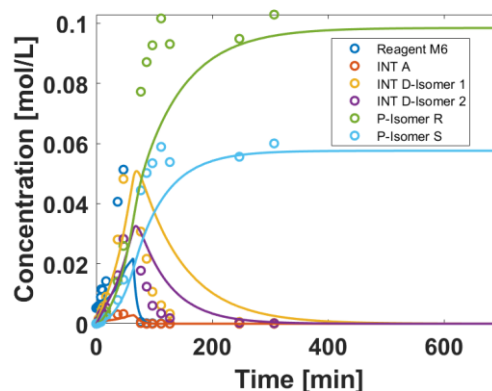


Figure 3. Process data fitted by new kinetic model

4. Conclusions

Established practices in pharmaceutical industry, such as LCAP method, can lead to underestimate the impact of physical processes, perhaps controlling the batch time significantly. Here the overlook of a critical dissolution step was spotted. Physical processes of heat and mass transfer are the key factors in scaling-up/down multiphase syntheses, and to properly identify the actual chemical kinetics.

References

- [1] R.A Sheldon, (2007) Green Chemistry, 9 (12), 1273-1283
- [2] C.L. Burcham, A.J. Florence, M.D. Annu. Rev. Chem. Biomol. Eng., 9 (2018), 253-281
- [3] K. Pandey et al., International Journal of Current Research and Review, 12 (2020), 188-192
- [4] V. Koganti, et al., AAPS PharmSciTech, (2010), 1541-1548, 11(4)
- [5] N.S. Marzifarani et al., Organic Process Research and Development, (2021), in Press
- [6] C. Bottecchia et al., Organic Process Research and Development, (2021), in Press

Reaping Chemical Engineering heritage by leveraging green solvents: opportunities and issues

Vittoria Sapone¹, Alessio Mazzelli², Marco Valentini¹, Agnese Cicci², Marco Bravi^{1*}

1 Dip. Ingegneria Chimica Materiali Ambiente, Sapienza Università di Roma, via Eudossiana, 18, 00184 Roma;

2 NextChem Spa, Via Di Vannina, 88, 00156, Roma, Italy

**Corresponding author E-Mail: marco.bravi@uniroma1.it*

1. Introduction

Renewably using biomasses in place of depleting fossil resources is seen as one major means for providing long-term viability to our civilization. However, the ubiquitous presence of oil refining products on today's market can be replicated by bio refined products only if biorefining technology achieves a degree of flexibility and optimisation resembling that attained by oil refining technology at a fraction of its current cost.

Learning the lesson from oil refining history begins with identifying a single (and ideally “universal”) unit operation, which should be flexible enough to be up to the hard challenge of addressing the fractionation of a diverse pool of biomass types, by providing an efficient separation of components with quite different physical characteristics [1]. Inasmuch as the diversity and complexity of biomasses is much higher than the diversity among crude oils, biomasses are solids, so the question arises as to whether, and in which way, extraction mediated by a solvent can be carried out to serve as a significant analogue of distillation in the “biomass age”.

As a route toward such an ambitious objective, the adopted unit operations might deploy reusable concepts and “pluggable” operating conditions and materials acting as solvents or modifiers thereof.

From a commercial point of view, compounds, or fractions, which can be obtained from biomasses (higher plants, macroalgae and microalgae) may have multiple markets which may require different specifications, impose different regulations, and consequently attach a different value to the very same semi-finished product. Hence, a process should aim at “market-neutrality” to avoid putting restrictions on the market placement of a product due to regulatory issues. In this scenario, beside the not yet solved issue of the primary biomass production costs, the evaluation and optimization of the biorefining costs is just as important and the level of optimization in this area is nothing but primitive.

The present article discusses two possible approaches to bio-refining whole biomass of the *Chlorella vulgaris* microalga, with different aims and readiness to market: obtaining raw primary fractions by a novel use of the so-called “switchable solvents” and fractionating tryglycerides and individual carotenoids by staged supercritical CO₂ (sCO₂)-assisted extraction.

2. Approaches and methods

2.1 Circular Extraction by using Switchable Solvents

One step in learning the lesson of oil refining may be taken by recalling analogies among unit operations from classical undergraduate unit operations courses in distillation, separation requires heat (the cost item), and is brought about by virtue of relative volatility (the driving force), under physical (diffusional) hindrances.

In solvent-mediated extraction separation requires a suitable solvent (the cost item) and is brought about by virtue of solubility in that solvent (the driving force), under physical (entanglement) and chemical bonding hindrances. Along oil refineries history, optimising distillation has implied optimising heat integration, in

turn obtained by reusing the “same heat” at “different temperature levels” by designing the whole required heat exchange network by using the thermal pinch technology. The question arises, hence, as to whether useful hints toward optimised biomass fractionation can be found by taking the analogy route and looking for “reusable solvents” across “different solubility features” (i.e., solvents that may be modified, and thus be adapted) for very different tasks in the extraction process.

Switchable hydrophilicity solvents have only been used in their hydrophobic form to extract hydrophobic solutes. However, the treated biomass might also contain hydrophilic solutes, as well as debris that might not be soluble in either hydrophobic or hydrophilic solvents; hydrophilic solutes may be expected to be easily removed by treating with a hydrophilic solvent the residue which remained after the extraction with the hydrophobic solvent. It should be noted that, after completing the hydrophilicity switch, the formerly hydrophobic switchable hydrophilicity solvent has the very needed hydrophilicity character. The hydrophilic form of the SHS, obtained after switching, may thus be suitable for extraction of hydrophilic material from the raw biomass or separation of the hydrophilic material from the solid residue, obtained after that biomass has undergone an extraction by the SHS in hydrophobic form. By noting that both hydrophilicity states of the original switchable solvent can be used in two specific and complementary extraction tasks, it can be concluded that the biomass extraction can begin with either the hydrophobic or the hydrophilic form of the solvent and may continue with the other form and can be started from either form of the solvent itself. This dual use of SHSs, denoted as “Circular Extraction”, has been touted to increase the utility of the extraction process and of the solvent itself because of the second (complementary) biomass extraction task, and to be potentially conducive to a reduction of the environmental impacts associated with the solvent because these latter are now amortized over two extractions per cycle [2].

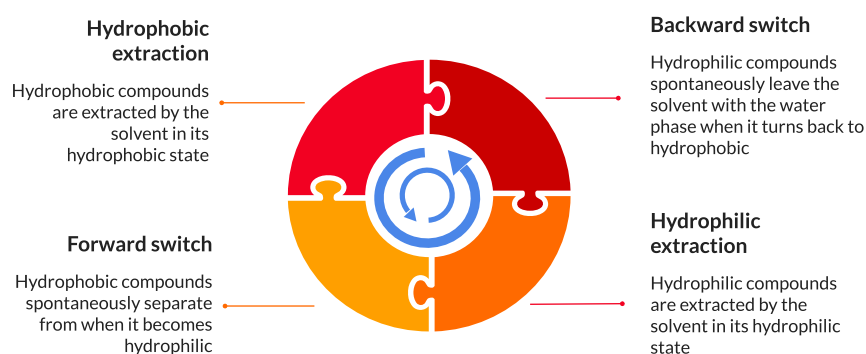


Figure 1. Sequential two-stage extraction by switchable solvents in Circular Extraction, in counterclockwise (“forward”) or counterclockwise (“backward”) arrangement..

Some chemicals exhibiting switchable behaviour provide a specific additional performance as a cell-breaking means or tolerate the presence of water in the biomass thus bringing a substantial process simplification and energy requirement. Here, we will demonstrate the bio-fractionating approach by dimethylcyclohexylamine (DMCHA), which can be switched by using CO₂ and a Natural Eutectic System (NaDES) based on the mixture of food-grade caprylic and lauric acid, which can be switched by a very low toxicity amine (Jeffamine) [3]. The microalgal biomass, produced in house by autotrophic growth in pure culture, was processed in the wet state in an orbitally agitated flask. Extraction rates were calculated: for lipids, by weighing the recovered material; for carbohydrates and proteins, by assaying the undissolved residue by the appropriate test (Lowry and Dubois).

2.2 Staged s CO₂-assisted extraction and fractionation

The extraction and fractionation of *C. vulgaris* to obtain high value-added components, including carotenoids and Omega-3, by employing sCO₂ and, when necessary, ethanol as co-solvent, was carried out as a two-stage process. During the first stage, triglycerides are extracted but carotenoids remain in the matrix and are removed in a second extraction phase. The operation was evaluated by an overall model implemented as a combination of two different sub models: a model describing the extraction of triglycerides, and a model for describing the extraction of carotenoids. Both models were adopted from the open literature. The extraction

of triglycerides was modelled according to Sovova [4][5] “Broken and the Intact Cell” model” by assuming an appropriate size of dried microalga beads. Equations (1) and (2) relevant to the “fast” and “slow” period, respectively, make up the extraction model:

while external mass transfer resistance, θ_f , was expressed as the ratio to the residence time t_r , of the fluid phase mass transfer characteristic time, t_f . This latter was estimated by calculating the Sherwood number of the microalgal beads and the diffusivity of lipids as described in detail in [6]. The carotenoids extraction process using sCO₂ and ethanol as a co-solvent was calculated by the Reverchon [7] kinetic model. In lack of a full set of experimental data that could allow adopting motivation either model structure (Sovová or Reverchon) for both molecule classes, the detailed motivation for using two separate models is discussed [6]. The characteristics of the microalgal biomass during the second extraction phase were assumed to be equal to those of unextracted biomass. The diffusivity of carotenoids in the microalgal matrix was assumed after Macías-Sánchez [8] who determined it in *Nannochloropsis gaditana* cells. The co-solvent-to-solvent ratio employed for the modelling was adopted after a literature survey and fixed to 5% w/w.

CO₂ density was calculated by the Huang equation [9], compounds solubility by the Chrastil model [10], whose thermodynamic parameters were estimated by a group contribution method. sCO₂ viscosity was estimated as done by Heidaryan [11] while the diffusivity of each component in the solvent was calculated as done by He [12].

The simulation of the entire process was carried out employing the Aspen Plus software (V10, AspenTech). The daily biomass feed was set to 360 kg. The optimal operating conditions were optimised by MATLAB, to estimate the saturation times and the equipment volume. The extraction process was carried out in batch. Therefore, as the spreadsheet software can only be employed for continuous processes, the simulation was integrated with the system analysis carried out by using MATLAB. An optimization of the operating conditions for each microalgal component was carried out, by using the previously described models and by assuming that carbohydrates are in starchy form and that proteins share the composition of the most represented aminoacid of the microalga, i.e. leucin. The design of the equipment was carried out according to classical engineering criteria, calculated residence times were confirmed by qualified industry professionals and the cost of equipment with the volumes processed was provided by vendors. When the amount of extract and the density of the currents were known, the sizing of vessels was done. Regarding the CAPEX, each equipment was designed according to manuals [13]. The compressors and pumps power and their minimum energy consumption was calculated by Aspen Plus. The use of Aspen plus software for energy and sCO₂ consumed allowed the calculation of OPEX.

3. Results and discussion

3.1 Biofractionation of *C. vulgaris* by Circular Extraction use of switchable solvents

Extraction results (Figure 2) showed that lipids extraction was nearly quantitative and confined to the hydrophobic phase, while the extraction of both proteins and carbohydrates occurs partly in the hydrophobic phase and partly in the hydrophilic phase, arguably according to the affinity with the solvent. For proteins, DMCHA still had some edge over NaDES-based extraction, while the reverse is true for carbohydrates. Carbohydrates are extracted for the most part during the hydrophobic stage, while the reverse is true for proteins. In “Backward mode”, observed yield is similar, but protein extraction was essentially carried out during the hydrophilic stage for the NaDES-based extraction, while with DMCHA some additional gain was observed also during the hydrophobic stage. Carbohydrates extraction, however, received a significant boost during the hydrophobic stage, and this was observed with both solvents.

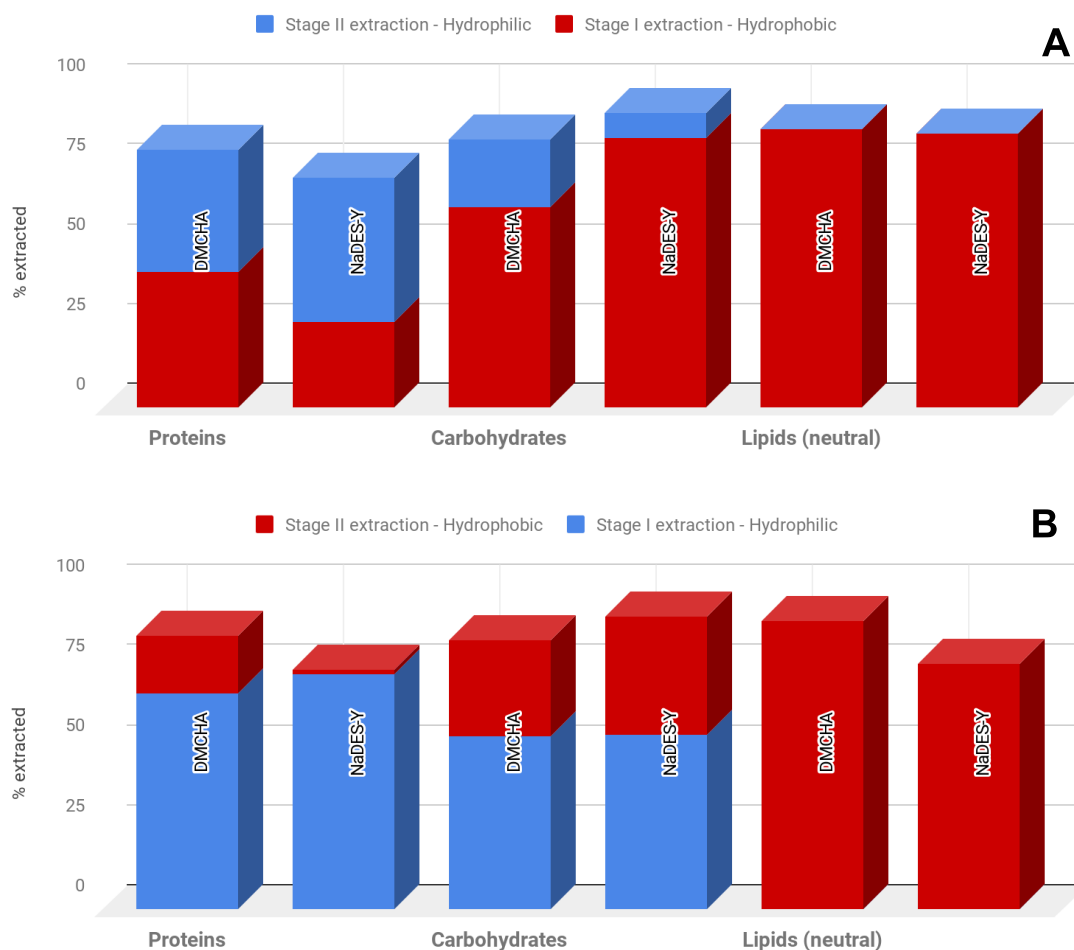


Figure 2. Results of *C. vulgaris* biofractionation into primary fractions by Circular Extraction use of switchable solvents with "forward" (subfigure A) and "backward" (s. B) ordering of extractions

3.2 Biofractionation of *C. vulgaris* into triglycerides and carotenoids by sCO₂

Given the different grounds and level of development of this application, the relevant part of results deals with the time-averaged results that are obtained in optimised conditions. These latter were found at 50 °C, 200 bar, and 5 kg/kg solvent to solid ratio for both extraction phases, thus allowing a total of 3 full biomass extractions per day. By recovering the extract from the two extraction phases in different vessels, the overall daily yield of the first phase is 38.3% of the feed, while that of the second is 2.3%. No carbohydrates or proteins were anticipated in the extracts. During the depressurization phase, the solvent contained in the extractor is not recovered; therefore, a daily CO₂ make up of 485 kg for all the extractions was calculated. A loss of ethanol with the extracts was also quantified. A process scheme was designed (Figure 3) and, by using the approximate costing procedure described previously, a Total Treatment Cost of the microalgal feed of 44 Euro/kg was anticipated, that lies within the range of values for pigment production from 12.50 D/kg to 107.95 D/kg cited by Slegers et al. (2020). In addition, the present work satisfies the conditions required by Slegers et al. [14] to develop a profitable microalgae production chain because there are technological innovations enabling cost reductions, especially in micro-algae production and is present a developing multiproduct biorefinery concepts aimed at valorizing the full biomass through the cascading principle deriving a range of new specialty products with applications in food, aquaculture and non-food.

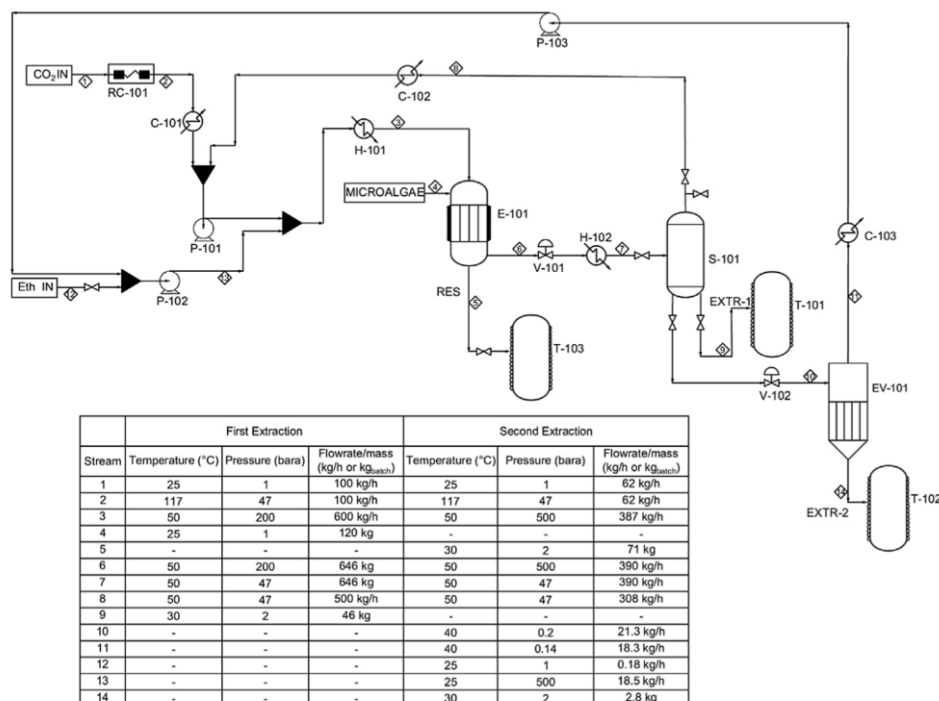


Figure 3. Process scheme for the batch biorefining of *C. vulgaris* to triglycerides and carotenoids by sCO₂.

4. Conclusions

Biorefining is a key “macro” operation of the biomass age and a fundamental one to obtain the full biologic and economic value of the processed biomasses. This article has shown that existing industry-standard bio-safe processes such as sCO₂-assisted extraction can provide an array of high value lipidic compounds. However, carbohydrates and proteins are left in the residue, and should be therefore extracted from the biomass residue by further, cascaded processes. Furthermore, sCO₂ turnover is highly energy intensive even more than most classical evaporative processes. Doing without phase change can prospectively save energy and keep the product safe and can be done in a neat way by using switchable solvents in a Circular Extraction approach, enabling one-pot processing, in some cases also dispensing biomass drying and fragilization needs with. However, a lot of work needs to be done from the thermodynamic, kinetic, and process development point of view to make bare “maximum yields” into reliable process development at the expected TRLs for industrial application.

References

- [1] González-Delgado, A.D. and Kafarov, V., 2012. Microalgae based biorefinery: evaluation of several routes for joint production of biodiesel, chlorophylls, phycobiliproteins, crude oil and reducing sugars. *Chem Eng Trans*, 29(1), pp.607-612.
- [2] C Ricci, A., Sed, G., Jessop, P. G., Bravi, M. (2018). Circular extraction: an innovative use of switchable solvents for the biomass biorefinery. *Green Chemistry*, 20(17), 3908-3911.
- [3] Sed, G., Ricci, A., Jessop, P. G., Bravi, M. (2018). A novel switchable-hydrophilicity, natural deep eutectic solvent (NaDES)-based system for bio-safe biorefinery. *RSC Advances*, 8(65), 37092-37097.
- [4] H. Sovová, Mathematical model for supercritical fluid extraction of natural products and extraction curve evaluation, *J. Supercrit. Fluids*. 33 (2005) 35–52. <https://doi.org/10.1016/j.supflu.2004.03.005>.

- [5] H. Sovová, Modeling the supercritical fluid extraction of essential oils from plant materials, *J. Chromatogr. A.* 1250 (2012) 27–33. <https://doi.org/10.1016/j.chroma.2012.05.014>
- [6] Mazzelli, A., Valentini, M., Ciccì, A., Iaquaniello, G., Bravi, M. (2022). Industrial bio-fractionation process of microalgae valuable products using supercritical CO₂. A techno-economical evaluation. *Chemical Engineering Research and Design*, 178, 50-60.
- [7] E. Reverchon, G. Donsi, L.S. Osseo, Modeling of Supercritical Fluid Extraction from Herbaceous Matrices, *Ind. Eng. Chem. Res.* 32 (1993) 2721–2726. <https://doi.org/https://doi.org/10.1021/ie00023a039>.
- [8] M.D. Macías-Sánchez, C.M. Serrano, M.R. Rodríguez, E. Martínez de la Ossa, Kinetics of the supercritical fluid extraction of carotenoids from microalgae with CO₂ and ethanol as cosolvent, *Chem. Eng. J.* 150 (2009) 104–113. <https://doi.org/10.1016/j.cej.2008.12.006>.
- [9] Huang, Z., Shi, X.-H., Jiang, W.-J., 2012. Theoretical models for supercritical fluid extraction. *J. Chromatogr. A* 1250, 2–26, <http://dx.doi.org/10.1016/j.chroma.2012.04.032>.
- [10] J. Chrastil, Solubility of Solids and Liquids in Supercritical Fluids, *J. Phys. Chem.* 86 (1982) 3016– 3021. <https://doi.org/https://doi.org/10.1021/j100212a041>.
- [11] E. Heidaryan, T. Hatami, M. Rahimi, J. Moghadasi, Viscosity of pure carbon dioxide at supercritical region: Measurement and correlation approach, *J. Supercrit. Fluids.* 56 (2011) 144– 151. <https://doi.org/10.1016/j.supflu.2010.12.006>.
- [12] C.-H. He, Prediction of Binary Diffusion Coefficients of Solutes in Supercritical Solvents, *AIChE J.* 43 (1997) 2944–2947. <https://doi.org/https://doi.org/10.1002/aic.690431107>.
- [13] R. Peters, M., Timmerhaus, K., West, *Plant Design and Economics for Chemical Engineers*, McGraw-Hill Education., 2002.
- [14] P.M. Slegers, G. Olivieri, E. Breitmayer, L. Sijtsma, M.H.M. Eppink, R.H. Wijffels, J.H. Reith, Design of Value Chains for Microalgal Biorefinery at Industrial Scale : Process Integration and Techno-Economic Analysis, 8 (2020) 1–17. <https://doi.org/10.3389/fbioe.2020.550758>.

Liquid Pyrolysis of Mixed Plastic Waste for the Co-production of Lubricants and Hydrogen: the Plasbreaker™ Process

Francesco Negri^{1,2}, Francesco Gallo³, Flavio Manenti^{1,2*}

1 Politecnico di Milano, Dipartimento di Chimica, Materiali ed Ingegneria Chimica “Giulio Natta”, Piazza Leonardo da Vinci 32, 20133 Milano, Italy;

2 Consorzio Interuniversitario Nazionale per la Scienza e Tecnologia dei Materiali, Via Giusti 9, 50121 Firenze, Italy;

3 Itelyum Regeneration SpA, Via Tavernelle 19, 26854 Pieve Fissiraga (LO), Italy;

**Corresponding author E-Mail: flavio.manenti@polimi.it*

1. Introduction

Plastic waste has become a major environmental issue in recent times. Thermo-mechanical recycling processes are suitable for less than a third of the total plastic waste production, and they work properly only with rather chemically homogeneous plastic waste, which is only a fraction of the total [1]. Mixed plastic waste is generally treated with environmentally impacting processes such as incineration and landfill disposal, which may generate harmful compounds such as pollutants, greenhouse gases, and microplastics [2-3]. The Plasbreaker™ is a possible solution for this problem: this process treats mixed plastic waste (according to COREPLA mass composition: PE 50%, PP 25%, PS 15%, PET 7%, PVC 3%) through a mild liquid pyrolysis process to turn them into high-performance lubricants while using a small amount of energy. The light ends of the process are then reformed and converted into blue hydrogen, leading to a significant reduction of the CO₂ emissions thanks to a final Carbon Capture, Utilization, and Storage (CCUS) step.

2. Methods

The Plasbreaker™ process was modeled in the commercial simulation software Aspen HYSYS® V11. A Process Flow Diagram of the process is reported in Figure 1. The scheme refers to the revamping of an existing refinery treating exhaust lubricant oils (Itelyum Regeneration). In the first section of the process a plastic waste stream of 15 kt/y is melted through oil-heated twin-screw extruders, exiting at 250°C and 5 bar. Two alternating production lines are present, so that continuous operations are guaranteed even during ordinary maintenance. An auxiliary line for treating vulcanized rubber is also present, where the sulfur is removed through a H₂-fed reactor. The molten plastic is fed to a buffer where off-gas is disengaged, and the liquid is sent to the de-halogenation section. Here, a 15.1 kt/y stream of non-regenerable mineral waste oil is co-fed with molten plastic to an oil-heated mixer working at 300-350°C. The mixture is de-halogenated, generating HCl that is sent to a packed washing column using a NaOH solution, leading to a removal efficiency higher than 99.9%. The de-halogenated liquid mixture enters the Plasbreaker furnace, which heats the mixture at 350-550°C for several minutes, leading to the depolymerization of the plastic feedstock. The waste oil acts as a heat carrier, facilitating the heat transfer in the mixture and enhancing the conversion of the plastic. The effluent from the tubular reactor is then separated in a full-reflux distillation column working at 350°C, 50 torr at the bottom and 50°C, 10 torr at the top. The heavy fraction exiting from the bottom of the column is recirculated to the de-halogenation mixer, while the main product is withdrawn from the bottom-half of the column. The light ends are removed from the top of the column and then pre-reformed at 500°C to transform them into methane, which is then converted into syngas in a steam reforming unit that produces an effluent at 850°C, 24 bar. The syngas is then cooled to 350°C and it is sent to a WGS reactor to generate hydrogen from CO. The WGS effluent is processed in a PSA unit, producing 99.999% pure hydrogen with an 86% recovery [4]. The PSA tail gas is sent to a thermo-oxidizer to generate high-pressure steam, which is used in the previous reforming section as well as a heating utility in the plant. The flue gas from this unit are treated in a DEA-based chemical washing step with CO₂ removal efficiency higher than 70%. The majority of the pure CO₂ captured by the amine loop is compressed and stored as product, while another fraction is sent to an AG2S unit [5] where it produces syngas by reacting both with O₂ produced from a renewable-based water electrolyzer and H₂S

produced in the refinery and in the rubber de-vulcanization step. After the reaction, the gas is sweetened before entering the PSA unit.

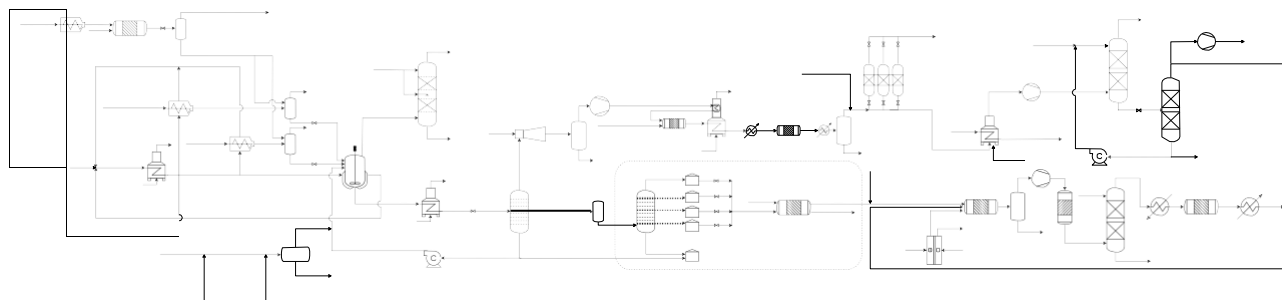


Figure 1. Process Flow Diagram of the Plasbreaker™ Process.

3. Results and discussion

The Plasbreaker™ process produces 22.5 kt/y of base oil for lubricants and 1.1 kt/y of blue hydrogen starting from 15 kt/y of mixed plastic waste and/or vulcanized rubber and 15.1 kt/y of non-regenerable mineral waste oil and/or oil from emulsions, reaching an overall product yield approaching 80%. Moreover, it has many environmental benefits compared with other processes: it produces no solid waste and it shows CO₂ emissions lower than 65%, 61%, and 57% compared with incineration, gasification, and pyrolysis, respectively [6].

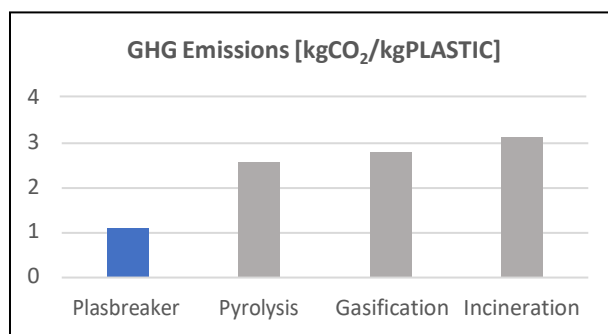


Figure 2. Comparison of CO₂ emissions between the Plasbreaker™ and other waste disposal processes.

4. Conclusions

The Plasbreaker™ process offers a feasible, low-impact solution for the conversion of plastic waste into high-value chemicals such as lubricant bases and blue hydrogen. Thanks to the low energy requirements, the presence of a DEA-based CCUS section and an AG2S unit, together with the lubricants production which act as carbon sink, the process minimizes the environmental impact, showing lower CO₂ emissions compared with other thermal treatments. A first industrial plant is at the EPC phase at the Itelyum Regeneration plant in Lodi.

References

- [1] W. d'Ambrières, Plastics recycling worldwide: current overview and desirable changes, [Http://Journals.Openedition.Org/Factsreports](http://Journals.Openedition.Org/Factsreports). (2019) 12–21.
- [2] L.M.S. Pandey, S.K. Shukla, An insight into waste management in Australia with a focus on landfill technology and liner leak detection, *Journal of Cleaner Production*. 225 (2019) 1147–1154. <https://doi.org/10.1016/J.JCLEPRO.2019.03.320>.
- [3] R. Verma, K.S. Vinoda, M. Papireddy, A.N.S. Gowda, Toxic Pollutants from Plastic Waste- A Review, *Procedia Environmental Sciences*. 35 (2016) 701–708. <https://doi.org/10.1016/J.PROENV.2016.07.069>.
- [4] S. Sircar, W.C. Kratz, Simultaneous Production of Hydrogen and Carbon Dioxide from Steam Reformer Off-Gas by Pressure Swing Adsorption, *Sep. Sci. Technol.* (1988). <https://doi.org/10.1080/01496398808058461>.
- [5] A. Bassani, C. Pirola, E. Maggio, A. Pettinau, C. Frau, G. Bozzano, S. Pierucci, E. Ranzi, F. Manenti, Acid Gas to Syngas (AG2STM) technology applied to solid fuel gasification: Cutting H₂S and CO₂ emissions by improving syngas production, *Appl. Energy*. 184 (2016) 1284–1291. <https://doi.org/10.1016/j.apenergy.2016.06.040>.
- [6] C. Mølgaard, Environmental impacts by disposal of plastic from municipal solid waste. *Resources, Conservation and Recycling*, 15 (1995) 51–63. [https://doi.org/10.1016/0921-3449\(95\)00013-9](https://doi.org/10.1016/0921-3449(95)00013-9).

Sustainable hydrogen production from corn stover hydrothermal liquefaction aqueous phase

Giuseppe Pipitone^{1*}, Giulia Zoppi¹, Samir Bensaid¹, Raffaele Pirone¹

1 Department of Applied Science and Technology, Politecnico di Torino, Corso Duca degli Abruzzi 24, 10129, Turin, Italy

**Corresponding author E-Mail: giuseppe.pipitone@polito.it*

1. Introduction

The hydrothermal liquefaction (HTL) has the aim of producing liquid biofuels starting from wet biomass [1]. In this scenario, the aqueous phase by-product stream (HTL-AP) needs a suitable treatment/valorization, because it can dissolve up to half of the carbon initially present in the feedstock, depending on the reaction conditions [2]. Therefore, its exploitation is a critical achievement for the commercial implementation of this process. Herein, we investigated the aqueous phase reforming as a possible strategy to reach this goal.

Aqueous phase reforming (APR) has been proposed in the pioneering work of Dumesic's research group for the production of H₂ from biomass-derived compounds under milder reaction conditions (220-270 °C, 30-60 bar) compared to conventional fossil-based steam reforming [3]. Most of the research focused on single-compound solutions, which were fundamental for the sake of comprehension of the catalyst structure-activity relationship and the influence of operating conditions. However, there is a lack of information on the catalytic behaviour when multi-components solutions are evaluated. As a matter of fact, the real streams present in industrially relevant environments are constituted by multiple species, belonging to several different classes of compounds (carboxylic acids, alcohols, hydroxyacids, ketones, aromatics, amides, etc.) [4]. In this work, APR was studied to exploit this strategic by-product and obtain a hydrogen-rich gas phase, which can be further used for the hydrotreatment (i.e., deoxygenation) of the biocrude. The corn stover HTL-AP was considered as model feedstock, due to the abundance of this lignocellulosic residue. Glycolic, acetic and propionic acid as individual acids and in combination were tested over different catalysts (5% Pt/C, 5% Pt/ γ -Al₂O₃ and 5% Pd/C) to investigate to which extent the presence of one molecule affected the reactivity of the other one. Furthermore, the kinetic of glycolic acid was evaluated on 5% Pt/C.

2. Methods

The APR reactions were performed in a 300 mL 4560 series mini benchtop reactor (Parr). In a typical reaction, 75 mL of solution and 0.15 g of catalyst (commercial, powder form) were used, with the desired concentration of glycolic, acetic or lactic acid. Once fastened, the reactor was purged with nitrogen to remove atmospheric oxygen, finally pressurized at 0.3 MPa with N₂, and heated up to the desired temperature (250-270 °C). At the end of the reaction, the reactor was cooled down, the gas phase collected in a syringe and analysed by μ GC, while the liquid phase was filtered to separate the catalyst and then analysed through HPLC.

3. Results and discussion

Firstly, the absence of external and internal mass transfer limitations was verified. Figure 1-left shows the results of the system constituted by acetic and glycolic acid with Pt/C catalyst. If acetic acid was the only compound in the solution (PtC-G0A1), its conversion was 23.7%. Adding glycolic acid in a 1:4 glycolic/acetic ratio (PtC-G0.25A1) dramatically reduced its conversion up to 2.4%. This outcome is significant of the strong adsorption of glycolic acid on the active metal compared to acetic acid. When glycolic-acetic acid ratio gradually increased up to 1:1 (PtC-G1A1), the final conversion of acetic was -8.1%. It means that eventually its concentration increased: this was attributed to the side reactions involving glycolic acid, which can be hydrogenated to acetic acid by removing its hydroxyl group. Being the evaluation of the actual conversion complicated by this side-reaction, an alternative approach can be followed by considering the methane production. In fact, it is scarcely produced by glycolic acid, while it is the main product (together with carbon dioxide) for acetic acid. Figure 1-left demonstrates that a slight production of methane was obtained also in the PtC-G1A1 test, but globally this conversion was wrapped by the higher production. A similar trend was reported also for Pt/Al₂O₃ and Pd/Al₂O₃ (data not shown). In particular, the Pd-based catalyst, due to the lower

activity, reported both a negligible acetic acid activation and formation, reaching higher hydrogen selectivity. The strong adsorption of glycolic acid was confirmed by the kinetic study, which highlighted the apparent zero-order reaction for this compound.

A similar approach was used for the acetic/propionic solution, and the results are displayed in Figure 1-right. Acetic acid conversion gradually decreased while propionic concentration increased in the feed; Despite this trend, the conversion was significantly higher than in the former binary solution. Since acetic acid was not significantly produced from propionic acid, the reported conversion may be considered as the real one, without considering the methane production. The study of these two binary mixtures allowed to derive a ranking in the adsorption of small biomass-derived oxygenates on platinum, being glycolic > propionic > acetic acid. The stronger adsorption of glycolic acid may be attributed to the presence of both a carboxylic and hydroxyl group, which favored the anchoring of the molecule on the platinum site. Further studies on this subject, in particular with the help of techniques such as density functional theory, could help to shed light on the adsorption path, and provide hints on the rational design of more effective heterogeneous catalysts.

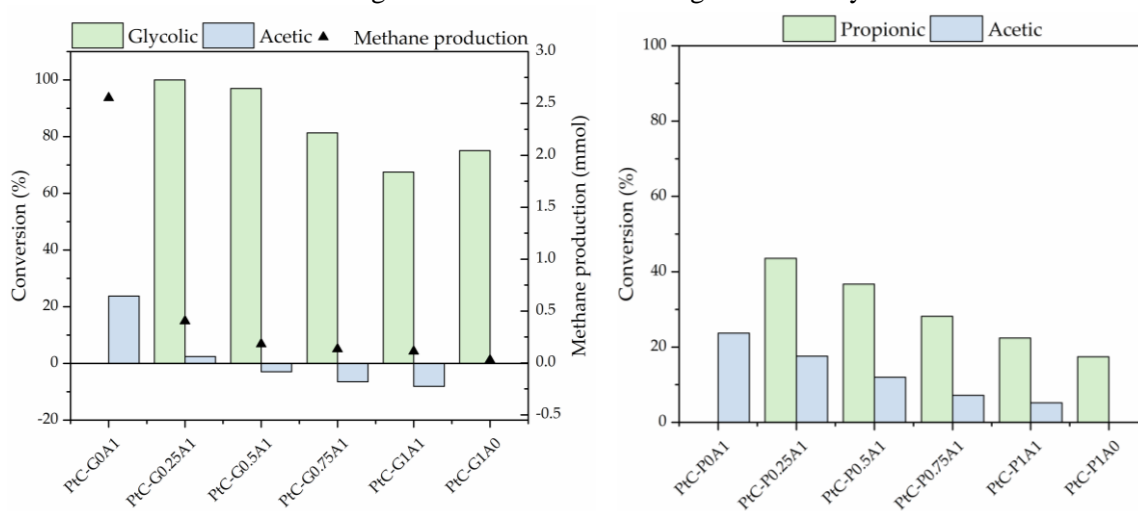


Figure 1. Influence of solution composition on APR performance. Reaction conditions: 75 mL solution, 270 °C, 0.15 g 5% Pt/C, 1 h.

4. Conclusions

APR of a model corn stover HTL-AP was performed to derive information on competitive adsorption phenomena. Glycolic, acetic and propionic acid were investigated alone and in mixtures to get an insight on their reactivities with different catalysts, the affinities with the active sites and the relative influences between the molecules. The full characterization of both liquid and gaseous products showed that acetic acid conversion was more influenced by the presence of glycolic acid rather than propionic acid. The insights gained from this work into the competition issues for the APR of complex mixtures can prompt future research in the design of catalysts for carboxylic acid activation, tackling the challenge of zero-waste biorefineries.

Acknowledgment

The project leading to this research has received funding from the European Union's Horizon 2020 research and innovation program under grant agreement N 764675.

References

- [1] L. Grande, I. Pedroarena, S.A. Korili, A. Gil, *Materials* (Basel). 14 (2021) 5286.
- [2] S.D. Davidson, J.A. Lopez-Ruiz, Y. Zhu, A.R. Cooper, K.O. Albrecht, R.A. Dagle, *ACS Sustain. Chem. Eng.* 7 (2019) 19889–19901.
- [3] G. Zoppi, G. Pipitone, R. Pirone, S. Bensaid, *Catal. Today.* 387 (2022) 224–236.
- [4] E. Panisko, T. Wietsma, T. Lemmon, K. Albrecht, D. Howe, *Biomass and Bioenergy.* 74 (2015) 162–171.

Sorption-enhanced gasification in dual interconnected fluidised beds – Behaviour of limestone-based sorbents

Antonio Coppola¹, Fabio Montagnaro^{2*}, Piero Salatino³, Fabrizio Scala^{1,3}

1 STEMS, Consiglio Nazionale delle Ricerche, 80125 Napoli

2 DSC, Università degli Studi di Napoli Federico II, 80126 Napoli

3 DICMaPI, Università degli Studi di Napoli Federico II, 80125 Napoli, Italy

**Corresponding author E-Mail: fabio.montagnaro@unina.it*

1. Introduction

Sorption-Enhanced Gasification (SEG) is a promising technology that can be based, Figure 1, on the use of Ca-based sorbents (like limestone) to selectively remove CO₂ from the gasification environment for production of a hydrogen rich syngas [1–3]. The SEG process benefits from the extensive understanding of the “calcium looping” process, a post-combustion technique aimed at removing CO₂ from combustion flue gas [4–6]. Calcium looping is most typically carried out in a Dual Interconnected Fluidised Bed (DIFB) reactor system, where the Ca-based sorbent is cycled between a carbonator, where it captures CO₂ from flue gas, and a calciner where the sorbent releases CO₂ and is regenerated for another cycle. Design of sorbent looping processes in DIFB reactors must consider: 1) sorbent deactivation (i.e., decay of CO₂ capture performance) over repeated cycling; 2) loss of sorbent material due to elutriation, that may be enhanced by attrition and fragmentation. The aim of this study was to investigate the performance of six different commercial limestones in terms of sorbent performance and attrition/fragmentation tendency under simulated SEG conditions.

2. Methods

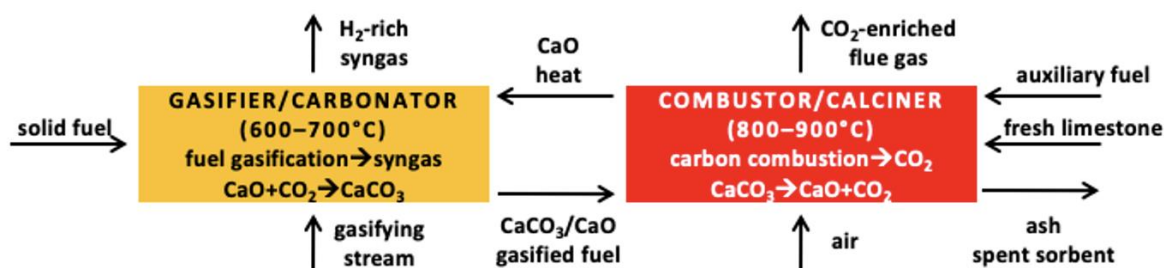
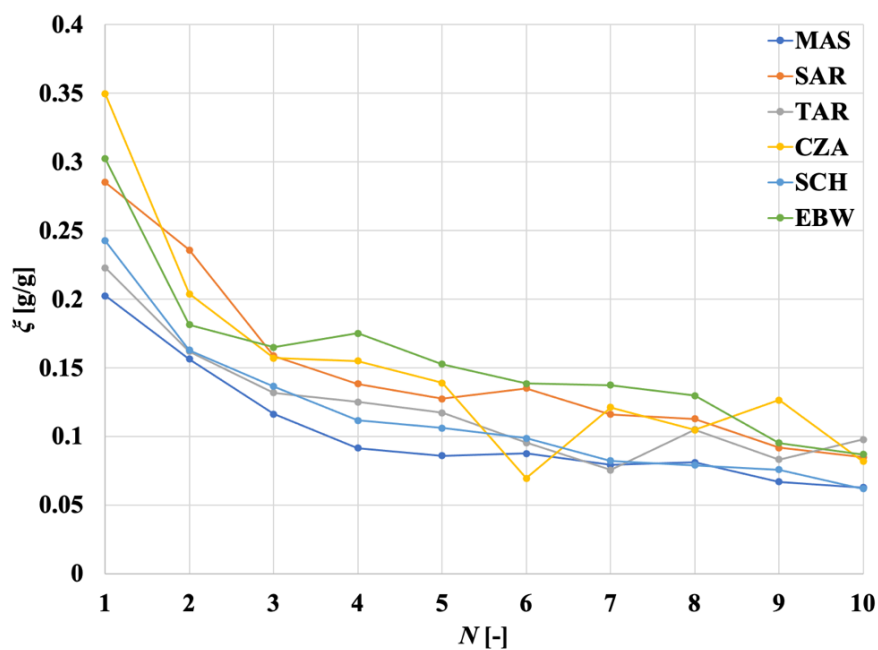
The experimental campaign was carried out in a batch-operated lab-scale DIFB reactor, electrically heated. The six sorbents were different limestones coming from different parts of Europe. A synthetic gas including air, CO₂ and N₂, was used to simulate SEG conditions. A “test” consisted of ten complete cycles of calcination/carbonation. Calcination was performed at 850°C fluidising the bed with a stream of 10% CO₂ (balance air) so as to simulate oxidising conditions typical of the combustor-calciner. In the carbonation stage, the temperature was kept at 650°C and the CO₂ concentration was set at 10% (balance nitrogen) to account for reducing conditions typical of the gasifier-carbonator. Operating conditions are summarised in Table 1. During each carbonation stage, the CO₂ concentration at the exhaust was continuously monitored to calculate the CO₂ specific capture performance. The sorbent attrition rate was determined by working out the mass of fines elutriated at the exhaust and collected in the filters, for each calcination and carbonation stage. After a test, each exhaust sorbent sample was sieve-analysed to obtain the particle size distribution and the fraction of generated fragments.

3. Results, discussion and concluding remarks

The preliminary characterisation of the six sorbents presented in this abstract shows that three of them (termed EBW, CZA and SAR) have good CO₂ capture performance (Figure 2), coupled with a limited production of both in-bed fragments and elutriable fines, while the sorbent named TAR is the worst in terms of the three features listed above. While results here presented can be useful for the determination of the make-up of fresh sorbent required for steady operation, and for optimal design and operation of sorption-enhanced gasification, further work is currently being carried out and concerns: i) the morphological (via SEM analyses) and porosimetric characterisation of the samples, in order to explain the features observed here; ii) the study of the impact fragmentation tendency of these sorbents, under a variety of impact velocity conditions.

Table 1. Main operating conditions for simulated SEG tests.

	Temperature, °C	Duration, min	%vol. CO ₂ (balance)	Fluidisation velocity, m/s
Calcination	850	10	10 (air)	0.5
Carbonation	650		10 (N ₂)	

**Figure 1.** Sorption-enhanced gasification in dual interconnected fluidised beds reactor.**Figure 2.** CO₂ specific capture performance ζ as a function of N , the number of carbonation stage, for DIFB-SEG tests (six different limestones).

References

- [1] A. Di Giuliano, K. Gallucci, P.U. Foscolo, *Ind. Eng. Chem. Res.* 59 (2020) 6840–6854
- [2] A.M. Parvez, S. Hafner, M. Hornberger, M. Schmid, G. Scheffknecht, *Renew. Sust. Energy Rev.* 141 (2021) 110756
- [3] A. Coppola, A. Sattari, F. Montagnaro, F. Scala, P. Salatino, *AIChE J.* (2022) <https://doi.org/10.1002/aic.17588>
- [4] N. Rodríguez, M. Alonso, J.C. Abanades, *AIChE J.* 57 (2011) 1356–1366
- [5] A. Perejón, L.M. Romeo, Y. Lara, P. Lisbona, A. Martínez, J.M. Valverde, *Appl. Energy* 162 (2016) 787–807
- [6] A. Coppola, O. Senneca, F. Scala, F. Montagnaro, P. Salatino, *Fuel* 268 (2020) 117371

The VIRTICHEM project: the virtual immersive education for chemistry and chemical engineering

Carlo Pirola^{1,*}, Alessandro Pedretti², Claude Jolival³, Farzaneh Arefi³, Ludek Mika⁴, Petr Smejkal⁴

1 Dipartimento di Chimica, Università degli Studi di Milano, via Golgi, 19 20133 Milano; 2 Dipartimento di Scienze Farmaceutiche, Università degli Studi di Milano, via Mangiagalli, 25 20133 Milano, 3 Sorbonne Université, CNRS, Laboratoire de Réactivité de Surface, LRS, 4 Place Jussieu, Paris F-75005, France, 4 Department of Chemistry Education, Charles University, Hlavova 2030/8, 128 00 Praha, Czech Republic

**Corresponding author E-Mail: carlo.pirola@unimi.it*

1. Introduction

Virtual immersive laboratories should be considered as an appealing and synergistic possibility for education in science, technology and engineering, strongly complementary to experimental activities performed in laboratory or exercises delivered in traditional rooms. Traditionally, degree courses in chemical sciences have been delivered using traditional teaching approaches, classroom exercises and real experiments in laboratories. Recently, innovative teaching methodologies have been proposed on the basis of the use of simulation science [1]. In this context, a new didactic project called VIRTICHEM was proposed by the three universities of Milan (Università degli Studi), Paris (Sorbonne Université) and Prague (Charles University) proposing virtual laboratories in the various fields of chemistry and chemical engineering. The project was based on the use of different types of virtual reality (VR) software for an immersive experience within the reproduction of chemistry laboratories, an industrial chemistry plant and investigation of structure of molecules. Students used these immersive programs in rooms equipped with VR workstations in the virtual rooms located in the departments of the three universities. During virtual exercises, specifically prepared according to educational goals, students collected information and data that required their interpretation, analysis and discussion in working teams to promote not only their learning but also their soft skills and critical thinking. Ten students from each university were selected to participate to the project. Preliminary lessons, about the theoretical background of the virtual exercises, were delivered as distance lessons and then three working weeks in Milan, Paris and Prague were conducted in presence during the spring of 2022 year. The project was funded by the 4eu+ European University Alliance (<https://4euplus.eu/4EU-183.html>).

2. Methods

VIRTICHEM project proposed immersive experiences in virtual laboratories by organizing preparatory lessons, virtual exercises, analysis of the data collected and a final meeting to share the teaching experiences. Expected educational outcomes were to promote innovative approaches such as student-centered and project-based learning by providing learning tools with improved flexibility and to provide an alternative to laboratory sessions when students are unable to attend the lab because of disabilities or attendance challenges (pregnancy, safety, pandemic issues). Another important goal of the project was to enable exploration of industrial platform or laboratory instrument set-up at a level inaccessible in “real life” such as inside process components and to take students on a realistic tour of an industrial plant since most of them never experience an in-person visit of an industrial site before their graduation. Particular attention was devoted to promote soft skills as to improve creativity, risk taking, social responsibility, teamwork ability, self-confidence and communication skills and to promote educational collaboration among universities.

3. Results and discussion

The project was based on the use of the following three simulation software Labsim, Eyesim and Nanome (Fig.1). LabSim is a laboratory simulator of inorganic analytical chemistry that allows to do solubility test, pH measurement and phase separation, and to perform a qualitative analysis of inorganic substances. The database allows to reproduce more than 3500 reactions. (<https://nova.disfarm.unimi.it/labsim>). Eyesim reproduces a Crude Distillation Unit plant from a physical and chemical point of view. The users can visit the plant and perform different exercises [2]. Nanome (Cuni, by Nanome Inc.) is a software for visualization and manipulation with molecules allowing immersion into a centre of almost any molecule to study its structure and properties. It is suitable for the educational purposes due to its wide platform support and illustrative way of molecule presentation. Webpage and short presentation is at <https://nanome.ai/>.

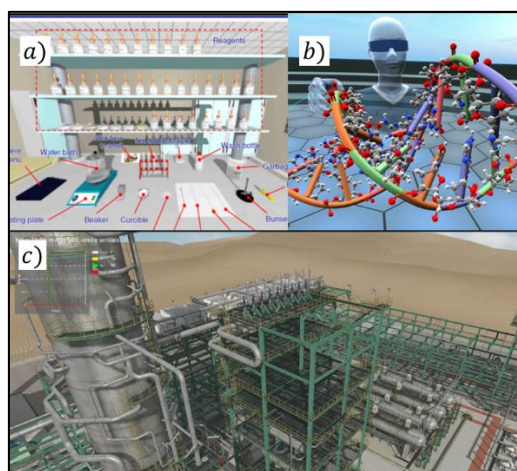


Figure 1. Example of screenshots of the software a) Labsim; b) Nanome; c) Eyesim.

The participation and evaluation of the students in the project was very positive. The planned activities, still in progress, are allowing students with heterogeneous basic preparation to be able to acquire basic notions on all the topics of the project. Quantitative results will be given during the GRICU conference, after the end of all the activities, including the final evaluation of the student groups' work scheduled for May 2022.

4. Conclusions

A new and innovative education project, VIRTICHEM, was proposed and delivered to students from different European Universities and degree courses. The project covered different areas of chemical sciences (chemical engineering, analytical and inorganic chemistry, molecular chemistry). The proposed activities resulted strongly complementary and synergic respect the traditional lessons and exercises.

References

- [1] V. Potkonjak, M. Gardner, V. Callaghan, P. Mattila, C. Guetl, V.M. Petrović, K. Jovanović, *Comput. Educ.* 95 (2016) 309–327
- [2] C. Pirola, C. Peretti, F. Galli, *Computer Chem. Eng.* 140 (2020) 106973

Deep learning-based non-intrusive detection of instabilities in formulated liquids

Maurizio De Micco¹, Diego Gragnaniello², Fabio Zonfrilli³, Massimiliano M. Villone^{1*}, Giovanni Poggi⁴, Luisa Verdoliva⁵, Vincenzo Guida³

1 Dip. di Ingegneria Chimica, dei Materiali e della Produzione Industriale, University of Naples Federico II, 80125 Naples, Italy; 2 Dipartimento di Ingegneria dell'Informazione ed Elettrica e Matematica applicata, University of Salerno, 84084 Fisciano (SA), Italy; 3 The Procter and Gamble Company, Brussels Innovation Center, 1853 Grimbergen, Belgium; 4 Dip. di Ingegneria Elettrica e delle Tecnologie dell'Informazione, University of Naples Federico II, 80125 Naples, Italy; 5 Dip. di Ingegneria Industriale, University of Naples Federico II, 80125 Naples, Italy

**Corresponding author E-Mail: massimiliano.villone@unina.it*

1. Introduction

Emulsions are metastable systems composed by at least two immiscible liquids and they have many industrial applications. Because of their thermodynamic instability, they have always represented a challenge for formulators and manufacturers. Emulsion stability is influenced by both chemical and physical factors and can be promoted by using emulsifying agents such as surfactants. This approach leads to the generation of formulated liquids, the prediction of whose long-term stability can be quite tricky due to both their complex chemical composition and the uncertain conditions to which they may be exposed. Instabilities lead to changes in the appearance, consistency, and performance of the products, thus an important aspect in their design is ensuring physical stability over shelf life. In the industrial field, the assessment of the physical stability of formulated liquids is typically done by placing samples of products in transparent jars and observing them at regular intervals of time under known operating conditions, e.g., temperature and pressure [1]. Observations are typically done by expert researchers and can be hardly repeated. This method allows to monitor potential long-term problems that might arise at given operating conditions. Visual observations can be eventually coupled with rheological measurements. This is a time-consuming task, which is ubiquitous in all the industrial sectors involving formulated liquids.

In order to automatize the process of stability assessment, time-lapse videos of the samples can be acquired and analyzed at a later time, which guarantees the repeatability of observations and allows studying also the temporal evolution of phenomena. In this work we leverage a large dataset of frames extracted by such time-lapse videos and use it to train several deep CNNs to perform frame-level instability detection. The dataset is strongly unbalanced, since it includes a very large number of stable samples with respect to unstable ones. Hence, we investigate different possible approaches to address this issue in order to improve the performance of the model. We also add results on interpretability to better understand which parts of the image impacted most on the final decision.

In recent years, image analysis methods have proven effective for addressing a number of chemical engineering-related problems, such as the prediction of physical phenomena and properties. This trend has further accelerated with the advent of deep learning, with its unprecedented performance. For example, Viitanen et al. [2] trained a CNN to predict the occurrence of specific events in dry foams by using just a single input frame. Likewise, a CNN combined with an auto-encoder has been employed by Khor et al. [3] to characterize microfluidic systems. The CNN has been trained to extract shape descriptors of emulsion droplets, whereas the auto-encoder has been trained to predict their break-up.

Besides good performance, deep learning-based image analysis is highly appreciated in several industrial applications because of its non-invasiveness. As an example, Hadikhani et al. [4] proposed a non-intrusive method to measure with high accuracy the flow rate of a water/oil emulsion and the concentration of each component of the system through a deep CNN. A hybrid deep CNN - Long Short Term Memory (LSTM)

network has been proposed by Lin et al. in [5] with the aim of predicting the membrane elasticity and viscosity of microcapsules from their dynamic deformation when flowing in a branched microchannel.

The high throughput of CNNs at inference time make them especially suitable for real-time tasks. Chu et al. [6] employed a CNN to classify newly-formed droplets in a microencapsulation system. In their experimental setting, a class weighting scheme is adopted in order to penalize misclassifications of under-represented classes in the loss function. A similar problem has been addressed by Anagnostidis et al. [7], who trained a deep CNN to count the number of micro-objects contained in droplets, cells or other systems at the time of image acquisition.

Instabilities of liquid formulations can be interpreted as product defects. Defect detection is a growing topic in the field of industrial applications and there are great efforts to automatize this process. CNNs have been investigated for this task by Wang et al. [8], who proposed a CNN composed of two major parts, one for classification and one for defect detection, while Zhou et al. [10] implemented a Region-based CNN to improve accuracy and speed of fabric defect detection.

Several image analysis techniques have been explored for the assessment of emulsion instability. Hosseini et al. [11] have used image processing and visual observations to maximize the stability of Arabic gum emulsions by calculating parameters such as creaming index, color, and average dimension of the droplets. Unnikrishnan et al. [12] adopted different machine learning methods, such as Random Forests, Multinomial Logistic Regression, and Neural Networks to perform classification into 4 categories on a set of emulsion micrographs previously labelled by experts. In this work, we study the effectiveness of CNN-based classifiers to detect instabilities in liquid formulations through the analysis of macroscopic images. To the best of our knowledge, this is the first time low-resolution images are automatically analyzed to detect liquid formulation instabilities.

2. Methods

We collected a large dataset of images extracted from time-lapse videos and labeled them thanks to expert researchers. In particular, the evolution of formulated liquids with various compositions when exposed to different operative conditions was observed. These experiments are of great importance to assess the so-called ‘shelf life’ of a product before its marketing. To this aim, images of the vials were periodically acquired to store snapshots of the content status. Images were cropped and stored by a fully automatic monitoring system, thus obtaining a time series of images for each experiment, with spatial resolution and temporal span changing from a series to another. For each series, a subset of 10 images equally spaced in time was selected and these were manually labeled as stable or unstable by a team of experts. Note that, during this process, the experts took advantage of the full series to reliably tell if and when an instability appears. Among the unstable samples, cases of phase separation, creaming, flocculation, cracking, and crystallization are present. Some examples of early, mid, and late snapshots of different failures are reported in Fig. 1. After discarding a small subset of ambiguous images for which the experts did not reach an agreement, as well as those erroneously cropped, we obtained a dataset comprising 32,078 stable and 4,857 unstable images, extracted from 6,341 time series. The dataset classes are heavily unbalanced, with 85% stable and 15% unstable samples, most of which show phase separation. This is a common problem in industrial applications since non-defective products outnumber defective ones [13].

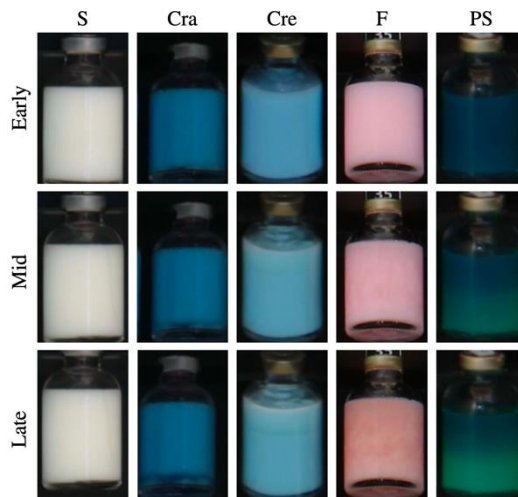


Figure 1. Early (top), mid (center), and late (bottom) stage of different experiments. From left to right: a stable sample and samples showing cracking (Cra), creaming (Cre), flocculation (F), and phase separation (PS).

The models we used rely on EfficientNet [14], a class of recently proposed CNNs that have been successfully employed in various computer vision applications. In order to train and validate the networks, a pre-processing pipeline was designed. Firstly, cropped images of different dimensions were resized to the same resolution, namely, 224×224 pixels. Since the average crop resolution is 150×240 pixels, this resizing operation did not produce significant information loss for the vast majority of the samples. After that, the whole dataset was split into training, validation, and test subsets by adopting a 70%-15%-15% proportion. The partitioning was carried out on whole time series rather than on individual images, so as to ensure that images from the same sequence, likely similar to one another, belong to the same subset. This avoids biases due to the presence of similar images in both training and validation/test sets.

Our dataset is heavily unbalanced, which may prevent the trained models from correctly generalizing to test data. To overcome this problem, we considered several approaches proposed in the literature. On one hand, we tested different loss functions beyond the classical cross-entropy loss. More specifically, we weighted the cross-entropy loss by using weights proportional to the inverse of the number of samples for each class, so as to discourage errors on the minority class. Alternatively, we adopted the focal loss [15] to down-weight examples whose labels are easily guessed by the network, likely those of the majority class. On the other hand, we synthetically increased the number of samples of the minority class. At each iteration, the mini-batch is composed by sampling images of the training set so as to balance the classes.

To further reduce the risk of poor generalization due to the unbalanced dataset, we combined the above mentioned strategies with augmentation techniques. We tested both geometrical transformations, like horizontal flipping and rotation, and color/illumination variation. In particular, we introduced random variations in hue, saturation, contrast, and brightness.

3. Results and discussion

For a preliminary set of experiments, we selected EfficientNet-B0, which ensures a performance almost as good as the deeper architectures of the family, but has a smaller number of parameters, and therefore is trained much faster. We trained it by combining different strategies in terms of loss functions, dataset balancing, and augmentation profiles. In this regard, we defined a *light* profile, involving only geometrical transformations, and a *strong* profile, which combines geometrical and color transformations. For comparison, we also trained the network without any form of augmentation. Results are reported in Tab. I. To assess the various solutions, we measure performance in terms of per-class weighted accuracy, which is not affected by the class unbalance, F-measure, and Pd@Q%. The latter is the probability of correctly

detecting the minority class of unstable sample (true positive rate) when the probability of false alarm (false positive rate) is fixed at $Q\%$, where Q here is 1 or 5. When considering the network trained using the classical cross-entropy loss, the light augmentation uniformly improves performance with respect to the case without any augmentation. In particular, this configuration achieves the highest F-measure, Pd@1%, and Pd@5% (boldface entries) among all the preliminary experiments. On the contrary, the training does not benefit from the strong augmentation. Probably, random color/illumination variations distort important features for this specific task. As for the mini- batch balancing, it appears to improve the performance in the absence of augmentation, providing more controversial results in the other cases, with improvements in terms of weighted accuracy achieved in particular with strong augmentation. Weighted cross-entropy loss and focal loss do not improve performance.

We then proceeded to explore alternative architectures. We selected two different training configurations, light augmentation with cross-entropy loss and strong augmentation with balanced batches. The former provides best FM, Pd@1% and Pd@5%, while the latter achieves comparable results with respect to other configurations, nevertheless it is interesting to understand to which extent including balanced batches can effectively represent an improvement.

Augm.	Loss	W. Acc	FM	Pd@1%	Pd@5%
None	XE	†0.920	0.803	0.714	†0.871
	W. XE	0.891	0.751	0.707	0.829
	Focal	0.885	0.767	0.706	0.819
	XE / BB	0.901	0.853	†0.789	†0.890
Light	XE	†0.917	0.872	0.812	0.908
	W. XE	†0.915	0.742	0.642	0.857
	Focal	†0.911	0.769	0.566	0.852
	XE / BB	†0.909	0.813	0.751	†0.880
Strong	XE	0.921	0.837	0.750	†0.888
	W. XE	0.897	0.776	0.622	0.843
	Focal	0.888	0.782	0.679	0.830
	XE / BB	†0.915	0.778	0.631	†0.880

Table I. Preliminary experiments using EfficientNet-B0. For each augmentation setting, the classical cross-entropy (XE) loss, its weighted version (W. XE), the focal loss, and the balanced batch approach (BB XE loss) are tested. Results with † are statistically similar to the top score (bold).

We trained deeper and wider EfficientNet models, as well as the popular ResNet50, and the architecture proposed in [17]. We also added two baseline approaches based on the Random Forest classifier trained on handcrafted features, namely the Local Binary Patterns (LBP) [18] and the Scale Invariant Descriptor (SID) [19] encoded using the Bag of Words (BoW) paradigm [20]. Results are reported in Tab. II. First of all, they confirm our initial preference for the EfficientNet architectures which dominate ResNet50 under all performance metrics and training settings. In any case, all CNN-based methods are much superior to handcrafted based approaches. A second notable result is that EfficientNet-B0 outperforms almost uniformly the deeper versions B1-B3, with both light and strong augmentation. This was somewhat unexpected, considering results reported in the literature for similar tasks, but can be explained with the relatively small size of the available training set, especially for the unstable class, probably insufficient to optimize a complex network with a large number of parameters. The comparison between training configurations confirms light augmentation to be preferable in all cases. This result suggests to pay special attention on testing proper forms of augmentation for this problem.

Setting/Input	Classifier	W. Acc	FM	Pd@1%	Pd@5%
Light augm. + XE loss	ResNet50	†0.904	0.845	0.751	†0.877
	Eff.-B0	0.917	0.872	0.812	0.908
	Eff.-B1	0.886	0.825	0.727	†0.880
	Eff.-B2	†0.913	0.844	†0.781	†0.897
	Eff.-B3	†0.908	0.845	†0.764	†0.883
	[17]	0.846	0.740	0.607	0.792
Strong augm. + XE / BB loss	ResNet50	0.900	0.768	0.614	0.843
	Eff.-B0	†0.915	0.778	0.631	†0.880
	Eff.-B1	0.887	0.767	0.590	0.827
	Eff.-B2	0.899	0.780	0.542	0.849
	Eff.-B3	0.889	0.766	0.590	0.827
	[17]	0.788	0.559	0.257	0.513
LBP	RF	0.618	0.375	0.187	0.358
SID+BoW	RF	0.732	0.556	0.257	0.462

Table II. Comparisons of architectures under two selected augmentation / loss settings: light augmentation with cross-entropy loss (top), strong augmentation with balanced mini-batch cross-entropy loss (bottom). Results with † are statistically similar to the top score (bold).

Besides the quantitative performance metrics, we also provide a visual interpretation of the result provided by the network. By relying on the Grad-CAM [16] method, we obtain a heat-map spotting the image regions that mostly contributed to the network decision. Example results from the test set are shown in Fig. 2 where images characterized by different types of instability are displayed together with the corresponding heatmaps. It appears that the network, although trained in a weakly supervised manner, with no information on the location of the instability, correctly focuses on the small regions of the input image where instability artifacts arise.

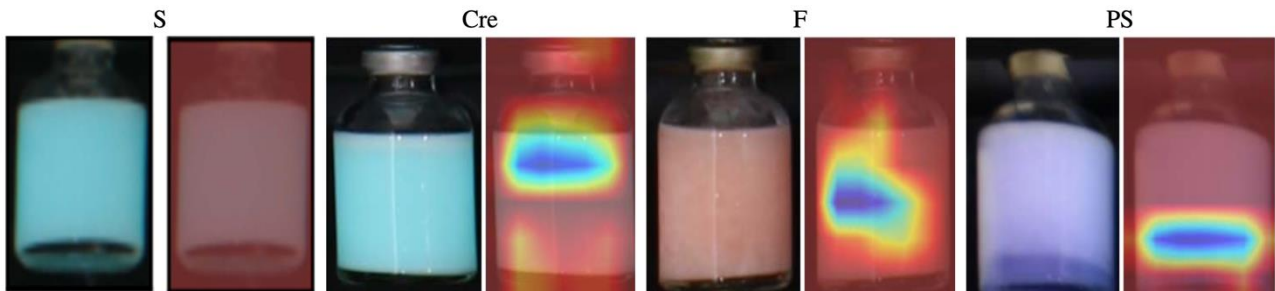


Figure 2. Sample images from the test set together with their GradCAM heatmaps. From left to right: stable (S), creaming (Cre), flocculation (F), and phase separation (PS). In all unstable cases artifacts are correctly spotted in the heatmap, while for the stable case there is no specific region that is highlighted.

4. Conclusions

We investigated CNN-based image analysis methods for non-intrusive detection of instabilities in formulated liquids. To the best of our knowledge, this is the first time deep learning is used to address this problem. Results are already very encouraging, confirming the potential of this approach. Nonetheless, there is much room for improvements. First of all, a larger and more refined dataset is necessary to train modern CNN architectures, and more specific losses and forms of augmentation need to be tested. After that, our focus will shift on more challenging problems, such as fine-grained instability classification, and early prediction of instability onset over time series.

References

- [1] G. Zografu, *J. Soc. Cosmet. Chem.* 33 (1982)
- [2] L. Viitanen, J.R. Mac Intyre, J. Koivisto, A. Puisto, and M. Alava, *Phys. Rev. Research* 2 (2020)

- [3] J.W. Khor, N. Jean, E.S. Luxemberg, S. Ermon, and S. K. Y. Tang, *Soft Matter* 15 (2019) 1361-1372
- [4] P. Hadikhani, N. Borhani, S.M.H. Hashemi, and D. Psaltis, *Sci. Rep.* 9 (2019)
- [5] T. Lin, Z. Whang, W. Wang, and Y. Sui, *Soft Matter* 17 (2021) 4027-4039
- [6] A. B. Chu, D. Nguyen, A. D. Kaplan, and B. Giera, *Applications of Machine Learning* (2019).
- [7] V. Anagnostidis, B. Sherlock, J. Metz, P. Mair, F. Hollfelder, and F. Gielen, *Lab Chip* 20 (2020) 889-900
- [8] T. Wang, Y. Chen, M. Qiao, and H. Snoussi, *Int. J. Adv. Manuf. Technol.* 94 (2018) 3465–3471
- [9] M. Wieler, and T. Hahn, *DAGM* (2007)
- [10] H. Zhou, B. Jang, Y. Chen, and D. Troendle, *AI4I* (2020) 52-55
- [11] A. Hosseini, S.M. Jafari, H. Mirzaei, A. Asghari, and S. Akhavan, *Carbohydr. Polym.* 168 (2015) 1-8
- [12] S. Unnikrishnan, J. Donovan, R. Macpherson, and D. Tormey, *Chem. Eng. Res. Des.* 166 (2021) 281-294
- [13] R. Shimizu, K. Asako, H. Ojima, S. Morinaga, M. Hamada, and T. Kuroda, *AI4I* (2018) 27-30
- [14] M. Tan, and Q. V. Le, *ICML* (2019) 6105-6114
- [15] T. Lin, P. Goyal, R. Girshick, K. He, and P. Dollar, *ICCV* (2017) 2999-3007
- [16] R. Selvaraju, M. Cogswell, A. Das, R. Vedantam, D. Parikh, and D. Batra, *ICCV* (2017) 618-626
- [17] T. Wang, Y. Chen, M. Qiao, and H. Snoussi, *Int. J. Adv. Manuf. Technol.* 94 (2018) 3465–3471
- [18] T. Ojala, M. Pietikainen, and T. Maenpaa, *IEEE PAMI* 24 (2002) 971–987
- [19] I. Kokkinos, M. Bronstein, and A. Yuille, *INRIA RR-7914* (2012)
- [20] D. Gragnaniello, G. Poggi, C. Sansone, and L. Verdoliva, *Pattern Recognit. Lett.* 82 (2016) 251-257

Technical and economic analysis of the decarbonization of steelmaking using green hydrogen

Antonio Trinca^{1*}, Giorgio Vilardi¹

Sapienza University of Rome, Dept. of Chemical Engineering Materials Environment, via Eudossiana 18, 00184 Rome, Italy;

**antonio.trinca@uniroma1.it*

1. Introduction

The environmental changes encountered nowadays are more and more worrying. In the recent years, several conferences and deals were programmed with the aim to reduce global greenhouse emissions. Steel is one of the most important raw materials for global industry. The main iron and steel making processes use energy and reduction agents derived from carbon sources, as carbon coke and natural gas. They are characterized by high energy consumption and high greenhouse gases emissions. The 4% of total European emissions and the 22% of total European industry emissions derives from steel sector [1]. Blast Furnace (BF) technology produces the 71% of global steel: the entire process has an energy demand around of 19.2 GJ/t of steel produced and emits 1.694 tCO₂/t of steel [8, 9]; the 24% of steel derives from the recycle of scrap in an Electric Arc Furnace (EAF) with an energy demand of 3.3 GJ/t and an emission of 0.190 tCO₂/t [3]. The remaining 5% is produced in Direct Reduced Iron (DRI) process where iron is reduced by gaseous reducing agents, under melting conditions [3]. The process can be coupled with EAF furnace. DRI/EAF process consumes 13 GJ/t [4], and 0,5-0,9 tCO₂/t of steel [3, 6]. DRI/EAF process is already a viable solution to reduce CO₂ emissions, moreover conventional direct reduction reactors can also use hydrogen as reductant [6].

This work will analyse the possibility to decarbonize iron and steel making process and its economic results compared with the fossil route, using green hydrogen and renewable energy in DRI/EAF process.

2. Process layout

The DRI/EAF with hydrogen process is a modified plant of DRI/EAF process. The plant uses hydrogen instead of syngas as reducing gas. Hydrogen is produced by a Proton exchange membrane (PEM) electrolyser from water and renewable energy.

DRI/EAF (Midrex layout) and DRI/EAF with hydrogen plants have been simulated using AspenPlus software. Following figures describe the process scheme of the two plants.

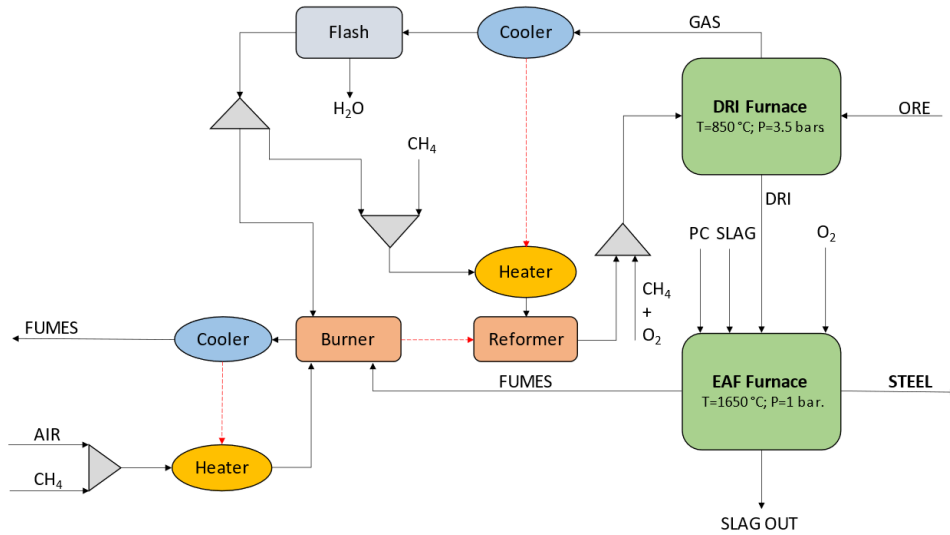


Figure 1. DRI/EAF scheme. Dotted lines represent heat streams, continued lines represent material streams.

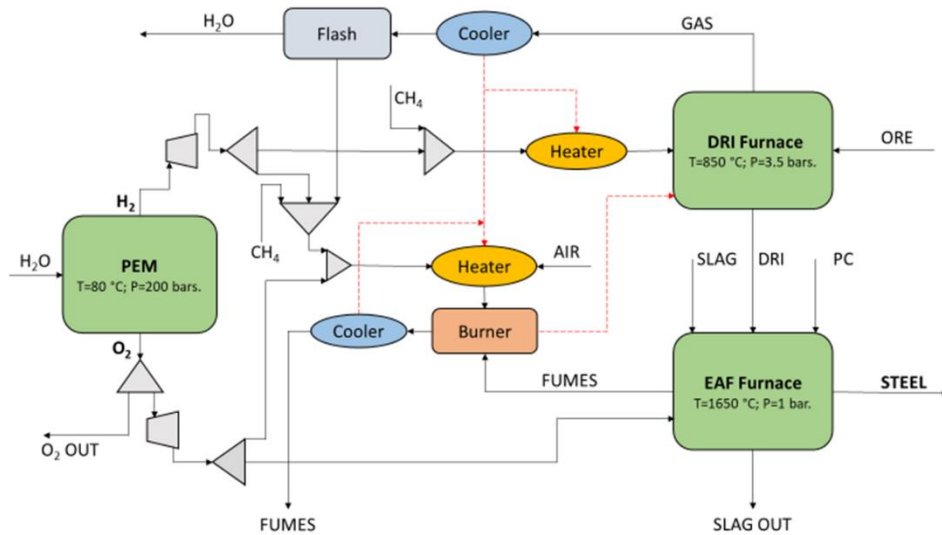


Figure 2. DRI/EAF with hydrogen scheme process. Dotted lines represent heat streams, continued lines represent material streams.

An energy, exergy, environmental and economic analysis of the two flowsheets have been made.

3. Results and discussion

Energy and exergy yield values are similar. Waste exergy of the DRI/EAF plant is 81,84 MW against 47,14 MW of the hydrogen plant. Certainly, there is room for improvement.

η_g	
DRI-EAF	0,63
DRI-EAF-H ₂	0,62
η_{ex}	
DRI-EAF	0,52
DRI-EAF-H ₂	0,51

Table 1. Energy (η_g) and exergy (η_{ex}) yield.

Hydrogen plant has an energy demand 15,9% and a power energy consumption 468% more than traditional DRI/EAF, because of the great demand of PEM electrolyser.

	<i>Methane</i>	<i>Carbon</i>	<i>Electricity</i>	<i>Total</i>	<i>Unit</i>
DRI-EAF	9,42	1,00	1,80	12,22	GJ/t
DRI-EAF-H ₂	2,94	1,00	10,23	14,73	GJ/t

Table 2. Energy demand.

CO₂ emissions, using hydrogen and renewable energy, decrease by the 71,7% with respect to DRI/EAF process; NO_x emissions decrease by the 49,3% with respect to DRI/EAF process.

	<i>CO₂</i>	<i>NO_x</i>
DRI-EAF	0.73	0.19
DRI-EAF-H ₂	0.21	0.01
Unit	t/t	kg/t

Table 3. Specific CO₂ emissions.

Operative cost, using hydrogen and renewable energy, increases by the 161%.

<i>Opex</i>	
DRI-EAF	389.21
DRI-EAF-H ₂	1017.84
Unit	\$/t

Table 4. Opex results.

4. Conclusions

This work is focused on the reduction of greenhouse gas emissions from iron and steel making process, in line with the global and European targets. The potential use of green hydrogen and renewable energy in a conventional DRI/EAF plant is investigated. The simulations of the conventional DRI/EAF plant and the DRI/EAF with hydrogen plant are carried out with the software AspenPlus. Energy and exergy analysis show the possible improvements in terms of efficiency. Economic and environmental results are compared. Despite a higher operative cost, green hydrogen allows a great reduction in CO₂ and NO_x emissions. About the economic feasibility, nowadays, this production way is not practicable in terms of economic results. However, author is confident that DRI/EAF with hydrogen process will become economical attractive in the next years, because of the great investment established by governments in new production routes and in renewable energy. Author is also confident that in the next years more efficient electrolysers will be designed and that the renewable energy availability will increase.

References

- [1] R. Berger, *The future of steelmaking – How the European steel industry can achieve carbon neutrality*. 2020.
- [2] M. Hammerschmid, *Evaluation of biomass-based production of below zero emission reducing gas for the iron and steel industry*. Biomass Conversion and Biorefinery, 2021, pp. 169–187.
- [3] Laplace Conseil, “Impacts of energy market developments on the steel industry,” *74th Session of the OECD Steel Committee*, no. July, pp. 1–2, 2013, [Online]. Available: [https://www.oecd.org/sti/ind/Item 9. Laplace - Steel Energy.pdf](https://www.oecd.org/sti/ind/Item%209.%20Laplace%20Steel%20Energy.pdf)
- [4] Olga Chiappinelli, *A green COVID-19 recovery of the EU basic materials sector: identifying potentials, barriers and policy solutions*. 2020.
- [5] F. Muscolino, A. Martinis, M. Ghiglione, P. Duarte, M. Ghiglione, and P. Duarte, *Introduction to direct reduction technology and outlook for its use*, pp. 25–31, 2016.
- [6] P. Cavaliere, *Direct Reduced Iron: Most Efficient Technologies for Greenhouse Emissions Abatement*. 2019.

The colors of hydrogen: a process simulation-based comparison of different production processes

Elena Barbera^{1*}, Andrea Mio², Marco Disnan², Alessandro Massi Pavan², Alberto Bertucco¹,
Maurizio Fermeglia²

1 Department of Industrial Engineering, University of Padova, Via Marzolo 9, 35131 Padova, Italy;

2 Department of Engineering and Architecture, University of Trieste, Via Valerio 10, 34127 Trieste, Italy.

**Corresponding author E-Mail: elena.barbera@unipd.it*

1. Introduction

Over the last decades there has been an accelerated growth in human energy consumption. The global average primary energy use has significantly increased, by about 42%, from 2000 to 2019, passing from 122073 to 173340 TWh. This, together with the need of a strong reduction in fossil fuels consumption in order to reach the objectives of greenhouse gases emissions for 2030, as indicated by recent reports of IPCC [1] and EIA [2], has put an increasing pressure on the energy sector. Since energy production from renewable sources is not dispatchable due to their fluctuating nature, great attention is given to energy storage and energy carrier systems. Hydrogen is one of the most suitable energy carriers for several applications, such as heavy transportation and logistics. It can be produced from different feedstock and according to different processes, each one identified by a color.

Decisions on the best strategies to pursue in this regard should be based on indicators able to summarize different aspects of the different routes, such as energetic efficiency, economic considerations, but also environmental impacts. These aspects can be quantified according to suitable indicators, namely the Energy Return on Energy Investment (EROEI), the Levelized Cost of Hydrogen (LCOH), and a thorough Life Cycle Assessment (LCA). In order for the analysis to be meaningful, it needs to be based on detailed and coherent process simulation-based mass and energy balances with reference to a specific production target

This work aims at providing reliable operating data for different hydrogen production processes, in order to obtain all the information needed for subsequent energetic, economic, and environmental assessments. Specifically, process simulations are developed to compare different hydrogen production pathways, each one defined by the appropriate color: (i) grey hydrogen, produced from natural gas using steam methane reforming (SMR); (ii) blue hydrogen, which is like the grey one but integrated with carbon capture and storage (CCS); and (iii) green/yellow hydrogen, produced by water electrolysis using electricity from renewable sources or grid electricity, respectively. In the latter case, different types of electrolyzers are simulated and compared, namely Alkaline Electrolysis Cells (AEC), Proton Exchange Membrane Electrolysis Cells (PEMEC), and Solid Oxide Electrolysis Cells (SOEC).

The analysis is carried out with reference to a daily hydrogen production corresponding to the estimated consumption required by the port of Trieste, taken as a case study, with the goal to feed fuel cells train locomotors and tugboats handled inside the port area. The production processes are sized according to the desired daily requirement, possibly avoiding the need to store high amounts of hydrogen within the port.

2. Methods

Process simulations were carried out using Aspen Plus v. 12.1. The software was used to develop the process flowsheet for each hydrogen production process considered, and perform material and energy balances, physical property estimations, design/rating calculations, sensitivity analysis and process optimization. In

addition heat integration by pinch analysis and economic analysis evaluation were performed with Aspen Energy Analyzer and (AEA) and Aspen Process Economics Analyzer (APEA) tools, respectively.

3. Results and discussion

Process flowsheets were developed for hydrogen production via SMR with and without CCS (grey and blue hydrogen) and via water electrolysis according to AEC, PEMEC and SOEC electrolyzers (green and yellow hydrogen). For the latter, electrochemical models to describe the stack performances were included by means of user unit models. The target daily hydrogen production was estimated to be about 800 kg/d. The Aspen Plus process flowsheets for SMR, AEC and SOEC are displayed in Figure 1, as an example.

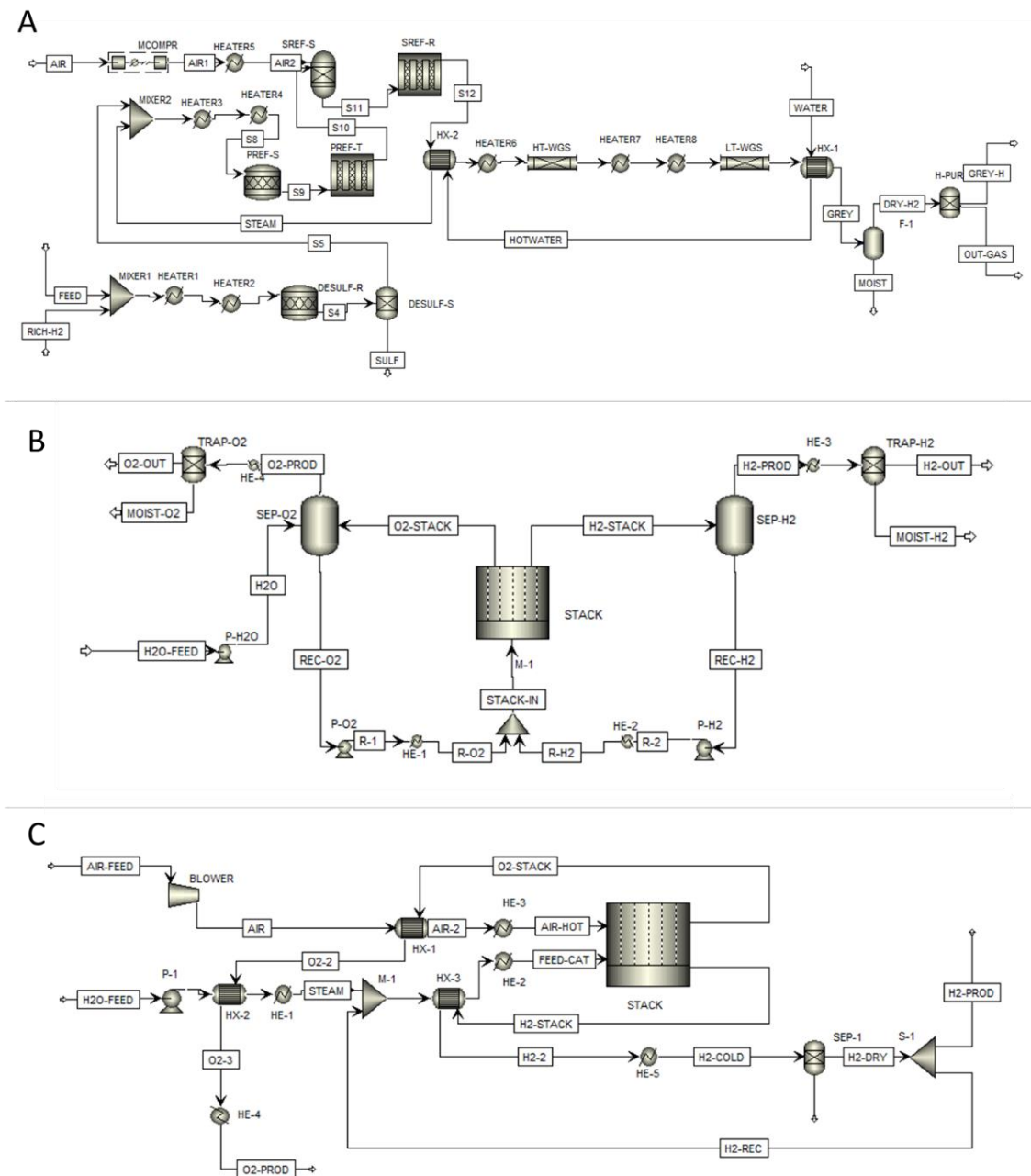


Figure 1. Aspen Plus Flowsheet of SMR (A), AEC (B) and SOEC (C)

The data obtained from process simulations were then elaborated in order to derive the inputs required for the evaluation of the EROEI, LCOH and LCA indicators, according to Table 1.

		EROEI	LCOH	LCA
Gross energy output	kW	x	x	x
Power energy requirement	%	x		x
Thermal energy requirement	%	x		x
Net energy output	kW	x	x	x
Total plant cost (TPC)	€		x	
Share of investment costs due to operation and maintenance (so&m)	%	x		
Fixed operation and maintenance costs (FO&MC)	€/kW/year		x	
Variable operation and maintenance costs (VO&MC)	€/kWh		x	
Total amount of solvent (for CCS)	kg			x

4. Conclusions

The data obtained by means of process simulations allowed a detailed estimation of the energy duties required for the production of hydrogen at a desired scale. Preliminary results indicate that green hydrogen is likely to be the preferred route.

References

- [1] <https://www.ipcc.ch/report/sixth-assessment-report-cycle/> AR6 IPCC 2021 report. Accessed on December 7, 2021.
- [2] <https://www.iea.org/reports/net-zero-by-2050> IEA (2021), Net Zero by 2050, IEA, Paris, Accessed on December 7, 2021.

Valuable C-based chemical intermediates and bio-char from “end of life” olive stone waste: analysis in thermal pyrolytic conditions

Sina Ebrahim Atakoochi¹, Elena Spennati¹, Alessandro A. Casazza¹, Paola Riani², Gabriella Garbarino^{1*}

1 Department of Civil, Chemical and Environmental Engineering, University of Genoa, Via Opera Pia 15, 16145 Genoa, Italy

2 Department of Chemistry and Industrial Chemistry, University of Genoa, via Dodecaneso 31, 16146, Genoa, Italy

**Corresponding author E-Mail: gabriella.garbarino@unige.it*

1. Introduction

Pyrolysis of biomass is a promising method for the production of distributed and renewable energy, producing pyrolytic gas, bio-oil and bio-char [1]. Produced bio-char and bio-oil can be used as starting materials for other added-value products such as carbon-based materials, chemical intermediates, and fuels that are attractive for several industrial applications. However, the presence of heteroatoms might lead to limitations in the exploitation of available technologies. In the first stage of evaluation, we considered several biomasses of potential interest, and “end of life” olive stone waste has been identified as a possible and promising raw material. In fact, among pros, olive stones have a great potential to be used as the biomass for pyrolysis because the world’s annual production of olive mill waste exceeds 30 million m³ [2]. In addition, the olive oil industry is an important economic sector in the European Union (EU), mainly Mediterranean Sea countries [3], and based on 2019 data of FAO report, Italy was the second producer of olive in the world with 2 million metric tons [4]. Therefore, the present work aims to evaluate the possible production of useful C-based products from this waste, when considering that the major use for “end of life” olive stones is energy generation through conventional combustion processes.

2. Methods

In this work, pyrolysis on a dried industrial “end of life” olive stone waste was performed in batch or semi-batch conditions using a tubular quartz reactor. For each test, 10.0 g of the starting material with a particle size of 1-4 mm were loaded. The thermal treatment was provided by an electric oven at a temperature of 500 °C and in the preliminary study two different operating conditions for N₂ have been investigated: fully batch conditions or a constant N₂ flow (100 mL min⁻¹). Also, for each condition, reaction times of 1 and 3 h were considered. A Liebig condenser with water as coolant was used to collect the condensable gas as liquid (hydrophilic and lipophilic parts), while gas has been collected in a latex balloon (batch experiment) or vented (N₂ continuous flow). In this preliminary study, the amount of liquid and bio-char were evaluated gravimetrically and the produced gas one was calculated by the difference method. The starting material has been characterized by ashes content and SEM-EDX. Produced liquid and gases have been analyzed by FT-IR and GC-MS as reported from previous investigations [5,6]. The produced solid materials have been characterized by SEM-EDX, FT-IR, UV-vis and the following treatment stages are under evaluation at the present time.

3. Results and discussion

The density of the starting olive stone material was measured to be 1480 kg·m⁻³ while after all the pyrolysis tests, it is reduced to 480 kg·m⁻³ (bio-char). Ashes content in the starting material is ~1%, thus supporting the correct choice of the raw material for the present study.

Yields to liquid, bio-char and pyrolytic gas has been evaluated as: $Y_i = \text{mass}_i / \text{mass}_{\text{biomass}}$, with the methodology described above. As shown in Figure 1, when the pyrolysis condition changed from batch inert environment to nitrogen flow, the yield of the liquid was decreased from 57 to 50 % and the yield of the bio-char was slightly increased from 24 to 26 %.

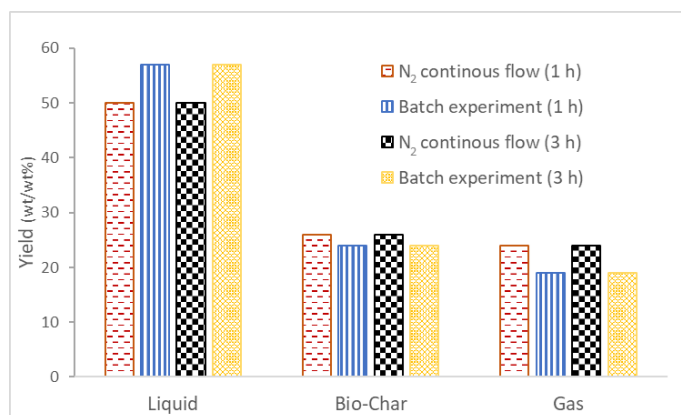


Figure 1. Yields to pyrolysis products as a function of reaction time and process conditions at 500°C

Conversely, the yield of the gas increased from 19 to 24 %. The reason for the reduction of liquid yield and subsequent increase of gas one when using nitrogen flow could be attributed to the different reaction conditions or removal of volatile liquid compounds. Likewise, a slight increase in bio-char yield could be attributed to the removal of the pyrolysis gas from the reactor by nitrogen flow, removing volatile compounds and maybe reducing possible interaction of bio-char with gaseous components [7]. Instead, no remarkable effect has been obtained by varying the reaction time mainly because, in the adopted experimental setup, pyrolysis process mainly occurs in the first 30 minutes, in agreement with reaction times reported in the literature on different biomasses [8]. Therefore, it could be concluded that pyrolysis time higher than 1 hour, will probably affect the properties and reactivity of bio-char [9] which is an important parameter for char use, currently under investigation. Assessment of the liquid composition and bio-char properties and morphology are currently under evaluation.

4. Conclusions

Pyrolysis of dried “end of life” olive stone waste was performed at 500 °C with different reaction times in both batch and semi-batch operating mode. The effect of the experimental process condition applied to the pyrolytic treatment on the yield of bio-char, liquid and gas was evaluated. Also, composition of produced liquid was analyzed. When the pyrolysis condition changed from batch to N₂ flow, the yield of char and gas was increased by 8% and 26% respectively while the liquid yield was decreased by 14%. No remarkable difference was observed upon a variation of the reaction time (1 vs. 3 h). An extensive discussion on stream composition and properties of the produced bio-char will be given.

References

- [1] G. Wang, Y. Dai, H. Yang, Q. Xiong, K. Wang, J. Zhou, Y. Li, S. Wang, *Energy & Fuels*. 34 (2020) 15557–15578.
- [2] M. Corral-Bobadilla, R. Lostado-Lorza, F. Somovilla-Gómez, R. Escribano-García, *J. Clean. Prod.* 294 (2021).
- [3] K. Khwaldia, N. Attour, J. Matthes, L. Beck, M. Schmid, *Compr. Rev. Food Sci. Food Saf.* (2022) 1–36.
- [4] NationMaster, 2022, www.nationmaster.com/nmx/ranking/olives-production-fao
- [5] M. Borella, A.A. Casazza, G. Garbarino, P. Riani, G. Busca, *Energies*, 15 (2022) 991.
- [6] E. Spennati, A.A. Casazza, A. Converti, G. Busca, *Energies*, 13 (2020) 5246.
- [7] M. Iwanow, T. Gärtner, V. Sieber, B. König, *Beilstein J. Org. Chem.* 16 (2020) 1188–1202.
- [8] Y.H. Chan, S. Yusup, A.T. Quitain, Y. Uemura, S.K. Loh, *Biomass Bioenergy* 107 (2017) 155–163.
- [9] H. Liu, M. Kaneko, C. Luo, S. Kato, T. Kojima, *Fuel* 83 (2004) 1055–1061.

A study on the adsorption on activated carbons as upgrading technology for Kraft lignin pyrolytic gas

Matteo Borella¹, Alessandro A. Casazza¹, Gabriella Garbarino^{1*}, Paola Riani² and Guido Busca^{1*}

¹ Department of Civil, Chemical and Environmental Engineering, University of Genoa, Genoa, Italy;

² Department of Chemistry and Industrial Chemistry, University of Genoa, Genoa, Italy;

* Corresponding authors E-Mail: Gabriella.Garbarino@unige.it; Guido.Busca@unige.it;

1. Introduction

Environmental and climate issues deriving from the exploitation of fossil resources led scientists towards the development of more ecological solutions to achieve the carbon neutrality within 2050 [1]. Biochemicals and biofuels production has raised in recent years attempting to reduce carbon dioxide emissions deriving from the combustion of non-renewable resources [2]. Lignocellulosic biomasses can represent one of the most promising alternative feedstocks due to their carbon matrix and their great availability [3]. In particular, from 10 to 30 wt. % of lignocellulosic biomass is represented by lignin, an aromatic-rich compound whose thermal degradation can have a key role in the in the production of bio-based relevant compounds[4]. Among all the different types of commercial lignin, almost 80% is obtained from Kraft process. In this process, Kraft lignin (KL) isolation is obtained by means of a solution of NaS₂ and NaOH (black liquor), and for this reason the final lignin still contains 3-4 wt.% of sulfur [5]. In particular, previous results of our group [6] showed that KL pyrolytic gas is rich in CH₄, CO, CO₂, and H₂S with the presence of other sulfur compounds in smaller amount (i.e., CH₃SH, CH₃-S-CH₃, SO₂, COS, and CS₂). In this work, the thermal degradation in inert environment of KL at 550°C has been studied, and the distribution of sulfur compounds in the gas phase formed during the cracking at high temperature has been investigated. The composition of the gas has been characterized and then compared to the one obtained forcing the gas to pass through a fixed bed of activated carbon with a high selectivity in the adsorption on S-containing compounds. Four different commercial activated carbons were adopted with different adsorption capacities and pore dimensions.

2. Methods

In this work, commercial Kraft lignin has been received from StoraEnso® (Lineo™ Classic Lignin, Kotka, Finland). Lignin morphology was investigated using scanning electron microscopy (SEM), while the elemental composition in terms of C, Na, S, and O content was determined through energy-dispersive X-ray spectroscopy (EDX). The pyrolysis has been carried out in an inert environment and batch conditions at 550 °C for 3 hours. The total absence of oxygen inside the reactor is guaranteed by a nitrogen purge performed before each test in order to avoid the occurrence of combustion reaction. The setup is characterized by a reaction unit constituted by a furnace where a quartz tubular reactor is collocated. This section is followed by a separation unit constituted by a Liebig condenser where condensable reaction gases are cooled and collected in a flask. Non-condensable gases have been collected in a latex balloon after forcing them to pass in a column packed with different commercial activated carbons. The efficiency of the adsorption process has been evaluated by comparing the results so obtained with those of a control test performed with the same setup without the adsorption bed. Qualitatively, the composition of the produced gas has been investigated using Fourier Transform Infrared Spectroscopy (FT-IR). A quantitative analysis of S-containing compounds was conducted injecting 100 μL of reaction gas every 45 minutes in a gas chromatography–mass spectrometer (GC–MS).

3. Results and discussion

In Figure 1 the FT-IR spectra of the pyrolysis gas of the control test (a) and the gas after the adsorption on activated carbons (b, c, d, e) have been reported. Even though most of the sulfur compounds produced during the pyrolysis cannot be detected using FT-IR analysis, the band at 2062 cm⁻¹ can be attributed to the presence

of COS. However, this band is only observable in the control test where the gas is not adsorbed on the activated carbon. Moreover, the band around 2364 cm^{-1} due to the presence of the CO_2 , has a decreasing intensity signal when adsorbed on the activated carbon bed. An activated carbon with high selectivity towards hydrogen sulfide, would likely interact with CO_2 because of its acid character. This results in a gas richer in CH_4 whose peaks at 3016 and 1304 cm^{-1} do not seem to be remarkably affected by the interaction with the bed.

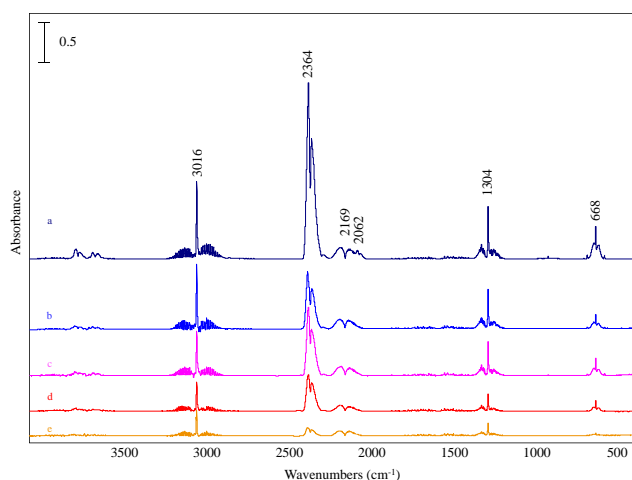


Figure 1. FT-IR analysis of pyrolytic gas for control test (a), and after the adsorption on activated carbons (b, c, d, e).

In order to monitor the evolution of sulfur compounds from a quantitative point of view, the GC-MS analysis has been performed and the peak area related to sulfur compounds has been evaluated. H_2S resulted the most abundant compound present in the gas phase, with relevant amounts of COS and CH_3SH too. Data have been expressed as the ratio between the peak area of the sulfur species normalized with the total area. The concentration of H_2S , COS and CH_3SH undergoes a remarkable drop after their interaction with the adsorption bed of activated carbon. Preliminary data from GC-MS show a reduction of the relative abundance of H_2S from 2.2% to 0.01%. COS and CH_3SH , whose relative abundance in control test is 0.2 and 0.8%, respectively, exhibit almost a total adsorption on the activated carbon bed.

4. Conclusions

Two different setup configurations have been compared to understand how a coupling of pyrolysis and one pot adsorption could affect the distribution of sulfur compounds in the pyrolytic gas of a commercial Kraft lignin, thus leading to the development of new process outlines. The effect of the adsorption is clearly observed in the disappearing of the band at 2062 cm^{-1} related to the presence of COS. From a quantitative point of view, a decrease of the peak areas of H_2S , COS and CH_3SH is revealed from the GC-MS analysis. Other sulfur compounds, i.e $\text{CH}_3\text{-S-CH}_3$, SO_2 and CS_2 that were also present in conventional test, were not detected in significant amounts after the adsorption on activated carbons. Thus the proposed upgrading process would be feasible for a sulfur rich pyrolytic gas cleaning.

References

- [1] F. Schreyer, G. Luderer, R. Rodrigues, R.C. Pietzcker, L. Baumstark, M. Sugiyama, R.J. Brecha, F. Ueckerdt, *Environ. Res. Lett.* 15 (2020).
- [2] P. Azadi, O.R. Inderwildi, R. Farnood, D.A. King, *Renew. Sust. Enegr. Rev.* 21 (2013) 506–523.
- [3] S. Nanda, J. Mohammad, S.N. Reddy, J.A. Kozinski, A.K. Dalai, *Biomass Convers.* 4 (2014) 157–191.
- [4] C. Chio, M. Sain, W. Qin, *Renew. Sust. Enegr. Rev.* 107 (2019) 232–249.
- [5] S. Kang, X. Li, J. Fan, J. Chang, *Renew. Sust. Enegr. Rev.* 27 (2013) 546–558.
- [6] M. Borella, A.A. Casazza, G. Garbarino, P. Riani, G. Busca, *Energies* 15 (2022) 991.

Analyzing the production of pure K₂SO₄ via rigorous process simulation to overcome lack of literature and experimental data

Marco Vaccari^{1*}, Livia Di Palma¹, Leonardo Tognotti¹, Giovanni Papa², Elisabetta Brunazzi¹

1 University of Pisa, Department of Civil and Industrial Engineering, Largo Lucio Lazzarino 2, 56126 Pisa (Italy)

2 Altair Chimica SPA, Saline di Volterra (PI), Italy

**Corresponding author E-Mail: marco.vaccari@ing.unipi.it*

1. Introduction

Potassium sulfate (K₂SO₄), a chlorine-free potash fertilizer, is commonly used to supply essential potassium for plant growth, and the traditional and most widespread production process is the Mannheim one [1]. Another production process composed of a larger number of phases but characterized by decidedly more moderate operating conditions include the co-production of K₂SO₄ and ammonium chloride (NH₄Cl) [2]. The maximum temperatures of the process considered reach 60°C against 600°C of the Mannheim case, and pressure is also moderate as 101,325 KPa are maintained up to the evaporative crystallization which instead occurs at 10 KPa. In addition, the chemicals involved are less dangerous than sulfuric and hydrochloric acids which necessarily follow the most stringent regulations that influence the production process, storage, and disposal of effluents.

A recent pilot plant of this process was designed in an Italian chemical company (later named Altair), in which facility the presence of several production lines covering part of the necessary reagents (KCl, FeSO₄) implied a strong saving on raw material costs and a more favorable integration with the existing plants rather than the Mannheim process. Few aspects concerning the complex chemistry behind the unit operations at stake together with its missing description in international reference documents [3], make the definition of the operating conditions for obtaining the maximum production of potassium sulfate not an easy task. In fact, the process yield strictly depends on the possibility of accurately predict the co-precipitation of salts in solution and therefore limiting the production of by-product as much as possible. For the aforementioned reasons, literature or experimental data on solubility of the salts in the particular solution of interest for this process are very difficult to find, whether not present at all at the operating conditions required.

In this context, the purpose of this work is to study the production process of K₂SO₄ with the help of rigorous process simulation to better analyze how the production of by-products (NH₄Cl) can be minimized by understanding how the solubility of these two main salts are affected by their interaction.

2. Methods

One of the main issues related to the original design and subsequent construction of Altair K₂SO₄ pilot plant is represented by the study of the fractional crystallization of the mother liquors after the first precipitation of K₂SO₄. The lack of solubility data for the fractional crystallization step and in general the influence of NH₄Cl on K₂SO₄ is crucial information to define the plant parameters to maximize the precipitation of the product.

The quantities of species present in the treated solutions in the processes examined give rise to complex electrolytic solutions. Consequently, it is necessary a simulator capable, through complex mathematical models, of creating a robust and reliable model able to predict the behavior of the various components.

For these reasons, the tool chosen in this work is the software UniSim Design R470 with OLI Engine as the thermodynamic package.

In the production process of K₂SO₄, it is important to have a reliable simulator for predicting solubilities as various competitive precipitations are at stake that can influence the crystallization of the main product. Consequently, the choice of the thermodynamic model falls on MSE for the following reasons: possibility to simulate solutions from infinite dilution down to pure solute, and high accuracy in the prediction of the properties of multicomponent systems with several concurrent solid phases. In addition, it is possible to

reproduce properties of systems with two ionic liquid phases and calculation of solid-gas (or sublimation) as well as vapor-liquid, solid-liquid and liquid-liquid equilibria are available.

The tools chosen for the analysis and the simulation of the process, possess different potentialities useful to better characterize this study and they can offset the lack of literature data in this area. Therefore, to study the reciprocal solubility of the main salts in solution, a first validation of the simulator has been performed by testing the solubility of the single salts in water with literature data [4]. As expected, the validation tests carried out demonstrated the reliability of the software, this allowed us to continue with the study of mixed salts in solution. Since the maximum temperature reached in the process is about 56 °C, solubilities of K₂SO₄ in function of percentage by weight of the NH₄Cl in solution and vice versa are studied in the range 10-60 °C as shown in **Errore. L'origine riferimento non è stata trovata.** This study is necessary as before the last crystallizer both salts coexist in an unsaturated ammonium chloride solution. In general, the greater the amount of NH₄Cl, the more K₂SO₄ remains in solution even if the trend in the left panel of Figure 1 is showing a non-monotone behavior of the solubility curve. The maximum solubility of K₂SO₄ occurs around 17% wt NH₄Cl at 55°C, while at lower temperatures the maximum shifts on greater amounts. Instead, the trend shown in the right panel of Figure 1 is monotone decreasing, indicating that as the %wt of K₂SO₄ increases in the solution, the greater is the amount of NH₄Cl that precipitates.

Hence, the two salts in solution actually influence each other, both counterproductively for the purposes of the objectives of the studied process. This explains the difficulty of the evaporative fractional crystallization since, compared to the design expectations based on salt-water solubility, less pure K₂SO₄ and a higher quantity of mixed salts are obtained.

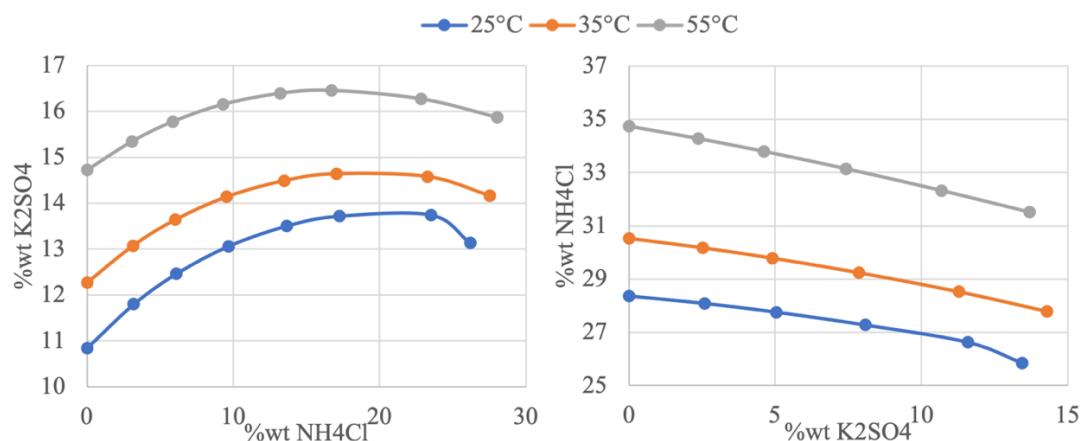


Figure 1. Trend of the solubility of the two salts with respect to the second one at different temperatures. On the left K₂SO₄ as a function of the % wt of NH₄Cl, and on the right NH₄Cl as a function of the % wt of K₂SO₄.

Once verified the combined solubility of the two salts, the entire pilot plant has been simulated to verify how the yield results are distant from the original design. The stationary batch pilot plant is simulated as a continuous process with the additional fictitious streams leaving each crystallizer. The purpose of these streams is to simulate the increase in flow rate accumulated in the various operating cycles of the equipment. The PFD of the simulated process production of K₂SO₄ as by design of the Altair pilot plant is reported in Figure 2.

The process starts with the carbonation of ammonia; the process feed constituted by a stream of 30% ammonia solution [33] (Stream 1 in Figure 2) diluted with fresh water (Stream 2) and a gaseous supply of CO₂, is sent to the reactive absorption column to obtain the production of a solution of (NH₄)₂CO₃ 2.2 M (Stream 4).

In the atmospheric batch column, the aqueous streams are recycled until a pH value of 9.4 is obtained. This value was fixed through experimental tests and selected as ammonium carbonate is formed complete, without precipitation. This unitary operation is simulated with a single state of equilibrium and the calculated pH is 8.8. In particular, the stage of equilibrium is simulated through a Flash evaporator (V-100) with an energy stream (E1) that controls the outlet temperature around the value of 50°C, counteracting the effects of the strongly exothermic absorption reaction.

The column outlet (Stream 4 in Figure 2) is sent to a first stirred reactor V-101 in which the ammonium sulfate ((NH₄)₂SO₄) is obtained through the reaction between FeSO₄ hydrate and (NH₄)₂CO₃. Also here, an energy

stream is needed (E2) to obtain the output at 25 C so that the reaction is completed correctly with a pH of 8.5. The reaction forms a by-product, solid iron carbonate, separated from the solution via a three-phase separator (SSS-100) as it represents an impurity for the final product (Stream 9).

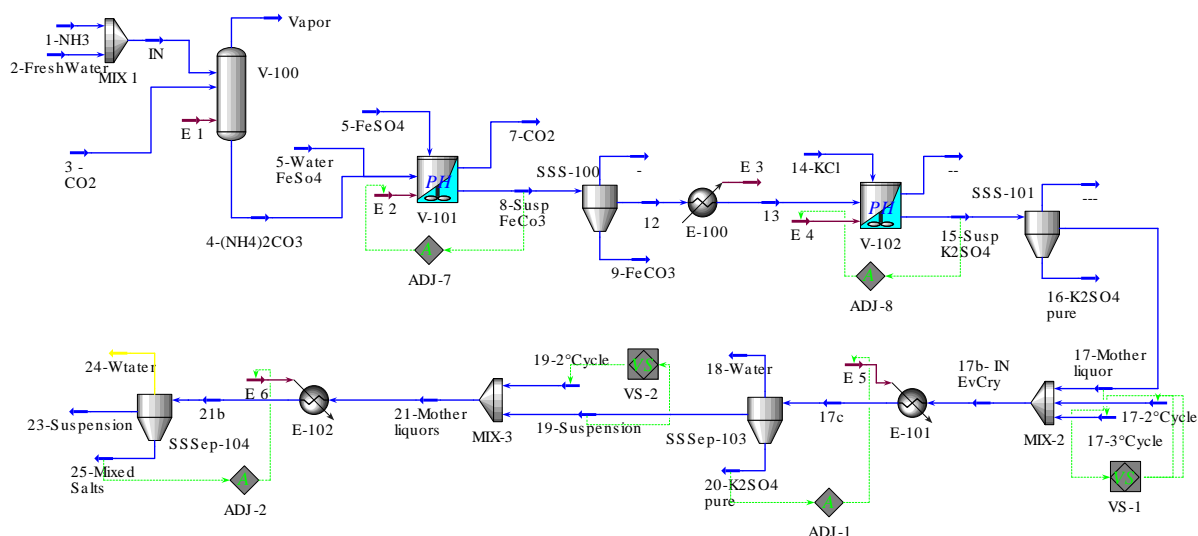


Figure 2. PFD of the K₂SO₄ pilot plant of Altair simulated with UniSim Design R470.

The suspension of (NH₄)₂SO₄ is sent to a second stirred reactor where the endothermic reaction with the potassium chloride (KCl) for the formation of K₂SO₄ takes place. Through the associated energy stream (E3) the resulting suspension (Stream 15) is maintained at 50°C for a complete formation of K₂SO₄, and then fed into a crystallizer (simulated as solid separator SSS-101) to obtain the first production of pure K₂SO₄ crystals. In real-life operation of the pilot plant, the mother liquors are stored for 3 cycles and then sent to the first evaporative crystallizer, hence two fictitious streams with the same conditions and compositions of the one leaving the stirred reactor are created in the simulator. Finally, the three streams are combined in a mixer (Mix-2) to obtain the same feed rate indicated in the reference process (Stream 17b).

The resulting stream is heated and laminated up to 10 KPa to be sent to the evaporative FC crystallizer in order to obtain more pure K₂SO₄. This phase is simulated via solid separator as the precipitation of the crystals is calculated through thermodynamic models and not as a function of the simulated equipment, while the separator allows the separation of the crystals from the solution.

The heat power of the exchanger (E-101) is varied through the logical unitary operation Adjust to avoid precipitation of the by-product NH₄Cl imposing zero its output flow. Again, the solution exiting the crystallizer (Stream 19) is stored up to the second cycle, then the same mechanism is used for its simulation. The resulting solution (Stream 21) is sent to a second exchanger (E-102) for the preheating necessary to obtain evaporation of the second evaporative crystallizer. Also in this case, the unitary Adjust operation is used to have the solid flow rate consistent with the description of the process at the output, by varying the power heat exchanger.

3. Results and discussion

The results obtained in the simulation compared with the reference values from the original design are shown in Table 1. As can be seen in Table 1., the phase of ammonia carbonation is satisfactorily simulated as the only relevant difference is in the pH value of the resulting stream slightly deviating from the reference one. On the other hand, the suspension (Stream 8) obtained for the iron carbonation coincides with the reference one also in terms of pH value. As expected, the difference between reference data and simulation results is encountered in the crystallization phases. The quantities of the products from crystallization with KCl (Streams 14/15 in Figure 2) are very similar even if the precipitation of K₂SO₄ differs by 10 kg with respect to the reference one. This is due to the possible approximations used in the design in the absence of electrochemical equilibria data that the simulator instead considers.

The thermal power used in the first evaporative crystallization is the maximum possible to avoid the precipitation of NH₄Cl, therefore the amount of pure K₂SO₄ obtained (Stream 20) is similar to the reference one, at expense of a greater amount of steam (Stream 18). Finally, having set up via the logical operation

Adjust the quantity of mixed salts to be obtained, the difference stands on the composition of the mother liquor and the amount of water evaporated. For both K_2SO_4 and NH_4Cl , the quantities are similar to the design data while the amount of water evaporated needed is almost half compared to the reference value.

To conclude, the simulated process is consistent with the design of the Altair pilot plant mostly in the early stages. The data regarding fractional crystallization, as expected, deviate from those provided. This is in fact the original design problem and approximation of the complex systems in solution. In fact, the solubility of the main product is influenced by the presence of NH_4Cl and its conditioning is difficult to predict without a complex mathematical model, such as that of the simulator.

Clearly this is not an arrival point, since *ad hoc* experiments are to be conducted on the real-life plant, but the simulation tool gives the opportunity to formulate and explore different alternative configurations possibly more efficient, or even the continuous scale-up of the system.

Table 1 Comparison between design data and simulation results for all the process phases. Quantities are expressed in kg and (aq) indicate compounds in solution.

	<i>Ammonia Carbonation</i>	<i>Iron Carbonation</i>		<i>Crystallization with KCl</i>		
	<i>(NH₄)₂CO₃(aq)</i>	<i>FeCO₃</i>	<i>(NH₄)₂SO₄(aq)</i>	<i>K₂SO₄(aq)</i>	<i>NH₄Cl(aq)</i>	<i>K₂SO₄</i>
Design	108.1	97.8	111.5	79.4	86.4	61.4
Simulation	106.7	97.71	11.52	89.11	91.3	52.48
	<i>First Evaporative Crystallizer</i>			<i>Second Evaporative Crystallizer</i>		
	<i>K₂SO₄</i>	<i>NH₄Cl</i>	<i>H₂O_{ev}</i>	<i>K₂SO₄</i>	<i>NH₄Cl</i>	<i>H₂O_{ev}</i>
Design	139.5	0	1071.4	124.5	242.7	848.9
Simulation	133	0	1202	120.2	242.26	430.9

4. Conclusions

This work focused on study the problematics encountered by a real pilot plant for an unconventional production process of pure K_2SO_4 . The presence of numerous electrolytical components in solution makes it difficult to predict how to best manage the minimization of the precipitation of by-products in the crystallization stages. The lack of literature data on the solubility of ternary solutions and the recent economical infeasibility to perform experiments, has led to analyze the fractional crystallization via rigorous process simulation. Unisim Design with OLI thermodynamic package gave the possibility to study the process by exploiting the mathematical models of the OLI package that consider complex electrochemical equilibria. Simulation results showed agreement with the original design of the plant based on solubility of binary solutions (salt-water), except for the crystallization phases. According to the simulator, less water is needed to be evaporated in the last phase to obtain the amount of mixed salts in the reference. This simulation can be the starting point for the formulation of alternative configurations. Indeed, even if the main purpose is the continuous scale-up of the system, such tool can be easily exploited to explore process variations for eventually a greater production of pure K_2SO_4 .

Acknowledgment

This work has been supported by Sviluppo Regione Toscana through the POR CREO FESR 2014 - 2020 funding program (GREEN FIELD PEAS, sub-project K_2SO_4).

References

- [1] O.G. Sheveleva, V.A. Rupcheva, V. Z. Poilov, Russ. J. Appl. Chem. 89 (1) (2016) 29–33
- [2] Y. Mubarak, Int. J. Eng.&Tech., 7:185,2018
- [3] EUROPEAN COMMISSION. Reference document on best available techniques for the manufacture of large volume inorganic chemicals - ammonia, acids and fertilisers. 2007
- [4] G. D. Perry R. Perry's chemical engineer's handbook. McGraw-Hill Education, 2007

Artificial Intelligence applied to Chemical Engineering

Luigi Piero Di Bonito^{1,2*}, Lelio Campanile¹, Mauro Iacono¹, Francesco Di Natale²

1 Dipartimento di Matematica e Fisica – Università degli Studi della Campania “Luigi Vanvitelli”

2 Dipartimento di Ingegneria Chimica, dei Materiali e della Produzione Industriale – Università degli Studi di Napoli “Federico II”

**Corresponding author E-Mail: luigipiero.dibonito@unicampania.it*

1.Introduction

Chemical engineers have found mathematical modeling to be extremely useful in understanding and creating chemical processes. However, for real systems, many of these models cannot be solved analytically and require a significant amount of processing power to for a numerical resolution. The transition towards a green and sustainable chemical industry necessitates the development of new design paradigms for flexible plants, smart molecules, and functional materials. Decades of modeling, simulations, experimental tests, and sensors deployed on chemical plants have generated huge amounts of data for Chemical Engineering (CE) community [1], adding the option of generating predictions based on experience, as an additional modeling toolbox for specialist designers. Machine Learning (ML) models are statistical and mathematical models that can "learn" from experience and find patterns in data without requiring explicit, rule-based programming. Machine learning including Deep Learning (DL) and Artificial Intelligence (AI), has the potential to overcome the constraints of mechanistic modeling: ML approaches can learn complicated behavior, model building is inexpensive, and optimization is possible. Moreover they allow modeling the structures governing the processes that generate the large data-collections, with problem-independent approaches.

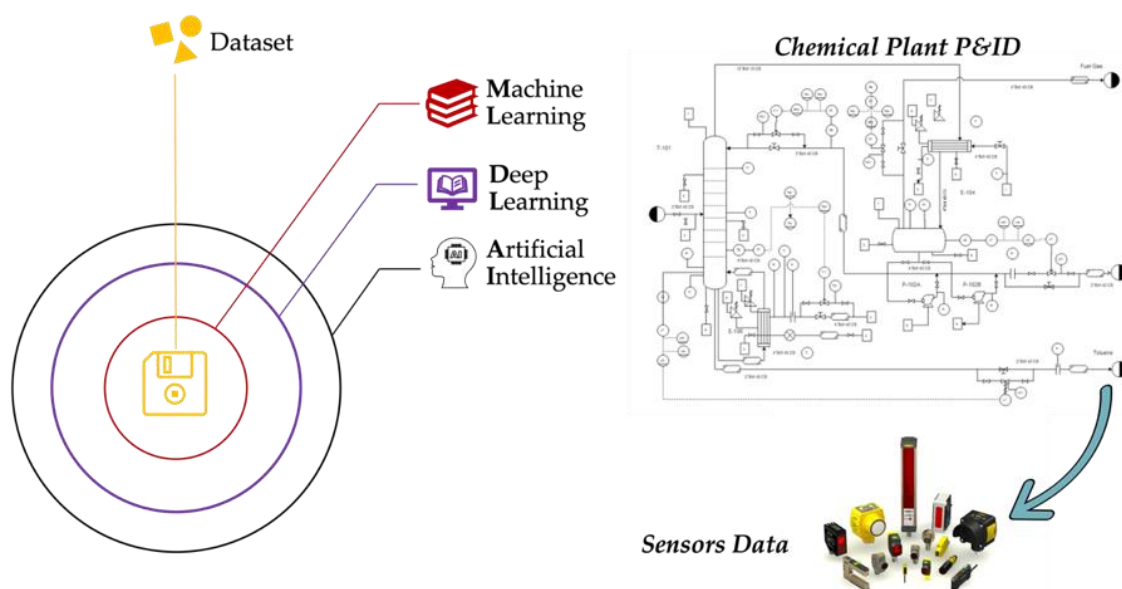


Figure 1. An example of raw materials: big data from chemical plants

This work is part of a new Italian Ph.D. Programme (funded by the PON Ricerca e Innovazione 2014-2020) aimed to development of new AI assisted methodologies for the design of chemical plants. In this paper we will present an overview of AI/ML approaches applied to CE, demonstrating how these techniques offer unique perspectives, but that only the integration between AI and CE groups can fully realize their promise.

2. Methods

The purpose of this work is an overview of the actual state of the art on ML/DL/AI methodologies used in the field of plant design and operation. The number of papers related to the application of ML/DL/AI on chemical plants has grown exponentially in the last ten years. The goal is to identify the primary study fields and applications in which they have been employed, as well as the approaches and datasets that have been collected, reorganized, and used. To achieve our goals, we explored the literature finding some paradigmatic references and our research work has been driven by the following research questions:

I. According to the literature, what types of issues have been solved?

II. What ML/DL/AI approaches are employed in these works?

III. What sort of dataset has been used?

3. Results and discussion

We decided to evaluate several aspects of this research subject, primarily to demonstrate to the chemical engineering community the potential of ML/DL/AI approaches applied to chemical processes. To succeed this goal, and in response to the first question (I), we investigated the types of issues solved using these strategies. To the best of our knowledge, there are no example of ML/DL/AI methods used for plant design, and the literature survey revealed that the majority of ML/DL/AI applications to chemical plants are related to prediction, optimization, fault diagnosis, and control issues.

For example, in terms of prediction/modeling challenges, AI has been used to predict NO_x emissions from coal-powder power plants [2] and the operation of a wet scrubber system for air pollution management [3]. In terms of optimization problems, Osuolale and Zhang [4] proposed a methodology for optimizing the energy efficiency of an atmospheric distillation unit without sacrificing product quality or process throughput, whereas Zhang et al. [5] present an AI-based real time optimization (RTO) for two chemical process examples: a Continuous Stirred Tank Reactor (CSTR) and a distillation column. Concerning control issues, after the RTO analysis, the authors successfully updated the control systems of both processes using AI approaches [5]. Al-Dunainawi and Abbod [6] established an AI based control-logic system to regulate product compositions of distillation column.

As regards fault analysis, Mamandipoor et al. [7] monitored and analysed flows and compositions of the intermediate streams of a wastewater treatment plant, while Li et al. [8] proposed a fault diagnostic system for a distillation process.

Regarding the second question (II), a classification of ML/DL approaches, which comprise AI techniques is needed, into two broad categories: supervised learning and unsupervised learning. Supervised learning approaches use labeled data to train a model with an explicit input-output structure and learn functions that translate an input to an output. Unsupervised learning refers to a set of approaches that explore "unlabeled data", or data that lack a clear input-output relationship. Table 1 resumes the artificial intelligence approaches used in the previously listed references based on this classification.

Table 1. Overview of ML/DL/AI Applied Techniques

ML/DL/AI TECHNIQUES	SUPERVISED	UNSUPERVISED	REFERENCES
Convolutional Neural Networks (CNN)	X		[2], [8]
Artificial Neural Networks (ANN)	X		[3], [5]
Bootstrap Aggregated Neural Networks (BNN)	X		[4]
Particle Swarm Optimization (PSO)	n.a.	n.a.	[6]
Recurrent Neural Networks (RNN)	X		[7]
Long-Short Term Memory Networks LSTM)	X		[7]
Deep Auto Encoders (DAE)		X	[8]

To answer the third and final question (III), it is important to quickly describe the most common datasets within CE. Chemical engineering data sources may be divided into five primary categories: 1) data from the factory, 2) data from the laboratory, 3) data from simulation, 4) data from the literature, and 5) data from the company. According to this classification, Table 2 shows what type of dataset was used in prior references.

Table 2. Kind of Dataset used in AI Applications to CE

KIND OF DATASET	REFERENCES
Plant Data	[2], [7]
Laboratory Data	[3]
Simulation Data	[4], [5], [8]

4. Conclusions

In recent years, the literature in chemical engineering has mostly explored the integration of traditional analytical models and artificial neural networks for prediction/modeling, optimization, fault detection, and control concerns based on plant, laboratory, or simulation datasets. No examples of AI based plant design have been found.

The authors envisage that in the design of chemical plants, a hybrid approach has a great advantage respect to pure ML/DL/AI methods [9]. Indeed, the conventional analytical design models developed by chemical engineering since the last century constitute a corpus of knowledge in the form of chemical-physical, balances, transport, reaction kinetics and “engineering” equations, graphs and dataset which allow to design a given

equipment (e.g., distillation towers, absorbers, mixers...) almost regardless of the specific chemical system at hand. This is the essence of the powerful concept of Unit Operations. Differently, a pure ML/DL/AI model may be exceptionally good in describing an existing process, but the design cannot be extended to different chemical systems. In a few words, its direct application to chemical plant design may push back chemical engineering development to the level of ancient alchemic recipes. Further efforts are thus needed to integrate the ML/DL/AI and conventional models to reach a better comprehension of plant design and operation, preserving the general schemes and design frameworks of Unit operations. A first example of a similar approach has been recently proposed by Napolitano et al. [10] for the case of a marine scrubber and in the review of McBride et al [9].

References

- [1] R. H. Hariri, E. M. Fredericks, and K. M. Bowers, "Uncertainty in big data analytics: survey, opportunities, and challenges," *J. Big Data*, vol. 6, no. 1, 2019, doi: 10.1186/s40537-019-0206-3.
- [2] I. Bukovský and M. Kolovratník, "A Neural Network Model for Predicting NO_x at the Mělník 1," *Acta Polytech.*, vol. 52, no. 3, 2012, doi: 10.14311/1538.
- [3] B. A. Danzomo, M. Salami, and R. M. Khan, "Artificial Neural Network Model for Wet Scrubber Performance," *Int. J. Sci. Eng. Res.*, vol. 3, no. 11, pp. 8–10, 2012, [Online]. Available: <http://www.ijser.org/researchpaper%5C%20Artificial-Neural-Network-Model-for-Predicting-Wet-Scrubber-Performance.pdf>.
- [4] F. N. Osuolale and J. Zhang, "Thermodynamic optimization of atmospheric distillation unit," *Comput. Chem. Eng.*, vol. 103, pp. 201–209, 2017, doi: 10.1016/j.compchemeng.2017.03.024.
- [5] Z. Zhang, Z. Wu, D. Rincon, and P. D. Christofides, "Real-time optimization and control of nonlinear processes using machine learning," *Mathematics*, vol. 7, no. 10, pp. 1–25, 2019, doi: 10.3390/math7100890.
- [6] Y. Al-Dunainawi and M. F. Abbod, "PSO-PD fuzzy control of distillation column," *IntelliSys 2015 - Proc. 2015 SAI Intell. Syst. Conf.*, pp. 554–558, 2015, doi: 10.1109/IntelliSys.2015.7361194.
- [7] B. Mamandipoor, M. Majd, S. Sheikhalishahi, C. Modena, and V. Osmani, "Monitoring and detecting faults in wastewater treatment plants using deep learning," *Environ. Monit. Assess.*, vol. 192, no. 2, pp. 1–12, 2020, doi: 10.1007/s10661-020-8064-1.
- [8] C. Li, D. Zhao, S. Mu, W. Zhang, N. Shi, and L. Li, "Fault diagnosis for distillation process based on CNN–DAE," *Chinese J. Chem. Eng.*, vol. 27, no. 3, pp. 598–604, 2019, doi: 10.1016/j.cjche.2018.12.021.
- [9] K. McBride, E. I. Sanchez Medina, and K. Sundmacher, "Hybrid Semi-parametric Modeling in Separation Processes: A Review," *Chemie-Ingenieur-Technik*, vol. 92, no. 7, pp. 842–855, 2020, doi: 10.1002/cite.202000025.
- [10] E. Napolitano, L. Campanile, A. Portolano, L. P. Di Bonito, and F. Di Natale, "Analysis of a marine scrubber operation with conventional and AI based methodologies," no. September, pp. 1–6, 2022.

Automated Machine Learning Framework for Surrogate Model Generation: Application to the Aspen HYSYS Process Simulator

Andrea Galeazzi^{1,2}, Kristiano Prifti^{1,2}, Flavio Manenti^{1,2*}

1 Politecnico di Milano, Dipartimento di Chimica, Materiali ed Ingegneria Chimica “Giulio Natta”, Piazza Leonardo da Vinci 32, 20133 Milano, Italy;

2 Consorzio Interuniversitario Nazionale per la Scienza e Tecnologia dei Materiali, Via Giusti 9, 50121 Firenze, Italy;

**Corresponding author E-Mail: flavio.manenti@polimi.it*

1. Introduction

A typical task of a chemical engineer is the modelling of complex systems with great accuracy. Usually, the main obstacle to overcome is the non-linearity of chemical processes which enhances exponentially the computational load required to obtain a significant solution. In the field of process systems engineering, one well-established tool created for lowering the complexity of these mathematical systems is the surrogate model [1]. Their purpose is to recreate the behaviour of a complex system through the usage of simpler mathematical tools that are easier to manipulate. For example, a simple surrogate model could be created using a polynomial equation for which it is possible to calculate its derivatives fast. This makes it possible to start using derivative-based optimization methods on systems where the derivative is either computationally costly or analytically impossible to evaluate [2].

The use case described in this work is for the complexity reduction of chemical process flowsheet simulations. In this specific case, the advantage is that by surrogating a steady-state simulation it could be possible to export the model (e.g. in C++, Python, etc.) and use it later for optimization purposes, ideally in real-time and online, without the need of using directly a licensed process simulator (e.g. Aspen HYSYS, PRO/II, gPROMS, etc.).

2. Methods

A process simulation is simplified using a surrogate model composed of many selected algorithms (i.e., in order of complexity, linear regression, second-order polynomial regression, support vector regression, decision tree, random forest, AdaBoost), chosen based on the accuracy with respect to the predicted variable and its complexity. Thus, the regressed models are evaluated with a cross-validation methodology against all the streams' predicted variables of a flowsheet simulation, and the algorithm with the smallest residual error is chosen. The variables identified for this study are the ones required to fully saturate the thermodynamic degrees of freedom of units, and in particular, streams (i.e. temperature, pressure, flow rate, and composition).

Step zero in generating a surrogate model is to choose the specific process or unit operation, or a mix of both to be approximated. It is possible to surrogate either an entire plant or a single specific piece of equipment. The drawbacks in approximating an entire plant with a lot of machinery with a single surrogate model are mainly the data generation and, consequently, the accuracy. On the other hand, surrogating only a single piece of equipment may not solve at all the problem of computational load since the units would be numerically connected as they were before the surrogate creation, thus recycle loops and other computationally intensive operations are still present.

The data generation, which is the first step, is conducted using a design of experiment (DoE) approach [4]. The analyzed domain depends on the number of existing variables and it grows exponentially larger as the number of variables increases. For this reason, surrogating a process with a high number of streams and equipment may result in a need for generating an enormous amount of process data to evaluate every possible interaction between the variables. A reasonable compromise must be found, for example by splitting a large process into several subprocesses in the case where some independence exists between one another.

3. Results and discussion

The framework described above has been applied on a steady-state digital twin (DT) of a sweetening process using diethanolamine in the exhausted oil circular refinery of Itelyum Regeneration, in Pieve Fissiraga (LO), Italy. A process flow diagram (PFD) is shown in Figure 1. The process main units are the three absorbers, one for the regeneration (REG, T-506) of the amine while the other two for high-pressure (HP, T-504) and low-pressure (LP, T-505) separation. The streams entering the process are rich in H_2S , H_2 , CO_2 , and hydrocarbons. The DT has been developed using Aspen HYSYS and the accuracy has been validated against process data coming from the distributed control system.

The process has been split into two parts, the regeneration section, and LP/HP section, thus creating two sets of surrogate models. The data generation step has been conducted using a Latin-Hypercube DoE [3] in two splits, with a total of 4000 data points for each section and a cut of 50% between each split. The first split is a domain closer to the steady-state ($\pm 10\%$) while the second one is far from the steady-state ($\pm 40\%$). The latter is also subject to convergence problems due to the possibility of encountering operating conditions that are thermodynamically unfeasible.

After the training of both surrogate models, the residual error is 2% and 5% for the smaller domains ($\pm 10\%$) of the HP/LP and the regeneration section, respectively. The error on the wider domain ($\pm 40\%$) is higher by orders of magnitude and this is caused by the unfeasibility of a high number of operating conditions which reduces the available converged solutions to a total of, e.g., 64 out of 2000 simulations, for the HP/LP section. Thus, the algorithms have a big disadvantage in that domain since there is approximately 2000 data point in the closest range so the wider range is neglected.

The resulting algorithms trained and chosen for each thermodynamic variable of the simulation are shown in Table 1. It is worth noting that simple linear regression is sometimes the better option with respect to other more advanced methods like random forests. This is especially true when there is a linear pressure drop imposed on a unit in Aspen HYSYS. Artificial neural networks have been tested but their efficacy has proven unworthy of their additional complexity and training time. For this reason and the lower accuracy, they have never been selected as the better option, as seen in Table 1.

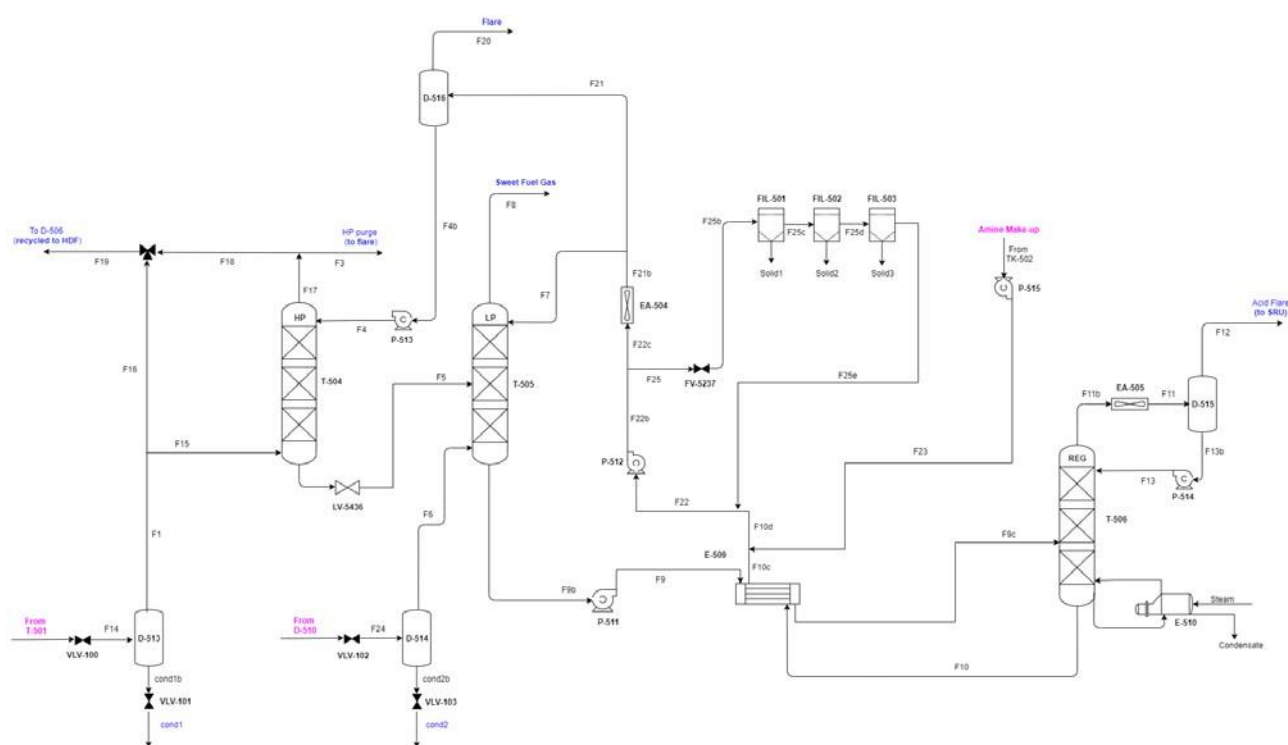


Figure 1. PFD of the amine washing section of Itelyum Regeneration exhausted oil refinery.

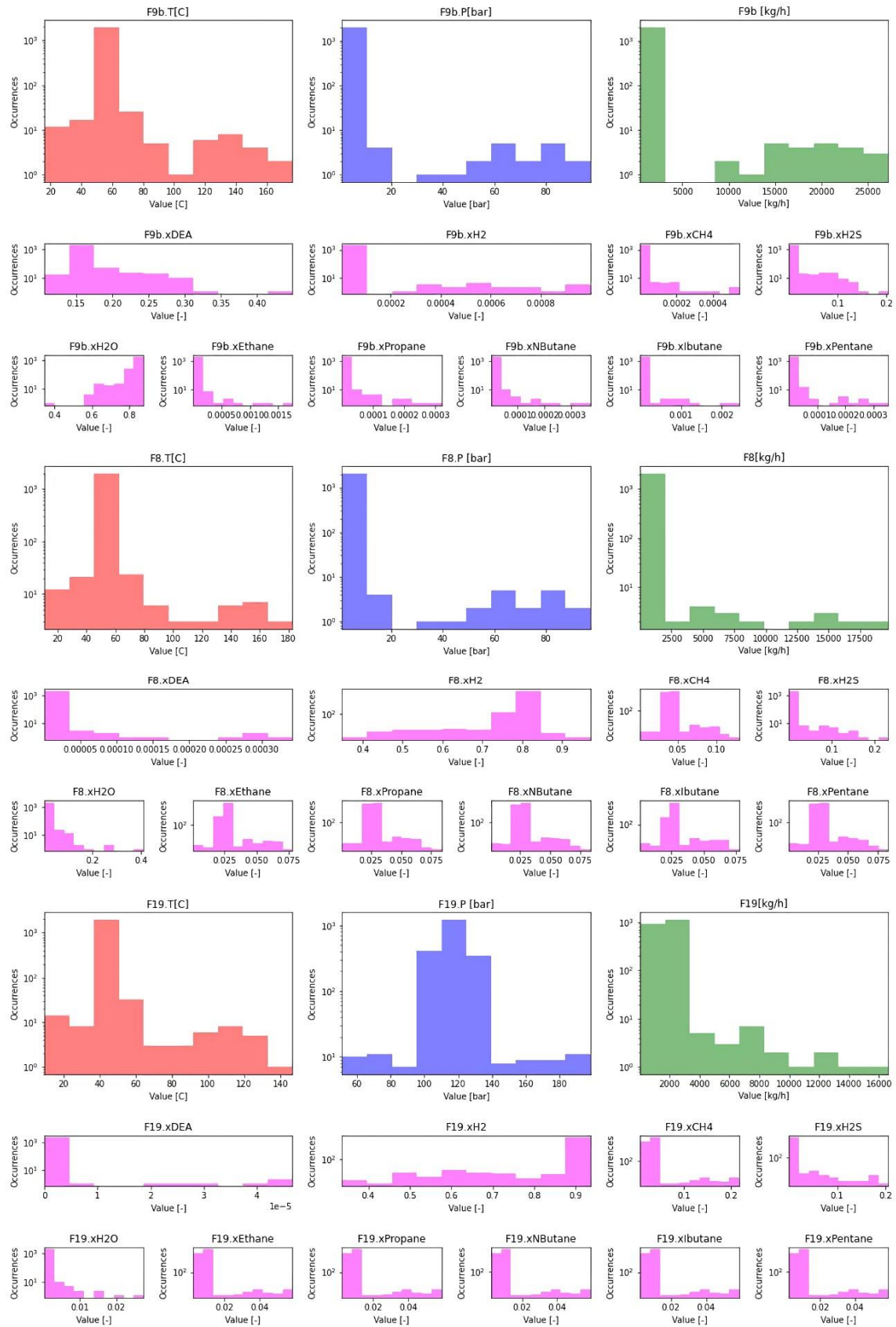


Figure 1. Histograms of the occurrences of data points in the range of process variables for several selected streams.

Table 1. Number of occurrences for each best-performing algorithm for the regenerator and HP/LP absorbers sections

	Regenerator section		Absorbers section	
	Occurrences (#)	Occurrences (%)	Occurrences (#)	Occurrences (%)
Linear regression	2	7.70%	3	7.70%
Polynomial order 2	1	3.80%	-	-
SVR	12	46.20%	-	-
Decision tree	2	7.70%	-	-
Random forest	6	23.10%	28	71.80%
AdaBoost	3	11.50%	8	20.50%

4. Conclusions

In conclusion, the surrogate modelling approach has been applied for a case study of a real industrial process. The approach described using a careful design of experiment together with domain split near and far from the steady-state operating conditions makes it possible to reduce the computational load of a flowsheet simulation, in this case, made in Aspen HYSYS, using simpler or less computationally expensive machine learning algorithms. This method could be suitable for creating surrogate models of steady-state digital twins of industrial plants, given the existence of a reliable digital twin. Thanks to the development of such a surrogate model it is now possible to subsequently perform optimization or other costly computational procedures, like, e.g., sensitivity analysis. This methodology should be further enhanced to make it able to treat dynamic digital twins. Furthermore, the final goal of this method is to substitute the need for a process simulator that generates the data and takes this data directly from the DCS of the industrial plant, automating the process of surrogate models' creation.

References

- [1] K. McBride, K. Sundmacher. *Chemie Ingenieur Technik* 91 (2019), 228–239.
- [2] A. Shokry, P. Baraldi, E. Zio, A. Espuña. *Industrial & Engineering Chemistry Research* 59 (2020), 15634–15655.
- [3] M. D. McKay, R. J. Beckman, W. J. Conover. *Technometrics* 21 (1979), 239.
- [4] J. Eason, S. Cremaschi. *Computers & Chemical Engineering* 68 (2014), 220–232.

Generalized Framework for the Simultaneous CapEx/OpEx Robust Optimization (CORO) of Production Processes Using Commercial Simulation Suites

Kristiano Prifti^{1,2}, Andrea Galeazzi^{1,2}, Flavio Manenti^{1,2*}

1 Politecnico di Milano, Dipartimento di Chimica, Materiali ed Ingegneria Chimica “Giulio Natta”, Piazza Leonardo da Vinci 32, 20133 Milano, Italy;

2 Consorzio Interuniversitario Nazionale per la Scienza e Tecnologia dei Materiali, Via Giusti 9, 50121 Firenze, Italy;

**Corresponding author E-Mail: flavio.manenti@polimi.it*

1. Introduction

During the design of a process, the most economically impactful choices are often taken with limited data and details available on the specifics of unit operations. Despite this fact, the effect that some of these choices have on the final economic performance of the plant can be dramatic and far more influential than later decisions[1]. The availability of fast and reliable preliminary cost estimations based on few key design parameters for the most common units can go a long way in improving flowsheet design. Due to the early design stage, these estimates do not need to be very accurate since errors in the range of 50% are admissible[2]. Automating the costs computation process and making the interface with the most common simulation packages standardized and easily accessible for users not accustomed to programming languages is very important in speeding up the cost evaluation of the plant and reducing the human resources tied to this task. Moreover, with such a tool it is possible to simultaneously optimize both CapEx and OpEx to reach the minimum payback time, contrarily to what is done in standard optimization routines where only the OpEx are optimized. These concepts stand at the core design of the CapEx OpEx Robust Optimizer (CORO) developed in this work. Aspen HYSYS serves as the commercial simulation package to estimate the input variable of the economic libraries. Excel is used both as a GUI (Graphic User Interface) and as a data extraction tool from Aspen HYSYS due to its widespread diffusion in industry and versatility provided by Visual Basic for Applications (VBA). The core of the computations is carried out by the proprietary process digitalization library BzzMath [3].

2. Methods

The automation process is based on three modules; the simulation package, the evaluation package, the optimization library. Each covers a standalone role and operates completely detached from the others except for a single file collecting the data in input and output of the module. The simulation package has the role of modeling the physical and chemical problem as well as the characteristic dimensions of the unit and process flowsheet with a consolidated structure. The evaluation package role is to provide a performance indicator for the optimization routine to use. The evaluation package used as a case study here is a financial key performance indicator: the payback time of the process. The optimization library role is the robust search of the minimum or maximum of the performance indicator in the system domain. The simulation package design is Aspen HYSYS V10 release. The ease of use and already included macro-enabled library for Microsoft Excel VBA allowed to develop the data extraction and writing add-on in a limited amount of time exploiting Excel spreadsheets for user data input and plotting of the results. All the data necessary for the evaluation library are organized in and eXtensible Markup Language file (.xml).

The data extracted from the simulation into the xml file are read by the CapEx/OpEx estimation BzzMath libraries. The economic libraries included in the software reach a study estimate precision on the final cost

estimation with an estimated error ranging from +30% to -25%. For the sake of direct comparison two different libraries are included: the Peter and Timmerhaus (2001) library based on percentage of delivered equipment cost and the Guthrie (1974) [1] and Turton (2012) [2] approach based on the bare module cost.

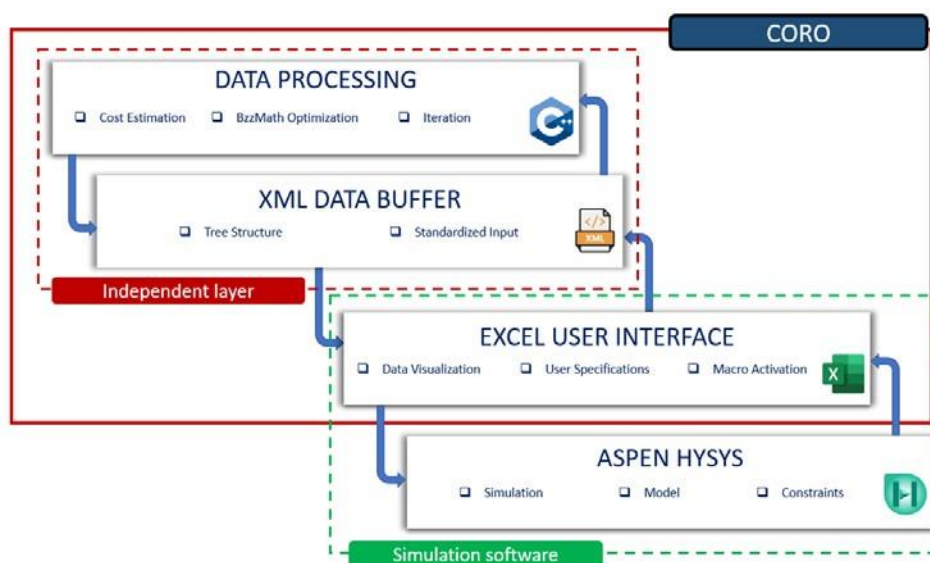


Figure 1. Data structure of the CapEx/OpEx robust optimizer

The detailed discussion on this costing approaches is not the topic of this paper and can be explored in detail in [1,2]. Both costing methods include in the Capital expenditure estimation:

- ISBL: Inside Battery Limits cost include purchasing and shipping costs of equipment, piping, catalysts, and any other material needed for final plant operation, or construction of the plant.
- OSBL: Off site battery limits are defined as utilities, common facilities, and other equipment and components not included in the ISBL definition
- Engineering and Construction: indirect expenses associated with the actual building of the plant such as supervision, engineering and legal expenses.
- Working Capital: is defined as the money required to start and run the already constructed plant until income can be obtained from the products
- Contingency: allows for variation from the predicted cost estimate

When the conventional approach to cost estimation fails due to out of boundary values then each library falls back to less precise, but more versatile methods such as the sixth tenth's rule.

4. Conclusions

A general automated framework for the evaluation of economic performance of chemical plants is shown in its structure. The overarching algorithm structure is made in such manner as to allow for further expansion with new, non economic, performance indicators and proposed as a standard to interface data between commercial software solutions and external packages.

References

- [1] G. Towler., R. Sinnott, Chemical Engineering Design. Principles, practice and economics of plant and process design, 2008.
- [2] W.W. R. Turton, J. Shaeiwitz, D. Bhattacharyya, Analysys, Synthesis, and design of chemical processes, 5th editio, Pearson, 2018.
- [3] G. Buzzi-Ferraris., F. Manenti, Comput. Aided Chem. Eng. 30 (2012) 1312–6. 10.1016/B978-0-444-59520-1.50121-4.

Hydroil, the opportunity to save leather

Omar Salmi¹, Giacomo Pacchi^{2*}, Massimiliano Franceschi³, Maurizio Maraviglia⁴, Roberto Lupi²,
 Maurizio Masi¹

1 Department of Chemistry, Materials and Chemical Engineering "Giulio Natta", Politecnico di Milano, via Mancinelli 7, 20131 Milan, Italy; 2 BCN Concerie S.p.A., via E. Fermi 25, 56029 S. Croce Sull'Arno (PI), Italy; 3 ARCHA Laboratories S.r.l., via di Tegulaia 10/A, 56121 Pisa, Italy; 4 Dermochimica S.p.A., via Euripide 27, 20864 Agrate Brianza (MB), Italy

*Corresponding author E-Mail: giacomo.p@bcn.it

1. Introduction

Leather tanning is today an important industry where a secondary raw material of the food compartment, the hide, is transformed in a relevant product for the apparel chain, that is, from a slaughter waste to a versatile luxury product. Tannery process chemically transform the perishable collagen of the raw skin in a long-time stable product under the most severe conditions of use.^{1,2} With tanned leather it is possible to produce as many as possible product like clothes, gloves, shoes, bags, wall panels, seat covers and more. As all the industrial products, tanned leather must fit the demand of sustainability well issued by the 17 goals of the UN 2030 Agenda.³ Accordingly, the main challenge for the XXI century tanneries is to guarantee the sustainability of used processes and, unfortunately, the tanning step is one of the most critical ones within the whole leather chain (e.g., because the huge amount of chemicals and water used). Today, more than 85% of the hides are tanned with metals, in particular with chromium (III) salts. These salts are not toxic but the possibility of their not voluntary oxidation to chromium (VI) salts even at level of ppm rises issue about human health.⁴ Of course, there are other ways to tan leather, like with vegetal or synthetic tannins, aldehydes, oils or resins. However, all these different recipes cannot express the process flexibility and the product quality of the chromium-based recipe. This is because the unique very stable structure that is produced by the chelation reaction between chromium (III) and collagen that creates an octahedral complex with six hydroxyl ligands as sketched in Figure 1.⁵

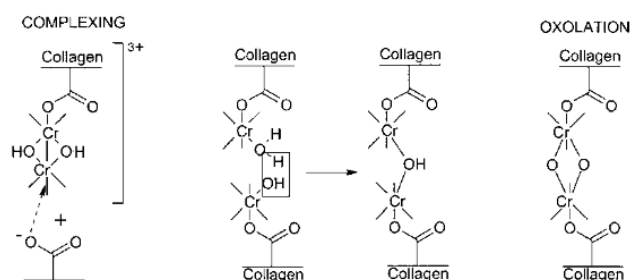


Figure 1. Complexing and oxidation mechanism of chromium.

In conclusion, there is a strong market demand for a final tanned product with the handy properties of the chromium tanned leather but obtained with a less critical process from the environmental and health issues.

Accordingly, the aim of this work is to present a new sustainable tanning agent that combine the properties described above.

2. Hydrooil

The tanning agent here under investigation has the commercial name of Hydrooil. It is a tanning agent derived from OMWW (Oil Mill Waste Water).⁶ This invention, disclosed a new kind of sustainable tanning element, derived from an environmental pollutant (i.e., OMWW)⁷ that it can be carefully dispersed in landfills because it can improve desertification⁸ for its very high COD and BOD5 values. Hydrooil transforms this toxic product in a tanning agent that can be classified as a circular economy product. Moreover, OMWW is expected to exploit important properties of olive oil and scraps contained in this waste water like: (i) antibacterial activity (important in various steps of tanning industry); (ii) tanning characteristics of polyphenolic tannins with or without other tanning reagents; (iii) antioxidant activity thanks to hydroxytyrosol and some other compounds.⁹ These characteristics, permit to use it to protect leather from different types of degradation. It is significant to remember that tannins are important tanning agents because their capacity to perform olations between their hydroxy groups and the carboxyls of the collagen as sketched in Figure 2.¹⁰ It is well known that common vegetable tannins produce time stable leathers but with a very slow mechanical flexibility than that tanned with chromium salts. Hydrooil tanning agent merge these characteristics: the leather handiness similar to that Cr(III) tanned, the product durability and the process sustainability.

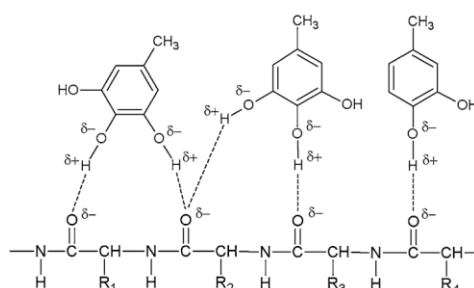


Figure 2. Olation interaction mechanism of tannins.

3. Methods

This paper will investigate the potential of this source of new tanning agent with a series of test summarized in Table 1. Different hides were processed using various recipes and then, after tanning, were tested using consolidated qualification tests, whose aims are explained in detail below. In all test the compositions are expressed in kg hides/kg bath ratio.

E1: For the evaluation of antimicrobial effect, dry hides were processed in a rotating jar mill together with OMWW at different concentration (25-50-75-100%) and water (100%). They were agitated for 2 hours at 25°C and after that, the material was left for remaining wet on a plastic bag for 24 hours. Finally, it was done a common test to evaluate the possible formation of rot; by hair pulling and smelling (evaluation of significant malodorousness or not).¹¹ The results were compared in parallel with blank test.

E2: For the evaluation of tanning capacity, the Folin-Ciocalteu and Chambort-Jamet methods were used. In particular, the first one is the most common test for polyphenols quantification, by firstly doing a basification with Na₂CO₃ and then using FCR (Folin-Ciocalteu Reagent), a mixture of phosphomolybdate and phosphotungstate; so, this solution could be analyzed by UV spectroscopy. The other method is the main one to know the capacity to absorb tanning species in hide powder. In particular, it was used standard leather Freiberg Hide Powder, bought in Forschungs institute für Leder und Kunststoffbahng GmbH in Germany. The formula for quantification of tanning capacity expressed is:

$$C.C. = \frac{c_i - c_f}{c_i} \times 100$$

Where: C.C. is tanning capacity; C_i is the starting concentration and C_f is the final concentration, after the tanning time.

E3: To know if OMWW has a microbiological inhibition activity, 10 kg calfskin hides were used in testing drums of 50 liters. These hides were previously worked in wet and Pickle phase; the product concentration was 100% and it was significant the density adjustment to 6°Be by salt. After 2 hours, hides were checked and took on a horse for a few days. So, they were ready to be tested by warm humidity conditions (climate chamber) of 40°C with 60% humidity for 7 days. Also, it was valuated Tg by the standardized method UNI EN ISO 3380.¹¹

E4: Then it was tested the capacity of OMWW to improve the metal-free tanning phase, by mixing with some other agents. One of the most important tests is using similar condition of the previous test for hides, in a batch with a pH of 2,8-2,9; 70% of product (OMWW) with 6% of glutaraldehyde, 1,5% of long chain sulfosuccinate and rolling the jars for 3 hours. After, it was added 2% of dihydroxydiphenyl sulphone and rolled for other 3 hours. Finally, it was putted inside jars 5% of tanning polyacrylic resin and rotated for 8 hours. Leathers were washed with 100% cold water, 1% sodium acetate and after a few hours wrapped in nylon bags, it was done a Tg analysis.¹²

E5: For a valuation of OMWW antioxidant activity, it was used wet-blue leather (chromium tanning) in a reproduction of retanning phase, by matching a vegetal tannin (Tara) and the Olive Mill Waste Water. After that, it was used as fatliquoring agent sulphited fish oil, really important to repeat normal passages to make a leather. The water was replaced with OMWW 150% p/p. It was used a jar, and after some rotation, leathers were left to rest for one day. Then were done drying operations on vacuum machine, hot roller machine and on air. Finally, these were submitted in strong condition to develop Cr VI, a strong carcinogenic product.¹³

- 1) 24h under UV rays at 30 cm away from a UV iron halides lamp (JELOSIL HG200 L) at 30°C with 55% of humidity
- 2) 24h in climate chamber at 60°C with humidity of 90%.

The quantification of Cr VI was done with spectrophotometric method UNI EN 17075:2008.

Table 1. summary of experimental activity used to test Hydroil tanning agent

Entry	Substrate	Phase	Instrument	Ingredients	Time	Temperature	Preparation		Evaluation test
							Time	Place	
E1	Dry hides	Soaking	Jar mill	Water + OMWW	2 h	25°C	24h	Plastic bag	Hair pulling + smelling
E2	Hide powder	Tanning	Beaker	Water + OMWW	Like the evaluation method		Folin-Ciocalteu quantification		Chambort-Jamet method
E3	Calfskin hides	Pickle	Testing drums	Water + Pickle bath + OMWW + salts	2h	rt	7 days	On a climate chamber	UNI EN ISO 3380
E4	Calfskin hides	Tanning	Jar mill	Pickle bath + OMWW + glutaraldehyde + sulfosuccinate + dihydroxydiphenyl sulphone + polyacrylic resin	14h	rt	hours	On a nylon bag	UNI EN ISO 3380
E5	Wet-blue leather	Retanning	Jar mill	Tara or OMWW + water + sulphited fish oil	1 day	rt	48 hours	Over UV lamp and on climate chamber	UNI EN 17075:2008

4. Results and discussion

E1: The evaluation of OMWW bactericide feature was done in base of tannins antimicrobial activity. In fact, these are a natural defence for fruits and vegetal tissues, thanks by the inhibition activity of bacterial cell wall synthesis and of some peculiar enzymes with a reproductive control action.¹⁴ Of course, in case of OMWW there is a difference on tannins presence, depends by: olive species, seasons and climate. But, OMWW used, had 500-10000 mg/l gallic acid determined by Folin-Ciocalteu assay (the most common polyphenol tannins quantification) and it is enough to have a strong activity. More concentration takes more bactericide activity like it was demonstrated in this first experiment. This is valuable thanks by physical tests; olfactory evaluation of malodorousness and hair pulling. The principle is: if there is a bacterial contamination, the keratinolytic activity and bad smelling are due by some products made by different species like: Bacillus, Staphylococcus and Micrococcus.

E2: For a valuation of tanning capacity Chambort-Jamet is a really important standardized method. But to do that, it must be normalize the tannins quantity on OMWW, so a previous Folin-Ciocalteu is mandatory. This assay is based on the polyphenol oxidation at pH 10, thanks by reduction activity of molybdenum and tungsten compounds.¹⁵ Then the tanning capacity has an easy principle, based on quantification of how much substances are absorbed in standard hide powder, in a beaker lab bath. It is done by weighting, at the beginning and at the end, filtrated dried tannins. The results were surprising: 82,94% phenols absorbed are quite similar to commercial wood tannins, so it exhibited a very high tanning power.

E3: The evaluation of using OMWW as preservative adjuvant against microorganisms, could be very interest for its using in another part of the process. In this case it was applied climate chamber conditions to improve microbial growth after OMWW. For a good preparation of hides, it was followed some tips like: checking thickness and permeation by lightness of bath and to increase fixation process it was putted hides on a horse for a few days. The deterioration evaluation in this case was done by smelling and observing mold formation, but without negative changes in hides. To know contraction or gelatinization temperature it was used a standardized procedure, consisting on shrinkage determination of leather sample piece by heating at a specified rate in water. The result of 60°C means an exciting tanning activity by OMWW.

E4: The chromium-free vegetal-like tanning test, can improve leather characteristics by using OMWW in an optimized procedure. The acidification permits to tannins to enter inside the material by modifying hide isoelectric point. Furthermore, an acid pH permits chelation and aggregation of phenols, so a fixed tannins improvement.¹⁶ The wrapping of leather was done to avoid excessive drying and to absorb and distribute chemicals inside. The test was done with or without PA (polyacrylic acid) and Tg was 82°C and 78°C, an enthusiastic result, considering vegetal and chromium tanning leather have 80 and 100°C. The PA prove was the best one; may be the use of polymer can improve the structure stability.

E5: At the end, an interest step for consumers health is the application of OMWW for the Cr VI decrease. This is possible thanks by the presence of some antioxidant agents inside olive drupe. They act like defending agents from different climates, rays, temperatures and humidity conditions. Without them fruits or some other vegetal products, could be more susceptible and easily altered. In fact, olive waste water protects chromium tanning leather from oxidizing conditions and the results were very encouraging (mg Cr VI/kg leather):

- Tara retanning process: 1) 6,31; 2) 5,68
- OMWW retanning process: 1) 0,29 2) 0,16

The principle of this standardized method is the extraction and quantification by a colorimetric method in presence of particular indicator, oxidized by all Cr VI presents in sample.

5. Conclusions

These results demonstrated some good characteristics of OMWW and in base of them it was developed the product Hydroil.⁶

Every single day human activities footprint becomes high and high, and linked with its, all of these days natural disaster risk increase drastically in every region of world ascertained by UNDRR (United Nations Office for Disaster Risk Reduction).¹⁷ So, it is the hour to find a solution and try to exploit this problem to a new kind of products, with important characteristics and less costs; not only for environment but also for the industry. Only with this strategy, leather and some other sector could survive and update. Hydroil is the method, the chance to do that by becoming stronger and competitive than before.

References

- [1] E. Onem, A. Yorgancioglu, H.A. Karavana, O. Yilmaz, J. Therm. Anal. Calorim. 129 (2017) 615–622
- [2] M. Tuckermann, M. Mertig, W. Pompe, G. Reich, J. Mater. Sci. 36 (2001) 1789–1799
- [3] General Assembly United Nations, (2015) A/RES/70/1
- [4] Z. Kirpnick-Sobol, R. Reliene, R.H. Schiestl, Cancer Res. 66 (2006) 3480–3484
- [5] S. Imer, T. Varnali, Appl. Organometal. Chem. 14 (2000) 660-669
- [6] Patent No. EP3494237B1, 2016
- [7] M. Elhag, J.A. Bahrawi, H.K. Galal, A. Aldhebiani, A.A.M. Al-Ghamdi Environ. Earth Sci. 76 (2017) 278
- [8] A.I. Khdaif, G. Abu-Rumman, Fresenius Environ. Bull. 4 (2017) 2537-2540
- [9] T.A. Wani, F.A. Masoodi, A. Gani, W.N. Baba, N. Rahmanian, R. Akhter, I.A. Wani, M. Ahmad, Trends Food Sci. Technol. 77 (2018) 77-90
- [10] G. Vyskočilová, M. Ebersbach, R. Kopecká, L. Prokeš, J. Příhoda, Herit. Sci. 7 (2019) 26
- [11] A. Riffel, S. Ortolan, A. Brandelli, J. Chem. Technol. 78 (2003) 855-859
- [12] B. Esteban, G. Baquero, R. Cùadros, J.M. Morera, Thermochim. Acta, 698 (2021) 178880
- [13] Q.Y. Chen, A. Murphy, H. Son, M. Costa, Toxicol. Appl. Pharmacol., 377 (2019) 114636
- [14] J.A. Field, G. Lettinga, Plant Polyphenols, 59 (1992) 673-692
- [15] C.R. China, S.S. Nyandoro, J.J.E. Munissi, M.M. Maguta, M. Meyer, M. Schroepfer, J. Leather Sci. Eng., 3 (2021) 13
- [16] A.E. Alexander, J. Soc. Leather Chem. Soc. 35 (1951) 230
- [17] Policy brief: Disaster risk reduction and climate change, United Nations Office for Disaster Risk Reduction (2021)

Scale-up of electro dialysis with bipolar membrane (EDBM) unit for valorisation of waste brine by experimental analysis

Calogero Cassaro, Andrea Culcasi, Andrea Cipollina*, Alessandro Tamburini, Giorgio Micale

Dipartimento di Ingegneria, Università degli Studi di Palermo - viale delle Scienze Ed.6, 90128 Palermo, Italy;

**Corresponding author E-Mail: andrea.cipollina@unipa.it*

1.Introduction

The valorisation of brines, of both natural and industrial origin, represents one of the most important challenges of modern society. Another equally desirable aspect concerns achieving a circular economy within various industrial processes to make the process itself more sustainable, from an economic and environmental point of view. The bipolar membrane electro dialysis (EDBM) process is particularly suited to achieving these goals [1]. It is an electro-membrane process that can valorize waste brines and produce acid and alkaline solutions, which can be recirculated inside the equipment located upstream/downstream. The bipolar membranes, which allow the dissociation of water into H^+ and OH^- ions, play a critical role. These ions, in turn, combine with those of the salt present in the waste brine, resulting in high value-added chemicals. The enormous potential inherent in this technology has piqued the European Community's interest. The European project H2020 WATER-MINING, in particular, has integrated this technology into a pilot-scale demonstrative treatment chain. The goal of using the EDBM is to produce chemicals in-situ, allowing for resource circularity and, ultimately, waste minimization. This work aims to design of an EDBM stack at the pilot scale exploiting the data collected by a laboratory-scale unit, with operating conditions similar to those of an industrial context.

2. Methods

The experiments were conducted using a Fumatech® laboratory unit equipped with FAB®, FKB®, and FBM® membranes, as well as PVC/ECTFE spacers. Five repeating units were used to assemble the stack. The experiments were carried out in closed-loop mode (i.e., with recirculation) to achieve a target concentration of 1M NaOH in the base compartment. The saline compartment was initially filled with 1.5M or 2M NaCl solutions, while the acid and base compartments were filled with 0.05M HCl and NaOH, respectively. The experiments were carried out galvanostatically with current densities ranging between 100 and 300 $A m^{-2}$. The identification of the best operating condition for the laboratory-scale stack allowed the calculation of parameters independent of the membrane surface. These parameters, along with the design constraints, were then inserted into a mathematical algorithm that provided the design of the equipment at the pilot scale.

3. Results and discussion

The results show that the tests at 200 $A m^{-2}$ and a salt input concentration of 2M are the best compromises between NaOH Specific Energy Consumption (SEC) and current efficiency. Indeed, this operating condition has a current efficiency of 79.9 percent, similar to the 80.8 percent obtained in the tests at 300 $A m^{-2}$. Excellent results were also achieved in terms of the relationship between real time and theoretical test time. This in fact, at 200 $A m^{-2}$, turns out to be equal to 1.25 which is close to the 1.2 obtained at 300 $A m^{-2}$. However, the specific consumption at 200 $A m^{-2}$ is equal to 1.27 $kWh kg^{-1}_{NaOH}$, which is comparable to the SEC obtained at 100 $A m^{-2}$. Furthermore, using a salt input concentration of 2M allows for the achievement of and exceeding the NaOH target.

The developed mathematical algorithm enabled the design of the EDBM pilot plant to be identified. The results show that a total membrane area of 6.71 m² is required to produce 500 moles of NaOH (corresponding to a solution of 500 liters and a NaOH concentration of 1M) over a 5h process time.

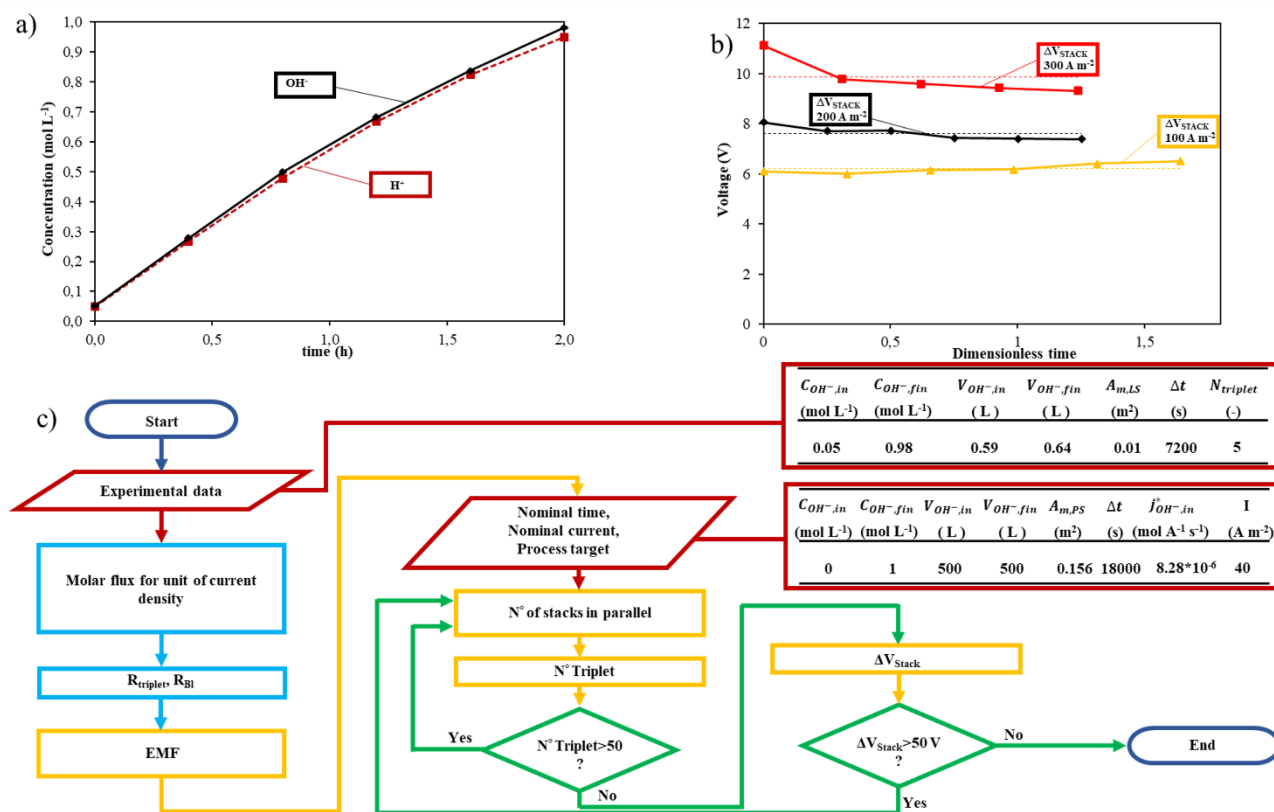


Figure 1. Illustration of the main results achieved. a) H⁺ and OH⁻ concentration profiles, b) voltage of the stack at three different applied current densities, c) Flowchart of the mathematical tool used for the design of the pilot plant.

4. Conclusions

This study investigated an EDBM unit on a laboratory scale, providing important insights into the best trade-off of process conditions in terms of current density and solution composition. Finally, this work resulted in the design of a pilot-scale EDBM stack that will be built and installed as part of a waste brine treatment chain, which is one of the main goals of EU project WaterMining. These studies may enable this system to progress from a Technology Readiness Level (TRL) of 4 to 7, laying the groundwork for future industrialization.

5. Acknowledgement

This project has received funding from the European Union’s Horizon 2020 research and innovation program under Grant Agreement no. 869474 (WATER-MINING – Next generation water-smart management systems: large scale demonstrations for a circular economy and society). www.watermining.eu.

References

- [1] L. Gurreri, A. Tamburini, A. Cipollina, and G. Micale, “Electrodialysis applications in wastewater treatment for environmental protection and resources recovery: A systematic review on progress and perspectives,” *Membranes*, vol. 10, no. 7. 2020. doi: 10.3390/membranes10070146.

Detailed Understanding of Transport Mechanisms during Sr²⁺ and Cs⁺ Adsorption onto Cryogels via Application of Rigorous Diffusion Models

Alzhan Baimenov¹, Marco Balsamo^{2*}, Vassilis Inglezakis³, Fabio Montagnaro²

¹ National Laboratory Astana, Nazarbayev University, Nur-Sultan, 010000, Kazakhstan

² Department of Chemical Sciences, University of Naples Federico II, Complesso Universitario di Monte Sant'Angelo, 80126 Napoli, Italy

³ Department of Chemical & Process Engineering, University of Strathclyde, Glasgow, G1 1XJ, UK

*Corresponding author E-Mail: marco.balsamo@unina.it

1. Introduction

The removal of heavy metals and radioactive elements from wastewaters is nowadays imperative to reach the goals of a sustainable development. In this context, adsorption is a consolidated purification technology characterized by generally low costs and high operating flexibility. In particular, polymeric cryogels are emerging adsorbents with high potentiality for the removal of different classes of adsorbates from liquid phase thanks to their tunable chemico-physical and microstructural properties [1]. Limited rigorous analyses on the complex transport mechanisms occurring along adsorption in porous sorbents are currently available in the literature (and, in particular, for cryogels), and most of the adopted dynamic models rely on empirical expressions [2].

In this work we investigate the batch adsorption dynamics of strontium and cesium ions onto two cryogels, and a detailed analysis of kinetic results was attained by adopting a rigorous diffusional model accounting for fluid film, pore volume and surface transport mechanisms coupled with a time-dependent expression for surface diffusivity.

2. Methods

Two kinds of cryogels (termed as AAC and SAC) were synthesized by means of free-radical polymerization performed at sub-zero temperatures [3]. Batch kinetic adsorption tests were performed at room temperature and by fixing both the initial concentration of Sr²⁺ and Cs⁺ ions (100 mg L⁻¹) and the sorbent mass/solution volume ratio (0.7 g L⁻¹). The time trend of the sorbent specific adsorption capacity $\overline{q}(t)$ was evaluated by monitoring the evolution of each metal ion concentration in the liquid phase via ICP-MS technique. Kinetic data were analyzed by means of the rigorous Pore Volume Surface Diffusion model (abbreviated as PVSDM [4]), in which we adopt our recently proposed fractal-like expression for surface diffusivity [5] (model named PVSDM-MBI):

$$\frac{1}{D_s(t)} = \frac{1}{D_{s0}} \left[\frac{\beta}{(t+1)^{-h}} + \frac{(1-\beta)}{(t+1)^\alpha} \right] \quad (1)$$

where $D_s(t)$ and D_{s0} are the time-dependent and zero-loading surface diffusion coefficient, respectively; β , h and α represent the fractional contribution of the fractal diffusion resistance, the fractal and hopping exponent, respectively. The resolution of ordinary and partial differential equations was carried out in the MATLAB R2019b numerical environment by adopting the method of lines.

3. Results and discussion

Figure 1a) reports, as an example, a comparison between experimentally and theoretically determined dynamic adsorption profiles for strontium capture onto AAC cryogel. In general, the PVSDM (with constant surface diffusivity) and PVSDM-MBI did not provide significant differences in the interpretation of $\overline{q}(t)$ vs. t trends, with the latter model providing a slightly better fitting accuracy, in particular when Cs⁺ and Sr²⁺ adsorption onto AAC is considered. Dynamic results highlighted that, for each adsorbent material, the capture rate for

cesium is greater than in the case of strontium, which can be ascribed to the greater value of the molecular diffusivity for the former ion. A comparison of the adsorbent materials, at fixed adsorbate species, revealed that the adsorption dynamics is faster for AAC when compared to SAC cryogels, due to more rapid fluid film, pore, and surface transport mechanisms. For instance, in the case of cesium capture onto AAC, the mean integral value of the fractal-like surface diffusivity is $5.43 \times 10^{-11} \text{ m}^2 \text{ s}^{-1}$, a figure about 1.3 times greater than the value retrieved for SAC. Modelling results according to the PVSDM–MBI also allowed to observe that, for all the investigated systems, the surface diffusivity exhibits a non-monotonic pattern in time with the occurrence of a maximum (see Figure 1b)). This demonstrates that the hopping contribution (increasing term of $D_s(t)$ in Eq. (1)) to surface transport prevails in the first stages of the adsorption process, whereas the fractal contribution (the time-diminishing term associated with hindered surface transport) rules thereafter. An analysis of results based on the average Biot number $\overline{Bi}(t)$ values (cf. [2]), witnessed that both fluid film and intraparticle transport resistances regulates the adsorption dynamics (the latter with a comparatively higher relevance) for the systems AAC-Sr²⁺, SAC-Cs⁺ and SAC-Sr²⁺ (with $\overline{Bi}(t)$ varying from 14 to 20). In the case of cesium adsorption onto AAC, intraparticle diffusion is significantly slower than the transport of the adsorbate in the fluid film ($\overline{Bi}(t)$ equals to 167). Finally, both surface and pores diffusion resistances are relevant for the intraparticle transport of Cs⁺ and Sr²⁺ ions.

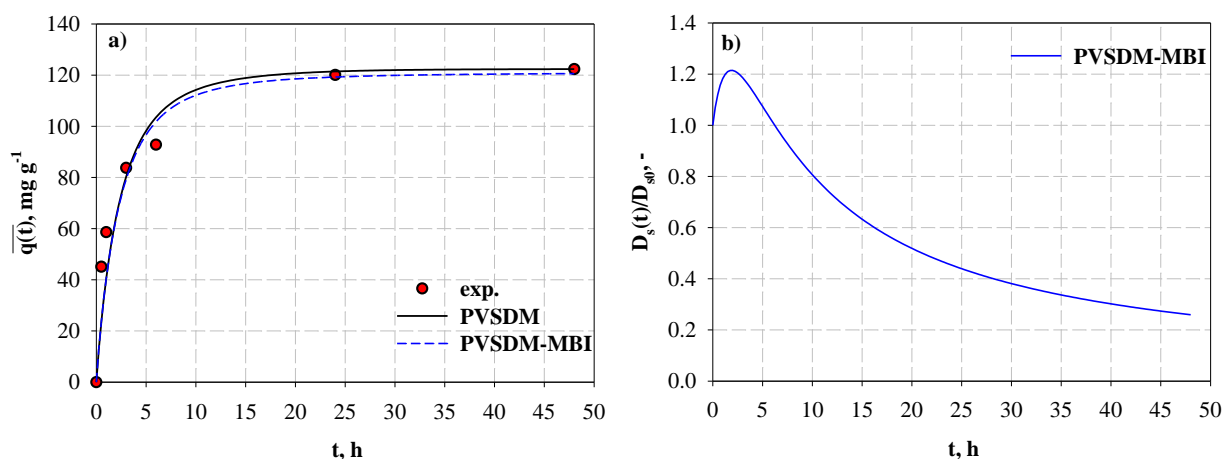


Figure 1. a) Comparison between experimental and theoretical kinetic adsorption patterns for the system AAC-Sr²⁺; b) Surface diffusivity ratio as a function of the adsorption time predicted by PVSDM–MBI for AAC-Sr²⁺.

4. Conclusions

In this work, the removal of strontium and cesium ions from liquid phase by adsorption onto two cryogels (named AAC and SAC) was investigated. Batch adsorption tests showed that the equilibrium removal efficiency of Sr²⁺ was 86% and 48%, for AAC and SAC, respectively. In the case of cesium, AAC attained a final removal efficiency of 58%, while 63% was reached for SAC sorbent. Mathematical modelling of dynamic capture results, according to a rigorous diffusional model accounting for all transport resistances, highlighted that the inclusion of a fractal-based expression for surface diffusivity is able to provide a very satisfying fitting accuracy. Moreover, surface diffusivity exhibits a non-monotonic pattern with the occurrence of a maximum in the time domain. Finally, the analysis of the average Biot number revealed that, in general, both external and intraparticle transport resistances are important, with the latter being comparatively more limiting in the capture process.

References

- [1] A. Baimenov, D.A. Berillo, S.G. Pouloupoulos, V.J. Inglezakis, *Adv. Colloid Interface Sci.* 276 (2020) 102088.
- [2] V.J. Inglezakis, M. Balsamo, F. Montagnaro, *Ind. Eng. Chem. Res.* 59 (2020) 22007–22016.
- [3] A. Baimenov, D.A. Berillo, V.J. Inglezakis, *J. Mol. Liq.* 299 (2019) 112134.
- [4] R. Ocampo-Pérez, R. Leyva-Ramos, M. Sanchez-Polo, J. Rivera-Utrilla, *Adsorption* 19 (2013) 945–957.
- [5] V.J. Inglezakis, M. Balsamo, F. Montagnaro, *Processes* 8 (2020) 1–11.

CO₂ sorption and diffusion in Fluorinated polymers for carbon transport application

Virginia Signorini^{1*}, Marco Giacinti Baschetti¹, Matteo Minelli¹

1 Department of Civil, Chemical, Environmental and Material Engineering (DICAM), Alma Mater Studiorum, University of Bologna, Via Terracini, 28, 40131 Bologna, Italy;

**Corresponding author E-Mail: virginia.signorini2@unibo.it*

1. Introduction

Polymeric materials play a relevant role in the protection for gas transport equipment (such as pipeline, pumps, vessels, compressor..), and they can thus be used in the value chain of Carbon Capture and Storage (CCS), which is considered as the most viable solution to limit the CO₂ emission in the atmosphere, with the potential to be applied at short-medium times [1]. Among the various classes of polymers, fluorinated material look promising for their potential application for CO₂ transport, either in pipelines or in ship vessels, due to their excellent thermal and chemical resistance [2,3].

This work explores the sorption and diffusion properties of three different fluorinated polymers (PVDF, PTFE and PVF) when they are exposed to Carbon Dioxide, since their industrial applicability is related to their barrier behaviour and their intrinsic mechanical response. In fact, industrial carbon transport chain requires to deal with dense CO₂ phases, either in its supercritical or in liquid state, which can affect the performance of the materials due to a physical change in their structure.

2. Methods

The materials characterized in this study for the CO₂ sorption are three commercial grades of fluorinated-based polymers (Table 1): polyvinylidene fluoride (PVDF), poly-(tetrafluoroethylene) (PTFE) and Polyvinyl fluoride (PVF).

The sorption experiments have been performed at 35°C in a fixed volume and variable pressure system, temperature controlled by a thermostatic bath. The sample is inserted into a cell and connected to a pre-chamber volume where the gas is loaded to the desired pressure. The CO₂ solubility in the polymer is then evaluated by considering the pressure variation during the gas absorption in the sample. The gas diffusivity in the polymer matrix is then calculated for each sorption step considering the Fick's law of diffusion.

The experimental results of CO₂ solubility in PVDF, PTFE and PVF have been modelled via thermodynamic model (Lattice Fluid equation of state [4]), whose optimization parameters for the three materials are reported in Table 1, obtained by the resolution of phase equilibrium problem, aiming to be able to predict both gas sorption and transport under different operating conditions. The ultimate goal of this work is indeed to inspect penetrant-polymer characteristic interaction and the polymer behaviour.

Polymer	ρ [g/cm ³]	Thickness [μm]	App Tg [°C]	App Tm [°C]	T* [K]	p* [MPa]	ρ^* [kg/L]
polyvinylidene fluoride (PVDF)	1.77	50	-35	180	630	620	1.79
poly-(tetrafluoroethylene) (PTFE)	2.20	50	120	330	629	388	2.16
Polyvinyl fluoride (PVF)	1.44	50	40	200	670	660	1.42

Table 1. Material properties and optimization parameters (T*, p*, ρ^*) for Lattice fluid EoS model [5]

3. Results and discussion

The results of the experimental CO₂ sorption in commercial PVDF, PTFE and PVF at 35°C are illustrated in Fig. 1 as a function of the pressure. The solubility behaviours observed are linear in all cases, with PVDF showing the larger uptake, followed by PVF and PTFE which results to have the lower solubility.

Their behaviour is then described by the thermodynamic Lattice fluid EoS model (continuous lines), which is able to represent the experimental results, and can be used for predictive purposes at lower temperatures and/or larger pressures. Figure 1b reports the diffusivity coefficient obtained from transient CO₂ sorption. In such fluorinated polymers, the diffusion coefficient increases by increasing the CO₂ concentration, following an exponential law with CO₂ mass fraction, as a direct consequence of the plasticization of the polymer matrix.

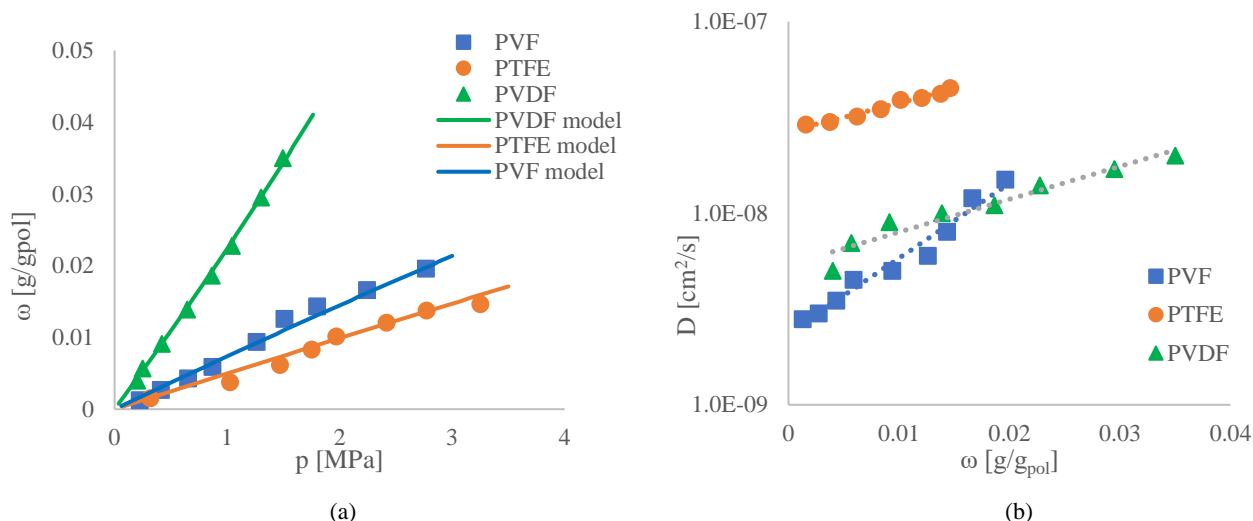


Figure 1. CO₂ solubility (a) and diffusivity (b) in PVDF, PVF, PTFE as obtained from sorption experiments and comparison with thermodynamic model for gas sorption

4. Conclusions

This experimental work characterizes the CO₂ sorption behavior in three commercial polymers PVDF, PTFE and PVF, potentially suitable as materials for CO₂ transport process, in view of their use in CO₂ transport to ensure the safe deployment of CCS. From the experimental CO₂ sorption data at room conditions, following a rigorous physically sound model, it is possible to evaluate thermodynamic and kinetic parameters, such as Solubility, Diffusivity and Permeability. That allows the penetrant-polymer interaction and the effect of dense phase CO₂ on polymer-based materials to be understood, as well as proving essential performance information for targeted applications.

Moreover, by fitting those sorption data through a thermodynamic model, based on EoS, it is possible to describe and predict the molecular behaviour of these commercial polymers in wide temperature and pressure ranges, including super-critical conditions, relevant for CO₂ transport application, and to evaluate their future use in industrial applications.

Acknowledgment

The authors acknowledge the financial support of the Research Council of Norway, under grant 308765.

References

- [1] D.Y.C. Leung, G. Caramanna, M.M. Maroto-Valer, An overview of current status of carbon dioxide capture and storage technologies, *Renew. Sustain. Energy Rev.* (2014). <https://doi.org/10.1016/j.rser.2014.07.093>.
- [2] L. Ansaloni, B. Alcock, T.A. Peters, Effects of CO₂ on polymeric materials in the CO₂ transport chain: A review, *Int. J. Greenh. Gas Control.* 94 (2020) 102930. <https://doi.org/10.1016/j.ijggc.2019.102930>.
- [3] R.W. Baker, B.T. Low, Gas separation membrane materials: A perspective, *Macromolecules.* 47 (2014) 6999–7013. <https://doi.org/10.1021/ma501488s>.
- [4] M. Minelli, G.C. Sarti, 110th Anniversary: Gas and Vapor Sorption in Glassy Polymeric Membranes - Critical Review of Different Physical and Mathematical Models, *Ind. Eng. Chem. Res.* 59 (2020) 341–365. <https://doi.org/10.1021/acs.iecr.9b05453>.
- [5] Zoller and Walsh, Standard pressure–volume–temperature data for polymers, Techn. Publishing Company, 1995.

CFD simulation and Convolutional Neural Networks Modelling for Flow and Transport in Porous Media

Agnese Marcato^{1*}, Gianluca Boccardo¹, Daniele Marchisio¹

1 Department of Applied Science and Technology, Politecnico di Torino, Torino, Italy

**Corresponding author E-Mail: agnese.marcato@polito.it*

1. Introduction

The modelling of flow and transport in porous media finds application in many fields of interest in chemical engineering such as packed bed catalytic reactors, carbon capture and storage, and battery modelling. Even though the nature of porous media is different in these applications – catalytic beads, rocks and electrodes – the modelling methodologies can be transferred from well established fields to new ones. Computational fluid dynamics (CFD) has been successfully employed for both macroscale and microscale modelling of porous media systems, thanks to the increasingly high performance computing resources available for research. Even though the simulations are feasible, the time required for their solution can take hours on multiple cores, so they cannot easily find application in multiscale modelling or optimization problems. The training of data-driven models can be useful to obtain fast models that can be employed without the need for new expensive simulations. Machine learning models can be trained for this purpose, in this work neural networks have been chosen since they can generalize well nonlinear problems and can be used when analytical correlations cannot be obtained for complex physical systems.

Neural networks must be trained on a dataset made by CFD simulations, which must explore the range of conditions of interest for generalization to new cases. The first step in the workflow [1] is the creation of a dataset based spanning the range of variation of the features that will be the input of the neural networks. A portion of the dataset is employed for training of the models, while another portion is used to test the generalization capability of the model itself.

The porous media systems in this work are sphere packings, the physics studied is flow in laminar conditions and the transport of a scalar that is consumed on the grains surface. This system models the transport of a colloid filtered by the grains or equivalently an instantaneous reaction on the grains surface, but the transport equations solved are the same that describe other physical systems of interest in the porous media and chemical engineering community, like the lithiation and de-lithiation in Lithium-ion batteries.

Depending on the prediction objectives and the input data it is possible to choose the most appropriate neural network architecture. If the objectives are numerical values, it is easily possible to transfer well established architectures from the data science community. Depending on the kind of input data, fully connected neural networks (FCNN) and convolutional neural networks (CNN) can be trained, in the first case the inputs are numerical values, instead in the second case the inputs are images (either 2D or 3D). For using FCNN it is necessary to hand-select the features which are the most effective for the prediction of the outputs, on the contrary CNN can grasp autonomously from the images the features to obtain an accurate output.

If the data-driven model objectives are fields, so image-like outputs, the neural networks architectures are more challenging to conceive. Some recent works propose neural networks for the flow field prediction in porous media systems [4]. To the authors knowledge little was done to extend the use of these models beyond the flow prediction, and generally to geometric and flow-related parameters, like the permeability. The extension of these models to transport or, generally, to more complex physical phenomena could find applications in the above-mentioned fields of chemical engineering, where multiphase and/or reactive systems are commonly studied.

In this work a rigorous setup of the CFD simulations is presented, as well as the technical issues related to the creation of the dataset. After that both FCNN and CNN were employed for the prediction of the permeability and the filtration rate in porous media. Particular attention was paid on the hyperparameter tuning of the neural

networks and on the effect of the dataset width on the prediction accuracy. The preliminary results for the prediction of concentration fields are presented.

2. Methods

The geometries employed for the CFD simulations are sphere packings, these realizations were created by means of the discrete element method implemented in toolbox Yade and they differ for the mean diameter and the standard deviation of the grains size distribution. The CFD simulations were solved by using the finite volume method implemented in the open-source toolbox OpenFOAM. A grid independence study is performed in order to build the mesh, after that the Navier Stokes and the continuity equations are numerically solved [1]:

$$\frac{\partial U_i}{\partial t} + U_j \frac{\partial U_i}{\partial x_j} = -\frac{1}{\rho} \frac{\partial p}{\partial x_i} + \nu \frac{\partial^2 U_i}{\partial x_j^2} \quad (1)$$

$$\frac{\partial U_i}{\partial x_i} = 0 \quad (2)$$

where U is the velocity, ρ is the density, ν is the viscosity, p is the pressure. A pressure drop between inlet and outlet is imposed as boundary condition for the pressure.

The fluid simulated is water (incompressible and Newtonian) at room temperature, the filtration simulation is a passive scalar transport governed by the advection diffusion equation:

$$\frac{\partial C}{\partial t} + U_j \frac{\partial C}{\partial x_j} = \frac{\partial}{\partial x_i} \left(D \frac{\partial C}{\partial x_i} \right) \quad (3)$$

where C is the concentration, and D is the diffusion coefficient. An inlet unitary concentration is set as boundary condition, and a null concentration on the grains surface.

The permeability is calculated from the CFD simulations results by the well-known Darcy's law, and the filtration rate is calculated by a relation obtained by volume averaging of the advection diffusion equation [3]:

$$K_f = \frac{F_{tot}^{in} - F_{tot}^{out}}{\langle C \rangle V}$$

where F is the total flux, $\langle C \rangle$ the volume-averaged concentration, and V is the porous media volume.

Concerning the data-driven models, the neural networks were trained and tested by using the Python's libraries Keras, Tensorflow and Pytorch. The FCNN receive as input the mean diameter and the standard deviation of the distribution, the porosity, the pressure drop across the porous medium and the diffusion coefficient, for the prediction of the permeability and the filtration rate. The tuning of the model was performed varying the learning rate and the architecture, i.e. the number of hidden layers and the number of neurons per layer. Concerning instead the CNN, the input is the entire porous media geometry for the prediction of the permeability, instead for the prediction of the filtration rate a multi-input CNN was conceived, in fact, the geometry together with the operating conditions numerical value (pressure and diffusion coefficient) were the inputs to the network. For the tuning of these models we focused on a preliminary choice of the architecture, and then on the effect of the input scaling and of the learning rate. Since the creation of the dataset for the training of neural networks is the most computationally expensive step of the workflow, the minimum number of samples necessary to obtain a satisfactory generalization accuracy was explored training the networks with a decreasing number of samples.

The neural networks models for the prediction of entire fields were elaborated starting from the multiscale convolutional neural network architecture developed by Santos et. al. [4], choosing the most appropriate features for the concentration field prediction. The pressure drop, the diffusion coefficient and the time of flight between the inlet and the outlet are the most effective features that lead the network to generalize accurately to new geometries.

3. Results and discussion

In Figure 1 two contour plots of the flow field and the concentration field are proposed for a sample of the dataset. In the concentration field contour, it is possible to appreciate the boundary conditions set for the solution of the advection diffusion equation. The time required to obtain a complete sample is around 15 hours, considering the creation of the mesh, the Navier-Stokes and the advection diffusion equation solution on OpenFOAM in single core.

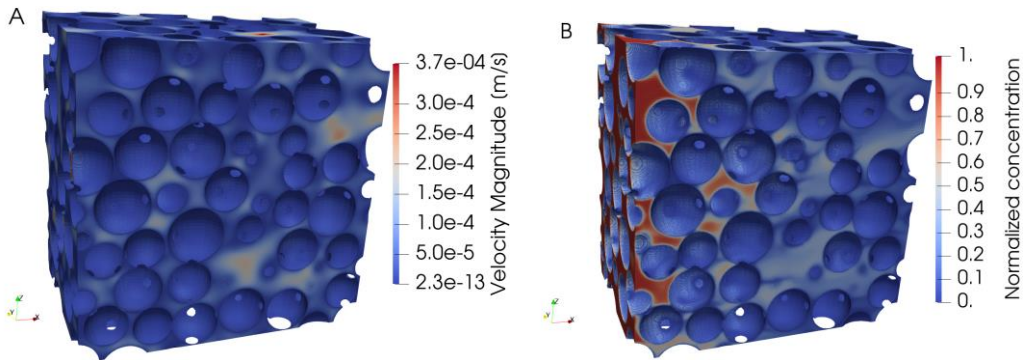


Figure 1. Contour plot of the flow field (A) and the concentration field (B)

The number of CFD simulations to be solved to obtain an accurate data-driven model is a question we focused in this study. In Figure 2 the average error and the maximum error on the test set is shown as a function of the dataset width. Using the complete dataset, the permeability was predicted with an average error lower than 2.5%, the filtration rate was predicted with an average error lower than 5%. These results can be achieved with a dataset of at least 100 CFD simulations. The time required for the training of the FCNN takes about 30 minutes, the training of the CNN on the full dataset take around 4 hours on GPUs nVidia Tesla V100. Instead, the prediction of a new sample is almost instantaneous.

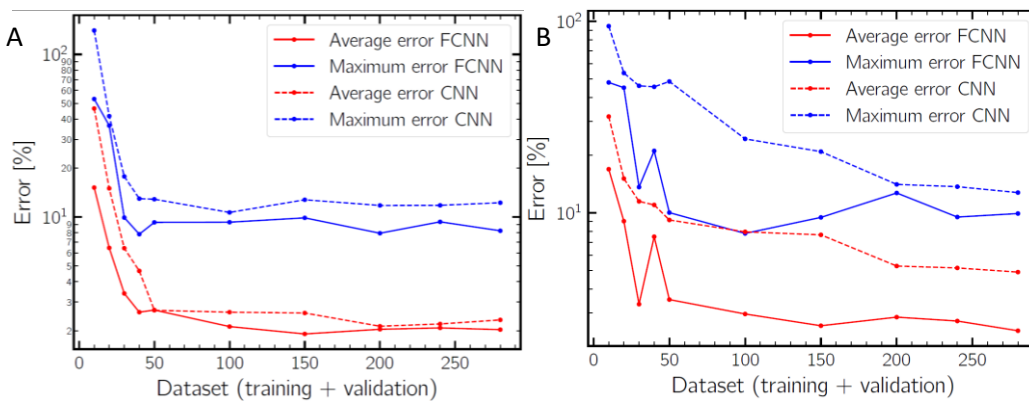


Figure 2. Average error on the test set for the prediction of the permeability (A) and the filtration rate (B)

In Figure 3 is reported a preliminary result on the prediction of the concentration field on a sample of the bidimensional dataset presented in our previous work [1]. It is possible to notice that the field is qualitatively well predicted by the CNN.

4. Conclusions

The use of neural networks is promising in porous media modelling, since the data-driven models trained can rapidly predict new inputs, so they can find application in multiscale modelling and optimization problems. For this reason, the models must be tuned in order to acquire the highest generalization capability on new

samples, the choice of the best hyperparameters and the construction of a dataset wide enough are essential to obtain a good data-driven model. Even though the training of FCNN is less expensive and the predictions are quite accurate, CNN represent a powerful tool for future applications, in fact, for more realistic geometries it would be hard if not impossible to hand select the most effective geometrical features for the output predictions.

Our objective for the future is to develop a workflow for the prediction of entire fields for complex physical phenomena in porous media such as the transport of a chemical species, in this case it is not sufficient to provide the neural network with only the geometry since the boundary conditions and specifically flow direction play an important role.

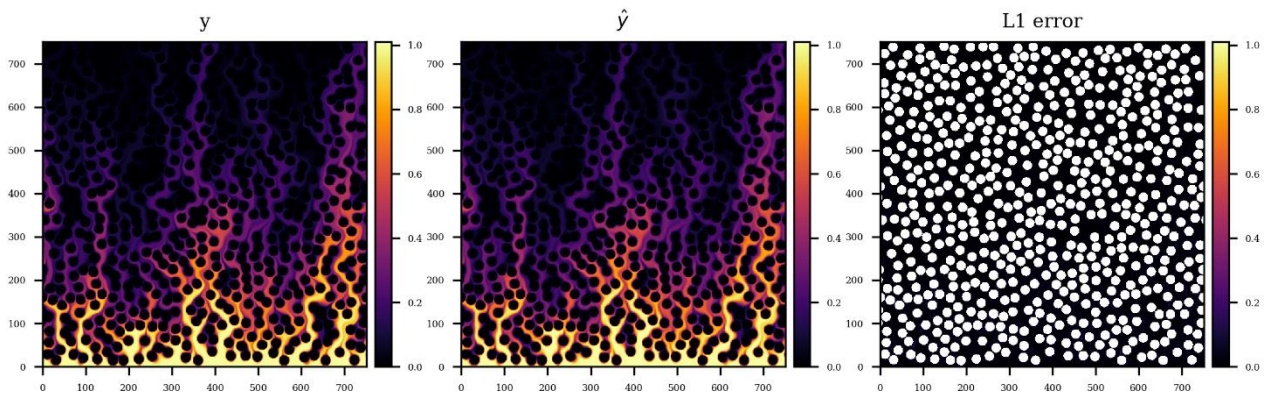


Figure 3. Prediction of the concentration field by MSNet [4].

References

- [1] A. Marcatto, G. Boccardo, D. Marchisio, *Chem. Eng. J.*, 417 (2021), 128936.
- [2] G. Boccardo, D. L. Marchisio, R. Sethi, *J. Colloid Interf. Sci.*, 417 (2014), 227–237
- [3] G. Boccardo, E. Crevacore, R. Sethi, M. Icardi, *J. Contam. Hydrol.*, 212 (2018), 3–13
- [4] J. E. Santos, Y. Yin, H. Jo, W. Pan, Q. Kang, H. S. Viswanathan, M. Prodanovic, M. J. Pyrcz, N. Lubbers, *Transport Porous Med.*, (2021) 1–32

Simulation of a methane-based Poly(3-hydroxybutyrate) production process: the effect of internal gas recycling

Claudia Amabile¹, Teresa Abate¹, Simeone Chianese^{1*}, Dino Musmarra¹

¹ Department of engineering, University of Campania "Luigi Vanvitelli", Via Roma 29, 81031, Aversa;

*Corresponding author E-Mail: simeone.chianese@unicampania.it

1. Introduction

Poly(3-hydroxybutyrate) (PHB) is a thermoplastic polyester belonging to the family of Polyhydroxyalkanoates (PHAs), which are well-known biobased and biodegradable biopolymers [1]. Many microorganisms, mainly type II methanotrophs, are capable to grow on methane and oxygen and to accumulate granules of PHB into the cell structure when a metabolic stress due to the lack of nutrients in the medium is induced (Figure 1) [2]. These granules can then be extracted from the cells, processed, and used to produce several products [3][4].

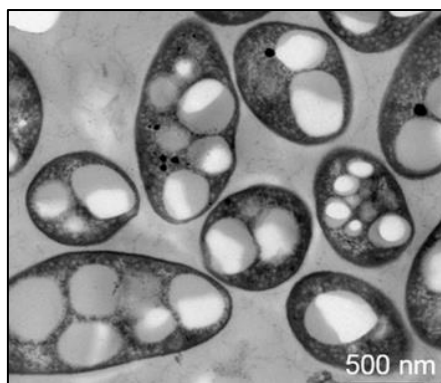


Figure 1. Granules of PHB

The properties of PHB make it a potential substitute for conventional plastics, which nowadays represent one of the main causes of environmental pollution [5]. Anyway, the high market price of these polymers and the poor scalability of the process result in inefficient PHB production. Moreover, the low productivities, which have been largely estimated using continuous bioreactors at a laboratory scale, remain at approximately $\approx 0.03 \text{ kg m}^{-3} \text{d}^{-1}$ [6]. In this context, among the several factors that affect the process yields, mass transfer from the gas to the liquid represent a key aspect [6]. Normally, methanotrophs use oxygen and methane for growing in presence of nutrients and accumulating the polymer into the cell structure under an induced metabolic stress, but the low solubility of methane often limits the availability of these gaseous reactants into the liquid phase. Many strategies for improving gas-liquid mass transfer and saving methane have been studied in the literature, some of them reporting interesting results in terms of PHB productivity [6]. For example, the use of an internal gas recycling strategy in a bubble column bioreactor operating in a continuous mode to produce Poly(3-hydroxybutyrate) from methane, resulted in a higher productivity of $1.4 \text{ kg m}^{-3} \text{d}^{-1}$.

In this work, a double step process was simulated to grow *Methylocystis Hirsuta* and to accumulate PHB in 400L bubble column bioreactors working in series in a semi-continuous mode. The process was simulated twice: first, a process scheme without internal gas recycling was considered, then, the same conditions were repeated in two reactors provided with a gas recycling unit and working at several recycling rate.

2. Methods

The process to produce Poly(3-hydroxybutyrate) was simulated using two 400L semicontinuous bubble column bioreactors working in series. The first step consisted in the growth of a Type II methanotroph in presence of NO_3^- and methane as nitrogen and carbon source, respectively; the second phase was aimed at the accumulation of PHB in absence of nutrients in the medium. The flowsheet was designed both with and without a gas recycling unit (Figure 2a and 2b) to assess the effects of gas recirculation on PHB yields with respect to the methane fed. When the recycling unit was not included in the flowsheet, the empty bed residence time (EBRT) (eq.1) was set to 2 min, which corresponded to a superficial gas velocity of 0.027 cm s^{-1} ; when gas recirculation was considered, the virtual residence time (VRT) (eq.2) was set to 2 min, to have a fixed final velocity of 0.027 cm s^{-1} . This condition was reached starting from empty bed residence time of 30, 15, 10 and 5 min and increasing the recycling ratio (eq.3) from 1.5 to 14. The summary of the scenarios simulated is reported in Table 1.

$$EBRT = \frac{V_r}{Q_{fed}} \quad (1)$$

$$VRT = \frac{V_r}{Q_{fed} + Q_{rec}} \quad (2)$$

$$RR = \frac{Q_{rec}}{Q_{fed}} \quad (3)$$

In the previous equations, V_r is the volume of the reactors, Q_{fed} is the fresh methane fed to the reactors and Q_{rec} is the recycled flow.

Table 1. Details of the scenarios simulated, with and without the internal gas recirculation

EBRT [min]	VRT [min]	$Q_{fed} [\text{m}^3_{\text{gas}} \text{ m}^{-3}_{\text{reath}} \text{ h}^{-1}]$	$Q_{rec} [\text{m}^3_{\text{gas}} \text{ m}^{-3}_{\text{reath}} \text{ h}^{-1}]$	RR
2	2	1.2	0	0
5	2	0.48	0.72	1.5
10	2	0.25	1.02	4
15	2	0.16	1.04	6.5
30	2	0.08	1.12	14

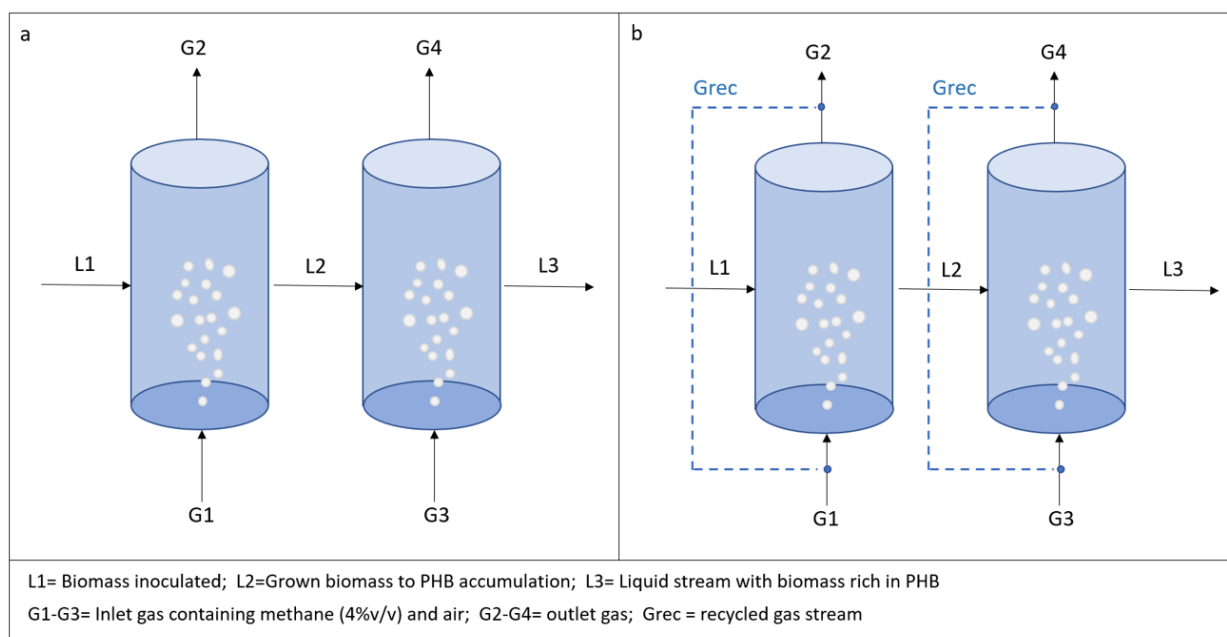


Figure 2. Flowsheet used for the simulations without a recycling unit (a) and with a recirculation system (b)

3. Results and discussion

The results of the simulations are reported in terms of biomass and PHB produced at the end of the cycle, production of PHB for unit of substrate (S_{PHB}) and methane utilization capacity (eq.4). When working with a recycling unit, methane saving was also evaluated.

$$EC - CH_4 = \frac{Q_{gas}(C_{CH_4in} - C_{CH_4out})}{V_r} \quad (4)$$

In eq.4, Q_{gas} is the gas fed to the reactor, C_{CH_4in} and C_{CH_4out} are the inlet and outlet methane concentrations, respectively, and V_r is the volume of the reactors (400L).

The total biomass produced at the end of the growth cycle was 1.22 kg, the PHB amounted to 0.76 kg after 12 days of accumulation, thus resulting in 38% w/w, and the methane utilization capacity calculated according to eq.4 remained constant at $59 \text{ gCH}_4 \text{ m}^{-3} \text{ h}^{-1}$. It should be noted that these results were the same for all cases, since the final operating conditions were fixed: the total methane fed (fresh + recycled) was kept constant at 300 g h^{-1} , the superficial gas velocity was set at 0.027 cm s^{-1} and the VRT at 2 min. Anyway, Figure 3 shows the convenience of using a recycling unit with a high RR: it resulted that, the higher the EBRT, the higher the recycling ratio and the production of PHB for unit of substrate, with an evident saving of methane (93% of methane saved at a RR=14).

The convenience in using a recycle stream for reducing the VRT and saving methane at the same time was previously stated, with an increase of $EC-CH_4$ which was function of the EBRT and of the recycling ratio. For example, an increase of methane utilizing capacity from $29.8 \pm 2.0 \text{ g CH}_4 \text{ m}^{-3} \text{ h}^{-1}$ at $EBRT=30 \text{ min}$ with no internal gas recirculation to $73.8 \pm 2.1 \text{ g CH}_4 \text{ m}^{-3} \text{ h}^{-1}$ with a final VRT of 1 min employing a recycle ratio of 30, was reported [6]. Others [7] confirmed the opportunity of enhancing the methane consumption by using a recirculation strategy, with an increase of $EC-CH_4$ from $8.5 \pm 0.3 \text{ gCH}_4 \text{ m}^{-3} \text{ h}^{-1}$ to $18.7 \pm 0.2 \text{ gCH}_4 \text{ m}^{-3} \text{ h}^{-1}$ when increasing the recycling rate from $0 \text{ m}^3_{\text{gas}} \text{ m}^{-3}_{\text{reatt}} \text{ min}^{-1}$ at $EBRT=60\text{min}$ to $0.25 \text{ m}^3_{\text{gas}} \text{ m}^{-3}_{\text{reatt}} \text{ min}^{-1}$ at $VRT=4 \text{ min}$ starting from $EBRT=60\text{min}$.

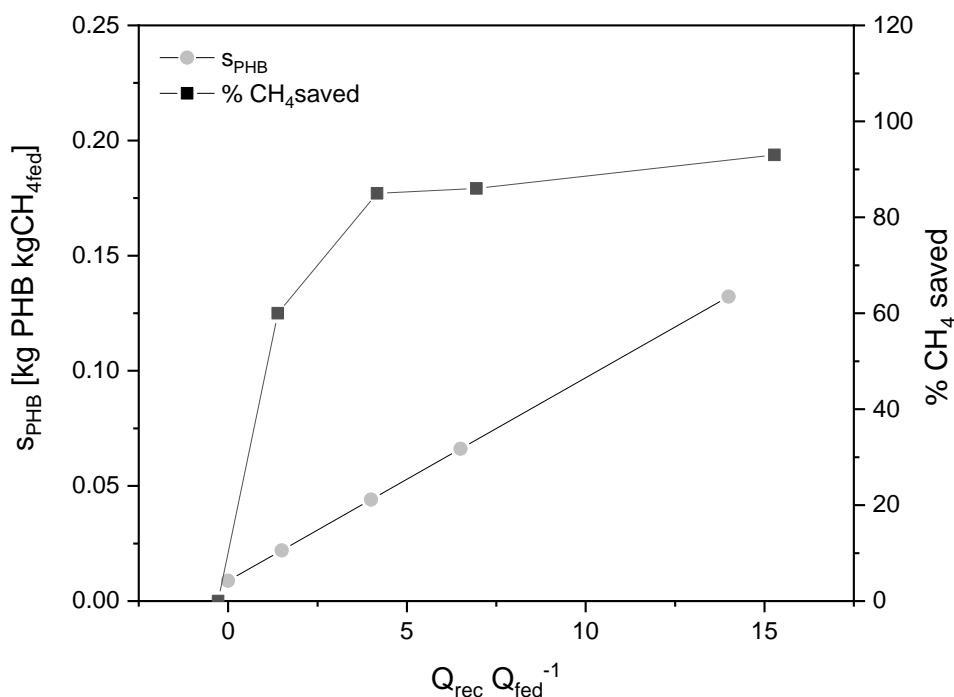


Figure 3. Elimination capacity of methane and production of PHB for unit of substrate fed as function of the recycling ratio

4. Conclusions

The process for producing PHB from methane through a double step configuration was simulated in this work. *Methylocystis hirsuta* was grown for 20 days and accumulated PHB in lack of nitrate. The opportunity for enhancing gas-liquid mass transfer and saving methane was evaluated through the addition of a gas recycling unit, with a recycling ratio ranging from 0 to 14. The production of PHB at the end of the cycle was 0.76 kg, which corresponded to 38%w/w of PHB with respect to the total suspended solids. The best condition, in terms of methane saved, was reached at the highest recycling ratio (14), saving 93% of methane compared to the condition in which no gas recycling was considered.

References

- [1] C. S. K. Reddy, R. Ghai, Rashmi, and V. C. Kalia, *Bioresour. Technol.* 87 (2003) 137–146
- [2] L.-Y. Liu, G.-J. Xie, D.-F. Xing, B.-F. Liu, J. Ding, and N.-Q. Ren, *Environ. Sci. Ecotechnology* 2 (2020) 100029
- [3] L. L. Madison and G. W. Huisman, *Microbiol. Mol. Biol. Rev.* 63 (1999) 21–53
- [4] G.Q. Chen, *China Plastic and Rubber Journal*, April Issue, 2010.
- [5] J. Chee, S. Yoga, N. Lau, S. Ling, and R. M. M. Abed, (2010) pp. 1395–1404
- [6] M. R. García-Pérez, C.J. López, F. Passos, R. Lebrero, S. Revah, “*Chem. Eng. J.* 334 (2018) 691–697
- [7] Y. Rodríguez, P. I. M. Firmino, V. Pérez, R. Lebrero, and R. Muñoz, *Waste Manag.* 113 (2020) 395–403

Multiscale modeling approaches to describe complex chemical engineering systems

Francesco Petrosino^{1*}, Giorgio De², Javier Luque Di Salvo³, Sudip Chakraborty¹, Stefano Curcio¹

1 Department of Computer Engineering, Modeling, Electronics and Systems (D.I.M.E.S.), University of Calabria, Via-P. Bucci, Cubo-42A, 87036 Rende (CS), Italy;

2 Institute on Membrane Technology, ITM-CNR, Ponte P. Bucci, Arcavacata, 87036 Rende (CS), Cosenza, Italy;

3 INFIQC, Universidad Nacional de Córdoba, Facultad de Ciencias Químicas, Departamento de Química Teórica y Computacional, CONICET, Ciudad Universitaria, X5000HUA Córdoba, Argentina

**Corresponding author E-Mail: f.petrosino@dimes.unical.it*

1. Introduction

Multiscale approaches are receiving more and more interest in different scientific and technological areas. “Multiscale simulation can be defined as the enabling technology of science and engineering that links phenomena, models, and information between various scales of complex systems [1]. Nowadays, one of the major challenges in chemical engineering resides in the description of complex phenomena, which are essentially multiscale in nature. Multiscale simulations allow properly modeling and analyzing the connections between different scales so to determine how a change or even a perturbation at one scale may influence the results at a different scale of detail [2]. Incorporating the transition from one to another scale within a multiscale approach is a real challenge in several chemical engineering applications. Localized properties at the microscale have to be incorporated directly in the macroscale description without any averaging due to their model key role. However, multiscale approaches are not restricted to chemical engineering problems: environmental, biological, medical, astrophysical situations would equally benefit from such approaches.

Given the importance of these modeling techniques and given the different studies carried out by our research group in this area [3]–[6], the present work is intended to propose two different applications to chemical engineering processes strictly related to multiscale approach.

The first application consisted on the study of concentration polarization phenomena during membrane processes. The macroscopic characterization of fouling structure formation occurring during the Ultra-Filtration (UF) of Bovine Serum Albumin (BSA) was analyzed from a theoretical point of view. A twisted Monte-Carlo (MC)/Computational-Fluid-Dynamic (CFD) approach was developed to calculate macroscopic fluid-dynamic proprieties. Different fluid-dynamic simulations were performed on the base of the knowledge acquired by an MC analysis that provided boxes of adsorbed molecules (i.e., 3D proteins meso configurations on the UF membranes surface). These represented the deposit layers, formed at different distances from the membrane. The 3D meso structure were imported into a bespoke simulation environment, and several meshes were created to perform micro-fluid dynamic calculations (m-FD). The resistance to flow of deposit layers accumulated on the membrane surface, R_{add} , usually estimated by experimental methods, was therefore, computed starting from the ab-initio knowledge acquired at sub-nanosopic scale.

The second application consisted of the simulation the long-range interactions between SARS-CoV-2 spike protein and three synthetic polymeric materials (Polypropylene (PP), Polyethylene Terephthalate (PET), and Polylactic Acid (PLA)) experimented by the virion when it is dispersed in the droplet before its possible adsorption. Some descriptors, namely the interaction potentials per single protein and global potentials, were calculated in this work. These descriptors, evaluated for the closed and open states of the spike protein, were correlated to the long-range noncovalent interactions between the SARSCoV-2 spikes and the considered polymeric surfaces. They were associated to the surface’s affinity towards SARS-CoV-2 dispersed in respiratory droplets or water solutions. For closed and open structures, the long-range interactions with the surfaces decreased in the following order PP ~ PLA > PET and PLA > PP > PET, respectively [6].

It is important to underline that the above-described works, although different in their subjects, are linked by a fundamental unifying basic strand, which is represented by the multiscale approach for the analysis of protein-protein and protein-surface interactions. Moreover, as already discussed, this unifying strand has fallen into a very broad and promising multidisciplinary field.

2. Methods

The density functional theory, used as the first-brick of the entire work, allowed the fundamental atomic proprieties calculations without resorting to any empirical or experimental parameter. The Molecular Dynamics and Monte Carlo approaches permitted the determination of a minimal energy structure of both the polymeric membrane at nanoscale level and the aggregated colloidal particles during ultrafiltration or virus interaction at microscale level. Despite the two approaches are aimed at the same minimization goal, the first one is based on the solution of the classical equation of motion, while Monte Carlo is a stochastic-based approach. To get some fundamental macroscopic properties like the Osmotic pressure and the Diffusion coefficient in the membrane process, the colloidal soft matter theory was used. In this field, different statistical thermodynamics approaches resulted of vital importance for the complete closure of the multiscale framework and the achievement of the final transition at macroscopic level by a completely ab-initio methodology. Moreover, a micro-Computational-Fluid-Dynamic approach was exploited for the final process simulation based on the previously defined quantities. To have a macroscopic estimation of the virus-surface potential energy different Molecular Mechanics optimizations were also performed.

3. Results and discussion

3.1 Micro-CFD modelling of UF bio-fouling

The ab-initio approach allowed acquiring a fundamental knowledge about the characteristics of the membrane system, i.e., the quantum mechanics colloidal surface charge at sub-nanoscale [3], [5]. A Monte Carlo based code was developed to simulate the fouling formation through a coarse-graining methodology. The schematic of such a methodology is shown in Fig.1.

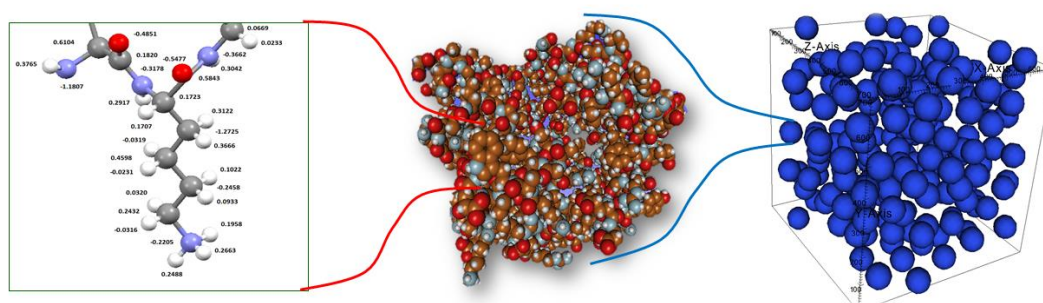


Figure 1: Developed multiscale framework from sub-nanoscale to nano/mesoscale level. Point charges on external amino acid atoms (on the left), a coarse-grained total colloid of overall macromolecule (in the middle) and a colloids box at nano/mesoscopic scale performed by MC simulations (on the right).

After defining both the boundary and the initial conditions, the 3D Navier-Stokes problem was computed through the defined mesh geometry based on the MC box. A schematic of MC/CFD procedure was reported in Fig.2.

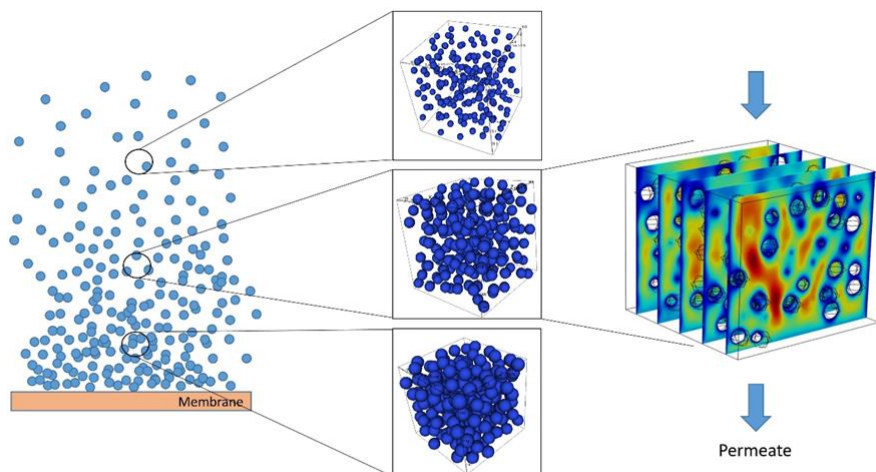


Figure 2: micro-CFD approach to develop a complete fluid dynamic study on the deposited cake layers during membrane filtration. The number of MC-CFD simulation boxes depends on the computational resources.

A set of fluid-dynamic simulations was performed, and a total pressure drop across the whole fouling layers was so calculated. If the average volume fraction for every fouling thickness range is known, the calculated pressure drop per unit length of the cake can be multiplied by the corresponding fouling thickness so to obtain a global fouling cake pressure drop summing all contributions: $\Delta P = \sum_{i=1}^n \Delta P_i \cdot \Delta d_i = 1.35 \text{ bar}$. Moreover, the additional resistance R_{add} at the specified filtration time $t=5\text{min}$, was estimated based on the well-known Darcy's law and resulted equal to $R_{add} = 1.91 \cdot 10^{13} \text{ m}^{-1}$.

3.2 Noncovalent interactions between SARS-CoV-2 spikes and polymer surfaces

The noncovalent interactions between the single S-protein and the target surfaces, as well as the global interaction potentials, were calculated using a classic Molecular Mechanics approach. In particular, the single-protein potential describes the potential energy of a single spike interacting with the polymer surface; thus, the surrounding protein's effects are not considered. The second potential is instead the interaction potential due to a protein ensemble formed by a reference spike, considered perpendicular to the polymer surface, and its surrounding proteins: i.e., the 1st and 2nd neighbors. Hence, both descriptors are correlated with the affinity of SARS-CoV-2 towards a target polymer surface.

In order to evaluate the contribution of various spikes around a reference protein, i.e., the effect of the 1st and 2nd neighbors, the global interaction potentials were evaluated and plotted in Fig. 3.

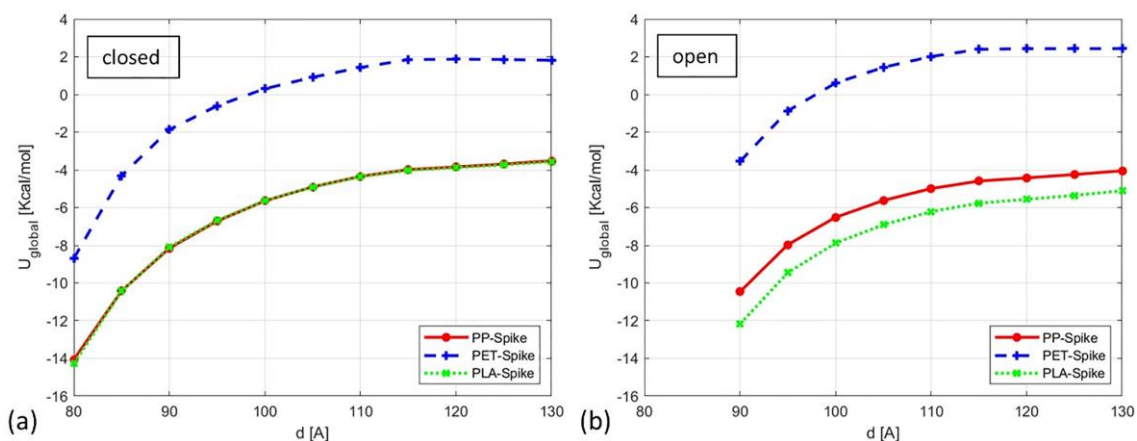


Figure 3: a) Global interaction potentials as a function of the protein-surface distance (d) for the closed structure of spike and target surfaces, b) global interaction potentials as a function of the protein-surface distance (d) for the open structure of spike.

PP and PLA surfaces interact with the S-proteins to a greater extent than the PET surface. Additionally, the global potentials highlight more clearly that the PP and PLA surfaces interact differently with the open state of the S-protein. Moreover, the global interaction potentials show that PP and PLA-based purification devices or membranes should retain the virus more effectively than PET-based devices.

4. Conclusions

A combined Monte Carlo/micro-CFD model was implemented in the present work. The overall aim was the calculation of the additional resistance, R_{add} , in the cake layers. This macroscopic quantity was calculated starting from the ab-initio surface charge obtained by Quantum Mechanics techniques. The pressure drop across the fouling layer was calculated and the fouling layer additional resistance resulted equal to $R_{add} = 1.91 \cdot 10^{13} \text{ m}^{-1}$. Long-range noncovalent interactions between the SARS-CoV-2 spikes and synthetic polymeric materials were investigated to suggest descriptors associated with the surface's affinity towards coronavirus. Single-protein and global interaction potentials, evaluated through a combined computational approach based on molecular mechanics and dynamics simulations, were proposed as versatile descriptors. The evaluated descriptors highlight that the protein-surface long range interactions decrease in the following order $PP \sim PLA > PET$ and $PLA > PP > PET$ for the closed and open structures of the spike, respectively. A completely multidisciplinary approach has been developed and applied in two areas substantially different but connected by a characterizing aspect such as the study of macromolecule-macromolecule and macromolecule-surface interactions at the nano/microscopic scale.

References

- [1] M. Fermiglia and S. Priol, "Multiscale modeling for polymer systems of industrial interest," *Prog. Org. Coatings*, vol. 58, no. 2–3, pp. 187–199, 2007, doi: 10.1016/j.porgcoat.2006.08.028.
- [2] R. E. Amaro and A. J. Mulholland, "Multiscale methods in drug design bridge chemical and biological complexity in the search for cures," *Nat. Rev. Chem.* 2018 24, vol. 2, no. 4, pp. 1–12, Apr. 2018, doi: 10.1038/s41570-018-0148.
- [3] S. Curcio, F. Petrosino, M. Morrone, and G. De Luca, "Interactions between Proteins and the Membrane Surface in Multiscale Modeling of Organic Fouling," *J. Chem. Inf. Model.*, vol. 58, no. 9, pp. 1815–1827, Sep. 2018, doi: 10.1021/acs.jcim.8b00298.
- [4] F. Petrosino, S. Curcio, S. Chakraborty, and G. De Luca, "Enzyme Immobilization on Polymer Membranes: A Quantum and Molecular Mechanics Study," *Computation*, 2019, doi: 10.3390/computation7040056.
- [5] F. Petrosino, Y. Hallez, G. De Luca, and S. Curcio, "Osmotic pressure and transport coefficient in ultrafiltration: A Monte Carlo study using quantum surface charges," *Chem. Eng. Sci.*, vol. 224, p. 115762, Oct. 2020, doi: 10.1016/j.ces.2020.115762.
- [6] G. De Luca, F. Petrosino, J. L. Di Salvo, S. Chakraborty, and S. Curcio, "Advanced descriptors for long-range noncovalent interactions between SARS-CoV-2 spikes and polymer surfaces," *Sep. Purif. Technol.*, vol. 282, Feb. 2021, doi: 10.1016/J.SEPPUR.2021.120125.

Design and Development of a Microfluidic Platform for Extracellular Vesicles Engineering

Caterina Piunti^{1,2}, Sara Micheli^{1,2}, Elisa Cimetta^{1,2*}

¹Department of Industrial Engineering, University of Padua, Padua, Italy;

²Fondazione Istituto di Ricerca Pediatrica Città della Speranza, Padua, Italy

*Corresponding author E-Mail: elisa.cimetta@unipd.it

1. Introduction

Despite great progress achieved in the understanding of cancer biology, metastases are still synonymous of terminal illness. Therefore, developing targeted therapies in cancer is a clinical imperative.

In recent years, extracellular vesicles (EVs) have been found to be involved in cancer development. EVs are small-sized vesicles (30-10000 nm in diameter) of endocytic origin, released from different cell types under both normal and pathological conditions. These vesicles contain proteins, RNA, miRNA, double-stranded DNA, and lipids that are highly representative of their cell or tissue of origin. As mediators of near and long-distance intercellular communication in health and disease, EVs and their cargo affect various aspects of recipient cell biology [1]. Growing evidence shows that cancer cell-derived EVs contribute to proliferation, angiogenesis, anti-tumor immune responses, and metastasis. For instance, EVs derived from Neuroblastoma (NB) - one of the most common solid tumors of childhood - are found to play a role in mediating its progression and metastasis [2]. Despite being the guilty part of cancer progression and metastasis, EVs could potentially also play a role in the treatment of cancers. Indeed, EVs can be used to our clinical advantage by transforming them into drug delivery systems in cancer therapy [3].

Although traditional methods for EVs studies and modifications will continue to play a significant role in the future, it is believed that microfluidic approaches will eventually replace benchtop methods for investigating EVs in speeding up precision therapeutics.

Considering such promises, the goal of the project is to evaluate the feasibility of designing and developing a microfluidic device for generating drug-loaded EVs. Currently, various strategies are being employed for EVs cargo loading; however, these approaches are faced with limitations of low loading efficiency, disruption of integrity, and aggregation. Taking advantage of *lab-on-chip* devices, passive cargo loading through microfluidic mixing and incubation may be an important strategy to produce functional engineered EVs. EVs can be loaded with various therapeutic agents, including Verteporfin (VP). VP is a small hydrophobic porphyrin recently identified as an inhibitor of YAP/TAZ complex. Notably, VP provided positive results for its anti-cancer activity in different tumors, including NB [4]. Although the utilization of EVs for therapeutic drug delivery is still in its infancy, a more advanced understanding and systemic evaluation of their use will boost the development of EVs as a superior and effective drug delivery system that can bring breakthroughs to the field of cancer nanomedicine.

2. Methods

The platform is designed so that both a perfect mixing between EVs and VP occurs within the mixing unit and the desired incubation time, set at 10 minutes, is achieved [5]. The platform is designed with AutoCAD® (Figure 1) and contains a “T” type inlet channel and is formed by two sections: the mixing and the incubation units. The mixing unit consists of a micromixer embedded with geometric features [6]; the 5-period mixing unit exists at the terminal of a 1.7 mm channel after the confluence of the two inlet channels and one mixing period is 500 μm wide by 500 μm long. The incubation section uses delay lines, allowing incubation for precise time periods as a function of the imposed flow rate. The delay lines consist of channels with a width of 700 μm and a total length of 30 cm. The entire device has a surface equal to 48 × 14.4 mm². The height of all elements is 100 μm.

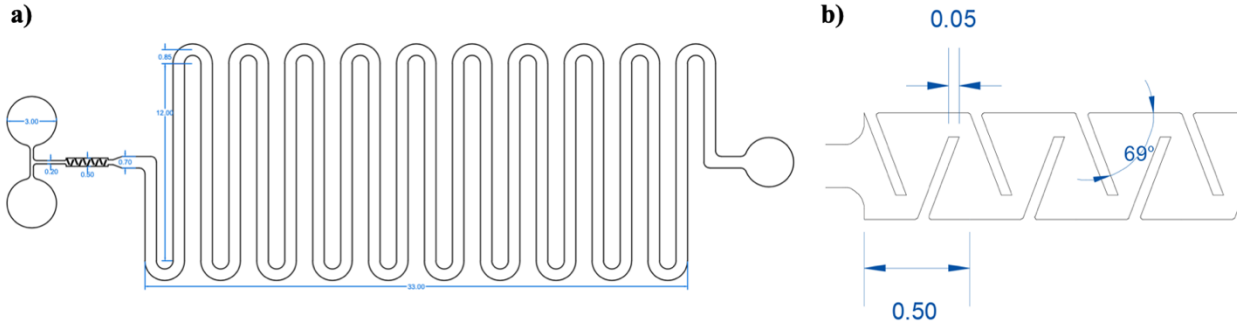


Figure 1. Platform layout: a) AutoCAD® design of the platform; b) detail of the micromixer. All dimensions are in mm.

The platform is then modeled, performing computational fluid dynamics simulations through COMSOL Multiphysics®. The master mold for the optimized device is fabricated with photolithography, and polydimethylsiloxane (PDMS) replicas of the chips were obtained with replica molding processes. There are several advantages of the technologies related to the use of PDMS which make it the first choice for most biochemical and biological applications: its cytotoxicity is nullified by full curing, its preparation is rapid and inexpensive and its optical transparency allows for high resolution live imaging. Finally, plasma treatment is used to form an irreversible hydraulic seal of the microfluidic platform to a glass coverslip (60 × 30 mm). The platform in this configuration is used to perform the fluid dynamic validations, using both food coloring and fluorescent tracers. The food coloring solution is simply prepared by mixing it with water, in a proportion suitable to obtain an intense color. The fluorescent tracers used are fluorescein isothiocyanate-dextran (Sigma-Aldrich) with maximum excitation at a wavelength of 490 nm, and maximum emission at 520 nm. Specifically, the dextrans used have an average molecular weight (MW) of 500 kDa and are prepared by dilution in phosphate buffered saline (PBS) in a proportion 0.5mg/10mL. A syringe pump (Harvard Apparatus) is used to infuse the solutions through the platform. The volumetric flow rate is set to 1 $\mu\text{L}/\text{min}$. Finally, images of the platform are taken using Invitrogen EVOS™ FL Cell Imaging System microscope (Thermo Fischer Scientific).

3. Results and discussion

The COMSOL Multiphysics® simulation is performed in a 3D geometry. The physics that are added to the simulation are: *a.* the laminar flow of a single-phase incompressible fluid, to describe fluid motion inside the platform and, *b.* the transport of a diluted species, to simulate the convective/diffusive behavior of a generic species *i* inside the platform. The addition of the transport of diluted species interface does not require the properties of the species *i*, except for the diffusion coefficient and the initial concentration *c* at the inlets. The diffusion coefficient (*D*) of a spherical particle in a viscous fluid is calculated with the Stokes-Einstein equation (Equation 1), where k_B is the Boltzmann constant [J/K], *T* is the temperature [K], μ is the viscosity of the fluid [Pa·s] and *r* is the radius of the particle [m]:

$$D_{EVs} = \frac{k_B T}{6\pi\mu r} \quad (1)$$

The diffusion coefficient of EVs in water is calculated using Equation 1 considering an average diameter of 70 nm and gives: $D_{EVs} \approx 6.14 \cdot 10^{-12} \text{m}^2 \text{s}^{-1}$.

The second information needed is the initial concentration *c* of the species at the inlets. At one inlet the concentration is set at an arbitrary value, while at the other one the concentration is set as equal to zero. The final graphs are created by normalizing the concentration, dividing it for the initial value, to obtain a dimensionless scale (from zero to one). Several simulations are performed in COMSOL, varying mainly two parameters: the inlet flow rates and the length of the mixing unit, with the aim of determining the optimal configuration for the perfect mixing of the species.

Once both variables are set, the length of the delay lines is calculated using Equation 2:

$$t = \frac{lwh}{Q} \quad (2)$$

Where Q is the flow rate and l , w , and h are the length, width, and height of the channel, respectively. By setting the ideal delay time t to 10 minutes, the calculated length of the delay lines is $l = 30 \text{ cm}$.

A concentration plot from the COMSOL Multiphysics® simulations is presented in Figure 2. At the set inlet flow rate of $1 \mu\text{L}/\text{min}$, the fluids completely mix after a 5-period mixing unit.

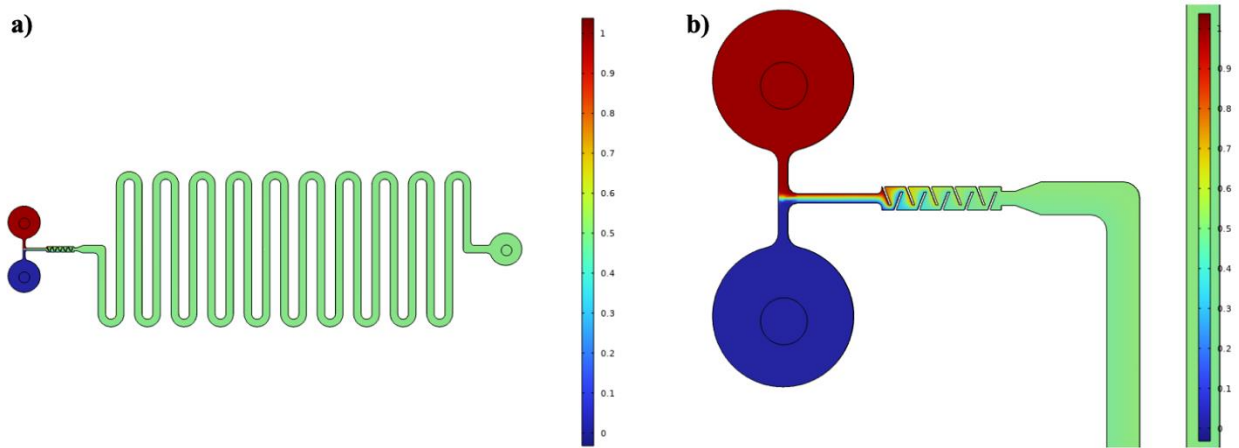


Figure 2. Concentration surface plots of the: a) entire platform; b) micromixer. The color indicates the mass fraction: the mass fraction of one is represented by red, while a mass fraction of zero is pictured in dark blue.

Based on the simulation result, the performance of the produced platform is then experimentally validated. First, both food coloring and dextran are used to obtain qualitative information about the fluid behavior inside the device (Figure 3). The validation confirms the correct production of the PDMS replica and the hydraulic seal of the platform.

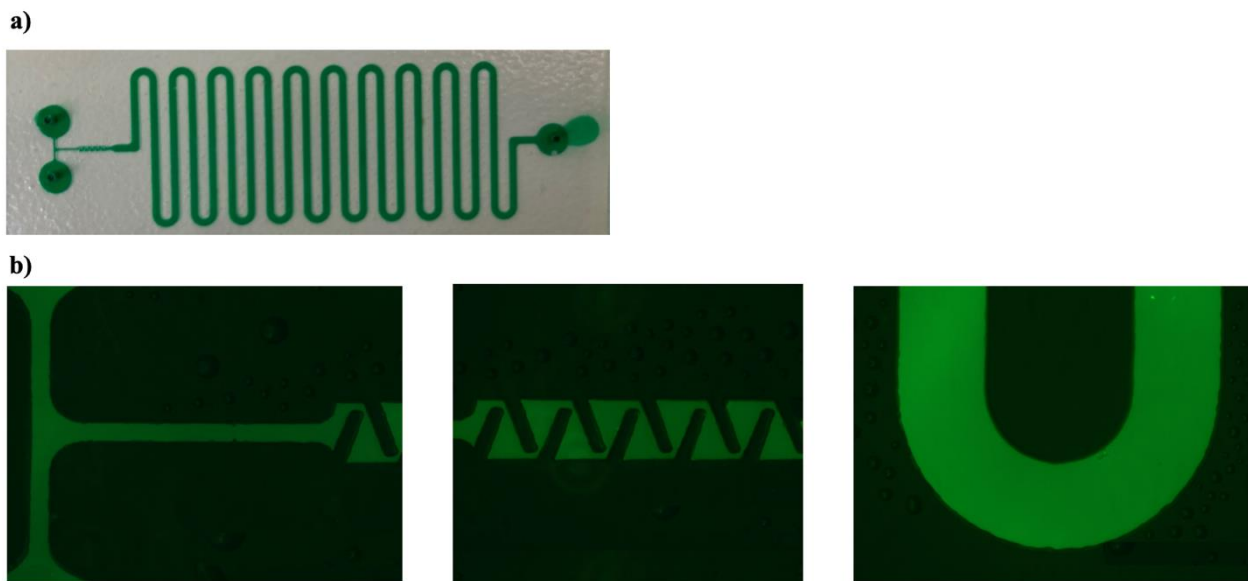


Figure 3. Result of the validation experiment on the irreversible configuration of the microfluidic platform. a) PDMS replica of the platform filled with green colorant; b) microscopy images of the platform filled with 500 kDa fluorescent isothiocyanate-dextran.

Then, different food coloring tracers are used to validate the mixing performance and achievement of the desired incubation time (Figure 4). The syringes with the blue and yellow colors are prepared and placed on the pump, which is then started setting the flow rate to 1 $\mu\text{L}/\text{min}$. After approximately 10 minutes, green fluid exit through the outlet, demonstrating that perfect mixing and incubation times is obtained using the platform, consistent with COMSOL simulations.

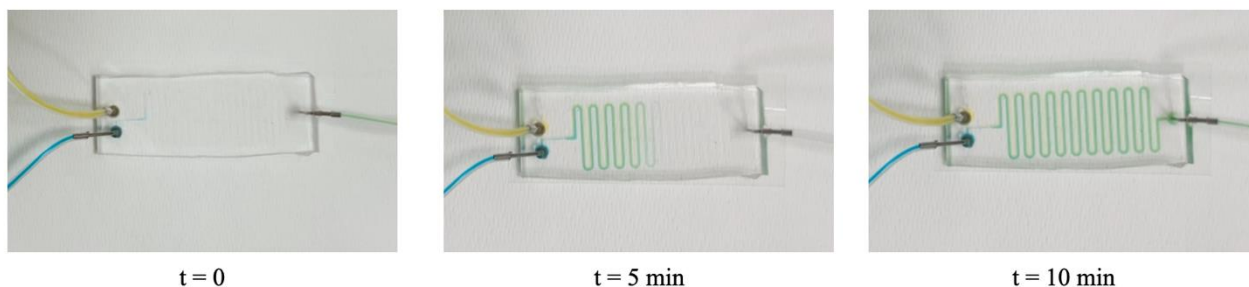


Figure 4. Result of the validation experiment on the irreversible configuration of the microfluidic platform at the beginning of the incubation time ($t=0$), after 5 and 10 minutes. Visually, the blue and the yellow colors become green, meaning that the microfluidic mixing is functioning.

4. Conclusions

The objective of this work is the design of an innovative microfluidic device that would allow drug-loading of EVs, using microfluidic mixing and incubation. The platform is produced using replica molding, employing PDMS as the production material. The performances of the device are simulated with COMSOL Multiphysics® software and used to perform a validation of the experimental data.

The biological experiments will be next carried out using EVs isolated from different cell types and VP as cargo. The loading methods employed in this study would be non-destructive and technically simple to allow application with a broad range of therapeutic molecules. Due to the relatively short history of EVs being utilized in therapeutics, there are only a few studies employing microfluidic platforms for engineering EVs for drug delivery, and the full potential and capability have not yet been well explored. Thus, as a versatile tool, microfluidic technology is expected to fully unlock the potential of EVs for speeding up precision medicine.

References

- [1] Walker, S., Busatto, S., Pham, A., Tian, M., Suh, A., Carson, K., Quintero, A., Lafrence, M., Malik, H., Santana, M. X., & Wolfram, J. (2019). Extracellular vesicle-based drug delivery systems for cancer treatment. *Theranostics*, 9(26), 8001–8017. <https://doi.org/10.7150/thno.37097>
- [2] Richard, H., Pokhrel, A., Chava, S., Pathania, A., Katta, S. S., & Challagundla, K. B. (2020). Exosomes: Novel Players of Therapy Resistance in Neuroblastoma. *Advances in experimental medicine and biology*, 1277, 75–85. https://doi.org/10.1007/978-3-030-50224-9_5
- [3] Zhu, Q., Heon, M., Zhao, Z., & He, M. (2018). Microfluidic engineering of exosomes: editing cellular messages for precision therapeutics. *Lab on a chip*, 18(12), 1690–1703. <https://doi.org/10.1039/c8lc00246k>
- [4] Fusco, P., Mattiuzzo, E., Frasson, C., Viola, G., Cimetta, E., Esposito, M. R., & Tonini, G. P. (2021). Verteporfin induces apoptosis and reduces the stem cell-like properties in Neuroblastoma tumour-initiating cells through inhibition of the YAP/TAZ pathway. *European journal of pharmacology*, 893, 173829. <https://doi.org/10.1016/j.ejphar.2020.173829>
- [5] Fuhrmann, G., Serio, A., Mazo, M., Nair, R., & Stevens, M. M. (2015). Active loading into extracellular vesicles significantly improves the cellular uptake and photodynamic effect of porphyrins. *Journal of controlled release : official journal of the Controlled Release Society*, 205, 35–44. <https://doi.org/10.1016/j.jconrel.2014.11.029>
- [6] Lee, Chia-Yen & Wang, Wen-Teng & Liu, Chan-Chiung & Fu, Lung-Ming. (2015). Passive Mixers in Microfluidic Systems: A Review. *Chemical Engineering Journal*, 288. <http://dx.doi.org/10.1016/j.cej.2015.10.122>

Steady and unsteady reactive flows in an X-microreactor

Sara Tomasi Masoni*, Matteo Antognoli, Roberto Mauri, Chiara Galletti, Elisabetta Brunazzi.

Dipartimento di Ingegneria Civile e Industriale, Università di Pisa, Largo Lucio Lazzarino 2, Pisa 56122, Italy

*Corresponding author E-Mail: sara.tomasimasoni@phd.unipi.it

1. Introduction

Microreactors are very attractive for intensifying chemical and biochemical reactions, as they ensure a high surface-to-volume ratio, leading to an extremely efficient heat and mass transfer [1]. These features allow a significant improvement of reaction yield and selectivity. Microreactors also offer the possibility of implementing continuous operation with respect to batch stirred reactors, which are traditionally used for mixing and reaction operations in fine chemical and pharmaceutical industries.

Since the flow is laminar, mixing should be triggered either using active (based on external energy sources) or passive methods (based on special configurations of the inlet and mixing channels). As for the latter methods, the mixing process has been extensively studied in simple geometries, which are interesting for the easy fabrication, such as T- and Y-mixers. Recent studies have highlighted how the X-mixer guarantees better mixing performance than the previously mentioned geometries. Most of the investigations concerned the characterization of flow regimes using only water in an X-mixer, conceived as an impingement jet [2]. At low Reynolds number, the flow regime is completely segregated, and mixing is mainly promoted by diffusion. At $Re=48$ [2], the engulfment regime occurs exhibiting a single vortical structure in the mixing channel that enhances the mixing of the two streams. Above $Re\approx 300$, the unsteady regime was found, leading to higher mixing efficiency.

Although large attention has been paid to the characterization of the mixing process in these regimes, there is scarce knowledge about their effect on the yield of a chemical reaction. Indeed, only recently the effect of the flow regimes on the reaction yield in the T-microreactor was investigated experimentally and numerically [3, 4]. At low Re , with segregated flow regimes, the reaction yield decreases with increasing Re because of the lower residence time. Instead, increasing Re in the steady and unsteady engulfment regime leads to an increase of reaction because of the enhanced mixing.

Still, more investigations are needed to study the relationship between mixing and yield of chemical reactions in X-shaped devices. In this work, experimental flow visualizations and numerical simulations are carried out jointly to characterize the steady and unsteady flow regime in an X-microreactor using reacting fluids.

2. Methods

The X-microreactor is represented in Fig. 1 and consists of four identical channels, i.e., two inlets and two outlets, with a square cross-section $1\times 1\text{ mm}^2$. The hydraulic diameter is $d=1\text{ mm}$, and the length of the channels is 60 mm. The experimental set-up consisted of KD Scientific syringe pump Gemini 88, equipped with two Becton Dickson plastic syringes of 60 mL, an upright microscope (model Nikon Eclipse 80i) with a magnifying lens of $4\times$, and a high-speed camera (Optomotive Velociraptor HS).

The considered reaction is the reduction of methylene blue (MB^+) to the colorless leucomethylene blue (LMB^+) using ascorbic acid (AsA) and hydrogen chloride (HCl) as a catalyst. The microreactor is fed with an aqueous solution of AsA in one of the inlet channels and an aqueous solution of MB^+ and HCl into the other. The former solution is prepared by dissolving L-ascorbic acid (Ultrafine vitamin C powder by Cutetonic Ltd, London, SW17 9SH, UK) in deionized water, and the concentration of AsA is $[AsA]=1.7\text{ M}$. Instead, the aqueous solution of MB^+ and HCl is obtained by dissolving methylene blue trihydrate powder (CAS No. 7220-79-3, Sigma Aldrich, St. Louis, USA) in aqueous solutions of HCl (CAS No. 7647-01-0)

supplied by Merck KGaA (Darmstadt, Germany); the concentrations of MB^+ and HCl are $[\text{MB}^+]=5.33 \times 10^{-5}$ M and $[\text{HCl}]=2.19$ M.



Figure 1. Picture of the fabricated PMMA device for the experiments.

The problem can be described by the Navier–Stokes with transport-reaction equations for the chemical species except water. The set of equations is discretized through the code ANSYS Fluent v. 19, using a steady solver with a second-order upwind scheme and a SIMPLE algorithm for pressure-velocity coupling. More details on the grid resolution and boundary conditions are provided in [6].

3. Results and discussion

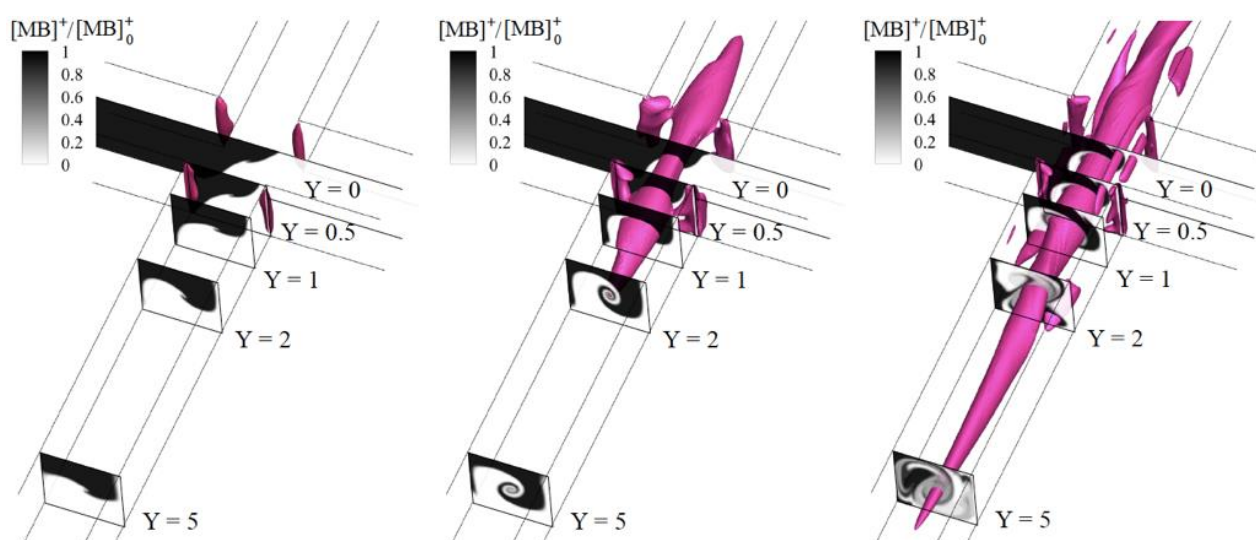


Figure 2. Isosurfaces of the vortex-indicator (λ_2) and contour of non-dimensional MB^+ concentration along the outlet channel in numerical simulations. Considered case (from left to right): $\text{Re}=40$, $\text{Re}=50$, $\text{Re}=200$.

The different flow regimes are analyzed within the interval $\text{Re}=10$ -600. The Reynolds number (Re) is evaluated by considering the physical properties of water. Figure 2 shows the isosurface of vortex-indicator (λ_2) and the contour of non-dimensional MB^+ concentration along the outlet channel in numerical simulations for $\text{Re}=40$, 50, and 200. At $\text{Re}=40$, the flow stratifies over the mixing channels, and no vortical structures are observed in the confluence region. The impingement plane is slightly tilted as the higher

density solution of ascorbic acid moves toward the lower part of the mixing channels. In this flow regime (i.e., stratified regime), mixing is promoted only by the diffusion of the two streams at the contact area. At $Re=50$, a single vortical structure forms at the channel intersection, extending the contact area and providing more efficient mixing. This central vortex is typical of the engulfment flow regime, which was observed at $Re \approx 50$ also in water-water and water-ethanol mixtures [5]. By further increasing the Reynolds number, the central vortical structure becomes stronger and elongated in the outlet channels. Furthermore, two additional vortices, counter-rotating with respect to the central vortex, are formed. This feature improves the mixing between the two inlet streams, and thus the reaction yield.

With the increase in Reynolds number, the flow becomes unsteady and time-periodic. Figure 3 shows the isosurface of vortex-indicator (λ_2) and the experimental flow visualization for two instants within a cycle at $Re=450$. A remarkable agreement between experimental results and simulations is found for the considered Reynolds number. The unsteady engulfment regime was found from $Re=375$. Here, as found for the steady engulfment regime, the initial flow pattern shows a single vortical structure with two lateral vortices. Subsequently, the central vortex splits into four main vortices, generating a blob of vorticity that is driven downstream along the mixing channels. At the end of the cycle, the four vortices merge into two, extending towards the mixing channels up to about 4 mm. Although the inlet streams are almost completely mixed during the unsteady engulfment regime, the reaction yield decreases with the Reynolds number owed to a reduction in residence time.

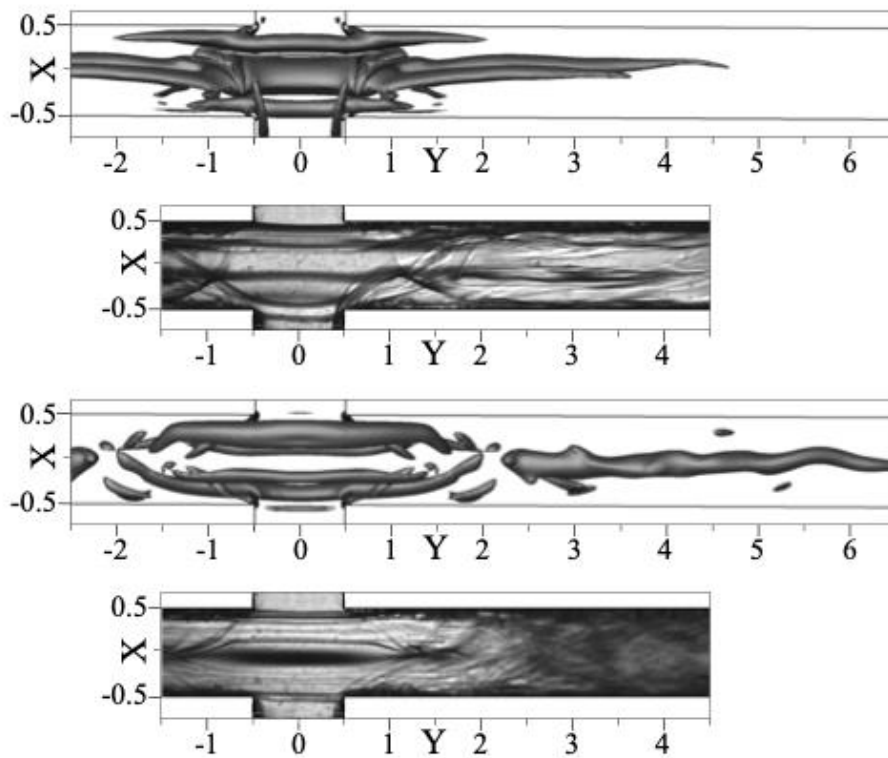


Figure 3. Isosurfaces of the λ_2 vortex-indicator (left) and experimental flow visualizations (right) at $Re=450$ at different times.

4. Conclusions

Steady and unsteady flow regimes in the X-microreactor were observed experimentally and numerically, finding a good match for the results. The CFD simulations provided an insightful analysis of the flow pattern and the vortical structures that characterized the regimes observed during the experiments. Compared to the stratified regime, the steady and unsteady engulfment regimes can ensure efficient mixing that enhances the microreactor performance, achieving a maximum value in reaction yield at $Re=80$. By increasing the Reynolds number, the reaction yield decreases as the time-to-react is reduced. When the unsteady engulfment regime occurs ($Re=375$), the reaction yield raises; then, it decreases again for higher Reynolds numbers. Future works may be addressed to produce nanoparticles through the flash precipitation determined by the rapid mixing of solvent and anti-solvent solutions.

References

- [1] I. Rossetti, M. Compagnoni, *Chemical Engineering Journal* 296 (2016) 56-70.
- [2] J.W. Zhang, W.F. Li, X.L. Xu, H.F. Liu, F.C. Wang, *Physics of Fluids* 31 (2019) 034105.
- [3] A. Mariotti, M. Antognoli, C. Galletti, R. Mauri, M.V. Salvetti, E. Brunazzi, *Chemical Engineering Journal* 396 (2020) 125223.
- [4] A. Mariotti, M. Antognoli, C. Galletti, R. Mauri, M.V. Salvetti, E. Brunazzi, *Micromachines* 12 (2021) 1–14.
- [5] M. Antognoli, S. Tomasi Masoni, A. Mariotti, R. Mauri, E. Brunazzi, C. Galletti, *Chemical Engineering Science* 248 (2022) 117254.
- [6] S. Tomasi Masoni, M. Antognoli, A. Mariotti, R. Mauri, M.V. Salvetti, C. Galletti, E. Brunazzi, *Chemical Engineering Journal*, 437 (2022) 135113.

Phase field modeling of phase separation in a binary mixture in presence of external forces

Roberto Mauri^{1*}, Antonio Bertei

1 Department of Civil and Industrial Engineering, University of Pisa, Largo Lucio Lazzarino 2, 56126 Pisa (IT)

**Corresponding author E-Mail: roberto.mauri@unipi.it*

1. Introduction

When a partially miscible binary mixture is brought from the stable region to the unstable region of its phase diagram, it separates into two coexisting phases since this corresponds to the minimization of the mixture free energy. Such a phase transition, called spinodal decomposition, is a reordering process that takes place isotropically. However, when an external force field (e.g., gravity or electric/magnetic fields) is applied to the mixture, provided that the force exerts a different acceleration to the species, demixing is enhanced, leading to stratification or to anisotropic phase separation.

In this study the process of phase separation of a regular binary mixture subject to an external force field is studied by extending the thermodynamics-based phase field model developed by the authors in a series of publications [1-3]. Numerical simulations show how the external force field breaks the isotropy of the mixture dynamics when starting from stable, unstable and metastable initial states of the phase diagram.

2. Methods

The phase field (a.k.a. diffuse interface) approach assumes that the interface between different phases is not a sharp bidimensional surface but, rather, it occupies a finite volume wherein all the mixture properties vary continuously, from the bulk region of one phase to the bulk region of the other phase [1]. In this way, capillary forces associated to the interfaces, such as the surface tension, are treated as volumetric forces in the governing equations of the mixture.

We basically start from the conservation of mass, species and momentum for a regular binary mixture, as follows [1-3]:

$$\frac{\partial \rho}{\partial t} + \nabla \cdot (\rho \mathbf{v}) = 0 \quad (1)$$

$$\frac{\partial (\rho \mathbf{v})}{\partial t} + \nabla \cdot (\rho \mathbf{v} \mathbf{v} - \eta (\nabla \mathbf{v} + \nabla \mathbf{v}^T)) = -\nabla p + \rho \mathbf{f} \quad (2)$$

$$\frac{\partial (\rho \phi)}{\partial t} + \nabla \cdot (\rho \mathbf{v} \phi + \mathbf{J}_\phi) = 0 \quad (3)$$

where t is time, ϕ is the mass fraction of species I in the mixture, ρ and η the density and viscosity of the mixture (which are assumed constant), p is pressure, \mathbf{v} is the mass-average velocity, \mathbf{f} is the force per unit mass and \mathbf{J}_ϕ is the diffusion flux. In particular, the volumetric force $\rho \mathbf{f}$ is the sum of two contributions: the Korteweg force (first term on the right-hand side of Eq. (4)), which is a non-equilibrium force that encodes the capillary stresses which arise from spatial inhomogeneities, and the applied external force (second term on the right-hand side of Eq. (4)), as follows [1,3]:

$$\rho \mathbf{f} = \rho \frac{RT}{M_w} \phi \nabla (a^2 \nabla^2 \phi) + \rho \phi \chi_{12} \mathbf{b} \quad (4)$$

where R is the universal gas constant, M_w the molecular weight of the species (assumed equal for both species), T is temperature, a is the characteristic length of the diffuse interface, while χ_{12} and \mathbf{b} are difference in species susceptibilities and the external body force, respectively.

The external force, being its effects different on the two species of the mixture, provides an additional contribution to species diffusion, so that the species diffusion flux results as [3]:

$$\mathbf{J}_\phi = -\rho D[(1 - 2\Psi\phi(1 - \phi))\nabla\phi - \phi(1 - \phi)\nabla(a^2\nabla^2\phi)] + \rho D \frac{M_w}{RT} \phi(1 - \phi)\chi_{12}\mathbf{b} \quad (5)$$

where D is species diffusivity and Ψ is the Margules coefficient, which describes the non-ideality of the mixture.

3. Results and discussion

Figure 1 shows the main results of the numerical solution of the system of Eqs. (1)-(5). The phase diagram of the mixture (Figure 1a) shows that while above the critical temperature T_c the mixture is always stable and does not phase separate, below T_c there is a miscibility gap, with unstable and metastable regions.

When the external force is applied to a mixture in the stable region of the phase diagram, as in point A, the two species undergo a stratification process, as shown in Figure 1b, where species I is pushed along the direction of the force field (which is the vertical one in this case). Even though there is no phase separation, the external force leverages on the thermodynamic repulsion between the species, which segregate following a continuous species distribution.

The application of the external force to an unstable mixture (point B in Figure 1a) leads to a specific directionality to phase separation, as show in Figure 1c. In particular, as small nuclei of the minority phase emerge, these are pushed by the external force, which speeds up demixing and makes it anisotropic, leading to two completely segregated phases at steady-state.

Finally, the external force field can trigger phase separation from the metastable region, as for point C in the phase diagram. If the force is sufficiently strong to stratify the species so that a significant fraction of the domain falls within the unstable region (see Figure 1d, in particular the grey line which denotes the spinodal composition), phase separation starts and proceeds following a nucleation process, where the interface forms first and then moves slowly to its final state.

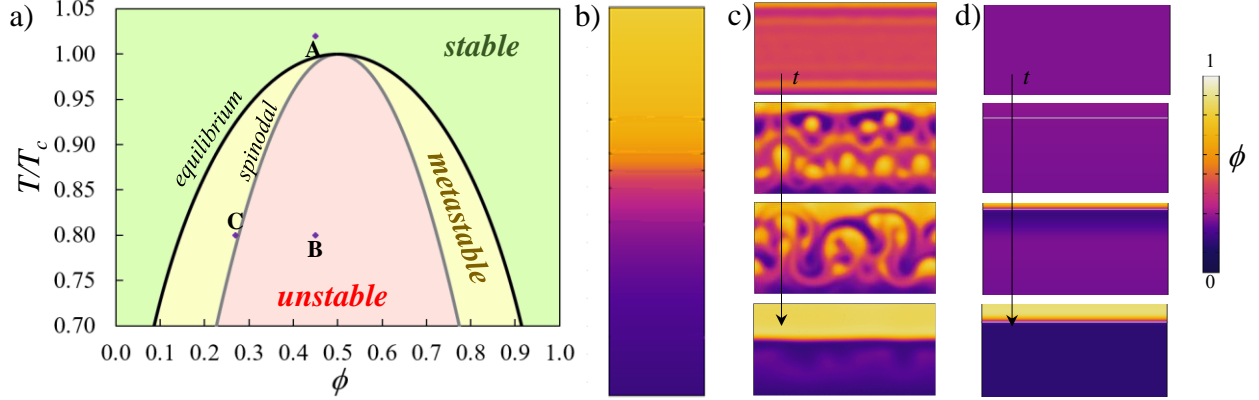


Figure 1. Effect of the external force in a binary mixture. a) Phase diagram, b) stratification induced for the stable point A, c) phase separation from the unstable point B and d) from the metastable point C.

4. Conclusions

The phase field model proves to be a versatile modelling framework to simulate the dynamics of multiphase flows from first principles, where external forces can be easily included within the modeling framework. This opens the scope for an extended use of phase field modelling to simulate mixtures subject to gravitational, electric or magnetic force fields.

References

- [1] A.G. Lamorgese, D. Molin, R. Mauri, Milan J. Math. 79 (2011) 597-642
- [2] C.-C. Chueh, A. Bertei, R. Mauri, Phys. Fluids 32 (2020) 023307
- [3] A. Bertei, C.-C. Chueh, R. Mauri, Phys. Rev. Fluids 6 (2021) 094302

One-way vs two-way coupling approach for predicting Brownian-Sieving Hydrodynamic Chromatography separation performance

Claudia Venditti^{1*}, Stefano Cerbelli¹, Alessandra Adrover¹

¹ Sapienza University of Rome, Dept. Chemical Engineering, Materials, Environment, Via Eudossiana 18, 00184 Rome, Italy.

*Corresponding author E-Mail: claudia.venditti@uniroma1.it

1. Introduction

Recently, a one-way coupling approach was exploited to optimize the geometry and the operating conditions of a Brownian Sieving Microcapillary Hydrodynamic Chromatography device (BS-MHDC), an unconventional MHDC double-channel device, where a Brownian sieving mechanism acting alongside the MHDC separation drive is enforced to boost separation resolution [1-2].

The BS-MHDC consists of a two-channel coaxial annular structure, where the core and the annular channel communicate through slit openings of assigned cut-off length A . The geometry is designed so that the core and the annular channel are characterized by significantly different average velocities of the eluent. When a mixture of particles of two characteristic sizes, say d_p^1 and d_p^2 with $d_p^1 > A > d_p^2$, is initially injected only within the core channel, both large and small particles flow downstream the channel under the action of the eluent pressure-driven laminar flow. Particles of diameter d_p^2 , smaller than A , can diffuse through the openings and eventually attain a uniform distribution onto the entire accessible cross-section, so their effective velocity will be affected by the average eluent velocity in both the core and annular channel. On the contrary, particles of diameter d_p^1 , bigger than A , are confined to the core region so that their effective velocity is influenced only by the average eluent velocity within this region.

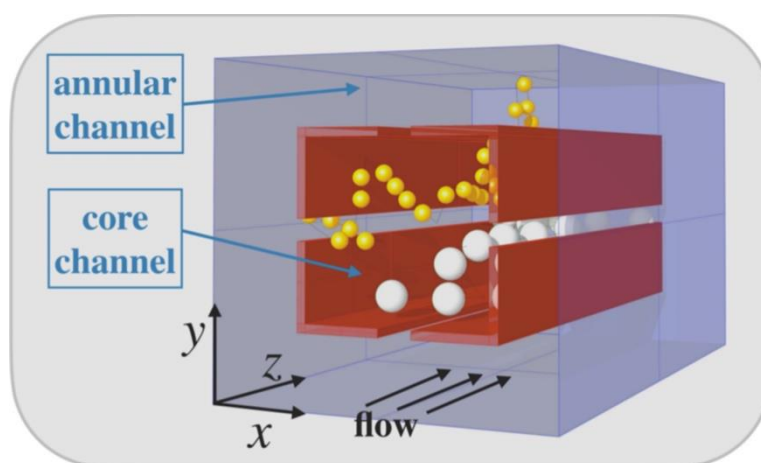


Figure 1. Schematic representation of the double-channel BS-MHDC device.

Previous approaches for quantifying the device performance hinged on the so-called one-way coupling excluded-volume approximation, in which the eluent flow is computed as a single-phase Stokes problem, and the particle-wall interactions are crudely simplified by only considering hindrance effects due to the finite size of the particle.

Bounds for the accuracy of the one-way coupling approach have been investigated in the literature only in single-channel geometries [3], where it is possible to single out a unique characteristic dimension of the cross-section which constitutes the reference length for scaling the particle size. On the contrary, the Brownian sieving device considered here possesses multiple reference lengths of the cross-section (the diameter of the core channel, the thickness of the annular channel and the slit opening A), which make the limits of validity of the one-phase approach uncertain.

The scope of this work is to explore these limits, comparing the predictions of the separation performance obtained with the one-way coupling approach with those obtained from a fully three-dimensional two-way coupling approach. Brenner's macro-transport theory [3-4] is used in both cases for obtaining the effective transport parameters, namely the effective particle velocity and the dispersion coefficient.

References

- [1] V. Biagioni, A. L. Sow, A. Adrover, and S. Cerbelli, "Brownian sieving effect for boosting the performance of microcapillary hydrodynamic chromatography. proof of concept," *Analytical Chemistry* 93, 6808–6816 (2021).
- [2] V. Biagioni, A. L. Sow, A. G. Fagiolo, A. Adrover, and S. Cerbelli, "Brownian sieving enhancement of microcapillary hydrodynamic chromatography. analysis of the separation performance based on Brenner's macro-transport theory," *Journal of Chromatography A*, 462652 (2021).
- [3] H. Brenner and L. J. Gaydos, "The constrained brownian movement of spherical particles in cylindrical pores of comparable radius: models of the diffusive and convective transport of solute molecules in membranes and porous media," *Journal of Colloid and Interface Science* 58, 312–356 (1977).
- [4] A. Adrover, C. Passaretti, C. Venditti, and M. Giona, "Exact moment analysis of transient dispersion properties in periodic media," *Physics of Fluids* 31, 112002 (2019).

Validation study of Windtrax backward Lagrangian model: critical discussion on model reliability and its optimisation

Francesca Tagliaferri^{1*}, Marzio Invernizzi², Selena Sironi³

1,2,3 Politecnico di Milano, Department of Chemistry, Materials and Chemical Engineering "Giulio Natta" - P.za Leonardo da Vinci 32, 20133 Milano, Italy;

**Corresponding author E-Mail: francesca.tagliaferri@polimi.it*

1.Introduction

In last years, urbanization and industrialization have been major contributing factors to the poor air quality. As the air quality deteriorates, exposure to air pollution remains a fundamental concern to public health (Pope, 2000). Passive chemicals in the atmosphere, such as NO₂, SO₂, CO, PM₁₀, PM_{2.5}, C₆H₆, could severely damage the health of the population (Leelóssy et al., 2014).

Having information on atmospheric pollution and its environmental impact on citizens is the starting point for improving air quality (Wang et al., 2008). Therefore, the evaluation of the extent of exposure to chemicals becomes a key issue. In this regard, dispersion modelling represents a useful tool for reproducing spatio-temporal distribution of contaminants emitted by a specific source thereby quantifying the areas of population exposure as well as the ground level concentrations of contaminants (Mangia et al., 2014).

There are several types of atmospheric dispersion models, Gaussian (Gifford, 1959), Eulerian (Jacobson, 2005; Seinfeld and Pandis, 1998), Lagrangian (Rodean, 1996) and fluid dynamics models (Moon et al., 1997). Overall, they calculate the concentration of a species in space, given the meteorological and emissive conditions of the source (Barclay et al., 2021; Capelli et al., 2012; Tagliaferri et al., 2020).

In recent years, dispersion patterns have increasingly evolved (Herring and Huq, 2018; Yudego et al., 2018). However, although these models have been refined, there are still some criticalities related to the input dataset: in some situations, the characterization of the emission source is not trivial. (Invernizzi et al., 2020, 2018; Tagliaferri et al., 2020). In particular, it is necessary to define the emissive flux released by the source whose estimation, in case of complex sources (e.g. floating roof tanks, tanks topped by grates), may be critical (Invernizzi et al., 2018). For point sources, such as stacks, concentrations and emission rates can be measured rapidly. On the other hand, area sources may be tricky: if they have a measurable outward flow such as biofilters, they can be treated similarly to point sources, but in case of passive area sources without an outward flow it is difficult to estimate an emission rate, since there is no well-defined airflow, and hoods must be used (Capelli et al., 2009). However, in case of area sources such as floating roof tanks or tanks topped by grates, hoods cannot be adopted (Capelli et al., 2009).

To this end, it would be extremely useful to apply an inverse dispersion model: so, by knowing a concentration value in space, to quantify the emission rate of the source.

The Windtrax software (Crenna, 2006) is a backward Lagrangian stochastic model, based on the principles of Monin-Obukhov Similarity Theory (MOST) (Flesch and Wilson, 2005, 1995), that computes an ensemble of random paths backward in time from the detectors to the sources thus quantifying the unknown emission rates from measured downwind concentrations.

Windtrax is widely used for the evaluation of emission rates in the agro-meteorology field, where emissions of greenhouse gases, methane or ammonia are typically measured (Gao et al., 2009; McBain and Desjardins, 2005; Yang et al., 2016). The studies available in literature regarding the application of the Wintrax model are generally focused on the evaluation of how well it predicts the emission of pollutants from area sources, which is typically the way in which agricultural sources are treated.

On the contrary, the present study focuses on the application of Windtrax for a different type of source. In fact, before tackling datasets with complex sources, it was decided to initially test the model by considering sources, such as stacks, never discussed in literature in similar studies. Also, when dealing with sources of this kind, being easy to characterize, the observed emission rate to compare with the model output is more reliable and consequently the model validation is more robust. In addition, in the agricultural field, point sources are of great interest, considering for instance flares in anaerobic digestion plants, vents of fixed roof tanks or conveyed emissions from livestock farming. Precisely, two experimental campaigns with a point source (i.e. stack) will be considered.

In this study, a validation of the model was carried out not limiting to this, but also trying to understand under which conditions (i.e. stability class, number and location of the sensors) it provides a greater accuracy. The aim of this work is to validate the Windtrax model by comparing the model results with observed values taken from datasets of real experimental fields available in literature.

The choice of the Windtrax model is mainly because it is free downloadable, not complex to use thanks to a user-friendly interface, widespread mentioned in the literature in the agro-meteorology field and it belongs to Lagrangian particle models which are advanced dispersion models.

2. Methods

2.1 Windtrax model

WindTrax 2.0.9.7 (Crenna, 2021) is a software that simulates the transport of gaseous substances in the atmosphere. It is based on the theory of the Lagrangian Particle Model (Crenna, 2006): the dispersion of pollutants is considered as a flow of dimensionless particles whose trajectory is described in a stochastic way.

It can be used either to calculate the concentration of a gaseous substance at a given point if the Emission Rate is known, or to calculate the Emission Rate if the concentration of the pollutant at a given point is known. The generic equations on which the model is based are:

$$\begin{aligned} a_{11}Q_1 + a_{12}Q_2 + \dots + a_{1n}Q_n + C_b &= C_1 \\ a_{m1}Q_1 + a_{m2}Q_2 + \dots + a_{mn}Q_n + C_b &= C_m \end{aligned} \quad [1]$$

Where C_b is the background concentration, Q_j are the emission rates, a_{ij} are the coefficients, computed by the model, relating the emission rate to the measured concentration C_i .

In order to solve the system of equations, there must be at least as many known concentration measurements as there are unknown emission rates. If the number of known concentrations C_i is greater than the number of unknown sources Q_j , the solution will be the best fit in the least squares sense (Crenna, 2006).

A full description of the Windtrax model is not presented here, since it has been widely discussed in literature (Crenna, 2006; Flesch and Wilson, 2005, 1995).

2.2 Uttenweiler and Round Hill campaigns

In this paragraph, a brief description of the field experiments used in the present study to validate the model is provided. Further details are described in the field test reports (Bachlin et al., 2002; Cramer et al., 1958).

The Uttenweiler campaign was conducted in a pre-existing pig farm in 12 and 13 December 2000 and 31 October 2001. The farm is situated outside the small village Uttenweiler, 20 km west of the city of Bielberach (5331621 N, 548508 E) in Germany. The surrounding area is mostly flat. This farm consists of the pig barn

and the feed processing room. The gas tracer, sulphur hexafluoride (SF₆) was continuously emitted by a single point source located on a building. It was at 8.5 m above the ground level, and it was connected to the internal ventilation system. 14 trials were performed, named in alphabetical order from B to O: the experiment A was an attempt.

The second campaign is the Round Hill experiment (Cramer et al., 1958). The site area, with a flat terrain, is close to the Round Hill Field Station of the Massachusetts Institute of Technology (338022 E, 4600793 N). The site roughness was around 7-30 cm and the vertical emission consisted of a stack at 30 cm from the ground releasing SO₂. A large number of experiments were conducted, some of them have been considered in the present study. The data set was obtained by means of the website <http://www.harmo.org/jsirwin>.

2.3 Model Validation

The first objective of this work was to estimate the performance of the Windtrax model in predicting the experimental data thereby performing a model validation. For this purpose, some statistical indicators were used (Chang and Hanna, 2004; Gustafson and Yu, 2012; Hanna and Chang, 2015; Willmott, 1981): Mean Bias (MB), Normalized Mean Bias (NMB), Root Mean Squared Error (RMSE), Normalized Mean Squared Error (NMSE), Index of Agreement (IOA) and FAC2.

The equations of each indicator are reported below:

$$MB = \frac{1}{N} \sum_{i=1}^N E_i = \bar{M} - \bar{O} \quad [2]$$

$$NMB = \frac{\sum_{i=1}^N (M_i - O_i)}{\sum_{i=1}^N O_i} = \frac{\bar{M}}{\bar{O}} - 1 \quad [3]$$

$$RMSE = \sqrt{\frac{1}{N} \sum_{i=1}^N (M_i - O_i)^2} \quad [4]$$

$$NMSE = \frac{\frac{1}{N} \sum_{i=1}^N (M_i - O_i)^2}{\bar{M}\bar{O}} \quad [5]$$

$$IOA = 1 - \frac{\sum_{i=1}^N (M_i - O_i)^2}{\sum_{i=1}^N (|M_i - \bar{M}| + |O_i - \bar{O}|)^2} \quad [6]$$

$$FAC2: 0.5 \leq \frac{M_i}{O_i} \leq 2 \quad [7]$$

Where M_i is the single modelled emission rate and O_i is the single observed value. The optimal values of these parameters indicating the best fit between the model results and the experimental data are: MB=0, NMB=0, RMSE=0, NMSE=0, IOA=1. Regarding the last index, FAC2, the percentage of values within the factor 2 range will be expressed.

The percentage (%) error of the modelled value with respect to the observed one has also been calculated. The latter is computed by means of the following formula:

$$ER\% = \frac{M_i - O_i}{O_i} \quad [8]$$

3. Results and discussion

3.1 Uttenweiler campaign

In this section, the validation of the model with the Uttenweiler experimental campaign will be discussed (Bachlin et al., 2002).

The Uttenweiler campaign was carried out in several experiments (14) lasting ten minutes each.

All these experiments had their own characteristics, such as weather data (wind velocity, wind direction, stability class) and instrument placements (sonic anemometer and concentration sensors). Therefore, each experiment was implemented separately in the software to obtain as many calculated Emission Rate values as the number of experiments. As an example, a picture of the spatial configuration of experiment B is given in Figure 1,a. In detail, the star with outgoing arrows having a question mark represents the point source having unknown emission rate; the columns having the symbol “C” are the concentration sensors (with known concentration values); finally, the remaining column represents the anemometer. In Figure 1b, an example of the Windtrax interface is shown while the simulation is running, with N particles emitted from the point source.

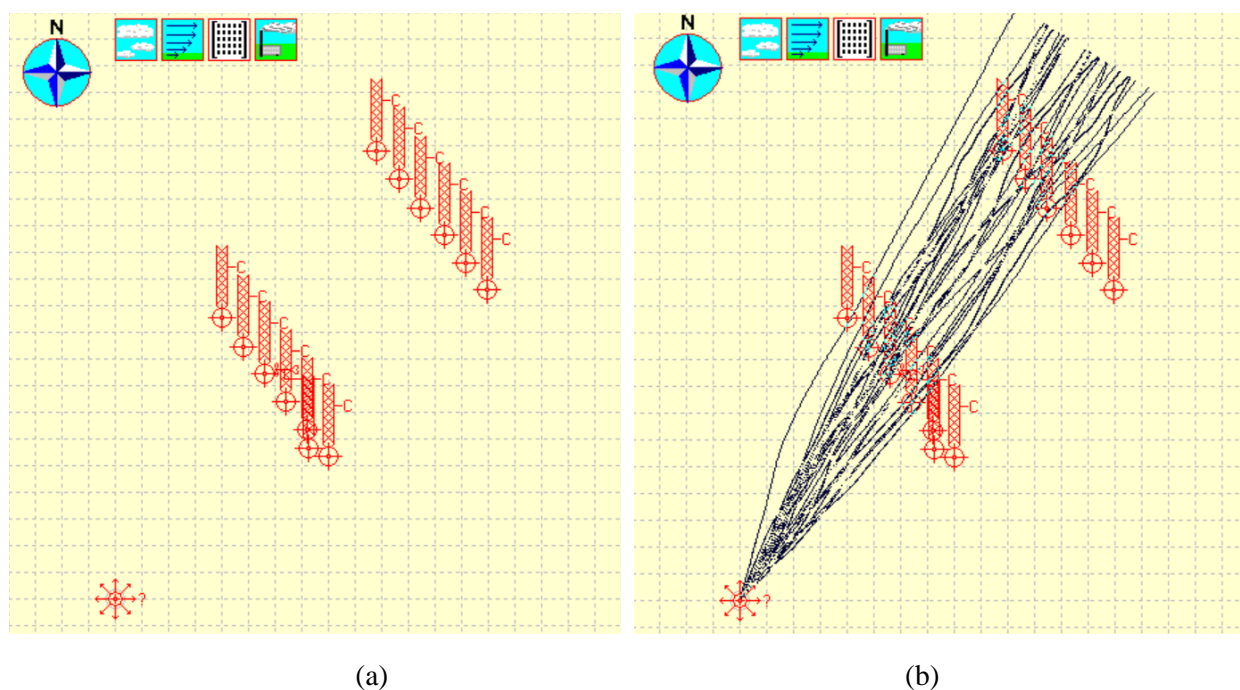


Figure 1. Experiment B spatial configuration on Windtrax on the left (a); Windtrax simulation, in which the trajectories traced by the N particles emitted by the source are visible (Crenna, 2006).

As first test, all the possible concentration sensors (12 measurement points) of the Uttenweiler campaign were entered as input data. In

Table 1 the statistical indicators computed by considering all the 14 experiments are reported.

Table 1. Statistical indicators computed by considering all the experiments; from the left: Mean Bias, Normalized Mean Bias, Root Mean Square Error, Normalized Mean Square Error and Index of Agreement.

MB	NMB	RMSE	NMSE	IOA
46.3	0.3	94.1	0.21	0.7

Focusing on the statistical indicators NMB, NMSE and IOA, the values predicted by the Windtrax model (Crenna, 2006) appear quite good. To confirm this, it is emphasized that the totality of the values obtained belong to the FAC 2 range.

From equation [1], it can be deduced that as many known concentration values are needed as there are unknown emission rates. Since in the investigated case-study there is just one unknown emission rate and given that such a large amount of concentration sensors (12) is rarely available, it was decided to evaluate the quality of the model progressively reducing the number of concentration sensors up to a single measurement point. The Uttenweiler campaign is characterized by a particular positioning of the concentration sensors: it develops in one or two transects (depending on the specific experiment) placed approximately perpendicular to the direction in which the wind was blowing. In experiments with two transects, these are placed parallel to each other and downwind of the emission source: so, one closer to the source and one further away, as visible in Figure 1. For the following test, i.e. validation of the model when reducing the number of measurement points, only the experiments having both transects were considered. Therefore trials (I, J, K, L) are neglected. This way it was also possible to test the influence of the distance of the receptor from the source on the accuracy of the results, i.e. to highlight if there is a significant difference when considering receptors closer or farther from the emission. To show the results of this test, a table with the percentage errors between the modelled and the observed value and the standard deviation of the modelled result for each experimental trial (B-O) is reported (**Errore. L'origine riferimento non è stata trovata.**). The different configurations implemented into the model are:

- 0) The entire concentration sensors,
- 1) The entire transect of concentration sensors closest to the source,
- 2) The entire transect of concentration sensors farthest from the source,
- 3) Two downwind sensors on the transect closest to the source,
- 4) Two downwind sensors on the transect farthest from the source,
- 5) One downwind sensor on the transect closest to the source,
- 6) One downwind sensor on the transect farthest from the source,
- 7) Two downwind receptors, one on the transect closest to the source and one farthest from the source.

It is worth underling that, for each experimental trial, the corresponding stability condition (N/S = neutral/stable; S = stable; VS = very stable) is indicated in the Table 2. In doing so, the way in which the stability class affects the performance of the model can be easily recognized in order to identify the optimal meteorological conditions to run the model.

Table 2. Percentage Error of the modelled value with respect to the observed value and standard deviation of the model result, for seven different spatial configurations of the concentration sensors (0-7), for the experiment considered (B-O).

	0		1		2		3		4		5		6		7	
	ER%	Standard Deviation	ER%	Standard Deviation	ER%	Standard Deviation	ER%	Standard Deviation	ER%	Standard Deviation	ER%	Standard Deviation	ER%	Standard Deviation	ER%	Standard Deviation
B	-13.6	14.1	-3.4	30.9	-2.9	18.5	-10.3	21.6	-2.3	19.6	-40.8	17.0	-9.9	26.0	-31.6	15.5
(N/S)																
C	-14.4	12.7	-13.2	29.3	-29.8	15.9	-22.5	16.1	-29.0	10.4	-26.0	17.1	-24.6	28.3	-18.8	18.9
(N/S)																
D	6.8	32.5	10.3	47.4	-30.0	35.0	1.9	28.0	-6.2	102.8	0.6	28.9	-31.7	39.6	4.8	28.8
(S)																
E	26.1	44.4	24.6	28.3	7.3	20.1	-3.7	31.1	29.8	24.5	-17.4	21.7	35.0	37.3	3.8	16.2
(N/S)																
F	54.7	15.2	72.8	56.8	8.8	18.4	43.3	53.1	-17.0	19.3	46.4	48.7	-5.9	45.3	13.3	27.3
(N/S)																
G	28.3	23.5	77.2	34.6	-6.1	16.7	39.1	27.4	-27.5	42.0	32.8	36.9	-29.0	19.5	23.2	26.5
(N/S)																
H	25.4	28.9	100.3	29.8	-27.3	13.8	151.3	95.8	-25.4	14.0	130.8	101.2	-30.6	22.1	35.6	41.8

(S)																
M	34.2	45.2	125.3	83.1	-24.1	29.2	94.9	101.3	-19.8	24.4	93.7	77.6	11.1	67.7	91.5	64.3
(S)																
N	-5.6	27.0	27.0	88.0	-22.3	46.6	27.1	56.5	-33.3	35.2	192.4	219.0	-40.4	20.6	-30.1	26.9
(S)																
O	-16.8	41.0	192.3	197.5	-35.3	32.4	169.1	114.2	-38.6	18.4	304.5	396.6	-39.3	25.7	-22.0	41.8
(VS)																

For the sake of clarity, a conditional formatting is used to have an easy-to-use overview of the model response: the percentage errors are shaded in yellow with increasing intensity as further away from zero (ideal value), the standard deviations in blue.

From Table 2, it is possible to observe that the highest values of percent error and standard deviation occur when considering experiments with stable and very stable conditions, particularly in situations where the concentration sensor was positioned on the transect closest to the source. This may be related to the fact that the plume emitted from the source under stable conditions is poorly dispersed in both the vertical and horizontal directions, so it is less likely having the plume to pass through the concentration sensors and this effect is more pronounced in the vicinity of the emission source where the pollutant is less diluted and dispersed.

The average percentage error computed by considering the absolute values of the percentage errors of the single experiments is about 41%, while considering only experiments in neutral/stable condition the average error decreases up to 24%. However, for the experiment D, performed in stable conditions, low percentage errors are detected, even on receptors positioned close to the source. This may be attributed to the fact that the location of the concentration sensors in all the configurations developed for this experiment and the wind direction are such that the plume always crosses only one sensor. Therefore, since this sensor is the only one which contributes to the quantification of the emission rate and it has been maintained in all the configurations, the removal of the other receptors does not affect the results.

Another consideration concerns the influence of the number of receptors on the model accuracy. From Table 2, it turns out that the reduction of the number of sensors does not necessarily improve the model performance. Thus, it can be inferred that the correct downwind placement of the sensor is much more significant than the number of sensors. In other words, the model results show a good accuracy even when considering a single measurement point provided that the sensor is properly located.

To conclude, the implementation of the Uttenweiler dataset highlights the good performance of the model in predicting the emission rate under neutral condition. Under stable conditions great care must be taken with the location of the sensor due to the fact that the plume is poorly dispersed. In this sense, a possible solution might be to move the sensor away from the source.

3.2 Round Hill campaign

In this section the validation of the model with the Round Hill Campaign (Cramer et al., 1958) will be discussed.

The dataset from the Round Hill campaign provides several concentration values measured from sensors positioned along arcs at different distances from the source (i.e 50 m, 100 m and 200 m). In particular, eight experiments characterized by different stability classes, were chosen to be tested: three of them are conducted under Moderately Unstable (MU) conditions, two in Neutral (NN) conditions, two in Moderately Stable (MS) conditions and only one in Extremely Stable (ES) conditions.

In this way, it was possible to test the performance of the model under different stability conditions, as for the Uttenweiler campaign.

In addition, for each experiment, different configurations of receptors were considered:

- 1) One arc of six downwind receptors at 50 m from the source (blue in Figure 2);
- 2) One downwind receptor at 50 m from the source (brown in Figure 2 **Errore. L'origine riferimento non è stata trovata.**);
- 3) One downwind receptor at 100 m from the source (green in Figure 2);
- 4) One downwind concentration at 200 m from the source (yellow in Figure 2);
- 5) Two downwind receptors, one at 50 m and one at 100 m from the source (red in Figure 2 **Errore. L'origine riferimento non è stata trovata.**).

In Figure 2 the % errors obtained for the different configurations of receptors (1-5) for the eight experiments are reported. It should be noted that in configuration 4, the first and third columns are missing, due to the failure to obtain a model result for the specific experiments.

From Figure 2, a general tendency of the model to overestimate in stable atmospheric conditions and to underestimate in unstable conditions may be observed.

In addition, higher accuracy of the model in predicting the experimental data under neutral condition is shown. The percentage errors for neutral stability class are always good, in the range between a $\pm 40\%$ with an average value of 10 %.

Conversely, the mean % error for experiments in unstable conditions is about -60%; while the mean error for trial in stable conditions is about 50%. It should be noted that in stable conditions, the average percentage error seems to decrease as the distance of the sensors from the source increases: in particular, in configuration 2 (receptor at 50 m from the source) the resulting error is about 60%, in configuration 3 (receptor at 100 m from the source) it decreases up to 40% and in configuration 4 (receptor at 200 m from the source) the (%) error is 32%. This outcome confirms what previously discussed for the Uttenweiler campaign.

By reducing the number of concentration sensors, it turns out what previously verified with the Uttenweiler dataset: even considering a single concentration value, it seems that the model still responds well. Thus, it can be concluded that the number of sensors is not so limiting, but rather their correct placement.

In Table 3, the statistical indicators discussed are shown. In particular, the performance parameters are computed distinguishing between the experiments conducted in neutral, stable and unstable conditions. Overall, looking at the absolute values of this statistical indicators, it seems that the model predicts the experimental data with a quite high level of accuracy, with the best values obtained in neutral conditions. The totality of the values obtained in neutral conditions belong to the factor 2 range.

Therefore, from this study, it appears that the model is more reliable for neutral conditions, where a good agreement between the experimental data and the simulated values are observed. Although the absolute values of the percentage errors obtained under stable and unstable conditions are comparable (50% vs 60%), it seems that the unstable conditions have a much more fluctuating error pattern (i.e. very low errors in some experiments, very high in others and eventually no results provided by the model). This behaviour is probably attributable to the high level of turbulence in unstable condition. For this reason, it might be concluded that the model is more reliable in stable conditions, even because, as discussed for the Uttenweiler campaign, the positioning of the sensor not too close to the emission source might help in the improvement of the model predictions.

GRICU 2022, Ischia, (Italy), July 3-6, 2022

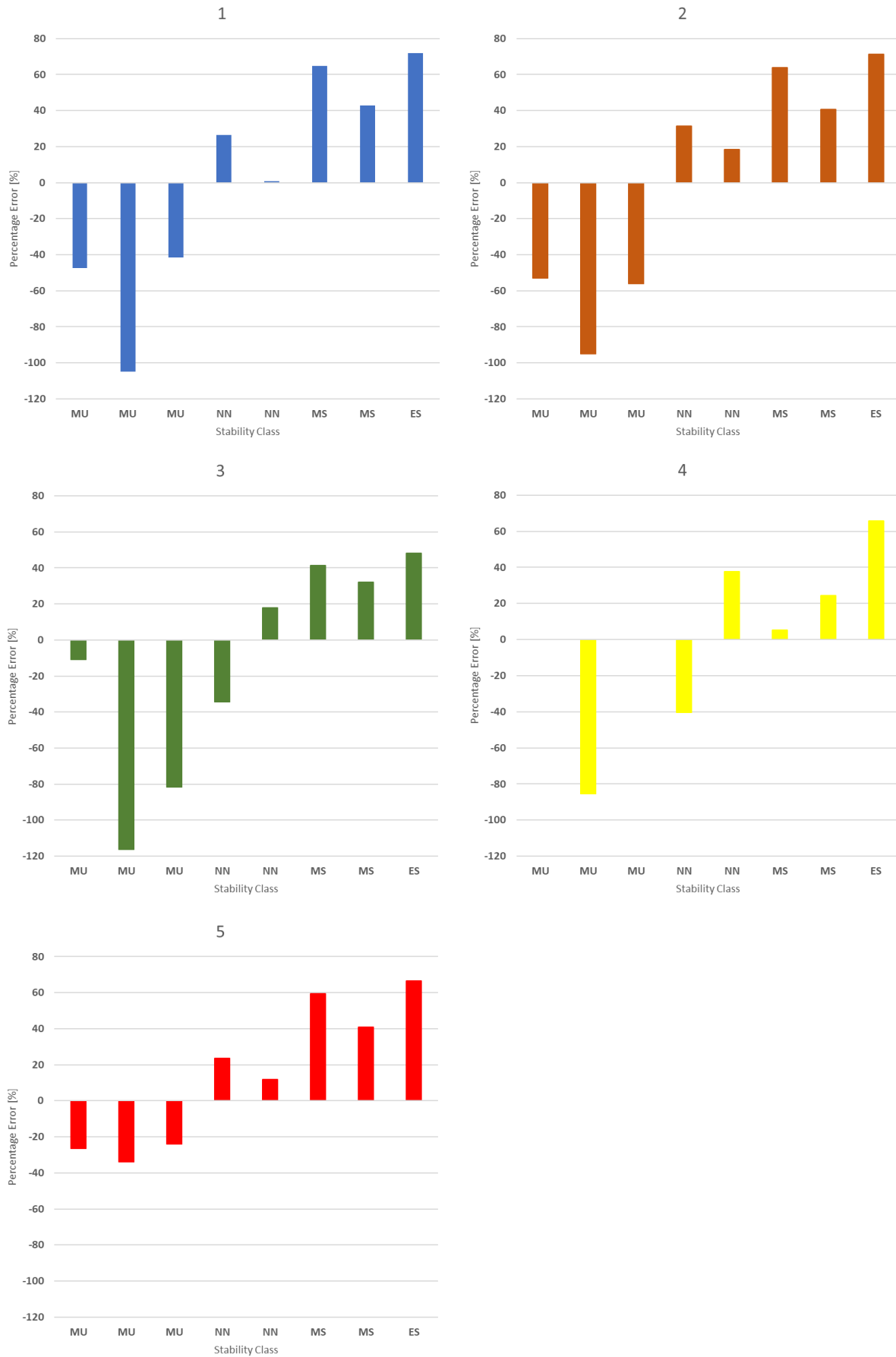


Figure 2. Percentage Error for the eight experiments with different stability class, in five different spatial configuration of concentration sensors (1-5). The absence of columns in configuration 4 means that there were no results provided by the model.

Table 3. Statistical indicators for all the considered experiments; from the left: Mean Bias, Normalized Mean Bias, Root Mean Square Error, Normalized Mean Square Error and Index of Agreement

MB			NMB			RMSE		
Unstable	Neutral	Stable	Unstable	Neutral	Stable	Unstable	Neutral	Stable
6.3	-0.6	-3.1	0.5	-0.1	-0.5	7.3	1.7	3.3

NMSE			IOA			FAC2		
Unstable	Neutral	Stable	Unstable	Neutral	Stable	Unstable	Neutral	Stable
0.3	0.1	0.5	0.005	0.1	0.4	81 %	100 %	50 %

4. Conclusions

Due to the high complexity associated, in some cases, to the characterization of emission sources, the availability of a reliable tool to estimate the source emission rate starting from a downwind measured concentration would be of great interest.

This work arises from this intent. It aims to test the performance of the backward Lagrangian model Windtrax, widespread mentioned in literature.

In particular, this validation study is not limited to investigate the reliability of the model in predicting the observed emission rate, but it also tries to understand under which conditions the performance of the model are expected to be higher.

From the results of this study, it turns out a general tendency of the model to predict the observed values with a good level of accuracy. In particular, for the Uttenweiler campaign, acceptable values of the performance indicators are obtained. For the Round Hill dataset, the model results are even better: in this case, an average percentage error of about 40% over all the experiments is estimated. In addition, this study highlights the importance of a correct positioning of the concentration sensor to make the model result reliable. In this regard, besides the downwind position of the sensor, in stable conditions, since the plume poorly dispersed, it is advisable to locate the measurement point not too close to the emission source. Another possible solution to adopt in stable conditions, might be the increase of the height of the sensor, so that it is more likely that the plume crosses the sensor box. Anyway, this possibility should be further investigated.

Also, from this evaluation, the performance of the model in different stability conditions were investigated. In this regard, it appears that the model is more reliable for neutral conditions, where a good agreement between the experimental data and the simulated values are observed.

In conclusion, Windtrax seems to be a very promising tool for the estimation of the emission rates. However, it is worth highlighting that it is not a trivial tool, and therefore, to obtain reliable results, it requires a deep preliminary study, regarding the position of the concentration sensor and the optimal meteorological conditions.

References

Bachlin, W., Rühling, A., Lohmeyer, A., 2002. Bereitstellung von validierungs-daten Für Geruchsausbreitungs-modelle – Naturmessungen, ingenieurbüro lohmeier. Badenwürttemberg, Germany.

- Barclay, J., Diaz, C., Galvin, G., Bellasio, R., Díaz-robles, L.A., Schauburger, G., Capelli, L., 2021. New International Handbook on the Assessment of Odour Exposure Using Dispersion Modelling 85, 175–180. <https://doi.org/10.3303/CET2185030>
- Capelli, L., Sironi, S., Del Rosso, R., Centola, P., 2009. Design and validation of a wind tunnel system for odour sampling on liquid area sources 1611–1620. <https://doi.org/10.2166/wst.2009.123>
- Capelli, L., Sironi, S., Delrosso, R., Bianchi, G., Davoli, E., 2012. Evaluating the dispersion of toxic odour emissions from complex sources. *J. Environ. Sci. Heal. - Part A Toxic/Hazardous Subst. Environ. Eng.* 47, 1113–1122. <https://doi.org/10.1080/10934529.2012.668068>
- Chang, J.C., Hanna, S.R., 2004. Air quality model performance evaluation. *Meteorol. Atmos. Phys.* <https://doi.org/10.1007/s00703-003-0070-7>
- Cramer, H.E., Record, F.A., Vaughan, H.C., 1958. The study of the diffusion of gases or aerosols in the lower atmosphere 19, 1–185.
- Crenna, B., 2021. Thunderbeachscientific [WWW Document]. URL <http://www.thunderbeachscientific.com/>
- Crenna, B., 2006. An introduction to WindTrax 19.
- Flesch, T.K., Wilson, J.D., 2005. Estimating Tracer Emissions with a Backward Lagrangian Stochastic Technique 513–531. <https://doi.org/10.2134/agronmonogr47.c22>
- Flesch, T.K., Wilson, J.D., 1995. Backward-Time Lagrangian Stochastic Dispersion Models and Their Application to Estimate Gaseous Emissions 1–27.
- Gao, Z., Mauder, M., Desjardins, R.L., Flesch, T.K., van Haarlem, R.P., 2009. Assessment of the backward Lagrangian Stochastic dispersion technique for continuous measurements of CH₄ emissions. *Agric. For. Meteorol.* 149, 1516–1523. <https://doi.org/10.1016/j.agrformet.2009.04.004>
- Gifford, F., 1959. Statistical Properties of A Fluctuating Plume Dispersion Model. *Adv. Geophys.* [https://doi.org/10.1016/S0065-2687\(08\)60099-0](https://doi.org/10.1016/S0065-2687(08)60099-0)
- Gustafson, W.I., Yu, S., 2012. Generalized approach for using unbiased symmetric metrics with negative values: Normalized mean bias factor and normalized mean absolute error factor. *Atmos. Sci. Lett.* 13, 262–267. <https://doi.org/10.1002/asl.393>
- Hanna, S., Chang, J., 2015. Skyscraper rooftop tracer concentration observations in Manhattan and comparisons with urban dispersion models. *Atmos. Environ.* <https://doi.org/10.1016/j.atmosenv.2015.01.051>
- Herring, S., Huq, P., 2018. A review of methodology for evaluating the performance of atmospheric transport and dispersion models and suggested protocol for providing more informative results. *Fluids* 3. <https://doi.org/10.3390/fluids3010020>
- Invernizzi, M., Ilare, J., Capelli, L., Sironi, S., 2018. Proposal of a method for evaluating odour emissions from refinery storage tanks. *Chem. Eng. Trans.* 68, 49–54. <https://doi.org/10.3303/CET1868009>
- Invernizzi, M., Teramo, E., Busini, V., Sironi, S., 2020. A model for the evaluation of organic compounds emission from aerated liquid surfaces. *Chemosphere* 240, 124923. <https://doi.org/10.1016/j.chemosphere.2019.124923>
- Jacobson, M.Z., 2005. *Fundamentals of atmospheric modeling.*, Second edi. ed. Cambridge university press.
- Leelőssy, Á., Molnár, F., Izsák, F., Havasi, Á., Lagzi, I., Mészáros, R., 2014. Dispersion modeling of air pollutants in the atmosphere: a review. *Cent. Eur. J. Geosci.* 6, 257–278. <https://doi.org/10.2478/s13533-012-0188-6>
- Mangia, C., Cervino, M., Gianicolo, E.A.L., 2014. Dispersion models and air quality data for population exposure assessment to air pollution. *Int. J. Environ. Pollut.* 54, 119–127. <https://doi.org/10.1504/IJEP.2014.065112>
- McBain, M.C., Desjardins, R.L., 2005. The evaluation of a backward Lagrangian stochastic (bLS) model to estimate greenhouse gas emissions from agricultural sources using a synthetic tracer source. *Agric. For. Meteorol.* 135, 61–72. <https://doi.org/10.1016/j.agrformet.2005.10.003>
- Moon, D., Albergel, A., Jasmin, F., Thibaut, G., 1997. The use of the MERCURE CFD code to deal with an air

pollution problem due to building wake effects. *J. Wind Eng. Ind. Aerodyn.* 67–68, 781–791.
[https://doi.org/10.1016/S0167-6105\(97\)00118-9](https://doi.org/10.1016/S0167-6105(97)00118-9)

Pope, C.A., 2000. Review: Epidemiological basis for particulate air pollution health standards. *Aerosol Sci. Technol.* 32, 4–14. <https://doi.org/10.1080/027868200303885>

Rodean, H.C., 1996. Stochastic Lagrangian models of turbulent diffusion. American Meteorological Society, Boston.

Seinfeld, J.H., Pandis, S.N., 1998. Atmospheric chemistry and physics: from air pollution to climate change. John Wiley & Sons.

Tagliaferri, F., Invernizzi, M., Sironi, S., Capelli, L., 2020. Influence of modelling choices on the results of landfill odour dispersion. *Detritus* 12, 92–99. <https://doi.org/10.31025/2611-4135/2020.13998>

Wang, G., Bosch, F.H.M. Van Den, Kuffer, M., 2008. Modelling urban traffic air pollution dispersion. *Int. Arch. Photogramm. Remote Sens. Spat. Inf. Sci.* 37, 153–158.

Willmott, C.J., 1981. On the validation of models. *Phys. Geogr.* 2, 184–194.
<https://doi.org/https://doi.org/10.1080/02723646.1981.10642213>

Yang, W., Zhu, A., Zhang, J., Zhang, X., Che, W., 2016. Assessing the backward Lagrangian stochastic model for determining ammonia emissions using a synthetic source. *Agric. For. Meteorol.* 216, 13–19.
<https://doi.org/10.1016/j.agrformet.2015.09.019>

Yudego, E.A., Candás, J.C., Álvarez, E.Á., López, M.S., García, L., Fernández-Pacheco, V., 2018. Computational Tools for Analysing Air Pollutants Dispersion: A Comparative Review. *Proceedings* 2, 1408.
<https://doi.org/10.3390/proceedings2231408>

Influence of cross-flows on the performance of open-channel liquid chromatography

Alessandra Adrover*, Valentina Biagioni, Claudia Venditti, Stefano Cerbelli

Dipartimento di Ingegneria Chimica, Materiali, Ambiente, Sapienza Università di Roma,

Via Eudossiana 18, 00184 Roma, Italy

**Corresponding author E-Mail: alessandra.adrover@uniroma1.it*

1. Introduction

Taylor-Aris dispersion represents an undesired phenomenon in pressure-driven liquid chromatography, often responsible for the unchecked increase of the Height Equivalent of the Theoretical Plate (HETP) when high throughput operating conditions are sought.

The augmented dispersion in empty microchannels can be contained by inducing cross-sectional velocity components yielding an overall helical structure of the flow streamlines, that speed up mixing in the direction orthogonal to the channel walls.

The cross-sectional components can be induced e.g. by AC or DC electroosmosis. A beneficial effect of the cross-flow in reducing axial dispersion is found in both cases, for adsorbing and non-adsorbing walls as well.

Removing the assumption that the flow is independent on the axial coordinate and steady (e.g. by enforcing a spatially periodic structure along the axis or an explicit time dependency, or a combination of the two) a remarkably complex geometry of the flow streamlines can be obtained, which is typically associated with the phenomenon of chaotic advection. Such strategy has been applied extensively (and successfully) for enhancing mixing rate in micromixers and microreactors. Remarkably, to the best of our knowledge, no thorough study of the impact of chaotic advection has been pursued in dispersion theory and it is quite reasonable that it represents a valuable approach for taming axial dispersion in pressure-driven liquid chromatography.

We consider a class of physically realizable incompressible flows, where alternate patterns of embedded electrodes along the channel axis create a DC-induced cross-sectional flow possessing different degrees of chaotic behavior.

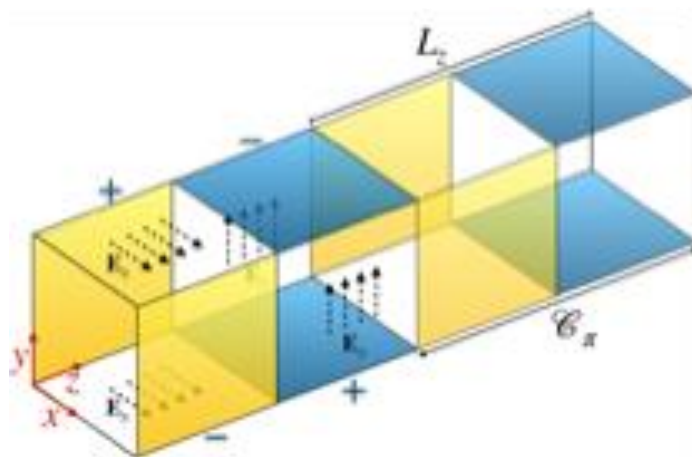


Figure 1. Electrode placement for the electroosmotically-induced spatially-periodic flow. The axial flow is created by a superimposed pressure gradient along the z coordinate.

Brenner's macrotransport approach is used to predict the axial dispersion coefficient D_{eff} in flows possessing regular, partially chaotic and globally chaotic kinematic features. Both cases of absorbing and non-adsorbing walls are investigated.

The validity and reliability of the numerical solution of the moment hierarchy as obtained by FEM 3-d simulations via Comsol Multiphysics is supported by independent Lagrangian stochastic simulations of particle ensembles.

4. Conclusions

Superimposing cross-sectional velocity components to the main pressure-driven axial velocity profile in an empty microchannel can drastically reduce the axial dispersion of an analyte carried by the flow and allows to increase the velocity of the eluent at moderate expenses as regards the increase of axial dispersion. The practical impact of our results is demonstrated by considering the chromatography of a mixture of three-species undergoing adsorption equilibrium with a stationary adsorbing phase coating the channel walls.

References

- [1] Zhao, H., Bau, H. H., Analytical Chemistry 79 (2007) 7792–7798.
- [2] Lester, D. R., Dentz, M., Le Borgne, T., Journal of Fluid Mechanics 803 (2016) 144–174.
- [3] Giona, M., Adrover, A., Cerbelli, S., Vitacolonna, V., Physical Review Letters 92 (2004) 114101.
- [4] Cerbelli, S., Adrover, A., Garofalo, F., Giona, M., Microfluidics and Nanofluidics 6 (2009) 747– 761.

Influence of side injection position on the mixing process in a tubular reactor equipped with Sulzer Static Mixers

Jody Albertazzi, Valentina Busini, Federico Florit, Renato Rota

Politecnico di Milano, Department of Chemistry, Materials and Chemical Engineering "Giulio Natta", Piazza Leonardo da Vinci 32, 20133, Milano, Italy

*Corresponding author E-Mail: valentina.busini@polimi.it

1. Introduction

Mixing is an important process in many food, pharmaceutical and chemical processes^{1,2,3}. The time (or space) needed to achieve complete homogenization is a key parameter depending on several variables such as fluid dynamics conditions and fluid properties.

While it is relatively easy to achieve complete mixing of chemical species for fully developed turbulent flows in pipes (i.e., for Reynolds numbers values greater than 4000)⁴, since vortexes and turbulent diffusion tend to lower the composition gradient along the radial coordinate, a much more compelling situation happens when laminar flows are involved, which is a common scenario for many chemical reactions that require long residence times to obtain satisfactory values of conversion; in laminar case, a parabolic profile velocity is obtained and strong gradients exist along the radial coordinate, which could only be lowered by molecular diffusion.

A complete homogenization can be obtained using active mixers, such as ultrasonic micromixers and pulse-flow mixers. However, these devices, while very efficient in mixing, are expensive and their operation is difficult, with high failure rates⁵.

A very promising alternative is represented by motionless mixers, or static mixers: these devices consist of a series of stationary and rigid inserts and are installed in tubular reactors, pipes and transfer tubes.

Unlike active mixers, they have no moving parts and require the mechanical energy coming from the flow momentum itself, so they need lower energy consumption and lower maintenance^{6,7}. Due to their relatively easy nature, they are employed in various industrial processes, such as wastewater treatment, paper, food, pharmaceutical, petrochemical and polymer industry⁷ and are considered to be key instruments in the transition from batch processes into continuous ones⁸.

There are various types of static mixers available: among them, the Sulzer SMX are known for being very efficient in mixing fluids, especially when fluids with very different properties (mass flow rate ratio and viscosity) are considered, as well as fluids with complex rheological behavior^{7,9}.

A complete understanding of the mixing process inside these devices is needed to optimize industrial processes in terms of productivity and energy consumption: indeed, pressure drops are known to be a critical factor in the choice of a static mixer¹⁰, and particularly Sulzer SMX are known to have higher pressure drops with respect to other passive mixing devices¹¹.

Various analyses varying the viscosity and the spatial velocity inside the reactor have already been performed¹²⁻¹⁴. Moreover, in previous works, both the mixing process as well as the residence time distribution (RTD) curve inside a side injection tubular reactor have been studied^{15,16}, finding that the Reynolds number and the Richardson number (for different densities flows) were the main parameters influencing the radial dispersion inside the reactor. Nevertheless, to the best of the authors' knowledge, the influence of the injection position on the mixing process has not been fully analyzed up to this: thus, the aim of this work is to expand

the mixing analyses previously done and to assess, through Computational Fluid Dynamics simulations, if a significant difference in terms of mixing efficiency exists when different configurations of injections are considered.

2. Methods

2.1 Reactor geometry

The modeled geometries consist of three tubular reactors, each one equipped with 15 Sulzer SMX and each one having a different typology of side injection: more in detail, Reactor A, reported in Figure 1a consists of a side-injection tubular reactor with the lateral injection placed on the section of the reactor before the static mixers, Reactor B, reported in Figure 1b is a side-injection tubular reactor having the injection exactly on the first static mixer, while Reactor C, shown in Figure 1c consists of a coaxial tubular reactor, with the side injection centered with respect to the reactor axis. The SMX element is formed by an array of adjacent crossed bars rotated with an angle of 90° with respect to each other. Several SMX mixing elements form together a mixer. Subsequent elements are rotated by 90° with respect to the previous element, so that the cross-flow mixing direction changes from one element to the next. Each SMX element is composed of eight blades and its aspect ratio, i.e., the length of the SM to the reactor diameter ratio, is equal to 1.

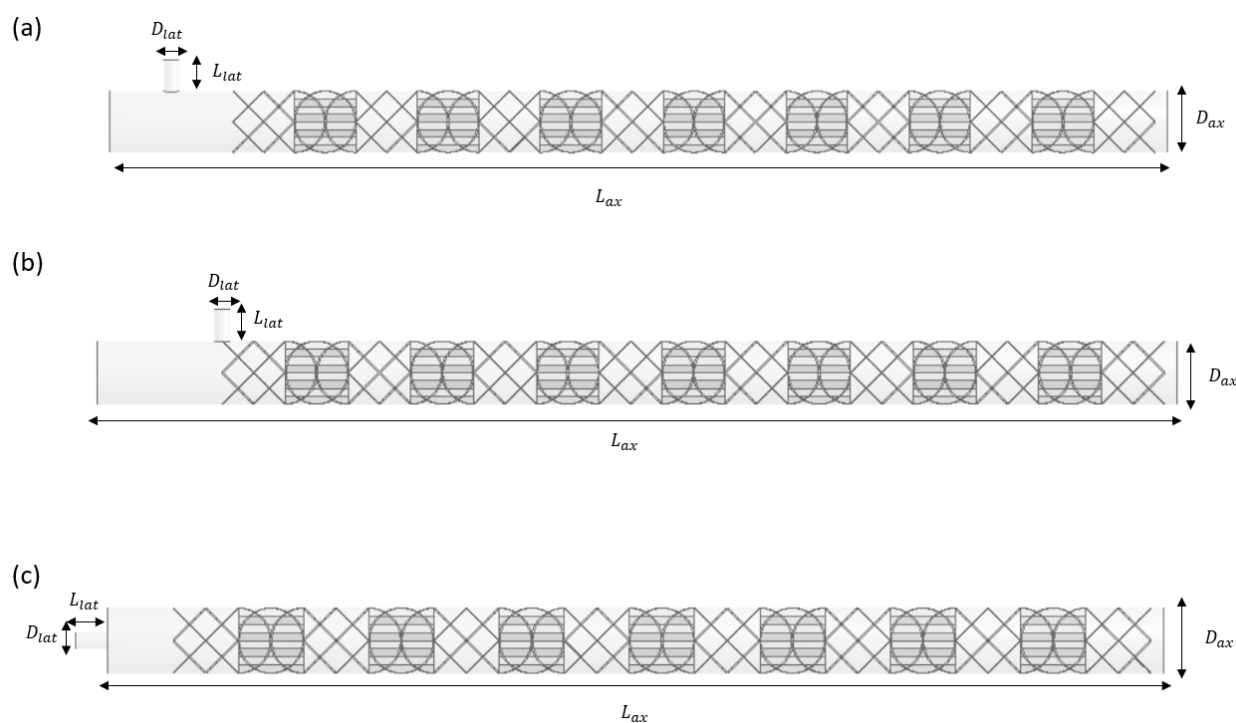


Figure 1. Reactor with side injection placed before the static mixers (1a); reactor with side injection placed on the First static mixer (1b); reactor with coaxial injection (1c).

The A component is fed through the axial tube inlet, which has a diameter equal to D_{ax} and a length equal to L_{ax} (in case of Reactor C, A is fed through the outer circular crown), while the smaller tube (diameter equal to D_{lat} and length equal to L_{lat}) allows the injection of the B component. The distance between the lateral tube and the first static mixer, in Reactor A and in reactor C is equal to one diameter. The geometrical properties of the reactors are resumed in Table 1.

Table1. Geometrical properties of the modelled reactors.

D_{ax} [m]	D_{lat} [m]	L_{ax} [m]	L_{lat} [m]
0,0508	0,0127	0,872	0,0254

In all the performed simulations, both the flow rates and the viscosity of the species A were varied to obtain various values of the Reynolds number (Re), which is defined as the ratio of inertial forces to viscous forces and it was calculated as follows:

$$Re = \frac{\rho_{mix} \cdot v \cdot D_{ax}}{\mu_{mix}}$$

where ρ_{mix} [kg/m^3] is the mass weighted mixture density and is calculated as $\rho_{mix} = (\omega_A/\rho_A + \omega_B/\rho_B)^{-1}$, with ω_A and ω_B being the mass fractions of the species A and B, respectively, v [m/s] is the spatial velocity inside the reactor and is obtained as $v = \frac{(m_A+m_B) \cdot 4}{\rho_{mix} \cdot \pi \cdot D_{ax}^2}$ and μ_{mix} [$Pa \cdot s$] is the mass weighted mixture viscosity, obtained through the following $\mu_{mix} = \mu_A \cdot \omega_A + \mu_B \cdot \omega_B$. The mass flow rate ratio between the streams A and B, \dot{m}_A/\dot{m}_B , was considered constant and equal to 10.

2.1 Mixing length analysis

The mixing of the two streams were characterized by the coefficient of variation, defined as follows:

$$COV(x) = \frac{\sqrt{(\overline{\omega_{B,x}^2} - \overline{\omega_{B,x}}^2)}}{\overline{\omega_{B,x}}}$$

where $\overline{\omega_{B,x}^2}$ is the mass-flow average of the squared mass fraction of B calculated at the axial position x and $\overline{\omega_{B,x}}^2$ is the mass-flow average of the mass fraction of B calculated at the axial position x. When $COV < 0.05$, uniformity over the cross section can be safely assumed. The mixing length is defined as the length from the injection of the B component for which $COV \leq 0.05$. The mixing length will be reported in terms of number of pipe diameters necessary to achieve perfect mixing, L_{mix}/D .

2.4 Mesh and CFD simulations

In this work, the results were obtained by solving continuity, momentum, and species mass fraction transport equations with the RANS approach by means of the Ansys Fluent 19.1 CFD suite of programs. A closure turbulence model is needed: the Shear-Stress Transport (*SST*) $k - \omega$ model was chosen, since it has been reported that it can correctly simulate the flow motions, from laminar to turbulent regime¹⁷.

The geometry was discretized through an unstructured mesh composed by tetrahedral cells, with cell refinement in correspondence of the static mixers wall, as shown in Figure 2a and 2b. In order to have reliable results, a mesh independent test must be performed: thus, a series of simulations (considering Reactor C) were performed considering mesh with increasing number of cells and the velocity outside the reactor was monitored.

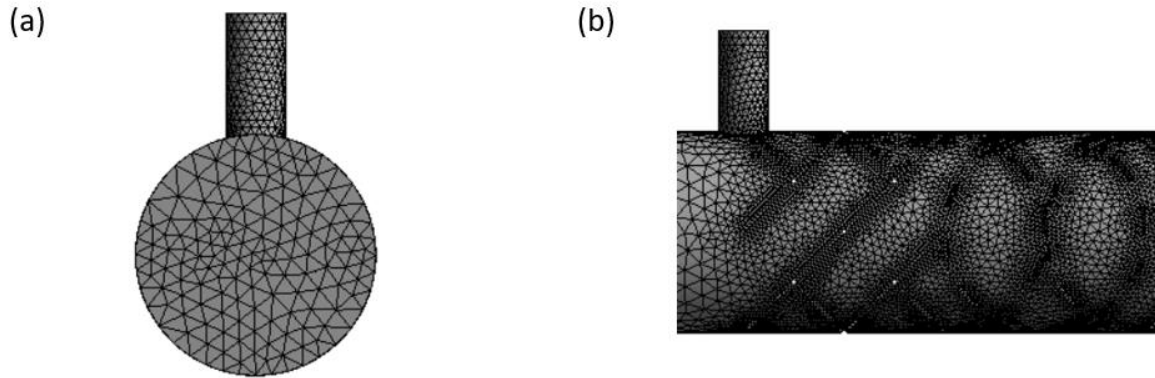


Figure 2. Inlet section mesh detail (a); Lateral reactor mesh detail (b).

Results are shown in Figure 3, which reports the values of the velocity as a function of the number of cells: the difference registered between the mesh with 6 million of cells and 13 million of cells is negligible, indicating a mesh independent result.

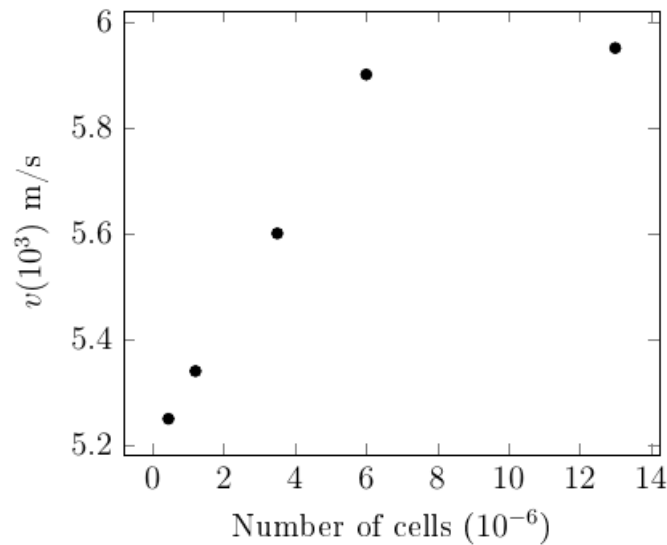


Figure 3. Grid independence test.

Moreover, since pressure drops are known for being particularly susceptible to flow perturbations³, as a further test the pressure drops obtained in a series of simulations at various Re , with the 6 million cells mesh were compared with the pressure drops obtained using a well-established empirical correlation⁷, defined as:

$$\Delta P = \frac{K_L}{Re} \cdot \rho \cdot v^2 \cdot \frac{L}{D}$$

where K_L is a dimensionless factor, which is comprised between 820 and 1280, depending on the technical details of the static mixer. In this case, considering a standard static mixer composed by 8 bars, K_L should be considered equal to 1070⁷. In the performed simulations the viscosity of the B component was kept constant

and equal to $\mu_B = 1 \cdot 10^{-3} [Pa \cdot s]$, while the viscosity of the A component was varied. Results are reported in Figure 4, confirming that the 6 million cells mesh can provide reliable results.

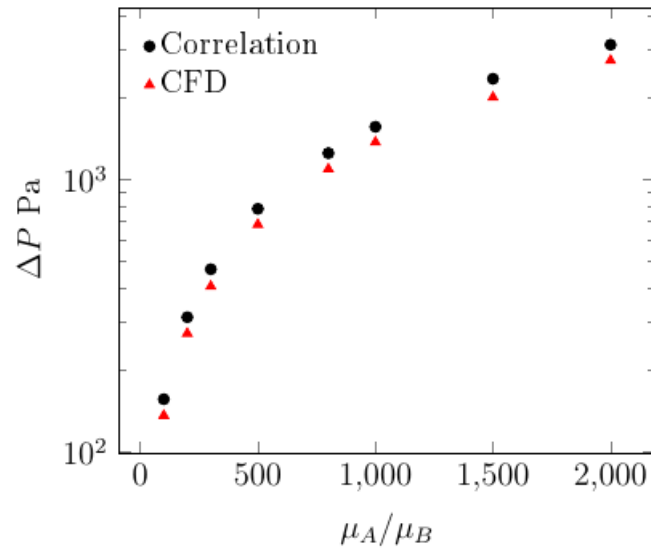


Figure 4. Validation of pressure drop with empirical correlation.

3. Results and discussion

A series of simulations were performed: in order to obtain various values of Re , both the mass flow rates and the mixture viscosity were varied. In all the simulations, the viscosity of the B component was kept equal to $\mu_B = 1 \cdot 10^{-3} [Pa \cdot s]$. Moreover, for sake of simplicity, buoyancy forces were neglected and the density of both species was kept constant and equal to $\rho_A = \rho_B = \rho_{mix} = 1000 [kg/m^3]$.

Table 2. Mixing length analysis boundaries conditions

$\dot{m}_A [kg/s]$	$\mu_A [Pa \cdot s]$	$\dot{m}_B [kg/s]$	Re
0,01	10	0,001	0,03
0,01	1	0,001	0,30
0,01	0,1	0,001	3,03
0,01	0,01	0,001	30,0
0,03	0,007	0,003	128
0,01	0,001	0,001	275
0,01	0,0005	0,001	505
0,04	0,001	0,004	1103
0,08	0,001	0,008	2206
0,2	0,001	0,02	5517

Results are reported in Figure 5, in which the mixing lengths as a function of Re obtained for the three reactor configurations are reported. It is possible to see that when a side-injection tubular reactor is adopted (reactor

A and reactor B), the mixing lengths obtained align on a curve which presents two asymptotes for, roughly, $Re < 10$ and $Re > 1000$. Considering the side-injection reactors, it is possible to see that positioning the lateral tube in the section before the static mixers has a negative effect on the mixing length: indeed, there is a difference in the mixing lengths between the two configurations of one diameter, which is the same distance that goes from the lateral injection and the first static mixer, in Reactor A. All the mixing lengths are comprised between 3 and 11 diameters, approximately.

On the other hand, when a coaxial reactor is considered (Reactor C), a very different trend is obtained: in this case, the mixing lengths obtained are approximately constant and equal to 5 diameters, even when strongly viscous flows are considered. This means that if a coaxial and centred injection is adopted, it is possible to neglect the influence of Re on the mixing process, since all the mixing lengths are comprised in a much smaller interval (roughly $5 < L_{mix}/D_{ax} < 4$). This represents a difference with respect to the other two reactor configurations, which mixing lengths appear to be strongly influenced by Re . These results suggest that a coaxial injection should always be preferred to efficiently achieve complete mixing. This is true for a single injection, but if more than one injection is needed in the same pipe (such as in reactor configurations used for the transition from semi-batch to continuous processes¹⁹⁻²¹), then a lateral injection must be adopted in practice (otherwise the SM cannot be inserted between the injection points). As an alternative, more injections in the same reactor can be achieved with flanged fittings between the various parts (this way coaxial flow can be implemented), but at a higher investment cost. Therefore, depending on the type of reactor (with single or multiple injections) coaxial flow can be exploited to lower the mixing length, otherwise lateral injections can be used considering larger mixing lengths.

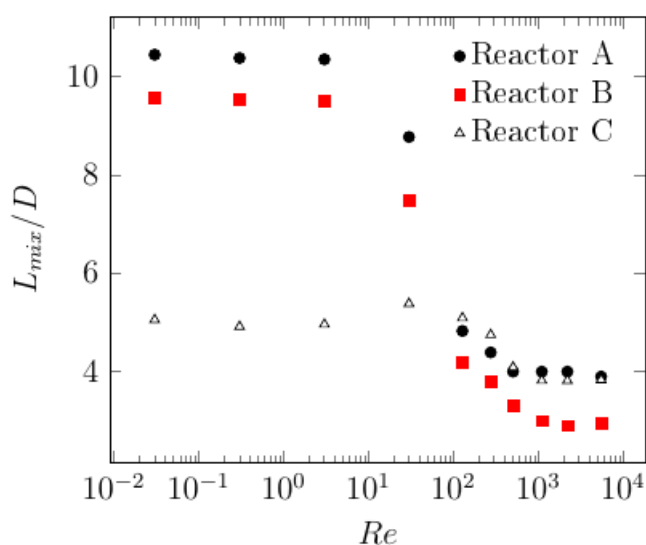


Figure 5. Mixing lengths as a function of Re for the three reactor configurations.

Figure 6 and Figure 7 show the contour of B mass fraction in the three reactors configurations for $Re = 3$ and $Re = 275$, respectively. It is possible to see that, considering Reactor A and Reactor B, the length in which the injected component is homogeneously dispersed across the section changes at the varying of Re ; on the other hand, when Reactor C is considered, the contours obtained for $Re = 3$ and $Re = 275$ do not differ significantly, thus confirming the results previously obtained. When $Re > 1000$ all the mixing lengths tend to align on an asymptote: indeed, it has been reported by experimental studies that, starting from this point, a complete turbulent regime is reached inside the Sulzer static mixers¹⁸. Thus the turbulent forces become

predominant and the influence of the side injection position on the mixing length, for Reactor A and Reactor C, becomes negligible, since in both cases the side injection was placed at the same distance from the mixing elements. On the other hand, the mixing lengths obtained with Reactor B and $Re > 1000$ are one diameter lower, because in this case the side injection was placed directly upon the first static mixer.

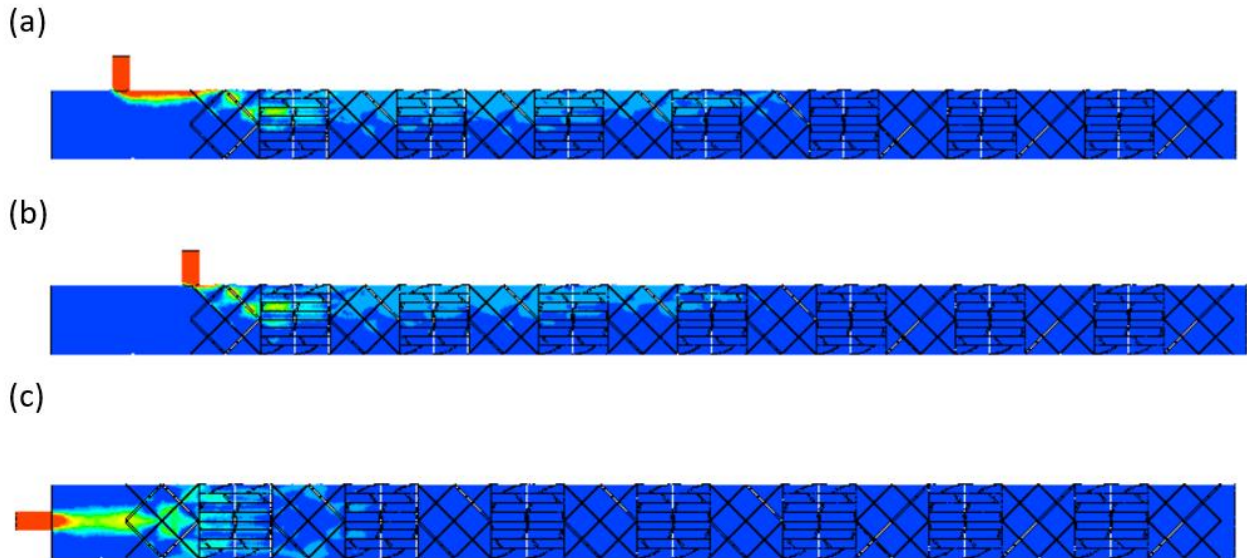


Figure 6. Mixing lengths obtained with the three reactor configurations for $Re = 3$.

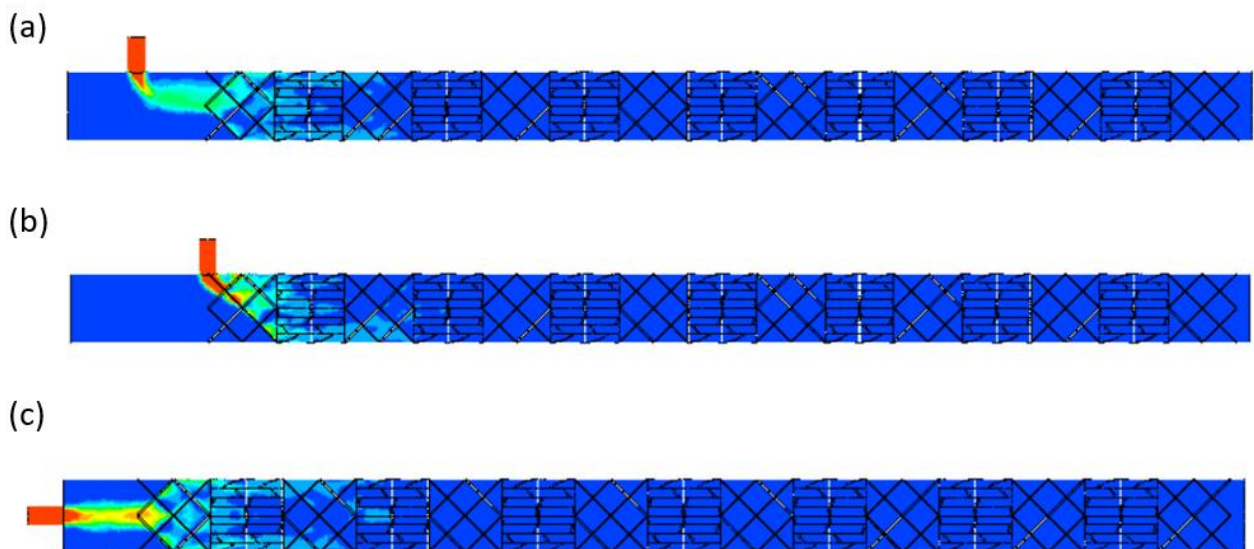


Figure 7. Mixing lengths obtained with the three reactor configurations for $Re = 275$.

4. Conclusions

A series of computational simulations were performed, with the aim of determine the influence of the injection position on the mixing efficiency of a tubular reactor equipped with Sulzer SMX. It was found that placing the side injection before the static mixers does not favor the mixing process; moreover, the mixing length is strongly reduced for $Re < 100$ when a coaxial injection is considered. These results should be considered in order to maximize the productivity and mixing efficiency of industrial processes, while at the same time lower

the total energy consumption: indeed, a lower mixing length means that a complete homogenization can be reached with less mixing elements, which implies that a lower pressure drop is needed in the reactor. Future studies may focus on the influence of the side injection position also when buoyancy forces are considered in a horizontal reactor, such as in the mixing of miscible fluids with different density and in multiphase flows.

References

- [1] R. Thakur, C. Vial, K. Nigam, E. Nauman, G. Djelveh, Static mixers in the process industry-a review *Chem. Eng. Res. Des.* 81 (2003) 787-826.
- [2] M. M. Haddadi, S. H. Hosseini, D. Rashtchian, M. Olazar, Comparative analysis of different static mixers performance by CFD technique: An innovative mixer, *Chin. J. Chem. Eng.* 28 (2020) 672-684.
- [3] B. W. Nyande, K. M. Thomas, R. Lakerveld, CFD Analysis of a Kenics Static Mixer with a Low Pressure Drop under Laminar Flow Conditions, *Ind. Eng. Chem. Res.* 14 (2021) 5264-5277.
- [4] C. Dyoike, U. Ngwaka, CFD Analysis of a Fully Developed Turbulent Flow in a Pipe with a Constriction and an Obstacle, *Int. J. Eng. Res. Technol.* 4 (2015) 2278-0181.
- [5] S. Klutz, S. K. Kurt, M. Lobedann, N. Kockmann, Narrow residence time distribution in tubular reactor for Reynolds number range of 10-100 *Chem. Eng. Res. Des.* 95 (2015) 22-23.
- [6] S. S. Soman, C. M. R. Madhuranthakam, Effects of internal geometry modifications on the dispersive and distributive mixing in static mixers, *Chem. Eng. Process* 122 (2017) 31-43.
- [7] S. Hirschberg, R. Koubek, F. Moser, F. Schöck, An improvement of the Sulzer SMXTM static mixer significantly reducing the pressure drop, *Chem. Eng. Res. Des.* 87 (2009) 524-532.
- [8] G. Montante, M. Coroneo, A. Paglianti, Blending of miscible liquids with different densities and viscosities in static mixers, *Chem. Eng. Sci.* 141 (2016) 250-260.
- [9] L. Z Huai, C. Fasol, L. Choplin, Residence time distribution of rheologically complex fluids passing through a Sulzer SMX Static Mixer, *Chem. Eng. Commun.* 165 (1998) 1-15.
- [10] R. Munter, Comparison of Mass Transfer Efficiency and Energy Consumption in Static Mixers, *Ozone Sci. Eng.* 32 (2010) 399-407.
- [11] G. Forte, E. Brunazzi, F. Alberini, Effect of residence time and energy dissipation on drop size distribution for the dispersion of oil in water using KMS and SMX+ static mixer, *Chem. Eng. Res. Des.* 148 (2019) 417-428.
- [12] C. Belhout, M. Bouzit, B. Menacer, Y. Kamla, H. Ameer, Numerical Study of Viscous Fluid Flows in a Kenics Static Mixer, *Mechanika.* 16 (2020) 206-211.
- [13] J. Zalc, E. Salai, F. Muzzio, Mixing Dynamics in the SMX Static Mixer as a Function of Injection Location and Flow Ratio, *Polym.* (43) (2003) 875-890.
- [14] M. Regner, K. Ostergren, C. Trägårdh, Influence of Viscosity Ratio on the Mixing Process in a Static Mixer: Numerical Study, *Ind. Eng. Chem. Res.* 47 (2008) 3030-3036.
- [15] J. Albertazzi, F. Florit, V. Busini, R. Rota, Mixing Efficiency and Residence Time Distribution of a Side-Injection tubular reactor equipped with Static Mixers, *Ind. Eng. Chem. Res.* 60 (2021) 10595-10602.
- [16] J. Albertazzi, F. Florit, V. Busini, R. Rota, Influence of Buoyancy Effects on the Mixing Process and RTD in a Side-Injection Reactor Equipped with Static Mixers, *Ind. Eng. Chem. Res.* 60 (2021) 16490-16497.
- [17] ANSYS Inc., ANSYS Fluent Theory Guide, release 19.1, 2018.
- [18] F. Theron, N. Le Sauze, Comparison between three static mixers for emulsification in turbulent flow, *Int. J. Multiph. Flow* 37 (2011) 488-500.
- [19] F. Florit, V. Busini, G. Storti, R. Rota, From semi-batch to continuous tubular reactors: A kinetics-free approach. *Chem. Eng. J.*, 354 (2018) 1007-1017.
- [20] F. Florit, V. Busini, G. Storti, R. Rota, Kinetics-free transformation from non isothermal discontinuous to continuous tubular reactors. *Chem. Eng. J.*, 373 (2019) 792-802.
- [21] F. Florit, V. Busini, R. Rota, Kinetics-free process intensification: From semi-batch to series of continuous chemical reactors. *Chem. Eng. Process.*, 354 (2020) 108014.

Flow features in a T-microchannel with cylindrical obstacles mixing water and ethanol

Matteo Antognoli*, Sara Tomasi Masoni, Roberto Mauri, Chiara Galletti, Elisabetta Brunazzi

Dipartimento di Ingegneria Civile e Industriale, Università di Pisa, Largo Lucio Lazzarino 2, Pisa 56122, Italy

*Corresponding author E-Mail: matteo.antognoli@phd.unipi.it

1. Introduction

Microfluidic reactor technology has become very attractive for a wide range of applications and research fields, such as engineering, chemistry, and biology [1-2]. Microreactors can manage with precise control fluids constrained in a small channel for a specific residence time. They also offer lower consumption of energy and raw materials, thereby increasing safety and economy. Regardless, considering the small sizes involved, the flow is inevitably laminar, so the fluid mixing mainly depends on molecular diffusion, which is usually a slow process. Therefore, it is necessary to devise the reactor geometry to enhance mixing [3-4]. The simplest passive micromixer has a T-shape, where two inlet flows join the main mixing channel through T-shaped branches. The complex flow regimes occurring in T-shaped microchannels have been investigated in detail through experiments and numerical simulations [5]. Recently, inserting obstacles such as cylindrical pins (pillars) into a T-microchannel has been a strategy to promote the chaotic advection and, thus, mixing and heat and mass transfer for the intensification of the yield and selectivity of chemical reactions and the reduction of energy cost in electronics cooling [6-9]. However, most of the studies on mixing in microreactors with obstacles are often limited in observing water mixtures that have limited use in practical applications, or the investigations can lack experimental results to validate the numerical ones.

The design of a T-microchannel with sequences of 20 cylindrical obstacles that differ in diameter dimension and position, was optimized for mixing water mixtures in [10]. The design approach based on the IAF (Interfacial Amplification Function) showed superior performance for efficiency and robustness compared to the Greedy and FIF (Final Interface Function) geometries.

In this work, experiments and CFD simulations were carried out on the IAF geometry using in addition to water-water (W-W) mixtures also water-ethanol (W-E) mixtures often employed in practical applications. Optical and numerical visualizations allowed us to gain insight into the flow behavior around the pillars for several Reynolds numbers. The numerical predictions were compared to measurements of depth-averaged concentrations to understand how physical properties affect the fluid dynamics at several sequence locations, observing the mixing progress. Eventually, a performance evaluation shows the efficiency and robustness of the device. These findings are relevant for processes dealing with the mixing of water and ethanol, such as the production of lipid particles, whose uniformity -- essential for the drug delivery purpose and cell targeting -- depends on the mixing quality.

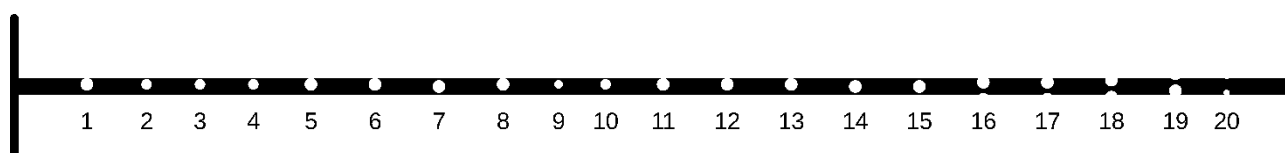


Figure 1. Sketch of the T-microchannel with pillars (distance between obstacles is reduced).

2. Methods

The experimental setup consisted of a syringe pump (KD Scientific syringe pump Gemini 88) provided of BD syringes of 30 mL, piping and luer lock fittings, an optical microscope (Nikon ECLIPSE 80i model) equipped with a magnifying lens of 4x, a high-speed camera (Optomotive Velociraptor HS model), a computer for the image processing, and a microfluidic device. The latter was made of PDMS and glass by adopting soft lithography and plasma etching techniques. The T-channel has an outlet cross-section of

$200 \times 50 \mu\text{m}^2$, and it contains 20 pillars of the IAF sequence obtained in [10]. The geometry is represented in the sketch of Fig. 1. The inlet channel width is $100 \mu\text{m}$. The mixing channel length is about 23 mm, and the pillar diameter ranges within $75\text{-}150 \mu\text{m}$.

Bidistilled water (CAS 7732-18-5, Titolchimica S.p.A.) and ethanol (VWR International S.A.S. CAS 64-17-5, content 99.97% v/v) were used for the experiments. Due to the hydrophobic channel surface, the surfactant SDBS (sodium dodecyl benzenesulfonate, CAS 25155-30-0, Sigma Aldrich) was dissolved in water at 0.5% to minimize the wettability difference between the ethanol and the water over the channel surface. The food dye Ponceau Red (E124) was employed to distinguish the two fluids in the flow visualizations from the top of the device using a low dye concentration to keep unchanged the fluid properties.

The CFD software Fluent ANSYS 19.2 was exploited to simulate the mixing in the microchannel by using the finite volume method. The fluid is incompressible, and the process takes place at isothermal conditions; thus, the governing equations consist of the Navier-Stokes equations and the transport equation for the mass-fraction of ethanol (Φ_E). The physical properties of the water-ethanol mixture varying the mass-fraction of ethanol were implemented in the CFD code through a bespoke subroutine. Indeed, this mixture has a non-ideal behavior as pictured in Fig. 2, showing the non-dimensional density ($\hat{\rho}$) and viscosity ($\hat{\mu}$), which are referred to the density and viscosity of water at 20°C , as a function of the mixture composition.

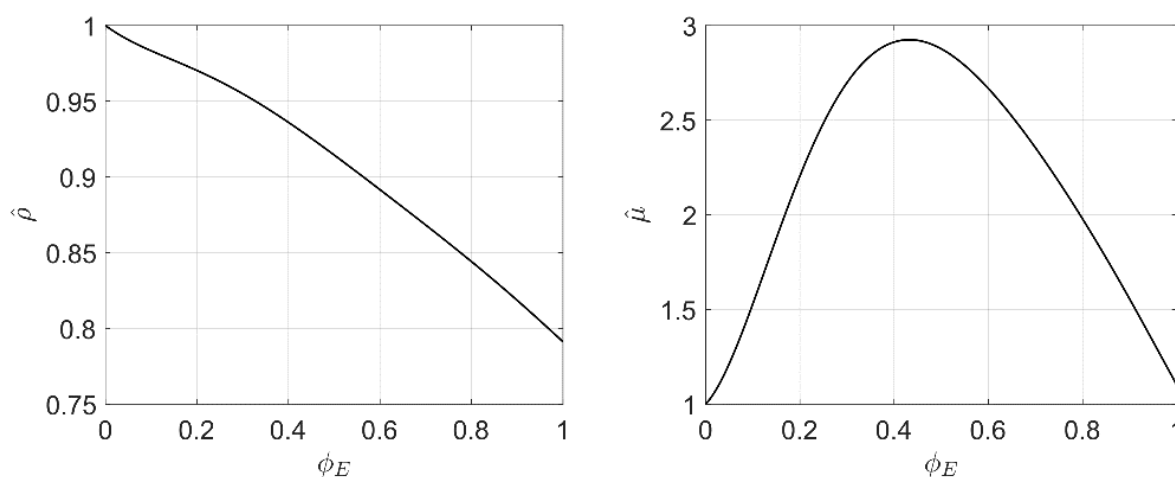


Figure 2. Non-dimensional density and viscosity of the water-ethanol system as a function of the ethanol mass-fraction.

A steady solver with a second-order upwind scheme was used, and the pressure-velocity coupling was treated with the SIMPLE algorithm. The convergence was ensured reaching normalized residuals below 10^{-9} . The computational grid is unstructured and formed by hexahedral elements, that are more refined near each pillar region. Hence, the minimum cell size is about $1.25 \times 1.6 \mu\text{m}^2$, and the maximum one is $1.25 \times 3.3 \mu\text{m}^2$. More details on the grid features and the independence from the solution are provided in [10].

3. Results and discussion

The W-W mixture is observed at $\text{Re}=40$ and compared with the W-E mixture at the same inlet volumetric flow rate; specifically, the Reynolds number (Re) is evaluated by considering the physical properties of water also in the W-E mixture. The experimental and numerical results show a fine agreement both at the beginning of the sequence (for instance at pillars 1-2 on the top panel of Fig. 3) and further down in the sequence (for instance at pillars 14-15 on the bottom panel of Fig. 3). The flow appears similar in both the

mixtures at the beginning of the pillar sequence. However, moving to the end of the channel, differences in the flow pattern between the two mixtures are observed. Indeed, the W-W mixture shows recirculations behind pillars 14 and 15 in Fig. 3, that are not present in the W-E case, where, instead, the flow remains attached to the pillar.

The formation of a viscosity layer at the fluid interface in the W-E system (see Fig. 4) may explain such a flow behavior. The pillars improve the mixing of the incoming fluids as a result of which however the viscosity of the mixture increases, and the formation of recirculations behind the obstacles is hindered. The effective Reynolds number of the mixture decreases along the channel as the mixing progresses.

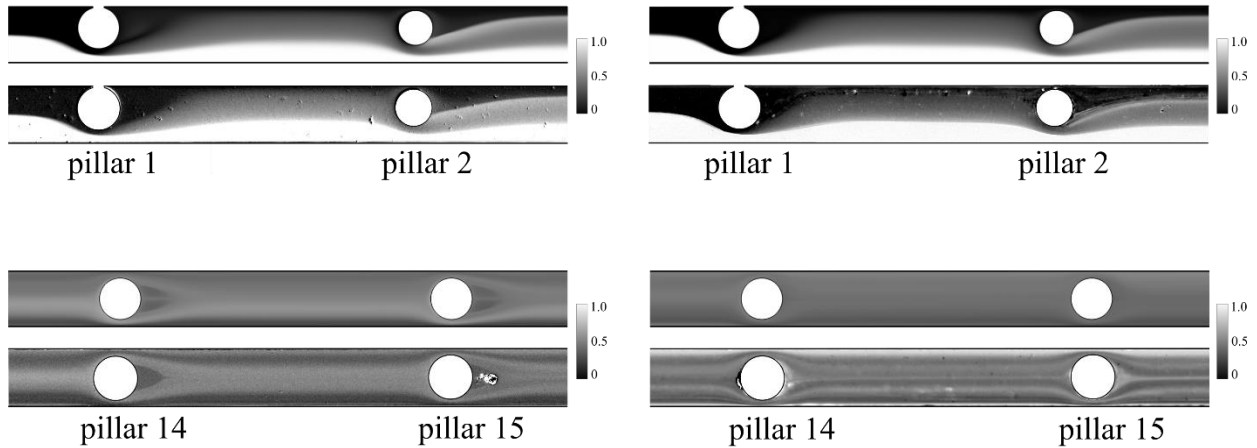


Figure 3. Top visualization of the device with experimental (top line) and numerical (bottom line) depth-averaged concentration fields for the W-W (on the left panel) and W-E (on the right panel) systems at pillar 1-2 and 14-15 at $Re=40$.

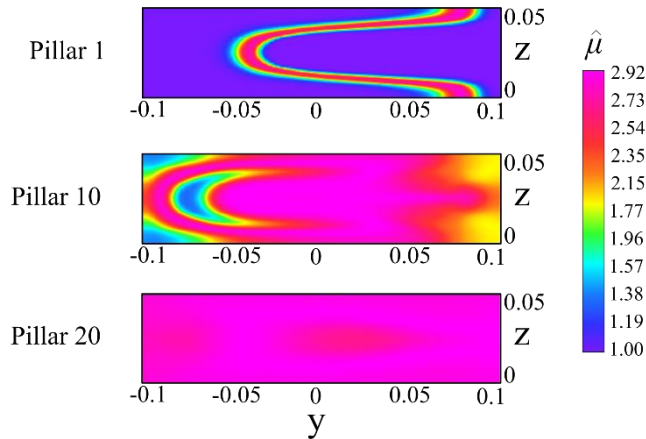


Figure 4. Cross-sectional contours of the non-dimensional viscosity of the W-E mixture for $Re=40$ at several channel locations.

For $Re = 40$, effective mixing is obtained, the values of the mixing index (MI, which is defined as $1 - \frac{\sigma}{\sigma_{max}}$, where σ is the standard deviation of the component mass-fraction field over a cross-section and σ_{max} is σ when the flow is completely segregated) are equal to about 85% for both mixtures. Nonetheless, the inertial forces lose intensity compared to the viscous forces in the W-E system, and the effective Reynolds number (Re^*_{outlet}) becomes 13 at the outlet section.

Similar results are observed for higher Reynolds numbers, as denoted in Table 1. On the contrary, mixing efficiencies are below 80% at $Re=10$. In particular, the W-E mixture achieves a value in Re^*_{outlet} that is very close to 1 and corresponds to the condition of Stokes flow. Hence, compared to the water-water case and

with the same volumetric flow rates at the T-microchannel inlet, in the case of water-ethanol, the predominance of viscous forces over inertial ones hinders the progress of the mixing along the channel.

Table 1. Mixing efficiencies of three cases ($Re=10, 40, 80$) for the W-W and W-E system and corresponding values of the Reynolds number of the water-ethanol mixture at the end of the microchannel (Re^*_{outlet}).

Re	10	40	80
MI^{W-W}	75.6 %	84.2 %	81.5%
MI^{W-E}	63.55 %	85.3 %	83.4 %
Re*_{outlet}	3.50	13.0	26.1

4. Conclusions

Numerical simulations and experimental visualizations provided an insightful analysis of the flow induced by pillars in a T-microchannel to mix water and ethanol. The alteration of the physical properties during the mixing process significantly affects the flow features, the Reynolds number of the mixture, and the mixing performance of the microreactor. The results of this study may support the optimization of the reactor design to improve the yield of chemical reactions and the quality of the products, e.g., to produce particles by using the flash precipitation method.

References

- [1] K.S. Elvira, R.CR Wootton, A.J. DeMello, *Nature chemistry* 5 no. 11 (2013) 905-915
- [2] I. Rossetti, M. Compagnoni, *Chemical Engineering Journal* 296 (2016) 56-70
- [3] N.-T. Nguyen, Z. Wu, *Journal of Micromechanics and Microengineering* 15 no. 2 (2005) R1-R16
- [4] J.M. Ottino, S. Wiggins, *Science* 305 no. 5683 (2004) 485-486
- [5] A. Mariotti, C. Galletti, R. Mauri, M.V. Salvetti, E. Brunazzi, *Chemical Engineering Journal* 341 (2018) 414-431
- [6] S. Zhang, N. Cagney, T. Lacassagne, S. Balabani, C.P. Naveira-Cotta, M.K. Tiwari, *Chem. Eng. J.* 397 (2020)
- [7] J. Wang, N. Zhang, J. Chen, V.G. J. Rodgers, P. Brisk, W.H. Grover, *Lab Chip* 19 (2019) 3618–3627
- [8] H.S. Santana, D.S. Tortola, J.L. Silva Jr., O.P. Taranto, *Chem. Eng. J.* 302 (2016) 752–762
- [9] A. Renfer, M.K. Tiwari, T. Brunschweiler, B. Michel, D. Poulikakos, *Exp. Fluids.* 51 (2011) 731–741
- [10] M. Antognoli, D. Stoecklein, C. Galletti, E. Brunazzi, D. Di Carlo, *Lab Chip* 21 (2021) 3910–3923

Using Dissipative Particle Dynamics as a Computational Rheological Tool: simulation of high Schmidt number fluids

Nunzia Lauriello¹, Antonio Buffo^{1*}, Gianluca Boccardo¹, Daniele Marchisio¹, Martin Lisa^{2,3}

1 DISAT – Institute of Chemical Engineering, Politecnico di Torino, C.so Duca degli Abruzzi 24, Torino 10129, Italy;

2 Department of Molecular and Mesoscopic Modelling, The Czech Academy of Sciences, Institute of Chemical Process Fundamentals, Prague, Czech Republic;

3 Department of Physics, Faculty of Science, J. E. Purkinje University, Ústí n. Lab, Czech Republic

**Corresponding author E-Mail: antonio.buffo@polito.it*

1. Introduction

One of the challenges of modern chemical engineering is to model the rheology of structured fluids, exploiting the increasing computational power together with more efficient computational methods. These modelling activities are extremely useful, as they contribute to reduce the number of experiments for investigating the scale-up and design of equipment for the processing of structured fluids. Structured fluids are very common in the food, personal-care, house-hold cleaner and pharmaceutical industries and include polymeric solutions and melts, suspension of colloidal particles, micellar solutions and liquid foams^[1]. Their rheological properties are very important as they define their possible applications, and they play a crucial role in the definition of design and scale-up rules for the corresponding processes and equipment. Depending on the system composition and the shear stresses, structured fluids arrange themselves in different micro-structures corresponding to different rheological behaviors. In the last years, several computational models have been developed to describe the behaviour of these fluids. At the largest scale of interest, Computational Fluid Dynamics (CFD) can be used to predict flow field in industrial scale equipment, giving the possibility to estimate important macroscopic quantities, such as pressure drop or power input, which are crucial for process design and optimization. However, the transport properties of the complex fluid are an input information of a CFD simulation, and such important information requires the fluid characterization at lower scales. Because of the characteristic size of the system and the time evolution of the process under investigation, conventional molecular simulation methods are not suitable for the description of structured fluids, in fact they rely on fully-atomistic approach, resulting in high computational costs. To overcome this limitation, Dissipative Particle Dynamics (DPD) is here employed^[2]. DPD is considered one of the most flexible simulation techniques: both static and flowing structured fluids, and more in general soft matter systems, are treated at physically interesting length- and time-scales. This method involves the use of Coarse-Grained (CG) models, in which groups of atoms and molecules, so-called “beads”, are processed as single units, each representing a complex molecular component of the system. In this perspective, it is therefore possible to simulate the hydrodynamic behaviour of structured fluids with a considerably lower number of particles, thereby reducing the computational effort. Dissipative Particle Dynamics is a powerful mesoscopic modelling technique widely used to qualitatively predict complex fluid morphology and structural properties. While its ability to rapidly scan conformational space is well known, it is unclear whether DPD can correctly calculate the viscosity of complex fluids^[3]. Indeed, although standard DPD gives good results in predicting static equilibrium properties, several studies in the literature report that the DPD method fails in reproducing the transport properties of real fluids. In particular, in their work, Groot and Warren showed that the original DPD scheme results in a Schmidt number of $O(1)$, unacceptably low for the simulation of liquid water at room temperature and pressure. The Schmidt number, Sc , is a dimensionless number defined as the ratio between the fluid kinematic viscosity ν , and the self-diffusion coefficient \mathcal{D} :

$$Sc = \frac{\nu}{\mathcal{D}}. \quad (1)$$

It groups two important transport properties giving a measure of the relative importance between fluid particle diffusion and momentum diffusion. For a typical liquid, the Schmidt number is $O(10^3)$, meaning that the momentum is usually transported more efficiently than fluid particles themselves, because of the caging effect of the interparticle potential. The dependence of the Schmidt number on the various DPD parameters can be expressed as:

$$Sc \sim \gamma^2 \rho^2 r_c^8, \quad (2)$$

where γ is the dissipative parameter, ρ is the density of DPD fluid and r_c is the cutoff radius for interparticle forces. However, even if these parameters strongly affect the Schmidt number simply by increasing them, also the computational costs would increase either directly, or indirectly by having to decrease the time step in order to maintain the simulation stability. In this work, we decided to investigate the performance of the transverse DPD thermostat, specifically formulated for the prediction of transport properties via DPD, in simulating high Sc number fluids with equilibrium simulations^[4]. We carried out a parametric study aiming at finding the DPD parameters capable of properly recovering the rheological behaviour of liquid water at room temperature and pressure, which is an important physical example requiring high Sc number and is a preliminary step to simulate complex fluids as aqueous polymer mixtures. We devoted particular attention to the numerical techniques for computing the transport properties from equilibrium simulations. Specifically, we compared the most adopted techniques for the viscosity calculation formulating a method that can be used for further investigations. Indeed, while non-equilibrium simulations are routinely employed in DPD to calculate both simple fluids and polymer viscosity with minimal computational cost it remains unclear whether the equilibrium approaches for the viscosity calculation can be confidently used with DPD, since these methods are subject to significant statistical error. This is a crucial point as we want to calculate the viscosity of morphologies resulting from the simulations without perturbing them, using an equilibrium simulation^[3].

2. Methods

As previously mentioned, DPD is a CG mesoscale simulation technique that simulates a fluid as a set of particles, often called beads which group together a certain number of atoms or molecules. In the case of a simple DPD fluid, bead i experiences the force, \mathbf{f}_i defined by

$$\mathbf{f}_i = \sum_{j \neq i} (\mathbf{F}_{ij}^C + \mathbf{F}_{ij}^D + \mathbf{F}_{ij}^R). \quad (4)$$

A conservative contribution, \mathbf{F}_{ij}^C , is a soft-repulsive force acting between two beads i and j and is defined as

$$\mathbf{F}_{ij}^C = \begin{cases} a_{ij} \left(1 - \frac{r_{ij}}{r_c^C}\right) \hat{\mathbf{r}}_{ij}, & r < r_c^C \\ 0, & r \geq r_c^C \end{cases} \quad (5)$$

where a_{ij} determines the strength of the repulsion between beads i and j and the compressibility of the simulated fluid; $r_{ij} = |\mathbf{r}_{ij}| = |\mathbf{r}_i - \mathbf{r}_j|$ is the separation distance between the beads, $\hat{\mathbf{r}}_{ij} = \frac{\mathbf{r}_{ij}}{r_{ij}}$ is the unit vector of the bead-bead separation distance and r_c^C is the cutoff radius for the conservative interactions. Dissipative and random contributions/forces, \mathbf{F}_{ij}^D and \mathbf{F}_{ij}^R , respectively, introduce viscous drag and thermal noise to the system, respectively, and act as a thermostat. Dissipative cutoff radius, r_c^D , is introduced for these forces. As originally introduced^[5,6], the dissipative and random forces act, similarly as the conservative force, along the bead-bead separation distance and are pairwise additive. In this work, the standard DPD thermostat is combined with the transverse DPD thermostat^[7] acting in the plane perpendicular to the bead-bead separation distance. The expressions for dissipative and random forces can then be written as

$$\mathbf{F}_{ij}^D = -\gamma_{\parallel} w_{\parallel}^2(r_{ij}) (\hat{\mathbf{r}}_{ij} \cdot \mathbf{v}_{ij}) \hat{\mathbf{r}}_{ij} - \gamma_{\perp} w_{\perp}^2(r_{ij}) (\mathbf{I} - \hat{\mathbf{r}}_{ij} \hat{\mathbf{r}}_{ij}^T) \mathbf{v}_{ij}, \quad (6)$$

$$\mathbf{F}_{ij}^R = \sigma_{\parallel} w_{\parallel}(r_{ij}) \frac{\xi_{ij}}{\sqrt{\Delta t}} \hat{\mathbf{r}}_{ij} + \sigma_{\perp} w_{\perp}(r_{ij}) (\mathbf{I} - \hat{\mathbf{r}}_{ij} \hat{\mathbf{r}}_{ij}^T) \frac{\xi_{ij}}{\sqrt{\Delta t}}. \quad (7)$$

Here γ_{\parallel} and γ_{\perp} are parallel and perpendicular dissipative parameters, respectively, analogously σ_{\parallel} and σ_{\perp} are parallel and perpendicular noise parameters, $w_{\parallel}(r_{ij})$ and $w_{\perp}(r_{ij})$ are weighting functions (WFs) for the parallel and perpendicular contributions. The dissipative and noise parameters are related to each other in order to satisfy the fluctuation-dissipation theorem:

$$\sigma_{\alpha} = \sqrt{2k_B T \gamma_{\alpha}}, \quad \alpha \in \{\parallel, \perp\}, \quad (8)$$

where k_B denotes the Boltzmann constant and T the system temperature. The WFs have the following functional form:

$$w_{\alpha}(r_{ij}) = \left(1 - \frac{r_{ij}}{r_c^D}\right)^{s_{\alpha}}, \quad \alpha \in \{\parallel, \perp\}, \quad (9)$$

and its exponent, $s_{\alpha} \in (0,1]$, plays an important role in modeling of dynamic properties of a DPD fluid.

The estimation of transport coefficients in DPD simulations takes place with numerical techniques developed for atomistic simulations. The self-diffusion coefficient in this work is calculated by the Einstein relation according to which it is proportional to the mean-square displacement (MSD) of the beads.

The methods for the evaluation of the viscosity from atomistic simulations are divided into two groups: equilibrium and non-equilibrium methods. To the first category belong methods such as Green-Kubo^[8,9] and Einstein-Helfand^[10], while to the latter one the reverse non-equilibrium molecular dynamics (RNEMD). We were interested in the use of equilibrium methods to estimate the viscosity from the simulation. However, the RNEMD method by Müller-Plathe^[11] is used as a benchmark to double-check and verify the evaluation of viscosity by the equilibrium methods. Green-Kubo relation allows to calculate the viscosity by integrating the stress autocorrelation function (SACF) and has the following form:

$$\mu = \frac{V}{k_B T} \int_0^{\infty} \langle \sigma_{\alpha\beta}(t_0) \sigma_{\alpha\beta}(t_0 + t) \rangle dt, \quad (\alpha \neq \beta), \quad (10)$$

where V is the system volume and $\sigma_{\alpha\beta}$ is the off-diagonal component of the stress tensor.

All simulations were performed by using the open-source software LAMMPS. The DPD model with extended thermostat was implemented as a user package. Regarding the calculation of the viscosity with the Green-Kubo approach, it is worth mentioning that LAMMPS uses an approximate algorithm to evaluate SACF, since the calculation according to its definition would be computationally intensive. Only a limited data set is actually employed in the SACF evaluation, namely the data points correlated every N_{ev} -th timestep for $N_{ev} \cdot (N_{rep} - 1)$ timesteps. Instead, the SACF averages are computed every N_{freq} timesteps. However, the final simulation time needs to be sufficiently long to carry out a correct estimation because, the algorithm makes use of the ergodic hypothesis to evaluate the ensemble average as a time integral. Therefore, the choice of N_{ev} , N_{rep} and N_{freq} is critical in the proper evaluation of SACF and, in general, in the viscosity evaluation.

3. Results and discussion

The crucial point for the viscosity calculation based on Green-Kubo method stands mainly in the numerical evaluation of the time integral of the SACF. This issue is linked to the well-known behaviour of the SACF which is reported in Fig. 1: after a first clear decaying trend the values of the SACF oscillate around zero with a certain noise, assuming also negative values. Therefore, the calculation of such time integral with a simple trapezoidal rule is affected by the tail oscillations. This behaviour results from the large fluctuations associated with the stress tensor element values affected by an extra noise due the presence of stochastic force leading to poor accuracy in the resulting viscosity. Moreover, the tail oscillations increase with increasing the friction coefficient. Different integration algorithms and the effect of finite timestep also play a role in the low statistical accuracy. A first challenge associated with the equilibrium method is both to improve statistical accuracy and to quantify results uncertainty. An additional challenge is to decide on the limit of the integration point. To overcome these issues, we tested several procedures. A first approach, denoted as ‘‘Procedure A’’, was to adopt the procedure proposed by Jung and Schmid^[12]. The procedure consists of the numerical integration by using the trapezoidal rule until the SACF values reached about 1% of their initial values. Then, the tail is fitted using a power-law, i.e.: At^{-B} , and integrated analytically. An alternative is to follow a procedure similar to the previous one, but with the preliminary application of a moving average filter to smooth

out the tail oscillations. This is denoted as “Procedure B”. However, the fitted power-law always approaches have a common problem: the power law tends to zero asymptotically more slowly than the actual values of the SACF. The latter begins to oscillate between positive and negative values when the power law still does not reach the asymptotic value. For this reason, we tried to use two approaches for the analytical integration of the fitted power-law. In the first approach, the final integration time is the final SACF available from the simulation post-processing, depending on the N_{rep} and Δt , and is labelled with number 1 in Table 1. In the second approach, the analytical integration is carried out up to ∞ and is labelled with the number 2 in Table 1. Despite of the second approach has a significant impact on final viscosity values the effect of the tail noise is still not quantified by using these procedures.

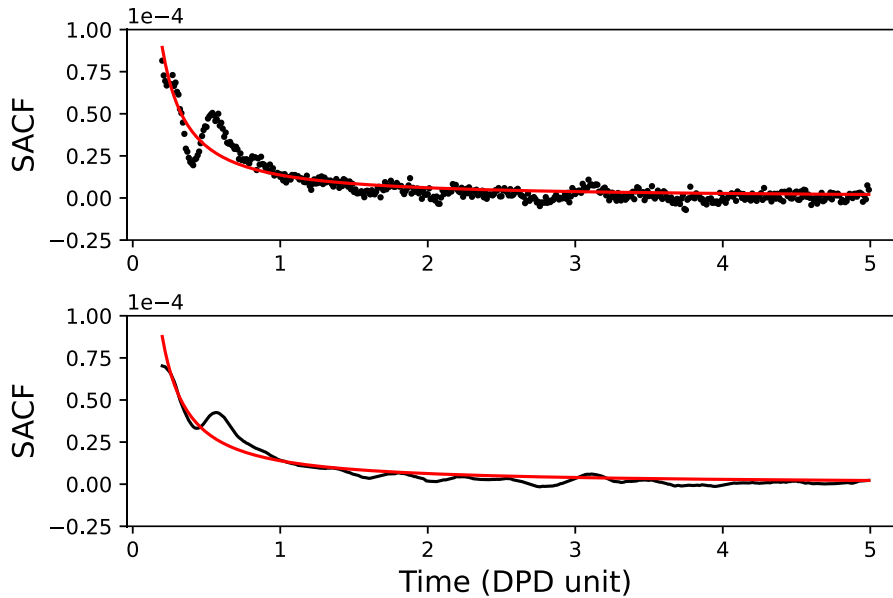


Figure 1. Two different representations of the tail of the same SACF. Top: procedure A. Black circles: points of the SACF. Red line: power-law fit. Bottom: procedure B. Black line: SACF after a moving average filter. Red line: power-law fit.

For this reason, we tried to use an approach based on the calculation of the viscosity cumulative integral function of time, denoted as in what follows as “Procedure C”. The idea behind this latter procedure is to evaluate the viscosity by using Eq. (10) progressively extending the integration interval up to the final SACF time. The result of Procedure C should theoretically be a monotonic curve that approaches an asymptotic value that corresponds to the system viscosity. However, this is impossible to reach exactly due to the intrinsic stochastic noise within DPD simulations and an example of such calculation is depicted in Fig. 2. Therefore, we opt to evaluate the system viscosity as the average value of the curve considering only the last DPD time units, avoiding the initial transient. Moreover, Procedure C is particularly convenient since it allows us to evaluate standard deviation and a coefficient of variation, providing therefore not only the expected viscosity value but also the associated uncertainty.

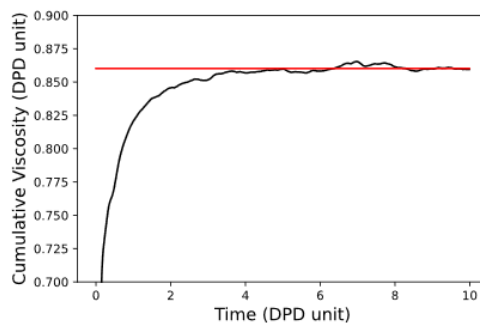


Figure 2 Cumulative integral of viscosity calculated using the Green-Kubo approach. Black line: viscosity cumulative integral. Red line: mean value and coefficient of variation calculated between $t = 5$ and 10.

Table 1. Viscosity values (in DPD unit) calculated with various approaches. Procedure A: power-law fitting. Procedure B: moving average filter before power-law fitting. The superscripts 1 and 2 correspond respectively to a final integration time of $N_{rep} \cdot \Delta t$ and infinite. Procedure C: cumulative integral. E-H and RNEMD refers to Einstein-Helfand and reverse non-equilibrium molecular dynamics methods.

γ_{\parallel}	A ¹	A ²	B ¹	B ²	C (mean)	C (Stand. dev.)	C (Coef. of var.)	E-H	RNEMD
4.5	0.8535	0.8846	0.8706	0.9399	0.860	0.002	0.002	0.847	0.860
9	0.9699	1.0018	0.9892	1.0613	0.957	0.004	0.004	0.923	0.930
15	1.1128	1.1468	1.1308	1.2065	1.065	0.002	0.002	1.071	1.055

Procedure C gives the closest results with the other two benchmark methods, and this procedure is then used in the rest of the work and has been automated. Furthermore, we integrated, also, this post-processing procedure into an iterative algorithm which during the simulation progressively identifies the simulation and the correlation post-processing parameters for the calculation of the SACF and capable to give us a value of viscosity within an acceptable range of uncertainty linked to the intrinsic stochastic noise of the method and timestep independent. This allows us to employ the minimal computational time in order to have an accurate statistic for the calculation of the SACF and consequently of the viscosity.

Once a reliable procedure for calculating the viscosity was found, the effect of different DPD parameters on Schmidt number of DPD fluid was investigated by performing different simulations, aiming to reproduce the Schmidt number of water at 25°C equal to about 370. The parameters varied are the dissipative cutoff radius, r_c^D , the weighting function exponent, s and the dissipative parameters, γ_{\parallel} and γ_{\perp} . We, also, investigated the combined effect of timestep and integration algorithm on the computation of transport properties.

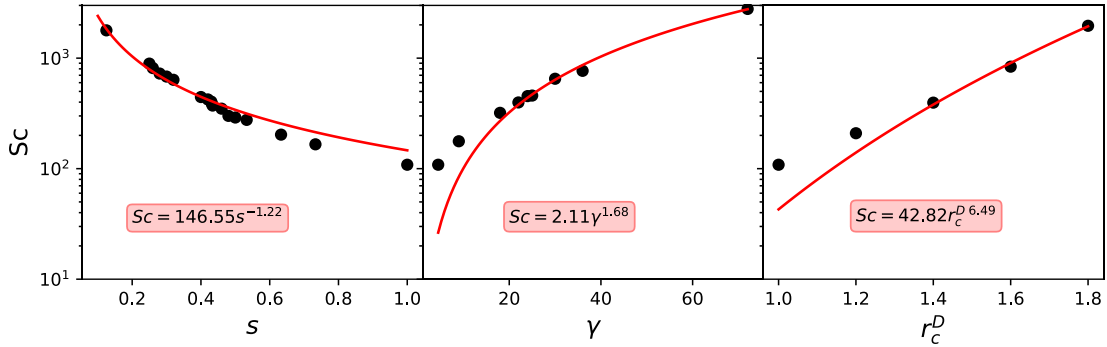


Figure 3. The Schmidt number as a function of (left) dissipative parameter γ , (center) GWF exponent s and (right) dissipative cutoff radius r_c^D . Dependences of the Schmidt number on the DPD parameters were fit to the power-law.

In Table 2, several aspects are worth to highlight. First, the conversion of viscosity and self-diffusion values from DPD units to real units, gives realistic results for liquid water at 25°C. Another important parameter reported in Table 2 is the so-called effective friction coefficient^[13], defined as follows:

$$\gamma^{eff} = \int_0^{r_c^D} \gamma w(r_{ij}) g(r_{ij}) 4\pi r^2 dr_{ij}, \quad (13)$$

where $g(r_{ij})$ is the radial distribution function (RDF). The effective friction coefficient is a measure of the overall bead friction and enables us to the effects of s , r_c^D , γ and implicitly of N_m into one single characteristic quantity. We can see from Table 2 that values of γ^{eff} for the three sets are rather similar. It is interesting that sets of parameters giving the same γ^{eff} give the same dynamical properties without perturbing the RDF which depends only on conservative contribution. In sight of this, we carried out a multi-parametric study aiming to investigate the Sc number scaling with γ^{eff} and to build curves that can help us to determine the proper parameters we should use in order to simulate a fluid with given dynamical properties.

Table 2. The properties of DPD fluid corresponding to the three sets of DPD parameters, calibrated against the Schmidt number of liquid water at 25°C equal to about 370.

	Set 1	Set 2	Set 3
s	0.434	1	1
r_c^D	1	1.38	1
γ	4.5	4.5	20.2
Δt	0.01	0.005	0.01
N_m	10	10	10
ρ	3	3	3
v^{DPD} (G-K)	5.89	5.87	5.88
ν (m ² /s)	$0.895 \cdot 10^{-6}$	$0.892 \cdot 10^{-6}$	$0.893 \cdot 10^{-6}$
D^{DPD}	0.016	0.016	0.016
D (m ² /s)	$2.43 \cdot 10^{-9}$	$2.43 \cdot 10^{-9}$	$2.43 \cdot 10^{-9}$
Sc	368.54	367.22	367.5
γ^{eff}	4.36	3.90	4.00

4. Conclusions

It can be concluded that, appropriately choosing the simulation parameters for the SACF calculation and adopting the developed method, the viscosity coefficient estimated via the Green-Kubo approach is comparable with that obtained by using reference techniques with the advantage that this method does not suffer of the intrinsic limitations of non-equilibrium methods. This becomes crucial for viscosity prediction in self-assembled non-Newtonian systems. Moreover, the proposed method of treating the noise of the SACF tail can give not only the mean viscosity value, but also the uncertainty of the numerical procedure associated with the viscosity evaluation. In this work, we show that such uncertainty is lower or comparable to the uncertainty of the experimental measurements.

The transverse DPD thermostat, including shear dissipation, can be used to simulate high Sc number fluids. It, in particular, can reproduce the proper momentum and mass transport behavior of liquid water, with at least three different sets of DPD parameters. The Sc number depends on model parameters whose effect can be grouped into the effective friction coefficient.

References

- [1] R.G. Larson, The Structure and Rheology of Complex Fluids, Oxford University Press, 1999.
- [2] R.D. Groot, P.B. Warren, Imperial College Press 107 (1997) 4423–4435
- [3] M. Panoukidou, C. R. Wand, P. Carbone, Soft Matter 17 (2021) 8343–8353
- [4] N. Lauriello, J. Kondracki, A. Buffo, G. Boccardo, M. Bouaifii, M. Lisal, D. Marchisio, Physics of Fluids 33 (2021) 073106
- [5] P.J. Hoogerbrugge, J.M.V.A. Koelman, Europhys. Lett. 19 (1992) 155–160
- [6] P. Español, P. Warren, Reviews in computational chemistry 30 (1995) 191–196
- [7] C. Junghans, M. Praprotnik, K. Kremer, Soft Matter 4 (2007) 156–161
- [8] M.S. Green, Journal of Chemical Physics, 20 (1952) 1281–1295
- [9] R. Kubo, J. Phys. Soc. Jpn. 12 (1957) 570–586
- [10] E. Helfand, Physical Review 119 (1960) 1
- [11] F. Müller-Plathe, Physical Review E. 59 (1999) 5
- [12] G. Jung, F. Schmid, The Journal of Chemical Physics 144 (2016) 204104
- [13] F. Lahmar, B. Rousseau, Polymer 48 (2007) 3584–3592

Open-cell foams modeling: workflows for geometry generation and CFD simulations for pressure drops and mass transport

Enrico Agostini^{1*}, Maxime Moreaud², Yacine Haroun², Gianluca Boccardo¹, Daniele Marchisio¹

¹ Department of Applied Science and Technology (DISAT), Politecnico di Torino, Torino, Italy;

² IFP Energies Nouvelles (IFPEN), Solaize, France.

*Corresponding author E-Mail: enrico.agostini@polito.it

1. Introduction

The interest of the process industry towards ceramic and metallic open-cell foams has greatly increased over the last twenty years. The reasons reside in the unique properties of these porous materials such as mechanical resistance, very high porosity, which results in lower pressure drops compared to other packing media, large specific surface area and high thermal conductivity, which are important factors for mass and heat transfer. Notable uses of these solid foams are filters, monolithic catalyst supports, column packing for packed bed reactors and heat exchangers.

Despite the great advancements in the scientific research and in the production technique during the last 30 years, correlations that links the key geometric parameters (porosity, specific surface) to the performances of these materials are still hard to find. The main parameters used to characterize commercially available open-cell foams are porosity ε and the *pore per inch* (PPI); which indicate the average pore diameter. However, these physical properties do not give any clue regarding specific surface S_v , which is important for the design of industrial devices and estimation of the pressure drops $\Delta P/L$ and heat and mass transfer coefficients, such as h and k_c . For all these reasons the optimization of such structures remains an open problem.

A first approach to model the geometric structure of open-cell foams, used by many authors, relies on the *Kelvin's Cell* structure, an ideal periodic polyhedron, called *Tetrakaidecahedron*, representing a single pore. The advantages of such an approach come from the limited computational effort required and the possibility of conceiving analytical correlations for the estimation of geometrical properties (S_v , ε), pressure drop $\Delta P/L$ and transfer coefficients. However, because of the random nature of open-cell foams, the necessity for more complex and realistic geometrical models has arisen in order to explain the key factor influencing transport phenomena occurring at the micro-scale. In literature there is evidence that random *Voronoi* or *Voronoi-Laguerre* tessellations can be effective in representing the cellular random nature of solid foams. The advantage of these algorithms, that subdivide a confined space into distinct regions, is that they allow the creation and the study of many more structures and configurations that would experimentally be viable.

The objective of this abstract is to introduce the digital workflows we have developed, tested and validated to reproduce a great variety of structures, exploring large parameter ranges, in order to be able to optimize the geometric structure according to the different application areas.

2. Methods

The first tool [1] relies only on the open-source computer graphics code `Blender` and on `Python` programming language code to calculate and create the final geometry. This workflow is able to create both ordered lattice geometries, such as the *Kelvin's Cell*, and random models such as those originated from *Voronoi-like* tessellations, by providing the coordinates of the nodes and edges of the structures.

In the first case, the coordinates are well known, whereas in the case of the random tessellations they must be generated starting from an initial set of points in space. The initial set of random points, called *seeds*, is

achieved by using the centers of spheres randomly packed (either mono- or poly-dispersed), following an already validated workflow proposed by [2], then the tessellation is calculated and the position of the edges and nodes of the tessellation is retrieved. Finally, Blender creates cylinders and sphere at the supplied coordinates to generate the foam structure. An example of a polydisperse foam geometry generated by the workflow is reported in Fig. 1.

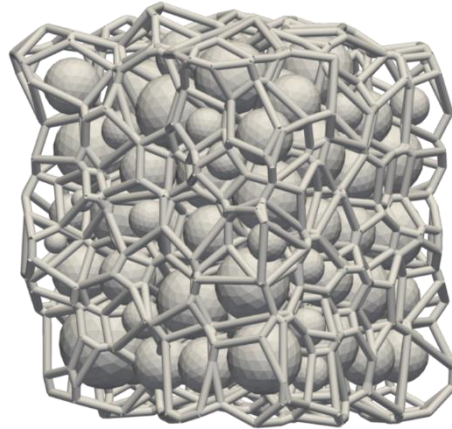


Figure 1. An example of an open-cell foam structure, obtained with a periodic Laguerre-Voronoi algorithm, overlapped to its generating sphere packing (which will be removed in the actual CFD simulation).

The resulting geometry is used to build a computational mesh and run CFD simulations in the OpenFOAM environment. First, the flow field is calculated by solving Navier-Stokes equations, to estimate the pressure drop and from them the hydraulic permeability k of the generated geometries, using Darcy's Law equation. Then, micro-scale mass transfer simulations are carried out to explore the transport of colloidal particles through these porous media, in the particular case of fast surface deposition occurring during clean-bed filtration[5].

In this situation the phenomena at the surface are driven by Brownian motion and steric interception mechanisms. Following the model and methodology proposed by [3] the results of the scalar transport simulations are used to calculate an effective macroscopic particle deposition rate coefficient K_d , which is used to estimate a macroscopic measure of the efficiency of clean-bed filtration for the open-cell foams in exam, estimated by means of the Damköhler number Da .

The geometrical model explored with the first workflow are: the Kelvin's Cell model, one mono-dispersed and two poly-dispersed structures originated from random tessellation, respectively from Voronoi and Laguerre-Voronoi tessellations. In the case of mono-disperse foam the originating sphere packings have grains with constant diameter, whereas for poly-disperse foams the packings have grains with normally distributed diameters around a mean value μ . Two different instances have been generated with same mean sphere diameter and different coefficient of variation $CV = \sigma / \mu$, namely 0.2 and 0.35.

The second tool was developed with the aim of creating realistic foam structures, with geometric features comparable to real foams. To achieve this result the new workflow is based on the creation and morphological modification of three-dimensional binary volumes, composed of regular grids of voxels. The advantages of working on voxelized volumes instead of on surfaces, like in Blender, is the much greater flexibility and potentials. These operations were carried out using the free software PlugIm! (<https://www.plugin.fr/>), which offers a great variety of plugins not only to create and modify voxelized volumes but also to create sphere packings. The overall process is very similar to the previous developed tool: spheres are packed in a cubic volume, then the centroids are retrieved and used as seed for the Voronoi algorithm, which creates the skeleton of the foam structure. Then, cylinders and spheres are placed according to the edges and nodes of the tessellation, creating a so called *balls and sticks* model of the foam. Finally, morphological operations, such as closing, opening, dilation and erosion, are carried out on the structure in order to achieve the desired values of porosity and specific surface. The additional novelty lies in the way spheres are packed: instead of using a *hard spheres* model, like in the previous tool, this new workflow relies on the sphere aggregation model

proposed by [4], which allows to modify the compactness of the spheres aggregates as well as the repulsion between spheres. This results in the possibility of creating a huge variety of foam structures with similar macroscopic characteristics (ε , S_V , τ) originated from spheres aggregates with different compactness. Fig. 2 report an example of comparison between a Nickel-Chrome metallic foam and its digital replica and Tab. 1 report the geometrical data.

	Porosity ε (%)	Specific surface S_V (m^2/m^3)	Tortuosity τ (-)
Experimental	92	1000	-
Tomography	91.9	1054	1.26
Digital replica	92.5	995.5	1.22

Table 1. A comparison between the values of the macroscopic geometrical descriptors for the Nickel-Chrome 14 PPI metallic foam, calculated with experimental technics, using digital reconstruction from tomographic images and from the digital replica

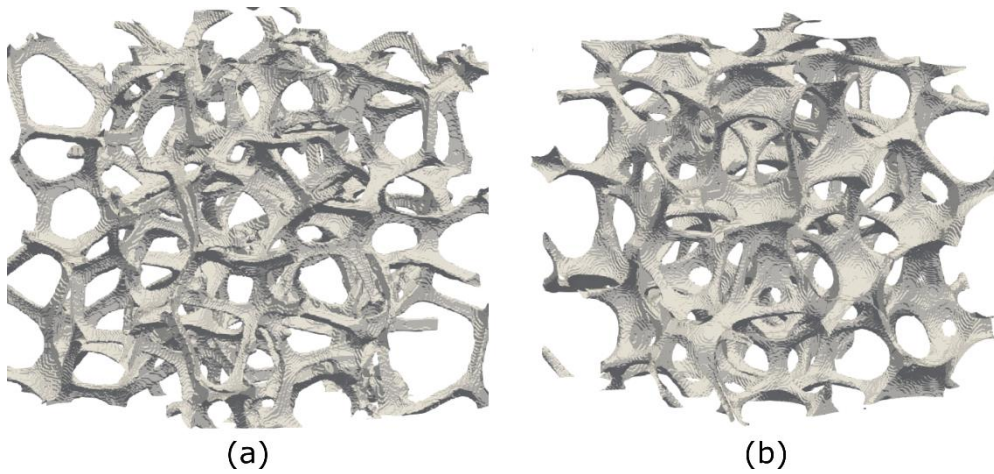


Figure 2. (a) metallic 14 PPI Nickel-Chrome foam geometry obtained from digital reconstruction of x-ray tomography, (b) Digital replica with the same target geometric parameters (ε , S_V , τ) obtained using the PlugIm! software. The error on porosity, specific surface and tortuosity of the digital model with respect to the real foam is inferior to 5%.

3. Results and discussion

For each type of geometry, four values of pore per inch (PPI) have been considered, namely 10, 20, 30 and 45, and five values of porosity ε , ranging between 77% and 95%, for a total of 20 different foams. The flow field simulations were carried out in steady state conditions, considering water as fluid, at constant atmospheric conditions, under laminar flow regime ($Re \approx 1 \cdot 10^{-3}$).

The obtained flow fields are then used in mass transport simulations, for five different values of colloidal particles dimensions, ranging from $1 \cdot 10^{-9}$ and $1 \cdot 10^{-6}$ m, with resulting Péclet number ranging between 5 and 500, for a total of 100 cases.

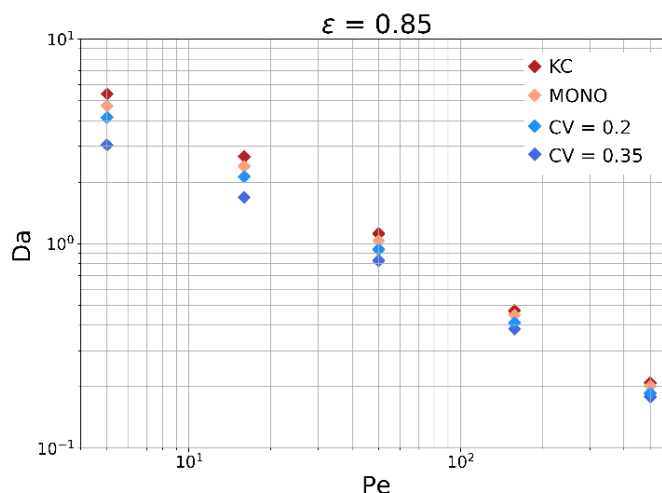


Figure 3. Particle deposition efficiency, as Da at constant porosity ($\varepsilon = 0.85$) for the four different geometries showing a power-law relationship between the Damköhler number and the Péclet number.

Fig. 2 shows the relationship between the advective Damköhler number Da and the Péclet number, for all the values of PPI and porosity $\varepsilon = 0.85$, for the four geometrical models (Kelvin's Cell, mono-disperse, poly-disperse with $CV = 0.2$ and $CV = 0.35$). At constant Pe values and geometry model, the Da values for different PPI collapse to the same point because the Damköhler number normalizes the deposition rate with respect to the operating conditions and dimension of the computational domain. Globally, at increasing Pe number, the quantity of colloids impacting on the solid surface of the foam decreases following a power law, as reported by previous studies [5] on Brownian clean-bed filtration. The results were first interpreted using well known constitutive equations ([6],[7]), and then several different power law functions, depending on S_v , ε and tortuosity τ and their combinations. This was done to verify if these relationships could be used to exactly predict the impact of the macroscopic parameters on the filtration efficiency of the foams. However, this strategy didn't bring out any significant correlation, since the global relative error, calculated as the sum of the mean squared relative errors of the data with respect to the fitting at each Pe value, showed values well over 100%. Therefore, the results show how this kind of (usually employed) macroscopic geometric features are insufficient in explaining the variations in filtration performance, highlighting the need for more detailed explorations of the pore-scale phenomena over a wider range of geometrical parameters.

To validate the second workflow, an experimental campaign was carried out to measure pressure drops on four open-cell foams: two Nickel-Chrome metallic foams (14 and 30 PPI) and two Alumina ceramic foams (20 and 40 PPI). Moreover, a three-dimensional digital reconstruction of these foam was obtained using images of the foam structure extracted using X-ray tomography. Pressure drop from experiments were compared to the results obtained from CFD simulations carried out both on the reconstructed foam models and the digitally generated models. The experiments were carried out on a column 60 cm long and 4.4 cm wide packed with foam pellets of the same size. Several different operating conditions were considered, with flow rate ranging between 12.5 and 1000 L/hr, resulting in Reynolds numbers ranging from 10 to 700.

An example of the results obtained is shown in Fig.4 which report the results for a Nickel-Chrome 14 PPI foam. Along with experimental and CFD results, two very commonly used literature correlations ([8],[9]) for the estimate of the pressure drops in open-cell foams are also reported for comparison. The results of the CFD are in good agreement with both the experimental data and the literature correlations. Moreover, the pressure drops estimated from the digital replica, created with `PlugIm!`, are in very good agreement with the other CFD results.

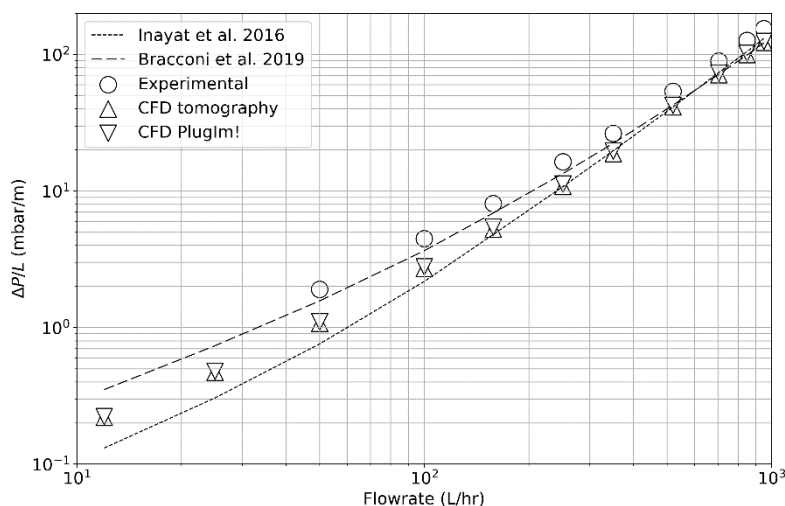


Figure 4. A comparison for a Nickel-Chrome 14 PPI metallic foam between experimental pressure drop measurements and CFD simulation results for the real foam structure and its digital replica. The plot report also two empirical correlations found in literature as a reference. The CFD results for both models are consistent with both experimental and literature data.

4. Conclusions

The results obtained in the first work highlight how the macroscopic parameters, such as porosity, specific surface, or tortuosity alone are not enough to derive macroscopic relations to describe the particle deposition during early filtration; neither by using available analytical correlations, nor by developing new simple ones based on these geometrical parameters. Thus, while we consider the value of the first workflow to lie in the capacity for users to create numerical analysis campaigns at a limited cost, decreasing the overhead of the foam modeling, the study of the different geometrical models and their performance in terms of colloidal particles deposition is conceived as just an example of the exploration capabilities. The second workflow has proved to be able to correctly describe foam structures and reproduce their performances in terms of pressure drops, at limited computational cost, while still being able to produce a wide range of digital foam structures at very low cost. Future perspectives on this topic are then to further improve the understanding of the transport phenomena occurring inside these foams, by exploring in-silico a wider number of cases and especially by better discerning the geometrical peculiarities of each - beyond simple, and oft-used, descriptors like porosity or tortuosity.

References

- [1] Agostini, E., 2021. Cefocat-public. <https://github.com/mulmopro/CeFoCat-public>.
- [2] Boccardo, Gianluca, et al. "Validation of a novel open-source work-flow for the simulation of packed-bed reactors." *Chemical Engineering Journal* 279 (2015): 809-820.
- [3] Boccardo, G., Crevacore, E., Sethi, R., Icardi, M., 2018. A robust upscaling of the effective particle deposition rate in porous media. *Journal of Contaminant Hydrology* 212, 3–13. URL: <http://dx.doi.org/10.1016/j.jconhyd.2017.09.002>, doi: 10.1016/j.jconhyd.2017.09.002, arXiv:1702.04527.
- [4] G. Ferri, S. Humbert, M. Digne, J.-M. Schweitzer, M. Moreaud. Simulation of Large Aggregate Particles System with a New Morphological Model. *Image Anal Stereol*; 40- 2 (2021).
- [5] Yao, K.M., Habibian, M.T., O'Melia, C.R., 1971. Water and wastewater filtration. concepts and applications. *Environmental science & technology* 5, 1105–1112.
- [6] Happel, J., 1958. Viscous flow in multiparticle systems: slow motion of fluids relative to beds of spherical particles. *AIChE journal* 4, 197–201.
- [7] Kuwabara, S., 1959. The forces experienced by randomly distributed parallel circular cylinders or spheres in a viscous flow at small reynolds numbers. *Journal of the physical society of Japan* 14, 527–532.
- [8] Inayat, A., Klumpp, M., Lämmermann, M., Freund, H., & Schwieger, W. (2016). Development of a new pressure drop correlation for open-cell foams based completely on theoretical grounds: Taking into account strut shape and geometric tortuosity. *Chemical Engineering Journal*, 287, 704-719.

- [9] Bracconi, M., Ambrosetti, M., Okafor, O., Sans, V., Zhang, X., Ou, X., ... & Tronconi, E. (2019). Investigation of pressure drop in 3D replicated open-cell foams: Coupling CFD with experimental data on additively manufactured foams. *Chemical Engineering Journal*, 377, 120123.

Fractionation of three-particles mixture by Brownian Sieving mechanism

Valentina Biagioni*, Alessandra Adrover, Stefano Cerbelli

Dipartimento di Ingegneria Chimica, Materiali, Ambiente, Sapienza Università di Roma,

Via Eudossiana 18, 00184 Roma, Italy

**Corresponding author E-Mail: valentina.biagioni@uniroma1.it*

1. Introduction

Measuring the size distribution of a population of nanometric particles is an important step in a variety of applications, ranging from biological essays to environmental sensors [1-3]. Due to its simplicity and high sample recovery, hydrodynamic chromatography remains a promising technique to sort nanoparticle mixtures. The separation mechanism of HDC is based on the combined effect between the drag action of a parabolic flow profile along the axial coordinate of the channel and transversal particle diffusion. Thanks to the latter, particles can experience different velocities depending on their size. Owing to reduced size, smaller particles can diffuse closer to the solid walls than the bigger ones and experience the low-velocity region of the eluent flow, whereas the largest particles are forced to travel in the central region, which is characterized by higher velocity values; consequently, they gain a higher average velocity than the smaller ones. The difference between the average velocity of particles of different sizes provides the driving force for the separation. This difference depends on the aspect ratio between the particle size and the width of cross-section. In standard HDC channels, this difference is typically weak, and it decreases as the particle size approaches the tens-of-nanometer range.[4] To avoid this problem and enhance the difference of the average velocities of the different types of particles, an alternative separation method, called Brownian sieving, has been theorized to separate a particle suspension [5-6]. The Brownian sieving HDC method exploits a two-channel annular geometry, where the internal (core) channel communicates with the external annular channel through openings of assigned length. The suspension is loaded inside the internal core. As they flow through the channel, particles smaller than the opening width are allowed to cross the openings and spread throughout the entire cross-section. Different average velocities of the eluent in the core and annular channel can be obtained by adequately designing the double channel geometry. Therefore, by tuning the width of the external section, it is possible to control the average velocity of particles of size below and above the opening width. Thus, in the Brownian sieving separation mechanism, the driving force is essentially governed by the width of the openings, and the ratio of the particle diameter to the characteristic dimension of the cross-section plays only a minor role. A proof of concept for BS-HDC has been demonstrated to separate a two-particle mixture. Here, we generalize the method and consider the simultaneous separation of suspensions of three nominal sizes in the same device. This is accomplished by changing the width of the openings along the channel (see. fig.1). Based on these preliminary results, the multi-stage Brownian sieving device could provide an efficient alternative to standard HDC methods.

2. Methods

The separation of three or more different sizes of particles can be obtained by enforcing different opening widths downstream the channel. The suspension is loaded inside the core channel, the first segment (Z1) of the device supports the smallest opening (λ_1). Thus, within this segment, only the smallest particles can spread into the entire cross-section of the channel. Once the smallest particles are separated from the others, the width of the openings increases and the medium-sized particles can spread into the entire cross-section. In light of this, the separation of three or more particle sizes can be achieved by sequentially increasing the width of the openings along the channel. The length of each segment is designed so that a complete separation of the particles passing through the openings from the rest of the suspension has been realized (see fig.1).

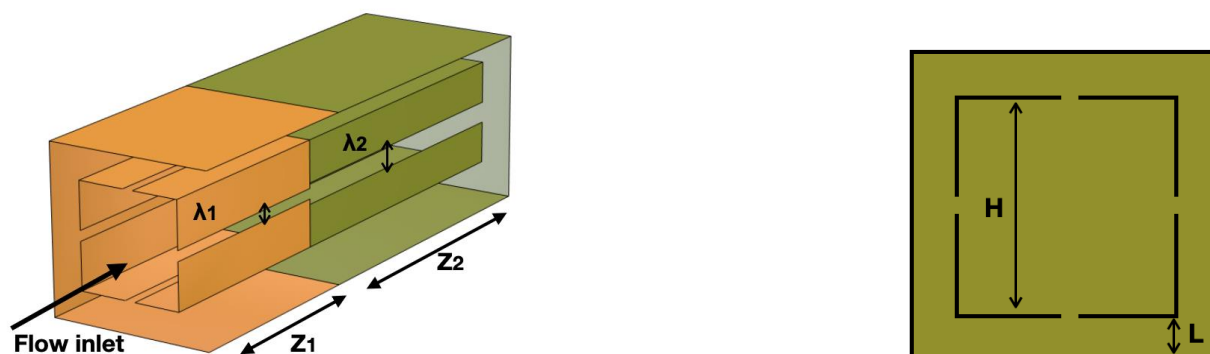


Figure 1. Device geometry

A Stochastic-Lagrangian approach has been used to simulate the trajectories of order fifty thousand particles for each size, and the separation efficiency of BS-HDC has been compared to the standard hydrodynamic chromatography. The model of particle dynamics considers the finite size of the particles, the fluid drag, and Brownian diffusion. The finite size of the particles is evaluated by simply excluding a volume equal to the radius of the particle from the solid walls. The convective term is quantified as equal to the velocity of the one-phase flow computed at the center of mass of the particle, thus assuming that the particles are in the overdamped regime. Finally, the Brownian diffusion is added as stochastic Wiener process.

3. Results and discussion

In figure 2 is shown the comparison between the swarms of particles characterized by a radius of 100 nm, 50 nm, and 25 nm, at an eluent velocity of 11 $\mu\text{m/s}$, for a width of 2 μm (H) and 0.6 μm (L) of the core and the annular channel, respectively. One can observe how the separation in the BS-HDC is reached by using a device long 1.5 mm while particles are all still overlapped in standard HDC. Note that to achieve the same BS-HDC resolution, standard hydrodynamic chromatography requires a device length of 40 mm. As regard the total analysis time, about 2 min and 60 min are needed for BS-HDC and HDC, respectively.

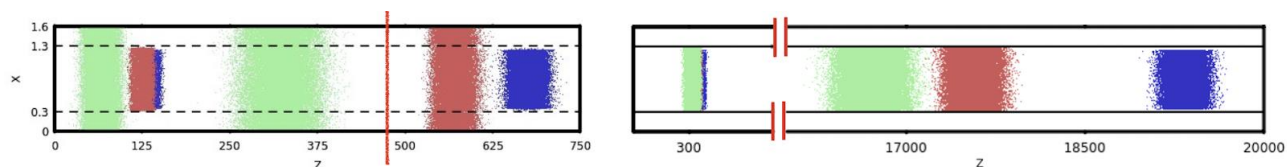


Figure 2: Particle dynamics for BS-HDC (right) and HDC (left) for particles of 100, 50 and 25 nm.

4. Conclusions

The Brownian sieving mechanism can separate nanoparticles in a very short length and low operation time, making the multiple BS-HDC a potentially useful technique for nanoparticles characterization.

References

- [1] L.Wang, W.Ma, L.Xu, W.Chen, Y.Zhu, C. Xu, N.A.Kotov . *Mater. Sci. Eng. R* 70 (2010) 265-274
- [2] J.P.Lafleur, S.Senkbeil, T.G.Jensen, J.P.Kutter. *Lab Chip* ,2012, 12, 4651-4656
- [3] M.Bouri, R.Saighi, M. Algarra, M.Zougagh, A.Rios. *RSC Adv.* 2015 ,5, 16672-16677
- [4] Striegel, A. M. *Anal. Chem.* 2005, 77, 104A–113A.
- [5] V Biagioni, AL Sow, A Adrover, S Cerbelli. *Anal. Chem.* 2021, 93, 17, 6808–6816
- [6] V Biagioni, AL Sow, A.G. Fagiolo, A Adrover, S Cerbelli. *J. Chromatogr. A* Volume 1659, 2021, 462652

Modeling Flux Reduction in Multiphase Gas Barrier Materials Trough 3D CFD Approach

Lorenzo Merlonghi^{1,3}, Marco Giacinti Baschetti^{1,3}, Maria Grazia de Angelis^{1,2,3}

(1) *Department of Civil, Chemical, Environmental and Material Engineering, (DICAM), Alma Mater Studiorum – Università di Bologna, via Terracini 28, 40131 Bologna, Italy*

(2) *Institute for Materials and Processes, School of Engineering, University of Edinburgh, Sanderson Building, Robert Stevenson Road, EH9 3FB, Scotland, UK.*

(3) *Dutch Polymer Institute (DPI), P.O. Box 902, 5600 AX Eindhoven, the Netherlands.*

*Corresponding author E-Mail: lorenzo.merlonghi2@unibo.it

1. Introduction

Semicrystalline polymers (SCP) and polymer matrix composites (PMC) are widely used for gas barrier applications, because crystalline and filler domains act as obstacles for small diffusing gaseous species. The main geometrical parameters that affect transport properties of such multiphase materials are volume fraction (VF) and aspect ratio (AR) of the dispersed particles. Analytical models like Maxwell [1] and Maxwell-Wagner-Sillars (MWS) [2] can be used to predict flux reduction in multiphase materials for simple geometries such as spheres and spheroids, while other methods based on finite elements or volumes methods (FEM, FVM) can be used to reproduce more complex geometries. In this preliminary work, a computational fluid dynamics (CFD) approach is proposed to investigate how particles morphology and size distribution (SD) affect overall transport coefficients of the homogenized material, with respect to the continuous matrix.

2. Methods

The study was based on the analysis of the permeation behavior of gases through a representative volume element (RVE) of the material of interest, obtained by inserting spherical inclusions in a cubic matrix with periodic or symmetric boundaries. Three levels of complexity were used to reproduce the geometry, changing impermeable phase VF, as well as AR, here defined as the ratio between the higher and the lower characteristic dimensions of oblate particles, and SD. For ARs higher than one, impermeable oblate spheroids were aligned perpendicular to the flux direction, reproducing an efficient gas barrier system. Initially, ordered spheroids with the same size were used to represent impermeable domains, then random distributed arrays in terms of size and positioning was generated. Finally, specific SDs of real LDPE samples [3] was reproduced to be more representative as possible of a real material microstructure. Once the microstructure was generated it was fed to a CFD tool for the solution of the transport problem. In particular, ANSYS Fluent 2020 R2 was used to mesh the geometry, set the correct boundary conditions, and solve a steady state pure diffusion problem. To do so, a fixed gradient was fixed between two faces of the cubic RVE, leaving other four as symmetric or coupled periodic boundaries, depending on the model used. Then, the elliptic partial differential equation was solved, setting a Neumann condition of null flux on the interface between amorphous matrix and impermeable phase. At the end, the constant flux was computed in the direction of the gradient and compared with the one obtained by solving the same problem using both the analytical and the numerical method by CFD analysis, in case of a pure amorphous matrix, in order to check the consistency. Finally, the ratio between the two fluxes, defined as flux reduction, is calculated and compared to analytical expressions available in the literature [1,2]. The size of the RVE was maximized in order to obtain the same result at least three times on three significant digits, by fixing RV, AR and SD, and also minimized in order to reduce computational time.

3. Results and discussion

In figure 1, the results for regular random and distributed spheres are compared with analytical models, showing better matching in diluted conditions, as expected. Random and ordered spherical arrays gives the same result of Maxwell [1], while real spherical distributions can give slightly different results. On the other hand, it was found that for oblate inclusions, MWS [2] gives better results for lower ARs and VFs. Moreover, increasing AR for regular and random arrays result in a lower effect on the flux reduction for the second configuration, due to the presence of diffusion shortcuts generated by the random algorithm.

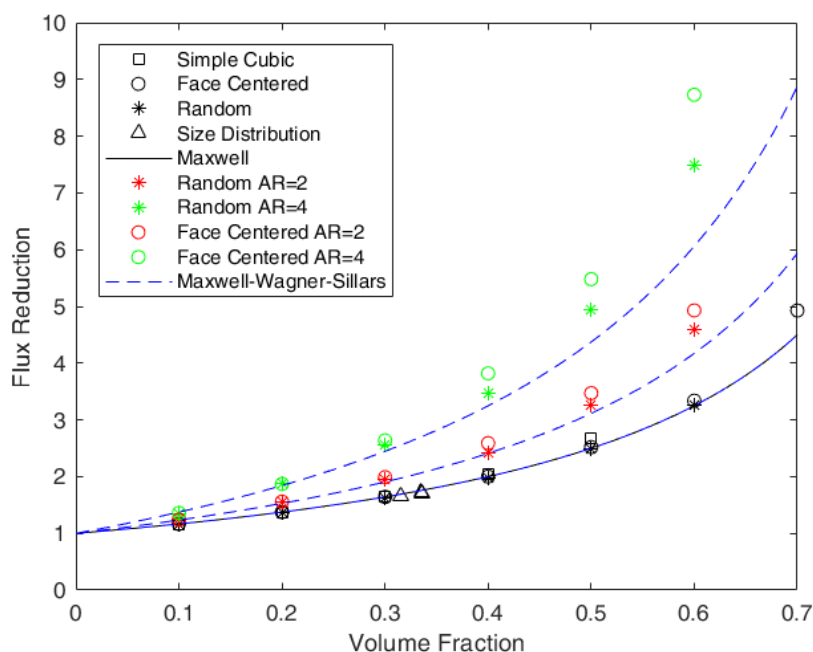


Figure 1. CFD results for spherical inclusions organized in different arrays compared with [1],[2].

4. Conclusions

In conclusion, this CFD approach was useful to understand the difference in terms of flux reduction, due to the presence of an impermeable phase in a continuous matrix, comparing ordered, random and distributed arrays. It was shown that all CFD results are consistent with analytical models available in the literature [1,2] and it was found that a real multiphase material can be easily reproduced using a specific size distribution, to have a more realistic prediction. In future works, this approach will be extended to different morphologies, like ellipsoids or fibers, and will be also improved inserting an interphase between the two main phases, when expected in real materials.

References

- [1] C. Maxwell, Treatise on Electricity and Magnetism, Oxford Univ. Press, 1873; Vol. 1.
- [2] R.W. Sillars, The Properties of a dielectric containing semi conducting particles of various shapes, Institution of Electrical Engineers, in: Proceedings of the Wireless Section of the Institution 12, 1937, pp. 139–155.
- [3] Leyva-Porras, C.; Balderrama-Aguilar, A.; EstradaÁvila, Y.; Espelosín-Gómez, I.; Mendoza-Duarte, M.; Piñón Balderrama, C.; Saavedra-Leos, M.Z.; Estrada-Moreno, I. Injection Molding of Low-Density Polyethylene (LDPE) as a Model Polymer: Effect of Molding Parameters on the Microstructure and Crystallinity. *Polymers* 2021, 13, 3597.

Acknowledgment: This research forms part of the research program of DPI, project 844 | Modelling and Design of Multiphase Polymeric Materials for High-Performance Applications Across Multiple Scales (MuMPol).

Slippage at the solid-liquid interfaces: implications for colloidal transport in confined geometries

Giuseppe Procopio¹, Massimiliano Giona^{1*}

1 DICMA, La Sapienza Università di Roma, via Eudossiana 18, 00184 Roma, Italy;

**Corresponding author E-Mail: massimiliano.giona@uniroma1.it*

1. Introduction

Transport of colloidal systems in viscous flows plays an important role in chemical engineering problems involving microfluidic devices, biochemical reactors, sol-gel processes, filtration, sedimentation and other separation operations.

The characteristic sizes of colloids (typically order of 1-1000 nm), much greater than that of the fluid molecules is however small enough to consider valid low Reynolds-number hydrodynamics for colloidal systems, making the Stokes equations, with no-slip boundary conditions at the solid (particle, wall) surfaces, the natural candidate for describing colloidal hydrodynamics and transport, and predicting the relevant emerging parameters: the resistance coefficient η (friction factor) characterizing the dissipation properties as regards momentum balance, and the diffusion coefficient D accounting for the intensity of fluctuations in particle motion. These two parameters are, for isothermal systems, related to each other by the simplest form of fluctuation-dissipation relation, namely $\eta D = k_B T$, where k_B is the Boltzmann constant and T the temperature of the system. The simplest approximation as regards diffusive transport properties consists in considering the system isotropic and diluted so that both η and D are scalar constant quantities (specifically, $\eta = 6\pi\mu R_p$ for spherical particles with radius R_p translating in a fluid with viscosity μ). However, in dealing with colloidal systems in a confined fluids, whenever the characteristic size of the particle L_p is comparable with the characteristic size of the system L , both η and D become position-dependent tensorial quantities. This is the case of particle transport in microfluidic devices, micro/nano-particle motion in porous media, chromatographic analytical methods, colloidal dynamics near a solid collector, dynamics of concentrated suspensions etc. . However, since the Stokes equations in the presence of no-slip boundary conditions at solid boundaries predict a singular behavior of the resistance of two surfaces getting in touch, i.e., $\eta \sim 1/h$, h being the distance between the surfaces, thus implying that $D=0$ at the solid surface, many paradoxes and difficulties arise in modeling surface phenomena. Specifically, since $\eta(h)$ is characterized by a non-integrable singularity at the touching point, Stokes hydrodynamics with no-slip boundary conditions predicts an infinite "touching time", for a particle to reach the surface, and similar paradoxes arise in dealing with surface chemical reactions or coalescence phenomena. Moreover, since $D=0$ for $h=0$, mixed boundary conditions accounting for surface chemical reactions cease to be valid. A way for overcoming these difficulties is to eliminate or mollify the singularity at the touching point by introducing slippage at the surfaces by means of the Navier slip boundary conditions. In fact, as shown in [1], if the slip length is the same at both the surfaces the singularity of the resistance coefficient becomes integrable as it is characterized by a logarithmic scaling $\eta \sim -\ln(h)$, providing a finite touching time. Starting from numerical simulations and using also the semianalytical approach proposed by Goren [2] we investigate in this presentation the quantitative behavior of the transport parameters $\eta(h)$ and $D(h)$ of a spherical particle close to a planar surface, proposing also solutions for solving the above mentioned paradoxes.

2. Methods

Hydrodynamic Finite Element Simulations have been used to characterize the scaling of the resistance matrix near a planar surface. In order take computational advantage from the axial symmetry of the problem of a sphere translating perpendicularly to a planar wall, cylindrical coordinates (r, φ, z) have been used reducing

the computation to a two dimensional (r, z) domain representing the flow region, with an empty disk, representing the spherical particle placed at distance h from planar wall. A finer mesh has been adopted along the perimeter of the disk representing the sphere, and the maximal length of the elements has been imposed to be less than 0.1 R_p. Both P2P1 and P3P2 finite elements have been used depending on the position of the particle. Furthermore, we solved the infinite system of Goren's equations furnishing the drag force on the particle [2] over the entire range of positions and for any values of the slip length at the wall λ_w and at the particle λ_p, truncating it to 500 equations (that was sufficient for the h-values considered to achieve convergence).

3. Results and discussion

If the no-slip boundary condition is imposed on just one of the two surfaces (particle or wall) the singular scaling η ~ 1/h is preserved independently of the value of the slip length imposed on the other surface. In the latter case, we can distinguish among three different regimes: (i) the scaling η ~ 1/h for λ < h < 10⁻¹ λ, (ii) an apparent logarithmic behavior for 10⁻² λ < h < λ and (iii) the asymptotic regime where η ~ 1/h for h < 10⁻² λ.

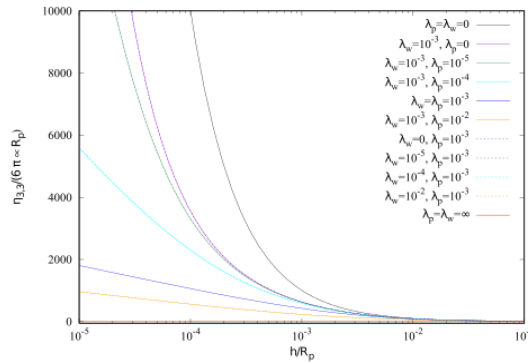


Figure 1. Dimensionless hydrodynamics resistance coefficient η(h)/ (6 π μ R p) vs h/R_p obtained by keeping fixed the slip length λ_i/R p = 10⁻³ on the i-th surface (i = w, p) and varying the slip length on the other obtained by solving the Goren's equations.

Keeping fixed the slip length at one of the surfaces (λ_i = 10⁻³, i = w, p) and increasing the slip length on the other λ_j, j = p, w, the logarithmic scaling occurs for d < λ_j, see Figure 1. This means that an arbitrarily small slip on both the surfaces is sufficient to determine an asymptotic logarithmic scaling of the transversal resistance and thus the occurrence of a finite value of the touching time [3].

4. Conclusions

We have thoroughly analyzed how the lack of integrability of mass-transport models (diffusion equation) in the presence of a surface chemical reaction depend on the simplifying assumption of no-slip boundary conditions. The inclusion of slippage effects at all the solid surfaces (walls and particle) transforms the non-integrable 1/h-singularity in the transversal resistance coefficient η(h) near a planar wall into a logarithmic singularity (η ~ - ln(h)) resolving the above mentioned integrability problem. However, there are physical reasons to conjecture that a more refined modeling of fluid-particle interactions (including compressibility and acoustic effects) could completely eliminate the singularity occurring for η(h) at the wall [3].

References

- [1] L. M. Hocking, J. Eng. Math. 7 (1973) 207–221.
- [2] S. L. Goren, J. Colloid Interface Sci. 69 (1979) 78-85.
- [3] G. Procopio and M. Giona, Fluids 7 (2022) 105.

Non-brownian suspensions: frequency-dependent irreversibility threshold

Simona Moliterno¹, Johanna Vargas Clavijo¹, Claudia Carotenuto¹, Mario Minale^{1*}

1 Department of Engineering, University of Campania "Luigi Vanvitelli", Real Casa dell'Annunziata, via Roma 29-81031 Aversa, Italy

** simona.molitierno@unicampania.it, johanna.vargasclavijo@unicampania.it, claudia.carotenuto@unicampania.it, mario.minale@unicampania.it*

1. Introduction

Concentrated suspensions are found in many engineering applications and understanding their rheological behaviour is often of fundamental importance. Dense particle suspensions in a Newtonian fluid are known to display a rich variety of rheologies, such as shear thickening/thinning, yielding, thixotropy, etc. [1-3]. These complex rheological behaviours are strongly affected by the details of the underlying microstructure, which is intimately related to various hydrodynamic/interparticle interactions, including e.g. lubrication, Brownian, electrostatic, van der Waals and contact forces [4].

Even the simplest suspensions made by non-Brownian particles suspended in a density matching Newtonian fluid, while exhibiting a Newtonian behavior in steady shear flow (SS), show a very rich rheology under oscillatory shear (OS) as the flow irreversibility, which induces a stochastic diffusion of particles [5], the transition towards an absorbing state [6, 7] and the microstructure reorganization at large accumulated strains [8, 9]. All these fundamental behaviors can be predicted using very few ingredients in the equation of motion that are in order: hydrodynamic forces, including lubrication, and hard sphere interactions.

These simple forces do not possess a characteristic time, or stress, scale and so their amplitude is proportional to the driving hydrodynamics force, thus the system and all its material functions result rate independent [10]. So far, in OS the microstructure has been considered strain history dependent and, both in OS and SS, strain rate history independent.

However, recent experiments challenge this assumption and demonstrate a frequency-dependent rheology in the absence of any rate-dependence in SS [11, 12]. The authors demonstrated that in OS the only parameter on which everything depends is the maximum shear rate (the product of angular frequency and strain amplitude). This finding is rather fundamental as it changes the understanding of the physics behind the simplest non-Colloidal Newtonian suspension. Ge, et al. [13] proved that the addition of the weak Van der Waals attractive forces to the equation of motion was enough to predict the rate dependence in OS while keeping the SS rate independent, as experimentally shown by Martone, et al. [11]. Ge, et al. [13] also showed that though the Van der Waals forces are always negligible with respect to the hydrodynamic forces or the lubrication ones or the forces deriving from the particle interactions they are able to mediate the microstructure evolution under oscillatory flow in such a way that the frequency plays a role in the predicted dynamics. In particular, Ge, et al. [13] confirmed that everything scales with the maximum shear rate, moreover their numerical predictions were in good agreement with the experimental data of [11].

Most interestingly Ge, et al. [13] also focused on the transition to irreversibility on Newtonian non-Brownian suspensions when the van der Waals (vdW) forces are added to the equation of motion. The classical equation of motion without the vdW forces were already able to predict the transition to an irreversible regime when the applied strain amplitude overcomes a critical value function of the particle volume fraction only. For values larger than the critical threshold the system enters an irreversible, eventually chaotic, regime dominated by particle collisions. For values smaller than the critical threshold the system under OS enters an adsorbing state where the particles rearrange so to give rise to a microstructure where particles collisions are minimised or

absent. This regime is reversible, i.e., when the flow is reverted each streamline is retraced. Ge, et al. [13] also showed the existence of a new critical strain amplitude, marking a new threshold of irreversibility, which depends on the frequency. In this case for strain amplitudes greater than this new critical strain amplitude, the system enters the reversible adsorbing state in which particles auto-distribute to avoid collisions, for values below it, the behaviour is irreversible with particles that form clusters where they continue colliding.

In this paper we experimentally study the existence of this frequency-dependent critical strain amplitude on a concentrated suspension focusing on two characteristic angular frequencies. We designed the experiments so to be able to catch this transition and by running the time sweep oscillatory shear tests at different imposed strain amplitudes for each angular frequency. The evolution in time of the complex viscosity was then interpolated with the classical law for the critical transitions, a hyperbolic/exponential decay. The divergence of characteristic time to reach the regime, τ , identifies the transition to the irreversible regime.

In the following we first describe the experimental protocol and results obtained, then discuss the modelling to identify the critical transition and finally draw our conclusions.

2. Materials and Methods

The suspension studied consists of hollow glass spheres suspended in a Newtonian PIB at a volume fraction of 40%. The microspheres are the Spherical-110P8 of Potter Industries LLC with sphericity ~ 1 and nominal density of 1.1 g/cm^3 . The particle distribution function reported [11] was obtained with a laser granulometer, Mastersizer 3000 (Malven). The average volumetric diameter resulted of $15.4 \text{ }\mu\text{m}$.

The suspension matrix is a Newtonian fluid, Poly-isobutene (PIB), Insopol-grade H50 from INEOS, with measured viscosity of 10.9 Pa s at 21.2°C and nominal density of 0.884 g/cm^3 [11].

The suspensions are prepared by manually mixing the microspheres and the PIB until a homogeneous milky sample is obtained. The sample is placed under vacuum overnight to remove most of the air bubbles entrapped in the suspension.

Before running each time sweep oscillatory shear test, the sample is preconditioned with a steady preshear at $\dot{\gamma} = 3\text{s}^{-1}$ for 500s such that the preshaer steady viscosity resulted always the same ($69,68 \text{ Pa s}$) with an experimental error of about 10%. Thi allows us concluding that the preshear is able to erase any history of deformation of the sample and let the OS experiments to start always from a similar initial microstructure.

The time sweep oscillatory tests were carried out with a strain-controlled rheometer, ARES-G2 (TA Instruments), equipped with a cone and plate geometry, with a diameter of 25 mm and a cone angle of 6.36° . A sinusoidal strain is imposed, $\gamma(t) = \gamma_0 \sin(\omega t)$, with strain amplitudes γ_0 ranging from 0.5% and 50% and two different angular frequencies, ω , equal to 5 and 50 rad/s.

The steady rheology of the suspension is Newtonian, and it was analysed in depth together with all the possible artifacts like wall slip, particle sedimentation, particle inertia and flow instabilities that may affect the data in [11, 14]. It was possible to conclude that none of these artifacts had effects on our data.

The complex viscosity was then followed in time since the very first instant until a regime vale was obtained. Our experiments always lasted a time necessary to reach an accumulated strain of 8000, that in the literature [8, 9] is considered enough to attain the final regime. The accumulated strain γ_{acc} is:

$$\gamma_{acc} = 4 n_{cyc} \gamma_0 = 4 t \frac{\omega}{2\pi} \gamma_0 \quad (1)$$

where n_{cyc} is the number of cycles in oscillatory shear. This parameter quantifies the strain history of the sample.

3. Results and discussion

The results in terms of relative complex viscosity $\eta_R^* = \eta^*/\eta_{PIB}$, with η_{PIB} the viscosity of the suspension matrix, are shown in Figure 1 as a function of the accumulated strain, γ_{acc} . Data are plotted parametric in the strain amplitude and each panel is dedicated to a frequency. The results clearly show that the evolution of the complex viscosity has different trends as a function of the applied strain amplitude, going from an increasing trend to a decreasing on by increasing the strain amplitudes. Non-monotonous trend are also measured in between the two monotonous behaviours.

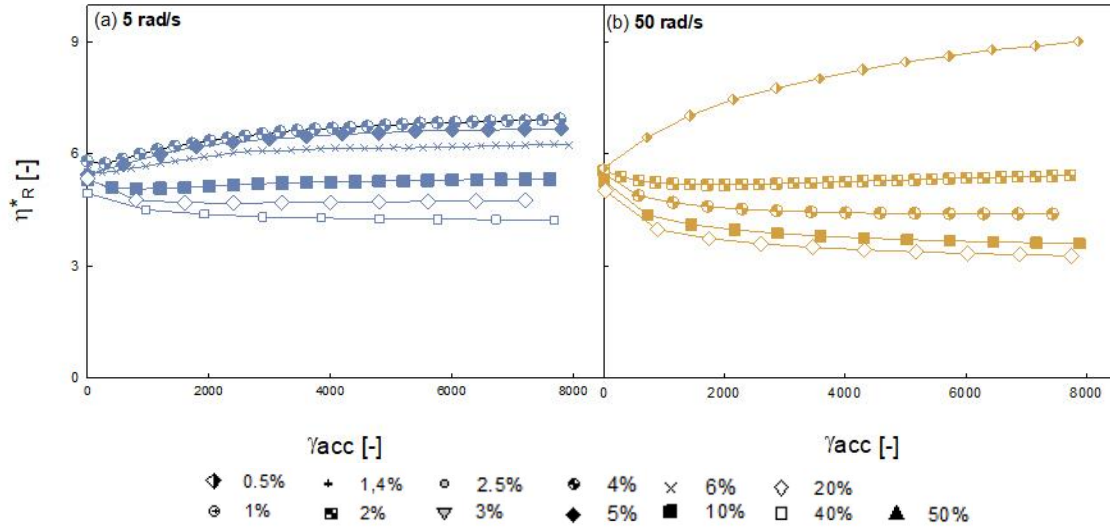


Figure 1 - Relative complex viscosity (η_R^*) vs the total accumulated strain γ_{acc} parametric in the strain amplitude: at 5 rad/s (a), and 50 rad/s (b).

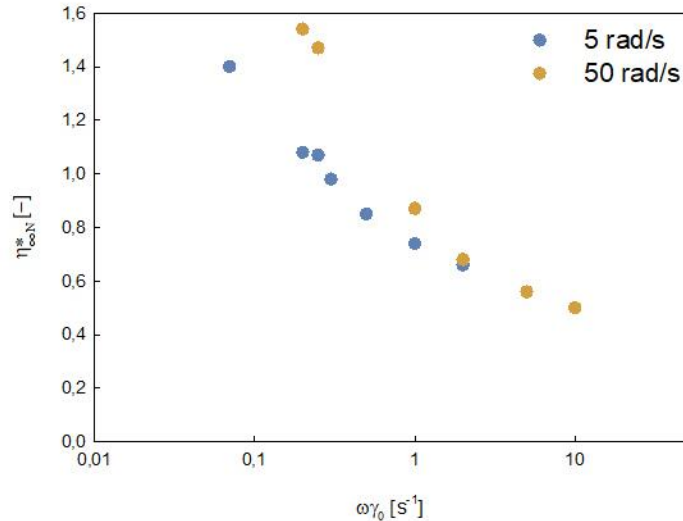


Figure 2 - Plateau values of the normalized complex viscosity η_N^* vs maximum shear rate $\omega\gamma_0$. Data (circles) are taken at 5 rad/s (blue) and 50 rad/s (yellow).

In Figure 2 we plotted the results in terms of η_N^* , the complex viscosity normalized with the steady preshear viscosity, (η_{st}): $\eta_N^* = \eta^*/\eta_{st}$. The normalized viscosities at regime $\eta_{N\infty}^*$, are plotted as a function the maximum shear rate, $\omega\gamma_0$, in agreement to what suggested by [11]. The data reasonably collapse on a single master curve, especially at the highest maximum shear rates.

In order to estimate the time required to reach the regime, τ , the complex viscosity vs. time plots were interpolated with the decay characteristic of critical phenomena [6]:

$$\eta^* = \eta_{\infty}^* + a \frac{e^{-t/\tau}}{t^2} \quad (2)$$

In Figure 3 we show the time evolution of the complex viscosity at $\gamma_0 = 4\%$ for the two angular frequencies. The data clearly show how both the regime value, and the entire transient are function of the applied frequency. The data are interpolated with equation 2 and the interpolating function is also shown in Figure 3. The accuracy of the interpolation is clearly appreciable in the Figure, and we always got a correlation coefficient $R^2 > 0.99$.

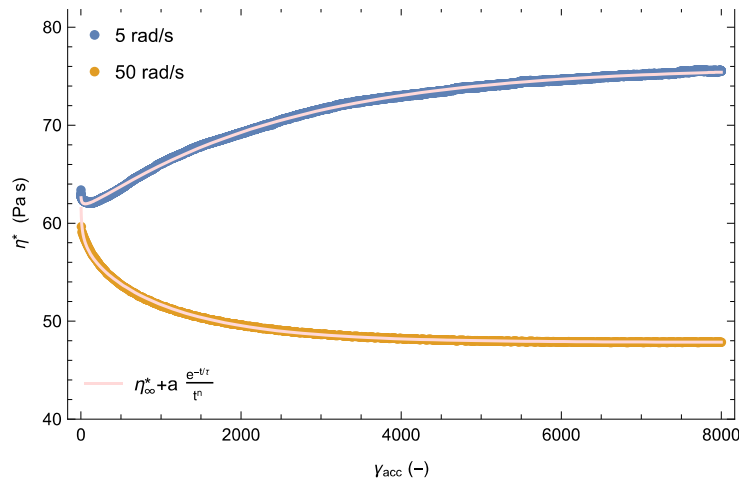


Figure 3 - Evolution of complex viscosity η^* with γ_{acc} . For the applied deformation amplitude γ_0 equal to 4%. Data (circles) are taken at 5 rad/s (blue) and 50 rad/s (yellow).

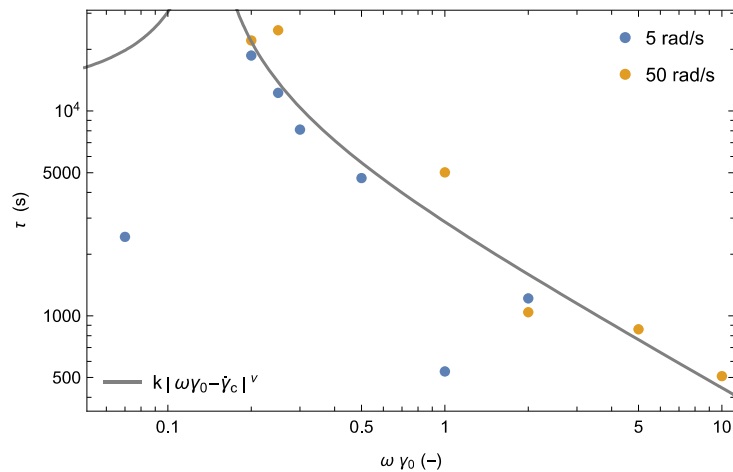


Figure 4 - Evolution of the time variable τ as a function of $\omega \gamma_0$. For $\omega = 5$ rad/s (blue circles), $\omega = 10$ rad/s (yellow circles) and $\omega = 50$ rad/s (green circles). Representation of the interpolating curve (gray).

The characteristic times, τ , are plotted vs. the maximum shear rate in Figure 4. A divergence of the characteristic time, marking the transition to the adsorbing state, can be guessed for $\omega \gamma_0$. between 0.1 and 0.2. To better estimate the critical value of the transition we interpolated the data with eq. (3) as suggested by [6]:

$$\tau = k |\omega \gamma_0 - \dot{\gamma}_c|^\nu \quad (3)$$

where $\dot{\gamma}_c$ is the critical maximum shear rate above which the system enters the adsorbing state and below which the system enters the irreversible collisional regime. The interpolation is also shown in Figure 4.

The interpolation parameters are reported Table 1. The correlation coefficient R^2 resulted larger than 0.99 and the critical maximum shear rate, $\dot{\gamma}_c = \omega \gamma_{0c}$, equal to 0.14. This implies that the critical strain amplitude is inversely proportional to the frequency:

$$\gamma_{0c} = 0.14/\omega \quad (4)$$

Table 1 – The interpolation parameters of the interpolation of the times. In this case the value of R^2 is 0.998661.

	Estimate	Standard Error
k	2.56 10 ³	4.6 10 ²
$\dot{\gamma}_c$	0.139	0.050
ν	-0,765	0,134

4. Conclusions

In our work we confirmed that a non-Brownian Newtonian suspension is rate dependent in oscillatory shear while remaining rate independent in steady shear. Most interestingly, in agreement with Ge, et al. [13], we individuated the new critical transition towards the adsorbing state marked by a critical strain amplitude inversely proportional to the frequency. In Figure 5, we added to the data already shown in Figure 2 a vertical line in correspondence of $\dot{\gamma}_c = \omega \gamma_{0c} = 0.14$ which intersects the viscosity data at a value very close to $\eta_{N\infty}^* = 1$. This suggests that when the system is in the adsorbing state, for $\omega \gamma_0 > \dot{\gamma}_c$ the regime complex viscosity is smaller than the preshear one, and the microstructure is somehow dilated so to limit the particles collisions; while $\omega \gamma_0 < \dot{\gamma}_c$ the regime complex viscosity is larger than the preshear one and the microstructure rearrange in a crystal-like state where particles continue colliding.

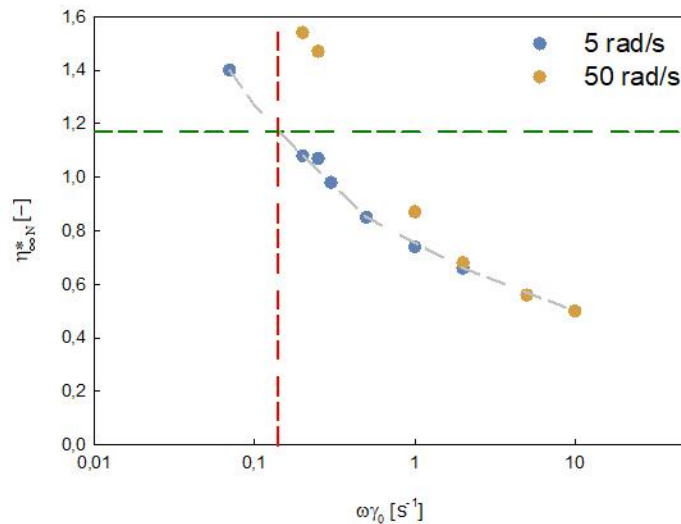


Figure 5 - Plateau values of the normalized complex viscosity $\eta_{N\infty}^*$ vs maximum shear rate $\omega\gamma_0$. Data (circles) are taken at 5 rad/s (blue) and 50 rad/s (yellow). The red line represents the interpolation value of $\dot{\gamma}_c$. The gray line serves to guide the eye and represents a hypothetical trend of the interpolating curve. The green line defines the corresponding value of the normalized complex viscosity $\eta_{N\infty}^*$ to $\dot{\gamma}_c$.

References

- [1] J. Mewis and N. J. Wagner, “Thixotropy”, *Adv. Colloid Interf. Sci.* **147-148**, 214-227 (2009).
- [2] J. Mewis and N. J. Wagner, *Colloidal Suspension Rheology*. (Cambridge University Press, Cambridge, 2011).
- [3] M. M. Denn and J. F. Morris, “Rheology of Non-Brownian Suspensions”, *Ann. Rev. Chem. Biomolecul. Eng.* **5** (1), 203-228 (2014).
- [4] J. Mewis and N. J. Wagner, “Current trends in suspension rheology”, *J. Non-Newton. Fluid Mech.* **157** (3), 147-150 (2009).
- [5] D. J. Pine, J. P. Gollub, J. F. Brady and A. M. Leshansky, “Chaos and threshold for irreversibility in sheared suspensions”, *Nature* **438**, 997-1000 (2005).
- [6] L. Corté, P. M. Chaikin, J. P. Gollub and D. J. Pine, “Random organization in periodically driven systems”, *Nature Phys.* **4** (5), 420-424 (2008).
- [7] L. Corté, S. J. Gerbode, W. Man and D. J. Pine, “Self-Organized Criticality in Sheared Suspensions”, *Phys. Rev. Lett.* **103** (24), 248301 (2009).
- [8] J. M. Bricker and J. E. Butler, “Oscillatory shear of suspensions of noncolloidal particles”, *J. Rheol.* **50** (5), 711-728 (2006).
- [9] J. M. Bricker and J. E. Butler, “Correlation between stresses and microstructure in concentrated suspensions of non-Brownian spheres subject to unsteady shear flows”, *J. Rheol.* **51** (4), 735-759 (2007).
- [10] R. N. Chacko, R. Mari, S. M. Fielding and M. E. Cates, “Shear reversal in dense suspensions: the challenge to fabric evolution models from simulation data”, *J. Fluid Mech.* **847**, 700-734 (2018).
- [11] R. Martone, C. Carotenuto and M. Minale, “Non-Brownian Newtonian suspensions may be rate dependent in time sweep oscillatory shear flow”, *J. Rheol.* **64** (5), 1075-1085 (2020).
- [12] R. Martone, L. P. Paduano, C. Carotenuto and M. Minale, “Dependence of suspension complex viscosity on frequency: Strain-controlled vs. stress-controlled tests”, *AIP Conf. Proc.* **1981** (1), 020185 (2018).
- [13] Z. Ge, R. Martone, L. Brandt and M. Minale, “Irreversibility and rate dependence in sheared adhesive suspensions”, *Physical Review Fluids* **6** (10), L101301 (2021).
- [14] C. Carotenuto, G. Rexha, R. Martone and M. Minale, “The microstructural change causing the failure of the Cox-Merz rule in Newtonian suspensions: experiments and simulations”, *Rheol. Acta* **60** (6), 309-325 (2021).

Thermodynamic characterization of Liquid-Vapor Equilibria of Propionic Acid-Water at atmospheric pressure

Leone Mazzeo^{1,2*}, Vincenzo Piemonte

1 Department of Engineering, University Campus Biomedico of Rome, Via Alvaro del Portillo, 21, 00128 Rome, Italy;

2 Department of Chemical Engineering Materials & Environment, Sapienza University of Rome, Via Eudossiana, 18, 00184 Rome, Italy;

**Corresponding author E-Mail: l.mazzeo@unicampus.it*

1. Introduction

Propionic acid is a Volatile Fatty Acid (VFA) which global market is projected to reach the size of US\$1.8 Billion by 2027 [1]. Such molecule finds its main application as a food preservative which account for nearly 78% of its total consumption. Propionic acid it is also employed in the food industry (as aroma additive, food additive and flavoring) and in the pharmaceutical industry (for pharmaceuticals and solvents formulation). The price of Propionic Acid was estimate to be 2000-2500 €/ton [2]. Although the main production of Propionic Acid occurs by means of ethylene carbonylation, oxidation of propanal and direct oxidation of hydrocarbons [3], nowadays increasing attention is given to the production of such molecule by means of Anaerobic Digestion [4]. As a matter of fact, currently it was investigated the potential of AD as an environmentally friendly alternative for the production of bulk chemicals such as Volatile Fatty Acids (VFAs) [5]. In this context rises the necessity to further investigate on the possible recovery of Propionic Acid from a fermentation broth which is basically a mixture of water and different types of VFA. This works sets a first step on this path studying the Vapor-liquid equilibrium of the mixture Propionic acid-water at 1 atm. Such mixture was already investigated in the past by other works [6–8], however none of them adopted the Non-Random Two-Liquid model for the description of the activity coefficient of the liquid phase. The aim of his work is then to increase the literature data for the liquid vapor equilibrium at 1 atm for the binary system Propionic Acid-Water and to evaluate the goodness of NRTL model in describing the liquid phase deviations from ideality.

2. Material and Methods

2.1. Experimental

Analytical grade Propionic acid (C₃H₆O₂) reagent was purchased from Sigma Aldrich (United States) and used without any further purification together with distilled water. The Refractive Indexes (RI) of both components were compared with literature data as shown in Table 1.

Table 1. Refractive index of pure compounds at 25°C.

Compound	RI measured	RI literature
Propionic Acid	1.3843 ± 0.0005	1.3837 [9]
Water	1.3340 ± 0.0005	1.3330 [10]

The experimental runs were carried out in a modified Gillespie vapor recirculation still (for further information see the work of Malanowski [11]) already used in other works [12]. Details of the apparatus are reported elsewhere [13]. The condenser of the still was open to the atmosphere in order to keep the system at

atmospheric pressure. The equilibrium temperature was measured by means of an Hg thermometer with an accuracy of ± 0.1 °C. Isobaric liquid-vapor equilibrium data were collected once no changes in the measured temperature were observed. Such condition was reached after 30 – 45 minutes from the beginning of each test. The liquid samples at equilibrium (liquid phase and the condensed vapor phase) were analyzed using a Bawch and Lomb Abbe-3L precision refractometer.

2.2. Modeling

The classical condition for vapor-liquid equilibrium, valid for each component i , is reported below in Equation 1:

$$Py_i\varphi_i = P_{s,i}(T)\gamma_i x_i \varphi_{i,s}^{\circ} \nu_{L,i} \quad (1)$$

where φ_i and $\varphi_{i,s}^{\circ}$ are the fugacity coefficients of the component i in the mixture at the system pressure P and pure at the vapour tension $P_{s,i}(T)$ calculated at the equilibrium temperature T respectively; γ_i is the liquid activity coefficient, $\nu_{L,i}$ is the Poynting coefficient and y_i , x_i are the compositions of the vapour and liquid phase respectively at equilibrium. In this work it was possible to neglect the Poynting effect due to the small difference between the vapour tension and the pressure of the system together with the small value of the specific molar volumes of the pure compounds. It is well known that carboxylic acids such as propionic acid have strong intermolecular interactions due to hydrogen bonds formation which leads to their tendency to form dimers in the vapour phase [8]. For this reason, the vapour phase wasn't considered ideal even if the experiments were conducted at 1 atm and hence $\varphi_i \neq 1$. According to this consideration, a calculation of liquid activity coefficients neglecting the non-ideality of the vapor phase may lead to inconsistent thermodynamic data. The chemical theory of vapor imperfections (fully explained in the work of Nothnagel et al. [14]) was commonly adopted for the description of the vapor phase non ideality for strong associating components up to pressures of 5 – 8 atm [9]. In this work the fugacity coefficient was calculated supposing the propionic acid (A_1) to react in the vapor phase forming dimers (A_2) with the following chemical reaction stoichiometry



while water was considered an inert. The chemical equilibrium is characterized by an equilibrium constant defined below in Equation 3:

$$K(T) = \frac{f_{A_2}}{f_{A_1}^2} = \frac{z_{A_2}}{z_{A_1}^2} \frac{1}{P} \frac{\xi_{A_2}}{\xi_{A_1}^2} \quad (3)$$

where f_{A_2} is the fugacity of the dimer, f_{A_1} is the fugacity of the monomer, and where z_{A_i} stands for the true mole fraction and ξ_{A_i} for the true fugacity coefficient. The latter can be easily calculated applying the definition of fugacity coefficient by choosing an Equation of State (EOS). In this work the following EOS was selected:

$$P = \frac{n_T RT}{V - n_T b_m} \quad (4)$$

where n_T is the total amount of moles and $n_T b_m$ is the is the excluded volume due to the finite size of the molecules (it is usually assumed that $b_{A_1} \equiv b_{A_2}$). Defining the fraction of moles dimerized α it is possible to express Equation 3 as a function of α and the measured mole fraction of the carboxylic acid (y_A) in presence of an inert as shown in Equation 5. The true mole fractions can be then calculated using Equation 6 - 7 where (z_I) indicates the true mole fraction of the inert compound.

$$K(T) = \left[\frac{(1 - y_A)\alpha}{2y_A(1 - \alpha)^2} + \frac{(1 - \alpha/2)\alpha}{2(1 - \alpha)^2} \right] \frac{1}{P} \quad (5)$$

$$z_{A_1} = \frac{y_A(1 - \alpha)}{(1 - y_A) + y_A \left(1 - \frac{\alpha}{2}\right)} \quad (6)$$

$$z_i = \frac{(1 - y_A)}{(1 - y_A) + y_A \left(1 - \frac{\alpha}{2}\right)} \quad (7)$$

The fugacity coefficients were then calculated with Equation 8

$$\varphi_i = \frac{z_i}{y_i} \xi_i = \frac{z_i}{y_i} \exp\left(\frac{b_i P}{RT}\right) \quad (8)$$

The Non-Random Two-Liquid Model (NRTL) was instead used to evaluate the liquid activity coefficients. The equations of the NRTL model for a binary system are reported below:

$$\begin{aligned} \ln \gamma_1 &= x_2^2 \left[\tau_{21} \left(\frac{G_{21}}{x_1 + G_{21}x_2} \right)^2 + \tau_{12} \frac{G_{12}}{(x_2 + G_{12}x_1)^2} \right] \\ \ln \gamma_2 &= x_1^2 \left[\tau_{12} \left(\frac{G_{12}}{x_2 + G_{12}x_1} \right)^2 + \tau_{21} \frac{G_{21}}{(x_1 + G_{21}x_2)^2} \right] \\ \tau_{12} &= \Delta g_{12}/RT \quad \tau_{21} = \Delta g_{21}/RT \\ G_{12} &= \exp(-\alpha_{12}\tau_{12}) \quad G_{21} = \exp(-\alpha_{12}\tau_{21}) \end{aligned} \quad (9)$$

The NRTL model was reduced to a two parameter model by fixing the non-randomness parameter $\alpha_{12} = 0.48$ and estimating only the parameters Δg_{12} and Δg_{21} . Even though both liquid and vapor composition were determined experimentally, only T-x data were used for regression and estimation of Δg_{12} and Δg_{21} . In fact, by adding Equation 1 for each component it is easy to verify that

$$P = \frac{P_{s,1}(T)\gamma_1 x_1 \varphi_{1,s}^\circ}{\varphi_1} + \frac{P_{s,2}(T)\gamma_2 x_2 \varphi_{2,s}^\circ}{\varphi_2} \quad (10)$$

Using NRTL equations for the calculation of the activity coefficients, for each set of T-x data it is possible to estimate pressure of the system by means of Equation 10. The estimated values of the two parameters of the NRTL model are the ones that minimize the following objective function:

$$\Phi = \sum_{i=1}^N \frac{1}{N} (P - P_{i,calc})^2 \quad (10)$$

where N represents the number of experimental data collected. Obviously this is an iterative method since the calculation of the fugacity coefficients φ_i can be accomplished only by knowing the vapour mole fractions at equilibrium. For this reason, as a first attempt the estimation is performed assuming $\varphi_i = 1$, while the vapour mole fractions obtained from the first regression can be used to evaluate the values of the fugacity coefficients that were inserted in the second iteration. The iteration continued until the values of the objective function Φ from an two consecutive iterations were $|\Phi_{j-1} - \Phi_j| < \varepsilon$ sufficiently small. This procedure (developed by J.A. Barker) was chosen since it intrinsically respects the conditions of thermodynamic consistency. Once finished the regression, the vapour mole fractions obtained were correlated with the experimental ones verifying simultaneously the consistency of the experimental data and the goodness of the model estimation. A schematic block of the algorithm used for the parameter estimation was given in Figure 1.

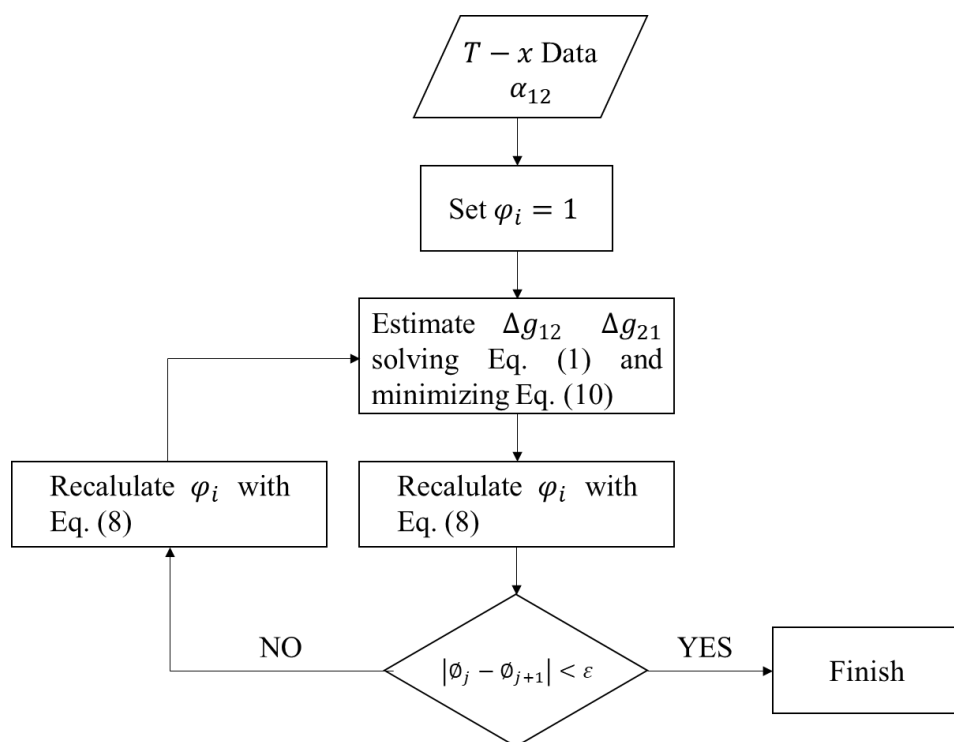


Figure 1. Algorithm for the estimation of NRTL Δg_{12} and Δg_{21} parameters.

3. Results and discussion

Liquid-vapor equilibrium data were reported in Table 2 and in Figure 1. Although the presence of minimum boiling azeotrope was observed, it was not possible to obtain a precise estimation of the azeotropic composition due to the “flatness” of the equilibrium curve in that region between 100.0 °C and 100.2 °C (see Figure 2).

Table 2. Vapor-liquid equilibrium data for Propionic Acid (1) – water (2) at 1 atm.

T, °C	x_1	y_1
100.2	0	0
100.0	0.106	0.081
99.9	0.030	0.034
99.9	0.063	0.059
100.2	0.147	0.094
100.3	0.203	0.113
101.1	0.250	0.127
102.0	0.420	0.165
103.8	0.497	0.216
104.1	0.543	0.216
107.2	0.650	0.301
121.3	0.874	0.593
125.1	0.921	0.682
141.2	1	1

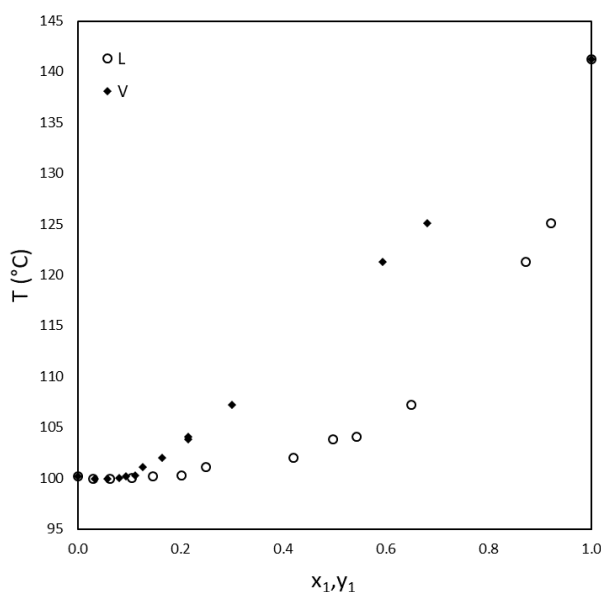


Figure 2. Propionic Acid-water Liquid-vapor equilibrium curve at 1 atm.

The expression for the calculation of the equilibrium constant of dimerization for propionic acid was taken by Tsonopoulos and Prausnitz [15] and reported in Equation 11:

$$\log_{10} K(T) = -10.13 + \frac{3075}{T} \quad (mm^{-1}Hg) \quad (11)$$

The relation used for the evaluation of the vapour tension of pure compounds was the one reported on Perry's Chemical Engineers' Handbook [10] and has the following expression:

$$\ln P_{s,i}(T) = C1 + \frac{C2}{T} + C3 \ln(T) + C4 T^{C5} \quad (Pa) \quad (12)$$

In both Equation 11 and 12 temperatures must be used in K. In Table 3 was given the value of the molecular excluded volume as well as the constants used in Equation 12 for each compound.

Table 3. Propionic Acid and water parameters.

Property	Symbol (UM)	Propionic Acid	Water	Reference
Molecular excluded volume	b (cm ³ /mol)	170.2	49.5	[14]
	C1	54.552	73.649	
Vapour tension constants	C2	-7149.4	-7258.2	
	C3	-4.2769	-7.3037	
	C4	$1.1843 \cdot 10^{-18}$	$4.1653 \cdot 10^{-6}$	[10]
	C5	6	2	

In figure 3 a) were reported the liquid activity coefficient values obtained by experimental data implementing the chemical theory for vapor imperfections, while in Figure 3 b) was given the Gibbs excess function (Δg^E) respect to the molar liquid composition of propionic acid: it is noticeable the positive deviation from ideality which leads to $\Delta g^E > 0$ and $\gamma_i > 1$.

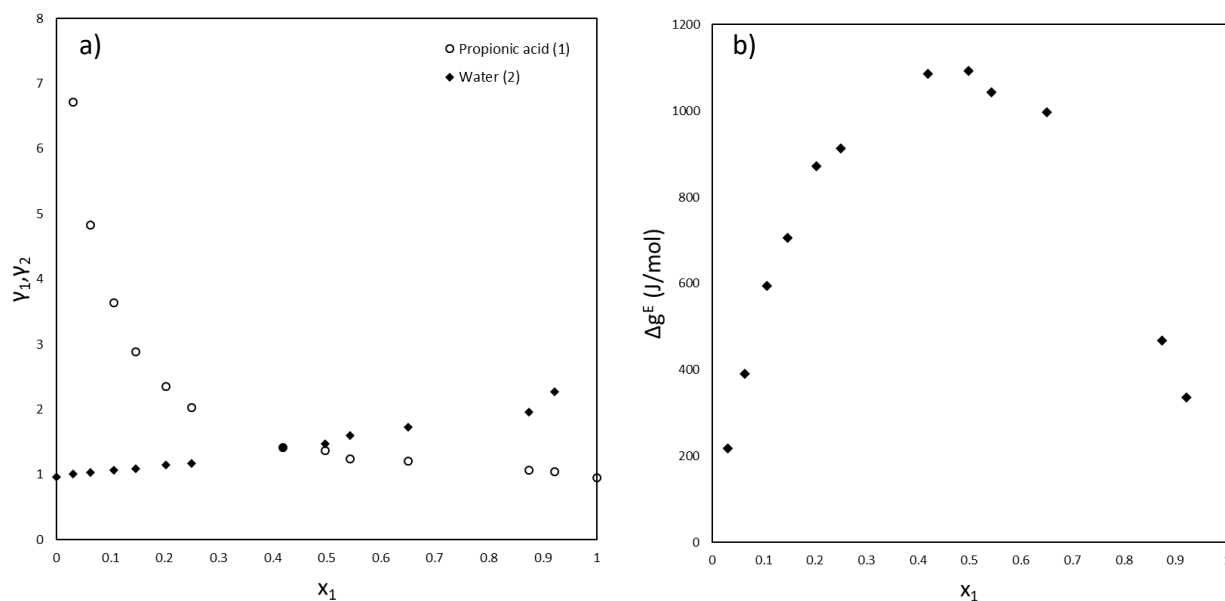


Figure 3. Propionic Acid-water liquid activity coefficients a) and Gibbs excess function (Δg^E) b).

Figure 4 shows the correlation between the calculated mole fraction of propionic acid in the vapour phase after performing the regression ($y_{1,cal}$) with the experimental one ($y_{1,exp}$). The goodness of the estimation is verified from the value $R^2=0.9954$ which indicates an extremely high correlation between the vapour mole fractions predicted by the model and the experimental ones. The NRTL values obtained are: $\Delta g_{12} = 446$ J/mol and $\Delta g_{21}=6399$ J/mol.

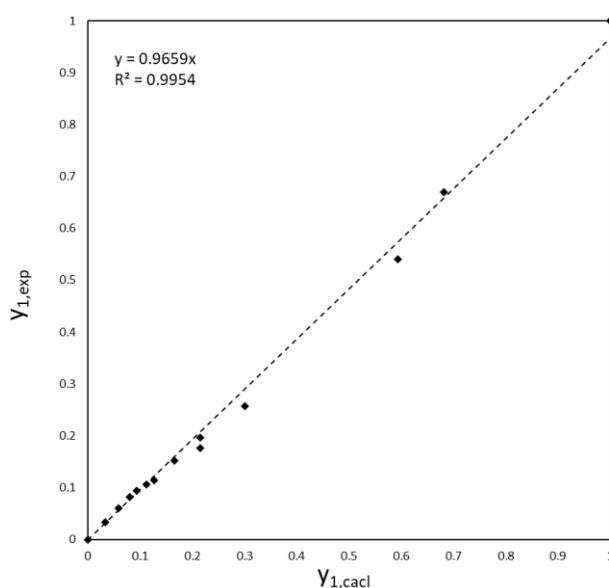


Figure 4. Correlation between the vapor mole fractions predicted by the model ($y_{1,cal}$) respect to the ones evaluated experimentally ($y_{1,exp}$).

4. Conclusions

In this work the atmospheric Liquid-Vapor equilibrium between the binary system Propionic Acid-water was investigated. The chemical theory for vapor imperfections was adopted for the evaluation of the fugacity coefficients considering the dimerization of propionic acid and water as an inert in the vapor phase. Although

were collected experimental data also regarding the composition of the vapor phase at equilibrium, it was chosen to utilize such data to verify the goodness of the regression. The system showed a positive deviation from ideality $\Delta g^E > 0$ and the presence of an azeotrope between the range of 100.0 °C and 100.2 °C. It was verified that the NRTL well represents the liquid phase non-ideality. Further studies should be conducted at different pressures and introducing others Volatile Fatty Acids (VFAs) in order to evaluate the selective separability of VFAs from water mixtures.

References

- [1] Research and markets, Propionic Acid - Global Market Trajectory & Analytics, 2021. <https://doi.org/ID:5030547>.
- [2] M. Atasoy, I. Owusu-Agyeman, E. Plaza, Z. Cetecioglu, Bio-based volatile fatty acid production and recovery from waste streams: Current status and future challenges, *Bioresour. Technol.* 268 (2018) 773–786. <https://doi.org/10.1016/j.biortech.2018.07.042>.
- [3] P.M. Brooks, Propionic acid derivatives, *Curr. Ther. (Seaforth)*. 22 (1981) 109–115. https://doi.org/10.1007/978-3-662-02384-6_18.
- [4] A. Gallipoli, A. Gianico, S. Crognale, S. Rossetti, L. Mazzeo, V. Piemonte, M. Masi, C.M. Braguglia, 3-routes platform for recovery of high value products, energy and bio-fertilizer from urban biowaste: The revenue project, *Detritus*. 15 (2021) 24–30. <https://doi.org/10.31025/2611-4135/2021.15092>.
- [5] K. Wang, J. Yin, D. Shen, N. Li, Anaerobic digestion of food waste for volatile fatty acids (VFAs) production with different types of inoculum: Effect of pH, *Bioresour. Technol.* 161 (2014) 395–401. <https://doi.org/10.1016/j.biortech.2014.03.088>.
- [6] B.P. Dakshinamurty, G.J. Rao, C.V. Rao, VAPOUR-LIQUID EQUILIBRIA IN THE SYSTEM WATER-PROPIONIC ACID, (1961) 226–228.
- [7] L.A. Román-Ramírez, F. García-Sánchez, R.C.D. Santos, G.A. Leeke, Vapour-liquid equilibrium of propanoic acid+water at 423.2, 453.2 and 483.2K from 1.87 to 19.38bar. *Experimental and modelling with PR, CPA, PC-SAFT and PCP-SAFT, Fluid Phase Equilib.* 388 (2015) 151–159. <https://doi.org/10.1016/j.fluid.2015.01.004>.
- [8] T. Ito, F. Yoshida, Vapor-Liquid Equilibria of Water-Lower Fatty Acid Systems: Water-Formic Acid, Water Acetic Acid and Water-Propionic Acid, *J. Chem. Eng. Data*. 8 (1963) 315–320. <https://doi.org/10.1021/je60018a012>.
- [9] A. Tamir, J. Wisniak, Vapor Equilibrium in Associating Systems (Water-Formic Acid-Propionic Acid), *Ind. Eng. Chem. Fundam.* 15 (1976) 274–280. <https://doi.org/10.1021/i160060a009>.
- [10] P.E. Liley, G.H. Thomson, D.G. Friend, T.E. Daubert, E.C.N.-D.-0020 Buck, Data: Physical and chemical data, in: *Perry's Chem. Eng. Handb.*, 1997: pp. 2-1-2-204 ST-Data: Physical and chemical data. t:%5CScholar E-library%5CDatabases%5CDataBase-0020.pdf LB - Chemical and Physical data.
- [11] S. Malanowski, Experimental methods for vapour-liquid equilibria. Part I. Circulation methods, *Fluid Phase Equilib.* 8 (1982) 197–219. [https://doi.org/10.1016/0378-3812\(82\)80035-6](https://doi.org/10.1016/0378-3812(82)80035-6).
- [12] A. Chlanesef, L. Marrelli, I. Chimica, U. Roma, Isobaric Vapor-Liquid Equilibria of the Ethylbenzene-p-Xylene System, (1985) 424–427.
- [13] A. Carli, S. Di Cave, E. Sebastiani, Thermodynamic characterization of vapour-liquid equilibria of mixtures acetic acid-dimethylacetamide and water-dimethylacetamide, *Chem. Eng. Sci.* 27 (1972) 993–1001. [https://doi.org/10.1016/0009-2509\(72\)80014-9](https://doi.org/10.1016/0009-2509(72)80014-9).
- [14] K.H. Nothnagel, D.S. Abrams, J.M. Prausnitz, Generalized Correlation for Fugacity Coefficients in Mixtures at Moderate Pressures. Application of Chemical Theory of Vapor imperfections, *Ind. Eng. Chem. Process Des. Dev.* 12 (1973) 25–35. <https://doi.org/10.1021/i260045a006>.

- [15] C. Tsonopoulos, J.M. Prausnitz, Fugacity coefficients in vapor-phase mixtures of water and carboxylic acids, *Chem. Eng. J.* 1 (1970) 273–278. [https://doi.org/10.1016/0300-9467\(70\)85014-6](https://doi.org/10.1016/0300-9467(70)85014-6).

Organic coatings from vegetable oils for corrosion protection

Leonardo Iannucci^{1*}, Camilla Noè¹, Valeria Gozzano¹, Marco Sangermano¹,
Emma Angelini¹, Sabrina Grassini¹

¹ *Department of Applied Science and Technology, Politecnico di Torino, Corso Duca degli Abruzzi 24, Torino, Italy*

**Corresponding author E-Mail: leonardo.iannucci@polito.it*

1. Introduction

The need to reduce oil consumption has stimulated an increasing interest in novel polymeric materials derived from vegetable oils, which can have wide applications, from composites production to coatings application [1][2]. Dealing with the anti-corrosion coatings field, major importance is attributed to the coating barrier properties, which determine the diffusion kinetics of aggressive species through the material [3]. Consequently, a widely recognized approach is to add fillers inside the polymeric matrix to slow down this process and improve corrosion protection effectiveness [4].

In order to evaluate the possible use of novel eco-friendly materials in the anti-corrosion field, this study characterizes UV-cured epoxy coatings from vegetable resources. Moreover, the effect of filler addition is investigated, assessing the effect of nanoclay content on the coating barrier properties.

2. Methods

Diglycidylether of vanillyl alcohol (DGEVA) was used as biobased epoxy monomer; it was synthesized and provided by Specific Polymers (Castrier, France). The photocurable formulations were prepared by mixing the epoxy resin with a 2 phr (per hundred resin) of photoinitiator (PhI) and with different concentrations of nanoclay (0 wt%, 3 wt%, 5 wt%). Subsequently, they were applied on mild steel substrates using a spiral bar coater (final coating thickness of 50 μm) and then cured under a DYMAX UV-lamp for 60 s with a light intensity of 125 mW/cm^2 . The photopolymerization reaction was conducted in air at room temperature.

Electrochemical measurements were performed in 3.5 wt% sodium chloride (NaCl) solution in a three-electrode cell, using an Ag/AgCl electrode as reference and a titanium sheet as counter electrode. Electrochemical Impedance Spectroscopy (EIS) measurements were carried out using an alternating voltage signal of 20 mV, in the frequency range from 10^4 Hz to 10^{-2} Hz, acquiring 10 points per frequency decade.

3. Results and discussion

The UV-curing process allows to obtain thermoset materials which, thanks to the low filler content, keep their transparency. In order to assess their corrosion protection effectiveness, EIS measurements were performed. Impedance spectra acquired after two hours of immersion in the electrolyte solution are presented in Figure 1 as Bode diagrams. All samples exhibit a resistive behaviour at high frequencies and then a capacitive-like behaviour at lower frequencies. Actually, phase values reach a maximum value of about -35° and then reach again values close to 0° in the low-frequency range. The relatively low maximum value in the measured phase can be attributed to the high aggressivity of the electrolyte solution.

Nanoclay addition has a clear effect on protective effectiveness, as can be seen from the impedance modulus. Actually, its value at low frequencies reaches about $10^5 \Omega \cdot \text{cm}^2$ for the sample without filler addition, while it increases up to about $6 \cdot 10^5 \Omega \cdot \text{cm}^2$ for the coatings containing the nanoclay. The positive effect is enhanced by the filler shape factor. Actually, clay has a lamellar shape which allows to increase the path tortuosity during diffusion of aggressive species from the environment towards the metal substrate. Thus, a lower filler content is needed, if compared to non-lamellar alternatives [6].

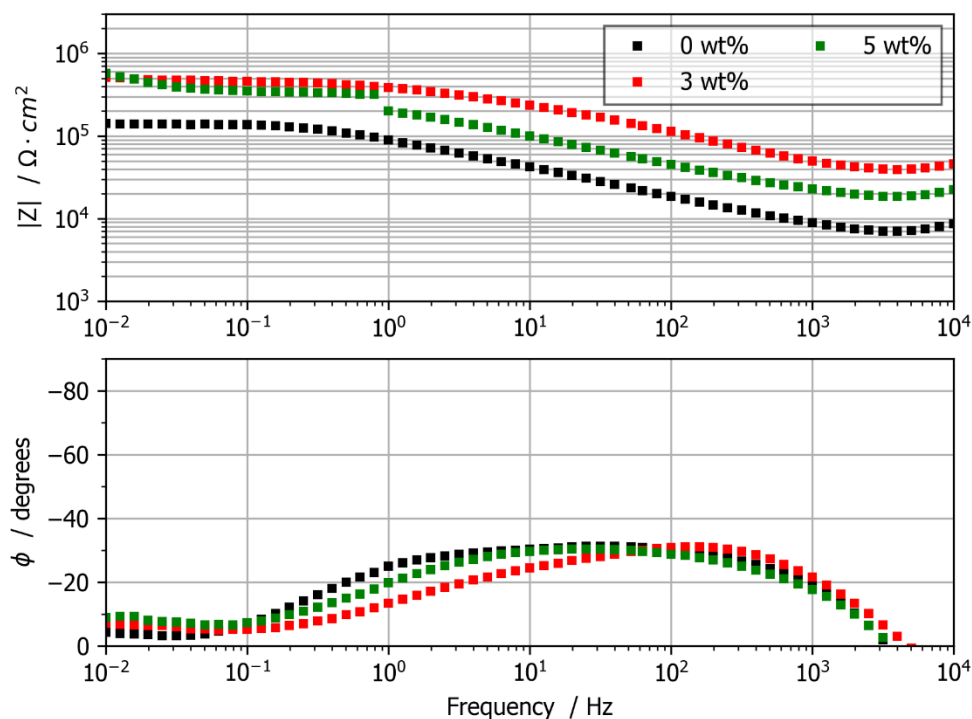


Figure 1. Impedance spectra recorded after 2 hours of immersion in 3.5 wt% NaCl electrolyte solution. Characterized samples are the three coatings, containing an increasing amount of filler (nanoclay).

It is interesting to highlight also that the beneficial effect is similar for samples containing 3 wt% and 5wt% of nanoclay, i.e. an additional increase in filler content above 3 wt% seems to have a limited effect. This can be attributed to aggregation phenomena, which often occur in nanomaterials when filler content is too high; thus, the optimal filler content is below 5 wt%.

4. Conclusions

The preliminary electrochemical measurements allowed us to assess the good protective effectiveness of the photocured coatings when immersed in an environment containing chlorides. Nanoclay addition had a positive effect on barrier properties, increasing the coating impedance modulus. Future work will be devoted to the characterization of the protective effectiveness after longer times of exposure to the electrolyte solution.

References

- [1] R. Auvergne, S. Caillol, G. David, B. Boutevin, J.-P. Pascault, Biobased thermosetting epoxy: Present and future, *Chemical Reviews*, 114-2 (2014), pp. 1082-1115.
- [2] C. Noè, M. Hakkarainen, M. Sangermano, Cationic uv-curing of epoxidized biobased resins, *Polymers*, 13-1,(2021), pp. 1-16.
- [3] C. Noè, L. Iannucci, S. Malburet, A. Grailot, M. Sangermano, S. Grassini, New UV-Curable Anticorrosion Coatings from Vegetable Oils, *Macromolecular Materials and Engineering*, 306-6 (2021), art. no. 2100029
- [4] R. K. Bharadwaj, Modeling the Barrier Properties of Polymer-Layered Silicate Nanocomposites, *Macromolecules*, 34, (2004), pp. 9189-9192
- [5] J. L. Varela Caselis, E. Rubio Rosas, J. D. Santamaría Juárez,
- [6] J. A. Galicia Aguilar, M. Sánchez Cantú, O. Olivares Xometl, M. Morales Sánchez, The use of montmorillonite organoclay in preparation of UV-cured DGBA epoxy anticorrosive coatings, *Corrosion Engineering, Science and Technology*, 53-5 (2018), pp. 362-369

Soot coatings wettability with different liquids. Preliminary results.

Raffaella Griffo^{1,*}, Arianna Parisi², Gianluigi De Falco², Mariano Sirignano², Francesco Di Natale², Mario Minale¹, Claudia Carotenuto¹.

¹Dipartimento di Ingegneria, Università della Campania "L. Vanvitelli", 81031 Aversa (CE), Italy

²Dipartimento di Ingegneria Chimica, dei Materiali e della Produzione Industriale, Università degli Studi di Napoli "Federico II", 80125 Napoli, Italy

*Corresponding author E-Mail: raffaella.griffo@unicampania.it

1.Introduction

The wettability of a solid surface is defined as the ability of the surface to hold contact with a liquid. It is frequently measured through the contact angle, CA, defined as the angle between the tangent to the liquid-vapor interface and the solid surface at the three-phase contact line (**Errore. L'origine riferimento non è stata trovata.**a). By convention, the contact angle is measured from the liquid side. The contact angle can assume values from 0° to 180° identifying different types of surfaces (**Errore. L'origine riferimento non è stata trovata.**b): superphilic surface (CA<5°), philic surface (5°<CA<90°), phobic surface (90°<CA<150°) and superphobic surface (CA>150 °)[1, 2].

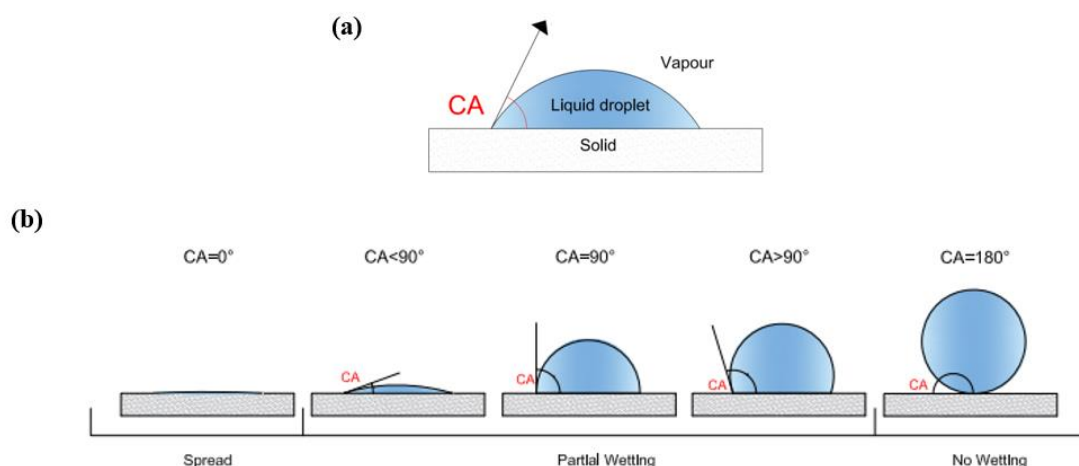


Figure 1– a) Profile of a drop deposited on a solid surface with the indication of the contact angle, b) Wettability scale.

In nature, there are numerous examples of superhydrophobic surfaces, which therefore have high water repellency, such as the lotus leaf[2]. The behavior of this surface is attributed to the peculiar leaf structure, in particular to its upper epidermis covered with wax crystals that create a nano/micrometric roughness. In recent decades, research has tried to "imitate" nature to create highly hydrophobic or even omniphobic surfaces with potential applications in the textile field, self-cleaning coatings, anti-icing coatings, anti-bacterial coatings, solar panels, etc[3].

If we refer to a smooth surface, for which the liquid/solid interactions are governed exclusively by the chemistry of the system, the maximum contact angle that can be found is 120°[4]. Therefore, to reach contact angles above 150°, and obtain a superhydrophobic surface, it is necessary to intervene on the surface texture and increase its roughness.

In this regard, it has been shown that soot deriving from flame can be used for the preparation of superhydrophobic surfaces[5, 6] with a rapid, modular and cost effective production process. Indeed, the first synthetic superhydrophobic surface was fabricated in 1907 by coating a substrate using candle soot [2].

One of the methods used to produce carbon nanofilm consists in repeatedly inserting the substrate that will host the soot deposit into a flame for a few milliseconds. The substrate and the forming film enter and exit intermittently from the combustion zone[7]. The residence time in the flame is short enough to prevent heating of the substrate but long enough to allow the deposition of the soot by thermophoresis (from the hot flame to the cold substrate). The chemical-physical properties of the nanofilm can be finely modulated by acting on various process parameters (type of fuel, fuel/comburent ratio, position, duration and number of insertions of the substrate in the flame, etc.).

This abstract reports preliminary results on wettability analysis of carbon nanofilms produced under different flame conditions. The wettability is firstly studied by measuring the contact angle using distilled water as the test liquid. To highlight the differences in the nanostructure of the various produced films, we also use water-ethanol mixtures to reduce and tune the interfacial tensions of the test liquid.
















2. Materials and Methods

A flat laminar premixed ethylene-air flame stabilized on a water-cooled McKenna burner was used to produce carbon nanofilms. The speed of the cold gas is set at 9.8 cm/s and the carbon/oxygen (C/O) ratios were: C/O = 0.72 (slightly sooty flame), C/O = 0.82, and 0.87 (more sooty flame).

The soot produced in flame is deposited on glass substrates. The glass plate is repeatedly inserted inside the burner to allow soot particle deposition by thermophoresis. The number of insertions varies from 1 to 32 (1, 2, 4, 8, 16, 32), each insertion lasts 2 seconds, and the rest time (that is the time for sample cooling before inserting it again in the flame) is set at 10 seconds. The distance from the burner surface (HAB) is fixed at 15 mm. Table 1 reports pictures of all the samples tested in this work; the degree of blackening increases by increasing the insertions number and the C/O ratio, indicating larger film depositions.

The wettability of the produced carbon nanofilms was tested with distilled water produced with a distiller (Ecotec) available in the laboratory of University “Luigi Vanvitelli” and with water-ethanol mixture (Ethanol, purity $\geq 99.8\%$, supplied by Honeywell). The surface tension, ST, of distilled water is high and equal to 73 mN/m. The use of water-ethanol mixtures allows tuning the surface tension of the wetting liquid. Figure 2a shows the surface tension as a function of water-ethanol mixture composition. The wettability of the glass substrate with distilled water and water-ethanol mixture is shown in Figure 2b.

Table 1 – Picture of the samples produced under different flame conditions

Samples		C/O		
		0.77	0.82	0.87
Insertions	1			/
	2			/
	4			/
	8			
	16			
	32			

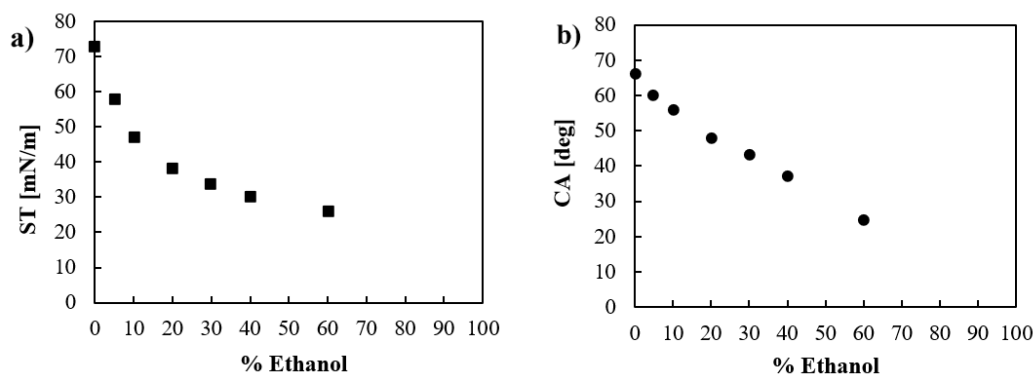










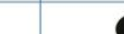

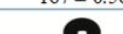

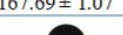
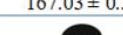

Figure 2–a) Surface tension and b) contact angle on the glass substrate as a function of the water-ethanol mixture composition.

The contact angle, CA, was measured with the First Ten Angstroms–1000tensiometer. The needle used for depositing the drop on the sample has an internal diameter of 0.406 mm. Depending on the wetting liquid, a drop of a certain volume is formed before it falls under its weight (*e.g.* for distilled water the drop volume is 8 μL) [8]. The distance between the needle tip and the surface is carefully evaluated to be minimized, so that the impact with the falling drop does not modify the nanostructure of the nanofilm. Despite this caution, soot particles may detach from the nanofilm and enter the drop. In any case, this is a negligible phenomenon not affecting the results. For each experimental test, at least ten replicates have considered and average values are reported therein.

3. Results and discussion

Table 2 shows, for each carbon nanofilm sample, the images of the water drops deposited on it and the corresponding average contact angle. It is immediately evident that by increasing the C/O ratio and the number of insertions, the samples passed from a hydrophilic to a superhydrophobic behavior. The increase of the contact angle is not gradual, but revealed an abrupt transition from hydrophilic surfaces ($CA < 90^\circ$) to superhydrophobic ones ($CA > 150^\circ$). As expected, the number of insertions necessary to observe this hydrophilic-superhydrophobic transition is smaller for a higher C/O ratio and occurs in correspondence of similar blackening of the sample (see Table 2 and 3).

Table 2–Images of water drops and corresponding contact angle for carbon nanofilms produced with ethylene-air flame with three C/O ratios and a different number of insertions.

ST: 73 mN/m		C/O		
		0.77	0.82	0.87
Insertions	Water			
	1	 42.58 \pm 0.79	 54.8 \pm 0.75	/
	2	 62.45 \pm 0.61	 59.31 \pm 0.86	/
	4	 67.96 \pm 3.57	 TRANSITION	/
	8	 64.82 \pm 2.12	 167 \pm 0.56	 166.22 \pm 0.85
	16	 167.69 \pm 1.07	 167.03 \pm 0.35	 165.38 \pm 1.07
32	 167.21 \pm 0.51	 164.62 \pm 1.57	 164.41 \pm 1.06	

The hydrophilic behavior is probably related to a not uniform soot coating of the glass substrate; when the soot completely covers the substrate the sample becomes superhydrophobic. It is worth noticing that the CA of all the superhydrophobic nanofilms does not depend on the flame conditions and it is on average equal to 166° . Furthermore, Table 2 shows a peculiar wettability behavior for $C/O = 0.82$ and 4 flame insertions: the surface was superhydrophobic for the first seconds after the drop deposition, then a sudden reduction of the CA, below 90° , was measured. This behavior individuates the limit conditions for a coating good enough to reach superhydrophobicity.

Errore. L'autoriferimento non è valido per un segnalibro. shows the results obtained with the water-ethanol 95/5 mixture (with 5% of ethanol) having a surface tension of 58 mN/m . The results are very similar to those observed with pure water in Table 2; in particular, the transition from philic to superphobic samples occurs in correspondence of the same flame conditions. For each sample, the CA measured with this water-ethanol mixture is equal or slightly smaller than the one obtained with pure water. In addition, the sample that previously showed an evolution from superhydrophobic to philic over time ($C/O = 0.82 - 4$ insertions) is immediately philic in this case.

Table3–Picture and contact angle of water-ethanol 95/5 drop deposited on carbon nanofilms produced with ethylene-air flame with three C/O ratios and a different number of insertions.







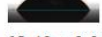








ST: 58 mN/m Water/ethanol 95/5		C/O		
		0.77	0.82	0.87
Insertions	1	 43.63 ± 1.91	 56.92 ± 0.31	/
	2	 44.81 ± 1.81	 58.56 ± 1.32	/
	4	 54.52 ± 4.35	 60.29 ± 0.2	/
	8	 65.49 ± 3.96	 164.2 ± 0.68	 163.09 ± 1.36
	16	 166.32 ± 1.48	 165.99 ± 1.2	 163.97 ± 1.59
	32	 164.94 ± 0.96	 163.58 ± 0.87	 164.53 ± 1.08

Table4– Picture and contact angle of water-ethanol 85/15 drop deposited on carbon nanofilms produced with ethylene-air flame with three C/O ratios and different number of insertions.







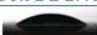
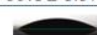

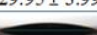


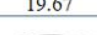
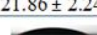
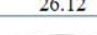
ST: 42 mN/m Water/ethanol 85/15		C/O		
		0.77	0.82	0.87
Insertions	1	 33.61 ± 2.22	 34.86 ± 3.33	/
	2	 37.46 ± 2.12	 36.9 ± 1.51	/
	4	 38.92 ± 2.40	 35.1 ± 1.37	/
	8	 29.95 ± 3.99	 28.28 ± 3.05	 27.23
	16	 19.67	 21.86 ± 2.24	 26.12
	32	 21.22 ± 3.77	 24.2	 26.38

Table 4 shows the results obtained with a 85/15 water-ethanol mixture, having a surface tension of 42 mN/m. With this low value of the surface tension, all the samples exhibit philic behavior. The contact angles are lower than those indicated in Table 3 and, unexpectedly, the lower CAs occur for those samples previously showing superhydrophobicity, i.e. for sample with higher C/O values and larger number of insertions.

The strong reduction of the surface tensions from 58 to 42 mN/m implies a complete switch of the wettability of all the superhydrophobic samples. We can better distinguish among them by individuating a wetting liquid with opportunely tuned surface tension. In particular, we selected a water-ethanol 93/7 mixture, with a surface tension of 51 mN/m and we measured the contact angle of samples obtained with 16 insertions and three different C/O values. With this selected liquid, the surface wettability of each sample results variable, as shown in Figure 3. In particular, by depositing liquid droplets in different points of the sample surface, we found both philic (blue dots) and superphobic (red dots) regions, together with regions showing transition from superphobic-to-philic (green dots) behavior (as already observed in Table 2 for the sample C/O = 0.82 and 4 insertions). Figure 4 shows that the nanofilm with C/O = 0.77 is prevalently philic with few superphobic and transition points, while for the nanofilms with C/O = 0.82 the number of superphobic points increases (with only three transition and one philic points). Nanofilms with C/O = 0.87 are almost entirely superphobic with only two transition points and no philic points.

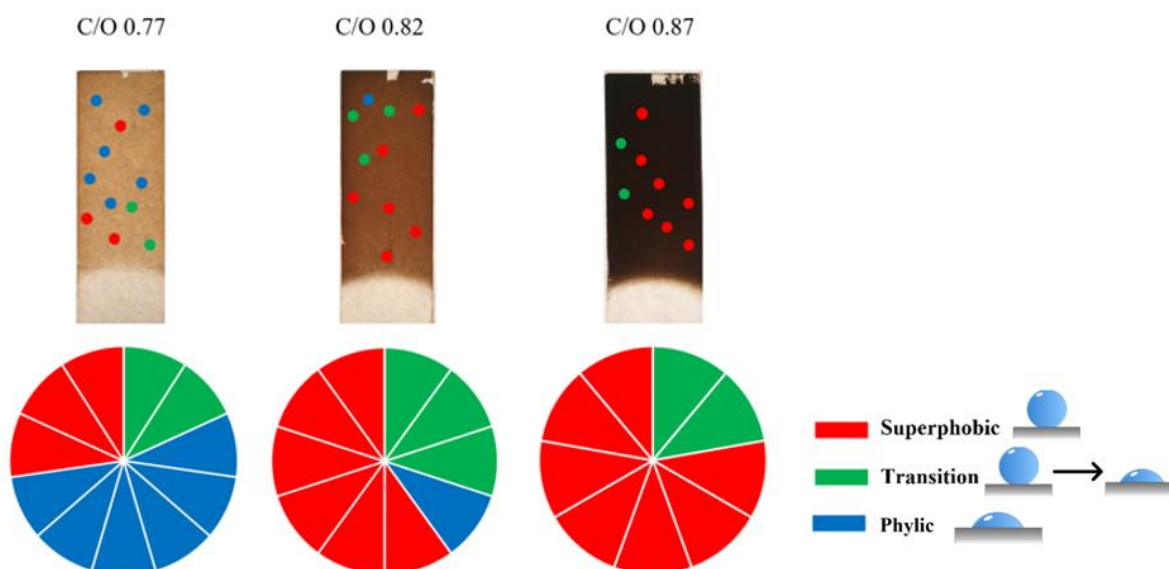


Figure 3 - Images representing philic, transition, and superphobic areas for samples made with 16 insertions and three different C/O ratios.

4. Conclusions

This study reports the preliminary results on the wettability of carbon nanofilms produced by depositing, on a glass substrate, soot deriving from premixed air-ethylene flame. Three C/O values equal to 0.77, 0.82 and 0.87 were tested and, in each case, we varied the number of substrate insertions in flame from 1 to 32 to obtain different coatings. Their wettability was measured with water, having a surface tension of 73 mN/m, and water-ethanol mixtures whose surface tension can be progressively reduced by increasing ethanol concentration.

Regarding tests with water, we observe that there is a critical soot coating level below which the carbon nanofilms are hydrophilic, above which they are superhydrophobic. In the latter case, CA is around 166° without any distinction among samples deriving from different flame conditions.

The nanofilms wettability measured with water-ethanol mixtures depend on the ethanol concentration. For low ethanol concentration (*e.g.* 95/5 water-ethanol mixture), no significant modification of the CA is observed with respect to the case of pure water. For high ethanol concentration (*e.g.* 85/15 water-ethanol mixture), all the nanofilms show philic behavior. For a selected ethanol concentration equal to 93/7 water-ethanol mixture, we can discriminate among samples produced with different C/O ratios and a fixed number of insertions. This mixture can highlight heterogeneity in the wettability of the sample's surface. In particular, the coating obtained with the less sooting flame (C/O = 0.77) has large philic areas and small superphobic ones, while passing to more sooting flame (C/O = 0.82 and 0.87) the superphobic regions progressively enlarges. These preliminary results demonstrate that the use of wetting liquid with tunable surface tension is a rapid and extremely sensitive tool to assess surface homogeneity/heterogeneity and to discriminate among nanofilms obtained under different flame conditions.

5. Acknowledgements

This work is financially supported by the PRIN project 2017PJ5XXX: "MAGIC DUST".

Reference

- [1] A. Marmur, "Solid-surface characterization by wetting," *Annual Review of Materials Research*, vol. 39, pp. 473-489, 2009.
- [2] S. Li, J. Huang, Z. Chen, G. Chen, and Y. Lai, "A review on special wettability textiles: theoretical models, fabrication technologies and multifunctional applications," *Journal of Materials Chemistry A*, vol. 5, pp. 31-55, 2017.
- [3] Z. Cai, J. Lin, and X. Hong, "Transparent superhydrophobic hollow films (TSHFs) with superior thermal stability and moisture resistance," *RSC advances*, vol. 8, pp. 491-498, 2018.
- [4] E. Fadeeva, S. Schlie-Wolter, B. Chichkov, G. Paasche, and T. Lenarz, "Structuring of biomaterial surfaces with ultrashort pulsed laser radiation," in *Laser Surface Modification of Biomaterials*, ed: Elsevier, 2016, pp. 145-172.
- [5] M. R. Mulay, A. Chauhan, S. Patel, V. Balakrishnan, A. Halder, and R. Vaish, "Candle soot: Journey from a pollutant to a functional material," *Carbon*, vol. 144, pp. 684-712, 2019.
- [6] B. Zhang, J. Duan, Y. Huang, and B. Hou, "Double layered superhydrophobic PDMS-Candle soot coating with durable corrosion resistance and thermal-mechanical robustness," *Journal of Materials Science & Technology*, vol. 71, pp. 1-11, 2021.
- [7] G. De Falco, M. Commodo, M. Barra, F. Chiarella, A. D'Anna, A. Aloisio, *et al.*, "Electrical characterization of flame-soot nanoparticle thin films," *Synthetic Metals*, vol. 229, pp. 89-99, 2017.
- [8] J. Drelich, "Guidelines to measurements of reproducible contact angles using a sessile-drop technique," *Surface innovations*, vol. 1, pp. 248-254, 2013.

Biodegradability evaluation of waste-derived Polyhydroxyalkanoates

Laura Lorini^{1*}, Marco Santini¹, Sara Alfano¹, Francesco Valentino², Andrea Martinelli¹, Marianna Villano¹, Mauro Majone¹

1 Department of Chemistry, La Sapienza University of Rome, Rome, 00185, Italy; 2 Department of Environmental Sciences, Informatics and Statistics, Ca' Foscari University of Venice, Venice, 30172, Italy

**laura.lorini@uniroma1.it*

1. Introduction

Biobased and biodegradable plastics are currently object of high interest within the biorefinery and circular economy approach. In this view, waste valorization and energy recovery can be realized through composting and anaerobic digestion of these materials since they are generally identified as biodegradable and compostable and then collected with the Organic Fraction of Municipal Solid Waste (OFMSW). Indeed, biodegradable bioplastics can be subjected to biological decomposition both in aerobic and anaerobic conditions, for the consequent production of carbon dioxide or methane. However, to be addressed to composting and anaerobic digestion treatments, either biodegradable and compostable plastics must meet the EU standards for SUP and packaging. Among biodegradable and biobased plastics, polyhydroxyalkanoates (PHA) are high added-value materials that can be recovered from waste activated sludge and different fermentable organic waste. They are biodegradable polyesters produced as intracellular carbon source by numerous microbes and have thermoplastic properties comparable to fossil-based plastics. The present study regards the evaluation of the Bio-Methane potential (BMP) of several PHA-based materials produced from mixed microbial culture and fermented mixture of OFMSW and sludge as substrate, within a pilot platform based in Treviso (Italy). PHA was produced from a feedstock composed by a mixture of the liquid slurry coming from squeezed OFMSW and the thickened sewage sludge from the treatment of municipal wastewater. The productive process is extensively described in a previous study [1]. Extraction with a mixture of aqueous-phase inorganic reagents was performed following a reserved protocol optimized by Biotrend S.A.. At the end of the extraction, the polymer was oven-dried obtaining a white powder (RU powder). In the framework of RES URBIS project, PHA purified by Biotrend was sent to SABIOMATERIALS for obtaining a melt-compounded pellet by mixing PHA with biodegradable additives (RU pellet). Finally, the pellet was sent to MiPlast, to produce blended PHA-PBS films by blown extrusion (Blend PHA-PBS). In this study, the powder and the pellet of RES URBIS PHA were melted and pressed (at a working T slightly below the melting point) to obtain films (RU film powder and RU film pellet, respectively). All these above-mentioned materials were tested for BMP in comparison with a commercial PHBV (HV 3%w/w) (Tianan powder) and thermal and chemical properties were determined before and after the biodegradation tests.

2. Methods

For the experimental set up, 14 serum bottles were filled with the 70 mL of mesophilic methanogenic sludge, 40 mL of mineral medium and 15mL of a 0.86 M NaHCO₃ solution as buffer. In order to maintain the Inoculum/Substrate ratio = 2:1 (g VSS/g material), about 175 mg of PHA material was added. The tests were carried out in duplicate for each material and for the blanks. From the headspace, 50 µL of gas phase were sampled with a gas syringe and directly injected into the gas chromatograph equipped with heat conductivity detector (TCD) for the determination of methane. Liquid samples were taken to monitor the volatile fatty acids (VFAs) concentration and the pH. VFAs analysis of filtered sample was conducted on GC equipped with flame ionization detector (FID). The materials were analyzed for viscosity average molecular weight (M_v)

determination, differential scanning calorimetry (DSC) and thermogravimetric analysis (TGA), following the procedures reported elsewhere [2].

3. Results and discussion

VFA concentration monitored for each material is reported in figure 1A for the first 60 days of BMP test. After an initial peak caused by the fermentation of PHA materials, the concentrations of acetic and propionic acid started to decrease, until zero from day 40 in all the bottles. This effect corresponded to the beginning of methane production, as it can be observed in Figure 1B, confirming the activity of the acetoclastic methanogens. Considering the kinetics of biodegradation and the produced methane, the highest conversion was obtained from both the PHBV powders (RU powder and Tianan) and from RU film powder, as a consequence of the high specific surface area. As regards RU pellet and Blend PHA-PBS, a significantly lower level of conversion into methane was obtained, as shown by the trends. Overall, considering the specific methane production (expressed as $L_{CH_4}/kgTVS$), a complete conversion to methane of PHA raw materials, including those produced from organic waste, can be confirmed [3]. Monomeric composition (i.e. HV content) of the whole RES URBIS set was in the range of 9 – 14 %w/w and the M_v of RU powder (207.4 kDa) and pellet (159.2 kDa) was lower than that one of Tianan (322.4 kDa). Melting temperatures (T_m) and temperatures at the highest rate of degradation (T_d^{max}) were determined by DSC and TGA analysis, respectively, for all the tested samples and also for RU pellet and Blend PHA-PBS residues. Indeed, since these latter were not easily biodegraded, it was possible to collect the residues at the end of the test. As an evaluation of the preliminary characterization of the recovered materials, it can be considered that they resulted macroscopically unchanged, as their properties, if compared to the original materials (158 – 167 °C and 263 – 288 °C, T_m and T_d^{max} ranges).

4. Conclusions

As a main result, the biodegradability of PHA raw materials has been confirmed in anaerobic conditions, suggesting the possibility to dispose PHA wastes together with the OFMSW for anaerobic digestion and compost applications. On the other hand, further investigation are required, since the presence of additives and plasticizers, necessary for plastic processing and depending from the application requested, affect the biodegradability. In this view, further characterization of the residual solid materials and tests conducted in different conditions (e.g. thermophilic anaerobic BMP tests) will be carried out.

References

- [1] Valentino F, Moretto G, Lorini L, Bolzonella D, Pavan P, Majone M, Ind. Eng. Chem. Res. (2019)
- [2] Lorini L, Martinelli A, Capuani G, Frison N, Reis M, Sommer Ferreira B, Villano M, Majone M, Valentino F, Front. Bioeng. Biotechnol. 9(2021) 1–13.
- [3] Battista F, Frison N, Bolzonella D, Environ. Technol. Innov. 22 (2021)101393.

Acknowledgements

The financial support from the H2020 EU project RES URBIS (GA 730349) is gratefully acknowledged.

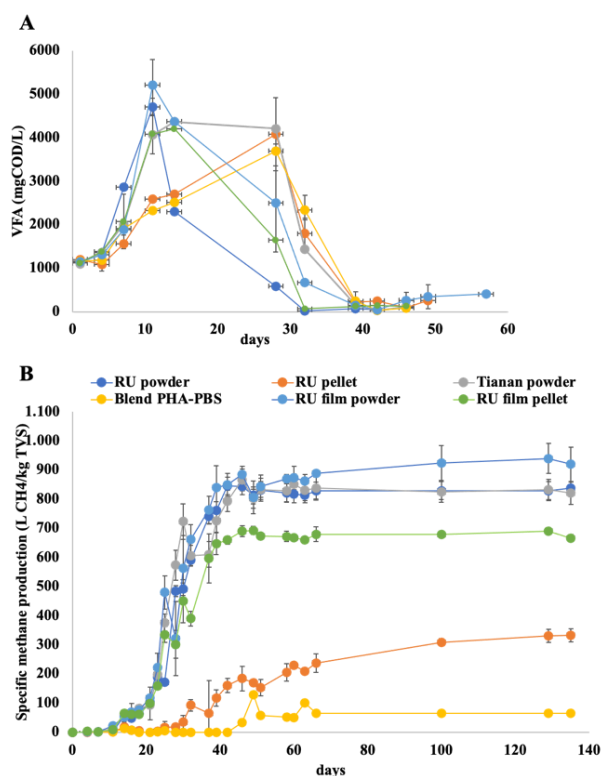


Figure 1. (A) VFA concentration; (B) specific methane production

Tuning the molecular architecture of 2D GO-based nanocomposites for gas separation application

Giacomo Foli,¹ Vincenzo Palermo,¹ Matteo Minelli^{2,*}

1 ISOF - CNR, via Gobetti 10, Bologna; 2 DICAM – University of Bologna, via Terracini, 28 Bologna

**Corresponding author E-Mail: matteo.minelli@unibo.it*

1. Introduction

Graphene Oxide (GO) is a 2D material derived from graphene oxidation and consists in a single sheet of graphite, functionalized by different oxygen-containing groups [1]. Thus, contrary to graphene, dispersion of GO can be easily accomplished in water, allowing a green and sustainable processability [2]. Among several possible applications, atomic-thick graphemic sheets spurs utilization in technological applications that demand 2D geometry, as fabrication of composite membranes for separation processes [3]. Ultrathin 2D composite membranes can be obtained by Layer-by-Layer (LbL) self-assembly [4], alternating the deposition of negatively charged GO and polycations [5], eventually leading to a layered molecular architecture with high order degree. In this work, we successively prepared nano-thick multilayers for gas-sieving applications such as hydrogen purification or pre-combustion carbon capture. The focus is on the gas couple He/CO₂, using He as a safer H₂ analogue, aiming to enhance the separation performances of existing membranes [6]. Furthermore, we demonstrated that membrane properties and performances can be conveniently modified by tuning the LbL procedure parameters or post-fabrication multilayers treatment that affect the 2D architecture, and consequently the gas sieving mechanism.

2. Methods

All chemical species were used as received. LbL self-assembled coatings were deposited on commercial polyimidic solvent-cast films (Matrimid[®] 5218) [7], used as substrate, and then superficially hydrolyzed, to allow self-interactions with charged species. LbL self-assembly was performed with a home-made apparatus following a previously reported procedure [4]. Briefly, Matrimid films were dipped in the polycation water solution (0.1wt%) for 5 minutes. Excess of deposited polycation was removed by a 20 min rising in neutralized water (pH = 7). Then, film was dipped in the GO water suspension (0.01wt.%) for 5 minutes and, once again, excess of deposited species removed with a 20 min rising in neutralized water. By repeating this procedure for 10 times, a coating of 10 BiLayers (BLs) was successfully prepared. Finally, coated films were hetaed for 30 minutes under an IR lamp to remove residual water in the coating. Gas transport properties of prepared coatings were evaluated with pure gas, by means of a manometric technique (ASTM D 1434). All the permeance were valued at 35°C. Permeances of the only coating (GPU_c) were calculated from the experimentally determined value of permeance (GPU_{Tot}) excluding the effect of the Matrimid (GPU_M) by means of the series resistance equation. All the presented results are the average of at least three analyses independently measured.

3. Results and discussion

LbL technique offers a large array of variables that can be opportunely tuned to modulate final molecular architecture, and thus modifying the resulting gas transport properties. The self-assembly with two different polycations (PEI or PDDA) lead to the fabrication of multilayers characterized by diverse perm-selectivities (Figure 1a). Indeed, while comparable values of selectivity were calculated for both multilayers, utilization of PDDA lead to a more permeable, and more attractive, coating. Interestingly, SEM imaging reveals that a smother surface was achieved when self-assembly was assisted by PDDA (Fig. 1b and c).

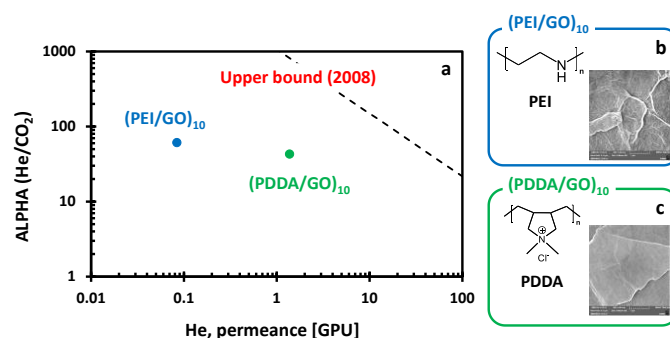


Figure 1. a) Perm-selectivity of the two differently self-assembled coatings; b) chemical structure of PEI and SEM image of outmost layer; c) chemical structure of PDDA and SEM image of outmost layer.

Even the possibility to accomplish post-fabrication modification was explored. Specifically, it is well known that an anoxic thermal annealing of GO results into its reduction (r-GO). Such conversion alters the structure of the multilayer, and the resulting transport phenomena. Water contact angle measurement confirm a gradual conversion of deposited GO into r-GO (increasing of the contact angle, Figure 2b). Interestingly, a 105°C (under vacuum) treatment lead to an improvement of perm-selectivity properties, while increasing the temperature a significant loss in selectivity was observed (Figure 2a).

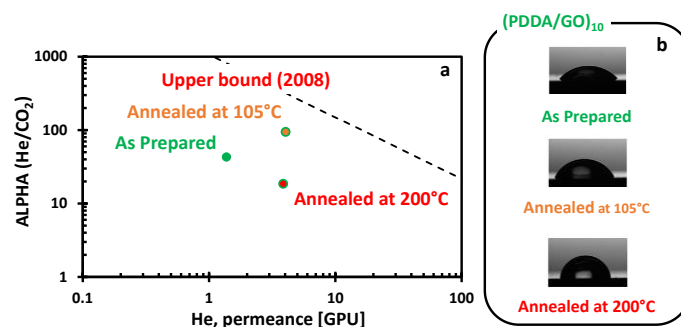


Figure 2. a) Perm-selectivity of differently post-fabricated annealed coatings; b) Water Contact Angles recorded for the outmost layers.

4. Conclusions

We presented a reproducible and scalable technology to self-assemble layered coating based consisting in an alternated deposition of a polycation and GO. Successively, we explore potential application of our multilayers as membrane for gas-sieving application, focusing our attention on the couple He/CO₂, and good results were obtained. Moreover, by performing proper modifications, a modulation of the coating nature was accomplished and perm-selectivity properties could be improved.

References

- [1] V. Palermo, Chem. Comm. 49 (2013) 2848–2857
- [2] D. R. Dreyer, A. D. Todd, and C. W. Bielawski, Chem. Soc. Rev. 43 (2014) 5288–5301
- [3] D. Bouša *et al.*, Chem. Eur. J. 22(2017) 11416-11422
- [4] D. Pierleoni *et al.*, ACS Applied Materials and Interfaces 10 (2018) 11242–11250
- [5] G. Decher, Science 277(1997) 1232–1237
- [6] L. M. Robeson, Journal of Membrane Science 320 (2008) 390–400
- [7] L. Ansaloni *et al.*, Oil and Gas Science and Technology 70 (2015) 367–379

Investigation of the effect of aeration time, storage and heating on the microstructure of oil-continuous foams with X-ray tomography and radiography

Lorenzo Metilli¹, Malte Storm², Shashidhara Marathe³, Aris Lazidis⁴, Stephanie Marty-Terrade⁵, and Elena Simone^{6*}

1 Laboratoire Rhéologie et Procédés, Université Grenoble Alpes, Grenoble 38000 (France)

2 Helmholtz-Zentrum hereon, 21502 Geesthacht (Germany)

3 Diamond Light Source Ltd., Harwell Science and Innovation Campus, Didcot OX110DE (UK)

4 Nestlé Product Technology Centre Confectionery, York YO318TA (UK)

5 Nestlé Research, Lausanne 26 1000 (Switzerland)

6 Department of Applied Science and Technology (DISAT), Politecnico di Torino, Torino 10129 (Italy)

**Corresponding author E-Mail: elena.simone@polito.it*

1. Introduction

Oil-continuous foams (also called oleofoams) are an emerging type of soft matter, which comprise a continuous liquid oil phase and a dispersed gas phase stabilized by fat crystals through a Pickering mechanism [1,2]. Oleofoams possess untapped potential for application in several manufacturing industries, such as food products with reduced calorific density, and topical delivery systems for active pharmaceutical ingredients. However, there is limited information available on these systems compared to their aqueous counterparts, due to the narrower choice of suitable stabilizers for the air/oil interface. Over the last 5 years research has focused on the relationship between the properties of the stabilizing crystals (size, shape, polymorphism) and the related foamability and stability of the oleofoams [1]. However, due to their opaque and soft nature, investigating the foam microstructure in a non-invasive fashion is challenging [3]. Such knowledge is required to understand the process-structure-function relationship, which in turn is required to prepare oleofoams with fine-tuned properties. In this work, a novel methodology for visualizing the microstructure of oil-continuous foams using synchrotron radiation X-Ray Tomography (SR-XCT) and Radiography (SR-XRR) is presented. A model system featuring cocoa butter and sunflower oil was chosen, due to the prominent role of these natural lipids in food and consumer products. The methodology was subsequently applied to the study of oleofoam microstructure during aeration, storage and heating, as these conditions are relevant for improving their manufacturing process, their shelf life and physical behaviour upon dissolution [4].

2. Methods

Mixtures of cocoa butter (CB) and high oleic sunflower oil (HOSO) were prepared by melting CB at 65°C and adding it to HOSO with a weight concentration of either 15% or 30%. The mixtures were cooled down using a Huber thermostat (Huber, Germany) under shear (DLH overhead stirrer, VELP Scientifica Italy) in a 1L capacity vessel until the formation of a gel (oleogel). The sample temperature was monitored with a Pt-100 thermocouple. Sample “15S” was prepared with 15% CB w/w and a cooling rate of -0.10 °C/min, while sample “30F” was prepared with 30% CB w/w and a cooling rate of -0.75 °C/min. The oleogels were then transferred to a planetary mixer (model 5KPM50, Kitchenaid, USA) and whipped with a constant shear rate (250 rpm). The oleogels were aerated for a total time of 30 minutes, pausing every 5 minutes to measure the amount of incorporated air (overrun). The overrun was calculated by filling a cup of a fixed volume (30 mL) with the foam and measuring its weight. The overrun is then calculated with Equation 1:

$$OR(\%) = 100 \times \frac{(w_{gel} - w_{foam})}{w_{foam}}$$

Where w_{gel} and w_{foam} are the weight of the unwhipped gel and the oleofoam, respectively. The samples were analysed with SR-XCT after each aeration step. For the stored samples, oleofoams kept at 20°C for 3 and 15 months were analysed as well.

The tomographic analysis was carried out at the I13-2 beamline at Diamond Light Source (DLS) synchrotron (Didcot, UK), using a pink beam source of 27 keV. The 2D projections were acquired with a PCO edge 5.5 CMOS camera (2560 x 2160 pixels). The effective pixel size was 0.8125 μm . A small amount of sample (approximately 1 mm^3) was placed on the top of a toothpick glued to the base of the cryocap. The samples were quickly immersed in liquid nitrogen (-196 °C) and installed on the tomography stage. The sample temperature was controlled using a Cryojet device (Cryojet XL, Oxford Instruments, UK) and set to -40 °C during the tomography acquisitions. The exposure time for each projection was set to 100 ms for 1001 projects, with a total time of 5 minutes. Each acquisition was repeated three times per sample.

The oleofoam samples were also subjected to controlled heating, and the changes in microstructure were studied using both SR-XCT and SR-XRR. The heating profile started from 20 °C until the melting temperature of the oleofoams (25 or 27°C) at a heating rate of 2 °C/min. Afterwards, the sample was cooled to 0°C at a rate of 6 °C/min and maintained at 0 °C for 5 minutes. A tomography acquisition was then performed. Radiography images were collected during the temperature ramp every 0.5 s. The radiography images were normalized and used to produce a set of difference images – where the i -th image is subtracted from the $i+1$ -th image – to highlight changes in the microstructure. The difference image stack was further analysed with Principal Component Analysis (PCA) using MATLAB R2021a (Mathworks, USA). The score of the first principal component was plotted against the temperature to detect the onset of structural changes in the oleofoam during heating.

The tomographic images were reconstructed using the *savu* framework developed at the Diamond Light source; the projections were corrected for dark images and flat-fields images, and a ring-removal algorithm was applied. A Paganin filter was applied to further enhance the contrast between the bubbles and the continuous phase. The reconstructed volumes were then processed using a custom ImageJ routine (National Institute of Health, USA), which includes median filtering, Otsu thresholding, and segmentation based on the 3D Euclidean distance map. Bubbles were counted using the BoneJ plugin, and their volume and surface area measured. BoneJ was also used to measure the thickness of the continuous phase.

3. Results and discussion

Result showed that both type of oleofoams (15S and 30F) displayed an average bubbles size of 20 μm , with a mean sphericity of 0.88. These values remained similar from 5 until 30 minutes of aeration, suggesting that an equilibrium size and shape distribution was reached at the beginning the process (Figure 1). The main difference between the two samples was seen in the overrun and the oleogel thickness. In particular, sample 15S reached a higher overrun (180%) and a thinner oleogel thickness ($11 \pm 6 \mu\text{m}$) in less time, compared to sample 30F which could reach only 130% overrun and retained a significant volume of unwhipped oleogel domains, resulting in a larger oleogel thickness ($20 \pm 13 \mu\text{m}$) after 30 minutes of whipping.

Sample stored for 3 months displayed a decrease in the amount of bubbles (hence the overrun), and an increase in the oleogel thickness. This change was more significant for 15S samples; after 15 months, only sample 30F retained a sufficiently aerated structure, however displaying a further decrease in overrun and a slightly larger bubble size distribution owing to occurrence of Ostwald ripening (Figure 2). Concurrently, growth of the CB crystals could be seen in the continuous phase.

Heating the oleofoams resulted in an increase in the volume-weighted bubble size, due to the melting of the stabilizing fat crystals and the resulting bubble coalescence. The average size increased by 130% for sample 15S and by 109% for sample 30F. At the same time, the bubble sphericity increased from 0.88 to 0.95 (Figure 3). By employing SR-XRR, it was possible to visualize in real time the coalescence of the air bubbles, which occurred over the span of few seconds. Furthermore, the PCA analysis of the radiography images showed that the destabilisation of the oleofoams due to heating could be promptly arrested by lowering the temperature below the melting point of the fat crystals

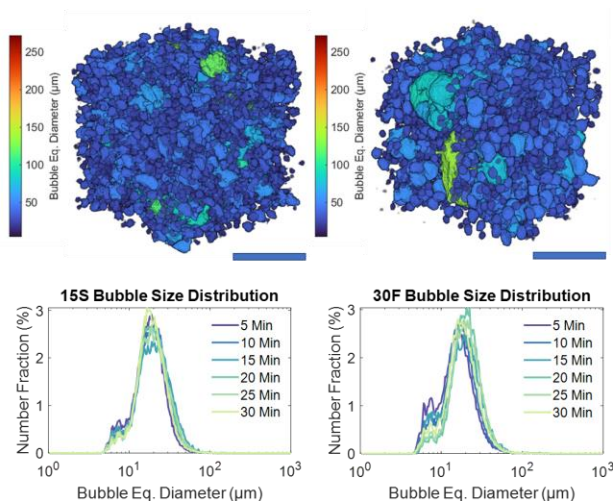


Figure 1. 3D renderings of two Volumes of Interest of a 15S (left) and a 30F sample (right) after 30 minutes of aeration. Scale bar is 250 μm . The bubble size distribution evolution during the aeration is plotted on the lower part of the figure.

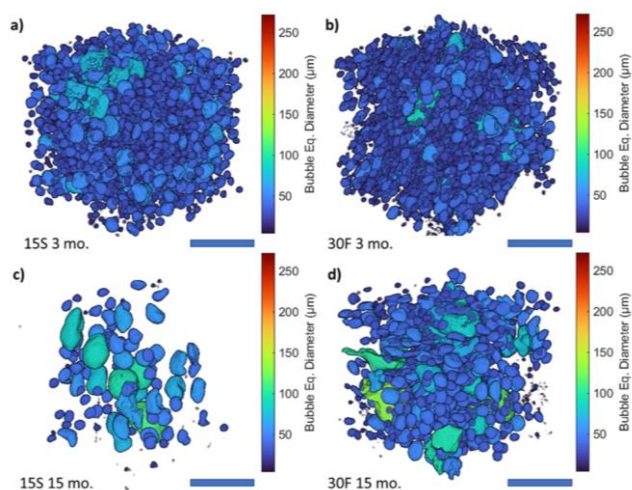


Figure 2. 3D renderings of representative Volumes of Interest for each of the aged oleofoam samples: 15S 3 months (a), 30F 3 months (b), 15S 15 months (c), and 30F 15 months (d). The scale bar is 250 μm .

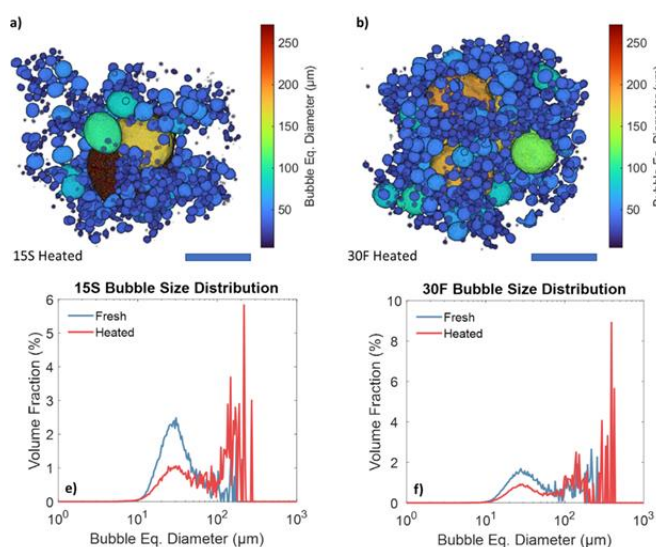


Figure 3. 3D renderings of samples 15S (a) and 30F (b) after being heated. The scale bar for the 3D renderings is 250 μm . Volume-weighted size distributions of sample 15S heated (e) and 30F heated (f) compared with their respective fresh samples.

4. Conclusions

In this work, the three-dimensional native microstructure of fat-stabilized oleofoams was investigated for the first time, both in static and dynamic experiments, using X-ray tomography and radiography. The aeration of oleofoams proceeded with a gradual increase in volume, concomitant with a decrease in the continuous phase thickness. Low-cocoa butter samples displayed a higher overrun (170%) and a lower oleogel thickness (10 μm), reaching an overrun equilibrium value after 15 min of whipping. High-cocoa butter samples, on the other hand, incorporated less air (125% overrun) and featured a coarse final microstructure, retaining fragments of unwhipped oleogel. The air bubble size distribution, centred at 20 μm , was not affected by the amount of solid fat or by the whipping time, suggesting that the shear induced during aeration produced stabilizing crystals with similar properties, regardless of the sample composition and the duration of whipping.

Oleofoam samples showed significant structural changes during storage, with the oleogel phase increasing its thickness, while the overrun decreased significantly for both samples analysed. The higher concentration of solid fat in the sample contributed to slowing down the disproportionation of the air bubbles, with sample 30F retaining a similar size distribution profile after 3 months. After prolonged storage conditions, however, only samples with 30% w/w CB maintained an aerated structure. Therefore, higher amounts of stabilizing crystals were beneficial to retaining the overrun and counteracting phase separation.

Heating the oleofoam samples to their melting point resulted in an increase in bubble sphericity, bubble coalescence, oleogel thickness, and a reduction of the total number of air bubbles. Sample 15S was more prone to coalescence than sample 30F, potentially due to the lower amount of stabilizing crystals. The increase in the bubble size followed by melting of the crystals both at the interface and in the bulk support the hypothesis that bulk contribution to stability in oleofoams is fundamental to prevent gas diffusion. The dynamic changes in the oleofoam microstructure were captured for the first time with XRR, showing clear evidence of bubble coalescence during heating. This body of work, owing to the non-invasive, three-dimensional approach to the study of oleofoams, contains significant information on the physical behaviour of these emerging materials, in relation to relevant processes such as their aeration, storage conditions that will contribute to their understanding, and their use in material formulation.

References

- [1] Binks BP, Vishal B. Particle-stabilized oil foams. *Adv Colloid Interface Sci* 2021;291:102404. doi:10.1016/j.cis.2021.102404.
- [2] Fameau AL, Binks BP. Aqueous and Oil Foams Stabilized by Surfactant Crystals: New Concepts and Perspectives. *Langmuir* 2021;37:4411–8. doi:10.1021/acs.langmuir.1c00410.
- [3] Metilli L, Storm M, Bodey AJ, Wanelik K, Tyler AII, Lazidis A, et al. Investigating the microstructure of soft, microporous matter with synchrotron X-ray tomography. *Mater Charact* 2021;180:111408. doi:10.1016/j.matchar.2021.111408.
- [4] Metilli L, Storm M, Marathe S, Lazidis A, Marty-Terrade S, Simone E. Application of X-ray Microcomputed Tomography for the Static and Dynamic Characterization of the Microstructure of Oleofoams. *Langmuir* 2022;38:1638–50. doi:10.1021/acs.langmuir.1c03318.

Fused Filament Fabrication of PLA: The Role of Interlayer Adhesion on the Mechanical Performances

Sara Liparoti*, Vittorio Alfieri, Annalaura Fabbricatore, Fabrizia Caiazza, Roberto Pantani

Department of Industrial Engineering, University of Salerno, via Giovanni Paolo II, 132 – Fisciano (SA)

**Corresponding author E-Mail: sliparoti@unisa.it*

1. Introduction

Additive Manufacturing (AM) techniques have triggered industrial innovations thanks to their ability to realize objects with so complex shapes that are impossible to obtain adopting conventional processes. AM is based on the bottom-up approach, during which the construction of parts is conducted layer by layer. Among the available techniques, fused filament fabrication (FFF) is devoted to the production of plastic parts. FFF can be spread out into four main stages: polymer melting inside the extruder, extrusion through the nozzle, deposition of the filament on the deposition plate and, subsequently, construction layer by layer. Up to now, FFF has been applied to the production of prototypes, medical devices and final parts for automotive and aerospace industry [1,2]. The parts generally exhibit poor and anisotropic mechanical performances, which make them not suitable for industrial applications and wherever structural properties are required. This drawback has been generally attributed to the layer-by-layer deposition approach. The filament is deposited on a previously deposited layer that is undergoing cooling: this induces the formation of a weld part between adjacent layers. The overall mechanical part resistance depends on the interlayer bond strength [3]. In turn, the interlayer bond strength depends on the molecular diffusion at the interface, namely on the possibility of the molecules to recover their entangled organization, also at the interface, after deposition. To further understand how the thermal history of the deposited layers is correlated to morphology and mechanical properties of the produced FFF object, the role played by crystallization phenomena, and a molecular weight between the entanglements must be considered. To this purpose, in the presented work, the morphology and the mechanical properties of FFF specimens have been correlated to the thermal history experienced by the polymer during deposition, including the role played by molecular diffusion in terms of molecular weight between entanglements. The results are aimed at investigating main phenomena that determine the performances of the parts. The final goal is to formulate a mathematical model of FFF, to reduce the needs for extensive experimental campaign in the future.

2. Methods

Poly(lactic acid) (PLA, grade 4032D, NatureWorks, Minneapolis, Minnesota, US) in the form of filament was adopted to perform FFF [4]. A Kloner3D 240 Twin (Kloner3D, Firenze, Italy) was used to produce the samples at 200°C nozzle temperature, with 100% infill density, without raft and supports. Two deposition velocities were adopted: 30, and 50 mm/s, and two temperatures of the bed: 60°C, and 80°C.

The layer thickness of the first layer was set constant to 0.1 mm. The razor direction of the adjacent layer was 90°. The shape and size of the samples (Figure 1) have been conveniently designed so that the deposition of the filament would be performed along a single direction for each wall. Each wall is formed by 3 filaments.

T-type thermocouples ($d = 120 \mu\text{m}$, Omega Engineering, Manchester, UK) were added along the deposition layer to monitor the evolution of the temperature at the interface between adjacent layers during the process. A thermocouple datalogger (TC-08, Pico Technology, St Neots, Cambridgeshire, UK) was adopted for temperature recording.

Dynamic mechanical analysis (DMA, Perkin Elmer DMA 8000) was conducted on the specimens to assess the mechanical behavior and evaluate the molecular weight between entanglements (the same procedure is reported in the literature [5]). The specimens were cut in a plane parallel to the building plate at 1, 2 and 3 cm distance from the plate, to inspect the accuracy of the deposition among consecutive layers; a cross-cut in a plane orthogonal to the direction of deposition was performed to investigate the occurrence of possible detachment.

The specimens were observed by an optical microscope (Eclipse L150, Nikon, Tokyo, Japan) equipped with a digital camera.

Atomic Force Microscopy (AFM, Veeco, Santa Barbara, CA, USA) was adopted to analyze the behavior of the material at the interface between adjacent layers [5].

3. Results and discussion

Figure 2 shows the evolution of the temperature recorded at the interface between adjacent layers at different distances from the deposition plate (see Figure 1). As the distance from the deposition plate increases, the average temperature decreases: at the deposition plate the average temperature is about 60°C (the set temperature), at 1 cm and 2 cm from the deposition plate the average temperatures are about 54°C, and 50°C, respectively. Furthermore, the deposition process determines a sudden increase of temperature of the previously deposited layers: the presence of several temperature peaks for the same position confirms this statement. The trend of temperature is time-shifted depending on the processing speed. Temperature distribution is expected to influence the distribution of the mechanical properties of the parts.

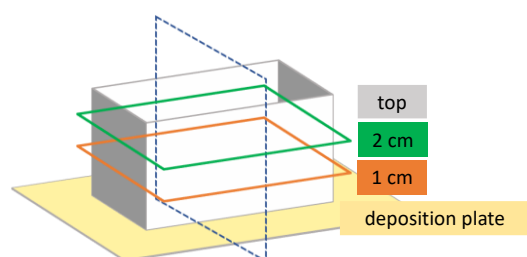


Figure 1 Sketch of the shape of the FFF specimen.

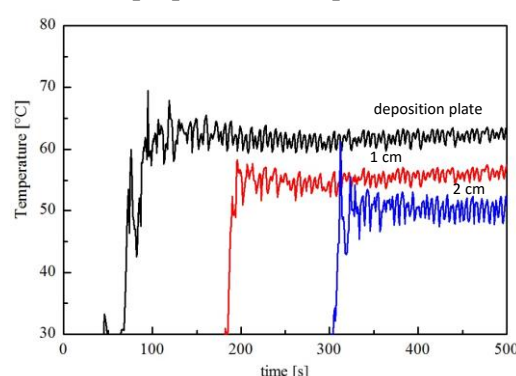


Figure 2 Temperature evolutions for the specimen obtained with 60°C deposition temperature and 30 mm/s as deposition velocity.

The morphology of the specimens was analyzed by optical microscopy to preliminary assess the dependence of the adhesion between adjacent layers on the operative conditions.

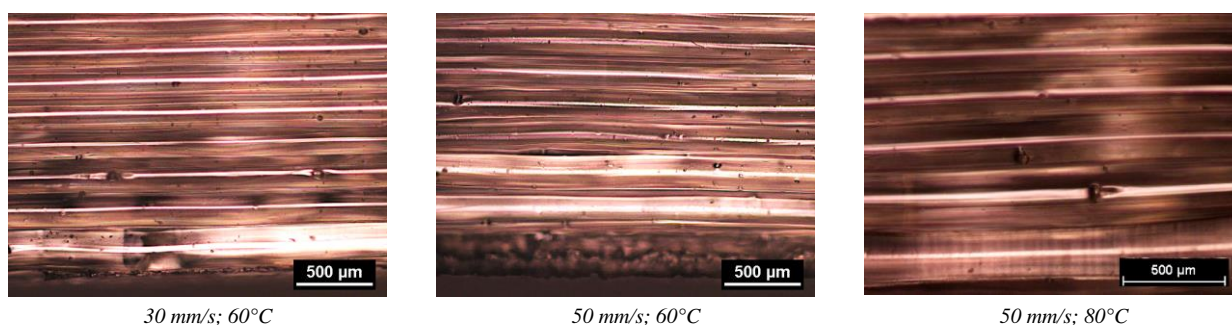


Figure 3 Optical micrographs of the specimens cut close to the deposition plate (at the bottom), for the cases obtained with several deposition velocities and two deposition temperatures, 60°C and 80°C.

The higher is the deposition velocity, the lower is the adhesion between adjacent layers. Particularly, the specimen obtained with 50 mm/s deposition velocity shows a clear detachment between the third and the fourth layers. The increase of the deposition temperature seems to reduce this phenomenon. Further investigations at the locations of detachment were conducted by means of AFM (Figure 4) for the specimens obtained with 60°C deposition temperature and different deposition velocities. Three AFM maps are shown: the height map, concerning the description of the topography, the phase map, and the elastic modulus map, concerning the mechanical performance of the parts. The height maps confirm the presence of a detachment in both cases; however, the detachment is more evident (therefore, the distance between the layers is wider) in the case obtained with 50 mm/s deposition velocity. The phase and the elastic modulus maps allow detecting differences in the mechanical behavior where the detachment occurs: where the detachment occurs, the elastic modulus is smaller. The distribution of the elastic modulus is almost homogeneous for the

specimen obtained with 30 mm/s deposition velocity; instead, the elastic modulus is significantly lower at the detachment positions, than in the surrounding area, for the specimen obtained with 50 mm/s.

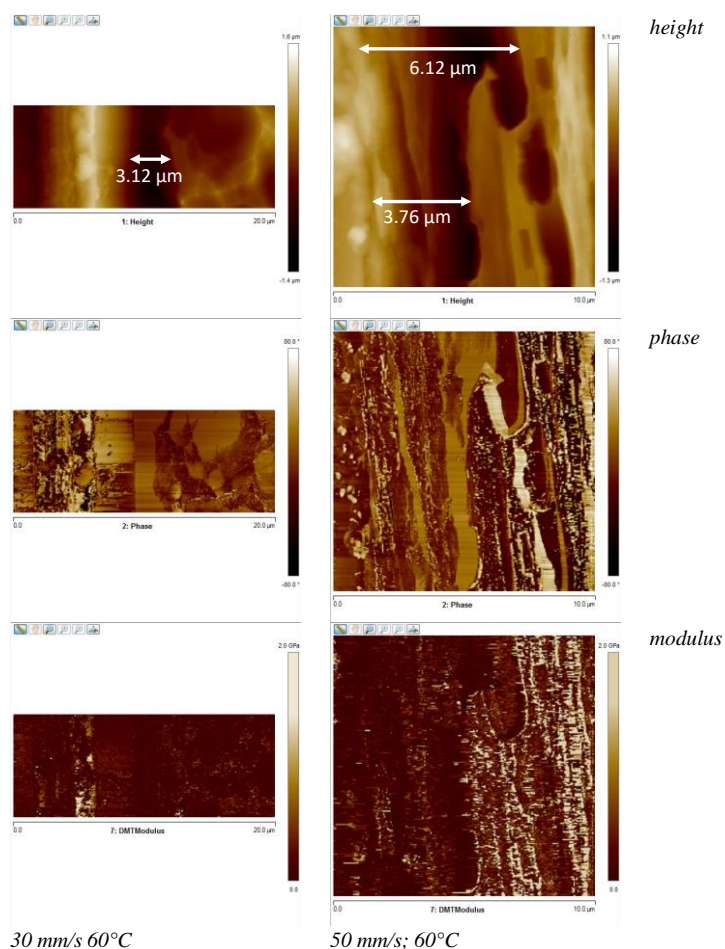


Figure 4 AFM of the specimens obtained with the same deposition temperature, 60°C, with two deposition velocities, 30 mm/s and 50 mm/s. The analyses are referred to interface between the third and the fourth layers already shown in Figure 2 (the white arrows indicate the distance between layers at the detachment).

The DMA analyses aim at understanding the effect of the deposition conditions and the distance from the deposition plate on the mechanical performance of the parts. The results are given in Table 1 in terms of elastic modulus and molecular weight between entanglements, for two specimens obtained with 60°C deposition temperature.

	position	E [GPa]	Me [g/mol]
30 mm/s	3 cm	1.43 ± 0.05	2151
	2 cm	1.50 ± 0.02	1901
	1 cm	1.26 ± 0.05	1901
	ortho	1.47 ± 0.05	2089
60 mm/s	3 cm	1.64 ± 0.05	2224
	2 cm	1.55 ± 0.02	2248
	1 cm	1.52 ± 0.05	2563
	ortho	1.33 ± 0.05	2260

Table 1 Elastic modulus (E), and molecular weight between entanglements (Me) for the specimens obtained with 60°C deposition temperature, and two different deposition velocities, 30 mm/s and 50 mm/s. The positions where the analysis was conducted with respect to the distances from the deposition plate are consistent with those indicated in Figure 1.

Two directions were analyzed, the first one is parallel to the deposition direction (positions 1, 2, and 3 cm), the second one is the direction transversal to the deposition direction (ortho). With reference to the positions parallel to the deposition direction, the elastic modulus increases with the deposition velocity, and, within the same specimen, with the distance from the deposition plate. The deposition velocity and the cooling time

determine the residual orientation in the final part. On its turns, the orientation determine the elastic modulus: the higher is the residual orientation, the higher is the elastic modulus [6]. The molecular weight between entanglements, M_e , can be used as an index of the residual orientation: the higher is M_e , the higher is expected to be the orientation, the wider is the distance between entangled molecules. M_e increases with the deposition velocity, thus the increase of this operating parameter induces more evident orientation in the molecules, whose relaxation is hidden by the fast cooling. The decrease of the average temperatures at longer distance from the deposition plate contributes to hide the molecular relaxation; consequently, M_e increases with the distance from the deposition plate. The increase of M_e , and orientation, determine the increase of the elastic modulus, in turn.

Concerning the positions along the direction transversal to the deposition direction, the elastic moduli are lower than those detected for the specimens cut along the deposition direction. This finding is consistent with the previous discussion since the elastic modulus along the transversal direction is influenced by the presence of detachments between adjacent layers. In this direction, M_e is high and comparable with the values measured for the specimens cut along the deposition direction at 3 cm from the deposition plate. A high residual orientation is not favorable to the molecular diffusion at the interface between adjacent layers, the molecules solidify before diffusion may occur determining poor mechanical performances (i.e small elastic modulus values).

4. Conclusions

FFF was conducted under different operating conditions, concerning the deposition temperatures and the deposition velocity with the aim of analyzing the effect of these parameters on the mechanical performances of the parts. To this purpose, several investigations were performed, adopting AFM and DMA to assess the mechanical characteristics. AFM analyses revealed that the effect of the detachment increases with the increase of deposition velocity; the increase of the deposition temperature partially compensate this effect. The DMA analyses contributed to determine the residual orientation within the specimens and to relate the orientation to the elastic modulus. The increase of the deposition velocity, coupled with the fast cooling experienced during the process, results in high residual molecular orientation in the final parts. The orientation increase, on its turn, determines the increase of the elastic modulus along the deposition direction. On the other side, the increase of the orientation prevents the molecular diffusion at the interface between adjacent layers, determining the detachments of adjacent layers. Consequently, the elastic modulus along the direction transversal to the deposition direction is smaller than the ones measured along the deposition direction. These finding suggest that, to produce isotropic objects with high mechanical performances it is crucial to allow the molecular relaxation, to favor the molecular diffusion. Therefore, where high deposition velocities are required to the purpose of increased productivity rate, the temperature must be conveniently shifted to allow relaxation in the whole deposited volume. These findings are intended to offer a solid basis for the implementation of a simulation tool to predict the temperature evolution of the deposited layer during FFF and extract the mechanical properties. A big effort has already been devoted in this direction, and the main finding will be shared in future works.

References

- [1] J. Korpela, A. Kokkari, H. Korhonen, M. Malin, T. Närhi, J. Seppälä, J. Biomed. Mater. Res. Part B Appl. Biomater. 101B (2013) 610–619. <https://doi.org/10.1002/jbm.b.32863>.
- [2] S. Singh, G. Singh, C. Prakash, S. Ramakrishna, J. Manuf. Process. (2020). <https://doi.org/10.1016/j.jmapro.2020.04.049>.
- [3] M. Spoerk, J. Gonzalez-Gutierrez, J. Sapkota, S. Schuschnigg, C. Holzer, Plast. Rubber Compos. 47 (2018) 17–24. <https://doi.org/10.1080/14658011.2017.1399531>.
- [4] V. Volpe, F. Foglia, R. Pantani, Polym. Cryst. 3 (2020). <https://doi.org/10.1002/pcr2.10139>.
- [5] S. Liparoti, D. Sofia, A. Romano, F. Marra, R. Pantani, Polymers (Basel). 13 (2021) 399. <https://doi.org/10.3390/polym13030399>.
- [6] S. Liparoti, V. Speranza, A. Sorrentino, G. Titomanlio, Polymers (Basel). 9 (2017) 585. <https://doi.org/10.3390/polym9110585>.

Rheological and Viscoelastic characterization of HDPE/LLDPE blends

Francesca Gentile*, Sara Liparoti, Valentina Volpe and Roberto Pantani

Department of Industrial Engineering, University of Salerno, via Giovanni Paolo II, 132 – Fisciano (SA) - Italy

*Corresponding author E-Mail: fgentile@unisa.it

1. Introduction

Polyolefins, including polyethylene (PE) and polypropylene (PP), are widely used in food and beverage packaging industry [1]. Linear polyethylene, such as high-density polyethylene (HDPE) and linear low-density polyethylene (LLDPE), is one of the most common materials for film applications due to its excellent performance in toughness, clarity, and thermal sealability [2]. Nevertheless, blown films from high density homo-polymers tend to be very brittle because they lack tie molecules [3], in fact, HDPE has a linear structure, without or with a few short branches, and a high degree of crystallinity [4].

It was suggested that bubble stability in film blowing is related to rheological properties [5], which are influenced by the molecular weight and molecular weight distribution. It is well known, in fact, that molecular weight parameters of a polymer impact also on its processability [6] and strongly affect the miscibility of PE blends [7]. For instance, blowability was found to be enhanced by the absence of long side chain branching in LLDPE [5].

Blending of polymers can lead to a balance of materials proprieties and processability [7], and this can also represent a viable way to achieve improved material proprieties avoiding the synthesis of new polymers [4]. A deep understanding of the rheological behavior is needed to ensure a good mixing during production of polymer blends.

In this work, rheological and dynamic mechanical behavior of blends of a HDPE and a LLDPE is investigated, to study their miscibility and processability.

2. Methods

Two different polyethylene were considered in this work, a high-density polyethylene (HDPE) and a linear low-density polyethylene (LLDPE). Proprieties of materials are listed in **Errore. L'origine riferimento non è stata trovata.** below.

Table 1 Proprieties of materials used in this study

PE Grade	Density	M_n (g/mol)	M_w (g/mol)	M_w/M_n	Comonomer
HDPE	0.956 g/cm ³ (Multimodal MMD)	8400	127000	15.12	Butene
LLDPE	0.941 g/cm ³ (Bimodal MMD)	7000	160000	22.86	Butene, Hexene

HDPE/LLDPE blends (Table 2) were produced by using a mini-extruder Thermo Scientific, Haake MiniLab II. The equipment is provided by a twin counter-rotating screws and a backflow channel which ensure an adequate mixing. Moreover, a slit capillary channel integrated in the close loop of the micro-compounder allows the possibility of performing rheological evaluations by measuring the pressure gradient in the recirculation channel (Figure 1).

Table 2 Blends composition

Blend No.	LLDPE content [%]	HDPE content [%]
1	100	-
2	60	40
3	70	30
4	80	20
5	-	100

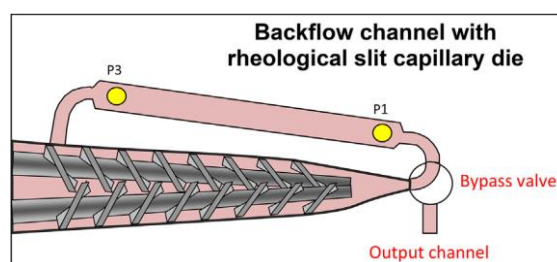


Figure 1 Schematic drawing describing the micro-compounder

The mini-extruder allows the possibility of performing rheological evaluations by measuring the pressure gradient in the recirculation channel; moreover the volumetric flow rate can be fixed by setting the screw rotation speed through a calibration curve. In this way, apparent shear rate in the recirculation channel can be evaluated with Hagen-Poiseuille equation, and consequently true shear rate is estimated by Rabinowitsch relationship [8]. Equations are reported below.

$$\text{Hagen-Poiseuille equation: } \dot{\gamma}_a = \frac{6 Q_v}{w h^2}$$

- Q_v is the volumetric flow rate
- w is the width of the capillary (10 mm)
- h is the height of flow channel (1.5 mm)
- n power law index

$$\text{Rabinowitsch relationship: } \dot{\gamma}_{\text{true}} = \left(\frac{2+n}{3}\right) \dot{\gamma}_a$$

The volumetric flow-rate depends on the material and on the rotation speed of the screws.

Apart from the recirculating channel, a distribution of polymer melt velocity within the mini-extruder should be taken into account. In fact, the presence of a distribution of velocity and different geometry in the recirculation channel and between the twin screws is evident. We estimate of having a velocity of polymer melts within the screws of about 1 order of magnitude greater than the velocity in the recirculation channel.

Materials were inserted between two steel plates covered with two Teflon tapes and positioned in a compression molded press (Carver press), that was previously heated to 130°C. A pre-heating time of 10 minutes ensures that pellets reached the temperature, after this waiting time, the press was closed, and materials compression occurred.

Rheological proprieties of pure materials and blends were measured using a Thermo Scientific HAAKE Mars II with parallel plate geometry. Frequency sweep experiments carried out at stress controlled with a frequency ranged between 0.1 and 100 rad/sec. The parameters used for the rheological characterization are listed in Table 3 below.

Table 3 parameters used for rheological characterization

	Temperatures [°C]	Frequencies [rad/sec]
LLDPE	140/ 160/ 180	0,1-100
HDPE	140/ 160/ 180/ 200	0,1-100

Dynamic mechanical analysis (PerkinElmer DMA 8000) was performed on films prepared through compression molding as already described. Dynamic mechanical analysis (DMA) was performed in multifrequency mode (frequencies: 0.1Hz, 0.3 Hz, 1 Hz 3 Hz and 10 Hz) and temperature scan, with a temperature ranged between 20°C-130°C and a heating ramp of 1°C/min. The ramp was select to allow a measurement at each frequency at each temperature.

3. Results and discussion

In the following we report the properties of the pure materials. Figure 2 shows the plots of the complex viscosity (η^*) as a function of the angular frequency (ω) of HDPE and LLDPE at each temperature. Rheological results of HDPE and LLDPE follow a pronounced shear thinning behavior. Furthermore, it is worth noting that at low shear rate, materials do not exhibit a Newtonian behavior, and this can be attributed to their wide molecular weight distribution.

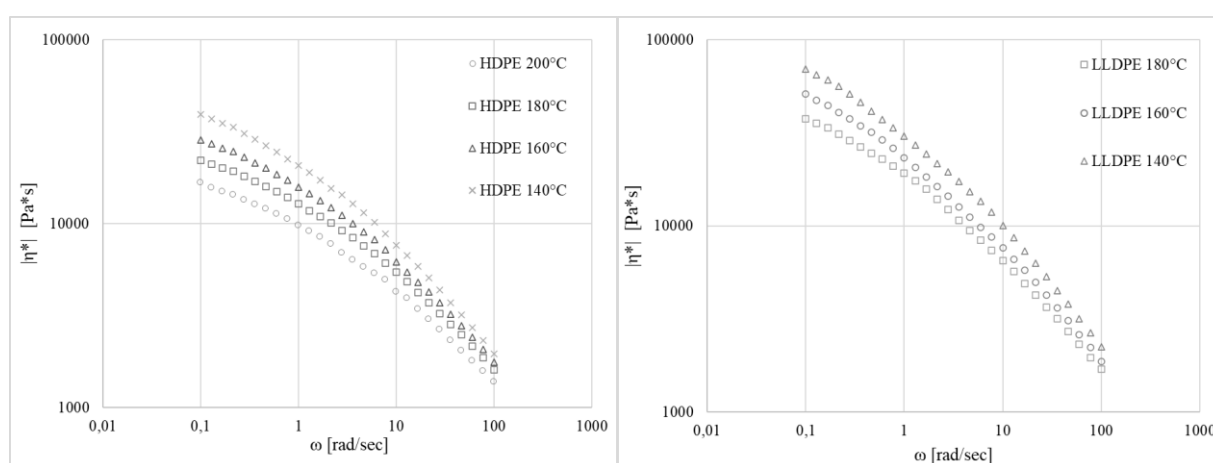


Figure 2 Complex viscosity of HDPE (left) and LLDPE (right) as a function of frequency for different temperatures

Viscosity measurements were found to be well described by Cross equation, shown below:

$$\eta(\dot{\gamma}, T) = \frac{\eta_0 \alpha_T}{1 + \left(\eta_0 \alpha_T * \frac{\dot{\gamma}}{T} \right)^{1-n}}$$

Where the zero-shear viscosity η_0 is given by Williams-Landel-Ferry (WLF) equation:

$$\alpha_T = \exp\left(\frac{-C_1(T - T_0)}{C_2 + T - T_0}\right)$$

Experimental data (solid line) and Cross (empty dot) equation results are plotted in Figure 3 and Figure 4. Experimental values of time-temperature shift factors α_T and the results of WLF equation are shown in the same figure.

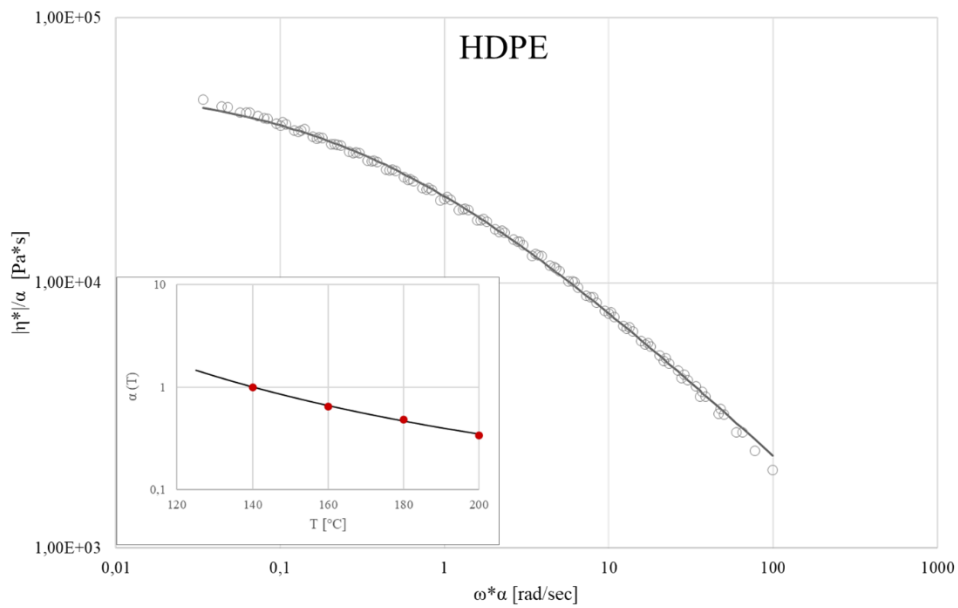


Figure 3 Master curve at 140°C: experimental data (solid line) and Cross (empty dot) equation results and time-temperature shift factor α_T for HDPE sample

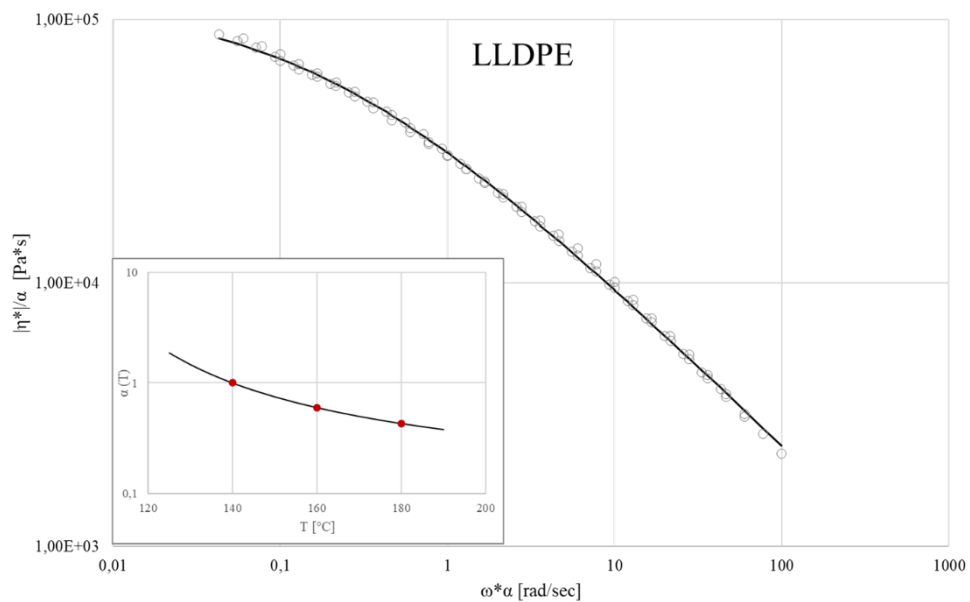


Figure 4 Master curve at 140°C: experimental data (solid line) and Cross-WLF (empty dot) equation results and time-temperature shift factor α_T for LLDPE sample

Rheological data provide an indication for identify process parameters in blends production. In fact, it can be noticed that for angular frequency greater than 50 rad/sec at temperature of 160°C (**Figure 5**), polymer melts exhibit comparable viscosities.

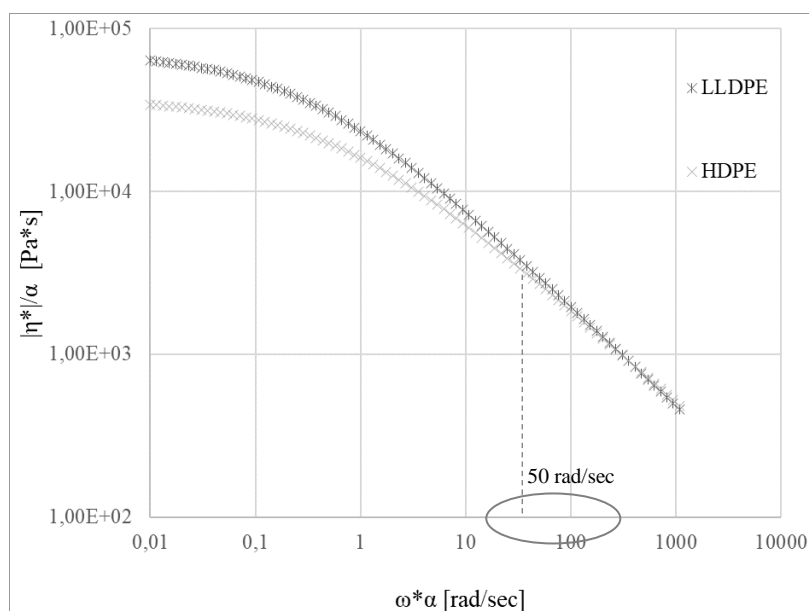


Figure 5 Complex viscosity evaluated by Cross equation of HDPE and LLDPE samples at 160°C

The generalized Maxwell model was used to describe the viscoelastic behavior of polymer melts. Results of modelling and the experimental data of the storage modulus (G'), loss modulus (G'') and complex viscosity are reported in **Figure 6**, while all the relaxation times and moduli of each Maxwell elements of the models are listed below (Table 4).

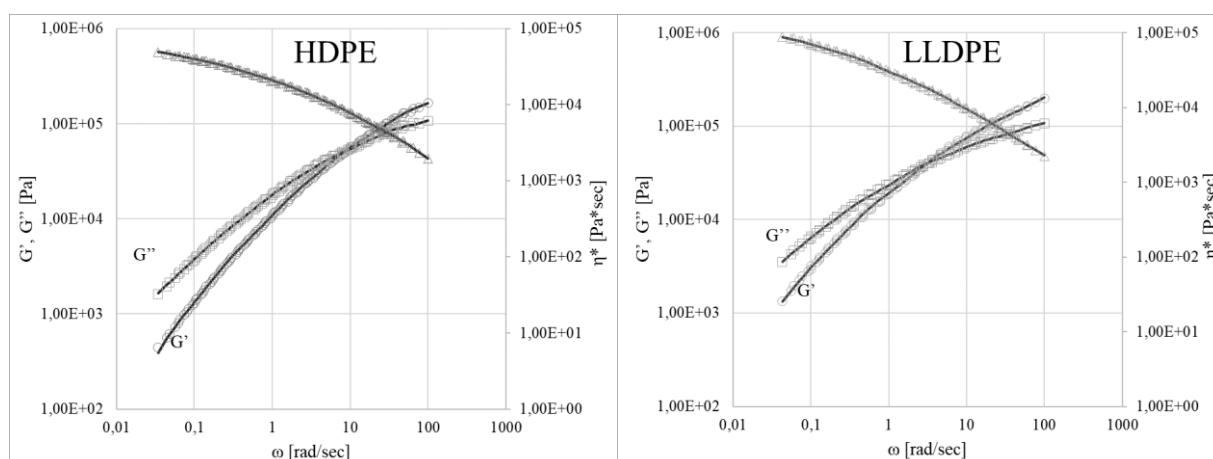


Figure 6 Experimental data of the storage modulus (G'), loss modulus (G'') and complex viscosity (η^*) plotted with the results of generalized Maxwell model.

Table 4 relaxation times and moduli of Maxwell's elements

	LLDPE		HDPE	
	τ_i	G_i	τ_i	G_i
1	4,19E+01	9,75E+02	-2,80E+00	5,69E+00
2	5,75E-02	7,54E+04	-1,56E+00	5,01E+00
3	7,86E-03	1,92E+05	-7,79E-01	4,61E+00
4	1,96E+00	1,40E+04	-1,10E-01	4,14E+00
5	3,19E-01	4,00E+04	5,75E-01	3,60E+00
6	9,52E+00	3,31E+03	1,35E+00	2,95E+00

Results of dynamic mechanical analysis are shown below in Figure 7. A remarkable change in slope is exhibited by both the HDPE and LLDPE samples soon below their melting point. This can be attributed to a softening of polymer during the test and can provide a measure of their processability at solid state. Furthermore, DMA was carried out in multifrequency mode, that allows the possibility of evaluating a time-temperature shift factor for materials at solid state. In this way, storage modulus and loss modulus data can be also used to perform a viscoelastic characterization of materials at solid state, by using the generalized Maxwell model, as already done for molten state.

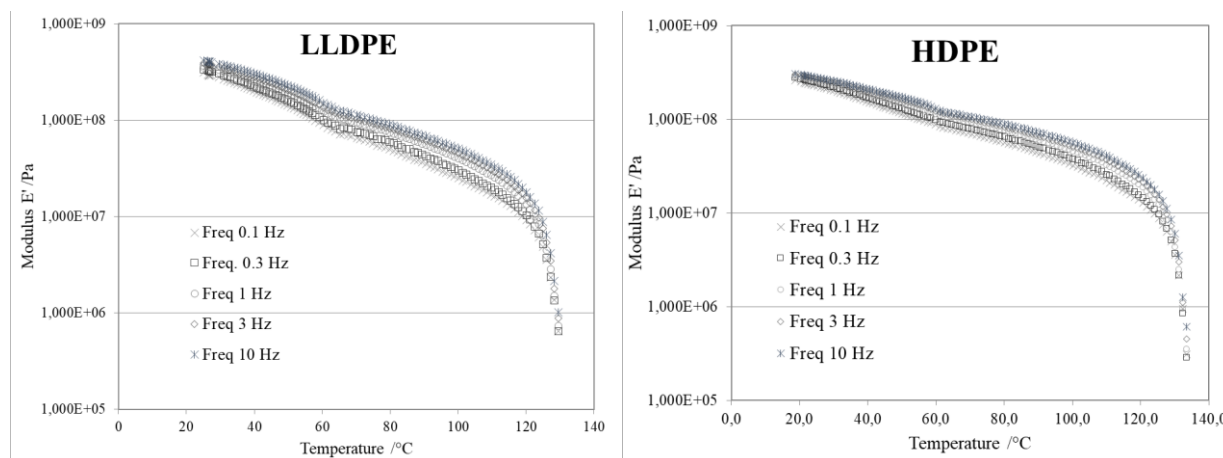


Figure 7 Dynamical mechanical analysis results for LLDPE (left) and HDPE (right) samples

4. Conclusions

Two different polyethylene, namely HDPE and LLDPE, were characterized and used for production of blends with various composition. Rheological characterization was performed on all the blends and pure materials, and the viscoelastic behavior of polymer melts was also investigated. Processing parameters for blends production was previously determined by the knowledge of rheological behavior of HDPE and LLDPE used in this work. Compression molded samples were produced to evaluate dynamical-mechanical behavior of all the materials considered in this study. DMA data were also interpreted by considering a viscoelastic approach.

References

- [1] F. Roberto Passador, A. Collà Ruvolo-Filho, and L. A. Pessan, *Polymer Engineering & Science*, vol. 56, no. 7 (2016), 765–775
- [2] W. Rungswang et al., *Macromolecular Materials and Engineering*, vol. 304, no. 9, (2019) 1900325
- [3] O. OGAH, *International Journal of Engineering and Management Sciences*, vol. 3, (2012) 85–90
- [4] P. Agrawal et al., *Polymer Bulletin*, vol. 79, no. 4, (2022) 2321–2343
- [5] A. Ajji, P. Sammut, and M. A. Huneault, *Journal of Applied Polymer Science*, vol. 88, no. 14, (2003) 3070–3077
- [6] C. L. P. Shan, J. B. P. Soares, and A. Penlidis, *Polymer*, vol. 44, no. 1, (2003) 177–185
- [7] Y. Chen, H. Zou, M. Liang, and P. Liu, *Journal of Macromolecular Science, Part B*, vol. 52, no. 7, (2013) 924–936
- [8] M. Yousfi, S. Alix, M. Lebeau, J. Soulestin, M.-F. Lacrampe, and P. Krawczak, *Polymer Testing*, vol. 40, (2014) 207–217

Biphasic porous structures formed by monomer/water interface stabilization with colloidal nanoparticles

Fabio Pizzetti¹, Alessandro Marchetti¹, Giovanna Massobrio¹, Valeria Vanoli¹, Franca Castiglione¹,
Filippo Rossi^{1*}

1 Politecnico di Milano. Department of Chemistry, Materials and Chemical Engineering "Giulio Natta", Via Mancinelli 7, 20131; Milano

**Corresponding author E-Mail: filippo.rossi@polimi.it*

1. Introduction

Bicontinuous jammed emulsion gels (known as bijels) are Pickering emulsion where the aqueous and organic phases are present as continuous phases [1]. These emulsions, stabilized by colloidal nanoparticles at the interface between the two phases, can be used in a variety of applications. The problem related to these systems is given by their low mechanical properties, thus limiting their use [2]. The goal of this study is that of using a hydrophobic monomer, able to polymerize in bulk, thus forming a bicontinuous structure with polymer and water present as immiscible phases. For this task, ϵ -caprolactone has been selected, thanks also to its biocompatibility. The system has been stabilized using hydroxyapatite as colloidal nanoparticles. The final product has been characterized with various techniques, among which DOSY experiments for ensuring the final structure bicontinuity. Furthermore, their ability to load and release both hydrophilic and hydrophobic drugs has been tested out. The strategy has been demonstrated to be highly versatile and can also be tuned changing the monomer used in the synthesis or the nanoparticles, in order to exploit also their functions and to satisfy specific industrial and medical needs [3]. Furthermore, current studies are also under development, shifting from inorganic NPs to organic ones, in particular nanogels.

2. Methods

ϵ -caprolactone, selected as monomer, has been inserted in the reacting cylinder, along with TBD as catalyst. The system was mounted on an orbital shaker, and a stirring velocity of 1000 rpm has been set. Once the polymerization has occurred, an aqueous solution of NPs (HAp or NGs) has been added, and the stirring speed has been increased up to 1700 rpm for 1 minute. Then, the stirring velocity has been decreased back to 1000 rpm until the bicontinuous structure formation occurred. For the HR-MAS analysis, deuterium oxide has been used instead of distilled water. Release tests have been performed by soaking the bicontinuous structures in 2 mL of PBS at 37 °C for mimicking the physiological conditions. After certain timepoints, 1 mL has been withdrawn and replaced with 1 mL of fresh PBS.

3. Results and discussion

After some initial tests, different parameters of pivotal importance during the synthesis have been selected in order to obtain a successful bijel-like structure. Temperature was shown to be one of the most important parameters, since if it was higher than a threshold value the structure was not able to solidify or mix well (two separate phases were obtained). We were able to successfully load some drug mimetics (both hydrophilic and hydrophobic) inside the structure, and release them in PBS solution. As far as the characterizations are concerned, fluorescent confocal microscopy successfully shown the bicontinuous structure of our samples and the presence of NPs on the interface between the two phases. Furthermore, bicontinuity has been confirmed from DOSY mapping using HR-MAS technique, as it can be observed from Figure 1 for the HAp-based sample.

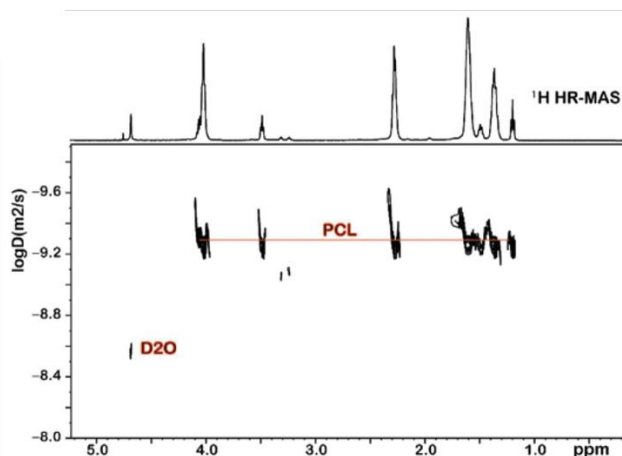


Figure 1. DOSY map of the HAP-based bicontinuous structure.

From Figure 1, it can be noticed how the water molecules (indicated as D2O) present only one value of the diffusion coefficient, thus confirming the presence of only one continuous phase. The same can also be deduced for the polycaprolactone (indicated as PCL). The preliminary results of the drug release experiments confirm that these bicontinuous structures can easily entrap and release in a controlled way both hydrophilic and hydrophobic drug mimetics. Furthermore, HR-MAS analyses on real drugs (ethosuximide and dimethyl fumarate) allowed the determination of the diffusion coefficients of such molecules, thus paving the way to a future modelling phase on the release dynamics for both single-loaded and co-loaded bicontinuous structures.

4. Conclusions

This study confirms that bicontinuous structures inspired from bijels can be successfully produced using monomers as organic phase. Both organic and inorganic NPs can be used for the structures formation, thus enhancing the versatility of these systems in biological applications. Finally, release tests were able to ensure the capability of loading both hydrophilic and hydrophobic drugs.

References

The reference format is provided below [1 – 3]. [Times New Roman 10].

- [1] S. Cha, H. G. Lim, M. F. Haase, K. J. Stebe, G. Y. Jung, D. Lee, *Scientific Reports* 9 (2019) 1-6.
- [2] P. S. Clegg, J. H. J. Thijssen, *Introduction to Bijels*, Soft Matter Series, 2020, 1-33.
- [3] F. Pizzetti, A. Rossetti, A. Marchetti, F. Castiglione, V. Vanoli, E. Coste, V. Veneruso, P. Veglianese, A. Sacchetti, A. Cingolani, F. Rossi, *Advanced Materials Interfaces* 8 (2021), 1-7.

Functionalized magnetite nanoparticles for the recovery of VFAs from a water solution

Elisa Lacroce^{1*}, Giovanna Massobrio¹, Filippo Rossi¹, Maurizio Masi¹

¹ Department of Chemistry, Materials and Chemical Engineering "Giulio Natta", Politecnico di Milano, via Mancinelli 7, 20131, Milan, Italy

*Elisa Lacroce E-Mail: elisa.lacroce@polimi.it

1. Introduction

Volatile fatty acids (VFAs) are widely used in chemical, pharmaceutical and food industry [1] due to their large application for producing paint, plastics, synthetic fibers, emulsions, coating formulations, pesticides, flavours, supplements and antibiotics [2]. About 90% of VFAs production is derived from petrochemical routes with negative effects on environment [2][3]. The recovery of chemical products from waste streams represents nowadays a promising strategy in the context of circular economy [4][5]. This work is focused on the recovery of VFAs from an aqueous solution by using functionalized magnetite nanoparticles as adsorbent agents with the aim of reusing them for other absorption/desorption cycles as schematized in figure 1.

2. Methods

Magnetite nanoparticles (MNPs) were synthesized by the co-precipitation method from hydrated FeCl_2 and FeCl_3 . Then, they were functionalized with adipic acid, oleic acid or APTES molecules (F-MNPs) and absorption tests were performed in order to extract the VFAs from a water solution. Gas chromatography analyses were conducted to estimate the percentage of absorption from the starting water solution.

3. Results and discussion

Magnetite nanoparticles with 8 nm of diameter were synthesized in order to have a high surface area to volume ratio. The functionalization with different molecules was performed to study the different effect on absorption capacity. Indeed, the absorption of VFAs on the nanoparticles was dependent on the interaction with the molecules used for the functionalization. In the case of functionalization with oleic acid and adipic acid the absorption was the results of hydrophobic interactions between the $-\text{CH}_2$ groups of the two chains. In the other case, in a pH environment of 7 the protonated amine groups of APTES molecules attracted electrochemically the unprotonated carboxylic groups of VFAs. Absorption tests were performed using different concentrations of nanoparticles and the best results showed around 30% of absorption using APTES and adipic acid functionalization and 21% using oleic acids.

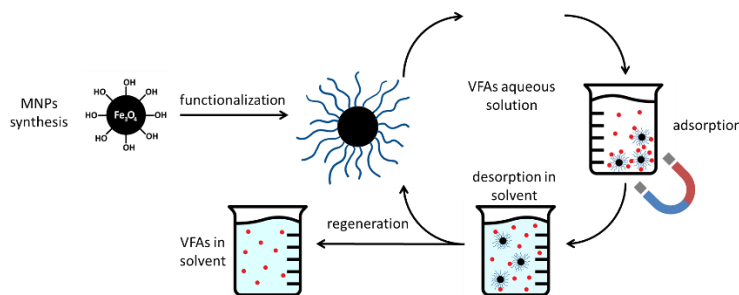


Figure 1. Schematic representation of the use of MNPs for VFAs recovery.

4. Conclusions

In this work we synthesized different functionalized magnetite nanoparticles for the recovery of VFAs from a water solution. The functionalization with different molecules was performed to allow different interactions between VFAs and MNPs and to find the best functionalization for having the maximum absorption percentage. The maximum absorption percentage was near 30% of the starting VFAs solution by using APTES and adipic acid-functionalized MNPs. Next steps of the project will be related to the desorption of VFAs and the use of recovered nanoparticles for other extraction cycles.

References

- [1] C. S. López-Garzón and A. J. J. Straathof, "Recovery of carboxylic acids produced by fermentation," *Biotechnol. Adv.*, vol. 32, no. 5, pp. 873–904, Sep. 2014, doi: 10.1016/J.BIOTECHADV.2014.04.002.
- [2] M. Atasoy, I. Owusu-Agyeman, E. Plaza, and Z. Cetecioglu, "Bio-based volatile fatty acid production and recovery from waste streams: Current status and future challenges," *Bioresour. Technol.*, vol. 268, pp. 773–786, Nov. 2018, doi: 10.1016/J.BIORTECH.2018.07.042.
- [3] E. V. Fufachev, B. M. Weckhuysen, and P. C. A. Bruijninx, "Toward Catalytic Ketonization of Volatile Fatty Acids Extracted from Fermented Wastewater by Adsorption," *ACS Sustain. Chem. Eng.*, vol. 8, no. 30, pp. 11292–11298, Aug. 2020, doi: 10.1021/ACSSUSCHEMENG.0C03220.
- [4] H. PA *et al.*, "Selective Extraction of Medium-Chain Carboxylic Acids by Electrodialysis and Phase Separation," *ACS omega*, vol. 6, no. 11, pp. 7841–7850, Mar. 2021, doi: 10.1021/ACSOMEGA.1C00397.
- [5] W. S. Lee, A. S. M. Chua, H. K. Yeoh, and G. C. Ngoh, "A review of the production and applications of waste-derived volatile fatty acids," *Chem. Eng. J.*, vol. 235, pp. 83–99, Jan. 2014, doi: 10.1016/J.CEJ.2013.09.002.

Comparative study on the effect of leucine and citric acid on calcium carbonate precipitation

Giuseppe Mazziotti di Celso¹, Marina Prisciandaro^{2*}, Despina Karatza³,
Dino Musmarra³, Amedeo Lancia⁴

1 University of Teramo, Faculty of Bioscience, Agri-Food and Environmental Technologies, 64100 Teramo, Italy;

2 University of L'Aquila, Dept. of Industrial and Information Engineering and of Economics, 67100 L'Aquila, Italy;

3 University della Campania Luigi Vanvitelli, Dept. of Engineering, 81031, Aversa (CE), Italy;

4 University Federico II of Naples, Dept. of Chemical, Materials and Production Engineering, 80125, Napoli, Italy

**Corresponding author E-Mail: marina.prisciandaro@univaq.it*

1. Introduction

This paper is concerned on the study of crystallization of calcium carbonate, when leucine – a green additive – is added in solution as an additive. The action of leucine of influencing calcium carbonate precipitation kinetic is particularly interesting since CaCO_3 is a so valuable product that it is worthy to recover from industrial liquid wastes (e.g. desalination brines), in the circular economy approach. An example is the post-distillation liquid from Solvay Process (production of sodium carbonate, soda-ash), that is a Ca-rich waste; if not correctly disposed of, this waste is responsible for the strong salinity of nearby groundwater with calcium chloride pollution of natural water reservoirs and soil [1]. Another example of wastes from which calcium carbonate can be recovered are brines: this is gaining increasing interest in scientific literature, also because this method limits CO_2 emissions or removes CO_2 from desalination plants [2].

In any case, either carbonate is a product of the process or a scale to be avoided, appropriate additives, under particular experimental conditions, allow to produce CaCO_3 with the desired characteristics, such as purity, water content, particle size and shape and polymorphic form [3].

Experimental runs have been performed in a laboratory scale plant at room temperature, by adding $\text{CaCl}_2 \cdot 2\text{H}_2\text{O}$ and NaHCO_3 as reagents, with a supersaturation range which spans from 2 to 60 mol/m³, using two different leucine concentration values (0.520×10^{-3} and 1.041×10^{-3} mol/l). Results obtained have been compared with previous published ones, carried out with no additive and with citric acid in solution. From the measurements of induction times for calcium carbonate nucleation, it was established that in solution the leucine, far from being a retardant, favours the precipitation of calcium carbonate, so it can be considered a promoter in calcium carbonate crystallization and this behaviour enhances when raising its concentration in solution.

2. Methods

Experimental apparatus is a laboratory scale plant, provided with a jacketed stirred reactor and an optical device. It is sketched in Figure 1, while a detailed description of the apparatus and the related optical technique used for the measurement of the induction time for nucleation is available elsewhere [4].

To prepare the calcium carbonate supersaturated solution to fill in the stirring reactor, three reagents have been mixed together with clear distillate water: calcium chloride dihydrate ($\text{CaCl}_2 \cdot 2\text{H}_2\text{O}$), sodium hydrogen carbonate (NaHCO_3) and L-leucine. EDTA titrimetric method was used to standardized all Ca^{2+} ions concentration as CaCO_3 .

Before filling in the reactor, the solution was passed through a suitable filter, to separate possible undesired materials. All experimental runs have been performed at room temperature ($T=25^\circ\text{C}$). Different values of $\text{CaCl}_2 \cdot 2\text{H}_2\text{O}$ and NaHCO_3 have been used, ranging from 2 to 60 mol/m³, while two concentrations of leucine 0.520×10^{-3} and 1.041×10^{-3} mol/l have been selected.

Experimental runs have been carried out at room temperature ($T=25^\circ\text{C}$), with supersaturation ratio values ranging from 2 to 120.

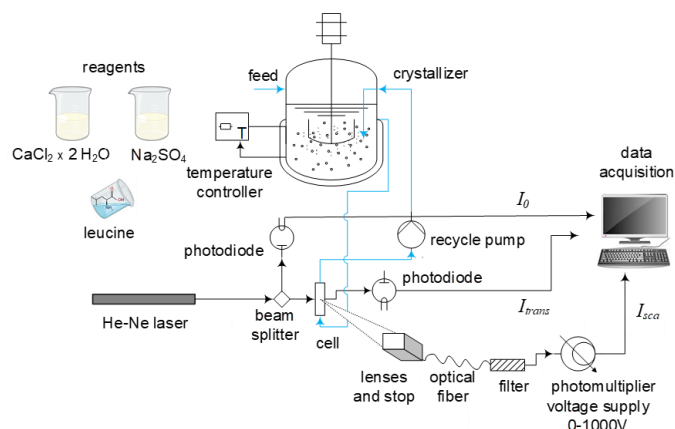


Figure 1. Experimental apparatus

3. Results and discussion

To study the effect of leucine addition on calcium carbonate nucleation, two experimental series for the induction time measurement have been performed at different leucine concentrations, keeping the temperature constant at $T=25^{\circ}\text{C}$ and varying the supersaturation ratio S . The first experimental series has been carried out at a leucine concentration (c_{LEU}) equal to $0.520 \times 10^{-3} \text{ M}$, the second one at $c_{\text{LEU}} = 1.041 \times 10^{-3} \text{ M}$. The experiments are reported in the following Figure 2, where induction times are plotted as a function of supersaturation ratios for two leucine levels.

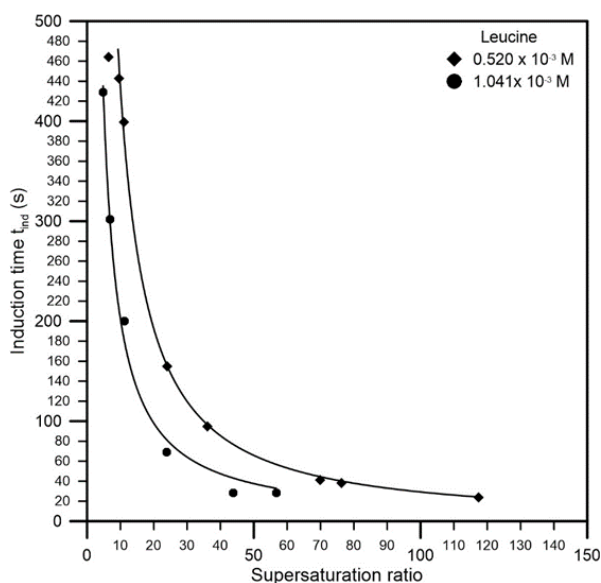


Figure 2. Induction time for CaCO_3 nucleation as a function of supersaturation ratio at different leucine concentrations.

As can be observed, for each curve at a fixed leucine concentration, the induction times decrease with increasing the supersaturation ratio. This is expected, since a higher ion concentration in solution results in a faster solid phase formation [5]. With increasing leucine concentration, passing from $0.520 \times 10^{-3} \text{ M}$ (rhombuses) to $1.041 \times 10^{-3} \text{ M}$ (circles), the induction times decrease and the curve moves downwards. Leucine seems to behave as a promoter for CaCO_3 crystallization. This behavior is likely due to the fact that when leucine is added in solution, the distance between the equilibrium and the metastable curves decreases, reducing the so-called metastable zone. This is an advantage if the target is to recover calcium carbonate with specific characteristics in terms of particle size, purity, shape and polymorphic form.

The promotion for CaCO_3 crystallization can be enhanced, as shown by the curves reported in Figure 2, if higher leucine concentration is added to the solution, which leads to lower induction times at the same supersaturation ratio.

Experimental results showed in Figure 2 have been compared with those obtained by the same research group in the absence of any additive [6-7] and in the presence of citric acid, which acts as a retardand for calcium carbonate nucleation [8-9]. This comparison is shown in Figure 3.

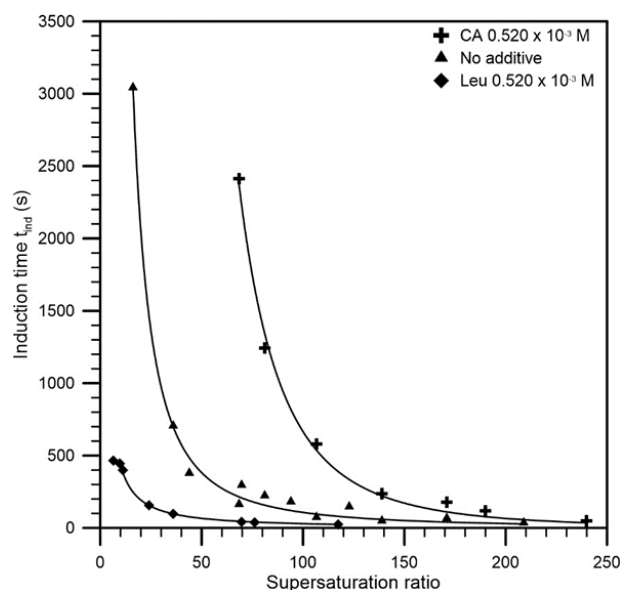


Figure 3. Induction time for CaCO₃ nucleation as a function of supersaturation ratio with additives (citric acid and leucine) and without any additive.

The figure shows the t_{ind} values measured in presence of citric acid (crosses) are higher, while t_{ind} values measured in presence of leucine (rhombuses), at the same concentration in solution, are lower than the induction times values obtained in the absence of any additives (triangles). This confirms the capacity of leucine to act as a promoter for calcium carbonate nucleation.

4. Conclusions

In this paper, the effect of leucine on the induction time of calcium carbonate crystallization has been studied. Two different concentrations of leucine in solution have been investigated, and the experimental runs, compared with previously published results with no additive and with citric acid in solution, have showed that leucine is a promoter for CaCO₃ precipitation and this behavior increases, if its concentration grows from 0.520×10^{-3} M to 1.041×10^{-3} M.

References

- [1] R. Chang, S. Kim, S. Lee, S. Choi, M. Kim, Y. Park, *Frontiers in Energy Research*.
- [2] J.H. Bang, Y. Yoo, S.W. Lee, K. Song, S. Chae, *Minerals* 7 (2017) 207.
- [3] A. Declat, E. Reyes, O.M. Suarez, *Reviews on Advanced Materials Science* 44 (2016) 87-107.
- [4] A. Lancia, D. Musmarra, M. Prisciandaro, *AIChE Journal* 45 (1999) 390-397.
- [5] J.W. Mullin, *Crystallization*, forth ed., Butterworth-Heinemann Ltd., Oxford, 2001.
- [6] G. Mazziotti di Celso, M. Prisciandaro, D. Karatza, A. Lancia, D. Musmarra, *Canadian Journal of Chemical Engineering* 95 (2017) 1671-1675.
- [7] G. Mazziotti di Celso, M. Prisciandaro, D. Karatza, A. Lancia, D. Musmarra, *Desalination and Water Treatment* 69 (2017) 173-177.
- [8] K.J. Wada, A.C. Ramuson, *Colloid Interface Science* 282 (2005) 359-369.
- [9] M.M. Reddy, G.H. Nancollas, *Desalination* 12 (1973) 61-73.

**Multiscale modeling of solubility in semi-crystalline polymers:
Bridging Molecular dynamics simulations with Lattice Fluid theory**

Omar Atiq^{1,4}, Eleonora Ricci^{1,3,4}, Marco Giacinti Baschetti^{1,4}, Maria Grazia De Angelis^{1,2,4}

*1 Department of Civil, Chemical, Environmental and Material Engineering, (DICAM), Alma Mater Studiorum –
Università di Bologna, via Terracini 28,40131 Bologna, Italy.*

*2 Institute for Materials and Processes, School of Engineering, University of Edinburgh, Sanderson Building, Robert
Stevenson Road, EH9 3FB, Scotland, UK.*

*3 Institute of Informatics and Telecommunications & Institute of Nanoscience and Nanotechnology, National Center for
Scientific Research Demokritos, 15341 Aghia Paraskevi, Athens, Greece.*

4 Dutch Polymer Institute (DPI), P.O. Box 902, 5600 AX Eindhoven, the Netherlands.

**Corresponding author E-Mail: omar.atiq2@unibo.it*

1. Introduction

The mechanical and barrier properties of semi-crystalline polymers are strictly related to their biphasic nature. In such polymers, upon cooling from the melt, partial crystallization occurs hence leading to the intercalation of two phases. Nevertheless, not all the chains have sufficient energy to fold into highly oriented lamellar structures hence random coils of chains, namely the amorphous domains, are always present along with the crystallites. An interesting feature of some semi-crystalline polymers is the limited gas and vapor permeability which therefore makes them excellent barriers. The permeability in non-porous materials, so are semi-crystalline polymers, is commonly derived, according to the solution-diffusion model as the product of the Solubility and the Diffusivity [1]. Both the solubility and diffusivity are strongly reduced by the presence of the crystal phase. The reduced solubility can be ascribed to the fact that the crystal domains are impermeable, thus the penetrant sorbs only in the amorphous phase. Moreover, the experimental evidence suggests that the amorphous phase exhibits a lower solubility than the one it would show in the absence of the crystalline domains hence suggesting that the crystals act as a physical constraint causing an increased rigidity and reduced swelling capacity of the amorphous phase.

In this context, a series of works addressed the modeling of the solubility in semi-crystalline polymers introducing the mechanistic effect provided by the crystal phase. We gathered and described such modeling strategies in a detailed review article that can be found in [2].

2. Methods

The new modeling strategy here presented follows a multi-scale paradigm that effectively couples molecular dynamics simulations with thermodynamic modeling. High-density polyethylene was chosen as a benchmark material for the development and optimization of the modeling strategy with carbon dioxide as a penetrant. The next pages are addressed to the description of the atomistic and macroscopic modeling and their integration.

2.1 Molecular Modeling

Since the penetrant does not sorb the crystal phase, the chosen molecular model was a fully amorphous polymer structure in which the crystal was implicitly accounted with the addition of a constraint pressure ' p_c^0 ' prevailing the gas pressure which mimics the increased density state and reduced swelling. NPT simulations were used to evaluate the volumetric properties of the amorphous polyethylene at different temperatures, pressures (gas + constraint), and CO₂ concentrations using LAMMPS software.

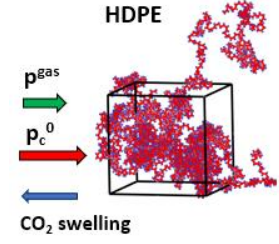


Figure 1 Constrained amorphous phase molecular representation

2.2 Thermodynamic Modeling

The thermodynamic modeling was performed via Lattice Fluid theory [3]. The idea behind our modeling is to consider the constrained amorphous phase of the semi-crystalline polymer as in a non-equilibrium fashion because of the volume relaxation hindered by the crystallites. In this context, the sorbing amorphous phase volume relationship with temperature, pressure (gas + constraint), and concentration was derived from molecular dynamics simulation results rather than an equation of state which is valid only for fully rubbery and molten polymers. The solubility evaluation was made at the macroscopic level using the Non-Equilibrium Lattice Fluid (NELF) model [4] fed with the polymer simulated density. Once the constraint pressure parameter p_c^0 was adjusted on one solubility isotherm, the same value was used to predict the solubility at different temperatures. Such an approach was tested for the modeling and prediction of carbon-dioxide isotherms.

2.3 Multiscale modeling

In the first stage, the Lattice Fluid theory in its equilibrium version was used to model CO₂ solubility isotherms in molten polyethylene. The pure penetrant equation of state solution provided the pure gas density and chemical potential. The penetrant chemical potential equalization gas-side and polymer side was then simultaneously solved with the mixture equation of state providing an estimation of the penetrant solubility in the molten polymer matrix (ω_1). The predicted solubility was matched with the experimental isotherm by adjusting the value of the binary interaction parameter k_{CO_2-HDPE} . The set of equations to be solved is reported in (1).

$$\left\{ \begin{array}{l} \tilde{\rho}_{CO_2} = 1 - \exp \left[-\frac{\tilde{p}_{CO_2}^2}{\tilde{T}_{CO_2}} - \frac{\tilde{p}_{CO_2}}{\tilde{T}_{CO_2}} - \tilde{\rho}_{CO_2} \left(1 - \frac{1}{r_{CO_2}^0} \right) \right] \\ \tilde{\rho}_{mix} = 1 - \exp \left[-\frac{\tilde{p}_{mix}^2}{\tilde{T}_{mix}} - \frac{\tilde{p}_{mix}}{\tilde{T}_{mix}} - \tilde{\rho}_{mix} \left(1 - \left(\frac{\Phi_{CO_2}}{r_{CO_2}} + \frac{\Phi_{pol}}{r_{pol}} \right) \right) \right] \\ \mu_{CO_2}^{pol}(T, p_{CO_2}, \omega_{CO_2}, k_{CO_2-HDPE}) = \mu_{CO_2}^0(T, p_{CO_2}) \end{array} \right. \quad (1)$$

Once the binary interaction parameter was fitted for all the solubility isotherms at the molten state it was possible to derive a linear expression for the binary parameter as a function of temperature $k_{12}(T)$ that was extrapolated even below melting temperature in the semi-crystalline state.

The modeling of the semi-crystalline solubility isotherms required to retrieve the experimental solubility isotherms on the sole sorbing amorphous fraction as follows:

$$\omega_{CO_2}^{am} = \frac{\omega_{CO_2}^{SC}}{(1 - \chi_{cr})} \quad (2)$$

where $\omega_{CO_2}^{am}$ and $\omega_{CO_2}^{sc}$ are the constraint amorphous and semi-crystalline solubility respectively and χ_{cr} the mass degree of crystallinity.

The modeling of the solubility isotherms in the constrained amorphous phase was performed solving the following set of equations fed with the binary interaction parameter temperature relationship previously retrieved $k_{CO_2-HDPE}(T)$ and adjusting the constraint pressure parameter p_c^0 to fit a sole experimental solubility isotherm.

$$\begin{cases} \tilde{\rho}_{CO_2} = 1 - \exp\left[-\frac{\tilde{p}_{CO_2}^2}{\tilde{T}_{CO_2}} - \frac{\tilde{p}_{CO_2}}{\tilde{T}_{CO_2}} - \tilde{\rho}_{CO_2}\left(1 - \frac{1}{r_{CO_2}^0}\right)\right] \\ \rho_{pol}^{am}(T, p_{CO_2} + p_c^0, \omega_{CO_2}^{am}) \text{ from MD simulations} \\ \mu_{CO_2}^{NE,am}(T, p_{CO_2} + p_c^0, \omega_{CO_2}^{am}, \rho_{pol}^{am}) = \mu_{CO_2}^0(T, p_{CO_2}) \end{cases} \quad (3)$$

3. Results

The yet presented modeling paradigm was used to predict carbon-dioxide solubility isotherms. In particular, the solubility prediction provided by the solution of the system reported in (3) at $T = 25^\circ\text{C}$ with the corresponding volumetric results coming from MD simulations was fitted on the experimental solubility isotherm adjusting the constraint pressure parameter. Once the constraint pressure parameter was adjusted on the solubility isotherm at 25°C , the fitted value was used to predict the solubility at other temperatures by using molecular dynamics simulations at the relative temperature.

The results of the MD simulated constrained amorphous density at $T = 25^\circ\text{C}$ are reported in Figure 2 while the solubility isotherms evaluation (fitted and predicted) derived from the coupling with the NELF model are displayed against the experimental results in Figure 3.

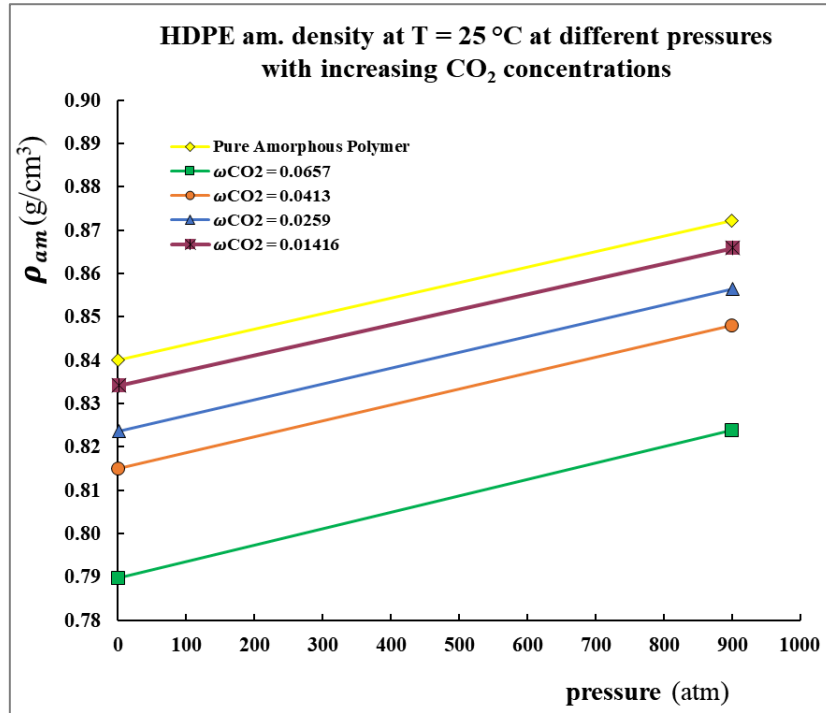


Figure 2 NPT simulations results at $T = 25^\circ\text{C}$. Constrained amorphous phase as a function of pressure ($p_{CO_2} + p_c^0$) for different concentrations: yellow (pure polymer), purple ($\omega_{CO_2} = 0.01416$), blue ($\omega_{CO_2} = 0.0259$), orange ($\omega_{CO_2} = 0.0413$), green ($\omega_{CO_2} = 0.0657$).

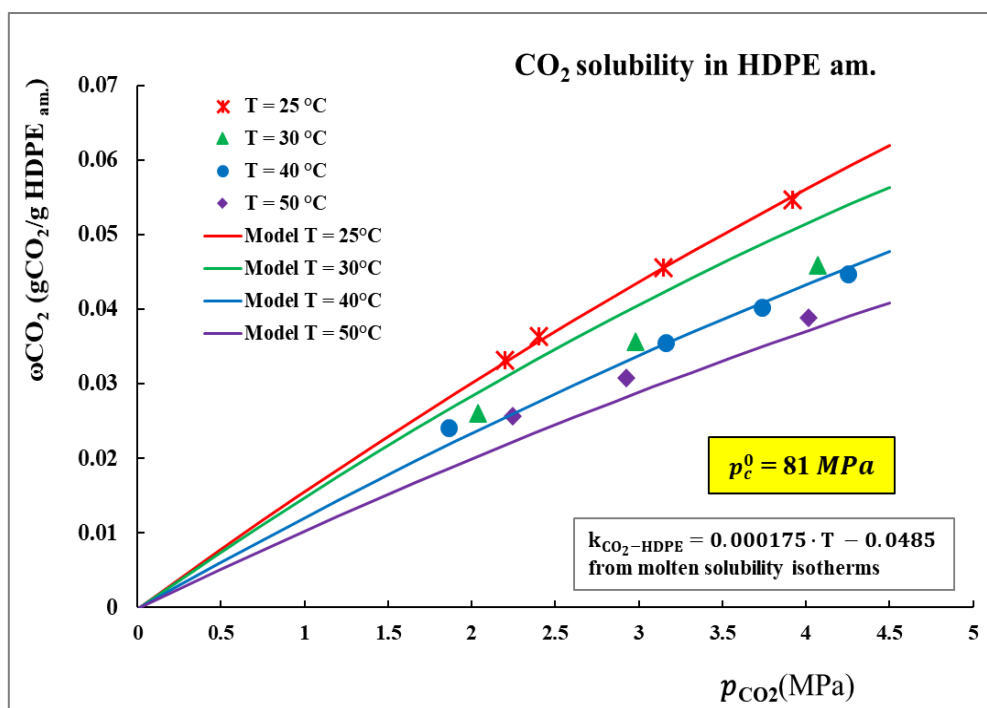


Figure 3 CO₂ Solubility isotherms in the constrained amorphous phase:

- Experimental solubility data ω_{CO_2} (gCO₂/gpol.am) [5]: T = 25 °C (red crosses), T = 30 °C (green triangles), T = 40 °C (blue circles), T = 50 °C (purple diamonds) .
- Multi-scale model (MD simulations + NELF) prediction: T = 25 °C (red line), T = 30 °C (green line), T = 40 °C (blue line), T = 50 °C (purple line).

4. Conclusions

A constant p_c^0 fitted parameter was demonstrated to reliably predict the CO₂ solubility data at other temperatures hence the modeling strategy showed as a promising tool for the estimation of sorption in semi-crystalline polymers. Nevertheless, the modeling strategy still needs to be optimized and tested with other penetrants and polymers.

References

- [1] J.G. Wijmans, R.W. Baker, The solution-diffusion model: a review, *J. Memb. Sci.* 107 (1995) 1–21. [https://doi.org/10.1016/S0166-4115\(08\)60038-2](https://doi.org/10.1016/S0166-4115(08)60038-2).
- [2] O. Atiq, E. Ricci, M.G. Baschetti, M.G. de Angelis, Modelling solubility in semi-crystalline polymers: a critical comparative review, *Fluid Phase Equilib.* 556 (2022) 113412. <https://doi.org/10.1016/j.fluid.2022.113412>.
- [3] I.C. Sanchez, R.H. Lacombe, Statistical Thermodynamics of Polymer Solutions, *Macromolecules.* 11 (1978) 1145–1156. <https://doi.org/10.1021/ma60066a017>.
- [4] F. Doghieri, G.C. Sarti, Predicting the low-pressure solubility of gases and vapors in glassy polymers by the NELF model, *J. Memb. Sci.* 147 (1998) 73–86. [https://doi.org/10.1016/S0376-7388\(98\)00123-9](https://doi.org/10.1016/S0376-7388(98)00123-9).
- [5] N. Von Solms, J.K. Nielsen, O. Hassager, A. Rubin, A.Y. Dandekar, S.I. Andersen, E.H. Stenby, Direct measurement of gas solubilities in polymers with a high-pressure microbalance, *J. Appl. Polym. Sci.* 91 (2004) 1476–1488. <https://doi.org/10.1002/app.13371>.

Acknowledgment: This research forms part of the research program of DPI, project 844 | Modelling and Design of Multiphase Polymeric Materials for High-Performance Applications Across Multiple Scales (MuMPol).

Geopolymer-zeolite composite materials for carbon capture applications: adsorption tests and modelling of thermal effects

M. Boscherini^{1,2*}, F. Miccio², E. Papa², V. Medri², E. Landi², F. Doghieri¹, M. Minelli¹

1 Department of Civil, Chemical, Environmental and Materials Engineering (DICAM), Alma Mater Studiorum, University of Bologna, via Terracini 28, 40136 Bologna, Italy

2 Institute of Science and Technology for Ceramics (ISTEC), National Research Council of Italy (CNR), via Granarolo 64, 48018 Faenza, Italy

**mattia.boscherini3@unibo.it*

1. Introduction

As the need for achieving carbon neutrality in industrial processes and energy production increases following rising worries of the scientific community towards the effects of climate change, researchers attention has been focused on finding competitive ways to obtain carbon dioxide sequestration from gaseous currents such as flue gas. Carbon capture is considered an essential strategy to contain the increase of global average temperature below the threshold of 1.5°C estimated by the Intergovernmental Panel on Climate Change to cause irreversible climate changes and environmental damage [1, 2]. Nowadays, the most common sequestration technology is the ammine absorption, but as this process presents limitations due to high costs, toxicity and volatility of amines other methodologies are being evaluated. In particular, adsorption processes offer a very promising solution, both clean and reliable, and are therefore becoming of increasing interest thanks also to their potential for retrofit application to existing industrial plants [3]. with research focused both on sorbent material development and process optimization. Different materials have been proposed for CO₂ sorption, from conventional sorbents such as active carbon to Metal-Organic Frameworks, zeolites and supported amines [4]. A good adsorbent material should possess an high adsorption capacity for CO₂ and large selectivity towards other gases, while also being thermally stable and possessing good mechanical resistance in handling and loading operations [5].

Adsorption is usually operated as a semi-continuous process: the CO₂ containing gaseous stream is fed to a sorbent bed until the breakthrough point is reached, then the feed is switched to a second bed while the first one undergoes regeneration. Two different approaches can be applied to regenerate the sorbent bed: either increasing the temperature, in a temperature swing adsorption (TSA), or decreasing the pressure, obtaining a Pressure Swing adsorption (PSA). Breakthrough time can be defined as the time when the concentration of the key component, CO₂ for carbon capture applications, reaches a preset threshold value (e.g. 5 or 10% of the inlet value), which can be optimized in order to maximize process efficiency. While fixed beds operate semi-continuously, continuous operation may be achieved by fluidized beds through the circulation of the sorbent from the adsorption to the regeneration bed [6].

This work presents the study of a CO₂ adsorption process in a composite geopolymer/zeolite material, with the purpose of evaluating material performance in dynamic conditions. Previous studies in pressure decay adsorption regime reported that this material presents a high affinity for CO₂ adsorption, thanks to a synergic effect between the zeolite and the geopolymeric matrix [7, 8]. Following these findings, cyclic adsorption/desorption breakthrough tests were therefore employed to investigate material performance in transient conditions. Particular focus was put on monitoring the temperature profile of the experimental sorption column, to inspect the strong thermal effects associated with the adsorption process and evaluate their potential influence on adsorption capacity and kinetics [9]. Adsorption/desorption cycles were examined under different thermal regimes, in order to compare the performance of PSA, without external temperature control, to TSA performed in a heating regime at constant temperature in a range between 50-80°C. Heating regimes are expected to improve material regeneration by favoring the endothermic desorption of carbon dioxide.

Numerical models are a useful tool for improving knowledge of processes, and in particular for process optimization. A model for the description of the adsorption process was developed and tested based on the obtained experimental data. The model accounts for both mass and energy transport in the sorbent bed, modelling concentration and temperature profiles both for the gas phase and the sorbent bed. The model was validated using the collected experimental data, and was then employed to predict the behavior of the sorbent in different operating conditions, such as different feed concentration and temperature. Useful indications on the internal profiles of temperature and concentration in the sorption bed are also obtained, in particular also predicting the effects of a possible scale up of the process.

2. Methods

2.1-Sorbent preparation and characterization

The sorbent is a composite of zeolite 13X and Na based geopolymer having specific surface area of 221 m²/g. The geopolymer-zeolite composite has been fabricated using formulations and procedures reported on previous works [7, 8]: geopolymer with theoretical Si:Al molar ratio equal to 1.2 was prepared by mechanically mixing metakaolin M1200S (Imerys) with a sodium hydroxide solution (10 M), and adding 27% wt. of Na13X zeolite powder, Na₈₆[(AlO₂)₈₆(SiO₂)₁₀₆]·H₂O (Sigma-Aldrich, average particle size = 2 μm, specific surface area = 791 m²/g and pore volume = 301 mm³/g) to the slurry. The material was then cured for 24 h at 80 °C in closed vessels and for other 24 h at 80 °C in open vessels. After consolidation, the obtained monoliths were crashed into granules and sieved in the ranges 400–630 μm.

2.2-Dynamic adsorption tests

A glass column (diameter 25.7 mm and height 200 mm) was filled by sorbent granules (400–630 μm size) forming a fixed bed. Two electronic mass-flow controllers (Brooks Instruments mod. 5850S) and a quick switching valve on the CO₂ line were used to provide the feed gas mixture of CO₂ and N₂, obtained from bottles of pure N₂ and CO₂. The valve allowed to switch between adsorption and desorption phases by intercepting the CO₂ flux before the column. Heating was provided through an external electric coil, and the column insulated with multiple layers of Teflon tape to avoid heat dispersion. A K-type thermocouple is inserted in the outlet section of the column to measure internal temperature. Outlet concentration of the gas is monitored by a multicomponent gas analyser (Testo 350). Both complete adsorption tests (bed is brought to saturation), and cyclic tests (adsorption step interrupted at breakthrough point, set at 5% of inlet CO₂) were performed. By integrating the mass balances for N₂ and CO₂, the amount of adsorbed CO₂ can be calculated from the outlet concentration profiled over time (N₂ adsorption is neglected):

$$q_{CO_2} = \frac{\dot{n}_{in}}{m_s} \int_{t_0}^{t_0+t_{ads}} \left(y_{CO_2}^{in} - y_{CO_2}^{out} \frac{1 - y_{CO_2}^{in}}{1 - y_{CO_2}^{out}} \right) dt \quad (1)$$

in which \dot{n} is the molar flowrate, $y_{CO_2}^{in}$ and $y_{CO_2}^{out}$ are respectively the CO₂ inlet and outlet molar fractions of the gas flow, m_s is the mass of the sorbent, and t_0 and t_{ads} are the initial time and the duration of the adsorption test, respectively. Sorption apparatus detailed description can be found in a previous work [10].

2.3-Model description

The model was coded in FORTRAN and is based on plug flow assumption for description of the sorbent bed (1-D model). Mass and energy balances are solved on the basis of continuum thermomechanics. The Peng-Robinson equation of state was chosen to describe the gas phase, while CO₂ adsorption in the solid sorbent is represented through the Sips equation in the sorbent phases. The 7 parameters employed in Sips equation were retrieved from best fit of experimental adsorption isotherms obtained from pressure decay at different temperatures). Only CO₂ is modelled to adsorb and sorption kinetics are modelled according to a linear driving force (LDF) approach [11]. The differential equations system solved includes mass, species, energy and momentum balances in the domain ($0 \leq t$; $0 \leq z \leq L$), where L is reactor length. A time implicit volume discretization method is used for calculation: a grid of 100 equally spaced nodes in the axial direction (z) and

a constant time-step are used. Three nested loop iterations are conducted for pressure, concentration and temperature profiles. The complete set of equations solved by the model is the following:

$$\left\{ \begin{array}{l} \varepsilon_t \frac{\partial c}{\partial t} + \frac{\partial n}{\partial z} + \rho_b \frac{\partial q_{CO_2}}{\partial t} = 0 \\ \varepsilon_t \frac{\partial (c y_{CO_2})}{\partial t} + \frac{\partial (n y_{CO_2})}{\partial z} + \rho_b \frac{\partial q_{CO_2}}{\partial t} - \varepsilon_b \frac{\partial}{\partial z} \left(cD \frac{\partial y_{CO_2}}{\partial z} \right) = 0 \\ \frac{\partial q_{CO_2}}{\partial t} + k_s (q_{CO_2} - q_{CO_2}^*) = 0 \\ \left[\varepsilon_t \hat{C}_g c + \rho_b (\hat{C}_s + q_{CO_2} c_{CO_2}^{ads}) \right] \frac{\partial T}{\partial t} + n \hat{C}_g \frac{\partial T}{\partial t} - \rho_b \Delta \tilde{H}_{ads} \frac{\partial q_{CO_2}}{\partial t} - \varepsilon_b \frac{\partial}{\partial z} \left(k_g \frac{\partial T}{\partial z} \right) + \frac{2}{R_p} h (T - T_\infty) \\ \frac{\partial p}{\partial z} + \left[1.75n + \frac{150\mu(1-\varepsilon_b)}{d_p} \right] \left[\frac{1-\varepsilon_b}{\varepsilon_b^3 d_p} \right] \frac{n}{c} = 0 \end{array} \right. \quad (2)$$

In these equations, y_{CO_2} is the fraction of active component in the gas phase, n is the molar flux density of the gas in the axial direction and q_{CO_2} is the concentration of active component adsorbed in the solid (q^* is the corresponding CO_2 capacity), c is the gas phase concentration (Peng-Robinson). C_g is the gaseous phase heat capacity linearly dependent on temperature and composition, while μ is the (constant) viscosity of the gas phase. The axial dispersion coefficients for mass transfer (D) and heat transfer (k_g) are calculated as functions of sorbent particle diameter, total void fraction, molar flux density, gas concentration and molecular diffusivity. R_p is the radius of the column, while ε_t and ε_b are respectively its total and bed void fractions. The following boundary conditions are used for integration:

$$\left\{ \begin{array}{l} z = 0 \Rightarrow y_{CO_2} = y_{CO_2}^{(in)}(t); \quad T = T^{(in)}(t); \quad n = \frac{\dot{V}_{CO_2}^{in} + \dot{V}_{N_2}^{in}}{\pi r^2} \frac{p}{RT} \\ z = L \Rightarrow \frac{\partial y_{CO_2}}{\partial z} = \frac{\partial T}{\partial z} = 0; \quad p = p^{(out)}(t) \\ p^0 = p^{(out)}(t=0) \end{array} \right. \quad (3)$$

The model is set to calculate the initial CO_2 content in the bed starting from the set regeneration conditions.

3. Results and discussion

The comparison of results obtained indicates that in breakthrough mode about 50% of the CO_2 amount sequestered in complete adsorption tests can be sequestered, while notably lessening required times (11 vs. 140 min). Appreciable thermal effects are observed in complete tests during adsorption and desorption steps, with a maximum of temperature during the exothermic adsorption and a minimum during the endothermic desorption. The increase of temperature in adsorption was observed to be larger than 10 °C, with peak observed shortly after the BT time, coinciding with maximum adsorption. Temperature then slowly decreases with adsorption rate as saturation of the bed is reached. Temperature decrease during desorption is less marked, due to slower kinetics. Higher CO_2 concentration in the feed leads to higher temperature peaks during adsorption, and interestingly this large temperature increase depresses adsorption more significantly than at lower values, so the resulting capacity at the BT deviates more appreciably from the that obtained in complete adsorption tests.

Fig. 1 and 2 shows adsorption cycles performed in different heating regimes, showing the effects of heating during desorption segment carried out up to the breakthrough point. Orange line represents feed concentration. As can be seen, desorption is much faster when heat is applied, achieving faster and better material regeneration.

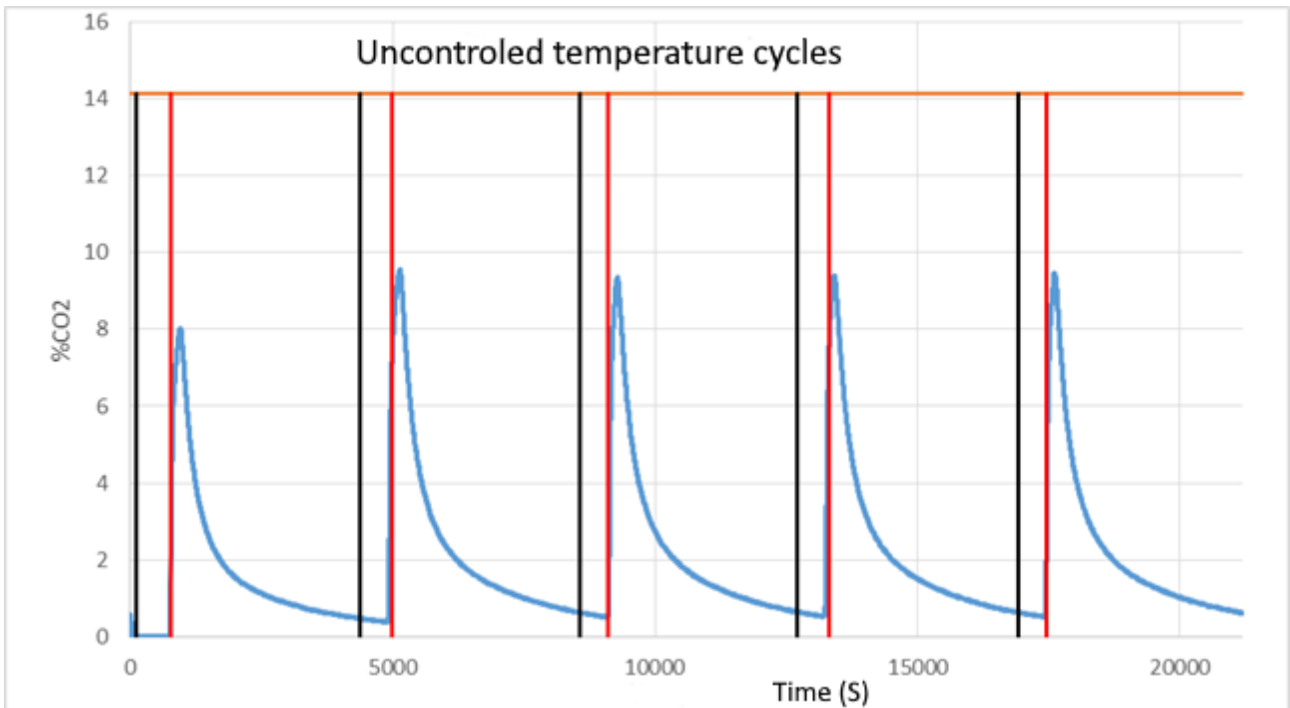


Figure 1. Adsorption/desorption cycles concentration profiles without external temperature control.

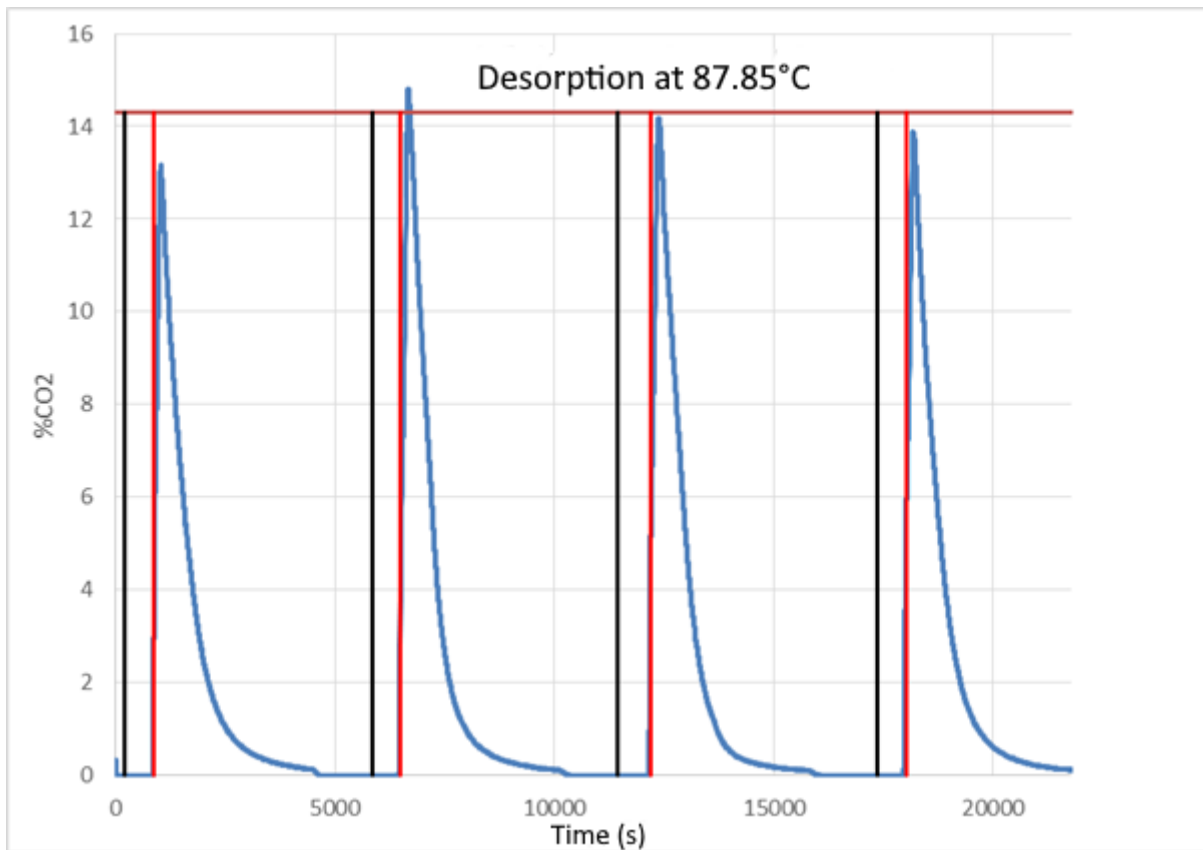


Figure 2. Adsorption/desorption cycles with external heating applied: desorption at constant temperature.

4. Conclusions

Experimental results demonstrate that a combined pressure-swing and temperature-swing strategy is the optimal solution to process optimization, leading to shortened sorbent regeneration time. A regeneration temperature above 80°C was found to be necessary to restore material sorption capacity along consecutive sorption/desorption cycles.

The model has been proven to represent well the experimental results obtained at different CO₂ feed concentrations, in terms of both concentration and temperature profiles in column outflow gas and in sorbent bed, and after validation has also been first tested to predict some effects of process scale up on sorption performance.

References

- [1] IPCC, 2014: Climate Change 2014: Synthesis Report. Contribution of Working Groups I, II and III to the Fifth Assessment Report of the Intergovernmental Panel on Climate Change [Core Writing Team, R.K. Pachauri and L.A. Meyer (eds.)]. IPCC, Geneva, Switzerland, 151 pp.
- [2] European Commission; COMMUNICATION FROM THE COMMISSION TO THE EUROPEAN PARLIAMENT, THE EUROPEAN COUNCIL, THE COUNCIL, THE EUROPEAN ECONOMIC AND SOCIAL COMMITTEE, THE COMMITTEE OF THE REGIONS AND THE EUROPEAN INVESTMENT BANK A Clean Planet for all A European strategic long-term vision for a prosperous, modern, competitive and climate neutral economy; COM/2018/773 final; Bruxelles
- [3] M. Younas, M. Sohail, L.K. Leong, M.J. Bashir, S. Sumathi, Feasibility of CO₂ adsorption by solid adsorbents: a review on low-temperature systems, *Int. J. Environ. Sci. Technol.* 13 (2016) 1839–1860.
- [4] Junya Wang, Liang Huang, Ruoyan Yang, Zhang Zhang, Jingwen Wu, Yanshan Gao, Qiang Wang, Dermot O'Hare and Ziyi Zhong; Recent advances in solid sorbents for CO₂ capture and new development trends; *Energy Environ. Sci.*, 2014, 7,3478
- [5] R. Ben-Mansour, M.A. Habib, O.E. Bamidele, M. Basha, N.A.A. Qasem, A. Peedikakkal, T. Laoui, M. Ali, Carbon capture by physical adsorption: Materials, experimental investigations and numerical modeling and simulations – a review, *Appl. Energy* 161 (2016) 225–255.
- [6] Gupta K.N., Kumar R., Kinetic modeling and optimization of fraction of bed utilized for the gaseous phase removal of toluene in fixed bed adsorption column: response surface methodology, 2020, *Separation Science and Technology* 55, 1062–1077
- [7] Minelli M., Papa E., Medri V., Miccio F., Benito P., Doghieri F., Landi E., 2018, Characterization of novel geopolymer – zeolite composites as solid adsorbents for CO₂ capture, *Chemical Engineering Journal* 341, 505–515.
- [8] Minelli M., Medri V., Papa E., Miccio F., Landi E., Doghieri F., 2016, Geopolymers as solid adsorbent for CO₂ capture, *Chemical Engineering and Science* 148, 267–274.
- [9] Xiao J., Peng Y., Bénard P., Chahine R., 2016, Thermal effects on breakthrough curves of pressure swing adsorption for hydrogen purification, *International Journal of Hydrogen Energy* 41, 8236-8245.
- [10] Boscherini M., Miccio F., Papa E., Medri V., Landi E., Doghieri F., Minelli M, 2021, The relevance of thermal effects during CO₂ adsorption and regeneration in a geopolymer-zeolite composite: Experimental and modelling insights, *Chemical Engineering Journal* 408, 127315.
- [11] Gholami M., Talaie M.R., 2010, Investigation of simplifying assumptions in mathematical modeling of natural gas dehydration using adsorption process and introduction of a new accurate LDF model, *Industrial Engineering Chemistry Resources* 49, 838–846.

Effect of flow induced crystallization on the flow length of injection molded polypropylene

Rita Salomone*, Vito Speranza, Sara Liparoti, and Roberto Pantani

Department of Industrial Engineering, University of Salerno, via Giovanni Paolo II, 132 – Fisciano (SA) - Italy

*Corresponding author E-Mail: rsalomone@unisa.it

1. Introduction

Micro injection molding (μ IM) represents one of the widespread processes for a large-scale production of micro components since it matches high automation, short processing time, and high flexibility. μ IM can be applied to several fields, from the electronic to the biomedical ones, where high dimensional and geometrical accuracy is mandatory. On its turn, geometrical and dimensional accuracy depends on the complete filling of the cavity during processing [1,2], which is a complex task in μ IM, due to the reduced cavity thickness (in the micrometrical range). The strong flow intensity coupled with the fast cooling occurring during μ IM induces the material solidification before the complete cavity filling. Many studies focused on the investigation of the effect of processing conditions on the filling length [3–6]. The main process parameter influencing the final filling length is the cavity temperature: a high cavity temperature delays the cooling, allowing for the complete filling of the cavity. The final morphology of the parts, which in turn determines the mechanical performances, is also influenced by the operating conditions, particularly, the cavity temperature [7,8]. In this work μ IM tests were conducted in an end-less cavity under several conditions of mold temperature and injection velocity, to assess the influence of those parameters on the final filling length.

2. Methods

The μ IM samples were obtained adopting a commercial isotactic polypropylene, T30G, supplied by Basell (Ferrara, Italy), and characterized in previous works [9,10].

The injection molding machine MegaTech H10/18-2 (Tecnica Duebi, ITA) was adopted for μ IM tests. Figure 1 shows the sketch of the cavity adopted for the experiments.

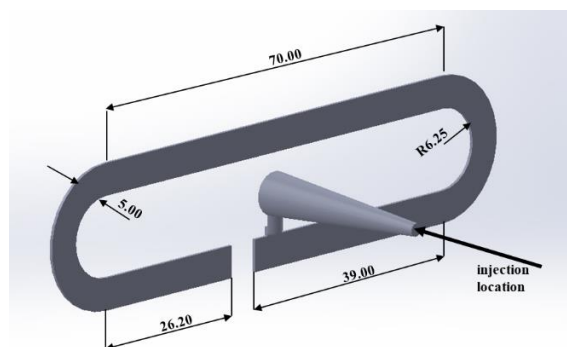


Figure 1. Sketch of the cavity adopted for the μ IM tests. Dimensions are expressed in millimeters. The cavity thickness is 0.50 mm.

Experimental conditions of μ IM tests are shown in table 1.

Table 1. Experimental conditions adopted for μ IM tests

Injection pressure [bar]	100
Injection temperature [°C]	230
Mold temperature [°C]	60 – 80 – 100
Injection velocity [mm/s]	13.2 – 26.4 – 39.6 – 52.8 – 59.4

3. Results and discussion

The final filling length depends on both the adopted mold temperature and the injection velocity. It must be noticed that in none of the considered cases the cavity is completely filled. In particular, the lower is the mold temperature, the shorter is the filling length. Figure 2 shows the results, in terms of final filling length achieved during μ IM on changing mold temperature and injection velocity.

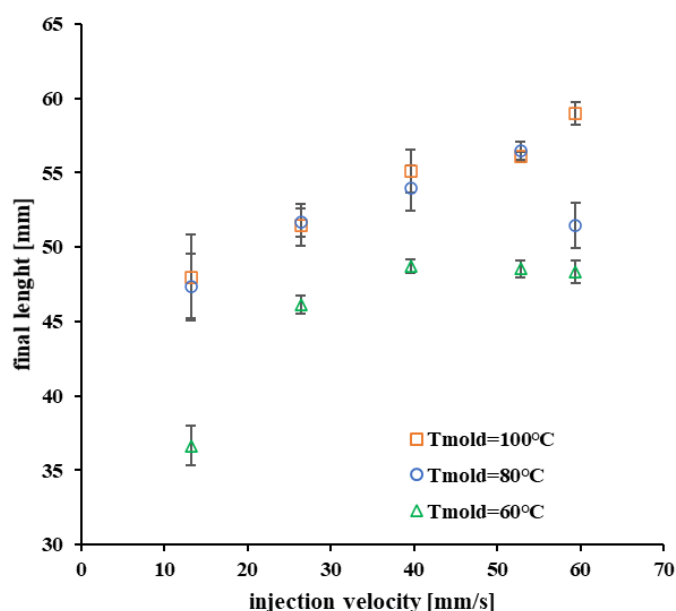


Figure 2. Final sample length obtained at different injection velocities for the three mold temperatures

The increase of mold temperature generally induces an increase of the final filling length. This finding is clearly detectable on increasing mold temperature from 60°C to 80°C. The samples obtained with 60°C mold temperature show the shortest filling length, because of the faster cooling and solidification. As a general effect, the increase of the injection velocity also induces an increase of the final filling length. This increase is due to the delay of cooling during the filling. A maximum value of the final filling length was achieved for an injection velocity of 59.4 mm/s, the longest one, with 100°C mold temperature. With 60°C and 80°C, a maximum value of the final filling length was detected at an intermediate velocity: 39.6 mm/s, and 52.8 mm/s, respectively. The injection velocity has indeed two effects: as the velocity increases, for the same solidification time a longer sample is obtained; furthermore, the crystallization rate increases and thus solidification time reduces. The effect of velocity on the crystallization rate depends on temperature: the crystallization growth rate shows a maximum at a given temperature [11], for higher/lower temperatures, the crystallization rate becomes smaller. Obviously, for temperature above the melt temperature, or for temperature below the glass transition, the crystallization is hindered. On its turn, the temperature which corresponds to the maximum value of the crystallization rate increases with the flow intensity, the injection velocity in these cases. The presence of a maximum in the final filling length at different injection velocities would depend on the complex interplay between the flow intensity and the temperature field.

4. Conclusions

The dimensional and geometrical accuracy of μ IM strongly depends on the operative conditions.

In this work the evolution of the final cavity filling lengths at different mold temperatures and injection velocities during μ IM tests was assessed. The final filling length strongly depends on the complex interplay between the flow and temperature fields since they both affect the crystallization rate. If crystallization occurs before the polymer has completely filled the cavity, any further filling is hindered. On its turn, crystallization rate increases with the flow intensity: the temperature at which maximum crystallization rate occurs shifts toward higher values on increasing flow intensity. This is the reason on the bases of the non-monotonous trend of the final filling length with velocity and temperature, especially when 60°C and 80°C were adopted for the mold. With 100°C mold temperature, the maximum of the final filling length was not detected, probably, it would be detected at higher injection velocities.

References

- [1] M.R. Mani, R. Surace, P. Ferreira, J. Segal, I. Fassi, S. Ratchev, *Journal of Micro and Nano-Manufacturing*. 1 (2013).
- [2] A. Eladl, R. Mostafa, A. Islam, D. Loaldi, H. Soltan, H. Hansen, G. Tosello, *Micromachines*. 9 (2018).
- [3] W.-W. Kim, M.G. Gang, B.-K. Min, W.-B. Kim, *The International Journal of Advanced Manufacturing Technology*. 75 (2014) 293-304
- [4] G. Fu, S.B. Tor, D.E. Hardt, N.H. Loh, *Microsystem Technologies*. 17 (2011) 1791-1798
- [5] D. Yang, C. Liu, Z. Xu, J.Z. Wang, L.D. Wang, *Key Engineering Materials*, 483 (2011) 53-57
- [6] S. Liparoti, V. Speranza, A. de Meo, F. de Santis, R. Pantani, *Journal of Polymer Engineering*. 40 (2020) 783-795
- [7] J. Zhang, C. Guo, X. Wu, F. Liu, X. Qian, *Part B*, 50 (2011) 2227-2241
- [8] J. Jiang, S. Wang, B. Sun, S. Ma, J. Zhang, Q. Li, G.-H. Hu, *Materials & Design*, 88 (2015) 245-251
- [9] F. de Santis, R. Pantani, G. Titomanlio, *Polymer*, 90 (2016) 102-110
- [10] R. Pantani, V. Speranza, G. Titomanlio, *Journal of Rheology*. 59 (2015).
- [11] R. Pantani, F. de Santis, V. Speranza, *Polypropylene Handbook*, Springer International Publishing, Cham 2019 pp. 243-294

Microwave-assisted hydrothermal preparation of photocatalytic fibrous membranes for water treatment

Carlo Boaretti, Jiayi Yin, Michele Modesti, Alessandra Lorenzetti, Alessandro Martucci, Martina Roso*

Dipartimento di Ingegneria Industriale (DII), Università degli studi di Padova

**Corresponding author E-Mail: martina.roso@unipd.it*

1. Introduction

Photocatalysis represents a widely recognized promising technique in the context of advanced oxidation processes for the oxidative degradation of organic pollutant for air and water purification. In this field the traditional benchmark is represented by TiO_2 which has been deeply investigated over the years in order to exploit its potential and solve issues related to its efficient employment [1]. From this point of view the use of TiO_2 nanoparticles for liquid phase treatment of polluted water can be problematic due to the necessity of recovery after use with additional costs for separation. Therefore, the use a substrate for its immobilization is a convenient strategy to overcome this problem and electrospun polymeric nanofibers have proved to be a flexible solution for this purpose [2]. On the other hand, the control of the morphology, crystal phase and correct exposition of the photocatalyst on the surface of such membranes plays a pivotal role on their performance. Microwave-assisted hydrothermal method, which combines the hydrothermal synthesis of nanomaterials from precursors in aqueous solution and the efficient heating of microwaves [3], can assist the synthesis and efficient deposition of TiO_2 particles on the surface of electrospun fibers to produce core-shell fibrous membranes. For this reason, in this study we investigated the effect of the different process parameters involved in the hydrothermal synthesis of TiO_2 particles (acidity of precursor solution, heating temperature and treatment time) on the surface of electrospun PVDF nanofibers for the production of photocatalytic fibrous membranes. The effect of such parameters was considered in relation to the final structure (morphology, TiO_2 crystalline phase and loading) and photocatalytic activity (photodegradation of organic dye and photocatalytic stability over multiple cycles) of the composite fibrous membranes.

2. Methods

PVDF nanofibrous substrate was obtained by conventional electrospinning equipment. For the microwave-assisted hydrothermal synthesis titanium butoxide was hydrolyzed in an aqueous H_2SO_4 solution at different molarities (1,2 and 3 M). The PVDF membrane was than soaked in this solution and treated under microwave heating at different temperatures (100, 120 and 140°C) and treating times (0.5, 1 and 2h) to induce the precipitation and crystallization of TiO_2 particles. The obtained membranes were characterized by scanning electron microscopy, infrared spectroscopy, x-ray diffraction, thermogravimetry. The membrane with the more uniform and homogeneous core-shell structure was further characterized by diffuse reflectance spectroscopy (DRS) and surface area measurement. The photocatalytic performance of the obtained membranes was evaluated by photo-oxidation of organic dye in liquid phase using a cylindrical quartz reactor equipped with a UVC lamp, using a 32 mg sample of membrane which was added to a 200 ml of a 2.5 mg/l solution of methyl orange (MO). The degradation was monitored by UV-vis spectroscopy using the characteristic absorption of MO at 465 nm after calibration with known concentrations. The membrane with the best performance was tested multiple time for performance stability evaluation.

3. Results and discussion

The mechanism for the production of TiO_2 particle can be divided into two step: hydrolysis of titania precursor followed by condensation under hydrothermal conditions which induces the formation of polymeric nuclei by

olation and oxolation reaction. Once reaching a critical dimension such nuclei are stabilized and induce the formation of titania particle which can be formed on the surface of the membrane. The SEM images of the samples revealed that the 2 M acidic precursor solution was the only concentration that effectively produced a uniform coverage of TiO₂ particles on the surface of PVDF nanofibers with a smooth morphology and a core-shell structure (Figure 1). For the other concentrations tested only partial coverage was achieved with a tendency to the formation of particle clusters. The amount of titania deposited increased both over time and by increasing the treatment temperature.

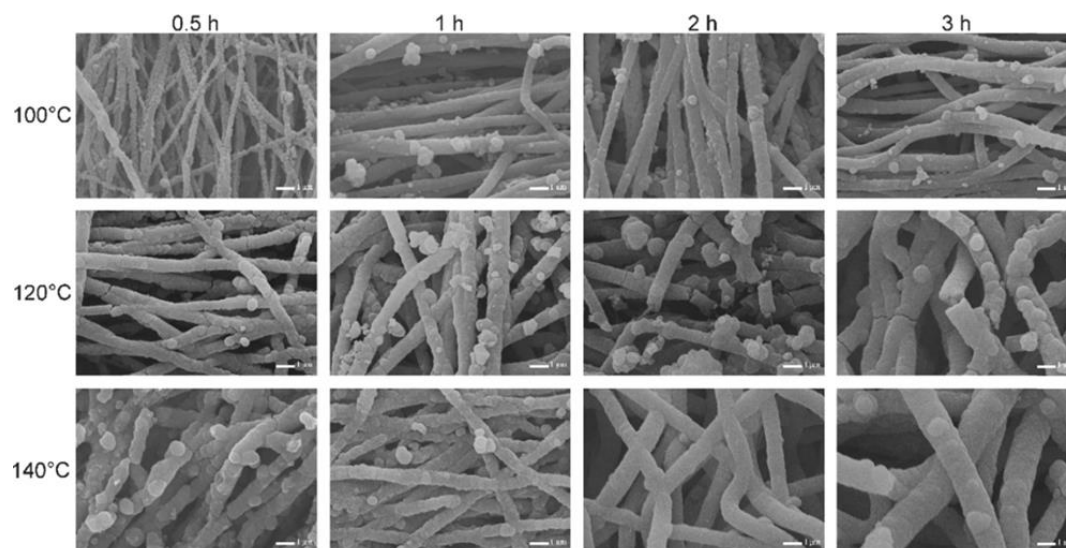


Figure 1. SEM images of PVDF-TiO₂ fibrous membranes produced by a 2M precursor solution (scale bar: 1 μ m)

XRD measurement revealed the presence of anatase as main crystal phase of the titania formed along with a minor content of rutile. The relative amount of the two polymorph is dependent on temperature and time. Low temperature tends to provide higher content of rutile which decreases over time. At 120°C only anatase is formed. In this last case the optical properties measured by DRS showed absorption limit and band gap energy in accordance to characteristic values of pure anatase phase. Photocatalytic experiment in liquid phase showed that although UV can to some extent induce degradation of methyl orange the combination with the membrane is capable to reach a 95% degradation after 200 minutes. The normalization of the data on the basis of the catalyst content (Figure 2) revealed that the best performance can be achieved for the membrane obtained at 120°C with a 2M solution and treated for 2 h.

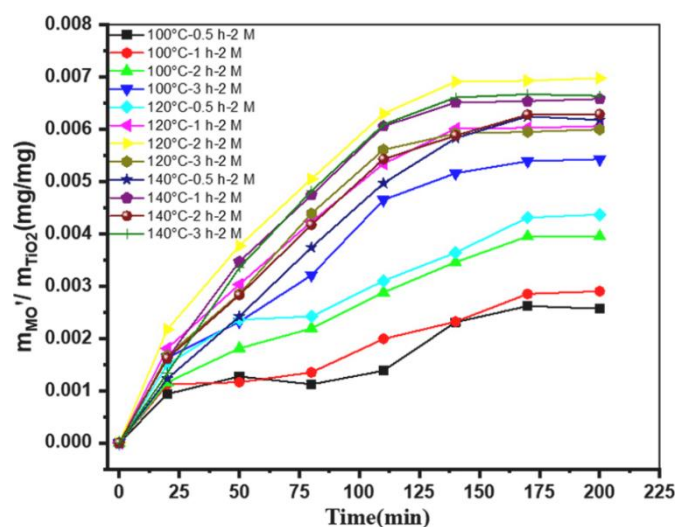


Figure 2 – The mass of MO degraded per mass of the different membranes as a function of time

The membrane was tested up to 5 cycles of degradation showing negligible variation in photocatalytic activity and no variation on the morphology of the core-shell structure thank to the high interaction between the polymeric core and the TiO₂ shell.

4. Conclusions

In this work we investigated a microwave-assisted hydrothermal method as a rapid and easy method for the deposition of TiO₂ particles on the surface of PVDF electrospun membrane to obtain core-shell fibrous membranes with photo-oxidation activity. The analysis of the acidity of the precursor solution revealed that optimum coverage of the fibers with smooth morphology can be obtained from 2 M solution. Although anatase was the predominant crystal phase the temperature influenced the rutile content both at 100 and 140°C, while at 120°C only anatase phase was observed. The obtained PVDF-TiO₂ core shell membranes showed good photocatalytic performance towards methyl orange degradation thanks to the high contact surface with the dye. The membranes also showed performance stability of multiple testing cycles and no leaching effect showing a good potential for organic pollution treatment in liquid phase.

References

- [1] K. Nakata, A. Fujishima, J. Photochem. Photobiol. C: Photochem. Rev (2012) 169-189
- [2] M. Modesti, M. Roso, C. Boaretti, S. Besco. D. Hrelja, P. Sgarbossa, A. Lorenzetti, Appl. Catal. B 144 (2014) 216-222
- [3] L.Y. Meng, B. Wang, M.G. Ma, K.L. Lin, Mater. Today Chem. 1-2 (2006) 2016-2027

Phosphorous removal and recovery from wastewater by adsorption using an innovative calcined pyroaurite

Dario Frascari^{1*}, Carla Maggetti¹, Tommaso Tabanelli², Davide Pinelli¹

¹ Dept. of Civil, Chemical, Environmental and Materials Engineering, University of Bologna, Via Terracini 28, 40131 Bologna; ² Dept. of Industrial Chemistry "Toso Montanari", University of Bologna, Viale Risorgimento 4, 40136 Bologna.

*Corresponding author E-Mail: dario.frascari@unibo.it

1. Introduction

Approximately 90% of phosphate rock is used for food production: 82% for fertilizers, 5% for animal feed, and 2–3% for food additives [1]. Furthermore, in current agricultural P utilization, nearly 90% of P is lost to the environment. Such losses enrich the P concentration in local streams, leading to environmental problems such as red tide and eutrophication. Municipal wastewaters (MWW) may contain from 5 to 20 mg/l of total phosphorous [2], making them an interesting source of P because of the possibility to simultaneously purify the water from P and recover it. Removal of ionic substances using the principle of adsorption by ion exchange resin has been used quite commonly in wastewater treatment. Adsorption guarantees full control of the effluent quality and allows P recovery, leading to a final product than might be used in fertilizer manufacture [3]. In comparison with alternative P recovery technologies, adsorption presents advantages such as operational simplicity, low capital and operational costs [4]. The choice of the adsorbent material must be done based on many parameters: capacity, selectivity, ease of regeneration, but also it must be able to bind phosphate at low concentration. This is fundamental since the MWW usually shows P concentrations around 7 mg/L, a very low concentration compared to those of other anions, such as sulfate and chloride, but with relatively high valence and weight. The consequence is that traditional ion exchange processes are not effective in removing phosphate anions. Various adsorbents and anion exchangers were found to show high adsorption capacity for phosphate ion, including metal oxides/hydroxides, hybrid anion exchangers HAIX and double-layered hydroxides LDH [5]. LDH are intensively studied due to their favorable properties such as high surface area, basicity, anion exchange properties and positive surface charge. In this work pyroaurite (used after calcination at 350°C for 5 hours), an LDH belonging to the group of hydrotalcite, has been studied as adsorbent material for the removal and recovery of P from a MWW from the purification plant of the municipality of Bologna (HERA). In particular, the research focused on (i) assessing the performances of calcined pyroaurite regarding P adsorption and desorption in batch and continuous flow tests with an actual MWW and (ii) evaluating the sorbent structure stability during 6 repeated breakthrough tests.

2. Methods

The performance of the material in terms of P adsorption has been estimated by adsorption isotherm tests, and continuous flow adsorption/desorption breakthrough tests, in a fixed-bed column packed with calcined pyroaurite. Cations analyses were performed with an HPIC method. All the procedures and methods followed are extensively described by Pinelli et al. [6]. The continuous tests were performed in a small-scale laboratory PVC column (0.40 m length, 0.013 m of diameter) packed with the adsorbent material for a height of 0.20 m.

3. Results and discussion

3.1 Adsorption Isotherm

A 9-points isotherm was performed with a real MWW effluent to investigate the performance of calcined pyroaurite in presence of competing anions. The results of the isotherm test are shown in Figure 1 in terms of

P sorbed concentration versus P the residual equilibrium concentration in the liquid. The experimental data were interpolated with the Langmuir and Freundlich models, with regression coefficient closer to 1. The experimental data showed a favorable isotherm: high solute adsorbed can be obtained even at low concentrations in the fluid. Indeed, the estimated P operating capacity at saturation resulted to be $13.1 \text{ mgP g}_{\text{dry resin}}^{-1}$.

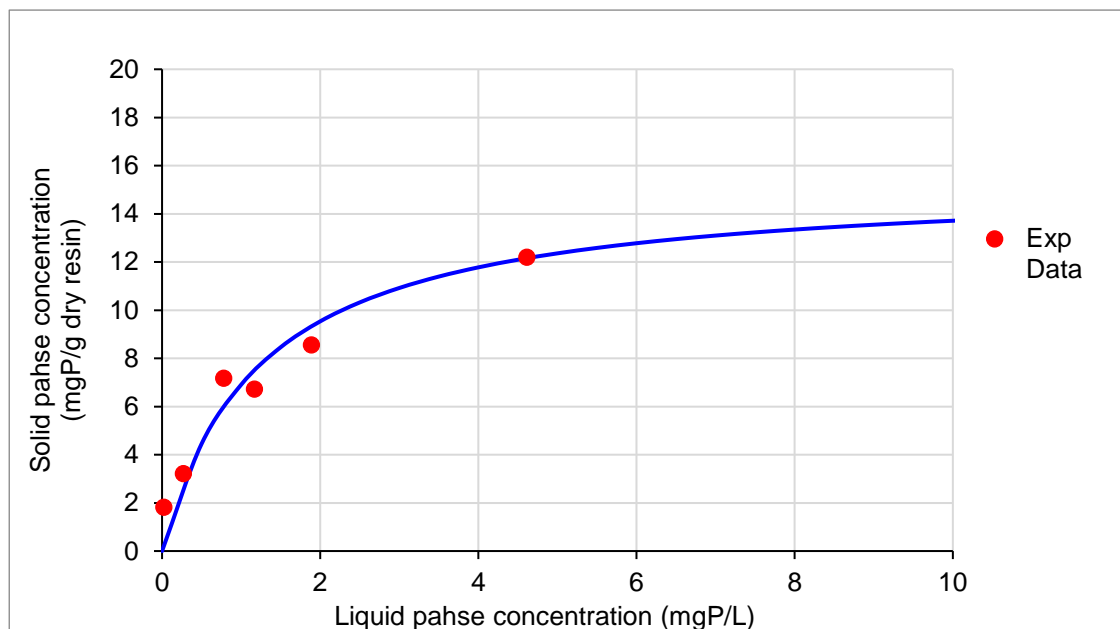


Figure 1. 9-point adsorption isotherm of calcined pyroaurite with HERA MWWT.

3.2 Continuous flow adsorption/desorption breakthrough tests

The adsorption/desorption breakthrough tests were conducted in a packed-bed column fed with the HERA WWTP effluent at 24-25°C. The adsorption phase was performed with an empty bed contact time (EBCT) of 5 min. The results obtained (Figure 2) show an excellent phosphate selectivity: all the other anions finish eluting even before the phosphate starts coming out: all the competing anions start to exit the column from 8 to 12 hours of operation (100 to 150 BVs) and their concentration became equal to the inlet one around hour 29 (350 BVs). Phosphate anions started to exit the column after about 40 h (500 BVs), meaning that large volumes of wastewater can be treated in a single adsorption cycle. The half saturation P concentration (3.5 mgP/L) has been reached after 77.5 h (928 BVs). The desorption/regeneration procedure was performed eluting the NaOH 2% with EBCT 10 min to regenerate the resin and recover the P rich product. The curves obtained (Figure 3) are partially overlapped, and this means that purity in P of the final desorbed solution cannot be expected.

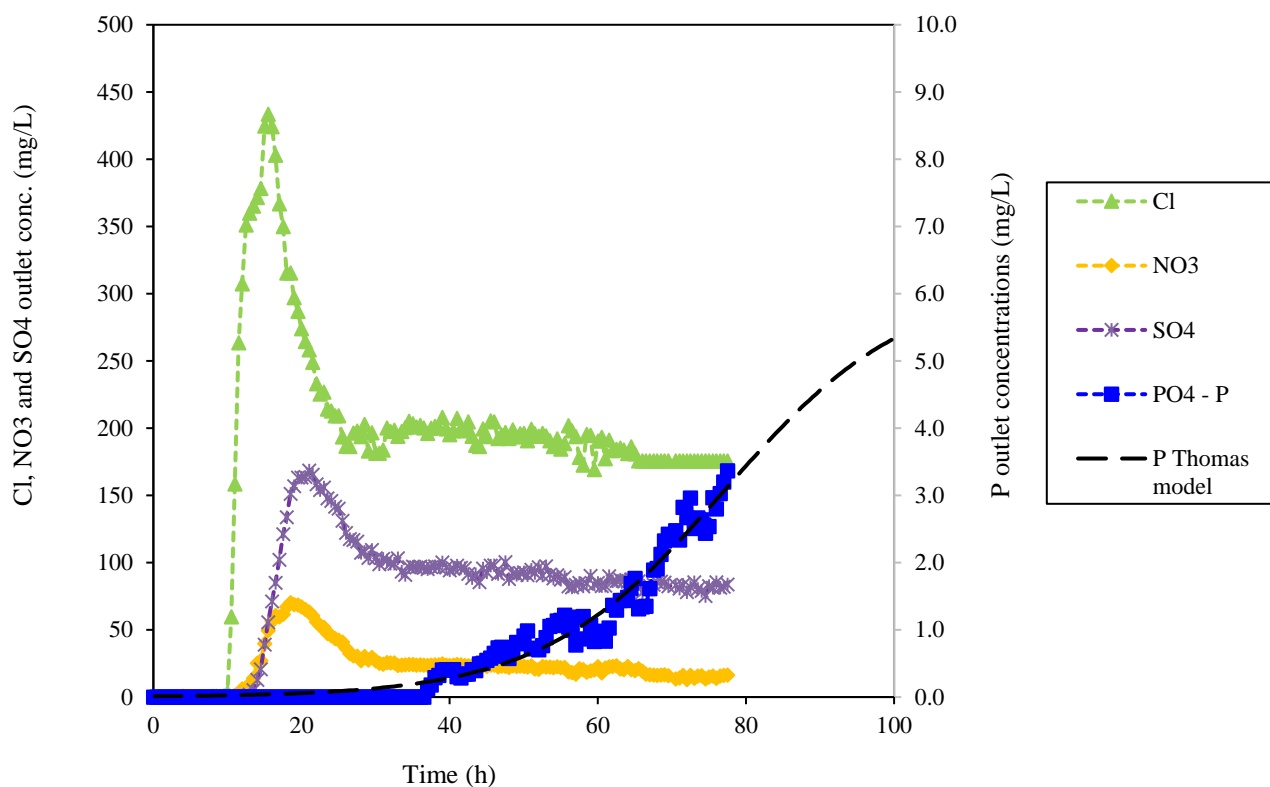


Figure 2. P adsorption continuous flow test conducted with calcined pyroaurite. Breakthrough curves of phosphorous and the competing cations obtained with P-spiked HERA WWTP effluent.

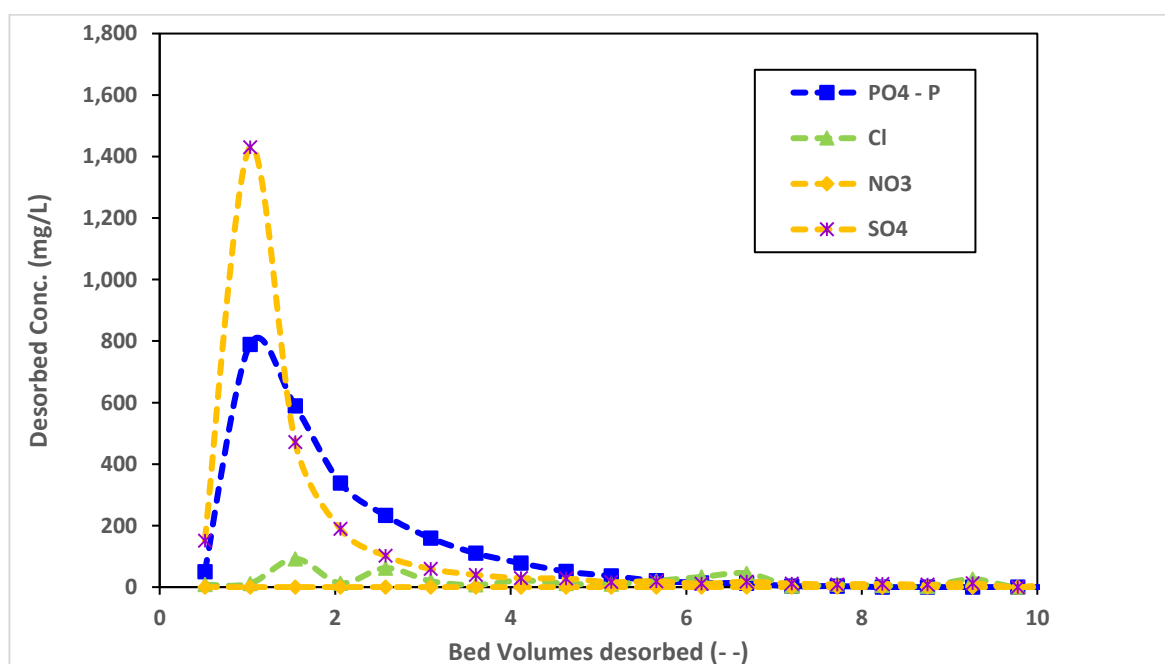


Figure 3. P desorption continuous flow test conducted with calcined pyroaurite. Breakthrough curves of phosphorous and the competing cations obtained with NaOH 2%.

To verify the repeatability of the adsorption/desorption process and the stability of the actual active phase after that the calcined pyroaurite is rehydrated, a set of 5 breakthrough tests has been conducted with the same operational conditions: the performances were similar, indicating a reproducible behavior of the process. Moreover, after the test, there was no sign of mechanical degradation of the resin, so mechanical stability and

structural integrity have been preserved, even if more tests are necessary to confirm the durability and regeneration capability of the material.

Calcined pyroaurite after 5 BTs shows very good average performances: for the adsorption phase 665 BVs of MWW effluent were treated at breakpoint BP (1mgP/L as law limits for P concentration in MWW), with an adsorption yield ($Y_{ads,P}$) of 95% and an operating capacity at BP (η_P) of 7.5 mgP/g_{dry resin}. The mean concentrations C_L at BP in the desorbed product were: 70 mgP/L for P, 81 mg/L for Cl⁻, 8 mg/L for NO₃⁻ and 257 mg/L for SO₄²⁻. The concentration factors (the ratio between the concentration in the desorbed product and that in the fresh MWW) were 32, 0.38, 0.49 and 2.99 for P, Cl⁻, for NO₃⁻ and SO₄²⁻ respectively confirming that the sorbent is very selective for P (only sulphate was partially concentrated in the desorbed product).

4. Conclusions

Calcined pyroaurite seems to be a very interesting material for P removal and recovery from MWW. The data collected after 5 breakthrough tests confirm that the process is reproducible and that, therefore, the adsorbent phase and structure is preserved after each test. The process seems to work well on a small scale with an EBCT of 5 min. BT curves of the other competing anions are well separated from the P one and the adsorbed amounts of the other anions are low, showing that the material is very selective toward P. The concentrations of the desorbed product confirm that the process leads to concentrate P by 30-70 times, sulphate by only 2-5 times, while nitrate and especially chloride dilute to less than half of the initial concentration of MWW. These are all promising results, but further tests in a pilot plant with a greater high resin bed are needed to optimize the process.

References

- [1] D. Cordell, S. White, «Life's Bottleneck: Sustaining the World's Phosphorus for a Food Secure Future», *Annu. Rev. Environ. Resour.*, vol. 39, n. 1, pp. 161–188, 2014, doi: 10.1146/annurev-environ-010213-113300.
- [2] M. Henze, *Biological wastewater treatment: principles, modelling and design*. London: IWA Pub., 2008.
- [3] S. Sengupta, A. Pandit, «Selective removal of phosphorus from wastewater combined with its recovery as a solid-phase fertilizer», *Water Res.*, vol. 45, n. 11, pp. 3318–3330, 2011, doi: 10.1016/j.watres.2011.03.044.
- [4] L. M. Blaney, S. Cinar, A. K. SenGupta, «Hybrid anion exchanger for trace phosphate removal from water and wastewater», *Water Res.*, vol. 41, n. 7, pp. 1603–1613, 2007, doi: 10.1016/j.watres.2007.01.008.
- [5] S. Gubernat, A. Masłoń, J. Czarnota, P. Koszelnik, «Reactive Materials in the Removal of Phosphorus Compounds from Wastewater—A Review», *Materials*, vol. 13, n. 15, 2020, doi: 10.3390/ma13153377.
- [6] D. Pinelli, S. Bovina, G. Rubertelli, A. Martinelli, S. Guida, A. Soares, D. Frascari, «Regeneration and modelling of a phosphorous removal and recovery hybrid ion exchange resin after long term operation with municipal wastewater». *Chemosphere* 286:131581, 2022, doi: 10.1016/j.chemosphere.2021.131581

Recycling of automotive waste for the recovery of precious and critical metals: Treasure Horizon 2020 project

Nicolò Maria Ippolito*, Marco Passadoro, Svetlana B. Zueva, Francesco Vegliò

Department of Industrial and Information Engineering and Economics – University of L'Aquila, Piazzale Ernesto Pontieri, Monteluco di Roio, 67100 L'Aquila, Italy

**Corresponding author E-Mail: nicolomaria.ippolito@univaq.it*

Electronic waste in the automotive sector is a valuable source of critical raw materials. Currently, because of the absence of dedicated European/national regulations for the recycling of car electronics components, the management practices show a low circularity level. Therefore, End-of-Life Vehicles are shredded by the dismantlers and the electronic components are not disassembled. This way of operating causes the loss of valuable and critical materials which has a negative environmental impact. Treasure Horizon 2020 project wants to support the transition of the automotive sector towards circular economy through the adoption of innovative technologies. Dedicated pilot plants exploit the advanced technologies to establish a new supply chain in the automotive sectors. Plants are related to car electronics disassembly, car electronics recycling and reuse of secondary materials from car electronics in new applications. New business opportunities will be created in the car electronic market, information on disassembly procedures will be provided to the dismantlers and the recovered materials will be reused by the carmakers to produce new electronic components for the automotive sector. University of L'Aquila is involved in the present project for the development of hydrometallurgical processes on lab-scale for different sets of critical materials (printed circuit boards, in-mold electronics, and indium tin oxide glass of LCD modules) in order to set up dedicated materials recovery processes. In addition, the reconfiguration of the pre-existing hydrometallurgical pilot plant is also planned with the aim of making it more flexible to the treatment of different types of materials and to ensure better connections with the pilot plants line. Testing and optimization of the recovery processes will be performed also on pilot scale. Based on the results, materials and energy balances will be described and technical-economic feasibility will be evaluated, taking into account also the environmental sustainability.

Multiscale modeling for the estimation of economic, energy and environmental indicators

Andrea Mio^{a,d*}, Elena Barbera^b, Alessandro Massi Pavan^{a,d}, Alberto Bertucco^{b,c},
 Maurizio Fermeglia^{a,d}

a. Department of Engineering and Architecture, University of Trieste, Italy

b. Department of Industrial Engineering (DII), University of Padova, Italy

c. Centro Studi “Levi Cases” for Energy Economics and Technology, University of Padova, Italy

d. Center for Energy, Environment and Transport Giacomo Ciamician, University of Trieste, Italy

* Corresponding author e-mail: amio@units.it

1.Introduction

One of the major challenges of the design of new processes and new products is the evaluation of indicators to support decisions makers and investors. The ultimate choice of the best process or product to be developed should be based on economic, energy and environmental indicators internationally recognized as standard and relatively easy to be calculated at design time. Such indicators are based on properties strongly related to the molecular structure of the product and to the details of the production processes of interest.

Multiscale molecular modelling is used to provide basic information for the estimation of such indicators thus allowing comparison among different products for the same application and different production processes for the same product. On one hand, the multiscale molecular modelling paradigm provides a full collection of material properties, such as mechanical, thermal, electrical, magnetic, and toxicological properties [1] as well as all the data estimated from a material and energy balance of a given production process. Multiscale molecular modelling permits all phenomena to be captured at each scale, with the essential information being transferred to the upper scale until the macroscopic system is achieved [2]. Multiscale molecular modelling, by definition, involves the generation of computational models at several length and temporal scales, which are frequently unconnected theoretically. The variety of methods and models commonly employed in the multiscale modelling hierarchy are shown in Figure 1, where the estimation of indicators methodology has been introduced on its top right corner.

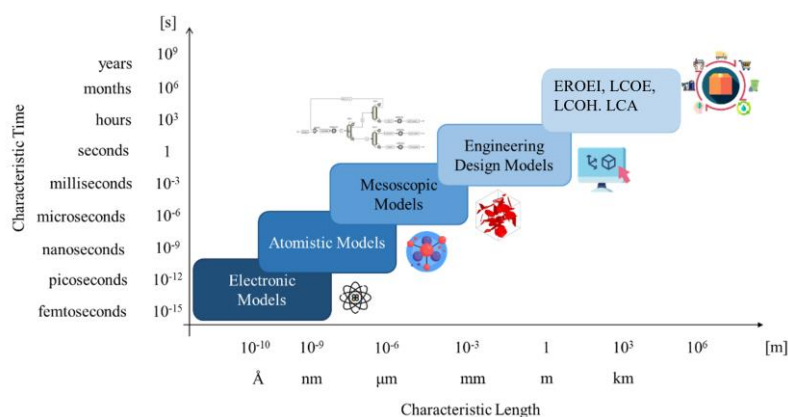


Figure 1. Multiscale molecular modelling scheme.

In the preliminary phase of the design of a new product or process, most of the relevant data for the calculation of the indicators are not available experimentally nor in the literature nor in the databases used for the estimation of the indicators. Furthermore, the accuracy of the data possibly present is missing or questionable: consequently, it is necessary to predict the properties of new products and perform material and energy balance for their production processes.

Despite the tremendous advances in the modelling of structural, thermal, mechanical and transport properties of products at the macroscopic level, there remains a high level of uncertainty about how to predict many critical properties related to advanced materials, which strongly depend on their structure.

Process simulators, an important component of the multiscale molecular modelling, emerged as powerful tools for solving the material and energy balances for any production process as well as for energy integration and costs evaluation. Specifically, they can deal with innovative processes for the production of new products involving batch operations, complex separations and reactions.

Collecting data for life cycle inventory, for instance, is generally a difficult task for practitioners. While reliable primary data is desirable, when case-specific information is lacking, it is standard practice to rely on recognized databases, such as ecoinvent [3] or Gabi [4]. However, even though current databases contain a wide range of information, data on innovative materials or unusual production methods is still lacking. In the event of insufficient data, ISO recommends using proxy inventories, i.e., the mass and energy balances of equivalent products/processes. Surely, the accuracy of the final outcomes is determined by the resemblance between the two systems. Therefore, several in-silico modelling approaches have been used to estimate LCI of products in order to reduce the inaccuracy of proxy data. Process modelling [5–6], dedicated frameworks [7], molecular structure-based models [8] or artificial neural networks [9] are some examples of computational approaches for generating raw materials inventories thus far. Similar difficulties apply also for the estimation of other indicators.

Aim of this paper is to propose a methodology for connecting the multiscale molecular modelling techniques to the main energy, economic and environmental indicators to be used for the selection of a process or a product. The methodology will be applied to two particularly relevant chemical process groups, namely the carbon capture and storage and the hydrogen production from methane steam reforming and from water electrolysis.

The paper is organized as follows: section 2 presents the methods used in this paper for the calculation of the EROEI, EROC, LCOE, LCOH and LCA; section 3 shows the results obtained with the methods previously described, applied to alternative production processes; lastly, some final considerations are reported in section 4.

2. Methods

Energy Return on Energy Invested (EROEI) and Energy Return on Carbon (EROC)

Several methods and indices can be used to assess the efficiency of production processes involving the generation of energy carriers (electricity and/or hydrogen), but the best method for comparing different energy production industries is Net Energy Analysis (NEA). The goal of NEA is to calculate whether the energy produced by any production process is greater than the energy required to build, operate and maintain the infrastructure. Among the possible indexes derived from NEA, the most suitable indicator for the processes of interest is the EROEI defined as:

$$EROEI = E_{out}/E_{in} \quad (1)$$

where E_{out} is the available energy that the process provides (which for hydrogen is the energy stored in a given quantity of hydrogen) and E_{in} is defined as:

$$E_{in} = E_{cap} + E_{o\&m} + E_f \quad (2)$$

In Eq. (2) E_{in} is the total energy that is provided and consumed during the production and operations periods of the plant and is made up of three contributions: E_{cap} is the capital energy embodied in the materials and used for construction and decommissioning of the plant; $E_{o\&m}$ is the energy needed for operating and maintaining the plant; E_f is the energy needed for procuring and distributing the fuels, which includes also the energy used for extracting, refining and transporting the fuels from the production well to the plant. All terms are expressed in GWh for consistency: the EROEI is thus dimensionless.

The Energy Return on Carbon (EROC) allows a comparison of processes under the constraint of climate change targets. The EROC is calculated as (C_{ef} is the carbon emission factor):

$$EROC = [((1 - 1/EROEI))/(C_{ef})] \quad (3)$$

Levelized cost of energy (LCOE) and levelized cost of hydrogen (LCOH)

The LCOE, which is a measure of the energy carrier generation cost, is used in order to compare different power technologies. The LCOE, which refers to electrical energy production, is calculated as follows:

$$LCOE = (OC \cdot P \cdot CRF \cdot FO\&MC) / (8760 \cdot cf) + VO\&MC \quad (4)$$

where OC [€/kW] is the overnight cost (cost per unit power produced), P [kW] is the net power output of the plant, CRF [-] the capital recovery factor, cf [-] the capacity factor, while FO&MC [€/kW/year] and VO&MC [€/kWh] are the fixed and the variable operation costs respectively. The overnight cost is calculated as the ratio between the total plant cost (TPC) and the net power output P. The CRF is:

$$CRF = \frac{i \cdot (i + 1)^L}{(i + 1)^L - 1} \quad (5)$$

where i [%] is the interest rate and L [years] is the plant life time.

The levelized cost of hydrogen (LCOH), which is used for hydrogen production processes, is an indicator specifically derived for hydrogen as an energy carrier. It is calculated as follows:

$$LCOH = \frac{(Total\ Costs - Electrical\ Revenue)}{H_2\ Annual\ Production} \quad (6)$$

Life Cycle Assessment

Following the International Standard Organization (ISO) 14040 and ISO 14044 guidelines, LCA enables practitioners to predict the potential emissions to environmental compartments (i.e., soil, water and atmosphere) coming from the system under investigation. The LCA procedure employs material and energy balances over the entire life cycle of the product system, taking into consideration the extraction of raw materials, manufacturing, use phase, end-of-life and the transportation between life cycle stages. The results of life cycle assessments are depicted by means of several impact categories, which are able to represent the entire range of ecological burdens associated with the product system, avoiding shifting the impact among environmental compartments. The LCA methodology prescribes the fulfillment of four stages as follows:

1. Goal and scope definition: this stage requires to specify the aim of the study, the system boundaries, the quality of data source, the assumptions and limitations introduced and the functional.
2. Life cycle inventory analysis (LCI): during this step, the practitioner needs to collect the mass and energy balances of the product system under investigation: the employment of primary data is preferred, since actual process data provide highest accuracy in comparison to secondary data.
3. Life cycle impact assessment (LCIA): this phase assigns specific environmental impacts to inventory data through recognized characterization factors, which typify the contribution of each substance to a determined impact category, providing harmonization on a shared unit of measure.
4. Life cycle interpretation: this stage provides an evaluation of the results obtained by previous steps: it embeds the overall LCA procedure including comments and recommendations. Usually, sensitivity analysis and uncertainty are assessed during this phase.

Table 1 summarizes the link between process simulation output and indicators' calculation methods.

		EROEI/ EROc	LCOH	LCOE	LCA
Gross power output	kW	x	x	x	x
Power energy requirement	%	x			x
Thermal power requirement	%	x			x
Net power output	kW	x	x	x	x
Total plant cost (TPC)	€		x	x	
Share of investment costs due to operation and maintenance (so&m)	%	x			
Fixed operation and maintenance costs (FO&MC)	€/kW/y		x	x	

Variable operation and maintenance costs (VO&MC)	€/kWh		x	x	
Total amount of solvent (for CCS)	kg				x

Table 1: Summary of data retrieved from process simulation for the estimation of EROEI, LCOH, LCOE and LCA.

3. Results and discussion

Carbon Capture and Storage (CCS)

The goal of this work was to assess the energetic, economic and environmental performance of natural gas-fired power plants without and with a CCS system. We integrated detailed process simulation (PS) outcomes with an evaluation of the Energy Return on Energy Invested (EROEI), the actual Levelized Cost of Energy (LCOE) and a Life Cycle Assessment (LCA). The application of comprehensive process simulations of two CCS processes suited to a Natural Gas Combined Cycle (NGCC) plant, chosen as typical of electrical energy generation from natural gas, is coupled to the above described calculation methods of indicators. We investigated two CCS processes using AspenPlus™ process simulation software: (i) a traditional one using monoethanolamine (MEA) as solvent and (ii) an innovative one based on hot potassium carbonate (HPC). The inventories of these absorption plants were not available, since CCS has not been successfully implemented at industrial scale yet. Therefore, we needed to resort to process simulation to provide the material and energy balances required for the following sustainability assessment. To ensure the greatest possible quality of the models used to forecast physical properties, a comprehensive thermodynamic and kinetic study was undertaken. Since the rigorous simulation of the NGCC was not the focus of this work, data related to material and energy balances of the power plant was retrieved in literature [20]. The process flow diagram of carbon capture from flue gases using a HPC is shown in Figure 2a, while the compression and transportation of CO₂ to the storage site is shown in Figure 2b. A detailed description of the procedure and processes is reported in [5].

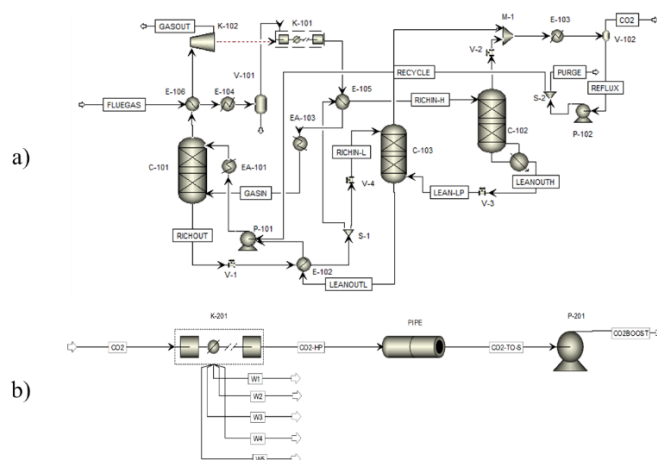


Figure 2: a) HPC carbon capture process flowsheet; b) CO₂ transport process flowsheet

Table 2 shows the results obtained for economic and energy indicators. It can be clearly noticed that at constant capacity factor, the EROEI decreases strongly when CCS is used, particularly when HPC process is used, due to the much higher energy consumption required in this CCS process. On the other hand, the effect of the higher costs of CCS reflects into an higher value of LCOE.

Process	cf	EROEI	EROC	LCOE
NGCC	0.40	17.60	16.81	78
	0.85	21.37	16.99	78
NGCC + CCS MEA	0.40	7.73	163.1	131
	0.85	12.36	167.1	102
NGCC + CCS HPC	0.40	5.21	163.1	178
	0.85	9.06	167.1	126

Table 2: calculated values of EROEI, EROC and LCOE for the processes of interest.

The LCA study shows that a comparison among 1 kWh produced using NGCC, NGCC coupled with MEA-based CCS, NGCC coupled with HPC-based CCS, photovoltaics and wind power has been performed using the environmental categories employed by Environmental Footprint (EF) v2.0 method, as shown in Figure 3.

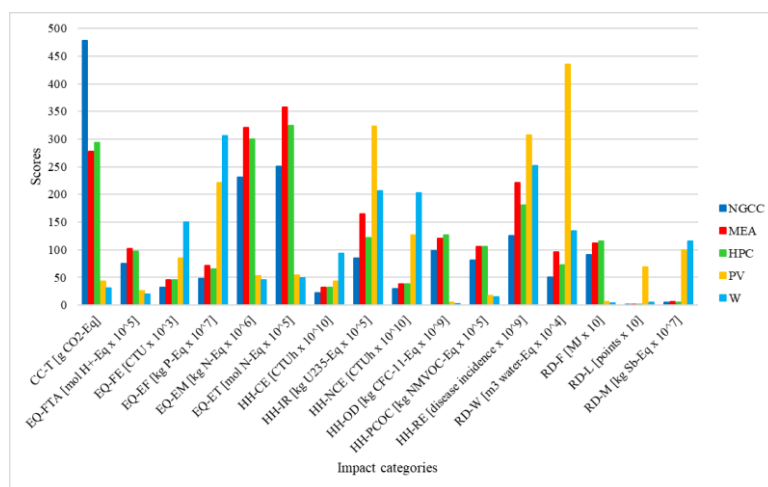


Figure 3: Impact categories scores for each power generation technology considered in this study. NGCC: Natural Gas Combined Cycle, MEA: MEA-based CCS, HPC: HPC-based CCS, PV: photovoltaics, W: wind.

It can be shown that natural gas use, in terms of extraction, refining, transportation, and burning, drives many impact category outcomes. Indeed, the largest impacts of HPC-based CCS on resource depletion of fossil fuels (RD-F) and human health (HH-OD and HH-PCOC) may be attributable to the configurations' maximum energy consumption. According to process modelling, this is due to the energy required for the compression of the high flow rate of flue gas, which exceeds the one required for MEA regeneration. Climate change (CC-T), like the previous impact categories, is linked to natural gas combustion. However, in this instance, owing to the carbon capture process, NGCC emerges as the worst option. Given that the development of CCS is motivated by the need to reduce greenhouse gas emissions as measured by CC-T, it is evident that renewable technologies, such as photovoltaic or wind installations, perform better than CCS in this regard. In fact, in terms of numerous impact categories (including climate change CC-T), it is worth noting how photovoltaic and wind installations have extremely low impacts when compared to fossil-fuel-based technologies. However, care must be taken to avoid burden shifting between the diverse natural compartments. The results of several sensitivity analyses were then used to examine various scenarios related to some assumptions adopted through the assessment. Sensitivity analyses dealt with natural gas power plant operating conditions, ranging over capacity factor, natural gas specific consumption and CO₂ specific emission. Despite the fact that impact categories values varied owing to parameter changes, the essential analysis previously stated on the benefits and downsides of each technology was confirmed, since sensitivity analyses had no effect on relative performance among the numerous options.

Hydrogen production process

The following processes have been simulated using Aspen plus™ 12.0: (i) water electrolysis (Figure 4), (ii) methane steam reforming (Figure 5) and carbon capture and storage (Figure 2).

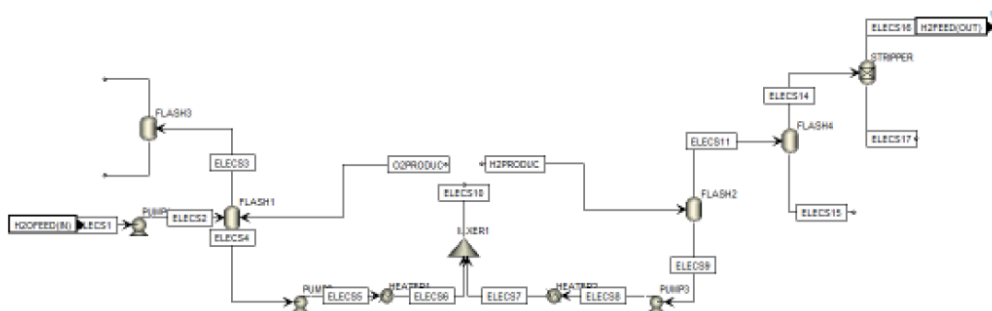


Figure 4. Water Electrolysis process flowsheet within Aspen Plus™.

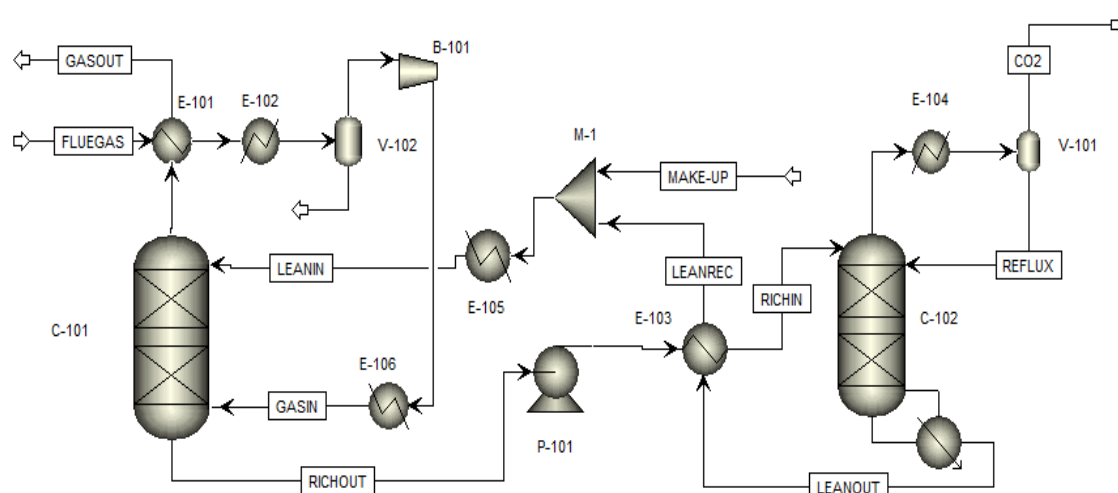


Figure 5: Methane steam reforming process flowsheet within Aspen Plus™.

Material and energy balance data coupled with cost estimation obtained by process simulation software are used to calculate the performance indicators: the detail of the data transferred from the process simulation are reported in Table 1. Values of the key performance indicators, namely EROEI, LCOH and LCA, indicates that the best route for producing hydrogen in terms of global impact is the green hydrogen. Table 3 shows as an example a comparison among EROEI values for the processes of interest.

	MSR	MSR & CCS	Electrolysis
Eout [GWh]	2,369.572	1,871.962	2,391.152
Ecap [GWh]	5.746	7.783	4.466
Eo&m [GWh]	6.895	9.340	5.359
Ef [GWh]	296.197	267.423	95.646
EROEI	7.8	6.58	22.67

Table 3: EROEI for methane steam reforming with and without CCS and water electrolysis hydrogen production processes.

4. Conclusions

The goal of this study is to demonstrate how in-silico techniques may be used to generate data to be used for the evaluation of different indicators: EROEI, LCOE, LCOH, LCA. The integration of indicators' evaluation into a multiscale molecular modeling framework produces a double benefit: i) we extended the scope of multiscale molecular modelling by taking the most comprehensive approach feasible, and ii) future evaluation applications, may benefit of this cutting-edge approach. This study shows how process simulation plays a fundamental role in providing material and energy balances as well as energy and costs information for the evaluation of the required indicators already at design time.

References

- [1] Fermeglia M, Mio A, Aulic S, Marson D, Laurini E, Pricl S.. Mol Syst Des Eng 2020; 5:1447–76.
- [2] Laurini E, Marson D, Aulic S, Mio A, Fermeglia M, Pricl S., Chem. Eng Trans 2019; 74:619–24.
- [3] Wernet G, Bauer C, Steubing B, Reinhard J, Moreno-Ruiz E, Weidema B., Int J Life Cycle Ass. 2016;21:1218–30.
- [4] PE-International. Gabi Database 2012.
- [5] Barbera E, Mio A, Massi A, Bertucco A, Fermeglia M. . Submitted 2021.
- [6] Petrescu L, Burca S, Fermeglia M, Mio A, Cormos CC., J Water Process Eng 2021;41.
- [7] Lodato C, Tonini D, Damgaard A, Fruergaard Astrup T., Int J Life Cycle Assess 2020;25:73–88.
- [8] Gonzalez-Garay A, Guillen-Gosalbez G. SUSCAPE., Chem Eng Res Des 2018;137:246–64.
- [9] Calvo-Serrano R, González-Miquel M, Papadokonstantakis S, Guillén-Gosálbez G., Comput Chem Eng 2018;108:179–93.

Techno-economic and life cycle assessment for the industrial implementation of hydrothermal liquefaction coupling with aqueous phase reforming

Edoardo Tito¹, Giulia Zoppi¹, Giuseppe Pipitone^{1*}, Edoardo Miliotti², Arturo Di Fraia², Andrea Maria Rizzo², Samir Bensaid¹, Raffaele Pirone¹, David Chiaramonti^{2,3}

¹ *Department of Applied Science and Technology, Politecnico di Torino, Corso Duca degli Abruzzi 24, 10129, Turin, Italy*

² *Renewable Energy Consortium for R&D (RE-CORD), Viale Kennedy 182, 50038, Scarperia e S. Piero, Florence, Italy*

³ *Energy Department DENERG, Politecnico di Torino, Corso Duca degli Abruzzi 24, 10129, Turin, Italy*

**Corresponding author E-Mail: giuseppe.pipitone@polito.it*

1. Introduction

Hydrothermal liquefaction (HTL) has shown to be an interesting technology for producing renewable advanced biofuels. HTL works in aqueous environment close to critical water conditions (374 °C, 22.1 MPa) and allows the conversion of waste biomass into an oil-like phase called biocrude. This phase is highly oxygenated and requires upgrading to produce a drop-in biofuel. Moreover, in addition to the biocrude, char, a gas phase and an aqueous phase are also produced as by-products, reducing the overall carbon recovery of the process. Thus, for an effective industrial application of HTL, it is critical to address the significant carbon loss in the aqueous phase (AP) and the need for biocrude upgrading [1]. In this work, we evaluated coupling hydrothermal liquefaction (HTL) with aqueous phase reforming (APR). APR is a catalytic process capable of converting the oxygenates contained in the aqueous stream into a hydrogen-rich gas, without requiring the energy-intensive vaporization of the feed. The gas thus produced can be used as an internal hydrogen source for the biocrude upgrading. In this work, a techno-economic assessment was performed for an HTL-APR integrated plant to produce biofuel. This allows to assess the feasibility of this novel integration and identify weaknesses that must be overcome in order to move to commercial-scale implementation. Finally, a life cycle assessment (LCA) was performed to assess the environmental impact of this technology as well.

2. Methods

Two cases were proposed, based on different lignocellulosic feedstocks: corn stover (CS), representative of several agricultural wastes that can be exploited, and lignin-rich stream (LRS), as by-product from cellulosic ethanol production. HTL-APR integrated plants were sized to work with a mass flow rate of 3.6 t/h and 10 wt.% of solid loading (input nameplate capacity of 20 MW for LRS and 16.5 MW for CS). Starting from mass and energy balances, the design of the main unit was performed; the calculations were based both on experimental data and the literature. The economic evaluation was carried out by calculating economic indicators: minimum selling prices (MSPs) and hydrogen production costs. The environmental analysis was carried out with LCA methodology (ISO 14040 and ISO 14044) [2]. The software GABI was used, and the impacts were evaluated by ILCD v1.09 method through to the global warming potential (GWP).

3. Results and discussion

With the LRS case, APR was able to supply 21% of the H₂ required for the biocrude upgrading. On the other hand, with the CS case this value increased up to 165%. The improved coupling in the latter was due to the coexistence of some factors: higher hydrogen productivity from the organics dissolved in HTL-derived wastewater, lower biocrude production, and lower oxygenation of the biocrude. The minimum selling prices, (internal rate of return 0%), for the two biofuels were 1.27 €/kg for LRS and 1.23 €/kg for CS. Despite, the higher biofuel production rate of the former, the lower value of the latter was justified by the much lower H₂ production cost through APR: 1.7 €/kg (CS) against 7.6 €/kg (LRS). The economic advantage deriving from the HTL-APR coupling was further assessed by evaluating the variation on the MSPs removing the APR section and using instead two established hydrogen production technologies: methane steam reforming (SR) and electrolysis (Figure 1). Unlike the LRS, with the CS the use of APR as hydrogen source showed lower

MSP than both SR and electrolysis. These results reveal that the HTL-APR integrated plant is a valid technology to internally produce the hydrogen required for biofuel upgrading, being the hydrogen production cost lower than that of electricity-intensive electrolysis and comparable to that of fossil-based SR.

Regarding the LCA, the two cases had similar impacts (Figure 2). Despite the lower thermal and electrical demand of the LRS case compared to the CS case, its impact was highly dependent on the supply of the hydrogen missing share. To allow a comparison with other biofuels the GWP was based on 1 MJ of biofuel; for this purpose the LHV was assumed as diesel (43 MJ/kg). The resulting CO₂eq/MJ was comparable with values for other biofuels.

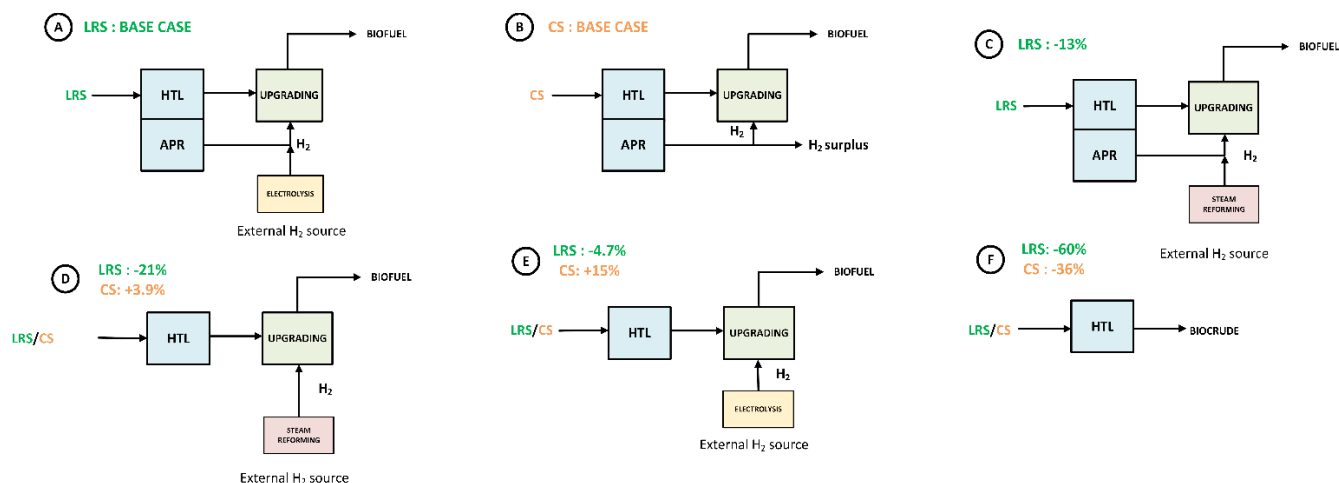


Figure 1. Plant configurations for hydrogen supply. A) APR+electrolysis, B) APR alone, C) APR+SR, D) SR alone, E) Electrolysis alone, F) No upgrading. The percentage values refer to the variation of the MSP of the considered configuration compared to the respective base case (A for LRS and B for CS).

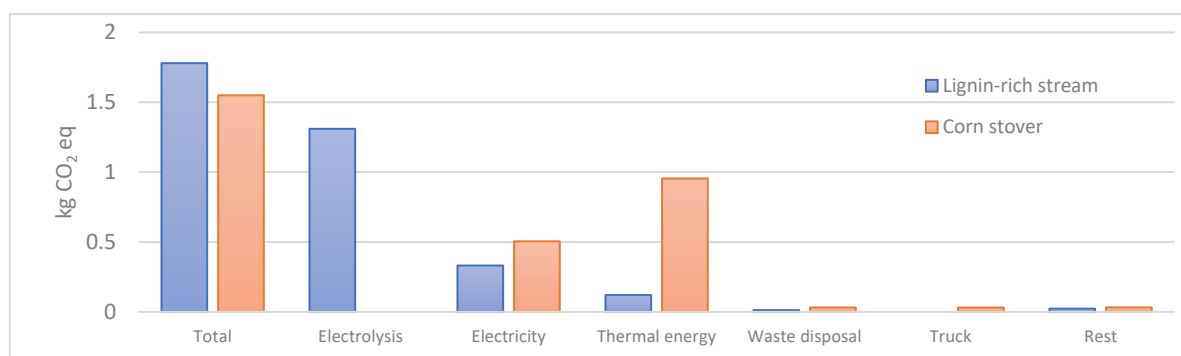


Figure 2. GWP for the CS and the LRS case based on 1 kg of biofuel. Subdivision among the different impact items.

4. Conclusions

HTL-APR coupling has been proven to be a valuable technology for biofuel production from an economic standpoint. In particular, this work has shown that the coupling is strongly dependent on the HTL carbon distribution and on the nature of the molecules dissolved in the HTL aqueous phase. H₂ production cost through APR was particularly interesting with corn stover, being it equal to 1.7 €/kg, which is lower than production cost through electrolysis. The GWPs for these two biofuels resulted in line with other biofuels.

References

- [1] J. Watson, T. Wang, B. Si, W. T. Chen, A. Aierzhati, and Y. Zhang, *Prog. Energy Combust. Sci.* 77 (2020) 1-45
- [2] European Commission-Joint Research Center, *ILCD Handbook: General guide for Life Cycle Assessment - Detailed guidance* (2010)

Energy valorisation of municipal sewage sludge for the production of renewable liquid fuels through the hydrothermal liquefaction process

Francesca Di Lauro^{1,*}, Marco Balsamo¹, Roberto Solimene², Piero Salatino³, Fabio Montagnaro¹

1 Dipartimento di Scienze Chimiche, Università degli Studi di Napoli Federico II, Complesso Universitario di Monte Sant'Angelo, 80126 Napoli, Italy

2 Istituto di Scienze e Tecnologie per l'Energia e la Mobilità Sostenibili, Consiglio Nazionale delle Ricerche, Piazzale Tecchio 80, 80125 Napoli, Italy

3 Dipartimento di Ingegneria Chimica, dei Materiali e della Produzione Industriale, Università degli Studi di Napoli Federico II, Piazzale V. Tecchio 80, 80125 Napoli, Italy

*Corresponding author E-Mail: francesca.dilauro2@unina.it

1. Introduction

The growing energy demand, together with necessity to reduce greenhouse gases emissions related to the power sector, has led in recent years to an increasing interest in renewable energies sources, alternative to traditional fossil fuels. In this context, the municipal sewage sludge represents an interesting biomass to develop efficient waste-to-energy techniques to reduce the volumes and environmental impacts of wastes commonly disposed of in landfills. However, the solid content in the municipal sewage sludge (mainly constituted by proteins, carbohydrates and lipids) is typically in the range of 10–20%_{wt}, and the energy content is low (higher heating value (HHV) of 10–25 MJ/kg on a dry basis). Thus, it is necessary to convert the organic matrix into high-energy-content fuels, in particular liquid ones required for many applications such as in the transport sector [1]. The production of bio-oil as liquid bio-fuel through the hydrothermal liquefaction (HTL) process is of particular interest, especially when applied to biomass with high moisture content, since the water in sub-critical state acts as solvent, catalyst, and reaction medium, and allows to convert the wet biomass into liquid fuels by processing it in a hot, pressurised water environment (250–350 °C and 15–220 bar). The HTL process enables the breaking down of the biopolymeric structure and the production of a liquid bio-oil as energy vector [2,3]. The target bio-oil is produced together with an aqueous phase, a bio-char and a gas phase [4]. In this study, HTL tests, carried out in batch autoclave reactors, were performed on a municipal sewage sludge to evaluate the yield of both the target bio-crude and other by-products at two different temperature levels.

2. Methods

The main properties of the municipal sludge used in this work are reported in a previous work [5]. Briefly, the sludge has a C, moisture and ash content of 34.6%, 12.1% and 21.2%, respectively, while its HHV is 13.5 MJ/kg. Prior to the HTL tests, the biomass was dried in an oven at 105 °C, until no change in weight was observed. HTL tests were carried out in a 500 mL Hastelloy C-276 batch reactor (Parr Instruments, series PA 4575A). The reactor was loaded with 30 g (dry basis) of a municipal sludge together with 270 mL of distilled water so to obtain a slurry with a 10%_{wt} solid content, enabling to reproduce the typical sludge concentration value obtained downstream of wastewater treatment plants. Then, the reactor was purged four times with N₂ at 5 bar to remove the O₂ present in the vessel. The following stages are thereafter performed: i) first pressurisation stage with N₂ fed; ii) second pressurisation stage at 200 bar by rapid heating of the system to the desired temperature; iii) running the HTL test at fixed temperature/time (300 °C and 350 °C – 20 min); iv) fast cooling of the reactor so to quench chemical reactions; v) depressurisation of the reactor. After the HTL test, the pressure difference measured between stages i) and iv) allowed to estimate the gas yield from van der Waals equation, considering that the produced gas is mainly composed by CO₂ [2]. Then, the gas phase was vented to the atmosphere to restore ambient pressure and allow reactor discharge. The liquid and solid phases were recovered from the vessel with a spatula, and 30 g of dichloromethane (DCM) were added to maximise the products recovery. Subsequently, the slurry was filtered on a Büchner under vacuum. After filtration, the solid phase was subjected to a Soxhlet extraction with DCM to recover the bio-oil from the solid pores, while the liquid phase was separated into bio-oil and aqueous phase in a separating funnel. Finally, the bio-oil fraction

obtained from the Soxhlet extraction and separating funnel underwent a distillation step with DCM (under vacuum at 30 °C and 0.45 bar), and subsequently weighed to estimate its yield. The bio-oil, solid and gas yields Y were calculated according to, respectively:

$$Y_{bio-oil} = \frac{m_{bio-oil}}{m_{biomass,dafb}} \cdot 100 \quad (1)$$

$$Y_{solid\ residue} = \frac{m_{solid\ residue,db}}{m_{biomass,db}} \cdot 100 \quad (2)$$

$$Y_{gas} = \frac{m_{gas}}{m_{biomass,dafb}} \cdot 100 \quad (3)$$

where $m_{bio-oil}$, $m_{solid\ residue}$, m_{gas} and $m_{biomass}$ represent the mass of bio-oil, solid residue, gas, and starting sludge, respectively. The subscripts “*db*” and “*dafb*” refers to dry basis and dry ash-free basis, respectively.

3. Results and discussion

Table 1 reports the effect of reaction temperature (300 and 350 °C) on the yields of bio-oil, solid residue and gas (taking into account that the gas produced by the HTL process is mainly composed by CO₂) products at a fixed reaction time of 20 min. $Y_{bio-oil}$ and Y_{gas} both increase by about 10% (in absolute terms) as the temperature rises from 300 °C to 350 °C. This result is likely linked to the favourable effect of the temperature increase in promoting the reactive pathways that determine the fragmentation of organic compounds to give the desired bio-oil and promote the production of gas via gasification reactions and secondary decompositions. Accordingly, the temperature increase determines a reduction of the solid residue yield from 33.6% to 25.9%. In this context, it should be emphasised that the solid fraction derives from multiple contributions: the inorganic fraction of the parent biomass (which could partially dissolve in the water medium as a function of the HTL conditions), an unreacted organic fraction of the starting matrix and the char fraction formed as a result of the HTL process through the recombination of free radicals.

Table 1. Yield of target bio-crude and other by-products at different temperature (runs performed in duplicate).

HTL Temperature [°C]	$Y_{bio-oil}$ [%]	Y_{gas} [%]	$Y_{solid\ residue}$ [%]
300	27.9 ± 1.4	5.6 ± 1.1	33.6 ± 0.9
350	38.3 ± 0.4	15.5 ± 1.1	25.9 ± 1.2

4. Conclusions

In this work, preliminary HTL tests were carried out on a municipal sludge to evaluate the yield of products at two different temperature levels. Best results were obtained in terms of bio-oil yield for the test conducted at 350 °C where, on dry and ash-free basis, $Y_{bio-oil}$ is 38.3% with a relative increase of about 37% with respect to the test performed at 300 °C. On the other hand, higher temperatures also promote the formation of the gaseous phase, whose yield increase from 5.6% at 300 °C to 15.5% at 350 °C. Future studies will focus on a more detailed study of the effect of operating conditions on the bio-oil yield and quality.

References

- [1] A.R.K. Gollakota, N. Kishore, S. Gu, *Renew. Sust. Energ. Rev.* 81 (2018) 1378–1392.
- [2] R. Mujahid, A. Riaz, R. Insyani, J. Kim, *Fuel* 262 (2020) 116628.
- [3] I.A. Basar, H. Liu, H. Carrere, E. Trably, C. Eskicioglu, *Green Chem.* 23 (2021) 1446.
- [4] T. Rahman, H. Jahromi, P. Roy, S. Adhikari, E. Hassani, T.S. Oh, *Energy Convers. Manag.* 245 (2021) 114615.
- [5] A. Cammarota, F. Cammarota, R. Chirone, G. Ruoppolo, R. Solimene, M. Urciuolo, *Combust. Sci. Technol.* 191 (2019) 1661–1676.

Hydrothermal liquefaction of sewage sludge: towards the effects of transition metals in the presence of homogeneous hydrogen producers

Claudia Prestigiacomio^{1,*}, Joscha Zimmermann², Ursel Hornung², Klaus Raffelt², Nicolaus Dahmen², Onofrio Scialdone¹, Alessandro Galia¹

1 Dipartimento di Ingegneria, Sezione Chimica Ambientale Biomedica Idraulica e dei Materiali, Università degli Studi di Palermo, Viale delle Scienze, 90128 Palermo, Italy.

2 Institute of Catalysis Research and Technology (IKFT), Karlsruhe Institute of Technology, Eggenstein-Leopoldshafen 76344, Germany

**Corresponding author E-Mail: claudia.prestigiacomio01@unipa.it (Dr. Claudia Prestigiacomio)*

1. Introduction

Waste carbonaceous matrices, such as sewage sludge (SS) seem to have a great potential, because they are namely costless matrices compared to the microalgae and hydrothermal liquefaction (HTL) can be considered an interesting route to dispose and valorize them [1-5]. However, SS are characterized by high amount of non-biogenic fractions, such as plastics, salts and metals. In particular SS contains a high amount of inorganics [5], such as Al, Ba, Ca, Cr, Cu, Fe, Ni, K, Mg, Mn, Na, P, S, Ti, Zn, Si which are distributed in the products at the end of the reaction. The presence of heavy metals represent a big challenge for the implementation of HTL on the industrial scale as they can affect product quality and/or the performances of the process. One of the hurdles of the transfer of the HTL from the lab to an industrial plant fed by SS is represented by the fact that the metals in the feedstock can be transferred to the biocrude (BC) affecting its placing on the market [6]. Some studies analyzed the distribution of metals in the phases produced by HTL of real SS and the main evidence was that the higher the reaction temperature, the higher is the fraction of metals entrapped in the produced BC [5, 7]. However, metals can positively affect the process behavior acting as catalysts [5]. Among the metals contained in residual biomass [6-8], Ni, Zn and Fe were selected as model compounds in this work and a systematic investigation was conducted to study their effect, individually and combined with homogenous hydrogen producer as formic acid (FA) and KOH, on the biocrude yield and quality.

2. Methods

SS provided by the wastewater treatment plant of Karlsruhe, Germany were used in HTL experiments. FA and KOH were selected as homogeneous additives. A slurry at 10% w/w of dry SS was used as feedstock and the metal powders of Ni, Fe and Zn and the homogeneous additives were added at 10% w/w (based on dry SS). Batch runs were performed at 350°C for 10 min in an AISI 316Ti high-pressure reactor with an internal volume of 25mL, processing 10 g of slurry in each experiment. A sand bath was used to heat the reactor until 350°C. The procedures adopted to separate the products downstream of HTL experiments were an optimization of those used in a previous work [2].

3. Results and discussion

Interesting results were obtained with Zn that when used alone or in the presence of KOH increased the cumulative biocrude yields from 29 to 42 and 46 % w/w respectively and resulted in energy recoveries (ER) higher than 100%. These results were accompanied by an improvement of the values of H/C and O/C of BC from 1.61 to 1.81 and from 0.13 to 0.06 respectively when Zn was added to the reaction mixture. Moreover when Zn was used with FA it strongly enhanced gas yield from 10 to 66% w/w leading to a significant hydrogen production that was determined to be generated mainly from SS or water. In fact, it is known that

Zn could react with sub/supercritical water promoting the production of molecular hydrogen inside the reactor [9]. Ni chips were used in two consecutive HTL experiments with no decrease of BC yields and ER.

4. Conclusions

According to results obtained in our study Zn, Ni and Fe powders used alone do not affect negatively the quality of BC and their effect can be improved by adding KOH or FA.

More in detail, it was found that:

- Zinc alone and in the presence of KOH, can promote improvement of BC yield and quality in terms of ER, H/C and O/C,
- Iron added in the presence of FA, was active in producing a BC with higher H/C and lower O/C, even it does not exhibit any positive effect on BC yield;
- Nickel in the metallic form was found stable in the HTL reactor after two HTL cycles.

Collected results suggest that metallic powders can be good catalyst to improve yield and quality of BC in the HTL of SS.

References

- [1] F. Lemoine, I. Maupin, L. Lemée, J.M. Lavoie, J.L. Lemberon, Y. Pouilloux, L. Pinard, *Bioresource Technology*. 142 (2013) 1–8.
- [2] C. Prestigiacomo, V.A. Laudicina, A. Siragusa, O. Scialdone, A. Galia, *Energy*. 201 (2020).
- [3] C. Prestigiacomo, P. Costa, F. Pinto, B. Schiavo, A. Siragusa, O. Scialdone, A. Galia, *Journal of Supercritical Fluids*. 143 (2019) 251–258.
- [4] A. Ali Shah, S. Sohail Toor, T. Hussain Seehar, K.K. Sadetmahaleh, T. Helmer Pedersen, A. Haaning Nielsen, L. Aistrup Rosendahl, *Fuel*. 288 (2021).
- [5] Y. Zhai, H. Chen, B.B. Xu, B. Xiang, Z. Chen, C. Li, G. Zeng, *Bioresource Technology*. 159 (2014) 72–79.
- [6] H.J. Huang, X.Z. Yuan, *Bioresource Technology*. 200 (2016) 991–998..
- [7] P. Manara, A. Zabaniotou, *Renewable and Sustainable Energy Reviews*. 16 (2012) 2566–2582.
- [8] C. Prestigiacomo, F. Proietto, V.A. Laudicina, A. Siragusa, O. Scialdone, A. Galia, *Energy*. 232 (2021).
- [9] B. de Caprariis, M.P. Bracciale, I. Bavasso, G. Chen, M. Damizia, V. Genova, F. Marra, L. Paglia, G. Pulci, M. Scarsella, L. Tai, P. de Filippis, *Science of the Total Environment*. 709 (2020).

Synthetic and natural surfactants for environmental applications using SEAR technology: process study by column continuous test

Berardino Barbati¹, Neda Amanat¹, Marco Bellagamba², Marco Buccolini², Marco Petrangeli Papini¹

¹ Department of Chemistry, Sapienza University, P.le Aldo Moro 5, 00185, Rome, Italy;

² Chimec SpA, Via Ardeatina, 0007, Pomezia, Italy,

*Corresponding author E-Mail: berardino.barbati@uniroma1.it

1. Introduction

Soils and aquifers contamination by Non-Aqueous Phase Liquids (NAPLs) is a serious problem on a global scale, due their strong toxicity [1, 2]. NAPLs are hydrophobic organic pollutants, characterized by a very low solubility and immiscibility in water and a high tendency to accumulate in the soil organic fraction [3]. NAPLs are classified into dense (DNAPLs) and light (LNAPLs) if the density is greater or less than water, respectively [4]. Among the DNAPLs, chlorinated solvents (ethanes, ethenes and chlorinated methanes) are certainly the compounds most widely identified, while LNAPLs are complex petroleum hydrocarbon mixtures [5, 6].

After a spill, NAPLs migrate downward through the vadose zone and remain trapped in the pore space at residual saturation by capillary forces in the form of separate phase droplets or ganglia [7]. Light NAPLs float at the water table, while DNAPLs can penetrate the water table and migrate downward the aquifer [8]. The groundwater flowing in contact with non-aqueous organic liquid phase causes a slow dissolution of pollutants, generating an aqueous plume that moves in the same direction of groundwater, resulting in long-term persistent sources of aquifers contamination [9]. Moreover, particularly in cases of historical contamination by NAPLs, become relevant the processes of molecular diffusion and adsorption of contaminants (present in a separate phase or dissolved in water) in low permeability layers. These layers can act as slow-release secondary sources due to slow back-diffusion and desorption processes which cause the return of contaminants in aqueous phase, triggering the so-called rebound phenomenon [10]. Therefore, the chemical-physical properties of NAPLs, the presence of a trapped and immobile non-aqueous phase, the heterogeneity of the subsoil and the rebound effect make the efficiency of conventional remediation technologies, such as Pump and Treat (P&T) very low [11]. In this regard, during the last years a great attention has been given to the development of innovative technologies that can greatly increase the mobilization of pollutants and, among these, the Surfactant-Enhanced Aquifer Remediation (SEAR) technology, based on *in-situ* soil flushing or *ex-situ* soil washing processes enhanced with surfactants solution, has been proved to be an efficient method for remediation of source areas containing hydrophobic organic compounds, such as NAPLs [12]. Surfactants are able to increase NAPLs mobilization by reducing interfacial tension between immiscible fluids and increasing apparent solubility of poorly soluble compounds by micellation at or above critical micelle concentration (CMC) [14, 15]. Thanks to these properties, SEAR technology may offer several advantages compared with P&T, like the greater efficiency in NAPLs recovery, lower costs, and greater activity on low permeability areas with the possibility of overcoming the rebound effect [16, 17].

The present work is focused on the operative context of contaminated aquifer remediation using SEAR technology. The aim of the research is the evaluation of potential applicability of two selected surfactants as mobilizing agents for adsorbed NAPLs in conditions representative of a real technological approach. In this regard, a continuous column test was carried out in which, under laboratory-controlled condition, a soil flushing process was simulated. In the experimentation toluene for LNAPLs and perchlorethylene (PCE) for DNAPLs were used as reference contaminants. Two sugar-based surfactants, belonging to the families of synthetic alkyl-polyglycosides (APG) and natural rhamnolipids (RL) was investigated, because in a previous study they had shown very low CMC values ($7 \cdot 10^{-3}$ %wt and $1.73 \cdot 10^{-2}$ %wt, respectively) and high capacity to reduce the adsorption of NAPLs on a reference adsorbent material.

2. Methods

For continuous test, plexiglas (PMMA) columns (13 cm height \times 2.6 cm internal diameter) equipped with two sampling points, door IN and OUT, respectively at the entry and the exit of the column, were used. Pine-wood biochar (PWB) was selected as reference sorbent material. It was mixed with silica sand in quantities equal to 4 wt% (equivalents to about 2 g of reactive material). In detail, the first and the last 3 cm of the column were filled only with sand to make the liquid phase front homogeneous in the central reactive zone (7 cm of bed height). A peristaltic pump was used to feed the column upwards at 0.6 mL min^{-1} as flow rate. Figure 1 illustrates a schematic draw of the experimental configuration. A total of six columns were set up, differentiated by type of used contaminant and flushing solution. Table 1 summarizes the test conditions in terms of contaminant and mobilizing agent used.

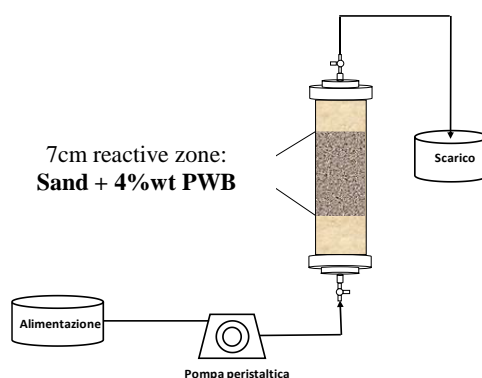


Figure 1. Experimental configuration of the fixed-bed column.

Table 1. Details of the set-up fixed-bed systems in terms of contaminant and flushing solution used.

Columns	Contaminant	Flushing solution
Toluene-APG	Toluene	APG2 (C=5x CMC), synthetic
Toluene-RL	Toluene	RL2 (C=5x CMC), natural
Toluene-H₂O	Toluene	Tap water (reference)
PCE-APG	Perchloroethylene (PCE)	APG2 (C=5x CMC), synthetic
PCE-RL	Perchloroethylene (PCE)	RL (C=5x CMC), natural
PCE-H₂O	Perchloroethylene (PCE)	Tap water, (reference)

A tracer test with Br^- was first performed to obtain the residence time (HRT), the porosity (ϵ), and the pores volume for each column. The experimental procedure was carried out in two consecutive steps. In the first *contamination phase*, each column was fed with a synthetic solution of toluene or PCE at concentration of 100 mg L^{-1} until the exhaustion of bed adsorption capacity when the outlet concentration (C_{out}) was equal to that of the input (C_{in}). In *flushing phase* columns feeding was a surfactant solution at concentration five time of CMC or tap water as reference test (details in Table 1). Flushing phase was stopped when the outlet concentration was about 5-6% respect the inlet in previous contamination phase. To monitor the system, samples of influent and effluent were daily collected and analyzed in gas chromatograph with FID detector.

3. Results and discussion

The contamination phase was monitored by reporting the concentration at the outlet normalized with the concentration in the inlet ($C_{\text{out}}/C_{\text{in}}$) as a function of the pore volume of contaminated water passed through the system. Then, the breakthrough curve was obtained (Figure 2a). Whereas, for the flushing phase curve (Figure 2b and 2c), the concentration at the outlet (C_{out}) is reported against the pore volume. From the area over the breakthrough curve and the area under the flushing curve it was possible calculate adsorbed and mobilized

contaminant mass, respectively. Lastly the yield of removal (%R) was calculated for all columns. from the ratio between the amounts of mobilized and adsorbed contaminant.

When flushing is carried out with surfactants, it is possible to see a rapid increase in the outlet concentration, as shown in Figure 2b, due to the increase in the solubility of insoluble compounds and to decrease in interfacial tension between immiscible phases. This behavior demonstrates, therefore, the positive contribution to the mobilization of hydrophobic compounds by surfactants. Instead, as can be seen in Figure 2c, the flushing with tap water led to a continuous slow decrease in the outlet concentration and no maximum point is observed.

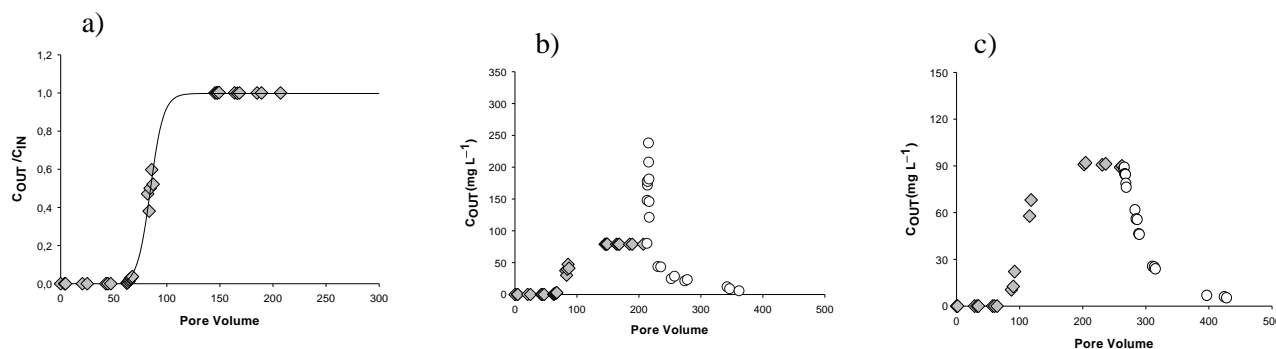


Figure 2. Breakthrough curve (a) and flushing curves using surfactant (b) or water (c) as mobilizing agent

All obtained results from continuous test, in terms of fluid-dynamic parameters pore volume needed for both process phases, the total amount of adsorbed and mobilized contaminant and yield of removal, are summarized in Table 2.

Table 2. Experimental results obtained from each set-up system

Column	HRT (min)	ε (%)	Contamination Phase		Flushing Phase			
			Pore Volume	Adsorbed mg	Pore Volume	$C_{out\ max}$ (mg L ⁻¹)	Mobilized mg	Yield (%)
Toluene-APG	65	57.5	145	296	150	238	204	69
Toluene-RL	50	43.5	117	274	102	316	225	82
Toluene-H ₂ O	65	57.5	202	305	160	/	126	41
PCE-APG	60	50.4	339	405	190	325	373	92
PCE-RL	50	42.7	293	372	229	323	361	97
PCE-H ₂ O	50	42.7	349	405	458	/	218	54

4. Conclusions

This work has been focused on the evaluation of the two investigate surfactants (APG and RL) mobilizing capacity towards NAPLs adsorbed through a continuous column test. Also, in this way it was also possible to carry out a comparative assessment and verify any possible difference in the mobilization capacity of the pollutants according to different origin of surfactant (synthetic and natural). The high capacity of surfactants to facilitate contaminants mobilization has been demonstrated by a significant increase in the effluent concentration of contaminant after a few hours of feeding of flushing solution, compared to a water-only feed where only a slow decrease in the output concentration was observed. Both surfactants investigated have guaranteed good removal yields, with both PCE and toluene. Specifically, the experimental results showed that the biosurfactant RL2 was particularly efficient in the mobilization of both PCE and toluene, compared to the synthetic surfactant APG2. In fact, it has been seen how the columns flushing with the solution of RL2 (5x

CMC) has determined a removal of 97% and 82% for PCE and toluene, respectively. While the flushing with APG2 solution (5xCMC) resulted in a removal of 92% and 70% for PCE and toluene, respectively.

The results obtained from continuous test have amply confirmed the validity of the use of surfactants, in particular of the biosurfactant RL2, in soil-flushing processes for the remediation of NAPLs contaminated sites using SEAR technology approach. Moreover, it should be considered that the RL2 biosurfactant, as produced by the secondary metabolism of microorganisms (*Pseudomonas Aeruginosa*), is completely biodegradable, and therefore able to offer a high environmental compatibility and reduce the effect of secondary contamination.

References

- [1] C. M. Steelman, J. R. Meyer, P. Wanner, B. J. Swanson, O. Conway-White, and B. L. Parker, "The importance of transects for characterizing aged organic contaminant plumes in groundwater," *J. Contam. Hydrol.*, vol. 235, Nov. 2020, doi: 10.1016/j.jconhyd.2020.103728.
- [2] Z. Guo, M. L. Brusseau, and G. E. Fogg, "Determining the long-term operational performance of pump and treat and the possibility of closure for a large TCE plume," *J. Hazard. Mater.*, vol. 365, pp. 796–803, Mar. 2019, doi: 10.1016/j.jhazmat.2018.11.057.
- [3] J. W. Liu *et al.*, "Surfactant-enhanced remediation of oil-contaminated soil and groundwater: A review," *Sci. Total Environ.*, vol. 756, p. 144142, 2021, doi: 10.1016/j.scitotenv.2020.144142.
- [4] L. Huo, G. Liu, X. Yang, Z. Ahmad, and H. Zhong, "Surfactant-enhanced aquifer remediation: Mechanisms, influences, limitations and the countermeasures," *Chemosphere*, vol. 252. Elsevier Ltd, Aug. 01, 2020, doi: 10.1016/j.chemosphere.2020.126620.
- [5] R. García-Cervilla, A. Romero, A. Santos, and D. Lorenzo, "Surfactant-enhanced solubilization of chlorinated organic compounds contained in dnapl from lindane waste: Effect of surfactant type and ph," *Int. J. Environ. Res. Public Health*, vol. 17, no. 12, pp. 1–14, Jun. 2020, doi: 10.3390/ijerph17124494.
- [6] K. Sookhak Lari, J. L. Rayner, and G. B. Davis, "Toward Optimizing LNAPL Remediation," *Water Resour. Res.*, vol. 55, pp. 87–96, Mar. 2019, doi: 10.1029/2018WR023380.
- [7] Y. Fu, C. Qin, S. Gao, C. Lv, C. Zhang, and Y. Yao, "Aquifer flushing using a SDS/1-butanol based in-situ microemulsion: Performance and mechanism for the remediation of nitrobenzene contamination," *J. Hazard. Mater.*, vol. 424, 2022, doi: 10.1016/j.jhazmat.2021.127409.
- [8] M. Le Meur, G. J. V. Cohen, M. Laurent, P. Höhener, and O. Atteia, "Effect of NAPL mixture and alteration on 222Rn partitioning coefficients: Implications for NAPL subsurface contamination quantification," *Sci. Total Environ.*, vol. 791, Oct. 2021, doi: 10.1016/j.scitotenv.2021.148210.
- [9] M. M. Rossi *et al.*, "Combined Strategies to Prompt the Biological Reduction of Chlorinated Aliphatic Hydrocarbons: New Sustainable Options for Bioremediation Application," *Bioeng. 2021, Vol. 8, Page 109*, vol. 8, no. 8, p. 109, Aug. 2021, doi: 10.3390/BIOENGINEERING8080109.
- [10] D. O'Connor *et al.*, "Sustainable in situ remediation of recalcitrant organic pollutants in groundwater with controlled release materials: A review," *Journal of Controlled Release*, vol. 283. Elsevier B.V., pp. 200–213, Aug. 10, 2018, doi: 10.1016/j.jconrel.2018.06.007.
- [11] E. H. Teramoto, M. A. Z. Pede, and H. K. Chang, "Impact of water table fluctuations on the seasonal effectiveness of the pump-and-treat remediation in wet–dry tropical regions," *Environ. Earth Sci.*, vol. 79, no. 18, Sep. 2020, doi: 10.1007/s12665-020-09182-1.
- [12] A. A. Befkadu and Q. Chen, "Surfactant-Enhanced Soil Washing for Removal of Petroleum Hydrocarbons from Contaminated Soils: A Review," *Pedosphere*, vol. 28, no. 3, pp. 383–410, 2018, doi: 10.1016/S1002-0160(18)60027-X.
- [13] T. Gaudin, P. Rotureau, I. Pezron, and G. Fayet, "New QSPR models to predict the critical micelle concentration of sugar-based surfactants," *Ind. Eng. Chem. Res.*, vol. 55, no. 45, pp. 11716–11726, 2016, doi: 10.1021/acs.iecr.6b02890.
- [14] S. T. Malkapuram *et al.*, "A review on recent advances in the application of biosurfactants in wastewater treatment," *Sustain. Energy Technol. Assessments*, vol. 48, no. August, p. 101576, Dec. 2021, doi: 10.1016/j.seta.2021.101576.
- [15] P. Ciampi, C. Esposito, G. Cassiani, G. P. Deidda, P. Rizzetto, and M. P. Papini, "A field-scale remediation of residual light non-aqueous phase liquid (LNAPL): chemical enhancers for pump and treat," *Environ. Sci. Pollut. Res.*, vol. 28, pp. 35286–35296, 2021, doi: 10.1007/s11356-021-14558-2/Published.
- [16] C. Yang *et al.*, "The role of surfactants in colloidal biliquid aphrons and their transport in saturated porous medium," *Environ. Pollut.*, vol. 265, Oct. 2020, doi: 10.1016/j.envpol.2020.114564.

Combustion of a biomass-derived syngas to decarbonize a tissue paper plant: impact of the turbulence-chemistry interaction treatment on numerical simulations

Chiara Galletti^{1*}, Lorenzo Giuntini¹, Luca Linari², Pietro Saccomano², Davide Mainardi³, Leonardo Tognotti¹, Rachele Lamioni¹

1 Dipartimento di Ingegneria Civile e Industriale, Università di Pisa, 56126 Pisa, Italy;

2 ANDRITZ Novimpianti S.r.l, Capannori (Lucca) – Italy

3 SOFIDEL S.p.A, Porcari (Lucca) - Italy

**Corresponding author E-Mail: chiara.galletti@unipi.it*

1.Introduction

In the papermaking industry is responsible of about 7% of the global industrial energy consumption mostly based on fossil fuels as natural gas and liquid petroleum gas, (LPG) with adverse effects on climate changes. The “Fit for 55” and “REpowEU” EU actions aimed at, respectively, 55% reduction of greenhouse gas emissions with respect to 1990 levels by 2030 and diversification of energy sources to reduce our dependence on suppliers of fossil fuels, both ask for a decarbonization of all industrial sectors, including the papermaking one. Here, the tissue paper constitutes one of the main products with a global average consumption per person of about 55 kg/year.

The tissue industry is very-energy demanding with a carbon footprint of around 0.6 kg eq. CO₂ per kg tissue paper [1]; this is mostly related to the thermal energy required for the drying process that in modern paper mills involves a steam-heated cylinder and two hot air hoods. The latter must supply hot air at about 500-600 °C to dry the surface of the tissue paper. These high temperatures are provided by burning fossil fuels.

Very recently, Frigo et al. [2] investigate the technical and economical possibility of feeding the combustion chamber located upstream of the hood for the tissue-paper drying, with a biomass-derived syngas, instead of LPG, to reduce the carbon footprint of the process.

However, further analysis is needed to elucidate how the switching to syngas may impact on the combustion process. Indeed, syngas is a mixture of hydrogen, carbon monoxide, nitrogen, carbon dioxide and therefore its combustion characteristics differ strongly from LPG [3]. The presence of H₂ which is characterized by laminar velocity and adiabatic flame temperature which are significantly higher than natural gas, can produce faster combustion rates [4] and generate higher temperatures which can augment NO_x emissions. The presence of inert gases, such as N₂, H₂O and CO₂, on the other hand, can naturally dilute the fuel and therefore produce flames with lower characteristic temperatures, which may help limiting NO_x emissions, but may lead to difficulties in the completion of the combustion process. All these differences due to the change of fuel must be analyzed in terms of the combustion system design, as the strategies used to handle fossil fuels could be ineffective or even worsen when using syngas.

This work, we intend to analyze the impact of replacing LPG with a biomass-derived syngas on the combustion process for tissue paper drying in a plant located in Sweden. The syngas is obtained from gasification in a fluidized bed of locally produced wooden pellets. To this purpose, the 2.4 MW burners are of dual-fuel type, to maintain the possibility of being able to use both fuels, i.e., LPG and syngas. The goal is to ensure stable combustion with low CO and NO emissions; besides, the drying requires an even distribution of the flow and temperature on the paper surface, which must be ensured. To this end, advanced numerical simulations, based on computational fluid dynamics, are performed to obtain detailed information on the flow and thermo-chemical fields in the combustion chamber and hood.

2.Methods

Errore. L'origine riferimento non è stata trovata. shows the reference geometry of the combustion system, consisting of a horizontal cylindrical combustion chamber and a hood collecting the exhaust stream towards the tissue paper to be dried. The chamber is equipped with a 2.4 MW dual-fuel swirled burner and a flame tube, confining the reaction zone.

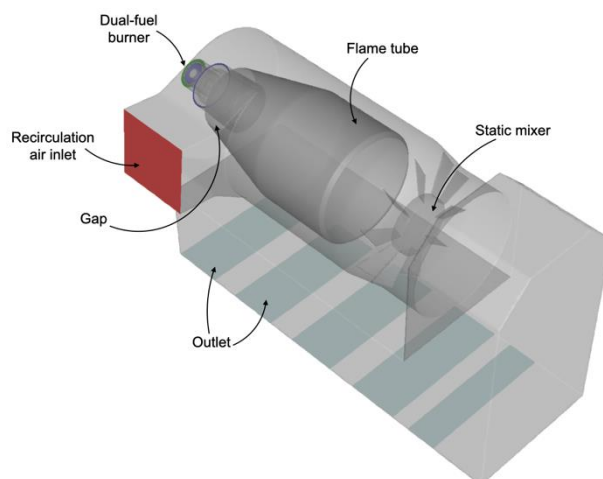


Figure 1. Sketch of the combustion system.

The syngas, whose composition is given in Table 1. Syngas composition., is fed through a swirled annular duct with a velocity of 20 m/s and a temperature of 323 K. The combustion air excess is 50%, with the total air being equally split into primary and secondary air. A large amount, i.e. about 14 times that of the combustion air, of humid (i.e., 28.61% by molar fraction of water vapor) recirculation air is also fed externally to the flame tube, to ensure its cooling. Such a recirculation air merges with the exhaust gases just upstream of a deflector cone, which protects the hood from flame radiation. In addition, a static mixer improves the temperature uniformity of the flow. A little amount of recirculation air is allowed to be entrained in the reaction region through an existing gap in the flame tube very close to the burner; this gas is crucial to dilute the flame to limit NO formation via the thermal route in case of LPG.

Table 1. Syngas composition.

Species	N ₂	CO	CO ₂	H ₂	H ₂ O	CH ₄	C ₂ H ₄	C ₆ H ₆
Mole fraction [%]	46.0	17.6	10.6	9.7	12.0	2.6	1.3	0.2

3-D numerical simulations are performed by solving the steady-state Favre-averaged Navier-Stokes equations for continuity, momentum, transport/reaction of chemical species and energy with the commercial code ANSYS Fluent v21 based on finite volume methods. Reynolds stresses are closed with the Realizable $k-\epsilon$ turbulence model with standard wall functions, while the turbulent transport of chemical species and heat respectively, are modeled through a gradient transport hypothesis with turbulent Schmidt and Prandtl numbers of 0.7 and 0.85, respectively.

For the closure of the mean reaction source terms two different approaches are compared, i.e.:

- the Eddy Dissipation Model (EDM) [5], based on an infinitely fast chemistry assumption is used with global kinetic scheme, where CH₄ is oxidized to CO, and CO to CO₂ [6] and H₂ is oxidized to H₂O with single step [7];
- the Eddy Dissipation Concept (EDC) [8], based on finite-rate assumption is used with the kinetic mechanism KEE58 [9], consisting of 17 chemical species and 58 reversible reactions.

Indeed, the purpose is to analyze the impact of chemistry on the numerical predictions; in fact, the global scheme ensures a much lower computational requirements, that make it interesting for practical applications. Radiation is considered by employing the P1 model with the Weighted-Sum-of-Gray-Gases model to estimate the spectral properties of the medium. As for NO_x formation, the thermal, prompt and N₂O-intermediate paths are considered, by including the effect of turbulence through a probability density function.

Velocity, temperature, and composition were set as boundary conditions at the inlets of the combustion system, while a pressure outlet condition was set at the exit. The fuel, primary and secondary air were fed with specific swirl angles.

A grid independence study was carried out by performing reactive numerical simulations, to verify that the flame front could be well captured by the mesh size. The chosen grid has 2.4M cells and is polyhedral with prism layers at the walls, ensuring an average value of Y^+ of 80, enabling a correct implementation of standard wall functions.

The set of equations was solved with a coupled solver and using a second-order upwind interpolation method with the PRESTO! algorithm for the pressure. Convergence was assessed by monitoring physical quantities at specified locations in the combustion chamber as well as by checking the normalized residuals, they are being always below 10^{-6} .

3. Results and discussion

Figure 2. Velocity-magnitude distribution obtained with EDC and KEE58 mechanism: 3D views on the (a) vertical and (b) horizontal planes. shows the flow field trough the contours of the velocity magnitude in vertical and horizontal planes of the combustion system as predicted by the EDC model and KEE58 kinetic scheme. The highest velocities can be found between the flame tube and the external case, thus allowing an effective cooling of the flame tube wall with the recirculation air. Inside the flame tube we can observe a low-velocity region along the burner axis, while higher velocities can be found near the walls, especially in the upper part. It is worth noting that here the flow field is not axisymmetric, due to a certain amount of recirculation air which unevenly enters the reaction zone, passing through an existing gap in the wall.

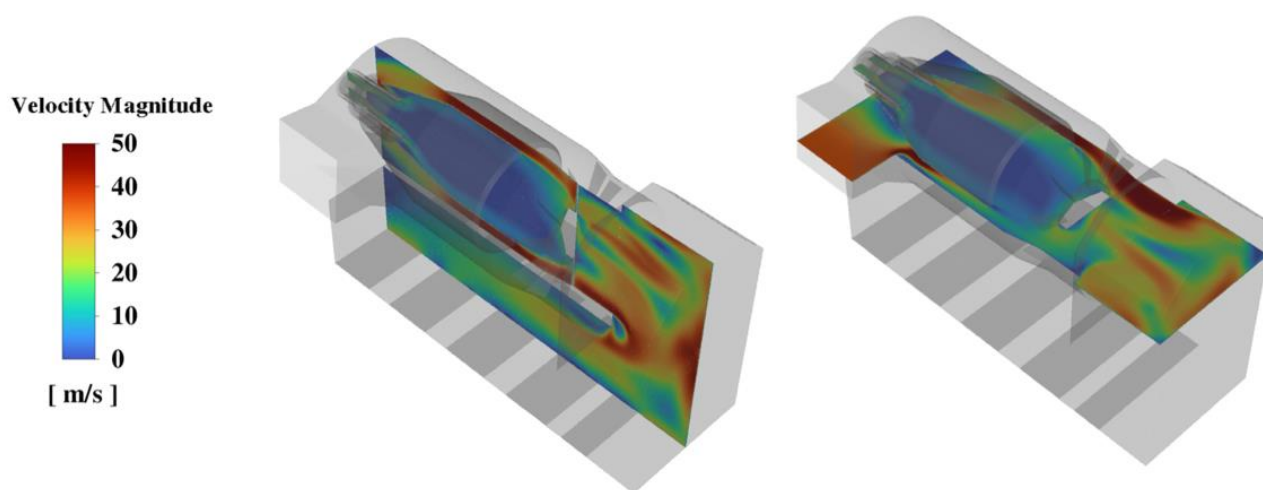


Figure 2. Velocity-magnitude distribution obtained with EDC and KEE58 mechanism: 3D views on the (a) vertical and (b) horizontal planes.

The thermal fields on the vertical and horizontal planes obtained with different combustion models and kinetic schemes are compared in Fig 3. The EDM and global kinetics (see left panels) predicts a flame, which is attached to the burner. This happens because the infinitely fast chemistry hypothesis, proper of EDM, along with a strong turbulent mixing at the inlets, make the syngas ignite as soon as it enters the computational domain. Conversely, the EDC, based on finite-rate, with KEE58 kinetic mechanisms, shows a lifted syngas flame (see right panels).

The carbon monoxide emissions are evaluated at the outlet of the hood, to appreciate the capability of the original combustion system to effectively deal with syngas. The EDM model with global kinetics predicts zero CO emissions; this behavior is imputed to the intrinsic hypothesis of the model, i.e., infinitely fast chemistry which leads to a complete combustion. Instead, EDC with a detailed oxidation scheme estimates rather high CO emissions, i.e., of approximately 400 ppm. Indeed, we can observe from Fig. 3 that the flame appears rather long and extends towards the static mixer: this indicates that in case of syngas the combustion process cannot complete within the flame tube upstream of the deflector. As for NO_x emissions, they are below 1 ppm in all cases. This is because the syngas is mostly composed of inert gases, i.e., N_2 , H_2O and CO_2 , which keep the maximum flame temperature below 1700 K, thus avoiding the thermal mechanism of NO formation.

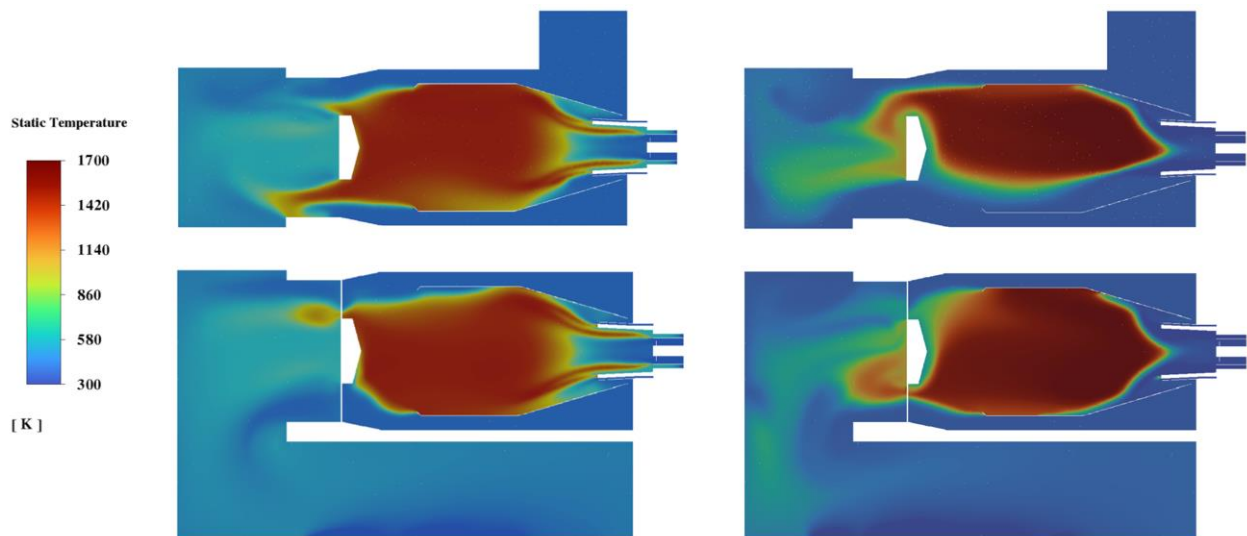


Figure 3. Temperature distribution on $z = 0$ (top) and $y = 0$ (bottom) plane. Global (left) and detailed (right) kinetic mechanism.

4. Conclusions

Numerical simulations were carried out of the combustion chamber equipped with an industrial hood used in the paper drying process and fed with a biomass-derived syngas. The study has shown how global oxidation schemes and a fast-chemistry hypothesis, largely employed in industrial practice for conventional fuels, cannot provide here the real morphology of the flame. By using a global chemistry approach, the flame is attached to the burner inlet and leads to zero CO emission. Instead, a finite-rate approach with detailed chemistry, which is remarkably more computationally expensive, predicts a flame which is lifted. However, the flame is rather unstable because of the presence of some recirculation air that dilutes it; as a result, syngas cannot be burned properly, thus leading to high CO emissions at the exit of the hood. This analysis represents a first step in the characterization the use of biomass syngas, to favor the decarbonization of the paper sector in place of LPG. In the context of the energy transition, combustion systems must be flexible in terms of fuel, therefore this work lays the foundations for a more in-depth analysis of the possibility of contributing to the retrofit of existing equipment in a decarbonized scenario.

References

- [1] E. D. Gemechu, I. Butnar, J. Goma-Camps, A. Pons, F. Castells, A comparison of the ghg emissions caused by manufacturing tissue paper from virgin pulp or recycled waste paper, *The International Journal of Life Cycle Assessment* 18 (2013) 1618– 1628.
- [2] S. Frigo, R. Gabrielli, L. Linari, Feasibility study of a chp plant with steam turbine and biomass gasification for tissue paper production, *Energy Procedia* 148 (2018) 751–757, aTI 2018 - 73rd Conference of the Italian Thermal Machines Engineering Association.
- [3] E. Jithin, G. Raghuram, T. Keshavamurthy, R. K. Velamati, C. Prathap, R. J. Varghese, A review on fundamental combustion characteristics of syngas mixtures and feasibility in combustion devices, *Renewable and Sustainable Energy Reviews* 146 (2021) 111178.
- [4] C. Liu, B. Yan, G. Chen, X. Bai, Structures and burning velocity of biomass derived gas flames, *International Journal of Hydrogen Energy* 35 (2) (2010) 542–555.
- [5] B. F.,
- [6] Magnussen, B. H. Hjertager, On mathematical modeling of turbulent combustion with special emphasis on soot formation and combustion. In *Symposium (international) on Combustion* (Vol. 16, No. 1, pp. 719-729) 1977.
- [7] C. K. Westbrook, F.L. Dryer, Simplified reaction mechanisms for the oxidation of hydrocarbon fuels in flames, *Combustion Science and Technology* 27 (1-2) (1981) 31–43.
- [8] N. M. Marinov, C. K. Westbrook, W. J. Pitz, Detailed and global chemical kinetics model for hydrogen.
- [9] B. Magnussen, On the structure of turbulence and a generalized eddy dissipation concept for chemical reaction in turbulent flow. In *19th Aerospace Sciences Meeting* 1981.
- [10] R. Bilger, S. Stårner, R. Kee, On reduced mechanisms for methane-air combustion in non-premixed flames, *Combustion and Flame* 80 (2) (1990) 135–149.

ELECTRONIC NOSE FOR REAL-TIME MONITORING OF ODOUR EMISSIONS AT A WASTEWATER TREATMENT PLANT

Stefano Prudenza, Carmen Bax*, Laura Capelli

Politecnico di Milano, Department of Chemistry, Materials and Chemical Engineering, piazza Leonardo da Vinci 32, 20133 Milano, Italy

**Corresponding author E-Mail: carmen.bax@polimi.it*

1.Introduction

Atmospheric emissions from industrial activities are subjected to control and regulation worldwide. Their monitoring and mitigation represent a common concern for chemical engineers who deal with the development and design of abatement systems [1], the study of new measurement techniques [2], the modelling of emissions impact [3, 4].

Odour emissions are nowadays recognized as atmospheric pollutants and consequently need to be monitored and kept under control such as any other emissions. Due to the particularity of these emissions, many efforts have been done by the scientific community to develop suitable methods for modelling and quantifying odour impacts, as well as for keeping odour emissions under control [5].

A development perspective for monitoring of odorous emissions from industrial activities in the Industry 4.0 era concerns the realization of networks of monitoring systems to be installed at emission sources or plant fencelines for a real-time analysis. Those systems can provide useful information for identifying potential malfunctioning and anomalies. In this scenario, electronic noses (e-noses), i.e. instruments combining a gas sensor array with machine learning algorithms, can serve as useful monitoring tool. If adequately trained, they are capable to provide a real-time qualitative and quantitative characterization of the odorous mixtures they are exposed to.

If installed at plant fenceline or directly at emission sources, e-noses can detect odours originating from anomalies during normal operating conditions: In other words, the e-nose can be trained to detect deviations from reference conditions. This in turn allows the setting of “warning” thresholds, enabling sudden intervention in case of malfunctioning. Thanks to its peculiarity to classify odours, the e-nose can also provide indications about the cause of the malfunctioning, thereby guiding maintenance operations.

In this context, this paper describes a feasibility study proposing the use of an e-nose to on-line monitor odorous emissions from a wastewater treatment plant (WWTP). The WWTP under exam receives both civil and industrial wastewaters from ca. 40 industries of different types (e.g., chemical, tanneries, paper mill, printing, food, car washes etc.). Civil wastewaters account for about 60-70% of the total incoming flowrate (i.e., about 22'000 m³/day), while industrial wastewaters account for the remaining 30-40%.

Due to the frequent reports of odour nuisance by citizens living in the proximity of the plant, in agreement with the regional guidelines on odour emission management, several olfactometric campaigns were carried out at the emissions sources with the purpose of determining odour concentrations and odour emission rates. This preliminary work allowed identifying the emission sources that are most responsible for the odour nuisance and evaluating the odour impact associated to the plant in the surrounding territories. As expected, based on experimental evidences collected so far, the arrival tank turned out to be the most problematic source of the plant. One peculiarity of this plant concerns the considerable variability of the concentration of odour emissions from the arrival tank: odour concentrations ranging from 2'000 to 120'000 ou_E/m³ were recorded. These results pointed out that there are some moments in which a particularly odorous wastewater arrives at the plant, causing the malodorous events. However, the origin of these odours, which could be related to the simultaneous presence of discharges from several different industries causing the release of compounds with a low odour threshold, has not yet been uniquely determined. Since these particular odorous conditions occur occasionally, the use of an instrument capable to provide a real-time monitoring of the odours emitted from

the arrival tank and activate specific alarms may allow the execution of targeted chemical and olfactometric analyses, when the “incriminated” wastewater is present in the plant. The chemical speciation of the substances contained in the liquid and in its headspace, compared with the respective olfactory threshold values, may enable the identification of the chemicals most responsible for the odour that is generated in the stages of wastewater ferment and pre-treatment.

In this context, this paper describes the experimental procedure involved for the e-nose training and evaluate its performance. The training is a crucial phase for the use of e-nose as monitoring tools, since in this phase the instrument develops its classification and quantification capability based on a reference dataset (i.e., the Training Set – TS), including samples showing the characteristic “patterns” of the odours that the instrument is expected to detect and recognize during the monitoring phase. To do this, the training involves the collection of odour samples at plant emission sources, according to specific sampling protocols. It is worthy to highlight that sampling is one of the main issues pertaining to odour characterization and measurement, on which the quality of results is heavily dependent [6]. Odour samples are characterized by dynamic olfactometry (EN 13725:2022) to assess their odour concentration and then analysed by the e-nose to build the TS. For the specific monitoring, the e-nose, equipped with an automatic gas sampling system, has been installed at the arrival tank of the WWTP. The training lasted about 1 month and involved the analysis of samples collected at the arrival tank under different meteorological and operating conditions of the plant. E-nose signals relevant to the training period were combined with the odour concentration, obtained by dynamic olfactometry, and with reports of presence/absence of odour by the citizens living nearby the plant to implement data processing models aimed at identifying a Normal Operating Region (NOR) [7], representative of moderate presence of odour on the arrival tank not causing odour events in surrounding territories. This paper reports also the results of the model validation. In this phase, gas samples have been randomly collected at the plant in order to verify the correct functioning of the model developed.

2. Methods

2.1 Monitoring system

2.1.1 Electronic nose

An electronic nose is an instrument capable to recognise and quantify odours by means of a gas sensor array and a multivariate machine learning algorithm. The architecture of an e-nose strictly depends on the specific application for which it is designed. In general, an e-nose comprises [8, 9]:

- A sampling system: it generally consists of a vacuum pump, which sucks the odorous mixture to be analysed and delivers it to the detection system. In some e-noses, specifically designed for the environmental monitoring, the sampling system is equipped with drying units or filters to generate odourless reference air, or compensate the moisture content of the sample.
- A detection system: it comprises an array of gas sensors, whose nature and number depends on the specific application, enclosed into an inert chamber, where gas to be analysed is sucked by means of a vacuum pump.
- A pattern recognition unit: it involves machine learning techniques for processing sensor signals, determining odour fingerprint and producing an estimate of the odour class or concentration for an unknown sample along with an estimate of the confidence placed on the assignment.

The instrument used in this project is an outdoor e-nose commercialized by Ellona, i.e., WT1 monitoring system. It is equipped with 4 metal oxide sensors (MOS), characterized by a high sensitivity to volatile compounds, 3 electrochemical sensors sensible to hydrogen sulphide, formaldehyde and ammonia, and a

photoionization detector (PID) calibrated in isobutylene for detection of volatile organic compound (VOC). The instrument comprises also sensors for evaluating the temperature and relative humidity of external environment.

The WT1 software enables the real-time visualization and preliminary pre-processing of signals (i.e., resistance values for MOS sensor, concentrations in ppm of H₂S, NH₃, formaldehyde and VOC for electrochemical sensors). The data processing pathway developed within the project, which is described in Section 2.2, was implemented in Rstudio.

2.1.2 Sampling system

The automatic gas sampler used in this study is an airtight suitcase of 25 liters produced by Scentroid (VC20) equipped with a membrane vacuum pump and Nalophan bags for sample collection. This system can be activated both manually and by the e-nose to which it is connected, when the alarm threshold is exceeded.

2.2 Training of the e-nose

The training phase represents a crucial phase for the use of e-nose for the environmental monitoring. It consists in the creation of a dataset from which identify, define and discriminate a “reference” condition on the arrival tank, representative of low odour concentration that do not create nuisance nearby the plant. It is worth to underline that an inappropriate training might compromise the performance of the e-nose and result in misclassifications or under/overestimations of the concentrations of odours detected.

In this research, the training phase lasted about 30 days. In this phase, the e-nose was installed at the arrival tank of the WWTP plant (

Figure 1) to acquire data representative of the odorous emissions from the tank. In order to avoid problems associated to the extreme environmental conditions of the arrival tank shed (high relative humidity and high levels of hydrogen sulphide), a dilution system was applied at the inlet of the e-nose. This system mixes the air from the arrival tank shed with outdoor ambient air in a ratio 1:1.

The gas sampler was placed nearby the e-nose (*Figure 2*) to allow the communication between the instruments and sucks the ambient air from the arrival tank shed by means of a Teflon tube.



Figure 1. The WT1 installed outside the arrival tank (on the left), the inlet section of arrival tank (in the middle) and the second section of the arrival tank (on the right) with sludge recirculation active.



Figure 2. The airtight suitcase placed nearby the WT1 outside of the arrival tank.

At the end of the training the data obtained from the e-nose sensors' generated a dataset consisting of 246570 observation and 6 features (i.e., the signals of 2 MOS, 3 electrochemical sensors and 1 PID sensor).

In order to correlate those e-nose signals relevant to the analysis of emissions from the arrival tank with their odour concentration, the training phase involved the collection of gas samples inside the arrival tank shed under different meteorological and operating conditions of the plant and their characterization by dynamic olfactometry. During this period, 18 gas samples were randomly collected on 10 different days, and characterized by dynamic olfactometry, with the purpose of combining sensors' signals with odour concentrations detected at the arrival tank. The samplings were carried out on different days under diverse conditions of the plant (e.g., different incoming wastewater flowrate, active or inactive recirculation of sludges) in order to include in the training dataset the variability of the source.

Once the data have been collected a specific procedure, illustrated in Figure 3 **Figure 3**, has been developed for their elaboration.

First of all, the sensors response is averaged on 5 minutes, to reduce the dataset dimensionality, and ease their elaboration and interpretation, preserving information useful for further processing. Then, a principal component analysis (PCA) [10] was applied in order to reduce even more the data dimensions, allowing for a better visualization and investigation of their structure. Finally, PCA scores were used as inputs of Support Vector Machine [11] (SVM) algorithm to define a rigorous NOR region representative of normal conditions at the plant.

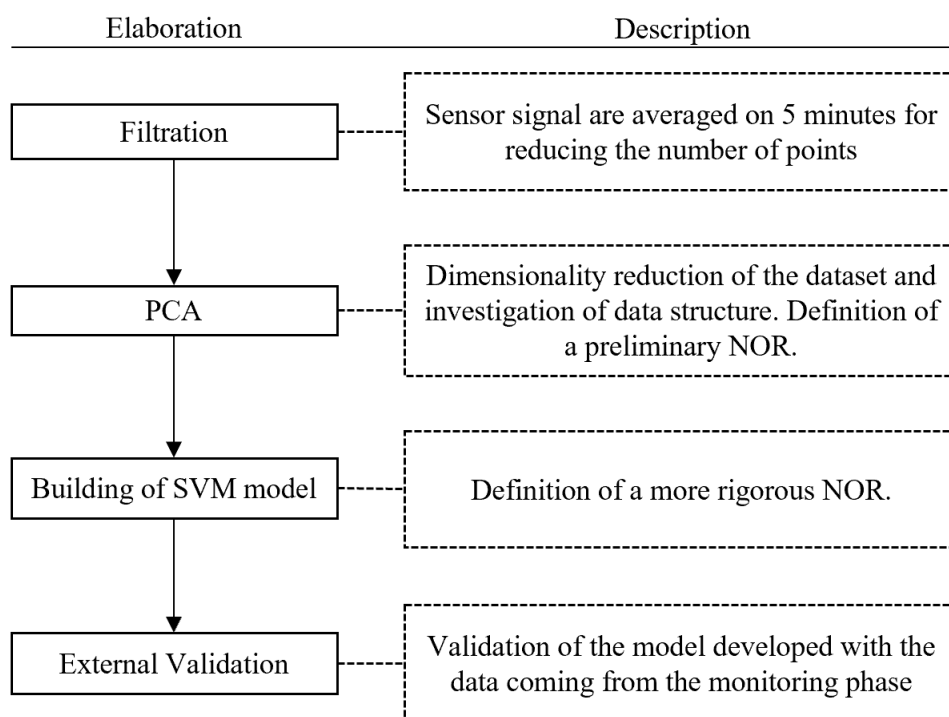


Figure 3. Block diagram of the data elaboration for the developing and validating the model.

2.3 Monitoring and validation

After the implementation of the model on the e-nose the monitoring phase started. The data collected by the nose in this phase follow the data processing pathway implemented on the training. The sensors response is averaged over 5 minutes, and then the data are projected onto the PCA model based on training data.

Then, the new PCA coordinates obtained from the monitoring points were used as inputs for the Support Vector Machine (SVM) algorithm to determine if they fall inside or outside the NOR. In case of projection outside the NOR boundaries, the e-nose report an alarm and activate the automatic sampler.

In order to validate the model, at the beginning of the monitoring phase, samples collected by the automatic sampler in case of alarm threshold exceedance and under normal conditions were analysed by dynamic olfactometry to determine their odour concentration and compare them with the predictions made by the monitoring system.

3. Results and discussion

3.1 Training

3.1.1 Preliminary considerations

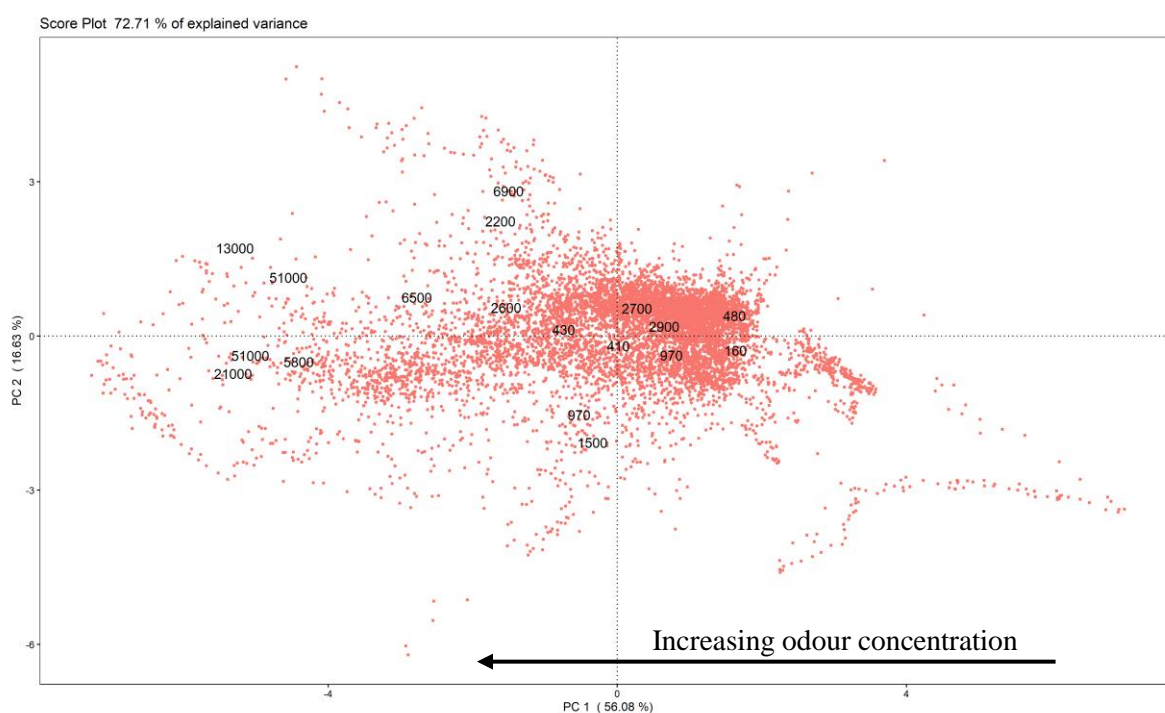
The data collected during the training phase were processed by PCA, whose results are reported in Figure 4. The model built on 2 principal components describes 72.7% of the variance of the data.

Figure 4-A reports the PCA score plot, illustrating the projection of observations into the new reference system defined by principal components, which provides information about the existence of clusters in the data. In this graph, the odour concentration of the gas samples taken from the arrival tank are highlighted. Figure 2-A points out that on the PC1 there is a clear correlation between the odour concentration and the signal registered by the sensors, since moving on the left part of the graph the ou_E/m^3 increases.

Conversely, Figure 4-B reports the PCA loading plot, which provide information about the correlation among variables and their importance for the purpose of differentiating different conditions. In order to identify the variables contributing to the dispersion of points in the PCA score plot, the visual investigation of the loading plot in Figure 2-B shows that that the region where peaks of odour are present is the left one, since all the features related to the electrochemical sensors point in this direction. Conversely, the MOS sensors' loadings point in the exactly opposite verse. Therefore, in the left portion of the plot, low resistance values are expected, in line with the MOS n-type behaviour when exposed to gas.

Moreover, this plot also enables determining correlations between the sensor signals. In this case, the MOS sensors are mainly correlated with the hydrogen sulphide, formaldehyde and PID sensors (i.e., the angle between the arrows is narrower than 90° , the one indicative of no correlation), while there is a negligible correlation with the ammonia sensor (i.e., the angle is close to 90°). This is probably due to the lower levels of ammonia registered on the arrival tank, varying among 0.3 and 1.5 ppm.

Finally, combining the point distribution of the score plot and the information coming from the loading plot, looking at the PC2 distribution of scores, 3 main regions of odours can be identified: one in the top-left part, one in the middle-left and one in the bottom-left part of the score plot. These 3 regions are relevant to different odour conditions at the arrival tank, associated to high levels of VOC, hydrogen sulphide/formaldehyde and ammonia respectively. Obviously, the odour presence will not be caused only by those compounds, but this information gives an estimation of the class of molecules most responsible for the specific odour peak.



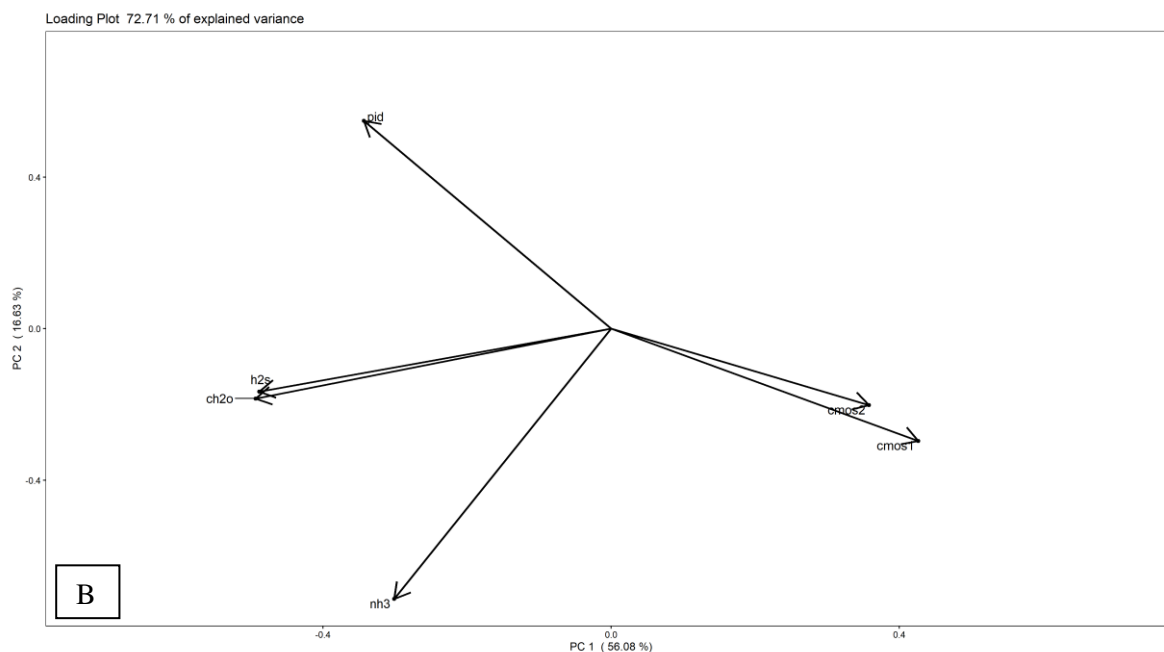


Figure 4. Loading (A) and scores (B) plot of the PCA on the training data. The numbers displayed in the score plot indicates the odour concentration of the gas samples taken from the arrival tank.

It is worthy to highlight that a multivariate approach, considering all the simultaneous sensors' responses, is needed to obtain reliable e-nose outputs. Figure 5 compares the responses of PID and H₂S sensors with the odour concentration of the gas samples collected at the arrival tank of the WWTP. It highlights a very poor correlation among single sensors response and odour properties of samples: R² of 0.28 and 0.48 were obtained for PID and H₂S sensors, respectively. Thus, single gas sensors cannot provide outputs directly correlated to the odour concentration of samples, which can be used to implement smart monitoring systems.

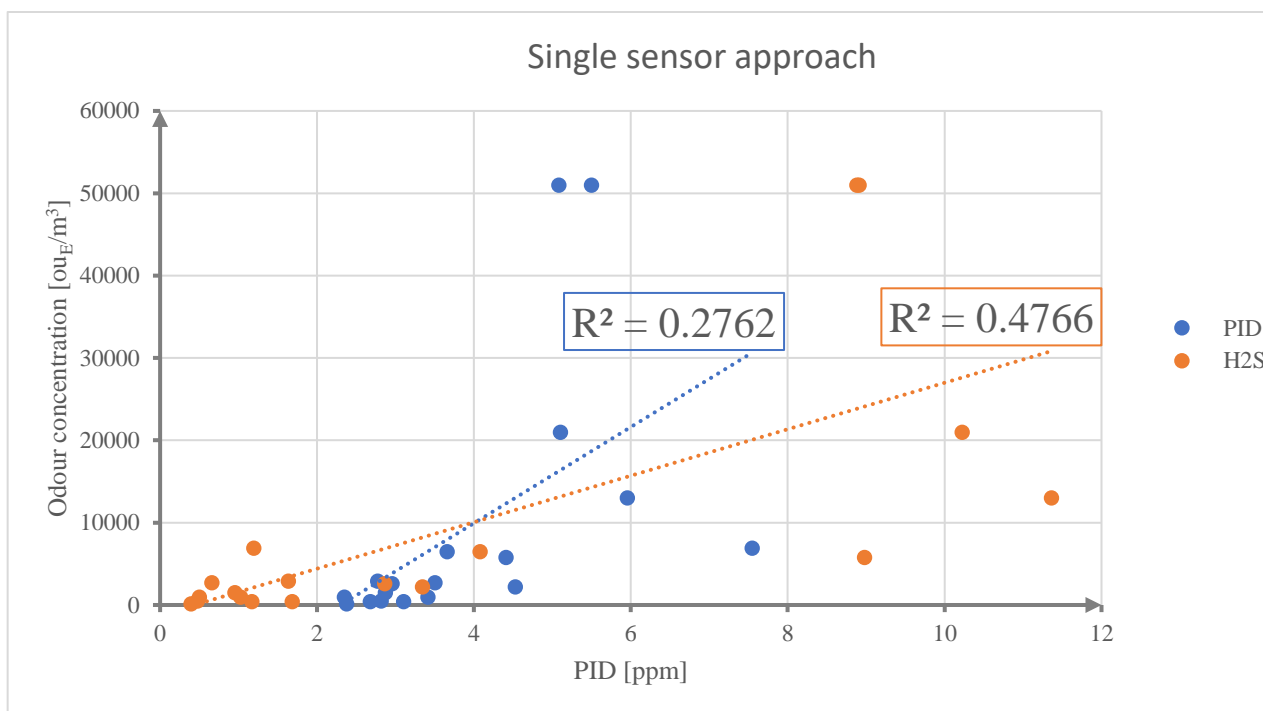


Figure 5. The PID values [ppm] versus the odour concentration [ouE/m³] of the samples taken from the arrival tank during the training phase.

3.1.2 E-Nose model for WWTP monitoring

Based on the information obtained from the loading and score plots, the results of the olfactometric analysis and the citizen reports, a NOR region of the arrival tank has been defined on the score plot (Figure 6) by selecting only the points of the score plot that satisfied the following conditions: $PC1 > 0 \wedge \forall PC2, -2.5 < PC1 < 0 \wedge -3 < PC2 < 2$.

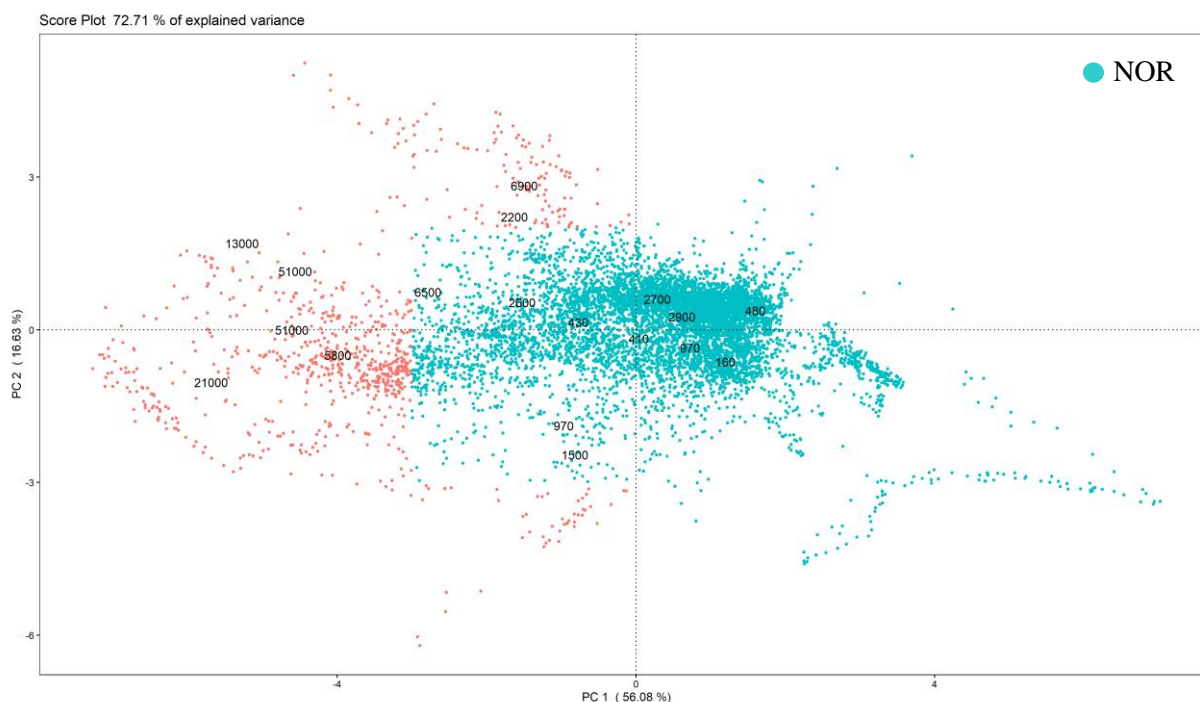


Figure 4. Score plot where the point satisfying the NOR condition are coloured in blue.

Once defined this region, the point satisfying the imposed condition has been used to develop a one-classification SVM model, able to define a more accurate confidence region through a radial kernel. In this type

of models two parameter are needed for the definition of the shape of the confidence region representative of the class. The “nu” parameter expressing the information of the percentage of possible outlier in the dataset, and the “gamma” parameter that define the shape of the boundaries of the NOR are defined based on training data distribution. In this case study, nu and gamma parameters have been set as 0.0001 and 0.03, respectively. The confidence region obtained as results is reported in Figure 7 **Errore. L'origine riferimento non è stata trovata.** With the purpose of introducing also an intermediate alarm region, representative of anomalous conditions that cannot be assimilated to the NOR region, but not so troubling in terms of odour concentration, a second area has been identified. This region is defined by PCA points satisfying the following requirements: $PC1 > 0 \wedge \forall PC2, -4 < PC1 < 0 \wedge -4 < PC2 < 3$. Also in this case, the SVM, using as parameters $\nu=0.0001$ and $\gamma=0.03$, has been used to define the boundaries of the intermediate region.

Thus, the final model illustrated in Figure 8 comprises two distinct regions: the NOR, representative of the typical odour concentration of the arrival tank for normal incoming wastewater, and an intermediate region indicating that the incoming wastewaters are creating anomalous odour on the arrival tank, but still characterized by acceptable odour concentrations not causing nuisance nearby the plant.

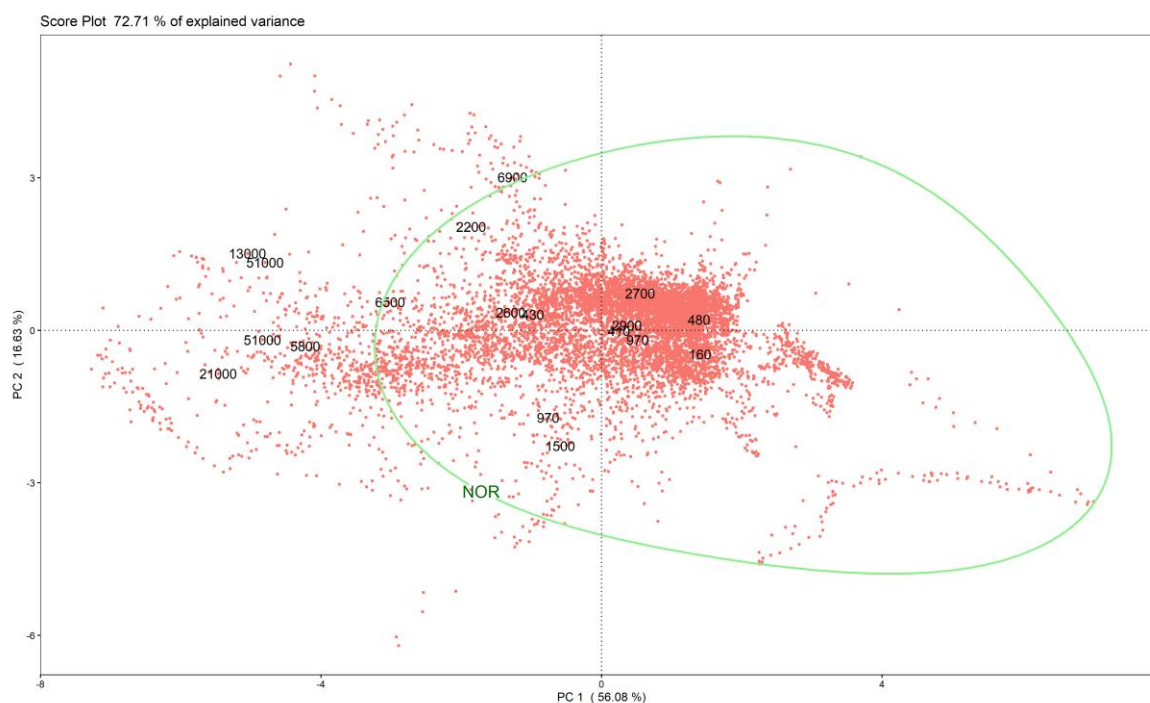


Figure 5. PCA score plot with the NOR defined through the use of one-classification SVM.

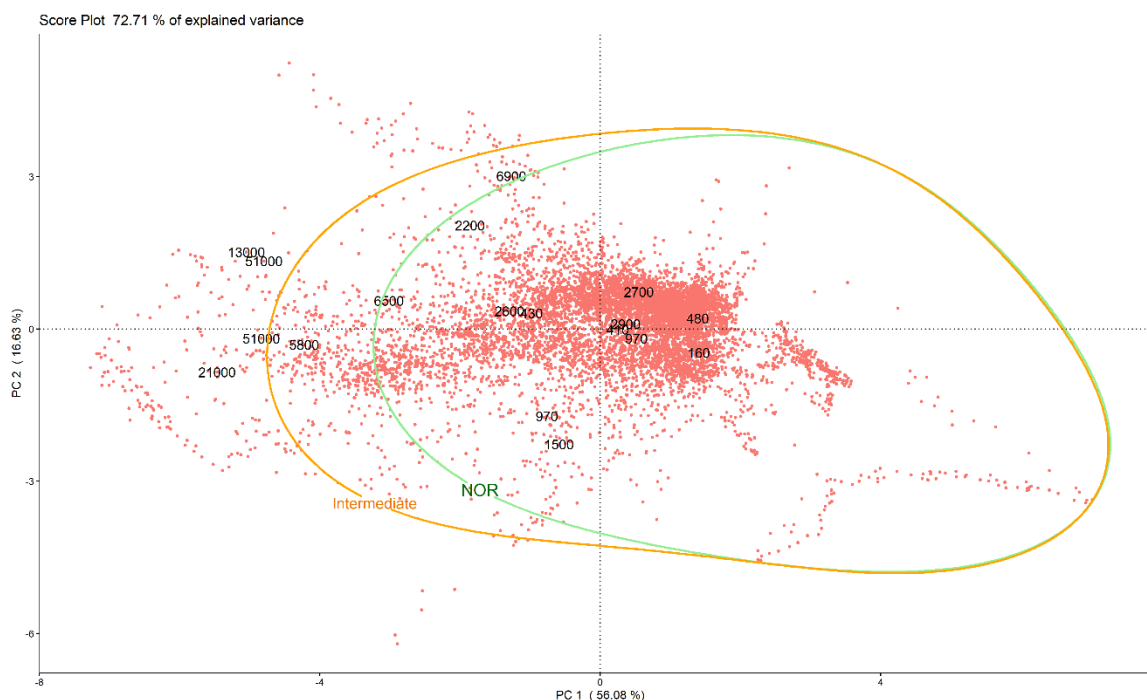


Figure 6. The PCA score plot with the NOR and the intermediate alarm region obtained with one-classification SVM.

3.2 Monitoring and Validation

During the monitoring phase, the data are continuously acquired by the e-nose and processed by the models implemented on the training data. With the purpose of evaluating the capability of the e-nose to recognize and reveal the presence of anomalous odours, verification tests are carried out. This phase involved the automatic withdrawal of samples representative of both reference and anomalous odour conditions, i.e. representative of different odour concentration levels, at the arrival tank. Specifically, 9 independent samples, collected in 5 different days, have been considered: 4 representatives of the NOR and 5 representatives of the anomalous conditions.

Figure 9 illustrates the results of this validation phase. Samples characterized by odour concentrations lower than $4'600 \text{ ou}_E/\text{m}^3$ fall within the NOR. Conversely, samples collected under anomalous conditions (i.e., odour concentrations ranging from $9'200 \text{ ou}_E/\text{m}^3$ to $26'000 \text{ ou}_E/\text{m}^3$) fall outside the NOR.

The NOR defined by the model proved to be suitable for the discrimination between conditions representative of normal functioning of the plant characterized by odorous emissions not causing odour events in the surroundings and anomalous odour peaks. Moreover, the alarm defined turned out to be effective in signalling the exceedance of the critical odour concentration, and activating automatic sampling systems with the purpose of identifying the causes of the odour event detected.

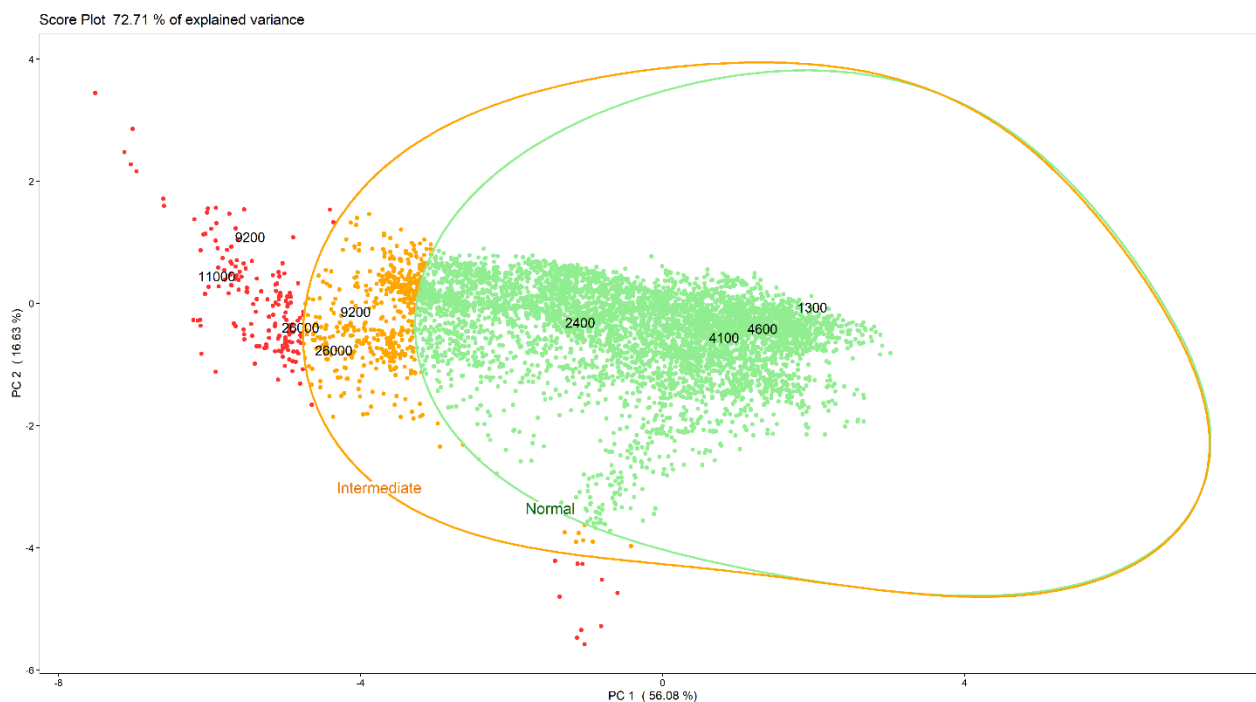


Figure 7. Score plot of the PCA on the first weeks of monitoring. The numbers displayed in the score plot indicates the odour concentration of the gas samples taken from the arrival tank.

4. Conclusions

This paper presented, as a case study, the e-nose monitoring of odorous emissions from the arrival tank of a WWTP. The e-nose was trained to signal the detection of malodours by implementing specific multivariate model, based on PCA and SVM algorithms, combining e-nose signals with odour concentration of gas collected on the arrival tank and the citizen reports about the presence or absence of odours nearby the plant.

The results achieved prove that the developed system is capable to real-time detect deviations from reference conditions (i.e. conditions with low-to-moderate odour emissions), and provide information about the potential causes of the malfunction. This system can serve the plant operator for different purposes. It could be useful for the identification of the substances responsible of odours peaks and consequently develop a specific tailored abatement system, thus optimizing the costs and benefits compared to more generic solutions. Moreover, if the wastewater source that cause the problems is identified it could be separated and pre-treated appositely before entering the WWTP for example with ozone treatments [12], ultraviolet light [13], nanoparticles [14] and other innovative treatments [15].

Future goals to be achieved within these applications concern the implementation of a more precise quantification model to estimate the odour concentration based on regression. Moreover, future work should focus on the validation over time of the model to spot the sensors drifting and intervene to compensate it with an appropriate drift correction model in order to extend the alarm model validity.

References

- [1] A. Setiabudi, M. Makkee, and J. A. Moulijn, "An optimal NO_x assisted abatement of diesel soot in an advanced catalytic filter design," *Applied Catalysis B: Environmental*, vol. 42, no. 1, pp. 35-45, 2003/04/15/ 2003.

- [2] Q. W. Wang, P. Zhou, N. Shen, and S. S. Wang, "Measuring carbon dioxide emission performance in Chinese provinces: A parametric approach," *Renewable and Sustainable Energy Reviews*, vol. 21, pp. 324-330, 2013/05/01/ 2013.
- [3] K. Li, S. Thompson, and J. Peng, "Modelling and prediction of NO_x emission in a coal-fired power generation plant," *Control Engineering Practice*, vol. 12, no. 6, pp. 707-723, 2004/06/01/ 2004.
- [4] J. A. Jahnke, "Continuous emission monitoring," 2000.
- [5] C. Bax, S. Sironi, and L. Capelli, "How Can Odors Be Measured? An Overview of Methods and Their Applications," *Atmosphere*, vol. 11, no. 1, 2020.
- [6] L. Capelli, S. Sironi, and R. Del Rosso, "Odor sampling: techniques and strategies for the estimation of odor emission rates from different source types," (in eng), *Sensors (Basel, Switzerland)*, vol. 13, no. 1, pp. 938-955, 2013.
- [7] D. Leung and J. A. Romagnoli, "Chapter 6.4 - Fault Diagnosis Methodologies for Process Operation," in *Computer Aided Chemical Engineering*, vol. 11, B. Braunschweig and R. Gani, Eds.: Elsevier, 2002, pp. 535-556.
- [8] J. A. Covington, S. Marco, K. C. Persaud, S. S. Schiffman, and H. T. Nagle, "Artificial Olfaction in the 21st Century," *IEEE Sensors Journal*, vol. 21, no. 11, pp. 12969-12990, 2021.
- [9] P. Boeker, "On 'Electronic Nose' methodology," *Sensors and Actuators B: Chemical*, vol. 204, pp. 2-17, 2014/12/01/ 2014.
- [10] H. Abdi and L. J. Williams, "Principal component analysis," *WIREs Computational Statistics*, vol. 2, no. 4, pp. 433-459, 2010.
- [11] M. Sun, "Support Vector Machine Models for Classification," in *Encyclopedia of Business Analytics and Optimization*, J. Wang, Ed. Hershey, PA, USA: IGI Global, 2014, pp. 2395-2409.
- [12] C. V. Rekhate and J. K. Srivastava, "Recent advances in ozone-based advanced oxidation processes for treatment of wastewater- A review," *Chemical Engineering Journal Advances*, vol. 3, p. 100031, 2020/11/15/ 2020.
- [13] W. Yang, H. Zhou, and N. Cicek, "Treatment of Organic Micropollutants in Water and Wastewater by UV-Based Processes: A Literature Review," *Critical Reviews in Environmental Science and Technology*, vol. 44, no. 13, pp. 1443-1476, 2014/07/03 2014.
- [14] S. Manikandan *et al.*, "Emerging nano-structured innovative materials as adsorbents in wastewater treatment," *Bioresource Technology*, vol. 320, p. 124394, 2021/01/01/ 2021.
- [15] J. M. Lema and S. S. Martinez, *Innovative wastewater treatment & resource recovery technologies: impacts on energy, economy and environment*. IWA publishing, 2017.

Upcycling of PU waste via microwave-assisted chemolysis process

Riccardo Donadini, Carlo Boaretti, Alessandra Lorenzetti, Michele Modesti*

Dipartimento di Ingegneria Industriale (DII), Università degli studi di Padova

**Corresponding author e-mail: michele.modesti@unipd.it*

1. Introduction

In this work we explored a microwave-assisted (MW) glycolysis process to chemically recycle rigid polyurethane (PUR) foam waste to obtain a single-phase product with suitable physio-chemical properties as secondary raw material for the synthesis of new PUR products. Such approach was compared to a conventionally heated (CH) process, analysing the performances of different catalysts.

In the last years, several emerging techniques have attracted the attention of the research community due to their considerable process intensification potential. Among them, microwaves heating has been established as an efficient strategy for both organic synthesis and extraction processes [1–3]. Through a controlled irradiation, microwaves can indeed be absorbed by suitable substances and readily converted into heat. Such mechanism is capable to produce a volumetric heating effect far more efficient than the surface conduction of traditional heating elements.

Polyurethane is the 6th polymer most used all over the world [4]. Polyurethane demand comes mainly from the construction sector, but its use is also widespread in the automotive, furniture, footwear sector and in the electronic industry. As a direct consequence of the commercial success of polyurethane, a growing amount of waste is being disposed of by landfilling in the last decades. Among possible polyurethane end-of-life scenarios chemical recycling could be the cornerstone for polyurethane recycling [5,6]. All reactions involve the cleavage of the urethane bonds of the polymer. Hydrolysis, aminolysis, phosphorolysis, acidolysis and glycolysis are different routes to recycle polyurethane [7]. Glycolysis is a transesterification reaction between the ester part of the urethane group of the waste polyurethane and the alcoholic groups of a glycol. MDA (methylenedianiline) is the main by-product of this process, and it is produced by hydrolysis, pyrolysis and by glycolysis of ureic groups in the polyurethane network [8]. Humidity present in the polymer foam is responsible for the hydrolysis. Pyrolysis occurs because of the high reaction temperature .

2. Methods

Glycolysis reactions

Glycolysis tests for the chemical depolymerisation of PUR foams were carried out using two different configurations to provide the heat necessary to sustain the reaction. The first configuration is based on a conventional heat conduction apparatus comprising an isomantle equipped with a flask, a temperature sensor and mechanical stirring. The second configuration is based on a microwave reactor equipped with hermetically sealed PTFE vessels, a magnetic stirring mechanism, and a fibre optic temperature sensor. All experiments were run at 200°C, to balance catalyst activation with minimal side products formation, and atmospheric pressure. According to different preliminary tests, a mass feed ratio ($m_{\text{PU}}/m_{\text{DEG}}$) equal to 1.5 was employed. Catalysts were tested at 30 and 50 mmol/100g_{PU} concentrations. According to several preliminary experiments, reaction times were set to 4h in the case of conventional heating and 15 min with microwave in order to obtain glycolysis product with comparable properties.

Glycolysis product were characterized in terms of aromatic amine content (HPLC), infrared spectroscopy (FT-IR), dynamic viscosity, hydroxyl value and gel permeation chromatography (GPC).

Foams

The polyols mixtures obtained from the glycolysis of PUR wastes were tested to evaluate PUR foam production suitability and subsequently characterized for performance evaluation. Several foams were produced, using different percentages of recycled polyol, and evaluated in comparison to equivalent products obtained from virgin polyols.

Foams were characterized in terms of apparent density, compression resistance, thermal conductivity, and morphology (SEM).

3. Results and discussion

Conventional and microwave-assisted glycolysis

Viscosity is the main property monitored in order to assess the extent of depolymerization of the waste polyurethane. The amount of MDA is measured to assess the extent of secondary reactions, whereas the hydroxyl value is useful during the subsequent synthesis of new foams. Table 3.1 summarizes experimental data, viscosity, and MDA, categorized by heating method and catalyst concentration.

Table 3.1: Properties of CH and MW products. Maximum errors for viscosity measurements is $\pm 80cP$, $\pm 0.1\%wt$ for MDA concentrations and $\pm 15 mg_{KOH}/g$ for hydroxyl values.

Cat	Heating		CH		MW		
	C _{cat} , [mmol/100g _{PU}]	μ , [mPa·s]	MDA, [%wt]	HV, [mg _{KOH} /g]	μ , [mPa·s]	MDA, [%wt]	HV, [mg _{KOH} /g]
KOAc	30	2346	1.65	505	1840	2.27	497
	50	2201	2.48	538	762	4.92	517
Sn(Oct) ₂	30	2541	1.33	540	2263	2.08	532
	50	2299	1.86	550	1154	3.22	549
MEA	30	8570	1.03	482	N.A.	0.19	512
	50	7025	0.38	475	11844	0.30	528

According to Table 3.1, the viscosity of the glycolyzate is highly influenced by both the type of catalyst and its concentration; the same can be said for the aromatic amine content. These two outputs are inversely related as the lower the viscosity, the higher the degree of depolymerization, and therefore the higher the amount of by-products formed at constant reaction time. On the one hand, a lower viscosity is desirable, as too viscous liquids are not easily handled in production facilities. Furthermore, the higher the viscosity of the glycolyzate, the higher the energy expenditure of the pump in the industrial foam production plant. On the other hand, MDA amount must be kept as low as possible; however, its abatement will be treated in another work.

From the catalyst point of view, it is clear that the higher the concentration of MDA, the lower the viscosity. However, the observed differences are notable in the use of monoethanolamine; it is the least active catalyst tested, producing high viscosities although having very low MDA concentrations. This evidence is confirmed and cleared when examining MW glycolysis results. In the case of 30 mmol/100g_{PU} it was not possible to measure the viscosity as the polyurethane was not completely dissolved and reacted.

In both the case of potassium acetate and stannous octoate, glycolyses proceeded quickly: microwaves drastically improved the recycling process since 15 minutes of microwave irradiation led to lower viscosities and higher MDA concentration than 240 minutes through conventional heating. This result is very interesting, since the reduction in reaction time is of 94%. The higher MDA concentration found in MW glycolyses can be explained by considering two facts. First, MW glycolyzates have viscosities lower than those of their CH counterparts, which means that less than 15 minutes is required to reach the same viscosity obtained through CH. Second, metal salts such as KOAc and Sn(Oct)₂ coupled with DEG provoke highly efficient dielectric heating and ionic polarization, providing the suitable conditions to let depolymerization reactions undergo.

Furthermore, stannous octoate and potassium acetate are equally capable of promoting transesterification as obtained viscosities are comparable, however, the latter allows hydrolysis and pyrolysis to occur more than the former. As a result, with Sn(Oct)₂, a lower concentration of MDA is achieved together with a comparable viscosity with the KOAc-catalysed product.

In addition to these considerations, in Figure 3.1 the characteristic peaks of the urethane structure can be monitored; optical path is constant when working with ATR. Peaks at 1515 cm⁻¹ (C-C carbon in the aromatic ring) and 1130 cm⁻¹ (C-O ether stretching) are used as reference peak to study relative variations of other significant peaks. Lower transmittances of peaks at 1720 cm⁻¹ (C=O carbonyl stretching of the urethane), 1540 cm⁻¹ (N-H amide stretching of the urethane), and 1230 cm⁻¹ (C-O carbonyl stretching of the urethane) indicate that the polymer structure is less degraded than in the other two cases. Shoulder-type peaks can be noticed at 1630 cm⁻¹: those are more marked for KOAc rather than Sn(Oct)₂ and MEA, testifying the presence of a higher concentration of free amino groups.

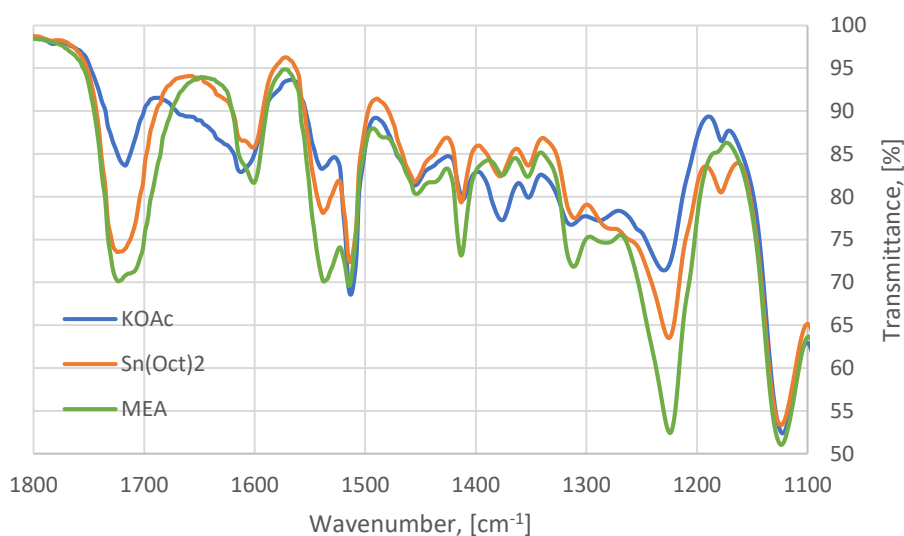


Figure 3.1: Infrared spectra of CH glycolyzates, catalyst concentration is 30mmol/100g_{PU}. Same trends were obtained with 50mmol/100g_{PU}.

The energy expenditure, EE, is calculated as the ratio between energy delivered to the system and total mass heated. In CH glycolysis, the power delivered by the isomantle is constant and 1400W as it has an on-off controller, the energy supplied is therefore the product of power and exposure time, t_h , the time the heating resistance is switched on. This is approximately 3h, considering both heating (one hour) and the reaction phase (two out of four hours). The hot plate has an on-off controller as the power cannot be controlled. Conversely, the energy given to the system in MW glycolysis is calculated as an integral of the power profile or as average power, P_{av} , multiplied by exposure time, therefore:

$$EE_{CH} = \frac{P_{max} \cdot t_h}{m_{tot}} = \frac{1.4kW \cdot 3h}{0.35kg} = 12 kWh/kg$$

$$EE_{MW} = \frac{\int_0^{t_h} P dt}{m_{tot}} = \frac{P_{av} \cdot t_h}{m_{tot}} = \frac{0.3kW \cdot 0.25h}{0.035kg} = 2.1 kWh/kg$$

The energy expenditure for the CH glycolysis is almost six times that necessary for the MW glycolysis, with an energy savings of 82%.

In conclusion, products obtained with potassium acetate and stannous octoate show a best performance from the glycolyzate point of view. 30 mmol/100g_{PU} as catalyst concentration is sufficient to reach an acceptable

viscosity (i.e. degree of depolymerization) keeping as low as possible by-product concentration. Stannous octoate displayed a higher selectivity with respect to potassium acetate as it allows for comparable viscosity but lower MDA content. In the case of monoethanolamine, conventional heating and 50 mmol/100g_{PU} as concentration are necessary to obtain a suitable product.

Synthesis and characterization of foams

Once it was proved that the CH and MW product are comparable, new foams were synthesized starting from MW products. New PUR foams were produced with an increasing percentage of glycolyzate as a substitute for virgin polyol, at 0, 15, 30, and 45% with respect to the total amount of polyol.

Figures 3.2-4 show the results related to the new foam synthesis in terms of average cell diameter, and compressive strength, for foams obtained with 30 mmol/100g_{PU} KOAc-catalysed glycolyzate.

Substitution of part of virgin polyol with recycled material allows for better thermal and mechanical performances with respect to a reference foam. The percentage of substitution reaches 30% without having a property decay. As can be seen in Figures 3.2 and 3.3, higher compression strength results from a smaller cell diameter. Aromatic rings already contained in the glycolysis polyol increase the compatibility with the isocyanate, leading to a finer cellular morphology. Same considerations can be made in terms of thermal performances, as the lower the average cell diameter, the lower the thermal conductivity (Figure 3.4). However, this was not observed as thermal conductivities are comparable. This may be caused by a higher percentage of open cells. With 45% substitution, a very slight and acceptable decrease (with respect to lower substitution percentages) of the properties is observed; this is due to a trade-off between two factors: glycolysis products contain aromatic rings that increase the miscibility with isocyanate component as well as diethylene glycol which decreases the average functionality of the mixture. At 45% substitution DEG contribution becomes relevant, leading to decrease in the mechanical performances due to lower crosslinking density in the foam. Best foams were obtained with KOAc-catalysed glycolysis product. A higher compression strength can be explained considering that potassium acetate is commonly used as trimerization catalyst. Isocyanurate structures formation promoted by trimerization catalysts leads to higher mechanical performances [9].

Foams obtained with an increasing amount of Sn(Oct)₂-catalysed glycolysis product showed no variations in thermal performances and an increased compression strength, up to 25% higher than reference with 45% substitution. However, reactive mixtures were difficult to deal with when stirring, reaction times were drastically shortened due to the fact that stannous octoate is a strong gel catalyst used also during PUR synthesis. When increasing the glycolyzate content, stannous octoate concentration is increased as well: for this reason maximum percentage substitution is limited to 15%. Above 15% foams obtained were dimensionally unstable.

Foams obtained with monoethanolamine showed higher mechanical performances than the reference foam, up to 40% higher with 45% substitution, and no thermal properties variations. Despite this, a brittle and chalky structure was observed. Even with MEA-catalysed products mixing problems were experienced as these have a higher viscosity, therefore the maximum substitution percentage was 15%.

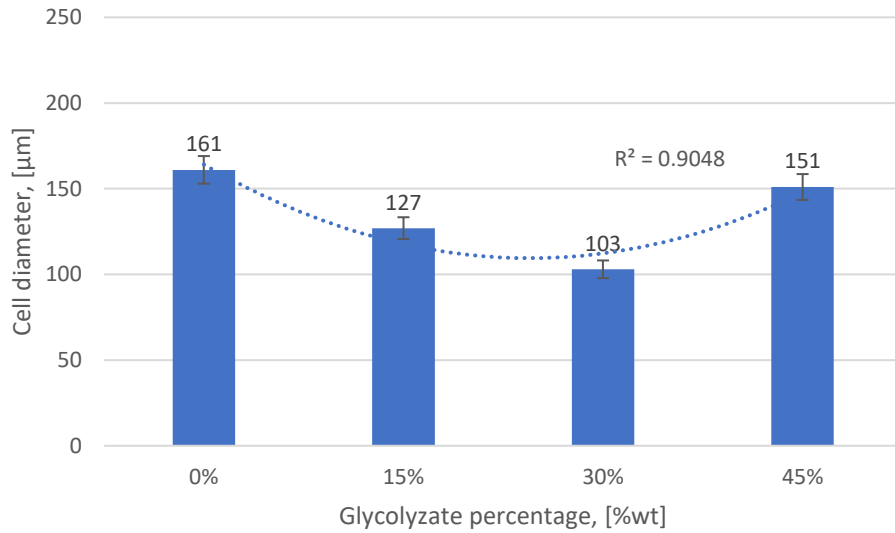


Figure 3.2: Average cell diameter of the foam along with substitution percentage.

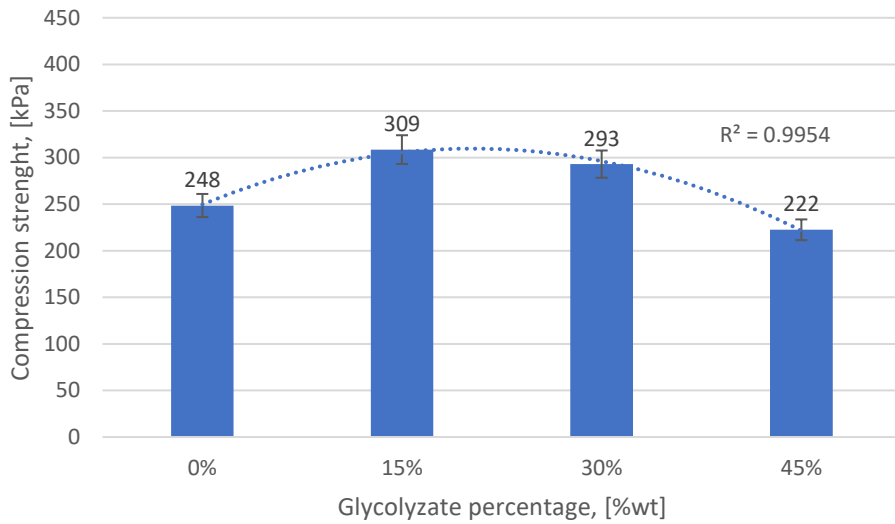


Figure 3.3: Compression resistance along with percentage substitution.

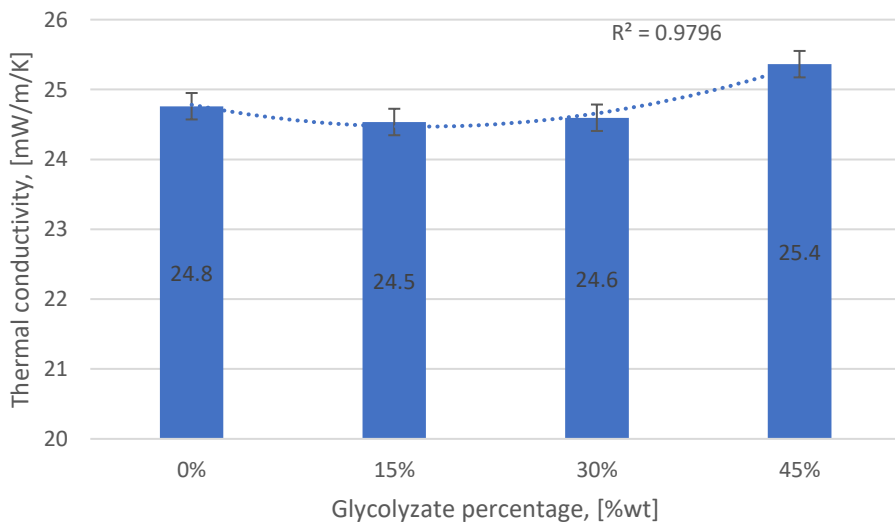


Figure 3.4: Thermal conductivity along with percentage substitution.

4. Conclusions

In this work, we assessed the feasibility of a microwave-assisted glycolysis reaction to recover a polyol-like liquid product from rigid polyurethane waste. Reaction conditions chosen allowed to obtain a single-phase product, which eases its handling with respect to a split-phase process, suitable for rigid foams production. In all trials, except on, microwaves drastically decreased the reaction time to reach a proper viscosity of the product, which decreases of 94% going from 240 minutes, with conventionally heated process to 15 minutes with microwave heating. Among the three catalysts were tested, products obtained with metal-based catalysts provided better properties than those obtained with organic catalysts. A simple energy balance showed microwave-assisted glycolysis is convenient with respect to the conventionally heated process as allowed for an energy saving of 82% (2.1 kWh/kg).

Foams obtained with metal-catalysed products, in particular KOAc, are also the ones that provide the best results. A substitution of virgin polyol up to 30% permits one to slightly reduce the thermal conductivity of the foam, coupled with an increase of roughly 20% of the compression strength. Maximum percentage of substitution with Sn(Oct)₂ and MEA-catalysed product is 15% as the mixing process was complicated by high reactivity of the first product and high viscosity of the second one. However, the higher substitution percentage with respect to other works was achieved improving the circularity of the process.

References

- [1] P. Lidström, J. Tierney, B. Wathey, J. Westman, Microwave assisted organic synthesis—a review, *Tetrahedron*. 57 (2001) 9225–9283. [https://doi.org/10.1016/S0040-4020\(01\)00906-1](https://doi.org/10.1016/S0040-4020(01)00906-1).
- [2] C.O. Kappe, Controlled microwave heating in modern organic synthesis, *Angew. Chemie - Int. Ed.* 43 (2004) 6250–6284. <https://doi.org/10.1002/anie.200400655>.
- [3] L. Rinaldi, D. Carnaroglio, L. Rotolo, G. Cravotto, A microwave-based chemical factory in the lab: From milligram to multigram preparations, *J. Chem.* 2015 (2015). <https://doi.org/10.1155/2015/879531>.
- [4] Polyurethane market size, share & trends analysis report by product, by end use, by region and segment forecasts, 2021-2028: <https://www.grandviewresearch.com/industry-analysis/polyurethane-pu-market>, (2021) 105. Last accessed 11.03.2022.
- [5] A.J. Martín, C. Mondelli, S.D. Jaydev, J. Pérez-Ramírez, Catalytic processing of plastic waste on the rise, *Chem.* (2021) 1–47. <https://doi.org/10.1016/j.chempr.2020.12.006>.
- [6] S.C. Kosloski-Oh, Z.A. Wood, Y. Manjarrez, J.P. de los Rios, M.E. Fieser, Catalytic methods for chemical recycling or upcycling of commercial polymers, *Mater. Horizons.* (2021). <https://doi.org/10.1039/d0mh01286f>.
- [7] D. Simón, A.M. Borreguero, A. de Lucas, J.F. Rodríguez, Recycling of polyurethanes from laboratory to industry, a journey towards the sustainability, 76 (n.d.) 147–171. <https://doi.org/10.1016/j.wasman.2018.03.041>.
- [8] M. Modesti, F. Simioni, R. Munari, N. Baldoin, Recycling of flexible polyurethane foams with a low aromatic amine content, 26 (n.d.) 157–165. [https://doi.org/10.1016/1381-5148\(95\)00031-A](https://doi.org/10.1016/1381-5148(95)00031-A).
- [9] M. Modesti, F. Costantini, E. dal Lago, F. Piovesan, M. Roso, C. Boaretti, A. Lorenzetti, Valuable secondary raw material by chemical recycling of polyisocyanurate foams, *Polym. Degrad. Stab.* 156 (2018) 151–160. <https://doi.org/10.1016/j.polymdegradstab.2018.08.011>.

Ammonia fuel cells onboard zero-emission ships: a comparison of different solutions

Roberta Russo^{1*}, Tommaso Coppola¹, Luca Micoli¹

1 Department of Industrial Engineering (DII), School of Polytechnic and Basic Sciences, University of Naples "Federico II", 80125 Naples, Italy

**Corresponding author E-Mail: roberta.russo5@unina.it*

1.Introduction

The reduction of the carbon footprint of maritime shipping is currently a debated topic and a primary goal [1]. In the last decades, the International Maritime Organization (IMO) has targeted greenhouse gas (GHGs) emissions on ships introducing several regulations aiming a 50% reduction in GHGs by 2050 up to a complete elimination in this century [1 - 2].

Several climate-friendly alternatives are being considered to reach that goal, these include both power energy technologies, such as fuel cells and batteries, and innovative fuels, like hydrogen and methanol [3 - 5].

Ammonia has recently attracted wide interest as fuel for shipping [6 - 7].

Nowadays, ammonia is primarily used to produce fertilizers and other chemicals rather than for energetic purposes. Nevertheless, in the future, there is potential for climate-friendlier production processes. Green ammonia can be synthesized by using green hydrogen coming from renewable or non-carbon sources, like wind or solar energy, and the so-called blue ammonia can be produced reducing the emission footprint of the production using carbon capture technologies [8 - 10].

Ammonia certainly has the energy potential for an alternative marine fuel: it's abundant and common, it has an energy density of around 3 kWh/l, it does not have to be stored in high-pressure tanks or cryogenic dewars (unlike hydrogen and GNL) [11].

The most relevant advantage of using ammonia in the marine sectors is that it does not release CO₂ and other harmful compounds, such as Sulphur oxides (SO_x) and particulate matter (PM), allowing to comply with the stringent environmental regulations [6 - 7, 12].

Ship-owners and industry analysts state that ammonia will play a pivotal role in decarbonizing ships, according to a DNV's report (2019), ammonia could make up 25 % of the maritime fuel mix by 2050, with nearly all newly built ships running on ammonia from 2044 onward [13]. However, the application of ammonia in the marine transportation sector is still at early stages: no vessels of any size today are equipped to use this fuel. Even if they were, the supply chain of green ammonia is almost virtually non-existent [8]. As green ammonia slowly scales up, the shipping industry will have to solve some other issues related to toxicity, corrosiveness, slow ignition and NO_x emissions [11 - 14]. Moreover, since ammonia's energy density is about half that of diesel, if it is used as a direct fuel in ICE, ships will need to accommodate larger storage tanks or to reduce the operating range of vessels.

Nevertheless, burning ammonia in ICE produces nitrogen dioxide (NO_x) which contributes to smog, acid rains and can harm people [14]. Combustion also yields small amounts of nitrous oxide (N₂O) is a GHG significantly more dangerous than CO₂. Therefore, shipbuilders have to consider special equipment to install onboard to avoid such outcome, e.g. a selective catalytic reduction system (SCR) [15].

An option to prevent air pollution with ammonia is to use the Fuel Cell (FC) technology instead of ICEs [16 - 19]. An FC is an electrochemical device that converts the chemical energy of a fuel directly into electrical energy with an efficiency higher than ICEs. Since no combustion process occurs in an FC, the release of harmful gases or particles in the air is avoided [20 - 21].

The mega-yacht is an interesting application for these technologies because it could favour a market in which passengers are allowed to enjoy a virtually silent and clean yachting experience.

The construction of yachts had an impressive growth in the last decades reaching an industrial production scale, therefore they cannot be considered "private ships" anymore and have to be developed accordingly to

commercial passenger ships rules (e.g. MARPOL). This means that yachts have to abide by the environmental rules as well [15].

The present work investigates the possibility of installing ammonia FCs onboard ships aiming to supply the hotel loads and to support the propulsion in different operating conditions. The main purpose is to reach the zero-emission condition and to allow the navigation in Emission Control Areas (ECA). A comparison has been made between three different FC technologies: Proton Exchange Membrane Fuel Cell (PEMFC), Solid Oxide Fuel Cell (SOFC) and Alkaline Fuel Cell (AFC).

2. Methods

2.1. Fuel Cell Systems

FC technologies considered in the present work are PEMFC, SOFC, AFC.

Ammonia can be fed to the SOFC and AFC directly, while to PEMFC is used as a hydrogen carrier [17, 18]. In the latter case, ammonia is dissociated easily into nitrogen (N₂) and hydrogen (H₂) through an endothermic reaction, then the produced hydrogen is concentrated before feeding an FC.

For all cases under consideration, the flow rate of fuel to be treated has been estimated using relation (1), assuming that the electrical efficiency (η) is constant:

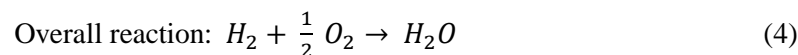
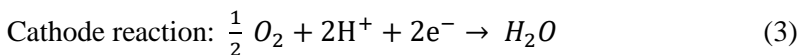
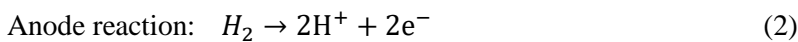
$$m = P/\eta LHV \quad (1)$$

Where P is the power generated, LHV is the lower heating value of hydrogen (120 MJ/kg) or ammonia (18.48 MJ/kg).

2.1.1. Proton Exchange Membrane Fuel Cell

PEMFCs use a polymer membrane with high proton conductivity as an electrolyte and operate at temperatures between 70 and 100 °C; they are mainly developed for automotive and small-scale power generation (1-250 kW) applications. The product FCgen®-HPS provided by Ballard (Canada) has been assumed as a reference [22], which operates at low temperature (70-80 °C). This PEM module provides 140 kW power with an electrical efficiency of 55%. The electrodes must be made of porous materials to allow diffusion of the reactant gases into the active zones, where the noble metal catalyst is in contact with the ionic and electronic conductor. The membrane is semi-permeable, allowing positive ions to pass through, but providing electrical isolation by not allowing electrons to pass, which are forced to travel through the external circuit set up to transfer electrical energy from the fuel cell to the user. The membrane must be impregnated with a precise amount of water, which is controlled during operation by humidifying the hydrogen and air introduced. A basic working scheme is shown in Figure 1 and other main characteristics are reported in Table 1.

The characteristic reactions at the anode, cathode and overall reaction are:



The pure hydrogen required for fuelling the PEM is supposed to be produced by the ammonia decomposition and purification systems, which constitute the ammonia processing system (AP). The ammonia is taken from the tanks, preheated in a heat exchanger (for better energy efficiency), vaporised and then separated in the main reactor. In this study, we referred to the specifics and performance of the reactor supplied by the SinceGas company (China), which can process an NH₃ flow rate up to 250 Nm³/h. Within the reactor, ammonia can be dissociated into hydrogen and nitrogen (N₂) via the endothermic reaction:

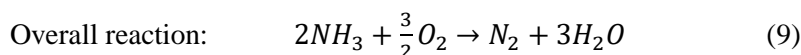
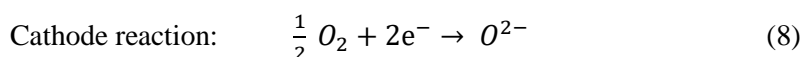
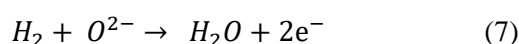
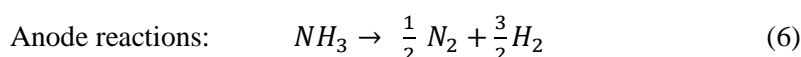


This reaction requires both a catalyst and a heat source, which is supposed to be produced electrically on board. Then, a Pressure Swing Adsorption (PSA) system, which generally uses special molecular sieves, is required for the separation of H₂ from N₂. Specifically, the PSA returns a quantity of pure hydrogen of about 15 kg/h.

2.1.2. Solid Oxide Fuel Cell

SOFCs operate at high temperatures (in the range 700-1000 °C) to ensure high conductivity to the electrolyte, which consists of ceramic material (zirconium oxide doped with yttrium oxide) [23]. SOFCs can be divided into two categories depending on the chemical specific of electrolyte. In the present study, it is considered a basic electrolyte, which conducts O²⁻ ions. They are particularly promising for stationary power generation and cogeneration in power ratings from a few kW to several tens of MW. For instance, the product “SOFC BOL module” provided by Bloom Energy company (United States of America) has been selected as reference. This module has an output power of 350 kW and an electrical efficiency of 55%; other specifics are reported in Table 1 and a basic working scheme is shown in Figure 1.

The overall and the electrodes' reactions are [24]:



2.1.3. Alkaline Fuel Cell

AFCs use an electrolyte consisting of a water solution of potassium hydroxide (≈30 %) and operate at temperatures of around 120 °C [21, 24]. They have reached a good degree of technological maturity, especially for special uses (military and space applications); their characteristics (requiring extremely pure feed gases) have severely limited their diffusion. A model from the AFC energy (United Kingdom) 350 kW HydroX-Cell(L) catalogue is chosen, with an electrical efficiency of 60%. The specifics are reported in Table 1; the working scheme is shown in Figure 1.

The overall reaction, the characteristic reactions at the anode and cathode are as follows [21, 24]:

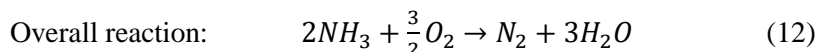
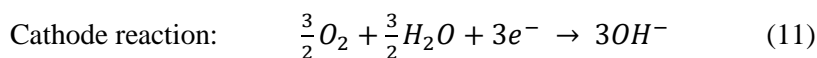


Table 1. Main specifics of the selected FC and AP power system

Specific	AP	PEM	SOFC	AFC
Inlet	NH ₃	H ₂	NH ₃	NH ₃
Operating temperature [°C]	100-300	70-80	700	120
Power [kW]	600	140	350	350
Efficiency [%]	88	55	55	60
Weight [kg]	47	55	18433	17500
Volume [m ³]	14	0.1	33	67

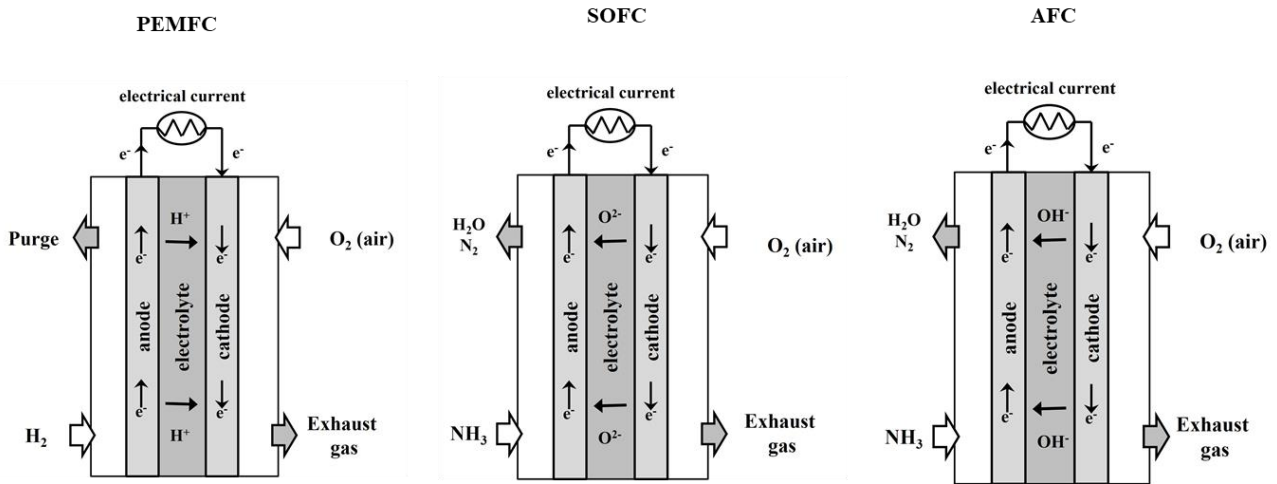


Figure 1. PEMFC, SOFC and AFC working schemes

2.2. Case study

The target ship is a mega-yacht with a length of about 64 m, which has an Atlantic autonomy of 4000 nm at 14 kn and reach a maximum speed of 18 kn. Shipowners generally establish the main requirements of the ship, i.e. the number of passengers and crew, size of cabins, public spaces, speed. These and other general characteristics of the mega-yacht are reported in Table 2.

Table 2. General specifications of the mega-yacht

Main dimension LxBxH [m]	64.4x11.3x6.2
Displacement [t]	921
Full load immersion [m]	3.6
Decks [num]	4
Passengers [num]	12
Crew members [num]	10
Cruise speed [kn]	14
Maximum speed [kn]	18
Autonomy [day]	14
Propulsion Diesel engine (×2) [kW]	1320
Shaft Generator engine (×2) [kW]	260
Gen-set [kW]	575

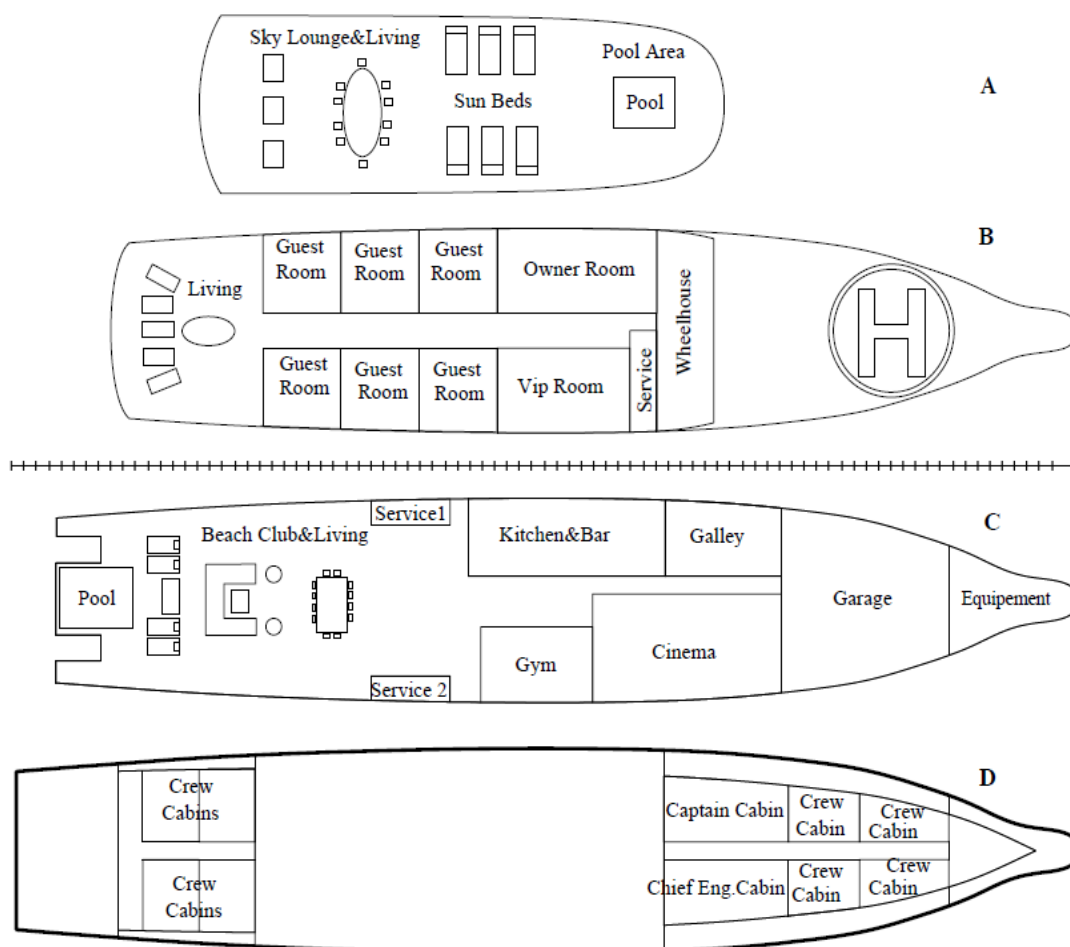


Figure 2. The layout of the mega-yacht: A: Sun Deck (12.9 m above BL); B: Upper Deck (9.2 m above BL); C: Main Deck (6.2 m above BL); D: Lower Deck (3.3 m above BL)

The ship's structure is laid out over four decks, as shown Figure 2. The engine room is placed between the Base Line (BL) and the Main Deck, while the fuel is stored between bulkhead 4th and the collision bulkhead. The initial configuration of the mega yacht includes two main Diesel engines (1320 kW Rolls Royce, model 4-stroke MTU 12V 4000 M33F) capable of supplying a maximum power of about 3021 kW to reach 18 kn. Additionally, it is considered the installation of two liquid-cooled permanent magnet synchronous motor shaft generators directly connected to the gearboxes (Type C SISHIP EcoProp from Siemens) to recover the engines' waste energy and to provide additional power to the propeller when the main engine is underperforming. This configuration allows both the “Power Take In” (PTI) and “Power Take-Off” (PTO) modes for the energy transmission [25]. A Diesel Gen-set (MTU 12V 2000 M41A by Rolls Royce) provides the non-propulsion power demand, with a power output of 575 kW at 1500 rpm.

3. Results and discussion

General Arrangements

The onboard installation of FCs has a different arrangement for the three technologies under consideration, depending on volume and weight of the FC system.

PEMFC are installed in a different area than the AP, though the footprint is limited, it can be arranged in a separate enclosed space within the engine room. The AP is arranged between the 3rd and 4th bulkheads. These rooms are classified as Hazardous Area Zone 1; therefore, a dedicated ventilation system and airlocks are provided.

SOFC and AFC have a very similar onboard layout: the FC space is larger than the case of PEMFC, which is due to the higher footprint. These are arranged between the 3rd and 4th bulkheads and enclosed by airlocks. The described arrangements are shown in Figure 3.

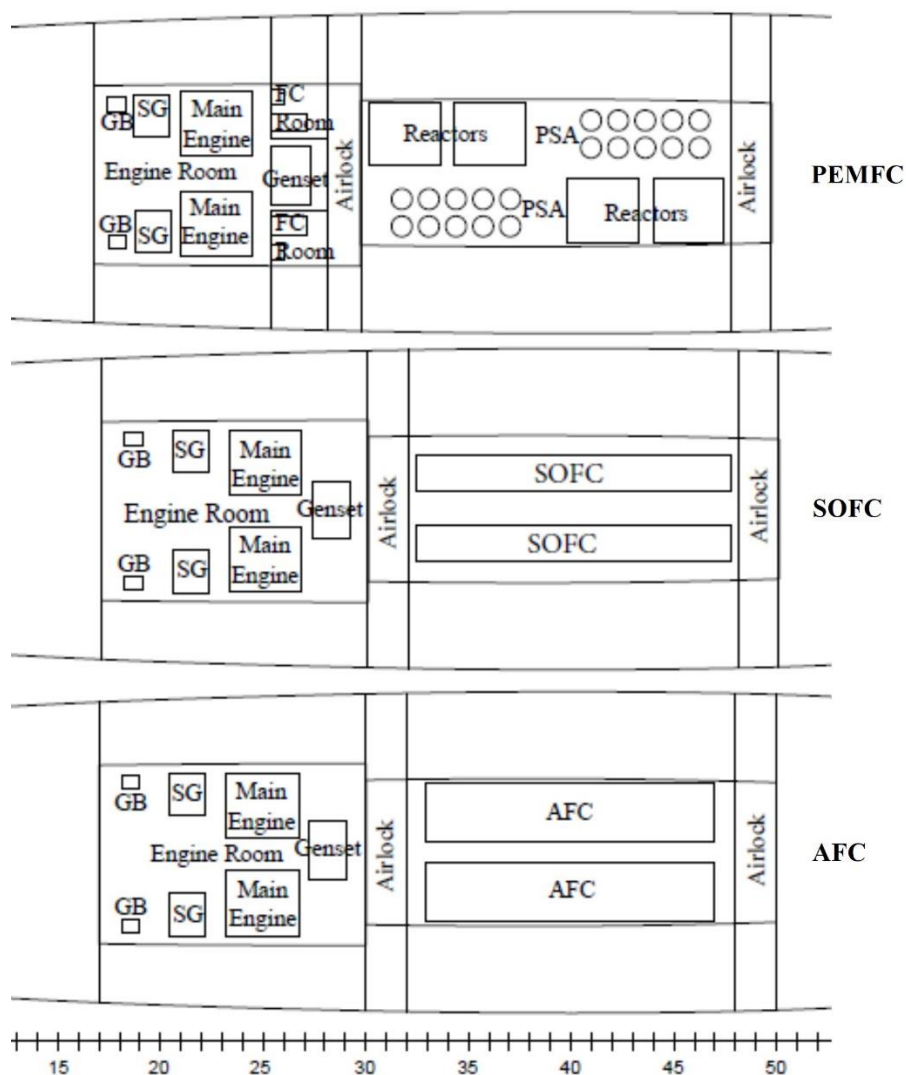


Figure 3. PEMFC, SOFC and AFC systems arrangement

Ammonia is supposed to be stored onboard in the liquid state at 98 kPa and 240 K. According to the international rules [26], ammonia cannot be contained in structural tanks but in type C double-walled tanks. Cemin Eurotank (Italy) tanks are chosen as reference for the study, these have an external diameter of 980 mm, an internal diameter of 950 mm and are specifically sized accordingly to the available space. It results that 48 m³ of ammonia can be stored in nine tanks with the main specifics reported in Table 3, and arranged on board as shown in Figure 4.

Table 3. Main specifics of NH₃ storage tanks

Tanks [num]	Volume [m ³]	Length [m]	Weight (empty) [t]
6	5.0	6.8	1.2
3	6.0	8.5	1.5

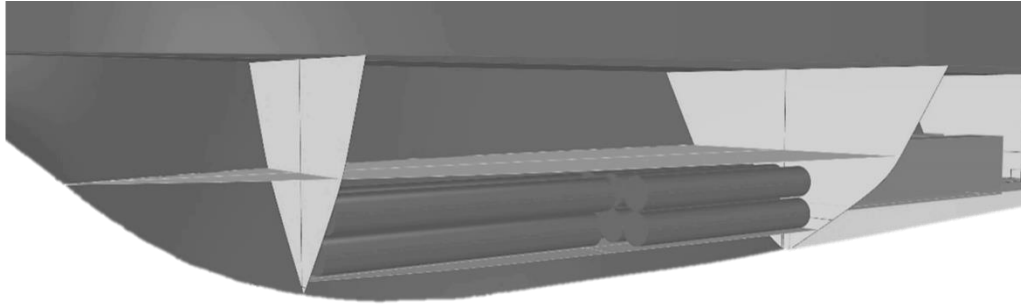


Figure 4. Ammonia storage tanks arrangement

3.1. Autonomy

The available volume for the storage tanks limited the amount of ammonia stored onboard, this affects considerably the autonomy of the ship depending on the FC and operating mode.

In the case that the FC system supplies only the hotel loads (kitchen, lightnings, air conditioning, rooms and deck), the autonomy is 6 days for PEMFC, 13 days for SOFC and 14 days for AFC. It must be noted that the lowest value for the PEMFC is due to the additional power required by AP.

The zero-emission condition can be achieved by FCs powering both the propulsion and the hotel loads during the navigation and mooring in ports. In this case, the autonomy is approximately the same for SOFC and AFC, while for the PEMFC is only 3 days.

If it is assumed that the zero-emission condition is limited to 250 nm at 8 kn, allowing entry and exit in ECA areas and anchoring in ports, the autonomy is 4 days for PEMFC, 11 days for SOFC and 12 days for AFC.

The autonomies are summarized in Table 4.

Table 4. Autonomy for different conditions and FCs

Condition	Autonomy [days]		
	PEMFC	SOFC	AFC
Hotel loads	6	13	14
Zero Emission	3	6	6
Zero Emission @ 8 kn, 250 nm	4	11	12

4. Conclusions

This work investigated the application of different ammonia-fuelled FC technologies (PEMFC, SOFC and AFC) for the electric power generation and to reach the zero-emission condition. A 64 m length mega-yacht was assumed as case study.

To identify the optimal solution, a comparison was carried out in terms of both the effect on the general arrangement and autonomy of the ship.

It resulted that, PEMFC was the most commercialized FC technology with the highest power density, but the presence of a bulky and heavy AP system was necessary to produce pure H₂. Although SOFC and AFC could be directly fuelled by ammonia, they required a significant space onboard for the installation.

The zero-emission condition was reached with all the FC configurations, but the limited ammonia volume stored affected the ship's autonomy. The autonomy was in the range 3-4 days in the case of PEMFC and 6-12 days in the case of SOFC and AFC. Allocating more spaces onboard to the ammonia storage tanks can increase the autonomy, but it requires fundamental modification of the original arrangement of the ship.

References

- [1] “Cutting GHG emissions from shipping - 10 years of mandatory rules.” [Online]. Available: <https://www.imo.org/en/MediaCentre/PressBriefings/pages/DecadeOfGHGAction.aspx>. [Accessed: 01-Feb-2022].
- [2] J. E. McCarthy, “Air pollution and greenhouse gas emissions from ships,” in *Air Pollution and Ship Emissions*, 2010.
- [3] J. Anders, “Comparison of Alternative Marine Fuels SEA\LNG Ltd,” 2019.
- [4] L. Ming Main Author, L. Ming, L. Chen, and L. Siu Lee Jasmine Sze Jia Yin Koh Eng Kiong Yang Mengyao Gou Xueni, “Methanol as a Marine Fuel-Availability and Sea Trial Considerations Alternative Fuels for International Shipping A Study on the Future Energy Options of Singapore Harbour Craft Electrification of Singapore Harbour Craft-Shore and Vessel Power System Considerations Executive Summary,” 2020.
- [5] E. A. Bouman, E. Lindstad, A. I. Rialland, and A. H. Strømman, “State-of-the-art technologies, measures, and potential for reducing GHG emissions from shipping – A review,” *Transp. Res. Part D Transp. Environ.*, 2017, doi: 10.1016/j.trd.2017.03.022.
- [6] J. Hansson, S. Brynolf, E. Fridell, and M. Lehtveer, “The potential role of ammonia as marine fuel-based on energy systems modeling and multi-criteria decision analysis,” *Sustain.*, vol. 12, no. 8, Apr. 2020, doi: 10.3390/SU12083265.
- [7] K. Kim, G. Roh, W. Kim, and K. Chun, “A Preliminary Study on an Alternative Ship Propulsion System Fueled by Ammonia: Environmental and Economic Assessments,” *J. Mar. Sci. Eng.* 2020, Vol. 8, Page 183, vol. 8, no. 3, p. 183, Mar. 2020, doi: 10.3390/JMSE8030183.
- [8] D. R. MacFarlane et al., “A Roadmap to the Ammonia Economy,” *Joule*, vol. 4, no. 6, pp. 1186–1205, Jun. 2020, doi: 10.1016/j.joule.2020.04.004.
- [9] Z. Cesaro, J. Thatcher, and R. Bañares-Alcántara, “Techno-Economic Aspects of the Use of Ammonia as Energy Vector,” *Techno-Economic Challenges Green Ammon. as an Energy Vector*, pp. 209–219, Jan. 2021, doi: 10.1016/B978-0-12-820560-0.00009-6.
- [10] S. Ghavam, M. Vahdati, I. A. G. Wilson, and P. Styring, “Sustainable Ammonia Production Processes,” *Front. Energy Res.*, vol. 9, Mar. 2021, doi: 10.3389/FENRG.2021.580808/FULL.
- [11] O. Elishav, B. Mosevitzky Lis, A. Valera-Medina, and G. S. Grader, “Storage and Distribution of Ammonia,” *Techno-Economic Challenges Green Ammon. as an Energy Vector*, pp. 85–103, Jan. 2021, doi: 10.1016/B978-0-12-820560-0.00005-9.
- [12] M. Gallucci, “The ammonia solution: Ammonia engines and fuel cells in cargo ships could slash their carbon emissions,” *IEEE Spectr.*, vol. 58, no. 3, pp. 44–50, Mar. 2021, doi: 10.1109/MSPEC.2021.9370109.
- [13] “Ammonia as a marine fuel DNV.” [Online]. Available: <https://www.dnv.com/Publications/ammonia-as-a-marine-fuel-191385>. [Accessed: 01-Feb-2022].
- [14] H. Kobayashi, A. Hayakawa, K. D. K. A. Somarathne, and E. C. Okafor, “Science and technology of ammonia combustion,” *Proc. Combust. Inst.*, vol. 37, no. 1, pp. 109–133, Jan. 2019, doi: 10.1016/J.PROCI.2018.09.029.
- [15] V. Ruggiero, “ScienceDirect Peer-review under responsibility of the scientific committee of the International Conference on Industry 4.0 and Smart Manufacturing. -NC-ND license (<http://creativecommons.org/licenses/by-nc-nd/4.0/>) Peer-review under responsibility of the s,” 2020, doi: 10.1016/j.promfg.2020.02.020.
- [16] A. Afif, N. Radenahmad, Q. Cheok, S. Shams, J. H. Kim, and A. K. Azad, “Ammonia-fed fuel cells: a comprehensive review,” *Renew. Sustain. Energy Rev.*, vol. 60, pp. 822–835, Jul. 2016, doi: 10.1016/J.RSER.2016.01.120.
- [17] D. Cheddie, “Ammonia as a Hydrogen Source for Fuel Cells: A Review,” *Hydrog. Energy - Challenges Perspect.*, Oct. 2012, doi: 10.5772/47759.
- [18] O. Siddiqui and I. Dincer, “A review and comparative assessment of direct ammonia fuel cells,” *Therm. Sci. Eng. Prog.*, vol. 5, pp. 568–578, Mar. 2018, doi: 10.1016/J.TSEP.2018.02.011.
- [19] L. Micoli, T. Coppola, and M. Turco, “A Case Study of a Solid Oxide Fuel Cell Plant on Board a Cruise Ship,” *J. Mar. Sci. Appl.*, vol. 20, no. 3, pp. 524–533, Sep. 2021, doi: 10.1007/S11804-021-00217-Y.
- [20] P. T. Moseley, “Fuel Cell Systems Explained,” *J. Power Sources*, 2001, doi: 10.1016/s0378-7753(00)00571-1.
- [21] A. Coralli, B. J. M. Sarruf, P. E. V. De Miranda, L. Osmieri, S. Specchia, and N. Q. Minh, “Fuel cells,” in *Science and Engineering of Hydrogen-Based Energy Technologies: Hydrogen Production and Practical Applications in Energy Generation*, 2018.
- [22] “FCgen HPS Spec Sheet.” [Online]. Available: https://www.ballard.com/about-ballard/publication_library/product-specification-sheets/fcgen-hps-spec-sheet. [Accessed: 24-Feb-2022].
- [23] S. J. McPhail, B. Conti, and J. Kiviahio, *The Yellow Pages of SOFC Technology - International Status of SOFC deployment 2017*. 2017.
- [24] P. Breeze and P. Breeze, “Chapter 7 – Fuel Cells,” *Power Gener. Technol.*, 2019, doi: 10.1016/B978-0-08-102631-1.00007-9.
- [25] “The Superyacht Directory | Superyacht Database.” [Online]. Available: <https://www.boatinternational.com/yachts/the-superyacht-directory>. [Accessed: 24-Feb-2022].
- [26] IMO, “the International Code of Safety for Ships Using Gases or Other Low-Flashpoint Fuels (Igf Code),” *Imo*, 2016.

Hydrodynamic cavitation as a treatment for the removal of methylene blue from synthetic textile wastewaters

Valentina Innocenzi^{1*}, Marina Prisciandaro¹

¹ *Department of Industrial and Information Engineering and of Economics, University of L'Aquila, Piazzale V. Pontieri 1, Monteluco di Roio, 67040 L'Aquila (Italy)*

**Corresponding author E-Mail: valentina.innocenzi@univaq.it*

1. Introduction

Azo dyes are recalcitrant pollutants that constitute a significant burden to the environment; they are organic compounds bearing the functional group $R-N=N-R'$ (R and R' are usually aryls) and are widely used to treat textiles, leather articles, and some foods. Many azo pigments are non-toxic, others are mutagenic and carcinogenic; partly after their uses they are discharged in the effluents and could result in environmental damages if are released without any treatment [1]. These effluents are usually treated to remove pollutants by means of chemical/physical processes (flocculation, coagulation, membrane filtration, and adsorption). But the above mentioned treatments often offer unsatisfactory removal for the presence of some types of color pigments, hard to degrade. Hence alternative processes to remove dyes become necessary, as advanced oxidation processes (AOPs). Among AOPs, hydrodynamic cavitation (HC) has been receiving increasing attention and interest in recent years; HC is the phenomenon of formation, growth, and collapse of microbubbles or cavities, with the release of a large magnitude of energy in a short span of time. It occurs at the transition from the liquid phase to the vapor phase when the local liquid pressure drops to the saturation pressure at a given temperature. HC can be generated by alterations in the flow and pressure, which are usually caused by specific constructions like a Venturi tube or an orifice plate [2, 3]. The main chemical effects of HC are the generation of highly reactive free radicals in the aqueous environment; it is possible to use these radicals for the intensification of chemical processes such as degradation of the water pollutants [4]. HC technology has thus unique advantages in wastewater treatment, however, HC alone is not efficient and cost-effective enough to provide a satisfactory degradation extent of target compounds [5]. By combining HC with other AOPS, the efficiency of degradation of the hybrid technology can be considerably promoted and the processing time and the amount of oxidant can be also reduced [6]. In the present study, the potentiality of hydrodynamic cavitation is analyzed for the degradation of an azo – dye, the methylene blue (MB) from synthetic solutions, mimicking textile effluent wastewaters.

2. Methods

Hydrodynamic cavitation experiments have been performed by using the lab-scale experimental apparatus showed in detail elsewhere [6]. The reactor has a volume capacity of 1 L and it has a thermostatic system to keep constant the temperature. The pump withdraws the liquid from the reactor and sends it into the main pipe and through the cavitation device (Venturi tube), where cavitation occurs, therefore it is reinjected in the tank. The liquid flowrate through a by-pass line is checked by a regulating valve. The diameter of the lines is equal to 12 mm. The pump (Fluid-o-Tech, TMFR2) has a maximum electrical power absorption of 375 W and rotation speeds in the range of 1100–3500 rpm. The system is equipped with a flow meter and two manometers (PI, Barksdale Control Products, UPA2 KF16809D). The cavitation device is a Venturi tube with maximum diameter of 12 mm as piping diameter, while the minimum one is 2 mm. The length of the converging and diverging section is 32 mm and 46 mm, respectively. The divergence angle value is 5.74° . Methylene blue dye was used to perform hydrodynamic cavitation tests. The solutions of dyes were prepared using distilled water for all the experiments. Sodium hydroxide (Fluka Chemika, >97%) and sulphuric acid (Carlo Erba, 96%) were used for adjusting the pH solution. Hydrogen peroxide (30% v/v, Carlo Erba) has been added in order to test their ability to improve the oxidant capacity of the process. The solutions were

circulated in the plant for 60 min as required by the experiments. The temperature was maintained constant ($T = 20\text{ }^{\circ}\text{C}$) by cold water that crosses in the jacketed system of the reactor. Three series of experiments have been performed in order to study the effect of initial inlet pressure to Venturi that has been varied up to 5.5 bar, the effect of initial pH of solutions (2, 4, 6, 8) and finally the effect of the addition of hydrogen peroxide (molar ratio dye/hydrogen peroxide = 01/30; 1/42; 1/85). The last two series of experiments have been conducted considering an inlet pressure of 5.5 bar (optimal condition found in the first series of test). The reaction time has been set to 60 min, and the samples were collected at regular intervals of 10 min and the analyzed to quantify the extent of MB degradation. The collected samples were analyzed using UV-Spectrophotometer (Cary 1E, UV Visible spectrophotometer Varian) in order to observe a change in the absorbance of MB with time at a specific wavelength (λ), that depended on pH value.

The concentration of dye was then calculated by the calibration curves. The decolourization efficiency η was determined according to Eq. (1):

$$\eta = \text{decolourization efficiency} = \frac{[MB]_0 - [MB]_t}{[MB]_0} \times 100 \quad (1)$$

Where $[MB]_t$ and $[MB]_0$ were the concentrations of methylene blue in ppm at a generic time (t) and at the initial time.

3. Results and discussion

3.1 Effect of the initial pressure on the HC process

The effect of the inlet pressure on MB decolourization was studied at different inlet pressures ranging from 2 – 5.5 bar. Fig.1 shows the results of this first series of experiments.

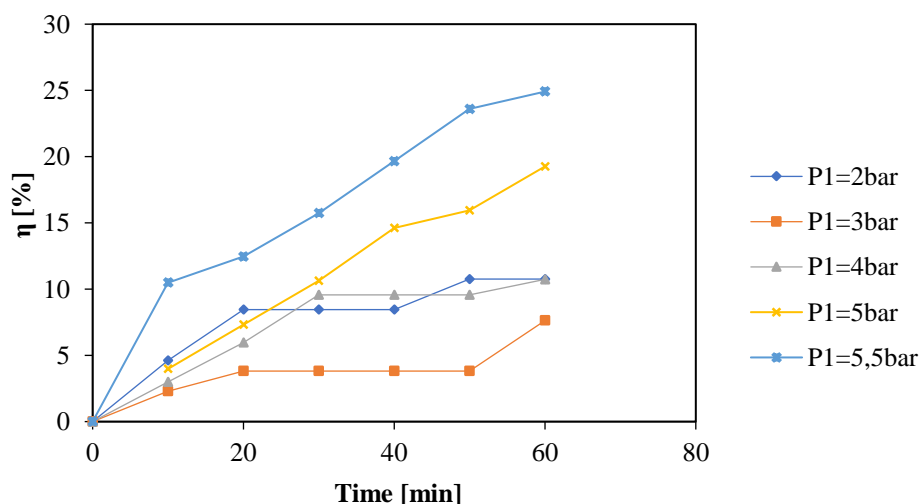


Figure 1. Degradation of MB as a function of inlet pressure; pH = 2 and MB initial concentration = 5 ppm

As reported in the scientific literature, the dye degradation increased with increasing the inlet pressure to the Venturi tube, except for the test carried out at 3 bar where a slight reduction in yield was measured. As a consequence of an increase in inlet pressure, a higher number of cavities formed, therefore more collapsing occurred generating additional OH radicals that react with dye. In this case, no reduction in yield was recorded and no higher pressure values were tested for system limits on a laboratory scale, and therefore the choked cavitation phenomenon could not be observed. The lowest and highest values of HC efficiency on the studied process after 1 h, were 7.63% and 24.91% at 3 bar and 5.5 bar, respectively.

3.2 Effect of the initial solution pH on the HC process

Fig. 2 shows the results of the second series of experiments. The tests have been performed varying the initial pH solution (2, 4, 6, 8) at the initial pressure of 5.5 bar (optimal pressure, Fig.2).

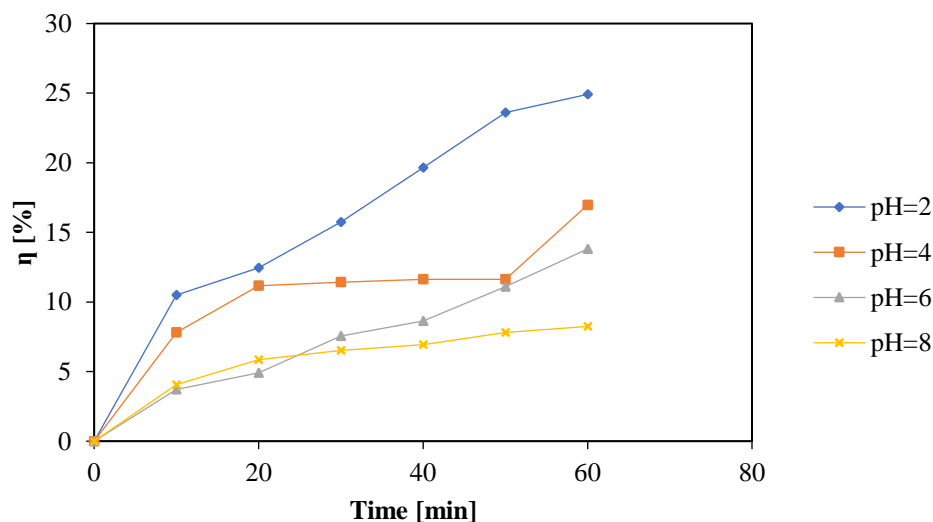


Figure 2. Degradation of MB as a function of inlet solution pH; inlet pressure =5.5 bar and MB initial concentration = 5 ppm

It was observed that the decolourization yield of MB increased with a reduction of the pH value of solutions. A maximum yield near to 25% has been observed at pH of 2, the minimum efficiency has been measured at the pH 8 (8.24%). As demonstrated by scientific literature the acidic pH favors the process, due to the increased production of OH-radicals necessary for the degradation reaction

3.3 Effect of the addition of hydrogen peroxide on the HC process

In a second series of experimental tests, the decolourization of MB solution (5 ppm) has been investigated by combining HC with different concentrations of hydrogen peroxide. The presence of this oxidant increases the free radical formation and consequently more OH[•] are available for the degradation of dye. A blank test of MB decolourization was also performed with hydrogen peroxide in the absence of HC under the operative conditions just described (5 ppm of dye, 20 °C, 60 min). After that, a synergism between H₂O₂ and HC was studied using a mixture of 5 ppm MB and oxidant in the following molar ratio dye/hydrogen peroxide: 1:30; 1:42; 1:85. The results of this third series of experiments are shown in Fig. 3. The degradation in the blanket test was negligible, the highest values of HC efficiency on dye decolourization (95.96%) has been obtained adding H₂O₂ at the molar ratio dye/hydrogen peroxide of 01/42. It can be seen the positive effect of oxidant combined with HC. A peak efficiency was also recorded during this test, beyond this concentration of hydrogen peroxide the yields decreased until 87.82% using a molar ratio of 01/85. This phenomenon is due to the recombination of radicals. Therefore, the use of oxidant increased the performance of the HC just in the optimum concentrations function of the concentration and type of the substances to degrade and also function of the cavitation intensity existing in the device which decides the capacity for the dissociation of hydrogen peroxide.

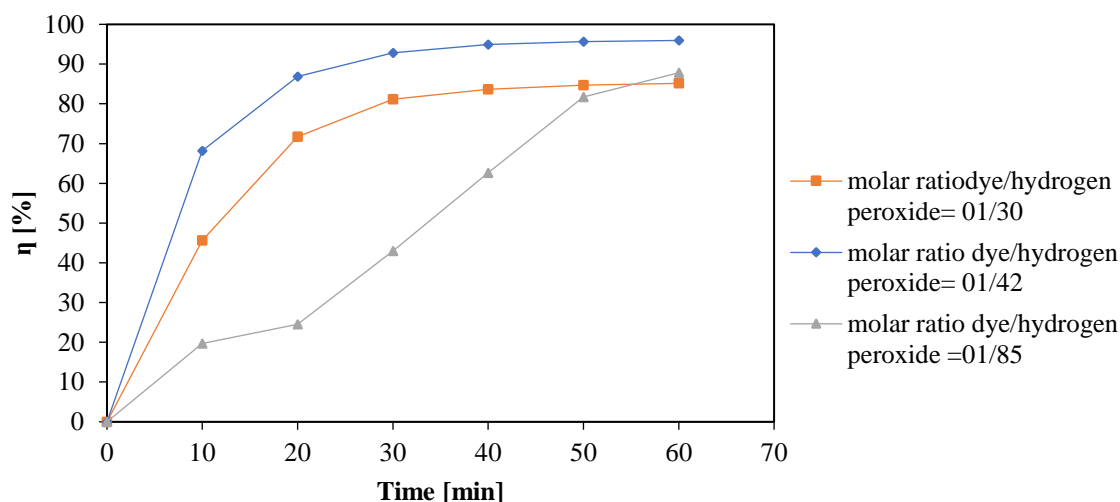


Figure 3. Degradation of MB as a function of molar ratio dye/hydrogen peroxide; inlet pressure = 5.5 bar, solution pH = 2, and MB initial concentration = 5 ppm

4. Conclusions

In the present work, the efficiency of the hydrodynamic cavitation for the decolourization of methylene blue has been studied by using a Venturi device. The effect of inlet pressure, solution pH and hydrogen peroxide concentration on dye degradation (5 ppm of MB) has been investigated. The efficiency of the process was significantly influenced by the inlet pressure and by pH of the solutions. More in details, an increase in pressure has a positive effect, while an increase in the pH of the solution has a negative effect. The maximum decolourization yield (24.91%) has been obtained in the following conditions: inlet pressure of 5.5 bar and pH of 2. Subsequently, the experiments were performed with adding hydrogen peroxide in the dye solutions and the efficiency of the combination HC-H₂O₂ was studied. The combined treatment showed an enhancement of the yields (until to 95.96%) using a molar ratio dye/hydrogen peroxide of 01/42, pH = 2, 5.5 bar after 60 min of treatment. It is clear that the use of the combined process has positive effects on the energy consumption of the HC process. Future research activities will be aimed to test the efficiency of a combined treatment with adding other oxidants, varying the dye concentration and adding more pollutants in order to simulate a textile industrial effluent closer to the real one.

References

- [1] Benkhaya S., El Harfi S., El Harfi A. Classifications, properties and applications of textile dyes: A review. *Appl. J. Envir. Eng. Sci.* 2017, 3, pp. 311-320.
- [2] Gogate, P. R., Pandit, A.B. Engineering design method for cavitation reactors: I. Sonochemical reactors. *AIChE journal*, 2000a, 46, pp. 372-379.
- [3] Gogate, P. R., Pandit, A.B. Engineering design methods for cavitation reactors II: hydrodynamic cavitation. *AIChE journal*, 2000b, 46, pp. 1641-1649.
- [4] Suslick, K. S. *Sonochemistry*. Science 1990, 247, pp. 1439-1445.
- [5] Wang, B., Su, H., Zhang, B. Hydrodynamic cavitation as a promising route for wastewater treatment—A review. *Chemical Engineering Journal*, 2021, 412, 128685.
- [6] Innocenzi, V., Prisciandaro, M., Centofanti, M., Vegliò, F. Comparison of performances of hydrodynamic cavitation in combined treatments based on hybrid induced advanced Fenton process for degradation of azo-dyes. *Journal of Environmental Chemical Engineering*, 2019, 7, 103171.

Removal and recovery of ammonium from municipal wastewater by adsorption/ion exchange on an innovative potassium based geopolymer adsorbent

Carla Maggetti^{1*}, Valentina Medri², Elettra Papa², Elena Landi², Davide Pinelli¹, Dario Frascari¹

¹ Dept. of Civil, Chemical, Environmental and Materials Engineering, University of Bologna, Via Terracini 28, 40131 Bologna; ² National Research Council of Italy, Institute of Science and Technology for Ceramics (CNR-ISTEC), Via Granarolo 64, 48018 Faenza, Italy

*Corresponding author E-Mail: carla.maggetti2@unibo.it

1. Introduction

Nowadays, 50% of food production relies on ammonia fertilizers. The industrial Haber-Bosch process is used to satisfy the rising demand for fertilizer, but it is very energy-intensive: it consumes 1% of the annual global energy supply, and produces about 1,4% of global CO₂ emissions [1]. On the other hand, wastewater (WW) is increasingly considered as a source of water, energy, and plant fertilizing nutrients such as nitrogen and phosphorous [2].

The adsorption/ion exchange process has proven to be a simple, cost-effective, and an environmentally friendly technique and an efficient way to remove and recover ammonium from wastewaters for further industrial uses, such as fertilizer production [3] [4]. Adsorption and ion exchange consist of mass transport between a liquid phase (adsorbate) and a solid phase (adsorbent). The adsorbent should have a particular affinity for the specific adsorbate relative to other substances in the solution [3] and the adsorption capacity and the selectivity of the sorbent materials may vary considerably. Many studies were carried out, but almost all are small-scale laboratory scale tests on natural and synthetic zeolites. However, there is still need for better materials that can achieve high adsorption capacities coupled with good mechanical properties suitable for the application in an adsorption bed. Geopolymers are innovative adsorbent materials that are gaining growing attention because of their excellent mechanical properties and the possibility of designing and fine tuning their adsorption properties. Geopolymers are inorganic polymers that resemble zeolites in many ways: they represent amorphous aluminosilicate materials with a three-dimensional anionic network of AlO₄ and SiO₄ tetrahedra in which the valence difference of Al(III) and Si(IV) results in a net negative charge, which is balanced by exchangeable cations. The main advantages of geopolymers compared to zeolites are: i) the milder synthesis conditions, ii) simpler preparation, and more importantly iii) the possibility of designing the Al/Si ratio in order to improve the adsorption capacity. The porous structure of geopolymers provides more binding sites, increases permeability, improves mass transfer, and reduces pressure drop. Franchin et al. [5] demonstrated that NH₄⁺ adsorption capacity of metakaolin-based geopolymers was 46% higher than that of natural zeolite and could be efficiently regenerated by NaCl/NaOH.

In this work, a potassium based geopolymer (referred as G13 [6]) synthesized by the Institute of Science and Technology for Ceramics of the National Research Council of Italy (CNR-ISTEC) was used to study the removal and recovery of NH₄⁺ from the effluent of a pilot-scale anaerobic membrane bioreactor (AnMBR), placed in side-stream configuration after an Up-flow Anaerobic Sludge Blanket reactor that treats the partly saline municipal wastewater (MWW) of Falconara Marittima (Italy). In particular, the research focused on: i) the assessment of the operative capacity and selectivity of the material in batch and continuous flow tests with an actual MWW, ii) the optimization of process parameters in order to maximise adsorption and desorption efficiency.

2. Methods

The performance of the material in term of N adsorption has been estimated by adsorption isotherm tests, and continuous flow adsorption/desorption breakthrough tests, in a fixed-bed column packed with geopolymer G13. Cations analyses were performed with an HPIC method. All the procedures and methods followed are extensively described by Frascari et al [7]. The continuous tests were performed in a complete automatized

pilot plant, consisting in an adsorption/ion exchange PVC column (1.2 m length, 0.21 m of diameter) packed with the adsorbent material for a height of 0.60 m, several LLDPE tanks (0.05-0.15 m³) used to stock the solutions, 1 volumetric pump (flow rate that can be controlled in the 0.25 - 25 L/h range), 3 sensors to monitor temperature, pressure and liquid levels, a datalogger to collect all the data and store them via PC, electrically operated valves to switch the flow in the plant during the adsorption, desorption, washing phases and 1 automatic sampler.

3. Results and discussion

3.1 Adsorption Isotherm

Two sets of isotherm tests were performed to investigate the performance of the G13: a preliminary 2-point isotherm test conducted with a synthetic NH₄Cl solution – to study the maximum operating capacity in absence of competition by other cations – and a complete isotherm with the Falconara MWW effluent. The complete isotherm was repeated after the adsorption/desorption breakthrough test (BT) in a continuous flow apparatus in order to evaluate potential changes in the performances of the geopolymer. The results of the isotherm tests are shown in Figures 1 in terms of NH₄⁺ sorbed concentration versus NH₄⁺ the residual equilibrium concentration in the liquid.

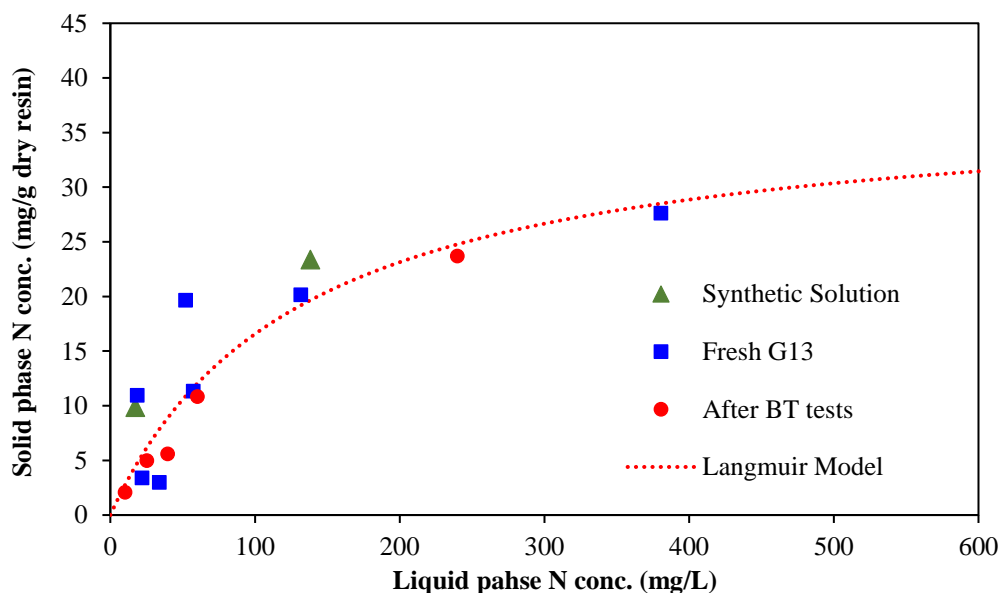


Figure 1 - Comparison of adsorption isotherms of Geopolymer G13 with (1) NH₄Cl synthetic solution, (2) UNIVPM MWW performed before the first breakthrough and (3) after seven cycles.

There are only small differences between the experimental points taken with the NH₄Cl synthetic solution (green triangles) and the ones taken with the real MWW (blue squares), suggesting that geopolymer G13 has a good selectivity towards NH₄⁺, in particular when compared to Na⁺. The latter is, indeed, the most abundant cation normally present in a MWW, it is also detrimental to agricultural purposes, and its presence must be as little as possible in a fertilizer. The isotherm points obtained from the isotherm performed after 7 breakthrough tests (BT) (red points) are consistent with those obtained with the fresh material (blue points). The experimental data were interpolated with the Langmuir and Freundlich models, with the former resulting in the best fitting, with an R² of 0.93.

3.2 Continuous flow adsorption/desorption breakthrough tests

The adsorption/desorption breakthrough tests were conducted in a packed-bed column fed with the Falconara MWW effluent at 24-25°C. The desorption/regeneration procedure was performed eluting the desorbing solution to regenerate the resin and recover the N rich product. The results obtained with Geopolymer G13 in the first BT (BT1) are shown in Figure 2 (adsorption phase) and 3 (desorption phase).

The results showed that the G13 geopolimer has a very good selectivity toward ammonium which is by far the last cation eluted. Ca^{2+} is the cation with the second-best affinity for the sorbent and, above all the affinity for Na^+ is very low (the first cation eluted). The breakpoint for NH_4^+ at the breakpoint BP (set at 4 mgN/L in the outlet concentration for a municipal effluent) occurs at 149 bed volumes (BVs), meaning that large amount of MWW can be treated before a regeneration step is needed. The NH_4^+ adsorption yield ($Y_{\text{ads, NH}_4^+}$) calculated at the breakpoint is 0.96, while the operating capacity ($\eta_{\text{NH}_4^+}$) is 8.42 mgN/g_{dry resin}.

Figure 3 shows that there is a good separation between the desorption of NH_4^+ and Na^+ and Ca^{2+} , allowing the possibility of recovery NH_4^+ as a pure solution.

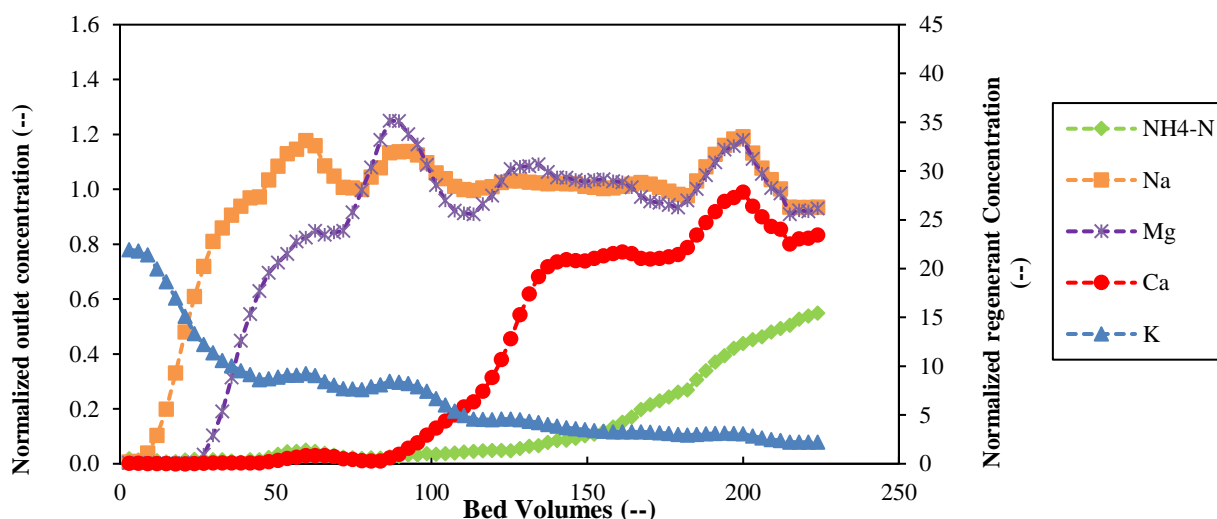


Figure 2. BT1 N adsorption continuous flow test conducted with Geopolymer G13. Breakthrough curves of ammonium and the competing cations obtained with N-spiked UNIVPM MWW effluent.

3.3 Optimization of process operational parameters

The next tests were dedicated to optimize the process by changing and testing various parameters, namely, the empty bed contact time (EBCT) of the adsorption step, the EBCT of the desorption step and the type and concentration of the desorbing solution.

Effect of different EBCTs on Adsorption: the effect of EBCT on the removal of N from WWTP has been studied by running three different adsorption breakthrough tests at different values; 10, 7.5 and 5 minutes. The remaining parameters have been kept unvaried. The EBCT reduction decreases the time of the BP, and so the BVs of WW treated. Indeed, the BP occurs at 149 BVs with an EBCT of 10 min, but it decreases to 135 BVs at 7.5 min, reaching a minimum of 124 BVs at 5 min. Operating capacity also follows this trend: it starts with a value of 8.42 mgN/g_{dry resin} for the curve with the higher EBCT, and it decreases to 6.45 and 5.28 mgN/g_{dry resin} for 7.5 and 5 min of EBCT, respectively. These values show that it is possible to reduce the EBCT to 7.5 min and increase the productivity of the plant with an almost negligible drop in performance, but the further reduction of the EBCT to 5 min caused a further and significant reduction in performances.

Desorption optimization: the effect of the EBCT in the desorption phase was preliminarily studied, varying it between 120, 60 and 20 minutes, with KCl 1% as desorbing solution. No drop in the performances was registered, so an EBCT of 20 minute was chosen to run all the following tests. The optimization of the desorption phase was mainly meant to test the feasibility of a fractionate desorption with the scope of separating Na^+ desorption from N and obtain two fractions: the first rich in Na^+ to be disposal, the second rich in ammonium to be reused in N fertilizer production. In a first step, KNO_3 has been tested as desorbing solution instead of KCl to avoid the presence of chloride in the desorbed product. Then the concentration of KNO_3 was increased from 1.3% to 6.7% in order to obtain a faster desorption and a more concentrated desorbed product. Since while desorbing with a 1% KCl about all the Na^+ eluted within the first 5 BVs, while N was almost retained, an optimization was performed to try a “fractionated desorption”: KCl 1% was used as the desorbing solution for the first 5 BVs, then it was switched with KNO_3 6.7%. The results showed (Figure 3) that the fractionated desorption is feasible also at higher regenerant concentration allowing to obtain a less Na^+

containing product even if with a lower ammonium concentration and recovery yield (part of the ammonium is lost in the first Na^+ rich fraction). The optimized fractioned desorbed product (from BV 5 to 9) has the following characteristics: 1020 mL of volume collected with a concentration of 1318 mg/L for N, 402 mg/L for Ca^{2+} , 21 mg/L for Mg^{2+} and only 36 mg/L for Na^+ .

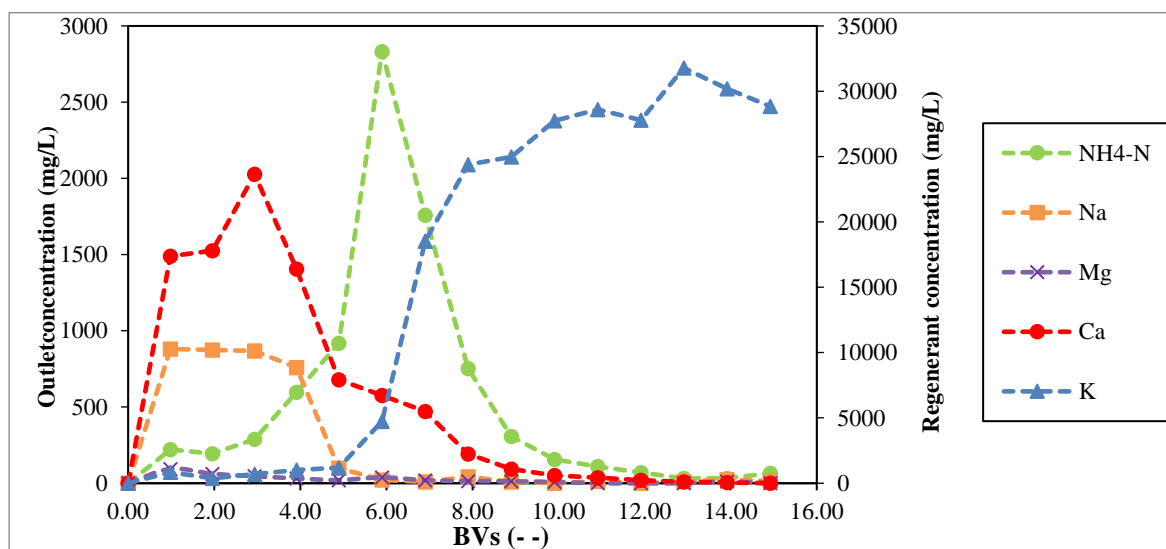


Figure 3. Optimised fractioned desorption. BT7, EBCT=20 min and different desorbing solutions.

4. Conclusions

Geopolymer G13 proved to be a good adsorbent material for N recovery. It showed a stable behavior during repeated breakthrough cycles, good adsorption and desorption yields and an elevated operating capacity. A preliminary optimization of operating parameters was successfully carried out, but more tests are needed in order to further optimize the whole process, especially the desorption step, in order to obtain a N concentrated solution suitable for agricultural purposes.

References

- [1] M. Capdevila-Cortada, «Electrifying the Haber–Bosch», *Nat. Catal.*, vol. 2, n. 12, Art. n. 12, dic. 2019, doi: 10.1038/s41929-019-0414-4.
- [2] D. Frascari *et al.*, «Integrated technological and management solutions for wastewater treatment and efficient agricultural reuse in Egypt, Morocco, and Tunisia», *Integr. Environ. Assess. Manag.*, vol. 14, n. 4, pagg. 447–462, 2018, doi: 10.1002/ieam.4045.
- [3] M. R. Adam *et al.*, «Current trends and future prospects of ammonia removal in wastewater: A comprehensive review on adsorptive membrane development», *Sep. Purif. Technol.*, vol. 213, pagg. 114–132, apr. 2019, doi: 10.1016/j.seppur.2018.12.030.
- [4] Hedström Annelie, «Ion Exchange of Ammonium in Zeolites: A Literature Review», *J. Environ. Eng.*, vol. 127, n. 8, pagg. 673–681, ago. 2001, doi: 10.1061/(ASCE)0733-9372(2001)127:8(673).
- [5] G. Franchin *et al.*, «Removal of ammonium from wastewater with geopolymer sorbents fabricated via additive manufacturing», *Mater. Des.*, vol. 195, pag. 109006, ott. 2020, doi: 10.1016/j.matdes.2020.109006.
- [6] E. Landi *et al.*, «Alkali-bonded ceramics with hierarchical tailored porosity», *Geopolymers New Smart Way Sustain. Dev.*, vol. 73, pagg. 56–64, mar. 2013, doi: 10.1016/j.clay.2012.09.027.
- [7] D. Frascari *et al.*, «Ammonium recovery from municipal wastewater by ion exchange: development and application of a procedure for sorbent selection», *Sep. Purif. Technol.* Submitted

A novel integrated technology to recover high-valuable minerals from seawater through a circular economy approach

Carmelo Morgante¹, Fabrizio Vassallo¹, Andrea Cipollina^{1*}, Alessandro Tamburini^{1,2}, Giorgio Micale¹

1 Dipartimento di Ingegneria, Università degli Studi di Palermo - viale delle Scienze Ed.6, 90128 Palermo, Italy;

2 ResourSEAs SrL, viale delle Scienze Ed.16, 90128 Palermo

**Corresponding author E-Mail: andrea.cipollina@unipa.it*

1. Introduction

Within the last few decades, the European Union (EU) has had to witness a gradual increase of its economic dependence on other non-EU nations due to mineral land mining depletion. Such matter has led to define thirty “critical” raw materials (CRMs), on which the EU has recently been focusing much attention, attempting to solve the issue via several action plans [1]. The discovery of new sources of the CRMs seems to be a solution to the problem, yet nowadays it still remains to be very challenging. It is no ground-breaking news the fact that seawater can be considered as an “infinite” source of valuable minerals, containing magnesium, lithium, calcium etc. These minerals have been recovered from seawater for centuries. Nevertheless, such method has never dominated the mineral production field due to the employment of inefficient technologies. Within this framework, a novel integrated process was proposed and tested at semi-industrial/pilot scale to recover high valuable minerals from Mediterranean seawater. More precisely, the integrated process comprises three different technologies: (i) a Nanofiltration unit NF, (ii) a Multiple Feed – Plug Flow Reactor MF-PFR and (iii) an Electrodialysis unit with Bipolar Membranes EDBM.

2. Methods

One semi-industrial and two pilot-scaled plants were installed and integrated in the minor Sicilian island of Lampedusa. A conceptual scheme of the integrated process is illustrated in Figure 1. The first plant (semi-industrial scale) was an NF unit, developed by Lenntech BV, with a feed capacity of ~ 2 m³/h. Seawater from Lampedusa Island was fed to the NF unit, producing two streams: (i) a permeate stream rich in monovalent ions e.g. sodium and chloride and (ii) a retentate stream rich in bivalent ions e.g. magnesium and calcium. The NF retentate was then fed to a second unit (pilot scale), MF-PFR. Such unit was designed and constructed by the University of Palermo [2]. The reactor consisted of two co-axial cylindrical tubes in which the NF retentate (rich in magnesium and calcium) was injected into one of the tubes whereas a sodium hydroxide (NaOH) solution into the remaining one. At controlled reaction pH values, it was possible to selectively promote the precipitation of magnesium hydroxide Mg(OH)₂ particles and calcium hydroxide Ca(OH)₂ particles in two consecutive steps. The pilot-scaled reactor had a feed capacity of 150 L/h. Since the second precipitation step occurred at a reaction pH value ~ 13 , the remaining effluent that exited the reactor was neutralized with a hydrochloric acid (HCl) solution and sent to the third and last plant: EDBM. The EDBM unit (pilot scale), with a feed capacity of 100 L/h, was also developed by the University of Palermo. By the effect of an electric field and the use of selective/bipolar membranes positioned in an alternative way, an alkaline solution (NaOH) and acidic solution (HCl) were produced other than a remaining salty effluent. The EDBM effluent was then mixed with the NF permeate and discharged back to the Mediterranean Sea. As far as the produced NaOH and HCl were concerned, a recycling strategy was adopted to re-use them within the process as the alkaline solution for the MF-PFR and for the neutralization of the MF-PFR effluent, respectively.

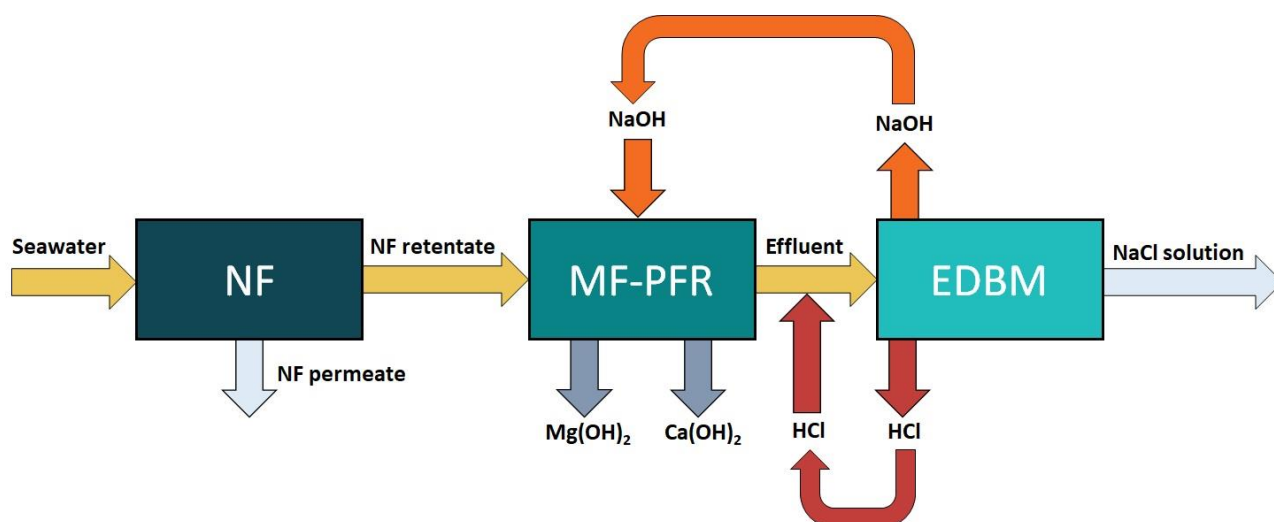


Figure 1. Conceptual scheme of the novel integrated technology for mineral recovery from seawater

3. Results and discussion

The entire plant was operated for 4 to 6 hours per day, testing its operational and performance stability. Given seawater (salinity ~ 35 g/L) as the feed of the process, the NF plant was able to produce a retentate with an average concentration of magnesium and calcium of ~ 5.5 and 1.5 g/L, respectively, with both ionic NF membrane rejections higher than 90%. This meant that it was possible to maximize the quantity of magnesium and calcium entering the MF-PFR. As for this unit, magnesium recovery equal to 100% was achieved whereas calcium recovery values were slightly lower ($\sim 90\%$). Finally, the EDBM unit was able to produce the desired/required concentrations of NaOH and HCl only when initial low concentrations of NaOH and HCl were fed to the EDBM unit along with the MF-PFR effluent.

4. Conclusions

A novel integrated technology was proposed and tested at the semi-industrial/pilot scale to recover high valuable products ($\text{Mg}(\text{OH})_2$ and $\text{Ca}(\text{OH})_2$) from Mediterranean seawater. Results obtained from its testing proved its performance stability, demonstrating its feasibility of being an alternative method to recover minerals with reduced environmental and economic impact (mainly due to its production of hydroxides and in-situ production of chemicals). Taking into account the process's future prospects, an application of possible greater interest could be the treatment of waste brines from the desalination field. In such scenario, larger quantities of hydroxides produced and a lower environmental impact could be contemporarily achieved, approaching the circular economy concept.

Acknowledgements

This project has received funding from the European Union's Horizon 2020 research and innovation program under Grant Agreement no. 869474 (WATER-MINING – Next generation water-smart management systems: large scale demonstrations for a circular economy and society). www.watermining.eu.

References

- [1] European Commission, Study on the review of the list of Critical Raw Materials - Final Report, 2020. doi:10.2873/11619.
- [2] F. Vassallo, D. La Corte, N. Cancilla, A. Tamburini, M. Bevacqua, A. Cipollina, G. Micale, A pilot-plant for the selective recovery of magnesium and calcium from waste brines, *Desalination*. 517 (2021) 115231. doi:10.1016/j.desal.2021.115231.

Olive Mill Wastewater treatment by a continuous-flow anaerobic co-digestion process with municipal sewage sludge

Davide Pinelli^{1*}, Dario Frascari¹, Alessandro Ragini¹, Francesco Avolio², GianNicola Scarcella²,
Sara Bovina¹

*1 Department of Civil, Chemical, Environmental and Materials Engineering, University of Bologna, via Terracini 28,
40131 Bologna, Italy;*

2 Hera Spa – Water Division, Via Cristina Campo 15, 40128 Bologna, Italy

**Corresponding author E-Mail: davide.pinelli@unibo.it*

1. Introduction

The disposal of olive mill wastewater (OMW) represents a significant environmental problem due to the high organic load, the presence of phenolic compounds (PCs), which are harmful for plants, soil and water microbial population, and the very unpleasant smell [1, 2]. The treatment of OMW represents a significant cost for olive mills and an issue for waste management treatment plant in Mediterranean countries. Numerous processes for OMW treatment have been proposed which have high cost and of difficult application due to the seasonality of OMW production and the small scale of several olive mills [3]. OMW anaerobic digestion (AD) is of high interest, but a challenging process because of the high concentration of inhibitory and recalcitrant compounds such as PCs. On the other hand, polyphenols recovery has become interesting as PCs found several applications in many industrial fields as they are used as antioxidants and antimicrobials in animal feeding, cosmetics and health care products. Adsorption proved to be a feasible and interesting possibility [2-5]. The co-digestion of OMW with the sewage sludge (SwS) represents a potential solution for OMW disposal thanks to the widespread presence of digesters used for the stabilization of the sludge produced by wastewater treatment plants (WWTP) [6]. Thus, combining OMW co-AD with a preliminary recover the OMW PCs by adsorption represents an interesting possibility to decrease potential inhibition effects on the AD process and to recover high-added value products [7]. In this work [8], the co-AD of OMW with SwS was investigated in continuous bioreactors, under different conditions. The targets of the research were: (i) to compare the performances obtained with untreated and dephenolised OMW; (ii) to assess operational conditions for a stable co-AD of OMW and SwS, with a high OMW content; (iii) to develop strategies for the integration of the OMW/SwS co-AD process in the network of existing SwS digesters; and (iv) to perform a cost-benefit analysis (CBA) relative to process both with and without a dephenolisation pre-treatment.

2. Methods

The OMW used in the present study was provided by a 3-phase olive mill located in Sant'Arcangelo di Romagna (Rimini, Italy). The partially dephenolised OMW (def_OMW) was produced by PCs adsorption on the neutral adsorbent resin Amberlite XAD16N (DOW Chemicals Europe GmbH, Horgen, Switzerland). The PCs concentration was reduced from 1010 ± 40 mg/L to 65 ± 5 mg/L (6.4 % of the untreated OMW concentration). However, the dephenolisation caused a loss of 32% of the COD, 35% of the BOD₅ as a significant amount of organic matter was removed together with the PCs. All continuous tests were made in laboratory-scale PVC bioreactors with a capacity of 1.7 L operated under at $34 \pm 1^\circ\text{C}$ and 12 different mixtures OMW/SwS ratios: from 5:95 to 40:60. The main parameters analysed to follow the process were: total solids (TS), VS, COD, volatile fatty acids (VFAs) and PCs. The CBA of the process was performed based on the

full-scale scenario of a 500000 people equivalent (PE) WWTP, in which it was assumed to co-digest OMW in the existing digester during a 4-month period, with an OMW / (OMW + SwS) volumetric ratio equal to 0.25. Two distinct CBA approaches were applied: i) untreated OMW co-AD and ii) OMW dephenolisation followed by co-AD. More details on materials, methods and apparatuses are in [5] and [8].

3. Results and discussion

Different volumetric OMW:SwS ratios up to 100% OMW were fed in continuous 1.7-L bioreactors. In the scenario to perform a OMW co-digestion process in an operating real SwS digester, the inlet volumetric flow rate increases and, if the liquid volume is kept constant, the HRT decreases. Thus, to simulate the co-AD process performances with a decreased HRT, the first part of this study was focused on OMW/SwS co-AD with an HRT equal to 23 days, close to the lower HRT limit of WWTP digesters operating range (20-40 days HRT). The reactor fed with 100% SwS was used as the internal benchmark of the AD process. The biogas and methane yield trends over time achieved a stable steady state after less than 7 days as the inoculum of the bioreactors were made with a digestate taken from an SwS industrial anaerobic digester. The average yields were 194 ± 13 NL/kg_{VS} fed and 110 ± 11 NL/kg_{VS} fed, for biogas (Y_{biogas}) and CH₄ (Y_{CH_4}) respectively. The mean production rates were 0.20 ± 0.02 NL_{biogas} L⁻¹ day⁻¹ and 0.12 ± 0.01 NL_{CH₄} L⁻¹ day⁻¹. The mean volatile solid (VS) conversion was 37% and the VS concentration was 16 ± 2 g/L. pH was stable at 7.2. In the AD tests with 100% of treated OMW, the OMW fraction in the feed was gradually increased from day 1 to day 35 in order to help the biomass adaptation to the new feed. Both biogas and methane yields increased during the first 35 days, with maximum values at the end of the OMW fraction increase (790 NL_{biogas}/kg_{VS} fed and 470 NL_{CH₄}/kg_{VS} fed) largely higher than those attained in the 100% SwS benchmark. However, starting from day 35, when the untreated OMW was the only feed, both the yields rapidly decreased and in 30 days the methanogenic activity completely halted. These results suggest that, as expected, the untreated OMW is a strong inhibitor on the methanogenic activity. VFAs, initially low, increased steadily up to a maximum value of 5.5 g/L and the pH gradually decreased, reaching 6.1 on day 63. These results confirmed the inhibition on the methanogenesis, with a consequent VFAs accumulation. Analogous results were obtained in the AD of dephenolised OMW: both the biogas and methane yield initially increased to maximum values on day 42 (1100 NL_{biogas}/kg_{VS} fed and 750 NL_{CH₄}/kg_{VS} fed), then, they yields decreased, though with a slower trend than in the case of the untreated OMW and after 100 day the methanogenic activity completely stopped. The trends of VFAs and pH were similar to that of untreated OMW. The results obtained with untreated OMW and dephenolised OMW showed that the OMW volatile solids have a large biomethane potential, higher than that of the SwS. The time evolution of methane yields for the co-AD bioreactors are shown in Figure 1. For both untreated OMW and dephenolised OMW fed bioreactors, the replacement of SwS with OMW caused the biogas and methane production yields and rates to increase with time and almost stabilized in about 60 days, showing that, contrary to the case of pure OMW AD, steady-state conditions can be successfully achieved. For both untreated and dephenolised OMWs the best performances were obtained with the higher OMW fraction (25%): methane yields of 226 NL_{CH₄}/kg_{VS} fed for untreated OMW and 179 NL_{CH₄}/kg_{VS} fed for dephenolised OMW, values much higher than that obtained with the sole SwS (110 NL_{CH₄}/kg_{VS}). The untreated OMW showed higher performances than the corresponding dephenolised OMW, indicating that dephenolisation did not lead to a beneficial effect in terms of methane production whereas the higher VS content of untreated OMW seems to be the reason of the higher methane yield. The results obtained so far showed that: i) the co-AD of OMW and SwS leads to a significant enhancement of the biomethanation performance, ii) the OMW dephenolisation is not economically justified, unless the produced PC mixture can be sold at a price high enough to repay the investment in the adsorption/desorption plant.

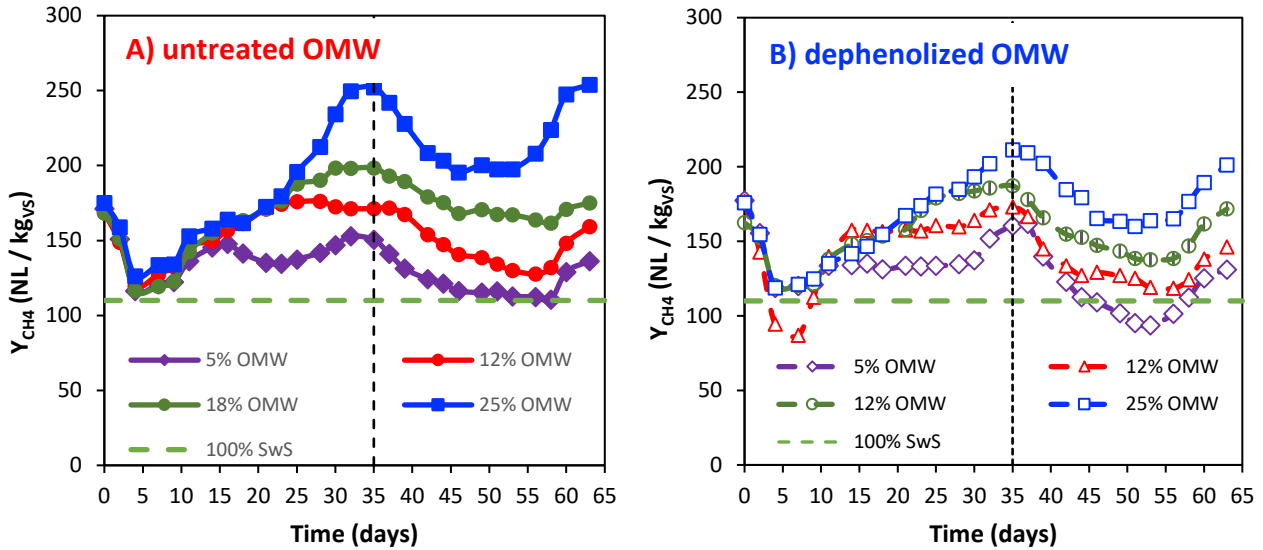


Figure 1 - Comparison between the CH₄ yields obtained in the bioreactors operated with different OMW/SwS ratios with a 23-day HRT. A) untreated OMW; B) dephenolised OMW.

At day 100, a second part of the work was started aimed at maximizing the OMW/SwS ratio and, in turn, the biogas productivity with a stable performance without a long adaptation time, hardly compatible with the typical seasonality of OMW production. The HRT of the bioreactors fed with 25% OMW contained a methanogenic microbial consortium acclimatized to a PCs concentration of 260 mg/L and 23 mg/L, respectively for untreated and dephenolised OMW, was raised from 23 to 40 days and the OMW fraction was increased to 40%. In both the bioreactors a rapid increase of the CH₄ yields, that reached 268 ± 3 NL_{CH₄}/kg VS fed for untreated OMW and 235 ± 13 NL_{CH₄}/kg VS fed for dephenolised OMW, corresponding to increases of 19% and 31% in methane yield respectively. The 40% untreated OMW bioreactor achieved a stable PCs concentration with a mean value of about 125 mg/L with a 70% PCs conversion. These results showed that the OMW PCs can be effectively degraded by a co-AD process and that the residual PCs does not significantly inhibit the methanogenesis.

Finally, the last part of the work was meant to assess the large-scale applicability of the OMW/SwS co-AD process and a cost-benefit analysis (CBA) on two possible scenarios. In particular, two Italian regions, Apulia and Tuscany, with a very high production of olives for oil were considered. For both the regions, the volumetric production of SwS was estimated and a mean volumetric OMW fraction in the feed of the OMW/SwS co-AD was estimated under the following simplifying assumptions: i) the OMW produced in a given region is treated in a fraction of the total AD capacity of that region (for example 1/4 to 1/3 of the total capacity), ii) the OMW co-AD process is distributed over a 4-month period. The estimated OMW fractions required to dispose all the regional OMW was 25-35% for Apulia and 6.8-9.1% for Tuscany, values below those successfully applied in this work. The CBA was based on the following scenario: i) a 500,000 PE WWTP, that receives $0.2 \text{ m}^3 \text{ d}^{-1} \text{ PE}^{-1}$, and therefore treats $100,000 \text{ m}^3/\text{d}$ of municipal wastewater (MWW), ii) the digester was assumed to treat $600 \text{ m}^3/\text{d}$ of SwS, iii) a OMW/SwS volumetric ratio equal to 0.25 is applied for a 4-month period with an untreated OMW (no dephenolisation) flowrate equal to $200 \text{ m}^3/\text{d}$, iv) a 10% spare capacity is present in the digester, that lead to an HRT reduction from 30 to 25 days. The benchmark scenario was the treatment of only SwS AD, assuming the characteristics and performance used in this work. The scenario to be compared was untreated OMW/SwS co-AD, assuming the characteristics and performance used in this work. The CBA estimated a total additional revenue associated to OMW co-AD in the existing digester varying in the 1,440,000-2,640,000 € range. Assuming a mean total cost of MWW treatment declared by several WWTP managers in Northern Italy of 0.65 €/m³ (average value), the additional revenues correspond to an 18-34%

reduction of the cost of MWW treatment, during the 4-month OMW season. In a second scenario with dephenolisation of the OMW and OMW/SwS co-AD, the market price at which the PC-rich antioxidant product obtained from OMW dephenolisation should be sold in order to attain a 6% FRR was estimated. This price resulted equal to 8.17 €/kg_{PC}. Considering that the market price of PC-rich antioxidants varies between 250 and 2500 €/kg_{PC}, even if the antioxidant product obtained from the above-described plant needs a further refining before being placed in the market, the resulting price for the generation of an attractive business case is considered a realistic one. In this scenario, a lower but significant 16-32% reduction of the cost of MWW treatment during the 4-month OMW season was calculated. The comparison between the two scenarios allows some conclusions: i) the benefit is substantial in both cases, ii) the largest fraction of the additional revenue is associated to the OMW disposal tariff, iii) the difference between the two scenarios is low, considering the uncertainties that affect this analysis, iv) the scenario of OMW dephenolisation requires additional investments in plants and personnel formation, and v) it has an economic uncertainty associated to the actual feasibility of selling at a reasonable price the entire PC-rich antioxidant mixture produced in each season, vi) a significant degradation of the OMW PCs is obtained also without the additional dephenolisation step. For these reasons, the scenario of untreated OMW co-AD is considered the best choice.

4. Conclusions

This work showed that it is technically possible and economically profitable to co-digest the entire OMW production in regions characterized by intense olive oil production by taking advantage the existing network of SwS anaerobic digesters. A substantial increase in methane production yield (144% increase in comparison to 100% SwS) was achieved. The increase of the revenues of the OMW treatment, mainly associated to the OMW disposal tariff, can potentially lead to a substantial decrease in the cost of MWW treatment during the 4-month of the OMW season.

References

- [1] A. Messineo, M.P. Maniscalco, R. Volpe, *Sci. Total. Environ.* 703 (2020) 135508.
- [2] D. Frascari, A.E. Molina Bacca, F. Zama, L. Bertin, F. Fava, D. Pinelli, *Chem. Eng. J.* 283 (2016) 293–303
- [3] D. Frascari, A.E. Molina Bacca, T. Wardenaar, E. Oertlé, D. Pinelli, *J. Chem. Technol. Biotechnol.* 94 (2019) 1968–81
- [4] D. Pinelli, A.E. Molina Bacca, A. Kaushik, S. Basu, M. Nocentini, L. Bertin, D. Frascari, *Int. J. Chem. Eng.* vol. 2016 (2016) Article ID 9349627
- [5] D. Frascari, G. Rubertelli, F. Arous, A. Ragini, L. Bresciani, A. Arzu, D. Pinelli, *Chem. Eng. J.* 360 (2019) 124–38
- [6] A.E. Maragkaki, M. Fountoulakis, A. Gypakis, A. Kyriakou, K. Lasaridi, T. Manios, *Waste Manag.* 59 (2017) 362–70
- [7] A.I. Vavouraki, M.A. Dareioti, M. Kornaros, *Waste Biomass Valorization*, 12 (2021) 2271–2281
- [8] S. Bovina, D. Frascari, A. Ragini, F. Avolio, G. Scarcella, D. Pinelli, *J. Chem. Technol. Biotechnol.* 2020 (2020)

Benchmark on literature data processes for precious metals recovery from spent auto-catalyst, waste printed circuit boards and photovoltaic panel

Ionela Birloaga*, Pietro Romano, Francesco Veglio

Department of Industrial and Information Engineering and Economics, University of L'Aquila,
Via Giovanni Gronchi 18, 67100, L'Aquila, Italy

The current paper has as main core to presents a literature overview of the processes developed for precious metals recovery from spent auto-catalyst (Pd, Pt and Rh), waste printed circuit boards (Au, Ag and Pd) and photovoltaic panel (Ag). The hydrometallurgical processes, which are generally more easily to handle than pyrometallurgical ones have been put more in evidence within this study. There have been chosen 6 types of hydrometallurgical processes with same reactive of solubilization but different kinds of reagents for precious metal recovery from solution or different leaching agents with different methods of recovery from solution. The final material balance of the processes was achieved by the processes simulation with Super Pro Designer and HSC Chemistry software. In this way, the economic feasibility was realized and put in balance between all the analyzed processes.

Key words: precious metals; spent auto-catalyst; waste printed circuit boards; spent photovoltaic panels; hydrometallurgy; recovery.

Corresponding author : ionelapoenita.birloaga@univaq.it

Eco-sustainable design of hybrid redox-active materials to remove (micro)plastics from water

Paola Amato^{1*}, Marica Muscetta¹, Claudio Imparato¹, Aurelio Bifulco¹, Mariacristina Cocca²,
Raffaele Marotta¹, Giuseppe Vitiello¹, Antonio Aronne¹

*1 Dipartimento di Ingegneria Chimica, dei Materiali e della Produzione Industriale, Università degli Studi di Napoli
Federico II, P.le Vincenzo Tecchio 80, 80125, Napoli.*

*2 Institute for Polymers, Composites and Biomaterials, Italian National Research Council -Via Campi Flegrei 34,
80078 Pozzuoli, NA, Italy*

**Corresponding author E-Mail: paola.amato@unina.it*

1. Introduction

Plastic waste has become a highly abundant and growing problem across global environments, as a result of increasing plastic manufacture, disposal and anthropogenic activities. In particular, microplastics (plastic particles <5 mm) are highly dispersive and have now caught both scientific and public awareness [1]. Due to their small size, microplastics can be discharged into the environment from wastewater effluents, causing damages to aquatic ecosystems. Therefore, the definition of solutions to deal with this threat is indeed of great interest. In this context, the green photocatalytic removal of microplastics from water, activated by visible and/or solar light can be a sustainable strategy. The main photocatalysts used for the photocatalytic degradation of (micro)plastics are TiO₂ and ZnO. TiO₂ has been widely used because of its high stability, non-toxicity and low cost. However, TiO₂ has a wide bandgap (3.0–3.2eV) and only the short-wavelength ultraviolet light (UV) stimulates its electron transition. ZnO (bandgap energy = 3.37 eV) is also widely used in the treatment of dye wastewater because of his high catalytic activity, non-toxicity, photostability, tunable size. To improve the effective sunlight utilization of photocatalysts, various modification techniques, such as using dopants must be investigated [2]. Moreover, the adsorption of suitable organic molecules has been proposed as a versatile photosensitization strategy, alternative to doping [3].

The aim of this work is thus to design and realize new eco-compatible hybrid materials:

1. Hybrid photocatalysts consisting of semiconductor oxides combined with a bioavailable organic component and/or derived from biomass (i.e. humic acids), thus able to generate ROS under the effect of UVA/solar radiation.
2. Organic-inorganic hybrid catalysts consisting of semiconductor oxides functionalized with bioavailable organic molecules (i.e. organic ligands) capable of stabilizing ROS through the formation of charge-transfer complexes without the need for irradiation, resulting therefore active in dark or in conditions of ordinary brightness.

These materials will be tested for the degradation of polymeric samples through Advanced Oxidation Processes (AOP), taking advantage of their ability of ROS production.

2. Methods

Specifically, humic acid sodium salt (low molecular weight humic acid model molecule) and dibenzoylmethane (DBM, organic ligand) have been used to functionalize the semiconductor oxides (ZnO and TiO₂). Bare/hybrid ZnO and TiO₂ have been tested on polymeric samples like LLDPE (linear low-density polyethylene) and PLA (polylactic acid). To investigate the photocatalytic properties, different glass supports were coated with about 0.4 mL of a 5 mg / mL suspension of each bare and hybrid photocatalyst samples. Then, these supports were dried in an oven for 30 minutes at 90 °C. Then, to perform photocatalytic tests, the

polymeric films were opportunely wrapped around the supports on which each type of nanocatalyst was deposited. All the sets of slides with each nanocatalyst were placed in a bath containing water and equally exposed to the UV lamp:



Figure 1. Images of the used UVA/Vis lamp.

To investigate the capability of production of ROS and their stabilization without the need for irradiation, the polymeric films chosen were coated with about 0.4 mL of a 5 mg / mL suspension of TiO₂-DBM at room light in presence of air.

3. Results and discussion

Preliminary characterizations of the polymeric films treated with the hybrid materials prepared have been realized by using ATR and SEM analysis which show promising results in terms of changes that can be ascribed to the activity of ROS generated.

4. Conclusions

Investigating the ROS degradation behavior of (micro)plastics is beneficial to better understand their elimination and to develop novel technologies for their removal. Although these materials show satisfactory polymers degradation efficiency, the identification of intermediates, reusability of the materials, and the application cost are still worthy of further exploration.

References

- [1] Alice A. Horton, David K.A. Barnes, Microplastic pollution in a rapidly changing world: Implications for remote and vulnerable marine ecosystems, *Science of The Total Environment*, Volume 738, 2020, 140349, ISSN 0048-9697
- [2] Jianhua Ge, Zhiping Zhang, Zhuozhi Ouyang, Mengxin Shang, Peng Liu, Huang Li, Xuetao Guo, Photocatalytic degradation of (micro)plastics using TiO₂-based and other catalysts: Properties, influencing factor, and mechanism, *Environmental Research*, Volume 209, 2022, 112729, ISSN 0013-9351
- [3] Ritacco, I., Imparato, C., Falivene, L., Cavallo, L., Magistrato, A., Caporaso, L., Farnesi, M., Aronne 2100629, A., Spontaneous Production of Ultrastable Reactive Oxygen Species on Titanium Oxide Surfaces Modified with Organic Ligands. *Adv. Mater. Interfaces* 2021, 8, 2100629.

A multi-objective optimization approach for preliminary design of economical and environmentally sustainable CO₂ transport pipelines

Francesco Zanobetti¹, Haroun Mahgerefteh², Sergey Martynov², Valerio Cozzani^{1*}

1 LISES - Laboratory of Industrial Safety and Environmental Sustainability,

Department of Civil, Chemical, Environmental and Materials Engineering, University of Bologna,

via Terracini 28, 40131 Bologna, Italy;

2 Department of Chemical Engineering, University College London, London, WC1E 7JE, UK

**Corresponding author e-mail: valerio.cozzani@unibo.it*

1. Introduction

Carbon Capture and Storage (CCS) is widely recognized as a key CO₂ emissions abatement strategy in meeting the ambitious 2050 net zero emission target [1]. In this regard, pressurized pipelines represent the most economic and safest method of large-scale CO₂ transport for final geological storage [1 – 2]. The design of such transport infrastructures with the aim of significantly reducing costs and environmental impacts is therefore paramount for boosting the large-scale deployment of CCS. In this study, an approach for multi-objective optimization with respect to economic and environmental issues is presented as a decision tool supporting the preliminary design of CCS transport pipelines. This consists in a first analysis of the Pareto Front [3] for identifying a set of cost-effective and environment-friendly design trade-offs, followed by a quantitative assessment procedure based on the aggregation of Key Performance Indicators (KPIs) to identify the most effective alternative. The application of the methodology is exemplified for a point-to-point CO₂ pipeline and benchmarked against an alternative single-objective optimization route.

2. Methods

The optimal CCS pipeline design with respect to economic and environmental performance is formulated in terms of a multi-objective optimization problem. Levelized Cost of CO₂ transport (LC) and the amount of greenhouse gases emitted annually due to electricity consumption are accordingly set as the economic and environmental objective functions respectively, whereas the Nominal Pipe Size (NPS) is assumed as the decision variable. LC is obtained by dividing the annualized sum of CAPEX, OPEX and Operational & Maintenance (O&M) costs of the pipeline and upstream compression plant with the mass of CO₂ transported annually [4]. A European-wide Electricity Emission Factor (EEF) [5] is considered to model the CO₂ equivalents of annual GHG emissions per unit of electrical power demanded by compressors and pumps. Solving the multi-objective problem leads to identify the Pareto Front, where none of the design option is best for minimizing both objectives. In order to aid the selection of optimal solutions, a Level Diagrams visualization techniques is used [3]. This involves computing norm metrics quantifying the distance between a given design option and the ideal solution simultaneously optimizing both objectives. Three design options lying on the Pareto Front and presenting the lowest values of norm metrics are therefore selected as the optimal solutions to be further assessed by a quantitative methodology based on impact indicators [6]. The economic performance is assumed being quantified by the LC of CO₂ transport, whilst the Global Warming Potential Impact Factor (PIF_{GW}) is considered to account for the environmental impact due to global warming. Economic and environmental impact indicators are then normalized and aggregated to produce an overall performance index for each alternative. A single CO₂ point-to-point pipeline is considered as a case-study, for which both the proposed multicriteria optimization route and the single-objective optimization of the transport cost of avoided CO₂ emission (i.e., CO₂ transported diminished by the amount of CO₂ equivalents emitted annually) are solved for a comparative analysis. The uncertainty affecting the estimation of CO₂ transport cost values is assessed by a Monte Carlo probabilistic approach.

3. Results and discussion

Figure 1 shows a graphical representation of the solution of the multi-objective optimization problem.

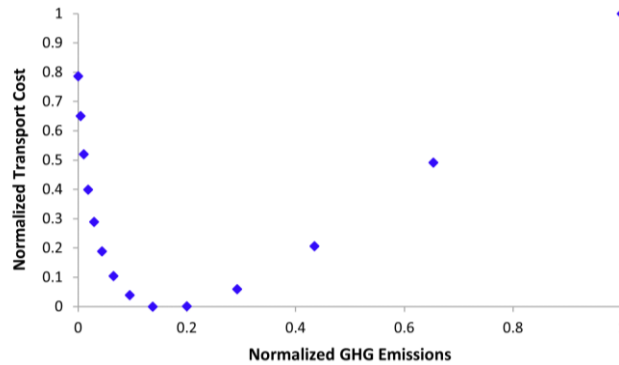


Figure 1. Representation of the multi-objective optimization problem and the corresponding Pareto Front.

As shown in Figure 1, a set of design trade-off points constituting the Pareto Front appears as the normalized value of GHG emissions spans the range from 0 to 0.2. The three optimal solutions minimizing the norm metrics are found to be NPS 28, 30 and 32. Therefore, these diameters were assessed by multi-criteria aggregation of economic and environmental KPIs. Equally weighing levelized cost of CO₂ transport and emitted GHG results in an overall optimal solution equal to NPS 30, whereas the design option given by the single-objective optimization of the transport cost of CO₂ avoided is NPS 28. Since compression power demand turns out to increase as NPS diminishes, it may be argued that lumping the minimization of economic and environmental issues in a single-objective problem rather than following the multicriteria route would lead to select a design option with a greater energy consumption and a higher global warming contribution, thus favoring lower transport costs over higher environmental impacts. The Monte Carlo sensitivity analysis of the transport cost considering the input variables giving the highest uncertainties in the cost assessment results in an unchanged economic ranking of alternatives, thus confirming the robustness of the CO₂ transport cost model used in the analysis.

4. Conclusions

A multicriteria optimization approach for the preliminary design of cost-optimal and environment-friendly CCS pipelines was developed and tested. The ranking of the overall economic and environmental performance of alternatives obtained by multicriteria weighted summation of KPIs turned out to provide an effective metric to guide the preliminary selection of one or more “best design” solutions. Comparing the proposed approach against a more conventional single-objective optimization pathway for a given case-study highlighted the possibility of underestimating environmental issues when not undergoing a multicriteria solution route. Overall, the optimization approach presented provides the decision makers with a flexible decision tool where each impact category may be appropriately weighed according to either local sustainability policies or case-specific expert judgment to arrive at the most economic and environmentally sustainable pipeline transport solution. A Monte Carlo probabilistic analysis is ultimately developed to assess the reliability of the applied CO₂ transport cost model when accounting for uncertainties in its input parameters.

References

- [1] B. Metz, O. Davidson, H. de Coninck, M. Loos, L. Meyer (Eds.), IPCC Special Report on Carbon Dioxide Capture and Storage. Prepared by Working Group III of the Intergovernmental Panel on Climate Change, Cambridge University Press, Cambridge, 2005.
- [2] World Resource Institute (WRI), CCS Guidelines: Guidelines for Carbon Dioxide Capture, Transport and Storage, WRI, Washington DC, 2008.
- [3] E. Zio, R. Bazzo, Reliab. Eng. Syst. 96 (2011) 569–580
- [4] M.M.J. Knoope, W. Guijt, A. Ramírez, A.P.C. Faaij, Int. J. Greenh. Gas Control 22 (2014) 25–46
- [5] The Covenant of Mayors, Technical annex to the SEAP template instruction document: the emission factors.
- [6] A. Tugnoli, F. Santarelli, V. Cozzani, Environ. Sci. Technol. 42 (2008) 4555–4562

Assessment of wastewater plant serving a paper industry: performances evaluation and proposal treatment for the reduction of freshwater consumption

Nicolò Maria Ippolito*, Giovanni Del Re

Department of Industrial and Information Engineering and Economics – University of L'Aquila, Piazzale Ernesto Pontieri, Monteluco di Roio, 67100 L'Aquila, Italy

**Corresponding author E-Mail: nicolomaria.ippolito@univaq.it*

The paper industries release wastewaters that requires adequate treatment for sustainable development. This work presents a case study of a wastewater plant serving a paper industry. A global approach has been adopted, taking into account the interactions between the production plant and the wastewater plant. The main objectives were the assessment of the current state of the plant for the aspects related to the production and the treatment of wastewater streams, as well as the feasibility study for the reuse of the purified water. Based on monitoring data the correlation between the characteristics of the wastewater and the quality of the raw materials used in the production plant was evaluated. Moreover, the trends of the main parameters (COD, SST, starch, N_{tot} , P_{tot} , pH) for all the sections of the wastewater plant were determined through a specific intensification of monitoring activity. In this way, the overall performances of each section of the plant have been evaluated. More in details, the abatement efficiency of the three oxidation sections is decreasing, MBBR abates about 54% of the COD, the second section about 32% and finally the third removes about 11%, for a total COD removal of 97%. The concentration of dissolved oxygen detected in the second and third oxidation sections is higher than the range of optimal values, which confirms the possibility of decreasing energy consumption by intervening on the regulation of the aeration system. The monitoring data have been used to perform a preliminary study to evaluate the technical feasibility and the limits of reusing wastewater in production, in order to decrease the withdrawal of freshwater and/or face situations of scarcity of water resources. In the present study has been proposed to treat the polluted water by reverse osmosis: the permeate is recirculated to the production plant while the retained is sent to the oxidation sections of the treatment plant. The addition of the reverse osmosis section decreases the wastewater flow rate to treat and, consequently increases the COD concentration and conductivity. Different scenarios have been considered as a function of reducing freshwater withdrawal (15%, 25%, and 40% from current withdrawal). For each scenario the main parameters (flow rate, conductivity, starch, COD) of the streams have been calculated and the preliminary sizing of the reverse osmosis section (membrane surface, energy consumption) have been described.

Experimental Study on VOCs Production during High Monomer Content Emulsion Polymerizations

Marco Barozzi¹, Luca Leopardi², Carlo Bottinelli², Jacopo Ghezzi², Anita Barni², Sabrina Copelli^{1*}

¹ Università degli Studi dell'Insubria, Department of Science and High Technology, via Valleggio 9, Como (CO), IT

² ICAP-SIRA Chemicals and Polymers S.p.A., via Filippo Corridoni 19, Parabiago (MI), IT

* Corresponding author E-Mail: sabrina.copelli@uninsubria.it

1. Introduction

Emulsion polymerizations are chemical reactions exploited for the synthesis of countless products, including adhesives for textile and labeling applications, colloids, synthetic rubbers, and plastics. The possibility of working with monomers in an aqueous medium offers a series of advantages, the main one is reducing the massive use of toxic solvents. However, such processes bring along several concerns, such as hard batch reproducibility, uncomplete conversions and particle size control^[1]. These reactions have been object of massive research for what concerns both modeling^[2] and optimization^[3] aspects. Concerning the optimization, the reduction of the Volatile Organic Compounds (VOCs) content is crucial for whatever latex synthesis as it can compromise the health of the product final users^[4]. For this reason, many works regarding the control of VOCs generation in such polymerization processes^[5] have been reported. Some studies have proposed a VOCs monitoring by enhancing monomer conversion with the introduction of a post-polymerization step^[6], which consists mainly in the addition of organic radical initiators which can migrate into the micelles/polymer particles and promote free monomer content reduction. Other works have investigated the use of devolatilization to physically separate VOCs from the latex^[7]. However, some reactions involve high boiling point VOCs, which cannot be removed by simple devolatilization. In this work, the effect of nitrogen fluxing on VOCs production on an industrial polymer, which is used as adhesive, was investigated. A high monomer content (about 55% w/w) polymer based on 2-ethylhexyl acrylate was proposed. Samples of reacting mixture were taken overtime and analyzed with a Gas Chromatography - Flame Ionizator Detector.

2. Reaction studied

The polymer studied within this work is produced via an emulsion polymerization process involving a high solids content (about 55% w/w). The main reactants are reported in the following: demineralized water (45% w/w), 2-ethylhexyl acrylate (2EEA, 49.5% w/w), acrylonitrile (1.12% w/w), anionic and nonionic surfactants (1.85% w/w). The reaction is exothermic, and the process is operated according to a semi-batch recipe. Radical generation is promoted using two initiators, ammonium persulfate and sodium bisulfite, dosed separately. At first, monomers, surfactants and water are mixed to form a stable pre-emulsion which will be dosed overtime. The reactor is loaded with water (10% w/w) containing 2.5% w/w of surfactants, and reactor temperature is kept at 82 °C. Then, the pre-emulsion is loaded in parallel with the aqueous initiator solutions over a dosing time of 280 min. After dosing, reaction is kept under temperature control for 30 min. After this, conversion is enhanced with the use of a post-polymerization process, which is carried out by dosing two solutions of an organic initiator, mixture of tert-Butyl hydroperoxide and Sodium formaldehyde sulfoxylate, for 60 min. The total amount of organic initiators is 2.1% w/w.

2. Methods

The experimental setup is reported in Figure 1.

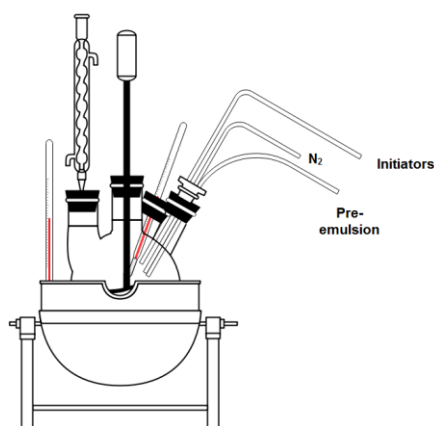


Figure 1. Scheme of the experimental setup

All the experiments were performed in a 5 L glass laboratory reactor. Recipes are formulated to synthesize 2 kg of latex per batch. Temperature control is manual using a controlled hot water bath. Pre-emulsion is prepared in a 1L glass flask with a magnetic stirrer at high speed. Pre-emulsions are very stable and do not separate during dosing. Dosing is performed using ISMATEC pumps. Nitrogen is introduced through a small rubber tube located at the top of the reactor. Thanks to a condenser, it is possible to both purge nitrogen and condense most of the vapors. Samples are taken with the use of a syringe: 10 g of latex are taken with each sample. Considering the potential high amount of residual monomer, samples required quenching, which was performed by adding 0.24 g of an aqueous solution saturated with 4-methoxy phenol. Samples were added with Dimethyl sulfoxide and sent to a Gas Chromatography – Flame Ionizator Detector (GC-FID) for analysis.

Substances analyzed are residual 2EEA and acrylonitrile, acetone, 2-ethylhexanol, 2-ethylhexyl acetate and tert-Butanol (tBuOH). Acetate is used because, as it is present in the reagent with a well-known composition and it is stable during the reaction, it is an index of the reliability of the sample. For each reaction, 5 samples were taken from the reactor according to Table 1:

Table 1. Samples characterization.

# sample	Reference	Reaction time
1	Half dosing	180 min
2	End of dosing	280 min
3	Before post-polymerization	310 min
4	After post-polymerization	370 min
5	Finale product	400 min

Redundant samples were not considered to avoid excessive changes in latex composition. The experimental campaign was carried out with the aim of studying the impact of introducing a nitrogen flux on the total VOCs production. 4 tests under different operating conditions were carried out, with a standard recipe synthesized in parallel (8 tests). In this way, it was possible to validate the reliability of the results. In tests a-b-c, nitrogen flux was activated after dosing (that is, after 280 min), with values equal to 10-50-60 L/h, respectively, resulting in about 3.3-16.7-20 exchanges/h on the gas phase, respectively. In test d, a nitrogen was plugged to the reactor from the beginning of reaction, with a flowrate of 50 L/min.

3. Results and discussion

Figure 2 reports the results on the final products for all the tests performed. In general, the use of nitrogen positively influences the VOCs content, showing a significative reduction. The most affected substances are A2EE, CAN, while tBuOH and 2ethylhexanol are mildly affected. It is interesting to notice how tert-Butanol reduction is not strictly enhanced increasing the total nitrogen supplied (ref. test d). One possible reason can be that, as tBuOH it is generated mainly during post-polymerization, it remains trapped within the polymer particles, making it harder to be stripped from the aqueous phase.

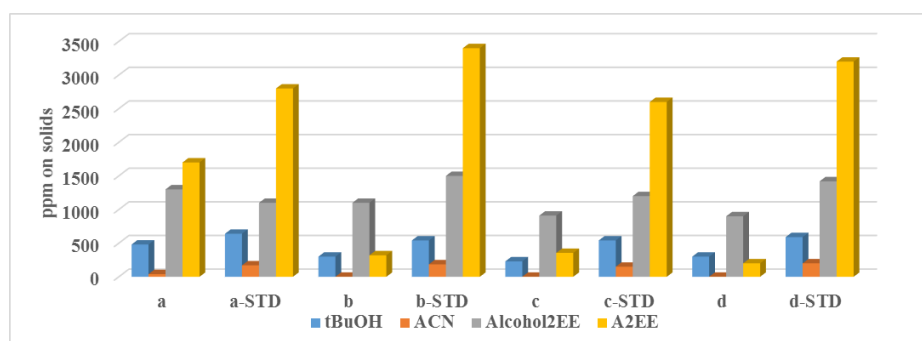


Figure 2. VOCs content in all the tests

Figure 3 shows the concentration of A2EE and CAN as a function of time for tests c and d. A2EE (B.P. 214°C) content is effectively reduced but such a reduction is most likely associated with the reduction of the oxygen content in the solution. Oxygen acts as a radical inhibitor, as it interacts with hydroquinone which is added to all monomers to prevent their auto-polymerization during storage. ACN (B.P 77°C) concentration is strongly reduced using high nitrogen fluxes as a consequence of a pure stripping effect.

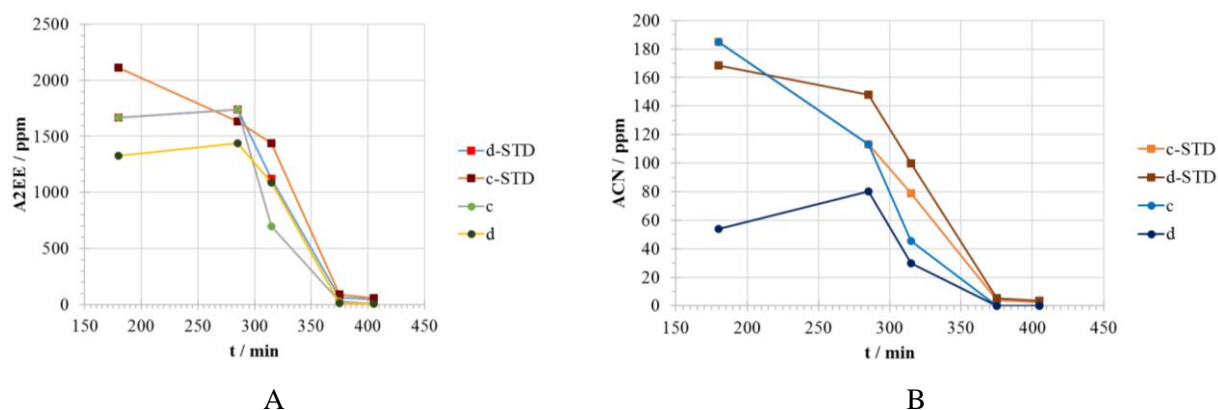


Figure 3. A2EE (a) and ACN (b) content for tests c and d (ppm are evaluated on the solids)

Concerning 2-ethylhexanol (B.P. about 185 °C) content, the ratio between alcohol and 2-ethylhexyl acetate on the pure monomer was tested and it was equal to 0.8. As acetate is basically inert, its concentration can be used to detect more precisely the amount of alcohol generated during the process. It can be noticed that only test d showed a noticeable reduction in the alcohol content, which is noticed already over the course of dosing. Alcohol can be generated by a lot of reactions, but the most likely reaction is the hydrolysis, which can occur both on pure monomer and on polymer chains.

Finally, latexes were tested for their applicability, according to the standards for total solid content, viscosity, pH and specific adhesivity (D 3330/D 3330 M; D6195 – 03; D 3654/D 3654M – 02).

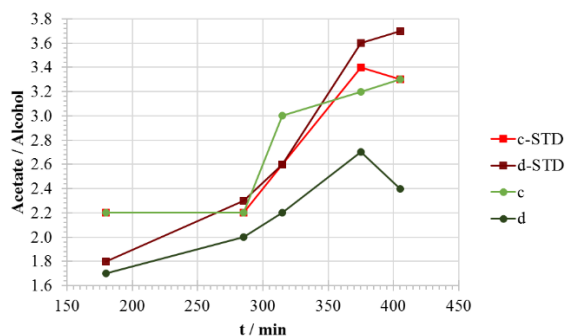


Figure 4. Acetate/alcohol ratio on tests c and d

Table 2 reports the results for tests c and d. Almost each analysis is in accordance with the acceptability standards. The only exception is represented by test d, whose viscosity is slightly lower than the minimum limit value.

Table 1. Accordance to standards for tests c and d

	Range	c	c-STD	d	d-STD
Solids content (%)	54,0 - 56,0	55,9	55,4	55,6	55,4
Brookfield Viscosity (mPa·s R3/V20)	600 - 3000	2100	1800	474	1654
pH	5,5 - 7,0	6,4	6,5	6,2	6,1
Peel (steel) (g/25mm)	300 - 700	365	380	360	440
Shear (steel) 15X20 mm (h)	5 - 50	5 C	5 C	3 C	9 C
Quick Stick (steel) (g/25mm)	-	390	370	435	410

4. Conclusions

In this experimental work, the impact of nitrogen flows on an emulsion polymerization was investigated. From results, it was noticed that nitrogen effectively reduces VOCs content. Possibly, this reduction is a combination of stripping and chemical effects. Tert-Butanol, despite being a light compound, is not particularly affected. ACN is eliminated with high nitrogen flows, but it is more likely stripped, as it is a low boiling VOC. 2-ethylhexanol is the most critical substance, its content is unaffected in most cases, showing a small reduction (about 30%) by using nitrogen during dosing. Working under these conditions allows to synthesize latexes which comply with industrial requirements except for the low viscosity of test d. Future works will investigate the impact of additional variables on VOCs generation, such as starting pH, particles diameter before post-polymerization and different working conditions, such as temperature and dosing times.

References

- [1] P- A. Lovell, F. Joseph Schork, *Fundamentals of Emulsion Polymerization*, *Biomacromolecules*, 2020, 21 (11), 4396-4441
- [2] S. Copelli, M. Dente, G. Bozzano, M. Barozzi, Simplified modeling and main constitutive parameters estimation for industrial emulsion copolymerization processes, *Chem. Eng. J.*, 2018, 335, 988–1003
- [3] S. Copelli, M. Barozzi, N. Petrucci, V. Casson Moreno, Modeling and process optimization of a full-scale emulsion polymerization reactor *Chem. Eng. J.*, 2019 358,1410–1420
- [4] A. De San Luis, C. C. Santini, Y. Chalamet, V. Dufaud, Removal of Volatile Organic Compounds from Bulk and Emulsion Polymers: A Comprehensive Survey of the Existing Techniques, *Ind. Eng. Chem. Res.* 2019, 58, 11601–11623
- [5] R. Salazar, P. Ilundain, D. Alvarez, L. Da Cunha, Ma. J. Barandiaran, and J. M. Asua, Reduction of the Residual Monomer and Volatile Organic Compounds by Devolatilization, *Ind. Eng. Chem. Res.* 2005, 44, 4042-4050
- [6] P. Ilundain, L. Da Cunha, R. Salazar, D. Alvarez, M. J. Barandiaran, J. M. Asua, Postpolymerization of vinyl acetate containing latexes. *J. Appl. Polym. Sci.* 2002, 83, 923.
- [7] R. J. Albalak, E. W. Merrill, J. M. Zielinski, J. L. Duda, A. V. Yazdi, E. J. Beckman, M. Favelukis, S. T. Lee, A. Tukachinsky, T. Chechik, Y. Talmon, Z Tadmor, *Polymer Devolatilization*; Marcel Dekker Inc: New York, 1996.

Managing the operative conditions in photobioreactors to improve photoconversion efficiency: LED applied to microalgae cultivation

Lisa Borella, Elena Barbera, Nicola Trivellin, Eleonora Sforza*

Department of Industrial Engineering, University of Padova, via Marzolo 9, 35131 Padova, Italy

*Corresponding author E-Mail: eleonora.sforza@unipd.it

1. Introduction

Understanding the major bottlenecks in microalgal growth is of crucial importance for the development of economically feasible and energetically sustainable large-scale cultivation systems. Light is a key process parameter, associated with many difficulties in terms of its control, in particular the assurance of temporal stability and spatial uniformity [1]. In the last years, light emitting diodes (LEDs) have been investigated as a promising alternative to natural sunlight for microalgae growth, offering high durability and efficiency (less than 10% of energy is lost as heat in highly efficient LED [1]), together with a monochromatic emission, which is useful to tune the emitted spectrum, in order to optimize light supply [2], [3]. To decrease the costs associated with artificial illumination, however, improvements in both light sources and photosynthetic efficiency are required [4]. Photosynthesis is a low efficiency process [5] and to date different strategies have been proposed to achieve a high level of light utilization, including the spectral matching of the light source to the photosynthetically active spectrum [6]. However, it should be considered that the operating condition of the system also play a role in the increase of photoconversion efficiency. Current pilot-scale plants for microalgal production usually apply batch or semi-continuous cultivation methods, even though the continuous system should be preferred as it is the most productive. Batch is simple, the cheapest, and most widespread operation mode, but its productivity is inversely proportional to growth curves duration, so that the average value depends on harvesting day (during exponential or stationary phases) [7]. A compromise is a semi-continuous system, where a certain amount of culture volume is harvested periodically from the reactor to recover biomass, and replaced with fresh medium. Nevertheless, productivity depends on the harvesting frequency which, on average, can be approximated to a residence time. The light supply mode is also responsible of a potential increase of biomass production: flashing light can reduce the degree of mutual shading by penetrating deeper into the cultures, owing to the increased intensity of the instantaneous photosynthetic photon flux [8].

2. Methods

Arthrospira maxima was cultivated under continuous illumination with red-blue (R/B) light-emitting diodes. Experiments were carried out in a continuous operating photobioreactor. Kinetic parameters were retrieved from respirometric tests and implemented in a comprehensive growth model, which examines the spectral composition of the light source, and identifies optimal culturing conditions. The model was experimentally validated by data obtained at various light intensities, near the predicted optimal conditions. Moreover, *Arthrospira maxima* was cultivated under flashing regime in the range 10-1000 μs , and pulse intensities up to 70000 $\mu\text{mol m}^{-2} \text{s}^{-1}$ on biomass growth were investigated. The overall energy efficiency of the process was evaluated by calculating both the photosynthetic efficiency (i.e. the efficiency of conversion of light energy into chemical energy stored in the biomass) and the LED efficiency (i.e. the efficiency of conversion of electrical energy into light energy).

3. Results and discussion

Respirometric tests showed that an acclimation to a Red/Blue LED light source is necessary and that, after this period, kinetic parameters values were not significantly different from a white LED-grown culture. The kinetic parameters retrieved by respirometry were implemented in a mathematical model, able to reproduce the experimental data quite well. Based on simulations, it was shown and experimentally validated that adjusting the residence time it is possible to properly exploit the spectrum of light provided (Figure 1) and increase the biomass productivity by 15%. Nevertheless, energetic efficiency analysis indicated that integrating tailored illumination in the microalgae cultivation process may be a valuable approach to increase overall process efficiency.

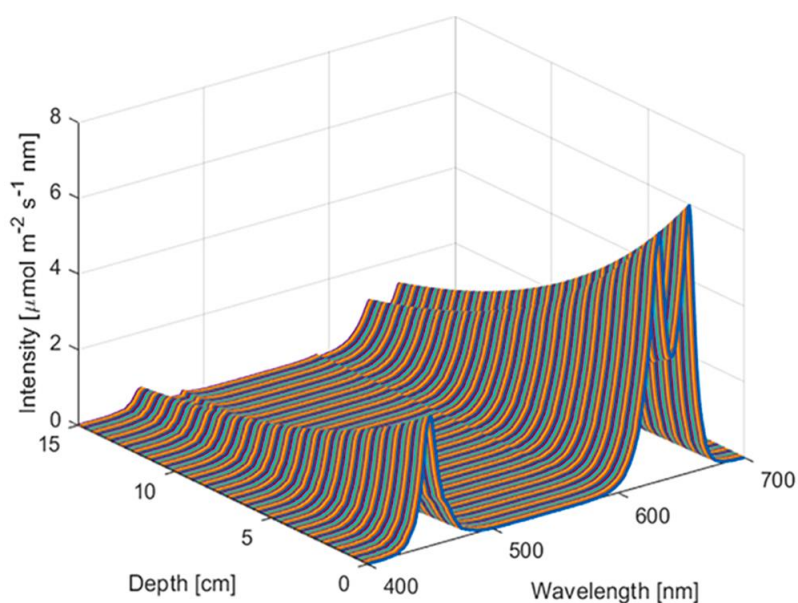


Fig.1 Light attenuation profile at the optimal conditions. $I_0 = 300 \mu\text{mol m}^{-2} \text{s}^{-1}$, $C_x = 315 \text{ g m}^{-3}$

In addition, LED technology was used to overcome self-shading limitation, taking advantage of the possibility of generating high-intense pulsed light, that allows greater light penetration through the reactor depth. In a first set of experiments, light periods ranging from 10 to 1000 μs were applied, followed by longer dark periods and light intensities ranging from 8000 to 178000 $\mu\text{mol m}^{-2} \text{s}^{-1}$. It has been found that flashing light effect (i.e. increased photosynthetic performance under pulsed light regime) occurs in both light-limited and light-saturated regime (120 and 300 $\mu\text{mol m}^{-2} \text{s}^{-1}$), and the optimal light period ranges between 100 and 200 μs , with a maximum observed biomass increase of 2.56 times with respect the control in continuous light. In the second set, different residence times (in the range between 0.8 and 5 days) and different pulse intensities (from 11605 to 37500 $\mu\text{mol m}^{-2} \text{s}^{-1}$) have been investigated, with a light period of 100 μs and average light intensity of 300 $\mu\text{mol m}^{-2} \text{s}^{-1}$. Results showed that for flash intensity up to 17850 $\mu\text{mol m}^{-2} \text{s}^{-1}$ flashing light effect (FLE) can be observed, while beyond this value photoinhibition is so strong that FLE is not so evident (Figure 3). On the contrary, at the optimal pulse intensity, biomass productivity almost doubles the optimal one obtained in continuous light regime, at much higher residence times. In addition, results suggest that the higher the pulse intensity, the more the wash out shifts toward higher residence times, due to the increasing photo-inhibition.

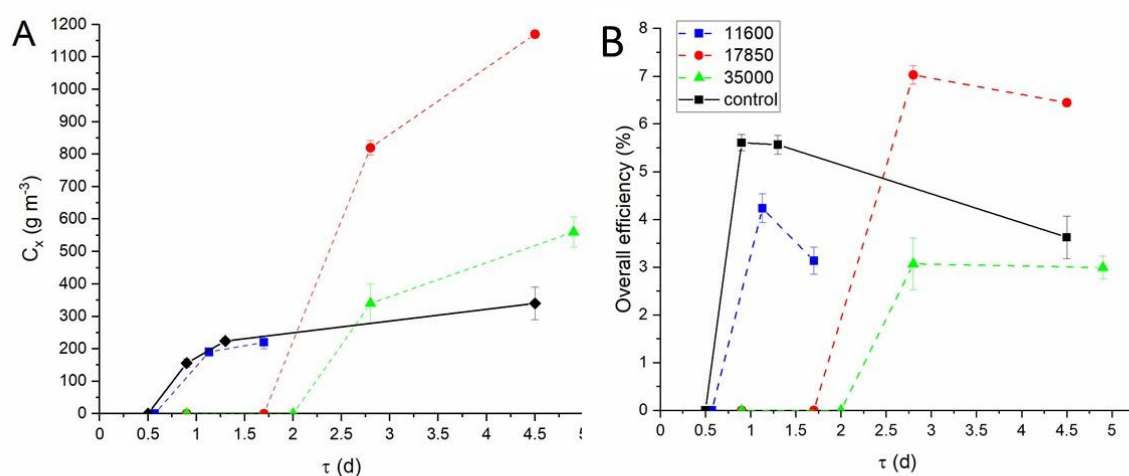


Figure 1: Overall efficiency at different residence time and different light periods for an incident light intensity of $300 \mu\text{mol m}^{-2} \text{s}^{-1}$

(A) and the corresponding energy conversion efficiency (B)

4. Conclusions

In this work, the possibility of increasing the production of microalgae by using tailored LED light was proved. A model approach demonstrated which should be the best operative condition of an artificially illuminated continuous system. The use of pulsed light at very high frequency showed an increased light penetration and biomass productivity, but only if the operating conditions (i.e the residence time) are properly set.

References

- [1] A. P. Carvalho, S. O. Silva, J. M. Baptista, and F. X. Malcata, *Appl. Microbiol. Biotechnol.*, (2011) 89, 5, 1275–88
- [2] E. Bland and L. T. Angenent, *Bioresour. Technol.*, (2016) 216, 579–586, , doi: 10.1016/j.biortech.2016.05.116.
- [3] E. G. Nwoba, D. A. Parlevliet, D. W. Laird, K. Alameh, and N. R. Moheimani, *Algal Res.*, (2019) 39, 101433, doi: 10.1016/j.algal.2019.101433.
- [4] P. S. C. Schulze, R. Guerra, H. Pereira, L. M. Schüler, and J. C. S. Varela, *Trends Biotechnol.*, (2017) 35, 11., 1088–1101, doi: 10.1016/j.tibtech.2017.07.011.
- [5] R. E. Blankenship et al., *Science (80-.)*, (2011) 332, 6031, 805–809, May, doi: 10.1126/science.1200165.
- [6] P. S. C. Schulze, L. A. Barreira, H. G. C. Pereira, J. A. Perales, and J. C. S. Varela, *Trends Biotechnol.*, (2014)32, 8, 422–430, doi: 10.1016/j.tibtech.2014.06.001.

- [7] L. Borella et al., Adv. Sustain. Syst,(2022) 2100346, doi: <https://doi.org/10.1002/adsu.202100346>.
- [8] K. H. Park and C. G. Lee, Biotechnol. Bioprocess Eng, (2000) 5, 3, 186–190, , doi: 10.1007/BF02936592.

A circular economy approach for olive oil industry: from olive pomace to microalgal biomass

Alessandro Alberto Casazza*, Patrizia Perego, Attilio Converti

1 Department of Civil, Chemical and Environmental Engineering, via Opera Pia 15, 16145 Genova, Italy

*Corresponding author E-Mail: alessandro.casazza@unige.it

1. Introduction

The circular economy is defined by the European parliament as “a model of production and consumption, which involves sharing, leasing, reusing, repairing, refurbishing and recycling existing materials and products as long as possible” [1]. This allows an extension of the life cycle of a product to be reused, thus adding a further value to it and reducing wastes. In this context, particular attention must be paid to olive oil production residues [2]. Olive oil production, which is a major industrial field in the Mediterranean countries, reached 1924 Mg in the season 2019/2020, while the worldwide production was around 3207 Mg [3]. In this work olive pomace was used to recover high added value compounds and produce biogas by anaerobic digestion. Moreover, in order to satisfy the circular economy concept, the digestate from the latter process was used as medium for the microalga *Chlorella vulgaris* growth. The microalgal biomass represents an important source of chemicals, and in the future, its use will be increasingly significant.

2. Methods

2.1 Polyphenols extraction

Polyphenols were extracted from the olive pomace (OP) of Taggiasca cultivar by means of a High Pressure High Temperature Extractor (HPTE) (model 4560, PARR Instrument Company, Moline, IL, USA). HPTE was selected because of better results obtained in polyphenols recovery if compared with other extraction methodologies [4]. Extraction parameters were selected based on previous works [2]. During the extraction, pressure and temperature inside the reactor reached 25 bar and 180 °C, respectively. Total polyphenols were quantified using a modified version of the Folin-Ciocalteu method [5].

2.2 Olive pomace anaerobic digestion

The digestion process was carried out in a bioreactor with a total volume of 6 L and a working volume of 5 L. After an initial period of acclimatization of the Anaerobic Digestion (AD) microorganisms present in the inoculum, the OP was fed to the bioreactor. Initially it was anaerobically co-digested with activated sludge and subsequently mono-digested alone (15 g of OP three times per week).

2.3 *Chlorella vulgaris* growth using digestate as a culture medium

Chlorella vulgaris CCAP 211 (Culture Collection of Algae and Protozoa, Argyll, UK) was used at an initial concentration of 0.2 g/L in 0.6 L column photobioreactors. Different concentration of digestate (25 and 50% v/v) in Bold Basal Medium were tested. *C. vulgaris* concentration was determined by optical density ($\lambda = 625$ nm) measurements using a UV-Vis spectrophotometer (Lambda 25, PerkinElmer) and a calibration curve, and the Chemical Oxygen Demand (COD) removal efficiency was quantified [6]. The microalga lipid content was quantified following the method described by Converti et al. [7].

3. Results and discussion

After the extraction at 180 °C, an ethanolic solution rich in polyphenols was obtained. The concentration of total polyphenols in the HPTE extract, expressed as caffeic acid equivalents (CAE) per unit volume, was 19.2 mg_{CAE}/mL. Concentrations of 3.59, 0.51, 0.23, 0.18 and 0.08 mg_{CAE}/mL were found by High Performance

Liquid Chromatography (HPLC, model 1260, Agilent) for oleuropein, tyrosol, caffeic acid, coumaric acid and apigenin, respectively. At the same time, OP anaerobic digestion led to a considerable biogas production, which achieved about 6.5 L using 40 g of dry OP (Figure 1).

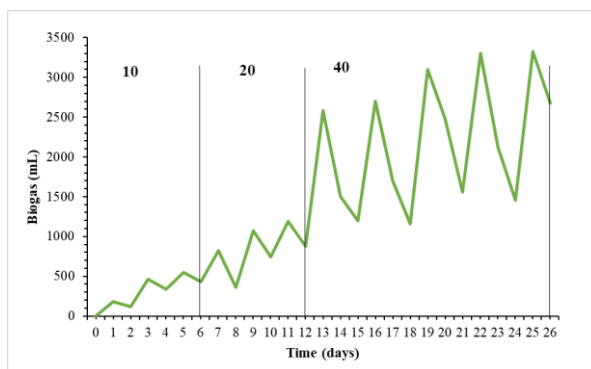


Figure 1. Biogas production obtained by feeding the anaerobic digester every three days with 10, 20 and 40 g of dry olive pomace.

The digestate resulting from the anaerobic treatment was mixed with the Bold Basal Medium (25 and 50 % v/v) and used as medium to cultivate *C. vulgaris* in column photobioreactors. Although the microalga was able to grow mixotrophically using both organic compounds present in the waste and carbon dioxide, its final concentrations, ranging from 1.0 to 1.4 g of dry biomass per L of medium (g_{DB}/L), were quite lower than those achieved in the control runs (2.0 g_{DB}/L). A possible negative influence of the digestate on the growth of the microalga can be supposed because the digestate can prevent light from deeply entering the culture medium. In addition, Merchuk and Wu [8], after applying a three-stage structured model integrating photosynthesis and photoinhibition to a column photobioreactor, demonstrated that cell productivity (v_{DB}), defined as the biomass produced per unit time and surface, is related to: the height of the column (H), the distance between adjacent column installations (d), the column diameter (D_c), the biomass concentration at the beginning (X_0) and at the end of the growth (X_f) (Eq. 1).

$$v_{DB} = \frac{D_c^2 H (X_f - X_0)}{(D_c + d)^2 \Delta t} \quad \text{Eq. 1}$$

As for the COD, the results showed a significant reduction in this parameter over time. In fact, after 20 days the COD decreased from 1500 and 750 mg_{O_2}/L in the photobioreactors containing 50% and 25% v/v of digestate to final values of 477 and 269 mg_{O_2}/L , respectively.

Conclusions

Olive pomace can be successfully used for the recovery of high added value compounds and for the production of biogas by anaerobic digestion. Moreover, the digestate can be further treated using microalgae, obtaining a waste with a less environmental impact and high added value biomass.

References

- [1] M. Smol, P. Marcinek, J Duda, D. Szoldrowska, Resources. 9 (2020), 5.
- [2] B. Aliakbarian, A.A. Casazza, P. Perego, Food Chem. 128 (2011), 704-710.
- [3] IOC, <https://www.internationaloliveoil.org/worlds-olive-oil-production-has-tripled/>. 01/04/2021.
- [4] A.A. Casazza, B. Aliakbarian, S. Mantegna, G. Cravotto, P. Perego, J. Food Eng. (2010), 100, 50-55.
- [5] A.A. Casazza, M. Pettinato, P. Perego, Sep. Purif. Technol. (2020), 240, 116640.
- [6] E. Spennati, S. Mirizadeh, A.A. Casazza, C. Solisio, A. Converti, Algal Res. (2021), 60, 102519.
- [7] A. Converti, A.A. Casazza, E.J. Ortiz, P. Perego, M. Del Borghi, Chem. Eng. Process. (2009), 48, 1146-1151.
- [8] J. Merchuk, X. Wu, J. Appl. Phycol. (2003), 15, 163-170.

Medium chain fatty acids production via biological chain elongation

Federico Battista*, David Bolzonella

University of Verona, Department of Biotechnology, Strada Le Grazie 15, 37134, Verona, Italy

*Corresponding author E-Mail: federico.battista@univr.it

1. Introduction

Medium-chain fatty acids (MCFAs) are saturated or unsaturated fatty acids having from 6 to 12 carbon atoms, which are mainly synthesized from fossil-base compounds or from vegetable oils such as palm oil, coconut oil or castor oil. Even in this last case, the MCFAs production cannot be considered sustainable as their extraction involves the adoption of no green solvents. Moreover, the MCFA content in the vegetable oils represents only the 5-15% w/w of the total compounds [1]. MCFAs are very attracting compounds as they have different applications in food, pharma, chemical and biofuel industries. The investigation of sustainable processes for MCFAs production has been receiving great attention from scientific community in last decade. In particular, anaerobic fermentation is a well-known technology for the organic wastes conversion into valuable bioproducts, such as Volatile Fatty Acids (VFAs), and biogas, a gaseous blend rich in methane. But the higher energy densities and economic value than the traditional methane and VFAs, make MCFAs more interesting in a biorefinery scope [2].

The biological process that appears as the most promising for MCFAs synthesis is represented by the “chain elongation”, where short chain VFAs, derived from the acidogenic fermentation of organic substrates, are converted into MCFAs through the addition in the reaction medium of electron donor-compounds, such as ethanol, lactate, methanol, n-propanol of biological origin. VFAs and ethanol conversion into MCFA is carried out by microorganisms able to elongate the VFAs’ carbon chain by reverse β -oxidation pathway, as reported in Figure 1.

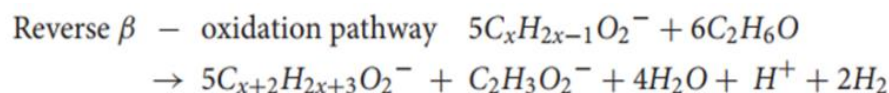


Figure 1. Reverse β -oxidation pathway for the VFAs conversion into MCFAs.

Considering the caproic acid production from ethanol and acetate, ethanol is first converted into acetyl-CoA before entering into two cycles of reverse β -oxidation. The acetyl-CoA is stretched into butyrate along the first cycle of reverse β -oxidation reacting with acetate. The remaining acetyl-CoA is then used in the second cycle of reverse β -oxidation, reacting with the butyrate to generate the caproate.

The challenge of this work is to select caproic acid producing microorganisms by reverse β -oxidation from Microbial Mixed Culture (MMC). Firstly, batch tests were performed using synthetic acetate and ethanol at different molar ratios in order to verify the possible MCFAs production yields. In order to assure the presence of MMC, agricultural digestate was adopted as inoculum. With the optimization of the acetate-ethanol ratio, the chain elongation for the caproic acid production was also tested in a 1 liter CSTR reactor.

2. Methods

One of the main parameters governing the chain elongation process is represented by the acetate-ethanol molar ratio. The theoretical acetate-ethanol molar ratio for a complete conversion of the two substrates into caproate is 1:2. Previous studies demonstrated that this ratio must be lower than 1:2 because only 5/6 of the acetyl-CoA derived from ethanol enters in the reverse β -oxidation cycle for the caproate production, while the remaining 1/6 of the acetyl-CoA is used to provide ATP. But, acetate:ethanol ratios lower than 1:10 stop the process as consequence of the lack of enough acetate to support the reactions of the first cycle of reverse β -oxidation [3].

2.1 Batch tests for the selection of the best acetate: ethanol molar ratio

Different batch tests were carried out to individuate the optimal acetate: ethanol molar ratio and the best pH. Tests were performed in 0.5L reactors with a working volume of about 250 mL under anaerobic condition and at mesophilic temperature (37°C). The MMC was assured by the addition of agricultural digestate (inoculum), having a Total Solids (TS) and Volatile Solids contents of 5.29 and 3.31% w/w, respectively. The inoculum:substrate ratio was of 2:1 in terms of VS content, as suggested by Liu et al. (2017) [4]. Two rounds of batch tests were performed according to the acetate: ethanol molar ratios of Table 1, at pH of 7 and 9, respectively.

Table 1. Batch tests' configuration

Acetate: Ethanol ratio	Inoculum (g)	Acetate (g)	Ethanol (g)
1:2	240	1.56	2.4
1:3	240	0.48	0.92
1:5	240	0.84	3.16
1:10	240	0.84	6.24

Batch tests had a duration of 10 days, considered the required time to allow the starting of the chain elongation for the acetate and ethanol conversion into caproic acid [4].

VFAs and MCFAs (C6, C8 and C10) concentrations were monitored at the end of the tests. The process performances were evaluated considering both the MCFAs and VFAs production yields, expressed as:

$$\text{MCFAs yield (Y}_{\text{MCFAs}}, \% \text{ w/w}) = \frac{\text{amount of MCFAs (g)}}{\text{initial VS amount from substrates (g)}} * 100$$

$$\text{VFAs Yield (Y}_{\text{VFAs}}, \% \text{ w/w}) = \frac{\text{amount of MVFAs (g)}}{\text{initial VS amount from substrates (g)}} * 100$$

In order to close the mass balance of the process, biogas production was also monitored following the Holliger et al. (2016)'s protocol [5].

2.2 Continuous test

The best acetate: ethanol molar ratio in terms of MCFAs yield from the batch tests was tested in continuous mode. A 1L CSTR reactor, with a working volume of about 0.6L, was initially fed with an inoculum amount of 580 g. Then, the CSTR were daily discharged and fed with about 5g of acetate and 20 of ethanol in order to have an acetate: ethanol molar ratio of about 1:5, the best one in term of MCFAs yield from the batch test. The Hydraulic Retention Time was set up at 25 days. Continuous test is still running and will be stopped at the end of 3 HRT. The corresponding results will not be included in the present abstract.

3. Results and discussion

The first main result from batch tests was that pH 9 inhibited completely any biological processes: acidogenic fermentation, reverse β -oxidation and biogas production, demonstrating that the neutral pH values are the ideal for all these processes.

Figure 2 summarized the MCFAs production yields for the batch tests carried at different acetate:ethanol molar ratios and pH 7.

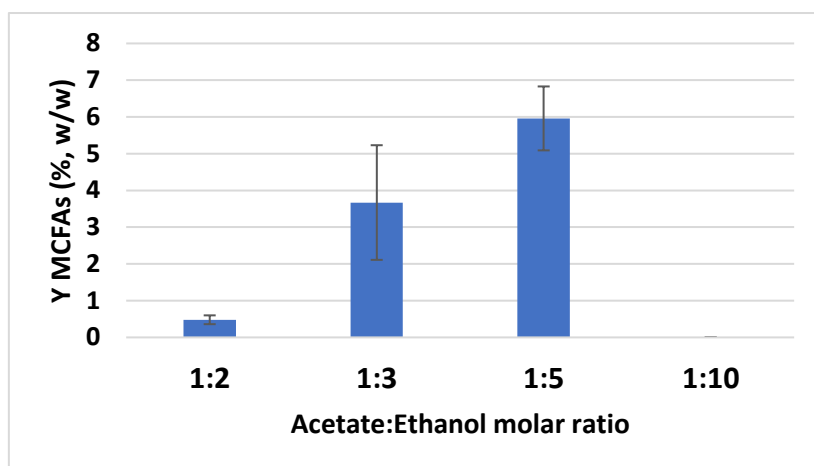


Figure 2. MCFAs production yield for the different acetate: ethanol molar ratio

The tests confirmed that acetate:ethanol molar ratio is a fundamental parameter for the beginning of reverse β -oxidation reactions. In particular, the theoretical molar ratio of 1:2 was not adequate, as ethanol is not employed exclusively for the chain elongation but also for providing energy by ATP production, as commented above [2]. Instead, a too low acetate: ethanol molar ratio of 1:10 did not assure the minimal acetate amount to provide its elongation into MCFAs. The best acetate: ethanol molar ratio was of 1:5 with a MCFAs production yield of 6% w/w of the initial substrates amount (ethanol and acetate) fed in the reactor. Caproic acids accounted for the 90-95% w/w of the total MCFAs produced along the batch tests, while octanoic and decanoic acids represented the remaining part, suggesting that probably more days are required for their production.

Considering only batch test with the best acetate: ethanol ratio of 1:5, the VFAs production yield was of about the 27% w/w of the total amount of VS fed in the reactor, with butyric acid as the main product (around the 85-90% w/w). It demonstrated that reverse β -oxidation reactions were still running at the end batch tests, which had a duration of 10 days. For this reason, the following continuous test was set up at higher HRT of 25 days, that is also consistent with some previous research works [3, 4].

It is important to note that most of the VS derived from acetate and ethanol was converted into biogas, whose produced amount was about 2.3L. It corresponded to about 580 mL_{biogas}/g_{VS}, for the batch test of an acetate: ethanol molar ratio of 1:5. Consequently, VS were converted for the 60% into biogas, for the 27% into VFAs and for the 6% into MCFAs. It demonstrated that batch configuration can assure the conversion of the substrates into MCFAs just for a minimal fraction, favoring the anaerobic digestion reactions for biogas production. The selection of MCFAs producing microorganisms could be made just with a continuous feeding of the acetate and ethanol, and consequently with a CSTR configuration.

4. Conclusions

A preliminary research work for MCFAs production at batch tests allowed the selection of the best operational conditions to increase the yield's process. It emerged that a neutral pH and an acetate: ethanol molar ratio of 1:5 optimized the MCFAs production yield, achieving a final conversion of the 6% w/w of the substrates (VS based). Considering the high VS conversion into VFAs (27% w/w) and of butyric acid (representing the 90% w/w of the total VFAs), it emerged that 10 days were not enough to assure the completing of reverse β -oxidation reactions of the VFAs into MCFAs. Finally, it was demonstrated that batch test favored the anaerobic digestion reactions for biogas production rather than the selection of MCFAs producing microorganism.

A continuous test operated at neutral pH, an acetate: ethanol molar ratio of 1:5 and at high HRT (25 days) is still running and its results will be available in the next future.

References

- [1] Venkateswar Reddy, M., Kumar, G., Mohanakrishna, G., Shobana, S., & Al-Raoush, R. I. (2020). Review on the production of medium and small chain fatty acids through waste valorization and CO₂ fixation.

Bioresource Technology, 309(April), 123400. <https://doi.org/10.1016/j.biortech.2020.123400>

- [2] Strazzera, G., Battista, F., Andreoli, M., ...Bolzonella, D., Lampis, S. (2021). Influence of different household Food Wastes Fractions on Volatile Fatty Acids production by anaerobic fermentation. *Bioresource technology*, 335, 125289. <https://doi.org/10.1016/j.biortech.2021.125289>
- [3] Zhang, C., Yang, L., Huo, S., Su, Y., & Zhang, Y. (2021). Optimization of the Cell Immobilization-Based Chain-Elongation Process for Efficient n-Caproate Production. *ACS Sustainable Chemistry and Engineering*, 9(11), 4014–4023. <https://doi.org/10.1021/acssuschemeng.0c07281>
- [4] Liu, Y., He, P., Shao, L., Zhang, H., & Lü, F. (2017). Significant enhancement by biochar of caproate production via chain elongation. *Water Research*, 119, 150–159. <https://doi.org/10.1016/j.watres.2017.04.050>
- [5] Holliger, C., Alves, M., Andrade, D., Angelidaki, I., Astals, S., Baier, U., Bougrier, Clair et al. (2016). Towards a standardization of biomethane potential tests. *Water science and technology*, 74(11), 2515-2522. <https://doi.org/10.2166/wst.2016.336>

Bioactive substances from hazelnut processing residues via Soxhlet extraction: set up, mass balances and yield

Michele Miccio^a *, Marcello Casa^a, Michela Fraganza^a, Aisylu Zainutdinova^c, Paola Brachi^b,
Giovanna Ferrari^{a, d}

^a University of Salerno – Department of Industrial Engineering, Via Giovanni Paolo II 132, 84084 Fisciano (SA), Italy

^b Inst. Sciences and Technologies for Energy and Sustainable Mobility, STEMS-CNR, P. Tecchio 80, 80125 Napoli (IT)

^c Department of Production Safety and Industrial Ecology, The Ufa State Aviation Technical University, Ulitsa Karla
Marksa 12, 450077 Ufa, The Republic of Bashkortostan, Russian Federation

^d ProdAl S.c.a r.l., Via Giovanni Paolo II 132, Edificio L6, 84084 Fisciano (SA), Italy

* Corresponding author E-Mail: mmiccio@unisa.it

1.Introduction

Hazelnut (*Corylus avellana L.*) is one of the most popular tree nuts consumed for human food worldwide, ranking second in production after almond. Turkey, specifically the Black Sea region, is the world leading producer of hazelnut, contributing over 72% to the global production, although other important producing areas include Georgia, Spain and Italy (FAO, 2020). In Italy, the Campania region has been the leader in the field production of hazelnut in 2020, with an amount of about 480000 q and less than half in the province of Avellino (ISTAT, 2020). The hazelnut skin (*perisperm*), hard shell (*pericarp*), green leafy cover (*floral bracts*) and the hazelnut tree leaves represent the byproducts of the roasting, the cracking, the shelling/hulling, and the harvesting processes, respectively.

The present paper is in the framework of a R&D project aimed at valorization of the above non-edible parts. As the public opinion is aware and under the focus of current R&D activities, residues and wastes of biogenic origin are more and more considered as a valuable source of both bioactive substances and biofuels, whatever their original moisture content is (Adiletta et al., 2020; Casa et al., 2021).

It is well known that a diet rich in tree nuts adds benefits because of their mono- and polyunsaturated fatty acid content (Ros et al., 2006), their high level of dietary fiber (Salas-Salvadó et al., 2006) and the presence of several bioactive molecules in the kernel and skin ranging from tocopherols to arginine and to polyphenols (Andrés et al, 2002), which might exert positive cardiovascular effects such as low-density lipoprotein (LDL) protection from oxidation or enhanced endothelial function (Andrés et al, 2002). The antioxidant capacity of various nut byproducts has been widely investigated, and several works have acknowledged that nut byproducts are especially rich sources of natural phenolic compounds with potential bioactivity (Shahidi et al., 2007). Phenolic compounds are the primary bioactive components in plants. Consequently, the utilization of natural phenolic antioxidants instead of synthetic ones has recently raised considerable interest among food scientists, manufacturers and consumers. In particular, the skins from roasted hazelnut (Shahidi et al., 2007) and green leafy covers (Alasalvar et al., 2006) have been investigated to exploit the content of some phenolic acids.

The bioactive compounds of interest can be separated, in principle, from the source hazelnut matrix by means of a conventional liquid-solid extraction triggered by an organic solvent. Nowadays, a switch to “greener” solvents like limonene or even water would represent a convenient step along the way to more environmentally sustainable processes. In any case, the extraction process generates solid residues, in a wet or dry state, which are to be disposed of. They are suitable candidates for subsequent valorization steps to biofuels, e.g., based on mild thermal processing: biomass torrefaction is the most representative one (Brachi et al., 2016; Chen et al., 2021).

Therefore, the idea underlying this work is to extract bioactive compounds using a “green” solvent.

Among the above-mentioned hazelnut residues, green leafy covers (or leafy husks) have been privileged here because, based on a preliminary bibliographic analysis, they appear now of greater interest and exhibit greater knowledge gaps. Samples at a different “maturation” degree have been tested, i.e., in a green (wet) and a dry

state.

2. Materials and Methods

Different samples of husks were directly collected from the trees in a hazelnut orchard at Pizzolano (Fisciano, SA). Dry brown ones (see Figure 1.A and Table 1) were taken in September 2020; green leafy husks were sampled on August 5, 2021. These latter, when not directly tested, have been frozen and stored at $-18\text{ }^{\circ}\text{C}$.



Figure 1. Pictures of the “as collected” hazelnut husks: A. Dry brown leafy husks sampled on September 8, 2020; B. Fresh green leafy husks sampled on August 5, 2021

Samples of dry cuticles separated from roasted hazelnuts were kindly provided by cooperating companies in the Campania region, precisely PRODAL Scarl and Grimaldi Srl. They (see Figure 2 and Table 2) were obtained after industrial roasting of hazelnuts harvested in 2020.



Figure 2. Picture of the roasted hazelnut cuticles

For the measurement of the moisture content, the KERN MLB analyzer was used, with a sample load of 2 g and a final T = 105 ° C. For all samples, the determinations of the moisture content have been conducted in triplicate.

A conventional Soxhlet extractor was adopted in the present study, which is equipped with a 250 W electric heater (by Falc), a 500 mL glass flask, a 43x123 mm cellulose thimble and a 300 mm long Graham condenser for solvent vapor condensation.

The selected solvent was the “greenest” one, i.e., water; actually, double-distilled water was used with a loaded volume of 300 mL. For comparison, pure ethanol of analytical grade was used at the same load in a few tests. The Soxhlet extraction tests were carried out on the “as collected” samples, without any grinding. In the case of frozen green leafy husks, they were gently thawed to room temperature and allowed to lose the dripping water. In the case of roasted cuticles, the PRODAL sample was taken as the first reference material and, for such a reason, was gently sieved to obtain a 2-4 mm size cut. It is worth saying that the cuticles have a skin-type shape and, as a consequence, the 2-4 mm size fraction yields particles that are very irregular and far away from the conventional sphere-like solids. The sample mass to be loaded into the cellulose thimble was varied according to the moisture content of the test sample (see Tables 1 and 2) to keep fixed the mass of dry solids in the extraction experiments. For the necessary verification, each test was at least duplicated, as it is possible to check from the color codes in the rows of the Tables 1 and 2.

Table 1. Summary of the Soxhlet extraction tests with “as collected” hazelnut husks

Soxhlet test No.	Sample	Sample mass (g)	Sample moisture content (% wt.)	Extraction solvent	Solvent volume (mL)
21	Dry husks “as collected” 2020-09-08	8.0	9.60	water	300
29	Dry husks “as collected” 2020-09-08	8.0	9.60	water	300
22	Green husks “as collected” 2021-08-05	22.5	61.84	water	300
23	Green husks “as collected” 2021-08-05	22.5	61.84	water	300
24	Green husks “as collected” 2021-09-08	22.7	67.53	water	300
30	Green husks “as collected” 2021-08-05 after thawing	22.5	62.64	water	300
31	Green husks “as collected” 2021-08-05 after thawing	22.5	63.50	water	300
26	Green husks “as collected” 2021-08-05	22.5	65.70	ethanol	300
27	Green husks “as collected” 2021-08-05	16.5	54.49	ethanol	350
28	Green husks “as collected” 2021-08-05	16.5	54.49	ethanol	500

The effectiveness of the extraction has always been confirmed by the change in color of the extracted solution (see Table 1 and 2). Then, each extracted solution was stored in a glass bottle away from light.

Table 2. Summary of the Soxhlet extraction tests with roasted hazelnut skins

Soxhlet test No.	Sample	Sample mass (g)	Sample moisture content (% wt.)	Extraction solvent	Solvent volume (mL)
25	PRODAL 2-4 mm size cut	14.3	7.25	water	300
1	Grimaldi “as collected”	20.0	9.19	n-hexane	300
4	Grimaldi (residue after extraction with n-hexane)	14.3	==	ethanol	400
2	Grimaldi “as collected”	20.0	9.19	ethanol	300

The UV spectrophotometric analysis has been preliminary used for a qualitative assessment of the actual presence of bioactive compounds in the Soxhlet extracted solutions. To this end, a laboratory UV spectrophotometer has been used and at least one extracted solution has been tested for each reference sample of hazelnut residue. In particular, the presence of polyphenols was expected in the 200-300 nm wavelength window.

All the Soxhlet extracted solutions have been subjected to a quantitative assessment of their content of polyphenols and tannins as representative families of bioactive compounds. The method of Singleton and Rossi

(1965) using *Folin and Ciocalteu's phenol reagent* was followed for the quantitative determination of total polyphenols as g (gallic acid equivalent)/L (extracted solution). The method of Price et al. (1978) was adopted for the quantitative determination of tannins as g/L (extracted solution).

3. Results and discussion

First of all, the Soxhlet experimental procedure has been checked for the correct closure of the mass balances. The most critical case has been taken into consideration, corresponding to the test condition in which there is contemporary presence in extraction of both ethanol (EtOH) and water, the latter being introduced as “moisture” of the wet husks (WH).

The test sample of the green hazelnut husks was weighed and the moisture content of another sample taken from the same feedstock was measured. This allowed the calculation of the masses of the two macro-components, i.e., water and dry solids (DS).

After extraction, the wet spent husk was accurately separated from the wet thimble, both were weighed on an analytical scale, after which they were dried under forced air circulation in a lab hood and re-weighed to determine the mass of the dry husk. The difference between the initial weight (i.e., wet spent husk and wet thimble) and the final weight (i.e., dried spent husk and dried thimble) provided the mass of the liquid (i.e., ethanol and water) removed from solids by evaporation during drying.

The liquid extracted solution was also weighed, then its density was simply measured with the aid of a precisely graduated balloon. By using the mixing rule for density of miscible liquids, the masses of the two components, i.e., ethanol and water, were determined by calculation.

Three simple mass balance equations were written for dry solids, ethanol and water, respectively. They are not reported here for brevity. Their solution, which was quite straightforward, yielded the masses of total solids dissolved in the extracted solution, and of EtOH and H₂O losses to atmosphere, these latter likely due to incomplete condensation in the Graham condenser.

The scheme of the material flows in the Soxhlet experimental procedure is shown in Fig. 3.

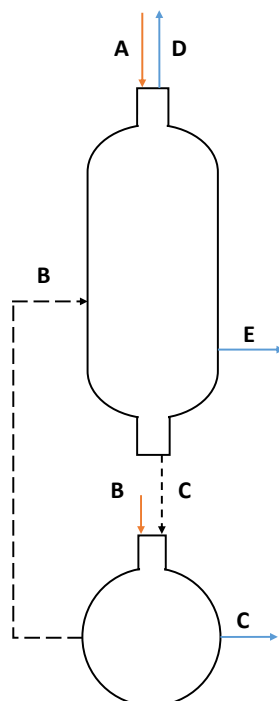


Figure 3. Schematic representation of the material flows in the lab Soxhlet apparatus: A – Biomass test sample; B – Reagent grade ethanol; C – Extracted solution; D – Loss due to incomplete condensation (Evaporation loss); E – Spent “wet” biomass solids;
NOTE: The recirculating streams are dashed.

The closure of the mass balances was quite satisfactory. Small and reasonable values were obtained for the masses of total solids dissolved in the extracted solution and the H₂O loss to atmosphere; only the EtOH loss to atmosphere appeared as a negligible mistake because of the negative sign (see the value –0.08 g for the “D”

stream in Table 3), but its absolute value was by far smaller than any other value reported in Table 3.

Table 3. A check of the mass balances during the Soxhlet extraction tests with ethanol as solvent

Samples	Corresponding stream in Fig.3	#26 Green hazelnut husks (WH)
INPUT, g		
H ₂ O in WH	A	14.78
DS in WH	A	7.72
EtOH (anhydrous)	B	236.70
TOTAL		259.20
OUTPUT, g		
EtOH evaporated from drying solids	E	47.84
H ₂ O evaporated from drying solids	E	2.66
Husk (dry)	E	7.00
H ₂ O in the extracted solution	C	10.51
EtOH in the extracted solution	C	188.94
EtOH loss due to incomplete condensation *	D	-0.08
H ₂ O loss due to incomplete condensation *	D	1.62
Dissolved solids in the extracted solution *	C	0.72
TOTAL		259.20

* Unknown variable obtained as the solution of mass balance equations

All in all, the Soxhlet experimental procedure proved to be both reliable and accurate enough.

Representative results of the UV spectrophotometric analysis of Soxhlet liquid extracts are shown in Fig. 4. The profiles reported in Fig. 4 have been smoothed with respect the originally acquired data by introducing a “baseline averaging” for absorbance in its profile as a function of the wavelength.

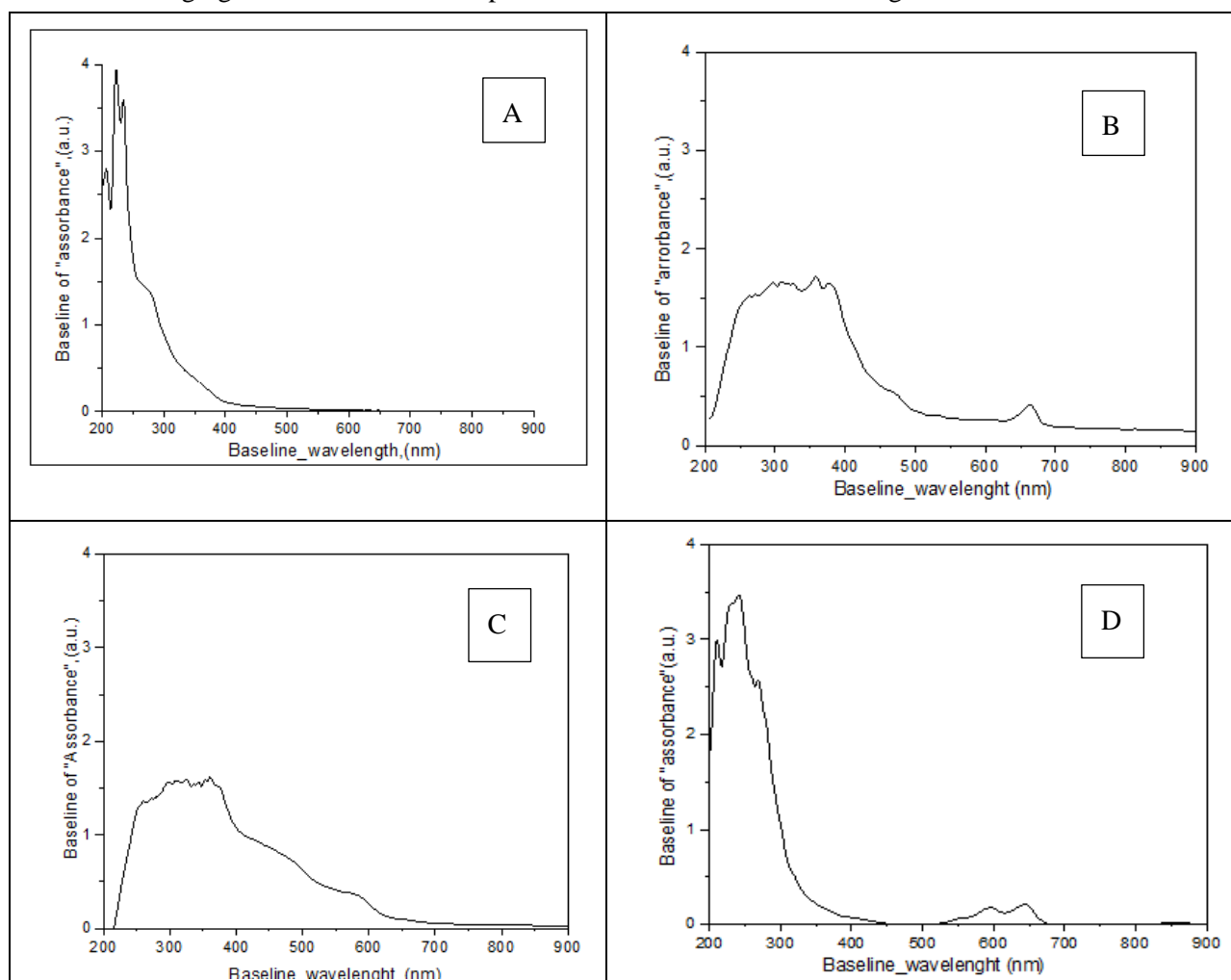


Figure 4. Representative UV spectrophotometric profiles: A. test #30: extract of husks in water; B. test #26: extract of husks in ethanol; C. test #2: extract of roasted cuticle in ethanol (after 1:1 dilution); D. test #1: extract of roasted cuticle in n-hexane

All of the Soxhlet extracted solutions exhibit a peak near and across 270 nm, which can be easily attributed to polyphenols, although the peak is different in height and shape from sample to sample.

The extracted solutions using ethanol or n-hexane in the Soxhlet apparatus exhibit another peak approximately in the range 600–700 nm, which is however one order of magnitude smaller in absorbance. In the case of green husks (Figure 3.B), it is located at 680 nm and reveals the presence of chlorophyll, likely to be present at a low extent.

Table 4. Results of the Soxhlet extraction tests with “as collected” hazelnut husks

Soxhlet test No.	Sample	Liquid-to-dry solids ratio (mL/g)	Polyphenols g (GAeq)/L	Tannins (g/L)	Theoretical yield in total Polyphenols (g/g DS)	Theoretical yield in Tannins (g/g DS)	Color of extract
21	Dry husks “as collected” 2020-09-08	41.48	0.26	0.16	0.0079	0.0049	Brown
29	Dry husks “as collected” 2020-09-08	41.48	0.19	0.29	0.0055	0.0084	Reddish yellow
22	Green husks “as collected” 2021-08-05	34.94	0.12	1.37	0.0024	0.0279	Light brown
23	Green husks “as collected” 2021-08-05	34.94	0.21	0.72	0.0049	0.0168	Light brown
24	Green husks “as collected” 2021-09-08	40.70	0.17	0.44	0.0048	0.013	Brown
30	Green husks “as collected” 2021-08-05 after thawing	35.69	0.18	5.68	0.0058	0.182	Amber yellow
31	Green husks “as collected” 2021-08-05 after thawing	36.53	0.21	1.51	0.0058	0.0414	Amber yellow
26	Green husks “as collected” 2021-08-05	34.94	0.11	1.56	0.0032	0.0454	Yellow
27	Green husks “as collected” 2021-08-05	46.61	0.11	4.51	0.0033	0.135	Light green
28	Green husks “as collected” 2021-08-05	66.59	0.04	2.34	0.0019	0.112	Light green

Table 5. Results of the Soxhlet extraction tests with roasted hazelnut skins

Soxhlet test No.	Sample	Liquid-to-dry solids ratio (mL/g)	Polyphenols g (GAeq)/L	Tannins (g/L)	Theoretical yield in total Polyphenols (g/g DS)	Theoretical yield in Tannins (g/g DS)	Color of extract
1	Grimaldi “as collected”	15.00	ND	ND	===	===	Pale yellow
4	Grimaldi (residue after extraction with n-hexane)	27.97	2.01	16.85	0.0337	0.283	Brown
2	Grimaldi “as collected”	16.52	2.34	7.10	0.0309	0.094	Brown
25	PRODAL 2-4 mm size cut	22.62	2.99	7.28	0.0620	0.151	Dark brown

* ND = Not Detected

As concerns hazelnut husks, testing of a “fresh feedstock”, i.e., the green leafy covers with a high moisture content in the order of 60–70% wt. (see samples in Table 1 and 4), was privileged in investigating the extraction potential of bioactive compounds. For brevity, the results available so far can be summarized as follows:

- the Soxhlet extraction turns out effective with both solvents tested on the “as collected” husks, even on the “fresh” ones with a water content as high as 65% wt. or more
- generally, the content of tannins in the extracted solution (g/L) exceeds that measured for polyphenols [g (GAeq)/L], sometimes by more than one order of magnitude (see tests #30 and #28), with both solvents tested
- water is more effective than ethanol in the Soxhlet extraction of polyphenols, with a minimum value of 0.12 g (GAeq)/L (see tests #22) that is in any case larger than the concentrations provided by ethanol
- the previous statement seems not applying to the Soxhlet extraction of tannins by ethanol (see tests #26-28) as compared to the corresponding water extraction tests (see tests #22-24)
- in any case, the measured concentration of tannins appears much more scattered within the same subset of tests (see the color code) in Table 4

The “theoretical” yield from the feedstock is calculated in Tables 4 and 5 by the relationship, respectively in total polyphenols and tannins:

$$\text{Theoretical yield} = \frac{\text{volume of extracted solution} \cdot \text{measured concentration}}{\text{mass of dry solids in the sample}} \quad (1)$$

under the assumption of “complete extraction” for the Soxhlet technique. The following comments apply:

- The theoretical yield in total polyphenols is three orders of magnitude lower than the mass of dry solids in the original (wet) feedstock. This finding provides a straight and sharp indication of the best attainable performance when a solvent extraction process is outlined for hazelnut husks taken as a biomass feedstock at a given processing capacity (e.g., in kg/h).
- The theoretical yield in tannins is more scattered, even within the same subset of tests (see the color code in Table 4), but it can reach a value that is just one order of magnitude lower than the mass of dry solids in the original (wet) feedstock (see tests #27 and #28 in Table 5), apparently when extraction is performed with ethanol.
- The water-based extraction seems to provide a slightly better performance than the ethanol-assisted Soxhlet: roughly, the theoretical yield in polyphenols is $5 \cdot 10^{-3}$ g (total polyphenols)/g (dry solid) in the average when water is used as a solvent against $3 \cdot 10^{-3}$ with ethanol.

As concerns the roasted hazelnut skins (see samples in Table 2 and 5), the early results are briefly commented here:

- It is confirmed that the compounds of interest here, i.e., the families of polyphenols and tannins, are not extracted by n-hexane as they have not been detected in the quantitative analytical tests on the extract (see test #1 in Table 5). In principle, a non-polar solvent like n-hexane can be used for defatting the roasted hazelnut cuticles and the defatted solid residue can undergo a subsequent extraction step devoted to polyphenols and tannins. This is what was done and is actually confirmed by the test #4 (see Table 5), which yielded a concentration of polyphenols in the extracted solution equal to 2.01 g (GAeq)/L and of tannins as high as 16.85 g/L. This latter result coming after the two-stage extraction is very promising but needs to be further confirmed because the one-stage extraction with ethanol seems to yield a concentration of tannins that is at least halved with the same sample of roasted hazelnut skins (see test #2 in Table 5) and with another one from a different source (see test #25 in Table 5), too.
- Generally, the concentration of total polyphenols [g (GAeq)/L] in the extracted solutions from the roasted hazelnut cuticles (see Table 5) appears larger than that obtained from the “as collected” hazelnut husks (see Table 4). Correspondingly, the theoretical yield in total polyphenols appears to be one order of magnitude higher, i.e., $5 \cdot 10^{-2}$ g (total polyphenols)/g (dry solid) in the average when roasted hazelnut cuticles undergo Soxhlet extraction against $5 \cdot 10^{-3}$ g (total polyphenols)/g (dry solid) in the above-mentioned case of “as collected” hazelnut husks. This comparison is to be confirmed, too.

4. Conclusions

- The Soxhlet technique shows that water, the greenest solvent overall, is suitable for extracting polyphenols from the green leafy covers of hazelnut, i.e., agricultural residues that have been poorly taken into consideration so far in the framework of waste valorization and appear now of great interest.
- Using a “*wet feedstock*”, i.e., fresh leafy cover samples with a moisture content as high as 60-70% wt., does not impair the extraction process and favors its performance even in the case another polar solvent like ethanol is used instead of water.
- An additional advantage of the extraction technique investigated in this work is that the green leafy covers are processed “as collected”, i.e., without any other pretreatment like drying or size reduction; this represents a significant simplification and provides added value in a possible industrial process implementation in terms of green solvent extraction of bioactive compounds.
- Further work is required. Apart from an additional set of Soxhlet tests for extension of the investigation conditions and verification of the reported results, especially for the case of roasted hazelnut cuticles, a further exploitation is currently in progress by means of other suitable analytical methods like HPLC in order to identify in the Soxhlet extracts individual phenolic acids, i.e., gallic, caffeic and p-coumaric acid, having the role and the appeal of being bioactive compounds.
- Finally, the present work analysis is one of the planned steps along the route to a biorefinery implementation project aimed at a thorough valorization of hazelnut (and possibly other nuts) residues while yielding valuable products (bioactive compounds and solid biofuels) and pursuing circular economy goals.

Acknowledgements

Funding and support are acknowledged by the project “Pasta for fun”, No. F/200122/02/X45, CUP: B41B19000620008 - COR: 1610092, Asse I, Azione 1.1.3 del PON Imprese e competitività 2014 – 2020.

References

- Adiletta, G., Brachi, P., Riianova, E., Crescitelli, A., Miccio, M., Kostryukova, N. (2020). A Simplified Biorefinery Concept for the Valorization of Sugar Beet Pulp: Ecofriendly Isolation of Pectin as a Step Preceding Torrefaction, *Waste Biomass Valor.*, 11(6), pp. 2721–2733, <https://doi.org/10.1007/s12649-019-00582-4>
- Alasalvar, C., Karamać, M., Amarowicz, R., & Shahidi, F. (2006). Antioxidant and antiradical activities in extracts of hazelnut kernel (*Corylus avellana* L.) and hazelnut green leafy cover. *Journal of Agricultural and Food Chemistry*, 54(13), 4826–4832. <https://doi.org/10.1021/JF0601259>
- Andrés, H., Fernández, B., Rodríguez, R., & Rodríguez, A. (2002). Phytohormone contents in *Corylus avellana* and their relationship to age and other developmental processes. *Plant Cell, Tissue and Organ Culture* 2002 70:2, 70(2), 173–180. <https://doi.org/10.1023/A:1016347921550>
- Brachi, P., Miccio, F., Miccio, M., & Ruoppolo, G. (2016). Torrefaction of Tomato Peel Residues in a Fluidized Bed of Inert Particles and a Fixed-Bed Reactor. *Energy and Fuels*, 30(6)
- Casa, M., Miccio, M., De Feo, G., Paulillo, A., Chirone, R., Paulillo, D., Lettieri, P., Chirone, Ric. (2021). A brief overview on valorization of industrial tomato by-products using the biorefinery cascade approach. *Detritus*, (15), pp. 31–39, available at: <http://dx.doi.org/10.31025/2611-4135/2021.14088>
- Chen, W. H., Lin, B. J., Lin, Y. Y., Chu, Y. S., Ubando, A. T., Show, P. L., Ong, H. C., Chang, J. S., Ho, S. H., Culaba, A. B., Pétrissans, A., & Pétrissans, M. (2021). Progress in biomass torrefaction: Principles, applications and challenges. *Progress in Energy and Combustion Science*, 82, 100887
- dativ7a.istat.it/index.aspx?DatasetCode=DCSP_COLTIVAZIONI accessed 17-11-2020
- Price, M. L., Scoyoc, S. van, & Butler, L. G. (1978). A Critical Evaluation of the Vanillin Reaction as an Assay for Tannin in Sorghum Grain. *Journal of Agricultural and Food Chemistry*, 26(5), 1214–1218.
- Ros, E., & Mataix, J. (2006). Fatty acid composition of nuts--implications for cardiovascular health. *The British Journal of Nutrition*, 96 Suppl 2(SUPPL. 2). <https://doi.org/10.1017/BJN20061861>
- Salas-Salvadó, J., Bulló, M., Pérez-Heras, A., & Ros, E. (2006). Dietary fibre, nuts and cardiovascular diseases. *The British Journal of Nutrition*, 96 Suppl 2. <https://doi.org/10.1017/BJN20061863>
- Shahidi, F., Alasalvar, C., & Liyana-Pathirana, C. M. (2007). Antioxidant phytochemicals in hazelnut kernel (*Corylus avellana* L.) and hazelnut byproducts. *J. of Agricultural and Food Chemistry*, 55(4), 1212–1220.
- Singleton, V. L., & Rossi, J. A. (1965). Colorimetry of Total Phenolics with Phosphomolybdic-Phosphotungstic Acid Reagent, *American Journal of Enology and Viticulture*, 16, 144–158
- www.fao.org/faostat/en/#data/QC accessed 22-07-2020

A new methodology for the selection of a methanogen-free acetogen inoculum from mixed sludge

Jacopo Ferretti, Marianna Villano, Mauro Majone, Marco Zeppilli

Department of Chemistry, Sapienza University of Rome, P.le Aldo Moro 5, 00185 Rome, Italy

*Corresponding author E-Mail: jacopo.ferretti@uniroma1.it

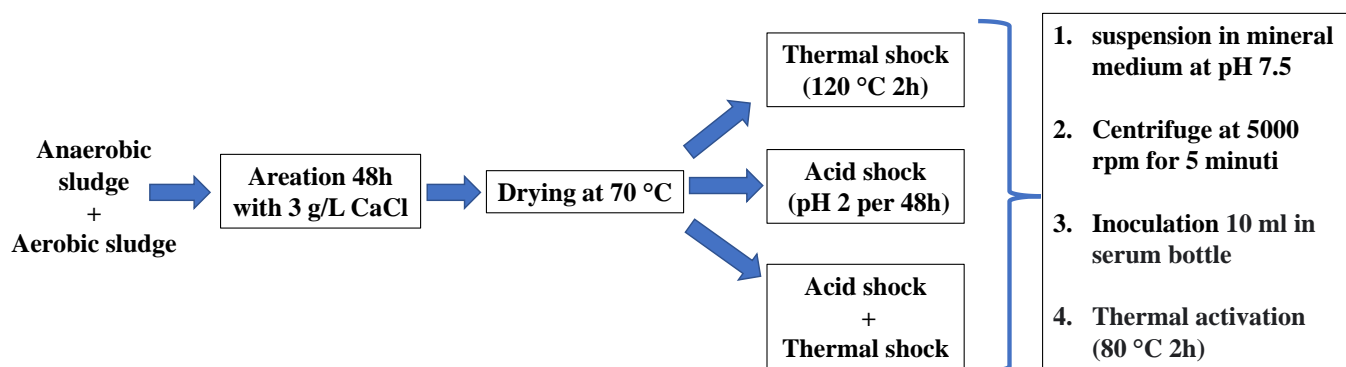
1. Introduction

Mitigation of CO₂ represents a major challenge to reduce emissions by 2030 as a global goal to limit global warming to an increase of 1.5 °C. The recycling of CO₂ through its fixation into precious metals such as fuels and chemical compounds represents an interesting strategy in the industrial sector where concentrated CO₂ flue gases are available such as the production of cement and steel or the treatment of wastewater. Many groups of microorganisms are able to biocatalyze similar reactions through the Wood-Ljungdahl pathway (WLP) [1], where CO₂ is fixed in acetate. Acetogens are ubiquitous and often share the same environments with methanogens, so to obtain an acetogenic inoculum from environmental samples it is necessary to inhibit methanogenesis [2]. This work proposes an innovative method for the inhibition of methanogenesis and the selection of acetogenesis based on the spore-forming nature of many acetogens. In fact, sporulation can be induced through multiple stresses, which simultaneously contribute to the inactivation of methanogenesis. The tests consisted in inducing sporulation, activating the biomass growth, and maintaining an active autotrophic community in hydrogenophilic condition growth.

2. Methods

2.1 Sludge treatment and inoculum activation

Figure 1 shows the sludge treatment and the preparation of the tests. Furthermore, part of the sludge was kept untreated to obtain the control suspension. The experimental set-up involved a first step in mixotrophic conditions, i.e. in the presence of organic substance and H₂, and a second step in hydrogenophilic autotrophic conditions (only in the presence of H₂ as electron donor), under hydrogenophilic autotrophic conditions, forcing the selected biomass to grow on H₂ and CO₂.



2.2 Analytical methods

The detection of H₂, CO₂, CH₄ was carried out with gas chromatographic analysis of the headspace using a Dani Master GC equipped with a packed column and TCD detector set with the following conditions: injection volume 50 µL, carrier gas nitrogen, flow 12 mL/min, inlet temperature 120 °C, column temperature 70 °C and TCD detector at 150 °C. Organic carbon was measured by TOC (total carbon analyzer)-V CSN (Shimadzu) on filtered samples with cellulose acetate filters, diameter 25 mm, pore diameter 0.2 µm. The biomass was monitored through the spectrophotometric reading and correlated to the concentration expressed in VSS (volatile suspended solids, mg/L).

3. Results and discussion

3.1 Microbial growth in mixotrophic and autotrophic conditions

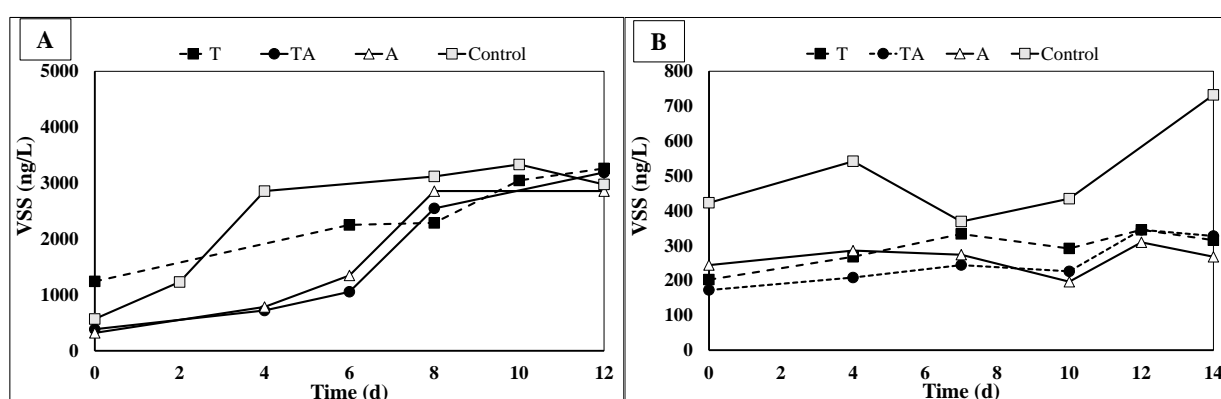


Figure 1. Biomass profile over time in mixotrophic (A) and autotrophic (B) conditions. The tests are denominated T= thermal shock; TA=thermal and acid shock; A= acid shock.

The speed of biomass in mixotrophic conditions (A) highlights the activation of the biomass following the different treatments. The control test shows a higher growth rate, considering however that this growth is also attributed to methanogens (methane data not reported). growth rate under autotrophic conditions (B) decreased for all tests, as expected. The test treated with acid and thermal shock showed a growth rate close to the control test (12 mgVSS/Ld vs 15 mgVSS/Ld), considering that the methanogenesis in the first was inactive, while in the control 0.3 mmol/Ld was produced.

4. Conclusions

The treatments contributed to the inactivation of methanogenesis and to the activation of the acetogenic autotrophic community, previously activated in mixotrophic conditions and subsequently maintained in autotrophic conditions, where methane production was not observed.

References

- [1] S.W. Ragsdale, Enzymology of the Wood-Ljungdahl pathway of acetogenesis, in: *Annals of the New York Academy of Sciences*, Blackwell Publishing Inc., 2008: pp. 129–136. <https://doi.org/10.1196/annals.1419.015>.
- [2] O.R. Kotsyurbenko, M. v. Glagolev, A.N. Nozhevnikova, R. Conrad, Competition between homoacetogenic bacteria and methanogenic archaea for hydrogen at low temperature, *FEMS Microbiology Ecology*. 38 (2006) 153–159. <https://doi.org/10.1111/j.1574-6941.2001.tb00893.x>.

Categorical Multifactor Design to Evaluate Different Operative Parameters During the Bioremediation of Hydrocarbon-Polluted Soil in Early Experimental Stages.

David Javier Castro Rodriguez^{1*}, Omar Gutiérrez Benítez², Enmanuel Casals Perez², Micaela Demichela¹, Alberto Godio¹, Fulvia Chiampo¹.

¹ Politecnico di Torino, Corso Duca degli Abruzzi 24, 10129 Torino, Italy.

² Centro de Estudios Ambientales de Cienfuegos (CEAC), Post mail 5, 59350, Ciudad Nuclear, Cuba

* David Castro E-Mail: david.castro@polito.it

1. Introduction

Pollution by hydrocarbons is associated with different industrial activities which may harm the environment and human health Shahryar [1]. It is generally accepted that this kind of pollution has an anthropogenic origin, often due to accidental spills from production units and transport pipelines, leakages from storage facilities and underground tanks, mining, human activities in the production, transportation, and improper or illegal behaviors in waste treatment and disposal. These contaminants can be accumulated in soil due to their low degradation rates, affecting the physical, physiological, and biochemical properties of this valuable resource [2]. The bioremediation of soils polluted with hydrocarbons demonstrated to be a simple and cheap technique, even if it needs a long time [3]. The current paper shows the application of statistical analysis, based on two factors involved in the biological process at several levels. We focus on the Design of Experiments to determine the number and kind of experimental runs, whereas the use of the categorical factors has not been widely exploited up to now. This method is especially useful to analyze factors with levels constituted by categories and define the interaction effects. Categories or labels built from the combination of interest predetermined variables should be useful especially in the early stages of bioremediation projects, where the effects of multiple ideas are tested at the same time. Particularly, we focused on the statistical analysis of 1) experimental runs carried out at laboratory scale (test M, in microcosm), on soil polluted with diesel oil, and 2) bench scale runs (test B, in biopile), on refinery oil sludge mixed with industrial or agricultural biodegradable wastes. Finally, the main purpose was to identify the factor's significance in both the tests and their potential interactions against the different response variables, by applying ANOVA.

2. Methods

Two categorical multifactor arrays were designed, randomized, and performed. In both cases, the effects of two factors on the interest response variables concentration were assessed. For each study case, the experimental runs are described, namely: i) Microcosms test (test M), based on a small amount of polluted soil (200 g); ii) Bench test (test B), based on a larger polluted mass (around 38 kg).

For both tests, a 6-levels categorical factor called "Treatment" was defined. In test M, the treatments M_i ($i=1, 2, \dots, 6$), corresponding to a combination of values water content (WC%) and carbon to nitrogen ratio (C/N). These combinations are labeled: M1 (8 WC%-120 C/N); M2 (8 WC%-180 C/N); M3 (12 WC%-120 C/N); M4 (12 WC%-180 C/N); M5 (15 WC%-120 C/N); M6 (15 WC%-180 C/N). On the other hand, the categorical factor levels in test B, B_i , correspond to the different treatments of the biopiles technique. Each run had a supplement of a specific organic waste as an additive bulking agent in the mixtures of soil and hydrocarbons. The levels were labeled as follows: B1 (sugarcane bagasse); B2 (sugarcane filter cake); B3 (sawdust); B4 (coffee pulp); B5 (beef manure); B6 (Thalassia testudinum residues). Likewise, in both the tests (M and B), the other factor was the "Time", defined at 5 levels T_{mi} ($i=0, 15, 70, 112, 131$). and T_{bj} ($j=0, 60, 90, 150, 240$) respectively. Each level corresponded to the time when the residual TPH concentration was monitored after the run started. This second factor was chosen under the hypothesis that the different treatments could have interactions during the bioremediation.

The Total Petroleum Hydrocarbon (TPH) concentration was the response variable in both tests. In the M test the TPH was measured in sample extracts achieved from each microcosm. The extraction was done by the EPA method 3546 (moisture 15-30% b.w.), based on microwave heating, as described in a previous paper [2]. Then, each extract was analyzed twice by the EPA method 8015 to measure the TPH concentration. On the other hand, the TPH in the B test was measured with samples collected from each biopile. The TPH

concentration was determined by adapting the EPA Method 1664 to the biopile system. The analysis was based on the TPH extraction from solid by an organic solvent and evaluation of the TPH mass by gravimetry. This method results reliable because the solid sample was over 5 g and the TPH concentration over 0.3% by weight.

Both experiments has combined all the levels of the factors (6x5). For M test, since two replicas were carried out, a total of 60 runs were available, achieving 30 degrees of freedom (Df). The statistical parameters of the DOE were considered statistically consistent with the strengths in the analytical determination method of the TPH concentration. On the other hand, for the B test a total of 120 runs due to 4 replicas of the experimental array. This ensured 90 degrees of freedom, which were considered statistically robust, compensating for the weakness of the gravimetric determination method if compared to the gas chromatographic one. All the analyses were performed using a confidence level of 95% employing the professional software STATGRAPHICS Centurion v. 16.1.18. Moreover, the assumptions for the model were corroborated. Table 1 offers the synthesized information for both tests.

Table 1. Operative conditions for the studied tests.

Operative conditions	Microcosms (Test M)	Biopiles (Test B)
Response variable	TPH	TPH
Factor 1-Treatments (6 categorical levels)	M1(8 WC%-120 C/N)	B1 (sugarcane bagasse)
	M2 (8 WC%-180 C/N)	B2 (sugarcane filter cake)
	M3 (12 WC%-120 C/N)	B3 (sawdust)
	M4 (12 WC%-180 C/N)	B4 (coffee pulp)
	M5 (15 WC%-120 C/N)	B5 (beef manure)
	M6 (15 WC%-180 C/N)	B6 (<i>Thalassia testudinum</i>)
Factor 2-Time (5 levels)	0	0
	15 days	60 days
	70 days	90 days
	112 days	150 days
	131 days	240 days
Mass	200 g	38 kg
Pollutant	Diesel oil	Oily Sludge
Water content (WC%)	8%	20%
	12%	
	15%	
Carbon to nitrogen ratio (C/N)	60	10
	120	
	180	
	300	
Kind of soil	Sandy soil	Sandy soil
pH	6-8	6-8

3. Results and discussion

Since the categorical multifactor was used under the hypothesis that different interaction between factors could influence the removal of the hydrocarbons, it is of interest to know which combination of treatment and time would ensure better results for any process period. Figure 1 shows the interactions plots of both factors in each experiments.

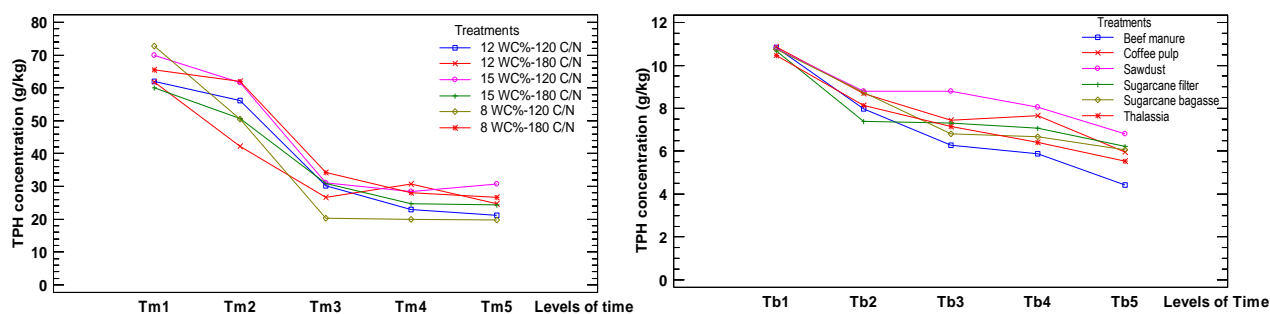


Figure 1. Interaction plot for the factors. a) test M b) Test B.

The lines in Figure 1 on both the left (a) and the right one (b) represents the interaction effect between the significant factors obtained in the Analysis of Variance (P-value= 0.000 for test M; P-value= 0.0012 for test B) and indicates that during the process, some treatments alternated their order of degradation.

Specifically, in test M, the Treatment M1 (8 WC%-120 C/N) had the lowest TPH concentration at each level of time after the first 15 days. Likewise, after 71 days M3 (12 WC%-120 C/N) was ranked second with lower TPH concentration, suggesting not only the best degradation of the treatments with the less C/N ratio but also the influence of water content in the first period of the run. These findings are consistent with the previous ones modelled by Raffa et al. [2] using an RSM model, confirming the accurateness of the categorical multifactor design. After the third month, the TPH concentration decreasing was negligible for all treatments. This could represent a crucial issue to estimate the times for the in situ exploitation of the technology.

In test B, in all treatments, the TPH concentration decreased until 240 days, with removal percentages between 40% and 60%. The treatments order rank was B5, B6, B2, B1, B4, B3. Specifically, Treatment B5 (beef manure) was the one that reported the lowest TPH concentrations at 240 days, keeping this trend after 60 days. The means obtained for B5 presented marked statistical differences with the rest of the treatment. In contrast, B3 (sawdust) presented the worst TPH removal, keeping this trend after the 60 days. Despite the rank order, the TPH means of B6, B2 and B1 do not present significant differences among them for a 95% confidence level. Furthermore, the differences between the levels in the factor Time evidence the evolution in the degradation process.

4. Conclusions

The categorical multifactor array based on categorical factors assessed at different levels demonstrated its applicability to studies done in different operative conditions. Particularly, we focused on a laboratory experiment and bench-scale test to evaluate the reliability of the proposed statistical method in testing the performance of biostimulation processes of contaminated soil, but the application is not limited to this kind of experiment or scales.

The structured method implemented in this study enables the identification of the best candidate in microcosms polluted with diesel oil (combinations of water content and carbon to nitrogen ratio were assumed as treatments). Specifically, the treatment M1 (8 WC%-120 C/N) showed the best diesel oil removal. In the experimental runs on biopiles to bioremediate oily sludge supplementing different renewable organic wastes as treatments, the treatment B5 (biopile with beef manure as a bulking agent) showed the best hydrocarbons removal.

References

- [1] J. Shahryar. Butterworth-Heinemann (Eds.), Chapter 3: Environmental Impacts of the Petroleum Industry. in: Petroleum Waste Treatment and Pollution Control, Elsevier Inc: Oxford, UK, 2017, Volume 3 pp. 86–115.
- [2] C.M. Raffa, F. Chiampo, A. GodioVergnano, F. Bosco, B. Ruffino. Kinetics and Optimization by Response Surface Methodology of Aerobic Bioremediation. *Geoelectrical Parameter Monitoring., Appl. Sci.* 10, 405 (2020) 1–21.
- [3] O. Gutiérrez, D. Castro, O. Viera, E. Casals, D. Rabassa, Kinetic of hydrocarbon degradation by biopile at a bench-scale (In Spanish). *Tecnología Química*, 41, 2, (2021) 349-369.

Advancements of scale-up methods for stirred aerobic fermenters

Federico Alberini, Francesco Maluta, Giuseppina Montante, Alessandro Paglianti*

Dipartimento di Chimica Industriale, Università di Bologna, viale Risorgimento 4, 40136 Bologna

**Corresponding author E-Mail: alessandro.paglianti@unibo.it*

1. Introduction

Aerobic fermentations are adopted in an increasing variety of industrial productions, but their application is often limited from high dissolved oxygen requirements, which result in unaffordable cost unless low volume and/or high value compounds are produced [1]. The issue of the determination of the most advantageous scale of the production is industrially relevant and it has been often tackled employing lumped correlations, both in design and techno-economic analysis. Since around 90% of industrial bioprocesses using bacteria and yeast are carried out in stirred bioreactors [2], the choice of the stirred tank geometry, its size and operating conditions is of primary importance. Scale-up and scale-down of aerated bioreactors is a very challenging and complex task, due to the interplay of many factors, such as oxygen transfer rates and flow regimes, that inherently depend on the system scale [3], and additional coupling with key variables related to morphology and physiology of microorganisms.

This contribution is focused on the experimental and computational investigation of a pilot scale gas-liquid stirred tank, with the main aim of deepening the detection and prediction capability of fundamental two-phase flow variables that affect aerobic fermentation. To this end, experimental and computational methods are adopted in a very challenging context combining the physical complexity of turbulent gas-liquid dispersions and the geometric complexity of baffled stirred tanks.

The experimental part of the investigation is based on the adoption of Electrical Resistance Tomography (ERT). It provides detailed information on the spatial distribution of the gas phase and on the effect of bubbles on the liquid homogenization dynamics. The selected experimental technique allows to overcome the typical limitations of optical methods and to gain insight into the two-phase flow characteristics of sparged stirred tanks without restriction on the upper value of overall gas hold-up, that is of great interest for industrial aerobic fermentation. The outcomes of the experimental work can be directly adopted for obtaining practical guidelines for design and intensification of aerobic fermentation in stirred tanks. In addition, novel local data suitable for detailed model validation are obtained. The computational part of the investigation is carried out in the realm of Computational Fluid Dynamics (CFD). The modelling method contributes to move a step forward in the development of a comprehensive model for the simulation of aerobic stirred bioreactors of complex geometry ensuring consistency of the predictions in a variety of multiphase conditions at any scale [4].

2. Methods

The investigated pilot-scale baffled stirred tank consisted of a cylindrical, flat bottomed vessel of diameter, T , equal to 0.48 m and height, H , equal to 1.6 m, equipped with four equally-spaced baffles of width, W , equal to $T/10$. In order to evaluate the gas dispersion features, a standard configuration, resembling a single stage of a typical multiple impeller stirred fermenter, was considered. The analysis was carried out under variable gas flow rates, Q_G , and impeller speeds, N , thus covering different regimes of gas-liquid and gas-impeller interaction, as obtained by the conventional Rushton Turbine and the innovative Bakker Turbine. Both the Rushton turbines of diameter, D , equal to 0.19 m ($D=0.40T$) and the Bakker Turbine of $D=0.215m$ ($D=0.45T$) were located at an off-bottom clearance, C , of $T/2$. In all the experiments, the tank was filled with

demineralized water up to a height, H_L slightly higher than T . Afterwards, air was fed in water through a ring sparger located at a clearance, C_s , equal to 85 mm ($C_s=0.18T$).

The mixing time and the gas hold-up distribution were determined on three horizontal planes by using an ITS P2000 ERT instrumentation by Industrial Tomography Systems Ltd. On each measurement plane, 16 equally spaced electrodes of 30 mm side and 1 mm thickness were fixed to the vessel wall. The electrodes were connected to the data acquisition system (DAS) by coaxial cables. The measurements were based on the circular adjacent strategy, in which electric current is injected from adjacent electrodes pair at a time and the voltage difference is measured from the remaining pairs of electrodes. The procedure is repeated for all the independent pairs of electrodes. The conductivity maps were reconstructed from the electric potential measurements by the linearized (non-iterative) modified sensitivity back projection (MSBP) algorithm.

The CFD modelling was based on the Two Fluid Model (TFM) formulation of the Reynolds averaged Navier-Stokes (RANS) equations. Details on the computational model can be found elsewhere [5].

3. Results and discussion

The local gas volume fraction distribution on the three measurement planes in the vessel stirred with the Bakker turbine is shown in Figure 1, together with numerical predictions on the same planes. By means of example, just the condition of $Q_G=25\text{L/min}$ and $N=200\text{rpm}$ is reported.

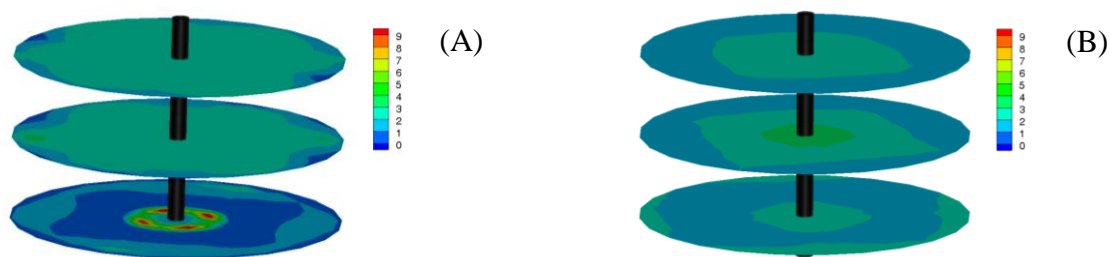


Figure 1. Percentage gas volume fraction obtained from (A) CFD and (B) ERT at the elevation $z=0.18\text{ m}$, $z=0.30\text{ m}$ and $z=0.42\text{ m}$ from the bottom of the tank. The impeller is located at $z=0.24\text{ m}$

In these conditions, the gas phase is in complete recirculation, having a consistent amount of gas below the impeller plane. On the other hand, the bubbles are not homogeneously distributed in the vessel volume, with the most peculiar features observed in the tank zone below the impeller. Here, large amounts of gas are found both towards the center of the vessel, where the coherent gas stream from the sparger is not dispersed by the action of the impeller, and at the radial periphery of the tank, where the lower recirculation loop generated by the impeller entrains the bubbles just in the proximity of the cylindrical walls of the system. At intermediate radial coordinates, there is a well-defined volume devoid of bubbles. This behavior is observed both from the ERT measurements and the CFD simulations, as apparent on the lowest plane of Figure 1. Overall, the proposed computational approach validated in this work may help in the design of industrial aerated stirred fermenters, since it proved very reliable in fully predictively reproducing the power consumption and the gas-liquid flow regimes, and it may be applied to other geometries and impeller types, without the need for global correlations and ad hoc experiments.

References

- [1] D. Humbird, R. Davis, J.D. McMillan, *Biochem. Eng. J.* 127 (2017) 161–166.
- [2] F. Garcia-Ochoa, E. Gomez, V.E. Santos, *Biochem. Eng. J.* 164 (2020) 107803.
- [3] H.J. Noorman, W. van Winden, J.J. Heijnen, R.G.J.M. van der Lans, *RSC Green Chem.*, Royal Society of Chemistry, 2018.
- [4] F. Maluta, A. Paglianti, G. Montante, *Biochem. Eng. J.* (2022) 108405.
- [5] F. Maluta, F. Alberini, G. Montante, A. Paglianti, *Can. J. Chem. Eng.* (2022) *in press*.

Caratterizzazione di un processo di co-digestione anaerobica di biomasse residuali

Giuseppe Cristian PISO¹, Pietro Bareschino¹, Erasmo Mancusi¹, Francesco Pepe^{1*}

*1 Dipartimento di Ingegneria, Università degli Studi del Sannio
Piazza Roma, 21 – 82100 Benevento - Italy*

**Corresponding author E-Mail: francesco.pepe@unisannio.it*

1. Introduzione

La necessità di ridurre l'impatto ambientale e la crescente richiesta di energia pongono l'attenzione della comunità scientifica su tecniche di sfruttamento energetico ecosostenibili. La digestione anaerobica (DA) è un processo biochimico di degradazione di matrici organiche in assenza di ossigeno [1], permettendo di ottenere biogas, quest'ultimo è costituito per il 50-70% da metano, 30-50% da anidride carbonica e per la restante parte da acqua e impurezze (principalmente solfuro di idrogeno, ossigeno e silossani). La variabilità nella composizione dipende dalle tipologie di substrato e dalle condizioni in cui avviene il processo di digestione anaerobica [2], inoltre la massimizzazione della resa come mostra questo studio è fortemente influenzata dal pretrattamento della biomassa. Pertanto la caratterizzazione di nuove matrici, che altresì sarebbero destinate a smaltimento perdendo sia il contenuto energetico nonché rappresentando un costo è uno degli aspetti di fondamentale importanza.

In questo lavoro sono stati adoperati due substrati in co-digestione: (i) refluo zootecnico da allevamento bovino; (ii) lettiera da stabulario. Dapprima il substrato è stato caratterizzato dal punto di vista chimico mediante analisi CHN e TGA, in seguito sono state condotte due prove di digestione anaerobica in un impianto da laboratorio batch. La prima delle quali alimentando il digestore con la biomassa tal quale: sono state monitorate le grandezze di interesse e valutata la resa complessiva. Mentre nella seconda prova la biomassa prima di essere alimentata al reattore è stata sottoposta ad un pretrattamento di idrolisi acida, anche in questo caso sono state monitorate le grandezze di interesse e valutata la resa complessiva. Infine è stato messo in evidenza il vantaggio in termini di resa in biogas e selettività in metano che il pretrattamento consente di ottenere.

2. Materiali e metodi

2.1 Biomasse

Sono state utilizzate due differenti tipologie di biomasse: una lettiera da stabulario e un refluo zootecnico da allevamento bovino. La prima delle due biomasse considerate è costituita da cippato di faggio frammisto ad escrementi di topi prelevato presso lo stabulario del centro di ricerca BIOGEM s.c.a.r.l. di Ariano Irpino (AV) al cui interno è presente una popolazione di oltre 7.000 topi e 200 ratti. Lo smaltimento della lettiera sporca rappresenta una voce di costo molto importante per il centro e per questo motivo si è cercato di trovare una metodologia innovativa per il suo smaltimento. I reflui zootecnici sono stati prelevati presso l'azienda agricola COCCA sita in S. Marco de' Cavoti (BN). L'azienda dispone di 8 capi, dal peso medio di circa 400 kg, di razza Marchigiana. Questi risiedono in una stalla chiusa a stabulazione libera che prevede l'utilizzo di abbondante paglia come lettiera per garantire il confort del bestiame. La pulizia della stalla viene realizzata conferendo i reflui nel letamaio dove è stoccato per un periodo variabile tra i 4-6 mesi.

Ciascuna biomassa è stata caratterizzata sia in termini di tenore di umidità, contenuto di volatili, carbonio fisso e ceneri in accordo alla norma ASTM D5142/02 mediante l'impiego di un analizzatore termogravimetrico che mediante analisi CHN in accordo alla norma ASTM D5373 condotta in un analizzatore LECO CHN2000. I risultati delle analisi sono riportati in tabella 1.

Analisi	Componente	Lettiera [%w]	Stallatico [%w]
CHN	Carbonio	33.2	35.85
	Idrogeno	7	4.89
	Azoto	2.4	2.11
TGA	Umidità	6.59	77.16
	Volatili	69.83	19.37
	Carbonio fisso	19.21	2.9
	Ceneri	4.37	0.85

Tabella 1. Risultati Analisi CHN e TGA.

2.2 Impianto di digestione anaerobica

L'impianto di digestione anaerobica è costituito da due digestori verticali di altezza 0.2 m e diametro interno 0.1m, all'esterno dei reattori vi è l'intercapedine per la circolazione del fluido termovettore gestita dall'impianto di termostatazione. Il dispositivo di miscelazione del reattore è costituito da un albero coassiale al digestore al quale sono solidali le pale di movimentazione del fluido. Il coperchio di chiusura superiore dispone di cinque fori filettati per consentire la raccolta del biogas prodotto nelle sacche di Tedral® e l'accesso della strumentazione di misura all'interno del reattore senza che si abbia interscambio di gas tra l'interno e l'esterno. In figura 1 è riportata una rappresentazione schematica del sistema di digestione adoperato.

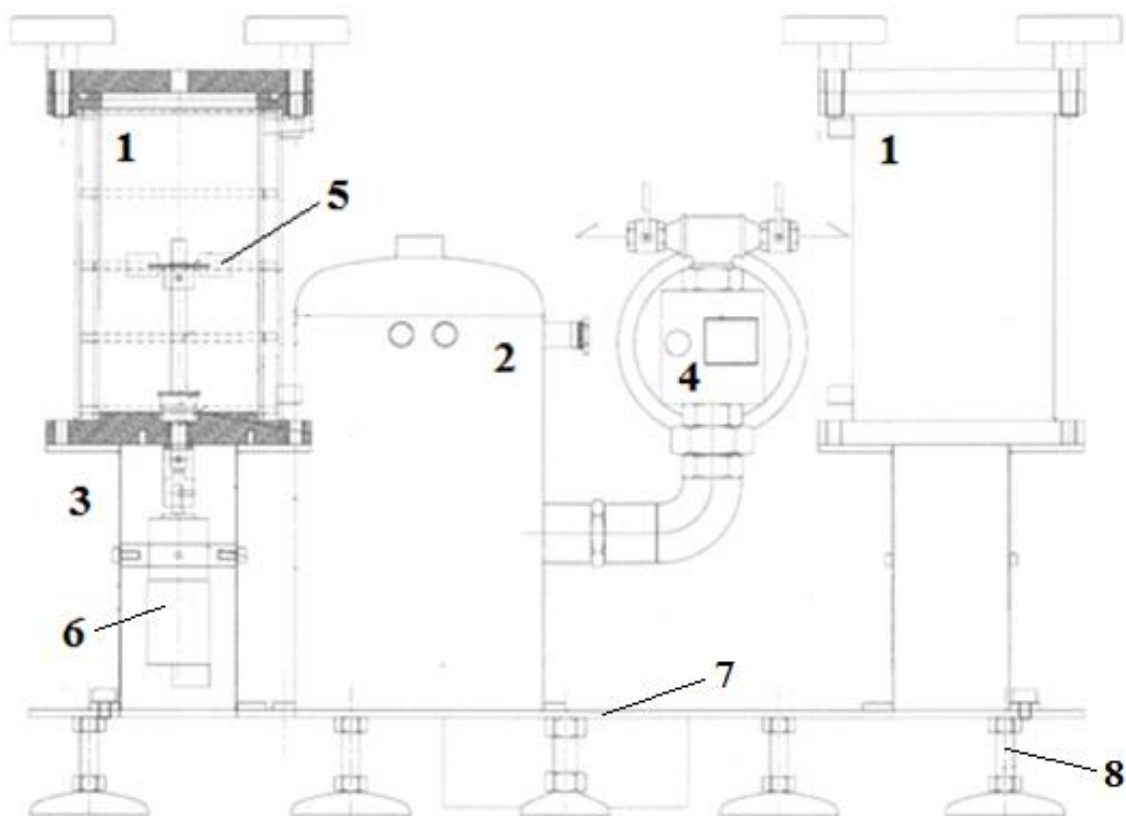


Figura 1. Rappresentazione schematica dell'impianto in scala da laboratorio: 1) digestori; 2) serbatoio fluido termovettore; 3) vano alloggiamento motore; 4) pompa di circolazione fluido termovettore; 5) pale di agitazione; 6) Motore; 7) base di appoggio; 8) Piedini regolabili.

2.3 Inoculo

Come inoculo per il processo di co-digestione anaerobica sono stati utilizzati fanghi secondari di depurazione derivanti da processi di ossidazione biologica (SANAV s.r.l. Ponte Valentino (BN)); la scelta di non utilizzare ceppi batterici selezionati è legata alla volontà di indagare la possibilità di utilizzo di un rifiuto altrimenti destinato allo smaltimento. I fanghi sono stati fatti sedimentare in un recipiente a chiusura ermetica per 45 giorni a temperatura ambiente: in questo modo, oltre a consentire la sedimentazione dei solidi in sospensione, si è favorita l'eliminazione dei ceppi aerobici dal *pool* di microorganismi presenti nei fanghi.

Prima di essere utilizzati come inoculo per le successive prove di digestione anaerobica è stata necessaria un'operazione preliminare di acclimatazione dei ceppi batterici alle condizioni operative di processo. All'interno del fermentatore sono stati versati 0.50 L di fanghi e, per fornire una fonte di carbonio facilmente degradabile, sono stati aggiunti 12.00 g di saccarosio. La miscela ottenuta è stata mantenuta, in condizioni di continua miscelazione, a 36°C per un periodo di 10 giorni, il fango è stato utilizzato come inoculo per tutte le successive prove di digestione anaerobica.

2.4 Pre-trattamento

È stato eseguito un pretrattamento di idrolisi acida della biomassa ponendo a contatto 20 g di biomassa con 200 mL di H₂O e 5,4 mL di una soluzione acquosa di acido solforico (H₂SO₄) al 5% in peso, il pH del sistema risultante è stato pari a 1.8 per la lettiera ed 1.6 per lo stallatico. La miscela così ottenuta è stata posta sul piatto agitatore a conduzione Kartell per un tempo di sei giorni. Il sesto giorno si è provveduto alla filtrazione per separare le particelle grossolane dalla fase liquida, utilizzata come substrato, e si è corretto il pH, neutralizzando il liquido con una soluzione 1M di idrossido di sodio (NaOH), fino ad un valore ottimale di 6 per la successiva fase di digestione anaerobica.

2.3 Test di digestione anaerobica

Il test di digestione anaerobica ha previsto due prove: la prima delle quali alimentando il digestore con la biomassa tal quale in co-digestione al 70% da stallatico ed al 30% da lettiera, mentre nella seconda prova la biomassa prima di essere alimentata al reattore è stata sottoposta ad un pretrattamento di idrolisi acida (Paragrafo 2.4) effettuando test sia in digestione singola che co-digestione con le stesse percentuali della prima prova. Entrambi i processi di digestione sono stati condotti in condizioni mesofile alla temperatura di 35°C e con un tempo di ritenzione di 30 giorni. Durante la prova si è provveduto alla misura del pH prelevando quotidianamente una quantità di 0.5 ml di fango dal digestore prevedendo una correzione quando il valore è risultato inferiore a 3.5 tramite una soluzione di acqua ed idrogenocarbonato di sodio (NaHCO₃).

3 Risultati e discussione

La produzione di biogas per il substrato senza pretrattamento è stata molto discontinua, influenzata dal pH dell'ambiente di reazione. Nella prima settimana, caratterizzata da un ambiente fortemente acido, non si è avuta alcuna produzione di biogas, si sono registrati aumenti di produzione in seguito alle correzioni del pH. Il picco nella produzione di biogas si è avuto tra il decimo e l'undicesimo giorno, in cui sono stati prodotti circa 8.6 L di biogas, con una percentuale massima di metano di circa 8%. La composizione del campione prelevato alla fine dell'undicesimo giorno è stata analizzata con un analizzatore di biogas "GAS 3200 BIOGAS Portable Analyser GEIT", i risultati sono riportati nella tabella 2.

Componente	Percentuale volume
CH ₄	8.24 %
CO ₂	57.37 %
O ₂	0.89 %
H ₂ S	498 ppm
Altri	33.14 %

Tabella 2. Composizione gas senza pretrattamento della biomassa all'undicesimo giorno.

La produzione cumulata di biogas è stata pari a 0.027 m³/kg_{substrato}, mentre quella di metano è pari a 0.0014 m³/kg_{substrato}. È stata effettuata l'analisi CHN del digestato residuo, esso ha mostrato un tenore di carbonio ancora molto elevato, si è ottenuta la trasformazione di piccole percentuali di carbonio alimentato in biogas. Ciò significa una difficoltà da parte delle colonie batteriche ad idrolizzare i co-substrati iniziali.

Il secondo test è stato effettuato con la biomassa pretrattata secondo le specifiche riportate nel paragrafo 2.3. La tabella 5 riporta i risultati in resa e composizione di biogas.

Biomassa	Volume biogas [mL]	% vol. CH ₄	% vol. CO ₂
Refluo bovino	55	64	36
Lettiera	60	68	32
Co-digestione	5000	65.2	34.8

Tabella 5. Produzione biogas e sua composizione volumetrica in seguito alla digestione con pretrattamento della biomassa.

Si può osservare che per tutti i campioni rispetto al test senza pretrattamento si hanno notevoli produzioni di biogas. Va sottolineato inoltre che i migliori risultati in termini di selettività in metano sono stati ottenuti con la lettiera da stabulario che fornisce 60 mL di biogas contenente il 68% vol. di CH₄. Questo è probabilmente dovuto al più elevato contenuto di zuccheri riducenti [3]. La co-digestione ha fornito i migliori risultati in termini di resa, infatti essa è caratterizzata dalla produzione di un volume di biogas pari a 5 L, una resa in biogas pari a 0.25 m³/kg_{substrato} ed una concentrazione media di metano di circa il 65%.

4. Conclusioni

Il lavoro condotto si è focalizzato sulla caratterizzazione sperimentale di un substrato in co-digestione, sui vantaggi in termini di resa in biogas e selettività in metano che un pretrattamento di idrolisi acida può produrre sul processo di digestione anaerobica. I substrati sono stati caratterizzati dal punto di vista chimico mediante analisi CHN e TGA, consentendo la determinazione del tenore di umidità e delle percentuali massiche di carbonio idrogeno ed azoto. L'esercizio sperimentale dell'impianto nelle due diverse condizioni ha sottolineato come il pretrattamento della biomassa consente un'elevata conversione dei solidi volatili. La differenza dei risultati ottenuti con biomassa pretrattata (resa di 0.25 m³biogas/kg_{substrato}, 65% in volume di CH₄ e 35% in volume di CO₂) e senza pretrattamento (resa di 0.027 m³biogas/kg_{substrato}, 5% in volume di CH₄ e 58% in volume di CO₂) evidenzia come il pretrattamento sia necessario per la riuscita del processo di digestione anaerobica. Fondamentale è anche la scelta della tipologia di pretrattamento, l'idrolisi acida ha mostrato ottimi risultati; in futuro potranno essere implementati ulteriori idonei pretrattamenti allo scopo di migliorare la resa del processo.

Riferimenti

- [1] Meegoda JN, Li B, Patel K, Wang LB (2018), A Review of the Processes, Parameters, and Optimization of Anaerobic Digestion, *International Journal of Environmental Research and Public Health*, 15(10), 2224.
- [2] Nwokolo N, Mukumba P, Oibileke K, Enebe M (2020), Waste to Energy: A Focus on the Impact of Substrate Type in Biogas Production, *Processes*, 8(10), 1224.
- [3] Ausiello A, Bareschino P, Micoli L, Florio C, Pepe F, Pirozzi D, Toscano G, Turco M (2016). Dark Fermentation di biomasse di scarto per la produzione di Biogas e BioIdrogeno, *GRICU 2016*.

Empowered Parameter Identification Procedure for Anaerobic Digestion Models Stability and Reliability

Federico Moretta, Federico Rocca, Flavio Manenti, Giulia Bozzano*

Politecnico di Milano, piazza Leonardo da Vinci, 32, 20133, Milan (MI), Italy

**Corresponding author E-Mail: giulia.bozzano@polimi.it*

1. Introduction

Mathematical modeling of anaerobic digestion systems is crucial as it allows for the prediction and optimization of quantities such as methane and carbon dioxide. Because of its simplicity and processing speed, the AM2HN model [1], an improved version of the AMOCO model [2], is the ideal tool for control purposes. However, the identification procedure in the latter is ineffective, resulting in useless outcomes and meaningless parameters values. Consequently, this work provides a new approach based on resilient linear programming and advanced statistical analysis to address the inefficiency and obtain more trustworthy results.

2. Methods

AMOCO has a linear regression-based procedure which use experimental data and evaluate the yield coefficients in a dual-step pathway; AM2HN identification is non-linear regression based, which involves a single step evaluation for all the yield coefficients, starting from steady-state values coming both from experimental data and evaluated through ADM1 simulation [3]. Because of its inherent instability to data fluctuations, these procedures result in deceptive results when the analysis is performed on the absolute values of the simulated quantity. In our model, at first, the kinetic parameters of the biomasses are calculated by means of two non-linear regressions, starting from their steady-state values obtained from ADM1 simulations. The hydrolysis constant (k_{hyd}) and the liquid-gas transfer coefficient are then obtained by two stable and robust linear regressions, accordingly to what has already been proposed by other authors. The innovativeness of our procedure relies on the yield coefficients identification since the results obtained from the latter are misleading. Consequently, it aims to simplify and improve its reliability, employing an adaptation of the approach originally proposed in AMOCO. Firstly, it identifies two yield coefficients (k_1 , k_6) with two linear regressions from the methane flowrate and the steady-state values (Eq. 1, 2). Finally, two other multi-variable regressions are performed to get the four ratios which allow the computation of the remaining ones (k_2 , k_3 , k_4 , k_5), starting from both carbon and methane flowrate values at steady state (Eq. 3,4).

$$D(S_1^{in} - S_1) + k_{hyd}X_T = k_1X_1(\alpha D + k_{d,1}) \quad (1)$$

$$q_M/X_2 = k_6\mu_2 \quad (2)$$

$$q_M = k_6/k_3 D(S_2^{in} - S_2) + k_6k_2/k_3k_1 [D(S_1^{in} - S_1) + k_{hyd}X_T] \quad (3)$$

$$q_C - D(C_{in} - C) = k_4/k_1 [D(S_1^{in} - S_1) + k_{hyd}X_T] + k_5/k_6 q_M \quad (4)$$

Matlab R2021a is used to perform all the regressions. The improved robustness is achieved by using the *Iterative Reweighted Least Squares (IRLS)* regression algorithm, which guarantees more reliable results where heterodasticity affects data.

3. Results and discussion

A results comparison between the two procedure (new one and AM2HN) demonstrates the efficacy of this new proposed methodology. Figure 1 shows the multi-variable regression of yield ratios in Eq. 3-4, where both non-robust (NR) and robust (R) algorithm are applied. As shown, both the models perfectly fit the data (Fig. 1a). While the second relation shows a similar slope for both the NR and R (Fig. 1c, $\beta_2 = k_5/k_6$), the slope of the first relation (Fig. 1b, $\beta_1 = k_4/k_1$) from NR give a negative value, bringing a further simulation to misleading trends (Fig. 2). The other regressions, which allow the effective evaluation of the ratios k_6/k_5 and k_6/k_5 , are not included due to space restriction, but the procedure is analogous.

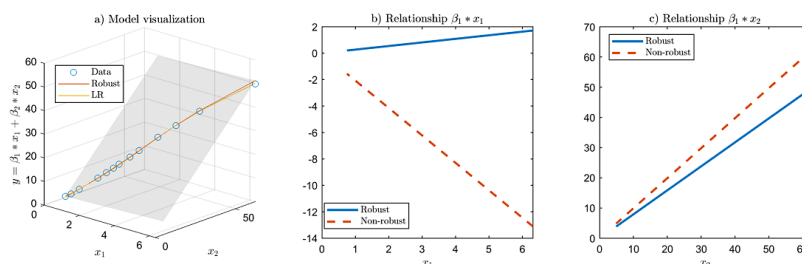


Figure 1. Model and data visualization (a); parameter validation (b, c) ($\beta_1: \frac{k_4}{k_1}$, $\beta_2: \frac{k_5}{k_6}$, $x_1: D(S_1^{in} - S_1) + k_{hyd}X_T$, $x_2: q_M$, $y: q_C - D(C_{in} - C)$).

The results of the simulation with the new identified parameters shows a more realistic trend of the principal variables, while preserving the model's simplicity and flexibility. In the Figure 2, the outlet molar gas fluxes of CH_4 (q_M) and CO_2 (q_C) are reported, being the most important. The new proposed identification leads to a difference in the result of variables related to inorganic carbon (i.e., pH) whereas the methane is almost equal with both models. The yield evaluated from the new procedure predicts a CO_2 percentage in the biogas around 20%, more realistic than the higher 70% resulted from the AM2HN simulation, without compromising any other result and eventually improving them.

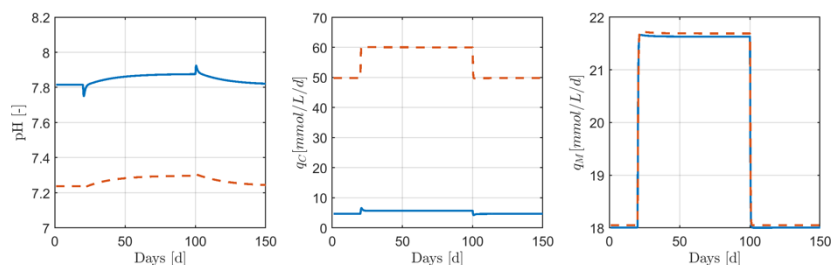


Figure 2. Results of model simulation. New identification procedure (solid line), AM2HN simulation (dashed line).

4. Conclusions

The new proposed identification method can be successfully applied to the AM2HN model and thus used to develop a model-oriented control strategy of an anaerobic digestion unit. The variables most affected are the ones related to the inorganic carbon, because of the improved accuracy of the estimation of the yield coefficients related to it (k_4, k_5). The reliability of the procedure had been further tested with another set of data available within the ADM1 model, obtaining excellent results.

References

- [1] S. Hassam, E. Ficara, A. Leva, J. Harmand, *Biochem. Eng. J.* 99 (2015) 193–203
- [2] O. Bernard, Z. Hadj-Sadok, D. Dochain, A. Genovesi, J. P. Steyer, *Biotechnol. Bioeng.* 75 (2001) 424-438
- [3] D. J. Batsone *et al.*, *Water Sci. Technol.* 45 (2002) 65-73.

Biological conversion of agricultural wastes into microbial proteins for aquaculture feed

Giovanna Pesante¹, Anna Zuliani¹, David Bolzonella¹ and Nicola Frison^{*.1}

1 Department of Biotechnology, University of Verona, Strada Le Grazie 15, 37134 Verona, Italy

**Corresponding author E-Mail: nicola.frison@univr.it*

1. Introduction

Due to the ever-growing population, the demand of protein-rich food for human and animal nutrition is continually increasing (FAO, 2018). The current use of plant and animal-based proteins is not environmentally sustainable because of the high CO₂ footprint of agriculture and livestock rearing (Vermeulen et al., 2012) and is also problematic because of the scarcity of land (Mekonnen & Hoekstra, 2014). The European Green Deal promotes the use of alternative sources of proteins, such as insects or single cell proteins (SCP) (Siddi, 2020). SCP or microbial proteins include dried microorganisms rich in proteins, vitamins and lipids (bacteria, algae, fungi and yeasts), which can be used as supplements in human food or as animal feed (Saeed et al., 2016), but also for the production of third-generation biofuels – bioethanol and biodiesel (Martínez et al., 2015) and the manufacture of bioplastics and adhesive materials (Yadav et al., 2020), as well as fertilisers replacing conventional nitrogen and phosphorous rich material. SCP have so far mainly been produced from raw materials with high commercial value, while they could be obtained by the fermentation of inexpensive feedstocks such waste, making them more economical, and helping with the environmental burden created by the disposal of wastes (Nasseri et al., 2011). In our study we set up the production of SCP of microbial origin from agricultural and zootechnical waste, using the VFA-rich fluid obtained from the fermentation of the waste as feed for a bioreactor, with the aim of using them microbial biomass in the aquaculture industry. The bacterial species used to produce the SCP were selected to be polyhydroxyalkanoates (PHAs) producers, because of the added value they provided in the fish feed. Indeed, these biological polymers have been shown to help protect aquatic animals from pathogenic bacteria acting both as prebiotics and probiotics (Laranja et al., 2014; Suguna et al., 2014). PHAs producing organisms can be used directly as SCP without the need of expensive extraction and purification PHAs procedures, which are at present hindering their use as bio-plastics (Chee et al., 2019).

2. Methods

2.1 Experimental set-up

The feedstock consisted in cattle's manure or digestate obtained at the end of an anaerobic digestion process, together with leftovers from a pasta making factory. This mixture was homogenized with water (total solids content 5-10%) and loaded in a 4 m³ acidogenic fermentation unit (AFU) at the anaerobic digestion (AD) plant "La Torre" located near Verona, Italy, where the initial acidogenic fermentation (AF) took place, according to Righetti and colleagues (Righetti et al., 2020). The volatile fatty acids (VFAs) stream obtained from the AFU was used to feed a 1.6 liters continuous stirred tank reactor (CSTR) after a solid-liquid separation step and a mechanical filtration phase up to 0.22 µm with a Juice Clarification System pump. The reactor was inoculated either with the bacterial consortium of the AF, or with a pure culture of the PHA producer *Thauera* sp. Sel9 (Conca et al., 2020; Sabapathy et al., 2020). The culture was supplied with oxygen, kept at 30° C and stirred at 180 rpm. Different hydraulic retention times (HRT) were tested, with steady-state conditions reached when MLSSs (mixed liquor suspended solids) variations were less than 5% for 3 times the value of the HRT. The bacterial biomass obtained from the culture at the end of the 38 days of the experiment was centrifuged, resuspended in deionized water to remove any remaining culture medium and was analyzed for the determination of its centesimal composition, with particular focus on the amino acid composition. Part of the

biomass obtained from the CSRT was also used, prior to the centrifugation step, for a PHAs accumulation test designed to produce the highest possible content of PHAs.

2.2 Fermentation fluid characterization

Total suspended solids (TSS), volatile suspended solids (VSS) and soluble COD (sCOD) were determined according to standard protocols (APHA et al., 1998; IRSA-CNR, 2003). Total nitrogen (TN) was determined using LCK338 LATON kit and ammonium (NH₄-N) with LCK303 kit, both by Hack, following manufacturer's protocol. VFAs concentration was verified by ion-chromatography using a Dionex ICS-1100 (Thermo Fisher Scientific, USA) equipped with IonPac ICE-AS1 column as described by Conca and colleagues (Conca et al., 2020). PHA contents were quantified by gas chromatography (GC) following Braunegg and colleagues (Braunegg et al., 1978) together with standards of pure poly(3-hydroxybutyric acid-co-3-hydroxyvaleric acid) (Sigma, 403105). PHA contents in experimental samples were calculated as percentage over the sample VSS with the following equation: (mgPHA/mgVSS)*100, whereas the PHA yields were calculated as mgPHA/mgCOD.

2.3 Bacterial biomass characterisation

The proximate composition and amino acid analyses were performed by Chelab Srl laboratories - Merieux NutriSciences (Resana, Treviso, Italy, www.merieuxnutrisciences.com/it/). Moisture and ash contents were determined gravimetrically according to standard methods (APHA et al., 1998; IRSA-CNR, 2003). Crude lipids, oils and cellulose were quantified using internal methods subject to copyright and therefore not disclosable. Nitrogen-free compounds were obtained by subtracting from 100 the other obtained values, which are presented as g/100g. Crude protein amounts were determined by quantifying the total nitrogen content with the Dumas method (Saint-Denis & Goupy, 2004) and then multiplying the result by the conversion factor of 6.25 (IRSA-CNR, 2003). The amino acid composition was determined in triplicates by oxidising and then hydrolysing the samples (or vice versa, depending on the amino acid under examination) and then determining each amino acid presence and quantity by ion chromatography with post-column derivatisation with ninhydrin. Cystine and cysteine were both determined as cysteic acid and then calculated as a sum expressed as cysteine; methionine was determined as methionine sulfone and then calculated as methionine. Tryptophan was determined according to the AOAC method 2017.03 (Draher & White, 2018). Total carbohydrate contents were calculated by a two-step acid hydrolysis with sulfuric acid (72% v/v) (Sluiter et al., 2008), followed by HPLC using a Jasco Extrema LC-4000 system equipped with a Rezex RoA H+ (Phenomenex) column.

2.4 PHAs accumulation test

500 ml of bacterial biomass extracted from the CSRT were placed at the concentration of 1g MLVSS/L in 1 litre flasks at the temperature of 27°C and 180 rpm. 5 hourly spikes of either fermentation fluid or VFAs mix (acetic, butyric, propionic, pentanoic, isobutyric, isopentanoic) were dosed to reach an sCOD concentration of 2 g/L and pH of 8.5 in the mixed liquor, and at the same time 100 ml samples were extracted for analysis of MLVSS, sCOD, PHAs, VFAs and pH.

3. Results and discussion

Table 1 and 2 present the results of the analysis of the fermentation fluid obtained from the AF of the zootechnical waste, and subsequently used to feed the CSRT. The sCOD had a value of 42.93 g/L, to which the VFAs contributed with 8.9 g/L. Among the VFAs, acetic acid was the most abundant (43.8%), followed by butyric (21.2%) and propionic acid (20.2%), while pentanoic, isobutyric and isopentanoic made up together to the remaining 14.8%. The pH of the fluid was quite acidic, and therefore it was increased to 8.5 before feeding it to the CSTR. The C/N ratio of the fluid was around 24, thus creating nitrogen deficiency conditions in the mixed liquor, which are favourable for cell PHAs accumulation.

Table 1. Characterisation of the fermentation liquid used to feed the CSTR bioreactor.

Parameter	Acronym	Unit	Value
Soluble COD	sCOD	gCOD/L	42.5
Volatile Fatty Acids	VFAs	gCOD/L	8.9
Total solids	TS	%	13.3
Ammonium	NH ₄ -N	g/L	1.6
pH	pH	-	3.9
Carbon to Nitrogen ratio	C/N	-	24

Table 2. Details of the VFAs composition of the fermentation fluid.

Volatile fatty acids			
Acetic	43.8%	Pentanoic	8.1%
Butyric	21.2%	Isobutyric	3.7%
Propionic	20.2%	Isopentanoic	3.0%

Figure 1 shows the variations of the HRT (from 17 to 1 days) and of the OLR (from 2.5 to 42.5 g/L per day), with the consequent increase of the bacterial biomass and of the sCOD (after an acclimatisation period during day 1 to 5), followed by a steady state up to day 28 (Figure 2). The best performances of the CSTR were obtained with an HRT of 2 days, with a productivity of 1.6-2.0 gMLVSS/L per day (Figure 1), with progressive bacterial death and CSRT wash out happening with higher ORL and lower HRT after day 28.

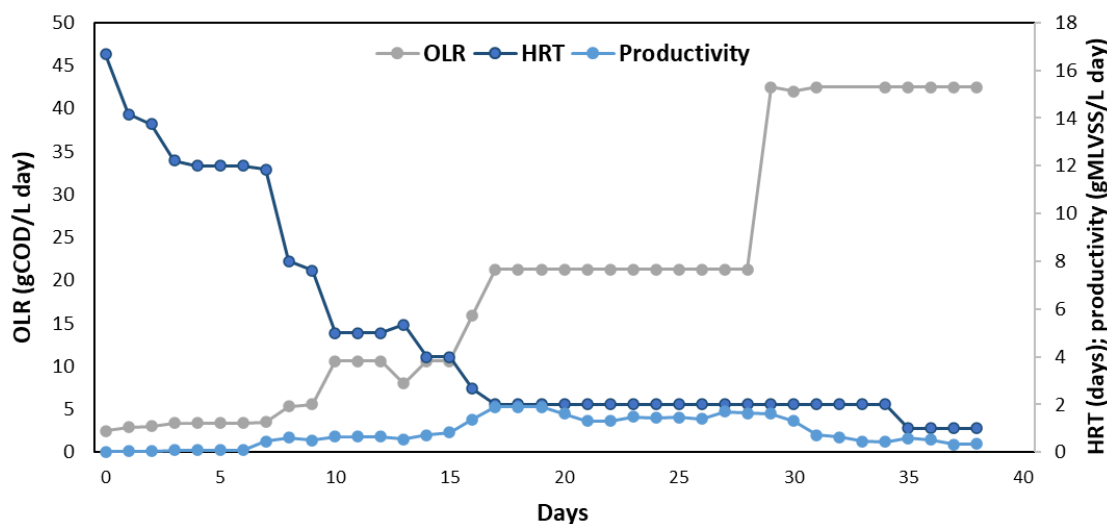


Figure 1. OLR, HRT and productivity during the 38 days of the CSTR operation.

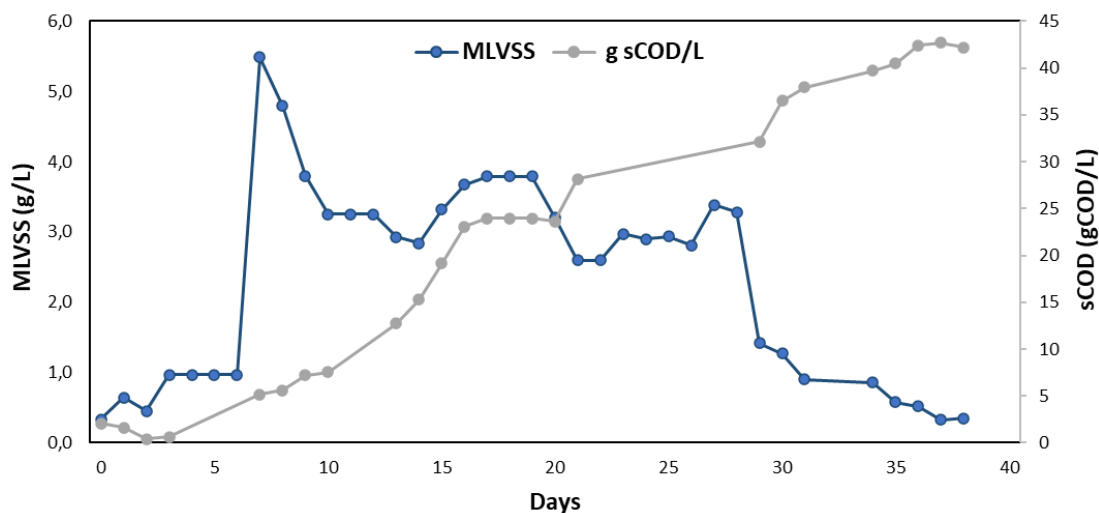


Figure 2. Biomass growth and sCOD of the mixed liquor during the 38 days of the CSTR operation.

The bacterial biomass presented a high protein content (70.4% of TSS, Table 3), with the amino acids glutamic and aspartic acid being the most abundant and histidine not possible to quantify (Figure 3). Most of the amino acids were found in quantities similar or higher to those necessary for the growth of commercial fish species. However, the absence of oils, carbohydrates and of the essential amino acid histidine, indicates that this biomass cannot be used on its own as fish feed, but it could however be part of a carefully formulated feed where SCP can make up to 50% of the diet and oils or PHAs are added to complement the formula.

Table 3. Centesimal composition of the bacterial biomass used as fish feed (% of dry sample).

Parameter	Value
Moisture	98.4%
Ash	8.9%
Crude proteins	74.0%
Crude lipids and oils	<LoQ
Carbohydrates	<LoQ

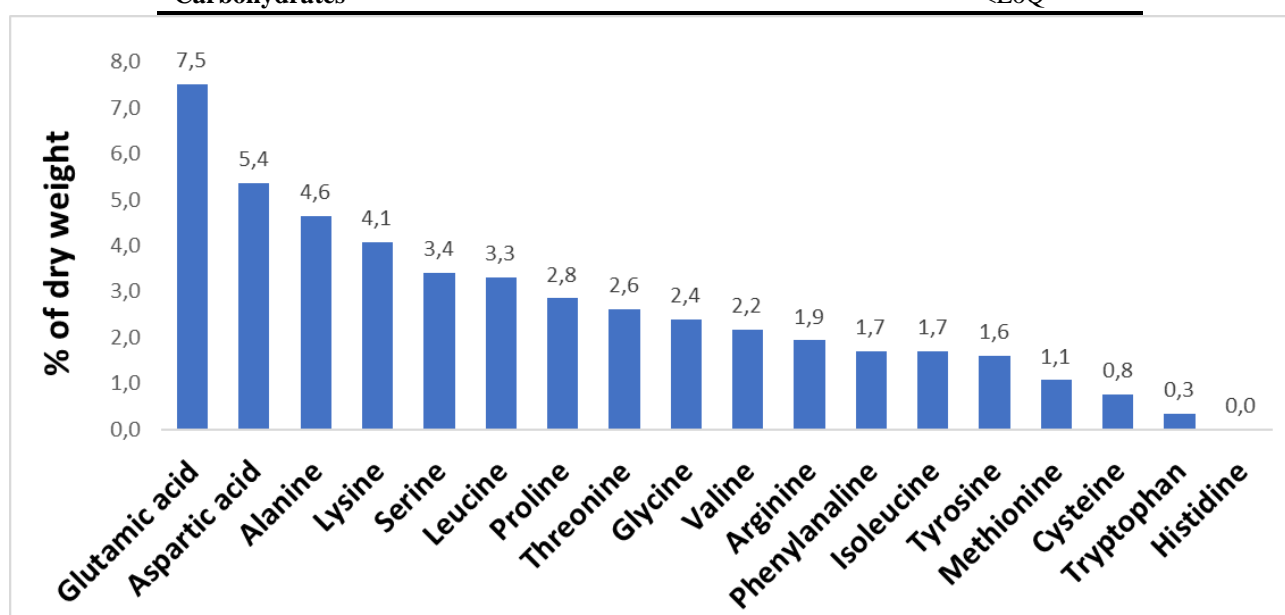


Figure 3. Amino acid profile (% of dry weight) of the bacterial biomass used as fish feed.

The accumulation of PHAs in the microbial cells was more evident with the fermentation fluid than with the VFAs mix, with percentages increasing from the initial 27.7% and reaching a maximum of 62.3% after the 4th spike (Figure 4), while the bacterial biomass remained constant. The PHAs composition indicated that methyl 3-hydroxypentanoate constituted 100% of the bioplastic at the beginning of the test, while methyl 3-hydroxybutanoate rose steadily during the experiment for both conditions, up to a final methyl 3-hydroxybutanoate/methyl 3-hydroxypentanoate ratio of around 4.21 (fermentate) and 3.77 (VFA mix) after the 5th spike%.

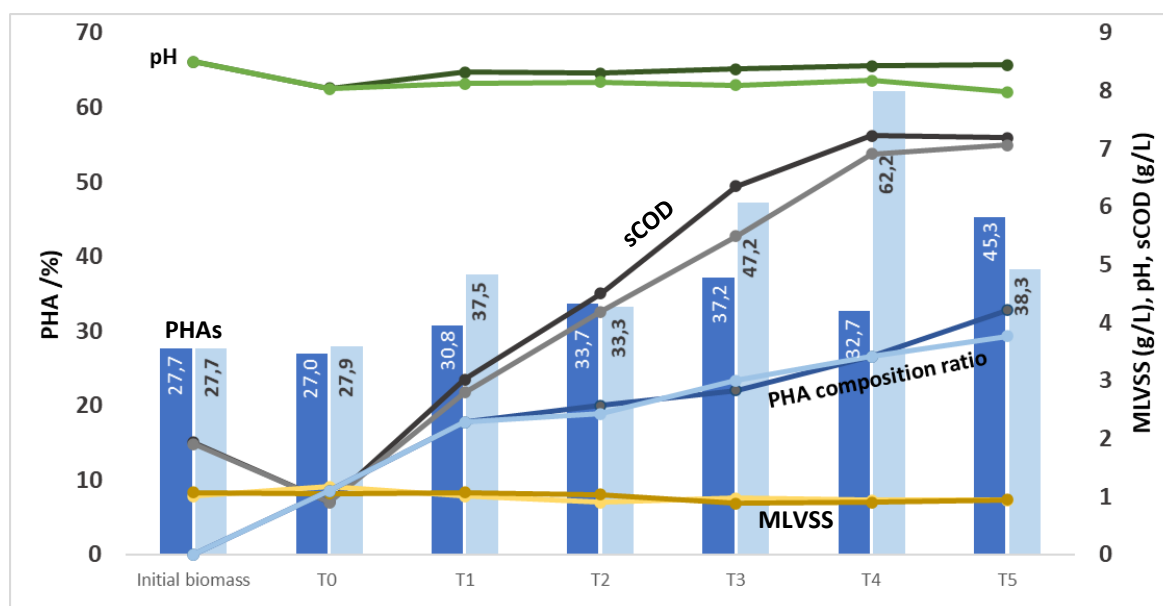


Figure 4. PHAs accumulation test performed with the biomass extracted from the CSTR. The data show the results for the flasks fed with either synthetic VFAs medium (dark shades) or with fermentation fluid (light shades).

4. Conclusions

Leftovers from food industries and from zootechnical and agricultural practices can be used to produce SCP and therefore fish feed, while at the same reducing the economic and environmental burden linked to waste disposal. The analysis of the microbial biomass produced from the bioreactor and from PHA accumulation test showed that high protein and PHA content can be achieved, therefore producing fish food of great nutritional value. Further work is needed to test the SCP feed on the survival and growth rates of commercial fish species, and to quantify the presence of unwanted compounds such as heavy metals and antibiotics in the feed.

References

- APHA, AWWA, WEF, 1998, Standard Methods for the Examinations of Water and Wastewater. Washington, DC, USA: American Public Health Association.
- Braunegg, G., Sonnleitner, B., Lafferty, R., 1978, A rapid gas chromatographic method for the determination of poly- β -hydroxybutyric acid in microbial biomass. European journal of applied microbiology and biotechnology, 6(1), 29-37.
- Chee, Y.Y., Lakshmanan, M., Jeepery, I.F., Hairudin, N.H.M., Sudesh, K., 2019, The Potential Application of Cupriavidus necator as Polyhydroxy-alkanoates Producer and Single Cell Protein. Applied Food Biotechnology, 6(1), 19-34.
- Conca, V., da Ros, C., Valentino, F., Eusebi, A.L., Frison, N., Fatone, F., 2020, Long-term validation of polyhydroxyalkanoates production potential from the sidestream of municipal wastewater treatment plant at pilot scale. Chemical Engineering Journal, 390, 124627.
- Draher, J., White, N., 2018, HPLC determination of total tryptophan in infant formula and adult/pediatric nutritional formula following enzymatic hydrolysis: single-laboratory validation, first action 2017.03. Journal of AOAC International, 101(3), 824-830.
- FAO, 2018. Future of food and agriculture 2018: Alternative Pathways to 2050.
- IRSA-CNR, A., 2003, Analytical methods for waters (Vol. 3). Rome, Italy.
- Laranja, J.L., Ludevese-Pascual, G.L., Amar, E.C., Sorgeloos, P., Bossier, P., De Schryver, P., 2014, Poly-beta-hydroxybutyrate (PHB) accumulating Bacillus spp. improve the survival, growth and robustness of Penaeus monodon (Fabricius, 1798) postlarvae. Veterinary Microbiology, 173(3-4), 310-317.
- Martínez, E.J., Raghavan, V., González-Andrés, F., Gómez, X., 2015, New biofuel alternatives: integrating waste management and single cell oil production. International journal of molecular sciences, 16(5), 9385-9405.

- Mekonnen, M.M., Hoekstra, A.Y., 2014, Water footprint benchmarks for crop production: A first global assessment. *Ecological indicators*, 46, 214-223.
- Nasseri, A.T., Rasoul-Ami, S., Morowvat, M.H., Ghasemi, Y., 2011, Single Cell Protein: Production and Process. *American Journal of Food Technology*, 6(2), 103-116.
- Righetti, E., Nortilli, S., Fatone, F., Frison, N., Bolzonella, D., 2020, A Multiproduct Biorefinery Approach for the Production of Hydrogen, Methane and Volatile Fatty Acids from Agricultural Waste. *Waste and Biomass Valorization*, 1-8.
- Sabapathy, P.C., Devaraj, S., Meixner, K., Anburajan, P., Kathirvel, P., Ravikumar, Y., Zaved, H.M., Qi, X., 2020, Recent developments in Polyhydroxyalkanoates (PHAs) production—A review. *Bioresource technology*, 306, 123132.
- Saeed, M., Yasmin, Y., Murtaza, M.A., Fatima, I., Saeed, S., 2016, Single cell proteins_ A novel value added food product.pdf. *Pakistan Journal of Food Science*, 26(4), 211-217.
- Saint-Denis, T., Goupy, J., 2004, Optimization of a nitrogen analyser based on the Dumas method. *Analytica Chimica Acta*, 515(1), 191-198.
- Siddi, M., 2020. The European Green Deal: Assessing its current state and future implementation. Finnish Institute of International Affairs, Helsinki.
- Sluiter, A., Hames, B., Ruiz, R., Scarlata, C., Sluiter, J., Templeton, D., Crocker, D., 2008, Determination of structural carbohydrates and lignin in biomass. *Laboratory analytical procedure*, 1617(1), 1-16.
- Suguna, P., Binuramesh, C., Abirami, P., Saranya, V., Poornima, K., Rajeswari, V., Shenbagarathai, R., 2014, Immunostimulation by poly-beta hydroxybutyrate-hydroxyvalerate (PHB-HV) from *Bacillus thuringiensis* in *Oreochromis mossambicus*. *Fish Shellfish Immunol*, 36(1), 90-97.
- Vermeulen, S.J., Campbell, B.M., Ingram, J.S., 2012, Climate change and food systems. *Annual review of environment and resources*, 37, 195-222.
- Yadav, B., Chavan, S., Atmakuri, A., Tyagi, R.D., Drogui, P., 2020, A review on recovery of proteins from industrial wastewaters with special emphasis on PHA production process: Sustainable circular bioeconomy process development. *Bioresource technology*, 317, 124006.

Protein-rich biomass production exploiting biological nitrogen fixation: respirometry as a tool to investigate diazotrophic cyanobacteria cultivation

Veronica Lucato¹, Elena Barbera², Eleonora Sforza^{1*}

1 Department of Industrial Engineering DII, University of Padova, Via Marzolo 9, 35131 Padova, Italy

2 Interdepartment Centre Giorgio Levi Cases, University of Padova, Via Marzolo 9, 35131 Padova, Italy

**Corresponding author E-Mail: eleonora.sforza@unipd.it*

1.Introduction

In a 7.9 billion people-world, expected to reach almost 10 billion by 2050, the need to get alternative solutions to meet increasing food demand turns pressing. Conventional food and feed production is not in itself capable to meet such a raised demand [1]. Moreover, food security and production are strongly threatened by global climate change, shortage and worsened quality of soil and water resources and biotic/abiotic stresses [2]. Hence, the time has come to dig up new food sources and to adopt sustainable production processes, which are not only eco-friendly but also cost-effective. In this sense, microalgae are attracting lots of interest as a promising forerunner high-nutrient food resource [3]. Microalgae is a broad term that refers to photosynthetic microorganisms, which can be both eukaryotes (microalgae) and prokaryotes (cyanobacteria). Their applications have historically been heavily carbon-centric [4], exploiting photosynthetic CO₂-fixation activity to get environmental benefits, including the possibility to grow in hostile and non-arable land, not competing with human activities [2]. However, now, microalgae attractive potential addresses also their ability to synthesize a vast plethora of bioactive compounds, such as proteins, lipids and carbohydrates [5]. Several among these macromolecules have already been highlighted for their healthy, antitumoral and antioxidant properties [2]. Great attention is posed on proteins because protein demand is expected to reach 175-361 Mt annually by 2050 [4]. Microalgal biomass stands out for equal or even better nutritional values when compared with vegetal biomass, taking into account amino acidic profile, protein quality and essential amino acid content, not synthesized by humans and necessarily supplied through nutrition [5].

Second only to carbon (about 50% of biomass), the most abundant element in microalgae is nitrogen (up to 14%). Since nitrogen composes approximately 16% of proteins [6], it is the most important parameter for high-protein production in microalgae farms [5]. Thus, commercial-grade and low-cost nitrogen sources are crucial for feasible microalgae farming. The use of wastewater as an economical nitrogen-rich source is not allowed in food production; however, noteworthy dinitrogen (N₂ gas) as a resource is nearly 2000-fold more abundant (78%) than CO₂ (0.04%) in the atmosphere. As a matter of fact, N₂ can be converted into a plethora of high-demand and high-value chemicals by N₂-fixing cyanobacteria, including proteins. Although microalgae applications are already ongoing, solar-powered nitrogen-fixing cyanobacteria capabilities have been largely ignored [4].

The biological nitrogen fixation (BNF) capability of many cyanobacteria has been traditionally investigated for biological fertilizers production replacing chemical ones to increase crop production [4]. Nevertheless, the direct use of biomass as a protein source could be more beneficial, avoiding inefficiency absorption by livestock or crop. In fact, only 30-50% of nitrogen fertilizer is absorbed by cereal crops and livestock converts this nitrogen into protein for human consumption at low efficiency (10%), resulting in nitrogen loss with respect to fertilizer [4]. Besides the reduction of upstream cultivation costs mainly due to nutrients (currently equal to 79 €/kg of produced biomass [5]), enhanced application of diazotrophic cyanobacteria will reduce the extent of Haber-Bosch process employment in the global nitrogen economy, which currently depends almost completely on such chemical process. Since it is highly energy-consuming and GHG-producing, the environmental impacts would be clearly positive. It is estimated that if cyanobacteria were cultivated on agricultural scales, cultures could fix nitrogen on a level equivalent to global ammonia demands [4].

Large-scale application of diazotrophic cyanobacteria could become competitive if we can maximize the efficiency of the nitrogen-fixation process and achieve improved biomass productivity. Thus, proper values of operative variables must be investigated in order to quantify kinetic parameters as well as to develop reliable growth models. However, modelling of BNF is challenging, since cyanobacteria metabolism relies on several environmental factors.

Respirometry is a technique typically used to study microbial metabolism. However, it also emerges as a successful tool to investigate microalgae phototrophic metabolism, based on the measurement of O₂ evolution in solution due to photosynthetic activity when light is supplied [7].

In this work, we propose respirometry as a promising tool to investigate the kinetic aspects of BNF.

2. Methods

The cyanobacterial strains *Anabaena cylindrica* and *Nostoc PCC 7122* (Pasteur Culture collection of Cyanobacteria, France) were used in this work. They were maintained and propagated in sterilized BG11₀ medium [8], modified by removing nitrogen and substituting HEPES with 1.5 g L⁻¹ of sodium hydrogen carbonate, to maintain the pH within the optimal interval of 6.5–7.5. Batch experiments were carried out to study and compare the growth of the two strains, in a thermostated incubator at a constant temperature of 24°C, both under control and phosphate-limited conditions. In phosphate-limited conditions, phosphate was reduced from 16.63 to 4.16 mg/L. 200 mL-volume Quickfit® Drechsel Bottles (5 cm diameter) were used and illuminated by a continuous light of 100 μmol photons m⁻² s⁻¹. Good mixing within the reactor was ensured by a magnetic stirrer and CO₂-air (5% v/v) mixture continuously bubbling at the bottom of the bottle (total gas flow rate of 1 L h⁻¹) for non-limiting CO₂ supply.

Continuous cultivation of *Nostoc PCC 7122* at 24°C in a vertical flat-panel polycarbonate photobioreactor with a working volume equal to 200 mL, an irradiated surface of 0.005 m and a thickness of 0.035 m was used to maintain the inoculum for respirometric tests. Light was provided by a white LED lamp with the incident light intensity equal to 150 μmol photons m⁻² s⁻¹. BG11₀ medium was modified by doubling nutrient concentration, reducing sodium hydrogen carbonate to 250 mg L⁻¹ and removing sodium carbonate. Steady-state was assessed by monitoring biomass optical density at 750 nm. Biomass concentration was also quantified by measuring dry cell weight concentration.

The respirometric protocol was adapted from E. Barbera et al. [9]

3. Results and discussion

Growth of *Anabaena cylindrica* and *Nostoc PCC 7122* was compared both in control and limited conditions. Growth curves are shown in Figure 1. Under control conditions, *A. cylindrica* growth rate was equal to 0.38±0.10 d⁻¹, while it was 0.42±0.14 d⁻¹ for *Nostoc PCC 7122*. The difference between growth rate values was not statistically significant. On the contrary, *Nostoc PCC 7122* was the most performing under limited conditions, achieving a growth rate equal to 0.33±0.01 d⁻¹ against 0.23±0.02 d⁻¹ of *A. cylindrica*. Thus, *Nostoc PCC 7122* was chosen for respirometric tests. Through respirometry, we evaluate the growth rate of *Nostoc PCC 7122* by varying one parameter at a time. Temperature, light intensity and nutrient concentration in the medium are taken into consideration. An example of a result that can be obtained from respirometry to describe the kinetic behaviour as a function of light intensity and temperature is shown in Figure 2.

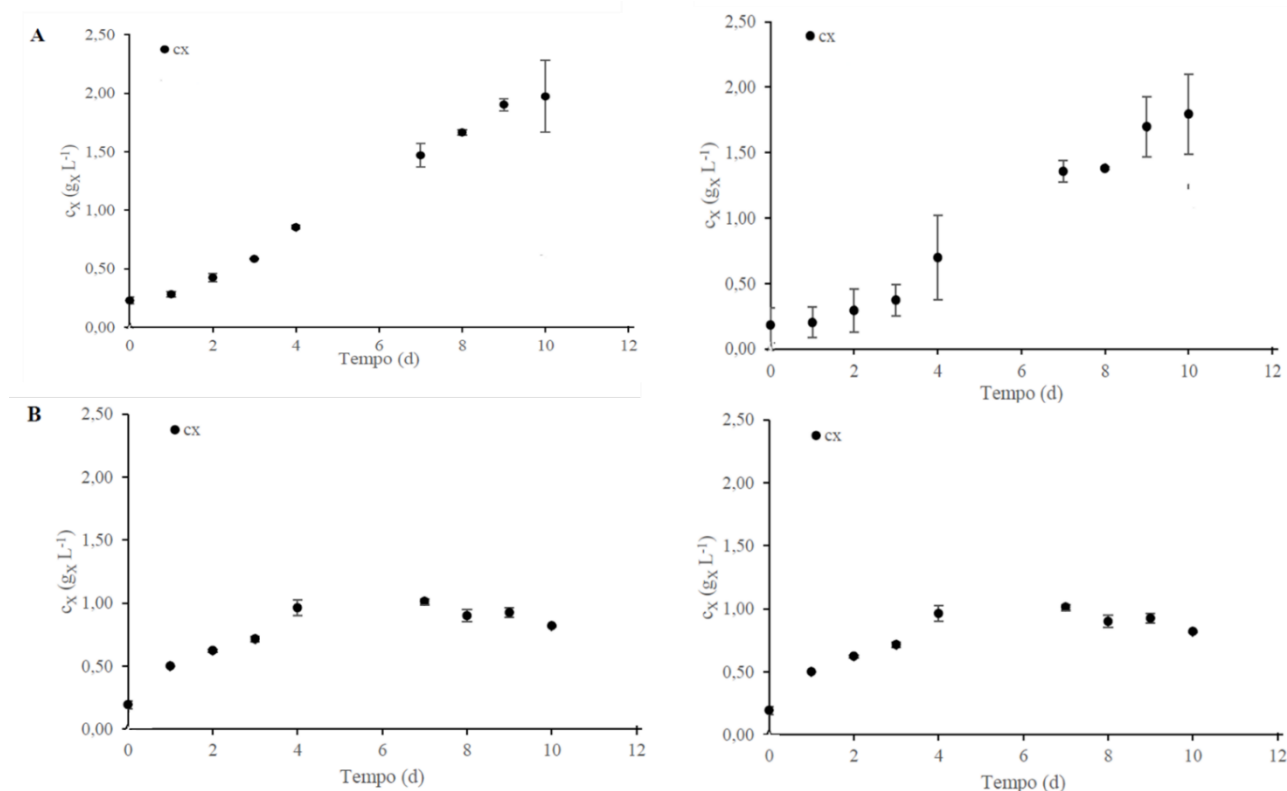


Figure 1. Biomass concentration C_x ($g_x L^{-1}$) over time (d) of *Anabaena cylindrica* (left) and *Nostoc PCC 7122* (right) under control (A) and limited conditions (B).

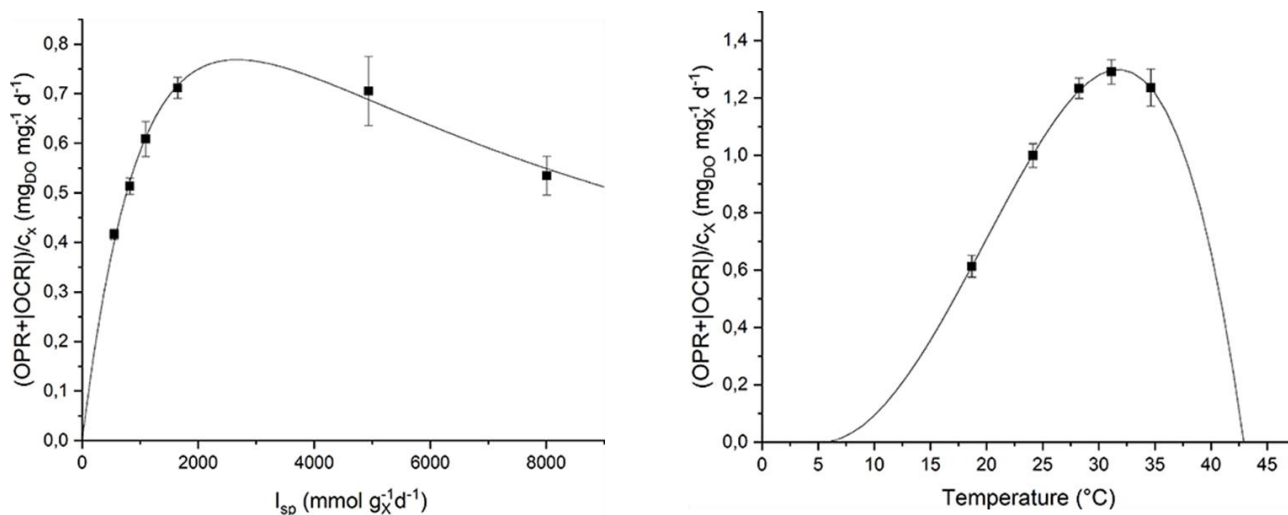


Figure 2. Specific oxygen production rate as a function of specific light supply rate (left) and temperature (right): experimental data (dots) and fitted model (continuous line).

4. Conclusions

Among the two nitrogen-fixing cyanobacteria species tested, *Nostoc PCC 7122* was the best performing and thus it was chosen for respirometric tests. Respirometry, which has already turned out as a useful method to study optimal growth conditions of photosynthetic organisms, was applied to identify growth kinetic parameters and determine growth conditions to achieve high diazotrophic species productivity.

References

- [1] M. Henchion, M. Hayes, A. M. Mullen, M. Fenelon, and B. Tiwari, "Future protein supply and demand: Strategies and factors influencing a sustainable equilibrium," *Foods*, vol. 6, no. 7, pp. 1–21, 2017.
- [2] C. M. Joan, L. Sbabou, and E. Arroussi, "Microalgae and Cyanobacteria: How Exploiting These Microbial Resources Can Address the Underlying Challenges Related to Food Sources and Sustainable Agriculture : A Review," *J. Plant Growth Regul.*, 2022.
- [3] L. Garcia, "Microalgae, old sustainable food and fashion nutraceuticals," vol. 2783, 2017.
- [4] P. Hudson, "Harnessing Solar-Powered Oxidic N₂-fixing Cyanobacteria for," *Front. Cyanobacteria Biotechnol.*, 2021.
- [5] M. L. Amorim, J. Soares, J. S. dos R. Coimbra, M. de O. Leite, L. F. T. Albino, and M. A. Martins, "Microalgae proteins: production, separation, isolation, quantification, and application in food and feed," *Crit. Rev. Food Sci. Nutr.*, vol. 61, no. 12, pp. 1976–2002, 2021.
- [6] S. O. Lourenço *et al.*, "Distribution of intracellular nitrogen in marine microalgae : Calculation of new nitrogen-to-protein conversion factors Distribution of intracellular nitrogen in marine microalgae : Calculation of new nitrogen-to-protein conversion factors," vol. 0262, 2007.
- [7] E. Sforza, M. Pastore, E. Barbera, and A. Bertucco, "Respirometry as a tool to quantify kinetic parameters of microalgal mixotrophic growth," *Bioprocess Biosyst. Eng.*, vol. 42, no. 5, pp. 839–851, 2019.
- [8] R. Rippka, J. Deruelles, J. B. Waterbury, and X, "Generic assignments, strain histories and properties of pure cultures of cyanobacteria," *J. Gen. Microbiol.*, vol. 111, no. 1, pp. 1–61, 1979.
- [9] E. Barbera, A. Grandi, L. Borella, A. Bertucco, and E. Sforza, "Continuous Cultivation as a Method to Assess the Maximum Specific Growth Rate of Photosynthetic Organisms," vol. 7, no. October, pp. 1–12, 2019.

Mixotrophic cultivation of *Phaeodactylum tricornutum* and value-added compounds extraction through a biorefinery concept

Caterina Celi^{1*}, Debora Fino¹, Francesco Savorani¹

¹ *Politecnico di Torino, DISAT, Corso Duca degli Abruzzi 24, 10129, Torino, Italy*

**Corresponding author E-Mail: caterina.celi@polito.it*

1. Introduction

Microalgae are photosynthetic organisms that own the possibility to produce high value phytochemicals and have the capacity to utilize CO₂ as a feedstock, potentially enabling economic and environmentally sustainable manufacturing solutions. (Butler, 2020) They have been extensively studied during the past years, firstly for the chance of biofuels production and then also for the extraction of valuable compounds, such as proteins, polysaccharides, polyunsaturated fatty acids (PUFAs), pigments, and sterols, widely used in pharmaceutical, nutraceutical, cosmetic and food sectors.

However, despite their advantages in high biomass productivity, photosynthetic efficiency, and adaptability to grow in a wide variety of substrates without depleting fertile lands, few industries based on these organisms have arisen, mainly because of the high costs to bear. The great demands in terms of materials and energy needed for their production and downstream processing, with the harvesting and dewatering steps being the most energy-intensive, prevented the microalgae-based industries to effectively establish themselves worldwide. Even more so when the industrial process is designed to obtain a sole product to be placed on the market.

In this context, biorefinery can be proposed as a valid approach towards sustainability and circular economy since it can increase production efficiency and economic feasibility by valorizing all biomass components. Such a strategy involves the building of several facilities close to each other to take advantage of the potential synergies arising from this set of processes. (Branco-Vieira, 2020) A microalgae-based biorefinery would then rely on a process chain starting from the optimization of biomass production to the development of a platform able to generate a wide range of products, such as bulk chemicals, food supply, bioactive compounds, and oils, exactly as occurs for petroleum-based processes. (Gilbert-López, 2015)

Nowadays, even if microalgae are mostly employed as feeding in aquaculture sector, there are anyhow some industries where they are grown to produce value-added products for feed and food market: e.g., astaxanthin, β-carotene, phycocyanin, fatty acids. Even if less commercially competitive, these microalgae-based molecules own specific advantages over standard synthetic alternatives: for instance, from a chemical point of view, synthetic molecules are only available in specific isomers, which are generally much less effective than natural variants for certain applications, such as in infant formula, fish pigment enhancers or dietary supplements (Enzing, 2014).

Some industries have specialized in the commercialization of one particular compound extracted from an algae source, but as underlined before, complete utilization of microalgae for multiple compounds extraction instead of the sole product is pivotal to increase the economic feasibility of bioactive compounds production from these natural sources.

Other studies have already focused on the possibility of multiple compounds production from microalgal biomass, such as *Thalassiosira weissflogii*, *Scenedesmus obliquus*, *Isochrysis galbana*, *Stauriosirella pinnata* and *Phaeodactylum tricornutum* (Marella, 2020; Amorim, 2020; Vieira, 2021; Zhang, 2018; Savio, 2020), but very few of them employed green extraction techniques. Therefore, this project shall focus on the comprehensive utilization of microalgal biomass to obtain diverse valuable products in a multi-stage cascade extraction based on sustainable technologies.

Marine diatoms are the most productive and adaptive microalgae, and account for 20% of global carbon fixation; among them, *Phaeodactylum tricornutum* is one of the most studied species. This is a marine pennate diatom belonging to the class of Bacillariophyceae of Heterokontophyta, containing about 36.4% of proteins, 26.1% of carbohydrates, 18.0% of lipids and 15.9% of ash on a dry weight basis, under normal growth conditions (Zhang, 2018). It is a commercially viable species for large-scale cultivation and can accumulate a large spectrum of marketable products, such as fucoxanthin, EPA, DHA and chrysolaminarin, which have been shown to be beneficial for human health.

P. tricornutum is a successful photoautotroph, converting sunlight energy into reduced carbon via photosynthesis, but it is also capable of mixotrophic growth on glucose, acetate, fructose, and glycerol; while heterotrophic growth via sugar fermentation in the dark is not possible, except upon metabolic engineering. Even if phototrophic growth could be a cheap way to produce biomass since only sunlight is used as an energy source, it is often limited by the difficulties in optimizing light penetration, gas diffusion, and temperature control. Therefore, mixotrophic cultivation making use of cheap and easily available carbon sources, represents an interesting alternative, having the potential to attain high biomass concentration while maintaining high contents of the photosynthesis-related compounds, that are usually lost under heterotrophic conditions. Glycerol appears to be the most suitable organic carbon source for *P. tricornutum*, leading to the highest biomass and EPA productivities. In fact, mixotrophy with glycerol mimics typical responses of N-starvation resulting in increases in TAGs, but also in biomass without loss of photosynthetic capacity due to nutrients' depletion (Butler, 2020).

2. Methods

P. tricornutum from Culture Collection of Algae and Protozoa (CCAP 1055/18, axenic culture of CCAP 1055/1) is cultivated mixotrophically with glycerol and in optimized enriched seawater artificial seawater (ESAW), which showed higher biomass yield than other conventional medium for diatoms (Villanova, 2021). Laboratory-scale photobioreactors of 2 L total working volume have been designed adapting a bubble column reactor system, which allows to obtain a certain degree of control over the lighting and temperature (Wang, 2019). Column reactors (10 with 200 mL working volume) are placed in a glass tank with a thermostatically controlled water bath; the light penetration is assured through two fluorescent lamps placed at the two sides of the tank (Fig. 1). The air and CO₂ mix (1% v/v CO₂) is supplied to the photobioreactors using flowmeters and the rising of gas bubbles is responsible for the gas exchange and the mixing in each reactor. Optimal growth conditions for *P. tricornutum* are maintained as: 21°C; pH=8÷8.50; 496 μmol/m²s of light intensity; light-dark cycle: 16:8 hours; final glycerol concentration of 4.6 g/L.

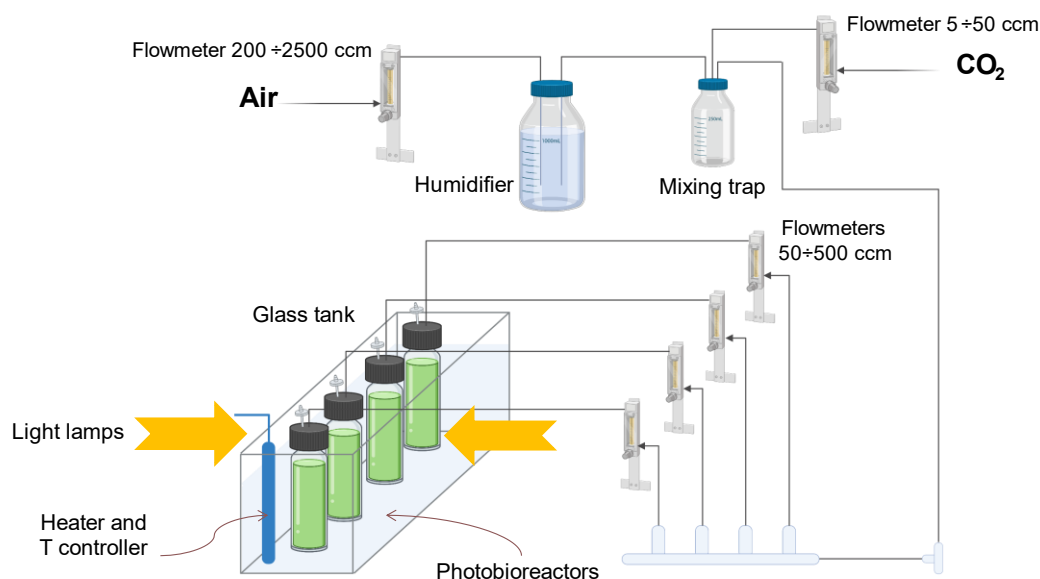


Fig.1 Tank with bioreactors for algae culturing, adapted from Wang et al. (2019)

To monitor algal growth, daily samples are taken to measure (i) OD at 750 nm in a spectrophotometer, (ii) cell density through a Thoma chamber and (iii) dry cell weight (DCW) after filtration through GF/C Whatman filters and drying oven of biomass.

A Design of Experiment will be carried out to find optimal culture conditions: two levels and three factors full factorial will be developed. The factors to be investigated in the DoE are Light intensity (low level of 150 $\mu\text{mol}/\text{m}^2\text{s}$ and high level of 400 $\mu\text{mol}/\text{m}^2\text{s}$), Temperature (low level of 20 °C and high level of 25°C) and Glycerol concentration for mixotrophic culture (low level of 0.05 M and high level of 0.1 M). The influence of these factors on biomass productivity, biomass maximum specific growth rate and biochemical composition (carbohydrates, lipids, proteins, pigments) will be studied in order to find the best operative conditions to obtain a high-value compounds rich biomass and the highest biomass productivity.

After cultivation step, dried biomass shall be characterized by lipid extraction and quantification with Bligh & Dyer method followed by GC-MS for fatty acids analysis; pigments extraction and quantification by spectrophotometric methods and use of equations for chlorophyll *a* and *c*; proteins quantification through elemental analysis and N-factor; carbohydrates extraction and quantification HPLC analysis.

Furthermore, different advanced environmentally friendly techniques shall be tested to design the optimal cascade extraction to exhaust all achievable compounds and fractionate microalgal biomass into valuable isolated fractions. For instance, microwave-assisted extraction (MAE), ultrasound-assisted extraction (UAE), pressurized liquid extraction (PLE), supercritical fluid extraction (SFE), and the use of enzymes, ionic liquids, or deep eutectic solvents will be considered for this purpose. With this regard, an interesting approach could be to design the extraction steps in increasing order of polarity (as done by Gilbert-López, 2015), by modulating extractive conditions and solvents used, so that different extracts are obtained in the various steps.

3. Conclusions

It is worth to stress that the extraction procedures targeted to specific compounds must not compromise the integrity of the other fractions to be extracted with the next steps; moreover, the solvents used must fulfill regulations related to the product's final use. If the latter can be true for GRAS (generally recognized as safe) solvents, the same can not be said with confidence for novel substances, such as ionic solvents and deep eutectic solvents, whose toxicity should be still investigated, especially if the target market is

pharmaceutical, nutraceutical or cosmetic. Lastly, the economic aspect should not be underestimated: even if biorefinery approach could allow to enhance economic viability, the selection of extraction techniques shall be performed carefully to not engrave overly on the total investment, which could occur in the case of using enzymes that are known to be very expensive.

Hence, taking account of the previous observations, results on extraction tests using cited techniques will be used to design the best cascade extraction suitable for *P. tricornutum*, aimed at valorizing all algal biomass components to their maximum extent; the possibility to develop a final valorization of the residual biomass intended to power upstream processes will also be evaluated.

References

- [1] Thomas Butler, Rahul Vijay Kapoore, Seetharaman Vaidyanathan, *Phaeodactylum tricornutum*: A Diatom Cell Factory, Trends in Biotechnology, Volume 38, Issue 6, 2020, Pages 606-622
- [2] Monique Branco-Vieira, Sergio San Martin, Cristian Agurto, Marcos A.V. Freitas, António A. Martins, Teresa M. Mata, Nídia S. Caetano, Biotechnological potential of *Phaeodactylum tricornutum* for biorefinery processes, Fuel, Volume 268, 2020, 117357
- [3] Bienvenida Gilbert-López, José A. Mendiola, Javier Fontecha, Lambertus A. M. van den Broek, Lolke Sijtsma, Alejandro Cifuentes, Miguel Herrero and Elena Ibáñez, Downstream processing of *Isochrysis galbana*: a step towards microalgal biorefinery, Green Chemistry, 2015, 17, 4599
- [4] Christien Enzing, Matthias Ploeg, Maria Barbosa, Lolke Sijtsma, Microalgae-based products for the food and feed sector: an outlook for Europe, Jrc Scientific and Policy Reports, 2014, Report EUR 26255 EN
- [5] Thomas Kiran Marella, Archana Tiwari, Marine diatom *Thalassiosira weissflogii* based biorefinery for co-production of eicosapentaenoic acid and fucoxanthin, Bioresource Technology, Volume 307, 2020, 123245
- [6] Matheus Lopes Amorim, Jimmy Soares, Bruno Bezerra Vieira, Willian Batista-Silva, Marcio Arêdes Martins, Extraction of proteins from the microalga *Scenedesmus obliquus* BR003 followed by lipid extraction of the wet deproteinized biomass using hexane and ethyl acetate, Bioresource Technology, Volume 307, 2020, 123190
- [7] Bruno Bezerra Vieira, Jimmy Soares, Matheus Lopes Amorim, Paula Viana Queiroz Bittencourt, Rita de Cássia Superbi, Eduardo Basílio de Oliveira, Jane Sélia dos Reis Coimbra, Marcio Arêdes Martins, Optimized extraction of neutral carbohydrates, crude lipids and photosynthetic pigments from the wet biomass of the microalga *Scenedesmus obliquus* BR003, Separation and Purification Technology, Volume 269, 2021, 11871
- [8] Wenyan Zhang, Feifei Wang, Baoyan Gao, Luodong Huang, Chengwu Zhang, An integrated biorefinery process: Stepwise extraction of fucoxanthin, eicosapentaenoic acid and chrysolaminarin from the same *Phaeodactylum tricornutum* biomass, Algal Research, Volume 32, 2018, Pages 193-200, ISSN 2211-9264
- [9] Saverio Savio, Serena Farrotti, Debora Paris, Esther Arnaiz, Israel Díaz, Silvia Bolado, Raul Muñoz, Carlo Rodolfo, Roberta Congestri, Value-added co-products from biomass of the diatoms *Staurisirella pinnata* and *Phaeodactylum tricornutum*, Algal Research, Volume 47, 2020, 101830
- [11] Qichen Wang, Haixin Peng, Brendan T. Higgins, Cultivation of Green Microalgae in Bubble Column Photobioreactors and an Assay for Neutral Lipids. J. Vis. Exp. (143), 2019, e59106
- [12] Valeria Villanova, Dipali Singh, Julien Pagliardini, David Fell, Adeline Le Monnier, Giovanni Finazzi and Mark Poolman (2021) Boosting Biomass Quantity and Quality by Improved Mixotrophic Culture of the Diatom *Phaeodactylum tricornutum*. Front. Plant Sci. 12:642199

A stochastic approach for modeling cell mass distribution of microalgae culture

Stefania Tronci^{1*}, Alexander Schaum²

¹ Dipartimento di Ingegneria Meccanica, Chimica e dei Materiali, Via Marengo 2, 09123 Cagliari, Italy;

² Chair of Automatic Control, Kiel University, Kiel, Germany,

*Corresponding author E-Mail: stefania.tronci@unica.it

1. Introduction

Microalgae are considered an important source to produce innovative foods, because they have several advantages in terms of the consumption of resources and energy when compared to traditional foods. Furthermore, they are rich in bioactive compounds, including pigments and polyunsaturated fatty acids [1]. The composition of microalgal biomass depends on the strain, the composition of the culture medium, and the operative conditions. Mathematically modeling microalgae growth can provide an effective tool for optimizing the biochemical process and maximize the production of specific high-value compounds. Several authors showed that the microalgae growth can be successfully described by the Droop model [2,3], that considers the dynamic behavior of biomass, substrate and quota. It has been observed that some bi-active compounds, e.g. astaxanthin, are produced by the microalgae during a particular phase of their growth, therefore the obtainment of cell-mass distribution can improve the value of the model. The cell population balance approach has recently been reported for microalgae in [4], showing a rather good correspondence with measurement data for extracellular substrate (i.e., nitrate) concentration, biomass concentration and cell-size distribution. The proposed approach led to good results but the modeling and identification was associated to a high experimental and analytic effort, the identification process and the model analysis showed to be rather complex, and the resulting model was difficult to be used for monitoring and control purposes. In this work, a different method based on Fokker-Planck equation is used to model the cell-size distribution.

2. Methods

Following the results reported in [5], the cell growth has been modelled by the following stochastic equation

$$\frac{dm}{dt} = f(m, t) + g(m)\eta(t) = r m \left(1 - \frac{m}{K}\right) + \sqrt{g(m)}\eta(t) \quad (1)$$

where m is the mass of a single cell, r and K are the parameters of the deterministic growth process and $\sqrt{g(m)}\eta(t)$ is the noise term, with $g(m)$ representing the diffusion term. It is assumed that

$$E[\eta(t)] = 0 \quad E[\eta(t)\eta(t')] = \delta(t - t') \quad (2)$$

according to [5], the following law has been used for the noise term

$$g(m) = \frac{q_v}{2} m^2 \quad (3)$$

Eqs. (1) and (2) implies that the cell mass behaves as a random variable, which is characterized by a certain probability density function $\psi(m, t)$. The dynamic behavior of the distribution can be calculated by resorting to the Fokker-Planck equation in Stratonovich form (4)

$$\frac{\partial \psi}{\partial t} = \frac{\partial}{\partial m} \left[\frac{q_v}{2} m^2 \frac{\partial \psi}{\partial x} - \left(f(m, t) - \frac{q_v}{2} m \right) \psi(m, t) \right] \quad (4)$$

along with the boundary and initial conditions

$$\frac{q_v}{2} m^2 \frac{\partial \psi}{\partial x} - \left(f(m, t) - \frac{q_v}{2} m \right) \psi(m, t) = 0 \text{ at } m = 0 \quad \frac{\partial \psi}{\partial t} = 0 \text{ at } m \rightarrow 0 \quad \psi = \psi_0 \text{ at } t = 0 \quad (5)$$

3. Results and discussion

Model parameters [r,K,q/2] has been calculated using experimental data obtained during the growth of microalga *Chlamydomonas Reinhardtii*. Results are reported in Figure 1, where a good agreement is shown between experimental histogram and calculated cell-size density (CSD) function.

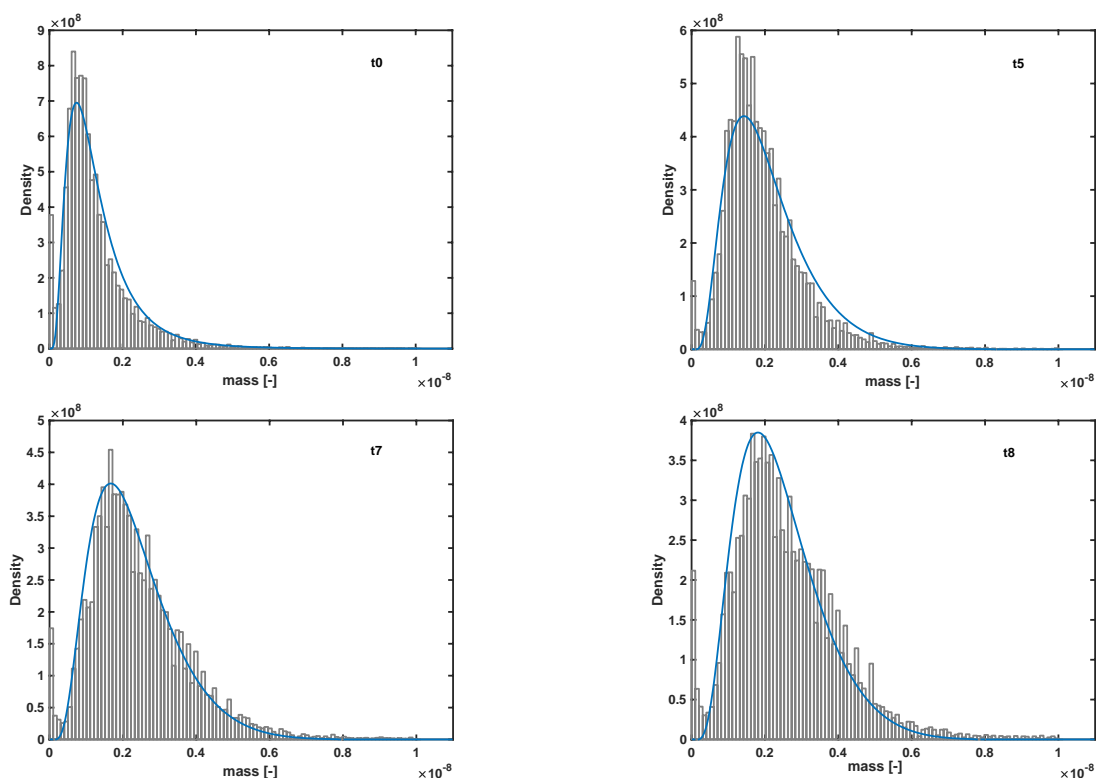


Figure 1. Experimental histograms (grey) and calculated CSD (blue line) at different sampling time.

4. Conclusions

The comparison of the model predictions with the experimental measurement data shows that this approach provides a valid tool for approximating cell-mass distribution. It is worth to noting that the resulting model is considerably simpler than alternative cell population balance equations, that have been previously applied to model the time evolution of the process.

References

- [1] Villaró, S., Ciardi, M., Morillas-España, A., Sánchez-Zurano, A., Ación-Fernández, G., & Lafarga, T. (2021). Microalgae Derived Astaxanthin: Research and Consumer Trends and Industrial Use as Food. *Foods*, 10(10), 2303.
- [2] Droop, M, Vitamin B12 and marine ecology IV: the kinetics of uptake growth and inhibition in *monochrysis lutheri*. *Journal of the Marine Biological Association*, 48 (3), (1968), 689-733.
- [3] Mairet, F., & Bernard, O. (2016). The photoinhibistat: Operating microalgae culture under photoinhibition for strain selection. *IFAC-PapersOnLine*, 49(7), 1068-1073.
- [4] Atzori, F., Jerono, P., Schaum, A., Baratti, R., Tronci, S., & Meurer, T. (2021). Identification of a cell population model for algae growth processes. *IFAC-PapersOnLine*, 54(7), 132-137.
- [5] Grosso, M., Cogoni, G., Baratti, R., & Romagnoli, J. A. (2011). Stochastic approach for the prediction of PSD in crystallization processes: Formulation and comparative assessment of different stochastic models. *Industrial & engineering chemistry research*, 50(4), 2133-2143.

A circular economy approach for *Cupriavidus necator* DSM 545 biosynthesis of polyhydroxybutyrate

Silvia Bellini^{1,2}, Tonia Tommasi¹, Debora Fino^{1,2*}

¹Dipartimento di Scienze e Tecnologie Applicate, Politecnico di Torino, Turin, Piemonte, 10129, Italy

²Italian Institute of Technology, Turin, Piemonte, 10144, Italy

*Corresponding author E-Mail: debora.fino@polito.it

1. Introduction

Since their first invention, the petrol chemical plastics have been rapidly and widely diffused worldwide. The huge rising in plastic demand and utilization have resulted in a proportional increasing of plastic pollution (about 6.2 million tonnes (MT) of macro-plastics and 3MT of micro-plastics were lost to the environment out of the 322 MT of plastics produced globally in 2015 [5]). In this scenario, there is the need of valid, sustainable, harmless, economically competitive, and biodegradable polymers, dealing with circular economy principles. The so called “green polymers”, including polyhydroxy alkanoates (PHAs), polylactic acid (PLA) and polybutylene succinate (PBS), are nowadays intensively studied for their applications and as replacement of conventional plastics. With respect to the synthetic and enzymatic polymerization of lactic and succinic acid of PLA and PBS respectively, PHAs polymerization can be mainly performed by a wide repertoire of bioplastics producers bacteria, which are able to store PHAs as carbon sink usually under restricted and nutrient shortage growth conditions [3, 6, 7, 9].

This research is focused on the poly hydroxybutyrate (PHB) biosynthesis, a member of PHAs, through *C. necator* DSM 545 fermentation using two different waste sources as carbon sinks. This work has been promoted by Regione Piemonte and Novamont® and it is included in the regional and circular economy-based project “PRIME” (Processi e pRodotti Innovativi di chiMica vErde), having the aim to study and develop advanced chemistry and biorefineries processes to produce new biomaterials and products belonging to several economic sectors (agriculture, automotive, textile, food, cosmetic, etc). The first waste substrate, the sugar waste, is furnished by Sedamyl S.p.A, a factory involved in PRIME project.

2. Methods

Cupriavidus necator DSM 545 has been grown following the protocol used by Mozumder et al. (2014) [4], i.e. using a medium containing a carbon source (sugar-based waste substrate) and sources of phosphate, sulphate, magnesium, and metals [4]. Fermentation has been carried out by keeping pH at 6.8 in a bioreactor (Sartorius®, working volume 0.5 L) firstly using the sugar base waste substrate coming from PRIME supply chain, then acetate at different concentrations (2, 3, 4 or 5 g L⁻¹) and hours has been added to the fermentation medium to increase PHB production, after 23 hours. During the test, samples have been taken at 12, 15, 21, 24, 36, 40, 44 and 48 hours from the beginning of fermentation and the biomass has been sampled (total volume of 3 mL) by centrifugation (5 min at 10000 rpm) and derived supernatant, filtered through 0.2-µm filters in PES, analyzed at HPLC using a Resex18 column using H₂SO₄ 5 mM in distilled water. The biomass has been dried at 80 °C for 15-20 h. PHB extraction has been performed digesting dried biomass in pyrex tubes using 1 mL of 96% sulphuric acid, in a silicon oil bath at 90°C for 1 h under stirrer agitation. The resulting solution was diluted 1:1000 to be then filtered through 0.2-µm filters in PES and analyzed by HPLC to check the production of PHB.

3. Results and discussion

C. necator has the extraordinary capability to accumulate up to 90% of PHB per cell dry weight (CDW), a polymer consisting of only short-chain-length (SCL) monomers, guaranteeing both high biomass and biopolymer yields [2]. The modified strain *C. necator* DSM 545 owns a constitutive expression of the gene codifying for glucose-6-phosphate dehydrogenase (G-6-PDH), resulting in increased NADPH molecule production, an important cofactor of acetoacetyl-CoA reductase (*phaB*), one of the three enzymes involved in

PHB biosynthetic pathway [8]. In this research work, the biopolymer biosynthesis has been induced two different wastes as carbon sinks. The first one is a waste sugar substrate, demineralized and isomerized, containing mainly glucose and fructose (about fifty percent each). This waste substrate has been used combined with another waste substrate, the consumed medium of *Acetobacterium woodii* autotrophic fermentation, whose carbon sink is acetate. This medium has been supplied to *C. necator* DSM 545 during the PHB accumulation phase.

C. necator can better grow on fructose rather than other sugars, but this modified strain can perform a glucose fermentation too, therefore the waste substrate containing both glucose and fructose (fifty percent each) can be used to ferment this strain. The fed-batch fermentation has been performed supplying and modulating the sugar substrate (12 g L^{-1} at the beginning of fermentation and 6 g L^{-1} after 15h and 21h), containing glucose and fructose, and acetate at different concentration during the whole fermentation, which lasted for 48h. Acetate feeding has been performed as resumed in the following scheme (figure 1):

substrate	time (hours)	concentration (g L^{-1})
sugar waste	0h	12 g L^{-1}
sugar waste	15h	6 g L^{-1}
sugar waste	21h	6 g L^{-1}
acetate	23h	2 g L^{-1}
acetate	27h	3 g L^{-1}
acetate	31h	4 g L^{-1}
acetate	34h	4 g L^{-1}
acetate	38h	5 g L^{-1}
acetate	42h	4 g L^{-1}
acetate	45h	4 g L^{-1}

Figure 1. Scheme of fed-batch feeding using the sugar waste coming from PRIME supply chain and pure acetate at different concentration and time during the whole fermentation in bioreactor ($V_w 0,5 \text{ L}$).

Using this strategy, the highest PHB concentration, about 7 g L^{-1} , has been reached after 35 hours of fermentation at 30°C , at a vvm of $0,5 \text{ h}^{-1}$ (using air and a Rushton impeller to oxygenate and mix the culture, and the biomass reached 10 g L^{-1} concentration at the same hour, as shown in figure 2 (about 70% of PHB content has been achieved).

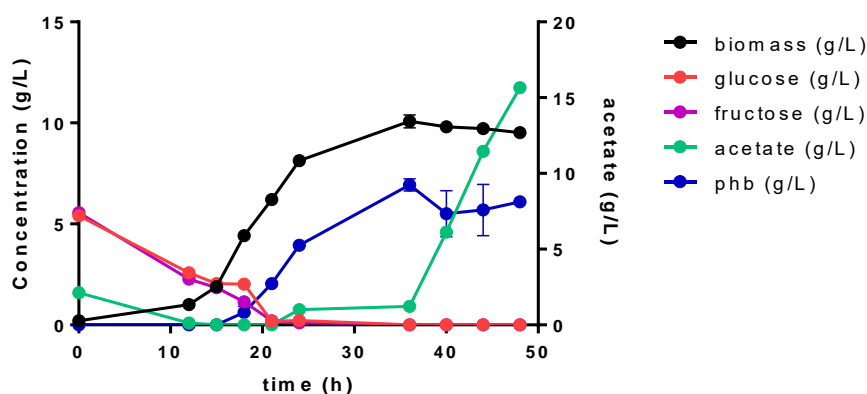


Figure 2: Fermentation in bioreactor (volume $0,5 \text{ L}$) of *C. necator* DSM 545 using sugar-based waste substrate and acetate at different concentration and hours. About 7 g L^{-1} of PHB has been obtained after 35 hours in a cell culture biomass of 10 g L^{-1} .

As shown in fig. 2, acetate still remains in the medium after the culture reached the highest PHB concentration, suggesting that the acetate concentration added could be reduced; furthermore, an additional step of sugar waste feeding may be added in order to achieve higher biomass concentration. Some other strategies to enhance the biopolymer accumulation could be the optimization of the operative conditions, such as those studied by Mozumder et al. (2014) [4] i.e. the application of exponential feeding and an alkali-addition monitoring strategies, and/or by using a three step C/N ratio approach [1]. This fermentation strategy could be implemented by using both sugar waste substrate and acetate to apply a pH-stat fed-batch feeding strategy in combination with an additional Dissolved Oxygen (DO)-dependent feed.

4. Conclusions

The development of fermentation based on wastes utilization, in agreement with circular economy perspective, can lead to a production process which can potentially reduce both environmental impact and production costs. Sugar waste and acetate utilization results in a good PHB production in *C. necator* DSM 545; still further studies must be done in order to improve PHB production, by also applying pH-stat and/or DO-stat feeding strategy, and monitoring C/N ratio.

References

- [1] Garcia-gonzalez, L., and Wever, H. De (2018). Acetic Acid as an Indirect Sink of CO₂ for the Synthesis of Polyhydroxyalkanoates (PHA): Comparison with PHA Production Processes Directly Using CO₂ as Feedstock. (2018) Appl. Sci. Vol. 8, Issue 9.
- [2] Hanisch, J., 1, 3 Marc Wa"ltermann, 1, Robenek2, 3 Horst, and Chel, and A.S. (2006). The Ralstonia eutropha H16 phasin PhaP1 is targeted to intracellular triacylglycerol inclusions in Rhodococcus opacus PD630 and Mycobacterium smegmatis mc 2 155, and provides an anchor to target other proteins Jan Ha Printed in Great Britain. Microbiol. 152, 3271–3280 3271–3280.
- [3] Kourmentza, C., Pl, J., Venetsaneas, N., Burniol-figols, A., Varrone, C., Gavala, H.N., and Reis, M.A.M. (2017). Recent Advances and Challenges towards Sustainable Polyhydroxyalkanoate (PHA) Production. Bioengineering 1–43.
- [4] Md. Salatul Islam Mozumder, Heleen De Wever, E.I.P.V., and A, L.G.-G. (2014). A robust fed-batch feeding strategy independent of the carbon source for optimal polyhydroxybutyrate production. Process Biochem. Vol. 49, Issue 3 49, 365–373.
- [5] Ryberg, M.W., Hauschild, M.Z., Wang, F., Averous-monneray, S., and Laurent, A. (2019). Resources, Conservation & Recycling Global environmental losses of plastics across their value chains. Resour. Conserv. Recycl. 151, 104459.
- [6] Shang, L., Jiang, M., and Chang, H.N. (2003). Poly(3-hydroxybutyrate) synthesis in fed-batch culture of Ralstonia eutropha with phosphate limitation under different glucose concentrations. Biotechnol. Lett. 25, 1415–1419.
- [7] Singh Saharan, B., Grewal, A., and Kumar, P. (2014). Biotechnological Production of Polyhydroxyalkanoates: A Review on Trends and Latest Developments. Chinese J. Biol. 2014, 1–18.
- [8] Uchino, K., and Saito, T. (2006). Thiolytic cleavage of Poly (3-hydroxybutyrate) with Polyhydroxyalkanoate Synthase from Ralstonia eutropha. J. Biochem. 139, 615–621 621, 615–621.
- [9] Verlinden, R.A.J., Hill, D.J., Kenward, M.A., Williams, C.D., and Radecka, I. (2007). Bacterial synthesis of biodegradable polyhydroxyalkanoates. J. Appl. Microbiol. ISSN 1364-5072 102, 1437–1449.

Monitoring and control of a bioreactor for yeast fermentation

Silvia Lisci¹, Massimiliano Grosso, Stefania Tronci^{1*}

1 Dip. Ingegneria Meccanica, Chimica e dei Materiali, Università di Cagliari, Via Marengo 2, Cagliari, Italy

**Corresponding author E-Mail: stefania.tronci@unica.it*

1. Introduction

In recent decades, biotechnological processes have shown significant growth. Although they concern different sectors (pharmaceutical, cosmetic, agro-food, biowaste treatment, etc.), they all have the cultivation of microorganisms as a common factor. Bioreactors are, in effect, the most important unit operations of biotechnological processes and the most difficult to control and monitor, being a complex combination of biological, chemical, and physical phenomena. Among the several biological processes, ethanol production through fermentation is surely one of the most investigated. Bioethanol represents an alternative to fossil fuels. It can be obtained from different sources such as agro-food residues, municipal waste, or dedicated energy crops collectively called “biomass”. Most of the worldwide production of ethanol occurs through fermentation. Although many advances have been made in ethanol fermentation technology in recent years, there are still significant challenges that need further investigations [1]. In this work, the problem of monitoring and control of a fermentation bioreactor has been addressed using a nonlinear estimator to obtain the direct control of product concentration. The proposed solution shows to be more effective than indirect temperature control [2] to reject disturbances affecting inlet composition, temperature and pH.

2. Methods

The bioreactor model used in this work is the same proposed in [2] and not reported here for brevity. The model is used as a virtual plant, and it describes the dynamic behaviour of six states, which are biomass concentration (b), ethanol concentration (p), substrate concentration (s), dissolved oxygen concentration (do), reactor temperature (T_r), and jacket temperature (T_j). Assuming that the substrate and dissolved oxygen concentration are measured online along with temperature, the proposed system is observable. It is thus possible to reconstruct all the states by using a proper estimation algorithm [3].

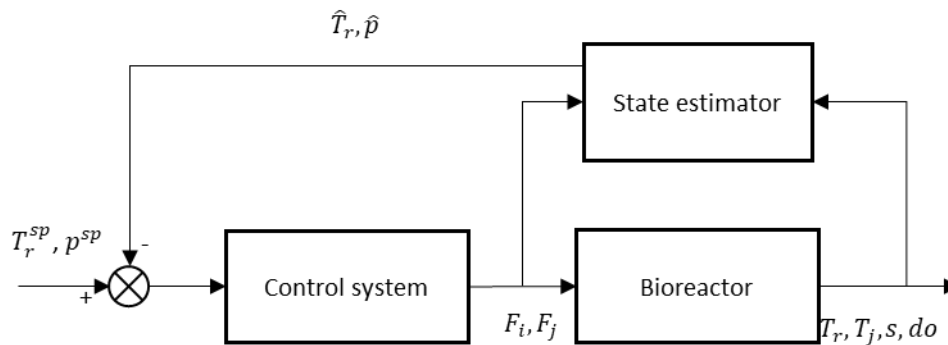


Figure 1. Control scheme for the bioreactor.

Because widely used in industry, the Extended Kalman Filter (EKF) has been used to infer ethanol composition in the bioreactor. The estimate is then used in a feedback control loop. According to previous studies [3], the estimator showed to be more robust and efficient if the ethanol concentration is not an innovated state. The dynamics of innovated $\hat{\mathbf{x}}_i = [s, b, do, T_r, T_j]$ and not innovated $\hat{\mathbf{x}}_u = [p]$ products along with the measurement processor are reported in Eq. (1-3).

$$\frac{d\hat{\mathbf{x}}_i}{dt} = \mathbf{f}_i(\hat{\mathbf{x}}_i, \hat{\mathbf{x}}_u, \mathbf{u}) + \mathbf{K}(\mathbf{y} - \hat{\mathbf{y}}), \hat{\mathbf{x}}_i(t_0) = \hat{\mathbf{x}}_{i,0} \quad (1)$$

$$\frac{d\hat{\mathbf{x}}_u}{dt} = \mathbf{f}_u(\hat{\mathbf{x}}_i, \hat{\mathbf{x}}_u, \mathbf{u}), \hat{\mathbf{x}}_u(t_0) = \hat{\mathbf{x}}_{u,0=0} \quad (2)$$

$$\mathbf{K} = \mathbf{P}(t)\mathbf{H}^T\mathbf{R}^{-1}, \dot{\mathbf{P}}(t) = \mathbf{P}(t)\mathbf{F}(t) + \mathbf{F}^T(t)\mathbf{P}(t) + \mathbf{Q}(t)\mathbf{K}(t)\mathbf{H}(t)\mathbf{P}(t), \mathbf{P}(t_0) = \mathbf{P}_0 \quad (3)$$

The control configuration is schematically reported in Figure 1. The cooling medium flowrate in the jacket (F_j) and inlet flowrate (F_i) are used as manipulated variables to control reactor temperature and product concentration. A PI algorithm is used in the control loops.

3. Results and discussion

The performance of the proposed control scheme has been evaluated for different conditions, and results are shown in Figure 2. The following variations have been introduced: decrease of specific growth rate equal to 20% (at time = 750 h), decrease of inlet substrate concentration from 60 to 40 g/l (at time = 1250) and increase of inlet temperature from 25 to 27°C (at time = 2000 h). Noise has also been introduced in the measured outputs. In all the conditions, the controlled system is able to maintain the set-points efficiently.

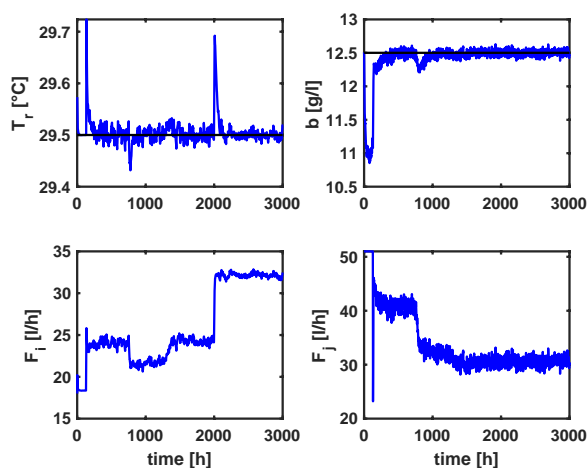


Figure 2. Temperature and biomass concentration (upper panels) manipulated inputs (lower panels). The set-points are indicated with black lines.

4. Conclusions

In this work, a state estimation and feedback control have been developed to maintain a bioreactor's desired conditions. Standard PI control algorithm is used to control reactor temperature and product concentration. The latter has been inferred by the available measurements by means of an Extended Kalman Filter. Results show that the proposed methodology can efficiently reject severe disturbances entering the system.

References

- [1] Devi, A., Singh, A., Bajar, S., Pant, D., & Din, Z. U. Ethanol from lignocellulosic biomass: an in-depth analysis of pre-treatment methods, fermentation approaches and detoxification processes. *Journal of Environmental Chemical Engineering*, 9 (2021) 105798.
- [2] Nagy, Z. K. Model based control of a yeast fermentation bioreactor using optimally designed artificial neural networks. *Chemical engineering journal*, 127 (2007) 95-109.
- [3] Lisci, S., Grosso, M., & Tronci, S. A geometric observer-assisted approach to tailor state estimation in a bioreactor for ethanol production. *Processes*, 8(4) (2020) 480.

From N₂ to cyanophycin: high-value compound production through biological nitrogen fixation in continuous systems

Giulia Trentin^{1*}, Boris Zorin², Inna Khozin-Goldberg³, Alberto Bertucco¹, Eleonora Sforza¹

1 Department of Industrial Engineering DII, University of Padova, Via Marzolo 9, 35131 Padova, Italy; *2* The Albert Katz International School for Desert Studies, Jacob Blaustein Institutes for Desert Research, Ben-Gurion University of the Negev, Sede Boqer Campus, Midreshet Ben-Gurion, 8499000, Israel; *3* The French Associates Institute for Agriculture and Biotechnology of Drylands, Blaustein Institutes for Desert Research, Ben-Gurion University of the Negev, Midreshet Ben Gurion, 8499000, Israel

*Corresponding author E-Mail: giulia.trentin@unipd.it

1. Introduction

Diazotrophic cyanobacteria have the ability to fix atmospheric nitrogen in their biomass during photosynthetic growth, so they could be a viable alternative to traditional and high energy demanding production processes, such as ammonia production [1–3]. However, photosynthetic cyanobacteria catalyse the reaction of nitrogen fixation at ambient temperature and pressure, driven by sunlight energy [4,5]. Cyanophycin is non-protein, non-ribosomally produced amino acid copolymer, composed of equimolar amounts of aspartic acid and arginine, which serves a temporary nitrogen reserve compound. The industrial application of cyanophycin is not still consolidated, but it is a promising starting point for the synthesis of many important chemicals. Industrial application focuses on its chemical derivatives, as cyanophycin can be chemically converted to poly-aspartic acid (PASP) and arginine by β -hydrolytic cleavage [6]. In this work, two diazotrophic cyanobacteria of the genus *Anabaena* were phototrophically cultivated in continuous system under N₂ fixing conditions to assess the possible stable production of cyanophycin. Indeed, *Anabaena* sp. was already cultivated in a continuous cultivation system diazotrophically, obtaining remarkable biomass productivities [7]. The effect of operating variables in continuous system as the inlet phosphorus concentration, the incident light intensity, the residence time, and the nitrogen availability, on biomass and cyanophycin productivities were investigated. In this way, it is possible to produce biomass having specific composition and constant quality over time, obtaining high productivities and, at the same time, reducing the costs associated with the process, thus developing a system compatible with large-scale production.

2. Methods

Anabaena sp. PCC 7122 (*Anabaena cylindrica*) and *Nostoc* sp. PCC 7120 were purchased from Pasteur Culture of Cyanobacteria in France. Cyanobacteria were maintained phototrophically in diazotrophic conditions at a constant temperature of 24±1°C in the BG11 medium [8], modified to remove all nitrogen compounds present. Continuous experiments were carried out in vertical flat-plate photobioreactors, irradiated by a white LED lamp. The mixing was ensured by both a stirring magnet placed at the bottom of the reactor and the bubbling of 1 L h⁻¹ of an air-CO₂ (5% v/v) mixture. Microalgae growth was monitored daily through optical density measurement. At steady state, dry cell weight was measured, and biomass composition was characterized in terms of phosphorus, nitrogen and cyanophycin internal quotas, following the protocols reported in Trentin et al. (2021) [9].

The effect of the inlet phosphorus concentration on cyanophycin productivity was investigated with both the cyanobacterial species. The residence time and the incident light intensity were kept constant, according to previous literature on cyanophycin production in continuous system [9] and on continuous cultivation of diazotrophic cyanobacteria [7]. Then, a second set of experiments was carried out with *Nostoc* sp. PCC 7120 to test the effect of the incident light intensity, the residence time, and the nitrogen availability. Each variable was varied keeping the other at a constant value, to see their effect individually. As for nitrogen solubility, it

was assessed how the pH could influence N_2 solubility in the cultivation medium. Thus, sensitivity analysis on N_2 solubility was carried out using Aspen Plus™ process simulator (V12.1).

3. Results and discussion

The effect of different inlet phosphorus concentrations on the growth of two diazotrophic species was addressed to identify which growth condition allows to obtain a higher cyanophycin productivity. For both species, the biomass concentration decreased at a decreasing inlet P concentration, whereas the cyanophycin quota increased, even if a species specificity was identified. (Figure 1).

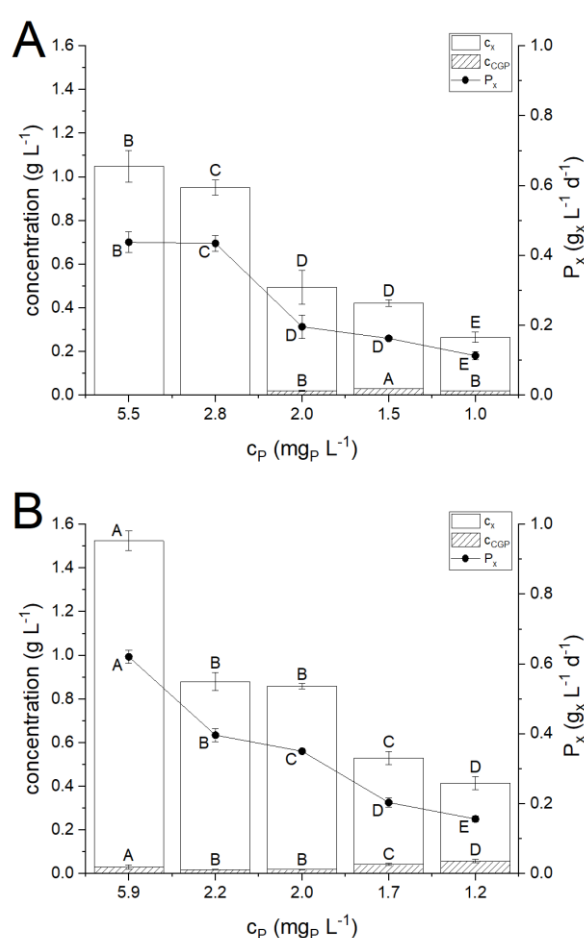


Figure 1. Steady state biomass concentration (c_x), cyanophycin concentration (c_{CGP}), biomass productivity (P_x) as function of the inlet phosphorus concentration (c_P) obtained with *Anabaena cylindrica* (panel A) and with *Nostoc* sp. PCC 7120 (panel B). Error bars represent the standard deviation of at least 4 samples for each steady state ($n \geq 4$). Statistical analysis was conducted separately for each category of data. Data that do not share a letter are significantly different. Lines are just eye guides.

As for nitrogen fixation, *Nostoc* sp. PCC 7120 was more efficient in all conditions. These preliminary results confirmed that in a continuous system the amount of phosphorus fed at the inlet was a fundamental variable when studying cyanophycin production, but also suggested that other operating variables (incident light intensity, residence time, nitrogen availability) can influence its accumulation and productivity in a continuous

system. Thus, the subsequent studies were carried out with *Nostoc* sp. PCC 7120, because in the preliminary experiments was more efficient both in biomass, nitrogen and cyanophycin productivity. In particular, a greater availability of nitrogen did not affect the internal quota of cyanophycin, but rather the growth of biomass. However, as a results, cyanophycin concentration and productivity increased. Overall, it was observed that the production of cyanophycin was strictly dependent on the concentration of phosphorus present in the culture medium: only decreasing the P quota, it was possible to measure a higher amount of cyanophycin in the biomass.

4. Conclusions

In this work, cyanophycin production by diazotrophic cyanobacteria (*Anabaena cylindrica* and *Nostoc* sp. PCC 7120) during photosynthetic cultivation was investigated in continuous experiments, with different inlet phosphorus concentration. The effect of other operating variables on biomass and cyanophycin accumulation was addressed, showing that P limitation is the main variable affecting the cyanophycin accumulation, and the internal quota of P in the biomass is the trigger for cyanophycin accumulation.

References

- [1] J. Nørskov, J. Chen, E. Al., DOE Roundtable Report, 2016.
- [2] M. Wang, M.A. Khan, I. Mohsin, J. Wicks, A.H. Ip, K.Z. Sumon, C.-T. Dinh, E.H. Sargent, I.D. Gates, M.G. Kibria, Can sustainable ammonia synthesis pathways compete with fossil-fuel based Haber–Bosch processes?, *Energy Environ. Sci.* 14 (2021) 2535–2548. <https://doi.org/10.1039/D0EE03808C>.
- [3] E. Mariani, L'industria dell'azoto, in: A. Girelli, L. Matteoli, F. Parisi (Eds.), *Trattato Di Chim. Ind. e Appl.* Vol. 1, Zanichelli, 1969: pp. 521–590.
- [4] N. Rascio, N. La Rocca, *Biological Nitrogen Fixation* ☆, Elsevier Inc., 2013. <https://doi.org/10.1016/B978-0-12-409548-9.00685-0>.
- [5] L.J. Stal, Nitrogen Fixation in Cyanobacteria, *ELS.* (2015) 1–9. <https://doi.org/https://doi.org/10.1002/9780470015902.a0021159.pub2>.
- [6] J. Du, L. Li, S. Zhou, Microbial production of cyanophycin: From enzymes to biopolymers, *Biotechnol. Adv.* 37 (2019). <https://doi.org/10.1016/j.biotechadv.2019.05.006>.
- [7] E. Barbera, A. Grandi, L. Borella, A. Bertuccio, E. Sforza, Continuous cultivation as a method to assess the maximum specific growth rate of photosynthetic organisms, *Front. Bioeng. Biotechnol.* 7 (2019) 1–12. <https://doi.org/10.3389/fbioe.2019.00274>.
- [8] R. Rippka, J.J.B.W. Deruelles, J.B. Waterbury, M. A. Herdman, R.Y. Stanier, *Generic Assignments, Strain Histories and Properties of Pure Cultures of Cyanobacteria*, *Microbiology-Sgm.* 111 (1979) 1–61. <https://doi.org/10.1099/00221287-111-1-1>.
- [9] G. Trentin, V. Lucato, E. Sforza, A. Bertuccio, Stabilizing autotrophic cyanophycin production in continuous photobioreactors, *Algal Res.* 60 (2021) 102518. <https://doi.org/10.1016/j.algal.2021.102518>.

Acknowledgements

The authors greatly appreciated the financial support from the Italian Ministry of Foreign Affairs and International Cooperation (MAECI) under award protocol number MAE01432042020-12-03, CUP C99C20001980005

Stabilization and characterization of microbial strains in liquid formulation

Chiara Bufalini^{1*}, Roberta Campardelli¹, Pier Francesco Ferrari^{1,2}, Domenico Palombo², Patrizia Perego¹

1 Department of Civil, Chemical and Environmental Engineering, University of Genoa, via Opera Pia, 15, 16145, Genoa, Italy

2 Department of Surgical and Integrated Diagnostic Sciences, University of Genoa, viale Benedetto XV, 6, 16132, Genoa, Italy

**Corresponding author E-Mail: chiara.bufalini@edu.unige.it*

1. Introduction

Emulsions are temporarily stable mixture of two immiscible fluids, such as oil and water, which are mixed using mechanical shear and surfactant. One phase, called dispersed phase, is mixed in the other, called the dispersing phase, in the form of droplets. The formation of emulsion requires surfactants which have the role of reducing the interfacial tension and facilitate dispersion of immiscible liquids [1]. There are different type of emulsifier and it is fundamental the choice of the correct one, not only for the formation of emulsion but also for its long-term stability. Emulsions can be conveniently classified according to the relative spatial distribution of liquid phases and the different type are: simple emulsion, like *oil-in-water* and *water-in-oil* type, and double emulsion, such as *water-in-oil-in-water* and *oil-in-water-in-oil* type. In particular, double emulsions have several advantages respect to single emulsion, such as carrying, protecting, or controlling the release of active ingredients [2]. Emulsions are used in many industrial sectors and are widely used in the food, pharmaceutical and cosmetic industries [3].

One of the most common applications of emulsions is the encapsulation of bioactive components, thanks to the compatibility with a wide range of lipophilic, hydrophilic and amphiphilic molecules, the high efficiency encapsulation and possibility of controlled release [4]. In addition to bioactive components, microorganisms can be encapsulated in emulsion with the objective of stabilization and protection from external environment [5]. One of the most application is encapsulation of probiotic bacteria for food applications [6]. Therefore, mainly strains with food application have been encapsulated and microorganisms with different applications have rarely been studied.

Therefore, this study is based on the encapsulation of different microbial strains, selected for improvement of soil microflora, in double emulsion of the *water-in-oil-in-water* ($W_1/O/W_2$) type, where the microbial strains in its growth solution constitute the internal phase of the emulsion (W_1). The effectiveness of this encapsulation technique is evaluated by analyzing the droplet size distribution, morphology of the emulsion, vitality and concentration of microorganisms within the emulsion.

2. Methods

Selected microorganisms consist of: microorganism belonging to the genus *Bacillus spp.* acronym B1, *Streptomyces spp.* acronym S1, *Pichia spp.* acronym P1 and 2 microorganisms belonging to the genus *Trichoderma spp.* acronym T1 and T2. Besides the selected strains, the emulsion is composed of soybean oil and water with a non-ionic surfactant soluble in water phase.

All microorganisms were stabilized individually in double emulsions of water-in-oil-in-water type ($W_1/O/W_2$) using a rotor-stator type emulsifier (Silverson Machines Ltd, Chesham, England). For the stabilization of the microorganism in double emulsion are necessary two steps: production of primary emulsion W_1/O setting agitation at 6000 rpm for 3 minutes and then production of secondary emulsion $W_1/O/W_2$ with 7000 rpm for

5 minutes. For the comparative study empty emulsion was produced, indicated as E, with the same procedure, but in this case the microorganism is replaced by deionized water.

The characterization of double emulsion after production has been done through the following analyses: analysis of morphology and homogeneity of the emulsion droplets by optical microscope (Olympus IX51), particle size analysis using the laser diffraction granulometer (Mastersizer 3000, Alphatest, Cinisello Balsamo, Italy) and study of microbial viability by cell seeding on an agar plate.

3. Results and discussion

Microorganisms were stabilized in W1/O/W2 emulsion based on soybean oil. The same conditions of emulsion procedure were adopted for all the microorganisms. All emulsions produced were homogeneous with milk white appearance. They were observed under an optical microscope to see the morphology soon after production (Figure 1). As can be seen from the microscope images, both empty emulsion and loaded emulsions are well formed with non-coalescent droplets. Furthermore, the morphology of loaded emulsions is similar to that of the empty emulsions, indicating that the microorganisms does not interfere with the formation of the emulsion. It is also confirmed by the average diameter of the various emulsions (Figure 2). In fact, it can be seen that emulsions have a uniform PSD, without particular difference between empty and loaded emulsions, and it is about 5 μm .

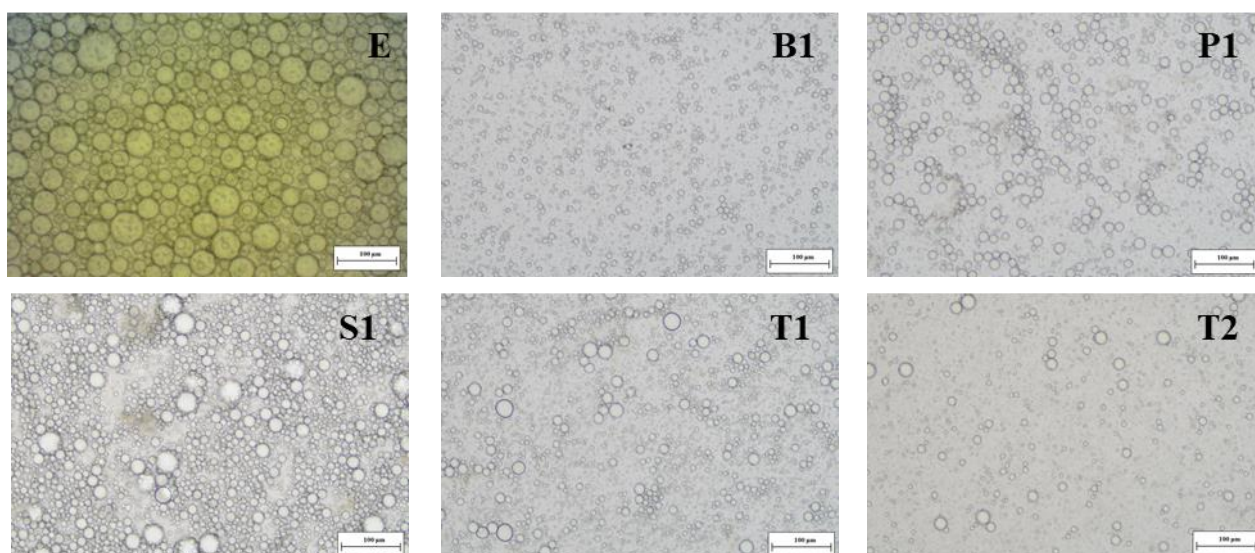


Figure 1. Optical microscope image of empty emulsion E and emulsion of strains B1, P1, S1, T1 and T2.

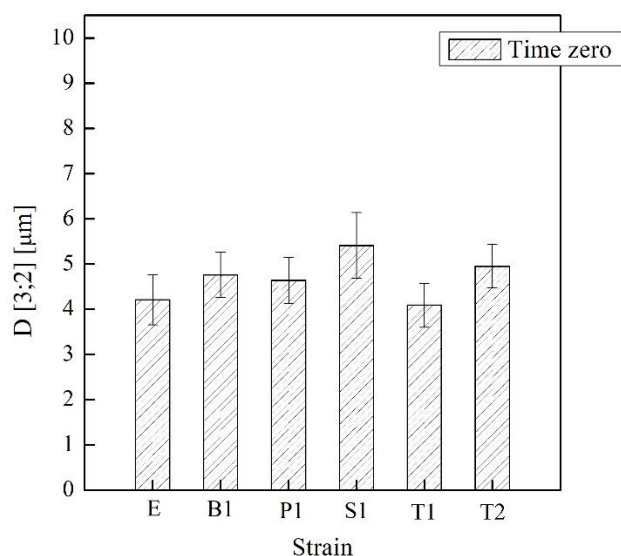


Figure 2. Average diameter and standard deviation of empty emulsion and emulsion of strains B1, P1, S1, T1 and T2 at time zero.

The study of microbial vitality of strains after encapsulation process was performed and the value of CFU/mL with standard deviation at time zero are reported in the histogram (Figure 3). As can be seen, all microorganisms are viable in double emulsion, with a concentration more than 10^6 . There is a drop in concentration from stock solution, that represents the starting microorganism in growth medium, to emulsion, that can vary from 10^1 to 10^3 . This decrease is probably due to the dilution factor and the loss of biomass. The vitality of strains is also confirmed by their appearance on the plate (Figure 4). In fact, each strains develop the typical morphology.

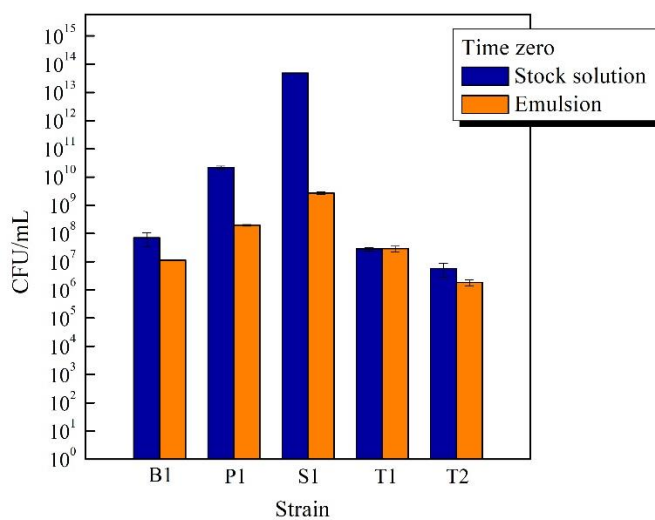


Figure 3. Histogram of CFU/mL and standard deviation at time zero for stock solution and emulsion of strains B1, P1, S1, T1 and T2 at time zero.

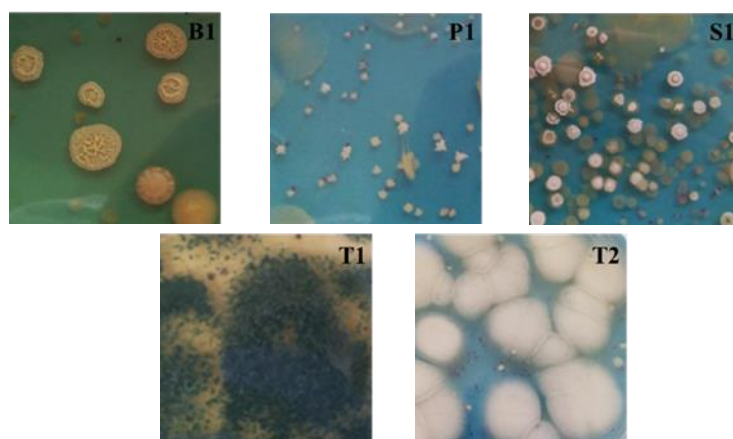


Figure 4. Detail of agar plate of emulsions containing B1, P1, S1, T1 and T2 strains at time zero.

Subsequently, the emulsions were analyzed over time in order to analyze the stability. From the results obtained it was possible to observe a good physical and microbial stability up to 360 days from production both for the sample stored at 4 ° C and at room temperature.

4. Conclusions

The aim of this work was to study the encapsulation of different strains in emulsion. From the obtained results, it can be verified that the emulsions are well formed and uniform, with the same average diameter of approximately 5 μm . Furthermore, the viability of all strains after encapsulation is guaranteed. There is only a decrease in concentration from stock solution to emulsion was found, which is attributable to the dilution factor and biomass losses. Thanks to these good results, future studies on the evaluation of the physical and microbial stability of these emulsions can be carried out to understand the shelf life of this formulation.

References

- [1] S.N. Kale, & S.L. Deore (2017). Emulsion Micro Emulsion and Nano Emulsion: A Review. *Sys Rev Pharm.*, 8(1), 39-47.
- [2] G. Muschiolik & E. Dickinson (2017). Double Emulsions Relevant to Food Systems: Preparation, Stability, and Applications. *Compr. Rev. Food Sci. Food Saf.*, 16, 532-555.
- [3] D.J. McClements (2016). *Food Emulsions: Principles, Practices, and Techniques*, Third Edition. Taylor & Francis Group.
- [4] D.J. McClements, E.A. Decker, Y. Park & Y. Weiss (2009): Structural Design Principles for Delivery of Bioactive Components in Nutraceuticals and Functional Foods. *Crit Rev Food Sci Nutr*, 49(6), 577-606.
- [5] N.S. Mohd Isa, H. El Kadri, D. Vigolo, & K. Gkatzionis (2021). Optimisation of bacterial release from a stable microfluidic-generated water-in-oil-in-water emulsion. *RSC Adv.*, 11, 7738-7749.
- [6] L. Wang, M. Song, Z. Zhao, X. Chen, J. Cai, Y. Cao, Y. & J. Xiao (2020). *Lactobacillus acidophilus* loaded pickering double emulsion with enhanced viability and colon-adhesion efficiency. *LWT- Food Sci Technol*, 121, 108928.

Comparison of kinetic models for *Chlorella vulgaris* growth in mixotrophic culture

Shabnam Mirizadeh*, Alessandro Alberto Casazza, Attilio Converti

Department of Civil, Chemical and Environmental Engineering (DICCA), University of Genoa, Via Opera Pia 15,
16145 Genoa, Italy

*Corresponding author E-Mail: shabnam.mirizadeh@edu.unige.it

1. Introduction

In the past few years, microalgae have become a promising candidate for large-scale biodiesel production, which is a solution for carbon dioxide emissions and energy shortages [1]. Despite many advantages, microalgae biodiesel production has not yet been commercialized due to low lipid productivity and the high cost of feedstock compared to diesel produced from fossil fuels [2]. Furthermore, biodiesel production from microalgae is highly dependent on the availability of biomass and the scale-up process, which must be optimized to reduce costs. Kinetic models simplify designing a bioreactor, controlling microbial processes, and predicting their behavior more easily than laboratory experiments [3]. Few reports are available on kinetic modeling of algae growth and lipid production under mixotrophic conditions. The Luedeking-Piret equation can adequately explain microalgae growth kinetics. It is an unstructured model, and growth and non-growth related contributions are combined towards product formation [4]. In this study, growth and substrate consumption kinetics of *Chlorella vulgaris* were modeled according to the distinguished Luedeking-Piret mathematical model with four different kinetics of Monod, Logistic, Tessier, and Bolton. Different parameters of K_S , K_P , μ_{max} , $Y_{X/S}$, $Y_{P/S}$, α , and β were estimated to obtain the most meaningful results and the most efficient model to describe growth, lipid production, and substrate consumption.

2. Methods

C. vulgaris was grown in a synthetic medium with 480 mg L⁻¹ COD (chemical oxygen demand), 200 mg L⁻¹ TN (total nitrogen), and 14 mg L⁻¹ TP (total phosphorus) for 12 days. Samples of the culture were centrifuged, and supernatants were analyzed for COD, TN, and TP [5]. Total lipids were determined according to the modified Bligh and Dyer method [6].

The growth, product, and consumption of substrates (COD, TN, and TP) were predicted according to equations (1), (2), and (3). Equations (2) and (3) are known as Luedeking-Piret equations.

$$\frac{dX}{dt} = \mu X \quad (1)$$

$$\frac{dP}{dt} = \alpha \left(\frac{dX}{dt} \right) + \beta X \quad (2)$$

$$-\frac{dS}{dt} = \frac{1}{Y_{X/S}} \left(\frac{dX}{dt} \right) + mX + \frac{1}{Y_{P/S}} \left(\frac{dP}{dt} \right) \quad (3)$$

where X is the biomass concentration (g L⁻¹), t is the growth time (days), μ is the specific growth rate (day⁻¹), P is the lipid concentration (g L⁻¹), α is the lipid formation coefficient, and β (day⁻¹) a non-growth correlation coefficient, S is the concentration of rate-limiting substrate (COD, TAN, and TP) (g L⁻¹), $Y_{x/s}$ is the growth yield coefficient; $Y_{p/s}$ is the lipid yield coefficient, m is the maintenance coefficient (day⁻¹). These parameters are correlated with biomass production rate (dX/dt), and therefore, solving them simultaneously results in more accurate results. The mentioned growth kinetic models are used to determine μ . The ordinary differential equations were solved by MATLAB software, and the predicted results were compared with experimental data.

3. Results and discussion

The Monod equation for phosphorus, which has the lowest concentration relative to COD and nitrogen, has calculated the lowest μ_{\max} (0.87 d^{-1}), which is not valid enough to determine the correlation coefficient R^2 (0.72). This model has reached a suitable R^2 for COD and nitrogen and has calculated a significant μ_{\max} (1.48 d^{-1}). Due to the exponential term, the Tessier equation includes the effect of severe inhibition of the substrate. However, when the substrate concentration is low in the medium, the comprehensiveness of the model in determining the kinetic parameters is well estimated, and the logical values for the kinetic parameters are calculated. The logistic equation in determining biomass growth is independent of the effect of substrate and product. Since the substrate concentrations were low and within the standard range, it is natural that no growth inhibition was observed in the medium. Compared to other models, this model best fits experimental data ($R^2 > 0.98$) and predicts the highest $Y_{X/S}$ (137.7 g/g) for phosphorus. The Bolton equation is independent of the concentration of the substance and includes the inhibitory parameter of the product. This model calculates the lowest μ_{\max} compared to other models. When the microalgae are in the growth phase, there is little change in the intracellular lipid content. As the biomass concentration increases, the amount of lipid in the medium also increases. Therefore, in reality, the product does not act as a deterrent to microalgae growth. In general, in the models that strongly (or even relatively) attributed the inhibition to the initial concentrations of the substance, there was no good agreement in determining the concentration of biomass or substrate with its practical reality.

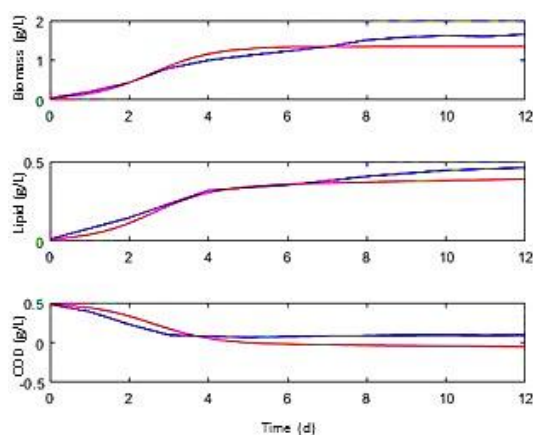


Figure 1. Fitting of biomass concentrations, lipid production and COD on logistic model (Blue diagrams are experimental data)

4. Conclusions

Examining the obtained results based on the performed modeling, it was found that the logistic model with a fitting coefficient of 0.98 has a good prediction. The greater complexity of the equations and the increase of the effective parameters will not increase the accuracy of their predictions but will sometimes deviate from the correct estimation.

References

- [1] A. Raheem, P. Prinsen, A.K. Vuppaladadiyam, M. Zhao, R. Luque, J. Clean. Prod. 181 (2018) 42–59.
- [2] K.T. Sukahara, S.S. Awayama, J. Japan Pet. Inst. 5 (2005) 251–259.
- [3] D. Surendhiran, M. Vijay, B. Sivaprakash, A. Sirajunnisa, 3 Biotech. 5 (2015) 663–669.
- [4] G. Halder, S.H. Dhawane, D. Dutta, S. Dey, Sustain. Energy Technol. Assessments. 18 (2016) 16–33.
- [5] E.W. Rice, R.B. Baird, A.D. Eaton, L.S. Clesceri, Standard Methods for the Examination of Water and Wastewater, 22 ed., American Public Health Association, Washington DC, 2012.
- [6] B.E. Kates, M. Volcani, Biochim. Biophys. Acta - Lipids Lipid Metab. 116 (1966) 264–278.

Electrochemically-steered processes for polyhydroxyalkanoates production with mixed microbial cultures

Gaia Salvatori¹, Matteo Di Luzio¹, Angela Marchetti¹, Ottavia Giampaoli^{2,3}, Fabio Sciubba^{2,3}, Alfredo Miccheli^{2,3}, Marianna Villano^{1*}

¹ Department of Chemistry, Sapienza University of Rome, P.le Aldo Moro 5, 00185 Rome (Italy);

² NMR-Based Metabolomics Laboratory, Sapienza University of Rome, P.le Aldo Moro 5, 00185 Rome (Italy);

³ Department of Environmental Biology, Sapienza University of Rome, P.le Aldo Moro 5, 00185 Rome (Italy)

* E-Mail: marianna.villano@uniroma1.it

1. Introduction

Polyhydroxyalkanoates (PHAs) are a family of biologically synthesized polyesters that are attracting considerable attention due to their chemical and physical properties similar to those of conventional plastics. Furthermore, PHAs can be considered three times bio since they can be produced from renewable feedstocks and are completely biodegradable in the environment under both aerobic and anaerobic conditions [1].

Currently, PHA production at industrial scale is based on pure culture processes and this involves high management costs due to the use of well-defined substrates and the maintenance of sterile conditions [2]. In order to limit the production costs, processes based on the use of waste organic substrates and mixed microbial cultures (MMC) are under investigation and are being tested at pilot scale. These are multistage processes that include, among the others, a preliminary acidogenic fermentation (AF) step of the substrate, followed by aerobic steps for MMC selection and enrichment in PHA-storing microorganisms and polymer accumulation. Here, an innovative electrochemically based approach to optimize each stage of the MMC-PHA production process, from feedstock AF to PHA production, has been investigated. As for AF, the introduction of a polarized electrode in the reaction medium represents an interesting and promising tool to control the spectrum of attainable products in terms of both composition and concentration. The process is referred to as electro-fermentation (EF) [3]. Here, EF has been investigated by supplying ¹³C-labelled glucose to anaerobic sludge in presence of a graphite electrode polarized at -0.70 V with respect to the Standard Hydrogen Electrode (SHE). Also, based on literature evidences reporting the enhancement of PHA production by pure cultures in bioelectrochemical systems [4-5], this study tested the PHA production capacity of an activated sludge in presence of a polarized electrode at +0.20 V and -0.20 V (vs. SHE).

2. Methods

2.1 Bioelectrochemical reactors configuration

Two chamber (H-type) cells have been used to perform all the tests herein described. The cells consisted of two gastight borosilicate glass bottles (each with a total volume of about 270 mL), functioning as the working- and counter- electrode chamber, respectively. A graphite rod electrode (10 cm length, 5 mm diameter, Sigma-Aldrich, Italy) equipped with a titanium wire (0.81 mm, Sigma-Aldrich, Milan, Italy) was placed in each chamber and a KCl saturated Ag/AgCl reference electrode (+199 mV vs. SHE) was also provided in the working- electrode chamber. The two chambers were separated by a Nafion[®] 117 proton exchange membrane (PEM) with a 3 cm² cross-sectional area. The working electrode was controlled by means of a potentiostat (BioLogic VSP-300) at -0.70 V, in the EF experiments with anaerobic sludge, and at +0.20 or -0.20 V when activated sludge was used as inoculum. All potential values are here reported with respect to SHE.

2.2 Analytical Methods

Volatile suspended solids (VSS) were measured according to Standard Methods (APHA, 2005). In the experiments with labelled glucose, acids production was monitored through nuclear magnetic resonance (NMR) spectroscopy, the elective technique for the C-labelled analysis [6].

3. Results and discussion

In this study, EF experiments have been performed inoculating the working chamber with anaerobic sludge at a final biomass concentration of 0.20 gL^{-1} (measured as VSS). The electrode potential, functioning as cathode, was fixed at -0.70 V and a synthetic mixture of ^{13}C -labelled glucose, acetate and ethanol was used as organic substrate. Tests were carried out in duplicate and compared to Open Circuit Potential (OCP) experiments, performed under identical conditions but in the absence of electrode polarization. Upon glucose depletion, preliminary analyses highlighted a different acids redistribution (with main reference to propionic and butyric acids) between EF and OCP experiments (Figure 1A). This finding is particularly relevant in the frame of the PHA production process, since a different ratio between acids with an odd and even number of C atoms affects the composition of the produced polymer and, in turn, its final application. As for the bioelectrochemical assisted MMC-PHA production, preliminary tests were conducted in the H-type cells wherein the working chamber was inoculated with activated sludge and operated under microaerophilic conditions. A synthetic mixture of acetic and propionic acids was used as substrate and the working electrode was polarized at $+0.20$ and -0.20 V . The electrode potential in OCP experiments decreased over time up to about 0 V , that is an intermediated value between those controlled with the potentiostat (Figure 1B). A little production of PHA was detected in all investigated conditions, likely due to the fact that the activated sludge was not previously enriched in PHA-storing microorganisms. Therefore, further experiments with selected MMC are ongoing, in order to gain a deeper insight on the effect of the polarized electrode on PHA synthesis.

4. Conclusions

This study deals with the possibility to use the bioelectrochemical approach to control the performance of a multistage MMC-PHA production process. EF preliminary experiments revealed a change in the distribution of organic acids with respect to OCP tests. This finding is particularly interesting, since the acids mixture affects the PHA production and composition in the following stages of the process. The use of a polarized electrode to directly control the polymer yield and composition (independently from the acids composition) in the aerobic stages of the MMC-PHA production process requires further investigation.

References

- [1] D. Jendrossek, R. Handrick, *Annu. Rev. Microbiol.* 56 (2002) 403–432.
- [2] M. Villano, F. Valentino, L. Martino, M. Scandola, M. Majone, *N. Biotechnol.* 31 (2014) 289–296.
- [3] M. Villano, P. Paiano, E. Palma, A. Miccheli, M. Majone, *ChemSusChem* 10 (2017) 3091–3097.
- [4] K. Nishio, Y. Kimoto, J. Song, T. Konno, K. Ishihara, S. Kato, K. Hashimoto, S. Nakanishi, *Environ. Sci. Technol. Lett.* 1 (2013) 40–43.
- [5] S. Srikanth, R. Venkateswar, M. Venkata, *Bioresour. Technol.* 125 (2012) 291–299.
- [6] D. Goritetti, E. Zanni, C. Palleschi, M. Delfini, D. Uccelletti, M. Saliola, C. Puccetti, A.P. Sobolev, L. Mannina, A. Miccheli, *Biochim. Biophys. Acta Gen. Subj.* 1850 (2015) 2222–2227.

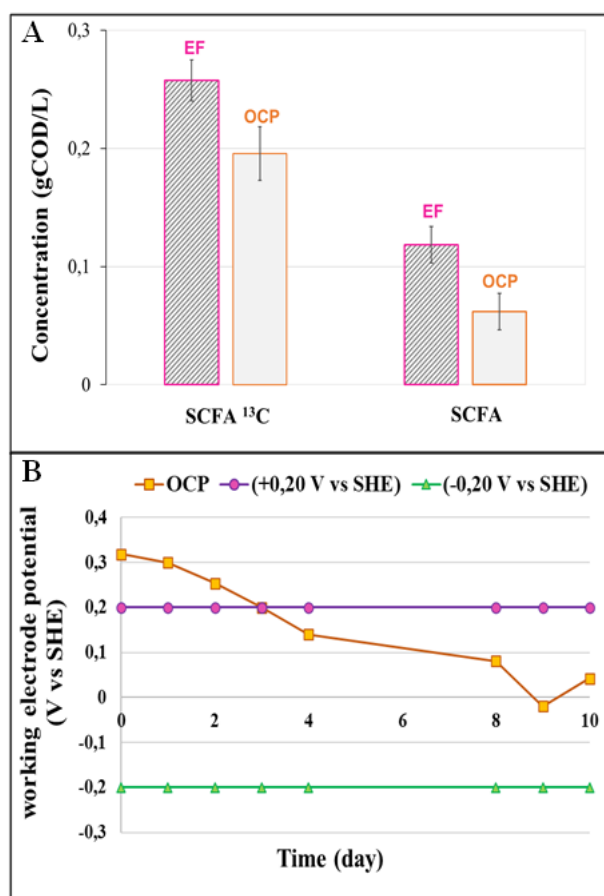


Figure 1. concentrations of short chain fatty acids (SCFA) determined by H-NMR (A); Trend of the electrode potential in experiments performed with activated sludge (B).

Scale up of a dechlorinating microbial consortium based on chemostat approach

Edoardo Dell'Armi¹, Marco Zeppilli, Mauro Majone, Marco Petrangeli Papini

1 Department of Chemistry, "Sapienza" University of Rome, P.zale Aldo Moro,5, 00185, Rome, Italy;

**Corresponding author E-Mail: edoardo.dellarmi@uniroma1.it*

1. Introduction

Chlorinated aliphatic hydrocarbons (CAHs) (eg Perchloroethylene (PCE), Trichloroethylene (TCE)) are organic compounds in which the chlorine atoms are directly bound to the carbon skeleton. Due to their peculiar chemical-physical properties, chlorinated solvents have been widely used for many industrial activities. The widespread utilization and the improper storage and disposal have made the CAHs ubiquitous pollutants of various types of environmental matrices [1]. Very often these matrices are remediate using technologies that exploit chemical-physical treatment technologies, even if in recent years are gaining the scientific community interest the technologies that utilize the microbial consortia naturally present in the contaminated matrices [2]. One of these technologies can take advantage of in situ reduction through a reaction called reductive dechlorination [3]. This is a reaction in which molecular hydrogen provides the reducing power to reduce the halogenated molecule. This study reports the increasing of the volume of a dechlorinating biomass with the chemostat approach in order to obtain a larger volume of active consortia with an high concentration of genes.

2. Methods

The scale up activity was carried out by PCE fed dechlorinating anaerobic culture, which was composed of 75% of *D. mccaryi*. Raw data of the 16S rRNA gene amplicon se-quencing of the consortium is available at the DDBJ/ENA/GenBank under the BioProject PRJNA705054 (SRA: SRX10172732). The anaerobic dechlorinating consortium used as inoculum a 150 mL PCE-fed enriched culture acclimated on lactate as electron donor and maintained under fill-and-draw conditions with a hydraulic retention time (HRT) of 30 days. The dechlorinating culture maintenance has been performed by the periodic feeding of TCE (0.5 mM) and a lactate 5 mM solution as hydrogen source through electron donor. Before each new feeding, any organic volatile metabolites were removed by flushing the liquid phase with a mixture of N₂/CO₂ (70:30 % v/v) which ensured the anaerobic environment necessary to the dechlorinating microorganisms. The scaled-up tank was constituted by a 25 L glass tank sealed with a rubber cap and provided with three glass tube for the liquid phase and gas phase sampling (Figure 1). he 25 L tank was provided with an internal recirculation loop by using a membrane pump which recirculate the liquid phase to avoid mass transfer limitation. The 25 L bioreactor was operated with the same HRT of 30 days which consists in the weekly substitution of 6 L of liquid phase with fresh mineral medium while the TCE and lactate concentration were maintained at 0.5 mM. During the volumetric increase of the liquid phase, the headspace was filled with a gas mixture of N₂/CO₂ (70:30 % v/v).

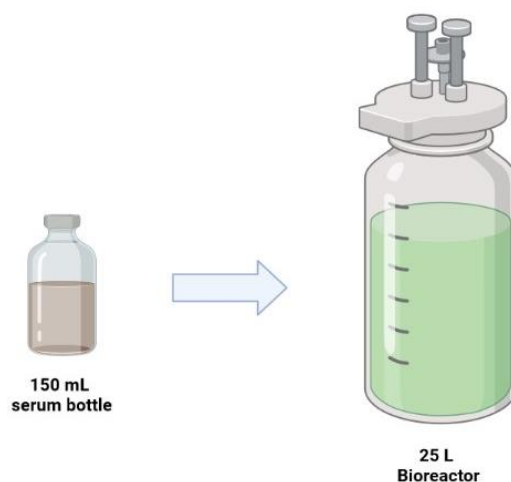


Figure 1. Schematic representation of the scale up activity

3. Results and discussion

The increase of the biomass volume with the chemostat approach had reported a good capability of the biomass to fulfill the PCE reductive dechlorination. After a small period of acclimatation the biomass gained the capability to completely reduce PCE in five days with the production of only vinyl chloride and ethylene with a concentration of 0.32 ± 0.03 mM and 0.2 ± 0.1 mM (fig2). The reductive dechlorination reduction rate resulted 0.1 mmol/L*d and the total amount of spiked PCE was utilized for the biomass growth as indicated by the mass recovery balance higher than the 95%.

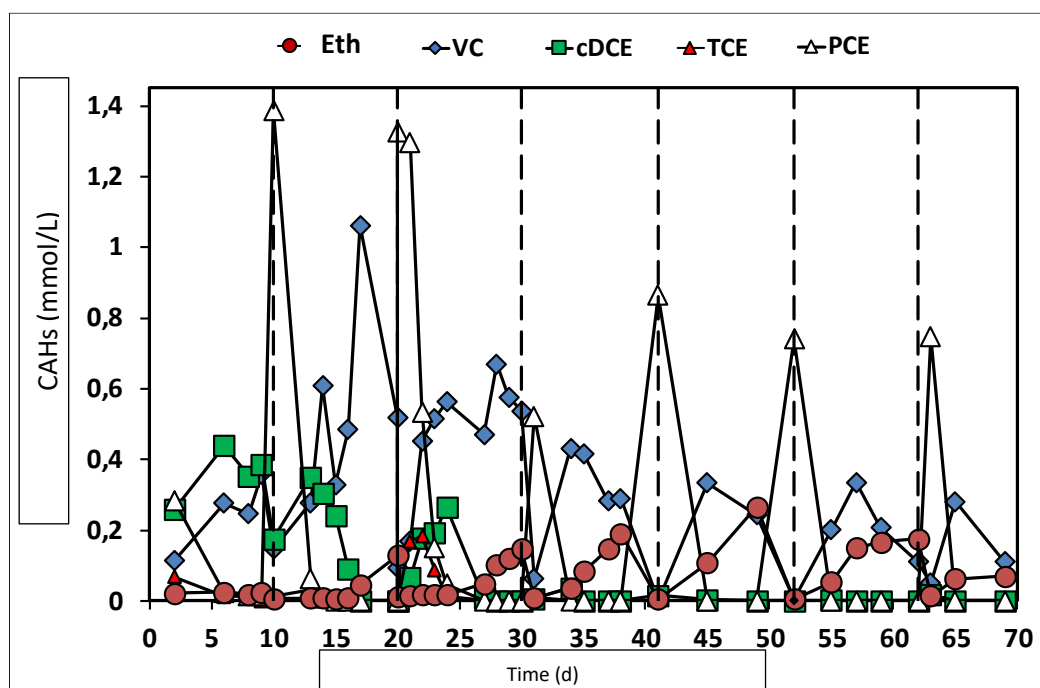


Figure 1. Time course of reductive dechlorination reaction in the 25L biological reactor

4. Conclusions

After the good performances offered by this consortia augmentation this biomass incrementation has allowed the inoculation and the biofilm formation on the electrodic surface on a 400 L bioelectrochemical reactor for a field test on a real contaminated site situated in northern Italy.

Acknowledgements

This project has received funding from the European Union's Horizon 2020 research and innovation program under grant agreement No 826244-ELECTRA.

Bibliography

- [1] R.E. Doherty, Environ. Forensics. 1 (2000) 69–81.
- [2] M.P. Papini, M. Majone, F. Arjmand, D. Silvestri, M. Sagliaschi, S. Sucato, E. Alesi, E. Barstch, L. Pierro, Chem. Eng. Trans. 49 (2016) 91–96.
- [3] M.M. Rossi, E. Dell'Armi, L. Lorini, N. Amanat, M. Zeppilli, M. Villano, M. Petrangeli Papini, Bioengineering. 8 (2021) 109.

3D Bioprinting for the production of a perfusable vascularized model of a cancer niche

Federico Maggiotto^{1,2}, Lorenzo Bova^{1,2}, Elisa Cimetta^{1,2*}

1 University of Padua, Department of Industrial Engineering (DII) - Via Marzolo 9, 35131 Padova, Italy;

2 Fondazione Istituto di Ricerca Pediatrica Città della Speranza (IRP) - Corso Stati Uniti 4, 35127 Padova, Italy.

**Corresponding author E-Mail: elisa.cimetta@unipd.it*

1. Introduction

The use of tumor models is increasingly advancing in the world of research. In particular, with the advent of three-dimensional (3D) cell cultures, new possibilities for investigation have opened up, making it possible to study tumor behavior in a more realistic environment that closely resembles cell physiology. However, one major limitation of 3D cell cultures is the size of the construct itself. Studies have shown that the limit of oxygen and nutrient diffusion in living tissues is about 100-200 μm - of course depending on the type of tissue analyzed [1]. Therefore, if the size of the 3D model exceeds this limit, it is necessary to employ techniques to simulate the behavior of a vascular network. We here propose to develop 3D models of cancers with a proper vascularization ensuring correct and uniform distribution of nutrients, especially in the bulk of the structure. Moreover, to represent in a more realistic way such a vascular channel, a method of endothelialization is here proposed, aimed at recreating endothelial coating of the walls of the channel [2].

3D cell cultures are mainly realized by exploiting 3D bioprinting techniques, through which structures are built by depositing biomaterials following precise instructions provided by the operator. Among the different possibilities available on the market today, we here used an extrusion 3D bioprinter (BioX; *Cellink*), which allows to sequentially extrude up to three different biomaterials, controlling their temperature throughout the process. Specifically, the structures are printed layer-by-layer, alternating - when necessary - the different biomaterials involved, thereby requiring each layer to act as a support for the following ones. The choice of materials and the geometry of the construct therefore play a key role in achieving the desired result, leading not only to proper cell attachment and proliferation but also providing the opportunity for their differentiation.

The creation of vascularized structures can be realized by exploiting the technique of sacrificial bioprinting, according to which two different materials are used: a matrix within which the cells are encapsulated and a sacrificial material that will be removed, leaving an empty channel in its place [3-4]. Several materials were tested in this study, identifying gelatin methacrylate (GelMA) and Pluronic F-127 (PLU) as the best candidates to be used as matrix and sacrificial ink, respectively [2].

2. Methods

Hydrogels are the most common choice as bioinks, so the first step of the work is the choice of the ideal materials. For our project, to create a structure that contains a vascular network exploiting sacrificial bioprinting, it is necessary to use two different hydrogels: one that acts as a matrix and one that can be easily removed - for example exploiting its thermoreversibility - to leave empty channels inside the other one. The hydrogel chosen as matrix is an 8% w/v methacrylate gelatin (GelMA) which is biocompatible, biodegradable and photo-crosslinkable in the presence of a crosslinking agent, such as Irgacure 2959. GelMA is a semi-synthetic hydrogel composed of gelatin and methacrylic anhydride: gelatin alone can form physical gels only at specific temperatures and concentrations; the addition of methacrylic anhydride has therefore the purpose of functionalizing the lysines of gelatin to chemically modify the polymer and support photo-crosslinking.

The sacrificial ink, Pluronic F-127 (PLU), is a synthetic copolymer that exhibits opposite thermoreversibility to GelMA: it liquefies at temperatures below 15°C while it gels at higher temperatures. In the world of

bioprinting this material is known for its excellent printability - especially at high concentrations (40 % w/v) - and it's often used as a sacrificial material.

Hydrogels are synthesized in the laboratory from raw materials: GelMA is made from gelatin and methacrylic anhydride through a reaction at controlled pH and temperature [5], while Pluronic F-127 is prepared by mixing the desired amount - to obtain the optimal concentrations - in a biocompatible solvent, such as 1xPBS (Phosphate-Buffer Saline) or water.

The focus then shifts on the design of a structure that can be fabricated using 3D bioprinting and that is suitable and efficient for the intended purpose. Using AutoCAD® software, we designed several structures each aimed at simulating different scenarios: a single channel, a serpentine, and a two-chamber structure that can accommodate multiple cell lines (Figure 1). To ensure efficient delivery of nutrients to all cells within the hydrogel, a vascular network was proposed consisting of a channel that crosses the entire structure covering as much surface area as possible.

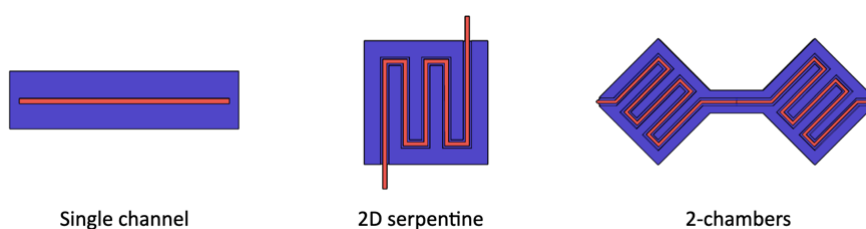


Figure 1. Different structure designs; in blue the matrix (GelMA), in red the sacrificial ink (PLU).

Once the desired structure is bioprinted, the PLU is liquefied by placing the entire construct at 4°C for 5 minutes, after which it is removed by injecting cold 1xPBS from one end of the channel.

The final aim is then to connect the structure to a hydraulic circuit in such a way as to ensure the transport of nutrients and removal of waste in a continuous way. To do this, a perfusion circuit is used in which the nutrients are continuously transported at a fixed flow rate by means of a peristaltic pump: the "fresh" medium is taken from a reservoir, injected into the structure by means of needles, collected at the outlet and returned to the reservoir.

3. Results and discussion

The method used to create the structures is multi-material bioprinting: the scaffolds are created layer-after-layer, alternating the printing of the different materials. Alternatively, the casting/bioprinting method can be employed, according to which a first layer of GelMA is cast into a mold, the PLU is bioprinted on top of it and finally the structure is completed with an additional layer of GelMA. The two methods were shown to be equivalently valid, leading to similar results. Figure 2 shows images of the different structures obtained through the casting/bioprinting method.



Figure 2. Bioprinted structures. The structures are contained in a 3D bioprinted silicone mold (SE-1700) to aid in needle placement at the ends of the channel.

The perfusion circuit is made up from a peristaltic pump through which two hoses are guided: one that transports the nutrients from a reservoir to the inlet of the vascular channel and the other that collects them after they have passed through the channel and returns them to the reservoir (Figure 3).

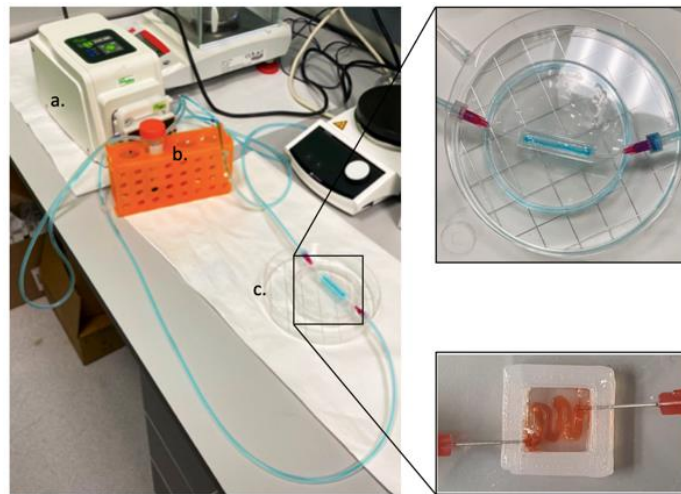


Figure 3. Perfusion circuit: a) peristaltic pump (Dülabo PLP 800); b) reservoir; c) vascularized structure.

The biological tests that have been performed are mainly two: endothelialization and perfusion.

The first are aimed at simulating the formation of a capillary, using endothelial cells (HUVECs) and mesenchymal stem cells (MSCs) to coat the surface of the vascular channel in a monolayer (Figure 4). To achieve this, once the vascularized structure is created and the PLU is removed, HUVECs and MSCs are injected inside the channel. After that, to ensure complete coverage of the channel, the structure is rotated at regular intervals and finally connected to the perfusion circuit.

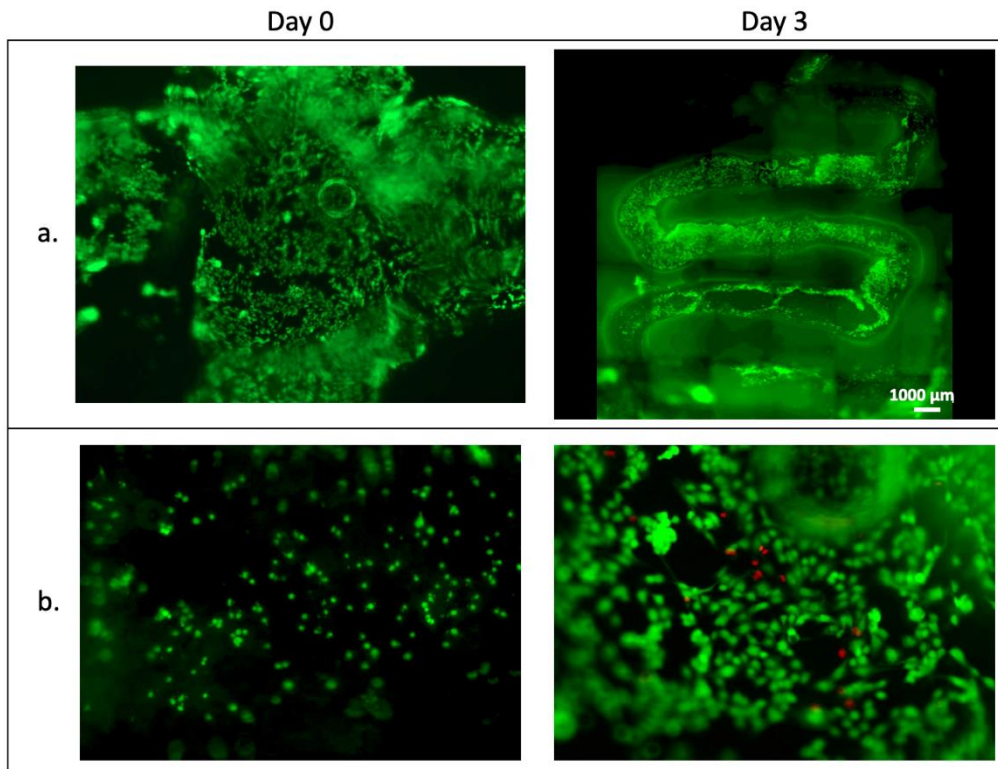


Figure 4. Endothelialization trials: HUVECs stained with a green cell-tracker inside the vascular canal at day 0 and day 3 after seeding. a) Representation of the entire channel; b) detail of cell morphology: it can be observed that at day 3 HUVECs tend to elongate and form a mono-layer on the surface of the channel.

Perfusion tests are aimed at validating the effectiveness of the vascular system. To do so, Neuroblastoma cells (SK-N-AS) are encapsulated in GelMA just prior to bioprinting step. After that, once the PLU is removed, the structure is connected to the perfusion loop to assess cell viability. A comparison of cell viability at day 7 for perfused, static vascularized, and non-vascularized structures can be seen in Figure 5.

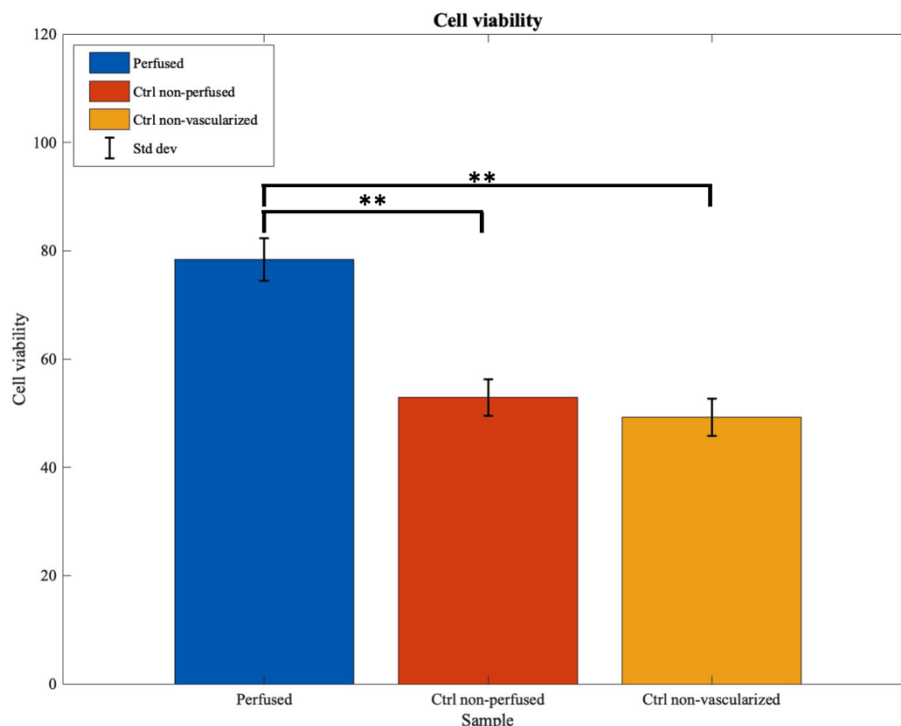


Figure 5. Perfusion trials: Live/Dead assay on SK-N-AS at day 7, comparing vascularized perfused construct (blue), vascularized non-perfused construct (red) and non-vascularized construct (yellow). The results show that perfusion significantly promotes cell viability. **p-value<0.01.

4. Conclusions

This work aims to create a 3D model of the tumor microenvironment by employing advanced 3D bioprinting techniques such as sacrificial bioprinting. The results show excellent success of vascularized structures, validated by different cellular assays. Due to the versatility and repeatability of the process, this model can be used to conduct more in-depth studies of the tumor microenvironment.

References

- [1] Carmeliet, P., Jain, R. Angiogenesis in cancer and other diseases. *Nature* 407, 249–257 (2000).
- [2] Kolesky et al. Three-dimensional bioprinting of thick vascularized tissues, *PNAS*, March 22, 2016, vol. 113.
- [3] Shen Ji et al. 3D bioprinting of complex channels within cell-laden hydrogels, *Acta Biomaterialia*, Volume 95, 2019, Pages 214-224, ISSN 1742-7061
- [4] Liliang Ouyang et al. Void-Free 3D Bioprinting for In Situ Endothelialization and Microfluidic Perfusion, *Adv. Funct. Mater.* 2020, 30, 1908349
- [5] Shirahama H, Lee BH, Tan LP, Cho NJ. Precise Tuning of Facile One-Pot Gelatin Methacryloyl (GelMA) Synthesis. *Sci Rep.* 2016

Modelling of the growth of *Nannochloropsis gaditana* in different reactor geometries, experimental kinetic parameters from batch cultures and biochemical analysis of the obtained biomass.

Luca Schembri^{1*}, Serena Lima¹, Alberto Brucato¹, Giuseppe Caputo¹, Silvia La Scala¹,
Francesca Scargiali¹

1 Università degli Studi di Palermo, Dipartimento di Ingegneria, Edificio 6, Viale delle Scienze 90128 - Palermo

*Corresponding author E-Mail: luca.schembri@unipa.it

Other authors E-Mail: serena.lima@unipa.it; alberto.brucato@unipa.it; giuseppe.caputo01@unipa.it;
silvia.lascalas@community.unipa.it; francesca.scargiali@unipa.it

Microalgae are unicellular and photosynthetic microorganisms that grow using inorganic salts, CO₂ and light, and are applied in numerous industrial sectors due to their variety and properties. Due to the lack of information on how microalgae respond to external inputs and to the different environments in which they grow, today the industrial application is not exploited as it should.

It is therefore necessary to create models that allow to predict microalgal growth in different photobioreactors to improve our knowledge, still poorly investigated.

In this work the Monod equation for the specific growth rate was combined with the Lambert-Beer law for the non-homogeneous light distribution in a flat photobioreactor.

Model kinetic parameters related to the cultivation of the microalga *Nannochloropsis gaditana* were obtained from batch cultivations under different photon-flux densities inside a quasi isoactinic photobioreactor. These parameters were applied in a mathematical model, based on the geometric system considered, for obtaining microalgae growth curves.

Biochemical analyses on the obtained biomass were also executed at the end of each batch cultivation to assess how light distribution influences biomass composition.

The obtained model allowed to successfully predict the growth of the microalga *Nannochloropsis gaditana* in the different photobioreactor geometries.

NiFe alloy based electrochemical sensor for sugars detection in food

Francesca Mazzara^{*1}, Bernardo Patella¹, Michele Russo², Alan O'Riordan³, Giuseppe Aiello¹,
Claudia Torino⁴, Antonio Vilasi⁴, Rosalinda Inguanta¹

¹Laboratorio Chimica Fisica Applicata, Dipartimento di Ingegneria, Università degli Studi di Palermo, Viale delle Scienze, 90128 Palermo;

² Dipietro Group, Siracusa, Italy

³Nanotechnology group, Tyndall National Institute, University College Cork, Dyke Prade, Cork, Ireland

⁴Istituto di Fisiologia Clinica (IFC)-Consiglio Nazionale delle Ricerche-Reggio Calabria-Italy

*francesca.mazzara04@unipa.it

1. Introduction

Sugars are essential organic compounds for humans, that play several fundamental roles in their life and development. They are naturally present in a wide range of food and produced in the human body. In fact, carbohydrates, consumed through a correct diet, are broken down into glucose, that is the most important source of energy for the body [1]. Sugars can be found in a range of foods including fruit, vegetables and honey and its quantification is very important to evaluate the quality of many foodstuffs. However, sugars may be added as additive during food processing, beverages and other preparations. While natural sugars are required by the body to satisfy the energy needs, added sugars are harmful to human health. Sugar consumption, especially added sugar, has been indicated as a major cause of several chronic diseases such as obesity, heart disease, diabetes and dental caries [2]. The World Health Organization (WHO) suggests that free sugars should make up no more than 10% of our daily energy intake [3]. Based on data relating to disease and mortality due to sugar intake, the European Commission has implemented a series of policies aimed to regulating sugar intake such as taxes on high-sugar foods [4]. To evaluate the concentration of sugars different techniques are available such as high-performance liquid chromatography and nuclear magnetic resonance. Among the quantification methods, electrochemical sensors have met with great success due to the simplicity of use, speed in response and high sensitivity and selectivity. In this work, non-enzymatic sensors were developed. In particular, a nanostructured electrode based on NiFe alloy was employed that exhibit very good catalytic properties [5].

2. Methods

Nanostructured electrodes based on nickel-iron (NiFe) alloys, obtained by template electrosynthesis method, were used as active materials for the electrochemical detection of glucose. This simple sugar was selected as a model to optimize the sensor. The nanostructured electrodes were fabricated through a two-step electrodeposition method. First of all, a thin layer of gold was sputtered onto a surface of a polycarbonate membrane to make it electrically conductive. On this surface, a Ni layer was electrodeposited by a potentiostatic deposition using a typical Watt's bath. This layer acts as a mechanical support and current collector for the nanostructures. The deposition solution of the NWs consists of the Watt's bath containing also $\text{FeSO}_4 \cdot 7\text{H}_2\text{O}$. NWs electrodeposition was carried out by pulsed potential. After NWs deposition, the polycarbonate membrane was etched in chloroform at room temperature. All samples were characterized by Xray diffraction (XRD), scanning electron microscopy (SEM) and energy dispersive spectroscopy (EDS) in order to study morphology and evaluate composition and crystalline phases of the alloy. The fabrication procedure and characterization methods are detailed in [6].

Sensor performances were evaluated by Cyclic Voltammetry (CV) technique at room temperature in a three-electrode cell with a Pt wire as a counter-electrode and a SCE as a reference. Sensors were also validated in real samples in order to compare our results with those obtained with conventional techniques. All tests reported in this work were repeated three times using a new electrode and fresh solution for each test and the main value was plotted to calculate the main properties of the sensor.

3. Results and discussion

The electrochemical deposition leads a nanostructured electrode consists of regular array of NWs. This morphology ensures a very high surface area and thus a very high electrocatalytic activity. As it possible to observe from Fig. 1, NWs have a cylindrical shape with a smooth and regular surface. They also present the typical interconnections due to template morphology. From EDS analyses, reported in Fig. 2, the composition of NWs was evaluated, founding a Fe content of about 79%. XRD pattern reveals the deposition of FCC Fe-Ni alloy (card no. 47-1405), with a preferentially oriented along the (200) plane.

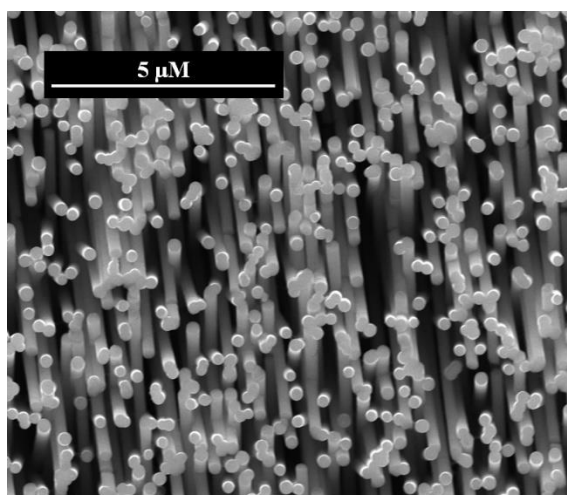


Figure 1 SEM image of NiFe NWs

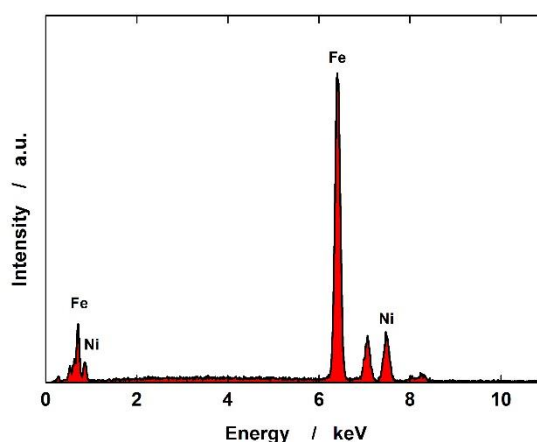


Figure 2 EDS spectrum of NiFe NWs

In order to perform the detection of glucose, CV was employed as electrochemical technique using NiFe NWs electrode as working electrode. In CV graph clearly appears the peak of glucose oxidation at about 0.1 V vs SCE that increases with the increase of glucose concentration. The NiFe electrodes show good behavior in terms of sensitivity and stability. Sensors were also validated with real samples of food. The achieved results were in good agreement with conventional techniques.

4. Conclusions

NiFe NWs based electrodes were fabricated by electrochemical deposition on a polycarbonate membrane that acts as template. Electrodes were tested for the detection of glucose. Sensors were fully characterized by means of several techniques, which revealed the deposition of both NiFe alloy with nanowire morphology that ensures a high surface area. Electrodes were tested in a basic solution in which good performance were obtained. The NiFe electrodes show good behavior in terms of sensitivity and stability. Sensors were also validated in real food and drink samples and the results appear good and comparable to values obtained by using standard technique.

References

- [1] V. Misra, A.K. Shrivastava, S.P. Shukla, M.I. Ansari, Effect of sugar intake towards human health, 1 (2016) 9.
- [2] L. Bonsembiante, G. Targher, C. Maffei, Type 2 Diabetes and Dietary Carbohydrate Intake of Adolescents and Young Adults: What Is the Impact of Different Choices?, *Nutrients*. 13 (2021) 3344.
- [3] World Health Organization, Food and Agriculture Organization of the United Nations, Strengthening nutrition action: a resource guide for countries based on the policy recommendations of the Second International Conference on Nutrition (ICN2), World Health Organization, Geneva, 2018.
- [4] N. Fidler Mis, C. Braegger, J. Bronsky, C. Campoy, M. Domellöf, N.D. Embleton, I. Hojsak, J. Hulst, F. Indrio, A. Lapillonne, W. Mihatsch, C. Molgaard, R. Vora, M. Fewtrell, Sugar in Infants, Children and Adolescents: A Position Paper of the European Society for Paediatric Gastroenterology, Hepatology and Nutrition Committee on Nutrition, *Journal of Pediatric Gastroenterology & Nutrition*. 65 (2017) 681–696.
- [5] T.-H. Yeh, C.-W. Liu, H.-S. Chen, K.-W. Wang, Preparation of carbon-supported PtM (M=Au, Pd, or Cu) nanorods and their application in oxygen reduction reaction, *Electrochemistry Communications*. 31 (2013) 125–128.
- [6] B. Buccheri, F. Ganci, B. Patella, G. Aiello, P. Mandin, R. Inguanta, Ni-Fe alloy nanostructured electrodes for water splitting in alkaline electrolyser, *Electrochimica Acta* 388 (2021) art. no. 138588.

A data-driven approach to assess the rheological properties of Durum Wheat Dough by indirect FTIR measurements

Fabio Fanari¹, Francesco Desogus¹, Massimiliano Grosso^{1*}, Manfred Wilhelm²

1 Dipartimento di Ingegneria Meccanica, Chimica e dei Materiali, Università degli Studi di Cagliari, Cagliari, Italia

2 Institute for Chemical Technology and Polymer Chemistry, Karlsruhe Institute of Technology, Karlsruhe, Germany

**Corresponding author E-Mail: massimiliano.grosso@unica.it*

1. Introduction

Fourier Transform Infrared Spectroscopy (FTIR) is an up-and-coming technique for dough characterization since measurements are easy to perform and fast. At the same time they can give both qualitative and quantitative chemical information about the microstructure. This work aims to propose and test a method capable to infer rheological information from indirect spectral measurements by resorting to a PLS model. The procedure could be important in view of a possible implementation of an online monitoring system based on rapid and non-invasive FTIR measurements.

2. Methods

Samples of semolina and distilled water in different amounts (40%, 50% and 60%) were kneaded using a measuring mixer type 350 (Brabender). Three different types of semolina were investigated. Two are non-commercial monovarietal species resulting from Karalis (KAR) and Cappelli (CAP) grains milling. The third kind is a commercial blend (COM). Their properties are quite different in protein amount, gluten percentages, and gluten index. The IR measurements were performed using a Vertex 70 spectrometer (Bruker), equipped with a Universal ATR sampling device. Spectra were collected at room temperature in the 600-4000 cm⁻¹ spectral range, as an average of 32 scans at 2 cm⁻¹ resolution. Rheological experiments were performed at 25 °C with an ARES-G2 strain-controlled rheometer (TA Instruments) with a 25 mm parallel plate geometry. Frequency sweep tests were performed with frequencies ranging from 1 to 100 rad·s⁻¹ with a constant strain of $\gamma_0 = 0.1\%$. Complex module data were modelled using the Weak Gel model [1], reported in Eq. 1, where parameter A_F is related to the network strength while z is linked to its extension.

$$G^*(\omega) = \sqrt{G'(\omega)^2 + G''(\omega)^2} = A_F \omega^{1/z} \quad (1)$$

The spectral data were related to the rheological parameters of the samples by means of a PLS model [2], which links the dependence of IR spectra to the rheological parameters A_F and z . After PLS regression had been accomplished, the interest was focused on selecting the wavelengths in which the absorption signal is the most influential on the changes in the rheological parameters. This can be carried out by computing the VIP scores. Wavelengths at which the VIP scores were above the unity value were considered significant [3].

3. Results and discussion

In Figure 1a, FTIR spectra of CAP, KAR and CAR samples are reported for a 50% water percentage. Interest is focused on the "Amide III" band (A₃), at 1200-1340 cm⁻¹, which mainly arises from N-H bending and C-N stretching vibrations. Although its intensity is limited, it is informative about the protein structure characterization. KAR50 and COM50 samples show similar spectra, especially in the water-linked peaks, while CAP50 presents quite different intensities. Figure 1b shows the semolina variety influence on $|G^*|$ together with the Weak Gel model predictions. Notice that the CAP50 sample has the highest G' and G'' values, so the Cappelli semolina variety is the strongest, followed by KAR. At the same time, COM turns out to be the weakest, in rheological terms. A PLS regression model relating A_F and z to the spectra of the A₃ band was developed to address a correlation between rheological properties and changes in the Amide III band spectrum.

The number of latent variables chosen was 5. The results for A_F are reported in Figure 2a. A good agreement was found, as confirmed by the high value of $R^2 = 0.832$. On the other hand, the PLS technique failed to establish a solid correlation for z . Therefore, one can assume that the strength of the network, related to the A_F value, is influenced by the protein structure's conformation and quantities.

VIP scores were then computed to establish the proteins' secondary structures more relevant in defining the rheological properties. VIP scores are reported in Figure 2.b as a function of the wavenumbers. As previously asserted [4], the amide III band can be divided into four spectral regions, corresponding to β -sheets (β -S), random coils (RC), β -turns (β -T), and α -helices (α -H), respectively. In this case, it is possible to see that VIP scores are higher than 1 in correspondence β -sheet and α -helix regions. Thus, one can conclude that these latter protein configurations are more important in defining the network rheological strength.

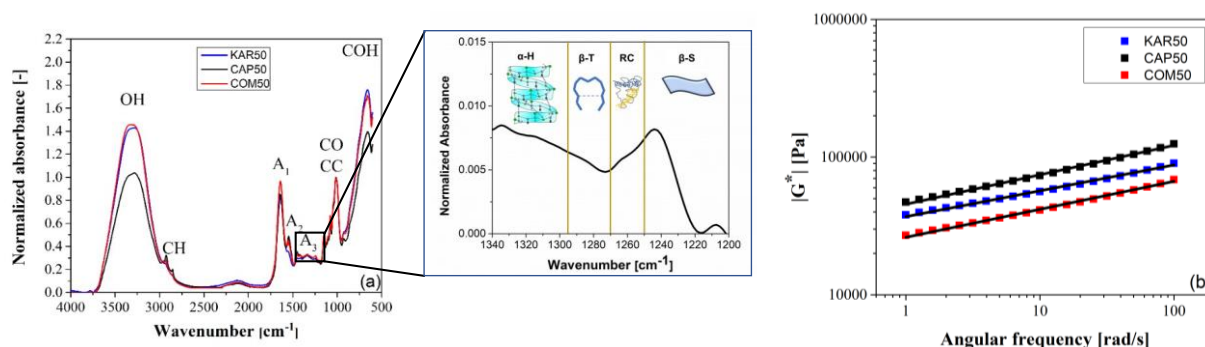


Figure 1. FTIR absorbance spectra (figure a) with particular focus on A3 band and complex modulus (figure b), measured for the CAP50 (black), KAR50 (blue), and COM50 (red) samples. Comparison with the Weak Gel model is also reported in Figure 1b

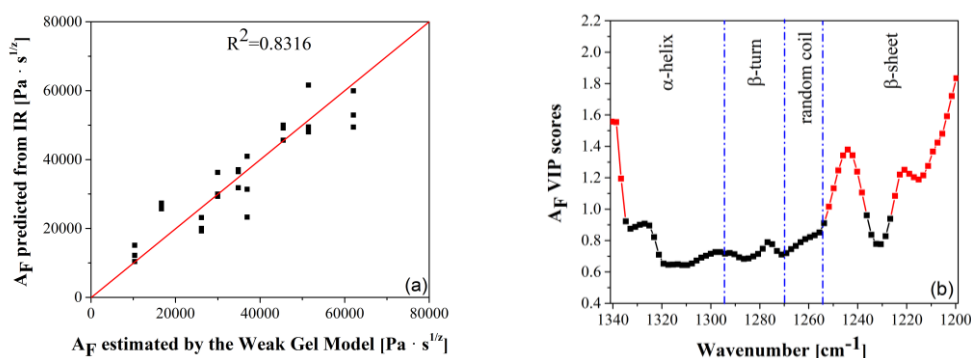


Figure 2. (a) A_F data predicted by the PLS regression reported as a function of the ones estimated by the Weak Gel model; (b) VIP scores for the PLS regression. Significant wavenumbers are highlighted in red

4. Conclusions

Rheological and infrared spectral analyses were used to infer rheological information from indirect spectral measurements. Satisfactory results were found regarding the prediction of the gluten network strength. Additionally, the methodology could give valuable insights into the interplay between protein conformations and rheological behaviour. In detail, β -sheets and α -helices protein conformations were shown to affect the gluten network's mechanical strength significantly. The method appears to be promising for future development of FTIR-based prediction systems for the online monitoring of rheological and structural properties of dough in the baking industry, considering the fast response times guaranteed by FTIR measurements.

References

- [1] D. Gabriele, B. De Cindio, P. D'Antona, *Rheol. Acta*, 40(2) (2001) 120–127.
- [2] P. Geladi, B. R. Kowalski, *Anal. Chim. Acta*, 185(C) (1986) 1–17.
- [3] L. Eriksson, N. Kettaneh-Wold, J. Trygg, C. Wikström, S. Wold, (2006). Multi- and megavariate data analysis: Part I: basic principles and applications. In *Computer and Information Science* (Vol. 1). Umetrics Academy, 2006.
- [4] S. Cai, B. R. Singh, *Biophys. Chem.*, 80(1) (1999) 7–20.

Calibration of a lyophilization model in the presence of limited industrial data for product transfer applications

Margherita Geremia¹, Gabriele Bano², Emanuele Tomba³,
Massimiliano Barolo¹, Fabrizio Bezzo^{1*}

1. *CAPE-Lab – Computer-Aided Process Engineering Laboratory
Department of Industrial Engineering
University of Padova
Via Marzolo 9, 35131 Padova PD (Italy)*
2. *GlaxoSmithKline, 1250 S Collegeville Rd, Collegeville (PA), United States*
3. *GlaxoSmithKline, Via Fiorentina 1, 53100 Siena SI, Italy*

**Corresponding author E-Mail: fabrizio.bezzo@unipd.it*

1. Introduction

In the pharmaceutical industry, lyophilization is used to extend long-time stability of valuable thermolabile medicines and vaccines. Primary drying is the most time-consuming and energy-demanding step of the entire process; therefore, minimizing its duration is a key process development goal. In the last years, the use of mathematical models as part of standard lyophilization development workflow has gained momentum in the industrial practice to accelerate and optimize the primary drying recipe. However, models typically require invasive sensors (i.e., product temperature) for parameter estimation, which are rarely available in good manufacturing practice (GMP) environment. In our study, we propose a new protocol for model parameter estimation exploiting limited industrial data, namely pressure measurements and gravimetric tests and we successfully verified results on the recently proposed model by Bano et al. (2020) [1].

2. Methods

We exploit the mathematical model by [1] to assist product transfer and cycle optimization on a specific equipment. Specifically, we estimate only six relevant equipment-dependent parameters [2] which describe the dependency of the heat transfer mechanisms on the operating conditions, and the mass transfer resistance on the length of the dried product. The proposed protocol for the estimation of those parameters consists of two sequential steps:

- Step S1: fitting of central zone gravimetric measurements for the estimation of conduction heat transfer parameters.
- Step S2: estimation of all other relevant equipment-dependent parameters via pressure measurements only.

3. Results and discussion

The effectiveness of the proposed protocol is evaluated for two different pieces of equipment (EQUIP #1 and EQUIP #2). The parameter estimation task is successfully assessed in terms of parameter precision and model accuracy with respect to experimental data (see Figure 1 representing the calibration run of EQUIP #1). The model performance is then validated through validation experiments, which confirm closeness to experimental data. Model efficiency at forecasting the sublimation endpoint is verified by comparing the prediction of the total sublimation flowrate with the one obtained using the reference model (i.e., the model calibrated using the current procedure based on the availability of pressure and product temperature measurements). Finally, model performance at minimizing the primary drying duration is found to be very similar to that obtained using the reference model.

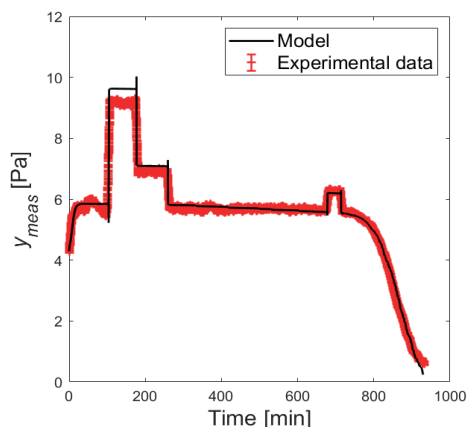


Figure 1. Model calibration for EQUIP #1: comparison of model profiles of pressure signal and the experimental observation.

4. Conclusions

The proposed workflow only relied on pressure measurements and gravimetric tests, which can be available on a large-scale equipment; no product temperature data is required. The effectiveness of our new protocol was successfully verified, thus confirming the possibility to use the model for aims of industrial interest. All tests were successfully passed for two different facilities, emphasizing the potential of the new protocol for the product transfer exercise and/or scale-up, thus making our approach particularly attractive in manufacturing environments.

References

- [1] G. Bano, R. De-Luca, E. Tomba, A. Marcelli, F. Bezzo, M. Barolo. Primary drying optimization in pharmaceutical freeze-drying: a multi-vial stochastic modeling framework. *Ind. Eng. Chem. Res.* 59 (2020) 5056–5071.
- [2] R. De-Luca, G. Bano, E. Tomba, F. Bezzo, M. Barolo. Accelerating the development and transfer of freeze-drying operations for the manufacturing of biopharmaceuticals by model-based design of experiments. *Ind. Eng. Chem. Res.* 59 (2020) 20071–20085.

Data-driven optimization of a freeze-drying unit using design of dynamic experiments

Christopher Castaldello¹, Pierantonio Facco¹, Fabrizio Bezzo¹,
Christos Georgakis², Massimiliano Barolo^{1*}

¹*CAPE-Lab – Computer-Aided Process Engineering Laboratory
Department of Industrial Engineering, University of Padova
35131 Padova, ITALY;*

²*Department of Chemical and Biological Engineering &
Systems Research Institute for Chemical and Biological Processes
Tufts University, Medford, MA 02155, USA*

**Corresponding author E-Mail: max.barolo@unipd.it*

1. Introduction and methods

Freeze-drying (lyophilization) is a unit operation commonly used in the biopharmaceutical industry to extend shelf-life of drugs in aqueous solution. Due to the very low temperature and low pressure, it is energy intensive and time-consuming [1,2]. Adoption of time-varying inputs (namely, shelf temperature and chamber pressure) allows faster operation [3,4], but finding the optimal input profiles experimentally is not trivial, because constraints exist on product temperature and sublimation rate. A recently developed detailed first-principles model of the process may help virtualize it [5]. However, optimization of the process performance using this knowledge-driven model is computationally expensive, due to model stochasticity.

In this study, a data-driven approach to process optimization is developed by designing time-varying inputs through design of dynamic experiments (DoDE) [6]. The first-principles model is used to carry out the designed experiments, through which one can calibrate appropriate response surface models (RSMs) describing the main response variables of the process. The best trajectories of the manipulated inputs are calculated by optimization from the RSMs, which are computationally inexpensive. Results are then compared with the direct optimization of the first-principles model.

2. Results and conclusions

Both optimization approaches (via first-principles or data-driven modeling) allowed reducing the duration of the freeze-drying operation significantly with respect to a time-invariant recipe (Figure 1). In particular, the data-driven approach is shorter by 15%, while the knowledge-driven one by 26%. However, the data-driven approach required about one-third of the computational time of the knowledge-driven approach. For the data-driven approach, the main drawback was related to a slight violation on the constraint of the maximum product temperature. This behavior was expected as no prior input-output relationship was available when the DoDE exercise was carried out, thus making its RSM slightly less accurate. This explains also why the duration is slightly increased with respect to optimization using the first-principles model.

From a general perspective, the data-driven approach can be very useful when dealing with complex models such as the one used in this case study, with results comparable to the knowledge-driven approach, but achieved in a much shorter computational time.

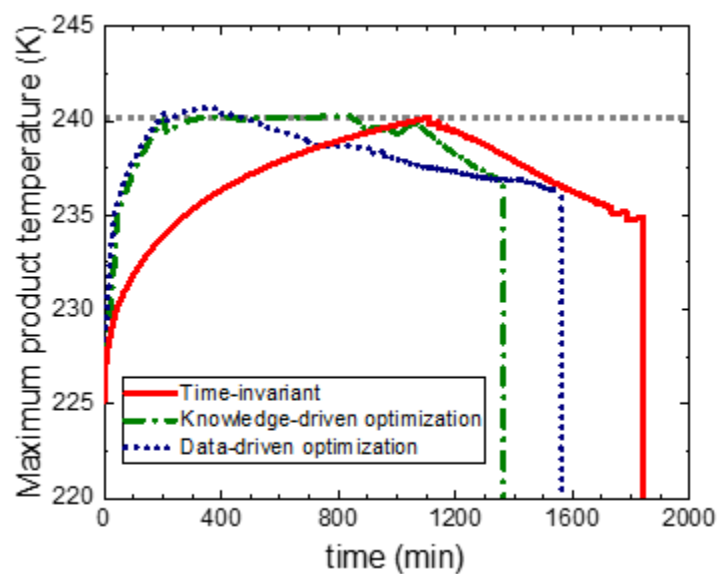


Figure 1. Maximum product temperature profiles for the time-invariant recipe and the two optimization approaches. End of sublimation is represented by a vertical line. Upper constraint is represented by the dotted gray line.

References

- [1] C. Ratti, *J. Food Eng.* 49 (2001) 311–319.
- [2] M. Bjelošević, K.B. Seljak, U. Trstenjak, M. Logar, B. Brus, P. Ahlin Grabnar, *Eur. J. Pharm. Sci.* 122 (2018) 292–302.
- [3] D. Fissore, R. Pisano, A.A. Barresi, *Dry. Technol.* 30 (2012) 946–958.
- [4] R. De-Luca, G. Bano, E. Tomba, F. Bezzo, M. Barolo, *Ind. Eng. Chem. Res.* 59 (2020) 20071–20085.
- [5] G. Bano, R. De-Luca, E. Tomba, A. Marcelli, F. Bezzo, M. Barolo, *Ind. Eng. Chem. Res.* 59 (2020) 5056–5071.
- [6] C. Georgakis, *Ind. Eng. Chem. Res.* 52 (2013) 12369–12382.

Carrier/curcumin microparticles obtained by supercritical antisolvent precipitation

Iolanda De Marco*

Department of Industrial Engineering, University of Salerno, Via Giovanni Paolo II, 132

84084 Fisciano (SA), Italy

**Corresponding author E-Mail: idemarco@unisa.it*

1. Introduction

Viral infections are still considered a persistent public health problem today. Viruses can be defined as non-living submicroscopic agents, composed mostly of RNA or stretches of DNA, capable of replicating and mutating within the host organism causing organoleptic and metabolic changes [1].

Coronavirus disease 2019 (CORonaVIRus Disease 19, COVID-19) is an infectious respiratory disease caused by SARS-CoV-2, belonging to the coronavirus family. The first cases were found in China, in Wuhan, in December 2019, and it was declared a pandemic in March 2020. Its rapid spread has caused severe difficulties in monitoring infected cases and drafting containment protocols in all countries involved.

Several natural substances belonging to different classes, most with antioxidant properties, have been considered excellent candidates for combating the COVID-19 pathology. In particular, those that have binding energy or a docking score similar to the drugs commonly used today and believed most effective are: polyphenols such as flavanones (including naringenin, quercetin and kaempferol) and flavones (including luteolin), terpenes and sesquiterpenes, curcumin, peptides, epigallocatechin gallate (EGCG), fatty acids and oleuropein [2,3].

Curcumin has been focused on these purposes. However, the effectiveness of this compound is limited by its poor solubility in water and, consequently, low bioavailability, as well as high sensitivity to light and heat. To overcome these problems, the active principle has been micronized through the supercritical antisolvent process (SAS) using two different types of carriers, namely β -cyclodextrin (β -CD) and polyvinylpyrrolidone (PVP). In particular, while aiming at a microparticle morphology of the powders in both cases, simple coprecipitates (microspheres) with PVP or inclusion complexes with β -CD were prepared to protect the active ingredient from degradation phenomena and increase its dissolution rate in an aqueous environment.

2. Materials and methods

β -cyclodextrin (β CD, purity 99.9 %) , polyvinylpyrrolidone (PVP, average molecular weight of 10 kg/mol) and curcumin (CURC, purity > 65 %) were provided by Sigma–Aldrich (Italy). Dimethylsulfoxide (DMSO, purity 99.5 %) was purchased from Carlo Erba (Italy). Carbon dioxide (CO₂, purity 99 %) was supplied by Morlando Group s.r.l. (Italy).

The experiments were performed in a homemade laboratory plant. Carbon dioxide is fed to the precipitation chamber with an internal volume of 0.5 L through a high-pressure pump. The liquid solution is prepared by dissolving the solutes in DMSO. The prepared solution is sprayed into the precipitation vessel through a stainless-steel nozzle through another pump. A micrometric valve regulates the pressure. The precipitated powder is collected at the bottom of the precipitation vessel on a stainless-steel filter. The liquid solvent is recovered in a separator located downstream of the vessel. The flow rate and the total amount of delivered CO₂ are measured at the exit of the separator by a rotameter and a dry test meter, respectively.

The morphology of the precipitated powders was determined by Field Emission Scanning Electron Microscopy (FESEM, mod. LEO 1525, Carl Zeiss SMT AG, Oberkochen, Germany). Fourier-transform infrared (FTIR) analysis was carried out using a Bruker spectrophotometer (Bruker Optics, Ettlingen,

Germany), model Vortex 70 FT-IR (scan wavenumber range of 4000–450 cm^{-1} , resolution of 0.5 cm^{-1} as the mean of 16 measurements). The dissolution kinetics of not processed or released from SAS-prepared samples CURC were studied using a UV/vis spectrophotometer (model Cary 50, Varian, Palo Alto, CA). The analyses were performed at a wavelength of 425 nm. In agreement with the literature, the dissolution tests were achieved in phosphate-buffered saline solution (PBS) at pH 6.8 (Rezaei and Nasirpour, 2019). Samples containing 2 mg of equivalent CURC were incubated in 300 mL of PBS at pH 6.8, continuously stirred at 150 rpm, and heated at 37 °C.

3. Results and discussion

Curcumin was coprecipitated with β CD (Figure 1a) or PVP (Figure 1b) at different process conditions. In particular, the effect of the pressure, the concentration of the liquid solution, and the ratio between the carrier and curcumin were investigated. At the optimized operating conditions, well-defined microparticles with a fast release were obtained using both the carriers.

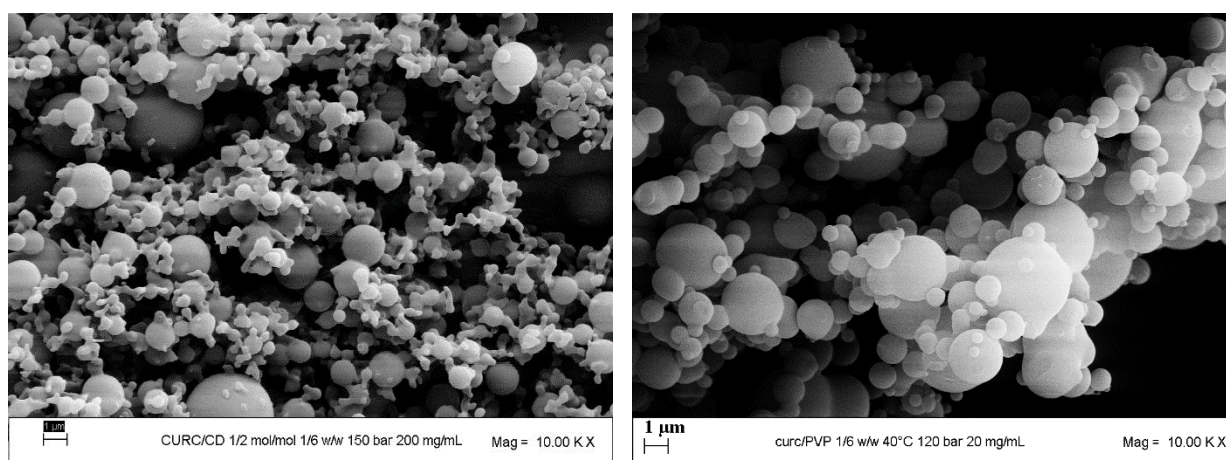


Figure 1. FESEM images of curcumin microparticles precipitated through the SAS process using β -cyclodextrin (on the left) and PVP (on the right) as the carriers.

4. Conclusions

The SAS process was effective using either cyclodextrin or PVP as carriers for the coprecipitation of curcumin. The production of β CD-based complexes or PVP-based coprecipitates allows to speed up the dissolution of curcumin, achieving the intended purposes. However, the use of β -CD compared to PVP seems to be more advantageous, as it reduces the amount of carrier in composite powders while ensuring a rapid release. Furthermore, cyclodextrin has the further advantage of allowing more significant powder recovery with the same process times. With the same injected solution, the concentrations used with CD are significantly higher than those used with PVP. Ultimately, this study made it possible to achieve the intended purpose, i.e., to produce composite systems capable of improving the therapeutic efficacy of curcumin, useful in the prevention or as adjuvant treatments for the pathology of COVID-19.

References

- [1] S. Modrow, D. Falke, U. Truyen, H. Schatzl, *Molecular Virology*, Springer-Berlin-Heidelberg, 2013, pp. 17-30.
- [2] A. da Silva Antonio, L. Silveira Moreira Weidemann, V.F. Veiga-Junior, *RSC Adv.* 10 (2020) 23379-23393.
- [3] K. Chojnacka, A. Witek-Krowiak, D. Skrzypczak, K. Mikula, P. Młynarz, *J. of Functional Foods* 73 (2020) 104146-104153.

Boosting butyrate and hydrogen production in acidogenic fermentation of food waste and sewage sludge mixture

Francesco Valentino^{1*}, Hojjat Borhany¹, Michele Rasera², Alessio Dell'Olivio¹, Paolo Pavan¹, Marco Gottardo¹

¹*Department of Environmental Sciences, Informatics and Statistics, Cà Foscari University of Venice, Via Torino 155, 30172 Mestre-Venice, Italy*

²*Contarina S.p.A., Via Vittorio Veneto 6, 31027 Lovadina di Spresiano (TV), Italy*

**Corresponding author: francesco.valentino@unive.it*

1. Introduction

The European Union (EU) 2030 strategy leads to ensure sustainable growth via a new and ambitious package of measures on “Circular Economy” (ec.europa.eu, 2020). These measures aim to increase products lifetime and their recyclability benefiting both the environment and the economy. Food waste (FW) management is part of this vision as it allows for conservative use of resources like carbon, nitrogen and phosphorous among the others. Separate collection, which allows to produce streams of recycled materials of good quality level, is a pre-requisite of this global approach. Once this material is collected it is the perfect substrate for the application of fermentative processes able to produce renewable biofuels in a sustainable way [1]. FW production in Europe accounts for about 87.6 million tons annually [2]; over past years, this waste was sent to landfill, without even any treatment, causing severe air, groundwater, and soil contamination due to its high biodegradability and leachate formation. The need different solutions led to food waste treatment with composting, allowing the production of high-quality compost for agricultural applications. However, this process is highly energy consuming and requires the occupation of large land quantities with possible GHG formation [3]. Similar disposal problems are encountered with other organic waste produced in urban areas, especially wastewater sludge (WWS) generated from municipal wastewater treatment processes. Anaerobic digestion (AD) of one or more organic substrates is a process currently applied also in existing wastewater treatment plants (WWTPs), to stabilize organic matter along with the production of biogas; however, the application of a biorefinery technology chain in urban scenarios, where organic substrates are always available, can foster the combination and valorization of different substrates into added-value marketable products other than biogas alone. In this work, acidogenic fermentation (AF) process has been chosen as key step for the anaerobic treatment of FW and WWS. Volatile fatty acids and hydrogen production has been monitored in terms of yield and process stability as an alternative option to the already established AD technology. In a coupled AF-AD process, a possible gas composition could be 10% H₂, 30% CO₂ and 60% of CH₄ (v/v), for a second-generation biofuel that can be of great interest for combined heat and power (CHP), cogenerated motors or automotive industry (after upgrade for the CO₂ elimination). In addition, within a context of a biorefinery development, the production of a VFA-rich stream at constant concentration and stable chemical features is a key aspect for the market exploitation or the synthesis of added value products.

2. Methods

The substrates used in this study were thickened WWS and mechanically screw-pressed FW, both available in Treviso wastewater treatment plant (northeast Italy). The mixture utilized in this study consisted of 50% of thickened WWS and 50% FW as volumetric ratio. For a part of experiments, the feedstock mixture was

thermally hydrolyzed (70°C) in 380 L hyper-thermophilic reactor for 24 h. Thickened WWS had the following characteristics: total solids (TS) 28.6 ± 0.4 g TS/kg, volatile solids (VS) 22.4 ± 0.2 g VS/kg, soluble COD (COD_{SOL}) 0.4 ± 0.1 g/L, total Kjeldahl nitrogen (TKN) 33 ± 2 g N/kg TS, phosphorus (P) 18 ± 1 g P/kg TS; screw-pressed FW had fluctuating characteristics: 44-54 g TS/kg, 37.5-46.0 g VS/kg, 13.2-30.0 g COD_{SOL}/L, 21-28 g N/kg TS as TKN and 4.0-6.0 g P/kg TS.

AF process was carried out in a 230 L Continuous Stirred Tank Reactor (CSTR) that was maintained at a fixed temperature (55°C) by an external thermostatic jacket and stirred with a mechanical impeller at 80 rpm. No inoculum was added. The reactor was fed once per day, in a semi-continuous manner. Three parallel CSTRs were operated for approximately 60 days, under three different hydraulic retention time (HRT): respectively 4.0, 5.0 and 6.0 days. In all the tested conditions, the hydrolyzed feedstock mixture was used the first 32 days; then, the hyper-thermophilic treatment was interrupted until the end of operation. Each condition was compared in terms of VFA yields and composition and hydrogen production. In each reactor, the effluent was collected before the feeding for pH measurements, COD_{SOL} and VFA analysis (roughly three times a week). Gas phase was analyzed twice a week.

The quantification of the VFA was conducted using AGILENT 6890N gas chromatograph equipped with a flame ionization detector (T 200°C), a fused silica capillary column, DB-FFAP (15 m x 0.53 mm x 0.5 µm thickness), and hydrogen was the gas carrier. Biogas production was quantified by a flow meter (Ritter Company™), while CO₂ percentage in the biogas was quantified through a portable infrared gas analyzer GA2000TM (Geotechnical Instruments™). H₂ and CH₄ percentage were determined by a gas chromatograph GC Agilent Technology 6890 NTM equipped with a column HP-PLOT MOLESIEVETM (30 m x 0.53 m ID x 25 µm thickness), using a thermal conductivity detector (TCD) at 250°C using Argon as gas carrier.

3. Results and discussion

The three CSTR runs were performed starting from hydrolyzed feedstock (first phase). The following figure 1 shows the trends of VFA, COD_{SOL} and specific hydrogen production (SHP) in the three runs performed at 4.0, 5.0 and 6.0 days as HRT (respectively A, B and C); the first and second phases are separated by the vertical axis. With reference to VFA and COD_{SOL} of figure 1A (HRT 4.0 days), the values tend to be close on days 9, 15, 21, 23 and 27 while for the rest of the period the VFA/COD_{SOL} ratio was substantially lower. Given the similarity of both parameters in the first phase (after the first week from inoculum), the application of hyperthermophilic pretreatment favored the feedstock acidification. The feedstock shift caused an immediate drop of the acidification performance and only in the last five days it was noticed a realignment of VFA and COD_{SOL} values, suggesting a slow acclimatization of the biomass to the feedstock. The CSTR conducted at HRT 5.0 days (figure 1B) denotes greater congruity of VFA and COD_{SOL} values over time and less variability. Both trends were stable after start-up in the presence of a pretreated feedstock. The growth of VFA and COD_{SOL} in the second period was due to the undesired increase in the organic load (because of the high solids content of the FW). Despite of this, such condition allowed to manage acclimation more efficiently than previously discussed condition. Finally, as regards the third investigated HRT (6.0 days; figure 1C), even reaching higher product concentrations during the second phase, the variability of the values during the entire period of experimentation is such as to make it less preferable than the previous run (HRT 5).

Hydrogen production was quantified as yield, compared to the VS of the feedstock. In all the three runs, hydrogen production seemed to be favored by the utilization of a pre-treated feedstock (first part of the run), achieving values even higher than 0.05 Nm³ H₂/kg VS and up to 33% v/v in the second CSTR at 5.0 days as HRT (figure 1B). As discussed below, the higher H₂ production was linked to the higher level of acetic acid (often above 30% of the total VFA; COD basin), generally observed in the runs conducted with hydrolyzed feedstock compared to the use of not hydrolyzed mixture, independently from the applied CSTR. Also commonly observed, the stability in H₂ yield values was often weak, independently from the hydrolyzation

of the feedstock. This is an intrinsic characteristic of the waste fermentation process, especially when a pH-control approach is not adopted. In all the CSTR, the pH was slightly above 5.0 without the need of any control strategy, given the sufficient alkalinity provided by the WWS.

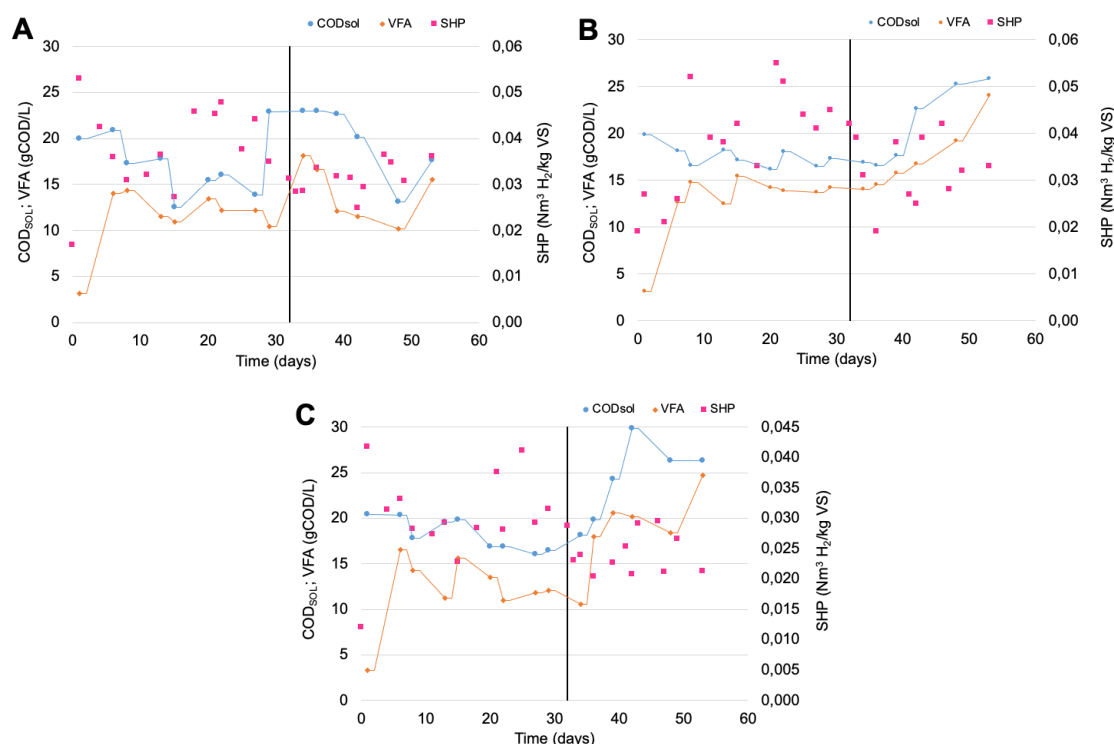


Figure 1. Trends of VFA, COD_{SOL} and SHP in the three runs performed at 4.0 days (A), 5.0 days (B) and 6.0 days (C) as HRT.

In terms of VFA spectrum, the three runs showed similar results, with a clear stability in the concentration of each single acid more noticeable when hydrolyzed feedstock was used. In general, all the conditions investigated, acids from C5 (valeric) to C7 (heptanoic) represented, individually, contributions equal to or less than 5% (COD basin) of the total VFA; therefore, the operating conditions applied must be considered unsuitable to produce longer-chain acids. Butyric acid was the main product, representing values between 30-45% with hydrolyzed feedstock and 55-70% with not hydrolyzed feedstock (COD basin). The contribution of acetic acid in the first phase, where H₂ production was higher, was in the range 15-40%, greatly reduced in the second phase where it was often below 10% (COD basin).

4. Conclusions

Acidogenic fermentation of FW and WWS was investigated in a total of six different conditions, by changing the HRT and applying a short-term hyperthermophilic pretreatment as hydrolysis. In terms of process stability, H₂ production potential and acidification yield, the condition having 5.0 days as HRT conducted with hydrolyzed feedstock gave better results: 0.042 ± 0.03 Nm³ H₂/kg VS, 0.52 ± 0.02 g VFA/g VS and 0.81 COD_{VFA}/COD_{SOL} ratio. Despite of the higher fluctuations observed on the performances when the not hydrolyzed substrate was used, the selective production of butyric acid (up to 70% COD basin) is of a remarkable interest, since it is one of the higher market values compared to other VFA, with many possible application (flavoring, pharmaceuticals, food additive).

References

- [1] F. Valentino, G. Munarin, M. Biasiolo, C. Cavinato, D. Bolzonella, P. Pavan, *J. Env. Chem. Eng.* 9 (2021) 106062.
- [2] B. Colombo, F. Favini, B. Scaglia, T.P. Sciarria, G. D'Imporzano, M. Pognani, A. Alekseeva, G. Eisele, C. Cosentino, F. Adani, *Biotechnol. Biofuels* 10 (2017) 201.
- [3] G. Moretto, I. Russo, D. Bolzonella, P. Pavan, M. Majone, F. Valentino, *Wat. Res.* 170 (2020) 115371.

Electrochemical detection of human immunoglobulin-G using immunosensor based on ZnO nanorods

Nadia Moukri^{1*}, Bernardo Patella¹, Gaia Regalbuto¹, Giuseppe Aiello¹, Chiara Cipollina², Elisabetta Pace³, Serena Di Vincenzo³, Alan O'Riordan⁴, Rosalinda Inguanta¹

1 Dipartimento di Ingegneria, Università degli Studi di Palermo, Palermo, Italy; bernardo.patella@unipa.it; gaia.regalbuto@community.unipa.it; giuseppe.aiello02@unipa.it; rosalinda.inguanta@unipa.it; *2* Fondazione Ri.MED, Palermo, Italy; ccipollina@fondazionerimed.com; *3* Istituto per la Ricerca e l'Innovazione Biomedica (IRIB)-Consiglio Nazionale delle Ricerche, Palermo, Italy; elisabetta.pace@cnr.it; serena.divincenzo@irib.cnr; *4* Tyndall National Institute, University College Cork, Ireland, alan.oriordan@tyndall.ie.

Corresponding author E-Mail: nadia.moukri@unipa.it

1.Introduction

In recent years, the demand for new types of analytical devices has been growing in several medical applications, such as clinical diagnosis and home patient monitoring. For this reason, research is focused on obtaining new devices capable of performing fast, accurate and *in situ* real-time analyses. In this work, an electrochemical immunosensor based on ZnO nanorods (ZnO-NRs) was developed for the detection of human immunoglobulin G (H-IgG). This protein was selected as model analyte because of its physical, chemical, and biological features similar to many other biomarkers.

Commercial methods for production of ZnO thin films are gas phase-based techniques such as sputtering and metal organic vapor deposition. These methods are highly expensive for both instrumentations and operational conditions and they also require specialized personnel. The fabrication methods are based on electro-generation of base that leads to the deposition of ZnO starting from a solution containing Zn²⁺ and nitrate ions. In particular, the electro-reduction of nitrate to nitrite leads to the generation of OH⁻ at electrode/electrolyte interface with a consequent increase of local pH [1]. This increase in pH allows the precipitation of ZnO on the electrode surface [2]. By tuning the electrodeposition parameters, it is possible to obtain ZnO with different morphologies such as thin film, self-assembled hexagonal nanorods (NRs), nanofibers, nanoparticles, nanorings and nanowires. The nanostructured morphology allows electrodes with higher surface area and thus high activity. For these reasons, in this work we explored the possibility of using electrochemically obtained ZnO nanorods (ZnO-NRs) as a basis for the fabrication of immunosensors.

In order to detect proteins, a sandwich configuration was assembled on the surface of the electrode. The sandwich layout is shown in **Figure 1**. This configuration consists of a) a primary antibody attached on the electrode surface, b) the antigen to be detected (analyte) that is selectively bound by the primary antibody, and c) a secondary labelled antibody. The immunosensor is electrochemically active thanks to the presence of gold nanoparticles tagging the secondary antibody. Therefore, it has been used to measure the current density of the hydrogen evolution reaction, which is indirectly related to the concentration of H-IgG antigens. In this way the calibration curve was constructed obtaining a linear range of 1-1000 ng mL⁻¹ with a detection limit of few ng mL⁻¹ and good sensitivity

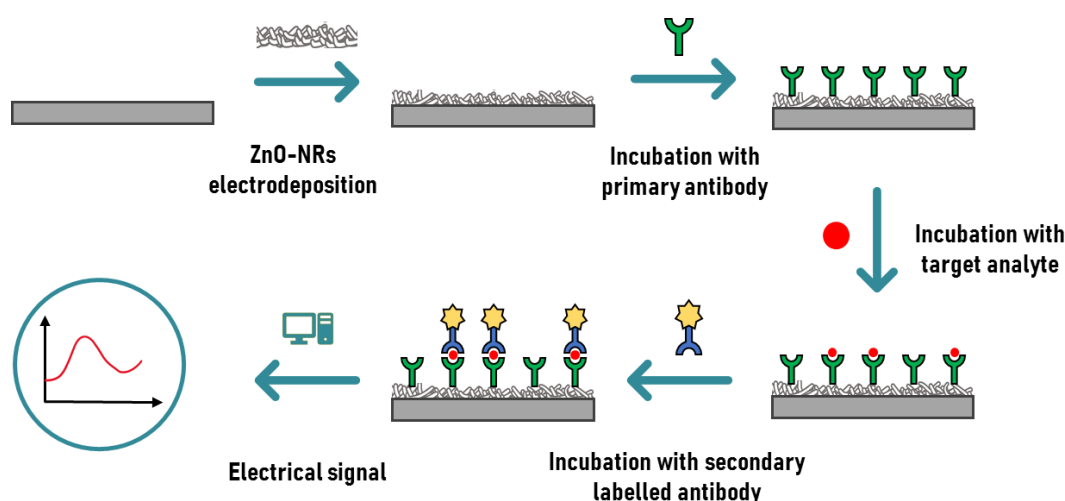


Figure 1. Scheme of immunosensor with a sandwich configuration based on ZnO nanorods.

2. Methods

ZnO nanorods were fabricated by means of an electrochemical deposition technique called electro-generation of base. This deposition was carried out over the flexible substrate ITO-PET (Indium Tin Oxide Polyethylene Terephthalate). The electrodeposition of ZnO-NRs was carried out applying a constant potential of -0.95 V vs Ag/AgCl for 60 min in an inert atmosphere under a continuous flow of nitrogen. A 3-electrodes cell was used, with a Pt mesh as a counter-electrode and a silver-silver chloride (Ag/AgCl) reference electrode. The deposition was carried out at 60 °C using an aqueous solution of ZnCl₂ 10 mM and NaNO₃ 10 mM as electrolyte.

To increase the covalent immobilization of the primary antibody, rGO (reduced graphene oxide) was deposited on top of the ZnO NRs electrodes using electrodeposition by applying a constant potential. This deposition was carried out in a homemade cell with small exposing area (0.07 cm²) of the NRs electrode that operates as working electrode; a rod of platinum and SCE were used as counter and reference electrodes, respectively. The electrolyte solution was an acetate buffer solution containing GO (graphene oxide) 5 mg mL⁻¹. A cathodic potential of -0.8 V (SCE) for 300 s was applied, to obtain the formation of rGO on electrode surface.

The method employed to obtain the immunosensor and to detect H-IgG consists of 5 different steps detailed in [3]. The first incubation step is a key step because it modifies the electrode surface with amino groups that can easily react with the primary antibodies, that were immobilized on electrode surface during the second step. In the subsequent step the modified electrode was treated with a solution of ETA to block all areas of the electrode not covered by the primary antibody. In this way, during the detection phase, the current signal will arise only from the sandwiches because they will be the only electrochemically active parts. Then, electrodes were incubated with different amounts of target H-IgG (ranging from 1 to 1000 ng mL⁻¹) diluted in PBS to define a calibration plot. Finally, the electrodes were incubated (1 h at room temperature) in a solution containing the secondary antibody, previously tagged with Au-NPs, to complete the sandwich. Au NPs were synthesized following the Turkevich method [4]. A chronoamperometry technique, performed by imposing a constant potential of -0.9 vs SCE, was employed for evaluate the immunosensor performance.

3. Results and discussion

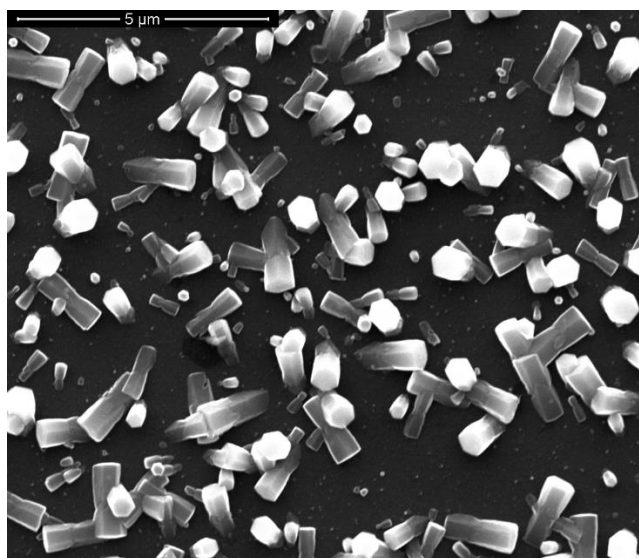


Figure 2. SEM image of ZnO nanorods electrode.

For sensing applications, the nanorods is the preferred morphology, due to its high surface area. By SEM we found that ITO-PET substrate is covered by nanorods with hexagonal shape characteristic of ZnO with wurtzite-type structure. SEM image of the electrode is shown in **Figure 2**. The presence of rGO film, that do not change the nanostructured morphology of the electrode, was also observed. On this electrode, after the different incubation steps, the immunosensor with sandwich configuration composed of primary antibody, antigen (immunoglobulin G), and secondary antibody labelled with gold nanoparticles, was fabricated. The greater the number of electrochemically active sandwiches, the greater the hydrogen developing current. By measuring this current, (0.1 M HCl polarized at -0.9 V vs SCE) the sensor calibration line was determined. The linear operating range of the sensor was found in the range 10–1000 ng mL⁻¹ with a detection limit of 1.25 ng mL⁻¹ and a sensitivity of 6.77 μA cm⁻²/log (ng mL⁻¹).

4. Conclusions

In this work, an electrochemical immunosensor based on ZnO nanorods was developed for the quantification of human immunoglobulin G. This protein is selected as it has physical, chemical, and biological characteristics similar to many others and can be used as a model analyte. The immunosensor was developed using the “sandwich” configuration in which the target antigen binds with the primary antibody and the secondary antibody labelled with gold nanoparticles (Au-NPs). With this configuration, the sandwich is electrochemically detectable, as the Au-NPs catalyze the hydrogen development reaction. Thus, the current density related to the hydrogen development reaction is indirectly correlated with the concentration of H-IgG. Through these measurements, the calibration curve of the sensor was obtained in the concentration range of the H-IgG from 1 ng mL⁻¹ to 1000 ng mL⁻¹. From the calibration curves it has been observed that the linear operating range of the sensor is included in the range 1-1000 ng mL⁻¹ with a detection limit of 1.21 ng mL⁻¹ and a sensitivity of 0.13824 μA cm⁻²/(ng mL⁻¹).

References

- [1] M. Nobial, O. Devos, O. R. Mattos, e B. Tribollet, «The nitrate reduction process: A way for increasing interfacial pH», *Journal of Electroanalytical Chemistry*, pag. 8, 2007.
- [2] M. Vaghayenegar, A. Kermanpur, e M. H. Abbasi, «Formation mechanism of ZnO nanorods produced by the electromagnetic levitational gas condensation method», *Scientia Iranica*, vol. 18, n. 6, pagg. 1647–1651, dic. 2011, doi: 10.1016/j.scient.2011.11.025.
- [3] B. Patella *et al.*, «Electrochemical Synthesis of Zinc Oxide Nanostructures on Flexible Substrate and Application as an Electrochemical Immunoglobulin-G Immunosensor», *Materials*, vol. 15, n. 3, pag. 713, gen. 2022, doi: 10.3390/ma15030713.
- [4] J. Kimling, M. Maier, B. Okenve, V. Kotaidis, H. Ballot, e A. Plech, «Turkevich Method for Gold Nanoparticle Synthesis Revisited», *J. Phys. Chem. B*, vol. 110, n. 32, pagg. 15700–15707, ago. 2006, doi: 10.1021/jp061667w.

Monoclonal antibody controlled and targeted delivery: the atherosclerosis case study

Roberta Campardelli^{1*}, Pier Francesco Ferrari¹, Giulia De Negri Atanasio¹, Domenico Palombo²,
Patrizia Perego¹

¹*Department of Civil, Chemical and Environmental Engineering, University of Genoa, Via Opera Pia, 15, 16145
Genoa, Italy;*

²*Department of Surgical and Integrated Diagnostic Sciences, University of Genoa, viale Benedetto XV, 6, 16132
Genoa, Italy*

**Corresponding author roberta.campardelli@unige.it*

1. Introduction

In the last years drug delivery systems have been deeply studied for the ability of preserving the payload activity and to control the release in order to maintain the drug concentration in the therapeutical window for prolonged time. The encapsulation of monoclonal antibody with a therapeutic activity represents an interesting new strategy that has been explored in the oncology fields, with encouraging results [1]. In this field, the external surface decoration of the drug delivery device can allow a targeted therapy with the main objective of decreasing the side effects since the drug is released directly in the pathological site.

For the controlled and targeted delivery of therapeutic monoclonal antibodies different materials have been tested for the micro and nanoparticles production such as synthetic polymers (i.e. poly (lactic-co-glycolic acid) (PLGA), poly (ϵ -capro-lactone) and poly (lactic acid)) [2], natural polymers (i.e. alginate [3] which is extracted from brown algae) and phosphatidylcholine (PC) for the production of liposomes [4].

In this project it will be described a comparative study of the preparation of different type of carrier which encapsulate a therapeutic monoclonal antibody Bevacizumab (BEV). It is a monoclonal antibody commercialized as Avastin[®] used to decrease the angiogenic correlated diseases [5]. In particular, this angiogenesis inhibitor has demonstrated to have positive effect on atherosclerotic plaques of various stages for which it demonstrated advanced inhibition of neovascularization. Therefore, a targeted delivery of this therapeutic protein directly on the target site is of great interest for cardiovascular field. The production of BEV loaded liposomes and PLGA micro and nanoparticles were optimized in order to obtain a good control over particles size distribution, suspension stability, high drug encapsulation efficiency and stability of entrapped therapeutic protein. Drug release kinetics were studied under simulated physiological conditions at 37 °C. Furthermore, the targeting of particles towards specific tissues was obtained via surface modification with the attachment of specific marker for angiogenesis.

2. Methods

To product polymeric particles, *water/oil/water* technique was used. Briefly, the PLGA was dissolved in ethylacetate until complete dissolution, then the aqueous inner phase was added (bevacizumab solution, at 25 mg/mL, or PBS solution for loaded or empty microparticles, respectively). The first w/o solution was obtained homogenising for 2 minutes (30 sec on-off) using a Vibra-Cell[™] ultrasonic probe with 60% of amplitude. After that, the first emulsion was added to 80 mL of ethyl acetate saturated water previously prepared. PVA was used as surfactant at 2% w/w in the aqueous solution. The secondary emulsion was obtained using a rotor-stator emulsifier (Silverson L5T) at 7000 rpm for 6 minutes. Finally, the obtained emulsion was left under magnetic stirring at 300 rpm in a fume hood to obtain the complete evaporation of the solvent. The obtained particles suspension was washed with Milli-Q water three times by centrifugation, 10.000 \times g for 15 minutes to remove the PVA excess.

Liposomes were produced using the thin-film hydration method. Briefly, 200 mg of PC was dissolved in chloroform. Then, the organic solvent was removed using a rotary evaporator (model Laborota 4000, Heidolph, Schwabach, Germany). The aqueous solution (with Bevacizumab) was used to hydrate the obtained thin-film layer. The solution was left under magnetic stirring for 3 h at room temperature. Then, it was homogenized for 2 min using the same Vibra-Cell[™] ultrasonic liquid processor reported above at the same conditions. The

obtained liposome solution was then centrifuged at $12.984\times g$ for 30 min at 4 °C three times and the pellet was washed with deionized water to remove the non-entrapped Bevacizumab. Liposome suspensions were stored at 4 °C after preparation. Empty nanoliposomes were also produced following the same procedure and used as control during the entire experimentation.

The functionalization with specific markers for angiogenesis was performed using the coupling reaction in the presence of carbodiimide hydrochloride (EDC) and N-hydroxysuccinimide (NHS).

3. Results and discussion

Empty and loaded PLGA microparticles and nanoparticles and PC liposomes were produced and optimized.

Polymeric microparticles were produced using the double emulsions evaporation process, whereas liposomes were produced using the thin layer hydration method. In general polymeric particles allowed to achieve higher entrapment efficiency, 77.15%. Indeed, the method is based on the formation of a stable emulsion in which the drug is contained in the inner water phase of the emulsion. In the case of liposomes, instead, the drug is dissolved in the water medium used for the hydration of the lipid layer. As a consequence, only a part of the water used to hydrate the layer effectively goes inside the vesicles, resulting in a lower entrapment efficiency of 51.13%.

Regarding the size of the particles and liposome, it is possible to precisely tune the desired dimensions from the nanometric to the micrometric one. In the case of PLGA particles the conditions of emulsification are the most responsible of emulsion droplet dimensions and then particles diameters. In the case of liposomes, since the thin layer hydration method is a spontaneous process, micrometric liposomes are generally obtained. In order to reduce liposome dimensions to nanometric level a post processing step of sonication is required. Changing the intensity and the duration of the sonication treatment it is possible to obtain the desired particle size distribution.

Regarding particles morphology an example of FESEM image of produced PLGA microparticles is reported in Figure 1.

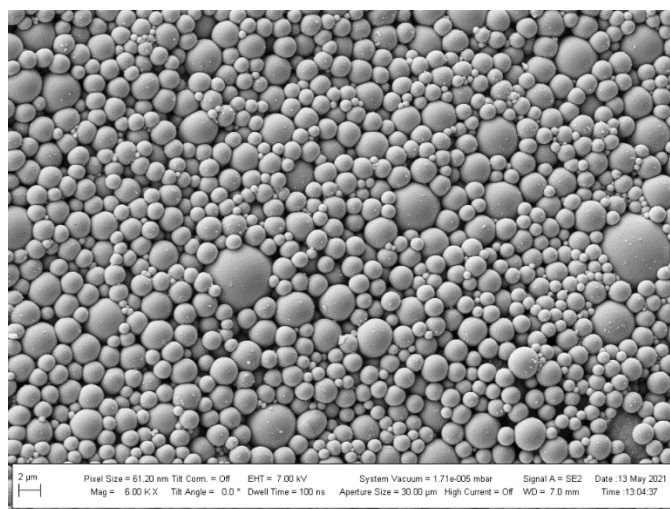


Figure 1. FESEM image of PLGA loaded BEV microparticles

Very different drug release kinetic can be obtained from the drug delivery devices produced, as shown in Figure 2. Indeed, polymeric particles allow the obtainment of a sustained release of BEV over very long time of observation, instead, liposomes, under simulated drug delivery conditions, rapidly release the cargo. The principle of drug release at the basis of the carrier systems selected is very different. This allow a modulation of the drug release according to the therapeutic need.

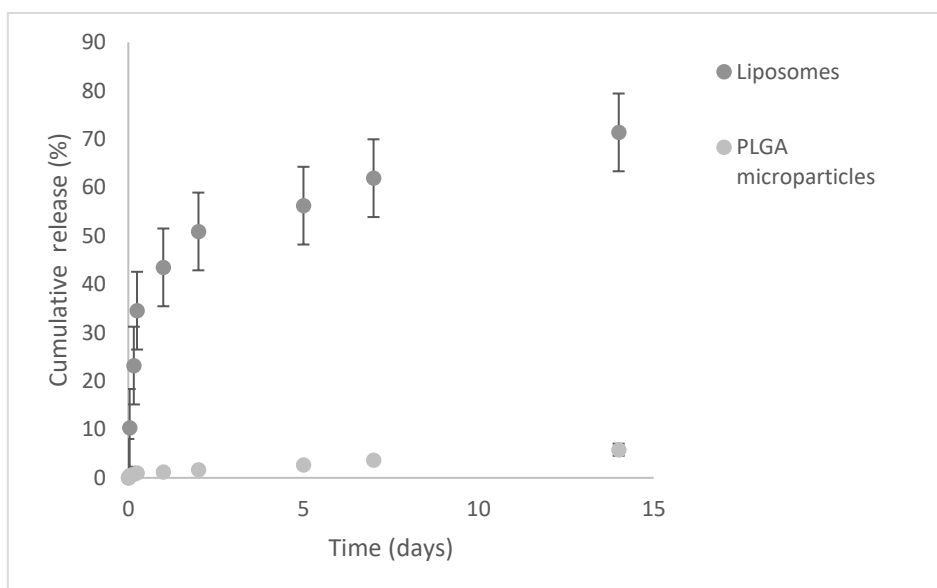


Figure 2. Drug release kinetics at 37°C

The possibility to drive the encapsulated BEV towards selected tissues was achieved by immobilizing the markers for angiogenesis on the produced carriers. The effective immobilization was demonstrated by FTIR and by circular dichroism analysis. Furthermore, after all the production steps, it was verified that BEV was structurally in its active form, thus maintaining its biological properties. Cell viability and hemocompatibility with human endothelial cells and human red blood cells confirmed the compatibility of this innovative drug delivery system as next generation therapy for angiogenesis based diseases, as atherosclerosis.

4. Conclusions

In this work a complete study about the encapsulation and targeting of Bevacizumab using different drug carriers was presented. At the optimized conditions of production, the best carrier for the application was selected in the PLGA nanoparticles. This carrier allowed the higher entrapment efficiency, the best particles size distribution and particle stability, the possibility of efficient and oriented attachment on the surface of functionalizing molecules, able to make specific targeting to selected tissues.

This work was financed by “Curiosity-driven project 2020” University of Genoa.

References

- [1] Baião, A., F. Sousa, A. V. Oliveira, C. Oliveira and B. Sarmento (2020). "Effective intracellular delivery of bevacizumab via PEGylated polymeric nanoparticles targeting the CD44v6 receptor in colon cancer cells." *Biomaterials Science* 8(13): 3720-3729.
- [2] M.L Hans, A.M Lowman, Biodegradable nanoparticles for drug delivery and targeting, *Current Opinion in Solid State and Materials Science*, Volume 6, Issue 4, 2002, Pages 319-327,
- [3] Lissette Agüero, Dionisio Zaldivar-Silva, Luis Peña, Marcos L. Dias, Alginate microparticles as oral colon drug delivery device: A review, *Carbohydrate Polymers*, Volume 168, 2017, Pages 32-43
- [4] Trucillo, P.; Campardelli, R.; Reverchon, E. Liposomes: From Bangham to Supercritical Fluids. *Processes* 2020, 8, 1022. <https://doi.org/10.3390/pr8091022>
- [5] Flávia Sousa, Harkiranpreet Kaur Dhaliwal, Florence Gattacceca, Bruno Sarmento, Mansoor M. Amiji, Enhanced anti-angiogenic effects of bevacizumab in glioblastoma treatment upon intranasal administration in polymeric nanoparticles, *Journal of Controlled Release*, Volume 309, 2019, Pages 37-47,

Integration and Digitalization in the Manufacturing of Therapeutic Proteins

Mattia Sponchioni, Tae Keun Kim, Ismaele Fioretti and Massimo Morbidelli ()*

Dipartimento di Chimica, Materiali e Ingegneria Chimica

Politecnico di Milano, Milano, Italy

**Corresponding author E-Mail: massimo.morbidelli@polimi.it*

Increasing costs and time pressure, as well as diversifying pipelines asking for more flexible production concepts and better product safety and efficacy, are driving the biopharmaceutical industry towards continuous and integrated manufacturing. However, we are still far from an efficient implementation of such technologies. The full exploitation of their potential requires significant advances in process digitalization for online monitoring, control, optimization and maintenance.

In particular, we consider hybrid approaches, where statistical methods based on machine learning techniques are used online in combination with ad-hoc mechanistic models. As an experimental basis for discussion, we take an automated end-to-end integrated platform to produce a monovalent monoclonal antibody of industrial relevance. The process consists of a perfusion bioreactor, a continuous protein A capture step, followed by low-pH virus inactivation, and frontal and flow-through chromatographic steps for final polishing.

Applications include: development of soft sensors for up and down stream monitoring (Raman based), the hierarchical online process control and optimization of a capture twin columns unit and online maintenance (replacement of protein A based stationary phase in a monoclonal antibody capture process).

We discuss the need for an efficient centralized process data collection and hierarchical control system, firmly based on hybrid algorithms, to allow continuous integrated manufacturing of biopharmaceuticals to develop and grow in agreement with the trends of industry 4.0.

Development of model-based strategies to accelerate the experimental campaign for the production of oral solid dosage through direct compression

Francesca Cenci¹, Gabriele Bano², Charalampos Christodoulou⁴, Yuliya Vueva³,
Simeone Zomer³, Massimiliano Barolo¹, Fabrizio Bezzo¹, Pierantonio Facco^{1*}

1 CAPE-Lab – Computer-Aided Process Engineering Laboratory,

Department of Industrial Engineering, University of Padova,

via Marzolo 9, 35131 Padova, Italy;

2 GlaxoSmithKline (GSK), 1250 S Collegeville Rd, Collegeville (PA), United States (USA);

3 GlaxoSmithKline (GSK), Park Road, Ware SG12 0DP, United Kingdom (UK);

4 GlaxoSmithKline (GSK), Gunnels Wood Road, Stevenage SG1 2NY, United Kingdom (UK)

**Corresponding author E-Mail: pierantonio.facco@unipd.it*

Abstract

Oral Solid Dosage (OSD) forms are widely used because they are easier to manufacture and transport with respect to other pharmaceuticals and they can be advantageous for patients, e.g. because dosage measurement is not needed. This impacts the market, too: Future Market Insights forecasts OSD market to grow from US\$493.2 bn in 2017 to US\$ 926.3 bn by the end of 2027 [9].

In this context, our study focuses on the production of solid tablets through direct compression: API, excipients and lubricants are fed to a blender and mixed for a precise blending time; then, the powder blend fills the dies of a tablet press and it is transformed into solid tablets thanks to the compression applied by the press punches. The only factor that facilitates tablets manufacturability is the lubrication step, which improves powder flowability [6] and prevents the powder from sticking to the die walls during compression [7,8].

Once the tablet has been ingested by the patient, it must be disintegrated, dissolved and absorbed in the desired point, usually in the gastrointestinal tract [3]. Such behavior is influenced by the manufacturing process, namely by lubrication and compression, and can be analyzed preliminarily through the assessment of tablets tensile strength, which is an intermediate property of the product. Different semi-empirical models have been proposed to describe the relation among these variables; for example, the Kushner and Moore model [4] relates tensile strength to the lubrication through three parameters. Then, Nassar et al. [5] expanded the expression of two of those parameters in order to take into account the effects of powder compression in the tablet press.

The extended Kushner and Moore model is very useful to the purpose of accelerating the design and scale-up of lubrication units, however it requires a considerable amount of data to be calibrated. Usually, up to 9 blends with different lubrication extents are prepared and then compressed in a compaction simulator. This leads to an excessive consumption of API, which is the most expensive species involved and that may not be available during drug development.

In our study we tackled this issue by proposing a science-driven method to select experimental conditions called “model-based design of experiments” (MBDoE). Differently from trial and error approaches, MBDoE does not rely on the experts’ knowledge, but on the mathematical representation of the process given by the model. More specifically, it is an optimization problem which finds the “optimal” experiments, namely the experiments that allow to maximize the information about the system. The information content of data is quantified by the Fisher information matrix [1], which is strictly related to the uncertainty region of model parameters: indeed, experiments that maximize a scalar measure of the FIM allow also to minimize the uncertainty region of parameters after calibrating the model.

However, the classical formulation of the MBDoE optimization problem was not suitable for the system under study: since the extended Kushner and Moore model used to build the objective function is algebraic, the result

of MBDoE was made of one optimal value of lubrication and one optimal value of solid fraction, therefore by one optimally lubricated and compressed tablet. However, it is not possible to perform only one compression point in the tablet press (i.e., to produce only one tablet). To overcome this limit, we adapted the Fisher information matrix calculation in order to get optimal “profiles” as MBDoE results, namely multiple optimal values of solid fraction for the optimal value of lubrication.

We applied the novel MBDoE approach to different drug formulations in order to test the methodology robustness in case of different drug behaviors in terms of lubrication sensitivity. The results were analyzed both in terms of parameters precision and model prediction accuracy: independently of the formulation considered, the model calibrated with three or four optimal profiles was characterized by statistically sound parameters estimates and by a good prediction of the tablet tensile strength, satisfying all the requirements set by the industry in this field. The high information content of the optimal experiments calculated through MBDoE allowed us to reduce the experimental burden up to 70% with respect to the standard industrial practice, thus cutting down the costs for materials and labor and the time to put new tablets formulations on the market.

References

- [1] Fisher, R., A. (1950). Contributions to Mathematical Statistics. Papers 10, 11 and 38, John Wiley and Sons.
- [2] Franceschini, G., Macchietto, S. (2008). Novel Anticorrelation Criteria for Model-Based Experiment Design: Theory and Formulations. *AICHE Journal*, **54**, 1009–1024.
- [3] Fung, K. Y. and Ng, K. M., 2003. Product-centered processing: Pharmaceutical tablets and capsules. *AICHE Journal*, **49(5)**, 1193–1215.
- [4] Kushner, J., Moore, F. (2010). Scale-up model describing the impact of lubrication on tablet tensile strength. *International Journal Pharmaceutics*, **399**, 19–30.
- [5] Nassar, J., Williams, B., Davies, C., Lief, K., Elkes, R. (2021). Lubrication empirical model to predict tensile strength of directly compressed powder blends. *International Journal Pharmaceutics*, **592**, 119980.
- [6] Podczek, F., Miah, Y., (1994). The influence of particle size and shape on the angle of internal friction and the flow factor of unlubricated and lubricated powders. *International Journal Pharmaceutics*, **144**, 187- 194
- [7] Sabir, A., Evans, B., Jain, S. (2001). Formulation and process optimization to eliminate picking from market image tablets. *International Journal of Pharmaceutics*, **215**, 123-135
- [8] Yamamura, T., Ohta T, Taira T, Ogawa Y, Sakai Y, Moribe K, Yamamoto K. (2009). Effects of automated external lubrication on tablet properties and the stability of eprazinone hydrochloride. *International Journal Pharmaceutics*, **370(1-2)**, 1-7.

Websites

- [9] www.futuremarketinsights.com

Accelerating cell lines selection in biopharmaceutical process development through machine learning on process and metabolomic dynamics

Gianmarco Barberi^a, Antonio Benedetti^b, Paloma Diaz-Fernandez^c, Daniel C. Sévin^d, Johanna Vappiani^d, Gary Finka^c, Fabrizio Bezzo^a, Massimiliano Barolo^a, Pierantonio Facco^{a,1}

^a *CAPE-Lab – Computer-Aided Process Engineering Laboratory, Department of Industrial Engineering, University of Padova, via Marzolo, 9 – 35131 Padova PD, Italy*

^b *Process Engineering & Analytics, Product Development and Supply, GlaxoSmithKline R&D, Stevenage, UK*

^c *Biopharm Process Research, Biopharm Product Development and Supply, GlaxoSmithKline R&D, Stevenage, UK*

^d *Cellzome GmbH, GlaxoSmithKline R&D, Heidelberg, Germany*

Abstract

The production of therapeutic drugs based on monoclonal antibodies has grown exponentially, in particular for the treatment of immunological and oncological diseases and, more recently, Covid-19.

The monoclonal antibodies are typically produced in mammalian cell cultures. The identification of the cell lines that guarantee the desired product quality attributes, such as productivity and stability, is extremely important in the development of new antibodies. The cell selection process requires an extensive and time-consuming experimentation, which can last several months, if not years.

In this work, we show how machine learning accelerates the selection of the best performing cell lines during bioprocess development and scale-up by exploiting the wealth of information retained in the process measurements from cell cultures and in the respective biological features, such as the metabolomic data. Metabolomics provides valuable information to increase the confidence in cell

¹ Correspondence regarding this paper should be addressed to: pierantonio.facco@unipd.it

lines selection. In fact, its integration with data on cell process performance allows inferring the metabolic characteristics and the biological functions related to a desired cell behavior along the culture. Furthermore, metabolomic dynamics fused with product quality attributes can be used to identify the metabolic traits of cell lines with industrially relevant phenotypes. Specifically, the accurate prediction of the product titer time trajectory from cell metabolism information and the identification of highly productive cell lines since the early stages of the culture, provided important pieces of information to improve and accelerate the cell selection.

Crystal Engineering as a tool for rational design of novel sustainable food, agrochemical and pharmaceutical formulations

Panayiotis Klitou¹, Lorenzo Metilli², Elena Simone^{3*}

1 School of Food Science and Nutrition, University of Leeds, Leeds, United Kingdom; 2 Laboratoire Rheologie et Procédés, Université Grenoble Alpes, Grenoble, France ; 3 Department of Applied Science and Technology, Politecnico di Torino, Torino, Italy

**Corresponding author E-Mail: elena.simone@polito.it*

1. Introduction

Recent progress in pharmacology, plant biology and biotechnology has led to a dramatic increase in potency and specificity of new generation drugs, active agrochemical ingredients and food nutraceuticals. Unfortunately, this has been accompanied by poor bioavailability and water solubility: it is estimated that around 40% of the active pharmaceutical ingredients currently on the market and 60% of the ones still in development are poorly soluble due to their high molecular weight and structural complexity. These issues have pushed scientific research towards the design of complex formulations, with enhanced dissolution rate

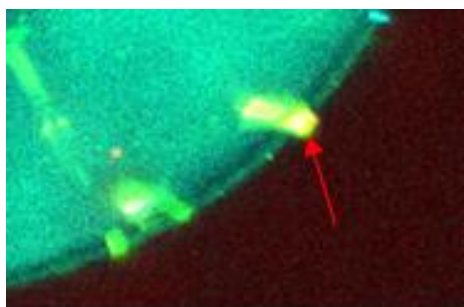


Figure 1. Confocal microscopy image of quercetin crystals stabilizing a water/oil emulsion.

and bioavailability, which allow more efficient and targeted delivery of active ingredients (AIs). Multiphase systems (e.g., emulsions, foams, creams) are a convenient and effective encapsulation and delivery strategy, particularly for oral and topical formulations. Currently, synthetic excipients, surfactants and specialty polymers are used to create formulations with enhanced properties. However, these compounds are derived from non-renewable resources through some of the most greenhouse gas-intensive manufacturing processes. For this reason it is necessary to replace the common synthetic stabilizers used for these products with natural, biocompatible and biodegradable materials. These include natural micro and nano-

particles (Pickering stabilizers) such as proteins, polysaccharides and various crystalline materials including cellulose, chitin, fat crystals and polyphenol crystals. Pickering systems are particularly promising since particles adsorb at interfaces more strongly than surfactants, providing significantly more stable formulations (Figure 1). The stability of Pickering systems is strongly affected by particle size and shape, but surface wettability is the most important property of Pickering particles. For faceted, anisotropic crystals surface wettability is not easy to determine. In fact, crystals present multiple crystallographic facets, whose surface properties (e.g., polarity, wettability) depend on the type and directionality of the intermolecular interactions that characterize each facet. The purpose of the presented work is to understand how crystal properties (size, shape and polymorphism) of Pickering particles affect their surface properties, hence their orientation and adsorption behavior at interfaces.

2. Methods

Molecular modelling (synthons analysis from crystallographic data) and experimental work (e.g., crystal properties characterization, stability studies) were conducted on two model systems: quercetin and cocoa butter. Two solid forms of quercetin, a solvate and a hydrate, were studied using Habit 98, a synthonic molecular modelling tool. The bulk intermolecular interactions and surface chemistry of the mentioned crystals

of quercetin were estimated. An empirical force field was used to calculate the strength, directionality and dispersive nature of the intermolecular interactions. The strongest bulk intrinsic synthons molecular interactions in the crystalline lattice have been identified and characterized, and conformational analysis was performed, evaluating how the presence of the solvent molecule(s) affect the crystal structure, packing and the stability of the different forms. The experimental study consisted in the production (crystallization and aeration) and characterization of oil-based foams stabilized by cocoa butter crystals (oleofoams). The crystals and the air bubbles incorporated in the foams were characterized with polarized and electron microscopy, small and wide angle X-ray scattering, X-ray tomography and differential scanning calorimetry. The effect of processing conditions and the concentration of cocoa butter crystals on the microstructure and the stability of the produced foams were tested.

3. Results and discussion

Two solid forms of quercetin were modeled, a 2:1 hydrate crystal and a 1:1 DMSO solvate. Figure 2 shows schematically the main results of the synthon analysis and the attachment energy study.

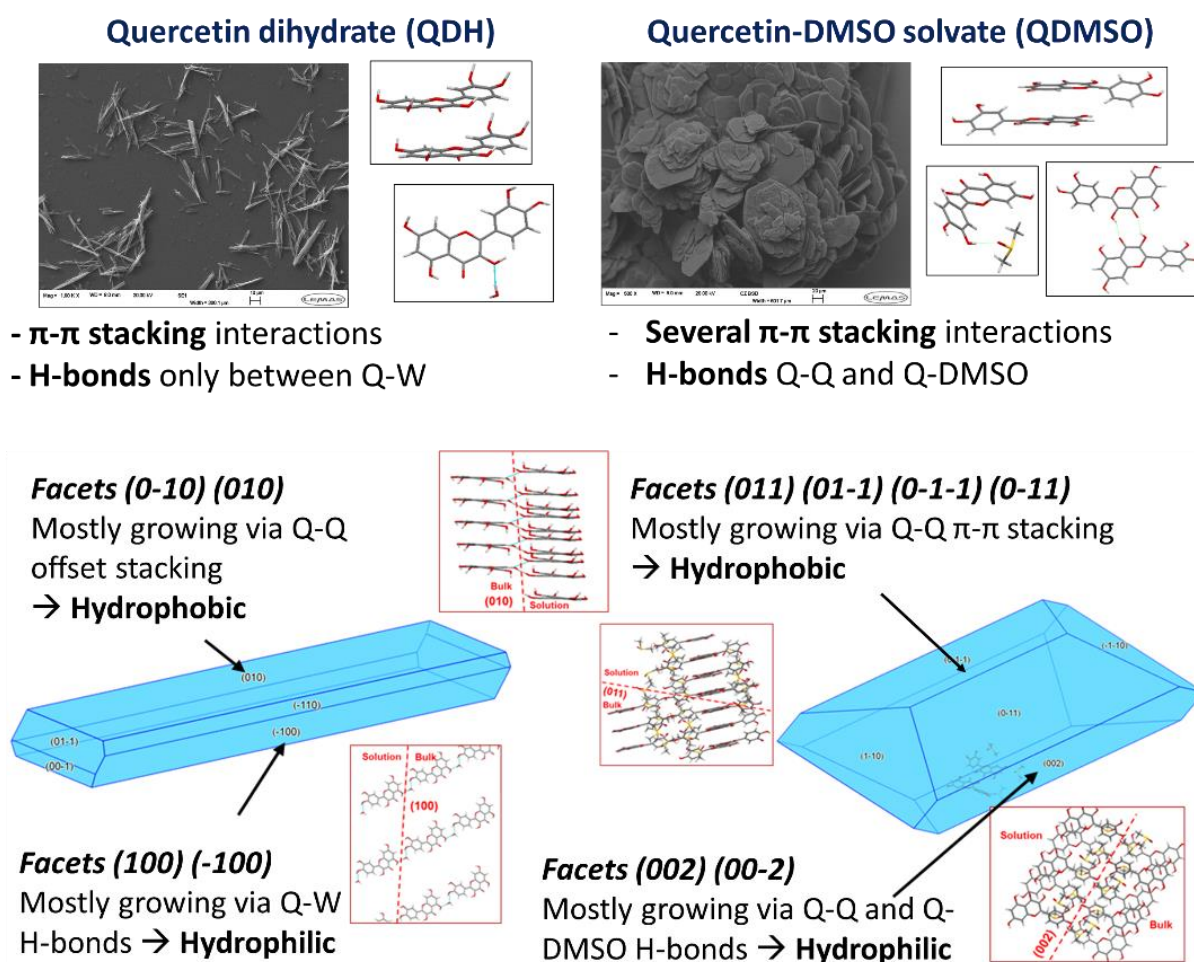


Figure 2. Main synthons of quercetin dihydrate and DMSO solvate. Chemical nature of the different facets of both forms from the attachment energy model.

Both structures show H-bonds and π - π stacking interaction; however, in the DMSO solvent H-bonds and dipole-dipole interactions contribute more to total lattice energy (around 39%) compared to the dihydrate structure (<10%). The attachment energy model showed that both structures are hydrophobic, with a more hydrophilic and a more hydrophobic facet. This indicates the possibility of modifying the overall surface nature

of both crystal forms of quercetin by modifying the morphology of the particles. Hence, both solid forms could be engineered to be either hydrophilic or hydrophobic, suitable for Pickering stabilization of a wide range of multiphase structures.

Experimental work was instead conducted on oil based foams stabilized by cocoa butter crystals. Crystals were produced by cooling from a liquid mixture of cocoa butter and high oleic sunflower oil. The effect of cooling rate and initial composition (percentage of cocoa butter in oil) on the foamability and storage stability of the produced oleofoam were tested. Figure 3 shows the microstructure of oleofoams characterized with polarized optical microscopy, electron microscopy and X-ray tomography. Evidence of Pickering stabilization is noticeable in the polarized and electron microscopy images.

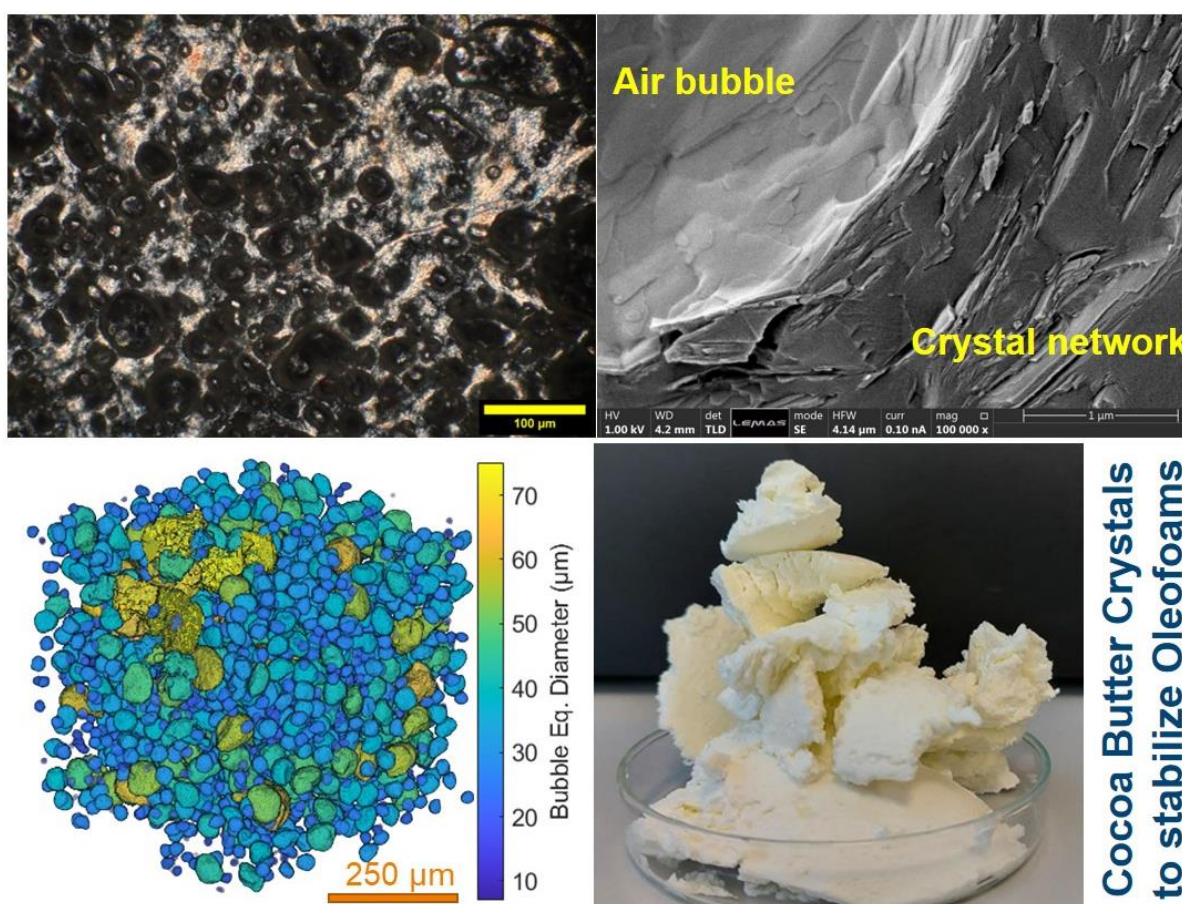


Figure 3. Oleofoams stabilized by cocoa butter crystals. Microstructure highlighted via polarized microscopy, electron microscopy and X-ray tomography.

The amount of cocoa butter crystals dispersed in oil was found to have a strong effect on both foamability and stability of oleofoams; whereas the cooling rate did not affect much the microstructure of these materials. At the concentrations and cooling rates used only one polymorphic form (β V) was observed after crystallization. Higher amount of cocoa butter in the oil determined a slightly lower volume of incorporated air but higher bubble stability during long term storage, with less Ostwald ripening and phase separation. Instead, the cooling rate affected the size and morphology of cocoa butter crystals agglomerates dispersed in the oil after crystallization; however, the size, shape and chemical nature of cocoa butter crystals nanoplatelets was independent of the cooling rate. During aeration crystals aggregates were destroyed due to the effect of shear and temperature increase, leaving only the nanoplatelets at the air bubble interfaces and, hence cancelling the effect of different cooling rates during crystallization.

4. Conclusions

Crystal engineering can help in the design of tailored crystalline particles that can stabilize multiphase formulations for a wide range of applications including pharma, food and agriculture. Molecular modelling is a powerful tool to study facet specific surface chemistry of crystalline materials. It can help in the design of the optimal solid form and morphology of Pickering particles for specific applications.

Furthermore, the mechanism of stabilization of cocoa butter crystals in oil based foams was studied with a multi-technique approach. In particular, the relationship between processing and microstructure was studied, with a focus on the role of crystals in the efficiency of incorporation of air bubbles and in their stability. Such information can help in determining the optimal cocoa butter crystals population for the design of ultra-stable oleofoams.

References

- [1] Klitou, P., Pask, C.M., Onoufriadi, L., Rosbottom, I., Simone, E. (2020) *Crystal Growth and Design*, 20 (10), pp. 6573-6584.
- [2] Klitou, P., Rosbottom, I., Simone, E. (2019) *Crystal Growth and Design*, 19 (8), pp. 4774-4783.
- [3] Metilli, L., Lazidis, A., Francis, M., Marty-Terrade, S., Ray, J., Simone, E. (2021) *Crystal Growth and Design*, 21 (3), pp. 1562-1575.
- [4] Metilli, L., Storm, M., Marathe, S., Lazidis, A., Marty-Terrade, S., Simone, E. (2022) *Langmuir*, 38 (4), pp. 1638-1650.
- [5] Metilli, L., Storm, M., Bodey, A.J., Wanelik, K., Tyler, A.I.I., Lazidis, A., Marty-Terrade, S., Simone, E. (2021) *Materials Characterization*, 180, art. no. 111408.

Cancer viscoelasticity: A dynamic compression assay for tumor spheroids characterization

Rosalia Ferraro, Sergio Caserta*

Università degli Studi di Napoli Federico II, Piazzale Vincenzo Tecchio, 80, 80125 Napoli NA

**Corresponding author E-Mail: sergio.caserta@unina.it*

1. Introduction

Cancer is a complex, heterogeneous and multifactorial disease, that is a leading healthcare problem worldwide. Several experimental and clinical studies of malignant neoplasms indicate that invasive growth and metastasis are the main manifestations of tumor progression, strongly influenced by the microenvironment, in particular chemical [1, 2] and mechanical [3-5] stresses.

Deep biomechanical differences between healthy and tumoral tissues exist, in fact, malignant transformations are associated with significant changes in the cytoskeleton structure and cell-cell interactions. Understanding the mechanical behavior and cellular organization is not easy. A novel approach here proposed is based on the analysis of living tissues as bio-soft matter, based on typical rheological models traditionally developed for non-bio complex fluids (polymers, surfactants, foams, etc.) [6].

Our work is focused on the development and validation of an innovative methodology to measure the role of external (bio-) mechanical stimuli on the capacity of tumors to invade the surrounding healthy tissue, using a 3D model of not-vascularized tumor: cell spheroid [7-9]. Tumoral spheroids are tightly bound cellular aggregates that tend to form when cells are grown in a nonadherent environment. To measure the mechanical response of the system, a dynamic compression was applied to the spheroids. Shape evolution of spheroids under controlled compression was modelled using standard springs and dampers rheological models available in the literature in order to estimate viscosity and elastic moduli of the system, quantifying the cell adhesion and invasive potential of different types of tumors.

2. Methods

2.1. Cell culture

A non-tumoral cell line (NIH/3T3) was used as control in the mechanical assay. Cells were cultured in their standard growth medium in 2D monolayers under the typical cell culture conditions, at 37°C in a humidified atmosphere (5% CO₂). In detail, NIH/3T3 mouse fibroblasts cells were cultured in Dulbecco's Modified Eagle's Medium (DMEM) supplemented with 10% (v/v) Fetal Bovine Serum (FBS), 1% (v/v) antibiotics (50 units/mL penicillin and 50 mg/mL streptomycin) and 1% (v/v) L-glutamine.

2.2. Spheroid formation

Spheroids were produced using the "agarose multi-well plate method". Specifically, 1% agarose solution was prepared by dissolving agarose powder (E AGAROSE, Conda, Cat n° 8100) in water at 200°C for 20' using a magnetic stirrer to homogenize the solution. Then, agarose solution was rapidly pipetted in 200 µl aliquots into the wells of a 48-well culture dish under sterile conditions and allowed to cool down. By capillary, agarose solution rises along the walls of the wells, thus gelifying in a few minutes forming a hemi-spherical meniscus. The non-adhesive concave surface promotes the collection of cells in the meniscus and cell-cell adhesion establishment; this leads to the formation of cell aggregates that finally evolve in compact spheroids after an adequate incubation time, depending on cell type and concentration. Typically, 5-10 days (depending on cell line) are required to obtain compact spheroids of adequate size.

2.3. Image and Chemotaxis Data Analysis

The dynamic evolution of tumoral spheroids was quantified by measuring different morphological parameters, i.e., area (A , μm^2) and diameter (d , μm). Spheroids images were analyzed using a commercial image analysis software (Image Pro Plus 6.0). Variations in the diameter as measured in the direction orthogonal to the compression was defined as strain ($\varepsilon = \frac{d_i - d_0}{d_0}$), and plotted as function of time, during the compression test.

2.4. Preparation of assay

In our compression assay, spheroids were placed in a Petri-dish, filled with Phosphate-Buffered Saline (PBS), and mechanical stress (σ , kPa) were applied to spheroids by using coverslip glasses. Images were acquired in time lapse using an inverted microscope (Zeiss Axiovert 200M) with a delay time of 2 seconds, in order to follow the spheroid deformation during the creep test experiment.

3. Results and discussion

Representative phase contrast microscopy images of NIH/3T3 spheroids are reported in **Figure 1**, comparing the undeformed spheroid with final image of, corresponding to the steady deformation. It is evident that spheroid size significantly increases after compression, proving the phenomena can be measured with high precision.

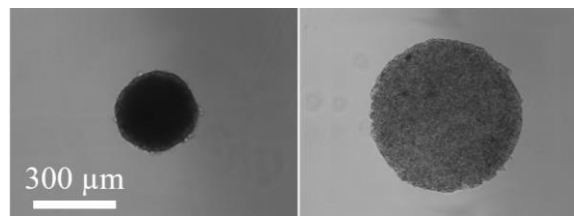


Figure 1. Representative phase-contrast microscopy images showing the morphological response of NIH/3T3 spheroids before (left) and after (right) mechanical stress.

To quantify spheroids morphological response, evolution of deformation, ε , is reported as function of time, t , in **Figure 2**, and compared to models inspired from standard non-bio soft matter systems. As shown, deformation value increases $\sim 20\%$ as response of mechanical stress. In addition, fitting experimental data using standard springs and dampers rheological models, available in the literature, viscosity, elastic modulus and relaxation time of the system can be estimated. For example, the relaxation time, intended as the time necessary for the cell reorganization, in this experimental condition, is $\sim 50\text{s}$, corresponding to the onset of linear plateau in the deformation.

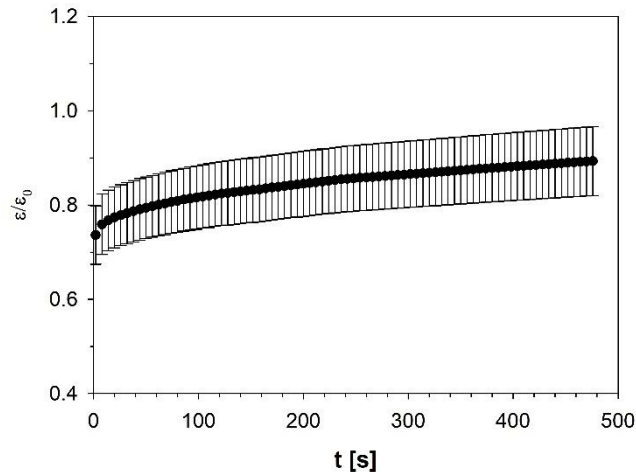


Figure 2. Creep test conducted at $\sigma \sim 54$ kPa.

4. Conclusions

In this paper, an innovative experimental assay aimed to quantify spheroid morphological response to a mechanical stress is proposed, in order to characterize rheological property of the system to be related to invasiveness of tumoral mass. The methodology is based on a mechanical analysis of living tissues as bio-soft matter.

Tumour spheroids were subjected to a stress by using a coverslip glass and observed by means of Time-Lapse video microscopy. The approach here proposed represents an innovative technique to investigate complex biological systems, such as cancer. The possibility to quantify differences in invasiveness of cancer cell types represents a key advancement that can be implemented in personalized medicine applications.

References

- [1] R. Ferraro, F. Ascione, P. Dogra, V. Cristini, S. Guido, S. Caserta, Diffusion-induced anisotropic cancer invasion: a novel experimental method based on tumour spheroids, *AICHE Journal* n/a(n/a) e17658. <https://doi.org/https://doi.org/10.1002/aic.17678>.
- [2] C.K.N. Li, The glucose distribution in 9L rat brain multicell tumor spheroids and its effect on cell necrosis, *cancer* 50(10) (1982) 2066-2073.
- [3] G. Helmlinger, P.A. Netti, H.C. Lichtenbeld, R.J. Melder, R.K. Jain, Solid stress inhibits the growth of multicellular tumor spheroids, *Nature biotechnology* 15(8) (1997) 778-783.
- [4] F. Montel, M. Delarue, J. Elgeti, D. Vignjevic, G. Cappello, J. Prost, Isotropic stress reduces cell proliferation in tumor spheroids, *New Journal of Physics* 14(5) (2012) 055008.
- [5] M. Delarue, F. Montel, D. Vignjevic, J. Prost, J.-F. Joanny, G. Cappello, Compressive stress inhibits proliferation in tumor spheroids through a volume limitation, *Biophysical journal* 107(8) (2014) 1821-1828.
- [6] M.S. Steinberg, Reconstruction of tissues by dissociated cells, *Science* 141(3579) (1963) 401-408.
- [7] D. Drasdo, S. Höhme, A single-cell-based model of tumor growth in vitro: monolayers and spheroids, *Physical biology* 2(3) (2005) 133.
- [8] F. Hirschhaeuser, H. Menne, C. Dittfeld, J. West, W. Mueller-Klieser, L.A. Kunz-Schughart, Multicellular tumor spheroids: an underestimated tool is catching up again, *Journal of biotechnology* 148(1) (2010) 3-15.
- [9] T.-M. Achilli, J. Meyer, J.R. Morgan, Advances in the formation, use and understanding of multi-cellular spheroids, *Expert opinion on biological therapy* 12(10) (2012) 1347-1360.

CFD-DEM simulations of shear-activated nanotherapeutic particles

Lorenzo Vasquez Giuliano^{1*}, Graziano Frungieri², Antonio Buffo¹, Marco Vanni¹

1 Department of Applied Science and Technology, Politecnico di Torino, Torino, Italy

*2 Lehrstuhl für Systemverfahrenstechnik, TUM School of Life Sciences,
Technische Universität München, Gregor-Mendel-Straße 4, 85354 Freising, Germany*

**Corresponding author E-Mail: lorenzo.vasquez@polito.it*

1. Introduction

The obstruction of blood vessels due to clots is a worldwide leading cause of death. The treatment of ischemic pathologies caused by obstruction clots is a major issue in this field: a tissue plasminogen activator is administered to the patient to dissolve the clot and restore the normal blood flow [1,2]. This is the only FDA-approved treatment, but it presents some limitations: it requires a tempestive administration of the protein (within 3 hours from the onset of the ischemic symptoms) and the administered dose must be monitored to limit the amount of active agent that is free to circulate in the patient's body.

A plethora of targeted drug delivery strategies have been considered to face this challenge. One of the most promising approaches is based on shear-activated nanotherapeutics and has been proposed by Korin and coworkers [3]. Polymeric nanometer-sized particles are coated with the active agent and constitute a micrometer-sized aggregate, or cluster. The strategy is inspired by the activation mechanism of natural platelets, and it is based on the effects of the flow field distortion caused by the obstruction itself. The cluster is designed to be stable, or de-activated, if subjected to a normal blood flow field, while it breaks when subjected to the local increase of the hydrodynamic forces caused by the clot. The breakup of the cluster generates smaller fragments that are more likely to adhere to the clot and perform the thrombolytic action. Among the other advantages, this approach does not require precise knowledge of the clot position or any external activation mechanism, thus offering a potential innovative approach for the treatment of life-threatening diseases that result from acute vascular occlusion.

An accurate tuning of the properties of the drug carrier is fundamental to achieve remarkable results in this field of application. At the early stage of drug carrier design, valuable insights can be obtained by coupling in-vitro experiments with numerical simulations. Breakup tests of plausible drug carrier morphologies can be performed in a microfluidic device that mimics an obstructed blood vessel, while computational fluid dynamics (CFD) simulations can be used to predict wall shear stress distribution inside the device. However, the mechanical response of clusters to the fluid dynamic stress is also crucial and needs to be investigated as well [4]. A discrete element method (DEM) can track the motion of every single primary particle in the cluster based on the forces acting on it, considering both the adhesive force binding a pair of particles together and the force exerted by the fluid on the discrete, dispersed phase [5,6]. Fluid dynamic forces are modelled by resorting to Stokesian dynamics [7], a method that has been widely employed to predict cluster restructuring and breakup in simple and complex flow field configurations [8-12].

The present work illustrates a numerical investigation of the flow field characteristics in obstructed blood vessels and in a microfluidic device realized for future in-vitro experimentations. The shear stress exerted by the fluid on the dispersed phase is converted by DEM simulations into the mechanical stress distribution acting in clusters, to predict the occurrence of breakup.

2. Methods

CFD simulations have been employed to compute the steady-state flow field of a fluid inside the vessel, whereas DEM simulations based on Stokesian dynamics have been used to investigate the mechanical response of three different drug carrier morphologies placed in the flow field. The simulated fluid is water. It is Newtonian and incompressible and its flow regime is assumed to be laminar. Clusters have been treated as

tracer particles passively carried by the flow field, to evaluate the hydrodynamic forces exerted by the fluid on them. CFD simulations have been conducted using *ANSYS Fluent 20* by solving the continuity and momentum transport equations and by coupling pressure and velocity with a SIMPLE algorithm.

Axisymmetric and asymmetric deformed cylindrical tubes have been chosen as a valuable approximation of an obstructed blood vessel [13,14], whereas the microfluidic device has a rectangular section. The three geometries present a pre-stenotic tract, a stenotic tract with 95% lumen obstruction, and a post-stenotic tract. The flow rate has been adjusted according to a trial-and-error procedure until the same pathological values of wall shear stress onto the obstruction were reached.

Three types of cluster morphologies have been considered: porous isostatic aggregates, spherical random close packing aggregates (RCP) and hollow aggregates (Figure 1). Porous aggregates result from a numerical reproduction of a diffusion-controlled aggregation process. These aggregates are isostatic, i.e., the failure of a single bond leads to the collapse of the entire structure. However, drug carriers are often produced via spray-drying. During a spray-drying process, the Péclet number plays a relevant role [15]. The Péclet number compares the diffusion velocity with the shrinkage velocity: if the diffusion of the particles inside an evaporating droplet is faster than the droplet shrinkage, the concentration of primary particles is kept homogeneous throughout the process and the resulting cluster is compact. On the other hand, particles accumulate at the periphery of the droplet if the shrinkage is faster than the diffusion, thus leading to shell-type aggregates with a pronounced void at their core. In this work the former output of a spray-drying process is generated by a Random Close Packing algorithm, i.e., minimizing the void fraction of the cluster, while the latter output is generated by removing internal particles from the RCP clusters. These classes of clusters are hyperstatic, and the failure of a single bond does not necessarily lead to the collapse of the entire structure.

Stokesian dynamics allows one to express the relationship between hydrodynamic force and torque and the relative velocity of primary particles compared to the velocity of the undisturbed flow at the particle position, through the definition of a mobility matrix. Therefore, hydrodynamic forces and torques acting on each primary particle of the aggregate can be evaluated. In our simulations, clusters are supposed to be rigid; hence deformation and breakup of clusters are not modelled, but tensile forces acting inside the clusters are known, thus giving valuable insights about the stability of the structure. The normal force acting at the contact region between each pair of primary particles is obtained by linearisation of the JKR theory [16], whereas the models by Dominik and Tielens and Marshall [17,18] are employed to calculate tangential force, bending moment and torsional moment.

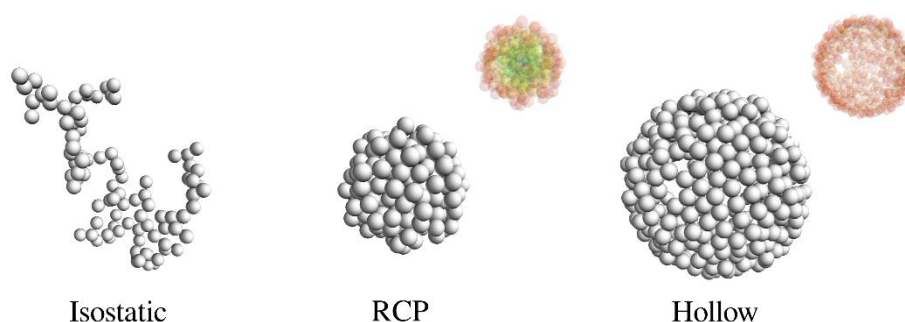


Figure 1. Isostatic, Random Close packing (RCP) and hollow aggregates. The difference between the compact core of RCP and the empty core of hollow aggregates is highlighted by a colormap.

3. Results and discussion

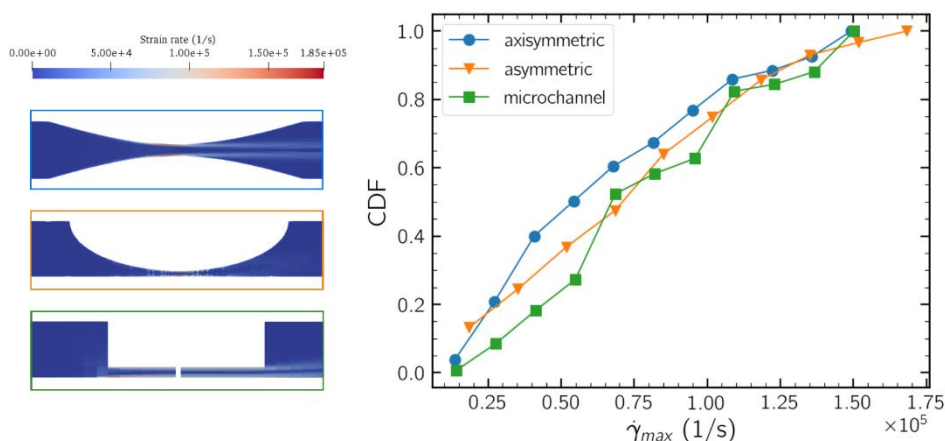


Figure 2. Left: strain rate contour on the longitudinal plane for axisymmetric and asymmetric obstruction and for the microchannel. Right: Cumulative Distribution Function of the maximum strain rate along trajectories in the three vessels.

The flow field in the three vessels has been fully characterized, and thus valuable insights about the hydrodynamic forces and the recirculation phenomena have been inferred. A peak of hydrodynamic forces has been found right onto the obstruction and the formation of vortices at the end of the stenotic tract has been observed. As mentioned above, the strain rate peak is a potential trigger for the activation of drug carriers flowing in blood vessels, i.e., for their breakup right onto the clot. Moreover, recirculation phenomena can keep the generated fragments in proximity to the stenotic tract. A large dataset of tracer trajectories has been extracted, and for every trajectory the maximum experienced strain rate has been calculated. A cumulative distribution function (CDF) of the maximum strain rate encountered by particles flowing in the three vessels can be extracted (Figure 2), thus proving that our microfluidic device well approximates the flow field in an obstructed blood vessel, and therefore it is suitable for experimental trials.

The breakup of clusters is a direct consequence of the internal tensile stress generated by the surrounding flow field, and the stresses acting on clusters depend on both the local strain rate and the geometry of the cluster itself. The strain rate signals obtained in the microchannel have been converted into tensile stress acting at contact regions between primary particles by using Stokesian dynamics simulations. The mechanical response of isostatic, RCP and hollow clusters to the hydrodynamic sollicitation exerted by the flow-field in the microfluidic device has been studied. The CDFs in Figure 3 have been obtained from the maximum tensile stress experienced by a cluster along its path in the vessel. Internal stresses inside RCP clusters are low, therefore they are the most resistant class. Isostatic clusters show intermediate behaviour, while hollow clusters are the most fragile ones. As shown in Figure 3, the highest tensile stresses in isostatic clusters have been found at the core of the cluster and the fragments generated after a breakup event should be expected to have comparable dimensions. In RCP clusters the highest tensile stresses are in the outer region of the cluster because of their hyperstaticity, so breakup should lead to the detachment of small fragments from their outer surface. The distribution of mechanical forces inside the hollow clusters is similar, the shell-shape of the cluster limits the discharge of mechanical stress that characterizes a hyperstatic cluster. Therefore, the breakup of outer bonds should lead to the opening of the shell structure.

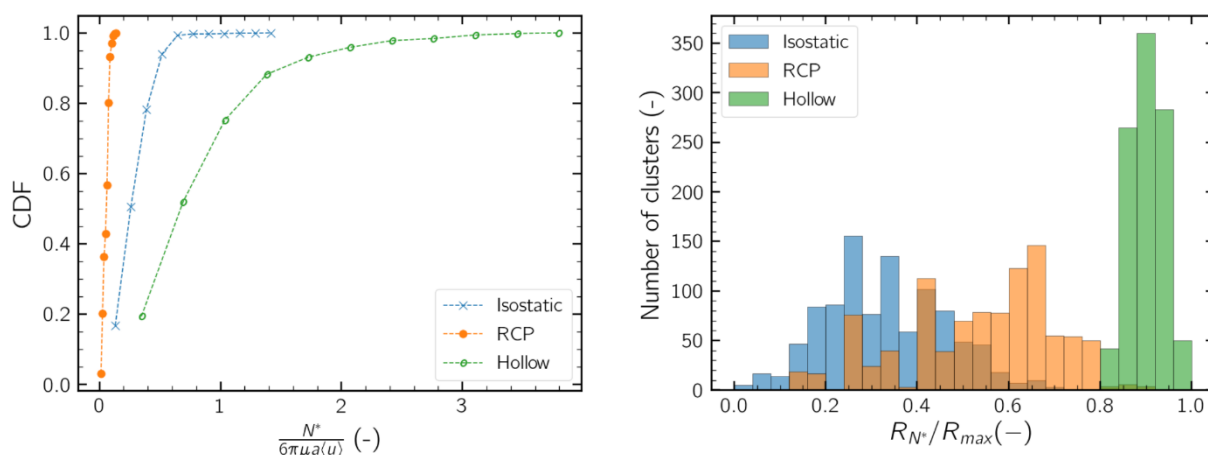


Figure 3. Left: Cumulative Distribution Function of the maximum tensile stress experienced by isostatic, RCP and hollow clusters flowing in the microchannel. Right: histogram showing the relative position of the most stressed bond in every aggregate.

4. Conclusions

CFD simulations of the flow field in obstructed vessels showed that fluid dynamic forces locally increase because of the lumen restriction. The microfluidic device represents a valid approximation of the flow field characteristics in clot-obstructed blood vessels and can therefore be employed for future in-vitro experimentations.

The local increase of fluid dynamic forces translates into a mechanical stress distribution inside clusters of particles flowing in the microchannel, and the magnitude of these mechanical stresses has been computed thanks to DEM simulations based on Stokesian dynamics. Compact aggregates are the most resistant ones, while hollow aggregates are the weakest class. The local increase of fluid dynamic stresses can effectively act as a trigger for the activation of drug carriers.

Such results will be used to effectively design drug carriers that are suitable for the proposed targeting strategy, thanks to an experimental campaign and the refinement of DEM breakup simulations.

References

- [1] J. Grotta, J. Marler, *Surg. Neurol.* 2007, 68, S12.
- [2] G. D. Graham, *Stroke* 2003, 34, 2847.
- [3] N. Korin, M. Kanapathipillai, B. D. Matthews, M. Crescente, A. Brill, T. Mammoto, K. Ghosh, S. Jurek, S. A. Bencherif, D. Bhatta, et al., *Science*, 2012, 337, 738.
- [4] M. Soos, L. Ehrl, M. U. Bäbler, M. Morbidelli, *Langmuir* 2010, 26, 10.
- [5] G. Frungieri, M. Vanni, *Powder Technol.* 2021, 388, 357.
- [6] G. Frungieri, M. U. Bäbler, M. Vanni, *Langmuir* 2020, 36, 10739.
- [7] L. Durlofsky, J. F. Brady, G. Bossis, *J. Fluid Mech.* 1987, 180, 21
- [8] M. Vanni, A. Gastaldi, *Langmuir* 2011, 27, 12822.
- [9] M. Vanni, *Comput. Phys. Commun.* 2015, 192, 70.
- [10] G. Frungieri, M. Vanni, *Can. J. Chem. Eng.* 2017, 95, 1768-1780.
- [11] Y. M. Harshe, M. Lattuada, *The Journal of Physical Chemistry B* 2016, 120, 7244.
- [12] G. Frungieri, G. Boccardo, A. Buffo, D. Marchisio, H. A. Karimi-Varzaneh, M. Vanni, *Can. J. Chem. Eng.* 2020, 98, 1880
- [13] Y. Zhou, C. Lee, J. Wang, *J. Healthc. Eng.* 2018, 2018.
- [14] G. Lorenzini, E. Casalena, *J. Biomech.* 2008, 41, 1862
- [15] E. Lintingre, F. Lequeux, L. Talini, N. Tsapis, *Soft Matter* 2016, 12, 7435
- [16] K. Johnson, K. Kendall, A. Roberts, *Proceedings Royal Society London A* 1971, 324, 301.
- [17] C. Dominik, A. Tielens, *Astrophysical Journal* 1997, 480, 647.
- [18] J. Marshall, *J. Comput. Phys.* 2009, 228, 1541.

Advanced Logistic in the Food Industry: a system engineering approach for a multi-layered solution

Maria Teresa Gaudio¹, Sudip Chakraborty², Stefano Curcio^{3*}

1,2,3 University of Calabria, Laboratory of Transport Phenomena and Biotechnology, Department of DIMES, Cubo-42a, 87036 Rende (CS), Italy

**Corresponding author E-Mail: stefano.curcio@unical.it*

1. Introduction

Final consumers are increasingly attentive to many aspects in our daily life. To achieve a sustainable in terms of both environmental footprint as well as the quality of the product new efficient and high performing systems is necessary. In this work the concept of "integrated logistics", which is able to account for all the phases and aspects of an innovative production system is optimized. This system also aims to combine the high quality and healthiness of the final product through process traceability, with the maximum possible environmental sustainability of the whole production process. It will not only reduce or eliminate hazardous waste or chemicals but also made ease of the whole logistics lines. In this context, food traceability is a key element for the safety and reliability of the entire food industry. It does not only respond to stringent regulations that differ from country to country, but it also requires ever greater access to data and information, making the processes of the supply-chain more complex and opening new market opportunities. Furthermore, the traceability of information along the supply-chain, "from fork to farm" and "from farm to fork", is essential to combat fraud and guarantee the quality of final products addressing different aspects of SDGs, such as: Good health and well beings (SDG 3), clean and safe water (SDG6), reducing GHGs (SDG-7) including climate actions (SDG 13). As the global food & beverage sector is very complex, improving traceability practices is a challenge and the use of blockchain technology along with the use of IoT sensors and other digital technologies, represents a possible solution for food traceability systems.

2. Methods

A traceability system in a supply-chain requires all stakeholders to link the physical flow of products with a corresponding flow of information. Each stakeholder should be able to identify the direct source and direct recipient of the traceable elements in the process so that all the stakeholders can access the information at any time. Therefore, the "one step forward and one step back" approach should be applied, to allow all actors in the food supply-chain to collect, record, archive and share the minimal useful information for a smoother traceability.

The agri-food supply chain is a complex system because it has a complex behavior. In this system, interactions between parts show self-organization, in which local interactions give rise to new, non-local, emerging patterns. Therefore, a holistic approach made it possible to always analyze the entire system, using an approach by aspects (e.g. technological and economic).

The system engineering approach is focused on defining the needs and requirements of the entire system, in particular the requirements of the different actors of the supply-chain. In this regard, it was decided to start from the evaluation of the process stages of some agri-food supply-chains which characterize the Calabrian

area. It may try to identify the main actors involved in the supply-chain through the main actions that they carry out, the resulting benefits and the problems.

In this research, we focused on different supply chains such as olive-oil supply-chain, wine supply-chain, tuna-fish supply-chain, ‘nduja supply-chain, dairy supply-chain, red-onion supply-chain. The analysis of the agri-food sectors has identified similar stakeholders in each supply-chain: Farmer, Producer, Packer, Distributor – who can be considered as actors of the company’s internal logistics – and Final Consumer at the end. So, the first step to develop this system was a need analysis of all the stakeholders in the supply-chain, both companies and customers, through some specific questionnaires dispensed by Google forms.

In particular, the customer’s point of view represents the driver for the realization of the real solution, because it provides objectives, needs and problems that will be transformed into requirements. In addition, legislative and environmental requirements were also taken into account.

Considering a high level of abstraction, the traceability system was considered and modelled in SysML using Papyrus tool. It has a requirements diagram as a core (see **Figure 1**) of the system that:

- it is able to “verify” the different test cases coming from the answer to the Google form by the single companies;
- it can be modelled by the identified and structured solution, also from the technological point of view;
- it is able to “refine” the agri-food supply-chain with each change that occurs.

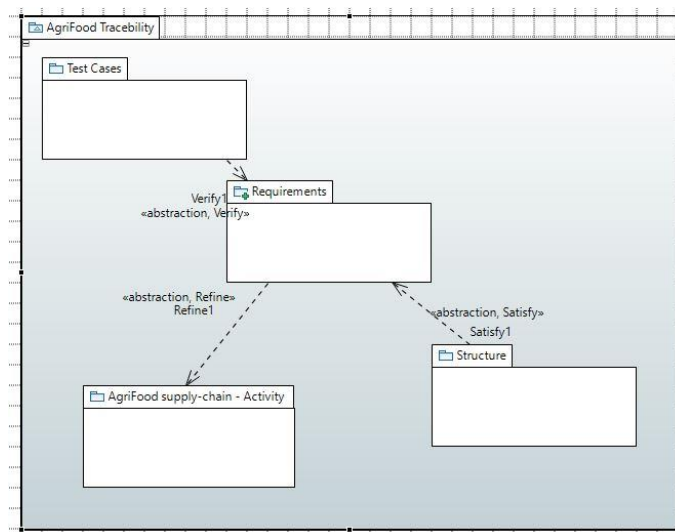


Figure 1 Agri-Food Traceability System

In this way, the change of any requirement can be an opportunity to better model the system as a whole. Other changes identified when the system takes on a change in its behaviour, that is when an unexpected event occurs – e.g. a tampering of a product – it could be correct and/or sanctioned almost immediately or in any case faster than now.

A general traceability structure of a traceability system follows the definition and attribution by ISO 8402, UNI 10939, European Regulation n. 178/2002 and UNI 10939. It can correspond to a blockchain solution, where the following considerations about a traceability system have been taken into account:

- there is a need to store and share a ledger state;
- multiple potential writers exist;
- the assignment of the maintenance of the ledger to a group of selected actors and not to an external third party (in this case, further increasing the complexity of the supply-chain logistics);
- there is a need of public verifiability of the ledger where the asset nature is public.

To implement the blockchain solution, Hyperledger Fabric technology – an open-source project hosted by the Linux Foundation – was chosen, because it is the most scalable and easily integrable with other technological and hardware solutions, such as IoT sensors.

3. Results and discussion

From the requirements analysis, the consumer's needs essentially identified in: clarity of information, safety and quality. They have been derived from the information on the label that the consumer considers most important when purchasing a product: net quantity, expiration date, ingredient list, conservation mode, batch of belonging, nutritional table, origin and provenance, headquarters of the production and packaging plant.

Given the features of the complex system, an open-permissioned blockchain could be implemented in Hyperledger Fabric. It can connect actors through a transparent, permanent, and shared record of food (e.g. origin and provenance, but also a specific characteristic of the product). The defined chaincode can be invoked by authorized participants in the supply-chain. All executed transaction records will be permanently saved in the ledger and all entities will be able to search for this information.

To meet the need for traceability of the agri-food supply-chain, a multi-layer network solution was developed. It was based on the integration of the blockchain technology and IoT devices.

Layer-1 consists of selecting of the information to be trace in the specific supply-chain, through the requirement analysis. Thanks to this layer, the specific IoT devices are built and installed at the critical points identified along the supply-chain. *Layer-2* is the “Device Layer”, that is the external interface layer, where a cluster of IoT devices collects sensing data, performs local computing, sends the results for storage and subsequent analysis. All the IoT devices used are based on microcontroller (e.g. Arduino), because they are cheaper than others and can be powered in different ways, including the battery.

Layer-3 is the “Network Layer”, where the different clusters of IoT devices distributed along the critical points of the supply-chain, perform data routing. Each IoT node corresponds to a unit of the supply-chain and also then, to a peer of the blockchain network. Generally, 4 IoT nodes are considered, one for each main unit of the supply-chain (Production, Processing, Distribution, Waste Management). *Layer-4* is the “Service Layer” and it consists in the data storage of all IoT data and an eventual unit of the Artificial Intelligence (AI) selection data. This layer is useful for reducing the size of the blockchain network. *Layer-5* is the “Platform Layer” and it is the real blockchain platform, where data is read, written and stored through query and invoke of a specific chaincode, which makes transactions take place.

The experimental measurements were carried out by first simulating the peer nodes with virtual machines in the cloud environment and then inserting the real data from the IoT devices. All to improve the cost-effectiveness of this solution and its adherence to the real supply-chain.

4. Conclusions

The agri-food supply-chain is a complex system. It has many different actors and many critical points, also depending on the specific product. Starting from an analysis of the needs of final consumers, it was possible to build a solution based on the stakeholder requirements. A technical solution based on the blockchain technology has been implemented in the Hyperledger Fabric open-source platform. A multi-layer networking solution was implemented with the interconnection of Hyperledger Fabric and IoT devices and compared with a simulated environment in a cloud platform. The use of the integrated multi-layer system guarantees greater securing of data coming from the IoT devices. At the same time, the use of the system engineering solution and the AI data selection system minimizes the size produced by the blockchain and the cost of the cloud environment. A large-scale application does not seem far off, thanks to this layered approach and its scalability.

References

- [1] INCOSE. 2015. Systems Engineering Handbook: A Guide for System Life Cycle Processes and Activities, version 4.0. Hoboken, NJ, USA: John Wiley and Sons, Inc, ISBN: 978-1-118-99940-0
- [2] Marianna Belotti, Nikola Božić, Guy Pujolle, Stefano Secci. A Vademecum on Blockchain Technologies: When, Which and How. Communications Surveys and Tutorials, IEEE Communications Society, Institute of Electrical and Electronics Engineers, 2019, 21 (4), pp.3796-3838. 10.1109/COMST.2019.2928178. hal-01870617
- [3] hyperledger-fabricdocs Documentation, Release master, <https://hyperledger-fabric.readthedocs.io/en/release-2.2/>

Wearable sensor for real-time monitoring of oxidative stress

Maria Giuseppina Bruno¹, Bernardo Patella¹, Giuseppe Aiello¹, Francesco Lopresti¹, Vincenzo La Carrubba¹, Claudia Torino², Antonio Vilasi², Chiara Cipollina^{3,4}, Serena Di Vincenzo⁵, Elisabetta Pace⁵, Alan O’Riordan⁶, Rosalinda Inguanta¹

¹ *Engineering Department, Università degli Studi di Palermo, Viale delle Scienze, 90128 Palermo, Italy*

² *Institute of Clinical Physiology, National Research Council, 89124 Reggio Calabria, Italy*

³ *Ri.MED Foundation, 90133 Palermo, Italy*

⁴ *Institute of Biomedical Research and Innovation, National Research Council, 90146 Palermo, Italy*

⁵ *Institute of Translational Pharmacology, National Research Council, 90146 Palermo, Italy*

⁶ *Nanotechnology Group, Tyndall National Institute, University College Cork, Cork, T12 R5CP, Ireland*

mariagiuseppina.bruno@unipa.it

1. Introduction

The recent spread of SARS-cov-2 has shown that existing health systems are not capable of enabling the effective management of rapidly spreading infectious diseases. However, the limitations and critical points that emerged during the pandemic provide an opportunity for the formulation of more efficient models to reduce the transmissibility and mortality of infectious diseases. In particular, pathologies concerning airways, such as asthma, lung cancer and chronic pulmonary diseases are on the rise according to World Health Organization: in total, 3.9 million deaths each year worldwide are caused by respiratory diseases. A large proportion of respiratory diseases are chronic and require frequent check-ups to monitor their progression [1]. This work aims at developing an original methodology and an innovative, inexpensive and miniaturized device for monitoring patients suffering from respiratory diseases, through the non-invasive detection of hydrogen peroxide in respiratory exhalations. In particular, the attention was focused on the fabrication of an electrochemical sensor that can be inserted into normal face masks in order to detect the concentration of hydrogen peroxide in exhaled air. H₂O₂ is one of the Reactive Oxygen Species (ROS) used to evaluate the level of oxidative stress in respiratory system: it is the most used biomarker because it is more stable than the other ROS and it diffuses through the cell membrane so it can be monitored in the extracellular space. High levels of this metabolic product are related to the onset of oxidative stress. This condition is a risk factor for several diseases, and therefore its early detection can help in risk assessment, disease monitoring and prevention. Therefore, the use of an electrochemical sensor allowing real time monitoring of hydrogen peroxide in breath exhalate can provide additional information and it is cost-effective, rapid and non-invasive compared to traditional diagnosis methods that are not suitable for a wearable continuous monitoring [2].

2. Methods

The sensor was realized from the silver layer present on the compact discs (CDs) and the three electrodes configuration was given through the use of a laser cutter [3]. An AgCl paste was applied to act as reference electrode and a graphite layer was applied to the counter electrode, while the Ag working electrode was not modified. In addition, electrospun polylactic-acid membrane (PLA) or an electrodeposited chitosan layer was used as absorber material. The application of this layer facilitates the wettability of the sensor in presence of a humid atmosphere such as that given by exhaled breath (relative humidity close to 100%). To study the performance of sensor, electrochemical tests (Linear Scan Voltammetry) were carried out in liquid solution at different concentrations of hydrogen peroxide between 10 μM and 5mM. These solutions were prepared

by dilution of H₂O₂ in 0.1 M PBS (Phosphate Buffered Saline) at pH=7.4. Then, these tests were repeated using aerosol of hydrogen peroxide solution in order to simulate humid atmosphere of exhaled breath [4].

3. Results and discussion

LSV tests were performed by placing the sensor in the liquid solutions at different concentrations of hydrogen peroxide and applying a variable potential between -0.2V and -0.9V vs Ag/AgCl. The obtained current density was proportional to the amount of hydrogen peroxide present in the solutions. The detection of hydrogen peroxide in the aerosol phase was carried out by exposing the sensor to the nebuliser for a time sufficient for homogeneously wets of the surface layer constituted by PLA membrane or electrodeposited chitosan. The electrochemical detection was performed with the same parameters used for liquid solutions. The experimental results showed that both layers are able to absorb the humidity of the aerosol and that the sensor is also able to quantify the hydrogen peroxide concentration in the aerosol phase.

4. Conclusions

In this study we reported the development of a wearable sensor for the detection of hydrogen peroxide in exhaled air since high levels of this metabolic product are related to the onset of oxidative stress. In order to facilitate the wettability of the sensor in presence of a humid atmosphere such as that given by exhaled breath a PLA membrane or a chitosan layer was used. The sensor developed was tested using hydrogen peroxide solution in a concentration ranging from 10 μ M to 5mM in liquid phase and in aerosol phase in order to simulate humid atmosphere of exhaled breath. LSV tests showed that current density was proportional to the amount of hydrogen peroxide present in the solutions and that the sensor is also able to quantify the hydrogen peroxide concentration in a humid atmosphere.

Acknowledgements: This work was partially financed by the project SENSOMAR- Sensore Nanostrutturato per Stress Ossidativo integrato in MAScherina per valutazioni in Remoto, MUR-FISR2020IP_03106

References

- [1] Maier, D., Laubender, E., Basavanna, A., Schumann, S., Güder, F., Urban, G.A., Dincer, C., 2019. Toward Continuous Monitoring of Breath Biochemistry: A Paper-Based Wearable Sensor for Real-Time Hydrogen Peroxide Measurement in Simulated Breath. *ACS Sens.* 4, 2945–2951.
- [2] Patella, B., Buscetta, M., Di Vincenzo, S., Ferraro, M., Aiello, G., Sunseri, C., Pace, E., Inguanta, R., Cipollina, C., 2021. Electrochemical sensor based on rGO/Au nanoparticles for monitoring H₂O₂ released by human macrophages. *Sensors and Actuators B: Chemical* 327, 128901.
- [3] Patella, B., Aiello, G., Drago, G., Torino, C., Vilasi, A., O’Riordan, A., Inguanta, R., 2022. Electrochemical detection of chloride ions using Ag-based electrodes obtained from compact disc. *Analytica Chimica Acta* 1190, 339215.
- [4] Fiore, L., Mazzaracchio, V., Galloni, P., Sabuzi, F., Pezzola, S., Matteucci, G., Moscone, D., Arduini, F., 2021. A paper-based electrochemical sensor for H₂O₂ detection in aerosol phase: Measure of H₂O₂ nebulized by a reconverted ultrasonic aroma diffuser as a case of study. *Microchemical Journal* 166, 106249.

Preliminary investigations on an experimental setup for nuclear graphite dissolution in the respiratory tract

Martina Mazzi^{1*}, Alessandro Antonio Porta², Fabrizio Campi², Marco Derudi¹

1 Politecnico di Milano, Dip. di Chimica, Materiali e Ingegneria Chimica "G. Natta", via Mancinelli 7, 20131 Milano - Italy; 2 Politecnico di Milano, Dip. di Energia, via Lambruschini 4, 20156 Milano - Italy

**Martina Mazzi E-Mail: martina.mazzi@polimi.it*

1.Introduction

This abstract aims to describe the preliminary study of an experimental setup to analyze the dissolution of nuclear graphite particles after accidental inhalation during decommissioning operations of graphite moderated nuclear reactors. Graphite is widely used for nuclear applications for its adequate properties, such as chemical inertness, high conductivity, good irradiation performance, corrosion resistance, good machinability, and good mechanical properties at high temperatures (Luo et al., 2004).

Despite of the fact that the first unit was shut down more than thirty years ago, nowadays most worldwide graphite moderated shutdown reactors are not dismantled and are just in a 'safe store' condition (Inno4graph, 2022). Tools for dismantling of components are usually safe and remotely operated, but workers could be present on site, and the eventuality of accidental exposure to highly contaminated graphite dusts must be considered.

The ICRP (International Commission on Radiological Protection) provides different dosimetry and biokinetic models, and ICRP Publication 66 and Publication 130 give a description about the Human Respiratory Tract Model. Inhaled contaminated particles can deposit on the upper or on the lower respiratory tract according to their size. The particle clearance is possible by two main mechanisms: absorptive (dissolution and adsorption to blood) and non-absorptive (physical mechanisms involving the transport to the alimentary tract with consequent excretion) (Keller et al., 2020).

The research focuses on the finer fraction of particles, which can reach alveolar region of lungs, and deposit in the lung extracellular environment or are engulfed by alveolar macrophages (Hettiarachchi et al., 2019). Therefore, mechanisms of dissolution in these two conditions have been investigated.

Solubility of inhaled particles or compounds is an important parameter that affects the uncertainty in a hazard evaluation of airborne that deposits in the respiratory tract. Indeed, the dissolving rate of a material can affect the extent and the rate at which it remains in the site of deposition, transported to other sites (e.g. target organs) or excreted (Ansoborlo et al., 1999).

Inhalable particles can be classified into three categories according to their dissolution rate: Fast, Moderate and Slow. This classification is a result of the assumption that each material that can be inhaled is characterised by a rapid dissolution fraction (fr) with the dissolution rate sr and a slow dissolution fraction (fs) with dissolution rate ss, their values are reported in Table 1 (Paquet, 2019).

Table 1. Dissolution fractions and rates values according to classification of ICRP Publication 130

	fr	fs	sr (day ⁻¹)	ss (day ⁻¹)
F	1.0	0	30	-
M	0.2	0.8	3	0.005
S	0.01	0.99	3	0.0001

In vivo data are the most reliable since the lung is a dynamic system, but developing an in vitro model has a really high importance because it could simplify the collection of data about different compounds and currently there are not standard procedures for in-vitro dissolution simulation. Moreover, it would be coherent with 3R

concept (Replacement, Refinement, and Reduction in the use of animals in science) with the aim of avoiding the infliction of unnecessary pain and other significantly unpleasant feelings to animals (Fröhlich, 2021).

2. Methods

The developed experimental setup is dynamic to better reproduce lung environment.

The system consists of two chambers, which are part of a circuit, and, in both of them, a membrane is inserted at a certain height.

The chambers are designed with the aid of the software Solidworks and 3D printed.

On the membrane the compound of interest is deposited and above it a fluid is inserted. In one chamber the fluid is SUF (Serum Ultrafiltrate Fluid), which simulates extracellular fluid of alveoli with pH 7.2-7.4; in the other chamber PSF (Phagolysosome Simulant Fluid) is inserted, and it simulates the environment inside macrophages with pH 4.5. Under the membrane, Human Body Plasma Simulant (HBPS) circulates for the presence of a peristaltic pump and removes dissolved particles, acting as blood in pulmonary capillaries.

The system is validated using as reference material BaSO₄, since in literature lots of in-vivo studies and data about dissolution of this compound can be found. The concentration of BaSO₄ in HBPS samples is assessed with the aid of ICP-OES to evaluate the dissolution during time.

The aim of this experimental campaign is to assess the dissolution of contaminated graphite particles from Politecnico di Milano research reactor L-54M. The radioisotopes that are present are the following: ¹⁴C, ³H, ¹⁵²Eu and ^{108m}Ag. In this case, to analyze dissolution, activity of the radioisotopes present in the samples have to be evaluated. The assessment is possible with the aid of a GEM p-type Coaxial Detector.

3. Results and discussion

HPBS samples were collected in different time instants and analyzed by ICP-OES technique to assess concentration of the compound in the fluid, and to build BaSO₄ dissolution curve.

The results of validation are promising, since the calculated displacement between dissolved BaSO₄ experimentally determined mass and the one assessed during an in-vivo study using the same compound on rats (Konduru et al., 2014) is less than 4%.

4. Conclusions

Since the results of the preliminary research on the setup were encouraging, further experimental campaigns will be carried out for the validation of the system and the procedure. After the validation phase, it is planned to assess lung dissolution of contaminated graphite dust.

References

- [1] X. Luo, J. C. Robin, Y. Suyuan, Effect of temperature on graphite oxidation behavior, *Nuclear Engineering and Design*, 227 (2004) 273–280
- [2] Inno4graph, n.d., accessed March 2022, <www.inno4graph.eu/objectives-results/>
- [3] J. G. Keller, U. M. Graham, J. Koltermann-Jully, R. Gelein, L. Ma-Hock, R. Landsiedel, M. Wiemann, G. Oberdörster, A. Elder, W. Wohlleben, Predicting dissolution and transformation of inhaled nanoparticles in the lung using abiotic flow cells: The case of barium sulfate, *Sci. Rep.* (2020) 10: 458
- [4] E. Hettiarachchi, S. Paul, D. Cadol, B. Frey, G. Rubasinghege, Mineralogy Controlled Dissolution of Uranium from Airborne Dust in Simulated Lung Fluids (SLFs) and Possible Health Implications, *Environ. Sci. Technol. Lett.* (2019) 62–67
- [5] E. Ansoborlo, M. H. Hengè-Napoli, V. Chazel, R. Gibert, R. A. Guilmette, Review and Critical Analysis Of Available In Vitro Dissolution Tests, *Health Phys* 77 (1999) 638-645
- [6] F. Paquet, The new ICRP biokinetic and dosimetric models, *BIO Web of Conferences* 14 (2019)
- [7] E. Fröhlich E., Replacement Strategies for Animal Studies in Inhalation Testing, *Sci.* (2021) 3, 45
- [8] N. Konduru, J. Keller, L. Ma-Hock, S. Groters, R. Landsiedel, T. D. Donaghey, J. D. Brain, W. Wohlleben, R. M. Molina, Biokinetics and effects of barium sulfate nanoparticles, *Particle and fiber toxicology* (2014) 11, 55.

MICRO-CHANNEL ARRAYS BY TWO PHOTON LITHOGRAPHY FOR CANCER CELL MIGRATION STUDIES

Sara Micheli^{1,2}, Elisa Varaschin^{1,2}, Caterina Piunti^{1,2}, Elisa Cimetta^{1,2*}

¹Department of Industrial Engineering, University of Padua, Padua, ITALY;

²Fondazione Istituto di Ricerca Pediatrica Città della Speranza, Padua, ITALY

*Corresponding author E-Mail: elisa.cimetta@unipd.it

1. Introduction

The study of tumor cell migration is of paramount importance in biological and medical research, as it is a key event in cancer metastasis. [1]. Metastasis is a dynamic process in which cancer cells begin to move in the surrounding microenvironment, driven mainly by different mechanical and chemical stimuli. Nowadays, classical migration studies are performed *in vitro* in culture plates where aggregates and cell populations are treated. However, recent studies have shown that initial stage migration information with *single-cell* resolution plays an exclusive role in metastasis [2].

The new frontier of microfluidics plays here a fundamental role. This technology is based on the manipulation of fluids at the nano- and micro-metric scale [3]. Unlike *in vitro* cultures, these devices improve experimental times, can reproduce an environment more faithful to the *in vivo* one, and reduce the number of reagents and substances needed for studies [4]. For this reason, the construction of devices with an innovative technique of two-photon polymerization (2PP) combined with microfluidics is a promising science for studying cell culture in a specific and controlled environment [5]. These devices could be suitable for the study of the migration of Neuroblastoma (NB), an embryonal malignancy of early childhood. For this reason, the goal is to build a device that allows the study of cell migration at a *single-cell* resolution, with micro-channel arrays that recall the shape and size of the lymphatic vessels.

2. Methods

The master mold for the micro-channels array was designed through AutoCAD (2019, Autodesk) and the fluid-dynamic behavior was simulated using COMSOL Multiphysics. The optimized mold was fabricated using a 2PP-based NanoScribe Photonic Professional GT 3D printer (Nanoscribe, Eggenstein-Leopoldshafe, Germany). To verify the quality of the produced master, Scanning Electron Microscopy (FEI Quanta 400, Scanning Electron Microscopy) and 3D optical profilometer (Sensofar S Neox profilometer) analyses were performed. The final device was then produced via standard replica molding. Briefly, Polydimethylsiloxane (PDMS) (Dow Corning, Sylgard® 184) was prepared by adding a curing agent, 10:1 (w/w), poured over the master mold and then polymerized for 90 minutes at 70 °C in an oven. The cured PDMS layer was gently peeled off from the rigid master. To create the microfluidic chip the PDMS slab was attached to a microscope cover glass (Sigma-Aldrich, 24 x 25 x 1 mm) with plasma treatment (PDC-002-CE by Harrick Plasma). Both the microscope glass slide and PDMS layer are inserted in the Plasma Cleaner under vacuum conditions for 2 minutes. The hydraulic seal of the final platform was validated with colored tracers. The microfluidic platform was then biologically validated using a human NB cell line (SK-N-AS) and human Mesenchymal stem cells (hMSCs), representative of one of the main NB metastatic target sites. Finally, migration was observed using a fluorescence microscope (EVOS FL Cell Imaging System, Thermo Fisher Scientific) following cell positions for up to 48 hours of incubation.

3. Results and discussion

The general platform design consisted in two lateral channels and chambers used to introduce different solutions of cells and micro-channels that connect the lateral chambers (Figure 1a and b). The key element is

the structure of the micro-channels that, designed with shrinkages and larger sections, recall the shape of lymphatic vessels, the main migration ducts. The hydraulic seal of the platform is validated with colorants (Figure 1c). This validation was favored by the optical properties of PDMS, as its transparency makes it easier to observe under the microscope.

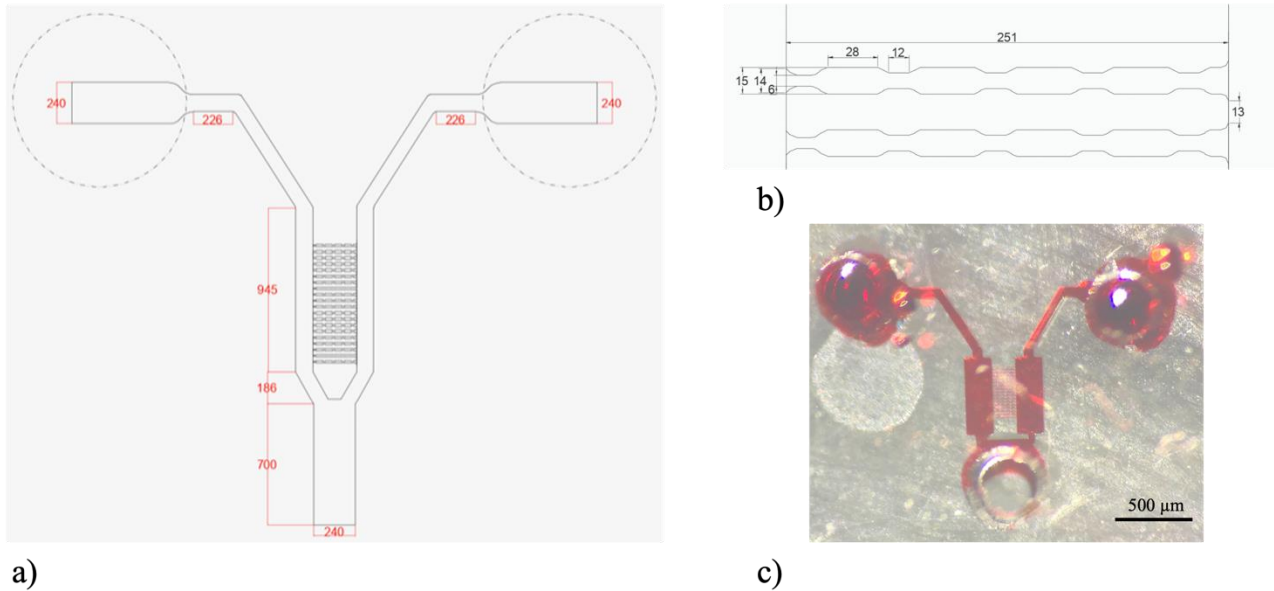


Figure 1. Platform layout: a) design of the platform; b) detail of the micro-channels; c) PDMS replica of the platform filled with red colorant. All dimensions are in μm .

To also verify the correct shape and size of all components, the platform was observed using Scanning Electron Microscopy (Figure 2).

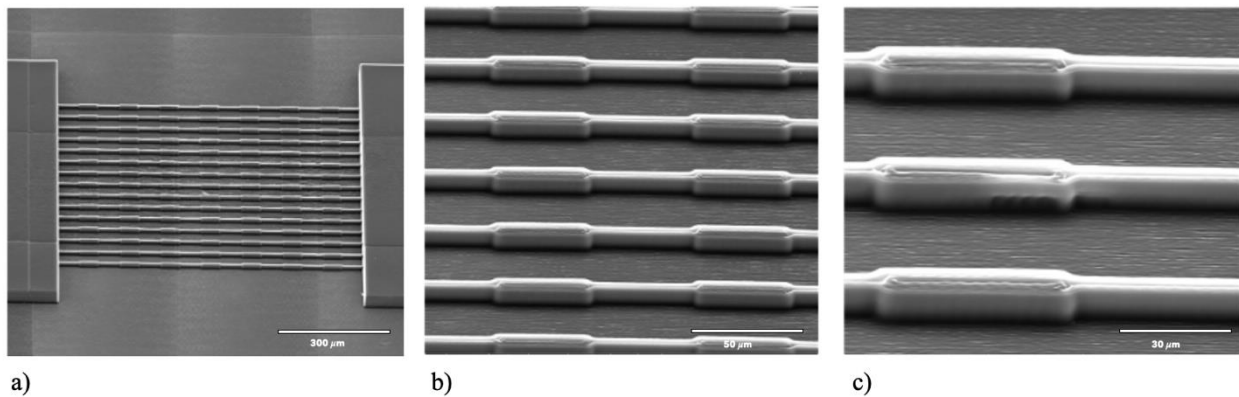


Figure 2. Scanning Electron Microscopy images of the platform, focusing on the micro-channels: a) 300x magnification; b) 1600x magnification; c) 3000x magnification.

The results of the profilometer analysis are shown in Figure 3 where the heights of specific area of interest are studied with the Confocal mode. Every channel is divided in three sections: top, center and bottom. The bar chart illustrates the results of the metrological characterization, demonstrating that the heights of each printed channel are higher than the nominal value. This can be attributed to a systematic error of the printer or to the

scattering effect that occurs when the sample is exposed to white light, altering its metrological measure. These differences are however not statistically different (Anova one-way Figure 3c).

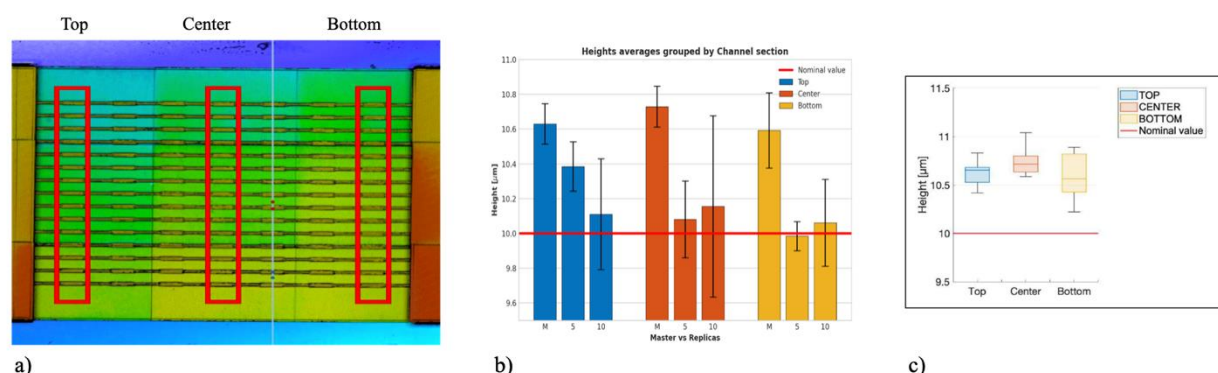


Figure 3. Profilometer analysis: a) Section of interest used to carry out the profilometric analysis; b) Metrological characterization of the heights of all channels in the master compared to the replicas: in blue the measures of the micro-channel top, in orange the one of the micro-channel center and in yellow the measures of micro-channel bottom. In red the line of the comparison CAD value; c) Box plot of the heights of all channels: in blue the measures of the micro-channel top, in orange the one of the micro-channel center and in yellow the measures of micro-channel bottom. In red the line of the comparison CAD value.

The platform was then biologically validated. To first fill the device with culture media inside all micro-channels and chamber, the device was kept under vacuum for 15 mins. SK-N-AS cells were resuspended in culture media to a concentration of $4 \times 10^4/\mu\text{L}$ and hMSCs of $1 \times 10^4/\mu\text{L}$. Then, $1 \mu\text{L}$ of these solutions was pipetted into each of the two main lateral channels, and the chip was put into the incubator. Figure 4 shows SK-N-AS and hMSCs seeded inside the platform at several time points. The cells are attached to the surface of the chamber demonstrating that this microfluidic chip is a favorable environment for cell culture.

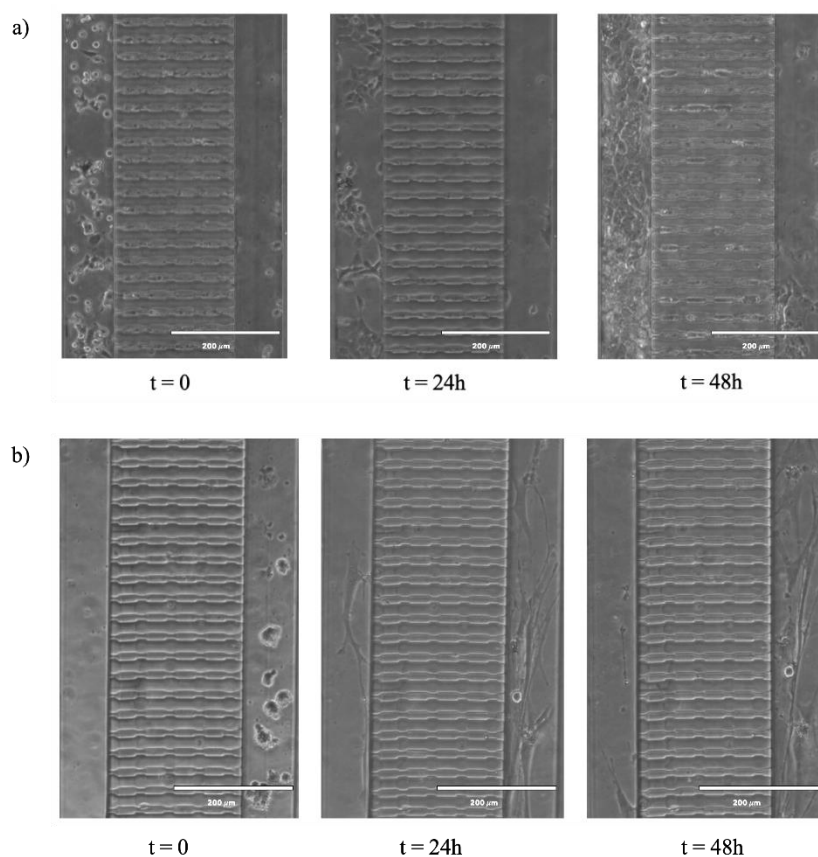


Figure 4. Biological validation of the platform: a) Microscopy images of SK-N-AS cells at seeding time ($t=0$) and at 24 and 48 hours from seeding; b) Microscopy images of hMSCs at seeding time ($t=0$) and at 24 and 48 hours from seeding.

Finally, migration was observed using a fluorescence microscope investigating cell positions at several time points for up to 48 hours of incubation. To improve the imaging quality, SK-N-AS and hMSCs cells were stained by red and green fluorescent tracers (Invitrogen, DiO and DiI), respectively. A preliminary result is shown in Figure 5 where it is evident that the red SK-N-AS cells tend to move through the channels reaching the chamber where the green hMSC cells are located.

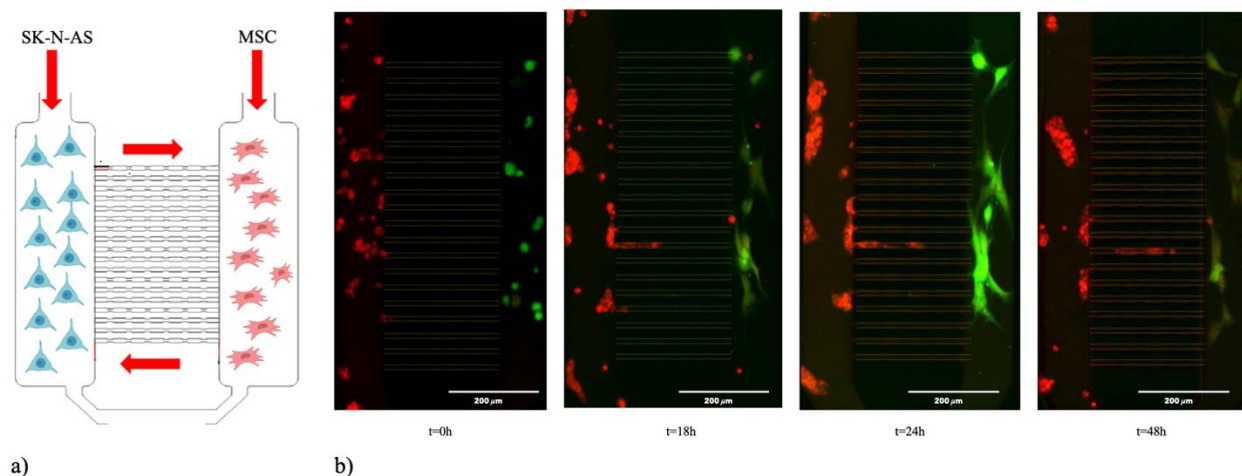


Figure 5. Preliminary migration studies: a) Schematic view of the experimental protocol; b) Fluorescence images of SK-N-AS (red) and hMSC (green) at seeding time ($t=0$) and at 18, 24 and 48 hours from seeding.

4. Conclusions

This work aimed to design an innovative microfluidic device that would allow studying the migration of cancer cells to a *single-cell* resolution and based on a novel production technology: two-photon polymerization. This new method resulted in a reduction of time, costs, and quantities of substances compared to established master production methods such as photolithography and micromilling. The result is a microfluidic platform, which successfully replicated the required micro- and nano-metric sizes and dimensions. With its excellent hydraulic sealing and very good cellular biocompatibility, this device can be, for all intents and purposes, a valuable tool for the study of cancer cell migration.

References

- [1] Disanza, A. et al. Is cell migration a selectable trait in the natural evolution of cancer development? *Philos. Trans. R. Soc. B Biol. Sci.* 374, 20180224 (2019).
- [2] Galarza, S., Kim, H., Atay, N., Peyton, S. R. & Munson, J. M. 2D or 3D? How cell motility measurements are conserved across dimensions *in vitro* and translate *in vivo*. *Bioeng. Transl. Med.* 5, (2020).
- [3] Nguyen, N.-T. & Wereley, S. T. *Fundamentals and applications of microfluidics*. (Artech House, 2006).
- [4] Breslauer, D. N., Lee, P. J. & Lee, L. P. Microfluidics-based systems biology. *Mol. Biosyst.* 2, 97 (2006).
- [5] Campbell, J. H. et al. Three-dimensional printing and deformation behavior of low-density target structures by two-photon polymerization. *Nanoengineering: Fabrication, Properties, Optics, and Devices XIV* (eds. Campo, E. M., Dobisz, E. A. & Eldada, L. A.) 66 (SPIE, 2017)

Using Machine Learning Tools for Residual Moisture monitoring in Freeze-Drying processes for Pharmaceutical Applications

Ambra Massei^{1,2}, Serena Bobba^{1,2}, Nunzio Zinfullino², Davide Fissore^{1*}

¹ Dipartimento di Scienza Applicata e Tecnologia, Politecnico di Torino, corso Duca degli Abruzzi 24, 10129 Torino

² Biotech Pharmaceutical Development Department, Merck Serono SpA, via Luigi Einaudi 11, 00012 Guidonia Montecelio (Roma)

*Corresponding author E-Mail: davide.fissore@polito.it (D. Fissore)

1. Introduction

Freeze-drying is a crucial step in many drug manufacturing processes as it provides long-term stability to formulations containing an active pharmaceutical ingredient (API). Approximately 46% of biopharmaceutical dosage forms approved by Food and Drug Administration (FDA) in the period 2003-2011 are prepared by freeze-drying.^[1]

A typical freeze-drying process starts with a freezing phase, in which most of the water, the *free water*, crystallizes as ice. A fraction of water, the *bound water*, is incorporated into the frozen product and remains unfrozen. After freezing, there is the primary drying phase, in which pressure is lowered in the chamber to promote sublimation of the ice. This leads to the formation of a porous solid structure, the cake, through which water vapor escapes from the product. Finally, secondary drying takes place, in which the temperature is increased to promote the desorption of bound water and achieve the target value of residual moisture in the final product.^[1]

Pharmaceutical companies must meet standards imposed by regulatory agencies, so final products must meet Critical Quality Attributes. Among all, the residual moisture (RM) plays an important role because it is closely related to the stability of the active ingredient. At the end of a freeze-drying cycle, the suggested moisture range is approximately 3-6%. So, it is necessary to monitor the residual amount of water in the final product. The residual moisture is generally investigated by Karl Fisher (KF) titration. This method is time-consuming, destructive and can therefore only be applied to a part of a production batch. Near-Infrared Spectroscopy (NIR Spectroscopy), on the other hand, is a fast, non-destructive method that can be applied to many samples. In NIR spectroscopy the sample is irradiated by a beam of NIR light and some of this NIR light is absorbed by the molecules, bringing them to a higher vibrational state. So, NIR spectroscopy is about studying the vibrational transitions in molecules, due to the absorbance of the system in the NIR region, i.e. in a region of the electromagnetic spectrum corresponding to 14300 - 4000 cm⁻¹.^[2]

This is in line with the Process Analytical Technology (PAT), a concept proposed by the U.S. FDA in 2002 that is expected to lie at the basis of the pharmaceutical “Good Manufacturing Practice” rules.^[3] This approach introduces the concept of Quality-by-Design (QbD) according to which the quality should be built into products. This is completely different from the Quality-by-Testing approach in which the quality is tested into products.^[4]

In this framework, NIR spectroscopy was used as method to measure RM in freeze-dried products. Here, a *robust* model was developed using *machine learning* tools: the goal of the model is to estimate RM from NIR spectra. The aim was to find a model able to predict the RM values of products also different from those used in the training phase of the model. In particular, the cases of a different percentage of solid fraction, a different excipient and the presence of another component in the product were considered. Great attention was paid in choosing the wavelength range over which to build the model. Looking at the spectra of the various sample data sets, it was chosen to focus on the range that contains 5150 cm⁻¹, the water peak. In fact, water is a component that all formulations have in common. As a result, it was thought that, to obtain a robust model, it

might be effective to focus on a narrow range of wavelengths that encompassed the water peak. In this way, specific peaks in product characteristics have a lower impact on the spectra. In addition, it would not become necessary to include all products in the calibration step, allowing for a reduction of the experimental effort for model development.

2. Methods

Some freeze-drying cycles were carried out to get the samples used for model development. In the first part of the study, a sucrose 6%_w solution, freeze-dried into 2R glass vial (Nuova Ompi, Piombino Dese, Italy) with a filling volume of 1 mL, was considered for samples preparation. Vials were placed according to a honeycomb layout surrounded by metal frames, in direct contact with the freeze-dried shelves, and processed in a lab-scale freeze-drier (Lyostar3, SP Scientific, Warminster, USA) in the laboratories of the Guidonia Montecelio (Italy) site of Merck Serono SpA.^[5] In order to get a RM in the range 1-5% some vials were humidified on purpose after the freeze-drying step. Sample sets having specific different features were necessary to test the robustness of the model. For this reason, the following samples were produced:

- 25 samples of sucrose 9%_w (sample set S9), thus having a solid fraction higher than S6;
- 22 samples of sucrose 3%_w (sample set S3), thus having a solid fraction lower than S6;
- 35 samples of trehalose 6%_w (sample set T6), thus a different amorphous excipient;
- 20 samples of sucrose 6%_w – arginine 1%_w (sample set SA14), thus 14.3% of arginine;
- 10 samples of sucrose 6%_w – arginine 0.5%_w (sample set SA7), thus 7.7% of arginine.

All RM values less than 1% were removed because they exceeded the lower limit of the experimental technique used (KF). So at the end the number of samples for each case was lower, as it can be seen in Table 1.

Table 1: Number of samples for each data set

<i>Data set</i>	<i>N° Samples</i>
<i>S6-V</i>	96
<i>S6-H</i>	96
<i>S3</i>	22
<i>S9</i>	8
<i>SA7</i>	8
<i>SA14</i>	5
<i>T6</i>	26

The samples listed above were all analyzed through a Fourier Transform NIR spectrometer (Antaris MX FT-NIR, Thermo Fischer Scientific, Waltham, USA), equipped with an InGaAs detector and a halogen NIR source. Pre-processing of the spectra was carried out by using a standard normal variate (SNV) approach, consisting in subtracting the mean value of the spectrum from all its points, and dividing for its standard deviation. It is possible to have get more in-depth details on the conduct of the trials in the paper by Bobba et al.^[5]

Machine Learning Tools

Machine Learning techniques differ from traditional algorithms because they also have the ability to learn as well as apply pre-programmed decisions. Traditional software receives input data and user-written code and generates an output. Machine Learning algorithms, on the other hand, are able to find the functional

relationship that binds the input data with the desired output. Models are obtained from a set of data, as shown in Fig. 1. Their formulation does not require a priori knowledge of the physics governing the system or of the relationships linking the input and output variables, although this may be useful.



Figure 1: Building a model using machine learning tools

The data set contains all the information necessary to obtain the model: in this case, they are the matrix of the spectra X and the vector of residual moisture y . The rows of the X -matrix are the observations and the columns represent the absorbance corresponding to a specific wavelength.

Building a machine learning model requires a data splitting into two different set:

- a) Training set: the model processes the spectra (input) with the RM values obtained with KF (output);
- b) Test set: the trained model is used to determine RM in samples not used in the calibration set. The values obtained, RM predicted by the model, are compared with those measured with KF.

For processing NIR spectra and modeling, scripts were written using Spyder (Python 3.9), exploiting the module *Scikit-Learn*. In particular, a multivariate linear regression problem was solved by using the “*LinearRegression*” tool. For regression, the general prediction formula for a multivariate linear model looks as:

$$y_{pred,i} = \theta_0 \cdot x_0^i + \theta_1 \cdot x_1^i + \dots + \theta_p \cdot x_p^i + b \quad (1)$$

Here, x_0 to x_p denotes the input variables (p is the number of features); i refers to the rows of the matrix X ; θ and b are parameters of the model that are learned, and $y_{pred,i}$ is the prediction the model makes.^[6]

In order to evaluate the performance of the model, the Root Mean Square Error (RMSE) and the Coefficient of determination, R^2 , were adopted. They give an idea of how much error the system typically makes in its predictions. So, linear regression finds the parameters θ and b that minimize the RMSE between predictions and the true regression targets, y , on the training set. Equations 2 and 3 show the mathematical formulas to compute the RMSE and R^2 .

$$RMSE = \sqrt{\frac{1}{N} \sum_{i=1}^N (y_{pred,i} - y_i)^2} \quad (2)$$

$$R^2 = 1 - \frac{\sum_{i=1}^N (y_i - y_{pred,i})^2}{\sum_{i=1}^N (y_i - y_m)^2} \quad (3)$$

The total number of observations and the mean value are designed respectively with N and y_m . The lower the RMSE value, the better the model performance.^[7] The closer the value of R^2 is to 1, the more the points are aligned to the bisector in the parity plot. Parity plots were also made, which correlate the RM values calculated by the model (y -axis) with the RM values measured by the KF (x -axis). It has been useful to report also the

diagrams that correlate the absolute error with the measured RM values considering an *intrinsic error* of the experimental technique of 0.3%.^[3]

Model Development

Data set S6-V was used for developing two models:

- 1) Model SR, based on a regression on a small wavelength range, 5290 – 4785 cm^{-1} ;
- 2) Model WR, based on a regression on a large wavelength range, 7100 – 4250 cm^{-1} .

The data set was split in two sets, in order to perform the training with a set and the validation with the other. The size of the training set was varied, from 30% to 70%, to find the minimum that would lead to an acceptable result in order to reduce the experimental effort. Then, the other data sets were used to perform the external validation of the model and challenge its robustness. Also a global model (GM) was developed by considering all the products previously listed as a single data set used also for the training phase. Since model GM was calibrated with different products, it was assumed to provide the best performances in prediction.

3. Results and discussion

Model SR, WR and GM are compared in the followings to establish which is the most suitable method for predicting the RM content. The most significant results obtained are reported. Both model WR and SR appeared to have comparable performance and seemed to be accurate enough to predict the RM content of formulations not included in the calibration set. In fact, the RMSE and R^2 values in the two cases are almost similar, as it can be seen in Table 2.

Table 2: Values of RMSE and R^2 for each data set

<i>Data set</i>	R^2 SR	RMSE SR	R^2 WR	RMSE WR
<i>S6-V</i>	0.993	0.119	0.995	0.074
<i>S6-H</i>	0.971	0.47	0.966	0.294
<i>S9</i>	0.997	0.281	0.992	0.248

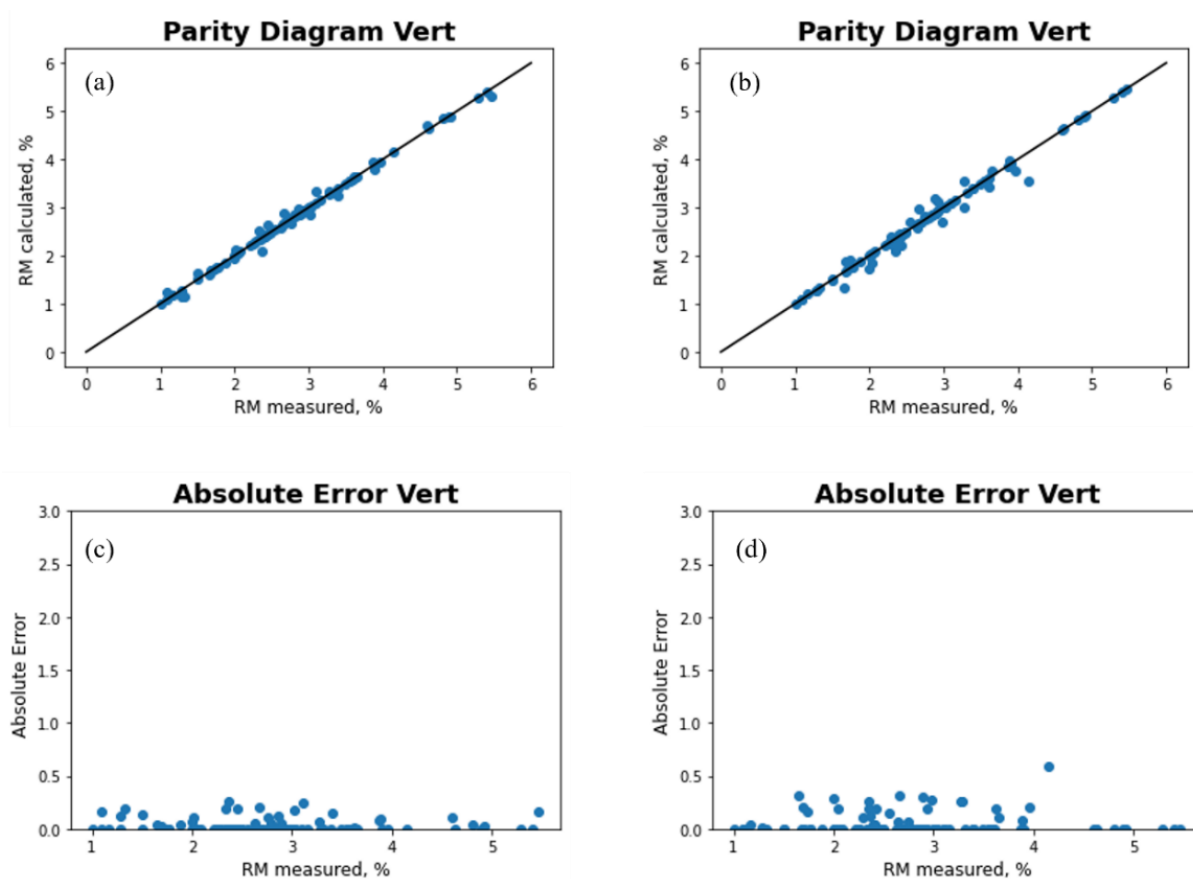


Figure 2: Correlation plots between RM (%) measured vs RM (%) calculated and Absolute error plots, obtained from the data set S6-V and processed by: (a),(c) model WR; (b),(d) model SR.

The correlation plots confirm the conclusions obtained from the RMSE and R^2 values shown in Table 2. In Fig. 2a and 2b it is possible to notice that the observations are distributed similarly along the bisector in the two cases, index of a good performance of the models.

To evaluate the percentage of success and failure of the obtained model, a vector called "*judgement*" was constructed. The intrinsic error in the KF experimental technique is 0.3%. The absolute error was calculated as the difference in absolute value between the value predicted by the model ($y_{pred,i}$) and the value measured by the KF (y_i). In the vector the value 1 occurs when the difference is greater than 0.3%; the value 0 if the difference is less than 0.3%. Figure 3 shows the trends obtained for the S6-V data set with both models. The number of times that in the diagram there is the value 1 corresponds to the number of times that the model exceeds the experimental error and, therefore, fails. The WR model had a good prediction of 100% as all observations were within the range given by the experimental error. In fact, all values in Fig. 3a are equal to 0. In contrast, the SR model was able to correctly predict 96.88% of the observations. In fact, 3 values equal to 1 are observed in Fig. 3b.

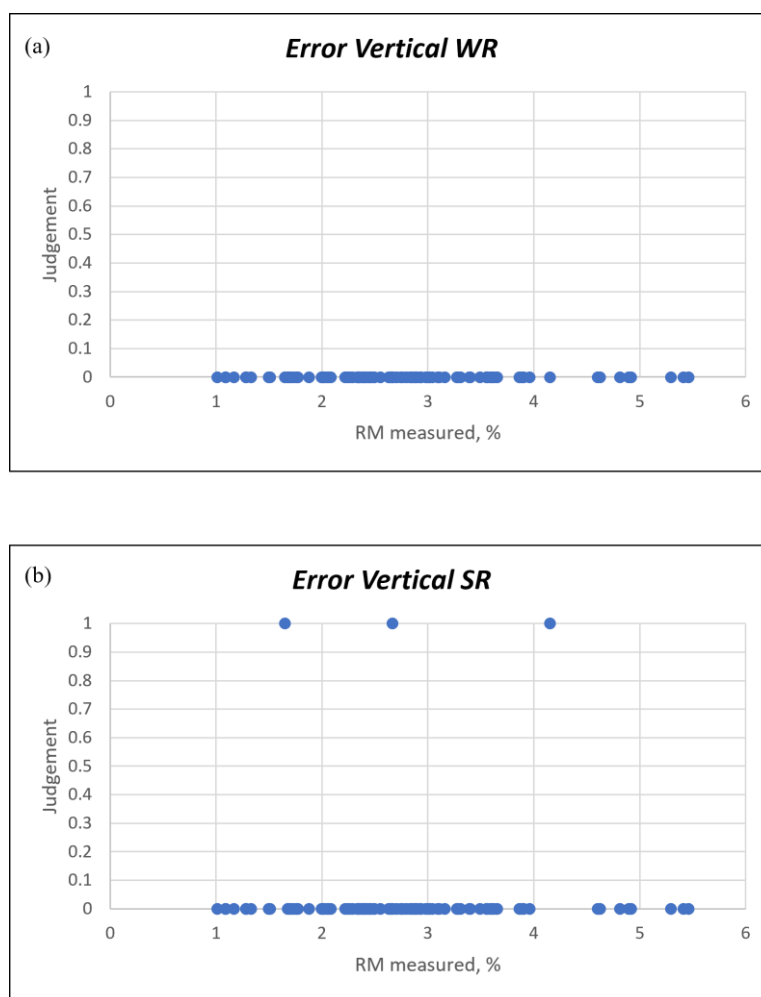


Figure 3: Success rate of the algorithm obtained with the S6-V data set: (a) model WR; (b) model SR.

The external validation of model WR and SR with S6-H spectra also yielded in very good performance parameters. Therefore, model SR and WR could be equally applied to spectra collected with vertical and horizontal layout. The fact that the spectra collected in vertical layout and in horizontal layout were similar was a confirmation of what Bobba et al. found by applying the PLS regression. This means that the spectra collected from two different spots of the cake are basically equivalent.^[5]

The effect of a different solid fraction was evaluated by means of data set S9. The external validation of model WR with data set S9 was less accurate at lower RM, where the distribution of the observations in the correlation plot is wider. For larger RM values, however, the points lie almost perfectly aligned to the bisector with both models. In order to confirm the robustness of the obtained model, however, it would be appropriate to expand the data set with new experimental tests. In fact, only 8 data were made available for the S9 data set.

The effect of adding an amino acid was studied with 7% and 14% sucrose-arginine mixtures. The case of 14% arginine concentration is reported in Fig. 4.

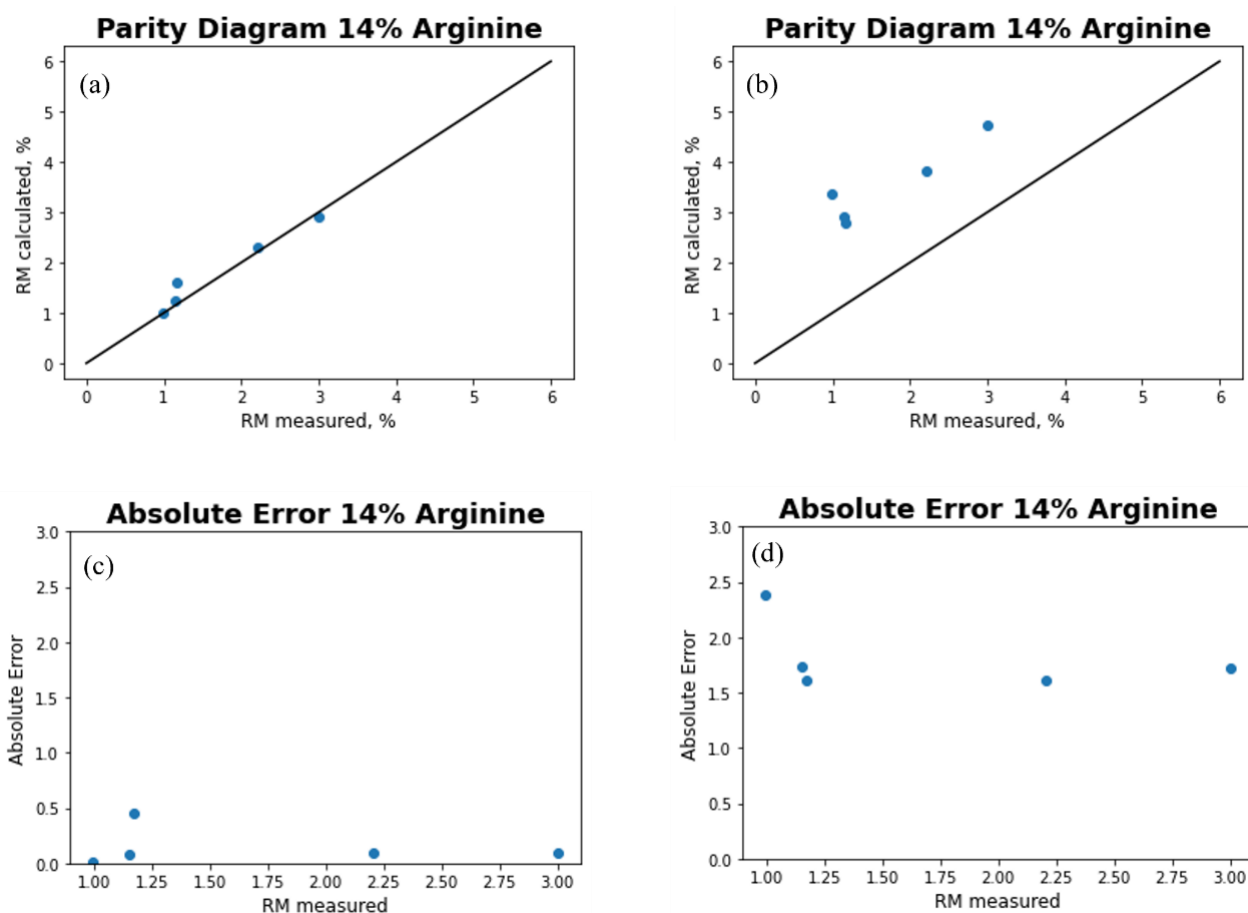


Figure 4: Correlation plots for sucrose-arginine mixture and Absolute Error plots processed by: (a),(c) model WR; (b),(d) model SR.

Model SR turned out to have the poorest performances in comparison with model WR to predict the residual moisture in a sample where an amino acid is added to the excipient considered in the training phase. In fact, in Fig. 4b it can be observed that the observations are much more spread from the bisector than those processed with the SR model (Fig. 4a). These findings are confirmed also by the values of R^2 and RMSE for both model, shown in Table 3.

Table 3: Values of RMSE and R^2 for sucrose-arginine mixture

<i>Data set</i>	R^2 SR	RMSE SR	R^2 WR	RMSE WR
SA14	0.863	1.837	0.949	0.211

These differences could be explained by looking at the spectra of the sucrose-arginine mixture. Significant differences can be seen in the region analyzed by the SR model compared to the 6% sucrose mixture used to calibrate the model.

Both the models were also tested using a different excipient, a 6% trehalose solution. The failure of the external validation applied to this data set appeared clear. The correlation plots showed a muddled distribution. The poor performance parameters confirm these findings. Due to the limited number of samples available, a more extended calibration might be advisable. Future work may try to use a nonlinear model, such as a neural network, which may have better performance in predicting an excipient different from the one used in the calibration step.

4. Conclusions

Machine learning tools were applied to develop a model suitable for the prediction of the RM content of freeze-dried products, focusing on its robustness and suitability for different products not involved in the training procedure.

Various tests have been done to find the minimum size of the training set that generates acceptable results, thus reducing the experimental effort required. Both models, SR and WR, were found to be very accurate in describing samples with high percentage of solid (S9). In contrast, they showed poor performance in predicting samples made from a different excipient (T6). Model WR was more accurate in predicting samples made from sucrose-arginine mixtures than the SR model. It has to be remarked that the accuracy of this method is strongly dependent on the accuracy of the KF titration used for model training.

A global model GM, calibrated with all products, gave basically the same results as models WR and SR, except for the samples containing trehalose, which were better described.

Future work may focus on applying more complex, nonlinear algorithms such as neural networks. Furthermore, the data set should be expanded to make the model more reliable.

References

- [1] D. Fissore, *Freeze Drying of Pharmaceuticals*, Encyclopedia of Pharmaceutical Science and Technology, New York, 2013, pp. 1723-1737.
- [2] H. Grohganz, D. Gildemyn, E. Skibsted, J. M. Flink, J. Rantanen, *Towards a robust water content determination of freeze-dried samples by near-infrared spectroscopy*, *Analytica Chimica Acta*, Elsevier, 2010, pp. 34-40.
- [3] T. De Beer, M. Wiggenhorn, R. Veillon, *Importance of using complementary process analyzers for the process monitoring, analysis and understanding of freeze drying*, *Analytica Chimica Acta*, Elsevier, 2009, pp. 7639-7649.
- [4] T. De Beer, A. Burggraeve, M. Fonteyne, S. Saerens, C. Vervaet, *Near infrared and Raman spectroscopy for the in-process monitoring of pharmaceutical production processes*, *International Journal of Pharmaceutics*, Elsevier, 2011, pp. 32-47.
- [5] S. Bobba, D. Fissore, N. Zinfolino, *Evaluation of the Robustness of A Novel NIR-based Technique to Measure the Residual Moisture in Freeze-dried Products*, *Journal of Pharmaceutical Sciences*, In press.
- [6] A. C. Muller, S. Guido, *Introduction to Machine Learning with Python*, O'Reilly, 2017.
- [7] A. Geron, *Hands-on Machine Learning with Scikit-Learn, Keras and TensorFlow*, O'Reilly, 2019.

Design and in vivo applications of decorated nanogels for selective drug delivery in spinal cord injury

Filippo Pinelli^{1*}, Filippo Rossi¹

¹ *Department of Chemistry, Materials and Chemical Engineering “Giulio Natta”, Politecnico di Milano, via Mancinelli 7, 20131, Milan, Italy*

**Filippo Pinelli E-Mail: filippo.pinelli@polimi.it*

1. Introduction

The spinal cord injury (SCI) is an invalidating disease that involves the spinal cord or the nerves connecting the spine to the central and peripheral nervous system. This disease is characterized by the primary SCI, that is the consequence of the primary traumatic event, and by the consequent inflammatory response, characterized by the activation of microglia/macrophages/astrocytes, the cells of the central nervous system, that leads to an aggravation of the pathology, causing neurodegeneration and persisting pain state [1]. A possible therapeutic approach is represented by the possibility to modulate the inflammatory response through the selective release of drugs in the damaged zone. Recent studies in polymer science and nanotechnologies show an increased interest for the nanogels (NGs), a new class of colloidal systems that can be used as carriers of drugs to treat SCI [2].

2. Methods

In this work we synthesized properly functionalized nanogels structures so that cells, especially astrocytes, involved in the inflammatory response of SCI, can selectively internalize them. This kind of devices represent a valuable tool in the treatment of the inflammatory response of SCI thanks to the possibility to release drugs and active molecules in situ once the nanocarrier has been internalized. The nanogels were synthesized using polyethylene glycol (PEG) and polyethyleneimine linear (PEI), after having functionalized the PEI with a chromophore using a “click” reaction. This functionalization is essential for being able to constantly trace the nanogels during the biological assays [3]. Two different chromophores and at the same time many different coating strategies (functionalization) of the nanogels were developed and tested: the 3-bromopropylamine hydrobromide was demonstrated to be the most effective coating molecule both during preliminary study and during *in vitro* and *in vivo* tests.

3. Results and discussion

The synthesized nanogels were characterized through dynamic light scattering analyses, to investigate their physical properties, and through drug release tests together with *in vitro* and *in vivo* biological assays. We demonstrated how the coating on the nanogels structure does not decrease the drug release ability of the carrier. The *in vitro* tests proved that the functionalized nanogels were able to be selectively internalized in mouse astrocytes and their degradation promoted drug release: the selective internalization in activated astrocytes

respect to microglia and neurons is a pivotal aspect for the efficacy of this kind of device for the treatment of the inflammatory state of the spinal cord injury [3-4]. *In vivo* subsequent assays on diseased mouse confirmed the result obtained *in vitro* and the potentiality of this kind of surface functionalization.

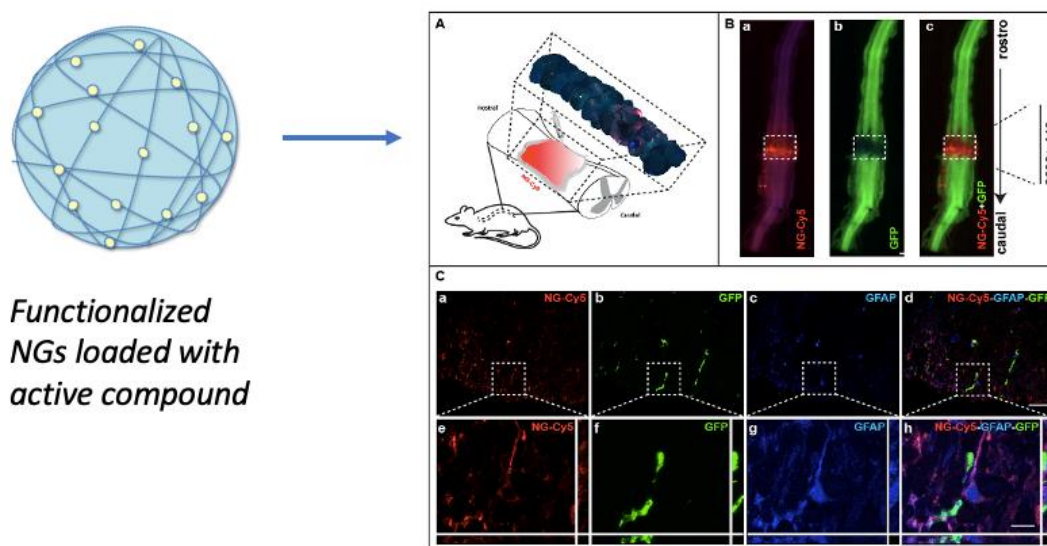


Figure 1. Schematization of the functionalized nanogels (NGs) loaded with active compound (on the left). On the right their applications in spinal cord injury are reported together with the results of the *in vivo* biological assays on diseased mouse (Fig.A). The co-localization of the NGs and the astrocytes markers (Fig.B and C) confirms their internalization.

4. Conclusions

In this work we successfully developed nanogel structures for drug delivery, characterizing their frameworks and their features. Moreover, we demonstrated their efficacy as selective devices for the treatment of the cells of the central nervous system in the spinal cord injury inflammatory state.

References

- [1] Thuret S., Moon L. D F, Gage F. H Nat. Rev. Neurosci. 7, 628, (2006).
- [2] Papa S., Veneruso V. et al. J.Control Release 330, 218, (2021).
- [3] Pinelli F., Pizzetti F. et al. Coll. Surf. A, 614, 126164, (2021).
- [4] Vismara I., Papa S. et al. ACS Nano 14, 360, (2020).

Development of active food packaging with thermal insulating properties

Emanuela Drago*, Roberta Campardelli, Antonio Barbucci, Patrizia Perego

Department of Civil, Chemical and Environmental Engineering (DICCA), University of Genoa, Via all'Opera Pia 15, 16145, Genova (GE), Italy

**Corresponding author E-Mail: emanuela.drago@edu.unige.it*

1. Introduction

Packaging plays a fundamental role in the protection of food products, the most well-known functions are: protection, communication, convenience and containment, but for some food products, such as fresh ones, this is not enough. In fact, according to the Food and Agriculture Organization of the United Nations (FAO), every year in the world, about 1/3 of all food produced for human consumption, is lost or wasted. One of the main causes is the loss of quality during distribution and storage which can occur due to sudden changes in temperature that can give rise to chemical, biological and physical degradation. Respect for the cold chain is a crucial aspect to guarantee the safety and quality of fresh food [1]. Traditional materials used in the packaging sector (e.g., plastic, cardboard, etc.) often have limited thermal insulation and poor thermal buffering capacity. Furthermore, the environmental impact deriving from the accumulation of non-degradable plastics, to which the packaging sector contributes greatly, is today an alarming problem to be taken into account globally. In this context, two new concepts have contributed, in recent years, to achievement of an advanced idea of packaging for safer and healthier foods: active and intelligent packaging [2], designed no longer as passive barriers but rather to interact with products. Among the active packaging, the most investigated are the migratory ones with antimicrobial and antioxidant action [3 - 5]. However, the innovative idea of this work is to use the active packaging concept to control temperature fluctuations of packaged foods. One way to attribute an insulating action to packaging is to use phase change materials (PCMs), substances that undergo a phase transition at a certain temperature, absorbing or releasing latent heat, i.e., paraffins, fatty acids and hydrated salts. To date, these interesting materials are widely used in the construction and textile fields, while in the food sector their use is limited to the development of insulated boxes and refrigerated equipment with only commercial paraffin mixtures [6]. Instead, very few information exists on incorporating PCMs directly into polymeric packaging materials [7]. Therefore, the main challenge and aim of this work was to use biodegradable and natural materials to develop an innovative active packaging with thermal insulating properties obtained through the direct loading of ecofriendly fatty acids (linoleic acid and oleic acid) into biopolymer matrices consisting of polycaprolactone (PCL) by means of the electrospinning process [8].

2. Methods

The first step of the work was dedicated to identifying the best solvent for the dissolution of PCL among those accepted as GRAS (Generally Recognized as Safe), thus excluding chloroform, the most used with PCL, and testing acetone, acetic acid and their mixtures. The work then focused on the electrospinning technique to obtain a fibrous material. In particular, the solution parameters (i.e., PCL molecular weight, polymer concentration) and process parameters (i.e., voltage, feed flow rate, needle-collector distance) were evaluated and optimized through a morphological investigation by means of SEM analysis. Once the fiber morphology was optimized, the selected PCMs (linoleic acid, oleic acid and dodecane as comparison compound) were loaded, separately, through electrospinning, evaluating their influence on the morphology of the fibers. The materials produced were characterized in terms of mean fibers diameter, film thickness and mechanical properties by means of tensile tests, to verify their potential use as materials for packaging applications. The thermal properties were investigated by Differential Scanning Calorimetry (DSC) and the peroxide values were studied to evaluate the possible degradation of fatty acids during storage time. Overall migration tests were also performed in food simulants according to the reference regulations [9].

3. Results and discussion

The first step of the work focused on optimizing the polymer solution, testing PCL at different molecular weights (14000-80000 Da), different concentrations (from 10 to 25% w/v) and different solvents, choosing from those accepted as GRAS and identifying a mixture of acetone and acetic acid 7:3 v/v as the most suitable. The polymeric solutions were then processed by electrospinning, systematically varying the process parameters in order to identify the optimal conditions for obtaining a good morphology. This study allowed to identify the operative limits and ranges of conditions that give rise to three types of morphologies, schematized in Figure 1, from only beads for low PCL concentrations to sub-micrometric fibers without imperfections for higher concentrations and voltages. Once the process conditions and therefore the morphology were optimized, the PCMs selected were loaded in different concentrations (from 5 to 15 % by weight with respect to the PCL content). The morphology of the fibers analyzed by SEM showed the maintenance of the good structure even after loading.

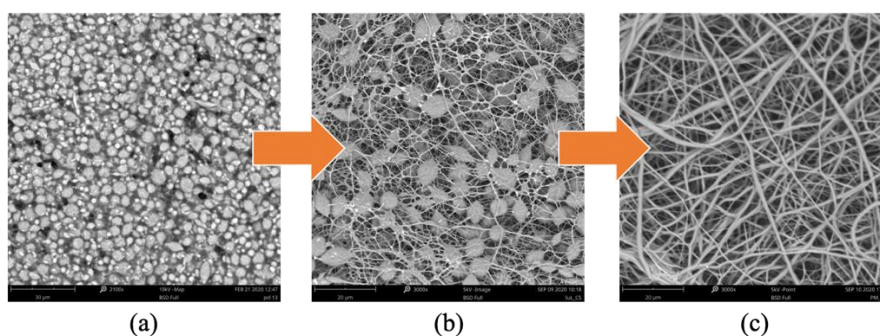


Figure 1. Morphological optimization of the electrospun PCL samples: from beads (a) and mixed morphology (b) to clean fibers (c).

In all cases, sub-micrometric fibers with a mean diameter of 860 nm were obtained, while the thickness of the films was quite variable between 85 and 335 μm due to the random deposition of the fibers on the collector during the electrospinning process. The variability of the thicknesses also influenced the mechanical tests conducted. Samples that showed more repeatability were those of linoleic acid, which showed a Young's modulus of about 9 MPa, better than that shown by PCL alone, highlighting a plasticizing action of fatty acid, elongation at break of 80% and a maximum stress value of about 4.5 MPa, higher than the value of 3.5 MPa identified as the minimum required for a material to be used as food packaging by conventional standards [10]. The thermal properties, peroxide value and the overall migration test allowed the selection of the best system.

4. Conclusions

The main challenge was posed by the goal of using biodegradable materials and non-toxic solvents, adopting green techniques to produce a packaging capable of protecting the shelf-life of food along the entire supply chain. Given these preliminary results, the materials produced seem to be suitable to be used as food packaging systems, since with the electrospinning technique it was possible to load rather high percentages of PCM while maintaining the desired structure. Furthermore, the produced materials exhibit good mechanical properties.

References

- [1] K.K. Gaikwad, S. Singh, Y.S. Lee, *Environ. Chem. Lett.* 16 (2018) 523
- [2] E. Drago, R. Campardelli, M. Pettinato, P. Perego, *Foods* 9 (2020) 1628
- [3] E. Drago, P. Franco, R. Campardelli, I. De Marco, P. Perego, *Food Hydrocoll.* 122 (2022) 107082
- [4] M. Pettinato, E. Drago, R. Campardelli, P. Perego, *Chem. Eng. Trans.* 86 (2021)
- [5] F. Topuz, T. Uyar, *Food Res. Int.* 130 (2020)
- [6] D. Leducq, F. Ndoye, G. Alvarez, *Int. J. Refrig.* 52 (2015) 133-139
- [7] W. Chalco-Sandoval, M.J. Fabra, A. López-Rubio, J.M. Lagaron, *J. Food Eng.* 192 (2017) 122-128
- [8] L. Zhao, G. Duan, G. Zhang, H. Yang, S. He, S. Jiang, *Nanomaterials* 10 (2020) 150
- [9] European Commission Regulation No. 10/2011, *OJEU*, 12, 75-80
- [10] S.F. Hosseini, M. Rezaei, M. Zandi, F. Farahmandghavi, *Food Hydrocoll.* 44 (2015) 172-182

PLA-based active food packaging production with antioxidant properties

Maria Bolla^{1*}, Margherita Pettinato¹, Roberta Campardelli¹, Giuseppe Firpo², Patrizia Perego¹

1 Department of Civil, Chemical and Environmental Engineering, University of Genoa, via Opera Pia, 15, 16145 Genoa, Italy;

2 Department of Physics, University of Genoa, via Dodecaneso 33, 16146, Genova, Italy.

**Corresponding author E-Mail: maria.bolla01@edu.unige.it*

1. Introduction

Food packaging is fundamental to protect food against mechanical damage, chemical, biochemical changes and microbiological spoilage, guarantying its stability over time. Nowadays, more rigorous food safety regulations, modernized manufacturing, retailing and distribution practices, led to the necessity of a suitable food packaging, with the aim of reducing food losses and extending the product shelf-life [1]. For these reasons, recent developments in materials and engineering resulted in new food packaging techniques, including active food packaging [2]. It plays an active role in the food protection by having direct interactions with food and/or its surroundings [1]. Among the most promising active materials, antioxidant agents are able to reduce reactive free radicals, providing higher food stability and nutritional value [3]. Spent coffee grounds (SCG) extracts are suitable candidates in this purpose, thanks to their high content of caffeine, phenolic compounds, flavonoids and melanoidins [4]. Furthermore, as other natural additives, they are safer and with a lower environmental footprint, with respect to the synthetic antioxidants [5,3].

In addition, in order to mitigate the alarming concern about the disposal and environmental issues raised from traditional oil-based plastics, natural and eco-friendly polymers represent an auspicious alternative. Among them, polylactic acid (PLA) is one of the most promising, thanks to its biodegradability, excellent transparency, good water resistance and good processability with standard plastic techniques, such as solvent casting [6].

Thus, the main aim of this work involved the production of active food packaging through a solvent casting technique, starting from PLA enriched with various amounts of spent coffee grounds extracts.

2. Methods

Antioxidant compounds were extracted from dried SCG using a hydroalcoholic solvent by a high pressure and temperature extraction (HPTE) at the operating conditions defined by a previous study [4]. The product was further purified through a liquid-liquid extraction (LLE) in chloroform. Both the obtained fractions were added to the PLA-based solutions during the packaging production process, by following the protocol reported by Cacciotti et al. [7].

The two final films were then characterized and compared in terms of morphology, gas permeability and specific migration of caffeine into a food simulant. Particularly, films morphology was investigated by the optical microscope (OM, Olympus BX51) and an ultra-high resolution field-emission-source scanning electron microscope (FESEM, Zeiss CrossBeam XB 1540). Furthermore, O₂ permeability measurements were carried out by the method reported by Firpo et al. [8]. Finally, packaging migration properties after eight days at 4°C, 25°C, 40°C and in 10% ethanol (v/v), as food simulant, were evaluated in accordance with the Plastic Regulation [9,10] and caffeine content was determined according to the protocol reported by Belay et al. [11].

3. Results and discussion

The packaging morphology, investigated by OM and SEM, is reported in Figure 1 for three representative samples: the blank and those enriched with the two fractions of extract at different caffeine contents.

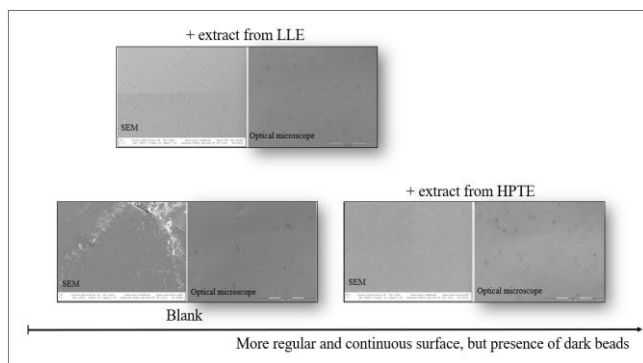


Figure 1. Packaging morphology. Images from OM and SEM.

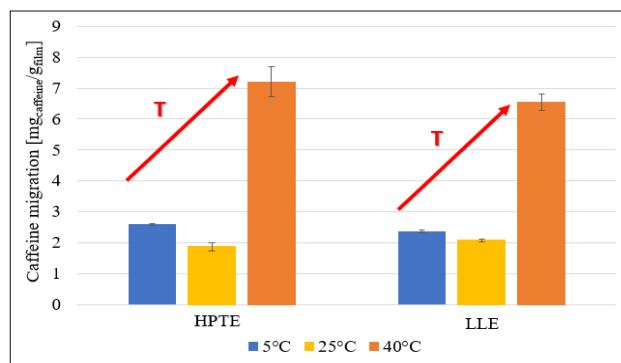


Figure 2. Comparison between films enriched with the HPTE extract and LLE extract.

Films enriched with the extract from HPTE exhibited a more continuous surface than the blank and that containing the fraction from LLE, but with some dark beads.

Regarding O_2 permeabilities, the same three samples were characterized by a decreasing permeability as the extract content increased. This can also be explained by considering the antioxidant action of the extracts.

Finally, in Figure 2 the specific migration of caffeine at 5°C, 25°C and 40°C in 10% ethanol (v/v) as food simulant is reported. As expected, as the temperature increased, caffeine release into the food simulant was facilitated by the improved mass transfer.

4. Conclusions

In this work, an innovative active food packaging was produced through the solvent casting technique, thanks to the use of a biodegradable polymer and the valorization of spent coffee grounds residue, which exhibits a considerable antioxidant action. The presence of the extracts affected the morphology of the final packaging, as well as its physical and chemical properties, showing higher barrier properties and antioxidant action.

References

- [1] M. Ozdemir, J.D. Floros, *Crit Rev Food.* 44 (2004) 185 – 193.
- [2] J. Ju, X. Chen, Y. Xie, H. Yu, Y. Guo, Y. Cheng, H. Qian, Y. Yao, *Trends Food Sci. Technol.* 92 (2019) 22– 32.
- [3] C. Vilela, M. Kurek, Z. Hayouka, B. Röcker, S. Yildirim, M.D.C. Antunes, J. Nilsen-Nygaard, M. K. Pettersen, C.S.R. Freire, *Trends Food Sci. Technol.* 80 (2018) 212–222.
- [4] M. Pettinato, A.A. Casazza, P.F. Ferrari, D. Palombo, P. Perego, *Food Bioprod. Process.* 114 (2019) 31–42.
- [5] E. Drago, R. Campardelli, M. Pettinato, P. Perego, *Foods.* 9 (2020).
- [6] M.J. Fabra, M.A. Busolo, A. Lopez-Rubio, J.M Lagaron, *Trends Food Sci. Technol.* 31 (2013) 79–87.
- [7] I. Cacciotti, S. Mori, V. Cherubini, F. Nanni, *Int. J. Biol. Macromol.* 112 (2018) 567–575.
- [8] G. Firpo G., J. Setina, E. Angeli, L. Repetto, U., *Vac.* 191 (2021).
- [9] Commission Regulation (EC) No 10/2011 of 14 January 2011 on plastic materials and articles intended to come into contact with food.
- [10] Commission Regulation (EC) No 2016/1416 of 24 August 2016 amending and correcting Regulation (EU) No 10/2011 on plastic materials and articles intended to come into contact with food.
- [11] B. Belay, K. Ture, M. Redi, A. Asfaw, *Food Chem.* 108 (2008) 310–315.

Oil-in-water nanoemulsions for encapsulation of lycopene from tomato waste

Junyang Li^{1*}, Giulia De Negri Atanasio¹, Roberta Campardelli¹, Patrizia Perego¹

1 Department of Civil, Chemical and Environmental Engineering, University of Genoa, Via Opera Pia, 15, 16145 Genoa, Italy;

**Corresponding author E-Mail: junyang.li@edu.unige.it*

1. Introduction

Lycopene is a carotenoid of industrial/commercial value, it can be found in ripe tomatoes, pink grapefruit, watermelon, guava and papaya, giving them their distinctive red color due to accumulation in the plant through photosynthetic pigment-pigment complexes [1]. Lycopene has anticancer action, is capable of preventing cardiovascular diseases and modulate the immune system. Therefore, it is widely used in functional foods, nutraceuticals, pharmaceuticals and/or other applications [2,3]. However, due to the presence of double bonds in the structure, lycopene is very unstable to factors such as oxygen, light, heat and humidity, which greatly affects its stability during processing and storage, as oxidation may promote its color and loss of functional activity. In this sense, encapsulation is considered an efficient method to improve the stability, bioavailability and effective delivery of lycopene [4]. In recent years, a wide range of colloidal delivery systems have been developed to encapsulate bioactive components, such as molecular complexes [5-7], micro/nano-encapsulation [8-10], micro/nano-emulsions [3], liposomes [11-13], microgels [14,15], and biopolymer particles [16,17]. Due to their easy application in the food industry, emulsion-based delivery systems are particularly suitable for protecting nutraceuticals. In this study, natural extract rich in lycopene obtained by tomato waste was stabilized in oil in water emulsions (O/W). The effect of different extract concentrations in the O/W emulsion on emulsion droplets size distribution emulsion, stability over time and lycopene entrapment efficiency was evaluated.

2. Methods

Preparation of lycopene O/W emulsion

To prepare the emulsion, isopropyl myristate was selected as oil phase, whereas the water phase was prepared dissolving pluronic at concentration of 1.5% (w/w). The ratio between the water and the oil phase was kept constant: 90/10 (w/w). Briefly, 9g of isopropyl myristate and 1g extracts was mixed with ultrasound at 40% amplitude, on/off = 30/30 s/s. Then 90g of pluronic solution was emulsified at 7000 rpm for 1 min using a high speed rotor stator. Then oil phase was slowly added and emulsified for 9 min. The emulsions were then analyzed with Mastersizer-3000 for drop size distribution (DSD). The emulsions were ultrasonicated at 70% amplitude with probe for 5 min (on/off = 30/30 s/s). At the end of the process emulsions were analyzed for DSD again. All the process was in ice bath.

Total lycopene amount and free lycopene content was determined according to. The encapsulation efficiency was obtained by the following equation:

$$\text{Encapsulation efficiency (\%)} = \frac{m_{\text{total}} - m_{\text{free}}}{m_{\text{initial}}} * 100 \text{ (Eq. 1)}$$

Where m_{total} is the total amount of lycopene loaded in the nanoemulsions, m_{free} is the free lycopene in the nanoemulsions, and $m_{initial}$ is the initial amount of lycopene added to the nanoemulsions. The m_{total} and m_{free} were measured following the protocol reported by [18].

To evaluate the storage stability of the nanoemulsions at different temperatures, samples (40 mL) were transferred into glass tubes and stored in the dark at 4, 25, 37 °C. The concentration of lycopene and the particle size of nanoemulsions were measured at regular intervals of three month. Samples were equilibrated at room temperature for 10 min before analysis.

3. Results and discussion

Emulsions were prepared using different amount of tomato waste extract. The extract was obtained by ultrasound assisted extraction at operative conditions of: T = 65 °C, t = 20 min, Liquid to solid ration = 72 mL/g, Amplitude = 65%, on = 33 s, Volume = 90 mL. Lycopene content in extract was $1536 \pm 53 \mu\text{g/g}$. Different emulsions were changing the O/W ratio and the extracts concentration.

Droplet size is the main parameter to describe the nanoemulsions; the viscosity of the oil phase can determine the final droplet size of nanoemulsions to a certain extent. The optical microscope images of Figure 3 show that the lycopene O/W nanoemulsions were characterized by droplet size of about 350 nm. In addition, the droplets are uniformly dispersed, without aggregations and fusion. Emulsions produced at different conditions were characterized by DSD between 200 nm and 800 nm.

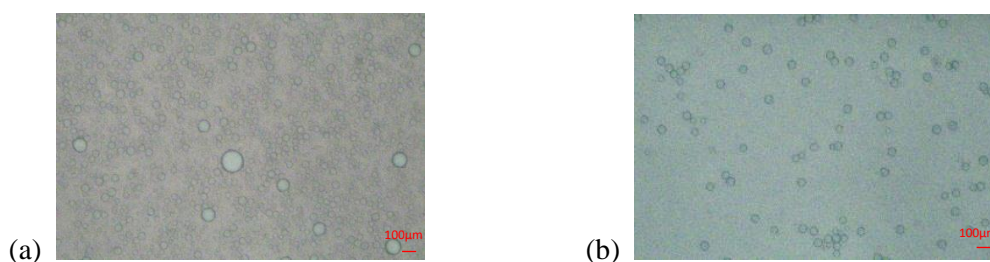


Figure 1. Optical microscope image of empty (a) and loaded (b) nanoemulsions.

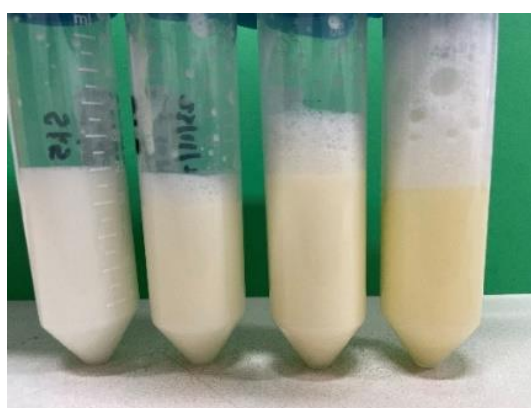


Figure 2. Emulsions loaded with different amounts of extract.

Increasing extract amount loaded in the O/W emulsion, a progressive increase of orange color was observed in the final product (Figure 2).

Storage stability of lycopene nanoemulsions

The stability of the lycopene nanoemulsion was determined at 4°C, 25°C and 37°C. Figure 3a shows that the appearance of the nanoemulsion at different storage temperatures showed significant changes after three months of storage at 37°C. The prepared nanoemulsions did not flocculate or precipitate at 4°C and 25°C. 37°C was a condition of accelerate aging. The stability of the nanoemulsion during storage was evaluated by measuring the change in particle size. Figures 3b shows that particle size did not change much at 4 °C and 25 °C during the first 4 weeks. In addition, the nanoemulsion becomes unstable at 37 °C, a phenomenon that may be due to the decrease in the repulsive force between droplets at relatively high temperature, and consequently, the increase of the average particle size from 300 nm to 800 nm, with the appearance of larger particles.

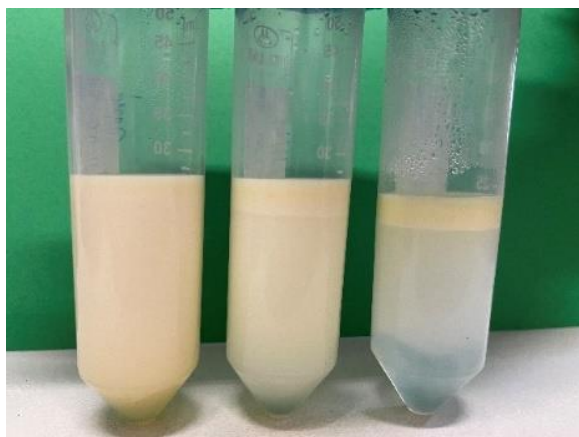


Figure 3a. Emulsion at 4°C, 25°C and 37°C after 3 months.

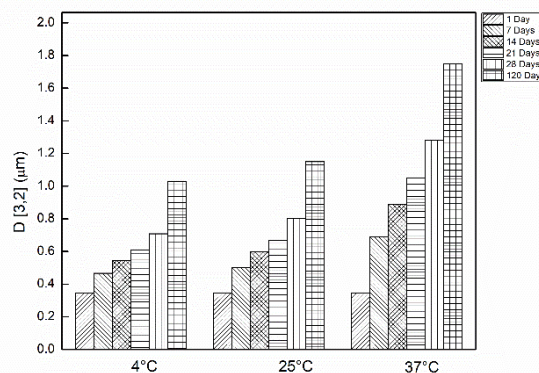


Figure 3b. Lycopene extracts (1g).

The encapsulation efficiency (EE) of lycopene in O/W nanoemulsion was calculated according to Eq. 1. Results demonstrated that after 3 months and at different temperature of the lycopene retention rate was in the range between 10.7-55.1 %.

4. Conclusions

In conclusion, O/W nanoemulsions can stabilize tomato waste extract, and different parameters can have a significant impact on the stability of lycopene nanoemulsions. The choice of extract ratio is crucial to improve the properties of nanoemulsions. Future work will regard the study of naturally stabilized emulsions.

References

- [1] S. Rahimi; M. Mikani. *Microchem. J.* 146 (2019) 1033-1042.
- [2] G. Vasapollo; L. Longo; L. Rescio; L. Ciurlia. *J Supercrit Fluids* 29 (2004) 87-96.
- [3] D. Sotomayor-Gerding; B.D. Oomah; F. Acevedo; E. Morales; M. Bustamante; C. Shene; M. Rubilar. *Food Chem* 199 (2016) 463-470.
- [4] G.L.A. Sampaio; S. Pacheco; A.P.O. Ribeiro; M.C. Galdeano; F.S. Gomes; R.V. Tonon. *Lwt* 116 (2019) 108589.
- [5] Y. Deswal; S. Asija; D. Kumar; D.K. Jindal; G. Chandan; V. Panwar; S. Saroya; N. Kumar. *Res. Chem. Intermed.* 48 (2021) 703-729.
- [6] A. Arora; S. Singh; P. Oswal; D. Nautiyal; G.K. Rao; S. Kumar; A. Kumar. *Coord Chem Rev.* 438 (2021).
- [7] H. Wang; S. Wang; H. Zhu; S. Wang; J. Xing. *Antioxidants (Basel)* 8 (2019).
- [8] R. Delshadi; A. Bahrami; A.G. Tafti; F.J. Barba; L.L. Williams. *Trends Food Sci Technol.* 104 (2020) 72-83.
- [9] Z. Akbarbaglu; S.H. Peighambaroust; K. Sarabandi; S.M. Jafari. *Food Chem* 359 (2021) 129965.

- [10] A.L.R. Souza; D.W. Hidalgo-Chávez; S.M. Pontes; F.S. Gomes; L.M.C. Cabral; R.V. Tonon. *Lwt* 91 (2018) 286-292.
- [11] M. Pettinato; P. Trucillo; R. Campardelli; P. Perego; E. Reverchon. *Chem Eng Process* . 151 (2020).
- [12] B.S. Esposto; P. Jauregi; D.R. Tapia-Blácido; M. Martelli-Tosi. *Trends Food Sci Technol* . 108 (2021) 40-48.
- [13] A. Najafi; R.A. Taheri; M. Mehdipour; G. Farnoosh; F. Martinez-Pastor. *Anim Reprod Sci* 195 (2018) 168-175.
- [14] F. Scheffold. *Nat Commun* 11 (2020) 4315.
- [15] S. Stock; R. von Klitzing. *Curr Opinion Colloid Interface Sci.* 58 (2022).
- [16] Y. Xiong; R. Georgieva; A. Steffen; K. Smuda; H. Baumler. *Journal of J. Colloid Interface Sci.* 514 (2018) 156-164.
- [17] Y. Li; S. Gong; X. Guan; H. Jiang; S. Tao; C. Yang; T. Ngai. *Adv. Mater. Interf.* 8 (2021).
- [18] C. Zhao; L. Wei; B. Yin; F. Liu; J. Li; X. Liu; J. Wang; Y. Wang. *Int J Biol Macromol* 153 (2020) 912-920.

Electrical conductivity of basil based sauces for MEF processing

Oriana Casaburi¹, Aldo Romano¹, Cosimo Brondi¹, Francesco Marra^{1*}

1 Dipartimento di Ingegneria industriale, Università degli studi di Salerno

**Corresponding author E-Mail: fmarra@unisa.it*

1. Introduction

The principle of moderate electric field (MEF) heating involves the passage of an alternating electric current (AC) through an electrically conductive material placed between two electrodes which has inherent resistance and as a result generates heat internally within the material [1]. The extent of power dissipated as heat in the material depends on the electrical conductivity of the product, and the electrical field strength applied. Generally, all food materials which contain water in excess of 30% and dissolved ions can sufficiently conduct electricity [2]. In literature, the electrical conductivity range between 0.01 S/m to 10 S/m is considered as satisfactory with optimum heat transfer efficiency experienced up to 5 S/m [3].

In this work, the heating behavior of heterogeneous complex food systems -such as sauces based on basil- undergoing MEF has been analyzed, with a focus on the dependence of electrical conductivity on the sauce composition.

2. Methods

2.1 Sample preparation

Samples of basil based sauces were prepared according with compositions reported in table 1.

Table 1. Compositions of the different samples.

Sample	Basil % [g/g]	Oil % [g/g]	Salt % [g/g]	Water* % [g/g]	Other components % [g/g]
A1	6.88	10.00	0.75	75.99	6.38
A2	13.75	20.00	1.50	51.98	12.77
A3	20.63	30.00	2.25	27.97	19.15
A4	27.50	40.00	3.00	3.97	25.53
B1	13.75	32.77	1.50	51.98	0
B2	13.75	20.00	1.50	64.75	0
B3	13.38	20.00	1.87	64.75	0
B4	26.52	20.00	1.50	51.98	0
C1	7.23	10.52	2.31	79.94	0
C2	15.76	22.93	1.72	59.59	0
C3	25.97	37.78	1.02	35.23	0
D1	7.34	10.68	0.80	81.17	0
D2	6.02	25.58	1.92	66.49	0
D3	4.03	47.81	3.59	44.58	0
E1	7.34	10.68	0.80	81.17	0
E2	18.56	9.23	2.03	70.18	0
E3	37.82	6.75	4.13	51.30	0

*Water already contained inside the basil.

2.2 MEF system

The used MEF system is depicted in figure 1

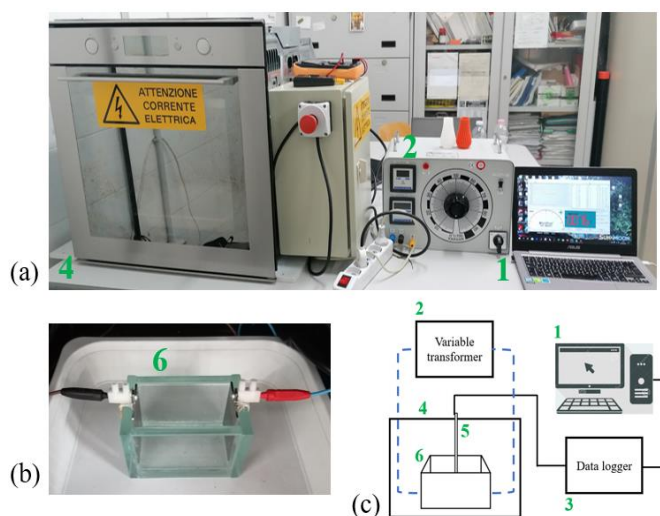


Figure 1. Pictures of the adopted MEF system and instrumentation: (a) assembly of the MEF heating equipment, showing the (1) data acquisition system, (2) the variable transformer and (4) the insulated chamber. (b) Detail of the (6) MEF cell with the electrodes. (c) Schematic diagram of the experimental setup representing the insertion of (5) the thermocouple into the cell.

2.3 Measurement of electrical conductivity

The electrical conductivity (σ) was evaluated from temperature, voltage and current data recorded at 2.5s intervals. Voltage and current readings were acquired by using a digital multimeter (model PicoLog, Pico Technology, UK) and a data acquisition software. Electrical conductivity was calculated according to the following equation:

$$\sigma = \frac{I}{V} \frac{L}{A} \quad (1)$$

where I is the current passing through the food item, V is the applied voltage, L is the length between the electrodes and A is the area of the electrodes occupied by the sample. The ratio L/A is known as the cell constant of the MEF heating unit. The cell constant of the MEF heater was 60.1 m⁻¹ when filled with a mass of 200 g. The cell was calibrated by using several aqueous solutions of NaCl in deionized water (concentrations were 1%, 2.5% and 5% w/w respectively).

3. Results and discussion

The change in σ with the temperature and the composition is shown in Figure 2. As the change in the electrical conductivity is independent of the applied $\Delta V/L$, the set of data obtained at the several applied voltage gradients (5.00 V/cm, 6.00 V/cm and 7.00 V/cm) are reported together. For all the considered samples, the electrical conductivity shows a positive linear dependence on temperature, which is a typical effect attributed to a reduced drag for the ions' movement within the medium [4].

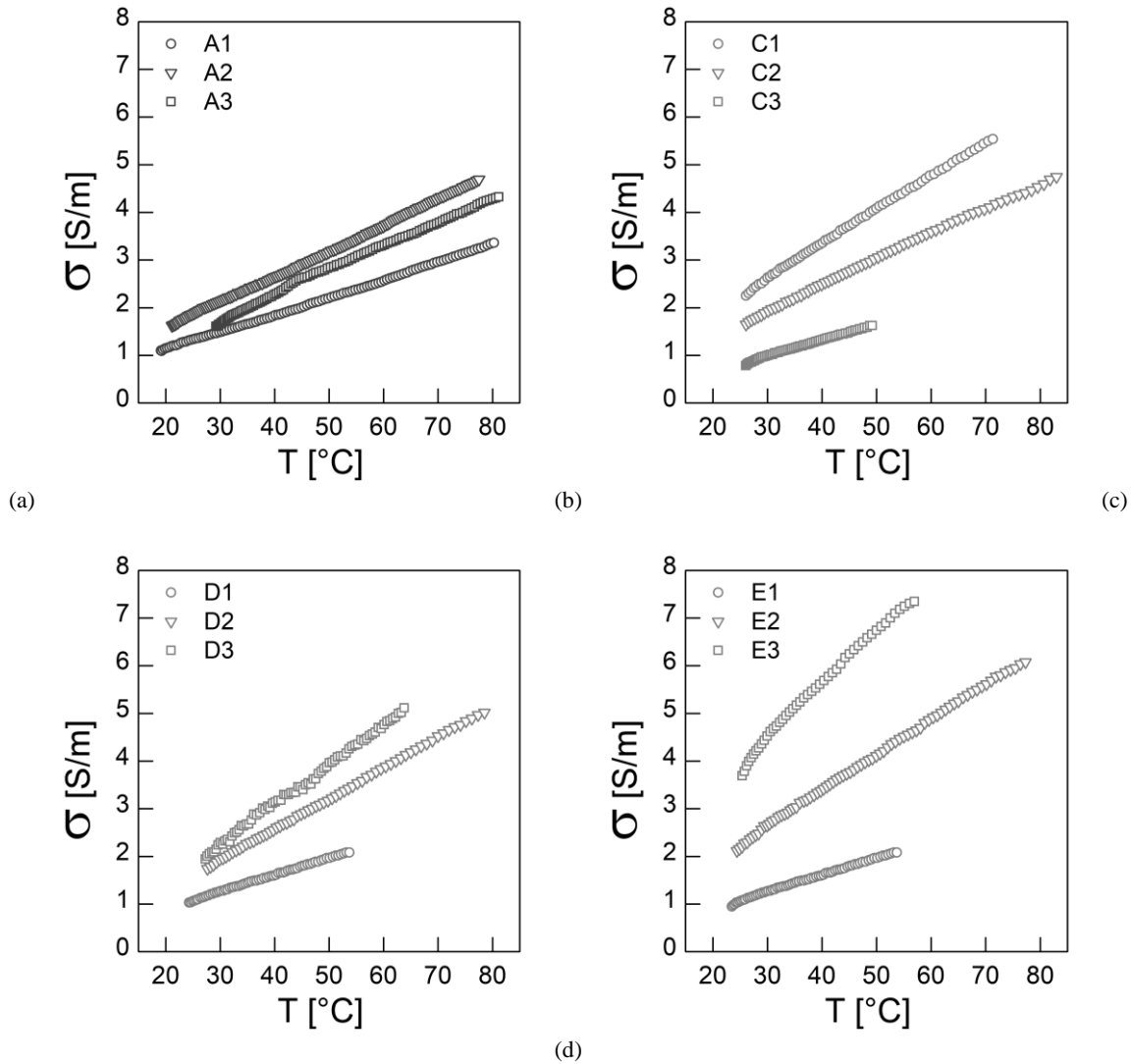


Figure 2. Electrical conductivity of (a) diluted pesto sauces and of basil suspension in oil-water emulsions: (b) competing effect between O/W and B/W at same S/W, (c) competing effect between O/W and S/W at same B/W, (c) competing effect between B/W and S/W at same O/W.

Experimental data were linearly fitted by linear equation:

$$\sigma = \sigma_0 + mT \quad (2)$$

where σ_0 and m respectively represent the intercept and the slope of the linear model. Results of the fitting procedure are reported in Table 2. R^2 values indicate a good agreement between the measured values and the linear fitting procedure. A1 is characterized by the lowest values of the electrical conductivity, while A2 has the highest values and A3 has intermediate values between A1 and A2. Indeed, it can be observed that m goes from 0.0365 S/(m °C) to 0.0537 S/(m °C) (for A1 and A2 respectively). In practice, the fat content and the vegetable solid particles are characterized by a lower electrical conductivity than liquids for particulate foods. For this reason, A2, diluted with 50% of deionized water, is characterized by higher values of electrical conductivity, as a lower fat concentration leads to a minor degree of resistance to the electrical current. A3 still has higher values of electrical conductivity than A1, characterized by higher amounts of the non-conductive phase. C1 is the sample that has the highest values of electrical conductivity. As ratios

basil/water and oil/water increase, the electrical conductivities of C2 and C3 progressively decrease, according the increasing amount of the oil and basil components. D1 is characterized by the lowest values of electrical conductivity. As the ratios oil/water and salt/water increase, also the electrical conductivities of D2 and D3 progressively increase, according the increasing amount of the salt component. E1 is characterized by the lowest values of electrical conductivity. As B/W and S/W increase, also the electrical conductivities of E2 and E3 progressively increase, according the increasing amount of the salt component.

Table 2. Parameters obtained from fitting of the experimental data by Equations 5.

Sample	σ_0 [S/m]	m [S/(m °C)]	R ²
A1	0.394	0.0365	0.999
A2	0.507	0.0537	0.999
A3	0.221	0.0512	0.997
C1	0.483	0.0716	0.999
C2	0.334	0.0530	0.999
C3	0.037	0.0341	0.996
D1	0.193	0.0355	0.999
D2	0.008	0.0644	0.999
D3	0.003	0.0833	0.999
E1	0.174	0.0360	0.998
E2	0.406	0.0744	0.999
E3	1.088	0.1132	0.994

4. Conclusions

Electrical conductivity of basil based sauces is influenced by relative ratios among basil, oil, water, and salt content. Some of the tested formulations showed a good heating behavior thanks to their electrical conductivities. This work demonstrated the applicability of heating assisted by moderate electric fields to complex heterogeneous food systems such as basil based sauces .

Acknowledgments

This study has been supported by the ERA-NET SusFood2 project, “Improving Sustainability in Food Processing using Moderate Electric Field (MEF) for Process Intensification and Smart Processing (MEFPROC).

References

- [1] Sastry, S. 2008. Ohmic Heating and Moderate Electric Field Processing. *Food Science and Technology International*, 14, 419-422
- [2] Samprovalaki, K., Bakalis, S. & Fryer, P. J. In: Yannotis, S. & Sunden, B. (eds.) *Heat Transfer in Food Processing: Recent Developments and Applications*. Southampton: Wit Press., 2007, pp.159-186
- [3] Zell Zell, M., Lyng, J. G., Cronin, D. A. & Morgan, D. J. 2009. Ohmic heating of meats: Electrical conductivities of whole meats and processed meat ingredients. *Meat Science*, 83, 563-570
- [4] Darvishi H., Khostaghaza M.H., Najafi G., 2013, Ohmic heating of pomegranate juice: Electrical conductivity and pH change, *Journal of the Saudi Society of Agricultural Sciences*, 12, 101-108

Coupling of experimental and computational approaches in the study of complex (nano)systems for industrial and biomedical applications

Domenico Marson^{*}, Maria Russi¹, Erik Laurini¹, Sabrina Pricl^{1,2}

¹ *Molecular Biology and Nanotechnology Laboratory (MolBNL@UniTS), DEA, University of Trieste, Piazzale Europa 1, 34127 Trieste, Italy*

² *Department of General Biophysics, Faculty of Biology and Environmental Protection, University of Lodz, ul. Pomorska 141/143, 90-236 Łódź, Poland*

** Corresponding author e-mail: domenico.marson@dia.units.it*

1. Introduction

In the contemporary material and drug development process, computer-assisted material design (CAMD) has proven to be a great asset in the prediction and characterization of different properties of complex molecular systems. Advancements in the last two decades, in high-performance computing (HPC) allowed researchers to share lights on increasingly multifaceted aspects of (nano)material development for industrial and biomedical applications. Nonetheless, to get detailed structure/property insights on the performance of a variety of materials – from (bio)proteins to micelles and synthetic polymers, a combination of HPC-based methods and experimental techniques are necessary. Accordingly, in this presentation we will give an overview of such hybrid approach with examples that, although referring to specific case-studies, hold a general validity and can be adapted to the study of any sophisticated (nano)systems.

2. Methods

Nowadays, HPC-based calculations allow researchers to design and predict the properties of highly complex materials with a great degree of accuracy, using computational techniques spanning different time and size scales [1]. In particular, focusing on molecular dynamic (MD) simulations is possible to follow the time evolution of a system of interest with atomistic resolutions, and describe a plethora of phenomena that pertain to the MD time/scale domain, including, *e.g.*, thermodynamics and kinetic events [2-7] (Figure 1). Yet, with the addition of tailored experimental investigations, other important information including – among many others – structural and mechanical properties of polymer (nano)composites and/or critical micellar concentrations (CMC) and aggregation numbers for (bio)surfactants (N_{agg}) can be precisely derived [8-17].

Among all physico-chemical experimental techniques available to the purpose, fluorescence spectroscopy (FS) and isothermal titration calorimetry (ITC) are the most versatile and powerful methods. For example, fluorescence quenching of aromatic amino acids induced by a ligand binding can unveil the underlying mechanism, and yield information of the overall ligand-receptor binding affinity [7, 18]. Contextually, ITC is becoming a gold standard approach for studying intermolecular and/or intramolecular interactions both in aqueous buffers and in different organic solvents [11-13]. Specifically, by measuring the heat exchanged during any interaction event it allows the direct derivation of the enthalpy variation, the stoichiometry of the species involved as well as the binding affinity constant. From the knowledge of these quantities the remaining thermodynamics parameters (entropy and free energy variations) can be directly estimated. K_d . With an eye on surfactants, the relevant CMC and N_{agg} can be retrieved with this technique; moreover, by re-elaborating

the ITC thermograms kinetics information (*e.g.*, the association (k_{on}) and dissociation rate constants (k_{off})) can be reliably calculated. Interestingly, all these data can find their counterpart *in silico*, for which more sophisticated techniques, which include metadynamics, free energy perturbation (FEP) and steered MD simulations, exist to investigate in detail the molecular rationales for these phenomena [5, 18-19].

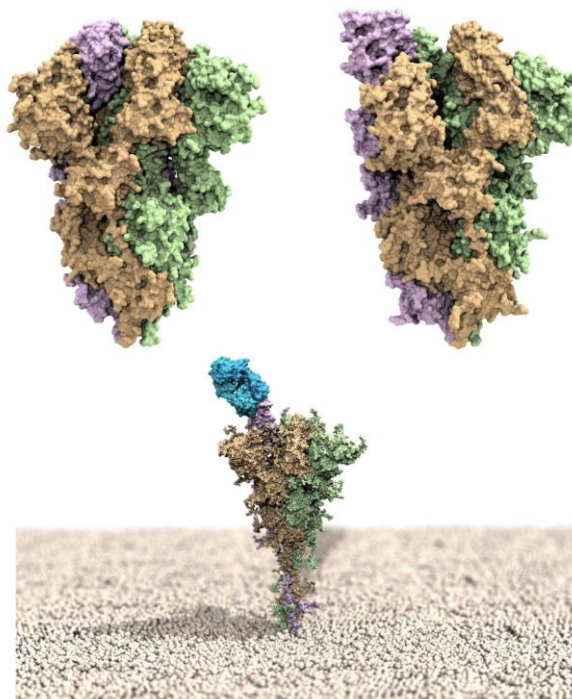


Figure 1. Upper panel: models of the SARS-CoV-2 spike homotrimeric protein in the down (left) and up (right) conformations. The three spike protomers are highlighted by their light green, tan and light purple van der Waals surfaces, respectively. Bottom panel: computer rendering of the full-length SARS-CoV-2 homotrimer embedded in a membrane model (polar heads in light tan spheres), showing one protomer in the up position and in complex with the LY-CoV555 (bamlanivimab) monoclonal antibody (light blue van der Waals surface) [3].

3. Results and discussion

To highlight the combined use of FS/ITC and HPC-based simulations, we will report a couple of examples dealing with protein/ligand binding [7, 18]. Purposely, the results obtained from the application of this hybrid approach to the thermodynamic and kinetic characterization of the interaction of human serum albumin (HSA) – the major protein component of human blood – with different ligands (two FDA anticancer drugs and a complex dendrimeric molecule) will be presented and discussed.

Next, we will report on the accurate determination of the binding stoichiometry among the radionuclide $^{111}\text{In(III)}$ (an element used in clinical single photon emission computed tomography (SPECT) bioimaging) with biocompatible nanocarriers bearing different terminal macrocyclic rings, *i.e.* DOTA (1,4,7,10-tetraazacyclododecane-1,4,7,10-tetraacetic acid) and NOTA (1,4,7-triazacyclononane-1,4,7-triacetic acid). For other self-assembling amphiphilic nanosystems we will also show some results stemming from the coupling of HPC- and experimental-based techniques, which allowed us to characterize their main micellar features, including their CMC and N_{agg} values [9, 12].

Finally, we will introduce a correlative analysis between the mechanical and structural properties exploited in the determination of the intrinsic changes of double strand DNA when interacting with different intercalant molecules (Figure 2). The procedures and results obtained in this study can be extended to a wide category of molecules and polymer of different nature, therefore finding further applications in different field, *e.g.*, from the optimal titration of chemotherapeutic drugs to environmental studies for the detection of heavy metals in human serum [17].

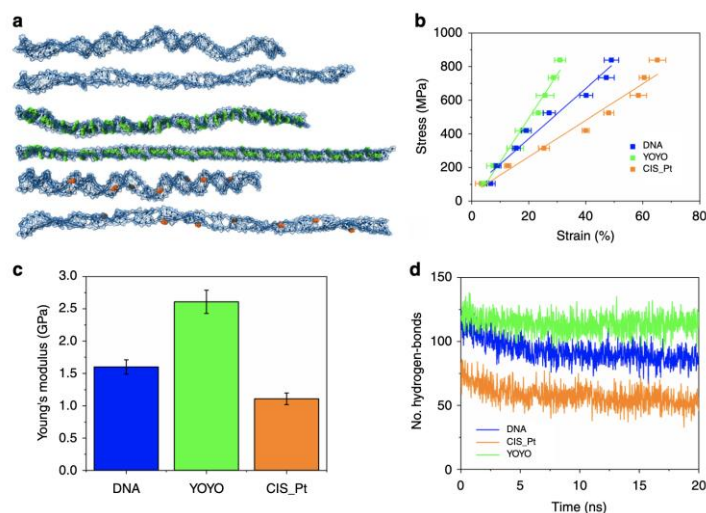


Figure 2. SMD simulations of pristine DNA and DNA intercalated with YOYO-1 and CisPt. a) Simulated conformational structures of the bare DNA (top), DNA intercalated with YOYO-1 (center), and CisPt (bottom) under uniaxial stretching deformation. In each figure, the first corresponds to the initial structure, while the second represents the final conformation reached at the maximum simulated strain. b) Stress-strain curve of the unidirectional traction applied to the DNA (blue), DNA/YOYO-1 (green), and DNA/CisPt (orange) systems. The Young's moduli for each complex are calculated from the slope of the linear fitting. The strain at each force has been averaged over three simulations and the corresponding standard errors are reported. c) Calculated Young's modulus values for DNA (blue), DNA/YOYO-1 (green), and DNA-CisPt (orange) complexes. d) Change in the number of hydrogen bonds of DNA (blue), DNA/YOYO-1 (green), and DNA/CisPt (orange) systems during the simulation time applying the maximum stress value [17].

4. Conclusions

With the advent of supercomputers, *in silico* methods are gaining a true momentum in the design, study and characterization of complex (nano)systems with high performance in different application sectors. Nonetheless, experimental routines based on chemico-physical techniques are still of age to corroborate computer-based predictions and/or to achieve a higher order of accuracy. In this presentation, we offered a necessarily confined yet significant number of examples in which the efficient combination of both methodologies led to effective material structure/property determinations for very complex systems of industrial and biomedical interest. As such, this approach holds a general validity and can be further expanded to the design and characterization of new, high-performance materials.

References

- [1] M. Fermeiglia, A. Mio, S. Aulic, D. Marson, E. Laurini, S. Pricl, *Molecular Systems Design & Engineering* 2020, 5, 1447-1476.

- [2] E. Laurini, D. Marson, S. Aulic, A. Fermeglia, S. Pricl, *Acs Nano* 2021, *15*, 6929-6948.
- [3] E. Laurini, D. Marson, S. Aulic, A. Fermeglia, S. Pricl, *Sci Rep* 2021, *11*, 20274.
- [4] E. Laurini, D. Marson, S. Aulic, M. Fermeglia, S. Pricl, *Acs Nano* 2020, *14*, 11821-11830.
- [5] D. Marson, E. Laurini, M. Fermeglia, D. K. Smith, S. Pricl, *Fluid Phase Equilibria* 2018, *470*, 259-267.
- [6] D. Marson, E. Laurini, P. Posocco, M. Fermeglia, S. Pricl, *Nanoscale* 2015, *7*, 3876-3887.
- [7] E. Laurini, D. Marson, P. Posocco, M. Fermeglia, S. Pricl, *Fluid Phase Equilibria* 2016, *422*, 18-31.
- [8] D. Marson, S. Aulic, M. Fermeglia, E. Laurini, S. Pricl, in *Design and Delivery of SiRNA Therapeutics* (Eds.: H. J. Ditzel, M. Tuttolomondo, S. Kauppinen), Springer US, New York, NY, 2021, pp. 267-296.
- [9] E. Laurini, S. Aulic, N. Skoko, D. Marson, M. Fermeglia, S. Pricl, in *Design and Delivery of SiRNA Therapeutics* (Eds.: H. J. Ditzel, M. Tuttolomondo, S. Kauppinen), Springer US, New York, NY, 2021, pp. 245-266.
- [10] E. Laurini, S. Aulic, D. Marson, M. Fermeglia, S. Pricl, in *Design and Delivery of SiRNA Therapeutics* (Eds.: H. J. Ditzel, M. Tuttolomondo, S. Kauppinen), Springer US, New York, NY, 2021, pp. 209-244.
- [11] L. Ding, Z. Lyu, B. Louis, A. Tintaru, E. Laurini, D. Marson, M. Zhang, W. Shao, Y. Jiang, A. Bouhleb, L. Balasse, P. Garrigue, E. Mas, S. Giorgio, J. Iovanna, Y. Huang, S. Pricl, B. Guillet, L. Peng, *Small* 2020, *16*, e2003290.
- [12] D. Dhumal, W. Lan, L. Ding, Y. Jiang, Z. Lyu, E. Laurini, D. Marson, A. Tintaru, N. Duseti, S. Giorgio, J. L. Iovanna, S. Pricl, L. Peng, *Nano Res* 2020, *14*, 2247-2254.
- [13] L. Ding, Z. Lyu, A. Tintaru, E. Laurini, D. Marson, B. Louis, A. Bouhleb, L. Balasse, S. Fernandez, P. Garrigue, E. Mas, S. Giorgio, S. Pricl, B. Guillet, L. Peng, *Chem Commun* 2019, *56*, 301-304.
- [14] Y. Dong, T. Yu, L. Ding, E. Laurini, Y. Huang, M. Zhang, Y. Weng, S. Lin, P. Chen, D. Marson, Y. Jiang, S. Giorgio, S. Pricl, X. Liu, P. Rocchi, L. Peng, *J Am Chem Soc* 2018, *140*, 16264-16274.
- [15] E. Laurini, D. Marson, S. Aulic, A. Mio, M. Fermeglia, S. Pricl, *Chemical Engineering Transactions* 2018, *74*, 619- 624.
- [16] E. Laurini, D. Marson, M. Fermeglia, S. Pricl, *J Comput Sci-neth* 2018, *26*, 28-38.
- [17] S. Stassi, M. Marini, M. Allione, S. Lopatin, D. Marson, E. Laurini, S. Pricl, C. F. Pirri, C. Ricciardi, E. Di Fabrizio, *Nat Commun* 2019, *10*, 1690.
- [18] M. Russi, G. Cavalieri, D. Marson, E. Laurini, S. Pricl, *Mol Pharmaceut* 2022, *in press*.
- [19] C. Holtschulte, F. Börgel, S. Westphäliger, D. Schepmann, G. Civenni, E. Laurini, D. Marson, C. V. Catapano, S. Pricl, B. Wünsch, *Chemmedchem* 2022, e202100735.

TURBOFLUX: A Mobile Transportable Unit to Produce Formulations for the Chemical and Health Sectors

Riccardo Bacci di Capaci*, Gabriele Pannocchia, Chiara Galletti, Elisabetta Brunazzi

Department of Civil and Industrial Engineering, University of Pisa, Italy

**Corresponding author E-Mail: riccardo.bacci@unipi.it*

1. Introduction

The COVID-19 emergency has put the Italian process industry and the various chemistry sectors in front of several crucial challenges [1]. Nevertheless, this unheard-of health pandemic has provided the opportunity for many chemical industries to enter new sectors, developing the ability to rapidly reconvert production and certify products, making efforts to adapt to the regulations in force. The pandemic has also revealed many major vulnerabilities, and it is clear how the need for process intensification is how much ever relevant [2]. Modular chemical process intensification indeed proves an attractive concept because factory-built modular plants can be easily distributed, repositioned, and stacked in parallel to achieve scale, while process intensification can overcome the inherent loss of economies of scale associated with a smaller process [3, 4].

This abstract is related to a recent project funded by Tuscany Region that aims to develop an innovative plant (called TURBOFLUX) to produce in continuous mode a set of specific formulations for the chemical and health sectors to face possible future sanitary pandemics. The recent COVID-19 emergency has now passed its most critical phase and has in the meantime become endemic, making the Italian production of surgical medical devices, such as sanitizing gel, settle on stable levels. Nevertheless, developing a plant with minimal complexity, but with peculiar features of high flexibility, modularity, agility, and availability, is very attractive for the very variable market of the future, especially for crisis areas or when rapid installation and start-up are required.

The project activities have concerned so far the analysis of rheological and physical/chemical properties of the substances of interest, the selection and analysis of the modular elements of the tubular flow reactor, and the run of a series of numerical simulations with CFD techniques. Furthermore, the work will focus on the definition and development of the automation software and the control system, the prototype integration and realization, and functional and performance tests in simulated and operational scenarios.

The desired formulations of TURBOFLUX are produced from a limited number of basic components in liquid state, directly inflow by means of a series of static mixing devices [5, 6] installed within the pipeline housed in a containerized mobile unit. The plant is specifically designed for three main types of final products: i) alcohol-based disinfectants; ii) synthetic environmental sanitizers; iii) modified acrylic resins. It is to be noted that the above-mentioned formulations are usually obtained in traditional batch-type processes; however, with the aid of static mixers, production can efficiently take place in continuous mode.

The plant consists of two maritime containers arranged adjacent by the long side, with standard dimensions. The first container includes the static mixing system and the pumps for the various components and the obtained formulate, as well as a buffer tank for temporary storing; the second container hosts the kegging machine for the final product and the control panels with external access in a safe area. In particular, the static mixing zone of the plant consists of a series of 5 parallel pipes connected by vertical curves, for a total of around 18m length, as shown in Figure 1. The main vector fluid is fed into the primary pipe and a series of secondary smaller pipes is used to introduce the additives to obtain the various final products.

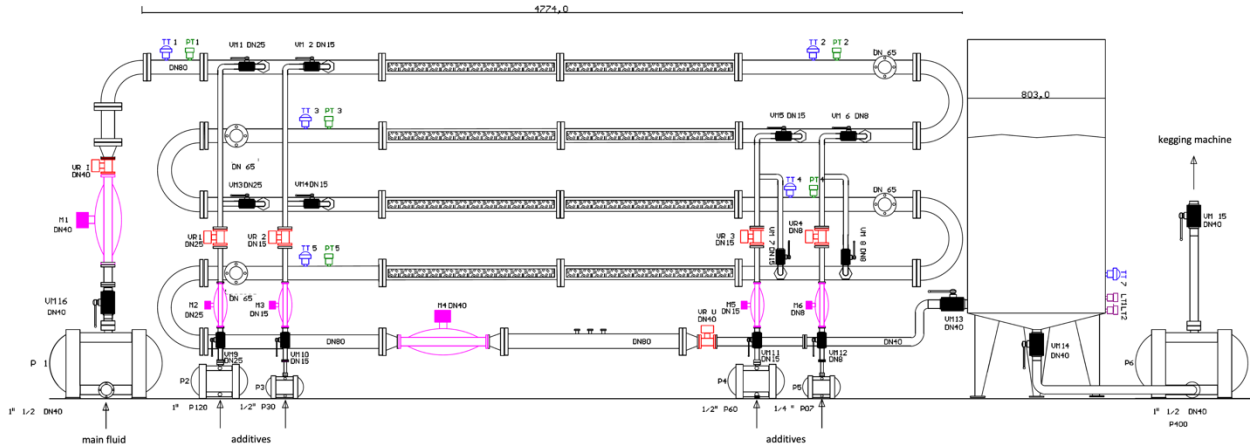


Figure 1. Sketch of the mixing zone of the TURBOFLUX system.

The main pipe represents the mixing and reaction environment: the first four sectors are used for feeding, mixing and reaction; the final sector is a calm zone to allow the product stabilization, the quality monitoring, and the properties control. Each component is fed with a dedicated volumetric pump and several mass flow meters are installed to guarantee a high precision in dosages. The relative quantitative and the procedure of injection of the various components are established in advance, according to the recipe developed for each final product. For every component, a control valve and two splitting valves are provided, so that the same additive can be fed in two different sectors of the pipe. The feedback basic control is guaranteed by a ratio logic between the main and the various additive flow rates. In addition, given the practical and economic difficulty of obtaining reliable real-time measures of product quality, an inferential system for monitoring and controlling the main performance variables will be adopted.

2. Methods

The present abstract reports only some results of the extensive CFD simulations carried out for the development of the hardware architecture of the tubular flow reactor. In details, the most suitable types of static mixer for the scopes were investigated and a series of operative conditions were evaluated. The simulation of a small portion of the real pipe, corresponding to the injection and the mixing area of an additive fluid with the main vector fluid, is here discussed. Despite being simplified, this preliminary model has anyway allowed one to analyze the influence of the main operating parameters and of the specific geometric configurations on the performance of mixing phenomena.

The studied geometry (see Figure 2) is characterized by a length $L = 800$ mm and an injection pipe far 50 mm from the inlet of the main pipe, with an inner diameter of 25mm and inclined by 45° . The various static mixing devices are installed 50 mm far from the additive inlet to ensure a premixing space, so that they cover only the last 700 mm of the overall geometry.

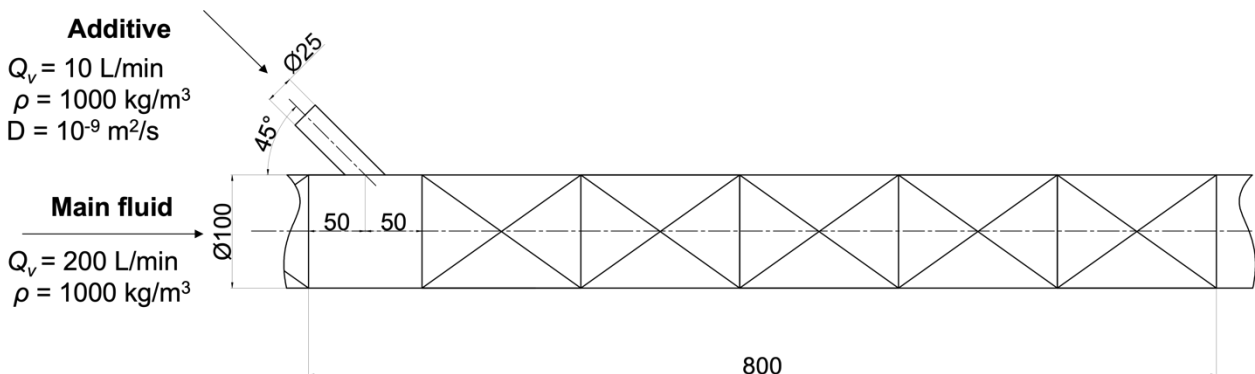


Figure 2. Sketch of the simplified geometry under study.

Note that the mixing of an ideal main fluid and an additive fluid, assumed as a tracer (scalar), is considered. The main fluid is a liquid with a density of 1000 kg/m^3 and different values of viscosity, according to the specific case study. The additive fluid has the same physical properties, and a molecular diffusivity in the main fluid equal to $D = 10^{-9} \text{ m}^2/\text{s}$. Therefore, ideal scenarios are investigated, since density and viscosity of the resulting mixture are assumed constant throughout all the mixing pipe.

The numerical model was developed with the commercial CFD code ANSYS Fluent v. 19, based on finite volume methods. The basic idea is to have a flexible numerical model, useful to investigate the effect of different design aspects on the mixing process and the pressure drops. The final objective is indeed to define the best configuration of the static mixer as to maximize mixing while limiting pressure drops, for different fluids. To this purpose, the numerical model is obtained by assembling different sections, each of them reproducing an inlet section, a kind of static-mixer, and an outlet section. Then, the resulting reactor length is covered by placing together the different elements as a "lego"-like assembly so to analyze different reactor configurations. The overall geometry can be easily modified by adding, removing, or replacing only some specific blocks. Polyhedral meshes with prismatic layers at the walls are generated for each block. The prismatic layers at the wall are needed in the turbulent regime to ensure the correct resolution on the wall boundary layer. Grid independence test was performed on a shorter geometry; 2 mm was set as the optimal grid dimension and then used in subsequent studies for both laminar and turbulent regimes. In this manner between 2.6 and 3.7 millions of cells were needed depending on the reactor configuration. Navier-Stokes equation and a transport equation for the tracer were solved; more specifically, in turbulent conditions, Reynolds-averaging was applied by closing Reynolds stresses with the RNG $\kappa - \epsilon$ model. The convective terms were discretized by a second-order upwind scheme. In laminar regime, the pressure-velocity coupling algorithm was treated with the SIMPLE algorithm, while in turbulent regime a pseudo-transient coupled scheme was adopted.

3. Results and discussion

Different reactor configurations were analyzed by assembling different blocks and related computational grids to cover the length $L = 800 \text{ mm}$. As shown in Figure 3, three different assembled geometries, for five levels of fluid viscosity (5, 50, 100, 500, 1000 cP) were tested, that is, five levels of Reynolds number, ranging from mid turbulent to pure laminar regime.

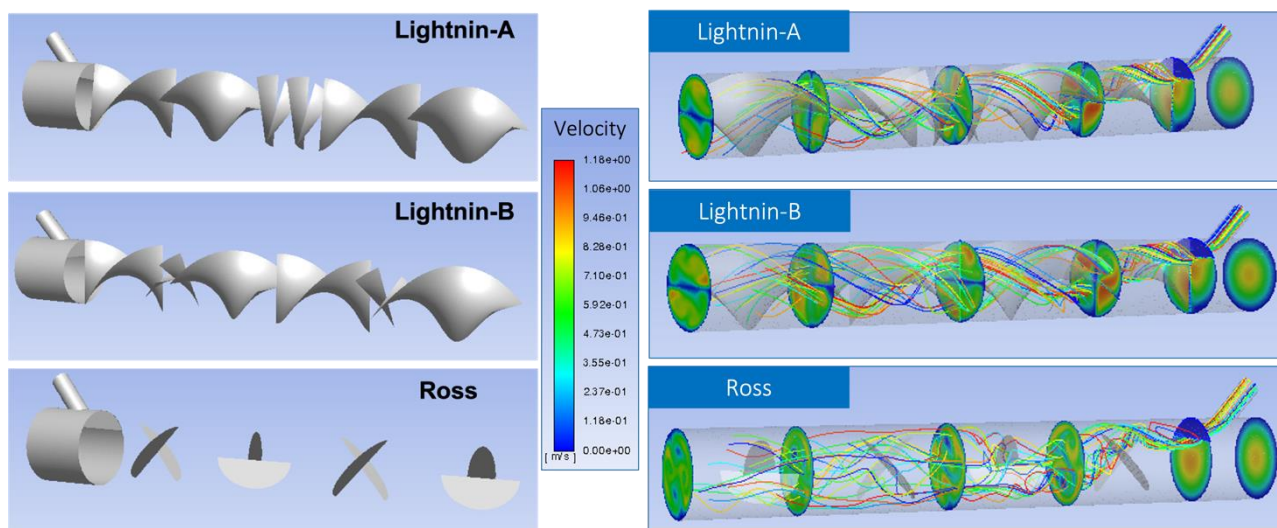


Figure 3. Assembled geometries; left) layouts built in Fluent; right) corresponding velocity fields.

Only some of the results of the extensive CFD study are here presented. Among others, the activities concerned the analysis of the beneficial effect of an entry bulkhead, and a comprehensive investigation of concentration and velocity fields (Figure 3); however, details are omitted for the sake of brevity. The various results were aggregated and compared by using two suitable performance indices, that is, the mixing degree (δ_m) and the pressure drops (ΔP). Figure 4 summarizes the results at the outlet section of the pipe: values of the mixing

degree normalized over pressure drops, for the different operating conditions and different geometries are here reported.

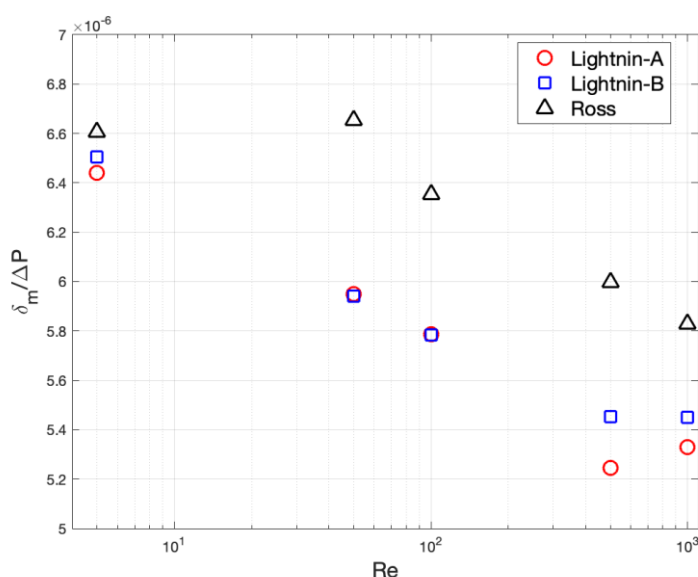


Figure 4. Mixing degree vs. pressure drops for different Reynold numbers and geometries.

The Ross geometry proves to guarantee higher mixing degree than the two Lightnin configurations for all the tested flow regimes, but it also produces higher pressure drops; nevertheless, keeping the ratio $\delta_m / \Delta P$ as the main key performance index, Ross reveals the best geometry for the scopes.

4. Conclusions

An innovative plant to produce in continuous mode a set of specific formulations for the chemical and health sectors to face possible future sanitary pandemics is here presented. Some results of the extensive CFD investigation of a section of pipe equipped with different typologies of static mixers are illustrated. This study aims to help the design of the flow tubular reactor to be hosted in a transportable plant unit. The mixing of the main flow rate of a carrier fluid with the injection of an additive component was studied, in which physical properties are the same for both fluids. Three different configurations of static mixers were tested and compared in terms of mixing degree and pressure drops. The Ross proves to outperform the two Lightnin configurations for all the tested flow regimes. As future developments, the mixing of real fluids with actual physical properties is to be considered to obtain more reliable indications for the plant run. In addition, different operating conditions will be tested to derive performance correlations to be used for the definition of a practical 1D model to be used as a digital twin of the real process.

References

- [1] M. Galimberti. SCI: la chimica ai tempi del Covid. Sfide e risposte, year V, n. 2, Online (March/April 2021).
- [2] D. Sengupta, P. Yelvington. Advanced manufacturing progress: Modular, intensified processes promote resilient manufacturing, online (June 2020). <https://www.aiche.org/resources/publications/cep/2020/june/advanced-manufacturing-progress-modular-intensified-processes-promote-resilient-manufacturing>.
- [3] A. Stankiewicz, T. Van Gerven, G. Stefanidis. The Fundamentals of Process Intensification, John Wiley & Sons, 2019.
- [4] R. Gani, et al. A multi-layered view of chemical and biochemical engineering, Chemical Engineering Research and Design 155 (2020) A133–A145.
- [5] G. Forte, F. Alberini, E. Brunazzi. Effect of residence time and energy dissipation on drop size distribution for the dispersion of oil in water using KMS and SMX+ static mixer, Chemical Engineering Research and Design 148 (2019) 417–428.

- [6] G. Forte, A. Albano, M.J.H. Simmons, H.E., Stitt, E. Brunazzi, F. Alberini. Assessing Blending of Non-Newtonian Fluids in Static Mixers by Planar Laser-Induced Fluorescence and Electrical Resistance Tomography, *Chemical Engineering and Technology* 42-8 (2019) 1602–1610.

Engineered small-diameter vascular prostheses: a study in bioreactor

Pier Francesco Ferrari^{1*}, Giulia De Negri Atanasio¹, Jan Oscar Pralits¹, Domenico Palombo²,
 Patrizia Perego¹

¹ Department of Civil, Chemical and Environmental Engineering, University of Genoa, via Opera Pia, 15, Genoa, Italy

² Department of Surgical and Integrated Diagnostic Sciences, University of Genoa, viale Benedetto XV, 6, Genoa, Italy

*Corresponding author: pier.francesco.ferrari@unige.it

1. Introduction

Cardiovascular diseases represent the global leading chronic-degenerative pathologies due to their high morbidity and mortality with a heavy impact on National Health Systems [1]. Among them, occlusive peripheral arterial diseases are caused by the accumulation of fatty material within the arterial wall, generating alterations of the blood circulation in downstream tissues as the main effect [2]. To overcome this problem, vascular bypass or stent are needed [3]. Synthetic vascular prostheses are not considered as a good choice for restoring the blood circulation in the case of vascular constructs with a diameter lower than 6.0 mm because of possible thrombotic events, intimal hyperplasia, calcification, inflammatory response, and arising of infections starting from the prosthesis itself. Different strategies, *i.e.*, electrospinning, 3D printing, freeze-drying, and decellularization of tissues and organs have been investigated in order to fabricate vascular constructs able to perform well even with a small-diameter. [4]. In this work, electrospun vascular prostheses, made of a polymeric blend, were obtained by electrospinning and they were engineered by incorporating quercetin, as a modulator of inflammation, and gelatin, as a coating protein. To predict the *in vivo* behavior of these engineered electrospun polymeric scaffolds, studies in an *ad hoc* bioreactor were performed. In details, it was studied the morphology of the vascular constructs, the influence of the testing conditions (pressure, residence time, *etc.*) on the release of quercetin and gelatin from the scaffolds, their physico-chemical properties (fluid uptake, degradation over time, *etc.*), their mechanical characteristics, and their bio- and hemocompatibility.

2. Methods

The studied vascular scaffolds were produced by electrospinning as reported by Ferrari et al., 2017 [5] using poly (ϵ -caprolactone) (PCL) and poly (glycerol sebacate) (PGS) in the presence of quercetin (Q) (0.05 %, w/v) and then they were coated with a thin layer of gelatin (G) at 37°C in order to reduce their porosity. These vascular grafts were tested in a bioreactor made up of a peristaltic pump, a flow chamber, pressure transducers, and a reservoir. A Newtonian fluid flowed in the bioreactor at different working pressures.

3. Results and discussion

In scanning electron micrographs, it was possible to notice that the fabricated scaffolds presented a randomized, bead-free microfibrinous structure (Figure 1).

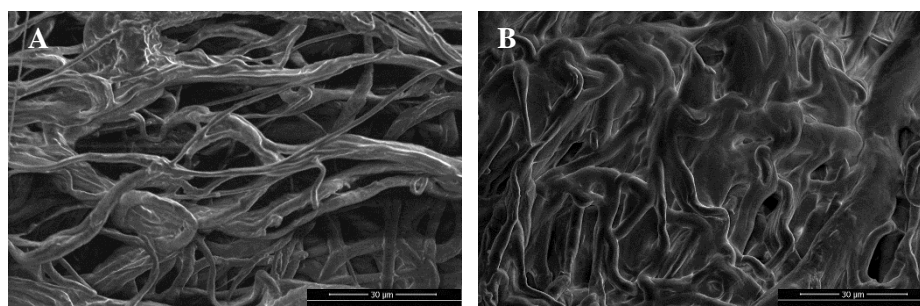


Figure 1. Representative scanning electron micrographs of (A) PCL:PGS scaffold and (B) PCL:PGS scaffold engineered with quercetin and coated with gelatin.

The addition of quercetin and the gelatin coating did not alter the mean diameter of the fibers (Table 1).

	PCL:PGS	PCL:PGS with Q and G
Fiber diameter (μm)	4.36 ± 1.37	4.03 ± 0.51

Table 1. Fiber diameter of electrospun polymeric vascular constructs.

The amount of released quercetin was able to modulate the post-implantation inflammatory response and the release of gelatin was sufficient to prevent blood leakage during the prosthesis implantation (Figure 2).

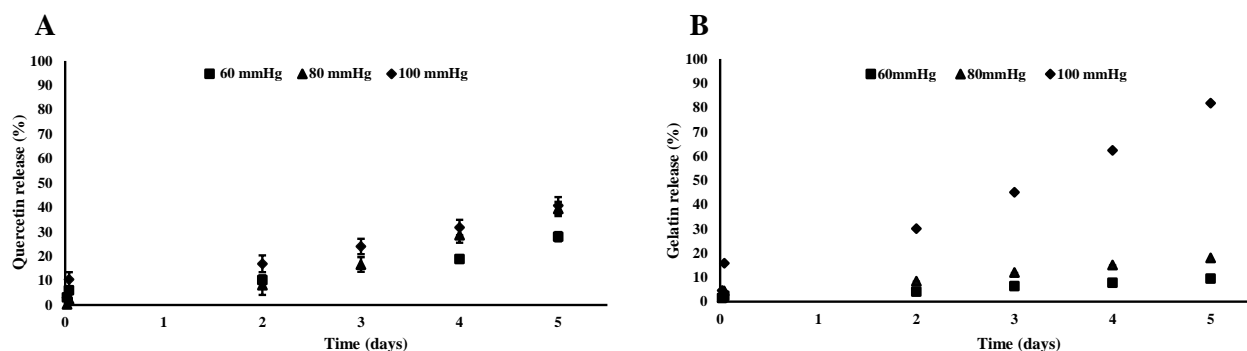


Figure 2. (A) Quercetin and (B) gelatin release from scaffolds at different working pressures.

The mechanical behavior, in terms of Young's modulus, tensile strength, and elongation percentage, was similar to that possessed by native human arteries (Figure 3).

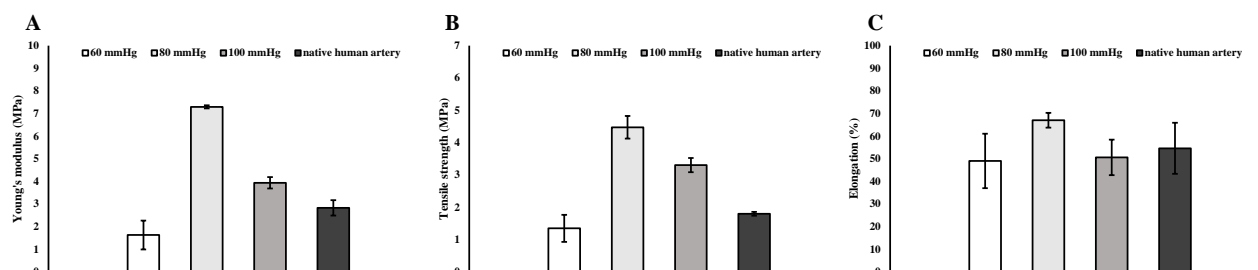


Figure 3. (A) Young's modulus, (B) tensile strength, and (C) elongation percentage of scaffolds after being tested at different working pressures.

4. Conclusions

The importance of testing engineered electrospun grafts in an *ad hoc* bioreactor at different working pressures was fundamental to develop mathematical models able to predict the *in vivo* behavior of the scaffolds. Considering all the obtained results, this engineered vascular prosthesis could become a promising tool for the next generation vascular tissue engineering.

References

- [1] M. Amini, F. Zayeri, M. Salehi, BMC Public Health 21 (2021) 1–12.
- [2] E.E. Bezsonov, I.A. Sobenin, A.N. Orekhov, Int. J. Mol. Sci. 22 (2021) 1–6.
- [3] Z. Wang, L. Liu, S.M. Mithieux, A.S. Weiss, Trends Biotechnol. 39 (2021) 505–518.
- [4] B.B.J. Leal, N. Wakabayashi, K. Oyama, H. Kamiya, D.I. Braghioroli, P. Pranke, Front. Cardiovasc. Med. 7 (2021) 1–18.
- [5] P.F. Ferrari, B. Aliakbarian, A. Lagazzo, A. Tamayol, D. Palombo, P. Peregó, Int. J. Polym. Mater. 66 (2017) 635–643.

Use of hydrofluorocarbon solvent for the recovery of lipid and aqueous extracts from olive pomace.

Rosa Colucci Cante^{1,2}, Isidoro Garella³, Alessandro Nigro³, Elisabetta Iannone¹, Marianna Gallo^{1,2} and Roberto Nigro^{1,*}

1 Department of Chemical Engineering, Materials, and Industrial Production, University of Naples Federico II, P. Tecchio 80, Napoli-Italy; 2 Department of Industrial Engineering, University of Niccolò Cusano, Via Don Carlo Gnocchi 3, Rome, Italy; 3 I. T. P. Innovation and Technology Provider S.r.l., Via Bisignano a Chiaia, 68, Napoli, Italy.

**Corresponding author: rnigro@unina.it*

1. Introduction

Re-use and valorisation of waste materials through low environmental impact recovery processes represent the fundamental principles on which the concepts of circular economy and sustainability are based.

For this reason, in recent years, recovery and transformation of agro-industrial wastes have been gaining more and more interest among the scientific community, industries, and the public opinion.

Olive pomace is the most abundant by-product generated during olive oil production process, consisting of olive pulp fragments, stones, and skins. It has an oil content of 8–12% w/w and a variable moisture content depending on the oil extraction system applied [1]. Since treatment and disposal of these huge volumes of solid and liquid wastes represent a very critical problem for the environment due to their high content of organic matter [2,3], residual oil can be recovered and used for consumption after refining.

Moreover, olive pomace contains other valuable bioactive compounds with health promoting benefits, such as phenolic compounds (phenolic acids and alcohols, lignans, and flavones) with antiviral, antimicrobial, antioxidant, anti-inflammatory, and anti-carcinogenic properties [4,5]. Conventional extraction processes currently applied to recover olive pomace oil involve the use of large amounts of organic solvents, such as hexane, long extraction times, and additional costs related to a preventive drying treatment of the matrix, solvent/extract separation processes, and disposal of solvent residues and exhausted solid.

The aim of this work was to propose an innovative extraction technique using hydrofluorocarbon Norflurane (1,1,1,2-tetrafluoroethane) in subcritical conditions as solvent, to recover oil from olive pomace.

Norflurane potential as extracting solvent for wasted materials was already tested in previous works [6-8].

The extraction yields reached using Norflurane were compared with those obtained by other extraction technologies, traditionally used, or recently studied. Furthermore, both dried and wet pomace was processed with this novel extraction system, confirming the possibility of recovering simultaneously both oil and vegetation water, rich in antioxidant compounds with high added value and beneficial effects on human health.

2. Methods

The initial moisture content of raw pomace was determined by drying the sample for 24 h at 105 °C, and a mean value of 57.4 % ($\text{g water/g pomace} \times 100$) was found. Soxhlet extraction was carried out for 6 h on 10 g olive pomace, preliminary dried in oven at 60 °C up to a final moisture content of 2% on wet basis.

The resulting oil content of 10.7 % ($\text{g oil/g dry solid} \times 100$) was used as reference for evaluating the extraction yields obtained using Norflurane.

Extraction tests were performed through a laboratory scale apparatus via a patented process [9] in which liquid Norflurane was percolated through the solid, placed in an extraction reactor (8–10 bar).

The oil-enriched solvent was then fed into an expansion vessel where it was gasified at a lower pressure (4–5 bar) and the oily extract was released at the bottom. Regenerated gaseous Norflurane was then recompressed and recycled in liquid form to the extraction chamber to restart the extraction cycle.

Extraction experiments were carried out on:

1. dried olive pomace, for 180 min of process and a solvent flow rate of 100 mL/min.

- raw olive pomace, without preventive drying treatments, for 440 min of process and a solvent flow rate of 100 mL/min.

Extract samples were collected at specific times during the process and the corresponding kinetic curves were determined.

Total polyphenol (TP) and flavonoid (TF) contents in the aqueous fraction recovered from wet pomace were determined using Folin-Ciocalteu reagent assay [10] and aluminium chloride colorimetric method [11], respectively. TP and FC were expressed as milligrams of gallic acid and quercetin equivalents (GAE and QE), respectively, as gallic acid and quercetin were used as reference standards. Moreover, antioxidant activity was determined using the ferric reducing/antioxidant power (FRAP) assay [10] and was expressed as both millimoles of Fe^{2+} produced and millimoles of Trolox equivalents (TE) per millilitres of water.

3. Results and discussion

Extraction on dried matrix led to a final yield (η) of 95.1% after 3 h of process.

As shown in Figure 1, an approximately constant extraction rate was observed at the beginning of the process; then, it started to decrease after 90 min of process, due to the gradual decreasing of available oil in the matrix. Chanioti and Tzia [1] reported an extraction efficiency of 73% after 10 min of process using hexane at 60 °C, while Norflurane system provided the same yield value in 1 h of process.

However, milder operating conditions, lower toxicity and environmental impact, and lower additional costs associated to the subsequent separation and purification phases, make the novel system a valid alternative to traditional technologies. Moreover, ultrasound assisted extraction technique studied by Chanioti and Tzia [12] provided pomace oil yields (88.93 % in 1 h, at 60 °C) comparable with those reached using Norflurane in the same process time.

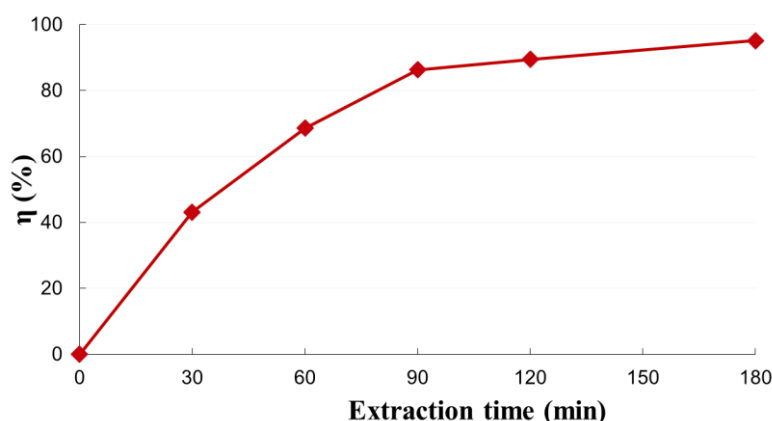


Figure 1. Extraction kinetic curve evaluated for oil extracted from dried olive pomace, using Norflurane system.

When extraction trials were performed on wet pomace, final extraction yields of 35 % and 88.6 % for oil and water, respectively, were reached after 440 min of process.

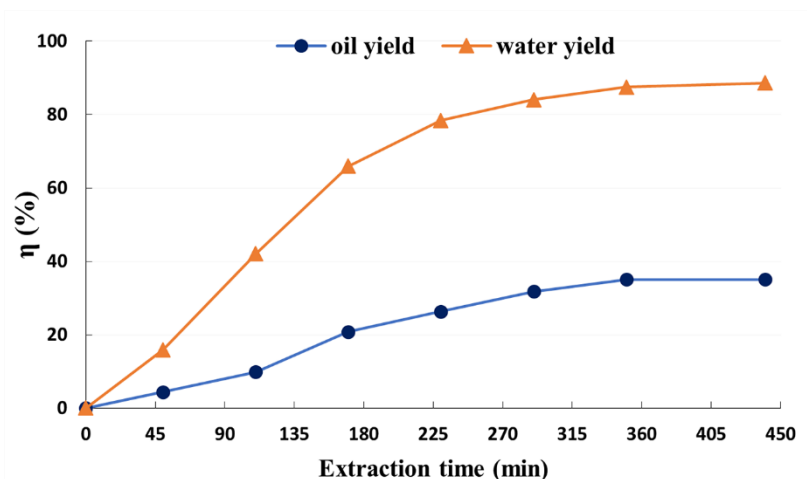


Figure 2. Extraction kinetic curve evaluated for oil and water extracted from wet olive pomace, using Norflurane system.

As shown in Figure 2, Norflurane solvent showed a higher selectivity towards water and a lower recovery of oil from the wet matrix was observed than that found with dried pomace. Probably, water competed with oil for solubilization in Norflurane and/or interfered with the oil diffusion of oil into the solid structure [7]. Total polyphenol and flavonoid contents equal to 0.214 mg GAE/mL and 4.56×10^{-3} mg QE/mL, respectively, were determined in the aqueous fraction, simultaneously extracted with oil during the process. In particular, the polyphenol concentration found in the extracted water was comparable with the values shown by Chanioti and Tzia [1], which reported a phenolic amount of approximately $13 \div 30$ mgGAE/g _{dry pomace} using different extraction techniques. Moreover, the antioxidant activity of Norflurane aqueous extracts was calculated as 0.0015 mmol (Fe²⁺)/mL, corresponding to 0.21 mg (TE)/mL. This suggested a much better antioxidant power than that reported by Böhmer-Maas et al. [13], where lower values of Trolox equivalents were reported for aqueous pomace extracts ($10 \div 20$ mg (TE)/mL).

4. Conclusions

The work was aimed at proposing a novel patented extraction method using hydrofluorocarbon Norflurane, as solvent, as alternative to traditional extraction techniques currently used for olive pomace oil recovery. Milder operating conditions, lower environmental impact, absence of expensive safety measures owing to the toxicity and flammability of organic solvents, and absence of all the additional costs associated to the subsequent phases of extract/solvent separation, purification, and disposal of the exhausted materials, represent the real strength of this technology.

Moreover, the process allowed to treat also wet matrices, without preventive drying, ensuring, essentially, the recovery of the water fraction rich in antioxidant compounds, such as polyphenols. Furthermore, as future purpose, the present results will be integrated with a technical-economic analysis of the traditional process compared to that evaluated for the innovative process using Norflurane, to verify the effective economic convenience of the proposed process.

References

- [1] S. Chanioti, C. Tzia, *J. Am. Oil Chem. Soc.* 95 (2018) 371-382.
- [2] S. Khoufi, M. Hamza, S. Sayadi, *Bioresour. Technol.* 102 (2011) 9050–9058.
- [3] E. Tsagaraki, H. Lazarides, *Food Bioproc. Tech.* 5 (2012) 584–592.
- [4] S. Chanioti, P. Siamandoura, C. Tzia, *Waste Biomass Valorisation*, 7 (2016) 831–842.
- [5] J. Fernandez-Bolanos, G. Rodríguez, R. Rodríguez Arcos, R. Guillen, A. Jiménez, *Grasas y Aceites*, 57 (2006) 95-106.

- [6] R. Colucci Cante, I. Prisco, I. Garella, M. Gallo, R. Nigro, *Chem. Eng. Res. Des.* 157 (2020) 174–181.
- [7] R. Colucci Cante, I. Garella, M. Gallo, R. Nigro, *Chem. Eng. Res. Des.* 165 (2021) 172–179.
- [8] R. Colucci Cante, M. Gallo, L. Varriale, I. Garella, R. Nigro, *Appl. Sci.* 12 (2022) 2822.
- [9] I. Garella, Patent n.0001396896, issued by C.C.I.A.A. 2012
- [10] P. E., Aikpokpodion, L.N., Dongo, *Int. J. Sustain. Agric. Res.* 5 (2010) 66-70.
- [11] H. F. Ismail, Z. Hashim, W.T., Soon, N.S.A., Rahman, A.N., Zainudin, F.A.A., Majid, (2017). *J. Tradit. Complement. Med.* 7 (2017) 452-465.
- [12] S. Chanioti, C. Tzia, *LWT-Food Sci. Technol.* 79 (2017) 178-179.
- [13] B. W. Böhmer-Maas, D. Murowaniecki, O. Rui, C. Zambiasi, B. C. Aranha, *Rev. Ceres* 67 (2020) 181-190

Injectable polymer-nanoparticle hydrogel with pH and thermo-responsive drug release

Elisa Lacroce^{1*}, Filippo Rossi¹

¹ Department of Chemistry, Materials and Chemical Engineering "Giulio Natta", Politecnico di Milano, via Mancinelli 7, 20131, Milan, Italy

*Elisa Lacroce E-Mail: elisa.lacroce@polimi.it

1. Introduction

Injectable polymer-nanoparticle hydrogels are promising tools in the field of cell and drug delivery. One of the principal advantages of the use of hydrogel for drug release is the possibility of being injected in a specific site of the body allowing a localized drug release, limiting the adverse effects related to its circulation in healthy tissues. In addition, the presence of polymeric nanoparticles inside the hydrogel improves the mechanical properties of the gel and guarantees the presence of hydrophobic and hydrophilic regions able to release drugs with different hydrophilicity and dimensions.

2. Methods

In this work we synthesized an injectable pH and thermo-responsive polymer-nanoparticle hydrogel following the procedure reported in literature by Eric A. Appel et al. [1] for the synthesis of HPMC-C₁₂ hydrogel and Chun-Liang Lo et al. [2] for the synthesis of poly(D,L-lactide)-g-poly(N-isopropylacrylamide-co-methacrylic acid) nanoparticles. In particular, a radical co-polymerization of monomers and a subsequent dialysis of the product were performed in order to obtain the polymeric nanoparticles. The release of a mimetic drug from nanoparticles was studied in acidic environment (pH=5) at different temperatures. Finally, the polymer-nanoparticle hydrogel was developed by mixing the functionalized HPMC-C₁₂ solution with the nanoparticle solution.

3. Results and discussion

The nanoparticles have pH and thermo-responsive behaviour due to the presence of PNIPAM, a thermo-responsive polymer, and methacrylic acid, sensible to pH changes. The presence of a temperature over 37°C and a pH 5 environment causes the collapse of the outer shell leading to structural changes of the core with the subsequent release of therapeutic drug encapsulated inside the nanoparticles. Results of the drug release at pH=5 from the PLA-g-P(NIPAm-co-MAA) nanoparticles showed a cumulative drug release of 60% at 42°C instead of 14% at 37°C after 96 hours. The formation of polymer-nanoparticle hydrogel was performed by mixing the two solutions with a luer lock mechanism and mechanical tests confirmed its injectability.

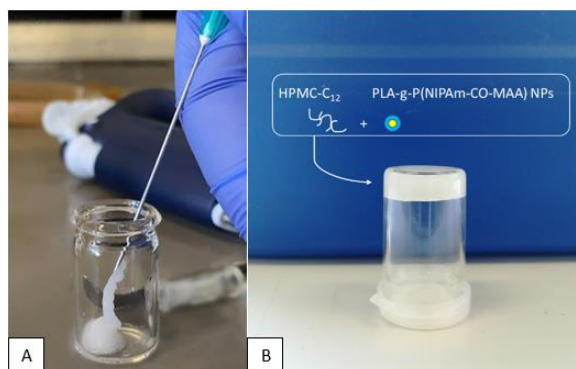


Figure 1. Representations of injectability (A) and schematic structure (B) of the polymer-nanoparticle hydrogel.

4. Conclusions

In this work we combined the injectability of the HPMC hydrogel with the pH and thermo-responsive properties of polymeric nanoparticles to develop a hybrid system for localized, controlled and temperature-dependent drug release.

References

- [1] E. A. Appel, M. W. Tibbitt, M. J. Webber, B. A. Mattix, O. Veiseh, and R. Langer, “ARTICLE Self-assembled hydrogels utilizing polymer-nanoparticle interactions,” *Nat. Commun.*, 2015, doi: 10.1038/ncomms7295.
- [2] C. L. Lo, K. M. Lin, and G. H. Hsiue, “Preparation and characterization of intelligent core-shell nanoparticles based on poly(D,L-lactide)-g-poly(N-isopropyl acrylamide-co-methacrylic acid),” *J. Control. Release*, vol. 104, no. 3, pp. 477–488, Jun. 2005, doi: 10.1016/j.jconrel.2005.03.004.

The production process of an injectable hyaluronic acid gel solution for regenerative medicine using two different crosslinking agents

Øystein Øvrebø^{1,2}, Zoe Giorgi¹, Giuseppe Perale^{3,4,5}, Håvard J. Haugen², Filippo Rossi^{1*}

1 Department of Chemistry, Materials and Chemical Engineering "Giulio Natta", Politecnico di Milano, Milano, Italy;

2 Department of Biomaterials, University of Oslo, Oslo, Norway; 3 Industrie Biomediche Insubri SA, Mezzovico-Vira, Switzerland; 4 Faculty of Biomedical Sciences, University of Southern Switzerland, Lugano, Switzerland; 5 Ludwig Boltzmann Institute for Experimental and Clinical Traumatology, Vienna, Austria

**Corresponding author E-Mail: filippo.rossi@polimi.it*

1. Introduction

Hydrogels are highly attractive biomaterials for regenerative medicine due to their ability to mimic the extracellular matrix and ease of delivery at defect site through needle injection. Particularly hyaluronic acid has received tremendous clinical attention due to its natural presence in the body, intrinsic ability to interact with cells, and readily ability to be chemically modified. This has given hyaluronic acid diverse application in medicine, and it has already been applied in orthopedics, dental, aesthetics, wound healing, and ophthalmology application, among others. An obstacle for hyaluronic acid has been the rapid clearance limiting the longevity of the therapy. As a response, an attractive strategy has been to chemically crosslink the hyaluronic acid to prevent rapid degradation and clearance. In this work we present a simple process for creating a crosslinked hyaluronic acid gel using two different crosslinking agents, BDDE and PEGDE, and making it injectable through a granulation process. The two different gels (HA-BDDE and HA-PEGDE) were compared using rheology characterization.

2. Methods

10 wt.% hyaluronic acid (HA, 1.5-1.8 MDa) was dissolved in 0.3N sodium hydroxide, before either 1.6 vol.% 1,4-Butanediol diglycidyl ether (BDDE) or 4 vol.% Poly(ethylene glycol) diglycidyl ether (PEGDE, 500 Da) was added to the solution. This gave a similar molar equivalence between the HA and the crosslinker for both gels. The solution was incubated for 5 hours at 40 °C to allow crosslinking. Thereafter the pH was neutralized by the addition of 0.25N hydrochloric acid in PBS, and the solution was dialyzed for 24 hours in distilled water to remove unreacted BDDE/PEGDE. To allow injectability, the crosslinked gel was granulated by extruding it through a steel mesh with 250 µm pores. The granulated gel was investigated in oscillatory rheology using an Anton Paar MCR501-machine, conducting shear strain amplitude sweeps between 0.01 and 100 % at a 10 rad/s frequency, and frequency sweep between 0.1-100 rad/s at an amplitude of 0.0347% shear strain. The temperature was controlled to 25 °C in all trials.

3. Results and discussion

Hyaluronic acid gels were created by crosslinking with either BDDE or PEGDE in a simple production process as presented in **Figure 1A**. The reaction was conducted under an alkaline environment at elevated temperature, leading to successful crosslinking of the hyaluronic acid, yielding a transparent hydrogel. An important factor for achieving crosslinking was to use 10 wt.% hyaluronic acid, as our trials with lower concentration failed. The pH of the gel was neutralized by addition of hydrochloric acid in PBS buffer. The alkaline environment is important for inducing the crosslinking; however, it also accelerates hydrolysis of the hyaluronic acid [1]. This gives a trade-off in the timing of the neutralization step to allow adequate time for crosslinking while limiting the degradation of the hyaluronic acid. Thereafter the gel was dialysed for 24 hours to remove unreacted crosslinking-agent. It has previously been demonstrated that high concentration of residual BDDE and PEGDE can cause cytotoxicity [2]. To go from a solid gel to a readily injectable gel, the gel was granulated by extruding

it through a mesh of 250 μm pores. The output was then characterized using rheology. From the rheology it can be observed that at a low shear strain both gels have a higher G'' than G' , suggesting they behave like gel. This is supported by that both gels behave linearly elastic across a wide frequency range at a low strain. Of the two, the HA-PEGDE has a higher modulus, however when the shear strain increases it, the HA-PEGDE gel reaches the crossover point earlier than the HA-BDDE gel. This can suggest that HA-PEGDE gel has a higher degree of crosslinking, thus fewer non-crosslinked hydroxyl groups to form intermolecular hydrogen bonds keeping the granules together.

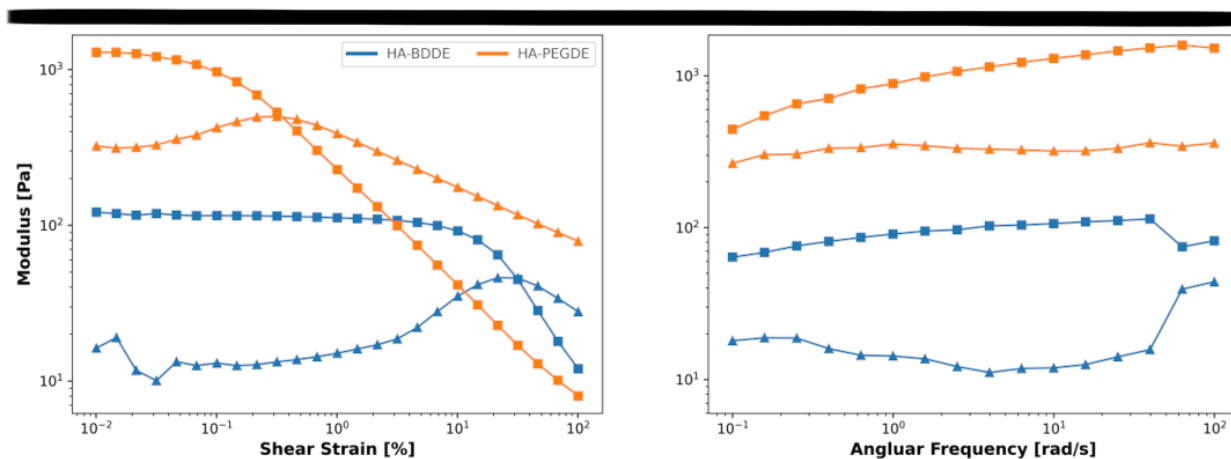
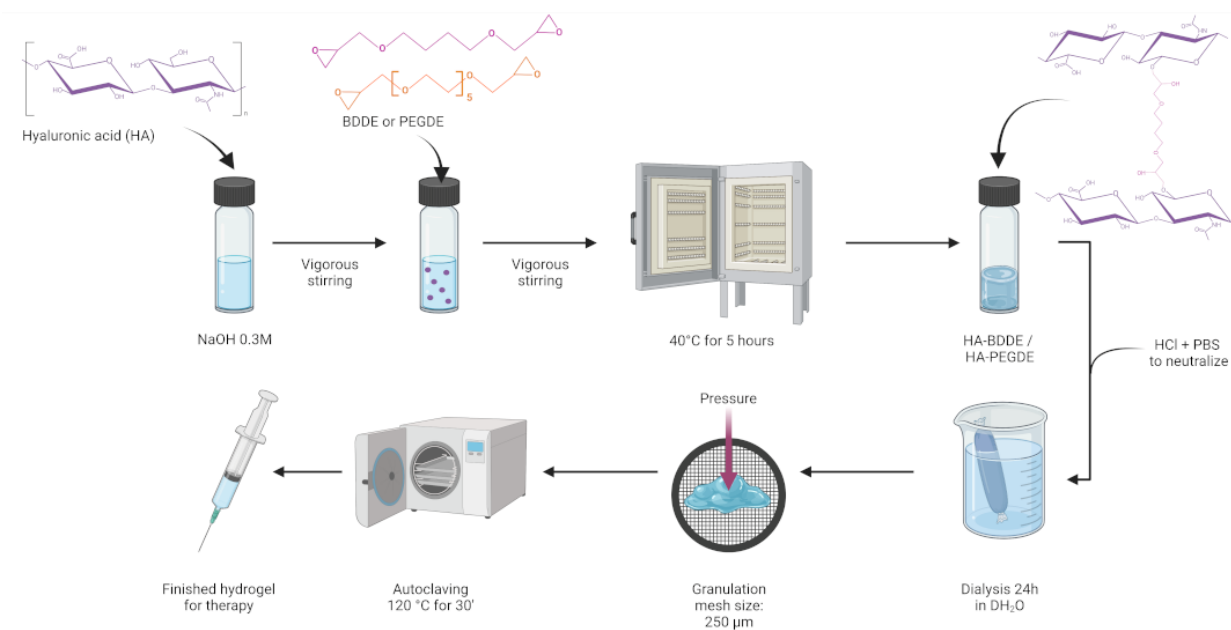


Figure 1. Top panel: Schematic illustration of hyaluronic acid gel production process (Created in Biorender). Bottom panel: Rheological properties for HA-BDDE (blue) and HA-PEGDE (orange) during shear amplitude (left) and angular frequency sweep (right). Squares (■) represents storage modulus, G' , and triangles (▲) represents loss modulus, G'' .

The current results are promising for creating an injectable hyaluronic acid gel for regenerative medicine. The last step which needs to be optimized is the sterilization of the gel, where autoclaving is a typically used method. If the sterilization can be conducted without compromising the properties of the gel, we have developed a successful method to produce a hyaluronic acid gel that can be utilized clinically. The method allows rapid crosslinking, and its simplicity allows readily scalability to an industrial size production while keeping the production costs low.

4. Conclusions

We have developed and presented a simple and scalable method for creating an injectable hyaluronic acid gel crosslinked with BDDE or PEGDE. The straightforward chemistry allows for readily industrial scaling, and we present methods for preventing excessive hydrolysis of the hyaluronic acid and removal of unreacted crosslinking agent. To make the solution injectable we suggest granulating the gel through extrusion through a mesh. The rheology analysis suggests that both HA-BDDE and HA-PEGDE behave gel like at a low shear strain. However, HA-PEGDE has a crossover point at a lower shear rate and a higher storage and loss modulus. Hence a lower degree of crosslinking can be used to open more hydroxyl groups for intermolecular bonding. After appropriate sterilization, this gel is ready for clinical translation for use in regenerative medicine.

References

- [1] B.A.G. de Melo, M.H.A. Santana, Structural Modifications and Solution Behavior of Hyaluronic Acid Degraded with High PH and Temperature, *Appl. Biochem. Biotechnol.* 189(2) (2019) 424-436.
- [2] C.H. Jeong, J.H. Yune, H.C. Kwon, D.-M. Shin, H. Sohn, K.H. Lee, B. Choi, E.S. Kim, J.H. Kang, E.K. Kim, In vitro toxicity assessment of crosslinking agents used in hyaluronic acid dermal filler, *Toxicol. In Vitro* 70 (2021) 105034.

Life Cycle Assessment of an innovative Thermochemical Water-Splitting Cycle for the production of *Green Hydrogen*

Maria Beatrice Falasconi¹, Alice Bertino^{1*}, Alberto Giaconia², Vincenzo Piemonte¹

1 Departmental faculty of engineering, Chemical-Physics Fundamentals in Chemical Engineering research unit, Campus Bio-Medico University, Via Alvaro del Portillo 21, 00128, Rome, Italy;

2 Department for Sustainability, ENEA, Casaccia Research Center, Via Anguillarese 301, 00123, S. Maria di Galeria, Rome, Italy;

**Corresponding author E-Mail: alice.bertino@unicampus.it*

*Thermochemical Water-Splitting Cycles (TWSCs) coupled with green energies as sources are the most promising renewable energy methods in terms of sustainability to produce *Hydrogen*, which is becoming one of the main candidates as energy carrier in a future sustainable economy. The greater sustainability of the TWSCs compared to other conventional methods has already been proved for the Cu-Cl cycle, which turned out to have an even lower carbon footprint than electrolysis [1].*

The main purpose of this work is to prove the environmental sustainability of an innovative *Thermochemical Water-Splitting Cycle* called “*MIS*” (*Metal/Iodine/Sulphur*) coupled only with concentrated solar thermal energy through a *Life Cycle Assessment (LCA)* of the entire flow-sheet. The “*MIS*” cycle is a modification of the more conventional “*IS*” (*Iodine/Sulphur*) cycle. The “*MIS*” cycle presents the same advantages as the “*IS*” cycle with respect to electrolysis and direct thermal dissociation and it also potentially has a simpler flow-sheet and higher thermochemical efficiency [2].

OpenLCA will be the tool to quantify and compare the carbon dioxide equivalent emissions and the energy equivalents of the “*MIS*” cycle with respect to the more conventional cycles, such as the IS or the Cu-Cl. This work is part of a larger frame which provides the realization of a *complete laboratory pilot* with a productivity of 2 Nm³/h. This realization will result in a complete set up of the cycle at laboratory level, including the design, implementation and coupling of each and all of its individual units, and will serve as the base for future scale-up to a pre-industrial pilot plant.

References

- [1] E. Cetinkaya, I. Dincer, and G. F. Naterer, “Life cycle assessment of various hydrogen production methods,” *Int. J. Hydrogen Energy*, vol. 37, no. 3, pp. 2071–2080, 2012, doi: 10.1016/j.ijhydene.2011.10.064.
- [2] P. P. Proisini, C. Cento, A. Giaconia, G. Caputo, and S. Sau, “A modified sulphur-iodine cycle for efficient solar hydrogen production,” *Int. J. Hydrogen Energy*, vol. 34, no. 3, pp. 1218–1225, 2009, doi: 10.1016/j.ijhydene.2008.11.011.

Simulation and optimization of an innovative Thermochemical Water-Splitting Cycle for the production of *Green Hydrogen*

Alice Bertino¹, Maria Beatrice Falasconi^{1*}, Alberto Giaconia², Vincenzo Piemonte¹

1 Departmental faculty of engineering, Chemical-Physics Fundamentals in Chemical Engineering research unit, Campus Bio-Medico University, Via Alvaro del Portillo 21, 00128, Rome, Italy;

2 Department for Sustainability, ENEA, Casaccia Research Center, Via Anguillarese 301, 00123, S. Maria di Galeria, Rome, Italy;

**Corresponding author E-Mail: maria.falasconi@unicampus.it*

Nowadays the increasing energy demand and greenhouses emissions are becoming more and more relevant problems. *Green Hydrogen*, produced by using water as raw material and renewable energies as sources, is becoming one of the main candidates as energy carrier in a future sustainable economy.

In particular, ENEA studied an innovative *Thermochemical Water-Splitting Cycle* called “*MIS*” (*Metal/Iodine/Sulphur*), which is a modification of the more conventional “*IS*” (*Iodine/Sulphur*) cycle. The “*MIS*” cycle presents the same advantages as the “*IS*” cycle with respect to electrolysis and direct thermal dissociation and it also potentially has a simpler flow-sheet and higher thermochemical efficiency [1].

The main purpose of this work is to prove the actual feasibility of the “*MIS*” cycle through an Aspen simulation of the entire flow-sheet. The Aspen simulation will be the tool to evaluate and even optimize the efficiency of the cycle, comparing the results with the ones of the conventional “*IS*” cycle. This work is part of a larger frame which provides the realization of a *complete laboratory pilot* with a productivity of 2 Nm³/h. This realization will result in a complete set up of the cycle at laboratory level, including the design, implementation and coupling of each and all of its individual units, and will serve as the base for future scale-up to a pre-industrial pilot plant.

References

- [1] P. P. Prosini, C. Cento, A. Giaconia, G. Caputo, and S. Sau, “A modified sulphur-iodine cycle for efficient solar hydrogen production,” *Int. J. Hydrogen Energy*, vol. 34, no. 3, pp. 1218–1225, 2009, doi: 10.1016/j.ijhydene.2008.11.011.

A compendium of behavioral characterizations of biomasses and oxygen carriers in the CLARA (Chemical Looping gAsification foR sustAainable production of biofuels) project

Andrea Di Giuliano^{1*}, Stefania Lucantonio¹, Barbara Malsegna¹, Katia Gallucci¹

1 Department of Industrial and Information Engineering and Economics (DIIIE), University of L'Aquila, Piazzale E. Pontieri 1-loc. Monteluco di Roio, 67100 L'Aquila, Italy

**Corresponding author E-Mail: andrea.digiuliano@univaq.it*

1. Introduction

University of L'Aquila has joined the ongoing Horizon 2020 European research project CLARA (Chemical Looping gAsification foR sustAainable production of biofuels, G.A. n. 817841), which includes 13 partners (universities, companies, research centers) from the European Union [1]. CLARA has investigated the Chemical Looping Gasification (CLG) of lignocellulosic biogenic residues, to obtain a syngas to be in turn converted into liquid fuel by a Fischer-Tropsch catalytic reactor, aiming to realize a complete biomass-to-fuel chain up to the 1 MW_{th} scale in an industrially relevant environment, with the following targets: cold gas efficiency of 82%, carbon conversion of 98%, and level of tar in the outlet syngas lower than 1 mg Sm⁻³ [1–3]. This project fully hinges on the European Green Deal objectives for promoting sustainable development [4].

Within CLARA, the CLG is intended to be performed by two interconnected fluidized bed reactors, holding a granular oxygen carrier (OC) as the internally circulated bed: (i) inside the “fuel reactor”, the biomass pellets are fed and gasified thanks to the lattice oxygen given by the fluidized OC particles; (ii) inside the “air reactor”, the reduced (i.e., exhausted) OC is re-oxidized by combustion and then returned to the fuel reactor, also bringing back part of the heat of combustion [1,5,6]. OCs are typically metal oxides which show some redox properties [7]. In comparison to traditional gasification configuration, CLG brings in the process the required oxygen to sustain endothermal gasification by the OC, avoiding air dilution (due to inert N₂) in the syngas or the usage of an air separation unit to feed pure oxygen into the gasifier [8].

The CLARA consortium selected pine forest residues and wheat straw as lignocellulosic feedstocks to be investigated for the CLG. Cereal straw, in general, is particularly attractive for heat and power generation, as it is largely available and do not compete with the fuel chain [9–12]. Unfortunately, the significant content of inorganic matter in biogenic residues may give place to the formation of ashes with high agglomeration and deposition tendencies, an important technological issue as far as their use in CLG-fluidized beds is concerned [13–15]. In fact, the increase of the average diameter of OC bed particles might substantially change their fluid dynamic properties and thus affect their fluidization quality and effectiveness in the CLG process [16,17]. In this sense, wheat straw is an even more risky feedstock, because of its high potassium, chlorine, and potassium–aluminum–silicates content [3]. In order to improve fluid-dynamic interactions between wheat straw and OCs and avoid the collapse of the fluidization quality, some pretreatments (torrefaction, washing, mixing with additive minerals, or their combination) were studied within CLARA for wheat straw pellets [6].

This manuscript represents a compendium of the experimental work carried out by this research group within CLARA, concerning some preliminary characterizations at laboratory scale of the behaviors of fourteen biomasses and three OCs, at process conditions relevant to CLG. Those behaviors were investigated by two campaigns: (i) devolatilization tests, to highlight the effects on syngas production; (ii) pressure fluctuation tests in heated fluidized beds obtained by mixing ashes from biomass pellets and OCs, to monitor the stability of the bubbling fluidization quality in the presence of potential agglomeration elements. Pieces of that work were already published elsewhere [3,6,8,18,19]; this manuscript provides the chance for an integral undisclosed discussion and more comprehensive conclusions.

2. Methods

2.1 Biomasses

Different kinds of biomass were investigated: raw pine forest residue pellets, raw wheat straw pellets, torrefied wheat straw pellets, torrefied and washed wheat straw pellets, torrefied wheat straw pellets with mineral additives, torrefied and washed wheat straw pellets with mineral additives. Torrefaction was always tried at three temperatures (250°C, 260°C, 270°C). The preparation of those pellets was carried out by National Renewable Energy Centre (CENER, Spain) with the contribution from Forschungszentrum Jülich GmbH (Germany) for the issue of minerals addition, both CLARA partners **Table 1** shows name abbreviations and associated pretreatments of the fourteen biomasses investigated in this compendium. Further details about torrefaction and washing could be found elsewhere [3].

Table 1. Biomasses investigated with the specification of the related pretreatments

Biomass acronym	Biomass features
RPR	Raw Pine Residue pellets
WSP	Wheat Straw Pellet (raw)
WSP-T1	Wheat Straw Pellet-Torrefied at T1=250°C
WSP-T2	Wheat Straw Pellet-Torrefied at T2=260°C
WSP-T3	Wheat Straw Pellet-Torrefied at T3=270°C
WSP-T1W	Wheat Straw Pellet-Torrefied at T1 and Washed
WSP-T2W	Wheat Straw Pellet-Torrefied at T2 and Washed
WSP-T3W	Wheat Straw Pellet-Torrefied at T3 and Washed
WSP-T1add	Wheat Straw Pellet-Torrefied at T1, with mineral additives
WSP-T2add	Wheat Straw Pellet-Torrefied at T2, with mineral additives
WSP-T3add	Wheat Straw Pellet-Torrefied at T3, with mineral additives
WSP-T1Wadd	Wheat Straw Pellet-Torrefied at T1 and Washed, with mineral additives
WSP-T2Wadd	Wheat Straw Pellet-Torrefied at T2 and Washed, with mineral additives
WSP-T3Wadd	Wheat Straw Pellet-Torrefied at T3 and Washed, with mineral additives

2.2 Oxygen carriers

Three OCs were investigated: ilmenite (ILM), a natural iron and titanium mineral [19,20]; calcined "Sibelco" (SIB), an iron and manganese ore [19]; Linz-Donawitz-slag (LD), a steelmaking waste material mainly composed of iron-manganese and calcium oxides [19,21,22]. These three OCs were provided by Chalmers University of Technology (Göteborg, Sweden), a CLARA partner. As previously verified [3], the provided samples of ILM, SIB and LD all belong to the generalized Geldart B group [16] at all tested conditions in this work (see Sections 2.3 and 2.4), i.e., their minimum fluidization velocity and minimum bubbling velocity coincide.

2.3 Devolatilization tests

Devolatilization tests were performed in a quartz fluidized bed reactor, at 700 °C, 800 °C, and 900 °C, loaded with a bed made up of one of the three OCs or sand (used as an inert non-redox bed material). N₂ was the fluidizing gas (1.5 times the minimum fluidization velocity u_{mf} of the tested bed at the chosen temperature). The devolatilized syngas, which left the bed with the N₂ carrier, was cooled, dried, and its volumetric concentrations of H₂, CO, CO₂, CH₄, and hydrocarbons (expressed as equivalent C₃H₈) were measured. Pellets of all biomasses in **Table 1** were devolatilized individually (i.e., the following pellet was fed into the reactor only when the devolatilization of the previous ended), so the process intrinsically resulted at unsteady state [8].

For each devolatilization, instantaneous flow rates of syngas components ($F_{i,out}$, with $i = \text{H}_2, \text{CO}, \text{CO}_2, \text{CH}_4$, equivalent C₃H₈) were calculated as functions of devolatilization time (t), by the insertion of experimental measurements in moles balances with the hypothesis of N₂ as the internal standard. In order to uniformly evaluate the devolatilization performances of each pellet, three integral-average parameters were obtained: gas yield (η^{av} , Equation (1)); H₂/CO molar ratio (λ^{av} , Equation (2)); carbon conversion into syngas components (χ^c , Equation (3)).

$$\eta^{av} = \frac{\sum_i \int F_{i,out} dt}{m_p} \quad (1)$$

with $i = H_2, CO, CO_2, CH_4$ and $C_3H_{8,eq}$; m_p = mass of pellet (g)

$$\lambda^{av} = \frac{\int F_{H_2,out} dt}{\int F_{CO,out} dt} \quad (2)$$

$$\chi_c^{av} = \frac{12 (g \text{ mol}^{-1}) \cdot \sum_j [n_j \cdot \int F_{j,out} dt]}{m_p \cdot \left(1 - \frac{\%moisture_{ar}}{100}\right) \cdot \left(1 - \frac{\%ash_{db}}{100}\right) \cdot \left(\frac{\%C_{daf}}{100}\right)} \cdot 100 \quad (3)$$

with:

$j = CO, CO_2, CH_4$ and $C_3H_{8,eq}$.

m_p = mass of biomass pellet (g)

n_j = number of carbons atoms in j

$\%moisture_{ar}$ = moisture content as wt% in as received (ar) biomass

$\%ash_{db}$ = ash content as wt% in biomass on dry basis (db)

$\%C_{daf}$ = elemental carbon as wt% in biomass on dry ash free basis (daf)

For each set "biomass/bed material/devolatilization temperature", three replications were performed, and the corresponding arithmetic means were analyzed in this manuscript.

For further details about the experimental apparatus, procedures, data calculations, please consider the other papers from this research group [8,19].

2.4 Study of pressure fluctuations in OC/ash mixed beds

Solid beds were obtained by mixing one OC with 10 % vol of an ash purposely produced by muffle combustion of one biomass from **Table 1**. Each of those beds was loaded in a quartz fluidized bed reactor, and the signals of dynamic pressure fluctuation were acquired at the temperature of interest for CLG (raised by 50°C per time from 700 °C to 1000 °C), using N₂ as the fluidizing agent at superficial velocity (u) which equaled 2 and 3 times the minimum fluidization velocity (u_{mf}) of the selected OC. For each set " u /bed temperature/OC/biomass ash", two replications of signal acquisition were performed. Power Spectral Density Functions (PSFD) of those signals were calculated and examined to estimate dominant frequencies; those dominant frequencies and the standard deviations of original signals were studied to assess the fluidization quality of beds, as fully described elsewhere [3].

Some selected OC/ash bed samples were characterized before and after the tests of pressure fluctuation acquisitions. Scanning Electron Microscopy (SEM) coupled with Energy Dispersive X-ray Spectrometry (EDS) for elemental analysis (by GeminiSEM 500 microscope or by SEM PHILIPS XL30CP equipped with an OXFORD ENERGY 250 INCAx-act LN2-free detector) and measurements of average particle diameters (d_p) by laser diffraction (Malvern Mastersizer 2000 analyzer) were performed.

Additional details about experiments and characterization procedures could be found elsewhere [3].

3. Results and discussion

3.1 Devolatilization tests

Figure 1 shows an example of instantaneous flow rates ($F_{i,out}$) of H₂, CO, CO₂, CH₄, other hydrocarbons (equivalent C₃H₈). All bed material/biomass combinations were tested at three temperatures, with three replications per operating condition; therefore, 504 pellet devolatilizations were performed and analyzed (i.e., 504 plots as that in **Figure 1** were obtained and studied). This do not allow a productive case by case discussion, so the related results were summarized by infographics (**Figure 2, Figure 3, Figure 4**).

As far as devolatilization temperature is concerned, some general results could be drawn from these infographics. For all bed materials (sand, ILM, SIB, LD) and biomasses (**Table 1**), the temperature increase from 700°C to 900°C generally made gas yield, carbon conversion and H₂/CO ratio increase (rare exceptions

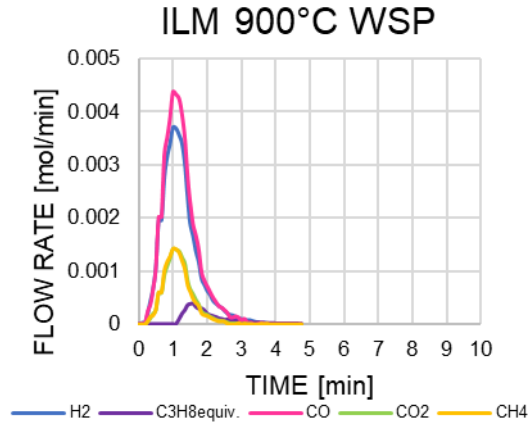


Figure 1. Example of outlet molar flow rates in the dried cooled syngas, obtained by the devolatilization of one pellet (WSP pellet, pyrolyzed in ILM bed at 900°C)

could be led back to this general observation by considering standard deviations reported in **Figure 2**, **Figure 3**, **Figure 4**)

No clear-cut trends were ascribable to the change of OC or kind of biomass; still, some trends emerged:

1. OCs action seems to be exalted by the increase of temperature in terms of gas yield (**Figure 2**) and carbon conversion (**Figure 3**): these quantities for sand and OCs were closer at 700°C (**Figure 2(a)** and **Figure 3(a)**) and 800°C (**Figure 2(b)** and **Figure 3(b)**), while the OCs generally ensured higher values at 900°C (**Figure 2(c)** and **Figure 3(c)**);
2. At 700°C, ILM coupled with some pre-treated biomasses (WSP-T1W, WSP-T1add, WSP-T1Wadd, WSP-T3Wadd) allowed noticeable gas yields (**Figure 2(a)**) and carbon conversions (**Figure 3(a)**); at 900°C the same emerged for LD with WSP, WSP-T3W and WSP-T1Wadd;
3. A higher torrefaction degree increased the chances to develop higher H₂/CO ratios (**Figure 4**);
4. Torrefaction appears as the most influential pre-treatment, having WSP behavior as a reference: carbon conversions of WSP were generally higher than those of pretreated biomasses, which have all undergone torrefaction (**Figure 3**); this was sensibly ascribed to the preliminary separation of volatile matter from wheat straw during the very same torrefaction process, which leaves only more recalcitrant carbon in the biomass pellet;
5. The other pretreatments did not drive to peculiar variations in pellets pyrolysis;
6. With regard to all considered parameters, the pyrolytic performance of the RPR – which is the closest representative of a commercial product – is comparable to that of WSP and pretreated wheat straw pellets.

3.2 Study of pressure fluctuations in OC/ash mixed beds

As occurred for devolatilization tests, the number of combinations “*u*/OC/ash/bed temperature” (each one corresponding to two replicated acquisitions) is too high for a fruitful case by case discussion. Therefore, related results were summarized by infographics (**Figure 5**), to be interpreted in the light of guidelines fully explained by Di Giuliano et al. [3]. In short (**Figure 5**): a green box means that the related pressure fluctuation signal and PSDF represent a bubbling bed; a red box means that the related pressure fluctuation signal and PSDF represented a not-bubbling bed; a yellow box indicates an intermediate situation, with incipient or fading bubbling fluidization; a white box indicates a not acquired signal.

Some general trends were drawn from these infographics (**Figure 5**):

1. There is not a unique ash ensuring the best performance independently on the coupled OC and process conditions; in other words, the fluidization quality in bubbling beds for CLG selected within CLARA depends on both process conditions and the chosen OC/biomass couple;

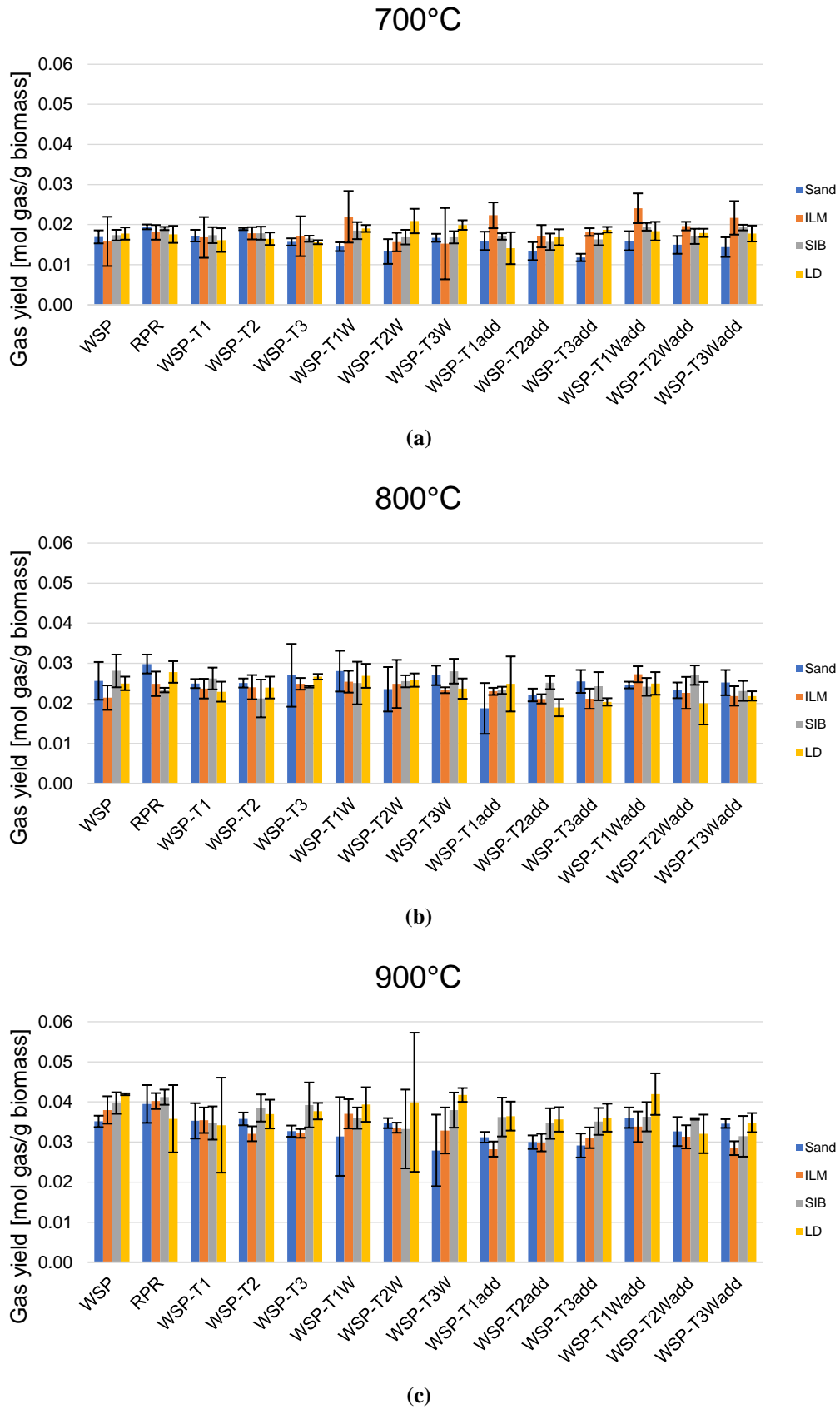


Figure 2. Gas yields from devolatilization tests at 700°C (a), 800°C (b), 900°C (c)

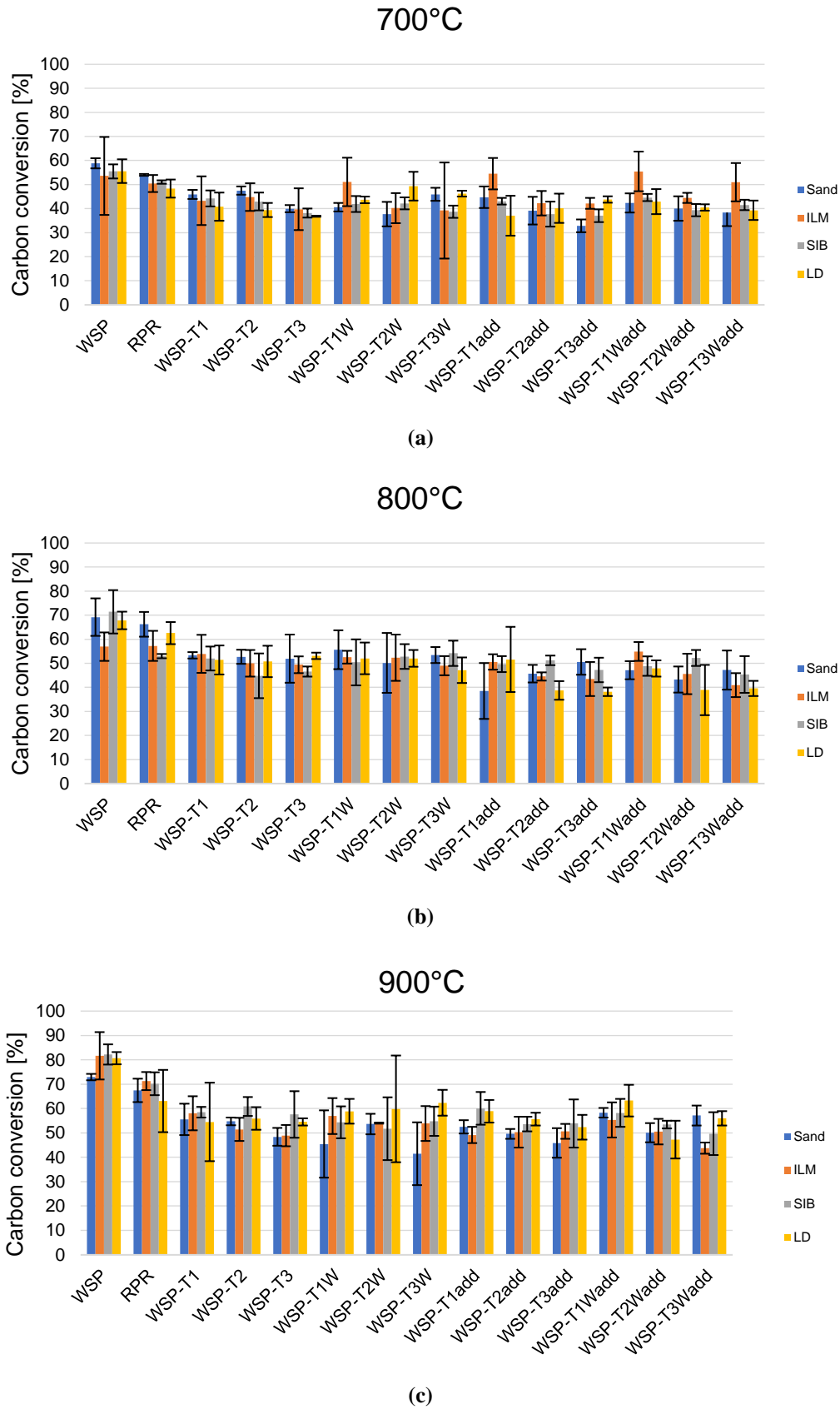


Figure 3. Carbon conversions from devolatilization tests at 700°C (a), 800°C (b), 900°C (c)

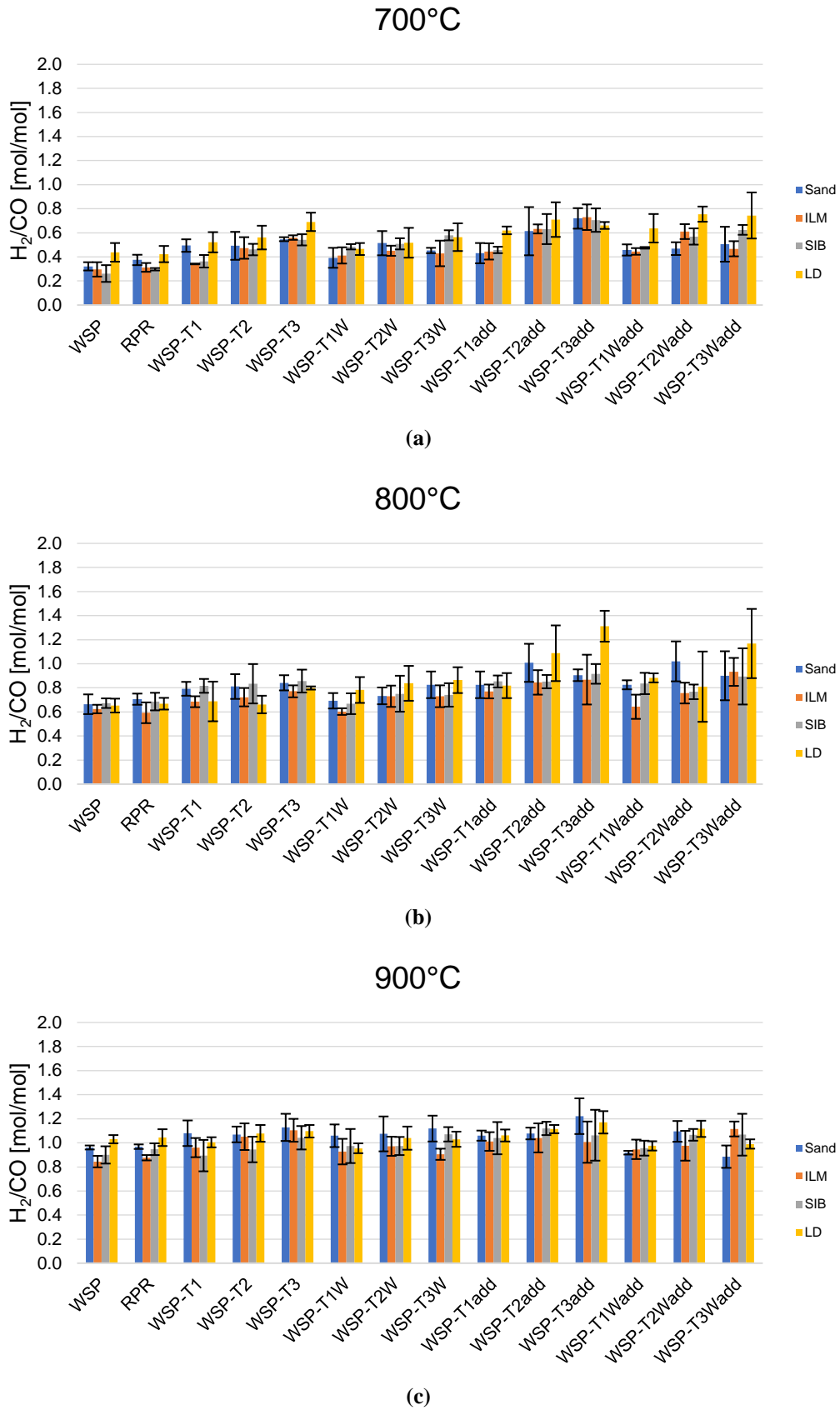


Figure 4. H₂/CO outlet molar ratio from devolatilization tests at 700°C (a), 800°C (b), 900°C (c)

2. LD, independently on the origin of mixed ash, had a worse bubbling fluidization quality than ILM and SIB, at both $2u_{mf}$ and $3u_{mf}$;
3. No clear trends emerged concerning the torrefaction temperature;
4. The increase up to $3u_{mf}$ generally improved the bubbling fluidization quality, with all the three OCs, and in many cases it brought back to the bubbling regime beds without bubbles at $2u_{mf}$.

The treatment of OCs in bubbling fluidized bed with ashes up to 1000°C engendered different types of modifications in bed particles, quantified by average particle diameters (d_p) measured by Malvern Mastersizer 2000. As to ILM and SIB, ashes from WSP caused the highest increase of OCs average diameters in comparison to fresh OCs (+14% for ILM, +25% for SIB), whereas ashes from pretreated wheat straw pellets always produced smaller variations than ashes from WSP, in the ranges from -3% to +13% for ILM, from -8% to +21% for SIB. As to LD, the outcomes were quite different: all after-test samples showed a substantial decrease of d_p , from -8% to -75%, only in one case lower than -25%; torrefied-washed samples seem to partially limit this behavior, while samples with additives enhanced it.

In the first place, the modifications observed by SEM-EDS, after fluidizations at 1000°C with ashes, were ascribable to the intrinsic nature of the OCs, rather than the type of ash joined in the fluidized bed. It is worth to observe a fundamental premise: EDS (**Figure 6**, **Figure 7**, **Figure 8**) determined that all the three OCs contained themselves some of the elements which are usually responsible of agglomeration issues in fluidized beds, generally due to ashes (e.g., Si, K). As to ILM, inferences from SEM-EDS observations revealed a good stability of chemical composition and particle dimensions, together with absence of evident agglomeration (some examples in **Figure 9**). As to SIB, samples at 1000°C systematically presented agglomerations in SEM micrographs, absent at 700°C, independently on the kind of coupled ash (some examples in **Figure 10**); this agglomeration tendency was explained by SEM-EDS, which evidenced an intrinsic chemical instability of Pb traces contained in SIB itself, which acted synergistically with low-melting elements such as Si and K, forming smooth bridges which hold the entire agglomerations together (**Figure 10(d)** and **Figure 10(h)**). In all cases, LD particles did not agglomerate, but fines with diameters lower than 100 µm formed, especially after treatments at 1000°C (some examples in **Figure 11**), jeopardizing the bubbling fluidization quality. This problem may be faced by selecting the most robust LD particles through a preliminary vigorous fluidization.

The results obtained by Malvern Mastersizer 2000 and SEM-EDS are in general good agreement one to each other, as well as with outcomes from pressure fluctuation signals.

4. Conclusions

Devolatilization tests at 700°C, 800°C, 900°C were carried out in fluidized beds made of sand (blank reference) or one of the three investigated OCs. For all the tested biomass/bed material combinations, the temperature increase was the parameter which mainly affected the thermochemical conversion, causing the increase of gas yield, carbon conversion, H₂/CO ratio (relevant for downstream Fischer-Tropsch conversion hypothesized in CLARA). Less clear-cut trends could be ascribed to the different OCs or kind of biomasses. Performance of wheat straw biomasses were comparable to those of the commercial benchmark RPR.

Pressure fluctuation acquisitions were performed in bubbling beds made of OCs and ashes from biomasses, at temperatures from 700°C to 1000°C, accompanied by measurements of particle size distributions and SEM-EDS analyses of pre- and post-test samples. ILM appeared as the most chemically and mechanically stable OC, ensuring reliable fluid-dynamic performances; SIB showed an inherent tendency to agglomeration, due to its content of Si, K and Pb in traces, probably enhanced by ashes; LD particles significantly generated fines during fluidization tests, severely jeopardizing the bubbling fluidization quality (a behavior avoidable with proper preliminary selection of more robust particles, as suggested by other CLARA partners). With regard to the various investigated biomasses, WSP generally behaved worse than RPR concerning bubbling fluidization quality, underlining the need of biomass pre-treatments. Probably, the benefits from washing were partially nullified by the presence of some low melting elements (e.g. Si, K) in fresh OCs themselves. In any case, acceptable

ILM-N ₂ -2U _{mf}	700°C	750°C	800°C	850°C	900°C	950°C	1000°C
WSP-T1	Green	Green	Green	Green	Green	Green	Red
WSP-T2	Green	Green	Green	Green	Green	Green	Red
WSP-T3	Green	Green	Green	Green	Green	Green	Red
WSP-T1W	Green	Green	Green	Green	Green	Green	Red
WSP-T2W	Green	Green	Green	Green	Green	Green	Red
WSP-T3W	Green	Green	Green	Green	Green	Green	Red
WSP-T1add	Green	Green	Green	Green	Green	Yellow	Red
WSP-T2add	Green	Green	Green	Green	Green	Yellow	Red
WSP-T3add	Green	Green	Yellow	Red	Red	Red	Red
WSP-T1Wadd	Green	Green	Green	Green	Green	Yellow	Red
WSP-T2Wadd	Green	Green	Green	Green	Green	Yellow	Red
WSP-T3Wadd	Green	Green	Green	Green	Green	Red	Red
WSP	Green	Green	Green	Green	Red	Red	Red
RPR	Green	Green	Green	Green	Green	Red	Red

(a)

ILM-N ₂ -3U _{mf}	700°C	750°C	800°C	850°C	900°C	950°C	1000°C
WSP-T1	Green	Green	Green	Green	Green	Green	Red
WSP-T2	Green	Green	Green	Green	Green	Green	Red
WSP-T3	Green	Green	Green	Green	Green	Green	Red
WSP-T1W	Green	Green	Green	Green	Green	Green	Red
WSP-T2W	Green	Green	Green	Green	Green	Green	Red
WSP-T3W	Green	Green	Green	Green	Green	Green	Red
WSP-T1add	Green	Green	Green	Green	Green	Green	Red
WSP-T2add	Green	Green	Green	Green	Green	Green	Red
WSP-T3add	Green	Green	Green	Green	Green	Green	Red
WSP-T1Wadd	Green	Green	Green	Green	Green	Green	Red
WSP-T2Wadd	Green	Green	Green	Green	Green	Green	Red
WSP-T3Wadd	Green	Green	Green	Green	Green	Green	Red
WSP	Green	Green	Green	Green	Green	Green	Red
RPR	Green	Green	Green	Green	Green	Green	Red

(b)

SIB-N ₂ -2U _{mf}	700°C	750°C	800°C	850°C	900°C	950°C	1000°C
WSP-T1	Green	Green	Green	Green	Green	Red	Red
WSP-T2	Green	Green	Green	Green	Green	Red	Red
WSP-T3	Green	Green	Green	Green	Green	Red	Red
WSP-T1W	Green	Green	Green	Green	Green	Red	Red
WSP-T2W	Green	Green	Green	Green	Green	Red	Red
WSP-T3W	Green	Green	Green	Green	Green	Red	Red
WSP-T1add	Green	Green	Green	Yellow	Red	Red	Red
WSP-T2add	Green	Green	Green	Yellow	Red	Red	Red
WSP-T3add	Green	Green	Green	Yellow	Red	Red	Red
WSP-T1Wadd	Green	Green	Green	Green	Green	Yellow	Red
WSP-T2Wadd	Green	Yellow	Yellow	Yellow	Yellow	Red	Red
WSP-T3Wadd	Green	Green	Green	Green	Green	Red	Yellow
WSP	Green	Green	Green	Green	Red	Red	Red
RPR	Green	Green	Green	Green	Green	Red	Red

(c)

SIB-N ₂ -3U _{mf}	700°C	750°C	800°C	850°C	900°C	950°C	1000°C
WSP-T1	Green	Green	Green	Green	Green	Green	Red
WSP-T2	Green	Green	Green	Green	Green	Green	Red
WSP-T3	Green	Green	Green	Green	Green	Green	Red
WSP-T1W	Green	Green	Green	Green	Green	Green	Red
WSP-T2W	Green	Green	Green	Green	Green	Green	Red
WSP-T3W	Green	Green	Green	Green	Green	Green	Red
WSP-T1add	Green	Green	Green	Green	Green	Green	Red
WSP-T2add	Green	Green	Green	Green	Green	Green	Red
WSP-T3add	Green	Green	Green	Green	Green	Green	Red
WSP-T1Wadd	Green	Green	Green	Green	Green	Green	Red
WSP-T2Wadd	Green	Green	Green	Green	Green	Green	Red
WSP-T3Wadd	Green	Green	Green	Green	Green	Green	Red
WSP	Green	Green	Green	Green	Green	Green	Red
RPR	Green	Green	Green	Green	Green	Green	Red

(d)

LD-N ₂ -2U _{mf}	700°C	750°C	800°C	850°C	900°C	950°C	1000°C
WSP-T1	Red	Red	Red	Red	Red	Red	Red
WSP-T2	Red	Red	Red	Red	Red	Red	Red
WSP-T3	Green	Red	Red	Red	Red	Red	Red
WSP-T1W	Green	Yellow	Red	Red	Red	Red	Red
WSP-T2W	Green	Red	Red	Red	Red	Red	Red
WSP-T3W	Green	Yellow	Red	Red	Red	Red	Red
WSP-T1add	Red	Red	Red	Red	Red	Red	Red
WSP-T2add	Red	Red	Red	Red	Red	Red	Red
WSP-T3add	Red	Red	Red	Red	Red	Red	Red
WSP-T1Wadd	Red	Red	Red	Red	Red	Red	Red
WSP-T2Wadd	Red	Red	Red	Red	Red	Red	Red
WSP-T3Wadd	Green	Red	Red	Red	Red	Red	Red
WSP	Yellow	Red	Red	Red	Red	Red	Red
RPR	Green	Red	Red	Red	Red	Red	Red

(e)

LD-N ₂ -3U _{mf}	700°C	750°C	800°C	850°C	900°C	950°C	1000°C
WSP-T1	Green	Green	Green	Green	Green	Green	Yellow
WSP-T2	Green	Green	Green	Green	Green	Red	Red
WSP-T3	Green	Green	Green	Yellow	Yellow	Red	Red
WSP-T1W	Green	Green	Green	Green	Green	Green	Red
WSP-T2W	Green	Green	Green	Green	Green	Green	Red
WSP-T3W	Green	Green	Green	Green	Green	Green	Red
WSP-T1add	Green	Green	Green	Green	Green	Yellow	Red
WSP-T2add	Green	Green	Green	Green	Red	Red	Red
WSP-T3add	Green	Green	Green	Yellow	Yellow	Red	Red
WSP-T1Wadd	Green	Green	Green	Green	Green	Red	Red
WSP-T2Wadd	Green	Yellow	Yellow	Yellow	Yellow	Red	Red
WSP-T3Wadd	Green	Green	Green	Green	Green	Yellow	Red
WSP	Green	Green	Green	Green	Green	Green	Red
RPR	Green	Green	Green	Green	Red	Red	Red

(f)

Figure 5. Evaluation of fluidization quality based on the experimental pressure fluctuation signals and their PSDf. Legend: green = bubbling bed, yellow = bubbling fluidization fading out, red = no bubbling, and white = not acquired

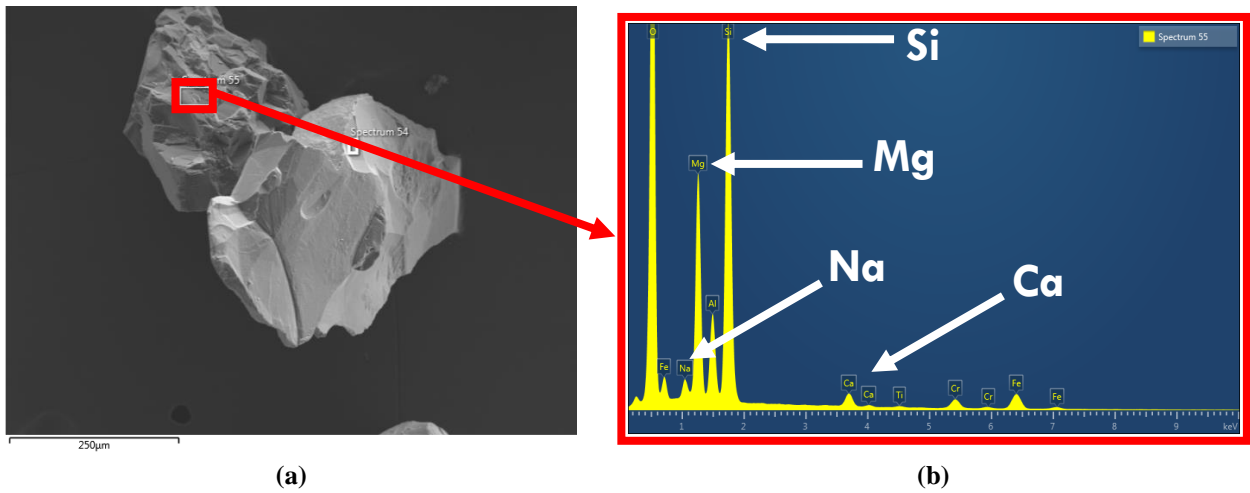


Figure 6. SEM micrograph of fresh ILM at 350× magnification (a) and related local EDS spectrum (b)

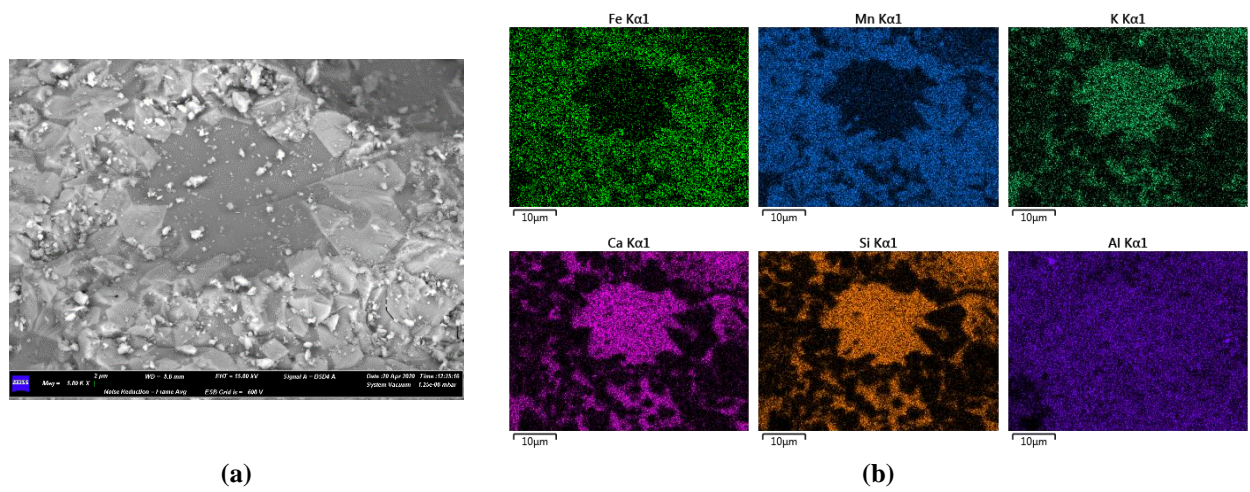


Figure 7. SEM micrograph of fresh SIB at 5000× magnification (a) and related elemental EDS maps (b)

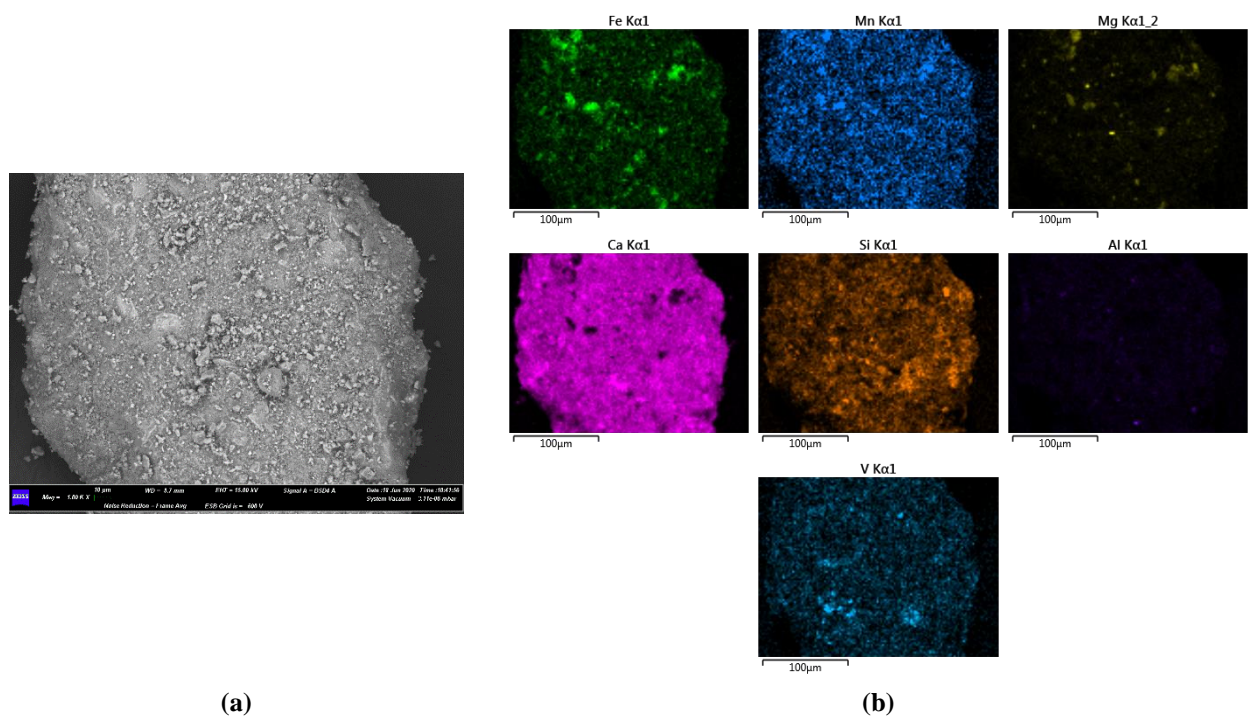


Figure 8. SEM micrograph of fresh LD at 1000× magnification (a) and related elemental EDS maps (b)

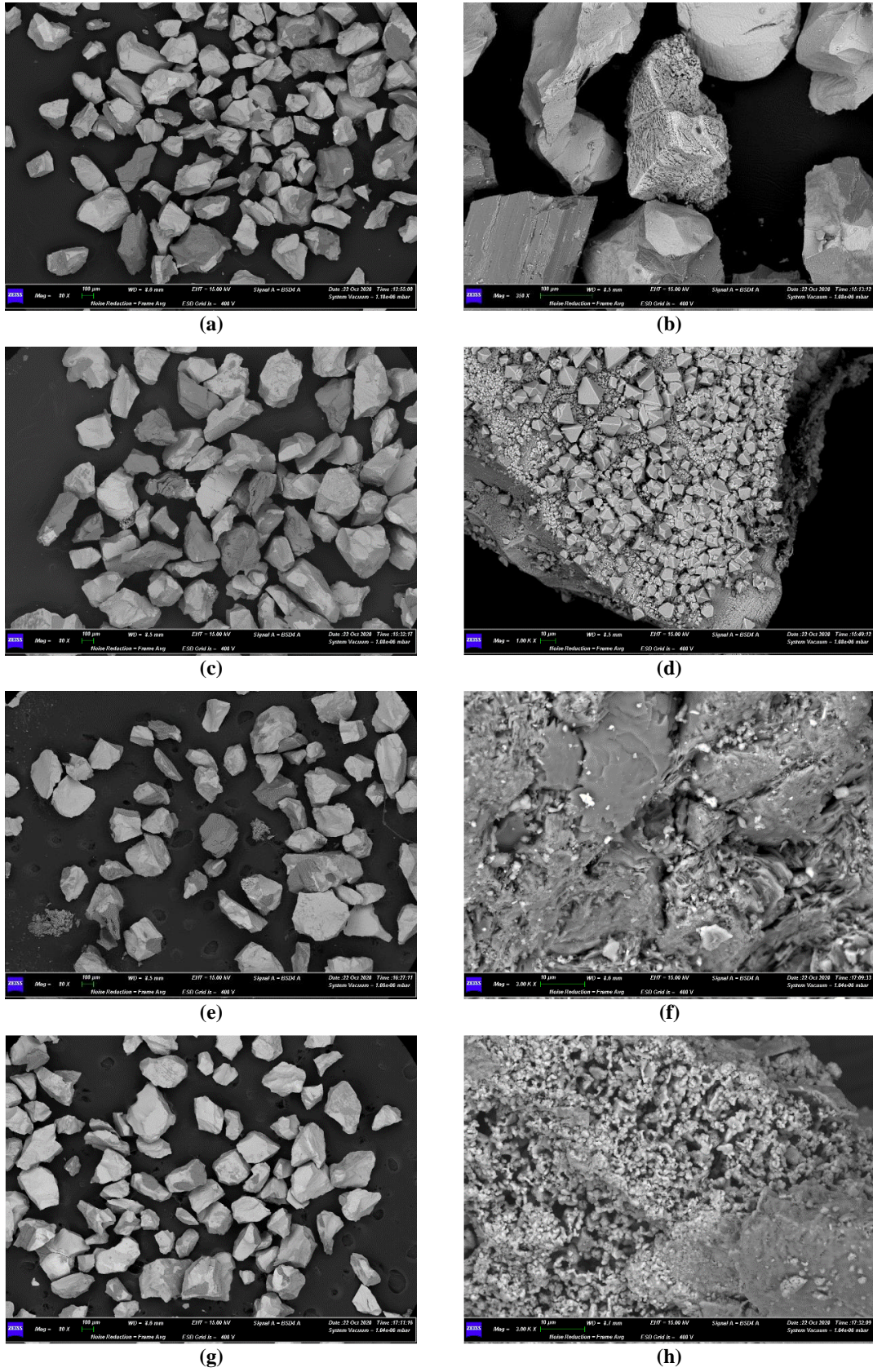


Figure 9. SEM micrographs of ILM after pressure fluctuations test with ashes from: WSP-T1Wadd at 700°C (80× (a) and 350× (b)) and 1000°C (80× (c) and 1000× (d)); WSP-T3Wadd at 700°C (80× (e) and 3000× (f)) and 1000°C (80× (g) and 3000× (h))

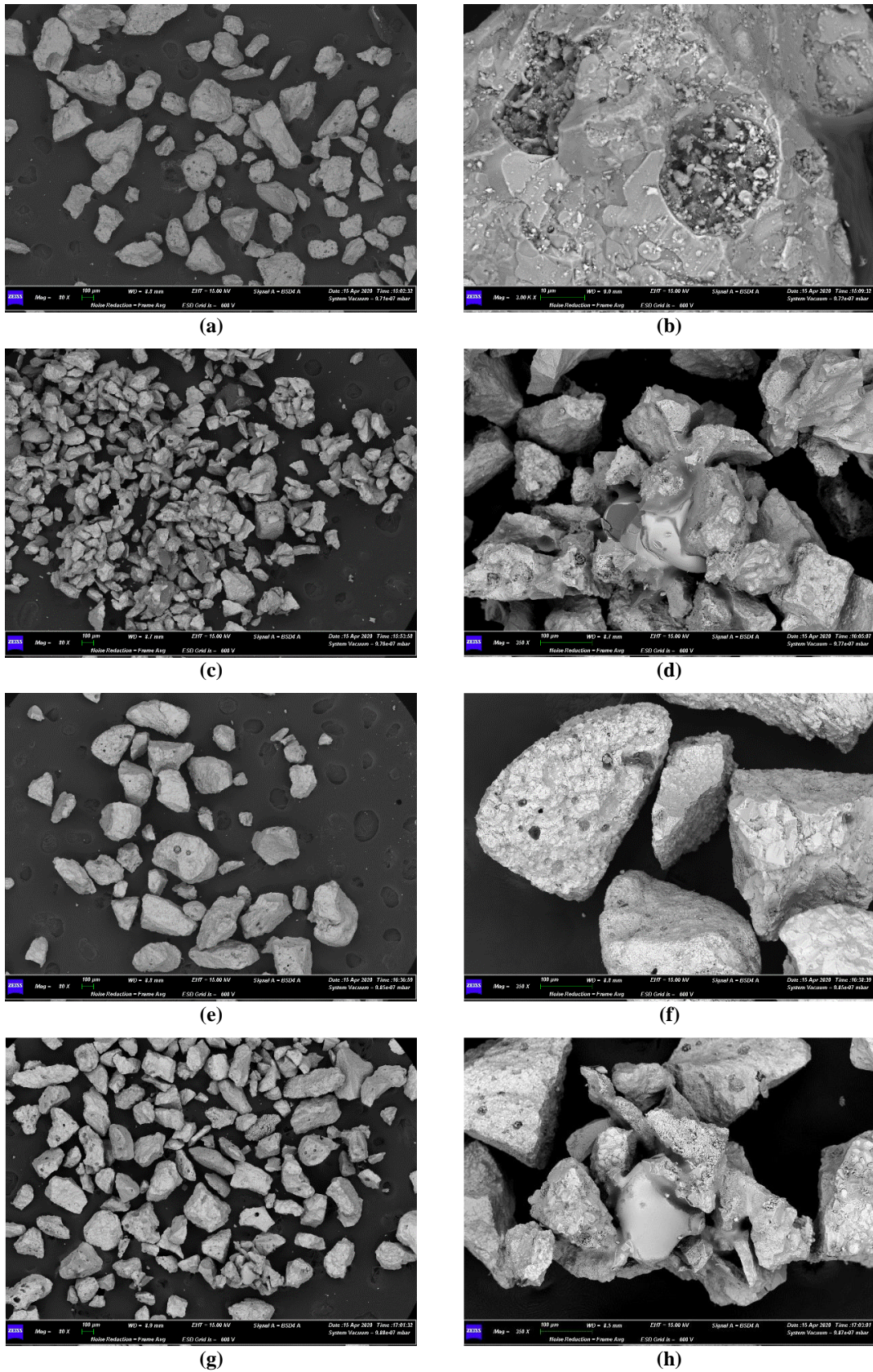


Figure 10. SEM micrographs of SIB after pressure fluctuations test with ashes from: WSP-T1 at 700°C (80× (a) and 3000× (b)) and 1000°C (80× (c) and 350× (d)); WSP-T3 at 700°C (80× (e) and 350× (f)) and 1000°C (80× (g) and 350× (h))

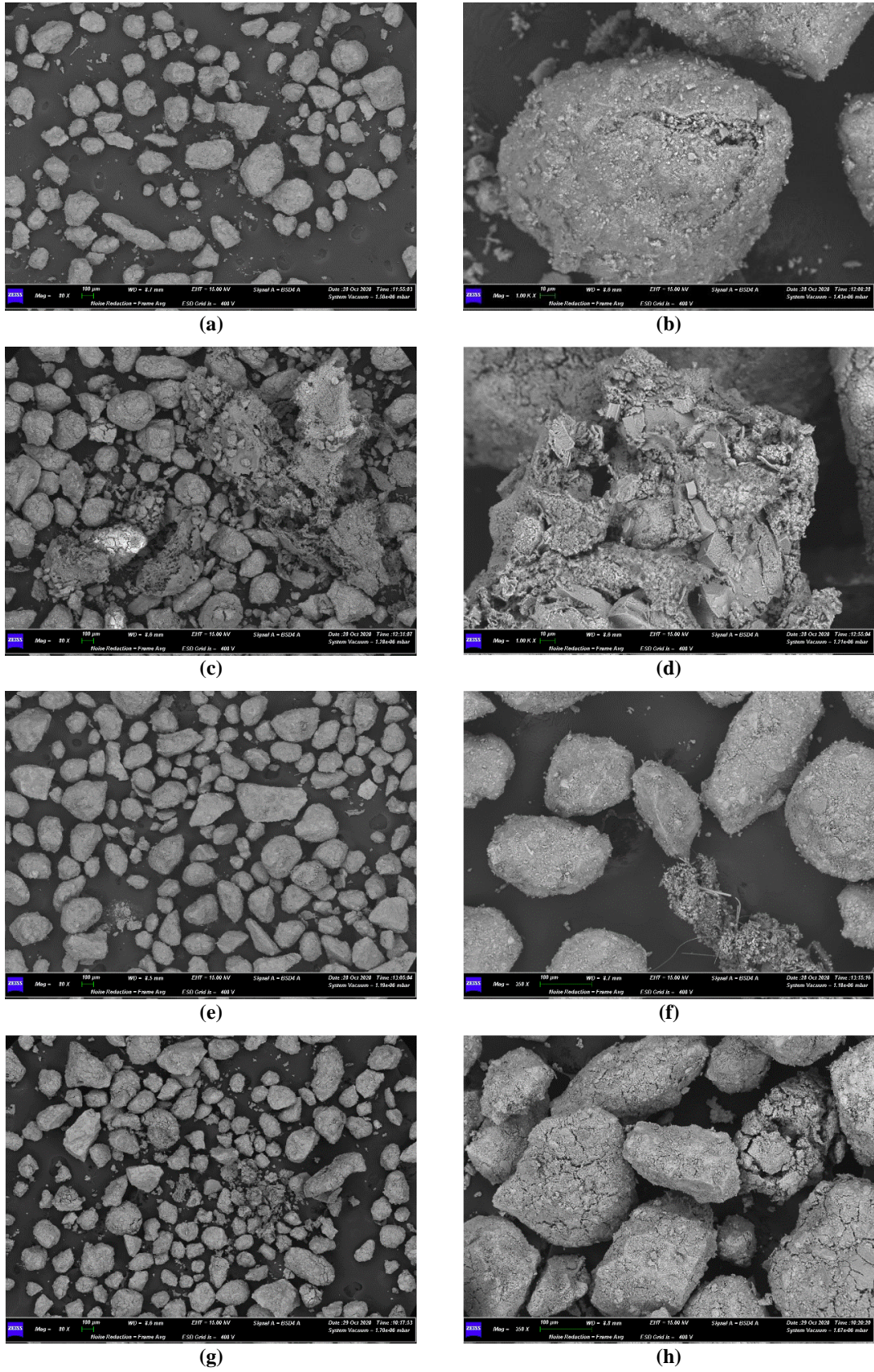


Figure 11. SEM micrographs of LD after pressure fluctuations test with ashes from: WSP-T1add ash at 700 °C (80× (a) and 1000× (b)) and at 1000 °C (80× (c) and 1000× (d)); WSP-T3add ash at 700 °C (80× (e) and 350× (f)) and at 1000 °C (80× (g) and 1000× (h))

bubbling fluidization quality was generally achieved by increasing the superficial velocity up to 3 times the minimum fluidization velocity of OCs: this is a precious indication for scale-up studies within CLARA, considering that the hypothesized CLG process should occur at even higher fluidization velocities.

The results summarized in this compendium allowed the selection of the most eligible materials (OCs and solid fuels) for CLG tests to be performed in the framework of CLARA at higher scales and gave relevant indications concerning the thermochemical conversion of considered biomasses, also providing pyrolysis experimental data which were useful for modelling investigations to other CLARA partners.

The two proposed experimental methodologies had the advantage of allowing performing a large number of tests – due to the many combinations of materials and process conditions required in the CLARA project – in a relatively short period of time, e.g., in comparison to more traditional continuous gasification tests. They have therefore proved to be useful and functional for the screening action requested by the other CLARA partners, leaving the more traditional, effort- and time-demanding experimental campaigns only to the worthiest materials and conditions.

Acknowledgements

This research was funded by the Horizon 2020 Framework program of the European Union, CLARA project, G.A. 817841.

The production and characterization of biomass pellets by the research team of National Renewable Energy Centre of Spain (CENER) and the contribution from Forschungszentrum Jülich GmbH (Germany) for the issue of minerals addition are acknowledged, as well as the provision of oxygen carriers by Chalmers University of Technology (Göteborg, Sweden), all occurred within the CLARA project. The authors thank Giampaolo Antonelli for his technical support, together with Lorenzo Arrizza and Maria Giammatteo from Microscopy Center of University of L'Aquila for their support to SEM-EDS analyses.

References

- [1] CLARA – Chemical looping gasification for sustainable production of biofuels, (n.d.). <https://clara-h2020.eu/> (accessed July 7, 2020).
- [2] F. Marx, P. Dieringer, J. Ströhle, B. Epple, Design of a 1 MWth Pilot Plant for Chemical Looping Gasification of Biogenic Residues, *Energies*. 14 (2021) 2581. <https://doi.org/10.3390/en14092581>.
- [3] A. Di Giuliano, I. Funcia, R. Pérez-Vega, J. Gil, K. Gallucci, Novel application of pretreatment and diagnostic method using dynamic pressure fluctuations to resolve and detect issues related to biogenic residue ash in chemical looping gasification, *Processes*. 8 (2020) 1137. <https://doi.org/10.3390/PR8091137>.
- [4] A European Green Deal | European Commission, (n.d.). <https://ec.europa.eu/info/strategy/priorities-2019-2024/european-green-deal/> (accessed March 7, 2022).
- [5] H. Ge, W. Guo, L. Shen, T. Song, J. Xiao, Experimental investigation on biomass gasification using chemical looping in a batch reactor and a continuous dual reactor, *Chem. Eng. J.* 286 (2016) 689–700. <https://doi.org/10.1016/j.cej.2015.11.008>.
- [6] A. Di Giuliano, S. Lucantonio, K. Gallucci, Devolatilization of residual biomasses for chemical looping Gasification in Fluidized Beds Made up of Oxygen-Carriers, *Energies*. 14 (2021). <https://doi.org/10.3390/en14020311>.
- [7] U. Mohamed, Y. Zhao, Q. Yi, L. Shi, G. Wei, W. Nimmo, Evaluation of Life Cycle Energy, Economy and CO2 Emissions for Biomass Chemical Looping Gasification to Power Generation, *Renew. Energy*. (2021). <https://doi.org/10.1016/j.renene.2021.05.067>.
- [8] S. Lucantonio, A. Di Giuliano, K. Gallucci, Influences of the Pretreatments of Residual Biomass on Gasification Processes: Experimental Devolatilizations Study in a Fluidized Bed, *Appl. Sci.* 2021, Vol. 11, Page 5722. 11 (2021) 5722. <https://doi.org/10.3390/APP11125722>.
- [9] N.E. Cazzaniga, R. Jonsson, D. Palermo, Sankey diagrams of woody biomass flows in the EU-28 Year 2009 EU-28, Luxembourg, 2019. <https://doi.org/10.2760/227292>.
- [10] S2Biom Project - Deliverable 8.2, (2016). https://www.s2biom.eu/images/Publications/D8.2_S2Biom_Vision_for_1_billion_tonnes_biomass_2030.pdf (accessed July 1, 2019).
- [11] IRENA, Solid biomass supply for heat and power: Technology brief, International Renewable Energy Agency, International Renewable Energy Agency, Abu DAhBI, 2019. www.irena.org (accessed July 18, 2020).
- [12] Transport & Environment, BirdLife International, How much sustainable biomass does Europe have in 2030?,

- Report. (2016) 1–7. [https://www.transportenvironment.org/sites/te/files/publications/How much sustainable biomass available in 2030_FINAL.pdf](https://www.transportenvironment.org/sites/te/files/publications/How_much_sustainable_biomass_available_in_2030_FINAL.pdf) (accessed July 18, 2020).
- [13] M. Coulson, J. Dahl, E. Gansekoele, A.V. Bridgwater, I. Obernberger, L. van de Beld, Ash characteristics of perennial energy crops and their influence on thermal processing, in: 2nd World Conf. Biomass Energy, Ind. Clim. Prot., ETA, Rome, 2004: pp. 359–362.
- [14] A. Demirbas, Combustion characteristics of different biomass fuels, *Prog. Energy Combust. Sci.* 30 (2004) 219–230. <https://doi.org/10.1016/j.pecs.2003.10.004>.
- [15] B.M. Jenkins, L.L. Baxter, T.R. Miles, T.R. Miles, Combustion properties of biomass, *Fuel Process. Technol.* 54 (1998) 17–46. [https://doi.org/10.1016/S0378-3820\(97\)00059-3](https://doi.org/10.1016/S0378-3820(97)00059-3).
- [16] L.G. Gibilaro, *Fluidization Dynamics*, 1st editio, Butterworth-Heinemann, Oxford, 2010. <https://doi.org/10.1201/9781420047509-c14>.
- [17] F. Scala, Particle agglomeration during fluidized bed combustion: Mechanisms, early detection and possible countermeasures, *Fuel Process. Technol.* 171 (2018) 31–38. <https://doi.org/10.1016/j.fuproc.2017.11.001>.
- [18] A. Di Giuliano, M. Gallucci, B. Malsegna, S. Lucantonio, K. Gallucci, Pretreated residual biomasses in fluidized beds for chemical looping gasification: Analysis of devolatilization data by statistical tools, *Bioresour. Technol. Reports.* 17 (2022) 100926. <https://doi.org/10.1016/J.BITEB.2021.100926>.
- [19] A. Di Giuliano, S. Lucantonio, B. Malsegna, K. Gallucci, Pretreated residual biomasses in fluidized beds for chemical looping Gasification: Experimental devolatilizations and characterization of ashes behavior, *Bioresour. Technol.* 345 (2022) 126514. <https://doi.org/10.1016/J.BIORTECH.2021.126514>.
- [20] O. Condori, F. García-Labiano, L.F. de Diego, M.T. Izquierdo, A. Abad, J. Adánez, Biomass chemical looping gasification for syngas production using ilmenite as oxygen carrier in a 1.5 kWth unit, *Chem. Eng. J.* 405 (2021). <https://doi.org/10.1016/j.cej.2020.126679>.
- [21] F. Hildor, H. Leion, C.J. Linderholm, T. Mattisson, Steel converter slag as an oxygen carrier for chemical-looping gasification, *Fuel Process. Technol.* 210 (2020) 106576. <https://doi.org/10.1016/j.fuproc.2020.106576>.
- [22] N. Menad, N. Kanari, M. Save, Recovery of high grade iron compounds from LD slag by enhanced magnetic separation techniques, *Int. J. Miner. Process.* 126 (2014) 1–9. <https://doi.org/10.1016/j.minpro.2013.11.001>.

Dynamic simulation and control of NGL recovery plant

Marta Mandis¹, Roberto Baratti¹, Stefania Tronci¹, José A. Romagnoli²

1 Dip. di Ingegneria Meccanica, Chimica e dei Materiali, Università degli Studi di Cagliari, Cagliari 09123 Italy;

2 Department of Chemical Engineering, Louisiana State University, Baton Rouge, LA 70809 USA

**Corresponding author E-Mail: roberto.baratti@unica.it*

1. Introduction

In the last 20 years, technological improvements in the gas extraction techniques such as hydraulic fracturing and horizontal drilling, have brought to the so-called "shale gas revolution" [1], allowing the extraction from unconventional reservoirs. This scenario is reflected in the increased availability of natural gas [1,2], an attractive energy source as cleaner alternative to coal and oil. The heavier hydrocarbon fraction contained in Natural gas is known as natural gas liquids (NGL), a valuable product that can be sold separately and used as feedstock for various industrial processes. For this reason, it possesses significantly higher market value than as part of the raw gas [3]. The increased availability of natural gas makes the separation process for the NGL recovery economically profitable. Different separation technologies have been developed for NGL production, and among them a technology that allows reaching high recoveries is the cryogenic distillation [4]. This process uses a separation train, where the first column is given by a cryogenic distillation unit for the methane separation, while the other columns are responsible for separating the heavier hydrocarbon fractions. The most common disturbances entering the process are related to the feed flow rate conditions. The plant inlet flow rate is dictated by the gas demand, as a result, variations are present on a daily but also seasonal basis, while the composition may be subject to fluctuations due to the characteristics of the extraction basin. To meet the product specification of the NGL separation process, it is thus necessary to design a control system based on dynamic analysis of the plant capable of mitigating or eliminating, as far as possible, the effect of these disturbances on the plant. Given the control objective of maintaining the purity of the products, the most intuitive control loop is represented by the direct control of concentrations. Unfortunately, this type of composition controller has drawbacks related to the long delay times due to measurement times and additionally, the use of composition analyzers involves high costs of purchasing and maintaining the equipment. An alternative to the direct control of composition, widely used in industry, is the indirect control of composition employing temperature measurements [5], a more convenient control strategy that gives the possibility to control the process by using online measurements. However, considering the complexity of the process and the not biunivocal relation between compositions and temperatures in multicomponent columns, it may not be the best control strategy to ensure process specifications in the presence of disturbances. This work aims to show the improvements obtained by modifying the control strategy of the NGL recovery process, starting from conventional temperature controllers. For this purpose, different control strategies are investigated and compared under feed flowrate disturbances.

2. Plant simulation and Control structures

The NGL fractionation process takes place in a separation train in a direct sequence arrangement which comprises a deethanizer, depropanizer, debutanizer columns, and a demethanizer column arranged in a cryogenic unit given by a CRR scheme. The process is simulated using the Aspen HYSYS® process simulator and based on realistic operating conditions [6]. The feed to the plant is represented by a natural gas mixture with low content of liquids, while the disturbance applied is represented by 10% variations in the feed flowrate, realized by manipulating the plant line pressure. The process targets are represented by the maintenance of product impurity level in the top and bottom product of deethanizer, depropanizer and debutanizer. Given the high cost of composition analysers and the delays in composition controllers, indirect composition controllers

based on temperature measurements are used along with reflux ratio controllers in the enriching section of the columns to mitigate the feed disturbances [7]. The effects on the functioning of the demethanizer downstream columns of a conventional control strategy, comprising only temperature controllers, are compared with a control scheme developed for improving the demethanizer transient operation [8]. The latter control scheme is given by a cascade control with boilup approximation plus a pressure compensator control in the separator upstream the demethanizer.

3. Results and discussion

The results obtained with the control strategies implemented in the separation plant are compared under the applied variations to the plant feed flowrate. The control performances are assessed by evaluating the production targets dynamic profiles for the different columns of the train, the corresponding ISE values are calculated and reported in Table 1.

Table 1. ISE values obtained under 10% variations in the plant feed flowrate for the proposed and the conventional control schemes.

	Deethanizer		Depropanizer		Debutanizer		Flowrate variations
	-10%	+10%	-10%	+10%	-10%	+10%	
CONV	1.43E+02	1.69E+02	2.43E+00	2.52E+00	2.38E+00	2.82E+00	Tray temperature
PROP	5.75E+01	5.01E+01	1.60E+00	1.70E+00	1.72E+00	1.76E+00	
CONV	4.90E-05	2.77E-05	4.82E-07	1.23E-07	1.95E-06	1.92E-06	Bottom impurity level
PROP	9.48E-06	1.42E-05	2.96E-07	3.55E-07	2.07E-06	2.02E-06	
CONV	2.95E-03	4.09E-04	2.47E-05	1.92E-06	3.61E-06	3.52E-06	Top impurity level
PROP	2.81E-04	4.07E-04	8.41E-06	9.16E-06	5.10E-06	4.93E-06	

As shown by the ISE values, the implementation of the cascade arrangement with PCT control in the CRR process scheme improves the performance of the temperature controls for deethanizer, depropanizer and debutanizer under both flow rate variations considered. Regarding the target concentrations, the higher improvement is recorded for the deethanizer column. With the proposed control scheme, the ISE values of both top and bottom products are reduced, and the responses result linearized, with symmetrical dynamic profiles obtained for changes in the applied flow rate. In addition, lower variations in the load of the manipulated variable represented by the reboiler duty are obtained. In the depropanizer top and bottom impurity level, the proposed control scheme succeeds to mitigate the disturbances in the worst-case variation represented by the decreasing in the feed flowrate, and also in this case the obtained response shows linear behavior.

4. Conclusions

The use of indirect composition control showed to be a successful strategy for guaranteeing specifics in the whole train of NGL recovery plants, when PCT control in the separator upstream the demethanizer and boil-up ratio control are used in the CRR separation scheme. When compared to a conventional control strategy, the proposed approach led the best control performance, especially under the worst-case variation.

References

- [1] M. Caporin, F. Fontini, *Energy Econ.* 64, (2017) 511–519.
- [2] G.F. Feng, Q.J. Wang, Y. Chu, J. Wen, C.P. Chang, *Energy Econ.* (2019), 104327
- [3] S. Mokhatab, W.A. Poe, J.Y. Mak, *Handbook of Natural Gas Transmission and Processing: Principles and Practices*, Gulf Professional Publishing, New York, 2015.
- [4] C. Olsen, T.A. Kozman, J. Lee, K. Yuvamitra *Distributed Generation and Alternative Energy Journal* 27, (2012) 42–55.
- [5] E.S. Hori, S. Skogestad, *Chem. Eng. Res. Des.* 85 (2007), 293-306.
- [6] J. Chebeir, S.D. Salas, J.A. Romagnoli, *J. Nat. Gas Sci. Eng.* 71, (2019), 102974.
- [7] W.L. Luyben, *Ind. Eng. Chem. Res.* 44, 20 (2005), 7800-7813.
- [8] M. Mandis, J.A. Chebeir, S. Tronci, R. Baratti, J. A. Romagnoli, *IFAC PapersOnLine* 54-3 (2021), 182-18

Hydrogen sulfide mix gas permeation in Aquivion® perfluorosulfonic acid (PFSA) ionomer membranes for natural gas sweetening

Virginia Signorini¹, Marco Giacinti Baschetti^{1*}, Diego Pizzi², Luca Merlo³

¹ Department of Civil, Chemical, Environmental and Material Engineering (DICAM), Alma Mater Studiorum, University of Bologna, Via Terracini, 28, 40131 Bologna, Italy;

² Renco S.p.A., Strada del Montefeltro, 51, Pesaro (PU), Italy

³ Solvay Specialty Polymers Italy S.p.A., V.le Lombardia 20, Bollate (MI), Italy

*Corresponding author E-Mail: marco.giacinti@unibo.it

1. Introduction

Hydrogen sulfide is one of the most toxic and acid contaminants presents in pre and post combustion processes of fossil fuel, such as coal or natural gas. Its attendance, together with that of CO₂ and higher hydrocarbons, must absolutely be removed from the natural gas streams prior to its commercialization [1].

Among the several process available for the Natural Gas Sweetening, gas separation with polymeric membranes become, in the latest years, one of the most suitable technologies because of its good performance, high efficiency in gas transport, mechanical and operational simplicity and relatively low cost of production and manufacturing [2–4].

Perfluorosulfonated acid ionomers (PFSA) have recently found wide use in various industrial applications, including membrane technology for Methane recovery due to their interesting affinity with polar compounds and good separation performances in humid conditions. In fact, PFSA membranes have a hydrophobic polytetrafluoroethylene-based fluorinated chain and a hydrophilic side chain ending in a SO₃H group. These sulfonic end-groups cause high water absorption and the formation, in humid environment, of interconnected water domains which become the preferential path for permeating gases (Fig.1) [5,6]. Thanks to this heterogenous structure, indeed, the gas can permeate in the water channels by solution-diffusion mechanisms where the most water-soluble compounds permeate faster respect to the other (so that H₂S > CO₂ > CH₄)[7].

In the present work, the membrane characterized is Aquivion® E87-12S, a short side chain perfluorosulfonic acid ionomer (PFSA) which exhibits high durability, good thermal and mechanical properties, high chemical stability to acidic compounds [8], and resulted to have extremely good resistance to plasticization and aging induced by CO₂ and H₂S [9].

Permeability of Aquivion® E87-12S films are tested with CO₂/H₂S/CH₄ ternary mixture at 35°C, and at relative humidity ranging from 20 to 95%.

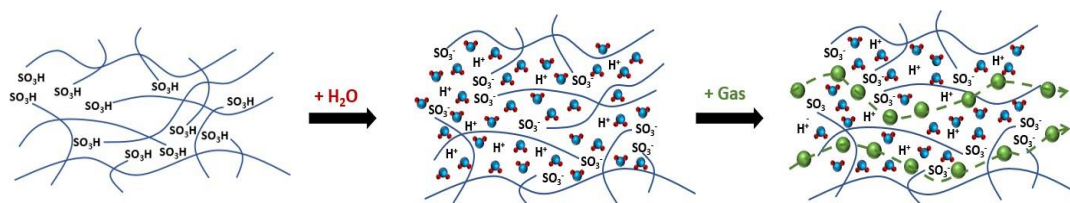


Figure 1. Humid gas permeation scheme in PFSA matrix

2. Methods

The material used for mixture permeation's studies is Aquivion E87-12S, a commercial perfluorosulfonic acid (PFSA) ionomer membrane characterized by an equivalent weight of 870 g_{pol}/mol_{SO₃H}. It is produced by Solvay Specialty Polymers Italy S.p.A. (Bollate (MI) Italy) by melt-extrusion process [10]. The experiments were carried out in a purposely developed manometric system with closed volume and variable pressure, which is immersed in a thermostatic bath to ensure temperature control. The system is designed to conduct both dry and humid test, so that before any test, the two side of the membrane are equilibrated to the desired water activity

in order to conduct humid test. Moreover, the sample cell is put in direct contact with a 2L upstream reservoir, where the mixture stream is loaded, while the downstream side is maintained under vacuum. Any possible concentration polarization phenomena related to the lack of flow in the upstream side were avoided by a magnetic driven mixer which ensured proper homogenization of gas composition during experiments. The composition of the feed and permeate flows was then characterized by a Micro Gas Chromatograph analyzer (Agilent Technology).

3. Results and discussion

In Figure 2 are displayed the permeability data for the three gases tested in the mixtures: H₂S, CO₂ and CH₄ as a function of relative humidity. The feed stream composition has been calibrated and checked by using the Micro-gas Chromatograph, and it has been taken more or less constant to a mol fraction of 0.1, 0.09 and 0.8 for CO₂, H₂S and CH₄ respectively.

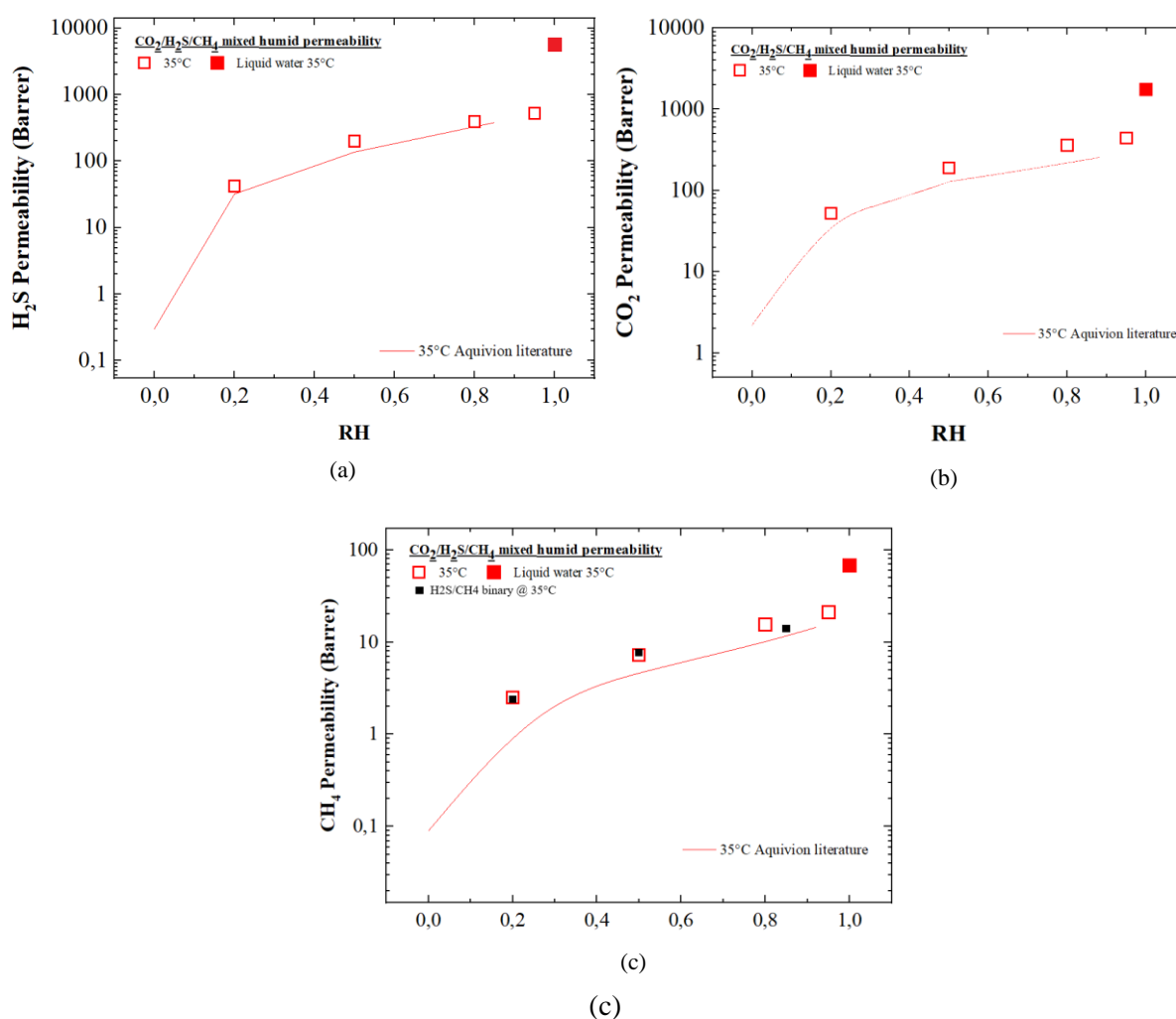


Figure 2. H₂S (a), CO₂ (b) and CH₄ (c) permeability as a function of relative humidity at 35°C and compare with literature data [7,11]

The results confirmed the major influence of water content on the gas permeation behaviour in PFSA as permeability strongly increased with RH, thanks to the hydrophilic characteristic of the material which tends to swell in humid condition, creating highly permeable water “channels” in the polymeric matrix.

The higher variation can be tracked down between 0 and 20% of humidity, where the permeability for all three gases increases sharply, since water vapor saturates the membrane and interconnected water channels start to be formed into the polymeric chain. At the higher humidity values investigate din the present work (from 20% to 95%), the permeability behaviour tends to rise more gently according to the water domains getting bigger and to the reduction of their tortuosity. At 95%RH, the permeability values obtained for all CO₂, CH₄ and H₂S

are similar to those in pure water, suggesting that the gas transport across the membrane is governed by solution-diffusion mechanism in the water swollen domains of the hydrated PSFA.

In particular, CO₂ and CH₄ results confirmed experimental data already available in the open literature, for pure components while H₂S reflects the behaviour already observed for binary data, (which are the only one, to the best of our knowledge, currently present in literature), showing a permeability increase by more than two orders of magnitude in the humidity range investigated.

In terms of separation behaviour hydrogen sulphide selectivity with respect to methane increased with water activity moving from 17 at RH 20% to 25 obtained at 95% RH. Regarding CO₂, the selectivity trend in Aquivion with respect to CH₄ is similar to the one observed for H₂S since they share the same acidic behaviour.

Even though this kind of polymer is not one of the best among studied in literature for natural gas sweetening, its selectivity to acid gases tends to achieve the upper bound limit, due to the great swelling of the membrane, especially for CO₂/CH₄ separation, as can be observed from the Robeson's Plot in Fig.3.

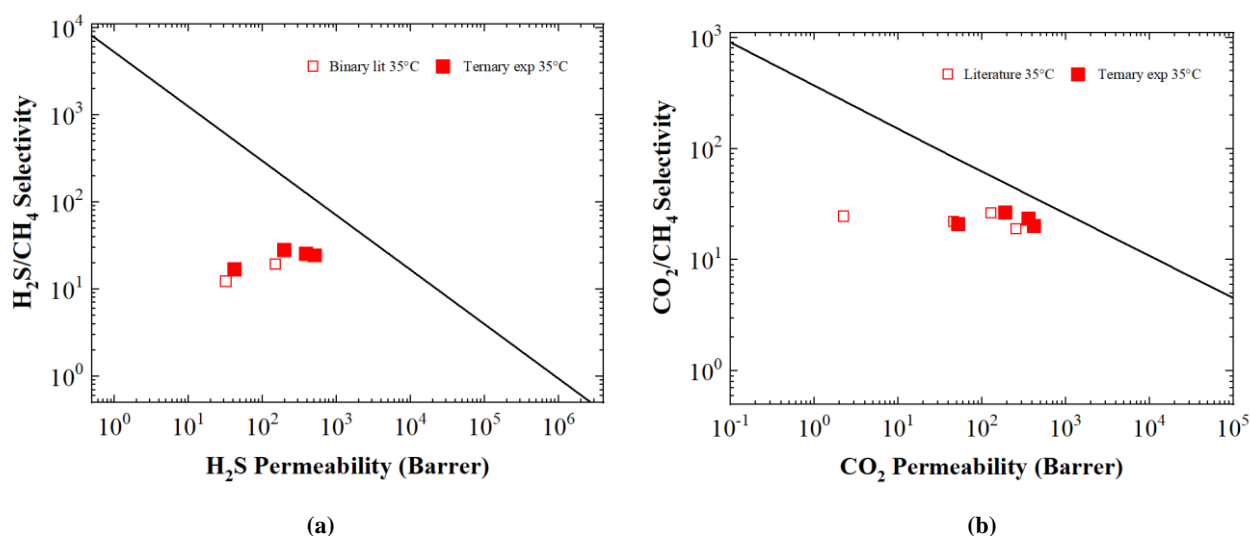


Figure 3. Robeson's plot for a) H₂S/CH₄ and b) CO₂/CH₄ system in Aquivion ® as a function of relative humidity. Literature data from [7,11]

4. Conclusions

Aquivion E87-12S® membrane has been tested for CO₂ and H₂S removal for natural gas sweetening through permeation test with ternary mixtures 35°C and relative humidity ranging from 20 to 95%.

The tests performed confirm that the membrane permeation behaviour is highly affected by the polymer hydrophilicity, which confer the ability of Aquivion® material to separate acidic compounds from natural gas. The presence of water indeed swells the materials positively affecting the permeability of acidic gases in the membrane, which tends to the values which could be calculated for a theoretical water membrane.

Current data therefore confirm that an interconnected network of hydrophilic domains exists in the hydrated polymer which speed up and control the gas permeation in the membrane.

Overall, the humid permeation tests carried on in the present work demonstrate good separation properties of Aquivion® E87-12S membrane with respect to the CO₂/CH₄ and H₂S/CH₄ system, even though permeability and selectivity are not the best observed in open literature; however, the separation performances obtained together with the high chemical and mechanical resistance, showed by this polymers makes it a potential candidate for industrial applications, also considering the excellent resistance of the membrane to plasticization and aging in H₂S.

References

- [1] T.D. Burchell, R.R. Judkins, M.R. Rogers, A.M. Williams, A novel process and material for the separation of carbon dioxide and hydrogen sulfide gas mixtures, Carbon N. Y. 35 (1997) 1279–1294. [https://doi.org/10.1016/S0008-6223\(97\)00077-8](https://doi.org/10.1016/S0008-6223(97)00077-8).
- [2] C.A. Scholes, G.W. Stevens, S.E. Kentish, Membrane gas separation applications in natural gas processing,

- Fuel. 96 (2012) 15–28. <https://doi.org/10.1016/J.FUEL.2011.12.074>.
- [3] R.W. Baker, K. Lokhandwala, Natural gas processing with membranes: An overview, *Ind. Eng. Chem. Res.* 47 (2008) 2109–2121. <https://doi.org/10.1021/IE071083W>.
- [4] P. Bernardo, E. Drioli, G. Golemme, Membrane gas separation: A review/state of the art, *Ind. Eng. Chem. Res.* (2009). <https://doi.org/10.1021/ie8019032>.
- [5] J. Catalano, T. Myezwa, M.G. De Angelis, M.G. Baschetti, G.C. Sarti, The effect of relative humidity on the gas permeability and swelling in PFSI membranes, in: *Int. J. Hydrogen Energy*, 2012. <https://doi.org/10.1016/j.ijhydene.2011.07.047>.
- [6] A.L. Rollet, O. Diat, G. Gebel, A new insight into nafion structure, *J. Phys. Chem. B.* (2002). <https://doi.org/10.1021/jp020245t>.
- [7] L. Olivieri, H. Aboukeila, M. Giacinti Baschetti, D. Pizzi, L. Merlo, G.C. Sarti, Humid permeation of CO₂ and hydrocarbons in Aquivion® perfluorosulfonic acid ionomer membranes, experimental and modeling, *J. Memb. Sci.* (2017). <https://doi.org/10.1016/j.memsci.2017.08.030>.
- [8] E.Y. Safronova, A.K. Osipov, A.B. Yaroslavtsev, Short Side Chain Aquivion Perfluorinated Sulfonated Proton-Conductive Membranes: Transport and Mechanical Properties, *Pet. Chem.* (2018). <https://doi.org/10.1134/S0965544118020044>.
- [9] M. Mukaddam, E. Litwiller, I. Pinnau, Gas Sorption, Diffusion, and Permeation in Nafion, *Macromolecules.* (2016). <https://doi.org/10.1021/acs.macromol.5b02578>.
- [10] T.D. Sheet, Aquivion® E87-12S, (2017).
- [11] V. Signorini, M. Giacinti Baschetti, D. Pizzi, L. Merlo, Hydrogen sulfide mix gas permeation in Aquivion® perfluorosulfonic acid (PFSA) ionomer membranes for natural gas sweetening, *J. Memb. Sci.* 640 (2021) 119809. <https://doi.org/10.1016/J.MEMSCI.2021.119809>.

Heterogeneous catalysts for hydrogen storage formates in aqueous solution

Marcella Calabrese^{1*}, Danilo Russo¹, Raffaele Marotta¹, Roberto Andreozzi¹, Almerinda Di Benedetto¹

1 Dipartimento di Ingegneria Chimica, dei Materiali e della Produzione Industriale, Università degli Studi di Napoli Federico II, P.le Vincenzo Tecchio 80, 80125, Napoli.

**Corresponding author E-Mail: marcellacalabrese.2@unina.it*

1. Introduction

In order to have reliable large-scale solutions for energy storage, hydrogen carriers are receiving special scientific attention. In recent years, there has been an interest in the development of new hydrogen vectors capable of releasing it at near ambient conditions. An interesting solution is represented by the salts of formic acid HCOOM ($M = \text{Li}^+, \text{Na}^+, \text{K}^+, \text{Cs}^+, \text{NH}_4^+$), prepared through the catalytic hydrogenation of bicarbonate ions. This can represent an alternative approach to safely and economically store and transport large quantities of H_2 , to be released when needed in the presence of a catalyst, at temperatures lower than 80°C .

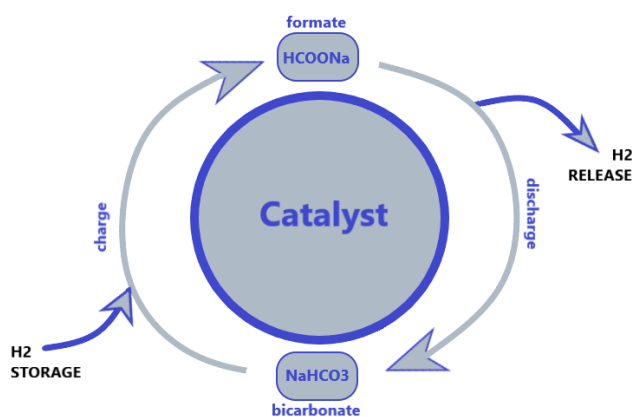


Figure 1 - Schematic representation of (sodium) formate-bicarbonate cycle [1]

Information on the stability of the proposed catalysts to release hydrogen from formiates is still scarce. Furthermore, most of the heterogeneous catalysts studied to date need to be reactivated often with the best ones showing a longevity of up to fifteen reversible cycles. [2] Based on the literature, [1]-[3-5] the most studied catalytic system is supported Pd on carbonaceous materials, oxides, etc. Some of these catalysts were found to be stable and capable of guaranteeing satisfying hydrogenation /dehydrogenation rates for industrial applications. In this work, particular attention will be devoted to identifying the supports among semiconductor oxides, that would permit to use a simple preparation technique such as the photodeposition of the palladium from solutions of its salts, as an alternative to impregnation.

2. Methods

All reagents were purchased from sigma-Aldrich and used as received. Dehydrogenation of formates tests were carried out using TiO_2 and WO_3 as the substrate of the catalyst. The photodeposition of palladium onto illuminated surfaces of TiO_2 [6] and WO_3 [7], was carried out in an annular photocatalytic reactor under UV irradiation and inert atmosphere. For the production of the catalyst an aqueous solution at 12wt. % of Pd in 180 mg of TiO_2 or WO_3 , starting from PdCl_2 , and at 10% v/v of EtOH was prepared. The photodeposition is done with a UV lamp with a wavelength $\lambda=254$ nm. The collected samples are centrifuged and dried at 75°C under inert atmosphere. Catalytic tests were run in a closed jacketed reactor, under N_2 inert atmosphere, adding 0.5 M sodium formate and the required amount of catalyst. Liquid samples were collected at different reaction time and analyzed by HPLC. Accumulated gas in the reactor was sampled at the end of each run and analyzed by GC.

3. Results

Various operating parameters that can influence the reaction (concentration of the reagent, preparation technique of the catalyst and its concentration, temperature, pH) have been investigated for dehydrogenation

of sodium formate. In Fig. 2, the most promising results are summarized with respect to catalysts obtained by photo-deposition of Pd on different semiconductors, with a particular focus on pH, temperature, and support influence on dehydrogenation kinetics. At present, photodeposited Pd on TiO₂ resulted in the best performances compared to WO₃ and ZnO (data not shown). pH affects reaction kinetics, the best range being 7-9. As expected, temperature increase significantly affects formates conversion and hydrogen release rates.

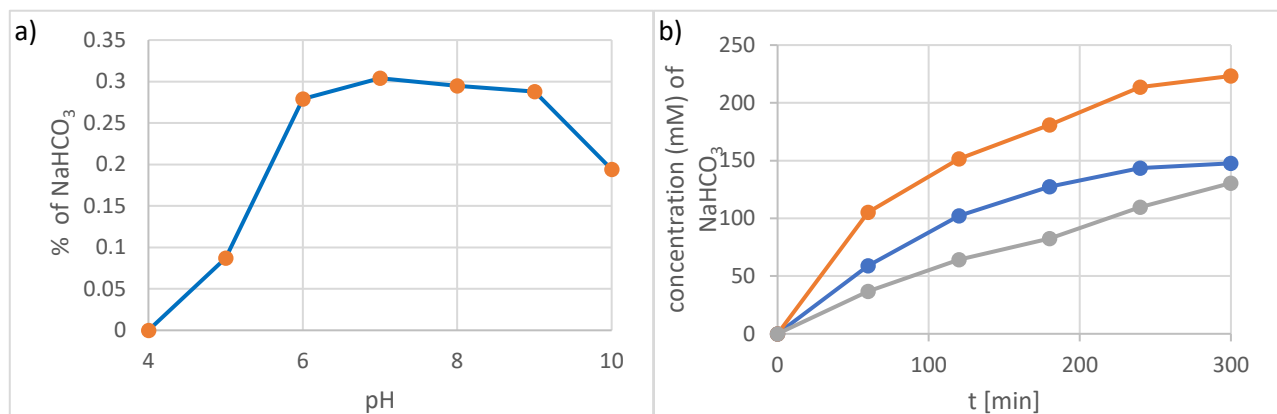


Figure 2 - a) effect of pH for the dehydrogenation reaction of HCOONa 0.5 M at T=75°C using 12 wt% Pd/TiO₂ as catalyst; b) production of NaHCO₃ starting from the dehydrogenation reaction at pH=8; orange: Pd/TiO₂, T=85°C; blue: Pd/TiO₂, T=75°C; grey: Pd/WO₃, T=75°C;

4. Conclusions

Preliminary results show the activity of photo-deposited noble metals on semiconductors to catalyze formates dehydrogenation. pH of the solution, as well as the choice of the support and the operating conditions are crucial to determine hydrogen release kinetics. Based on this, in an approach based on the principles of the circular economy, the possibility of using solutions containing the noble metal coming from leaching processes (solid-liquid extraction) of waste materials such as exhausted catalytic converters or cards from electronic waste will be evaluated. The activity will also be extended to the activity of other noble metals, such as Ru, Pt, Cu, and Ni, and alloys deposited on suitable supports.

References

- [1] A. Bahuguna and Y. Sasson, "Formate-Bicarbonate Cycle as a Vehicle for Hydrogen and Energy Storage," *ChemSusChem*, vol. 14, no. 5, pp. 1258–1283, 2021, doi: 10.1002/cssc.202002433.
- [2] X. Zhu *et al.*, "Tandem catalysis induced by hollow PdO: Highly efficient H₂ generation coupled with organic dye degradation: Via sodium formate reforming," *Catal. Sci. Technol.*, vol. 8, no. 23, pp. 6217–6227, 2018, doi: 10.1039/c8cy01551a.
- [3] E. González *et al.*, "Hydrogenation of sodium hydrogen carbonate in aqueous phase using metal/activated carbon catalysts," *Appl. Catal. B Environ.*, vol. 224, pp. 368–375, 2018, doi: 10.1016/j.apcatb.2017.10.038.
- [4] C. Fellay, P. J. Dyson, and G. Laurency, "A viable hydrogen-storage system based on selective formic acid decomposition with a ruthenium catalyst," *Angew. Chemie - Int. Ed.*, vol. 47, no. 21, pp. 3966–3968, 2008, doi: 10.1002/anie.200800320.
- [5] X. Shao, X. Miao, T. Zhang, W. Wang, J. Wang, and X. Ji, "Pd Nanoparticles Supported on N- And P-Co-doped Carbon as Catalysts for Reversible Formate-Based Chemical Hydrogen Storage," *ACS Appl. Nano Mater.*, vol. 3, no. 9, pp. 9209–9217, 2020, doi: 10.1021/acsanm.0c01830.
- [6] H. Yoneyama, H. Shiotani, N. Nishimura, and H. Tamura, "ACTIVE SITES OF TiO₂ SINGLE CRYSTAL SURFACE FOR PHOTODEPOSITION OF PALLADIUM," *Chem. Lett.*, vol. 10, no. 2, pp. 157–160, 1981, doi: 10.1246/cl.1981.157.
- [7] S. Y. Toledo Camacho, A. Rey, M. D. Hernández-Alonso, J. Llorca, F. Medina, and S. Contreras, "Pd/TiO₂-WO₃ photocatalysts for hydrogen generation from water-methanol mixtures," *Appl. Surf. Sci.*, vol. 455, no. September 2017, pp. 570–580, 2018, doi: 10.1016/j.apsusc.2018.05.122.

Basing offshore energy vectors production on optimized energy mixes: a methanol facility in the Adriatic Sea

Mariasole Cipolletta^{*}, Valeria Casson Moreno, Valerio Cozzani

*Laboratory of Industrial Safety and Environmental Sustainability – DICAM
University of Bologna, Via Terracini 28, Bologna, 40131, Italy*

** mariasole.cipolletta@unibo.it*

1. Introduction

When the extraction from end-of-life wells is claimed to be no more economically viable, reservoirs still have high amounts of potentially exploitable fossil fuels [1]. These residual resources may be valorized if combined with offshore energy generation, where near-to-decommissioning platforms can be converted into stations for energy collection, transmission and storage, once the structure's integrity is ascertained [2]. Power to X (PtX) strategies enable to convert Renewable Energy (RE) into liquid or gaseous chemical vectors that can be transported anywhere easily by conventional means, overcoming the issues of either lack of electricity infrastructure or grid saturation [3]. This solution is particularly interesting in the framework of energy transition to boost Blue Economy and exploit the offshore potential of multiple Renewable Energy Sources (RESs) [4].

This contribution introduces a methodology for the valorization of multiple RESs in a selected site. The outcome is the design of an integrated energy system based on offshore RESs that can provide the required energy to an offshore facility producing a targeted energy vector. The proposed method has two main aims: i) identifying the more sustainable energy mix in any location where a RES exploitation opportunity is present; ii) optimally designing the hybrid power system so that it can independently support a facility producing an energy carrier of interest. The method is demonstrated by its application to an offshore platform in Northern Adriatic Sea where residual natural gas (NG) and oxygen in air are the in-loco substrates used for methanol production via methane partial oxidation [5].

2. Methods

The methodology starts with the selection of a site where the exploitation potential of multiple RESs is attractive. A set of factors that represent constraints for the application of the methodology are then checked, i.e. surface limitations and regulations in force for the installation of renewable systems. Then, the available energy from each RES is estimated in order to evaluate the site energetic potential. The estimation of the available power starts from real site data retrieved on a reference period on a hourly basis, specifically for each source [6]. Then, the selection of the Renewable Energy Conversion Technologies (RECT) is carried out on the basis of RESs potentials on the site. Per each RES, a first screening step is performed to exclude the converters that do not suit the location features in terms of observed RES parameters, site characteristics and installation requirements. The operation performance of remaining RECTs is simulated in the reference period. Each power output profile is studied through power classes in order to identify the optimal RECT for each source. Subsequently, several energy mixes are considered by varying properly the number of RECTs applied to each RES. In parallel, a set of power duties likely to be coupled with the energy mixes are also defined. Finally, the optimal coupling “energy mix – duty” is found as the one assuring the higher number of energy-independent hours with respect to the minimal relative increase of nominal potentiality of the integrated system. The resulting conservative steady power provision that is assured by the system is set as the total energy supply available for methanol production, based on the most appropriate production process. The plant potential is thus derived using an iterative scale-up procedure. The facility technical, safety and environmental performances are then assessed by specific key performance indicators (KPIs).

3. Results and discussion

The site considered for a case-study with the aim of demonstrating the method is the offshore Garibaldi C platform in the Northern Adriatic Sea, close to decommissioning [7]. After data retrieval, RESs potential are

evaluated for year 2017: yearly averages obtained are 1 kW/m for waves, 189 W/m² for solar power, 114 W/m² for wind energy.

Based on the low marine potential, wave energy converters are excluded from the project. RECTs screening and simulation provide an average-performance PV panel [8] and a 1.5 MW horizontal-axis wind turbine [9] to properly exploit solar irradiation and wind speeds. The optimal combination “energy mix – duty” results in an integrated renewable energy plant of 1.68 MW nominal capacity (780 m² of PV panels, 1 wind turbine) coupled to a fixed duty of 150 kW insured for the 50% of time by RES. The final methanol facility (in Figure 1) is thus designed in order to steadily operate with 150 kW supply.

Section 1 aims at NG dewatering, section 2 consists of an air separation unit and the related oxygen compression train. In section 3, the reactants are heated before entering the methane partial oxidation reactor, which operates at 50 bar and 450 °C [10]. The reacted gases are separated in section 4 where fuel grade purity methanol is obtained. In section 5, recovery, compression and storage of propane-rich gaseous streams is carried out. These can be directed to a flexible turbine operating as a back-up system. The iterative sizing leads to a methanol productivity of 285 t/y, with a steady propane accumulation from purge gases of 97.5 kg/h, sufficient to satisfy the power demand by the back-up turbine in the time periods when RES generation is lower than 150 kW. The designed methanol plant fully relies on the electric power obtained by the in situ RE exploited.

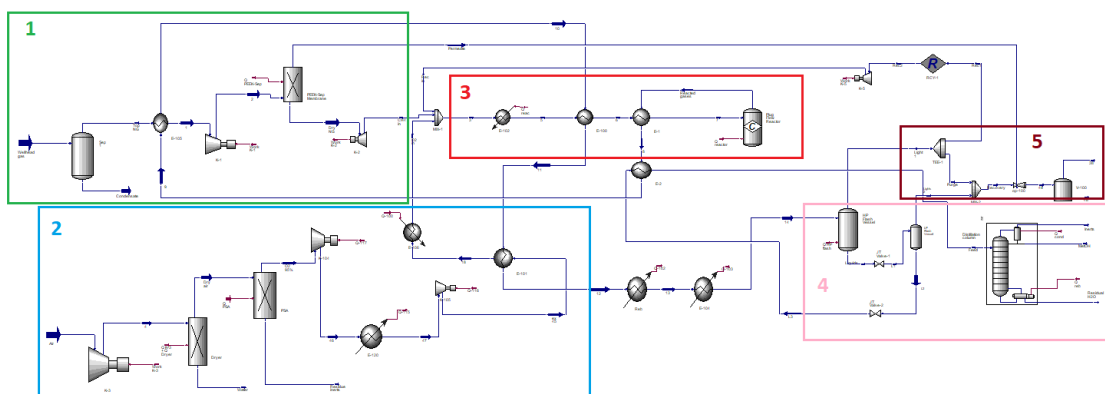


Figure 1. Process scheme of the methanol facility.

4. Conclusions

A methodology for the valorisation of integrated multiple offshore RESs through the coupling with Power-to-X processes is presented and is applied to a case-study. Methanol production on an offshore platform in the Adriatic Sea is considered. The methodology allowed the definition of the optimal design for both the RE exploitation systems and the methanol facility. The energy requirements of the methanol production process are totally satisfied by the RE exploitation system. The results also allow carrying out the assessment of the broad sustainability of the project.

References

- [1] J. Chécko, T. Urych, M. Magdziarczyk, A. Smolński, *Energies* 13 (2020), 1–20
- [2] S. R. Kolian, M. Godec, P. W. Sammarco, *Ocean. Coast. Manag.* 167 (2019), 52–59
- [3] A. Buttler, H. Spliethoff, *Renew. Sustain. Energy Rev.* 82 (2018), 2440–2454
- [4] V. Aryai, R. Abbassi, N. Abdussamie, F. Salehi, V. Garaniya, M. Asadnia, *Process Saf. Environ. Prot.* 148 (2021), 437–461
- [5] G. A. Olah, A. Goepfert, G. K. S. Prakash, *Beyond Oil and Gas: the Methanol Economy*, third ed., Wiley-VCH, 2018
- [6] E. Dallavalle, M. Cipolletta, V. Casson Moreno, V. Cozzani, B. Zanuttigh, *Renew. Energy* 174 (2021), 426–443
- [7] Ministero dello Sviluppo Economico, 2020
- [8] SUNPOWER, Datasheet MAXEON 3 - 400 W (2020)
- [9] GOLDWIND, 1.5 MW PMDD wind turbine - Technical report (2020)
- [10] P. S. Yarlagadda, L. A. Morton, N. R. Hunter, H. D. Gesser, *Ind. Eng. Chem. Res.* 27 (1988) 252-256

Biogas upgrading by adsorption: experimental performance of commercial zeolites and comparison with carbon-based sorbents

Fabrizio Rainone^{1*}, Sabrina Mauro¹, Marco Balsamo², Amedeo Lancia¹, Alessandro Erto¹

1 Dipartimento di Ingegneria Chimica, dei Materiali e della Produzione Industriale, Università degli Studi di Napoli Federico II, Piazzale Vincenzo Tecchio 80, 80125 Napoli, Italy; 2 Dipartimento di Scienze Chimiche, Università degli Studi di Napoli Federico II, Complesso Universitario di Monte Sant'Angelo, 80126 Napoli, Italy

**Corresponding author E-Mail: fabrizio.rainone@unina.it*

1. Introduction

Biomethane, a renewable form of natural gas, can be produced by biogas upgrading, which consists in the removal of CO₂ to a maximum allowed concentration lower than 3% by volume. For its renewable origin, biomethane utilization is incentivized to mitigate CO₂ emissions but a cost-effective production, which mainly includes the CO₂ removal step, must be assured. Among the different options currently available for upgrading, adsorption has gained high attention, mainly due to the easy operation and, if coupled with a well-reasoned definition of the working condition, for the high efficiency assured. This work focuses on biogas upgrading to biomethane by adsorption of CO₂ onto commercial zeolites (13X BFK, 5A, 4A), whose CO₂/CH₄ separation performance is assessed by dynamic breakthrough tests in a fixed bed employing binary feed gas mixtures at environmental conditions (1 atm, 30 °C). Furthermore, an overall comparison between zeolites and carbon-based sorbents is presented, based on previously published results obtained with the same lab-scale plant [1].

2. Methods

Adsorption/regeneration tests were conducted in a lab-scale plant consisting of a 12 cm glass adsorption column encased in a heated shell and an ABB NDIR gas analyzer to monitor CO₂ and CH₄ concentration in the outlet flow rate.

The experimental campaign consisted in a full characterization of the performance of the three sorbents by performing adsorption and desorption runs with feed mixtures characterized by different CO₂/CH₄ compositions. Lastly, the best performing sample was subjected to cyclic adsorption and desorption runs with a model biogas mixture, to determine its regenerability in conditions closer to those of an actual industrial adsorption process.

Prior to the adsorption runs, the sorbent was loaded into the column and heated above 100 °C for an hour in a nitrogen flow to remove the adsorbed water; afterwards, the dehydrated sample was weighed and 4 g of dried sample were loaded in the column. All the adsorption tests were conducted with a gas temperature of 30 °C and atmospheric pressure, with a constant total flow rate of 0.7 L/min (calculated at 1 atm and 20 °C); different feed mixtures were employed (10, 20, 30, 40, 50, 60% vol. CO₂, balance CH₄). Desorption runs were carried out at atmospheric pressure and either 30 or 80 °C, with a constant N₂ flow of 0.7 L/min acting as the purge gas; these tests were useful to assess the rate and degree of regenerability of the sorbents.

3. Results and discussion

The CO₂ breakthrough curves obtained from the adsorption tests with model biogas mixture (40% CO₂ in CH₄, T = 30 °C, P = 1 atm) on 13X BFK, 5A and 4A zeolites are shown in Figure 1.

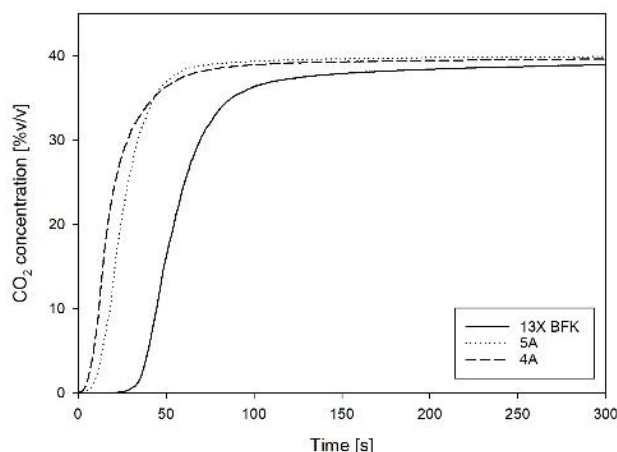


Figure 1. Comparison of CO₂ breakthrough curves for a model biogas mixture (40% CO₂ in CH₄, T = 30 °C, P = 1 atm) between the three zeolite samples (13X BFK, 5A and 4A)

Zeolites 5A and 4A show quite similar dynamic behaviors, as they belong to the same zeolite class and only differ for the average pore diameter. A slight difference can be retrieved in terms of adsorption rate, as the breakthrough curve of 5A sample is characterized by a steeper shape due to its wider mean pore diameter with respect to zeolite 4A. On the other hand, the 13X BFK sample exhibits a higher breakpoint time and, therefore, significantly greater adsorption capacity for CO₂. This result can be correlated to the higher BET surface area and micropore volume of this zeolite, thus confirming the better performance of this sample with respect to the other. Moreover, 13X BFK is characterized by the absence of the usual binder for pellets formation (substituted by a mechanical extrusion process). This result also testifies the positive effect of the removal of the binders for the separation performance of 13X zeolites, which is also in agreement with existing literature on this subject [2-3].

The desorption tests highlighted the main criticism of the 5A and 4A samples: the CO₂ desorption curves of these zeolites were characterized by extremely long tails, reaching a zero concentration level after more than three hours; even so, the curve integration showed that the amount of CO₂ desorbed was around the 70% of the amount previously adsorbed, indicating a critical lack of regenerability for these zeolites, at least by means of thermal swing processes. 13X BFK sample showed much faster desorption kinetics and displayed much better regeneration capabilities, which were also confirmed by the cyclic adsorption/desorption tests, showing a steady equilibrium CO₂ capture capacity ($\omega_{CO_2}^{eq}$) of 4.05 ± 0.05 mol/kg.

For these reasons, 13X BFK was deemed as the best sorbent for the biogas upgrade application among the investigated zeolites, and its $\omega_{CO_2}^{eq}$, selectivity and regenerability were compared to those of the carbonaceous sorbents tested in our previous experimental campaign, i.e., two carbon molecular sieves (CMSs, Carbotech and Xintao) and an activated carbon (AC, Desotec) [1]. This analysis underlined that the CMSs exhibited an overall behavior comparable to that discussed for the zeolites (i.e. low CH₄ breakpoint time and adsorption capacity, leading to high selectivity), while the Desotec AC stood out and showed different performance indicators, specifically a much higher CH₄ breakpoint time indicative of a substantial CH₄ adsorption capacity, which is indeed almost an order of magnitude higher than the average of the other samples and is associated to the lower selectivity value among all sorbents. These results translate into poor applicability of this sorbent to the biogas upgrade process, although another positive aspect of this carbon is its regeneration time, as its CO₂ desorption times are the lowest at both temperatures investigated.

On the other hand, the comparison between zeolite 13X BFK and Xintao, the best performing CMS, highlighted some interesting results, and their CO₂ breakthrough curves for a model biogas mixture (40% CO₂ in CH₄, T = 30 °C, P = 1 atm) are reported in Figure 2. However, it is important to underline that the adsorption tests for carbon-based sorbents and zeolites were conducted with different sorbent mass values (equal to 12 and 4 g, respectively), therefore the comparison between the curves can only lead to qualitative considerations.

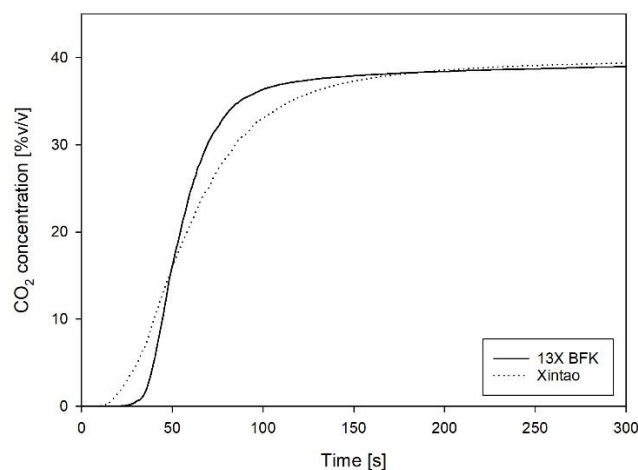


Figure 2. Comparison of CO₂ breakthrough curves for a model biogas mixture (40% CO₂ in CH₄, T = 30 °C, P = 1 atm) between zeolite 13X BFK (4 g) and Xintao CMS (12 g)

It can be noticed that, despite the significant difference in the mass employed, 13X BFK zeolite shows a higher CO₂ breakpoint time than the Xintao CMS. This is also reflected in a noticeably higher adsorption capacity at breakpoint (i.e., when CO₂ outlet concentration reaches 3% vol., $\omega_{CO_2}^b$), which is a first indication of the higher CO₂ adsorption capacity of this sample. Furthermore, 13X BFK curve also exhibits a higher slope, which can be associated to a narrower mass transfer zone (MTZ), which is in agreement with the higher temperature increase recorded for this sample (peak temperature of 70 °C for 13X BFK versus less than 40 °C for Xintao) and the lower fractional length of unused bed (LUB, 61% for 13X BFK versus 68% for Xintao). Moving on to the comparison of the desorption tests (which were also performed employing the previously reported sorbent masses), we noticed that CO₂ desorption times are much lower for Xintao both at 30 and 80 °C, and this is once again a counterintuitive result considering the higher mass of sorbent employed in its tests. Therefore, it is possible to infer that the regeneration of this sorbent is much faster and equally effective, as confirmed by the results of the 9 adsorption/desorption cycles performed on this sorbent. Moving on to the equilibrium results, zeolite 13X BFK showed higher $\omega_{CO_2}^{eq}$ and $\omega_{CH_4}^{eq}$ (4.02 and 1.24 mol/kg, respectively) with respect to Xintao (1.34 and 0.67 mol/kg), and also a higher selectivity (4.9 and 3); however, considering a real biogas upgrade application, it is generally better to minimize the methane losses rather than maximizing the CO₂ capture since the first is the product of interest while the latter is merely a by-product. Therefore, this is also a result favorable for Xintao, which can be considered the best sorbent among those investigated in our tests for the biogas upgrade application, mainly thanks to its kinetic sieving properties and smooth regenerability, at least in the case of a Temperature Swing Adsorption (TSA) process.

4. Conclusions

The breakthrough tests on 13X BFK, 5A and 4A zeolites highlighted their good kinetic separation capabilities for biogas-like mixtures (40% CO₂ in CH₄), as their CO₂ and CH₄ breakpoint times differ by at least 10-15 seconds. In comparison to the other tested zeolites, 13X BFK breakthrough curve was shifted toward longer times, resulting in higher CO₂ breakpoint time and greater adsorption capacity. However, the subsequent desorption tests underlined serious criticalities for the regeneration of the 5A and 4A zeolites. Lastly, the zeolites were compared with two CMSs and an activated carbon which were investigated in a previous experimental campaign. While the AC performance stood out because of its poor selectivity, which heavily penalizes its applicability for the biogas upgrading process, the comparison with the CMSs was particularly interesting, as they exhibited comparable selectivities (since a lesser CO₂ capture capacity was balanced by much lower CH₄ adsorption values) and far better regenerability than the zeolites. In conclusion, the good kinetic and equilibrium separation performance of zeolites is heavily downsized by their poor regenerability, at least by the means of temperature swings; therefore, other regeneration techniques (i.e., pressure or vacuum swings) should be evaluated to optimize their cyclic performance and assess their applicability for biogas upgrading at a commercial scale.

References

- [1] F. Rainone, O. D'Agostino, A. Erto, M. Balsamo, A. Lancia, *J. Environ. Chem. Eng.* 9 (2021) 106256.
- [2] M.C. Campo, A.M. Ribeiro, A.F.P. Ferreira, J.C. Santos, C. Lutz, J.M. Loureiro, A.E. Rodrigues, *Fuel Process. Technol.* 143 (2016) 185–194.
- [3] P.A.S. Moura, D.P. Bezerra, E. Vilarrasa-Garcia, M. Bastos-Neto, D.C.S. Azevedo, *Adsorpt.-J. Int. Adsorpt. Soc.* 22 (2016) 71–80.

Oxymethylene ethers as the next-generation energy carriers: kinetic model development

Alessandro Pegurri, Alessandro Stagni*

Department of Chemistry, Materials, and Chemical Engineering "G. Natta", Politecnico di Milano, Milano 20133, Italy

**Corresponding author E-Mail: alessandro.stagni@polimi.it*

1.Introduction

Implementing a life-cycle carbon neutrality in the third-millennium energy production, without sacrificing economic prosperity, requires the adoption of a multifaceted strategy, ultimately leading to the independence from fossil fuels [1]. Unsurprisingly, the transportation sector is among most involved ones in such a shift, as it is responsible of more than a quarter of the greenhouse gases in Europe [2]. On the other hand, when switching from fossil fuels to renewables (e.g. wind, sun), several scientific and technological challenges must be overcome, specifically due to their intermittent availability. For this reason, the chemical storage of the excess energy produced by renewable sources has recently gained interest, and synthetic electrofuels, or e-fuels, for energy accumulation and an "on-demand" release, have become a hot topic in the scientific community.

For these reasons, oxymethylene ethers (OME_n), with a structure CH₃O(CH₂O)_nCH₃, have acquired increasing importance due to their physical and chemical properties, making them good candidates to replace diesel fuels in the related engines [3], with the added value of decreased soot emissions, due to their oxygenated nature [4]. Thus, several studies have investigated the chemical kinetics of OMEs, and experimental, theoretical, and kinetic modeling activities have been performed in the latest years, especially involving dimethyl ether (DME, or OME₀) [5] and dimethoxymethane (DMM, or OME₁) [6]. Recently, the experimental activity also involved longer-chain OMEs [7,8], with kinetic mechanisms of single OMEs or their mixtures [7,9] being developed in parallel.

From a modeling perspective, the main disadvantage in describing the oxidation chemistry of the heavier OMEs is related to the growing complexity of the related detailed kinetic models, since the number of radicals and intermediate species increases more than linearly with the OME length. As a result, they cannot be used as such for the Computational Fluid Dynamic (CFD) simulations of real-scale devices, and their applicability in this context is subject to a preliminary simplification.

A significant reduction in size can be obtained by leveraging the hierarchical structure of OMEs, which are then well suited for a lumped formulation of their kinetic model. The potential of lumping procedures in the development of reduced but accurate kinetic models has already been shown in the previous literature [10–12], especially for such fuels exhibiting a low-temperature chemistry behavior. Moreover, the accuracy of the model can be further enhanced by performing a downstream optimization procedure, which is computationally eased by the reduced size of the starting model.

In this work, both of these classes of methods are combined to develop a kinetic model of OME₀₋₄ pyrolysis and oxidation. Starting from a detailed kinetic mechanism available in literature, a recently-developed lumping procedure is implemented to obtain a more compact model. On a successive step, the accuracy of the mechanism with respect to the experimental data is further improved via a data-driven optimization, after collecting a vast database of experimental data in ideal reactors (jet stirred, flow reactors, shock tubes, laminar flame speeds). Finally, the performance of the optimized mechanism is verified in a wide range of operating conditions, and compared to the detailed and the intermediate lumped one.

2. Methods

The lumping procedure was performed on a detailed kinetic mechanism, built up following a hierarchical methodology, leveraging the state-of-the-art submodels for the single fuels: the core C₀-C₂ model was taken from the work of Keromnes et al. [13] and Metcalfe et al. [14], while the C₃ mechanism was adopted after Burke et al. [15]. The implementation of the ethers chemistry followed a hierarchical procedure, too: DME, or OME₀, was taken from the work of Burke et al. [5], while DMM, or OME₁, was implemented by using the recent model by Jacobs et al. [6]. On top of them, the model by Cai et al, describing OME₂₋₄ chemistry using a reaction-classes approach, was added. For all of the species, thermodynamic properties were updated from the database of Burcat and Ruscic [16]. Overall, the detailed mechanism accounted for 282 species and 2657 reactions.

On the other hand, the chemical lumping procedure was performed by adapting a recently-developed methodology, initially devised for master equation solution techniques [17]. After dividing the mechanism in separate submechanisms, according to the global stoichiometry, and identifying the species to be grouped using a structural-isomerism criterion, the composition of the new, fictitious pseudospecies was evaluated by performing 0-dimensional simulations, and evaluating in this way the branching fractions of each of the composing isomers. With this approach, it was possible to reduce the size of the mechanism up to 176 species and 2486 reactions.

Finally, the lumped mechanism was optimized by applying a recently-developed data-driven methodology [18], implemented in the OptiSMOKE++ software [19]. After identifying the critical reactions via sensitivity analysis in the whole range of operating conditions, their modified-Arrhenius parameters were optimized by using an evolutionary algorithm, after an objective function was built up using the Curve-Matching methodology [20,21], and using the experimental data as reference. The use of the Curve-Matching algorithm allowed for a more complete comparison between experimental data and modeling predictions.

3. Results and discussion

The described lumping procedure was applied on each of the identified blocks constituting OME₁₋₄ fuel oxidation chemistry. The reactivity of the related block was also lumped, by weighting the isomers according to the respective branching fractions, as found in 0D simulations. As a result, the procedure allowed to significantly reduce the size of the mechanism. Figure 1 compares the number of species constituting the lumped and reduced mechanism, respectively. Compared to the detailed model, the increase in the number of species is linear with the ether length, which results in significant computational advantages.

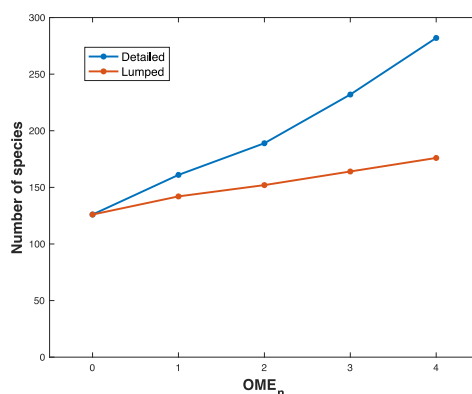


Figure 1. Comparison between the number of species of detailed and lumped mechanism

The optimization process involved the modified-Arrhenius parameters of 57 reactions, among the different OMEs. The optimized mechanism was validated against the detailed and lumped ones. Figure 2 shows the predictions in terms of ignition delay time for OME₂₋₄, evaluated at variable pressures and equivalence ratios.

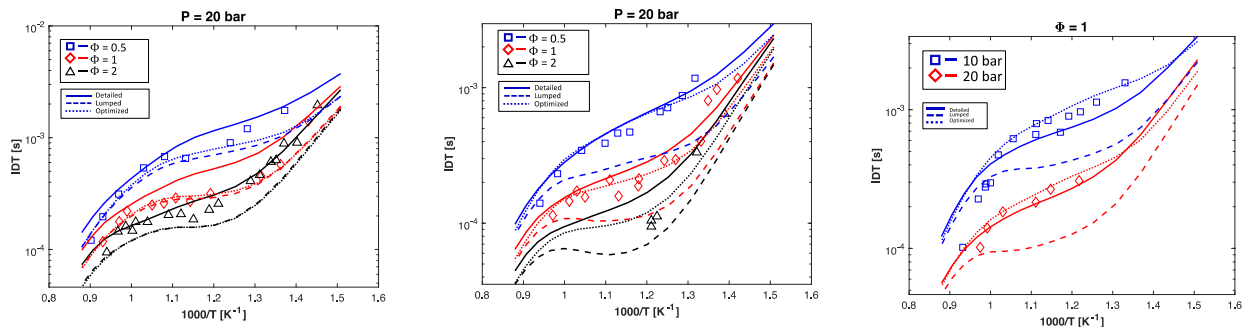


Figure 2. Comparison about the ignition delay time predictions of OME₂ (left), OME₃ (center) and OME₄ (right). Experiments [7] vs modeling predictions.

The lumping procedure resulted in a general acceleration of the predictions at all the conditions. When performing optimization, significant improvements were obtained on a global perspective, with the best results obtained for OME₃₋₄, while a slight worsening was obtained for OME₂. Indeed, it must be considered that, due to the kinetic coupling between the OMEs oxidation mechanisms, they must be optimized as a whole, i.e. with a single objective function, such to find the best trade-off between all the experimental targets. The very good performance of the kinetic mechanism is shown in Figure 2, too, in terms of laminar flame speed predictions. In this case, slight underpredictions can be observed for OME₄, while predictions for OME₂₋₃ are in much better agreement. However, it must be pointed out that the optimization margins for laminar flame speeds are much smaller than for the remaining experimental targets since, as already reported in literature [22], flame propagation is dominated by small-species chemistry (C₀-C₂).

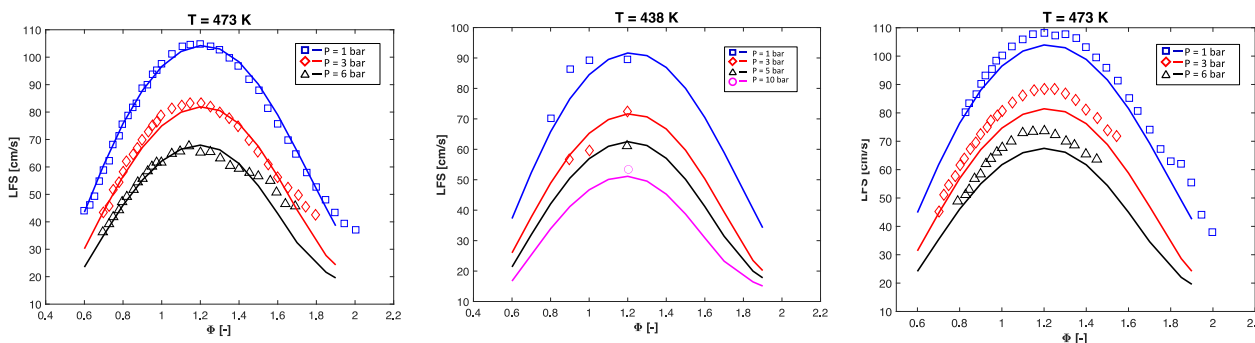


Figure 3. Comparison about the Laminar Flame Speed predictions of OME₂ (left), OME₃ (center) and OME₄ (right). Experiments [23–25] vs modeling predictions.

4. Conclusions

Chemistry of energy carriers has been gaining an increasing importance in the latest years, due to their potential key role in the energy transition scenario. In this work, a comprehensive kinetic modeling of oxymethylene ethers (OME₁₋₄) was hierarchically carried out by combining two novel methodologies, with the ultimate target of obtaining a compact, yet accurate and predictive mechanism. Drawing from master equation solution approaches [17], a lumping methodology was applied to simplify an OME₁₋₄ detailed kinetic mechanism, on turn developed by including the state-of-the-art submechanisms involving the core C₀-C₃, dimethyl ether, dimethoxymethane and longer-chain OMEs up to OME₄. As a second step, the obtained mechanism was optimized by leveraging a recently-developed data-driven technique, based on an evolutionary algorithm, and a single, Curve-Matching based, objective function in order to obtain the best trade-off among all the experimental datasets. The validation of the 176-species kinetic mechanism showed a satisfactory agreement throughout the whole experimental range, in terms of devices (shock tube, jet-stirred reactors, flow reactors, laminar flames) and operating conditions (low-to-high temperature, pressure and equivalence ratio). Such a mechanism can be rightfully considered as a first milestone for a wide-range implementation of OME chemistry into the full-scale CFD simulation of combustion devices. To make it feasible, such a coupling could need further extension for an additional simplification of the output mechanism, e.g. by a downstream implementation of additional mechanism reduction techniques [11]. Also, the successful application of the

lumping-optimization coupling on OME chemistry paves the way to an extensive use of such a procedure for a compact, efficient hierarchical modeling of other fuel classes [22].

References

- [1] European Parliament and the Council of the European Union, Off. J. Eur. Union 2018 (L 328) (2018) 82–209.
- [2] European Environment Agency, (2019).
- [3] K. Kohse-Höinghaus, Proc. Combust. Inst. 38 (1) (2021) 1–56.
- [4] A. Omari, B. Heuser, S. Pischinger, C. Rüdinger, Appl. Energy 239 (2019) 1242–1249.
- [5] U. Burke, K.P. Somers, P. O’Toole, C.M. Zinner, N. Marquet, G. Bourque, E.L. Petersen, W.K. Metcalfe, Z. Serinyel, H.J. Curran, Combust. Flame (2015).
- [6] S. Jacobs, M. Döntgen, A.B.S. Alquaity, W.A. Kopp, L.C. Kröger, U. Burke, H. Pitsch, K. Leonhard, H.J. Curran, K.A. Heufer, Combust. Flame 205 (2019) 522–533.
- [7] L. Cai, S. Jacobs, R. Langer, F. vom Lehn, K.A. Heufer, H. Pitsch, Fuel 264 (2020) 116711.
- [8] K. De Ras, M. Kusenberg, G. Vanhove, Y. Fenard, A. Eschenbacher, R.J. Varghese, J. Aerssens, R. de Vijver, L.-S. Tran, J.W. Thybaut, K.M. Van Geem, Combust. Flame 238 (2022) 111914.
- [9] T. He, Z. Wang, X. You, H. Liu, Y. Wang, X. Li, X. He, Fuel 212 (2018) 223–235.
- [10] E. Ranzi, A. Frassoldati, S. Granata, T. Faravelli, Ind. Eng. Chem. Res. 44 (14) (2005) 5170–5183.
- [11] T. Lu, C.K. Law, Prog. Energy Combust. Sci. 35 (2) (2009) 192–215.
- [12] C. Saggese, A. Frassoldati, A. Cuoci, T. Faravelli, E. Ranzi, Proc. Combust. Inst. 34 (1) (2013) 427–434.
- [13] A. Kéromnès, W.K. Metcalfe, K.A. Heufer, N. Donohoe, A.K. Das, C.J. Sung, J. Herzler, C. Naumann, P. Griebel, O. Mathieu, M.C. Krejci, E.L. Petersen, W.J. Pitz, H.J. Curran, Combust. Flame (2013).
- [14] W.K. Metcalfe, S.M. Burke, S.S. Ahmed, H.J. Curran, Int. J. Chem. Kinet. 45 (10) (2013) 638–675.
- [15] S.M. Burke, U. Burke, R. Mc Donagh, O. Mathieu, I. Osorio, C. Keese, A. Morones, E.L. Petersen, W. Wang, T.A. DeVertter, M.A. Oehlschlaeger, B. Rhodes, R.K. Hanson, D.F. Davidson, B.W. Weber, C.J. Sung, J. Santner, Y. Ju, F.M. Haas, F.L. Dryer, E.N. Volkov, E.J.K. Nilsson, A.A. Konnov, M. Alrefae, F. Khaled, A. Farooq, P. Dirrenberger, P.A. Glaude, F. Battin-Leclerc, H.J. Curran, Combust. Flame 162 (2) (2015) 296–314.
- [16] A. Burcat, B. Ruscic, Tech. Rep. ANL-05/20 (September) (2005) ANL-05/20 TAE 960.
- [17] L. Pratali Maffei, M. Pelucchi, C. Cavallotti, A. Bertolino, T. Faravelli, Chem. Eng. J. 422 (2021) 129954.
- [18] A. Bertolino, M. Fürst, A. Stagni, A. Frassoldati, M. Pelucchi, C. Cavallotti, T. Faravelli, A. Parente, Combust. Flame 229 (2021) 111366.
- [19] M. Fürst, A. Bertolino, A. Cuoci, T. Faravelli, A. Frassoldati, A. Parente, Comput. Phys. Commun. 264 (2021) 107940.
- [20] M.S. Bernardi, M. Pelucchi, A. Stagni, L.M. Sangalli, A. Cuoci, A. Frassoldati, P. Secchi, T. Faravelli, Combust. Flame 168 (2016) 186–203.
- [21] M. Pelucchi, A. Stagni, T. Faravelli, in: Comput. Aided Chem. Eng., 2019, pp. 763–798.
- [22] E. Ranzi, A. Frassoldati, R. Grana, A. Cuoci, T. Faravelli, A.P. Kelley, C.K. Law, Prog. Energy Combust. Sci. 38 (4) (2012) 468–501.
- [23] J.M. Ngugi, S. Richter, M. Braun-Unkhoff, C. Naumann, M. Köhler, U. Riedel, J. Eng. Gas Turbines Power 144 (1) (2021) 11014.
- [24] C. Fritsche, K.P. Shrestha, S. Eckart, F. Mauss, H. Krause, in: Proc. Eur. Combust. Meet., Naples, 2021, pp. 443–448.
- [25] S. Richter, T. Kathrotia, M. Braun-Unkhoff, C. Naumann, M. Köhler, in: Proc. Eur. Combust. Meet., Naples, 2021, pp. 1314–1319.

Novel process for cyan hydrogen production

Alessandra Di Nardo^{1*}, Maria Portarapillo¹, Danilo Russo¹, Almerinda Di Benedetto¹, Giuseppina Luciani¹, Gianluca Landi², Giovanna Ruoppolo²

¹ Dipartimento di Ingegneria Chimica, dei Materiali e della Produzione Industriale, Università degli Studi di Napoli Federico II, P. le Vincenzo Tecchio 80, 80125, Napoli.

² Istituto di Scienze e Tecnologie per l'Energia e la Mobilità Sostenibili STEMS-CNR, P. Le V. Tecchio 80, 80125, Napoli.

*Corresponding author E-Mail: alessandra.dinardo@unina.it

1. Introduction

Hydrogen is one of the main building blocks of the bulk and fine chemical industry as well as a promising energy carrier. The main advantages of hydrogen as an energy carrier are related to its high calorific value (HCV) and the absence of carbonaceous gases deriving from its combustion. However, most of hydrogen is currently produced from fossil fuels, via hydrocarbon reforming or pyrolysis processes or from renewable sources, via biological and thermochemical treatment of biomass and water splitting. Hydrogen production both from fossil fuels and from renewable sources shows several critical issues such as high operating temperature, high energy costs, limited yields, and selectivity.¹

In this work, we propose a novel process for cyan hydrogen production. The proposed process is a combination of *blue* H₂, derived from the traditional methane steam reforming with CO₂ capture and storage, and *green* H₂, produced by water electrolysis powered by renewable energy sources. More precisely, the proposed process combines H₂ production from water splitting and CO₂ capture and valorisation through the conversion of bio-derived chemicals to a high-value polymer, thus resulting in H₂ production and waste valorisation.

A patent on the process of cyan H₂ production has been submitted (submission number 102021000030875). It is based on redox cycles starting from bio-based organics and water under mild conditions, low pressure, and relatively low temperature. A solid catalyst is used which is a readily available and relatively cheap oxide with a wide range of industrial applications.

2. Methods

The process consists of a series of repetitive units, each composed by two consecutive steps in which organic reducing agent and water are charged alternately, as shown in Fig. 1. The gas phase is analyzed by gas chromatography (GC) technique, while the solid and liquid residue with FTIR and ATR-FTIR spectroscopy and TGA.

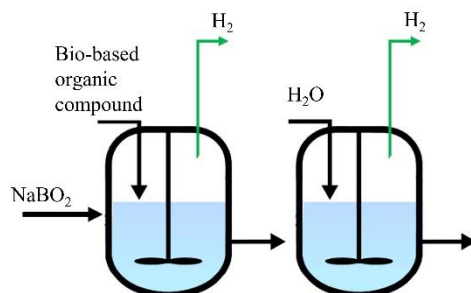


Figure 1. Scheme of the repetitive units in the cyan hydrogen production process.

3. Results and discussion

For two consecutive redox cycles, products consist of a gas phase stream rich and quite pure in hydrogen (as shown by GC analysis reported in Tab. 1), a solid residue composed by a mixture of the solid catalyst and an organic compound with high molecular weight, and a liquid phase that contains process intermediate products. The FTIR spectrum of the double-cycle residue shows the presence of bond vibrations typical of organic compounds, e.g., the stretching of the C-H bond in the zone 3000-2800 cm^{-1} .

	H₂	CO₂	OTHER
STEP 1	0,948	0,016	0,035
STEP 2	0,935	0,057	0,008
STEP 3	0,986	0,011	0,003
STEP 4	0,952	0,025	0,022

Table 1. GC analysis results.

4. Conclusions

The *cyan* hydrogen production process represents a totally innovative process. Surprisingly, starting from bio-based compounds and a by-product of low industrial interest, it is possible to produce a pure hydrogen stream under milder conditions than conventional processes and to capture the carbon in a high-value polymeric product.

References

- [1] C.C. Elam, et al., *Realizing the hydrogen future: the International Energy Agency's efforts to advance hydrogen energy technologies*, *Int. J. Hydrog. Energy* 28 (6) (2003) 601–607.

A comprehensive chemical kinetic framework for the thermo-catalytic pyrolysis of light hydrocarbons for value added carbon solids and turquoise hydrogen production.

Matteo Pelucchi^{1*}, Francesco Serse¹, Clarissa Giudici¹, Zhaobin Ding², Andrea Nobili¹, Davide Cafaro², Daniele Micale², Matteo Ferri², Mauro Bracconi², Matteo Maestri²

¹CRECK Modeling Lab. Department of Chemistry Materials and Chemical Engineering, Politecnico di Milano, Piazza Leonardo da Vinci 32, 20133, Milano

²Department of Energy, Politecnico di Milano, Via La Masa, 34, 20156, Milano

*Corresponding author E-Mail: matteo.pelucchi@polimi.it

1. Introduction

The large majority of fossil sources (gas, oil, coal, ~10 gigatonnes/yr) are exploited to generate energy through combustion, the main responsible of CO₂ emissions (>30 GT/yr) and of climate change. More than 12% of this energy is used by the metal industry to process materials that currently cannot be fully replaced by plastic polymers (e.g. low thermal/electrical conductivity, insufficient strength). In this context, value added carbon solids (VACS) pave the way for sustainable energy and large-scale advanced materials production as well as climate change mitigation¹. Specifically, the contextual production of hydrogen and carbon materials from methane and hydrocarbons cracking allows to overcome challenges in storage or disposal of carbon in the form of gas or liquid (e.g. CO₂) or solid side products, currently limiting the large scale implementation of carbon capture and storage technologies, by creating valuable products that can be used at large scale (above 1 million tons/yr) by displacing metals, ceramics, fertilizers and other materials with high carbon dioxide footprint. Beyond the widely known and implemented technology of carbon black (i.e. amorphous carbon) production, direct conversion of hydrogen rich feedstock such as methane or light hydrocarbons to VACS and H₂ is becoming of increasing scientific and industrial interest. This work proposes a first semi-detailed chemical kinetic framework, hierarchical and modular in nature, able to describe qualitatively and quantitatively the relationships between catalyst, reaction conditions and VACS (carbon black, carbon nanotubes-CNT) properties in the thermo-catalytic pyrolysis of methane.

2. Methods

An amorphous carbon model and a VACS growth model are coupled to a homogeneous gas-phase pyrolysis model to follow the transition from gas-phase to particulate matter particles in the gas phase and to carbon nanotubes (CNT) at the catalyst surface. The amorphous carbon model has been described and extensively validated in a previous work² and implements recent experimental and theoretical findings on the persistent radical behavior of particles and aggregates³. It discretizes heavy PAHs and soot particles into 25 sections of lumped pseudo species, called BINs, from 20 to over 10⁸ C-atoms, with a spacing factor of two. Each section consists of three subsections covering different H/C ratio, with thermochemical and diffusion properties computed through group additivity method and aerosol dynamics theory². Different reaction classes are implemented to rigorously describe the main chemical and physical pathways involving amorphous carbon such as particle inception, growth, coagulation, and dehydrogenation. Reference kinetic parameters for particles are derived by analogy from model PAHs molecules accounting for the transition from gas to solid as resulting from extensive density functional theory calculations on large PAHs molecules and graphene layers⁴. The flexibility of the amorphous gas-phase carbon model (soot) is here extended to include surface adsorption of gas phase species and successive growth of solid carbon deposits according to a similar systematic approach. Further extension to catalytic surface deposition mechanisms paves the way for a semi-detailed approach to turquoise hydrogen and carbon materials production modelling.

3. Results and discussion

Figure 1 summarizes the capability of the model to reproduce both (a) gas species formation and evolution (including hydrogen) and deposition rates as a function of temperature (b) and residence time (c) for propane

pyrolysis at $p=2.7$ kPa in a perfectly stirred reactor, as reported in [5]. Panel (d) shows the competition between amorphous carbon formation (black lines) in the gas stream and carbon deposition (red lines).

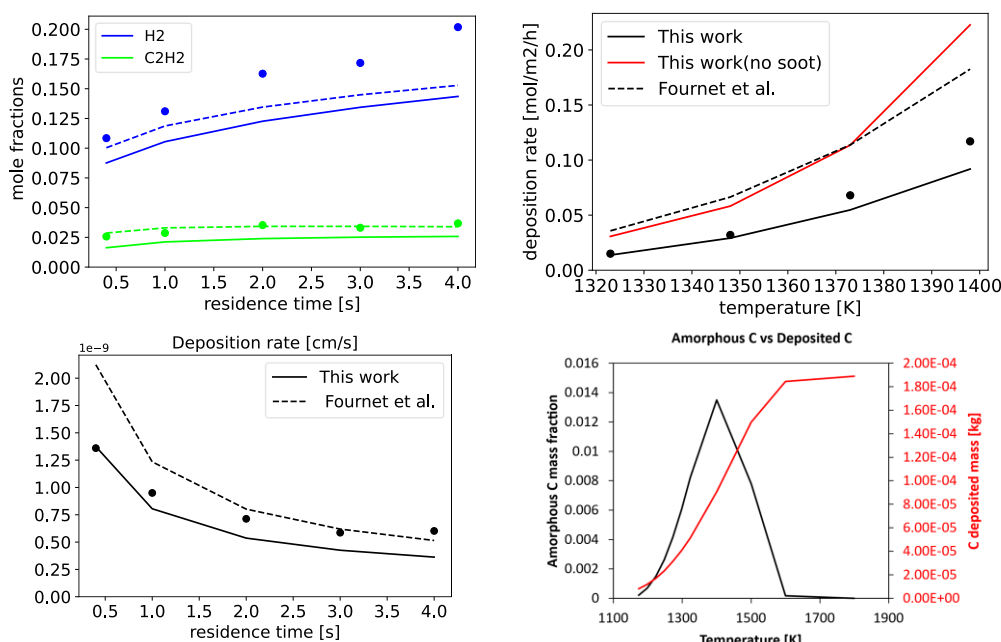


Figure 1. Model performances for methane pyrolysis: from gas-phase (a) to amorphous and pyrolytic carbon (b,c) and their competing formation (d). Experiments and dashed lines from [5], solid lines: this work.

4. Conclusions

The novel approach here presented overcomes the state-of-the-art modelling efforts for carbon materials growth. Indeed, available models are largely based on purely phenomenological approaches (i.e. power-law single step kinetics) of limited validity. This work provides a fundamentally based semi-detailed kinetic model describing both homogeneous gas-phase species evolution and amorphous carbon formation and surface carbon deposition. The approach has been extended also to catalytic CNT growth, providing promising results. Further model reduction makes our framework applicable to reactor scale simulations. However, a scarcity of kinetic relevant data suitable for model validation is highlighted in the literature. On one hand, this limits model reliability assessments, and on the other hand forces a systematic approach for modeling activities of such complex multiphase and multiscale phenomena. In addition, the systematic theoretical investigation of chemical pathways, potential energy surfaces and kinetic rate constants for H-abstraction reactions provides an effective methodological workflow for investigating heterogeneous gas/solid chemistry.

5. References

- [1] Pasquali, M., & Mesters, C. (2021). Opinion: We can use carbon to decarbonize—and get hydrogen for free. *Proceedings of the National Academy of Sciences*, 118(31).
- [2] Nobili, A., Cuoci, A., Pejpichestakul, W., Pelucchi, M., Cavallotti, C., & Faravelli, T. (2022). Modeling soot particles as stable radicals: a chemical kinetic study on formation and oxidation. Part I. Soot formation in ethylene laminar premixed and counterflow diffusion flames. *Combustion and Flame*, 112073.
- [3] Nobili, A., Maffei, L. P., Baggioli, A., Pelucchi, M., Cuoci, A., Cavallotti, C., & Faravelli, T. (2022). On the radical behavior of large polycyclic aromatic hydrocarbons in soot formation and oxidation. *Combustion and Flame*, 235, 111692.
- [4] Ding, Z.B., Di Marco, E., Pelucchi, M., Faravelli, T., Maestri, M., “First-principles assessment of the analogy between gas-phase and gas-solid H-abstraction reactions at graphene edges”, *Chem. Eng. J.* 377, 119691 (2019).
- [5] Lacroix, R., Fournet, R., Ziegler-Devin, I., & Marquaire, P. M. (2010). Kinetic modeling of surface reactions involved in CVI of pyrocarbon obtained by propane pyrolysis. *Carbon*, 48(1), 132-144.

Acknowledgements

The authors acknowledge the financial support from the industry members of the Carbon-Hub consortium.

Coupling machine learning and engineering judgment to reduce the cycle time of an industrial batch process

Francesco Sartori¹, Federico Zuecco², Pierantonio Facco¹, Fabrizio Bezzo¹, Massimiliano Barolo^{1*}

¹*CAPE-Lab – Computer Aided Process Engineering Laboratory
Department of Industrial Engineering, University of Padova
35131 Padova, ITALY*

²*BASF Italia SpA
40037 Pontecchio Marconi (BO), ITALY*

**Corresponding author E-Mail: max.barolo@unipd.it*

1. Introduction

Batch processes are ubiquitous in many industries producing low volumes of high value-added goods. They consist of cyclic repetitions of a sequence of operations, or recipe, performed in specialized process equipment. Even if the recipe is fully automated, variability may arise from several factors, e.g. variability in raw materials, environmental conditions, initial status of the equipment. For a fixed recipe, this variability can affect both the time duration of a batch run and the product quality. A large variability in the time duration of a processing step can cause that step to become a bottleneck for the entire process, leading to a loss of productivity.

In this study, an industrial batch reactor that is a key step in the industrial manufacturing of a polymer additive is studied. The available data historian revealed that the batch length experienced a large variability, but no apparent cause was initially identified to explain this behavior.

2. Results and conclusions

Data historians for this process included the logs of 468 batches operated along a time window of 12 months. Over this period, the batches carried out in the reactor under investigation (~7.5 m³ in volume) showed a length ranging between 0.9 and 2.8 h, with an average value of 1.4 h. This variability resulted to be a limit to the performance of the manufacturing system. Principal component analysis [1] applied to the dataset revealed that over 40 % of the historical batches had been affected by the anomalous intervention of a safety interlock. This anomaly proved to strongly correlate to an increase of the batch length, which in turn determined an increase in energy consumption. Reconfiguration of the interlock system resulted in a reduction of both batch length variability and average batch length (Figure 1). A 6-month assessment following the intervention on the interlock system revealed a reduction both of the batch length variability (which ranged between 0.8 and 2.1 h) and of the average batch length (which settled to 1.0 h).

Application of advanced analytics therefore allowed for a 29 % reduction in the average batch length and an 8 % reduction of the overall process cycle duration, together with significant energy savings.

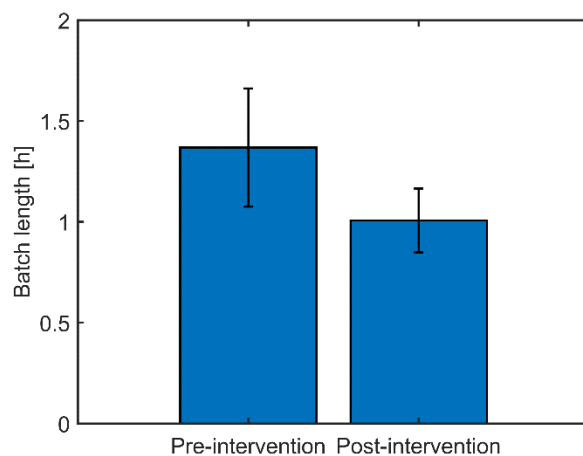


Figure 1. Comparison between the average batch length before and after the reconfiguration of the reactor safety interlock system

References

- [1] I.T. Jolliffe, J. Cadima, Principal component analysis: A review and recent developments, *Philos. Trans. R. Soc. A Math. Phys. Eng. Sci.* 374 (2016). <https://doi.org/10.1098/rsta.2015.0202>.

Feasibility study of a soft sensor predicting the vapor composition inside a flammable liquid storage tank

Gabriele Baldissone, Micaela Demichela, Davide Fissore

Politecnico di Torino, C.so Duca degli Abruzzi 24 Torino, Italy;

**Corresponding author E-Mail: gabriele.baldissone@polito.it*

1. Introduction

Often process plants include the storage of flammable liquids. Storage is generally considered a low-risk part of the plant, even if it can be involved in major accidents [1, 2, 3]

To guarantee tanks safety, the blanketing is usually adopted; despite it is a technique widely used in industry, it was scarcely investigated in the literature [4, 5]. In blanketing [6] the atmosphere inside the tank is kept far from the flammability conditions thanks to the presence of an inert gas, usually nitrogen. PSVs are installed on the tank to avoid damage from critical pressure deviations. In case of high pressure, the PSVs release the vapor phase contained in the tank. On the other hand, in the case of low pressure, the PSV allows air (or other gas) to enter. In this situation, the entry of air can bring the atmosphere in the tank in flammability conditions.

To keep the tank safe even when the PSV is open, it is necessary to know the composition of the vapor phase inside the tank. As an alternative to the direct monitoring of the composition of the vapor phase, a soft sensor can be adopted.

A soft sensor allows to obtain an indirect measurement of a variable from the measurement of related variables, through a mathematical model [7]. In the specific case, by measuring the inlet and outlet flow rates and the liquid level, an estimate of the composition of the atmosphere inside the tank is obtained.

This paper presents a first feasibility test of a soft sensor to estimate the composition of the vapor phase of a storage tank of liquid methanol. To develop the soft sensor, a dynamic model of the tank operation is used, as detailed in the subsequent paragraphs.

2. Methods

A dynamic model of the tank is developed as a preliminary step for the development of the soft sensor. The tank model is used to get the data required for soft sensor training and subsequent soft sensor validation.

Dynamic model

An isothermal model of the tank operation has been developed, which derives the liquid level and the composition of the internal atmosphere of the tank as a function of the inlet and outlet flow rates, according to the following equations:

$$\left\{ \begin{array}{l} \frac{dN^L}{dt} = N_{L,in} - N_{L,out} - A \cdot \phi \\ \frac{dN^V}{dt} = N_{Nit,in} + N_{Air,in} + A \cdot \phi - N_{V,out} \\ \frac{dN_{Nit}^V}{dt} = N_{Nit,in} + N_{Air,in} \cdot y_{Air,Nit} - N_{V,out} \cdot y_{Nit} \\ \frac{dN_{Ox}^V}{dt} = N_{Air,in} \cdot y_{Air,Ox} - N_{V,out} \cdot y_{Ox} \\ \frac{dN_{Met}^V}{dt} = A \cdot \phi - N_{V,out} \cdot y_{Met} \\ \phi = k_{Met}^v (y_{Met}^* - y_{Met}) \\ V_{TOT} = V_L - V_V \end{array} \right.$$

where N^L is the number of moles of liquid, in the tank $N_{L,in}$ is the flow rate of liquid methanol entering the tank, $N_{L,out}$ is the flow rate of liquid methanol leaving from the tank, A is the tank area, ϕ is mass transfer rate between the liquid and the gas phase. N^V is the number of moles of gas in the tank, $N_{Nit,in}$ is the flow rate of nitrogen entering the tank, $N_{Air,in}$ is the flow rate of air entering the tank, $N_{V,out}$ is flow rate of gas leaving from the tank. N_{Nit}^V is the number of moles of nitrogen in the gas phase, N_{Ox}^V is the number of moles of oxygen in the gas phase and N_{Met}^V is the number of moles of methanol in the gas phase. Instead $y_{Air,Nit}$ is the nitrogen concentration in the air, $y_{Air,Ox}$ is the oxygen concentration in the air, y_{Nit} is the nitrogen concentration in the tank gas phase, y_{Ox} is the oxygen concentration in the tank gas phase and y_{Met} is the methanol concentration in the tank gas phase. And k_{Met}^v is the methanol transfer coefficient between liquid and gas phase, y_{Met}^* is the equilibrium concentration of methanol in the gas phase. V_{TOT} is the tank volume, V_L is the liquid volume and V_V is the gas volume.

For the calculation of the pressure the law of ideal gases is used.

The incoming air flow and the outgoing gas flow through the PSV is calculated according to the API2000:1998.

The model estimates the composition of the vapor phase of a tank containing methanol, of a capacity of 100m³. Tank's height is approx. 5.3 m and 245 kg/h of methanol are removed from the tank to be used in the process downstream. With the nitrogen supply, the pressure inside the tank is kept constant. Due to process consumption, when the methanol level falls below 30%, the tank is re-filled to 80% of its capacity. The PSV is set to intervene at an overpressure of 7 kPa and a depression of 1 kPa.

Soft sensor

A soft sensor is developed to estimate the composition inside the tank. The soft sensor estimates the concentration of nitrogen and methanol vapors in the atmosphere inside the tank, the concentration of oxygen is obtained as a complement to one of the other concentrations. The soft sensor uses the structure shown in figure 1. The soft sensor consists of two neural networks, one estimates the concentration of methanol and the other the concentration of nitrogen.

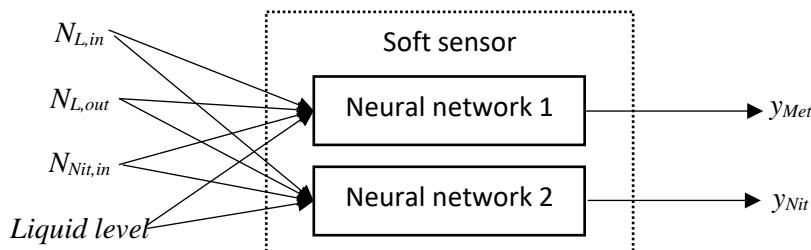


Figure 1. Soft sensor structure

To develop the neural networks constituting the soft sensor, a set of data is generated that describes the operation of the tank in different conditions. The data set obtained is used for the training of the neural networks.

Subsequently, the neural networks are tested in different operating conditions to evaluate the accuracy.

3. Results and discussion

In the test case study, after around 8353 h (5000 time steps of 10 minutes, needed to reach the steady state conditions for the initial conditions here considered) the nitrogen flow is reduced to 30% of the nominal value, with a step deviation. As a result, a pressure reduction occurs, and air enters following the intervention of the PSV. After another 5000 time steps, the nitrogen flow is restored.

Figure 2 shows the nitrogen, methanol and oxygen concentrations trends, both obtained from the model and from the soft sensor. Figure 2 shows that the soft sensor approximates the trend of the concentrations obtained with the model.

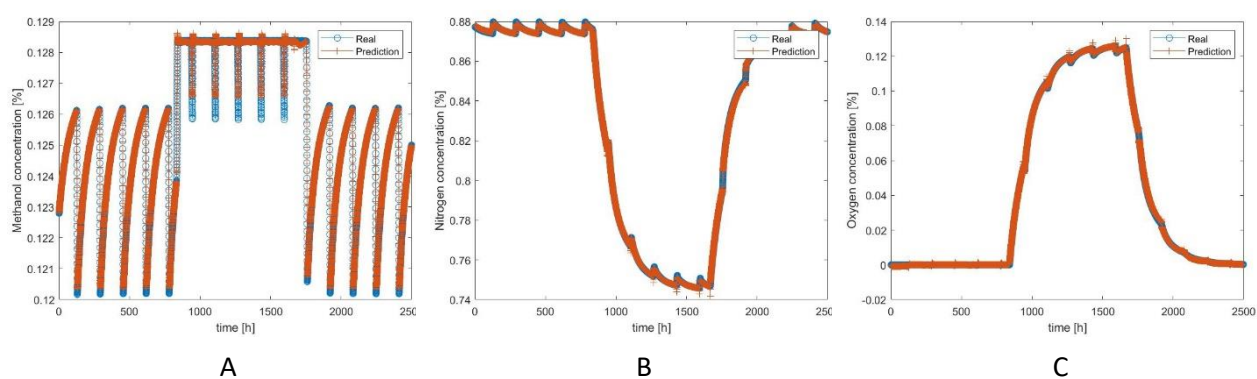


Figure 2. Composition trend, A: Methanol, B: Nitrogen, C: Oxygen

Figure 3 shows the prediction error of the soft sensor, identified as the difference between the values obtained from the model and those obtained from the soft sensor. As shown in the Figure, the maximum prediction error is about 0.6%.

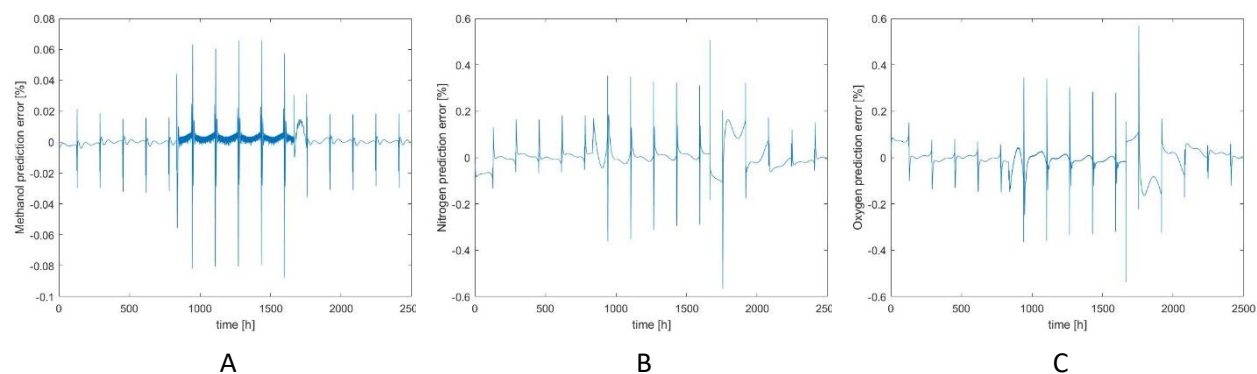
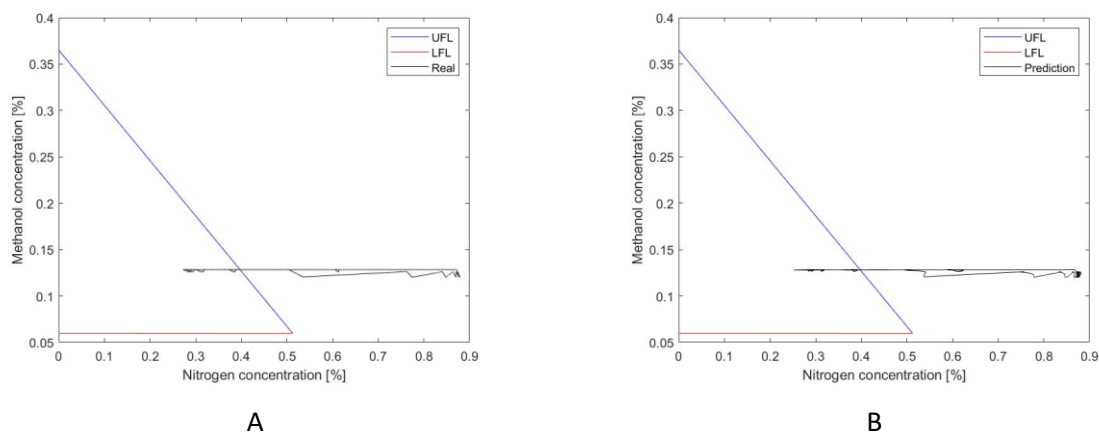


Figure 3. Prediction error A: Methanol, B: Nitrogen, C: Oxygen

Figure 4 shows the trend of the composition of the atmosphere inside the tank. The composition of the internal atmosphere of the tank enters the flammability peninsula, the flammability peninsula is obtained in accordance with Ma [8]. Figure 4 indicates that the soft sensor returns a trend close to that obtained from the model.

Figure 4. Atmosphere composition trend A: Real, B: Soft sensor



4. Conclusions

To keep tanks that contain flammable liquids safe, blanketing is usually adopted. In case of a pressure drop in the tank, generally related to the unavailability of blanketing gas, the opening of the PSV allows air to enter. The entry of air can bring the the atmosphere inside the tank to flammable conditions.

A soft sensor is developed to estimate the composition inside the tank. The soft sensor, based on the inlet flow rate of liquid and nitrogen, the outflow of liquid and the liquid level, that are usually monitored, or, in any case, easier to be measured than the internal concentrations, estimates the composition of the atmosphere inside the tank. The soft sensor consists of 2 neural networks, one estimating the nitrogen concentration and the other the concentration of methanol. The oxygen concentration is obtained as a complement to one.

The soft sensor has been tested in a case study in which the nitrogen flow is reduced to 30% and then restored. In this case, the soft sensor reported results in line with what is obtained from the model.

These encouraging initial results will be further extended, gradually reducing the initial simplifying hypothesis adopted in the model.

References

- [1] N. C. Markatos, C. Christolis, C. D. Argyropoulos, Mathematical modeling of toxic pollutants dispersion from large tank fires and assessment of acute effects for fire fighters, *International Journal of Heat and Mass Transfer*, . 52(2009) 4021–4030.
- [2] D. Wang, P. Zhang, L. Chen, Fuzzy fault tree analysis for fire and explosion of crude oil tanks, *Journal of Loss Prevention in the Process Industries*, 26(2013) 1390–1398.
- [3] J. I. Chang, C. C. Lin, A study of storage tank accidents, *Journal of Loss Prevention in the Process Industries*, 19 (2006) 51–59.
- [4] D. A. Crowl, J. F. Louvar, *Chemical Process Safety: Fundamentals with Applications*, Prentice Hall, Upper Saddle River, 2002.
- [5] T. J. De Paola, C. A. Messina, Nitrogen Blanketing, *Plant operations progress*, 3(1984) 203–212.
- [6] Y. Amrouche, C. Dave, K. Gursahani, R. Lee, L. Montemayor, General rules for aboveground storage tank design and operation *Chemical Engineering Progress*, 98 (2002) 54–58.
- [7] L. Fortuna, S. Graziani, A. Tizzo, M. G. Xibilia, *Soft Sensors for Monitoring and Control of Industrial Processes*, London: Springer, 2007.
- [8] T. Ma, A thermal theory for estimating the flammability limits of a mixture, *Fire Safety Journal*, 46(2011) 558–567

Identification of cyber-risks due to the malicious manipulation of Industrial Automation and Control Systems in chemical and process facilities

Matteo Iaiani^{1*}, Alessandro Tugnoli¹, Valerio Cozzani¹

*1 LISES – Dipartimento di Ingegneria Civile, Chimica, Ambientale e dei Materiali,
Alma Mater Studiorum – Università di Bologna, via Terracini n.28, 40131 Bologna, Italy*

**Corresponding author E-Mail: matteo.iaiani@unibo.it*

1. Introduction

Cyber-attacks to Industrial Automation and Control Systems (IACSs) in chemical and process facilities such as the Basic Process Control System (BPCS) and the Safety Instrumented System (SIS), are of major concern due to the potential severity of consequences on humans, assets, and the environment, which are comparable to those caused by safety-related causes [1–3].

The ISA/IEC 62443 series of standards provide a systematic and practical approach to address cybersecurity issues of IACSs. In particular, it requires the evaluation of all the impacts (including those on the physical plant (process equipment, storage equipment, interconnections)) that can result from intentional malicious attacks to the BPCS and SIS in order to evaluate the actual level of cyber-risk of a facility and implementing proper cybersecurity countermeasures for its reduction. However, neither specific methods nor guidelines are provided to conduct the proposed approach. Similarly, also the common methodologies dedicated to process plant Security Vulnerability/Risk Assessment (SVA/SRA) such as the VAM-CF methodology, the CCPS methodology, and the one proposed by API RP 780, consider attacks to the BPCS and the SIS in the evaluation, but no specific procedures for assessment of the link between malicious manipulations and consequences is provided [4].

In the present study a toolbox was developed to fill the gap in the availability of tools aimed at supporting cyber-risk identification in the context of SVA/SRA and cybersecurity risk assessment of ISA/IEC 62443.

2. Methods

Two complementary approaches were used. The first approach consisted in the population and analysis using Exploratory Data Analysis (EDA) of a dedicated database of cybersecurity-related incidents that occurred in chemical and process facilities worldwide in the last 50 years. Data was gathered from a broad set of sources (open source databases on industrial accidents/incidents, scientific literature, and the web) using a specific set of keywords translated in different languages (English, Italian, German, French and Spanish).

The second approach consisted in the development and application of two systematic qualitative procedures in order to systematically identify the possible scenarios affecting the operability and system integrity of a chemical process plant, of the malicious manipulations by which they may be initiated, and of the existing inherent/passive and active/procedural safeguards in place (safety/security barriers). Both the methodologies were demonstrated on case studies (upstream onshore Oil&Gas plant for the preliminary treatment of crude oil and offshore Oil&Gas platform for natural gas production).

3. Results and discussion

A database of 82 cybersecurity-related incidents was populated (see the structure in Figure 1a). Its analysis using EDA evidenced important differences as regards the geographical distribution, the distribution among the industrial sectors, the impacts of the attacks, the type of attackers and the target system infected. The analysis of a sub-set of more detailed incidents allowed also the identification of the general steps of a cyber-attack, the main hacking techniques used by the attackers and the more common cybersecurity countermeasures. Overall, the results obtained can be used to define generic cybersecurity-related scenarios that can be employed by authorities and practitioners as a reference starting point to undertake a case specific

cybersecurity risk assessment (approach very consolidate in the safety management practice). The detailed method used and results obtained are reported in [2].

Two rigorous systematic qualitative procedures for cyber-risk identification were developed, exploiting a reverse-HazOp concept (see the flowchart in Figure 1b): PHAROS (Process Hazard Analysis of Remote manipulations through the cOntrol System) for the analysis of system integrity and POROS (Process Operability analysis of Remote manipulations through the cOntrol System) for the analysis of process operability. Overall, the results from PHAROS and POROS application can be used by a team of experts to perform a case-specific cyber risk identification, to define protection requirements for the safeguards in place (inherent/passive and procedural/active), and to support the design of the network systems (e.g. network segmentation). Detailed information on PHAROS and POROS can be found in [5] and [6] respectively.

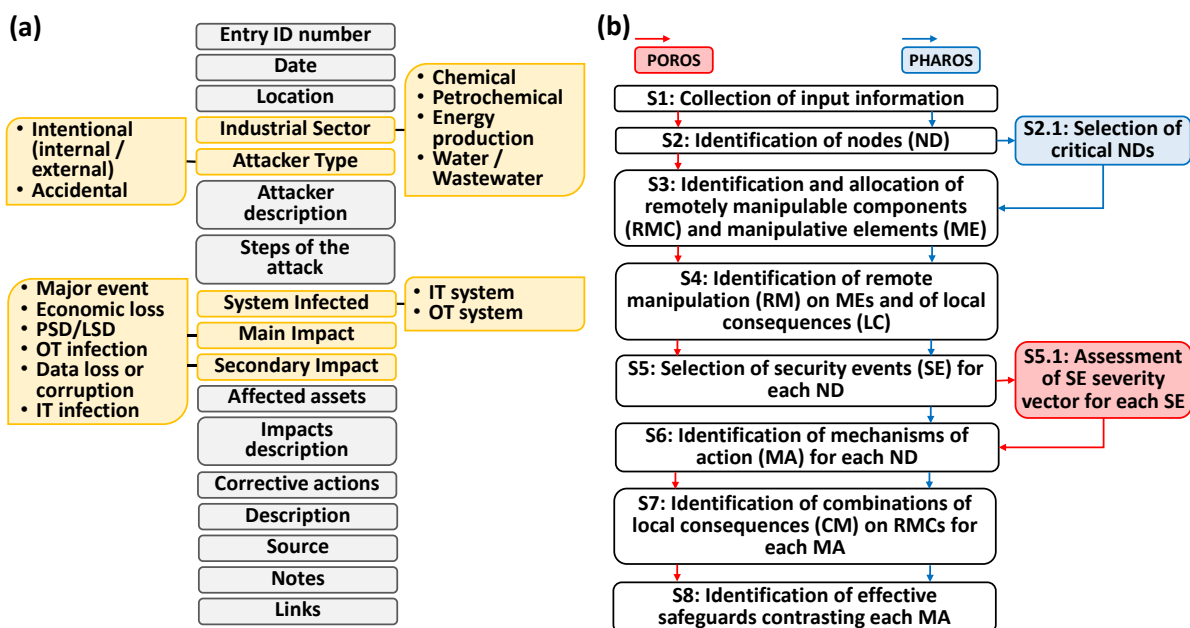


Figure 1. a) Structure of the developed database (grey boxes: free text fields; orange boxes: itemized fields); b) Flowchart of POROS (red arrows) and PHAROS (blue arrows).

4. Conclusions

A synergic toolbox aimed at supporting cyber-risk identification in the context of SVA/SRA methodologies and the cybersecurity risk assessment proposed by ISA/IEC 62443 was developed and tested on case studies that proved the quality of the results that can be achieved. The provided toolbox paves the way to future developments in strategies for a more secure network architecture design and supports quantitative approaches for assessing the probability of success of a cyber-attack aiming at interfering with the operability and/or system integrity of a process plant.

References

- [1] G. Landucci, G. Reniers, Preface to special issue on quantitative security analysis of industrial facilities, *Reliab. Eng. Syst. Saf.* (2019).
- [2] M. Iaiani, A. Tugnoli, S. Bonvicini, V. Cozzani, Analysis of Cybersecurity-related Incidents in the Process Industry, *Reliab. Eng. Syst. Saf.* 209 (2021) 107485.
- [3] M. Iaiani, V. Casson Moreno, G. Reniers, A. Tugnoli, V. Cozzani, Analysis of events involving the intentional release of hazardous substances from industrial facilities, *Reliab. Eng. Syst. Saf.* 2012 (2021) 107593
- [4] A. Matteini, F. Argenti, E. Salzano, V. Cozzani, A comparative analysis of security risk assessment methodologies for the chemical industry, *Reliab. Eng. Syst. Saf.* 191 (2019) 106083
- [5] M. Iaiani, A. Tugnoli, S. Bonvicini, V. Cozzani, Major accidents triggered by malicious manipulations of the control system in process facilities, *Saf. Sci.* 131 (2021) 105043
- [6] M. Iaiani, A. Tugnoli, P. Macini, V. Cozzani, Outage and asset damage triggered by malicious manipulation of the control system in process plants, *Reliab. Eng. Syst. Saf.* 213 (2021) 107685

An innovative application of the Advanced Recursive Operability Analysis to the Bhopal Accident Reconstruction

Federico Florit¹, Marco Barozzi², Martina Silvia Scotton², Sabrina Copelli^{2*}

¹ Politecnico di Milano, Dipartimento di Chimica, Materiali ed Ingegneria Chimica "G. Natta", via Mancinelli 7, Milano (MI), IT

² Università degli Studi dell'Insubria, Dipartimento di Scienza e Alta Tecnologia, via Valleggio 9, Como (CO), IT

* Corresponding author E-Mail: sabrina.copelli@uninsubria.it

1. Introduction

Nowadays chemical industry plays a leading role in our daily life, satisfying the needs of a large portion of the world population. The safety of chemical products is guaranteed by rigorous standards and control systems, which lead the chemistry sector to be one of the most prepared and equipped industrial sectors in terms of safety and health at work. Nevertheless, it is important to remember that the current success in terms of awareness and perception of chemical hazards owes much of its development to the lessons learned, at great cost, after the occurrence of catastrophic accidents.

The 70s and 80s were the scene of some of the biggest industrial accidents in the world, among which we can find the disasters of Flixborough, Seveso and Pasadena. But historically, the most serious accident is undoubtedly the Bhopal disaster. We will never know the precise number of people who died that terrible night; however, more than 25,000 victims were estimated and more than 120,000 people still suffer today from discomfort due to MIC exposure.

Aim of this work was to demonstrate, using an Advanced Recursive Operability Analysis (AROA)^[1,2], that the dynamics of whatever accidental scenario can be always traced whether a non-standard Hazard Identification (HI) procedure is carried out on the final operative plant. The terms "non-standard" refers to an analysis carried out under operative conditions which deviate from the normal plant operations (with respect to all process variables deviations are normally computed), e.g. during a temporary shut-down.

In the Bhopal case study, the presence of such non-standard operative conditions had led to multiple losses of safety at very different levels: plant equipment operations, control systems efficiency, presence of active protective measures and ad hoc procedures to be followed by the operators in case of emergency. Such losses of safety could not be traced carrying out a standard HI procedure.

2. Methods

Quantitative Risk Analysis (QRA) is a complex task performed to either quantify or minimize the hazards associated with the operation of potentially dangerous installations. A QRA procedure can be ideally subdivided into four main phases: 1) Hazards Identification (HI); 2) Frequency Estimation (FE); 3) Accident Consequence Evaluation (ACE); 4) Individual and Societal Risk Calculation (I&SRC). This work considers only the first two phases. Hazard identification represents a fundamental activity: not identified hazards will remain hidden until the occurrence of the related accidents. Among the various available methodologies, HazOp is the most known and widely applied. On the other hand, the probabilistic quantification of the hazardous states frequency is usually done using a Fault Tree Analysis (FTA). Unfortunately, FTA is a time-consuming task because of the general difficulty of extracting the necessary information from HazOp tables. To make FTA less expensive, an Advanced Recursive Operability Analysis (AROA) was applied to the portion of the plant involved in the Bhopal accident. AROA is based on a procedure which allows collecting plant perturbations data in a structured way. At the end of the AROA study, it is possible to systematically construct all fault trees of interest.

A typical AROA format presents the following fields to be correctly compiled:

1. Node – Process variable – Deviation
2. Causes
3. Consequences due to failure of safety functions
4. Plant state following the correct intervention of safety functions
5. Protections, made up by: a. Alarms; b. Operator actions; c. Automatic safety systems
6. Remarks

The AROA format must be used exclusively to collect information on the relationships between process variables deviations. Indeed, with the aim of simplifying the work of the HazOp team (i.e. to reduce the cost of HazOp analysis), the information to be collected will concern mainly plant perturbations (i.e. the relationships among cause-consequences of process variables deviations) leaving out the construction of fault trees of protection and control systems, as well as the analysis of spurious failures.

In the present work, an AROA was applied considering the deviations of the different process variables with respect to the non-standard state of the plant (that was, for the Bhopal plant, a shutdown state before plant dismissing). This is an important difference with respect to all the already presented applications of the ROA, which consider deviations from standard (or normal) operative conditions of the plant. Such a modification was necessary to correctly describe the dynamics of the Bhopal accident.

3. Results and discussion

Figure 1 reports the simplified P&ID of the portion of the Bhopal plant involved in the accident.

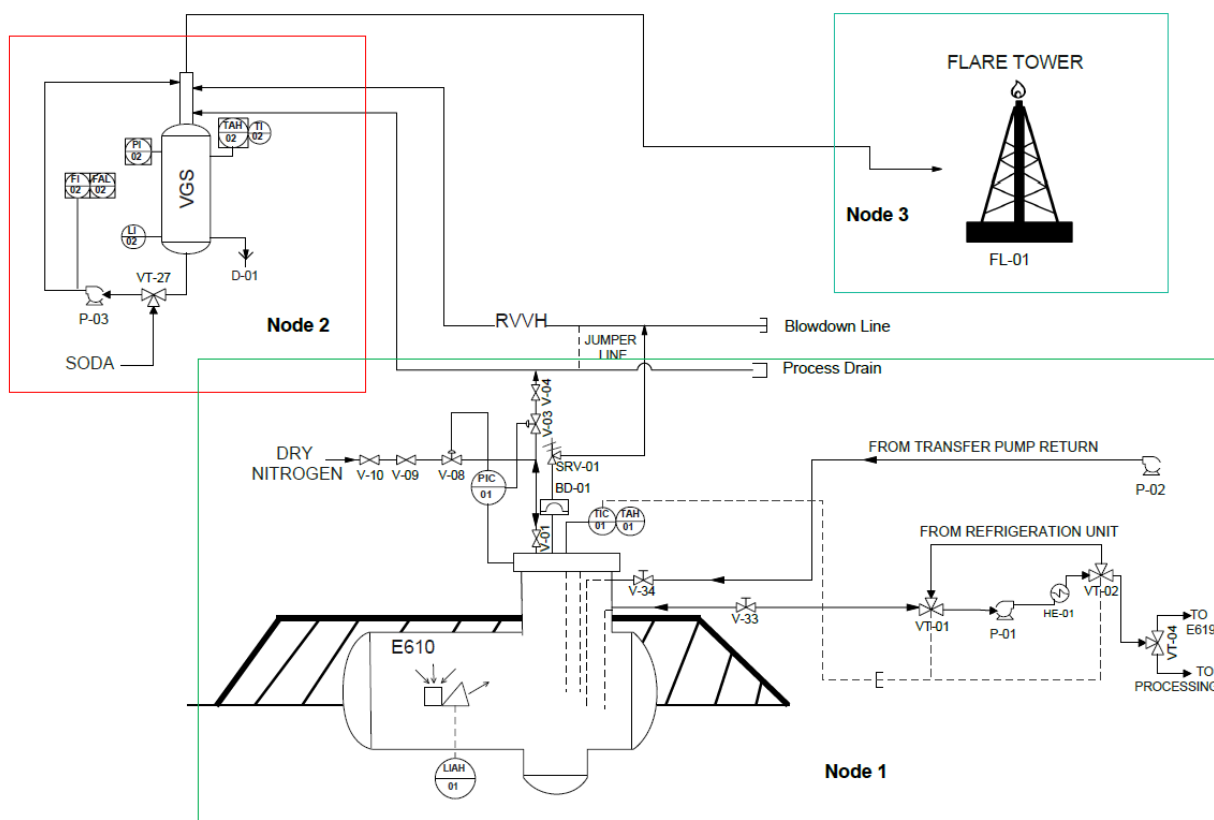


Figure 1. Simplified P&ID of the Bhopal plant (portion involved in the accident).

Referring to the P&ID reported in Figure 1, the system can be divided into 2 nodes:

- Node 1: identifies all the lines and equipment belonging to the E-610 tank. Process variables considered and their deviations (between square brackets) are reported in the following:
 1. (L) MIC level [h]
 2. (T) Temperature [h]
 3. (P) Pressure [h, hh, hhh]
- Node 2: identifies all the lines and instrumentation belonging to the safety devices (Vent Gas Scrubber - VGS and torch). Process variables considered and their deviations (between square brackets) are reported in the following:
 1. (F_{SC}) Flow rate of caustic soda [l]
 2. (F_{MIC}) MIC Flow rate [h]
 3. (C_{MIC}) MIC concentration in atmosphere [h]

The deviations indicated by the letters in the square brackets stand for high (h) and low (l). The repetition of the letter expresses an intensification of the deviation. For example (hh.P) symbolizes a very high pressure, while (hhh.P) corresponds to an even greater pressure. The information is represented using a classic AROA model in Table 1.

Table 1. AROA of the Bhopal plant (accident section)

Node 1: Tank E-610								
R E C	Node- Deviation- Variable	Causes	Consequences due to protections failure	Plant state following the correct intervention of safety functions	Alarms	Operator Actions	Automatic safety systems	Top Event
1	1.h.L [%] (L>50)	P-02 fail to operate OR Human Error (Excessive MIC Loading or V-34 open)	1.h.P	Normal Level State due to Human Action	LIAH-01	Manual intervention on V-34	-	No
2	MIC reaction with water	Water (from cleaning operations) AND Human Error (V-34 open)	1.h.T	1.h.T	-	-	-	No
3	1.h.T [°C] (T>11)	REC 2 OR HE-01 no cooling OR P-01 fail to operate OR VT-01 fail closed OR VT-02 fail closed OR	1.h.P	1.h.P	TAH-01	Check on HE-01	-	No

		TIC-01 fail low							
4	1.h.P [psig] (25<P<40)	1.h.L OR 1.h.T OR PIC-01 fail low OR V-03 fail closed OR V-04 closed (fail closed OR HE)	1.hh.P 2.h.F _{MIC}	1.hh.P	Discharge to VGS (2.h.F _{MIC})	-	-	RD-01 SRV-01	No
5	1.hh.P [psig] (40<P<300)	1.h.P	1.hhh.P	Tank collapse	Tank Damaged but not collapsed	-	-	Resistance to Rupture	TE1
6	1.hhh.P [psig] (P>300)	1.hh.P	Tank collapse	Tank Damaged but not collapsed	-	-	Resistance to Rupture	TE1	
Node 2: Vent Gas Scrubber and Node 3: Torch									
REC	Node-Deviation-Variable	Causes	Consequences due to protections failure	Plant state following the correct intervention of safety functions	Alarms	Operator Actions	Automatic safety systems	Top Event	
7	2.1.F _{SC}	P-03 fail to operate OR VT-27 fail closed	2.h.F _{MIC}	2.h.F _{MIC}	FAL-02	-	-	No	
8	2.h.F _{MIC}	REC 4 OR 2.1.F _{SC} OR REC 5*	3.h.F _{MIC}	C _{MIC} <TLV (atm)	-	-	FL-01	No	
9	3.h.F _{MIC}	2.h.F _{MIC}	C _{MIC} >>TLV (Toxic Release)	C _{MIC} >>TLV (Toxic Release)	-	-	-	TE2	

Analyzing Table 1, two main potential Top Events (TEs) can be easily identified:

1. The physical collapse of E-610 tank due to an uncontrolled increase in pressure beyond the maximum tolerable value;
2. The release of toxic gas into the atmosphere if both VGS and flare fail to intervene.

Starting from the AROA Table, it was possible to automatically generate the related FTs. As the sake of example, Figure 2 reports the Fault Tree corresponding to TE1.

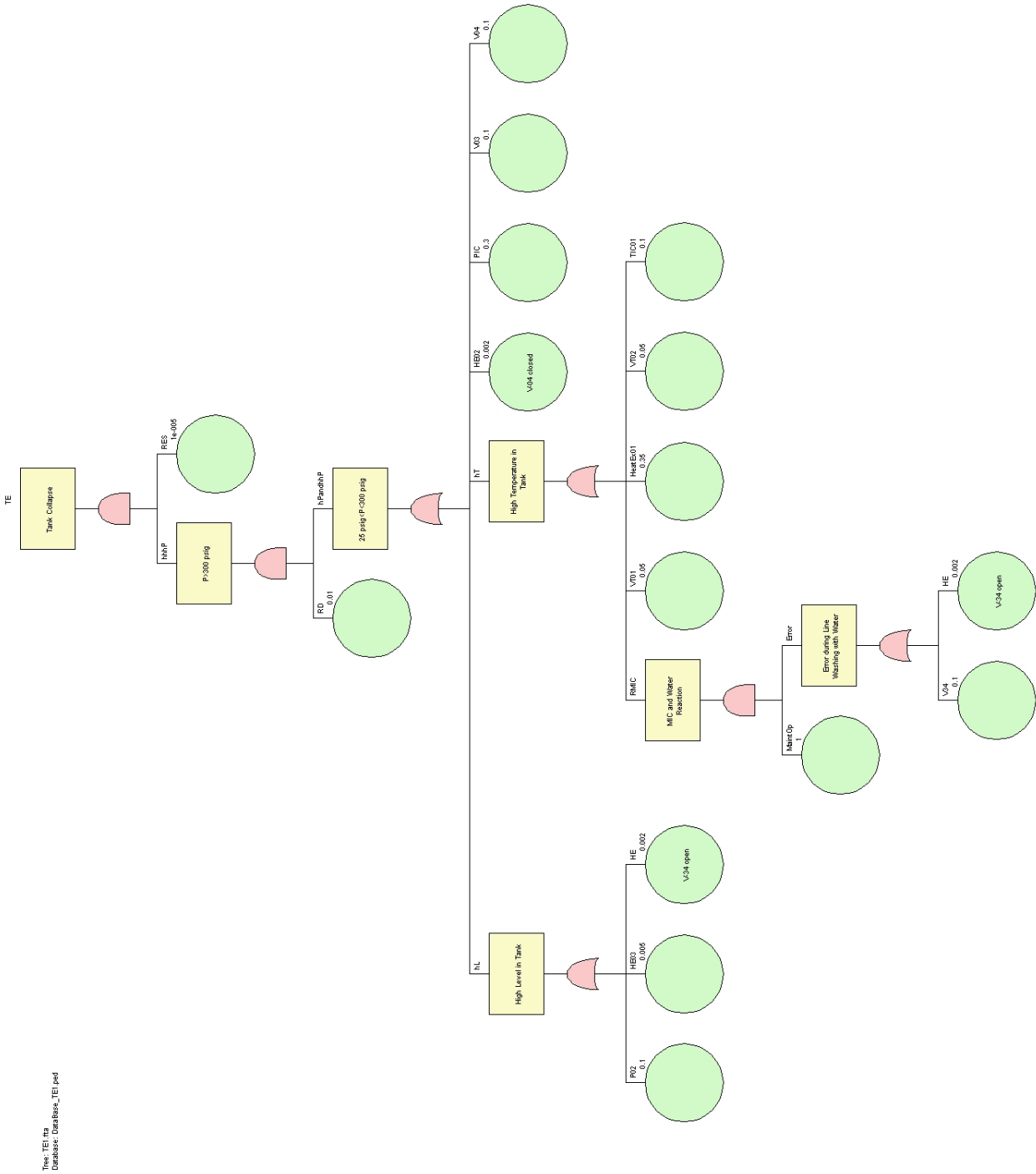


Figure 2. Fault tree for TE1.

From the calculation of the fault tree related to Node 1, we found the presence of 12 Minimal Cut Sets (MCS) 11 of order 3 and 1 of order 4, with respect to a total number of primary events which was equal to 15. The calculated TE probability was: $7.59 \cdot 10^{-8}$; such a value can be considered as acceptable because it is lower than the usually adopted reference value of 10^{-6} (base: 1 year of mission time). Concerning the relative importance of the different components of the system in determining the TE (collapse of the tank), we found that the failure of the rupture disk (RD) and the exceeding of the resistance of the tank material are the most important components, followed by the heat exchanger (HE-01) and the tank pressure controller (PIC-01). All these

components must receive more attention with respect to the others; this means that they must be subjected to frequent maintenance operations because they contribute heavily to the occurrence of the TE.

Regarding the tree related to Node 2, 13 MCS of order 2 and 1 of order 3 were calculated (over 17 total primary events). The calculated probability value obtained was $7.94 \cdot 10^{-1}$ that, considering a risk acceptability value equal to 10^{-6} , is a not acceptable value. The calculation showed that the flare together with the failure of the heat exchanger unit and the pressure controller constituted the most important components of the plant and, therefore, should have required greater attention and maintenance.

It is important to notice that, considering the state of “temporary shutdown” of the plant, the unavailability of the flare is 1; in case of normal operating conditions such a value would have been 2 or 3 order of magnitude lower. This is a very interesting point which highlights the importance of considering the deviations not only from normal plant state but also from upset plant state due to temporary operations.

4. Conclusions

This work highlighted how fundamental the contribution of a complete and adequate risk analysis is in the field of industrial prevention of potentially dangerous scenarios such as major accidents.

From the recursive operability analysis related to E-610 tank and associated equipment, it was found that the release of toxic gas into the atmosphere was to be considered as the worst unwanted event. Of course, it should be noted that the analysis carried out concerned only the E-610 system, which represented only a small part of a much larger and more complex plant. Assuming a detailed study of all the subsystems of the Bhopal chemical industry, countless TEs of similar nature to the one here analyzed could have been traced.

Using a modified version of the AROA it was possible to demonstrate that the dynamics of the Bhopal disaster was similar to that of all the major industrial chemical accidents: some deviations of the process variables have occurred when the plant was operating in a non-standard state as either a temporary shutdown or a maintenance, etc..

The lack of suitable procedures and protection devices specifically designed to operate when the plant is in a non-standard state is the first point of “no return” which foregoes the occurrence of an industrial accident: such evidence was demonstrated even in the case of Bhopal accident.

References

- [1] P.M. Contini, S. Contini, S. Copelli, R. Rota, M. Demichela, Safety and Reliability of Complex Engineered Systems - Proceedings of the 25th European Safety and Reliability Conference, ESREL 2015 (2015) 347-355
- [2] M. Barozzi, S. Contini, M. Raboni, V. Torretta, V. Casson Moreno, S. Copelli, Journal of Loss Prevention in the Process Industries 71 (2021) art. no. 104468

Risk of Major Accidents in Plants producing Energy from Wastes

Sabrina Copelli^{1*}, Marco Barozzi¹, Martina Silvia Scotton¹, Vincenzo Torretta², Federico Florit³

¹ *Università degli Studi dell'Insubria, Dipartimento di Scienza e Alta Tecnologia, via Valleggio 9, Como (CO), IT*

² *Università degli Studi dell'Insubria, Dipartimento di Scienze Teoriche e Applicate, via Dunant 2, Varese (VA), IT*

³ *Politecnico di Milano, Dipartimento di Chimica, Materiali ed Ingegneria Chimica "G. Natta", via Mancinelli 7, Milano (MI), IT*

** Corresponding author E-Mail: sabrina.copelli@uninsubria.it*

1. Introduction

Biomasses and wastes are a renewable source of energy whose main characteristics are to be: 1) intrinsically linked to the territory as they are available everywhere and widely distributed; 2) one of the tools indicated for the reduction of greenhouse gas emissions into the atmosphere: the CO₂ balance relating to the conversion of biomasses and wastes into energy is considered neutral. Due to their diversity, numerous conversion technologies are available, producing many final forms of energy: electricity (thermal energy), liquid fuels, biogas, synthesis gas, etc.

However, the technologies currently available for the conversion of biomasses and wastes into useful forms of energy entail critical issues from the point of view of either the operability of the plants or the health of the workers. Therefore, even for these types of systems, it is not possible to neglect the conduction of an accurate risk assessment. However, universally accepted hazard identification techniques such as HazOp are too expensive both in terms of money, personnel employed, and time dedicated to the analysis. Furthermore, they are not strictly targeted to the type of plant being analyzed. Therefore, in this work, a simple but effective hazard identification technique called Advanced Recursive Operability Analysis (AROA) was selected. Such a technique, coupled with others for either the qualification of the failure modes of plant components or the quantification of the probability of occurrence of accidents, allowed to carry out a complete risk analysis with limited time efforts.

The AROA technique was applied to an incineration plant using a fluidized bed waste gasifier. The results showed how it is possible to quickly identify the main criticalities of this type of systems also making the identification of the ATEX zones around the equipment practically straightforward.

2. Methods

Quantitative Risk Analysis (QRA) is a complex task performed to either qualify or quantify the risks associated with the operation of potentially dangerous installations. The first step of whatever QRA procedure is the identification of all hazards present into the plant: this is called, Hazards Identification (HI) phase. Hazards identification represents a fundamental activity: not identified hazards will remain hidden until the occurrence of the related accidents^[1]. Among all the different HI methodologies, HazOp is the most known and widely applied. Unfortunately, all information collected in a HazOp table are not structured for the following step of the QRA, that is the probabilistic quantification of the hazardous states of the plant. Such step, which is usually done using a Fault Tree Analysis (FTA), can be made less expensive using an Advanced Recursive Operability Analysis (AROA)^[2] instead of a classic HazOp.

A typical AROA Table is structured as presented in Table 1 (the progressive numeration of the records, that is of each row, was omitted).

Table 1. Structure of a AROA Table.

Node-Deviation-Variable	Causes	Consequences due to protections failure	Plant state following the correct intervention of safety functions	Protections			Top Event
				Manual		Automatic safety systems	
				Alarms	Operator Actions		
1	2	3	4	5	6	7	

In the present work, an AROA was applied to a standard incinerator using a fluidized bed gasifier which processes organic wastes.

3. Results and discussion

Figure 1 reports the simplified P&ID of the gasification plant layout.

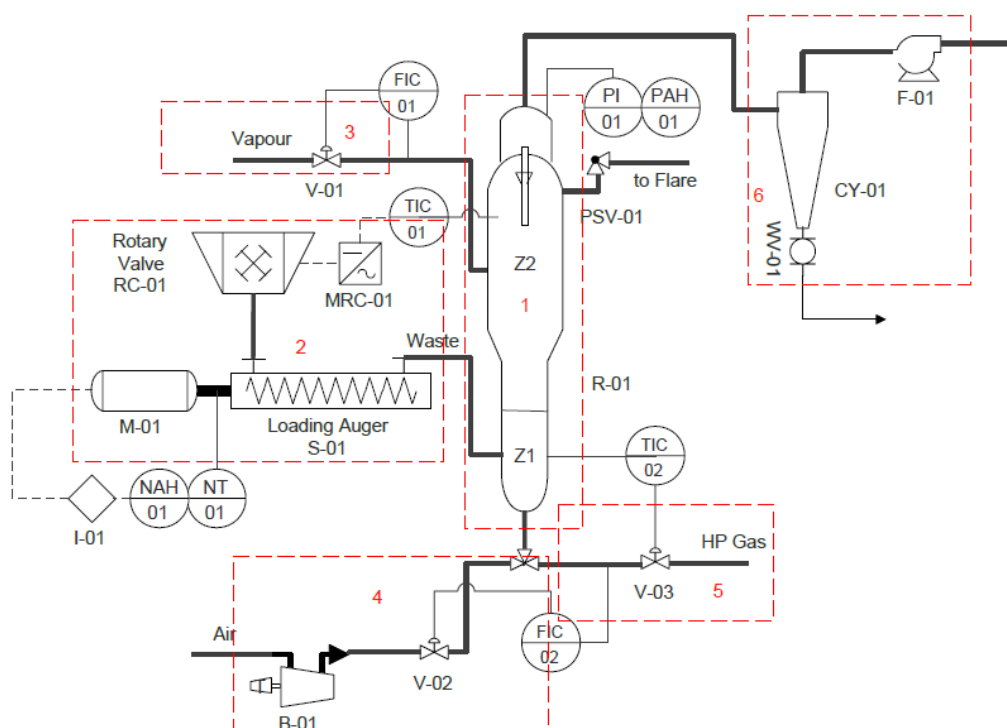


Figure 1. Simplified P&ID of the fluidized bed gasifier.

Referring to the P&ID reported in Figure 1, the system can be divided into 6 nodes:

- Node 1: identifies the fluidized bed reactor (R-01) where either the combustion (Z1) or the pyrolysis of the wastes (Z2) occurs. Air and a high-pressure assistant gas enter from the bottom of R-01. Process variables considered and their deviations (between square brackets) are reported in the following:
 1. (T_{Z1}) Temperature in Zone 1 (Combustion Zone) [h, l]
 2. (T_{Z2}) Temperature in Zone 2 (Pyrolysis Zone) [h, l]
 3. (P) Pressure [h, hh]
 4. (CH_2) Hydrogen concentration [h]
- Node 2: identifies the loading auger section. Process variables considered and their deviations (between square brackets) are reported in the following:
 1. (F) Flow rate of wastes [No, h]

2. (N) Torque at the loading auger [h]
- Node 3: identifies the vapor line used to adjust the syngas composition. Process variables considered and their deviations (between square brackets) are reported in the following:
 1. (F) Water vapor flowrate [l]
- Node 4: identifies the air supply necessary for correctly operating the combustion zone of the gasifier. Process variables considered and their deviations (between square brackets) are reported in the following:
 1. (F) Air flowrate [l, h]
- Node 5: identifies the High-Pressure (HP) combustible gas necessary to correctly operate the combustion zone of the gasifier. Process variables considered and their deviations (between square brackets) are reported in the following:
 1. (F) HP gas flowrate [l, h]
- Node 6: identifies the cyclone used for the abatement of the dusts generated from the waste processing and flow. Such a node was analyzed only from the embrittlement point of view (see Table 2).

The deviations indicated by the letters in the square brackets stand for high (h), low (l) or absence (No). The repetition of the letter expresses an intensification of the deviation (except for the absence). For example (hhP) symbolizes a very high pressure.

Table 2 summarizes the analysis carried out in the present work.

Table 2. AROA for the gasification plant portion analyzed within this work.

NDV	Causes	Consequences due to protections failure (3)	Plant state following the correct intervention of safety functions (4)	Protection			TE
				Manual		Automatic safety systems	
				Alarms	Operator Actions on components		
4hF	1) FIC-02 Fail High OR 2) V-02 Fail Open	1hTz1	1hTz1	-	-	-	-
5hF	1) TIC-02 Fail Low OR 2) V-03 Fail Open	1hTz1	1hTz1	-	-	-	-
1hTz1	1) 5hF OR 2) 4hF	1hTz2	1hTz2	-	-	-	-
1hTz2	1hTz1	1hP 1hCH ₂	1hP 1hCH ₂	-	-	-	-
1hP	1hTz2	1hhP	Gases to Flare	PAH-01	-	PSV-01	-
1hhP	1hP	Reactor Collapse + VCE	2hN PSV-01 collapse (H ₂ and CO release – Jet Fire from PSV-01)	-	-	Reactor Resistance Pressure	TE1 (3) TE2 (4)
1hCH ₂	1hTz2 OR 3IF	Embrittlement of CY-01	Embrittlement of CY-01	-	-	-	
Embrittlement of CY-01	1hCH ₂	H ₂ and CO release – Possible Jet Fire	Operability not compromised -	-	-	Resistance to corrosion of CY-01	TE3 (3)

GRICU 2022, Ischia, (Italy), July 3-6, 2022

NDV	Causes	from hydrogen cracks	Maintenance required	Protection			TE
		Consequences due to protections failure (3)	Plant state following the correct intervention of safety functions (4)	Manual		Automatic safety systems	
				Alarms	Operator Actions on components		
3IF	1) FIC-01 Fail High OR 2) V-01 Fail Closed	1hCH ₂	1hCH ₂	-	-	-	-
2NoF	2hN (I-01) OR M-01 broken OR MRC-01 broken (no rotation)	1IT _{Z1}	1IT _{Z1}	-	-	-	-
2hN	1hhP OR Clogging (water in the feed)	Tearing of the RC-01/S-01 connection with further dispersion of combustible material (Dust Explosion)	2NoF	NAH-01	-	I-01 (M-01 off)	TE4 (3)
2hF	1) MRC-01 fail to operate OR 2) TIC-01 Fail High	1IT _{Z2}	1IT _{Z2}	-	-	-	-
1IT _{Z1}	1) 2NoF OR 2) 4IF OR 3) 5IF	1IT _{Z2}	1IT _{Z2}	-	-	-	-
1IT _{Z2}	1) 2hF OR 2) 1IT _{Z1}	1ICH ₂ (Syngas out of specifics)	1ICH ₂ (Syngas out of specifics)	-	-	-	TE5 (3 and 4)
4IF	1) FIC-02 Fail Low OR 2) V-02 Fail Closed	1IT _{Z1} 1IT _{Z2}	1IT _{Z1} 1IT _{Z2}	-	-	-	-
5IF	1) TIC-02 Fail High OR 2) V-03 Fail Closed	1IT _{Z1} 1IT _{Z2}	1IT _{Z1} 1IT _{Z2}	-	-	-	-

Analyzing Table 2, five main potential Top Events (TEs) can be easily identified:

1. TE1: Reactor collapse followed by a Vapor Cloud Explosion (VCE)
2. TE2: PSV-01 collapse with subsequent H₂ and CO release - Jet fire from PSV-01
3. TE3: H₂ and CO release with possible jet fire from hydrogen cracks (CY-01)
4. TE4: Tearing of the RC-01/S-01 connection with further dispersion of combustible material (Dust Explosion)
5. TE5: Production of a syngas out of specifics

Top Events from 1 to 4 represent criticalities linked to safety problems while TE5 is well representative of an operability concern linked to the composition of the syngas produced. It is very important to underline that 5 Top Events were identified using only 16 records of an AROA Table. This means that a strong reduction of the time necessary for the overall analysis of the plant portion was achieved.

Starting from the AROA Table, it was also possible to automatically generate the related Fault Trees for a subsequent risk quantification step. Figure 2 reports a portion of the overall Fault Tree corresponding to the AROA Table.

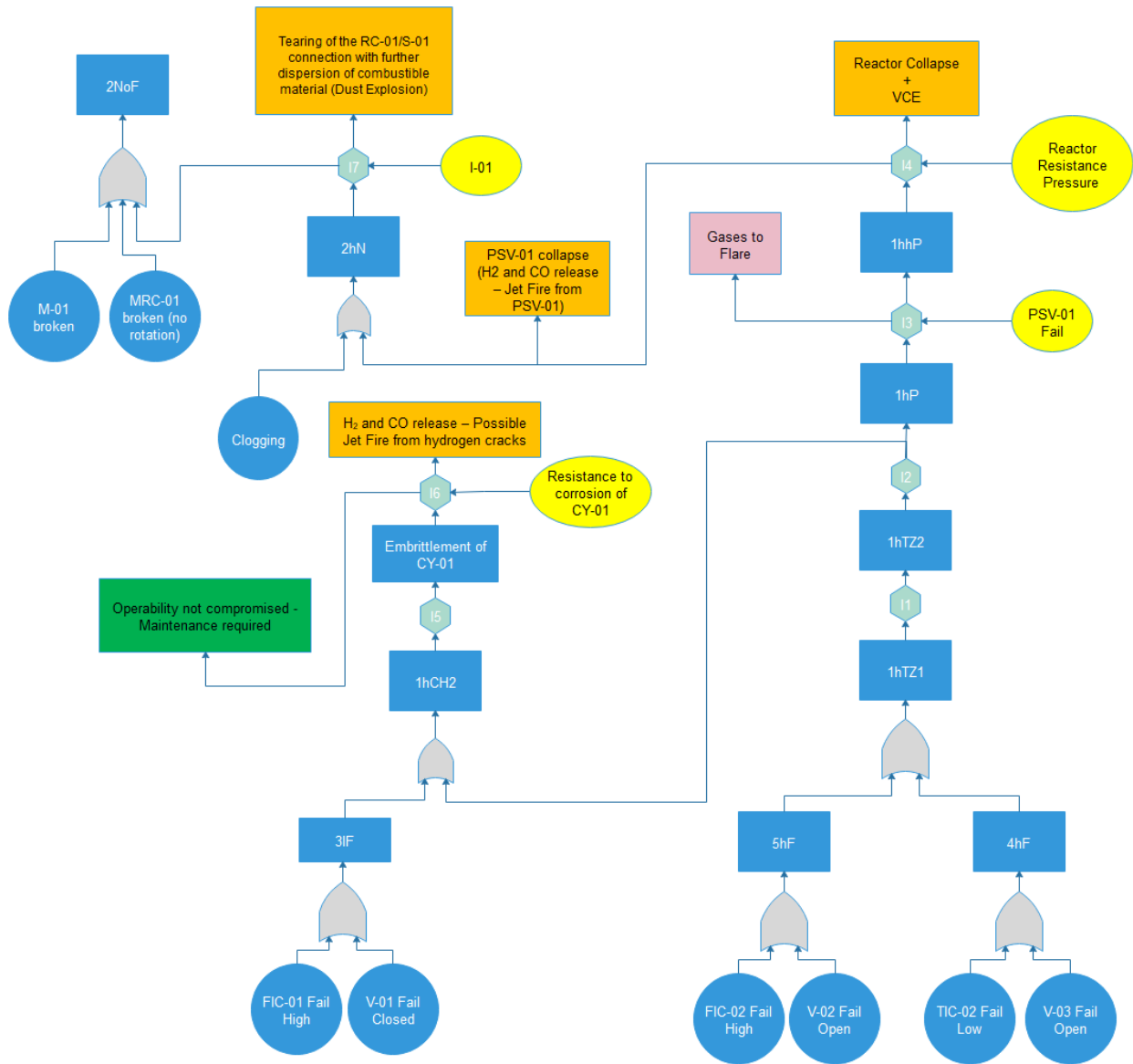


Figure 2. Portion of the overall Fault Tree.

In order to simplify the logic representation of each record (REC) in terms of either consequences due to either the failure or the correct operation of the protection means, the exits from each inhibitor gate (I) assume the following meaning: the direct exit (upward) refers to the consequences reported in column (3) of the AROA Table (Table 2), while the lateral exit refers to the consequences listed in column (4): practically, either the NOT gate or the relative protection are tacit.

Observing Figure 2, it is possible to notice that gates I1, I2 and I5 are not “saturated” from a safety point of view; this means that no protective means have been forecast at that level for the analyzed plant. This represents a huge loss of safety that must be properly counteracted. As the sake of example, I5 could be saturated by introducing a hydrogen analyzer with the related alarms in case of either too high or too low hydrogen concentrations. Successively, proper actions could be also scheduled.

Another relevant point arising from Figure 2 is that all Top Events are linked together in a compact structure: that is, all TEs can be found in a unique fault tree. Only TE5 is missing in Figure 2 for a pure “criticality of representation” reason: TE5 comes from the 2NoF line of failures (as it comes out from Table 2), which was terminated to provide a better visibility of all the other TEs (instead concentrated in a more compact logic structure).

4. Conclusions

This work highlighted how fundamental the contribution of a complete and adequate risk analysis is in the field of industrial prevention of potentially dangerous scenarios in gasification plants.

From the recursive operability analysis carried out on a simplified portion of a real fluid bed waste gasifier it was possible to trace a 5 Top Events using only 16 records of a suitably customized ROA Table. This is a very important advantage of the ROA with respect to all the standard Hazard Identification techniques.

Moreover, the possibility of a direct logic conversion of each record of the AROA table in a portion of a more complex fault tree permits to easily identify potential criticalities of the plant in terms of: 1) lack of protective means (both devices or procedures); 2) design problems linked to the processes to be carried out.

Particularly, the lack of suitable procedures and protection devices specifically designed to saturate, from the safety point of view, each level of the plant can be easily identified by simple observation of the final fault tree. This greatly simplify and target the subsequent plant modification to comply with the maximum reasonably achievable level of safety.

References

- [1] P.M. Contini, S. Contini, S. Copelli, R. Rota, M. Demichela, Safety and Reliability of Complex Engineered Systems - Proceedings of the 25th European Safety and Reliability Conference, ESREL 2015 (2015) 347-355
- [2] M. Barozzi, S. Contini, M. Raboni, V. Torretta, V. Casson Moreno, S. Copelli, Journal of Loss Prevention in the Process Industries 71 (2021) art. no. 104468

Investigation of the bottom corrosion of atmospheric storage tanks for the management of safety

Maria Francesca Milazzo^{1*}, Elpida Piperopoulos¹, Amani Khaskhoussi¹, Giuseppe Scionti¹, Paolo Bragatto², Edoardo Proverbio¹

1 Department of Engineering, University of Messina, Contrada di Dio, 98166 Messina, Italy;

2 Department of Technological Innovation, INAIL Workers' Compensation Authority, via Fontana Candida, 00040 Monteporzio Catone, Italy.

**Corresponding author E-Mail: mfmilazzo@unime.it*

1. Introduction

Given the types of handled substances in chemical and process industry and the operating conditions, all equipment is exposed to several corrosion phenomena causing losses of containment [1, 2]. Damage mechanisms are variegated and depend on the interaction between the construction material and the process fluid as well as the surrounding environment. These could also lead to economic losses due to unplanned stops and repairs or replacements of corroded items. Corrosion is a relevant issue in atmospheric storage tanks of hydrocarbons. The monitoring of the integrity of these tanks is particularly critical as regards the measures of the thickness loss in the bottom due to pitting or other phenomena. Available techniques require that tank is taken out of service, emptied and reclaimed. The thickness measurements are repeated after a certain time interval and allow scheduling next inspection usually according to popular standards. In addition, these measures are useful for the estimation of the probability of release, essential for the assessment of the risk associated with the release of dangerous substances as well as the environmental risk in accordance with current legislations [3, 4].

This research focuses on the investigation of the evolution of the corrosion phenomenon of the bottom of the storage tanks, with respect to a case-study that is a large atmospheric tank with a floating roof, used for the storage of various light aromatic naphtha-based solvents. The scope is to contribute to the understanding of the damage mechanism and provide some basic elements useful for the application of statistical analysis formulating the probability of bottom perforation.

2. Methods

To investigate the evolution of the deterioration mechanism of the storage tanks bottoms, two corrosive environments were simulated in the laboratory. By mixing the naphtha solvent and the solutions, two hydrocarbon mixtures were realized at different pH. The solvent is a commercial hydrocarbon, Shellsol A100 (Kremer Pigmente GmbH & Co., Aichstetten, Germany). The first solution (A) at pH 4 contained the hydrocarbon and an aqueous solution of NaCl, NaSO₄ and acetic acid according to [5, 6]. The second solution (B) at pH 2.5 contained the hydrocarbon and Sour Water as indicated in the NACE TM0177 Test Solution B (5.0 wt.% NaCl, 2.5 wt.% glacial acetic acid and sodium thiosulphate (Na₂S₂O₃) 10⁻¹ to 10⁻³ M in replacement of H₂S [7]. The ratio between the hydrocarbon and the A or B solution was in both cases 4/1.

The carbon steel specimens, 20 x 30 x 3 mm (width x length x thickness) were immersed in the two hydrocarbon solutions. Before the immersion, the specimens were treated in ultrasound (frequency 30 kHz), with acetone (CH₃-CO-CH₃), to remove the possible grease residues present on the surface. Subsequently, they were pickled in a Clarke solution (250 ml of hydrochloric acid (HCl), 5 g of antimony oxide (Sb₂O₃), 12.5 g of stannous chloride (SnCl₂), in continuous stirring, at room temperature, for 35 minutes. Then, they were washed sequentially with soda, distilled water and ethanol.

Periodically 2 specimens (one from the solution A and one from the B one) were extracted, pickled, always through Clarke solution, and structurally and morphologically characterized, respectively by X-Ray Diffraction (XRD) and Scanning Electron Microscope (SEM). The XRD instrument used for the structural analysis of the material was a Bruker D8 Advance (Bruker, Billerica, MA, USA), in Bragg-Brentano θ - 2θ configuration, with $\text{CuK}\alpha$ radiation (40 V, 40 mA). XRD patterns were collected in the range 10° – 80° with a step of $0.1^\circ/\text{s}$. The morphological investigation was conducted through an instrument FEI Quanta FEG 450 (FEI, Hillsboro, OR, USA), operating at high vacuum with an accelerating voltage of 20 kV.

3. Results and discussion

Before the immersion, specimens are structurally characterized by XRD analysis (Figure 1a). The presence of the Fe peak (JCPDS # 04-007-9753) is evidenced, constituting more than 98 wt.% of a carbon steel. The results of morphological characterization, after the extraction of the specimens, are compared with carbon steel specimens before the immersion procedure (Figure 1b). A homogenous morphology of the sample is observed by SEM analysis, free of particular relevant cracks.

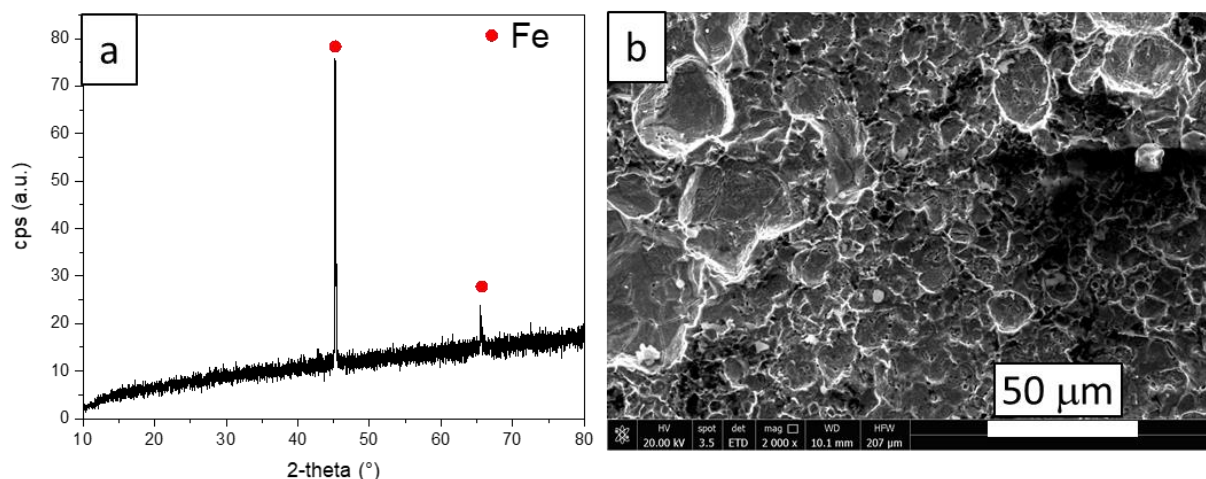


Figure 1. XRD diffractogram (a) and SEM image (b) of carbon steel specimen before the immersion procedure.

The results of the surface characterization of the specimens show two different ways of evolving the corrosive phenomenon. At 238 days all the specimens appear corroded (Figure 2). A selective attack can be noted for the sample extracted from solution A (Figure 2a). While corrosion is manifested itself in the form of pits for samples extracted from solution B (Figure 2b), where the sodium thiosulfate is probably the cause of this behavior.

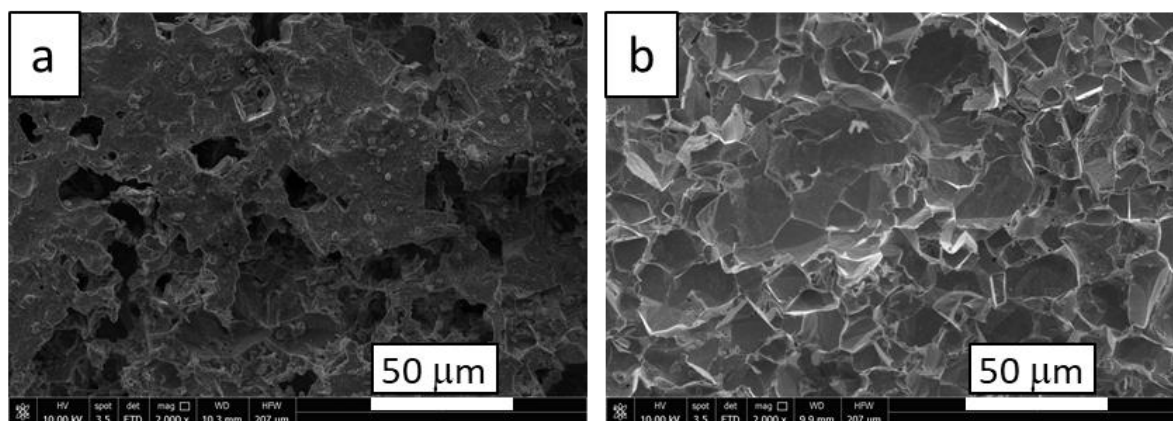


Figure 2. SEM images of samples extracted from solution A (a) and B (b), after 238 days of immersion

Pit depth measurements are useful for the estimation of the probability of the occurrence of the critical pit at the bottom of an atmospheric tank based on the application of the extreme value theory (EVT). The EVT is well known in the field of corrosion and in this study could represent a useful method to extrapolate the trend of the phenomenon from the specimens to the bottom of a tank for which the simulation system is representative. The limiting corrosion depth for safety purpose can be determined by means of popular standards [8].

The results of the study allow the establishment operator to integrate more appropriate investigations about the release scenarios due to the corrosion mechanisms within the risk assessment. These integrations consist in the quantification of the release probability accounting for the actual evolution of the phenomenon obtained through the simulation in the laboratory; moreover, through the use of more sophisticated models, the prediction of the probability of perforation and the remaining useful lifetime (RUL). These models combine the EVT and the Bayesian inference [9].

4. Conclusions

The study highlights the importance of underestimating the evolution of the corrosion in major hazard establishments, as it could be the cause of industrial accidents with the release of dangerous substances. To control and manage this problem, the operator usually carries out inspections and applies statistical modelling to calculate the probability of release, therefore, the investigation of the corrosive phenomenon certainly allows improving the understanding of its evolution.

Acknowledgments

This work has been funded by INAIL within the BRIC/2018 ID = 11 project MAC4PRO and the BRIC/2021 ID = 3 project DRIVERS.

References

- [1] M.H.Wood, A.V.Arellano, L.Van Wijk, Corrosion Related Accidents in Petroleum Refineries, European Commission Joint Research Centre Report no. EUR 26331, 2013.
- [2] OECD, Organisation for Economic Cooperation and Development, Ageing of hazardous installations, OECD Environment, Health and Safety Publications - Series on Chemical Accidents, no. 29, 2017.
- [3] EU Council, Directive 2010/75/EC on industrial emissions (integrated pollution prevention and control) (Recast), Official Journal of the European Union L334(2010), 17–119, 2010.
- [4] EU Council, Directive 2012/18/EU on the control of major-accident hazards involving dangerous substances, Official Journal of the European Union L197(2012), 1-37, 2012.
- [5] A.Rajasekar, S.Maruthamuthu, N.Muthukumar, S.Mohanan, P.Subramanian, N.Palaniswamy, Bacterial degradation of naphtha and its influence on corrosion, *Corros. Sci.*, 47(1), 257-271, 2005.

- [6] A.Groysman, N.Erdman, A Study of Corrosion of Mild Steel in Mixtures of Petroleum Distillates and Electrolytes, *Corrosion*, 56(12), 1266-1271, 2000.
- [7] L.Calabrese, M.Galeano, E.Proverbio, D.Di Pietro, F.Cappuccini, A.Donato, Monitoring of 13% Cr martensitic stainless steel corrosion in chloride solution in presence of thiosulphate by acoustic emission technique, *Corrosion Science*, 111, 151-161, 2016.
- [8] EEMUA, Users' Guide to the Inspection, Maintenance and Repair of above Ground Vertical Cylindrical Steel Storage Tanks, EEMUA 159, 2014.
- [9] M.F.Milazzo, G.Ancione, P.Bragatto, E.Proverbio, 2022, A probabilistic approach for the estimation of the Residual Useful Lifetime of atmospheric storage tanks in oil industry, *Journal of Loss Prevention in the Process Industries* (forthcoming).

Multi-Objective Optimization of a Carbon Capture and Sequestration Chain Under Seismic Risk Constraints

Daniel Crîstiu¹, Federico d'Amore², Paolo Mocellin¹, Fabrizio Bezzo^{1*}

¹ CAPE-Lab - Computer-Aided Process Engineering Laboratory, Department of Industrial Engineering, University of Padova, via Marzolo 9, IT-35131 Padova, Italy; ² Politecnico di Milano, Department of Energy, via Lambruschini 4, IT-20156 Milano (Italy)

*fabrizio.bezzo@unipd.it

1. Introduction

Carbon dioxide (CO₂) remains the primary anthropogenic greenhouse gas (GHG). It is expected that global surface temperature will surpass the limit established by the Paris Agreement of 2°C unless, in the near future, urgent actions are taken in reducing CO₂ emissions on a global scale [1]. CO₂ (carbon) capture and sequestration (CCS), which is a sequence of technologies targeted at cutting anthropogenic CO₂ emissions, has been acknowledged as a key technology for decarbonizing carbon intensive industries. In particular, CO₂ capture entails separating CO₂ from a process stream using various methods depending on the industry and technology used, followed by a transport step of the captured CO₂ from emission sources to areas suitable for sequestration in deep underground geological formations. Among the large stationary sources, cement plants, refineries and steel mills represent the most relevant sources of carbon dioxide emissions as part of the industrial sector around the world [2]. However, transporting CO₂ via pipelines may raise public concern with respect the possibility of leakages. This is particularly critical in the Italian context as widespread seismic activity poses an additional requirement during the planning, installation, and operation of a CCS system, particularly with regards to pipelining. In this contribution, a mixed integer linear programming modelling approach is employed to perform a countrywide multi-objective optimisation for the adoption of a CCS network. The multi-objective optimisation aims at minimizing the total cost of the CCS network, while simultaneously minimizing the seismic risk which, considering the seismic profile of the Italian Peninsula, can represent a vulnerability for the installation and operation of a CCS system.

2. Methods

The location of industrial plants and their corresponding annual CO₂ emissions in 2019 are taken from EEA (2020) database. The dataset of CO₂ emitting nodes n is subdivided into 23 cement plants (c), 7 refineries (r) and 2 steel mills (s), selected in such way to account for at least 80% of the emissions from each sector. A comprehensive explanation of the modelling approach can be found in [3]. The CO₂ transportation is achieved through onshore or offshore pipelines, while the sequestration stage takes into account both onshore and offshore sites. The seismicity-related parameters over the entire Italian peninsula are averaged into seismic areas and are used to calculate the risk specific to each pipeline in the transport stage.

The MILP model is formulated as minimizing total cost TC [€/year] and the total risk TR [ruptures/year]:

$$objective = \min\{TC; TR\} \quad (1)$$

The TC is a sum of capture (TCC [€/year]), transport (TTC [€/year]), and sequestration stages (TSC [€/year]):

$$TC = TCC + TTC + TSC \quad (2)$$

TR is the sum of all the repair rates $RR_{n,n'}$ [ruptures/year] concerning the pipelines of the transport stage:

$$TR = \sum_n (RR_{n,n'}) \quad (3)$$

3. Results and discussion

The CPLEX solver in GAMS software was used to solve the MILP multi-objective optimization problem. The Pareto optimal solution allows assessing how the CCS chain configuration changes when moving from a purely economic optimization to the solution where seismic risk is minimized. As a matter of example, by equally weighting the cost and the risk functions into the objective function, a trade-off is found between the two conflicting objectives: the resulting infrastructure is illustrated in Figure 1 for a carbon capture target of 50%.

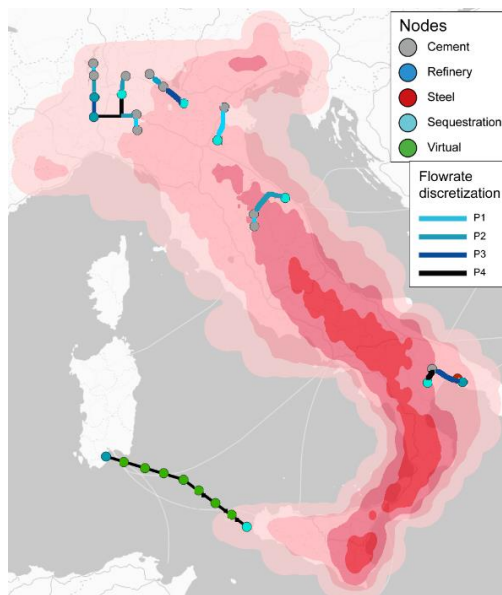


Figure 1. Trade-off configuration for the CCS supply chain.

This configuration gives a Total Risk of 2.36 ruptures/year with a Total Cost of 81.3 €/t of CO₂. By analysing the three components of the Total Cost, the significant contribution is seen in the capture step which accounts for 64.8 €/t of CO₂, while the transportation and sequestration costs give the value of 9.2 €/t of CO₂, respectively 7.2 €/t of CO₂.

4. Conclusions

For decarbonizing the Italian industry, a countrywide carbon capture and sequestration supply chain was optimized through a mixed integer linear programming framework. The model aimed at minimizing simultaneously the total cost (economic objective) and the total seismic risk (risk objective) by means of a multi-objective framework capable of providing useful insights to investors and policy makers.

References

- [1] IPCC, 2021: Climate Change 2021: Report of the Intergovernmental Panel on Climate Change. Cambridge University Press. In Press.
- [2] EEA, 2020, European Pollutant Release and Transfer Register, <https://prtr.eea.europa.eu/#/pollutantreleases>.
- [3] F. d'Amore, M.C. Romano, F. Bezzo, J. Clean. Prod., 65 (2021) 99-116.

Safe operation of reactors: an investigation on the thermal stability of hydroxylamine solutions.

Paolo Mocellin^{1*}, Gianmaria Pio², Chiara Vianello^{1,3}, Ernesto Salzano², Giuseppe Maschio¹

1 Dipartimento di Ingegneria Industriale. Università degli Studi di Padova. Via Marzolo 9, 35131 Padova, Italia.

2 Dipartimento di Ingegneria Civile, Chimica, Ambientale e dei Materiali. Università di Bologna. Via Terracini 28, Bologna, Italia.

3 Dipartimento di Ingegneria Civile, Edile e Ambientale. Università degli Studi di Padova. Via Marzolo 9, 35131 Padova, Italia.

*paolo.mocellin@unipd.it

1. Introduction

The knowledge of the substance behavior under atypical conditions is essential when dealing with the safe operability of chemical reactors, storage systems and the sizing step of safety and control devices. In this framework, the processing of hydroxylamine (HA) and HA-derived compounds may pose hazards and additional complexity, being intrinsically unstable under specific operative and storage conditions [1,2]. These are often responsible for a thermal decomposition leading to uncontrolled mechanisms that may affect inherent safety and equipment integrity. Investigating runaway conditions in chemical reactors processing HA and HA-derived compounds is essential to obtain the set of safe operative conditions to be maintained to avoid uncontrolled reactions. In addition, detailed calorimetric studies can be used to provide guidance concerning safe conditions and appropriate storage [4,5].

This work focuses on the behavior of solutions of HA in water at a concentration of 10%-50% w, respectively. A thermal screening unit, arranged with different cells made of stainless steel and Hastelloy, is used to collect batch data on the thermal stability of HA.

2. Methods

Reported measurements are made with a TS^U – *thermal screening unit* apparatus that allows for the collection of temperature and pressure profiles during the time of a closed-cell environment [3]. A specified thermal profile can be imposed in order to analyze the sample response to increasing temperatures that may trigger thermal decompositions. Different heating methods are used, namely an isothermal mode and an increasing ramp mode. The latter is employed to search for the onset of *runaway* conditions that are then investigated while keeping the system under constant temperature.

In this study, heating rates of $2\text{ }^{\circ}\text{C min}^{-1}$ and $5\text{ }^{\circ}\text{C min}^{-1}$ are adopted along with isothermal steps around the onset temperature. The selected rates are representative of external failures leading to respectively - uncontrolled - moderate and severe temperature increases. Besides, isothermal conditions may apply to operational storage targets.

Related cell internal temperature and time derivatives (dT/dt and d^2T/dt^2) are considered in the *onset* temperature evaluation according to [3]. The temperature is monitored through a type K thermocouple placed in the test cell while a pressure sensor tracks the cell internal pressure. HA aqueous solutions at 50, 30, 20 and 10 % on an HA mass basis (at 99.99 % purity) are used in addition to diluted systems.

3. Results and discussion

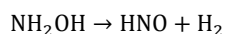
Collected data show that HA solutions may undergo *runaway* scenarios once subjected to external thermal perturbations. Results are reported in Table 1 for the HA solution heated at $2\text{ }^{\circ}\text{C min}^{-1}$ and $5\text{ }^{\circ}\text{C min}^{-1}$.

Table 1. Sample mass variation, maximum sample temperature T_{max} , sample pressure $(P_{max}-P_v)/P_v$ and onset temperature T_{on} of HA solutions.

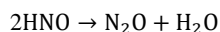
Sample	Mass variation /g	T_{max} /°C	$(P_{max}-P_v)/P_v$ /-	T_{on} /°C	Mass variation /g	T_{max} /°C	$(P_{max}-P_v)/P_v$ /-	T_{on} /°C
Heating rate: 2 °C min ⁻¹					Heating rate: 5 °C min ⁻¹			
HA 10 %	0.46 ± 0.26	202 ± 3	0.02 ± 0.01	n/a	0.04 ± 0.01	253 ± 5	0.03 ± 0.01	n/a
HA 20 %	0.45 ± 0.12	215 ± 3	0.09 ± 0.06	175 ± 5	0.15 ± 0.03	249 ± 4	0.13 ± 0.05	198 ± 7
HA 30 %	0.43 ± 0.23	239 ± 4	0.13 ± 0.03	143 ± 3	0.20 ± 0.05	245 ± 8	0.15 ± 0.04	158 ± 4
HA 50 %	0.31 ± 0.04	230 ± 9	0.10 ± 0.04	153 ± 5	0.36 ± 0.09	264 ± 8	0.11 ± 0.02	163 ± 4

First, it should be noted that for all tests, the increase in the pressure up to P_{max} is only ascribed to the water pressure. In addition, a difference between the maximum cell pressure (P_{max}) and the related mixture saturation pressure (P_v) at experimental conditions exists. The discrepancy is almost negligible for 10 % HA solution while more concentrated solutions lead to a difference increase up to 15 percent. Within the experimental error, results for 20, 30 and 50 % HA solutions are comparable, and the pressure increase with respect to P_v can be ascribed to HA decomposition mechanisms.

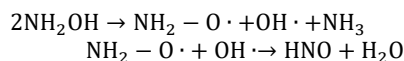
On the other hand, as reported in Figure 1, the onset of a runaway reaction is clearly observed for all the tests but the 10 % HA solution, which does not exhibit uncontrolled dynamics. This behavior is due to the hydroxylamine decomposition, which can be defined by the following set of reactions (in the absence of oxygen), producing a large increase of moles ([6; 7]):



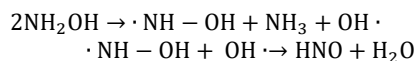
H₂ elimination forming nitroxyl and H₂



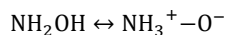
rapid decomposition of HNO (1)



bimolecular, intermolecular H shift termination, followed by (1)



bimolecular, two intermolecular H shift termination, followed by (1)



mono (or bimolecular) H · shift from O to N, forming ammonia oxide (zwitterionic tautomer of $\text{NH}_2 - \text{OH}$) $4\text{NH}_2\text{OH} \rightarrow$

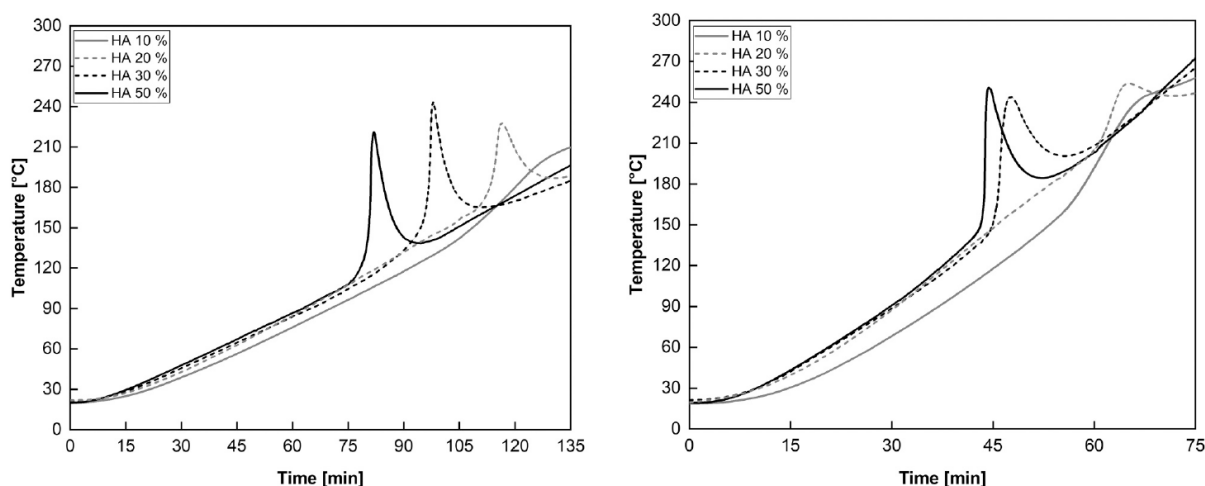
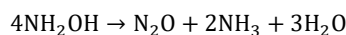


Figure 1. Thermal behaviour of aqueous solutions of HA at different concentrations (%w) at oven heating rate of 2 °C min⁻¹ (left) and 5 °C min⁻¹ (right).

4. Conclusions

The thermal decomposition of HA in aqueous systems is investigated. Runaway events are observed in the range of concentration considered, except for the 10 % HA solutions. Onset temperatures range from 143 to 198 °C depending on solution concentration and imposed heating rate, with lower onset temperatures at 2 °C min⁻¹. The maximum temperature is observed in the 50 % HA solutions sample with an associated maximum pressure of 50 ± 5 bar.

References

- [1] Kletz, T., 1998. *Process Plants: A Handbook for Inherently Safer Design*. Taylor and Francis, 1998.
- [2] Wei, C., Rogers, W.J., Mannan, M.S., 2006. Thermal decomposition hazard evaluation of hydroxylamine nitrate. *J. Haz. Mat.*, 130, 163-168.
- [3] Adamopoulou, T., Papadaki, M.I., Kounalakis, M., Vazquez-Carretero, V., Pineda-Solano, A., Wang, Q., Sam Mannan, M., 2013. Thermal decomposition of hydroxylamine: Isoperibolic calorimetric measurements at different conditions. *J. Haz. Mat.*, 254-255, 382-389.
- [4] Cisneros, L.O., Rogers, W.J., Sam Mannan, M., 2001. *J. Haz. Mat.*, A82, 13-24.
- [5] Lee, H., Litzinger, T.A., 2003. Chemical kinetic study of HAN decomposition. *Combustion and Flame*, 135, 151-169.
- [6] Wei C. (2005). *Thermal runaway reaction hazard and decomposition mechanism of hydroxylamine system*, PhD thesis, Texas A&M.
- [7] Pio, G., Mocellin, P., Vianello, C., Maschio, G., 2021. A detailed kinetic model for the thermal decomposition of hydroxylamine. *J. Haz. Mat.*, 416, 125641.

Flashback phenomenon in domestic condensing boiler in H₂-enriched admixtures

Rachele Lamioni^{1*}, Filippo Fruzza¹, Leonardo Tognotti¹, Chiara Galletti¹

1 Dipartimento di Ingegneria Civile e Industriale, Università di Pisa, 56126 Pisa, Italy;

**Corresponding author E-Mail: rachele.lamioni@ing.unipi.it*

1. Introduction

In the context of the energy transition, hydrogen may play a fundamental role following the European road map which forecast its use for up to 24% of the final energy demand by 2050 [1]. Hydrogen can be produced through the electrolysis of water, from the excess of solar and wind energy, representing the carbon-free energy vector par excellence. Furthermore, in controlled quantities, it can be directly introduced into the existing gas network. Moreover, current EU policies are focusing on regional hydrogen ecosystems, so-called hydrogen valleys, exploiting the local availability of renewable energies to promote decarbonization of local industrial processes and domestic heating.

However, the conversion of this green fuel in existing end-user appliances, as domestic condensing boilers, must be carefully evaluated as hydrogen has thermo-chemical characteristics that are extremely different from natural gas. With the same equivalence ratio, hydrogen has significantly higher adiabatic temperatures and laminar flame velocities (S_L) than natural gas. In particular, the laminar velocity of the flame increases from $S_L = 0.4$ m/s to $S_L = 2.5$ m/s when switching from natural gas to hydrogen under stoichiometric conditions. Hence, a serious problem can be flashback phenomena, i.e., with the flame returning to the injection, that can lead to significant safety problems.

Domestic appliances such as condensing boilers are equipped with perforated burners injecting a premixed gas mixture into the combustion chamber. Such burners are typically designed through the experience of the manufacturer [2] based, of course, on the use of natural gas. In this context, with the desire to switch to green fuels a better understanding of the combustion process and, above all, of the mechanisms for stabilizing the premixed flames is fundamental.

This work aims to suggest a numerical model to evaluate the possible occurrence of flashback when feeding H₂-admixtures in conditions relevant for domestic boilers. Indeed, the analysis of the minimum issuing velocity needed to avoid flashback is of key importance. It is worth mentioning that such issuing velocity may be remarkably different from the laminar flame speed as it depends on the manner the flame anchors to the burner.

For this purpose, a preliminary analysis is carried out using one-dimensional flames to estimate the characteristics of the premixed flames as the H₂ content varies, such as laminar speed and adiabatic flame temperature. Then, 2D transient numerical simulations (in axial symmetry) are performed with detailed kinetics to characterize the flame from a circular hole, exploiting periodic boundary conditions to simulate a perforated burner of condensing boilers domestic. Since the burner plate is crucial in flame stabilization, the numerical model also includes the corresponding solid domain with a conjugated heat transfer approach.

2. Methods

Initially, 1D simulations of freely propagating premixed flames are carried out with the open-source software Cantera [3], to estimate the characteristics of the flames at different operating conditions in terms of equivalence ratio (in the range from 0.5 to 1.0) and percentage of H₂ (from 0% to 100%).

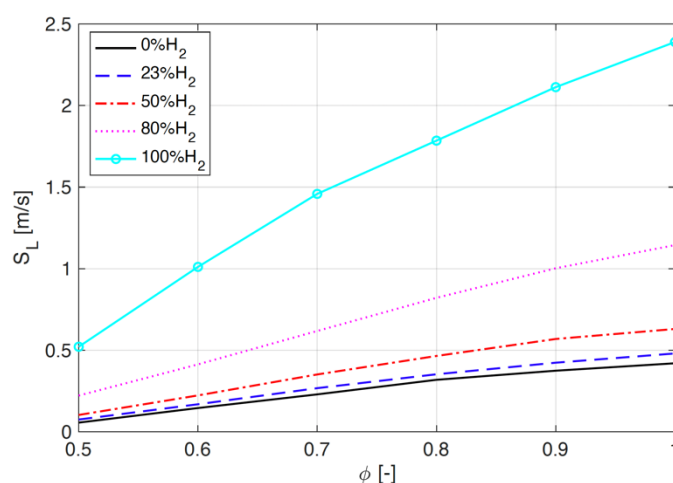
Then, numerical simulations with computational fluid dynamics (CFD) techniques are performed on hydrogen-methane/air premixed laminar flames in a 2-D field. In particular, the geometry of an axially symmetrical hole of diameter D is considered using detailed chemical kinetics through the KEE58-Mech [4] mechanism,

consisting of 17 chemical species and 58 reversible reactions. The system of conservation equations of the equations of mass, momentum, energy, and transport/reaction of chemical species with both a stationary and transient approach is solved through the ANSYS Fluent 2021.v1 code, based on finite volume methods. The computational grid is structured with 11k cells.

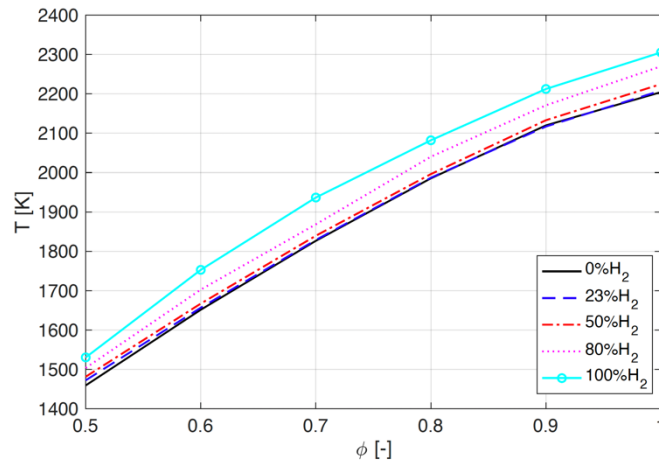
A sufficiently high flow rate, corresponding to the 50% of the nominal boiler power (i.e., 12 kW) in the steady-state is simulated to have a stable and developed condition for the flame, even in the vicinity of the burner plate. The latter is treated as a solid domain, through a conjugate heat transfer (CHT) approach. The interaction between the fluid and solid allows us to also estimate the burner temperature as operating conditions vary. To evaluate the flashback phenomenon, transient simulations are set up starting from the stable steady-state condition, progressively decreasing the input flow rate. An implicit second-order method and a time-step $\Delta t = 5.0e-6$ s are used for time advancement, using the PISO pressure-velocity coupling algorithm. This procedure, for decreasing the input speed, allows estimating the speed at which the backfire phenomenon. In particular, we have considered 23% of H_2 content, corresponding to the G222 gas test, using an equivalence ratio fixed, $\phi = 0.8$, typical for this type of operation.

3. Results and discussion

The laminar flame speed and adiabatic temperature, estimated through the 1-D simulations of freely propagating premixed flames, are reported in Figure 1(a) and Figure 1(b), respectively, for different CH_4-H_2 mixtures, namely 77%-23%, 50%-50%, 20%-80% and pure H_2 , and equivalence ratio $\phi = 0.5-1.0$, all corresponding to lean conditions. It is noted that as the percentage of H_2 in the mixture increases, the laminar flame speed increases up to values of 2.5 m/s when considering the mixture of pure H_2 . The laminar flame speed represents the speed at which the flame propagates from the burnt gas to the cool zone. Hence, in theory, the burner flow rate must exceed this speed to avoid flashback. However, this speed is the result of 1-D simulations of freely propagating flame, hence they do not consider the real domain of use and in particular the solid-fluid interaction as well as radiation effects. Figure 1(b) shows that by increasing the H_2 content, the adiabatic flame temperature T increases, and this trend may pose issues regarding the NO_x emissions, whose formation via the thermal route may be promoted.



(a)



(b)

Figure 1. Laminar flame speed (a) and adiabatic temperature (b) for different H₂ content and different equivalence ratio.

Subsequently, an equivalence ratio equal to $\phi = 0.8$ is chosen to carry out the CFD simulations in the 2-D field, considering the geometry of the hole in axial symmetry. This value is chosen as it represents a typical operating condition of domestic condensing boilers [5].

Figure 2 shows the temperature distribution for G222 gas mixture, having 23% H₂, as predicted to estimate the issuing velocity at which flashback occurs. Note that the axes are normalized with the diameter of the hole, which is D. The top panel of the Figure 2 shows the stable conditions for high velocity inlet. From this condition, the burner wall temperature is 950 K, which complies with the experimental values. Note that as the speed decreases, the flame front moves towards the entrance until it reaches the wall, here depicted through a dashed line.

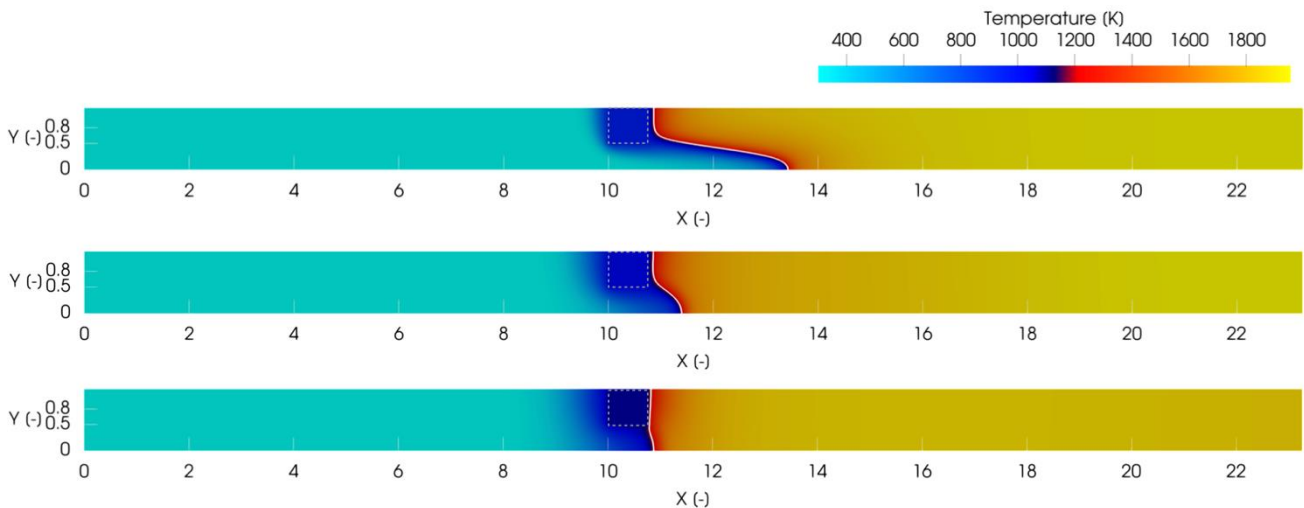


Figure 2. Temperature distribution for 23% H₂ and different velocity inlets: $V_i=0.6-0.16-0.08$ m/s.

In particular, for an input speed equal to $V_i = 0.08$ m/s the flashback phenomenon is triggered and the temperature of the solid increases up to 1150 K, as can be seen from the bottom panel of the Figure 2. Following this analysis, it was estimated that the flashback speed is 1.29 times higher than the S_L calculated by 1-D free-propagating flame simulations, as $S_L = 0.35$ m/s.

4. Conclusions

This work proposes a numerical procedure, based on CFD simulations, to estimate the velocity at which flashback of H₂-admixtures may occur in conditions that are relevant for domestic condensing boiler. Preliminary, the characteristics of the freely propagating premixed flames in terms of adiabatic flame temperature and laminar flame speed are analyzed for different H₂ contents and equivalence ratios. through 1-D simulation. It is observed that the interaction of the flame with the solid walls is fundamental in triggering the flashback phenomena. In particular, it was found from the transient 2-D CFD simulations, that the issuing velocity at which flashback occurs is 1.29 time higher that the laminar flame speed in case of the G222 test gas with 23% of H₂. This study may help investigating strategies of burner design aimed dealing with high H₂ contents in the perspective of decarbonize the domestic heating sector.

References

- [1] F. Cell and H. J. Undertaking, "Hydrogen roadmap europe: A sustainable pathway for the european energy transition," Hydrogen Knowledge Centre, no. 2019, 2019.
- [2] F. Schiro and A. Stoppato, "Experimental investigation of emissions and flame stability for steel and metal fiber cylindrical premixed burners," *Combustion Science and Technology*, vol. 191, no. 3, pp. 453–471, 2019.
- [3] D. G. Goodwin, R. L. Speth, H. K. Moffat, and B. W. Weber, "Cantera: An object-oriented software toolkit for chemical kinetics, thermodynamics, and transport processes." <https://www.cantera.org>, 2021. Version 2.5.1.
- [4] R. Bilger, S. Stårner, and R. Kee, "On reduced mechanisms for methane-air combustion in non-premixed flames," *Combustion and Flame*, vol. 80, no. 2, pp. 135–149, 1990.
- [5] Lamioni, R., Bronzoni, C., Folli, M., Tognotti, L., & Galletti, C. (2022). Feeding H₂-admixtures to domestic condensing boilers: Numerical simulations of combustion and pollutant formation in multi-hole burners. *Applied Energy*, 309, 118379.

A comparative analysis of software codes for the consequence assessment of CO₂ leakage scenarios from onshore facilities and pipelines

Federica Tamburini*, Sarah Bonvicini, Valerio Cozzani

LISES – Dipartimento di Ingegneria Civile, Chimica, Ambientale e dei Materiali

Alma Mater Studiorum – Università di Bologna, via Terracini n.28, 40131 Bologna, Italy

**Corresponding author E-Mail: federica.tamburini9@unibo.it*

1. Introduction

In recent years, the global concentration of CO₂ in the atmosphere has increased drastically. At present, the continuous rise in atmospheric CO₂ levels is driving climate change and temperature shifts on a worldwide scale. Carbon dioxide Capture and Storage (CCS) technologies have been suggested as a viable option for reducing CO₂ emissions. CCS involves mainly three successive steps: capture of CO₂ (and possible intermediate storage), transport (usually via pipeline and/or sealine), and permanent geological storage. The safety of CCS infrastructures is of high relevance for the future implementation of this technology. Thus, it is necessary to evaluate the risk caused by accidental CO₂ leakage scenarios for humans, for the environment (in particular in case of offshore permanent storage), and for the assets, during all the stages of CCS [1].

Thermodynamically, CO₂ behaves differently from the hazardous substances generally considered in the context of the consequence assessment of major accident scenarios. In fact, at atmospheric conditions CO₂ is below its triple point, which corresponds to $P = 5.2$ atm and $T = -56.6$ °C. This peculiarity implies the formation of a two-phase release of gas containing CO₂ solid dry ice particles, as a consequence of the rapid depressurization and phase change the substance undergoes during the release from pressurized equipment into the atmosphere. From a safety point of view, CO₂ represents both a mildly toxic and a physical stressor for humans, due to the extremely low temperatures it reaches (-78 °C) after the release. Furthermore, CO₂ leakage events might cause damage to assets, because of both the low temperatures and the presence of the abrasive solid particles. In case of an underwater release from a sealine or from a submarine reservoir, CO₂ releases have the potential to affect the marine biota, in virtue of the reduction of the seawater pH [2].

In the present study, a benchmarking of the most recent versions of the software codes available for simulating the atmospheric release and the dispersion of CO₂ from onshore facilities and pipelines has been carried out, also by their application to some relevant case studies. More specifically, the PHAST software by DNV-GL [3], EFFECTS by Gexcon [4], and OLGA by Schlumberger [5] have been considered. PHAST and EFFECTS are well-known software tools usually adopted for estimating the consequences of major accidents. In fact, they implement source models for characterizing the accidental outflow of hazardous substances from vessels and pipes, as well as dispersion models for simulating the fate of clouds dispersing as plumes or puffs into the atmosphere. Both PHAST and EFFECTS have been adapted to allow their application to the gas-solid outflows of CO₂, also taking advantage from the data provided by experimental CO₂ leakages [6]. Instead, OLGA is a dynamic multiphase flow simulator capable of modeling the multiphase transportation of oil, gas, and water throughout pipelines. However, it may be adapted to the evaluation of the source term of loss of containment events.

2. Methods

In order to compare the OLGA, PHAST and EFFECTS codes, first of all an extensive work has been carried out in order to highlight the input data required by each tool, the assumptions adopted, and the results provided. A specific focus has been devoted to pipeline spills, performing a sensitivity analysis of the features of the CO₂ outflow and of the damage distances of the CO₂ cloud with respect to the length of the conduit, its diameter, its length, its slope, its inlet pressure, the dimensions of the hole and its position along the pipeline, the depth at which the pipeline is buried and the influence of sectioning by means of the blocking valves. Furthermore, the influence of dry ice on the dispersion has been considered. As a second task, the three codes have been applied to some case studies. A first set of case studies refers to the loss of

containment events reported in [7], which include high-pressure cold and high-pressure supercritical releases from vessels, short pipes, and long pipes. A second set of case studies considers leakage scenarios from onshore pipelines differing for the pipeline diameter and the hole size, selected on the basis of the release characterization provided in [8].

Damage distances have been evaluated for both people and assets. The damage thresholds considered for human toxicity are the IDLH (40,000 ppm) and the LC50_{hmn,30min} (92,000 ppm) limits [9]. For cold burns, both the value of -18 °C [10] and the temperature at which solid CO₂ particles are totally sublimated [2] have been considered, since there is no accordance in the technical literature on the value to be adopted for this limit. The highest temperature at which dry ice particles are present has to be used also to determine the risk of erosion on assets [11], while the damage threshold for cold embrittlement has been assumed as equal to -40 °C, being this a typical embrittlement temperature of steels [12].

3. Results and discussion

As a result of the case studies, the discharge release rates provided by the EFFECTS and OLGA codes were found to differ from the values obtained with PHAST by -34% ÷ +95%, while the concentration profiles of CO₂ in air obtained with EFFECTS differ from the ones provided by PHAST by -76% ÷ +58%. Thus, the values of the mass release rate and the damage distances calculated with respect to people and assets typically differ less than a factor 2. Furthermore, the results of the sensitivity analyses allowed determining a set of baseline assumptions for the consequence assessment of pipelines in order to provide a standard for risk analysis, so that the results obtained for different pipelines are consistent and comparable.

4. Conclusions

A detailed benchmarking activity has been carried out on the PHAST, EFFECTS and OLGA software codes applied to the consequences of CO₂ spill events. Despite significant differences in the modeling approach of the codes, the differences in the results match the expectations. Thus, all the three software tools seem suitable for the consequence assessment of CO₂ leakage events. It has also been demonstrated that, in regard to the cold temperature effects on people, the two damage criteria reported in the technical literature provide different damage distances. In addition, the effects of solid particles and low temperatures on both people and assets usually occur at distances below 20 m, where it is acknowledged that the results provided by integral dispersion models are not accurate. For these reasons, in order to get a better understanding of the consequences of the CO₂ leakage events near the source point, the adoption of CFD modeling seems more suitable than the application of integral models. Moreover, further experimental data are necessary to reduce the uncertainty concerning the damage thresholds related to cold temperature effects on people and assets.

References

- [1] B. Metz, O. Davidson, H.C. de Coninck, M. Loos, L.A. Meyer (Eds.), IPCC Special Report on Carbon Dioxide Capture and Storage, Cambridge University Press, Cambridge, UK and New York, NY, USA, 2005, pp. 442.
- [2] DNV GL, 2020, CO₂ RISKMAN - Guidance on CCS CO₂ Safety and Environment, Major Accident Hazard Risk Management, Level 3 – Generic Guidance.
- [3] DNV GL, PHAST [Software version 8.4].
- [4] Gexcon, EFFECTS [Software version 11.0].
- [5] Schlumberger, OLGA [Software version 2017.2.0].
- [6] H.W.M. Witlox, M. Harper, A. Oke, J. Stene, Journ. Loss Prev. Proc. Ind. 30 (1) (2012) 243–255.
- [7] H.W.M. Witlox, J. Stene, M. Harper, S.H. Nilsen, Energy Procedia 4 (2011) 2253-2260.
- [8] IOGP, Risk Assessment Data Directory, “Riser & Pipeline Release Frequencies”, Report No. 434-04, 2019.
- [9] P. Harper, Assessment of the major hazard potential of carbon dioxide, Health and Safety Executive (HSE), 2011.
- [10] E.K. Ungar and K.J. Stroud, Proc. 40th Int. Conf. Environ. Syst. ICES 2012.
- [11] S. Connolly and L. Cusco, IChemE SYMPOSIUM SERIES NO. 153 (2007).
- [12] BS EN 10225:2019, 2019, Weldable structural steels for fixed offshore structures - Technical delivery conditions.

Assessment of Failure Frequencies of Pipelines caused by Earthquakes in the Natech Risk Assessment Framework

Fabiola Amaducci*, Alessio Misuri, Valerio Cozzani

LISES - Laboratory of Industrial Safety and Environmental Sustainability, DICAM – University of Bologna, Italy

*Corresponding author E-Mail: fabiola.amaducci2@unibo.it

1. Introduction

During a seismic event, underground pipelines can undergo significant damages releasing relevant quantities of hazardous substances with severe implications in terms of life safety and economic impact. This type of scenarios falls under the definition of Natech [1]. In recent years, quantitative risk analysis became a pivotal tool to assess and manage Natech risk. Among the tools required to perform the quantitative assessment of Natech risk, vulnerability models are aimed to characterize equipment damages from natural events. This contribution is focused on the review of the pipeline vulnerability models available for the case of earthquakes. Furthermore, a comparison of the features of the models deemed more suitable for the application to a QRA framework for Natech events is proposed.

2. Methods

A review of the academic literature was carried out in order to find empirical vulnerability models for pipelines. The search focused on the Natech area using keywords such as “pipeline”, “earthquake”, “fragility curves”, “vulnerability model” and “Probit” and their combination. In addition, more references were found looking at each reference cited by the retrieved contributions [2]. For each model, information was collected on the number of earthquakes considered for its development, the type of model proposed, the inputs required and the damage states. Finally, the most suitable models for QRA analysis are implemented for a comparison.

3. Results and discussion

The overview of the complete models found in the literature is shown in **Table 1** and **Table 2**, where the input parameters and the number of earthquakes considered in the development are also reported. Two main categories of models have been identified in the literature. A first category proposes the repair rate as a performance indicator for the damage of pipeline due to seismic load, and provides as output the number of required repairs per unit length. A second category proposes fragility curves associated with risk states depending on the mechanism of ground failure.

Table 1 Summary of models expressing the result in terms of repair rate. N = Number of past earthquakes used to develop the models.

Reference	Seismic intensity parameter	N	Reference	Seismic intensity parameter	N
[3]	PGA	6	[4]	PGV, PGD	3
[5]	PGA	6	[6]	PGV	1
[7]	PGA	1	[8]	PGA	1
[9]	PGV	3	[10]	PGV, PGD	12
[11]	MMI	4	[12]	PGA	1
[13]	PGA	2	[14]	PGA, PGV	1
[15]	MMI, PGD	7	[16]	PGV	1

[17]	PGD	2	[18]	PGA, PGV	1
[19]	PGV	6	[20]	PGV	5
[21]	PGV	7	[22]	PGV	1
[23]	PGD	5	[24]	PGA	1
[25]	PGV	7	[26]	PGV ² /PGA	1
[27]	PGA, PGV, PGD, MMI	4	[28]	PGV	4
[29]	PGA, PGV	1	[30]	PGV	2

Table 2 Summary of models expressing the result in terms of fragility curves. N = Number of past earthquakes used to develop the models.

Reference	Seismic intensity parameter	N
[31]	PGV	40
[32]	PGA, PGV	20

Only the models proposed by ALA [10] (12 earthquakes), by Lanzano [32] (20 earthquakes) and by Lanzano [31] (40 earthquakes) are suggested because they are developed on a consistent number of empirical data. Following, this subset is implemented to compare their relative merits and shortcomings. The curves for SGS (strong ground shaking) and GF (ground failure) are shown in **Figure 1** and **Figure 2**, specifying the material and (where present) also the types of joints and the damage state.

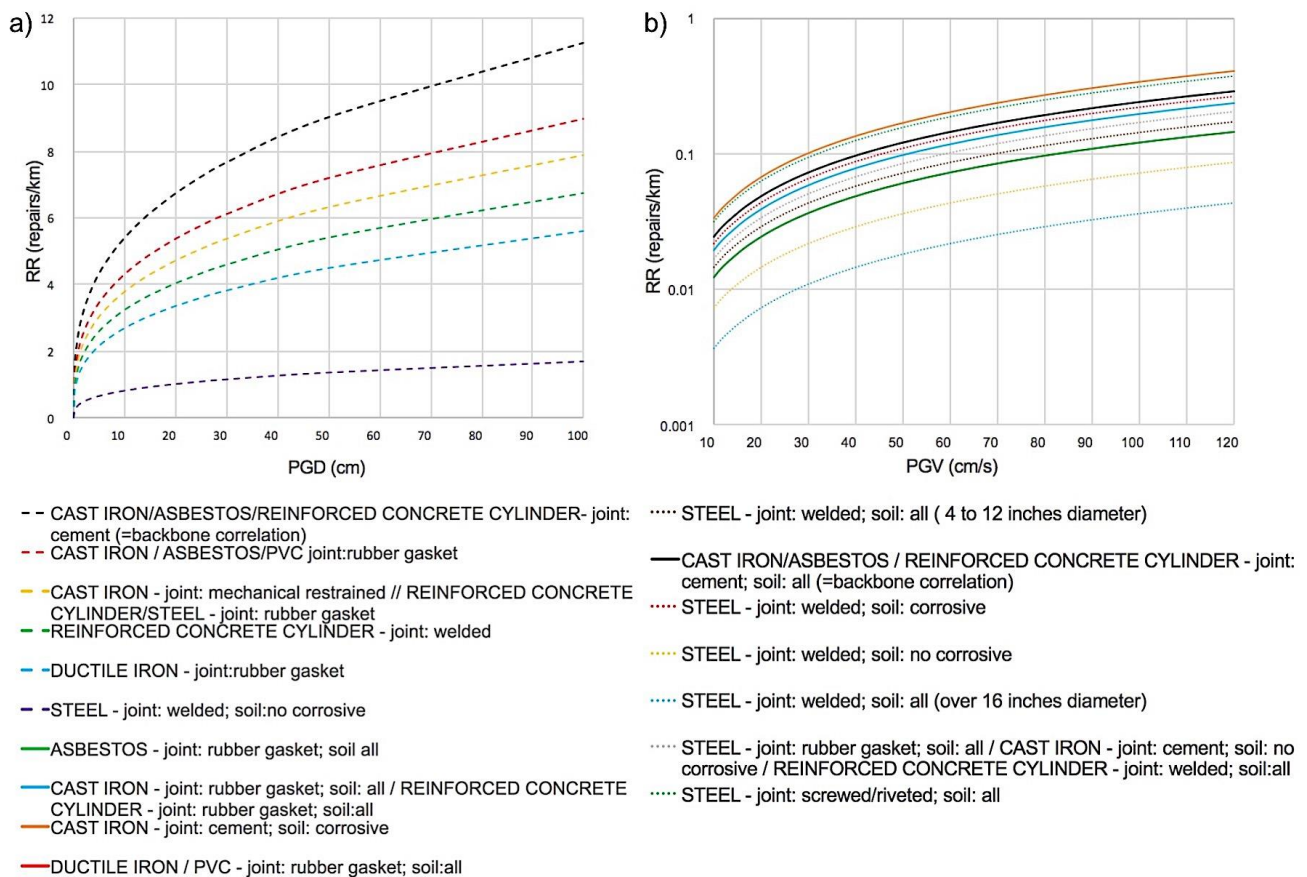


Figure 1 Vulnerability model for buried pipes developed in [10] for a) GF and b) SGS

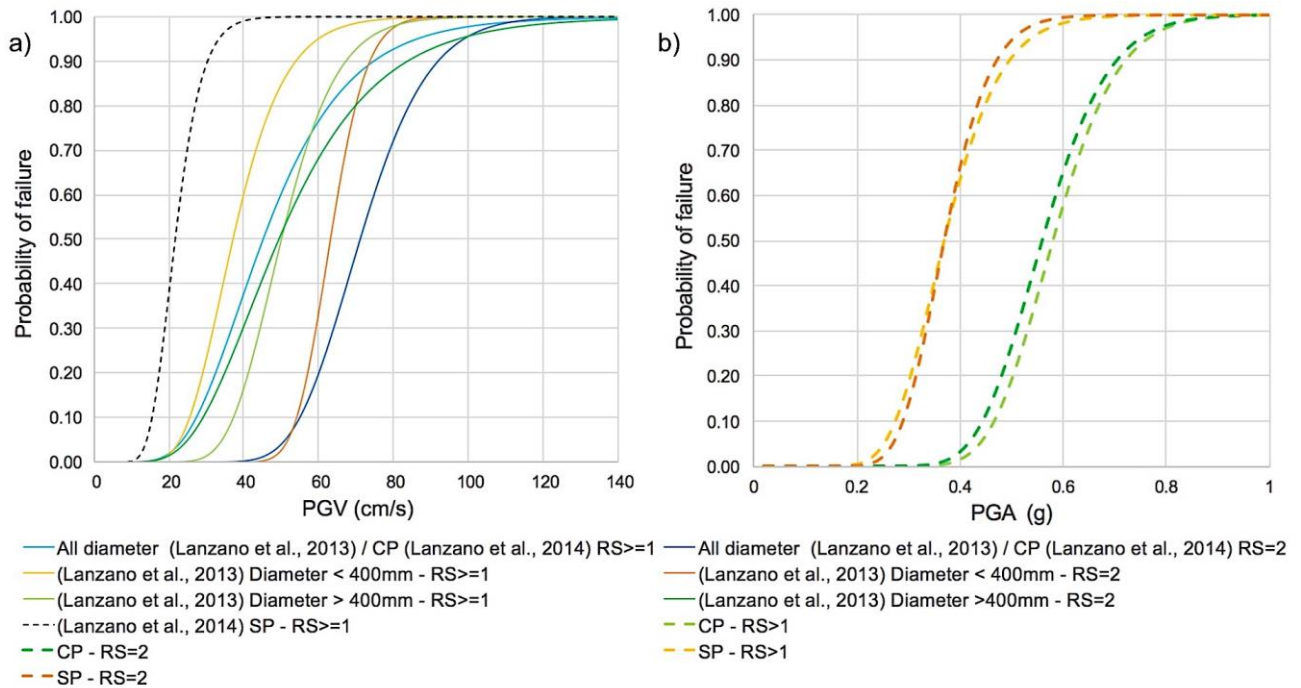


Figure 2 Vulnerability model for buried pipes developed in a) [31,32] for SGS and in b) [32] for GF

The models proposed by ALA [10] have been conceived for water-carrying pipelines, whereas the curves developed in the works of Lanzano [31,32] are possibly more generalizable. In addition, the former is more detailed in the type of soil and joint material. For what concerns the definition of risk states, the works of Lanzano [31,32] are more rigorous, while the models by ALA [10] give only thumb rules on the typology of expected failures. But in spite of this, the models by ALA [10] are suggested because to use the models of Lanzano [31,32] it is necessary to make strong assumptions about the unit length for which the failure probability is calculated, unlike the ALA [10] model.

4. Conclusions

A review of vulnerability models for pipelines subjected to seismic events is presented. Furthermore, the models deemed most suitable for a Natech QRA are implemented and discussed.

References

- [1] Krausmann E, Cruz AM, Salzano E. Natech risk assessment and management: reducing the risk of natural-hazard impact on hazardous installations. Amsterdam ; Boston, Massachusetts: Elsevier; 2017.
- [2] Fatemi F, Ardalan A, Aguirre B, Mansouri N, Mohammadfam I. Social vulnerability indicators in disasters: Findings from a systematic review. *International Journal of Disaster Risk Reduction* 2017;22:219–27.
- [3] Katayama T, Kubo K, Sato N. Earthquake damage to water and gas distribution systems. 1975:396–405.
- [4] Eidinger J, Avila E. Guidelines for the seismic evaluation and upgrade of water transmission facilities. American Society of Civil Engineers; 1999.
- [5] Katayama T, Kubo K, Sato N. Quantitative Analysis of Seismic Damage to Buried Utility Pipelines. *Proceedings Sixth World Conference Earthquake Engineering Institute Association* 1977:3369–75.
- [6] O'Rourke T, Jeon S-S. Factors Affecting the Earthquake Damage of Water Distribution Systems 1999.
- [7] Isoyama R, Katayama T. Reliability evaluation of water supply systems during earthquake. *Report of the Institute of Industrial Science, University of Tokyo* 1982;30:64p.
- [8] Isoyama R, Ishida E, Yune K, Shirozu T. Seismic damage estimation procedure for water supply pipelines. *Anti-Seismic Measures on Water Supply (Tokyo, 15-18 November 1998)* 2000:63–8.
- [9] Barenberg ME. Correlation of Pipeline Damage with Ground Motions. *Journal of Geotechnical Engineering* 1988;114:706–11.
- [10] ALA. Seismic fragility formulation for water systems 2001.
- [11] Eguchi RT, Chrostowski JD, Tillman CW, Ayala AG. Rapid post-earthquake damage detection method for underground lifelines, Publ by ASCE; 1991, p. 714–24.
- [12] Jui Huang Hung. The Analysis of Water Pipeline Damages of Wufeng Shiang in the 921 Ji-Ji Earthquake 2001.

- [13] Hamada M. Estimation of earthquake damage to lifeline systems in Japan. Proceedings of the Third Japan-US Workshop on Earthquake Resistant Design of Lifelines Facilities and Countermeasures for Soil Liquefaction (1991) 1991.
- [14] Chen WW, Shih B, Chen Y-C, Hung J-H, Hwang HH. Seismic response of natural gas and water pipelines in the Ji-Ji earthquake. *Soil Dynamics and Earthquake Engineering* 2002;22:1209–14.
- [15] O'Rourke TD, Gowdy TE, Stewart HE, Pease JW. Lifeline and geotechnical aspects of the 1989 Loma Prieta earthquake. *International Conference on Recent Advances in Geotechnical Earthquake Engineering and Soil Dynamics [Proceedings]* 1991;2, Vol. 2:1601–12.
- [16] Pineda-Porras O, Ordaz-Schroeder M. Seismic Vulnerability Function for High-Diameter Buried Pipelines: Mexico City's Primary Water System Case. *New Pipeline Technologies, Security, and Safety*, Baltimore, Maryland, United States: American Society of Civil Engineers; 2003, p. 1145–54.
- [17] Porter KA, Scawthorn C, Honegger DG, O'Rourke TD, Blackburn F. Performance of water supply pipelines in liquefied soil. *Publ by Natl Inst of Standards & Technology*; 1992.
- [18] Hwang H, Chiu Y-H, Chen W-Y, Shih B-J. Analysis of Damage to Steel Gas Pipelines Caused by Ground Shaking Effects during the Chi-Chi, Taiwan, Earthquake. *Earthquake Spectra* 2004;20:1095–110.
- [19] O'Rourke M, Ayala G. Pipeline Damage Due to Wave Propagation. *Journal of Geotechnical Engineering* 1993;119:1490–8.
- [20] O'Rourke M, Deyoe E. Seismic Damage to Segmented Buried Pipe. *Earthquake Spectra* 2004;20:1167–83. <https://doi.org/10.1193/1.1808143>.
- [21] Eidinger JM, Maison BF, Lee D, Lau B. East Bay Municipal Utility District Water Distribution Pipe Damage in 1989 Loma Prieta Earthquake, New York, NY; ASCE; 1995, p. 240.
- [22] Jeon S-S, O'Rourke TD. Northridge Earthquake Effects on Pipelines and Residential Buildings. *Bulletin of the Seismological Society of America* 2005;95:294–318.
- [23] Heubach WF. Seismic Damage Estimation for Buried Pipeline Systems, New York, NY; ASCE; 1995, p. 312.
- [24] Yeh C-H, Shih B-J, Chang C-H, Chen WYW, Liu G-Y, Hung H-Y. Seismic Damage Assessment of Potable Water Pipelines, 2006.
- [25] Eidinger JM. The Loma Prieta, California, Earthquake of October 17, 1989 - lifelines. US Gov. Print. Off.; 1998.
- [26] Pineda-Porras O, Ordaz M. A New Seismic Intensity Parameter to Estimate Damage in Buried Pipelines due to Seismic Wave Propagation. *Journal of Earthquake Engineering* 2007;11:773–86.
- [27] O'Rourke TD, Toprak S, Sano Y. Factors affecting water supply damage caused by the Northridge earthquake. *Proceedings of the Sixth US National Conference on Earthquake Engineering* 1998.
- [28] Maruyama Y, Yamazaki F. Construction of fragility curve for water distribution pipes based on damage datasets from recent earthquakes in Japan. *9th US National and 10th Canadian Conference on Earthquake Engineering 2010, Including Papers from the 4th International Tsunami Symposium*, vol. 1, 2010, p. 781–90.
- [29] Toprak S. Earthquake effects on buried lifeline systems. 1998.
- [30] Sakai H, Pulido N, Hasegawa K, Kuwata Y. A new approach for estimating seismic damage of buried water supply pipelines: New Water Supply Pipeline Damage Estimation Approach. *Earthquake Engng Struct Dyn* 2017;46:1531–48.
- [31] Lanzano G, Salzano E, de Magistris FS, Fabbrocino G. Seismic vulnerability of natural gas pipelines. *Reliability Engineering & System Safety* 2013;117:73–80.
- [32] Lanzano G, Salzano E, Santucci de Magistris F, Fabbrocino G. Seismic vulnerability of gas and liquid buried pipelines. *Journal of Loss Prevention in the Process Industries* 2014;28:72–8.

Emergency Response Management in the Risk Assessment of Cascading Events caused by Natech Accidents

Federica Ricci^{1,*}, Ming Yang², Genserik Reniers^{2,3,4}, Valerio Cozzani¹

1 LISES - Department of Civil, Chemical, Environmental and Material Engineering, University of Bologna, Bologna, Italy. 2 Safety and Security Science Section, Faculty of Technology, Policy and Management, TU Delft, Delft, Netherlands. 3 Faculty of Applied Economics, Antwerp Research Group on Safety and Security (ARGoSS), University Antwerp, Antwerp, Belgium. 4 CEDON, KULeuven, Campus Brussels, Brussels, Belgium

**Corresponding author E-Mail: federica.ricci18@unibo.it*

1. Introduction

Accidents triggered by natural events are becoming an increasing issue for industrial practitioners and policy-makers. These events are called Natech (Natural Hazards Triggering Technological Disasters), and their study has attracted attention due to their uncertain and complex nature, increasing occurrence, and severe consequences. Moreover, the increase in the number of natural events in the last decades has led to a growing number of Natech accidents [1]. In addition, the magnitude of the accident can escalate when it is triggered by a natural event. Natech accidents are characterized by the occurrence of cascading events [2], the possibility of multiple simultaneous failures [3], and the disruption of utilities, safety systems, and lifelines [4]. Besides active and passive barriers, human intervention plays a vital role in mitigating the effects of technological scenarios. The emergency response is widely considered a procedural safety barrier [5] and its role in risk assessment and management is paramount. Moreover, it is important in avoiding the occurrence of cascading events when considering fire-driven domino effects [6]. In fact, accidents that result in a fire are characterized by a time-lapse between the start of the primary fire and its spreading to neighbouring tanks [7]. This time-lapse represents the time available to perform an effective emergency response to avoid cascading events. Nevertheless, limited attention has been paid to date to the study of the emergency response, due to the complexity and the variety of actions and to the technical requirements needed to complete the procedures. Moreover, requirements differ when considering the aims of the intervention and the type of target considered. The three main targets of emergency response are human health, the environment, and assets [8]. Moreover, when considering the emergency response during Natech accidents, some actions can be delayed or unsuccessfully completed because of specific contingencies. In addition, technical elements can be unavailable or damaged due to the natural event. These elements should be considered to correctly actuate emergency response plans. Neglecting them could lead to a reduction of the effectiveness of the intervention, and to an underestimation of the overall risk in the framework of the quantitative risk assessment of Natech accidents and related domino effects.

2. Methods

Despite the criticality of the issue, scarce attention has been devoted to the study of emergency response in the case of natural events. To fill this gap, the present work aims to address the issue of emergency response in the case of natural events. In this framework, past accidents represent a source of detailed, complete and useful information considering the complexity of the phenomena involved. In the present study, accidents related to the Kocaeli earthquake (occurred on August 17th, 1999, in Turkey) [9] and the Great East Japan earthquake and tsunami (occurred on March 11th, 2011, off the Pacific Coast of Tohoku) [3] are considered. Through the analysis of these accidents, the actions of emergency response teams that can be hindered by natural events are highlighted, as well as the technical needs that resulted unavailable or damaged by the natural event.

3. Results and discussion

The accident dynamics that occurred in the events considered in the present study revealed that safety barriers alone cannot prevent the accident nor reduce the consequences, emphasizing that the role of emergency response is crucial to effectively counter Natech accidents. Nevertheless, past accidents also highlighted that the emergency response can be affected by natural events as well. According to the information available, shortcomings and lesson learned were derived and the main elements that should be improved to perform an effective emergency response are summarized as follow:

- a. **Design of mitigation safety systems.** Examples: length of hoses were not enough to reach industrial items; sprinkler systems were implemented in a limited number of tanks.
- b. **Capacity of fire-fighting materials.** Examples: shortage of fire-fighting materials; possibility of multiple and simultaneous fires not accounted.
- c. **Utility systems.** Examples: lack of the main power supply; unavailability of the fire-fighting system; inadequate design of backup systems.
- d. **Size of the internal fire-fighting team.** Examples: emergency teams on site were not enough to counteract the accident; unavailability of additional and supporting teams.
- e. **Training for any emergency teams.** Examples: lack of proper training specifically for the case of Natech accidents; lack of proper training specifically for multiple and simultaneous accidents.
- f. **Emergency response plans.** Examples: lack of proper emergency response plans specifically for Natech accidents and related cascading events.
- g. **Accessibility of the site.** Examples: disruption of external infrastructure (roads and bridges); inaccessibility of the site.
- h. **Communications.** Examples: disruption of standard communication means; an incomplete set of information shared within the teams.

The factors identified above provide the starting point for the evaluation of the effects of natural events on emergency response. Accounting for these aspects allows the correct and complete assessment of the risk associated with Natech events and improves the emergency response plans of industrial sites.

4. Conclusions

Appropriate and effective emergency response is a crucial aspect in the risk assessment and management of Natech events. The present study evidenced several shortcomings related to the emergency response during and after natural events, highlighting criticalities that should be considered when evaluating the emergency response in these accidents. Eventually, the results of the study can guide an improvement of existing emergency response plans for natural events and Natech accidents.

References

- [1] F. Ricci, V. Casson Moreno, V. Cozzani, 2021. *A comprehensive analysis of the occurrence of Natech events in the process industry*, Process Saf. Environ. Prot., 147, 703–713, 10.1016/j.psep.2020.12.031.
- [2] A. Misuri, G. Antonioni, V. Cozzani, 2020. *Quantitative risk assessment of domino effect in Natech scenarios triggered by lightning*, J. Loss Prev. Process Ind., 64, 104095, 10.1016/j.jlp.2020.104095.
- [3] E. Krausmann, A. M. Cruz, 2013. *Impact of the 11 March 2011, Great East Japan earthquake and tsunami on the chemical industry*, Nat. Hazards, 67/2, 811–828, 10.1007/s11069-013-0607-0.
- [4] A. Misuri, G. Landucci, V. Cozzani, 2021. *Assessment of risk modification due to safety barrier performance degradation in Natech events*, Reliab. Eng. Syst. Saf., 212, 107634, 10.1016/j.res.2021.107634.
- [5] S. Yuan, M. Yang, G. Reniers, C. Chen, J. Wu, 2022. *Safety barriers in the chemical process industries: A state-of-the-art review on their classification, assessment, and management*, Saf. Sci., 148, 105647, 10.1016/j.ssci.2021.105647.
- [6] G. Landucci, F. Argenti, A. Tugnoli, V. Cozzani, 2015. *Quantitative assessment of safety barrier performance in the prevention of domino scenarios triggered by fire*, Reliab. Eng. Syst. Saf., 143, 30–43, 10.1016/j.res.2015.03.023.
- [7] F. Ricci, G. E. Scarponi, G. Landucci, V. Cozzani, 2021. *Fire driven domino effect*, in Methods in Chemical Process Safety - Volume five, Academic Press, An imprint of Elsevier, 71–117, 10.1016/bs.mcps.2021.05.003.
- [8] J. D. Flynn, 2009. *Fire Service Performance Measures*.
- [9] S. Girgin, 2011. *The natech events during the 17 August 1999 Kocaeli earthquake: aftermath and lessons learned*, Nat. Hazards Earth Syst. Sci., 11/4, 1129–1140, 10.5194/nhess-11-1129-2011.

Catalytic activity of Si-modified Ni/Al₂O₃ catalysts for CO₂ hydrogenation to methane

Elena Spennati¹, Paola Riani^{*2}, Guido Busca¹, Gabriella Garbarino^{1*}

1 Department of Civil, Chemical and Environmental Engineering, University of Genoa, Via Opera Pia 15, 16145 Genoa, Italy

2 Department of Chemistry and Industrial Chemistry, University of Genoa, via Dodecaneso 31, 16146, Genoa, Italy

**Corresponding authors E-Mail: gabriella.garbarino@unige.it, paola.riani@unige.it*

1. Introduction

Nowadays, environmental pollution represents one of the main international concerns. In this context, CO₂ emissions achieved the remarkable value of 31.5 Gt in 2021, increasing greenhouse gases concentration and correlated global warming [1]. A possible strategy to mitigate this environmental problem is the conversion of CO₂ into methane by the Sabatier reaction using green hydrogen i.e., arising from renewables. Conventional catalysts for this application are based on Ru- and Ni- [2-6]. Thanks to their high activity and robustness, the low cost of Ni and its remarkable natural abundance, Ni-based catalysts represent a suitable choice for Sabatier reaction. Several supports have been investigated to enhance the catalytic performances i.e., Al₂O₃, SiO₂ [7], TiO₂, zeolites etc [8]. However, Ni-based catalysts showed low activity at low temperature, low dispersion of the active phase and, high deactivation mainly due to particles sintering or coking. For these reasons, the study for the possible industrial application of nickel-based catalysts requires further efforts in order to make them more efficient and competitive than noble metals-based catalysts. In this work [9], a series of Ni-based catalysts (from 1 to 33 wt. % NiO) was prepared and the influence of the addition of SiO₂ to Al₂O₃ supports was investigated.

2. Methods

The series of Ni-based catalysts with NiO content ranging from 1 to 33 wt.% were prepared by incipient wetness impregnation over commercial silica-alumina with different silica content, 1 and 20 wt.% (SA01 and SA20, respectively) and pure silica (S100), by relying on comparison with Ni/Al₂O₃ [10]. Ni(NO₃)₂·6H₂O was used as precursor salt. The precursor solution was added to the support and dried at 353 K for 12 hours, then the catalysts were calcinated at 1023 K for 5 hours with a heating ramp of 2 K/min. Fresh and exhaust catalysts were characterized by means of XRD, FE-SEM, FT-IR, and UV-Vis techniques. Before the catalytic test, 88 mg of catalyst was mixed with 700 mg of quartz sand, placed into a fixed-bed silica glass reactor, and reduced in situ at 1023 K for 30 minutes in a reducing environment (20% v/v of H₂ in N₂, total flow 80 NmL/min) with a heating ramp of 25 K/min. The catalytic tests were performed in N₂ diluted flow with an H₂/CO₂ ratio of 5. The reaction temperature was increased from 523 to 773 K (ascending temperature test) and decreased from 773 to 523 K (descending temperature test), in order to assess stability and eventual deactivation effects. The products composition was analyzed online by means of a FT-IR spectrophotometer.

3. Results and discussion

The addition of silica to the support led to a reduction of catalytic activity at all the investigated NiO loading, as observed in Figure 1, where the CH₄ yields obtained using the catalysts with 16 wt.% of NiO over the investigated supports are reported. Above 673 K, all catalysts approached the forecasted thermodynamic equilibrium evaluated in the chosen experimental conditions by using a Gibbs reactor and Redlich-Kwong-Soave equation of state.

It is possible to observe that, at low temperature (T<623 K), only the catalyst with the lowest SiO₂ content produced a remarkable methane yield (23% at 573 K). Moreover, only at high temperature (673 K, around the thermodynamic equilibrium) it was obtained a sufficient amount of CH₄ yield using Ni/S100 (27%), even if

its performances are significantly lower than that one obtained by using SA01 and SA20 (73 and 66%, respectively). On the other hand, an increase of Ni loading in the catalysts enhanced the catalytic activity with a positive effect towards methanation reaction and a negative effect on reverse water gas shift reaction, leading to the production of CO. The CH₄ yield obtained at 623 K using SA01 was increased from 1 to 74% by increasing the NiO content from 1 to 33%. This effect has been further investigated by kinetic measures carried out in differential reactor conditions together with the determination of apparent activation energies.

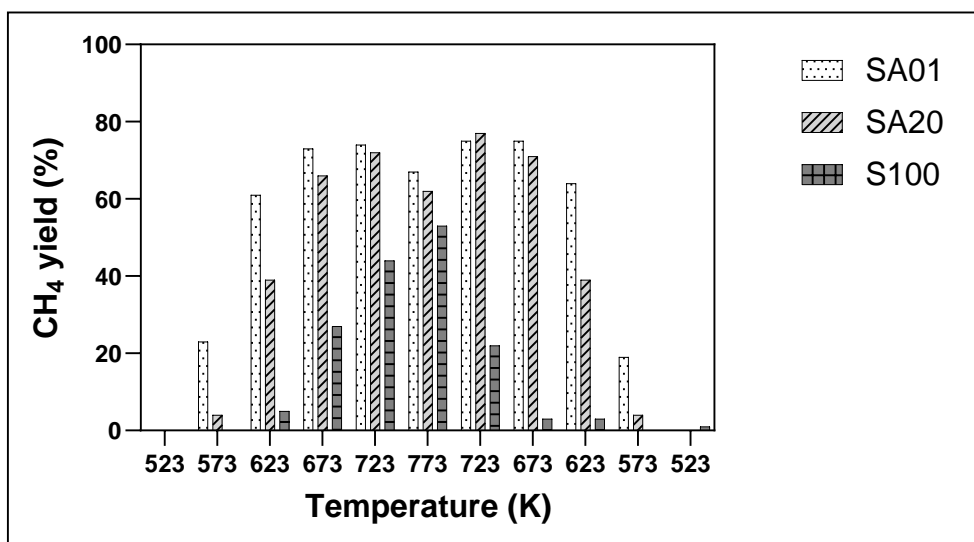


Figure 1. Methane yield obtained using the catalyst with 16 wt.% of NiO load over SA01, SA20 and S100.

4. Conclusions

Silica addition is beneficial at very low loadings, but it reduces the catalytic activity towards carbon dioxide methanation. At the same time, it slightly enhances the production of carbon monoxide, thus leading to the careful determination in-between improved catalysts stability, optimum nickel loading, high CO₂ conversion and methane selectivity. The best nickel loading for the CO₂ methanation over all the investigated supports was the 16 wt.% NiO. Among tested catalytic materials, 16 wt.% NiO supported on SA01 resulted the best catalyst in terms of both catalytic and morphological point of view, by achieving a methane yield of 73% at 673 K at atmospheric pressure and at a GHSV of 55000 h⁻¹.

References

- [1] Iea.org/reports/global-energy-review-2021/CO₂-emissions
- [2] G. Garbarino, P. Riani, L. Magistri, G. Busca, *Int. J. Hydrog* 39 (2014) 11557-11565
- [3] G. Garbarino, D. Bellotti, P. Riani, L. Magistri, G. Busca, *Int. J. Hydrog* 40 (2015) 9171-9182
- [4] G. Garbarino, D. Bellotti, E. Finocchio, L. Magistri, G. Busca, *Catal.* 277 (2016) 21-28
- [5] G. Garbarino, F. Pugliese, T. Cavattoni, G. Busca, P. Costamagna, *Energies* 13 (2020) 2792
- [6] G. Garbarino, P. Kowalik, P. Riani, K. Antoniak-Jurak, P. Pieta, A. Lewalska-Graczyk, W. Lisowski, R. Nowakowski, G. Busca, I. S. Pieta, *Ind. Eng. Chem. Res.* 60 (2021) 6554-6564
- [7] F. Meirer, B.M. Weckhuysen, *Nat. Catal.* 1 (2018) 127-134.
- [8] W. Gac, W. Zawadzki, M. Rotko, M. Greluk, G. Słowik, G. Kolb, *Catal. Today* 357 (2020) 468-482.
- [9] P. Riani et al., Effect of Si- in the formulation of Ni-based catalysts for Sabatier reaction, Manuscript in preparation.
- [10] G. Garbarino, C. Wang, T. Cavattoni, E. Finocchio, P. Riani, M. Flytzani-Stephanopoulos, G. Busca, *Appl. Catal. B* 248 (2019) 286-297.

Enhancing fluidized operations in heterogeneous catalysis through dynamically structured pulsed reactors

Davide Cafaro¹, Daniele Micale¹, Riccardo Uglietti¹, Kaiqiao Wu², Mauro Bracconi¹, Marc-Olivier Coppens² and Matteo Maestri^{1*}

¹Laboratory of Catalysis and Catalytic Processes, Dipartimento di Energia, Politecnico di Milano, Via la Masa 34, 20156 Milano (Italy);

²Centre for Nature Inspired Engineering, Department of Chemical Engineering, University College London, Torrington Place, London WC1E7JE (United Kingdom)

*matteo.maestri@polimi.it

1.Introduction

The coupling between heterogeneous catalysis and fluidization technologies is pivotal to tackle the challenges to achieve a sustainable economy. On the one hand, the peculiarity of this reactor technology (i.e., homogeneous reactive environment, the motion of the solid phase) can promote the development of novel processes [1] aimed at the valorization of the natural resources and the CO₂ capture. On the other hand, the complex fluid dynamics of conventional fluidized units is strongly influenced by the reactor size hampering their design and scale up. In particular, the motion of the bubbles strongly affects both conversion and selectivity since it causes a wide distribution of the gas-particle contact time and thus it must be properly managed to maximize the performances of such units.

A possible solution to face these problems is to achieve a dynamically structured bed by injecting a pulsed inlet gas flowrate [2]. Accordingly, an ordered bubble pattern is experienced providing additional degrees of freedom in their design and scale-up [2,3]. Despite the potential of such fluidization technique [3], its combination with catalytic processes has not already been analyzed in the literature. Thus, this work aims at investigating dynamically structured fluidized reactors in the context of heterogeneous catalysis by means of a multiscale Euler-Lagrange approach.

2. Methods

The numerical investigation of catalytic pulsed fluidized beds is performed by adopting a multiscale reactive particle tracking methodology [4], sketched in Figure 1. This CFD-DEM framework is based on the coupling between the LIGGGHTS[®] DEM code for the tracking of the solid materials and the catalyticFOAM [5] framework for the solution of the governing equations for non-isothermal catalytic reactive flows. By adopting this numerical framework, it is possible to provide insights into the interplay between macro-scale transport phenomena, particle-scale gas-solid and solid-solid interactions, considering also elementary steps at the catalyst sites, leading to predictions in agreement with experimental evidence [6].

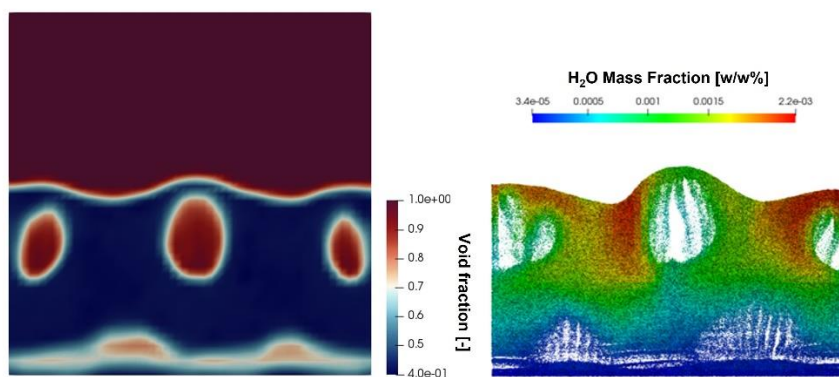


Figure 1. Maps of the void fraction (left) and water mass fraction in the solid catalyst (right) computed by the multiscale particle tracking methodology [4].

3. Results and discussion

A pseudo-2D lab-scale reactor configuration [2] has been investigated in this work by adopting a sinusoidal inlet flow rate. The hydrogen oxidation over Pt at ambient temperature in diluted conditions with oxygen as limiting reactant has been used as benchmark process to reproduce units working under almost isothermal conditions. First, the effect of the pulsation frequency on the bubble size (Figure 1a) has been analysed. The flow pulsation determines the generation of an ordered pattern of bubbles [2] whose dimensions decrease with the increment of the frequency, asymptotically reaching the value of the non-pulsed unit for a frequency higher than 13 Hz. At the same time, the pulsation also affects the solid mixing in the reactor. Indeed, Figure 1(b) shows the evolution over time of the Lacey's mixing index [6], which ranges from 0 (unmixed system) to 1 (ideal, perfect mixing). An enhancement of the mixing rate with frequency (shifting the emulsion phase towards a CSTR behavior) is observed up to 9 Hz. Then, the mixing decreases since the bed structure is gradually lost, approaching the non-pulsed condition. The complex interplay between the aforementioned parameters influences the reactive behavior of the bed. The higher bubble dimension with respect to the non-pulsed configuration leads to a lower conversion in the whole range of investigated frequencies. In particular, the O₂ conversion decreases from 5 Hz to 7 Hz, due to more pronounced mixing, leading to a more pronounced CSTR-like behavior of the emulsion phase, despite the smaller bubble diameter which favors the bubble-emulsion mass transfer. Thus, the minimum of the conversion is observed at a frequency of 7 Hz, where the limited decrease in bubble size is counterbalanced by the high mixing. Then, an increment of the conversion is experienced for higher frequency since both the bubble diameter and the mixing efficiency decrease.

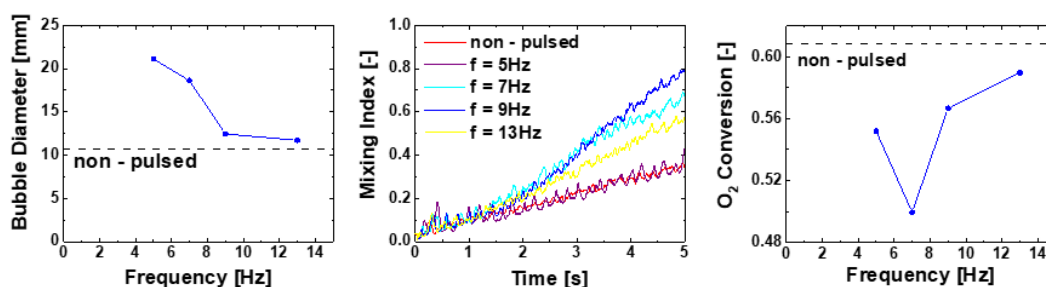


Figure 2. Catalytic pulsed fluidized bed investigation: impact of the pulsation frequency on bubble size (left), particle mixing (middle) and O₂ conversion (right).

4. Conclusions

This fundamental investigation highlights the strong relationship between the pulsation frequency and the overall catalytic performance in a dynamically structured fluidized bed, reflecting the intrinsic multiscale behavior of this system. In particular, the higher mixing rate and the more careful control of the gas-solid contact time with respect to the conventional fluidized units make this fluidization concept promising for the management of processes affected by selectivity issues (i.e., Oxidative Coupling of Methane) or characterized by strong exothermicity (i.e., methanation).

Acknowledgments

European Union's Horizon 2020 research and innovation programme under G.A. no. 814416 (ReaxPro) is gratefully acknowledged.

References

- [1] F. Raganati, V. Gargiulo, P. Ammendola, M. Alfe, R. Chirone, *Chem. Eng. J.* 239 (2014) 75-86
- [2] K. Wu, L. de Martin, M.-O. Coppens, *Chem. Eng. J.* 329 (2017) 4-14
- [3] V. Francia, K. Wu, M.-O. Coppens, *Chem. Eng. Sci.* 248 (2022) 117189
- [4] R. Uglietti, M. Braconi, M. Maestri, *React. Chem. Eng.* 5 (2020) 193-396
- [5] M. Maestri, A. Cuoci, *Chem. Eng. Sci.* 96 (2013) 106-117
- [6] N.G. Deen, G. Willem, G. Sander, J.A.M. Kuipers, *Ind. Eng. Chem. Res.* 49 (2010) 5246-5253

Catalysis by Confinement: an application to Diels-Alder reactions within voids of molecular dimensions

Gabriele Contaldo¹, Zhao-Bin Ding², Matteo Maestri^{1*}

1 Politecnico di Milano, Milano, Italy; 2 Sun Yat-Sen University, Zhuhai, China

**matteo.maestri@polimi.it*

1. Introduction

Zeotypes are effective catalysts for many chemical reactions. These structures are characterized by voids of molecular dimensions. Recent studies have shown that the catalytic consequences of confinement define reactivity and selectivity differently, depending on the reaction temperatures. Such effects of confinement are noteworthy at low temperature range and for low enthalpic barrier reactions and have been experimentally proven for the oxidation of NO in mesoporous silicas and pure silicious frameworks (SIL, CHA, BEA) [1]. The main cause of this enhanced reactivity is identified as the trade-off between the enthalpic stabilization, provided by the van der Waals (vdW) interactions between the molecules and the confining walls, and the entropic penalties inferred by a loss of mobility upon confinement. In particular, the enthalpic effects predominate over the concomitant entropy losses at low temperature, hence lowering the confined Gibbs free energy with respect to the homogeneous route. Furthermore, these interpretations are consistent with the theoretical treatments which predict no detectable enhancement when the vdW interactions are excluded [2]. Such catalysis by confinement is expected to be the real consequence for the Diels-Alder cyclization of buta-1,3-diene to 4-vinyl-cyclohexene [3]. Hence, we explain the experimentally observed rate enhancement on the basis of transition state enthalpic stabilization brought forth by dispersive forces.

2. Methods

Density Functional Theory (DFT) calculations that include dispersive forces (Grimme D2) were performed by adopting a generalized gradient approximation for the exchange functional proposed by Perdew, Burke and Ernzerhof (PBE), plane-waves basis-set and ultrasoft pseudo-potentials using the QuantumEspresso package. Brillouin zone samplings were restricted to the Γ -point. The transition states and the minimum energy paths were identified using the climbing image nudge elastic band methodology (CI-NEB). Statistical thermodynamic formalisms were adopted for the description of the entropy, enthalpy and Gibbs free energy for reactants, products and transition states, by accounting for the translational, rotational and vibrational contributions. Vibrational frequency calculations were performed by using a finite-difference approximation of the Hessian matrix implemented in Atomic Simulation Environment (ASE). Molecules in gas phase are assumed ideal.

3. Results and discussion

Here we performed a detailed study of the confinement effects induced by the narrow pore dimensions of chabazite (CHA), zsm-12 (MTW) and beta (BEA) zeolites for a set of three Diels-Alder reactions. In particular, the first reaction analyzed involves (1) the cycloaddition of ethylene and butadiene to cyclohexene, while the second and the third ones are two isomeric forms of the cyclodimerization of butadiene to (2) *cis*-4-vinyl-cyclohexene (VCH) and (3) *trans*-VCH. The analysis conducted in all the frameworks show larger rates when temperature decreases, as reported in Figure 1 for the showcase reactions (1) and (3), demonstrating how enthalpic stabilization more than prevails over the concomitant entropy losses in this range. Indeed, entropic penalties of confinement become more relevant when temperature increases. DFT-derived rates under confinement are up to 10^8 times larger than the homogeneous routes, as a consequence of differences between the energy of the confined transition states and the correspondent value in gas phase. In particular, reaction (1) is found to be more strongly stabilized (by 71.4 kJ mol^{-1}) by the smallest zeolite cavity of MTW; reactions (2) and (3), instead, show larger rates because the bigger TS structures are closer to the internal walls of the cavity, thus exhibiting stronger stabilization effects, as observed for CHA (89.7 kJ mol^{-1} for (2) and 92.6 kJ mol^{-1} for

(3)) and MTW (91.6 kJ mol⁻¹ for (2) and 89.7 kJ mol⁻¹ for (3)). As a result, the size and the shape of the pores play a fundamental role in stabilizing molecules under confinement without affecting the geometrical properties of confined structures with respect to the gas phase counterpart. However, this effect is compensated by repulsive interactions when molecules are too close to the internal surface of the cavities, giving rise to a decrease of the rate enhancement as shown by the confinement within CHA and MTW in Figure 1.b). Finally, these results further confirm how the size of molecules and cavities notably affects the strength of dispersion forces, key contribution in catalysis by confinement for reacting systems under confined spaces.

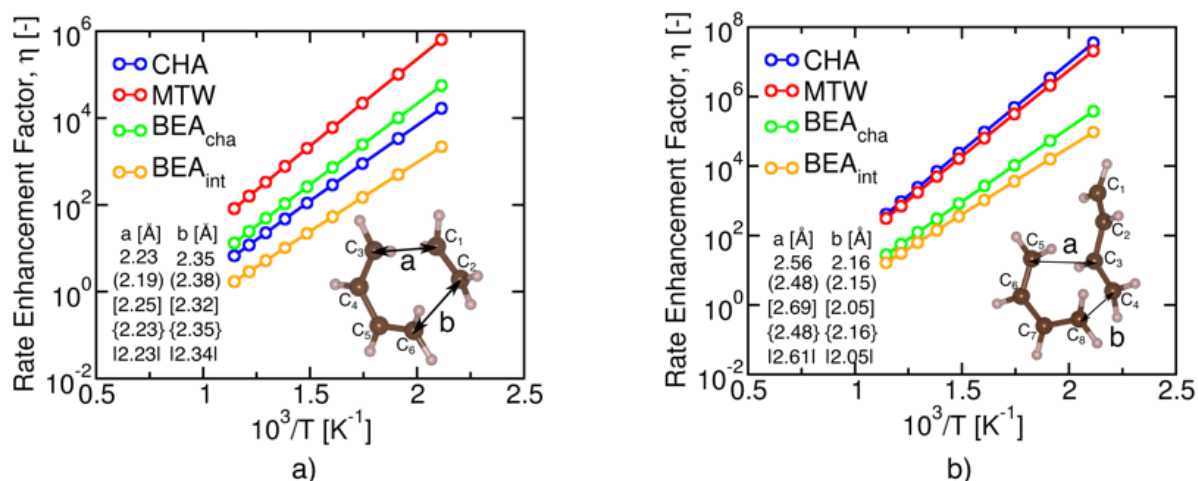


Figure 1. a) Rate Enhancement Factor for reaction (1) and b) Rate Enhancement Factor for reaction (3). Confinement prevails at low T because enthalpic stabilization more than compensates for the entropy losses. () = CHA, [] = MTW, { } = BEA_{cha}, | | = BEA_{int}.

4. Conclusions

This work provides fundamental underpinnings on the role of pore dimensions in the stabilization under confined environments. We provide the mechanistic underpinnings for interpreting the rate enhancements for Diels-Alder reactions under confined environments. The results will allow to improve and optimize the catalyst design for industrially relevant catalytic processes by a molecular scale investigation within the framework of multiscale reaction engineering. Computational time at CINECA-Bologna is gratefully acknowledged.

References

- [1] Artioli, N.; Lobo, Raul F.; Iglesia, E. *J. Phys. Chem. C* 2013, 117, 40, 20666-20674
- [2] Maestri, M.; Iglesia, E. *PCCP* 2018, 20, 23, 15725-15735.
- [3] Dessau, R. M. *J. Chem. Soc.* 1986, 15, 1167-1168

Optimization of the lifetime of CeO₂-carrier material over consecutive conversion cycles of methane for hydrogen and syngas production

Matteo Minelli¹, Mattia Boscherini¹, Francesco Miccio², Elena Landi², Ferruccio Doghieri¹, Alba Storione^{1*},

1 DICAM, Alma Mater Studiorum Università di Bologna, via Terracini 28, 40136 Bologna, Italy;

2 CNR-ISTEC, National Research Council, via Granarolo 64, 48018 Faenza, Italy

** alba.storione2@unibo.it*

1. Introduction

Despite all efforts to mitigate climate change, new energy sources cannot replace fossil fuels on a large scale at the short term and the supply of energy and fine chemicals must be addressed with the smart utilization of resources most largely available. The US energy information administration reports that there are abundant natural gas and shale gas reserves in the world and most of them are recoverable [1], as a consequence processes involving methane conversion are worthy to be investigated and optimized.

Traditional processes involving methane utilization suffer severe carbon deposition and sintering of the active phase, especially when CO₂ is present as co-reagent. Moreover, the majority of such processes relies on the use of expensive catalytic materials where the active phase is often a noble metal with high cost of raw material and also greater cost associated to the disposal of the exhausted catalyst. In the past years the utilization of CeO₂, a rare earth mineral, for reforming processes has constantly increased due to its remarkable redox properties and its resistance in harsh environments, including temperatures up to 2000 °C [2]. Furthermore, cerium, despite being a lanthanide, is rather abundant in the earth's crust, comparable to copper [3]. However, its use poses kinetic limits of the reforming reaction that requires temperature around 900-950°C [4] to achieve appreciable yields of syngas.

The energy requirements represent a growing concern since they are strictly related to the CO₂ emissions and become more and more relevant to find alternative source of energy or a most successful approach to intensify the utilization of the energy available in the overall process [5,6].

Chemical looping technology could offer a route to optimize the energy utilization, splitting in two steps the overall process with the reforming in one unit and the carrier regeneration in a second unit. The energy needed by the endothermic reaction in the reforming could be partially supplied by the exothermic heat released during the oxidation step and CO₂ emissions could be limited employing CO₂ itself as oxidant agent in the prospective of a CO₂ net-zero emission process.

However, even in this case one of the main issues hindering large scale implementation of the process is given by the carbon deposition associated to methane decomposition that strongly affects the durability of the carrier. Thus, in this work large attention has been paid on the regeneration efficiency and its optimization to increase the performance and the lifetime of material. The process has been simulated with the thermodynamic tools of Aspen Plus software simulator to check the feasibility and restrict the number of experiments. Several conditions for the regeneration of CeO₂ carrier have been tested experimentally at different composition (air content 3%, 5%, 21%) and the lifetime of the material after repeated cycles has found to be satisfactory.

2. Methods

2.1 Simulations approach and description

Process analysis was performed by means of thermodynamic tools available in Aspen Plus simulator. All the simulations were carried out at the steady state using MIXCISLD model for the evaluation of vapors and conventional solids phases. A reactor of Gibbs type was selected to perform the simulations and the related results were obtained employing the Gibbs minimization energy method, in combination with the ideal gas law for the description of the equilibrium in the gaseous phase only. A sensitivity analysis was performed in the reforming unit in presence of cerium oxide and selecting the temperature as only variable to evaluate the effect of small variation in temperature on reagent conversion, carbon deposition, and syngas purity. The conditions required for carrier regeneration were investigated in a preliminary inspection at different temperature and oxidant composition (air, CO₂).

2.2 Material Preparation

Commercial cerium oxide powders (Pi-kem UK, purity 99.9 %) were pelletised in a hydraulic press (8-9 MTons which corresponds to an actual pressure on the sample of 250 MPa) and then sieved to the desired size fraction of 0,595-0,841 mm. The particles were calcinated with a heating rate of 3 °C/min, left in isothermal condition at 900 °C for 1 h, then cooled to room temperature.

2.3 Experimental apparatus and test procedure

The test rig consists of a stainless steel (AISI 316) fixed bed reactor with an inner diameter (ID) of 10 mm. The reactor is enclosed in a tubular furnace which allows to keep a constant temperature. A K-type thermocouple is located along the reactor to measure the bed (internal) temperature at mid-length. The system is entirely insulated with external layer of quartz wool.

The feed flow rate and composition are controlled by Bronkhorst mass flowmeters, while the outlet gases are analyzed continuously by means of an online analyzer (GEIT 3100 P+ Syngas) equipped with a thermal conductivity detector (TCD), an infrared detector (NDIR) and an electrochemical oxygen sensor.

The apparatus was used to conduct test at different temperature (900 °C and 950 °C) while keeping constant the feed flow rate, the reagent partial pressure and the loading of the carrier. It was set up to work in cyclic mode by switching gases atmosphere from reducing to oxidizing in order guarantee the material regeneration over consecutive cycles.

In a typical experiment, the reactor was loaded with 15 g of cerium oxide oxygen carrier prepared as previously described and employed without any further treatment. The sample was heated up to 900° at atmospheric pressure and the temperature of the material bed was monitored and recorded approximately every two minutes while the composition of the gases evolved during the reaction was analyzed continuously.

First experiments were conducted at 900°C and at 950 °C in CH₄ (10% in N₂, 1 NL/min) and last until no more gaseous products were detected while the reduced carrier was re-oxidized at different content of oxygen (3%,5%, 21%) in N₂ at the same reforming temperature. These tests were also repeated for both the conditions to check reproducibility and the maintenance of performance over 3 consecutive cycles. At a later time shorter experiments were performed increasing the cycle number up to five.

3. Results and discussion

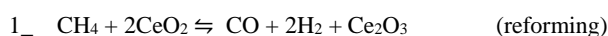
The thermodynamic analysis (Table1) obtained by Aspen+ for the stoichiometric ratio of the reactants showed a large variability of the syngas ratio with the temperature and a significant contribution of coke to the scheme of reaction when temperature lower than 900°C is reached on CeO₂ carrier.

T[°C]	χ_{CeO_2}	$\frac{\text{H}_2}{\text{CO}}$	nC/nCH _{4,in}
860	0.33	6.19	0.65
870	0.45	4.59	0.55
875	0.52	3.94	0.48
880	0.60	3.37	0.40
890	0.83	2.43	0.17
900	1	2.02	0.01
910	1	2.02	0.01
920	1	2.01	0.01
930	1	2.01	0.01

Table 1: Simulation results for [O]/CH₄ ratio of 0.5 at different Temperature and 1 atm.

The results also pointed out an incomplete conversion of the carrier under the same temperature. In this light, all the experiments were conducted with a starting temperature at least equal to 900 °C and recording the temperature profile along the material bed for all the duration of the reforming reaction.

Preliminary results at 900 °C and at 950 °C showed a lower reproducibility of the experiments when the first is preferred as reforming temperature. Moreover the effect of an increase in temperature turned out to be more relevant on the CeO₂ average conversion than on the syngas ratio variability. Indeed, the CeO₂ conversion varied from 79.7 ± 9.5 to 86.8 ± 1.7 % with the increase in temperature while modest variation interested the syngas ratio (max. variation of 0.7 for the case at 900 °C against the 0.5 for 950 °C). An explanation to this evidence was found in the analysis of the trend of the bed temperature profile with the extent of the involved reaction:



Indeed, when the carrier is at 900°C, it strongly reacted with methane in the endothermic reaction (1) decreasing the bed temperature under 900°C and going below the minimum threshold suggested by simulation where the variables are more sensitive to changes of temperature. However, setting the temperature 50 °C higher permitted to avoid this effect leading to the obtainment of more stable values. The same analysis also allowed to determine an optimal time for the reduction reaction selecting the one for which the bed temperature's profile was close to the isothermal condition. Next experiments were conducted at 950°C with 30 minutes for each reduction (10% CH₄ in N₂, 1 NL/min) and for a larger number of redox cycles. The regeneration of carrier was initially performed with a low partial pressure of oxygen to avoid to handle too much higher increase in temperature (up to 1000 °C) due to the occurrence of the exothermic reactions. Results are shown in the figure 1.

As one can see the minimum temperature reached during methane conversion corresponds to 920 °C and never goes below this value.

Furthermore, the plots show an evident correlation between the tendency of the minimum temperature of reduction and the values obtained for carrier conversion (figure 1a, 1b). The trend suggests that the fresh carrier undergoes under more severe reduction (superior contribution of the reaction 1) and this is also confirmed by the higher value of CeO₂ conversion at the beginning in comparison with the following cycles (figure 1b). However, the carrier reached appreciable conversions in all the cases with a degradation in

performance over the cycles due to the presence of carbon accumulated on the carrier (figure 1c, 1d). Indeed, the carbon derived from the thermolysis side reaction was only partially consumed in the regeneration step.

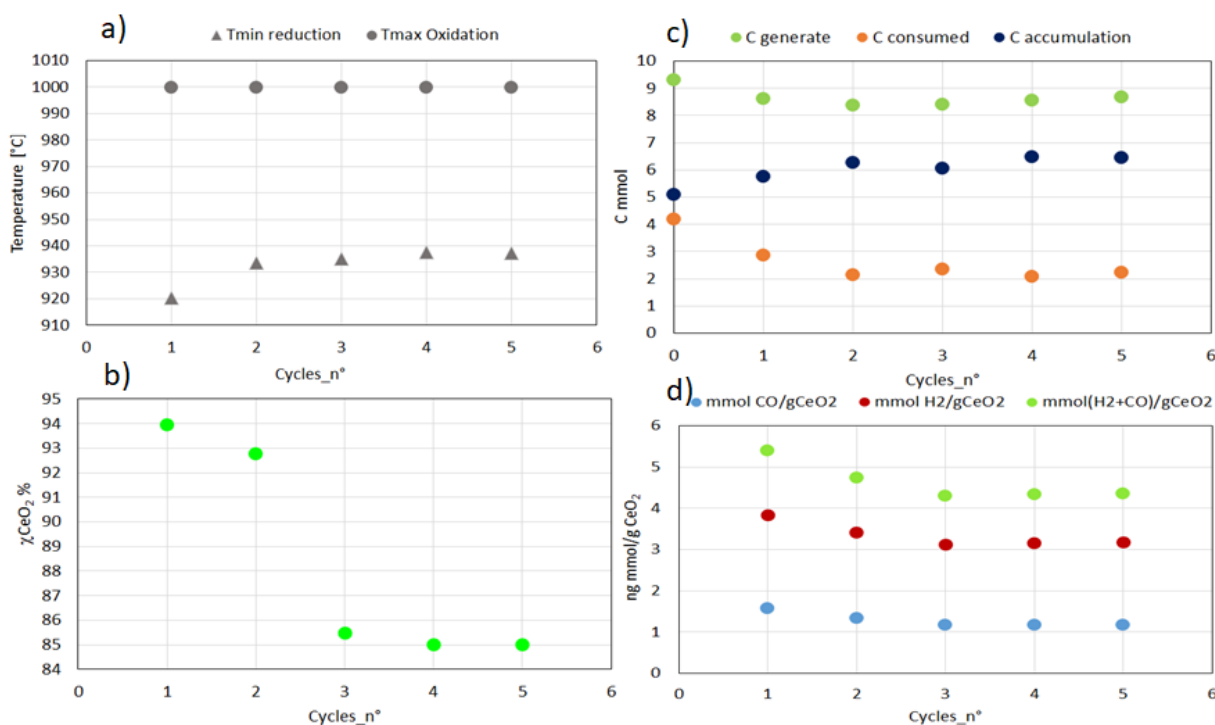


Figure 1: Main results obtained at 950°C and 1 atm with a CeO₂ loading of 15,34g. The plot reported as a function of the number of redox cycles: a) operative temperature; b) carrier conversion; c) carbon deposition; d) syngas productions for g of carrier.

The same plot also reports as cycle 0 the data related to an experiment conducted in absence of carrier material. The related data showed that in absence of oxygen carrier only the thermolysis occurs and a content of 3% of oxygen in air is not enough to guarantee the consumption of all the carbon during oxidation. The same trend was confirmed even in presence of the oxygen carrier where a greater content of oxygen is available due to the nature itself of the carrier. Additionally, the data collected during regeneration were also analyzed to rule out the possibility of an incomplete regeneration of the carrier material and to estimate the time desired by oxidation (Figure 2a). The image reports the results of the mass balance on the oxygen where the oxygen released was quantified directly account the total fed and the molar fraction at the exit of the analyzer while the oxygen consumed was estimated as the sum of oxygenated compounds measured at the reactor exit and the oxygen needed back by the carrier accounting the quantity released for the methane oxidation.

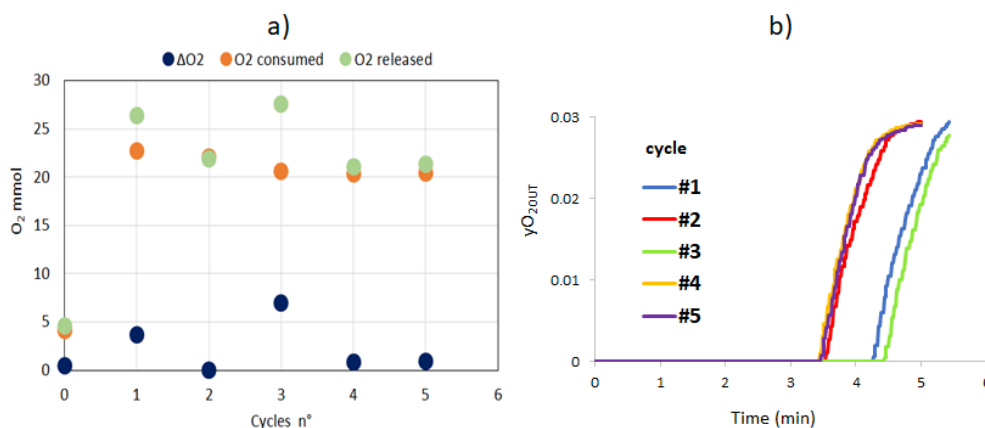


Figure 2: Results, over five consecutive cycles, of: a) regeneration efficiency and b) duration.

As evidence in the plot there is compliance in the oxygen mass balance proving the complete regeneration of the carrier over five consecutive cycle. It is also worth noticing that for all the cycles the oxidation lasts no more than five minutes (figure 2b) thus allowing a considerable decrease in the time of conduction of the overall process.

4. Conclusions

This work has showed that CeO₂ is promising as oxygen carrier material for looping methane conversion in fine chemicals. The carrier proved to be selective for syngas obtainment and to be easily and rapidly regenerated during several cycles without drastic changes in the performances. However, the presence of accumulated carbon on the CeO₂ material has been considered the cause of a decrease in the carrier conversion and of a drop of syngas production thus hindering the implementation of the process on a greater scale. Future works will aim to enhance the carbon removal, by studying the system with different oxygen partial pressure and testing the feasibility of the employment of other oxidant agent such as CO₂ even in consideration of a further optimization of the process that involved also energy balance assessment.

References

- [1] Z. Sun, X. Wu, C. K. Russell, M. D. Dyar, E. C. Sklute, S. Toan, M. Fan, L. Duan, W. Xiang, J. Mater, Chem. A 7, (2019) 1216.
- [2] R. Schmitt, Chem. Soc. Rev., 49 (2020), 554
- [3] G. Haxel, J. Hedrick and G. Orris, US Geological Survey, US Geological Survey, 2002
- [4] A. Storione, M. Minelli, F. Doghieri, E. Landi, F. Miccio, Chemical Engineering Transactions, 86(2021), 1267-1272.
- [5] A. Ozbilen, I. Dincer, MA. Rosen, Environ Impact Assess Rev, 9 (2013), 1-42.
- [6] B. Chen, Z. Liao, J. Wang, H. Yu, Y. Yang, Int J Hydrogen Energy, 200 (2012) 37-3191.

Methane cracking in molten tin to produce pure hydrogen and carbon.

Benedetta de Caprariis^{1*}, Paolo De Filippis¹, Francesco Anania¹, Gaetano Iaquaniello^{2*}

1 Department of Chemical Engineering, Sapienza University of Rome; 2 NextChem S.p.A.

**Benedetta de Caprariis E-Mail: benedetta.decaprariis@uniroma1.it*

1. Introduction

Methane cracking is considered a bridge technology linking the production of grey and green hydrogen. Processes with the aim of producing hydrogen from renewable and green sources are still not ready for an industrial scale-up. The price of the green hydrogen is too high compared to the grey hydrogen produced by fossil fuels [1]. Scientific and industrial research activities in this sector are continuously improving the state of the art and a possible industrialization of these processes at a competitive price is expected in no less than 10 years. Electrolysis of water is the only green process which was scaled up at industrial level and which contributes for a quote of 4 % to the total hydrogen production. The rest of the hydrogen comes from fossil fuels contributing thus to the CO₂ emissions. To respect the limits imposed by European Union in 2050, waiting for the industrialization of green hydrogen production processes, a viable alternative is the methane cracking.

Methane cracking involves the reaction (1).



Methane at high temperature is cracked into carbon and hydrogen. The produced hydrogen is pure and the carbon is a solid and, thus, easy to be separated. The carbon is a key product of the process, depending on its physical and chemical properties, it can be valorized or sequestered making the process zero CO₂ emission. As already demonstrated the carbon can be produced in different forms such as carbon coke, carbon nanotubes and others, some of which can have a very high commercial value. However, this process presents several issues which should be addressed before it can be scaled up. The reaction takes place at very high temperatures (about 1000 °C) and a catalyst is needed to obtain reasonable conversion of methane. The process produce carbon and thus the traditional catalysts (such as supported Ni) are immediately deactivated, furthermore the production of carbon creates serious problems of reactor clogging [2]. To overcome these problems traditional reactors should be completely revolutionized.

Aim of this work is to develop an innovative methane cracking reactor using molten tin as medium for the methane cracking reaction. The use of molten tin leads to several advantages; tin has an excellent thermal conductivity and thus the heat transfer between the medium and the methane is enhanced, its melting temperature is low, its vapor pressure is very low at the used temperatures assuring a low vaporization of the tin and thus low tin loss in the outlet gas flow. Furthermore, its density is higher than that of the produced carbon which implies the floating of the carbon on the tin and thus an easy separation between them. The use of tin has already been explored in literature for methane cracking [3,4], however a systematic study where the influence of temperature, residence time, and presence of filler is investigated is not present.

2. Methods

The tests are conducted in a quartz fixed bed tubular reactor (1.7 cm in diameter and 35 cm height) filled with liquid tin and heated by an external electric furnace. The methane is injected into the reactor by a capillary with internal diameter of 0.25 mm. The tested temperatures range between 950 and 1070 °C and the methane inlet flow rate between 30 ml/min to 60 ml/min. The effect of the bed height on the methane conversion was also investigated, the tests were performed in three different bed heights, 15, 18, 20 cm. The filler used has spheric shape with a diameter of 3 mm made of aluminosilicate. At the reactor exit the produced carbon is

separated in a flask and characterized by SEM, XRD and Elemental analyzer and the gas is sent to a Mass Spectrometer for the analysis. The experimental set-up is reported in Figure 1.

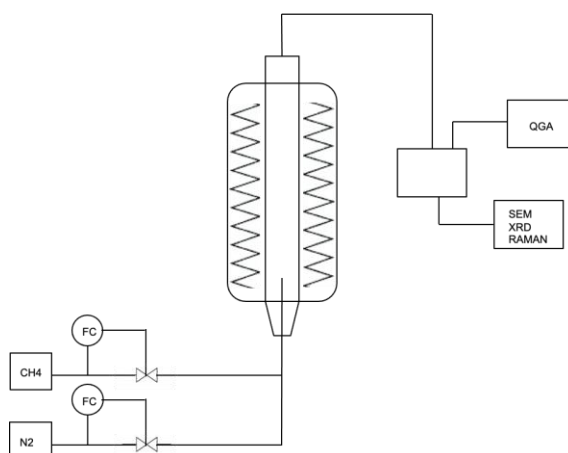


Figure 1. Experimental set-up.

3. Results and discussion

In Figure 2 the results of the tests made for different bed heights and different flow rates are reported. The maximum conversion, about 20 %, is reached for 15 ml/min of methane flow rate and 150 mm of bed height. The conversion at 1070 °C is quite low but it was expected in absence of a catalyst and a filler. The conversion decreases when the flow rate is increased since the residence time decreases, however a strange behavior is noted increasing the bed height. It seems that the increase of the bed height and, therefore, of the residence time led to a worse conversion for a constant flow rate.

However, the increase of the bed height favors the formation of carbon, in fact when the tests are made using a bed height of 150 mm the carbon is produced in form of a very sticky liquid which by the GC-MS analysis resulted to be made of PAH. The carbon formation in fact involves several reactions; the carbon can be formed directly from the methane decomposition or can be formed passing through the production of PAH which needs higher residence time to dehydrogenate to form pure carbon. Pure carbon is produced only when the bed height is increased to 210 °C. The carbon is in form of fine sheet having a depth of 200 nm.

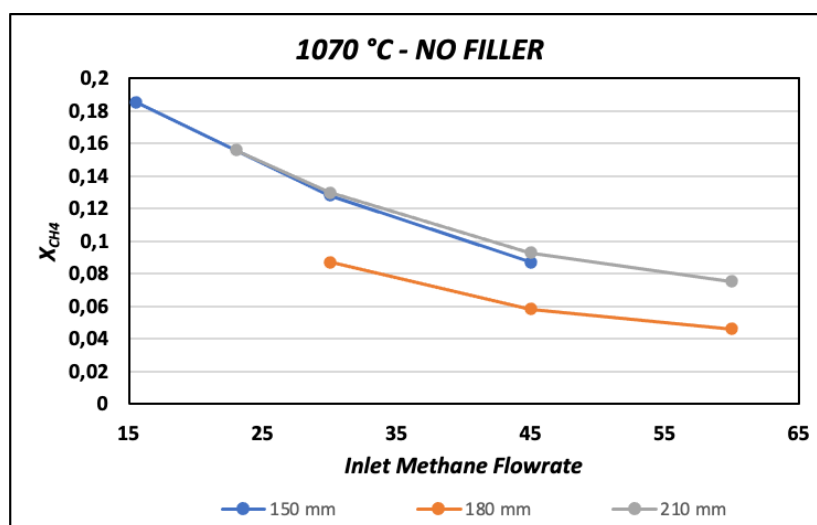


Figure 2. Tests made at different methane flow rate and bed height at a constant temperature of 1070 °C

One of the critical points of the process is the separation between the carbon and hydrogen. The carbon is collected on the top of the tin bed. To avoid the presence of tin entrained by the carbon it is important to create a calm zone in the reactor where the carbon and the tin can have the time to be divided into two distinct layers.

The tests at different temperatures were made at a constant bed height of 15 cm and at a flow rate of 30 ml/min. The tests (Figure 3) show that the reaction in absence of catalyst is activated at temperature higher than 1020 °C. The conversion for lower temperature is almost zero.

The tests made with the spherical filler into the tin bed

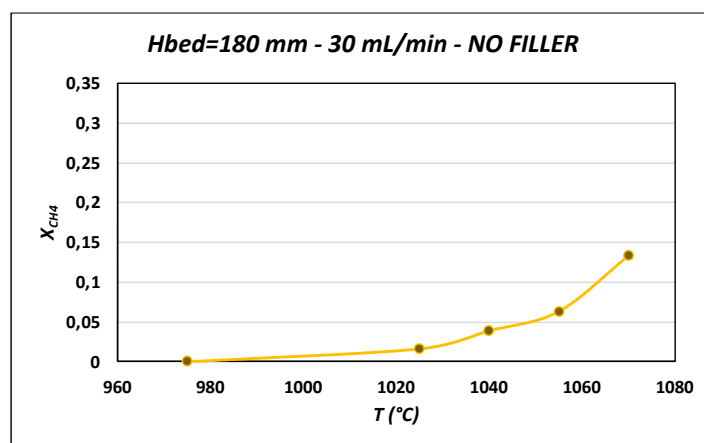


Figure 3. Tests made at different temperature (Bed height 15 cm and CH₄ flow rate 30 ml/min)

The tests with the filler show that the conversion can be increased consistently. In Figure 4 the results of a long duration test are reported, it can be noted that the filler has a very good stability since the conversion remains constant all the 24 hours.

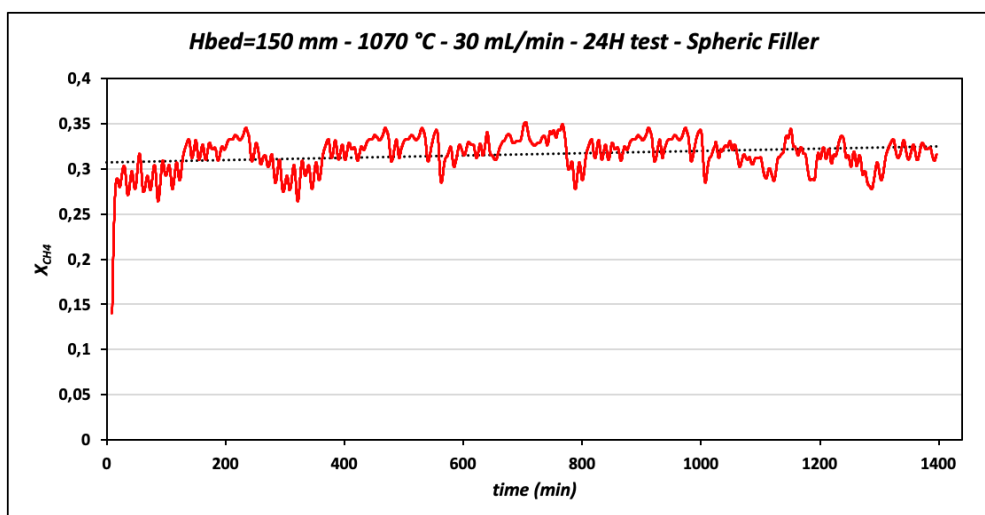


Figure 4. Long duration test with spherical filler.

4. Conclusions

The results show that residence time and bubble dimension play a fundamental role on the process. The average methane conversion is about 15 % which is enhanced in presence of the filler up to 30 %. However, the presence of the filler makes the separation between carbon, filler and tin not trivial. The bed height is also a fundamental parameter, higher is the bed, higher is the quality of the obtained carbon but the increase of the bed height seems not favor the methane conversion. This study demonstrates the feasibility of the methane cracking in molten tin reactor for the production of pure hydrogen without CO₂ emissions. The value of methane conversion obtained in the tested conditions are satisfactory to envisage a scale up in the reactor which was designed for this application.

References

- [1] L. Weger, A. Abanades, T. Butler, *Int. J. Hydrogen Energ.* 42 (2017) 720-731.
- [2] A. Amin, E. Croiset, W. Epling, *Int. J. Hydrogen Energ.* 36 (2011) 2904-2935.
- [3] I.V. Kudinov, A.A.Pimenov, Y.A.Kryukov, G.V.Mikheeva, *Int. J. Hydrogen Energ.* 46 (2021) 10183-10190.
- [4] M.Msheik, S.Rodat, S.Abanades, *Energies*, 14 (2021) 3107-3112.

3D-CFD simulation of a vessel with inside catalytic filter candles for particulate abatement and tar steam reforming

Andrea Di Carlo¹, Elisa Savuto¹, Alessandra Tacconi¹, Alessandro Antonio Papa¹, Bora Aydin²

1 University of L'Aquila, Piazzale E. Pontieri 1, L'Aquila, Italy;

2 Walter Tosto S.p.A., Via Erasmo Piaggio 62, Chieti, Italy

**Corresponding author E-Mail: andrea.dicarlo1@univaq.it*

1.Introduction

Biomass gasification is a very promising process to produce energy from agricultural wastes [1]. In order to meet the increasingly stringent environmental regulations, and increase the efficiency of biomass thermochemical conversion in useful gas and/or hydrogen syntheses, it is necessary to clean the product gas from particulate and tar [2]. The gas cleaning from dust is compulsory before any other treatments such as steam reforming of high molecular weight hydrocarbons (tar). Tar content in syngas produced in a fluidized bed gasifier ranges between 5 and 100 g/Nm³ [3] and may cause different problems. For example, in high temperature fuel cell units (i.e. SOFC) the catalysts might be deactivated as a consequence of carbon deposition. Therefore, the gas cleaning units play an important role, also for the fly ash removal. Furthermore, the presence of tar among the products of gasification reduces gas yield and conversion efficiency. Catalytic filter candles are an innovative solution for hot gas cleaning and conditioning. The main advantage of this concept, differently from the low temperature gas purification systems, is that it avoids tar condensation and the operating temperature is closer to the gasification temperature. Catalytic filter candles can be inserted directly in the freeboard of a fluidized bed biomass gasifier or in a separated vessel just downstream the gasifier. Characterization of catalytic ceramic candles in terms of gas flow field, particle separation and tar reforming exhibited at different operating conditions has been the subject of a previous work [4] addressed to 2D-CFD simulations. To by-pass technical problems related to the impregnation of Ni directly on the ceramic filters and to render the overall process more feasible in practice, commercial ceramic candles for particulate abatement at relatively high temperature could be filled with commercial pelletized steam reforming catalyst in their inner empty space. To verify this hypothesis, both experimental and simulation work is required. This work summarizes the results of one of the simulation tasks of the European project BLAZE[5]. The project aims to develop an innovative integrated biomass gasifier and fuel cell CHP plant to produce renewable electricity and heat. The CHP system integrates an innovative dual fluidized bed gasifier, hot gas cleaning and conditioning, industrialized solid oxide fuel cells (SOFC), and off-gas recirculation. This work partially summarizes the results of the 3D-CFD simulations carried out for the BLAZE project. In particular the simulations were carried out on a vessel with 6 ceramic filter candles inserted in, and with commercial pelletized steam reforming catalyst in the inner empty space of each candle, see the work of Savuto et al. [6] for more details about this configuration. The effect of temperature and the fluidized bed inventory was studied in order to evaluate the performance of the system in terms of gas composition and tar conversion. The aim is to obtain the optimal conditions for the effective syngas cleaning and conditioning within the limits required for the safe operation of the SOFC that will be used in the project. Deliverable 3.2 [7] of the BLAZE project gives an indication on the tolerable limit for toluene and naphthalene:

- the toluene concentration in the gas must be lower than 750 mg/Nm³, but preferably lower than 250 mg/Nm³

- the naphthalene concentration must be lower than 75 mg/Nm³, but preferably lower than 25 mg/Nm³

2. Methods

Development of the model

The system simulated by the model is the stainless steel vessel (0.3 m I.D. x 1.8 m H) realized by Walter Tosto SpA that will contain the 6 filter candles (0.06 m O.D., 0.04 m I.D. 1.5 m length) supplied by Pall Filtersystems GmbH. The six cylindrical catalytic candles are placed vertically and suspended from the top, for filtration and conditioning of the syngas.

The system was simulated in Fluent. The 3D domain simulated is shown in Figure 1.

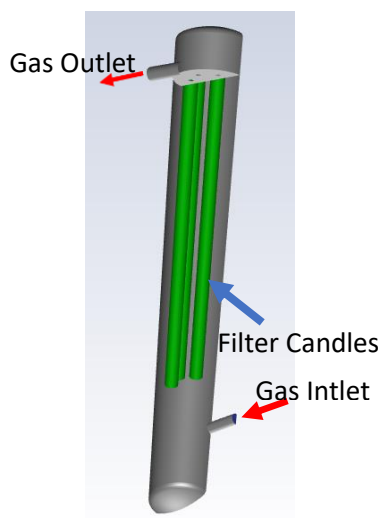


Figure 1-3D Domain simulated in Fluent

The ceramic candles are defined as porous media made of alumina characterized by porosity and permeability. The inner empty space inside the candle was partially filled by an annular bed of catalyst pellets, leaving a cylindrical, internal hollow space of 20 mm diameter for the gas to flow towards the candle head, see the work of Savuto et al. [6] for more details about this configuration. The vessel is surrounded by a layer of 0.3 m of Insulfrax LT 128 ceramic blanket, an insulation material simulated as a solid region. The chemical species considered are typical of a steam gasification gas product: H₂, CO, CO₂, CH₄, H₂O, and benzene (C₆H₆), toluene (C₇H₈) and naphthalene (C₁₀H₈). The tar key compounds taken into account in this work are well representative of the overall, complex tar mixture, since they are found in major quantity in a typical syngas produced from biomass gasification.

The mass and momentum balances, given by the Navier-Stokes equations, chemical species and energy conservation equations are solved for the gas phase in the vessel volume, in the porous zone of the candle and in the porous volume of catalyst pellets.

Vessel Region

For the vessel region the following equations are solved for gas phase:

$$\nabla \cdot (\rho \vec{v}) = 0 \quad (1)$$

$$\nabla \cdot (\rho \vec{v} \vec{v}) = -\nabla p + \nabla \cdot (\overline{\tau}_g) \quad (2)$$

$$\nabla \cdot (\vec{v}(\rho h)) = \nabla \cdot [(\overline{\tau}_g \cdot \vec{v}) + k_g \nabla T] + S_h \quad (3)$$

$$\nabla \cdot (\vec{v} \rho y_i) = \nabla \cdot (D_i \nabla y_i) + S_i \quad (4)$$

where i indicates each of the chemical species. S and S_h are the source (or sink) terms due to any reactions occurring in the vessel, if considered.

Porous structure of the filter candle and bed of catalyst pellets inside the candle

The continuity equation is equal to Eq.1.

The momentum balance is similar to Eq.2, modified to consider porosity (ε_c) of the solid (candle and catalyst bed) with an extra source term composed of two parts: a viscous loss term, that depends on permeability α (Darcy law) and an inertial loss term (due to an inertial resistance factor C):

$$\nabla \cdot (\varepsilon_c \rho \vec{v}\vec{v}) = -\varepsilon_c \nabla p + \varepsilon_c \nabla \cdot (\overline{\tau_g}) - \left(\frac{\mu}{\alpha} + \frac{C\rho}{2} |\vec{v}| \right) \vec{v} \quad (5)$$

Obviously, both α and C are different for the candle and for catalyst bed (see below).

The conservation of energy for the gas g is:

$$\nabla \cdot (\varepsilon_c \vec{v}(\rho h)) = \nabla \cdot [k_{eff} \nabla T] + \sum_j r_j \rho_{cat} (1 - \varepsilon_c) \Delta H_{j0} \quad (6)$$

where h is the sensible enthalpy for an ideal gas, involving only the sensible heat, ΔH_{j0} is the enthalpy of reaction j and k_{eff} is the effective thermal conductivity computed as:

$$k_{eff} = \varepsilon_c k_g + (1 - \varepsilon_c) k_c \quad (7)$$

where k is the thermal conductivity of the gas phase g and of the catalyst/solid phase c .

The following chemical species balance was finally set:

$$\nabla \cdot (\varepsilon_c \vec{v} \rho y_i) = \nabla \cdot (\varepsilon_c \rho D_i \nabla y_i) + \sum_j v_{ij} r_j \rho_{cat} (1 - \varepsilon_c) M_i \quad (8)$$

In Eq. 6 and 8 r_j is zero in the porous structure of the candle (where reactions can be considered negligible) and is different from zero only in catalyst bed.

The thermo-physical properties of the syngas were implemented in the model; its specific heat was calculated by the weighted average of the specific heat of its components.

The thermal conductivity and the viscosity of the syngas are polynomial functions of the temperature. A piecewise polynomial function was implemented to define the thermal conductivity and viscosity coefficients.

A k - ε model was adopted to model the gas turbulence in the freeboard of the simulated volume. The laminar flow model was used in the porous zones of the candle because the small pore diameters (in the order of 70 μm) guarantee very low Reynolds numbers ($\text{Re}=0.05$ - 0.07).

The chemical-physical parameters integrated in the model for the porous layer of the candle and for the catalyst pellets were obtained from typical properties of alumina (density: 3939 kg/m^3 , specific heat: $731.04 + 1.2119 T - 0.0007 T^2$ $\text{J}/(\text{kg K})$, thermal conductivity: $34.274 - 0.0644 T + 4\text{E-}5 T^2$ $\text{W}/(\text{m K})$). The porosity of the candle structure (ε_{cand}) was set to 0.3, as reported by the manufacturer, while the porosity of the catalyst pellet (ε_{cat}) was set to 0.4, as that measured experimentally. The permeability and the inertial resistance factor of the candle structure was obtained by experimental measures of the pressure drop, for different temperatures and filtration velocities. The Ergun equation was used instead to evaluate the same factors for the catalyst. The values adopted for the candles are reported in the following Table:

Table 1-Permeability and inertial resistance factor of the candle structure

α (m^2)	4.38E-12
C	2.88E8

The mass diffusivity of each component D_i was calculated with the Wilke equation:

$$D_i = \frac{1}{\sum_{k \neq i} \frac{x_k}{D_{ki}}} \quad (12)$$

where x_k are the molar fractions of different species.

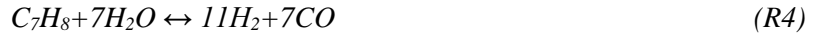
The binary diffusion coefficient D_{ik} was calculated using the Chapman and Enskog equation:

$$D_{ik} = 0.0018583 \sqrt{T^3 \left(\frac{1}{M_k} + \frac{1}{M_i} \right) \frac{1}{p \sigma_{ik}^2 \Omega_{ik}}} \quad (13)$$

where σ and Ω are the Lennard Jones parameters that can be found in Bird [8].

Reactions rates

The chemical reactions of tar and methane steam reforming and water gas shift taking place in the catalyst bed inside the candles were considered in the model:



The reaction rate dependencies on concentrations (reaction order) and on temperature (activation energy) for the steam reforming of benzene and naphthalene were taken from Depner and Jess [9] that describes the catalytic conversion with a Nickel based catalyst (15% wt) in presence of H_2O , H_2 and traces of H_2S .

$$r_{R3} = \frac{k_{R3} c_{C6H6}}{1 + K_{R3} c_{C6H6} + K_{R3, H_2S} c_{H_2S}} \quad (14)$$

$$r_{R5} = \frac{k_{R5} c_{C10H8}}{1 + K_{R5} c_{C10H8} + K_{R5, H_2S} c_{H_2S}} \quad (15)$$

Swierczynski et al. [10] gave apparent first order kinetic parameters for the steam reforming of toluene over a Ni based catalyst:

$$r_{R4} = A_{R4} \cdot e^{-E_{R4}/RT} c_{tol} \quad (16)$$

For the steam reforming of methane (SMR-R1) and the water gas shift reaction (WGS-R2), the model of Numaguchi and Kikuchi [11] was used as the reference model:

$$r_{R1} = A_{R1} e^{-E_{R1}/RT} \frac{(p_{CH_4} p_{H_2O} - p_{CO} p_{H_2}^3 / K_{eq,R1})}{p_{H_2O}^{1.596}} \quad (17)$$

$$r_{R2} = A_{R2} e^{-E_{R2}/RT} \frac{\left(p_{CO} p_{H_2O} - \frac{p_{CO_2} p_{H_2}}{K_{eq,R2}} \right)}{p_{H_2O}} \quad (18)$$

Insulation Region

The insulation region has been simulated as a solid body. The only equation solved for this zone is the energy equation:

$$\nabla \cdot (k_{ins} \nabla T) = 0 \quad (19)$$

where k_{ins} is the thermal conductivity of the Insulfrax LT ceramic blanket used for insulation (average values between Insulfrax LT 96 and 128, respectively), as a function of temperature:

$$k_{ins} = 2.05 \cdot 10^{-7} T^2 + 9.11 \cdot 10^{-5} T + 5.26 \cdot 10^{-2} \frac{W}{mK} \quad (20)$$

At the outer wall of the solid region a heat flux boundary condition with air at ambient conditions has been assumed:

$$k_{ins} \left(\frac{\partial T}{\partial n} \right)_{wall} = h_{amb} (T_{amb} - T_{wall}) \quad (21)$$

h_{amb} has been set to 5 W/m²K, typical value for air natural convection on vertical cylinder, and $T_{amb}=298$ K.

Model validation

The experimental values obtained in the bench scale gasifier equipped with a catalytic candle in its freeboard were exploited for the validation of the model. An axisymmetric model, as already done in the past [4], was used to simulate half of the cylindrical reactor of the bench scale tests. The inputs to the simulation were gas and tar compositions obtained in a biomass steam gasification test with a non-catalytic candle [12]. The operating conditions were those used for the gasification tests: the reactor wall temperature was set to 900°C in order to reproduce the effect of the electric furnace used to heat the bench scale gasifier, the gas input temperature was set to 800°C, and the upward superficial gas velocity was set to 0.365 m/s that corresponds to a face filtration velocity of 100 m/h through the candle. Input composition and operating conditions are reported in Table 2.

Table 2 – Gasifier freeboard input compositions and operating conditions for simulation

Input composition	
H ₂ (% vol dry, N ₂ free)	40.04
CO (% vol dry, N ₂ free)	29.05
CO ₂ (% vol dry, N ₂ free)	22.35
CH ₄ (% vol dry, N ₂ free)	8.56
H ₂ O content (%)	15.67
C ₆ H ₆ (g/Nm ³)	10.40
C ₇ H ₈ (g/Nm ³)	2.30
C ₁₀ H ₈ (g/Nm ³)	2.04
H ₂ S (ppm _v)	100
Operating conditions	
T in (°C)	800
T wall (°C)	900
v in (m/s)	0.365

Kinetic data for benzene, toluene, naphthalene, methane steam reforming and water gas shift found in literature provided the functional dependencies of the respective reaction rates as functions of the concentration of species and temperature (activation energies). The simulation outputs were compared with the results obtained in the experimental tests carried out in the bench scale reactor equipped with a ceramic candle filled with commercial Ni-catalyst pellets for steam reforming of hydrocarbons. The pre-exponential factors of the kinetic constant in each reaction rate expression were thus estimated to obtain simulation results close to the experimental outcomes. The chosen pre-exponential factors are reported in Table 3.

Table 3– Values of pre-exponential factors adopted in the chemical reaction rate expressions

Reaction	Pre-exponential factor
$\text{CH}_4 + \text{H}_2\text{O} \leftrightarrow \text{CO} + 3\text{H}_2$	235 kmol/m ³ Pa ^{-0.404} /s
$\text{CO} + \text{H}_2\text{O} \leftrightarrow \text{CO}_2 + \text{H}_2$	1.39 E-6 kmol/m ³ Pa ^{-0.404} /s
$\text{C}_6\text{H}_6 + 6\text{H}_2\text{O} \leftrightarrow 6\text{CO} + 9\text{H}_2$	1.68 E+5 s ⁻¹
$\text{C}_7\text{H}_8 + 7\text{H}_2\text{O} \leftrightarrow 7\text{CO} + 11\text{H}_2$	4.47 E+11 s ⁻¹
$\text{C}_{10}\text{H}_8 + 10\text{H}_2\text{O} \leftrightarrow 10\text{CO} + 14\text{H}_2$	4.63 E+10 s ⁻¹

Setting the pre-exponential factors to their respective values reported, simulation results eventually close to the experimental data were obtained at different operating temperature, as shown in the following Figure in term of tar concentration.

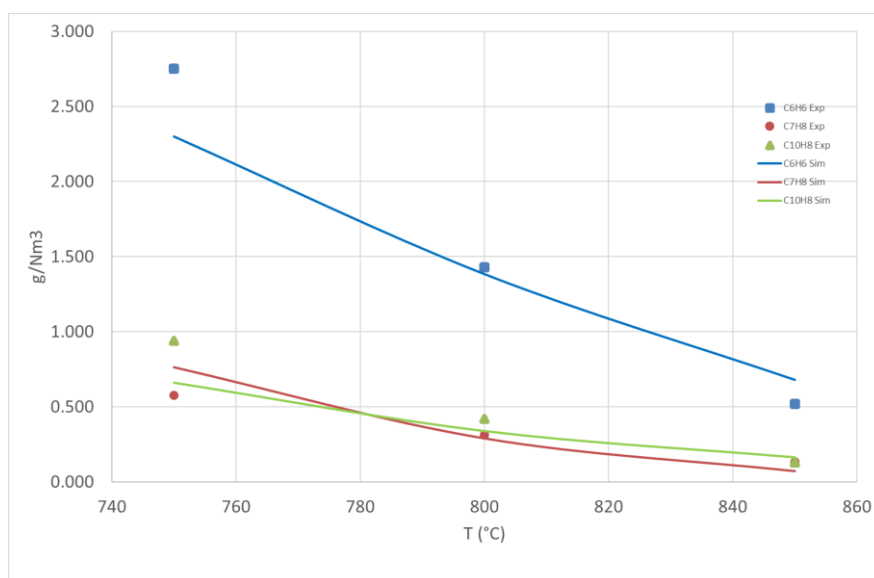


Figure 2– Comparison of experimental and simulation results

The Figure shows that there is very good correspondence between the simulation and experimental results.

3. Results and discussion

The 3D-CFD model was then used to simulate tar conversion in the vessel with the 6 commercial candles. The input data used for simulations were taken from the results recorded in the 100 kWth pilot scale dual fluidized bed gasifier. The input gas and tar composition are summarized in the next Table:

Table 4– Input data for simulations

	Input data
H ₂ (% vol, dry)	35.2
CO (% vol, dry)	24.2
CO ₂ (% vol, dry)	20.2
CH ₄ (% vol, dry)	8.0
H ₂ O (% vol)	24
C ₆ H ₆ (g/Nm ³)	6.3
C ₇ H ₈ (+1-ring) (g/Nm ³)	5.5
C ₁₀ H ₈ (+2-ring) (g/Nm ³)	5.4

T gasification (°C)	850
T in vessel (°C)	800-850-900

Results of simulations with the above mentioned input parameters are reported in Figure 3.

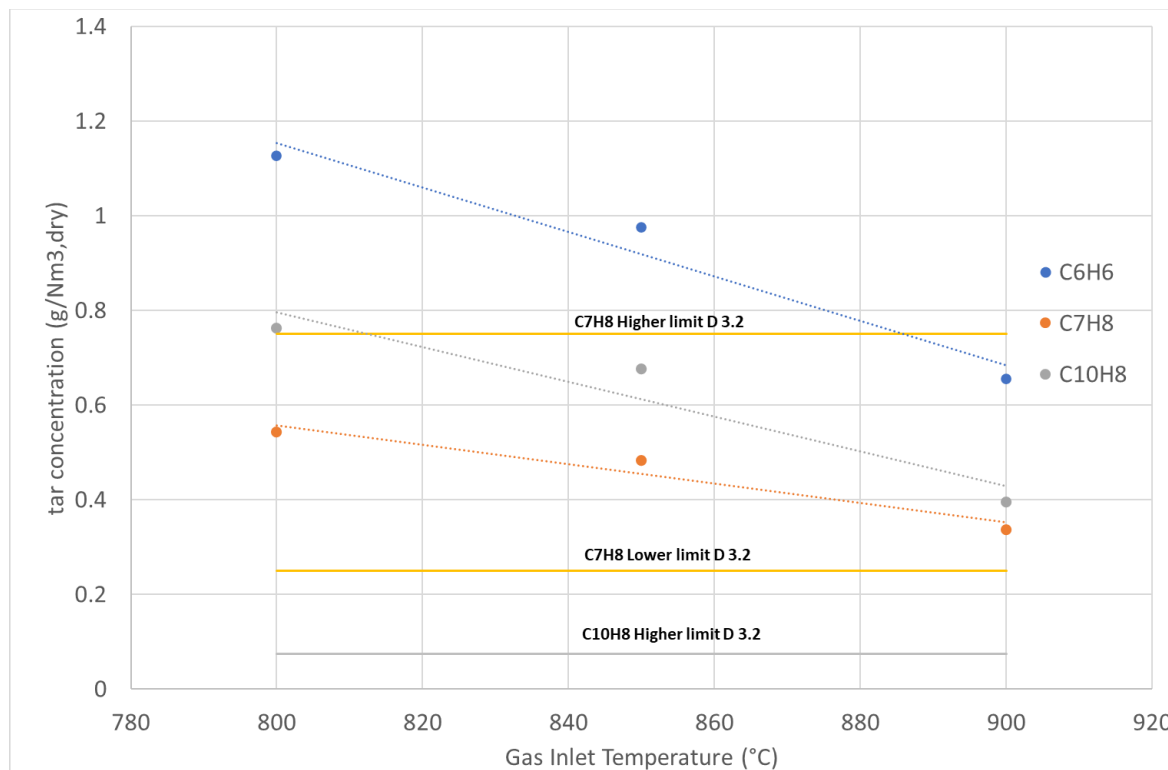


Figure 3-Results of the CFD simulations using the input of Table 4

The tar conversion yields obtained in this simulation are in the range of 80-90% at 800°C and increase to values higher than 90% at 900 °C. Naphthalene concentration is still too high at each temperature if compared with the required limits, while toluene is always lower than the higher limit.

Furthermore, it was observed that the temperature strongly drops along the reactor height due to the thermal dispersion with the external and because of the endothermic reactions that take place in the catalyst bed, these being probably the cause of the low tar conversion rate; tar steam reforming over Ni catalysts is in fact effective at temperatures much higher than 700 °C. Next Figure shows the temperature distribution at the inlet of the catalytic layer in the candles.

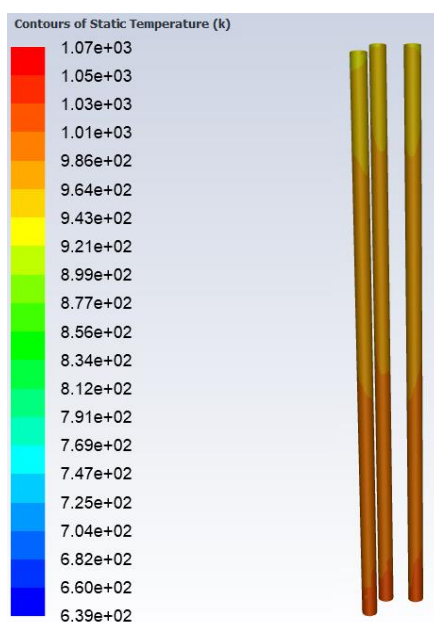


Figure 4-Temperature distribution at the inlet of the catalytic layer in the candles

Further simulations were carried out using a composition of the gas that can be obtained using dolomite in the bed. No experimental data on the pilot plant were available at that time for tar and gas composition when dolomite is used in the fluidized bed. Rapagnà et al. [13] carried out test, at the same bench scale test rig used in BLAZE project, test adding 20% of dolomite in a fluidized bed of olivine. The results showed that tar (without benzene) was reduced of a value between 68 and 76 %. Barisano et al. in the Deliverable 2.2 of BLAZE [14] demonstrated that adding 30% of dolomite in a fluidized bed of olivine, Benzene can be reduced of 19%, Toluene of 43% and hydrocarbons heavier than toluene of 52%. For the simulation it was assumed that the gas composition is the same of the previous one, while tar compounds were reduced using the data of Barisano et al.

Table 5– Input data for 2nd simulations, assuming dolomite in the bed

	Input data
H ₂ (% vol, dry)	35.2
CO (% vol, dry)	24.2
CO ₂ (% vol, dry)	20.2
CH ₄ (% vol, dry)	8.0
H ₂ O (% vol)	24
C ₆ H ₆ (g/Nm ³)	5.1
C ₇ H ₈ (+1-ring) (g/Nm ³)	3.1
C ₁₀ H ₈ (+2-ring) (g/Nm ³)	2.6
T gasification (°C)	850
T in vessel (°C)	800-850-900

Results of the simulations with the above mentioned input parameters are reported in the next figure.

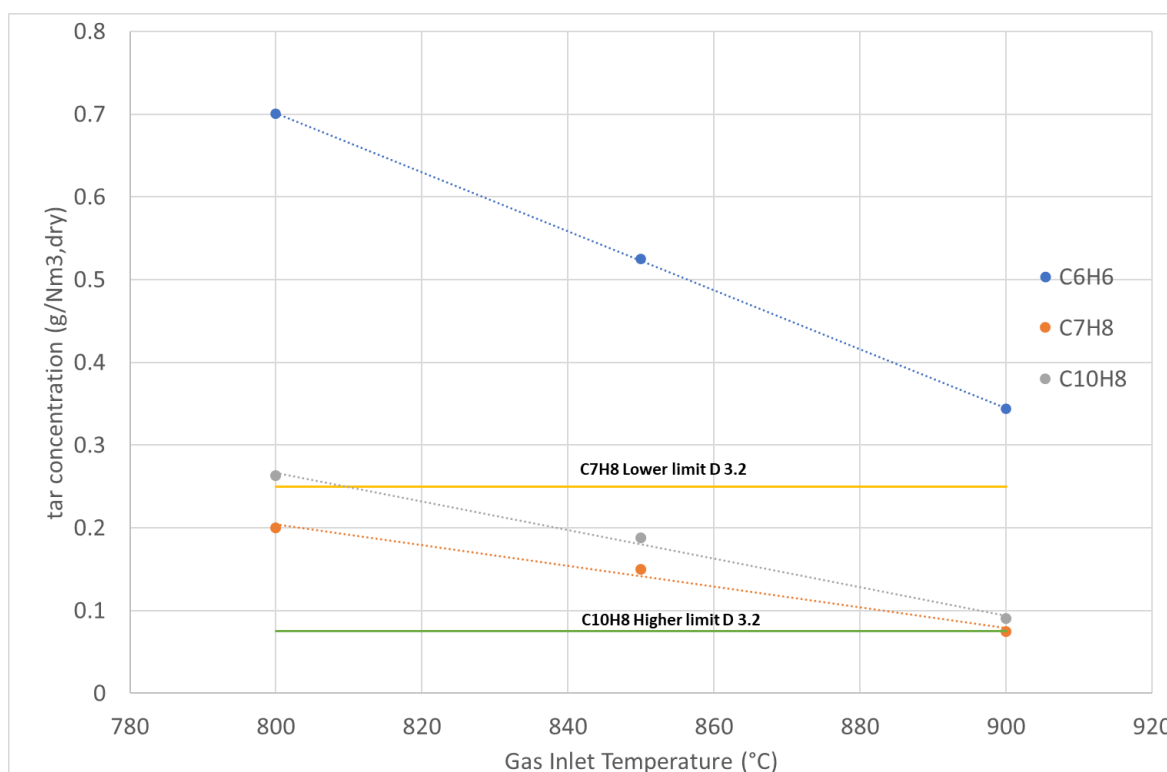


Figure 5-Results of the CFD simulations using the input of Table 5

The results show that naphthalene concentration is close to the higher limit for temperature of 900 °C, while toluene is always much lower than the lower limit. These results show that in order to meet the required limit for a safe operation of the SOFC the inlet temperature of the gas in the vessel with the filter candles should be higher than 900 °C, that is also higher than the operating temperature of the gasifier. A solution could be to inject small quantity of enriched air at the inlet of the filter candles vessel, to burn a really small portion of the gas and increase the temperature. This solution in anycase was not the one adopted for the project. To solve the problem a secondary catalytic reformer will be placed downstream the vessel of the filter candles. With this solution the contact time between gas and catalyst will be increased. In order to re-increase also the temperature of the gas, and thus improve the tar conversion, at the inlet of this secondary reactor, small quantity of enriched air will be injected. The evaluation of the performance of this new equipment is now in progress.

4. Conclusions

This work partially summarizes the results of the 3D-CFD simulations carried out for the BLAZE project. In particular the simulations were carried out on a vessel with 6 ceramic filter candles inserted in, and with commercial pelletized steam reforming catalyst in the inner empty space of each candle. The effect of the inlet gas temperature at the vessel was firstly investigated. The results showed that the tar conversion is really high between 80 to 90 %. Naphthalene concentration resulted still too high at each temperature if compared with the required limits, while toluene was always lower than the higher admissible limit. In order to find a solution, the same simulations were carried out again but with the tar concentration in the gas that can be obtained adding 30% of calcined dolomite in the bed. In this case the results show that naphthalene concentration is finally close to the higher limit for an inlet gas temperature of 900 °C, while toluene is always much lower than the admissible lower limit. In any case these results showed that in order to meet the required limit for a safe operation of the SOFC the inlet temperature of the gas in the filter candles vessel should be higher than 900 °C, that is also higher than the operating temperature of the gasifier. To solve this problem a secondary catalytic reformer will be placed downstream the vessel of the filter candles.

References

- [1] R. Alipour Moghadam Esfahani, L. Osmieri, S. Specchia, S. Yusup, A. Tavasoli, A. Zamaniyan, H₂-rich syngas production through mixed residual biomass and HDPE waste via integrated catalytic gasification and tar cracking plus bio-char upgrading, *Chem. Eng. J.* 308 (2017) 578–587. <https://doi.org/10.1016/J.CEJ.2016.09.049>.
- [2] T.A. Milne, R.J. Evans, N. Abatzoglou, Biomass Gasifier “Tars”: Their Nature, Formation, and Conversion, (1998). <https://doi.org/10.2172/3726>.
- [3] P. Basu, Biomass Gasification, Pyrolysis and Torrefaction: Practical Design and Theory, 2013. <https://doi.org/10.1016/C2011-0-07564-6>.
- [4] E. Savuto, A. Di Carlo, E. Bocci, A. D’Orazio, M. Villarini, M. Carlini, P.U. Foscolo, Development of a CFD model for the simulation of tar and methane steam reforming through a ceramic catalytic filter, *Int. J. Hydrogen Energy.* 40 (2015) 7991–8004. <https://doi.org/10.1016/j.ijhydene.2015.04.044>.
- [5] H2020 BLAZE-Biomass Low cost Advanced Zero Emission small-to-medium scale integrated gasifier-fuel cell combined heat and power plant G.A. 815284, (n.d.). <https://cordis.europa.eu/project/id/815284>.
- [6] E. Savuto, A. Di Carlo, A. Steele, S. Heidenreich, K. Gallucci, S. Rapagnà, Syngas conditioning by ceramic filter candles filled with catalyst pellets and placed inside the freeboard of a fluidized bed steam gasifier, *Fuel Process. Technol.* 191 (2019) 44–53. <https://doi.org/10.1016/j.fuproc.2019.03.018>.
- [7] J.P. Ouweltjes, Deliverable D3.2-BLAZE Selection of Representative Syngas Compositions including Organic and Inorganic Contaminants-BLAZE GA 815284, 2019.
- [8] R.B. Bird, W.E. Stewart, E.N. Lightfoot, *Transport Phenomena*, 2002. <https://doi.org/10.1016/j.ijhydene.2006.08.059>.
- [9] H. Depner, A. Jess, Kinetics of nickel-catalyzed purification of tarry fuel gases from gasification and pyrolysis of solid fuels, *Fuel.* 78 (1999) 1369–1377. [https://doi.org/10.1016/S0016-2361\(99\)00067-8](https://doi.org/10.1016/S0016-2361(99)00067-8).
- [10] D. Świerczyński, S. Libs, C. Courson, A. Kiennemann, Steam reforming of tar from a biomass gasification process over Ni/olivine catalyst using toluene as a model compound, *Appl. Catal. B Environ.* 74 (2007) 211–222. <https://doi.org/10.1016/j.apcatb.2007.01.017>.
- [11] T. Numaguchi, K. Kikuchi, Intrinsic kinetics and design simulation in a complex reaction network; steam-methane reforming, *Chem. Eng. Sci.* 43 (1988) 2295–2301. [https://doi.org/10.1016/0009-2509\(88\)87118-5](https://doi.org/10.1016/0009-2509(88)87118-5).
- [12] A. Di Carlo, E. Savuto, A. Di Giuliano, A. Tacconi, A. Papa, S. Rapagnà, Deliverable 2.3-Tar catalysts selection and filter candles configurations and management to guarantee reliable and high efficiency particulate and tar abatement below SOFC limits-BLAZE GA 815284, 2021.
- [13] S. Rapagnà, K. Gallucci, P.U. Foscolo, Olivine, dolomite and ceramic filters in one vessel to produce clean gas from biomass, *Waste Manag.* 71 (2018) 792–800. <https://doi.org/10.1016/J.WASMAN.2017.07.038>.
- [14] D. Barisano, F. Nanna, A. Villone, E. Catizzone, Deliverable D2.2 Bio-syngas composition and contaminants that affect SOFC and related gasifier parameters and bed materials to reduce sofc hazardous effects, n.d.

Study on mesoporous-supported catalysts for simultaneous CO₂ and steam reforming of biogas

Camilla Galletti, Fabio A. Deorsola, Samir Bensaid, Nunzio Russo, Debora Fino

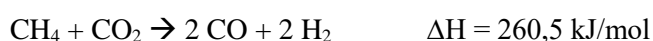
Applied Science and Technology Department, Politecnico di Torino,

Torino (Italy)

**camilla.galletti@polito.it*

1. Introduction

Conversion of methane and carbon dioxide, which are two of the most abundant carbon-containing materials, into useful products is an important area of the actual catalytic research. The methane-CO₂ reforming (dry reforming) to produce syngas



is a very attractive route to produce energy and valuable compounds. This reaction offers advantages over methane steam reforming to produce a H₂/CO ratio of about 2, adequate for processes such as the production of higher hydrocarbons and derivatives [1,2].

The process is inevitably accompanied by deactivation due to carbon deposition. In order to reduce the carbon deposition, CO₂ reforming of methane with a feed gas containing steam has been suggested. Moreover, in the presence of steam, methane steam-reforming occurs simultaneously and thereby higher selectivity for both CO and H₂ can be achieved, and also the H₂/CO ratio of the product gas can be controlled [3,4].

Recently, the most widely used catalysts for CO₂ steam reforming reaction are based on Ni. However, many of these catalysts undergo severe deactivation due to carbon deposition. Noble metals have also been studied and are typically found to be much more resistant to carbon deposition than Ni catalysts but are generally more expensive [5,6].

Moreover, the silica SBA-15, which possesses larger pores and higher thermal stability, may be used as a promising catalyst support [7,8].

In the present study, 10%Ni/SBA-15 and 0.5%Rh/SBA-15 catalysts were prepared, and their performances over the reaction of combined carbon dioxide and steam reforming of methane were investigated.

2. Methods

Ordered mesoporous silica SBA-15 was synthesized in a spherical shape, according to the procedures reported by Hussain et al. [9] and used as catalyst carrier.

The supported Rh and Ni catalysts were prepared with the Incipient Wetness Impregnation (IWI) method by using Rh(NO₃)₃ and Ni(NO₃)₂·6H₂O as precursor, respectively. The catalyst powders, after grinding in an agate mortar, were calcined in air for 1 h to remove the nitrate ions.

The phase structures of the samples were characterized by X-ray powder diffraction (XRD). CO₂ temperature programmed desorption (CO₂-TPD) analysis was performed using an analyzer equipped with a TCD detector. Multi-point BET surface area and pore volume of catalysts were measured via N₂ physisorption at 77 K. Morphology was observed by a Field Emission Scanning Electron Microscope (FESEM). In order to verify real amount of deposited metal, ICP-MS apparatus was used.

The activity of the prepared catalysts was analyzed feeding a gas mixture, composed by CO₂, CH₄ and steam (CO₂/CH₄ > 0.75 ÷ 1.5, H₂O/CH₄ ≅ 1.5), to a catalytic fixed-bed micro reactor. The gas hourly space velocity (GHSV) through the catalytic bed was varied.

3. Results and discussion

The first tests were carried out on both Ni and Rh supported catalysts at GHSV = 26000 h⁻¹ and with CO₂/CH₄ ratio equal to 0.85. Results in terms of CH₄ conversion, H₂ yield and H₂/CO ratio are shown in Fig. 1. The two catalysts reached similar methane conversion and H₂ amount produced was about comparable. Otherwise, H₂/CO ratio doubled with Rh based catalyst, meaning higher selectivity toward H₂ production. In particular, with 0.5%Rh/SBA15 catalyst H₂/CO ratio was equal to 2.

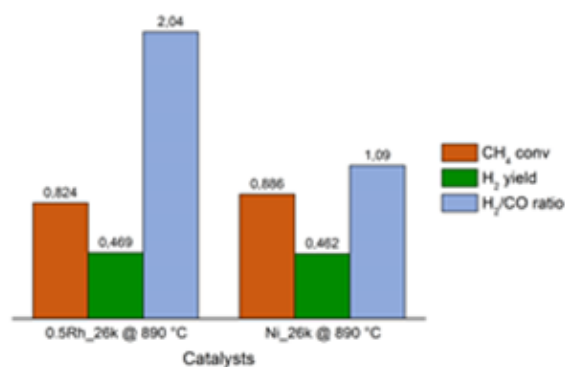


Figure 1. Comparison between Rh/SBA15 and Ni/SBA15 at GHSV=26000 h⁻¹ and CO₂/CH₄=0.85.

Deeper studies were performed on Rh/SBA15 catalyst by varying space velocity. Activity test at GHSV equal to 44000 and 15000 h⁻¹ were carried out and performances were compared with those obtained at GHSV = 26000 h⁻¹. As expected, CH₄ conversion and H₂ yield decreased by increasing space velocity, but H₂/CO ratio was maintained about 2.

4. Conclusions

Two SBA15 supported catalysts (Rh 0.5 wt% and Ni 10 wt%) were tested for CO₂ and steam reforming reaction. SBA15 supported Ni showed high CH₄ conversion but poor H₂ yield and low H₂/CO ratio, that reached very promising value using Rh supported catalyst. By increasing GHSV on Rh/SBA15 catalyst, CH₄ conversion and H₂ yield was decreased but the H₂/CO ratio was maintained. In conclusion, SBA15 supported 0.5 wt% Rh was proved to be a promising catalyst over the reaction of combined carbon dioxide and steam reforming of methane.

References

- [1] A.M. Gadalla, B. Bower, Chem. Eng. Sci., 43 (1988) 3049.
- [2] A.E.C. Luna, M.E. Iriarte, Appl. Catal. A: General, 343 (2008) 10.
- [3] V.R. Choudhary, K.C. Mondal, Appl. Energy, 83 (2006) 1024.
- [4] M.A. Al-Nakoua, M.H. El-Naas, Int. J. Hydrog. Energy, 37 (2012) 7538.
- [5] Z. Hou et al., Int. J. Hydrog. Energy, 31 (2012) 555.
- [6] A. Alvarez et al., Top Catal., 59 (2016) 303.
- [7] A. Carrero, J.A. Calles, A.J. Vizcaino, Appl Catal A, 327 (2007) 82.
- [8] S. Singh et al., Appl. Cat. A, 559 (2018) 57.
- [9] M. Hussain, D.Fino, N. Russo, J. Hazard. Mater., 211 (2012) 255.

Experimental Study of Sorption-Enhanced Methanation in a Lab-Scale Fluidized Bed System

Fiorella Massa¹, Antonio Coppola², Fabrizio Scala^{1,2*}

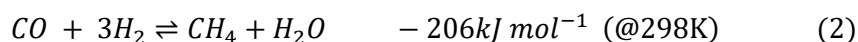
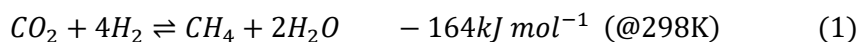
1 DICMaPI, Università degli Studi di Napoli Federico II, 80125 Napoli, Italy;

2 STEMS, Consiglio Nazionale delle Ricerche, 80125 Napoli, Italy

**Corresponding author E-Mail: fabrizio.scala@unina.it*

1. Introduction

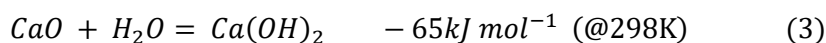
Climate change has become one of the most important issues of our time, but the demand for energy is still increasing worldwide. Many efforts are being made to replace fossil resources by renewable energy. One of the main drawbacks of renewable sources is their discontinuity: to overcome that, energy storage systems are needed. Chemical storage has been proposed among the suitable options and, in particular, there is an increasing interest towards the catalytic and biological production of renewable methane. Methane is an important energy carrier that benefits from an already developed infrastructure in many countries and a quite large public acceptance. Methanation of CO₂ is known as a Power-to-Gas technology (converting surplus electric energy into a gaseous fuel): the process can be a biogas upgrading or a CCU (Carbon Capture and Utilization) process using CO₂ streams captured from industrial plants [1-3]. In both cases “renewable” hydrogen from water electrolysis [4] reacts with CO₂ to produce the so called Synthetic or Substitute Natural Gas. Among the paths to “renewable” methane production also methanation of syngas from biomass gasification should be mentioned [5,6]. Catalytic methanation of CO₂ and/or CO (discovered by Sabatier and Senderens in 1902 [7]) occurs exothermically with a net reduction of gaseous moles:



Commercial methanation processes are typically applied in ammonia synthesis plants to remove carbon monoxide, and rely on a cascade of adiabatic catalytic fixed bed reactors operated at temperatures between 250 and 600°C with intermediate cooling steps and recycles, and at high operational pressure [5]. Among the typical metals that catalyze methanation (Ru, Ni, Co, Fe, and Mo), Ni is the most used for commercial applications due to the good activity and selectivity and the low price, compared to other metals [8]. Unfortunately, commercial Ni-based catalysts are subject to different deactivation mechanisms (chemical, thermal and mechanical) [9]. In particular, the main chemical deactivation of Ni catalysts is represented by carbon (coke) deposition, produced by the Boudouard reaction, on the catalyst surface [10].

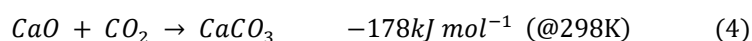
In the last years, several research projects were directed to innovate traditional methanation, typically considering processes operated at high pressure to improve methane production. However, the possibility of supplying reactants at lower pressures would be rather appealing to decrease the energy duty for compression work. With this respect, the application of the Le Chatelier principle to shift the reaction equilibrium towards the products formation has been recently proposed: sorption-enhanced methanation with in-situ H₂O removal using a suitable sorbent material could be applied to overcome the thermodynamic limits at low pressure [11,12]. These studies were carried out in lab-scale cyclically operated fixed beds and demonstrated that the SEM process has the potential for high-grade methane production at low pressure using commercial materials, with the consequence of a relevant energy saving for the entire process. The feasibility and the possible positive effects of sorption-enhanced conditions have also been tested in different chemical looping systems, such as the sorption-enhanced steam reforming of ethanol [13-16]. Considering the reactor design, fixed beds have the advantage of a compact design, but they imply transient operation and difficult heat management, especially at the industrial scale. In order to overcome such issues, fluidized bed reactors have been suggested as a possible alternative since they are known to be favorable for large-scale steady operation of highly exothermic

reactions. Moreover, the use of a fluidized bed reactor would be advantageous in a SEM process due to the ability of these reactors to easily transfer solid sorbent materials during steady operation [6]. On the basis of this consideration, a novel configuration for SEM, based on the technology of dual interconnected fluidized beds was investigated. This scheme has the advantage of a steady operation of the plant, thus avoiding the unsteady cyclic operation used for sorbent regeneration in fixed bed SEM concepts. The behavior of CaO particles as a steam sorbent during hydration-dehydration cycles was previously studied [17], since calcium oxide reacts with H₂O in the temperature range of interest for methanation:



In addition, CaO is an eco-friendly, abundant and low-cost material.

However, if CO₂ is present in the system, the following reaction also takes place:



The carbonation reaction, which is irreversible in the temperature range of interest, competes with hydration and could decrease the performance of CaO during CO₂ SEM. In this work, for the first time, the catalytic methanation with simultaneous CaO hydration was tested under different conditions in a fluidized bed system. The focus of the activity was the proof of concept of the enhancement effect with respect to traditional methanation, and the characterization of the possible detrimental effect of the carbonation reaction on the process.

2. Methods

2.1. Catalyst and sorbent preparation

The chosen material to catalyze methanation was a Nickel-based catalyst supported on alumina. As for the support, a commercial material was used: a spherical-shaped γ -alumina with an average size of 600 μm , specifically purchased for fluidized bed application, having a significant attrition resistance (provided by Sasol). The active phase was obtained by a precursor salt, the Nickel nitrate exahydrate Ni(NO₃)₂·6H₂O provided by Alfa Aesar. The preparation method, widely reported in the literature for this type of catalysts [18], was the incipient wetness impregnation technique: the volume of the aqueous solution prepared was exactly the volume needed to fill the porous structure. In this amount of water, the precursor was dissolved in order to obtain a 10%_{wt} of Nickel after two cycles of impregnation-dehydration. The impregnation stage lasted 2 hours, followed by dehydration, carried out by means of a heating plate at 95 °C. The impregnated spheres were calcined to obtain Nickel oxide in the active phase; air calcination was carried out in a fluidized reactor for 1 h at 500 °C, as commonly suggested by other studies [18-20]. The final active phase (Ni) for methanation was obtained after reduction, carried out in a stream of H₂ (4%) and N₂ for 1 h at 600 °C in a lab-scale fluidized bed reactor.

CaO was used as the H₂O sorbent, and was prepared in a laboratory-scale fluidized bed reactor heated to 850 °C and fluidized at a velocity of 0.5 m/s. For each preparation process, 20 g of fresh limestone, sieved in the size range 400-600 μm , was introduced in the reactor when the set-point temperature was reached. Complete calcination was achieved in about 10 min.

2.2. Experimental setup

The experimental apparatus used for the tests consisted of a system called Twin Beds (TB) [21], reported in Figure 1: two identical interconnected reactors, East Bed (EB) and West Bed (WB). Each reactor is composed of 3 sections: the wind-box, 0.66 m high, filled with metal elements and acting as a pre-heater/pre-mixer, the 1 m high fluidization column and, in the upper part, a system of a three-way valve that can be connected to the analyzers. This apparatus was conceived with the aim of studying looping processes: it enables the pneumatic transport of granular material in about 5 seconds between the two reactive environments by means of a connecting tube (ID 10 mm) immersed in both reactors. The fluidization column and the wind-box are composed by a tubular steel element (AISI 316) with an internal diameter of 40 mm.

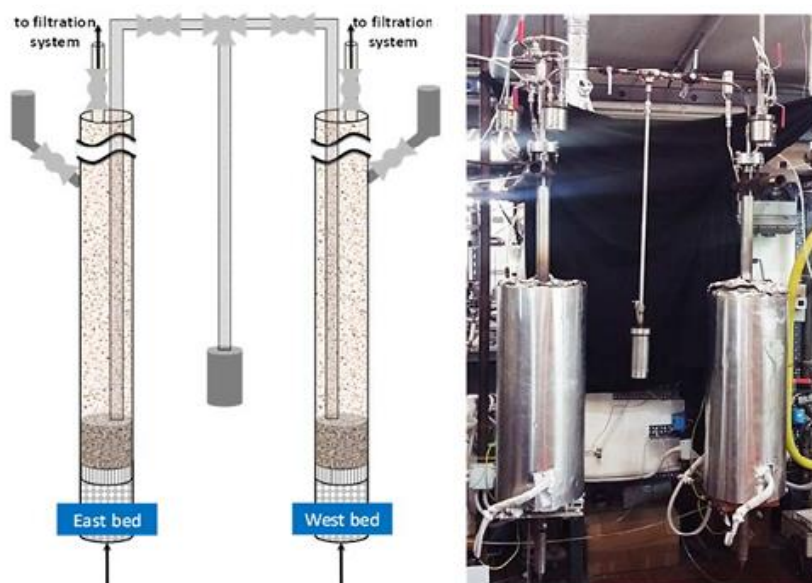


Figure 1. Twin bed apparatus.

Between the two sections, connected by a flange, a perforated plate is located to uniformly distribute the gas inside the reactor. A hopper is placed on the top of each reactor to carry out the bed loading. The electrical heating system consists of two semi-cylindrical furnaces on each reactor (Watlow, Ceramic Fiber Heaters) with a heating length of 457 mm and a power per semi-cylinder of 2100 Watts. A PID controller (Watlow, EZ-Zone ST) is connected to each bed via a K-type thermocouple (Cr-Al) inserted 40 mm above the distribution plate. During the methanation tests, the output concentrations of the species were measured by a mobile analyzer (MRU VARIO LUX) able to detect CH₄, CO, CO₂ by means of a NDIR sensor and H₂ via a TCD sensor. The pneumatic transport of the solids between the reactors was carried out generating an overpressure by means of a system of valves that enables and modulates the flow of the material. Specifically, as for the transport duct, three valves are present on it: two ball valves close to each reactor, which modulate the flow through the duct and a centrally located three-way valve connected to a discharge duct, which allows to direct the material either between the two reactors or towards the discharge vessel. Above each reactor, another valve allows the outlet gas to be sent to the analyzer system and the vent.

2.3. Experimental procedure

The methanation/hydration cycles were performed in the EB reactor, while the dehydration of the sorbent in the WB. Before each SEM test, traditional methanation was carried out to set the basis for comparison of the performance of SEM. To perform conventional methanation in the EB reactor, once the temperature was reached, the reduced catalyst was loaded into the reactor, already fluidized with a bed of silica sand in the size 800-900 micron. The presence of silica sand was necessary to keep temperature variations to a minimum and to assure the segregation of both sorbent and catalyst to the top of the bed (in order to perform smooth solids transfer between the reactors [17]). After catalyst loading, the mixture H₂/CO₂ in the desired ratio and diluted in N₂ (H₂ lower than 5%_{vol}), was fed to the EB. Two different mixtures of H₂ and CO₂ were investigated, corresponding to two different values of α^1 , the typical parameter used to characterize methanation feeding: $\alpha = 2$ and $\alpha = 3$. The latter value corresponds to stoichiometric feeding, while the former one corresponds to a sub-stoichiometric feeding with respect to H₂. The choice to work in sub-stoichiometric conditions is linked to the attempt to compensate for the subtraction of CO₂ due to CaO carbonation, trying to obtain an almost stoichiometric ratio between H₂ and CO₂ in the reactive environment.

The first traditional methanation and the subsequent cycles of methanation/hydration lasted 10 min, a sufficient time to achieve sorbent saturation. Once the first methanation stage was over, the sorbent material was

¹ $\alpha = (\text{H}_2 - \text{CO}_2) / (\text{CO} + \text{CO}_2)$ where H₂, CO₂ and CO are the respective species molar flows in the feeding.

introduced into the reactor and four complete cycles of SEM/regeneration were carried out for each test, plus a last fifth SEM in the East Bed reactor, after which the bed material was discharged and separated by means of sieving. As for the regeneration steps, they were carried out in N₂, lasting 5 minutes at a fixed temperature of 450 °C. Table 1 summarizes the operating conditions investigated for the SEM tests with the selected sorbent. The amount of catalyst used was selected in order to ensure an optimal solid transfer between the twin beds in the cycles. However, such mass was not sufficient to reach chemical equilibrium at the temperatures of interest. This was also due to the extremely diluted conditions and to the gas by-pass, due to the bubbles, typically occurring in fluidized bed reactors.

Table 2. Conditions adopted in the SEM tests.

SORBENT MASS (g)	10
SORBENT SIZE (mm)	0.5
CATALYST MASS (g)	10
CATALYST SIZE (mm)	0.6
FLUIDIZATION VELOCITY (m/s)	0.5
SEM TEMPERATURE (°C)	300-350
$\alpha = (\text{H}_2\text{-CO}_2)/\text{CO}_2 (-)$	2-3

3. Results and discussion

Figure 2 (a-b) reports the methanation test results in terms of the ratio between the molar flows (mol/h) of CH₄ at the outlet and that of H₂ fed to the fluidized bed, for a fixed bed temperature of 300°C and at different feed ratios ($\alpha = 2$ and $\alpha = 3$, a and b respectively), as a function of time. The figure reports results for all the cycles constituting a complete SEM test. The curves relative to traditional methanation (always performed before each SEM test) are indicated with MET while the other ones are relative to the 5 SEM cycles. Considering the qualitative trend of the curves along the cycles, three distinct behaviours can be identified. In particular: 1) the first curve corresponding to traditional methanation; 2) the trend characterizing the first cycle under SEM conditions; and, finally, 3) the trend for the other four SEM cycles after the first one.

During traditional methanation (black line) the production of CH₄ shows an increasing trend with an initial transient behaviour before reaching a stable value after about 240 s. During the first SEM cycle (grey line) a similar trend is observed, but exhibiting a distinct slowing down in reaching the asymptotic value with respect to conventional methanation. This behaviour can be explained by considering that fresh CaO immediately starts to irreversibly carbonate, subtracting CO₂ reactant from the methanation reaction. Carbonation then rapidly slows down as a CaCO₃ shell is gradually formed around the sorbent particles. Finally, the “enhanced-behaviour” trend is already visible in the second SEM cycle, and even more evident in the subsequent three cycles. This trend involves the achievement of a maximum in the CH₄ outlet molar flow within approximately the first few minutes (around 90 s) of the cycle during which the produced steam was captured by CaO. To quantify this effect, the integral amount of CH₄ produced, with respect to the H₂ fed, was calculated and it is reported in Table 2, for the two α values. In particular, the CH₄ moles were calculated at two characteristic times: one corresponding to the peak of the “enhanced-behavior” (t_{90}), and the other at t_{210} , corresponding to complete saturation of the sorbent and stabilization of the curves to the asymptotic value. For both times considered, the percentage variation in the produced methane with respect to the “MET” case, is also reported in brackets. By comparing the outlet methane corresponding to the different gas feed ratios, the largest CH₄ amount was found for $\alpha = 3$, i.e. for the stoichiometric case (H₂/CO₂=4). This may be due to the effect of a higher H₂ concentration on kinetics.

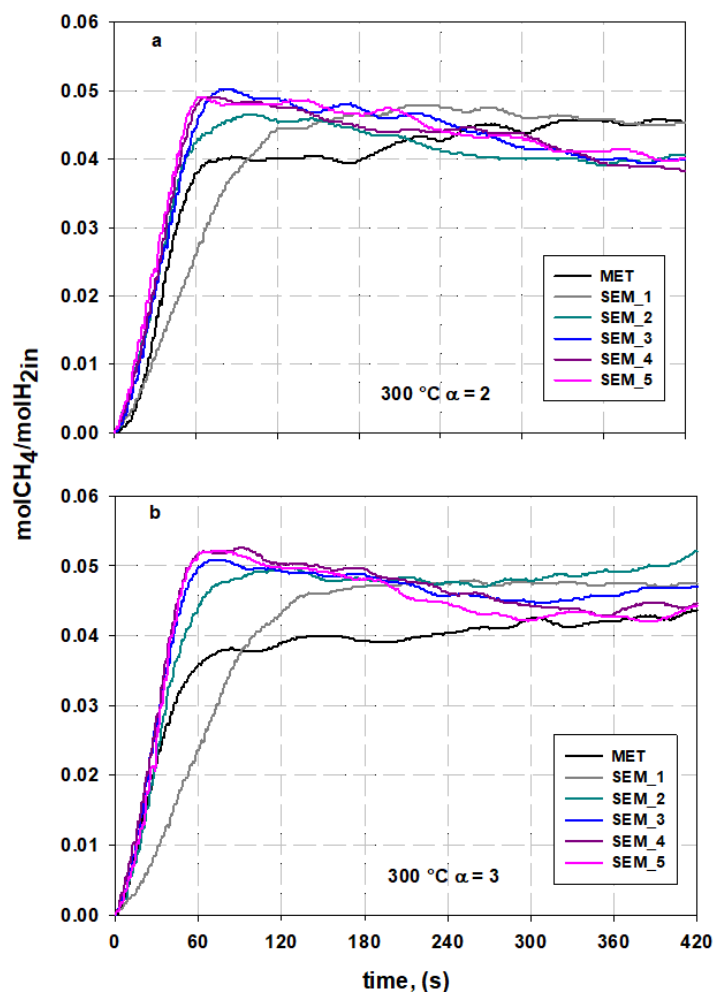


Figure 2. Molar flow ratio between outlet CH₄ and inlet H₂ as a function of time at 300°C, at $\alpha=2$ (a) and $\alpha=3$ (b).

For both α considered, the effect of H₂O sorption was evident in all the cycles except in the first one, when CaO carbonation clearly prevailed over hydration. In fact, during the first SEM cycle, a dramatic decrease in the CH₄ produced, if considering t_{90} , took place: -23% and -34% for $\alpha = 2$ and $\alpha = 3$, respectively. Feeding a CO₂ excess ($\alpha = 2$) with respect to the stoichiometric value was able to partly compensate the negative effect of carbonation in the first cycle. Noteworthy, along the cycles, the sorbent tended to rapidly saturate with respect to carbonation while concurrently the hydration effect became stronger with a higher amount of CH₄ produced. As far as the last cycles are concerned, the SEM effect for $\alpha = 2$ produced an enhancement amounting to around 20% (calculated at t_{210}). This value is about 30% lower than the increase corresponding to the peak value (t_{90}), where the maximum CH₄ productivity occurred. For a stoichiometric feed ($\alpha = 3$), this enhancement was even higher, with an average value over the last three cycles equal to about 30%.

Table 2. Ratio of total CH₄ produced to H₂ fed in each cycle at 300°C, and relative percentage variation with respect to standard methanation (MET).

	nCH _{4out} /nH _{2in}											
	MET		SEM_1		SEM_2		SEM_3		SEM_4		SEM_5	
	t ₉₀	t ₂₁₀	t ₉₀	t ₂₁₀	t ₉₀	t ₂₁₀	t ₉₀	t ₂₁₀	t ₉₀	t ₂₁₀	t ₉₀	t ₂₁₀
$\alpha = 2$	0.0237	0.0331	0.0182 (-23%)	0.0333 (0.34%)	0.0285 (20%)	0.038 (14.6%)	0.0295 (24.6%)	0.04 (20.4%)	0.03 (29.5%)	0.0396 (19.4%)	0.0317 (34%)	0.0408 (23%)
$\alpha = 3$	0.0252	0.0332	0.0165 (-34%)	0.0327 (-1.4%)	0.03 (18.6%)	0.04 (22.3%)	0.0336 (33.3%)	0.0423 (27.5%)	0.035 (39%)	0.0435 (31.3%)	0.0339 (34.5%)	0.0425 (28.3%)

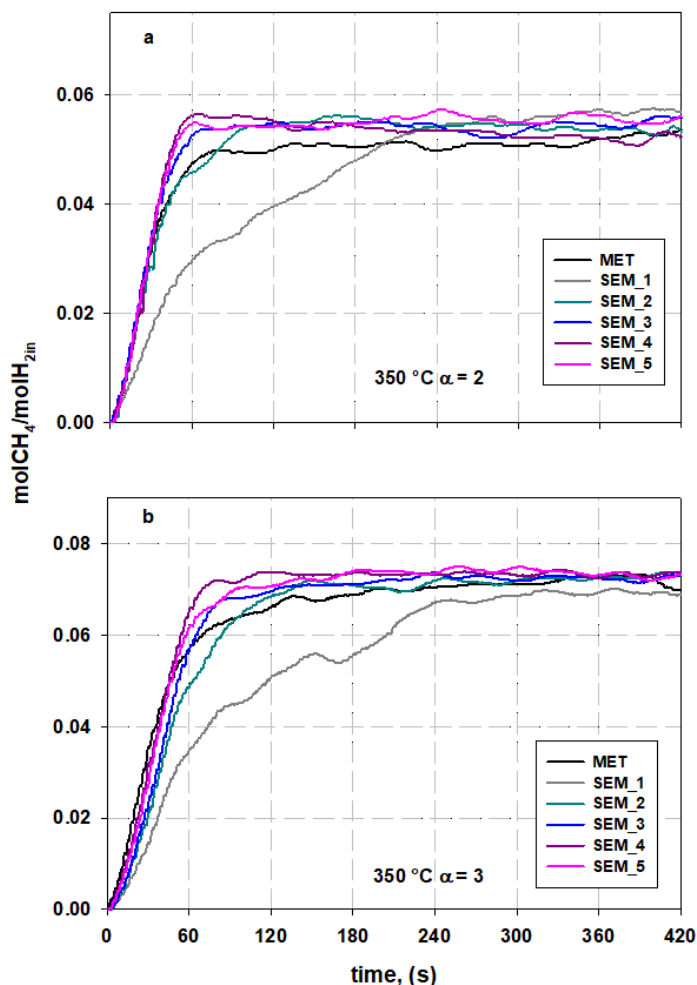


Figure 3. Mole flow ratio between outlet CH₄ and inlet H₂ as a function of time at 350°C, at $\alpha=2$ (a) and $\alpha=3$ (b).

Considering the other methanation temperature investigated, 350°C, the results are reported in similar graphs (Figure 3 a-b), and the integral amount of CH₄ produced, with respect to the H₂ fed, is reported in Table 3, for the two α values. It can be observed, for both gas feed ratios, that the qualitative trend of the curves along the cycles is similar but with some differences from those obtained at 300°C. At 350°C the SEM curves do not show a pronounced maximum in the first part of the cycle due to the water sorption effect, but tend to reach more smoothly the asymptotic value. Moreover, in the first SEM cycle the sorbent reaction with CO₂ needed more time to be completed with respect to 300°C.

At 350 °C, as expected, more methane was produced during each cycle with respect to the 300°C case: this is due to the fact that the system did not reach equilibrium and the kinetic effects prevailed. For example, if considering the total amount of CH₄ produced at $\alpha = 3$ in the last two cycles, it amounted to 0.0074 moles for 350°C compared to 0.0057 moles at 300°C.

The increase in CH₄ productivity in the last cycles was lower than that found in the same cycles at 300°C, for both α values considered, reaching the maximum enhancement, around 10%, for $\alpha = 2$. Apart from a stronger effect of the carbonation reaction, this result is most likely linked to the effect of temperature on the thermodynamic equilibrium limit on the hydration reaction of CaO, which worsens by increasing temperature in this range.

On the whole, these results are closely related to the effect of the operating conditions on the kinetics and thermodynamics of both the carbonation and hydration reactions of CaO, calling for a more in-depth analysis.

Table 3. Ratio of total CH₄ produced to H₂ fed in each cycle at 350°C, and relative percentage variation with respect to standard methanation (MET).

	nCH ₄ _{out} /nH ₂ _{in}											
	MET		SEM_1		SEM_2		SEM_3		SEM_4		SEM_5	
	t ₉₀	t ₂₁₀	t ₉₀	t ₂₁₀	t ₉₀	t ₂₁₀	t ₉₀	t ₂₁₀	t ₉₀	t ₂₁₀	t ₉₀	t ₂₁₀
α = 2	0.0339	0.0434	0.0209 (-38.5%)	0.0337 (-22.3%)	0.035 (2.7%)	0.0464 (7%)	0.0364 (7.3%)	0.0468 (7.8%)	0.0389 (14.7%)	0.0479 (10.4%)	0.0387 (14%)	0.0477 (10%)
α = 3	0.0397	0.0555	0.0238 (-39.9%)	0.0406 (-26.8%)	0.0345 (-12.9%)	0.0545 (-1.8%)	0.0383 (-3.2%)	0.0567 (2.1%)	0.0443 (11.8%)	0.0608 (9.6%)	0.041 (3.4%)	0.0588 (5.9%)

4. Conclusions

In this work, the CO₂ sorption-enhanced methanation process using CaO as sorbent was investigated in a novel configuration consisting of two interconnected fluidized beds. The performance was evaluated at different temperatures compatible with both methanation and chemical sorption of H₂O (300°C and 350°C). In addition to a stoichiometric feed (H₂/CO₂=4), the effect of an over-stoichiometric feed in terms of CO₂ (H₂/CO₂=3) was also considered to partly counteract the influence of the undesired CaO carbonation on the SEM performance. The results were analysed in terms of the amount of produced methane (with respect to the H₂ fed), compared to the traditional methanation case, during 5 SEM cycles. For both temperatures considered, the effect of the fresh CaO fed to the system, which immediately tends to carbonate, was dramatic, leading to a significant decrease in the methane productivity with respect to the conventional case during the first SEM cycle. However, when CO₂ was fed in excess with respect to the stoichiometric value, this negative effect seemed to be partly compensated.

On the other hand, in the subsequent SEM cycles the negative effect of carbonation tended to vanish and a clear enhancement of the methane productivity was observed. The enhancement of the produced methane during the last cycles, with respect to traditional methanation, was around 20-30% and 8-10% at 300°C and 350°C, respectively. The highest increase was found at 300°C for both feed conditions: the best performance occurred for a stoichiometric gas feed for which the average increase was around 30%. It is worth noting that if considering a shorter time with respect to the entire cycle, i.e. a time corresponding to the peak methane productivity, the CH₄ percentage enhancement was even higher and reached on average a value around 37% over the last two cycles.

Acknowledgements

The experimental support of Ms. Michela Vignola is gratefully acknowledged.

References

- [1] Cuéllar-Franca R. M, Azapagic A., Carbon capture, storage and utilisation technologies: A critical analysis and comparison of their life cycle environmental impacts, *J. CO2 Util.* 9 (2015) p. 82–102.
- [2] de Boer H. S, Grond L, Moll H, Benders R, The application of power-to-gas, pumped hydro storage and compressed air energy storage in an electricity system at different wind power penetration levels, *Energy* 72 (2014) p. 360–70.
- [3] Pleßmann G, Erdmann M, Hlusiak M, Breyer C, Global energy storage demand for a 100% renewable electricity supply, *Energy Procedia* 46 (2014) p. 22–31.
- [5] Smestad G. P, Steinfeld A, Review: photochemical and thermochemical production of solar fuels from H₂O and CO₂ using metal oxide catalysts, *Ind. Eng. Chem. Res.* 51 (2012) p. 11828–11840.
- [6] Götz M, Lefebvre J, Mörs F, McDaniel Koch A, Graf F, Bajohr S, Renewable Power-to-Gas: A technological and economic review, *Renew. Energy* 85 (2016) p. 1371–1390.
- [7] Sabatier P, Senderens J-B, New methane synthesis, *J. Chem. Soc.* 82 (1902) p. 333-337.
- [8] Rönsch S, Schneider J, Matthischke S, Schlüter M, Review on methanation – From fundamentals to current projects, *Fuel* 166 (2016) p. 276–296.

- [9] Mills G. A, Steffgen F.W, Catalytic methanation, *Catal. Rev.* 8 (1974) p. 159–210.
- [10] Bartholomew C. H, Mechanisms of catalyst deactivation, *Appl. Catal. A* 212 (2001) p. 17–60.
- [11] Seemann M.C, Schildhauer T.J, Biollaz S.M.A, Stucki S, Wokaun A, The regenerative effect of catalyst fluidization under methanation conditions, *Appl. Catal. A* 313 (2006) p. 14–21.
- [12] Borgschulte A, Gallandat N, Probst B, Suter R, Callini E, Ferri D, Arroyo Y, Erni R, Geerlings H, Züttel A, Sorption enhanced CO₂ methanation, *Phys. Chem. Chem. Phys.* 15 (2013) p. 9620-9625.
- [13] Walspurger S, Elzinga G.D, Dijkstra J.W, Saric M, Haije W.G, Sorption enhanced methanation for substitute natural gas production: Experimental results and thermodynamic considerations, *Chem. Eng. J.* 242 (2014) p. 379–386.
- [14] Dou B, Zhang H, Cui G, Wang Z, Jiang B, Wang K, Chen H, Xu Y, Hydrogen production and reduction of Ni-based oxygen carriers during chemical looping steam reforming of ethanol in a fixed-bed reactor, *Int. J. Hydrogen Energy* 42 (2017) p. 26217–30.
- [15] Dou B, Zhang H, Cui G, Wang Z, Jiang B, Wang K, Chen H, Xu Y, Hydrogen production by sorption-enhanced chemical looping steam reforming of ethanol in an alternating fixed-bed reactor: Sorbent to catalyst ratio dependencies”, *Energy Convers. Manag.* 155 (2017) p. 243–52.
- [16] Müller S, Fuchs J, Schmid J. C, Benedikt F, Hofbauer H, Experimental development of sorption enhanced reforming by the use of an advanced gasification test plant, *Int. J. Hydrogen Energy* 42 (2017) p. 29694–707.
- [17] Coppola A, Massa F, Salatino P, Scala F, Fluidized bed CaO hydration-dehydration cycles for application to sorption-enhanced methanation, *Combustion Science and Technology* 191 (2019) p. 1724–1733.
- [18] Lechkar A, Barroso Bogeat A, Blanco G, Pintado J.M, Soussi el Begrani M, Methanation of carbon dioxide over ceria-praseodymia promoted Ni-alumina catalysts. Influence of metal loading, promoter composition and alumina modifier, *Fuel* 234 (2018) p. 1401–1413.
- [19] Rahmani S, Rezaei , Meshkani, F, Preparation of promoted nickel catalysts supported on mesoporous nanocrystalline gamma alumina for carbon dioxide methanation reaction, *Journal of Industrial and Engineering Chemistry* 20 (2014) p. 4176–4182.
- [20] Abate S, Mebrahtu C, Giglio E, Deorsola F, Bensaid S, Perathoner S, Pirone R, Centi G, Catalytic Performance of γ -Al₂O₃-ZrO₂-TiO₂-CeO₂ Composite Oxide Supported Ni-Based Catalysts for CO₂ Methanation, *Industrial & Engineering Chemistry Research* 55 (2016) p. 4451–4460.
- [21] Coppola A, Scala F, Gargiulo L, Salatino P, A twin-bed test reactor for characterization of calcium looping sorbents, *Powder Technology* 316 (2017) p.585–591.

Core-shell structures to enhance the formation of gasoline products via CO₂ hydrogenation

Elena Corrao¹, Fabio Salomone¹, Emanuele Giglio², Raffaele Pirone¹, Samir Bensaid^{1*}

¹Department of Applied Science and Technology (DISAT), Polytechnic of Turin, Corso Duca degli Abruzzi, 24, Turin, 10129 (Italy)

²Chemical Engineering and Catalysis for Sustainable Processes (CECaSP) Laboratory, University of Calabria, Via Pietro Bucci, Rende, 87036 (Italy)

*elena.corrao@polito.it

1. Introduction

Nowadays, CO₂ emissions affect climate change, generating a wide range of adverse impacts on society and on the environment. To counteract this phenomenon, CO₂ could be captured and converted into high-value chemicals. In this scenario, the modified Fischer-Tropsch synthesis (FTS) is one of the most promising processes since it enables the production of hydrocarbons through the direct hydrogenation of CO₂. Furthermore, if H₂ is produced by exploiting renewable energy, a sustainable pathway to produce synthetic hydrocarbons can be carried out [1]. Since CO₂ is a very stable molecule, in-depth study of catalysts is required to produce molecules with two or more carbon atoms (C₂₊). In the open literature, many Fe-based catalysts have been investigated due to their good activity and stability in the production of hydrocarbons. Among them, Fe₃O₄-based materials are very promising since they allow the CO₂ to be directly converted into fuels. Fe₃O₄ sites are responsible of the endothermic reverse water gas shift (RWGS) reaction. Fe₅C₂ active sites formed in situ under reaction condition enable the FTS. Promoters like sodium are generally added to Fe₃O₄ to enhance the formation of Fe₅C₂ sites and to reduce the methane production, favoring the selectivity of olefins. Hence, the olefins obtained via FTS could oligomerize, aromatize and isomerize on the surface of a zeolite to produce a gasoline-like product [2]. In addition, core shell structures represent interesting catalyst configurations because they could break the Anderson-Schulz-Flory distribution (ASF) production distribution and increase the selectivity to target products thanks to a synergistic effect between core and shell materials [3], probably due to the forced back-diffusion of olefins formed on the active phase over the zeolite.

The aim of this work is to study the optimization of those particular structures made of a Fe-based active phase as core and a zeolite as shell. As a kind of effective investigation on the role of the core shell structure Na-Fe₃O₄@HZSM-5, several physical mixtures of catalysts were also tested at the same conditions.

2. Methods

To obtain 1%Na-Fe₃O₄, pure Fe₃O₄ (synthesized according to the method proposed by Zhong et al. [3]) was necessary. Pure Fe₃O₄ was subsequently impregnated with NaNO₃[4]. ZF1 (1%Na-Fe₃O₄@HZSM5), ZF2 (1%Na-Fe₃O₄@Fe₅C₂@HZSM5) and ZF3 (Na-Fe₃O₄@HZSM5) core-shell catalysts were synthesized by means of a physically adhesive technique [5]. More in detail, ZF1 was prepared mixing a certain amount of 1%Na-Fe₃O₄ particles (300 – 500 μm), with 1/4 of ludox (aqueous solution with 30 wt.% SiO₂) diluted with 2 times of milli-Q water. Subsequently, HZSM5 (SiO₂:Al₂O₃=80:1) powder were manually added to the moist granules (mass ratio between active phase and zeolite equal to 1:1). The core-shell pellets were calcined at 400 °C for 3 h (heating rate: 2.5 °C/min). ZF3 was prepared at the same but using a different active phase (Na-Fe₃O₄). Na-Fe₃O₄ was synthesized by the coprecipitation method with NaOH [6]. Lastly, ZF2 was prepared according to a similar procedure, but using glucose instead of ludox as glue. Also in this case, the core is made of 1%Na-Fe₃O₄ as active phase. Once the core-shell structure was obtained, the pellets of ZF2, were taken in a quartz boat and were heated at 400 °C at a heating rate of 2.5 °C/min under N₂ atmosphere for 3 h. Physically mixed 1%Na-Fe₃O₄-HZSM5 catalyst (mass ratio 1:1) was prepared as reference. In addition, physically mixed 1%Na-Fe₃O₄-HZ catalyst (mass ratio 1:1) was tested. HZ (SiO₂/Al₂O₃=80) was synthesized by hydrothermal synthesis method [4] and controlling appropriately the amount of AIP. The properties and the structure of the catalysts were investigated by means of N₂-physisorption, scanning electron microscopy (SEM), X-ray diffraction (XRD), temperature-programmed measurements (H₂-TPR, CO₂-TPD and NH₃-TPD), and X-ray photoelectron spectroscopy (XPS). The catalysts were loaded and pre-treated in a fixed bed reactor at 380°C for 3 h under N₂/H₂=50:50 and 0.2 MPa and tested at 2.1 MPa, 20 NL·g⁻¹_{active phase}·h⁻¹, H₂/CO₂/N₂ molar ratio equal to 15/5/1 at the temperature of 330 °C. Both inlet mixture and gaseous outlet stream were analyzed with

an on-line gas analyzer and a 2-columns GC system equipped with a thermal conductivity detector (TCD) and a flame ionization detector (FID). The collected liquid oil extract was instead analyzed using a GC-MS.

3. Results and discussion

The reaction pathway related to the conversion of CO₂ into hydrocarbons occurs on three different sites: Fe₃O₄, Fe₅C₂ and acid sites of the zeolite. Various configurations of multifunctional catalysts with different distances between iron-based sites and zeolite sites were synthesized. Physical mixing of the active phase 1%Na-Fe₃O₄ with the commercial zeolite HZSM-5 and physical mixing of the active phase 1%Na-Fe₃O₄ with the homemade zeolite HZ results were compared with core-shell structures. Results are reported in Figure 1 a); the different CO₂ conversion and CO selectivity between the two physical mixing catalysts, respectively 1%Na-Fe₃O₄-HZSM-5 and 1%Na-Fe₃O₄-HZ, could be attributed to the different pore size of involved zeolite. Focusing on the core-shell structures, the CO₂ conversion (especially for ZF2) is very low. This is probably due to the small amount of Fe₃O₄ rather than Fe₅C₂, and to the metallic iron found according to the XRD analysis Figure 1 b). Concerning ZF1, the decrease of CO₂ conversion and the increase of CO selectivity compared with the physical mixture, could be ascribed to the migration of Na from the surface of the catalyst to the zeolite. These assumptions were confirmed from the H₂-TPR and NH₃-TPD profiles. On the other hand, the last core-shell structure (ZF3) is the most promising. Also in this case, there is a small amount of metallic iron, but the ratio between Fe₃O₄ and Fe₅C₂ allows this catalyst to have good performance. H₂-TPR profile of the ZF3 catalyst suggests that there is no migration of sodium between the two phases. This is probably related to the different synthesis of active phase. Additional investigation is required to support our thesis. It is important to highlight the difference in the liquid oil extract, in fact with the zeolite the product obtained are especially aromatic compounds, while in the presence of only 1%Na-Fe₃O₄ active phase the product are olefins and paraffins.

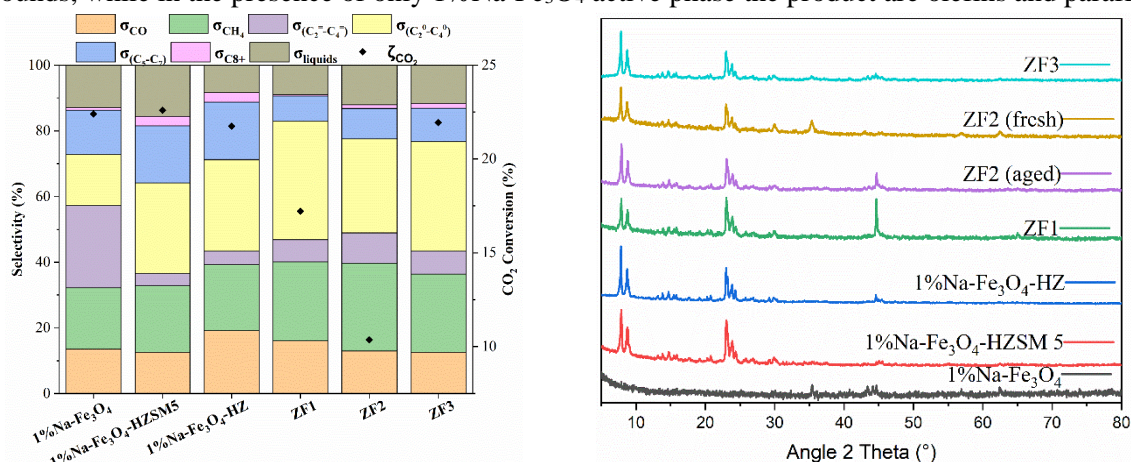


Figure 1. a) Selectivity of hydrocarbons distribution, CO and conversion of CO₂ over different structures. b) XRD pattern

4. Conclusions

The investigated process enables the production of liquid hydrocarbons via a sustainable pathway involving carbon dioxide hydrogenation over innovative catalysts, as an alternative to the conventional fossil-based route. Further studies are needed to investigate core-shell structures without diffusion problems. The challenge is to increase the conversion of CO₂, by limiting the selectivity towards to CO and CH₄, and by pushing the reaction over longer chains that lead to the formation of gasoline like products.

References

- [1] W. Wang, X. Jiang, X. Wang, and C. Song, *Ind. Eng. Chem. Res.*, vol. 57, no. 13, pp. 4535–4542, Apr. 2018.
- [2] P. Gao *et al.*, *ACS Catal.*, vol. 8, no. 1, pp. 571–578, 2018.
- [3] Y. Zhong *et al.*, *ACS Appl. Mater. Interfaces*, vol. 11, no. 35, pp. 32251–32260, Sep. 2019.
- [4] C. Wen *et al.*, *Energy and Fuels*, vol. 34, no. 9, pp. 11282–11289, 2020.
- [5] F. Song *et al.*, *Appl. Catal. B Environ.*, vol. 300, no. June 2021, p. 120713, 2022.
- [6] J. Wei *et al.*, *Nat. Commun.*, vol. 8, no. May, pp. 1–8, 2017.

Evaluation of transition metal heterogeneous catalysts deactivation in green chemistry processes

Gabriella Garbarino¹ *

¹ Department of Civil, Chemical and Environmental Engineering, University of Genoa, Genoa, Italy

**Corresponding author E-Mail: gabriella.garbarino@unige.it*

1. Introduction

In heterogeneous catalysis, at industrial level catalyst deactivation is translated in a reduced production in terms of conversion or selectivity losses. It is mainly compensated by optimization of process parameters up to a non-return point, where a shut-down of the full plant and catalysts reloading are mandatory. To this step, an expensive start up procedure follows. It is clear that this has a strong impact on process economics and as well on the catalyst market, accounting for 25 billion USD (datum 2019). Main deactivation mechanisms have been reviewed [1,2] and often parallel or multiple effects might play together, and, at the industrial level, this is mostly managed on experience basis. Chemical deactivation includes both the reversible and irreversible poisoning due to traces molecules or elements present in the flue gas or coke formation; physical deactivation includes fouling while thermal deactivation includes sintering and loss of active phase (i.e. vaporisation, solid state reactions and loss of surface sites due to secondary reactions). Mechanical deactivation is mainly due to attrition or erosion phenomena. In the frame of development of green industrial chemistry processes, the challenge is not only to develop catalysts or processes but also to investigate catalysts deactivation for key-challenge catalytic processes i.e., ethanol dehydrogenation [3] and/or oxidative dehydrogenation to acetaldehyde [4,5], CO₂ hydrogenation to CH₄ [6] and fuels or even S- poisoning over Ni catalysts [7] for green hydrogen production or in hot syngas cleaning after biomass gasification.

2. Methods

Experiments were performed on home-made synthesized catalysts by choosing suitable synthetic procedures and evaluating not only the preparation in terms of performances but also on the improvement in deactivation. Among suitable supported catalysts, abundant metal-based catalysts are certainly of interest and we will focus mainly on Co-, Ni-, Mo- and Cu- catalysts developed for mentioned reactions and extensively characterized both as fresh and after catalysis experiments by means of XRD, FE-SEM, FT-IR, UV-vis-NIR and TP techniques. Catalytic experiments have been performed in laboratory scale plants with the parameters reported in [3-7]. Online analyses have been performed by means of FT-IR spectroscopy by allowing the evaluation of concentration profile as a function of time. Mathematical fitting of concentration profile has been carried out to evaluate the activity factor and characteristic deactivation time upon which steady state is reached.

3. Results and discussion

For Co- based catalyst upon CO₂ hydrogenation an effect of preparation procedure and methane production has been observed upon both the precursor and the exposure of the catalysts at high temperature, that exhibit a reduction in methane production and a remarkable increase in CO one, suggesting the existence of two independent sites and the killing of methanation one in reactant stream. Moreover, cubic cobalt particles rapidly become deactivated by encapsulating carbon according to their high activity in favoring the formation of C-C bonds [6,8]. In the case of ethanol dehydrogenation to acetaldehyde, Cu-based catalysts mainly supported over an oxidic carrier with tailored acido-base properties are used i.e., ZnAl₂O₄ or MgAl₂O₄. In this frame, copper suffers of both sintering, occurring already at low temperatures, and of coke deposition. A typical experiment is reported in Figure 1, where a decay of acetaldehyde concentration and an increase in ethanol one can be clearly envisaged. In all cases, the mathematical fitting by using an exponential decay

function allowed the evaluation of characteristic deactivation time, by helping the interpretation of obtained results. As well, in an analogous way, the behavior of Ni- based catalysts in CO₂ hydrogenation to methane will be presented and extensively discussed.

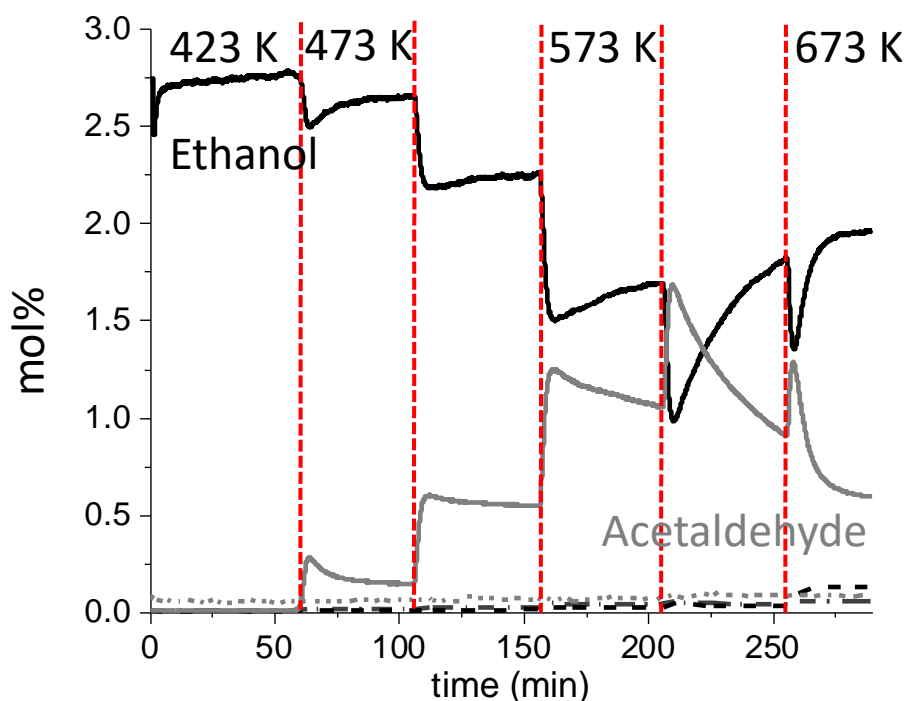


Figure 1. Ethanol Dehydrogenation over Cu/ZnAl₂O₄ catalyst - concentration of ethanol (black) and acetaldehyde (grey) as a function of time and temperature

4. Conclusions

Catalyst deactivation has been observed and evaluated over several transition metal materials devoted to the exploitation of green industrial chemistry processes. All the results will be widely discussed in the frame of the understanding of catalysts deactivation and possible strategies to reduce it.

References

- [1] J.M. Dreimann, E. Kohls, H.F.W. Warmeling, M. Stein, L.F. Guo, M. Garland, T.N. Dinh, A.J. Vorholt, *ACS Catal.* 9 (2019), 4308-4319
- [2] C.H. Bartholomew, *Appl Catal A: Gen* 212 (2001) 17-60
- [3] G. Pampararo, G. Garbarino, P. Riani, M. Villa Garcia, V. Sanchez Escribano, G. Busca, *Appl. Catal. A:Gen.* 602 (2020) 117710.
- [4] G. Pampararo, G. Garbarino, N. Ardoino, P. Riani, G. Busca, *J. Chem. Tech. Biotech.* 96 (2021) 3293–3303
- [5] G. Pampararo, G. Garbarino, N. Ardoino, P. Riani, G. Busca, *J. Chem. Tech. Biotech.* 96 (2021) 3204–3313
- [6] P. Riani, G. Garbarino, T. Cavattoni, G. Busca, *Catalysis Today* 365 (2021) 122-131
- [7] G. Garbarino, A. Romero Perez, E. Finocchio, G. Busca, *Cat. Commun.*, 38 (2013), 67-73
- [8] G. Garbarino, T. Cavattoni, P. Riani, G. Busca, *Catal. Today*, 345 (2020) 213-219

Past, present and future of a Spouted Bed reactor

Cristina Moliner¹, Filippo Marchelli², Elisabetta Arato^{1*}

¹ Dipartimento di Ingegneria Civile, Chimica e Ambientale, Università di Genova,
 Via Opera Pia 15, 16145 Genoa, Italy

² Dipartimento di Ingegneria Civile, Meccanica e Ambientale, Università di Trento
 Via Mesiano 77, 38123 Trento (Italy)

*Corresponding author E-Mail: elisabetta.arato@unige.it

The use of biomass to produce renewable energy and new bio-materials can provide a sustainable and low-carbon alternative to traditional fossil fuels based technologies. This is one of the main research areas of the Process Engineering Research Team (PERT) at the University of Genova. The group applies a multiscale-based approach to evaluate new and traditional technologies through a complementary experimental and theoretical point of view.

This approach is widely applied by the group in the study of Spouted Beds (SB) [1]. In contrast with traditional fluidization, the fluid flow enters the SB through a single central inlet orifice creating three well differentiated zones: the central core of the reactor through which air flows is the spout, the surrounding annular region is the annulus and the solids above the bed surface entrained by the spout and going down the annulus form the so-called fountain. This configuration promotes mass and energy transfer phenomena and makes them suitable for a wide range of industrial applications as drying of solids, coating or chemical reactors [2].

Several lab and pilot-scale SB have been developed by the group in collaboration with both academic and non-academic research teams to perform thermo-chemical conversion of biomass and other residuals as textile waste. A first lab-scale device (Figure 1a) working at room temperature permitted to optimise its fluid dynamic properties through the combination of experimental data [3] and validation of developed numerical models using Ansys Fluent[®] (Figure 2a) [4, 5] and MFIx [6]. In a successive step, the best fluid dynamic configuration led to the construction of a pilot plant (Figure 1b) able to treat 200 g/min of biomass with a potentiality of 200 kWth [7]. Again, the experimental activity was complemented with models using Aspen Plus[®] (Figure 2b) [8] and COCO [9] to optimise the operational conditions and maximise the target outputs. Recently, the pilot unit has been successively scaled up to design and construct a plant with 4x4 units (Figure 1c) combining pyrolysis and gasification reactions with a potentiality of 0.5 MWth. Its fluid dynamic properties have been optimized (Figure 2c) [10, 11] and now an extensive experimental campaign to maximise the production of H₂ is ready to start.



(a)



(b)



(c)

Figure 1. Experimental SB devices: (a) lab-scale; (b) pilot plant (20 kWth); (c) scaled-up plant (0.5 MWth)

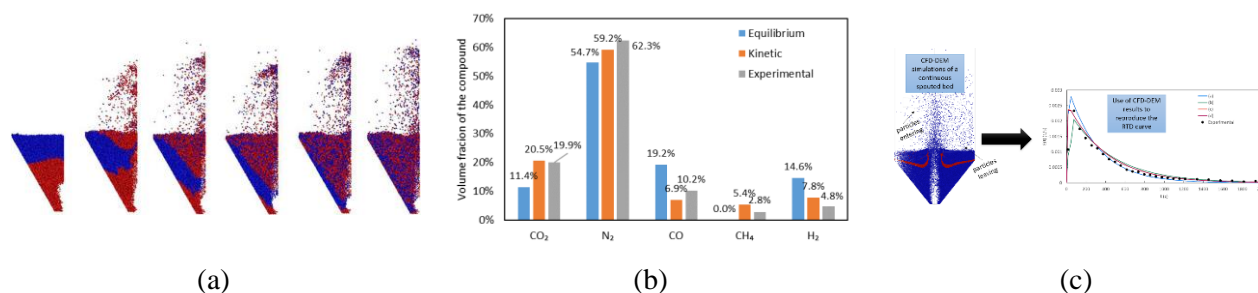


Figure 2. Results of simulation activities of the SB: (a) spouting phenomena using Ansys Fluent[®]; (b) distribution of gas products from the gasification of apple pruning using Aspen[®]; (c) residence time using Ansys Fluent[®]

The importance of valorising second-generation residues (i.e., by-products of valorisation technologies: char) has been identified and highlighted in all the developed systems. The different recovered biochar types (Figure 3a) have been used as an adsorbent for the removal of H₂S (Figure 3b) [12] and CO₂ (Figure 3c) [13] from exhausted gas.

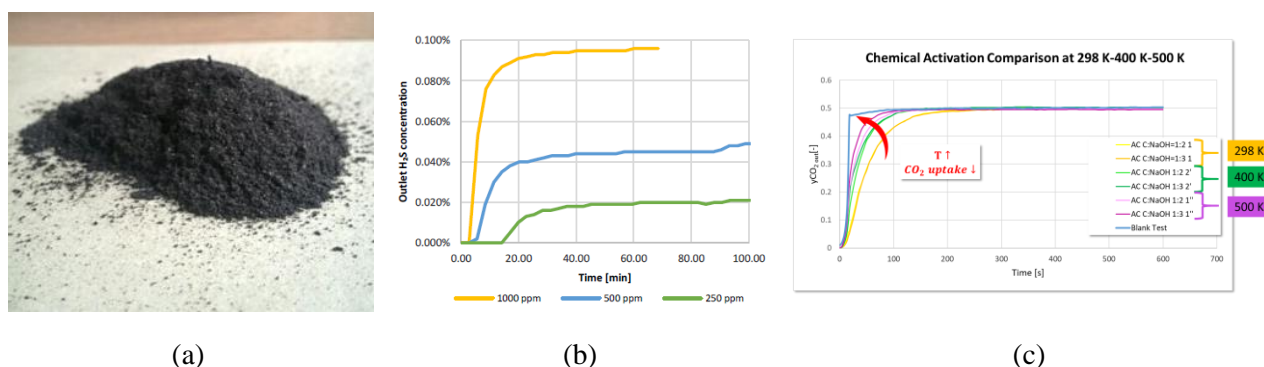


Figure 3. (a) apple pruning char; (b) breakthrough curves of H₂S adsorption on char from the gasification of biomass; (c) CO₂ uptake on chemically activated char from the pyrolysis of palm tree.

Within this framework, the present work aims to provide a description of all the above-mentioned research activities highlighting their most relevant outcomes and opportunities and providing an overview of the main challenges that the current state of the art is facing.

References

- [1] Epstein, N., Grace, J.R. Spouted and Spout-Fluid Beds. Cambridge University Press, Cambridge (2010).
- [2] Moliner, C., Marchelli, F., Bosio, B., Arato, E. Modelling of spouted and spout-fluid beds: Key for their successful scale up. *Energies*, 10(11), 1729 (2017).
- [3] Moliner, C., Marchelli, F., Curti, M., (...), Rovero, G., Arato, E. Spouting behaviour of binary mixtures in square-based spouted beds. *Particuology* 43, pp. 193-201 (2019).
- [4] C. Moliner, Marchelli, F., Spanachi, N., (...), Bosio, B., Arato, E. CFD simulation of a spouted bed: Comparison between the Discrete Element Method (DEM) and the Two Fluid Model (TFM). *Chemical Engineering Journal* 377, 120466 (2018).
- [5] Moliner, C., Marchelli, F., Ong, L., (...), Van der A, D., Arato, E. Sensitivity analysis and validation of a Two Fluid Method (TFM) model for a spouted bed. *Chemical Engineering Science* 207, pp. 39-53 (2019).
- [6] Marchelli, F., Di Felice, R. A comparison of ansys fluent and mfix in performing cfd-dem simulations of a spouted bed. *Fluids*, 6(11), 382 (2021).
- [7] D. Bove, C Moliner, M. Curti, M. Baratieri, B. Bosio, G. Rovero, E. Arato. Preliminary tests for the thermo-chemical conversion of biomass in a spouted bed pilot plant. *Canadian Journal of Chemical Engineering* 97(1), pp. 59-66 (2019).
- [8] Marchelli F., Moliner C., Baratieri M., Bosio B., Arato E. From equilibrium to kinetic modelling: the gasification of apple pruning residues in a spouted bed reactor. Poster. European Biomass Conference and Exhibition Proceedings Lisbon May (27thEUBCE) pp. 813-820 (2019).
- [9] Moliner, C., Marchelli, F., Bosio, B., Arato, E. Simulation of the gasification of agricultural residues using coco simulator. Poster. European Biomass Conference and Exhibition Proceedings Copenhagen (26thEUBCE), pp. 764-768 (2018).
- [10] Marchelli, F., Moliner, C., Curti, M., Bosio, B., Arato, E. CFD-DEM simulations of a continuous square-based spouted bed and evaluation of the solids residence time distribution. *Powder Technology* 366, pp. 840-858 (2020).
- [11] Marchelli F., Curti M., Tognin M., Rovero G., Moliner C., Arato E., Bosio B. Experimental study on the solids residence time distribution in multiple square-based spouted beds. *Energies* 13, 4694 (2020).
- [12] Marchelli, F., Patuzzi, F., Cordioli, E., ...Bosio, B., Arato, E. Adsorption of H₂S on residual biomass gasification char. European Biomass Conference and Exhibition Proceedings, (26thEUBCE), pp. 493-499 (2018).
- [13] Moliner, C., Antonucci, B., Focacci, S., ...Martín, C.F., Martínez-Felipe, A. Molecular dynamics simulation of the interactions between carbon dioxide and a natural-based carbonaceous microporous material. *Chemical Engineering Transactions*. Volume 86, Pages 1111 – 1116 (2021).

CeO₂ and Ce_xZr_{1-x}O₂ for the direct synthesis of diethyl carbonate from CO₂ and ethanol in presence of 2-cyanopyridine as dehydrating agent

Mara Arduino¹, Fabio Alessandro Deorsola^{1*} and Samir Bensaid¹

1 Politecnico di Torino, Department of Applied Science and Technology, Corso Duca degli Abruzzi, 10129, Turin, (Italy)

** Corresponding author E-Mail: fabio.deorsola@polito.it*

1. Introduction

The exponential increase of carbon dioxide levels in the atmosphere has attracted a great attention because of its significant impact on global warming. The reduction of atmospheric CO₂ concentration by carbon capture and utilization technologies is recognized as one of the possible solutions to mitigate the climate change. Among the various CO₂ utilization paths, organic carbonates attract a great deal of interest because of their promising properties[1,2]. Short chain dialkylcarbonates, such as DMC or DEC, are gaining popularity as replacements for hazardous chemical reagents or reactive solvents. DEC is most extensively researched as an electrolyte for lithium-ion batteries. Being an excellent solvent, it is widely used in pharmaceutical products, fertilizer, pesticide and manufacture of dyes. The presence of ethoxy and carbonyl groups in DEC help in its conversion to important chemicals which include polycarbonates and carbamates. Furthermore, due to its high oxygen content (40.6 wt%), it has been proposed to replace the gasoline fuel additive MTBE (methyl tertiary-butyl ether)[3,4]. With the global phase-out of the harmful phosgenation processes, the ENIChem process (liquid-phase oxycarbonylation of EtOH), the UBE process (ethylnitrite carbonylation) and the Texaco process (transesterification of EtOH and ethylene carbonate) have been successively transferred to the industrial scale for the production of DEC[4,5]. However, the corrosion, separation and catalyst deactivation remain bottlenecks of these processes despite recent significant improvements[6]. On the other hand, new synthetic routes are put forward under the framework of sustainable developments for the DEC synthesis, such as the alcoholysis of urea [7] and the direct conversion of ethanol and CO₂ [8–11]. However, the direct synthesis is extremely constrained by kinetics and thermodynamic limitations, hence, great efforts have been made to overcome these issues. A wide range of homogeneous and heterogeneous catalysts have been tested for this purpose. Heterogeneous catalysts are more suitable from the viewpoint of the easier separation of the catalyst from the products. Ceria (CeO₂), zirconia (ZrO₂) and ceria-zirconia (Ce_xZr_{1-x}O₂) mixed oxides have extensively studied as catalysts for direct DEC synthesis because of the bifunctionality of their active sites[9,10,12,13]. To shift the equilibrium and improve product yields, dehydrating agents such as orthoesters, and molecular sieves have been explored for the direct synthesis route. Nevertheless, nitriles were more effective as they are efficiently hydrated by CeO₂. Furthermore, water capture with nitriles leads to amides, which can later be converted back to the corresponding nitrile and enable the regeneration of the dehydrating species[14,15].

In this work CeO₂ and Ce_xZr_{1-x}O₂ catalysts with different morphologies and various Ce/Zr ratio were synthesized and tested, coupled with 2-cyanopyridine (2-CP) as dehydrating agent, for the direct synthesis of DEC from ethanol and CO₂ with the aim of developing a process which can operate at mild conditions of moderate temperature and pressure.

2. Methods

CeO₂ and Ce_xZr_{1-x}O₂ catalysts were prepared by the precipitation, hydrothermal and sol-gel methods and characterized by various techniques, such as N₂-adsorption (BET-SA), XRD, FE-SEM, CO₂-TPD and NH₃-TPD analyses.

Tests were carried out in a laboratory scale autoclave reactor with an inner volume of 310 mL. A known amount of catalyst, dehydrating agent and ethanol were charged, the reactor was then purged three times with

CO₂ at room temperature. The reaction system was then pressurized up to 2 MPa with CO₂. After a stabilization time, required for the CO₂ dissolution in ethanol, the reactor was then heated to the desired temperature and mechanically stirred constantly for a given time. Finally, the reactor was cooled to about room temperature and depressurized. The catalyst was then separated by filtration and the reaction mixture was analysed by GC-MS.

3. Results and discussion

The scanning electron micrograph was used to determine the morphology of the synthesized CeO₂ and Ce_xZr_{1-x}O₂ catalyst. Three types of morphologies were obtained: cubes, octahedra and rods. The morphology highly influenced the properties of the catalysts such as the amount of acidic and basic sites. Ceria cubes exhibited the lowest catalytic activity while octahedra and rods showed better performances.

The addition of a dehydrating agent was crucial to enhance the process yield. Furthermore, an increase in the quantity of 2-CP increased the selectivity.

References

- [1] M. Décultot, A. Ledoux, M.C. Fournier-Salaün, L. Estel, Kinetic modelling of the synthesis of diethyl carbonate and propylene carbonate from ethanol and 1,2-propanediol associated with CO₂, *Chem. Eng. Res. Des.* 161 (2020) 1–10. <https://doi.org/10.1016/j.cherd.2020.06.013>.
- [2] T. Tabanelli, D. Bonincontro, S. Albonetti, F. Cavani, *Conversion of CO₂ to Valuable Chemicals: Organic Carbonate as Green Candidates for the Replacement of Noxious Reactants*, 1st ed., Elsevier B.V., 2019. <https://doi.org/10.1016/B978-0-444-64127-4.00007-0>.
- [3] E. Leino, P. Mäki-Arvela, V. Etsä, D.Y. Murzin, T. Salmi, J.P. Mikkola, Conventional synthesis methods of short-chain dialkylcarbonates and novel production technology via direct route from alcohol and waste CO₂, *Appl. Catal. A Gen.* 383 (2010) 1–13. <https://doi.org/10.1016/j.apcata.2010.05.046>.
- [4] S. Huang, B. Yan, S. Wang, X. Ma, Recent advances in dialkyl carbonates synthesis and applications, *Chem. Soc. Rev.* 44 (2015) 3079–3116. <https://doi.org/10.1039/c4cs00374h>.
- [5] D. Delledonne, F. Rivetti, U. Romano, Developments in the production and application of dimethylcarbonate, *Appl. Catal. A Gen.* 221 (2001) 241–251. [https://doi.org/10.1016/S0926-860X\(01\)00796-7](https://doi.org/10.1016/S0926-860X(01)00796-7).
- [6] B. Schöffner, F. Schöffner, S.P. Verevkin, A. Börner, Organic carbonates as solvents in synthesis and catalysis, *Chem. Rev.* 110 (2010) 4554–4581. <https://doi.org/10.1021/cr900393d>.
- [7] K. Shukla, V.C. Srivastava, Synthesis of organic carbonates from alcoholysis of urea: A review, *Catal. Rev. - Sci. Eng.* 59 (2017) 1–43. <https://doi.org/10.1080/01614940.2016.1263088>.
- [8] X. Zhang, D. Jia, J. Zhang, Y. Sun, Direct synthesis of diethyl carbonate from CO₂ and ethanol catalyzed by ZrO₂/molecular sieve, *Catal. Letters.* 144 (2014) 2144–2150. <https://doi.org/10.1007/s10562-014-1403-5>.
- [9] I. Prymak, V.N. Kalevaru, S. Wohlrab, A. Martin, Continuous synthesis of diethyl carbonate from ethanol and CO₂ over Ce-Zr-O catalysts, *Catal. Sci. Technol.* 5 (2015) 2322–2331. <https://doi.org/10.1039/c4cy01400f>.
- [10] T. Chang, M. Tamura, Y. Nakagawa, N. Fukaya, J.C. Choi, T. Mishima, S. Matsumoto, S. Hamura, K. Tomishige, An effective combination catalyst of CeO₂ and zeolite for the direct synthesis of diethyl carbonate from CO₂ and ethanol with 2,2-diethoxypropane as a dehydrating agent, *Green Chem.* 22 (2020) 7321–7327. <https://doi.org/10.1039/d0gc02717k>.
- [11] M. Honda, S. Kuno, N. Begum, K.I. Fujimoto, K. Suzuki, Y. Nakagawa, K. Tomishige, Catalytic synthesis of dialkyl carbonate from low pressure CO₂ and alcohols combined with acetonitrile hydration catalyzed by CeO₂, *Appl. Catal. A Gen.* 384 (2010) 165–170. <https://doi.org/10.1016/j.apcata.2010.06.033>.
- [12] I. Prymak, V.N. Kalevaru, P. Kollmorgen, S. Wohlrab, A. Martin, Application of Ce_xZr_{1-x}O₂ catalysts for the synthesis of diethyl carbonate from ethanol and carbon dioxide, *DGMK Tagungsbericht.* 2013 (2013) 249–256.
- [13] G.G. Giram, V. V. Bokade, S. Darbha, Direct synthesis of diethyl carbonate from ethanol and carbon dioxide over ceria catalysts, *New J. Chem.* 42 (2018) 17546–17552. <https://doi.org/10.1039/C8NJ04090G>.
- [14] M. Tamura, A. Satsuma, K.I. Shimizu, CeO₂-catalyzed nitrile hydration to amide: Reaction mechanism and active sites, *Catal. Sci. Technol.* 3 (2013) 1386–1393. <https://doi.org/10.1039/c3cy00033h>.
- [15] K. Tomishige, M. Tamura, Y. Nakagawa, CO₂ Conversion with Alcohols and Amines into Carbonates, Ureas, and Carbamates over CeO₂ Catalyst in the Presence and Absence of 2-Cyanopyridine, *Chem. Rec.* 19 (2019) 1354–1379. <https://doi.org/10.1002/tcr.201800117>.

Comparative study of catalytic methane dry reforming, with microwave heating vs. conventional heating

Francesco Esposito, Paolo Canu*

University of Padua, Department of Industrial Engineering, Via Marzolo 9, Padua, 35131, Italy

*Corresponding author E-Mail: paolo.canu@unipd.it

1. Introduction

The minimization of energy consumption is a key factor in process intensification. To be minimized, energy should be transferred from the source to the sample in the required form, amount, at the required time and position [1]. This is particularly important in processes where high energy inputs are required, such as in endothermic gas-solid catalytic reactions like methane-dry reforming (MDR), where Methane and Carbon Dioxide reacts to produce Syngas, a source of various added-value chemicals. Energy is usually supplied in furnaces as heat, generated by flames or electrical resistances (conventional heating systems); however, these heating methods do not fulfill the conditions required to achieve energy minimization. Dielectric heating using microwaves (MW) represents an alternative heating strategy, which can meet the requirements imposed by process intensification [2]. In this work a high-temperature microwave reactor was developed by modifying a commercial MW oven; a suitable temperature measurement and control strategy were developed. The highly endothermic MDR was performed under either MW or conventional heating (CH), using the same reactor and catalytic bed; the most significant performance indices were analyzed, to quantitatively compare the effectiveness of both heating strategies.

2. Methods

The MW reactor used in the tests was internally developed in our lab, by modifying a household oven, to include a temperature control loop and a crossing quartz tube used as flow reactor. The reactor position into the oven cavity was determined by a numerical simulation of the electromagnetic field, and is located where the electromagnetic field intensity was higher [3]. The temperature control strategy is selected among three different measurement methods: air thermometers, infrared (IR) pyrometry coupled with fiber optics (FO), and metallic thermocouples. The catalytic bed is made by a mixture of SiC as MW-absorbing material, and an industrial catalyst (JM, Katalco 25-4). Temperature distribution in the fixed bed is analyzed by 3 grounded thermocouples. The feed mixture used is $\text{CH}_4:\text{CO}_2=1:1$; 5% v of Ar is added as internal standard, to determine the volumetric variations of the reacting mixture. A GHSV of 2000 h^{-1} based on the catalyst bed volume was set in both heating systems. The heat required to perform the MDR reaction is supplied using microwaves or electrical resistances, in two separate tests. The same reactor is used in both heating systems, to maintain the tests conditions as similar as possible. Prior to the tests, the catalyst is reduced to its active form in a Temperature Programmed Reduction (TPR) using Hydrogen. After the test, the catalytic bed is regenerated through a Temperature Programmed Oxidation (TPO), which removes the Carbon deposited on the catalyst during the test, re-establishing the initial catalytic activity. The product mixture is condensed to remove steam and it is analyzed in a gas chromatograph. Different temperatures (500°C , 600°C , 700° , 800°C and 900°C) have been investigated, and the results compared to the equilibrium. Under MW heating, the reactor is not insulated, to allow for a visual detection of hot-spots.

3. Results and discussion

Temperature measurement and control in the MW heating system is achieved with metallic thermocouples, properly grounded. Both the air thermometer and IR pyrometry measurement techniques were discarded, since the former only allows for an average bed temperature measure (making it impossible to measure temperature locally), while the latter is only able to measure the superficial reactor temperature (making it impossible to measure the reactor's center temperature). To be used, a thermocouple must be grounded [4] to avoid charge

accumulation in the sheath, which may lead to electric discharges; the thermocouple's hot junction, located beneath the tip, has to be shielded by a sufficiently thick layer of SiC, estimated in about 3 mm from studies on the penetration depth of MW into SiC. Significant axial temperature gradients have been measured in the bed, under MW heating; such gradients changes with the set temperature, being influenced by variations of the SiC dielectric properties with temperature. Gradients are limited by implementing a short catalytic bed, of 2 cm, having high SiC mass fraction (80%), the rest being catalyst. Interestingly, too small (< 0.1 mm) SiC particles were proved unable to absorb enough radiation to achieve temperature above 200°C without leading to magnetron overheating. This bed configuration allows to easily reach 900°C , while simultaneously prevent excessive reflected radiation to the MW source (magnetron), protecting it from overheating. The low catalyst content prevents arching (formation of electric discharges) in the bed, while maintaining a satisfactory catalytic activity. Fig.1 shows the CH_4 conversion and selectivity to H_2 from CH_4 profiles as function of temperature; the CH systems appear to perform better than the MW heating system. However, the lack of insulation in the MW heating system may contribute to the lower performances. Differences in selectivity may be traced back to the very different temperature distribution in the two heating systems: however, this result may also suggest different reaction pathways. Finally, energy consumption in the MW oven was measured to be more than twice the one of the CH system.

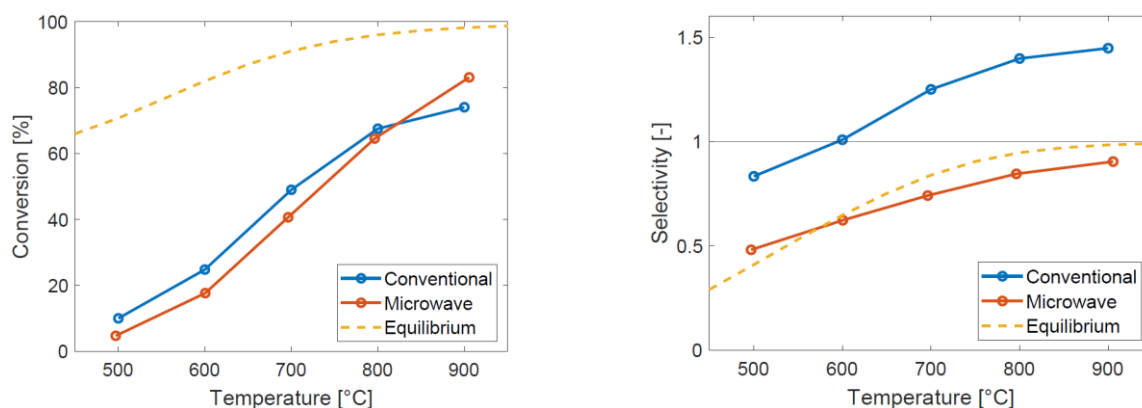


Figure 1. Conversions (left) and Selectivity to H_2 from CH_4 (right) as function of temperature, under microwave (red line) and Conventional (blue line) heating.

4. Conclusions

The possibility of operating highly endothermic reactions in a microwave oven has been demonstrated in this study. Temperature control can be achieved using metallic thermocouples; however, appropriate precautions must be taken to ensure the probe's correct operation. In particular, the thermocouple needs to be grounded and shielded with a sufficiently thick layer of MW-absorbing material. The effect of several operating parameters (thermocouple diameter, bed height, SiC particle size, catalyst loading, magnetron temperature) was assessed, and often a compromise between reactor performances and the oven component's integrity was required. The comparative study reported a superior performances of conventional heating, contrary to most literature studies (not directly comparative). Inhomogeneous temperature distribution and lack of insulation impact the MW heating system performances. Also the measured energy consumption was found higher in the MW oven, suggesting a poor radiation use. A systematic optimization on all the operating parameters is underway and may lead to a consistent improvement of the MW reactor performances.

References

- [1] G.D.Stefanidis, A.N.Muñoz, G.S.J.Sturm, A.Stankiewicz. *Reviews in Chemical Engineering* 30.3 (2014), 233-259
- [2] V.Palma, D.Barba, M.Cortese, M.Martino, S.Renda, E.Meloni. *Catalysts* 10.2 (2020), 246
- [3] C. Bianchi, P. Bonato, F. Dughiero, P. Canu. *Chemical Engineering and Processing - Process Intensification*, 120, 2017, 286-300
- [4] S.Hamzehlouia, J.Shabanian, M.Latifi, J.Chaouki. *Chem. Eng. Sci.* 192 (2018), 1177-1188

Facile and Scalable Synthesis of $\text{Cu}_2\text{O-SnO}_2$ Catalyst For The Photoelectrochemical CO_2 Conversion

Zoli Maddalena^{1*}, Roldán Daniela¹, Guzmán Hilmar¹, Castellino Micaela¹, Chiodoni Angelica²,
Bejtka Katarzyna², Russo Nunzio¹, Hernández Simelys^{1*}

¹ CREST group, Department of applied science and technology (DISAT), Politecnico di Torino, Turin, Italy;

² Center for Sustainable Future Technologies, IIT@Polito, Istituto Italiano di Tecnologia, Turin, Italy

*Corresponding author E-Mail: maddalena.zoli@polito.it; simelys.hernandez@polito.it

1. Introduction

CO_2 concentration in the atmosphere is increasing every year from the 50s, at the beginning of industrial acceleration, up to now, when it exceeds 410 ppm. Since natural CO_2 sink cannot keep up with the constant anthropogenic emissions, a renewable and green approach to CO_2 recovery is increasingly necessary to minimize its worrying impact on the environment. Within the depicted scenario, electrochemical and photoelectrochemical CO_2 reduction processes have been widely investigated as promising methods to transform CO_2 , under mild reaction conditions, into useful chemicals or fuels [1,2]. The first challenge of such processes is to find suitable catalysts with a high activity, good charges separation and improved solar conversion efficiency. Within this work, we focused on the CO_2 reduction reaction (CO_2RR) path directed towards products like CO (the syngas production is also taken into consideration) and formic acid, for which the transfer of 2 electrons is required. Cu_2O is a cheap, abundant, and intrinsically p-type semiconductor. Due to its narrow band gap (~ 2.1 eV) and the suitable positioning of conduction and valence bands, Cu_2O is an ideal photocatalyst for CO_2RR . Despite these promising features, Cu_2O is limited by its instability and continuous decrease of photoactivity under operative conditions [3]. The coupling cuprous oxide with a with a n-type wide bandgap semiconductor is here investigated as an effective way to prevent its self-photoreduction or oxidation. A noticeable electron mobility together with a good intrinsic stability have driven the choice towards tin oxide (SnO_2), which is also able to form a p-n junction with the Cu_2O photocatalyst. In this work we target the development of a facile and scalable synthesis method for the $\text{Cu}_2\text{O-SnO}_2$ catalyst. A particular focus is given to the preparation of photoelectrodes for the photo-electrocatalytic CO_2 reduction process and, finally, the evaluation of the catalyst performances in terms of stability and faradaic efficiencies of the target products.

2. Methods

The synthesis of photoactive copper-tin-oxide-based catalyst was optimized by an ultrasound assisted co-precipitation method. The significant advantages of the sonochemical synthesis approach [4] guided the choice of coupling these two methods. In addition, the reproducibility of the synthesis is boosted by using a completely automatised set-up made of peristaltic pumps. The characterization steps included several techniques: Transmission Electron Microscopy (TEM), Field Emission Scanning Electron Microscopy (FESEM), X-ray photoelectron spectroscopy (XPS) X-rays Diffraction Analysis (XRD), among others, and allowed the morphological assessment and the crystalline phase evaluation.

3. Results and discussion

From XRD on catalyst powder, it was found a correspondence to the cubic crystalline phase (cuprite) of Cu_2O which points out the suitability of the synthesis method. The elemental composition of the material was evaluated by comparing XPS and EDX (Energy Dispersive X-Ray) results both in the bulk and on the surface. It appears that the stannous compound presence is mainly present onto the surface of the catalyst, constituting a protection layer to Cu_2O . The study on specific surface area and porosimetry of the material, measured from N_2 adsorption/desorption isotherms, revealed a mesoporous structure with a BET surface area value of $142 \text{ m}^2/\text{g}$, a pore volume of $0.12 \text{ cm}^3/\text{g}$ and an average pore width of 5.9 nm, which were detected via BJH method.

From UV-Visible Spectroscopy analysis, the band gap energy value of 2.5 eV was calculated via Tauc plot method. The composition of a catalyst-based ink was optimized to avoid the Cu(I) oxidation during the electrodes preparation and preserve the catalyst photoactivity, which was assessed for the photo-electrocatalytic CO₂ reduction in an H-cell system. The PEC behaviour of Cu₂O-SnO₂ catalyst was evaluated using these photocathodes, for the photo-electroreduction of CO₂ in bicarbonate-based electrolyte. Cyclic Voltammetry tests carried out in both N₂ and CO₂ saturated environment showed more than double current density values with CO₂ (-1.25 vs. -2.75 mA cm⁻²), confirming an higher activity towards CO₂ reduction. Moreover, Linear Sweep Voltammetry and Chronoamperometry tests were led under the alternance of dark and light conditions, in order to show up the photoactivity of the catalyst. As reported in Figure 1, the photocurrent density was maintained stable for one hour (red dots), as evidence of the system stability. Chronopotentiometry tests at different current density values were performed, and the Faradaic efficiencies (FE) of both gaseous and liquid products were evaluated. CO was detected from the test at -1 mA cm⁻² with a FE = 8%, and it reached a maximum (FE = 18.5%) by applying -3 mA cm⁻². Also, we investigated how the simulated sunlight illumination can affect the products composition. Test carried out under light conditions were found to hinder the H₂ evolution (by a factor 1.5) and to produce around a double amount of CO (4.02% vs. 8.43%) and Formate (2.48% vs. 4.75%) with respect to dark conditions. Finally, ex-situ characterizations (XRD) of the electrodes after the photo-electrocatalytic tests pointed out a partial change of the Cu oxidation state, from Cu(I) to metallic Cu.

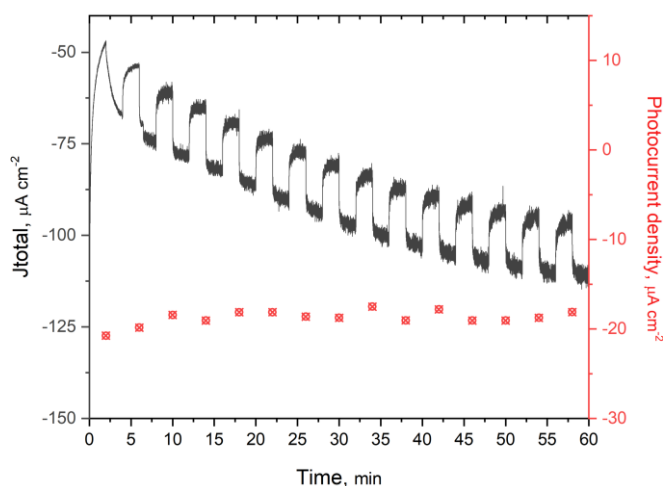


Figure 1. Chronoamperometry test plot, -250mV vs. RHE, under an alternated enlightenment (each 2 mins).

4. Conclusions

In conclusion, a simple, scalable, and reproducible method was developed for the Cu₂O-SnO₂ synthesis. A complete characterization allowed to investigate the catalyst morphology and the Cu(I) phase was found onto the photocathodes. Photo-electrocatalytic CO₂ reduction tests were carried out to finally assess the stability of the catalyst during time and the syngas and Formate production was evaluated in terms of their Faradaic efficiencies, showing a noticeable increase of C-based compounds under light conditions. It confirmed that the use of visible light seems to be highly appealing for the photoexcitation of CO₂⁻ richly mentioned in literature as the activated species of CO₂. Further developments will be devoted to optimize the SnO₂ loading into the Cu₂O photocatalyst and the sunlight utilization of this photo-electrocatalytic system.

Acknowledgements: The research leading to these results has received funding from the EU's Horizon 2020 Research and Innovation Action under the SunCoChem project (Grant Agreement No 862192).

References

- [1] S. Hernández et al., *Green Chem.* 19 (2017) 2326-2346
- [2] H. Guzmán, S. Hernández, N. Russo, *Green Chem.* 23 (2021) 1896-1920
- [3] Paracchino, A., Laporte, V., Sivula, K. et al., *Nature Mater* 10 (2011) 456-461
- [4] S. Yadav et al., *Ultrasonics Sonochemistry* 61 (2020) 104839

Electrification of methane steam reforming on Joule-heated SiSiC foams washcoated with a Rh/Al₂O₃ catalyst

Matteo Ambrosetti, Lei Zheng, Francesca Zaio, Alessandra Beretta, Gianpiero Groppi and Enrico Tronconi *

1 Laboratory of Catalysis and Catalytic Processes, Dipartimento di Energia, Politecnico di Milano, Italy

**Corresponding author E-Mail: enrico.tronconi@polimi.it*

1. Introduction

Methane steam reforming (MSR) is the process of choice for more than half of the global hydrogen production. Industrial scale MSR is typically carried out in multi-tubular reactors operated at high flow rates and externally heated by burning an additional amount of methane, which is responsible for roughly half of the CO₂ emission of the process.[1] In view of largely accessible renewable electricity, the so-called power-to-X (P2X) represents a promising way to address the challenge of decarbonization and provide an option for chemical storage of the excess energy. Electricity can be converted into heat and transferred to thermally driven chemical reactors. Recently, Wismann et. al. [2] proposed an innovative reactor concept for direct Joule heating of a washcoated FeCrAl-alloy tube for methane steam reforming. CH₄ conversion close to 87% was obtained with outlet temperature up to 900 °C. As an environmental benefit, a CO₂ reduction of 20-50% was achieved when compared with industrial reformers.

Open cell foam-based substrates can be also conceived as heating resistances for the electrification of catalytic processes.[3] The porous structure of foams enables a higher catalyst inventory than washcoated tubes thanks to their high specific surface area and allows uniform heating inside the reactor tubes. Therefore, the application of foams has the potential to overcome heat and mass transfer limitations in electrified methane steam reforming (eMSR), being the external mass transfer one of the limiting factors in the configuration proposed by Wismann and coworkers.[2] In this work, a novel reactor configuration is proposed and experimentally demonstrated for the electrification of MSR using direct Joule heating of a washcoated foam. A cylindrical Si-infiltrated silicon carbide foam was washcoated with Rh/Al₂O₃ catalyst and electrically connected to power supply as shown in Figure 1a. We show that it provided optimal heat and mass transfer properties and efficient inner heating for the steam reforming reaction.

2. Methods

A commercial SiSiC foam (Erbicol, CH) with cylindrical geometry ($d_{\text{foam}} = 3.2$ cm, $L_{\text{foam}} = 9.9$ cm) was adopted in the present work. A 1% Rh/Al₂O₃ catalyst was prepared via an incipient-wet impregnation method by using Al₂O₃ powder (Sasol, PURALOX) and rhodium precursor (Rhodium (III) nitrate solution, Alfa Aesar). The washcoating of the SiSiC foam was obtained by dipping, spinning and flash drying processes. Foams with different loadings, from 2.2 up to 4 g of catalyst over $\frac{1}{2}$ and $\frac{3}{4}$ of the foam length were prepared, corresponding to a catalyst inventory in the range of 40-85 g/lit.

Catalytic tests were performed at different GHSV up to 200.000 cm³/h/gcat (STP) with a non-diluted gas feed of CH₄ and H₂O (steam to carbon ratio of 4.1) at ambient pressure. Downstream from the reactor, water was removed from the products by a condenser and the dry gas mixture was analyzed using an online micro-GC (Agilent, 900 Micro GC).

3. Results and discussion

Figure 1 shows the schematic representation of the electrified methane steam reforming reactor layout proposed in the present work. The washcoated SiSiC foam was placed in a tubular stainless-steel tube reactor (OD = 5 cm). A ceramic tube was inserted between the foam and the stainless-steel tube to avoid electric contact. To connect the foam with the power generator, home-made electric sockets were adopted. A thin layer of copper

foam was placed between the foam and the electric plate to ensure a good electrical contact. The electric plates are connected to a DC power generator. K-type thermocouples, electrically insulated by ceramic thermocouple wells, are placed inside the electric contactors to measure the temperatures at the upper side and at the bottom of the foam.

Thanks to the interconnected geometry and the proper bulk resistivity of the SiSiC foam, the structured catalyst could be directly heated by the Joule effect (ohmic heating). Methane conversions approaching equilibrium were obtained across a range of conditions, with almost full methane conversion achieved above 700 °C, as shown in Figure 2(a). The foam-based eMSR system showed a high energy efficiency, which was found to be a strong function of the space velocity and reached a maximum of nearly 70% at lab-scale conditions.

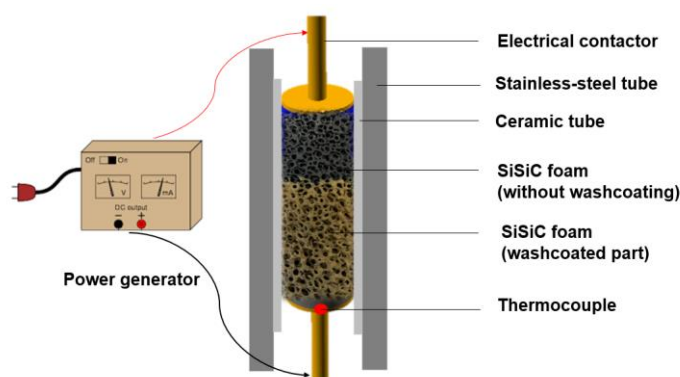


Figure 1 Schematic representation of the electrified methane steam reforming reactor layout

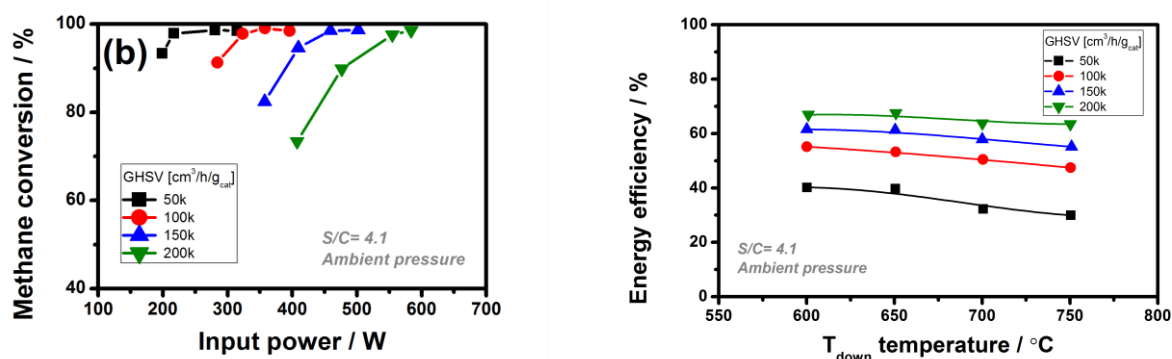


Figure 2. (a) CH₄ conversion and (b) thermal efficiencies as a function of GHSV for different space velocities

4. Conclusions

When driven by renewable electricity, such a reactor configuration promises a high potential to reduce CO₂ emissions in hydrogen production providing potential for process intensification with high H₂ productivities per volume and per kg of catalyst. Such a concept can be exploited also for many other endothermic processes, granting CO₂ savings.

References

- [1] Holladay J.D., Hu J. et. al., *Catalysis Today* 139, 244 (2009).
- [2] Wismann S.T., Engbæk J.S. et al, *Science* 364, 756 (2019).
- [3] Badakhsh A., Kwak Y. et al, *Chemical Engineering Journal*, 426, 130802 (2021).

Acknowledgements

We acknowledge financial support from MIUR - Progetto PRIN 2020N38E75 “PLUG-IN”.

Evaluating the mass transfer properties of 3D printed catalyst substrates with catalytic H₂ oxidation in rich conditions

Federico S. Franchi¹, Matteo Ambrosetti¹, Mauro Bracconi¹, Riccardo Balzarotti¹, Gianpiero Groppi^{1*}, Enrico tronconi¹

1 Dipartimento di Energia, Politecnico di Milano, Via La Masa, 34, Milano (Italy)

**Corresponding author E-Mail: gianpiero.groppi@polimi.it*

1. Introduction

Nowadays, the need to comply with more and more stringent environmental legislations is leading towards the implementation of innovative, high performance catalytic systems. The advancement in 3D printing technologies is enabling the manufacture of catalyst supports with better tradeoffs between gas/solid mass transfer and pressure drops than state of the art honeycomb monoliths [1]. To characterize the large number of geometries that can be manufactured with these techniques, an efficient screening methodology is required. Among the different additive manufacturing techniques, stereolithography (SLA) combine high precision and accuracy with low cost and fast production times resulting in the ideal technology for fast prototyping machines. The technique can use a wide range of polymeric materials, of which, a resin with a significant resistance to high temperature is selected. CO oxidation over noble metal catalysts in external mass transfer regime, was used in previous works [2-4], as a probe to evaluate the gas/solid mass transfer performances. However, the range in which this reaction is limited by external mass transfer is usually limited to temperatures above 300°C which will lead to the degradation of the resin substrate. To cope with the temperature limits of the resin samples (290°C), catalytic H₂ oxidation is a good candidate. Moreover, O₂ was used as the limiting reactant to reduce the conversion in the mass transfer regime.

SLA 3D printed samples have been used for other process intensification devices (e.g. static mixers), however, no catalytic applications have been yet reported in the literature. In this work, we propose the use of 3D printed resin samples for the investigation of external mass transfer properties by running H₂ oxidation catalytic tests in rich conditions.

2. Methods

POCS samples (cylinders, id = 9 mm, length = 15 mm) are printed using FLHTAM01 high-temperature (HT) resin (HDT_{@0.45MPa} = 289°C) and a Form2 SLA 3D printer. The finished samples are washcoated with a 3% Pd/CeO₂ slurry and the excess slurry is removed by spin-coating and flash dried in air at 200°C for 3 min. Samples are then reduced in situ at 200°C in a 2.5% v/v H₂ in N₂ feed mixture. Catalytic tests are performed using a N₂/H₂/O₂ 95/4/1 % v/v feed mixture. Operation with H₂ excess allows to avoid the potential oxidation and degradation of the polymer; furthermore, O₂ diffusion (5.6*10⁻⁵ m²/s @ 250°C) avoid the reach of complete conversion. O₂ conversion is evaluated at increasingly high temperatures until full external mass transfer limited regime is reached.

For validation purposes, a resin POCS tested with the presented protocol, is directly compared with an identical FeCrAlloy sample tested in mass transfer limited CO oxidation tests (1.5% CO in Air). Mass transfer coefficients, expressed as $ShSc^{-1/3}$, are calculated from O₂ conversion (for the resin sample) and CO conversion (for the FeCrAlloy POCS) in the external mass transfer regime assuming a PFR behavior.

3. Results and discussion

The dip/spin-coating procedure followed by flash drying resulted in a thin and homogeneous catalyst layer that does not significantly modify the geometrical properties of the investigated structures. Moreover, the Pd-based

catalyst used for the activation procedure, resulted in the light-off of the reaction at room temperature and allows to reach the diffusional regime at a temperature of 200°C, as shown in Fig 1 A).

As shown in Fig 1 B), that the dimensionless mass transfer coefficients evaluated through the use of the presented protocol are in very good agreement with the results provided by CO oxidation. A parametric investigation of mass transfer properties in POCS structures is currently ongoing.

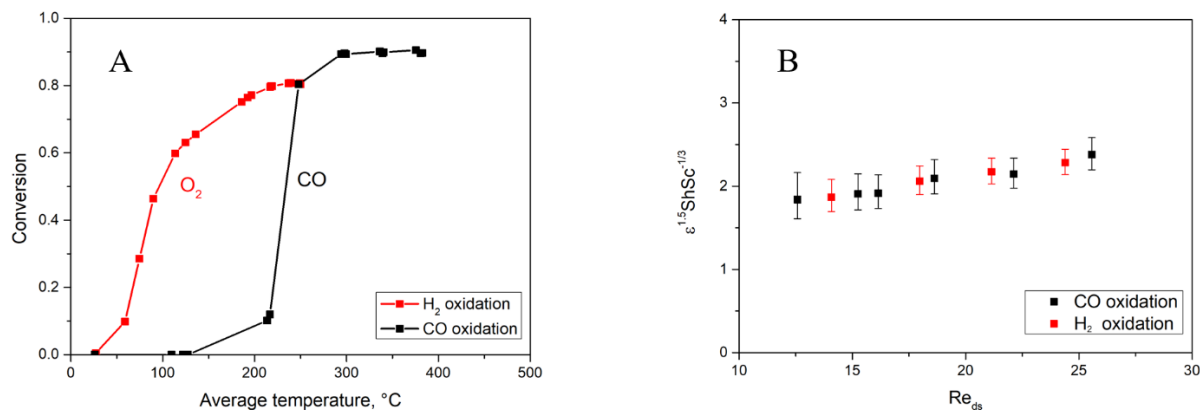


Figure 1. Limiting reactant conversion for CO and H₂ oxidation. Q = 3 l/min (STP), (A) and $\epsilon^{1.5}ShSc^{-1/3}$ vs. Re for TKKD POCS: cell diameter = 2.5mm, $\epsilon = 0.90$ (B)

4. Conclusions

A novel experimental protocol has been developed to allow accurate, fast and low-cost screening of complex 3D cellular substrates through the use of: i) HT resin for the manufacturing of 3D printed catalyst supports, and ii) rich H₂ oxidation as the test reaction.

5. References

- [1] Busse C., et al., Chem. Eng. Process., (2018), 124, 199
- [2] Groppi G., et al., Ind. Eng. Chem. Res., (2007), 46, 3955
- [3] Ullah U., and Waldram S.P., Chem. Eng. Sci., (1992), 47, 2413
- [4] Bracconi M., et al., Chem Eng. J., (2018), 352, 558

Experimental Campaigns and In-silico Assessment for the Conceptual Design of a Catalytic Splitting Process of Hydrogen Sulfide into Hydrogen and Elemental Sulfur

Anna Nova^{1,2}, Flavio Manenti^{1,2*}

1 Politecnico di Milano, Dipartimento di Chimica, Materiali ed Ingegneria Chimica "Giulio Natta", Piazza Leonardo da Vinci 32, 20133 Milano, Italy;

2 Consorzio Interuniversitario Nazionale per la Scienza e Tecnologia dei Materiali, Via Giusti 9, 50121 Firenze, Italy;

**Corresponding author E-Mail: flavio.manenti@polimi.it*

1. Introduction

Hydrogen sulfide (H₂S) is a synthetic and natural compound, the presence of which can affect both fossil (e.g., gas fields, oil processing) and renewable (e.g., biogas, geothermal wells) resources. H₂S processing is quite cumbersome since this species is lethal, corrosive and flammable. Today, H₂S is mainly disposed of through the Claus process [1], which performs an oxidative conversion able to transform it into elemental sulfur and water and, at the same time, to recover thermal energy. In this case hydrogen in H₂S cannot be recovered and is finally wasted in the form of water [2]. The production of hydrogen results of great interest since this compound is a highly valuable product with a wide range of applications, especially in the energy and chemicals industry. Therefore, a variety of splitting techniques, aimed at producing hydrogen and sulfur from H₂S, have been studied. These includes thermal [3] and catalytic [4 - 6] technologies. In this work, a MoS₂ catalyst-based decomposition method is presented and integrated into a conceptual process design.

2. Methods

The technology performing the H₂S catalytic splitting, called Sulfidric Acid Catalytic Splitting (SACSTM), has been tested by setting up an ex-novo experimental apparatus. This consists of an open circuit system fed by a gaseous H₂S/N₂ mixture with a H₂S concentration up to 8 vol%. The reactor, designed according to the ideal Plug Flow Reactor (PFR) model, is made of quartz and is composed of three sections: the inlet section, the central body and the outlet section. To ensure the adequate thermal conditions required by the process, the reactor is placed inside a tubular oven. The catalyst is constituted by MoS₂ powder supported on quartz wool. Upon exiting the reactor, the sulfur is condensed into a cold trap and subsequently the gases are analyzed with a Micro GC (Micro Gas Chromatograph). The experimental campaigns are currently in progress. Experimental observations are the backbone for the definition of a plant-scale conceptual process design for the conversion of an H₂S stream into hydrogen and sulfur. The detailed process simulation has been developed using Aspen HYSYS V11 suite. As thermodynamic model, the SRK (Soave-Redlich-Kwong) equation of state has been chosen for the reactive section of the process, while the Aspen HYSYS amine package has been chosen for the separation section.

2. Results and discussion

The process design shows how the catalytic conversion of H₂S can be exploited in a plant to convert a stream of H₂S into hydrogen and sulfur. The gaseous H₂S enters the SACSTM reactor and is converted at a pressure slightly higher than the atmospheric pressure and at a temperature between 500 and 1000 °C. Sulfur vapors are removed by condensation and the residues are hydrogenated at 260 °C in a dedicated reactor. The obtained gas stream (containing hydrogen, unreacted H₂S and H₂S produced by the hydrogenation of sulfur vapors) is treated in an amine scrubbing process. A first absorption column employs a water solution of MEA (20 wt%) to remove H₂S from the gaseous stream. The residual concentration of H₂S in the sweetened gases is around 1 ppm. This stream is then cooled to 5 °C in order to condense the water entrained during the washing step. The clean gases are compressed up to 16.5 bar and the last traces of water and H₂S are separated by means of a filter. The stream, now containing only hydrogen, is finally sent to a compression train and reaches a pressure

of 200 bar. The contaminated amine is regenerated in a distillation column operating at 1.2 bar. The top product is an acid stream containing H_2S and saturation water. After a water condensation step H_2S is recirculated to the SACSTM reactor. The purified amine leaving the bottom is cooled to 60 °C and recirculated to the absorption column. In this stream a water make-up is required. For this purpose, it is possible to exploit the two H_2S contaminated water streams obtained by the condensation steps of the process.

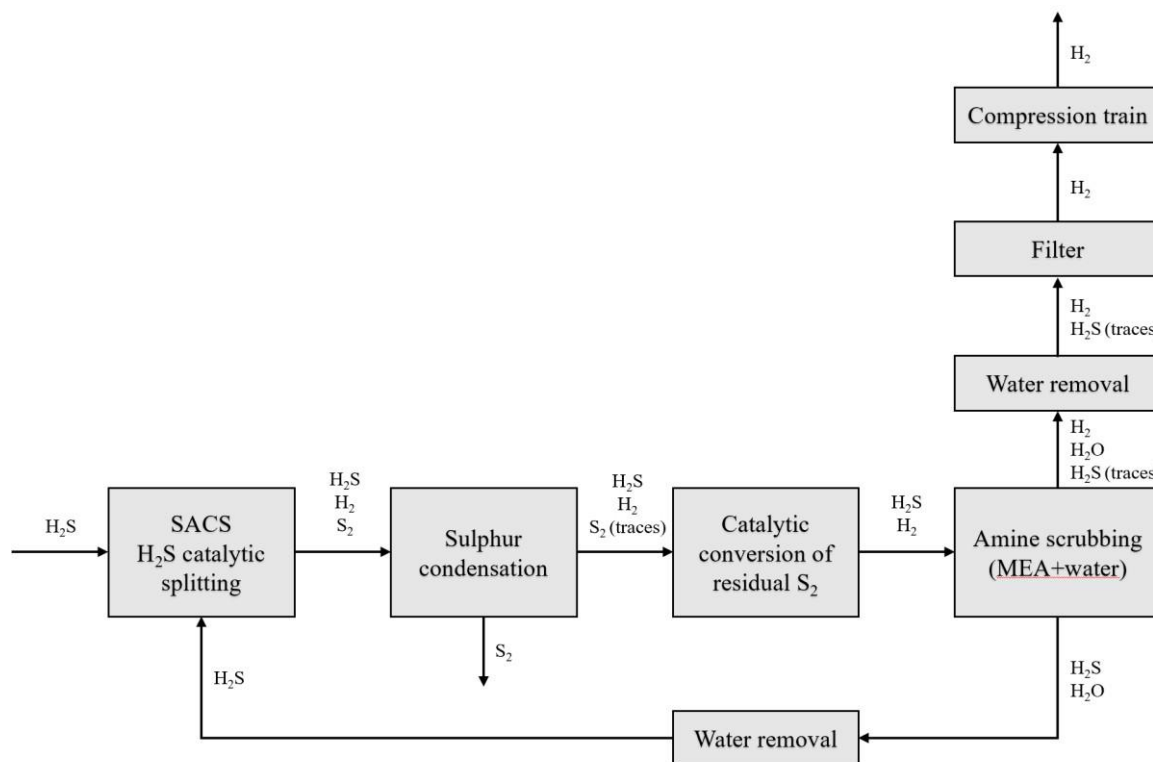


Figure 1. Block-flow diagram of the conceptual process for H_2S conversion.

4. Conclusions

The SACSTM process exploits the catalytic splitting of H_2S to allow the simultaneous production of H_2 and elemental sulfur from the undesired molecule H_2S . A process simulation that integrates experimental observations into a conceptual process design has been developed, proving how it is possible to achieve 100% conversion of H_2S streams into H_2 and elemental sulfur. This process could improve the performances of refineries or other industrial plants, since it changes the role of H_2S from waste to commodity. Also, the emissions would be reduced, both in terms of CO_2 and flue gases. The experimental campaign is still ongoing and aims at studying different possible catalysts, defining the kinetics of the reaction and optimizing the process.

References

- [1] J.A. Lagas, J. Borsboom, P.H. Berben. Selective-oxidation catalyst improves Claus process. *Oil Gas J*, 86 (1988) 68–71.
- [2] F. Manenti, D. Papisidero, G. Bozzano, E. Ranzi. Model-based optimization of sulfur recovery units. *Computers and Chemical Engineering*, 66 (2014) 244–251.
- [3] F. Faraji, I. Safarik, O.P. Strausz, E. Yildirim, M.E. Torres. The direct conversion of hydrogen sulfide to hydrogen and sulfur. *Int J Hydrogen Energy*, 23(6) (1998) 451–456.
- [4] K.R.G. Burra, G. Bassioni, A.K. Gupta. Catalytic transformation of H_2S for H_2 production. *Int J Hydrogen Energy*, 43(51) (2018) 22852–22860.
- [5] L. Zhao, X. Liu, X. Mu, Y. Li, K. Fang. Highly selective conversion of H_2S-CO_2 to syngas by combination of non-thermal plasma and MoS_2/Al_2O_3 . *Journal of CO_2 Utilization*, (2020) 45–54.
- [6] V. Preethi, S. Kanmani. Photocatalytic hydrogen production. *Materials Science in Semiconductor Processing*, 16(3) (2013) 561–575.

Nanostructured nickel–zinc alloy electrodes for hydrogen evolution reaction in alkaline electrolyzer.

Sonia Carbone^{1*}, Francesco Bonafede^{1,2}, Fabrizio Ganci¹, Bernardo Patella¹, Giuseppe Aiello¹, Rosalinda Inguanta¹

1 Applied Physical Chemistry Laboratory, Department of Engineering, Università degli Studi di Palermo, Viale delle Scienze, 90128 Palermo, Italy

2 Department of Civil Engineering and Architecture, University of Catania, 95123 Catania, Italy

*Corresponding author E-Mail: sonia.carbone@unipa.it

1. Introduction

Over the last decade, the interest towards green hydrogen has drastically increased due to need for the global decarbonization of energy processes. Green hydrogen is obtained by water electrolysis using the electricity obtained only from renewable sources [1]. It is considered one of the best vector energy in terms of environmental sustainability but it is not yet cost-competitive [2]. Nowadays, the research is focused on improving the Alkaline Water Electrolysis (AE) to reduce the cost of hydrogen produced. In this frame, the development of more efficient electrolyzers with low-cost electrode–electrocatalyst materials can play a key role [3]. The eligible materials must have some fundamental characteristics, such as good electrocatalytic properties, high conductivity, high availability, low cost, and good chemical stability. In alkaline environment, transition metals, in particular the iron group elements, are the most suitable electrocatalyst for hydrogen evolution reaction (HER) [4]. In this work, we have studied the electrochemical fabrication of electrodes of nickel-zinc alloys with nanowires morphology to use for the hydrogen evolution reaction in alkaline solution and at room temperature.

2. Methods

Ni-Zn nanowires (NWs) electrodes were obtained by template electrosynthesis by means of polycarbonate nanoporous membranes. The NWs were obtained by potential-controlled pulse electrochemical deposition in a solution containing ammonium chloride, sodium acetate, boric acid and different concentration of nickel sulphate hexahydrate and zinc sulphate heptahydrate at pH 5. After NWs deposition, the polycarbonate membrane was etched in chloroform. The performances of the obtained electrodes were evaluated through electrochemical and electrocatalytic tests that were performed in KOH 30% w/w aqueous solution. The tests were performed in a three electrodes cell using as counter electrode a Ni sheet and Hg/HgO as reference electrode. The electrochemical characterization was performed at room temperature and without agitation. The electrodes have been studied morphologically and chemically through scanning electrode microscopy (SEM), Xray diffraction (XRD), and energy dispersive spectroscopy (EDS). Fabrication methods and characterization are detailed in [5].

3. Results and discussion

NiZn alloys with different composition were obtained by changing the Zn/Ni ratio of the electrodeposition bath. The Zn atomic composition in NWs almost follows the Zn composition in the electrodeposition bath. Morphology of the electrodes consists in ordered arrays of nanowires well anchored to the Ni current collector also obtained by electrodeposition (Figure 1). The electrochemical and electrocatalytic behavior was evaluated by cyclic voltammetry (CV), quasi steady-state polarization (QSSP), galvanostatic-step polarization (GS) and galvanostatic polarization to evaluate the mid-term behavior of nanostructured electrodes. All electrochemical tests show that nanowires with about 44.4% (obtained from an electrodeposition bath containing 50% of the two elements) of zinc have the best performances. Particularly,

an overpotential (η_{10}) of -0.251 mV was measured while the Tafel's slope is -99 mV/dec, suggesting that the hydrogen evolution reaction is controlled by the Volmer step. This overpotential value is lower than pure Ni nanowire. NiZn nanowires show also a good stability over time because are able to work at a constant current of -10 mA cm^{-2} for 18 h without noticeable signs of performance decay.

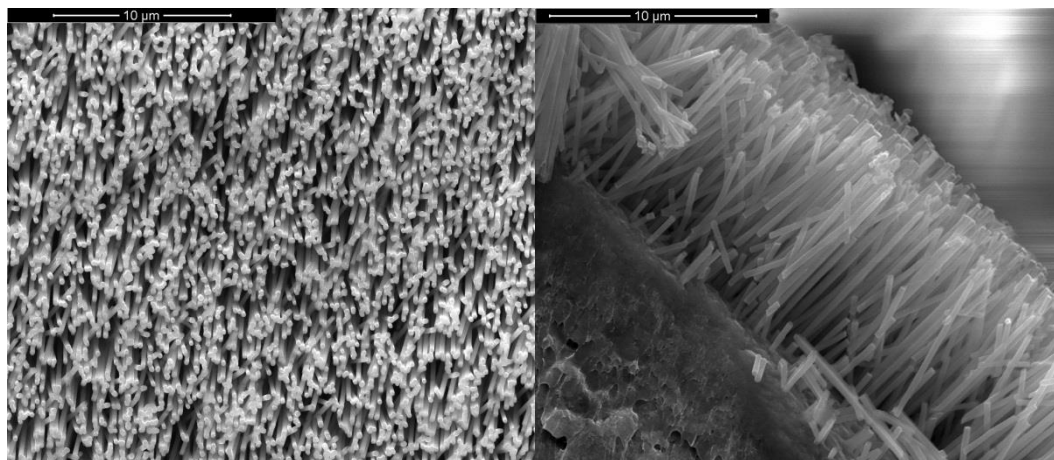


Figure 1. SEM images of NiZn nanostructured electrode

4. Conclusions

Template electro-synthesis method was employed for the fabrication of nanostructured NiZn alloys. Electrodes were obtained by pulsed electrochemical deposition and consists of regular arrays of nanowires uniformly distributed on Ni current collector. The alloys composition was controlled by tuning the concentration of Ni and Zn in the electrodeposition bath. The nanostructured NiZn alloy electrodes were tested as cathodes for alkaline electrolyzers in 30% w/w KOH aqueous solution at room temperature. All obtained alloys have good electrocatalytic performance compared to electrodes of pure Ni even if the most promising electrodes are those obtained from electrodeposition bath containing an almost similar concentration of Ni and Zn. In particular, the electrodes containing 44.4% of Zn showed the best performance for HER.

References

- [1] B. Ceran, Multi-Criteria Comparative Analysis of Clean Hydrogen Production Scenarios, *ENERGIES*. 13 (2020). <https://doi.org/10.3390/en13164180>.
- [2] J.L.L.C.C. Janssen, M. Weeda, R.J. Detz, B. van der Zwaan, Country-specific cost projections for renewable hydrogen production through off-grid electricity systems, *Appl. Energy*. 309 (2022). <https://doi.org/10.1016/j.apenergy.2021.118398>.
- [3] Y. Chen, G. Zhao, W. Sun, Strategies of engineering 2D nanomaterial-based electrocatalysts toward hydrogen evolution reaction, *Mater. Renew. Sustain. Energy*. 9 (2020). <https://doi.org/10.1007/s40243-020-00170-w>.
- [4] Q. Hu, G. Li, Z. Han, Z. Wang, X. Huang, H. Yang, Q. Zhang, J. Liu, C. He, Recent progress in the hybrids of transition metals/carbon for electrochemical water splitting, *J. Mater. Chem. A*. 7 (2019) 14380–14390. <https://doi.org/10.1039/c9ta04163j>.
- [5] F. Ganci, B. Patella, E. Cannata, V. Cusumano, G. Aiello, C. Sunseri, P. Mandin, R. Inguanta, Ni alloy nanowires as high efficiency electrode materials for alkaline electrolyzers, *Int. J. Hydrog. Energy*. 46 (2021) 35777–35789. <https://doi.org/10.1016/j.ijhydene.2020.11.208>.

Electrically driven SiC-based structured catalysts for hydrogen production

Vincenzo Palma*, Eugenio Meloni, Giuseppina Iervolino

Department of Industrial Engineering, University of Salerno (Italy)

**Corresponding author E-Mail: vpalma@unisa.it*

1. Introduction

The environmental issues raising from the chemical industry has reached the attention of people all over the world, and the reduction in greenhouse gas (GHG) emissions has been identified as a strategy for the mitigation of climate change. Nowadays, chemical industry is mostly powered by the combustion of fossil fuels, which is responsible for a significant portion of anthropogenic GHG emissions. In this context, many energy experts have agreed that the electrification is the most promising route for reaching the targets, even if electricity generation and transmission involve substantial energy losses and thus its application as a heat source in chemical industry is less efficient than onsite combustion from an energy efficiency point of view. However, the potential of electrification mainly lies in a future scenario where there is a pathway leading to zero-carbon electricity [1]. There are many types of electrification that can be implemented in current chemical industry: power-to-gas (PtG), power-to-chemicals (PtC), power-to-electricity (PtE), power-to-heat (PtH) and power-to-liquids. In the last years, an energy transition has been underway, and many leading energy, transport and industrial companies have taken initiatives to develop the energy transition with hydrogen [2], which is a versatile energy carrier, that can be integrated in different areas such as power grids, transport, heating, fuel-cell electric vehicles, and energy storage. Hydrogen can be produced through different processes, such as natural gas or biogas reforming, gasification of coal and biomass, water electrolysis, water splitting by high temperature heat, photoelectrolysis, and biological processes. Currently, among the above cited processes, the conventional large-scale production of hydrogen is mainly obtained by the reforming of fossil fuels, among which the main processes are methane steam reforming (MSR) and methane dry reforming (MDR). The two mentioned processes are highly endothermic; therefore, the constant supply of heat to the catalytic sites is one of the main constrain limiting their efficiency. In these reactors huge temperature gradients occur from the reactor external side to the catalyst bed, due to the heat transfer resistance mainly linked to the low thermal conductivity of the commercial catalysts actually used [3]. In this work the process intensification of both MSR and MDR is proposed by using an innovative structured catalyst which combines two fundamental features (i) a high thermal conductivity, that aim to flatten the thermal profile inside the reactor, and (ii) an integrated joule heating, that allow to perform a direct electricity-driven process. In this way, the energy is directly supplied to the catalyst, due to its intimate contact with the electric heat source, therefore the removal of thermal limitations and a better control of the reaction front may be obtained.

2. Methods

In this work a laboratory-scale reactor has been realized, using a commercial silicon carbide (SiC) electrical heating element that simultaneously acted as heating medium and support for the catalyst. In this way, the sense of the heat flux has been inverted (from the center to the external) with respect to the conventional reformer (from the external to the center). Commercial ceramic material was employed as support for the Ni-based catalysts preparation. A fixed amount of 5 wt% Ni was deposited on the support, previously dried and calcined at 850 °C in air. The catalysts were prepared via wet impregnation, with a solution of $\text{Ni}(\text{NO}_3)_2 \cdot 6\text{H}_2\text{O}$ as Ni precursor; the resulting catalysts were dried at 120 °C for 2 h and calcined at 850 °C in air for 1 h. The catalysed SiC element has been enclosed in a properly shaped quartz reactor and a mixture consisting of 10 vol% of CH_4 , 30 vol% of Steam and diluted in argon has been fed from the top to the bottom of the reactor. As regards the preliminary electrified MDR tests carried out on Ni catalysed SiC

element, the same reactor configuration described in the previous paragraph was used. In particular, a mixture consisting of 50 vol% of CH₄ and 50 vol% of CO₂ has been fed to the reactor.

3. Results and discussion

The results of the preliminary MDR test evidenced that the methane conversion and hydrogen yield (Figure 1) are particularly promising. In particular, it is possible to observe that the catalytic SiC element is able to reach the reaction temperatures by means of the Joule heating. It is possible to note that the MDR reaction proceeds following the equilibrium thermodynamic profile of the reaction (black curve) even at low temperatures.

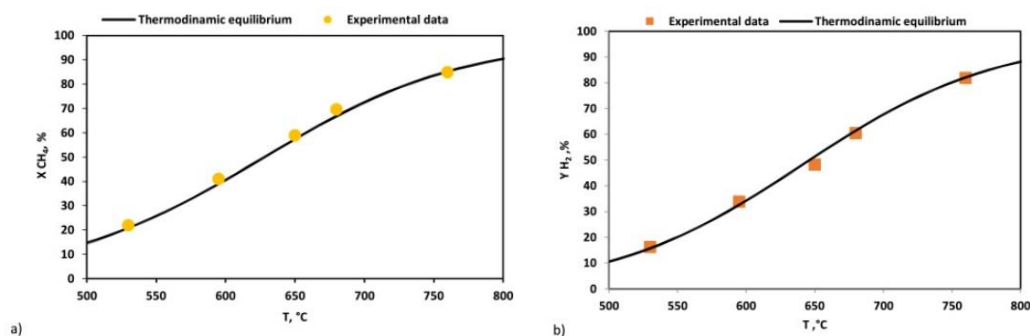


Figure 1. catalytic activity test results (MDR) a) CH₄ conversion; b) H₂ yield; CO₂/CH₄ ratio for MDR reaction = 1; WHSV = 70 h⁻¹.

As expected, the energy consumption of the system is strictly linked to the H₂ productivity; in fact, the higher is this amount the lower is the energy consumption. Moreover, at lab scale, the effects of heat dissipation have a big role with respect to the low gas flow rate fed to the reactor and for this reason higher energy consumption was observed at the lower WHSV values. The direct comparison in terms of energy consumption for H₂ production with other electrified reforming processes is very difficult, since not a so high number of data is available in literature. However, from preliminary results, it is possible to confirm that energy consumption values close to that reported for other electrified processes, including the modern electrolyzers,

4. Conclusions

The results reported in this work demonstrate that a commercial SiC based heating element, coated with a Ni-based catalyst, can be used in the context of the chemical processes electrification scenario, a topic that is acquiring more and more focus from the scientific and industrial world. The investigation concerning the adoption of the Ni catalysed SiC electrically heated element pointed out its effective capacity of heating up the reaction zone without any external source till temperature of 900 °C. It is possible to summarize that the results have shown values close to that reported for other electrified processes, including the modern electrolyzers. These results can be considered even more promising if one takes in to account the laboratory scale of the reactor, where the effects of heat dissipation have a big role with respect to the low gas flow rate fed to the reactor.

References

- [1] C. Chen, Y. Lu, R. Banares-Alcantara Direct and indirect electrification of chemical industry using methanol production as a case study *Appl. Energy*, 243 (2019), pp. 71-90, H.V. Patel, J.A.M. Kuipers, E.A.J.F. Peters, *Chem. Eng. Sci.* 193 (2019) 243–254 .
- [2] F.J. Durán, F. Dorado, L. Sanchez-Silva Exergetic and economic improvement for a steam methane-reforming industrial plant: simulation *Energy*, 13 (2020), p. 3807, G.F.Froment, K.B.Bishoff, *Chemical Reactor Analysis and Design*, second ed., Wiley, New York, 1990.
- [3] E. Meloni, M. Martino, V. Palma A short review on Ni based catalysts and related engineering issues for methane steam reforming *Catalysts*, 10 (2020), p. 352.

Design of an offshore renewable energy-based process for hydrogen production by electrolysis

Leonardo Bozzoli*, Valeria Casson Moreno, Valerio Cozzani

LISES – Laboratory of Industrial Safety and Environmental Sustainability, Dipartimento di Ingegneria Civile, Chimica, Ambientale e dei Materiali, Alma Mater Studiorum - Università di Bologna, via Terracini 28, 40131 Bologna, Italy

** leonardo.bozzoli@unibo.it*

1. Introduction

Green hydrogen is one of the most promising energy vectors in the perspective of energy supply chains decarbonization. Currently, the production of hydrogen is mostly carried out using natural gas, oil and coal as precursor. To obtain green hydrogen, renewable energy sources (RESs) are required in order to avoid the fossil fuel consumption and CO₂ production [1]. Offshore RESs, such as wind, wave and sun offer several advantages compared to the onshore ones, for example a more stable energy intensity, a higher energy density and significant amount of available space for devices installation [2]. Furthermore, close to decommissioning-phase, offshore platforms could represent an opportunity to create a hub for hydrogen production, avoiding platform removal, a technically complex and highly impacting process from both environmental and economic standpoints. The aim of this study is to provide design criteria for an offshore process for green hydrogen production able to exploit the energy available from sun, wind and wave.

2. Methods

The following steps allow the optimal selection of the energy converters for each RES considered in a selected offshore site (for the present case sun, wind and wave):

- 1) Selection of the offshore site that must have the following characteristic: the presence of a close to decommissioning phase platform and the availability of data related to RESs. Data collected for each RESs must cover at least one year to investigate all seasonal variations and timestep have to be of one hour or lower to analyze RESs unpredictability.
- 2) Elaboration of collected data to calculate the potentiality for each RES and to allow the selection of the most suitable converter for the maximum source exploitation. Such selection is driven by the potentiality of the source and by the nominal operativity conditions of each converter.
- 3) Calculation of power produced by each converter based on the timestep selected.
- 4) Determination of converters mix and power availability for the processes.
- 5) Calculation of energy requirement for MVC and AEL processes and quantification of green hydrogen production.

In the present study, the production of green hydrogen is based on Alkaline Electrolysis (AEL) [3], considering an upstream step for seawater desalination through Mechanical Vapour Compression (MVC) [4]. The AEL technology is selected because of its lower water consumption with respect to the PEM technology, while MVC is selected for its lower power consumption if compared to Multi-Stage Flash Distillation and Multi-Effect Distillation.

3. Results and discussion

A platform located 18 km offshore Ravenna (Adriatic Sea), called Garibaldi C, is selected as a case-study, in compliance with the constrain reported in step 1: indeed, the natural gas in the reservoir is depleting and wave data are provided by a metric wave buoy called Nausicaa, while for wind and sun data European Centre for Medium-Range Weather Forecast database is used, for a representative year (i.e. 2017) with hourly timesteps. Data are elaborated to evaluate the solar potentiality, wind yearly average velocity and wave potentiality, amounting respectively to: 5950 kJ/m²/y, 4.2 m/s and 1 kW/m. Given such potentialities, the most suitable converter for each RES is selected, i.e. high efficiency photovoltaic (PV) panel (226

W/m²), wind turbine (WT) designed for low wind potentiality (1500 kW of nominal power) and point absorber (20 kW of nominal power) as wave energy converter (WEC). Then, for each converter, the hourly average power production is calculated. For what concern solar panel, to calculate the power production the procedure reported in “UNI/TS 11300-4” is used; regarding WEC and WT, power matrix and power curve are used respectively, two tools providing the power produced from the converters based on the wind velocity and the significant wave height and the equivalent wave period respectively for WT and WEC. To equilibrate the power production from each RESs, the area of PV panels and the number of WECs are settled in order to obtain the same peak power production of the WT; the nominal power of 1500 kW is selected as target because is the nominal power of the single wind converter selected, resulting in the simplest possible case study. The area needed for PV panels is 8540 m², the number of WECs needed is 100. With the given potentiality for each RES converter, the hourly green hydrogen production is calculated as the power needed from the AEL and the MVC. In this work 1.5 MW of available power for the processes is selected. As shown in Figure 1, lower processes potentiality increases load factor (total energy used by AEL divided by total energy AEL would consume operating full time), but also increase the number of hours in which the power production by converters mix exceed 1.5 MW (waste of power), while higher processes potentiality decreases the load factor without sensibly increasing the hydrogen production. The power consumption of the MVC process is about 10 % of all energy consumption while the power consumption of AEL is 90 %. Given the energy mix, the resulting green hydrogen production is equal to 1.05 million of Nm³/y.

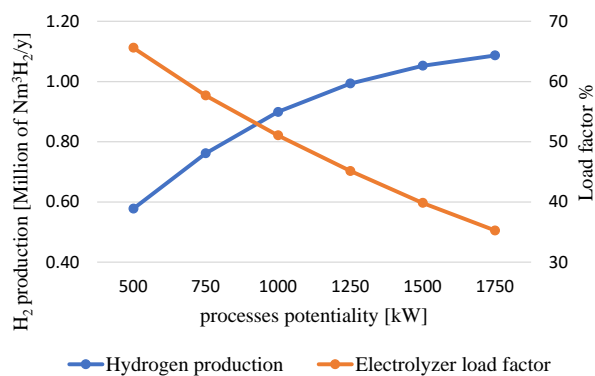


Figure 1. Green Hydrogen production and load factor for different AEL potentiality.

Due to its high transient response, the AEL system do not need a backup system to provide a steady electricity; thus, the use of a back-up system can be avoided, therefore fossil fuel consumption, representing an advantage for both environmental and economic aspects related to the process under design.

4. Conclusions

The conceptual design of a green hydrogen production system based on electrolysis fed by electricity provided by RESs converters was carried out. The aim is to prove the feasibility of the system, resulting in a significant amount of hydrogen production, providing the required data for economic optimization and footprint evaluation.

References

- [1] T. Capurso, M. Stefanizzi, M. Torresi, S. M. Camporeale, Perspective of the role of hydrogen in the 21st century energy transition, *Energy Convers. Manag.*, vol. 251, no. July 2021, p. 114898, 2022.
- [2] I. Dincer, V. Cozzani, A. Crivellari, Offshore renewable energy options, *Hybrid Energy Syst. Offshore Appl.*, pp. 7–18, 2021.
- [3] M. Rizwan, V. Alstad, J. Jäschke, Design considerations for industrial water electrolyzer plants, *Int. J. Hydrogen Energy*, vol. 46, no. 75, pp. 37120–37136, 2021.
- [4] A. Al-Karaghoul and L. L. Kazmerski, Energy consumption and water production cost of conventional and renewable-energy-powered desalination processes, *Renew. Sustain. Energy Rev.*, vol. 24, pp. 343–356, 2013.

Nanostructured Ni–Fe alloy electrodes for seawater electrolyzer.

Francesco Bonafede^{1,2}, Sonia Carbone¹, Bernardo Patella¹, Fabrizio Ganci¹ Giuseppe Aiello¹, Rosalinda Inguanta¹, Giuseppe Inturri³.

¹*Dipartimento di Ingegneria, Università degli Studi di Palermo, Viale delle Scienze, 90128, Palermo*

²*Department of Civil Engineering and Architecture, University of Catania, 95123, Catania, Italy*

³*Department of Electrical, Electronic and Computer Engineering, University of Catania, 95123, Catania, Italy*

bonafedef97@gmail.com , francesco.bonafede@phd.unict.it

1.Introduction

The climate change, caused by the increase of greenhouse gas emissions (GHGs), has incited governments and societies to change their environmental policies in favor of more sustainable method for energy generation and consumption [1]. Furthermore, there is a growing interest in reducing pollution in all transportation fields, in particular for naval transport that is one of the fastest growing sector in terms of GHGs, and also improve comfort by avoiding acoustic emissions inside ports and harbors [2].[3]

The renewable resources are considered a viable opportunity also for the carbonization of all transportation fields, although the difficulty of storing the surplus of produced energy still represents a fundamental problem to solve. In such regard, hydrogen can play a key role since it can be used as an energy vector. Hydrogen is a clean energy source, during its conversion into electricity, no toxic or polluting substances are emitted. Converting electricity into hydrogen and using hydrogen as energy carrier may be a technical and economically interesting option. In fact, hydrogen is currently receiving significant attention as energy carrier in many country roadmaps and studies, especially if short-term storage (weeks) is required.

Hydrogen [4] can be cleanly generated by means of electrolyzer technology [1]. The research of electrolysis for hydrogen production using freshwater has yielded good results; however, research of seawater electrolysis for hydrogen production is still at the early stage [5]. To make seawater electrolysis energy-efficient and cost-effective, highly active non-noble-metal-based catalysts for boosting the oxygen evolution reaction (OER) and the hydrogen evolution reaction (HER) are necessary. In this frame could be a winning choice, for the electrochemical property, using a nanostructured system based on Fe. In this work, we have fabricated and tested NiFe nanostructured electrodes for sea water electrolyzers.

2. Methods

All nanostructured electrodes were fabricated with a two-step electrodeposition method. The nanostructures were obtained by nanoporous polycarbonate membrane (Whatman) which acted as template. On a surface of membrane, after gold sputtering, a Ni layer was electrodeposited via potentiostatic deposition using as Watt's bath. This layer acts as a mechanical support and current collector (CC) for the nanostructures. NWs electrodeposition was carried out by pulsed potential using the Watt's bath containing different concentrations of $\text{FeSO}_4 \cdot 7\text{H}_2\text{O}$. All electrodepositions were carried out at room temperature using a three-electrode cell with a Pt mesh as a counter-electrode and a SCE as a reference. After NWs deposition, the polycarbonate membrane was dissolved in CH_2Cl_2 at room temperature. The electrochemical and electrocatalytic tests were carried out at room temperature in 30 wt% KOH aqueous solution using a three electrodes cell. A Ni sheet was employed as counter-electrode, and Hg/HgO (0.165 V vs. SHE) as reference. In the following, all potentials will be referred to the value of reversible hydrogen electrode (RHE, -0.826 V vs. SHE) at pH 14. A FEG-ESEM microscope (QUANTA 200 by FEI) was employed to investigate morphology of nanostructured electrode. Energy Dispersive Spectroscopy (EDS) was used to analyze NWs composition. RIGAKU X-ray diffractometer (D-MAX 25600 HK) was used for x-ray diffraction (XRD).

3. Results and discussion

EDS analyses reveals that the NWs composition does not change linearly with the composition of deposition bath but are richer in Fe. This result is coherent with literature data [6], in fact the electrodeposition of iron alloys is known as anomalous co-deposition consisting in the preferentially deposition of the less noble metal with respect the noble one, that complicates the control of alloy composition. The SEM images show that NWs replicate the morphology of the template. The electrochemical and electrocatalytic characterizations of the electrodes were performed by cyclic voltammetry (CV), quasi steady-state polarization (QSSP) and galvanostatic polarization. By CVs at different scan rates, specific capacitance was evaluated, by the double layer capacitance method, that is directly proportional to the real electrode surface. By comparison with a Ni planar sheet, we found that specific capacitance of each nanostructured electrode is at least 5-7 times higher. Thus, the nanostructured electrodes have a very high real surface area compared to planar electrode. To study the stability over time, constant current density mid-term tests were carried out for 6 h at -50 mA cm^{-2} and 50 mA cm^{-2} for HER and OER,

respectively. The results showed good stability over time. For both HER and OER, the NiFe alloy with 79% of Fe was found to be the most stable and the best performing.

Test was carried out both in 30% w/w KOH solution and in the same solution also containing 0.5 M of NaCl, in order to simulate the possible use of these electrode in sea water. In the presence of NaCl, during the 125 h of electrolysis, the electrode potential remained below 1.6 V vs. RHE, i.e., lower than the hypochlorite formation potential. Consequently, it is possible to conclude that there is no formation of hypochlorite. The electrodes used for the long-term tests were further analyzed by SEM showing a good mechanical and chemical stability of NiFe electrodes also in solution containing NaCl.

4. Conclusions

In this work, nickel-iron alloy nanostructured electrodes obtained by template electrosynthesis method are investigated for both hydrogen and oxygen evolution reactions. We found that alloy rich in Fe, about 79% have good performance for both HER and OER.

The key test was carried out in alkaline solution also containing 0.5 M NaCl to simulate seawater condition. We found that the presence of chlorine does not seem to affect the stable functioning of electrode in the short or long term. This is a very promising result because it would allow the application for seawater electrolyzers.

References

- [1] R. Ortiz-Imedio *et al.*, “Power-to-Ships: Future electricity and hydrogen demands for shipping on the Atlantic coast of Europe in 2050,” *Energy*, vol. 228, p. 120660, 2021, doi: 10.1016/j.energy.2021.120660.
- [2] U. Desideri, R. Giglioli, G. Lutzemberger, G. Pasini, and D. Poli, “Auxiliary Power Units for pleasure boats,” *2017 6th Int. Conf. Clean Electr. Power Renew. Energy Resour. Impact, ICCEP 2017*, pp. 650–655, 2017, doi: 10.1109/ICCEP.2017.8004758.
- [3] H. Winnes, L. Styhre, and E. Fridell, “Reducing GHG emissions from ships in port areas,” *Res. Transp. Bus. Manag.*, vol. 17, pp. 73–82, 2015, doi: 10.1016/j.rtbm.2015.10.008.
- [4] E. S. Hanley, J. P. Deane, and B. P. Ó. Gallachóir, “The role of hydrogen in low carbon energy futures—A review of existing perspectives,” *Renew. Sustain. Energy Rev.*, vol. 82, no. July, pp. 3027–3045, 2018, doi: 10.1016/j.rser.2017.10.034.
- [5] S. Dresch, F. Dionigi, M. Klingenhof, and P. Strasser, “Direct electrolytic splitting of seawater: Opportunities and challenges,” *ACS Energy Lett.*, vol. 4, no. 4, pp. 933–942, 2019, doi: 10.1021/acsenergylett.9b00220.

Physics-based modeling opportunities to overcome critical challenges in lithium-ion batteries

Marco Lagnoni¹, Xuekun Lu², Antonio Bertei^{1*}

1 Department of Civil and Industrial Engineering, University of Pisa, Largo Lucio Lazzarino 2, 56126 Pisa (IT)

2 Department of Chemical Engineering, University College London, WC1E 7JE London (UK)

**Corresponding author E-Mail: antonio.bertei@unipi.it*

1. Introduction

The commercialization of electric vehicles powered by lithium-ion batteries is one of the main strategies towards a future society based on renewable energy systems. However, the effective and sustainable use of lithium-ion batteries still faces several critical challenges.

One of the desirable requirements is the capability of the automotive battery to be charged in less than 15 min. Such a difficulty comes mostly from the microscopic electrochemical phenomena occurring at the anode, namely the sluggish intercalation of lithium within a phase-separating material like graphite, leading to degradation phenomena such as lithium plating. Understanding the interplay among phase separation, plating and other parasitic phenomena can stimulate significant advancements in the field.

A second related challenge stems from the possibility to early detect such degradation phenomena during operation. This would allow the battery management system to actively control the charge/discharge of single cells, prolonging their cycle life and reduce risk concerns. At the moment only semi-empirical indicators of battery state of health are used in the battery management system.

Another critical aspect regarding the sustainable use of lithium-ion batteries refers to their recyclability. The European Union is setting up a new regulation, pushing towards an increased content of recycled materials in new lithium-ion batteries. Although achieving such a target will likely reduce the environmental impact associated to battery production from raw materials, it is still unclear whether a recycled battery material, with potentially reduced intrinsic properties, can be effectively used for demanding automotive applications.

In this study we show how all these critical challenges can be quantitatively addressed by adopting a physics-based microscopic modeling approach to lithium-ion battery research, taking into account the interplay among different electrochemical phenomena across multiple length scales.

2. Methods

The modelling approach is based on porous electrode theory, which describes a single-repeating unit of a battery cell by means of mass and charge conservation equations in a pseudo-2D fashion (Figure 1). Along the through-thickness coordinate the model solves for the charge and species transport in the liquid electrolyte as well as for the conservation of electrons in the electron-conducting phase. A second dimension is added to solve for the transport of intercalated lithium across the radius of active material particles. At the negative electrode side, both intercalation and Li plating kinetics are enforced at the interface between graphite particles and the electrolyte. Details of the model derivation can be found in previous dedicated papers [1–4].

3. Results and discussion

Figure 2 summarizes the main results of the application of the modeling framework. Figure 2a shows the graphite state of lithiation across the electrode thickness and the particle radius upon fast charge as predicted by the model (solid and dashed lines) and as obtained by optical experiments. The comparison shows that the model correctly captures the phase transitions of graphite during lithiation, as denoted by the different colors, indicating that a significant plating risk is present when the graphite surface is saturated by intercalated lithium.

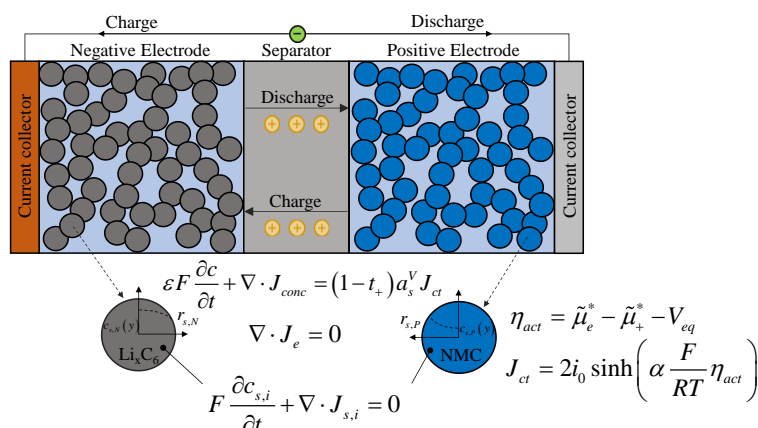


Figure 1. Physics-based modeling framework for the simulation of lithium-ion batteries.

Figure 2b reports the comparison of simulated (line) and experimental (symbol) discharge curves after a current pulse. During relaxation the model predicts the system dynamics, enabling the identification of the characteristic time of each microscopic process: intercalation kinetics takes place at short time scales (< 1 min), the relaxation of electrolyte concentration gradient occurs at medium time scales (ca. 5 min) while solid-state diffusion within active material particles occurs at long time scales (> 30 min). Thus, based on the shift of the characteristic time of the process, the model can efficiently detect any early signal of degradation.

Finally, Figure 2c shows practical indications about the compensatory measures of electrode design when recycled cathode active materials are used. Compared to the electrode thickness and particle diameter of a reference battery cell, a decrease in gravimetric capacity of the recycled cathode materials can be compensated by a small increase in electrode thickness while a reduction in solid-state diffusivity can be mitigated by a reduction in particle diameter. All these modifications indicate that compensatory measures are technically feasible, thus opening for a large share of recycled materials in the manufacturing of lithium-ion-batteries.

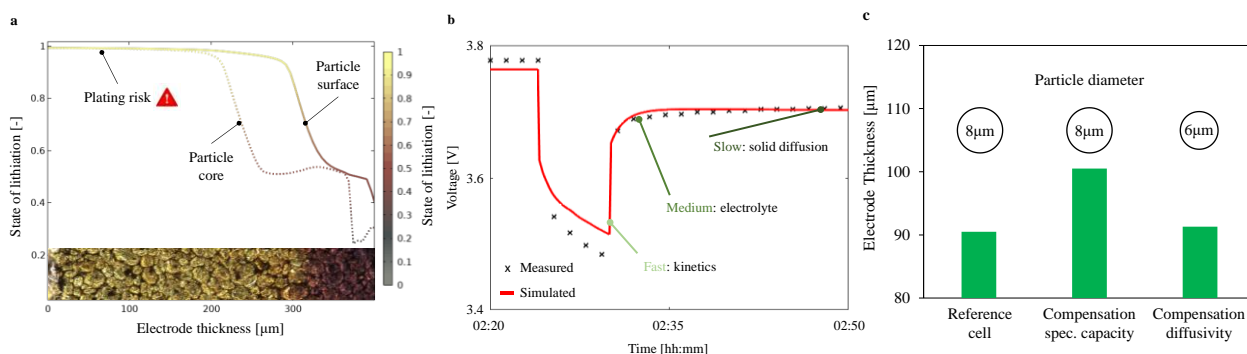


Figure 2. Potential of physics-based model in predicting a) intercalation and degradation phenomena during fast charge, b) time scale of processes for early detection of degradation, c) guidelines for recycled materials.

4. Conclusions

This study shows how physics-based electrochemical modelling of coupled transport and reaction phenomena in lithium-ion batteries has the potential of guiding the research towards viable solutions to the critical challenges of this technology. In particular, fast charge protocols, algorithms for early detection of degradation and guidelines for recycled battery designs can be effectively explored by using this approach.

References

- [1] M. Lagnoni, C. Nicolella, A. Bertei, *Electrochim. Acta* 394 (2021) 139098
- [2] X. Lu et al., *Energy Environ. Sci.* 14 (2021) 5929
- [3] L. Barzacchi, M. Lagnoni et al., *J. Energy Storage* 50 (2022) 104213
- [4] M. Lagnoni, D. Latini et al., *J. Energy Storage* 50 (2022) 104237

An experimental investigation on ionic shortcut currents reduction in Acid-Base Flow Battery systems

Alessandra Pellegrino, Andrea Culcasi, Alessandro Cosenza, Alessandro Tamburini*, Andrea Cipollina, Giorgio Micale

Dipartimento di Ingegneria, Università degli Studi di Palermo, Viale delle Scienze ed.6, 90128 Palermo, Italy

**Corresponding author E-Mail: alessandro.tamburini@unipa.it*

1. Introduction

In recent years, the global scenario has been shifting toward energy transition and widespread of renewables. However, the discontinuity nature of the most commonly used renewable resources, such as solar and wind, intrinsically requires the use of suitable Energy Storage Systems (ESS). In this regard, the Acid-Base Flow Battery (ABFB) is a novel and sustainable storage system based on two membrane technologies: Electrodialysis with Bipolar Membrane (EDBM) for the charging phase and Reverse Electrodialysis with Bipolar Membrane (REDBM) for the discharging phase [1]. The EDBM process, in particular, can store electrical energy in the form of pH and salinity gradients, whereas the REDBM process can supply electricity by consuming these gradients when needed [2]. The ABFB technological feasibility is strongly related to the reduction of the main detrimental phenomena affecting the process. Among these, the passage of ionic shortcut (or parasitic) currents through manifolds is the ABFB most important issue. Indeed, when parallel channels of the same solution are exposed to a voltage difference, a portion of the ionic current can pass through alternative pathways constituted by the manifolds [3]. As a result, during the charging phase, the cell current decreases, reducing acid and base production. On the contrary, during the discharging phase, the dissipated current increases, causing the battery to discharge faster. The present work aims to reduce the impact of this critical issue, thereby improving the ABFB Round Trip Efficiency (RTE).

2. Methods

A lab-scale setup was provided by Fumatech®. The stack was equipped with FAB®, FKB®, and FBM® membranes, as well as PVC/ECTFE spacers. The system was assembled with 30 triplets and the inlet operating conditions were: 0.5 cm s⁻¹ average velocity of the solutions in the channels, 1 M inlet acid (HCl) and base (NaOH) concentrations, and 0.25M salt (NaCl) concentration.

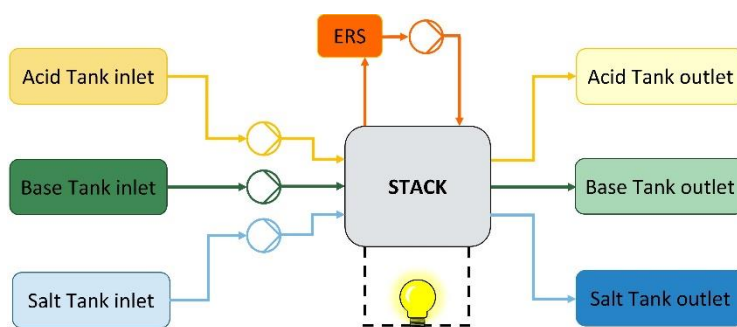


Figure 1. Configuration of REDBM Open Loop tests.

In order to study the effect of the ionic shortcut currents, plastic non-conductive sticks were used to reduce the manifold section. In detail, the sticks were made of plexiglass and occlude the section by approximately 90%: this reduction increases the electrical resistance of the manifolds and is therefore expected to reduce the relevant ionic shortcut currents. On the other hand, pressure drops are expected to increase. In this work REDBM tests (i.e. the discharge phase of the battery) in open loop (i.e. without recirculation, Figure 1) with a

unit assembled without the sticks (classic configuration, referred to as “test 1”) and with the sticks (referred to as “test 2”) are shown. Moreover, the battery gross and net power densities, voltage, and Round Trip Efficiency were all evaluated.

3. Results and discussion

Figure 2 shows the external voltage and power density as a function of the current density. The external voltage values in test 2 were higher than in test 1: Open Circuit Voltage (OCV) was 36% higher and the voltage at the highest investigated current density for REDBM (i.e., 29 Am^{-2}) was 30% higher. Moreover, as the current density increases, the difference between the two curves of external voltage wasn't constant. The introduction of plastic sticks into the manifolds has increased the internal global resistance of the stack, as evidenced by the slope of the curves. Furthermore, tests were performed to determine the pressure drops in the two different configurations. Finally, the achievable power density was computed, after subtracting the pumping power consumption. The maximum net power density of test 1 (at 29 Am^{-2}) was $4.3 \text{ Wm}^{-2}\text{N}_{\text{r}}^{-1}$, while for test 2 was $5.4 \text{ Wm}^{-2}\text{N}_{\text{r}}^{-1}$. Therefore, the effect of the plastic sticks may potentially result in a RTE increase of 25%.

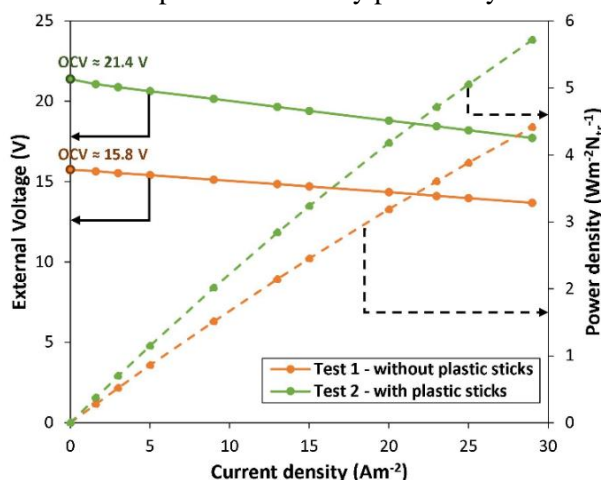


Figure 1. Comparison between test 1 and test 2: trend of external voltage and power density as the current density changes.

4. Conclusions

This work demonstrates how the inclusion of isolating material inside the manifolds can reduce the effect of parasitic currents in the system. The best design of plastic sticks cross-sectional area can be chosen to achieve a balance between reducing parasitic currents and increasing stack pressure drops. As demonstrated, the technology has significant potential for future growth, although additional experimental and modelling tests are required to improve the battery performance.

Acknowledges

This work was performed in the framework of the BAoBaB project (*Blue Acid/Base Battery: Storage and recovery of renewable electrical energy by reversible salt water dissociation*). The BAoBaB project has received funding from the European Union's Horizon 2020 Research and Innovation program under Grant Agreement no. 731187 (www.baobabproject.eu).

References

- [1] R. Pärnamäe, L. Gurreri, J. Post, W. J. van Egmond, A. Culcasi, M. Saakes, J. Cen, E. Goosen, A. Tamburini, D. A. Vermaas, M. Tedesco, The Acid–Base Flow Battery: Sustainable Energy Storage via Reversible Water Dissociation with Bipolar Membranes, *Membranes* 2020, 10, 409; <https://doi.org/10.3390/membranes10120409>
- [2] A. Culcasi, L. Gurreri, A. Zaffora, A. Cosenza, A. Tamburini, G. Micale, On the modelling of an Acid/Base Flow Battery: An innovative electrical energy storage device based on pH and salinity gradients, *Applied Energy* 277 (2020) 115576, <https://doi.org/10.1016/j.apenergy.2020.115576>
- [3] A. Culcasi, L. Gurreri, A. Zaffora, A. Cosenza, A. Tamburini, A. Cipollina, G. Micale, Ionic shortcut currents via manifolds in reverse electro dialysis stacks, *Desalination* 485 (2020) 114450, <https://doi.org/10.1016/j.desal.2020.114450>

Scale up of a sequential reductive/oxidative bioelectrochemical process for chlorinated aliphatic hydrocarbons (CAHs) removal from contaminated groundwater

Marco Zeppilli, Edoardo Dell'Armi, Marco Petrangeli Papini, Mauro Majone

Department of Chemistry University of Rome Sapienza Piazzale Aldo Moro 5, 00185 Rome

**Corresponding author E-Mail: marco.zeppilli@uniroma1.it*

1. Introduction

Chlorinated Aliphatic Hydrocarbons (CAHs) as Perchloroethylene (PCE) and Trichloroethylene (TCE) are worldwide contaminants due to their uncorrected disposal and storage in the past years. An effective remediation strategy for CAHs contaminated groundwaters is the stimulation of dechlorinating microorganisms which can carry out reductive and oxidative reactions which allowed for the complete mineralization of CAHs [1]. More in detail, dehalorespiring microorganisms can reduce PCE and TCE via the reductive dechlorination reaction (RD), while aerobic dechlorinating microorganisms oxidize low chlorinated compounds such as cis-dichloroethylene (cDCE) and vinyl chloride (VC) into CO₂. The combination of reductive and oxidative dechlorination can be easily tuned by the adoption of bioelectrochemical systems, in which an electrodic material interact with so-called electroactive microorganisms acting like electron acceptor or donor of the microbial metabolism. Microbial electrolysis cells (MECs) are a particular bioelectrochemical systems application that require the utilization of an electric potential to overcome the thermodynamic and kinetic limitations of non-spontaneous reactions. MECs have been successfully adopted in the last years for the stimulation of the reductive and the oxidative dechlorination of CAHs through the polarization of a biocathode or a bioanode [2]. A sequential reductive and oxidative environment has been obtained by the utilization of different MEC configurations including the utilization of an ion exchange membrane as ionic separator or, the adoption of two membrane-less unit. Recently, as reported in previous paper, our research group adopted a new membrane-less MEC configuration consisting in a tubular reactor provided with an internal graphite counterelectrode [3]. The new MEC concept has been tested opening a new perspective for bio-electro remediation allowing a simple and cheap design of the reactors, particularly advantageous for the scale up of the technology. In this study, a sequential reductive/oxidative bioelectrochemical process developed by the combination in series of two membrane-less microbial electrolysis cells (MECs) has been applied for the treatment of a CAHs contaminated groundwater coming from a polluted site in northern Italy. More in detail, the study presents the development and the validation of the sequential bioelectrochemical process under laboratory conditions and the and subsequent scale-up of the process for a field scale application. The scale-up increased the reactor volume 42 times (from 10 L to 420 L) dividing the reductive and the oxidative sections into 4 different columns with a geometric volume of 105 L.

2. Methods

The lab scale sequential bioelectrochemical process consisted of two tubular reactors as reported in figure 1.1, the reductive and the oxidative reactor with an empty volume of 8.24 and 3.14 L (Table 1), respectively. Both reactors were equipped with an internal counter electrode made by a tube filled with graphite granules enveloped by a double layer of a grid in plastic material and a permeable textile membrane that avoided the shortcut of the circuit while allowing for electrolyte migration. The reductive reactor external chamber was filled with graphite granules as electrodic material to sustain the reductive dechlorinating biofilm while the oxidative reactor external chamber was filled with silica bed and present three pieces of a mixed metal oxide (MMO) electrode connected by a titanium wire. Both upscaled reductive and oxidative reactors have been realized keeping a constant dimensions and geometry with respect the lab scale reductive reactor. In order to allow a simpler handling of the pilot, the projected volume of 420 L has been split into 4 identical tubular units with a geometric volume of 105 L (Table 1). The reductive units consisted of a working and counter electrode

made of graphite granules, while the two oxidative units were assembled with an external mixed metal oxides (MMO) electrodes inserted in a gravel bed, in which a graphite granules counter electrode was inserted.

Table 1. Volume of the working and counter electrodes in the lab scale and upscaled reactors.

	Working electrode volume (L)	Counter Electrode volume (L)
Lab scale reductive reactor	8.24	1.70
Lab scale oxidative reactor	3.14	0.18
Upscaled reductive reactor	105	23
Upscaled oxidative reactor	105	23

3. Results and discussion

The preliminary results performed on the upscaled reductive and oxidative reactors allowed for the determination of the hydraulic parameters by tracer tests while information about their electrochemical behaviour have been performed by some polarization tests. Figure 1 shows the polarization curves obtained for the upscaled reductive and oxidative reactor by controlling the reactor with a three-electrode configuration. More in detail, the polarization test for the reductive reactor was performed by controlling the external graphite cathodic chamber in the range of 0 to -750 mV vs SHE, while the oxidative reactor working electrode (i.e., the MMO anode) was polarized in the range of +0.8 to +2.0 V vs SHE.

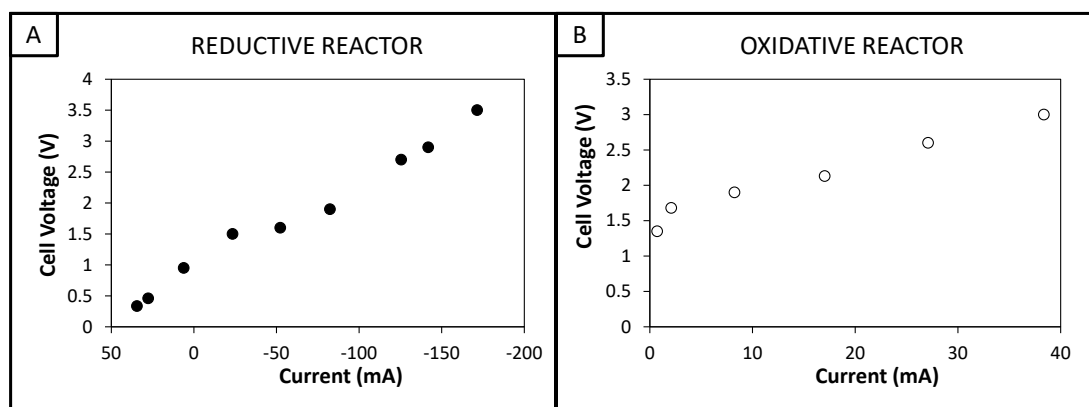


Figure 1. Polarization curves of the upscaled reductive (A) and oxidative (B) reactors.

4. Conclusions

The presented study presents the characterization and the design of an upscaled bioelectrochemical process for chlorinated aliphatic hydrocarbons (CAHs) removal. After the laboratory validation of the technology under several operating conditions, the design, and the realization of an upscaled process allowed for a 42 times volume increase of the technology for its filed scale validation. Preliminary polarization curves and tracer tests allowed for the characterization of the electrochemical and hydraulic behavior of the upscaled units.

Acknowledgements

This project has received funding from the European Union's Horizon 2020 research and innovation programme under grant agreement No 826244-ELECTRA.

References

- [1] B. Matturro, E. Presta, S. Rossetti, *Sci of Total Environ.*, (2016), 445-452
- [2] M. Zeppilli, E. Dell'Armi, M. P. Papini, M. Majone, *Chem. Eng. Transactions*, 86 (2021), 373-378.
- [3] M. Zeppilli, B. Matturro, E. Dell'Armi, L. Cristiani, M. P. Papini, S. Rossetti, M. Majone, *Journal of Environ. Chem. Eng.*, 9, (2021), 104657.

Influence of the morphology of the precursors on the electrochemical capacity of cathodes of Li-ion batteries

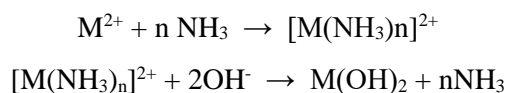
M. L. Para^{1*}, A. Querio¹, M. Shiea¹, S. Bodoardo¹, D. Marchisio^{1*}.

¹ Dep. of Applied Science and Technology, Institute of Chemical Engineering, Politecnico di Torino, Torino, Italy.

*maria.para@polito.it, daniele.marchisio@polito.it

1. Introduction

Lithium-ion batteries are widely spread from small portable devices to stationary battery storage systems. Particularly, for portable application and electric vehicles (EV) the favorite batteries are those made from layered nickel-manganese-cobalt oxides (NMC) [1]. The precursor for this kind of materials are nickel-manganese-cobalt hydroxide, $\text{Ni}_{1-x-y}\text{Mn}_x\text{Co}_y(\text{OH})_2$, which is produced via a co-precipitation typically conducted in continuous stirred tank reactors (CSTR). This process consists of mixing the metal sulphate solutions with an ammonia solution and a basic solution, represented by the following equations:[2]



Complexes are formed between NH_3 and metal cations ($\text{M} = \text{Ni}, \text{Co}, \text{Mn}$), the basic media promotes a quantitative precipitation. Then, the active material NMC, can then, been obtained by a calcination with a lithium source as LiOH .

The coprecipitation process consists in nucleation, molecular growth and aggregation, particles are formed by large aggregates of smaller particles. These large aggregates are referred as secondary particles, whereas their building blocks as primary particles.

Previous studies were carried out in our research group to determine the effect of the synthesis conditions on the characteristics of the $\text{Ni}_{0.8}\text{Mn}_{0.1}\text{Co}_{0.1}(\text{OH})_2$. Those studies focused on the first stage of coprecipitation, in the order of a few seconds, and it was analyzed the influence of inlet solution concentration, flow rate, and ratio between metal and complexing agent, on the characteristics of the particles obtained (particle size distribution, morphology, crystallinity and tap density).

Based on these studies, the objective of this work is to further study the effect of the mean size particles and subsequent aging of the precursor suspension, on the electrochemical properties of the active material.

2. Methods

The $\text{Ni}_{0.8}\text{Mn}_{0.1}\text{Co}_{0.1}(\text{OH})_2$ synthesis is carried out within a four-inlet vortex mixer. Two opposite inlets are fed with NaOH solution, the other two opposite inlets are fed with the NH_3 and the metal sulfate solution. The metal sulfate solution had 80 % of NiSO_4 , 10 % of MnSO_4 and 10 % of CoSO_4 . All solutions are prepared with boiled milliQ water and then injected with the same flow rate. The suspension obtained in the outlet of the micromixer is aged in a round flask with a top stirrer and under N_2 atmosphere. Different precursors were synthesized using inlet concentrations of 1 or 2 M at different flow rates, due to experimental constrain that does not allow us to work with lower concentrations.

The active material, $\text{LiNi}_{0.8}\text{Mn}_{0.1}\text{Co}_{0.1}\text{O}_2$ (NMC811), is synthesized by calcining the precursor with a lithium source, under air flux. The precursor is mixed with a 7% mol excess LiOH , grinded and then a three-step calcination protocol is applied. First calcination step consists in 3 hours at 460 °C, flow by 3 hours at 560 °C and finally 15 hours at 800 °C.

The active material obtained is used to prepare a slurry that is casted in a carbon coated aluminum foil. The slurry composition is 80 % active material, 10 % of conductive carbon C65 and 10% of binder polyvinylidene difluoride (PVDF) in N-methyl-2-pyrrolidone (NMP) solvent. All components are mixed in a ball miller and then casted, with a blade height of 200 μm , then is dried at room temperature at open air. Finally, 15 mm disc are cut to used them as cathodes in coin cells 2032. They are dried under vacuum and transferred into an Ar glove box.

The coin cell are assembled with the commercial separator Celgard 2500, using metallic Li discs as counter electrodes, and 1M LiPF_6 in Ethylene Carbonate:Diethyl Carbonate 1:1 (EC:DEC (1:1)) as electrolyte.

The precursor and active material are characterized by different techniques to determine its particle size distribution (PSD) by light scattering, morphology, and crystallinity. Finally, it is determined its electrochemical performances by charge discharge cycling.

3. Results and discussion

First is analyzed the effect of the mean size of $\text{Ni}_{0.8}\text{Mn}_{0.1}\text{Co}_{0.1}(\text{OH})_2$ on the specific capacity of the NMC obtained. Based on previous studies, that shows that an increase in flow rate leads to smaller and more monodisperse particles, the precursor is synthesized at three flow rates, 35, 70 and 280 mL/min, to obtain sufficiently different $\text{Ni}_{0.8}\text{Mn}_{0.1}\text{Co}_{0.1}(\text{OH})_2$ particles. The suspension was immediately filtrated and washed as it goes out from the mixer.

It is seen that the specific capacity increases with the inlet flow rate of the precursor synthesis (see Figure 1). This can be correlated with a decrease in the mean size, that is 56, 32 and 16 μm , to the synthesis made at 35, 70 or 280 mL/min, respectively.

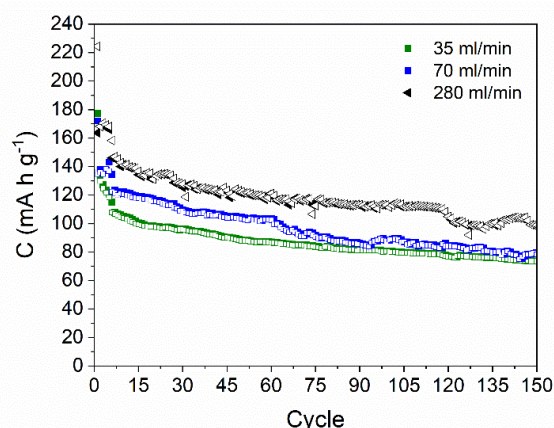


Figure 1. Specific capacity vs. cycling for NMC811 obtained from the precursors synthesized at three flow rates (see inlet). The precursor synthesis conditions were: reagents solution 1M, mixed at room temperature. Filled symbols correspond to discharge capacity and empty symbols to charge capacity.

To further study the effect of aging the suspension of the precursor, it was selected a flow rate of 70 mL/min aged at 60 °C under N_2 atmosphere, for 3 hours and overnight (t_{ON}). In Figure 2 are shown the specific capacities of the NMC811 obtained from these syntheses. For comparison it is also shown the capacity of a material obtained without aging (sample collected at the outlet of the mixer: t_{mix}).

Is observed that both materials obtained from aged precursors have higher capacity. Additionally, there is not a significantly difference between the suspension aged 3 hours or overnight. This behavior can be attributed to the different morphologies of the primary and secondary particles of the materials (see Figure 3). When analyzing the $\text{Ni}_{0.8}\text{Mn}_{0.1}\text{Co}_{0.1}(\text{OH})_2$ precursors particles (first row Figure 3) it is seen that secondary particles become more compact when they are aged, also primary particles (see zoomed images inserted) change their shape from spherical to lamellar. Meanwhile, when the secondary particles of $\text{LiNi}_{0.8}\text{Mn}_{0.1}\text{Co}_{0.1}\text{O}_2$ are analyzed,

it seems that there are not big changes, however the primary particles show a correlation with the aging time of the precursor, they become more compact and smoother.

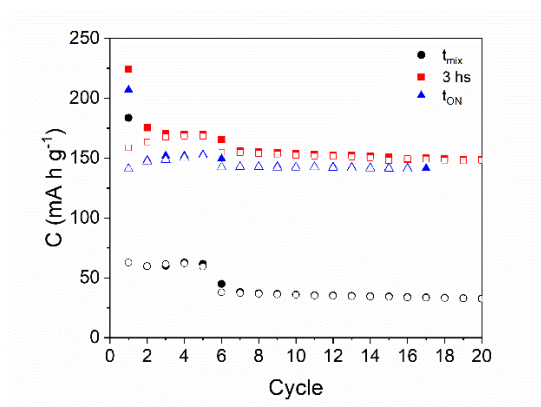


Figure 2. Capacity versus cycling (a) for NMC811 obtained from the precursor at different aging times. The precursor synthesis conditions were: reagents solution 2M, fed at 70 ml/min flow rate, and aged at 60 °C, with top stirrer. Without aging (black), aged 3 hours (red) and aged overnight (blue).

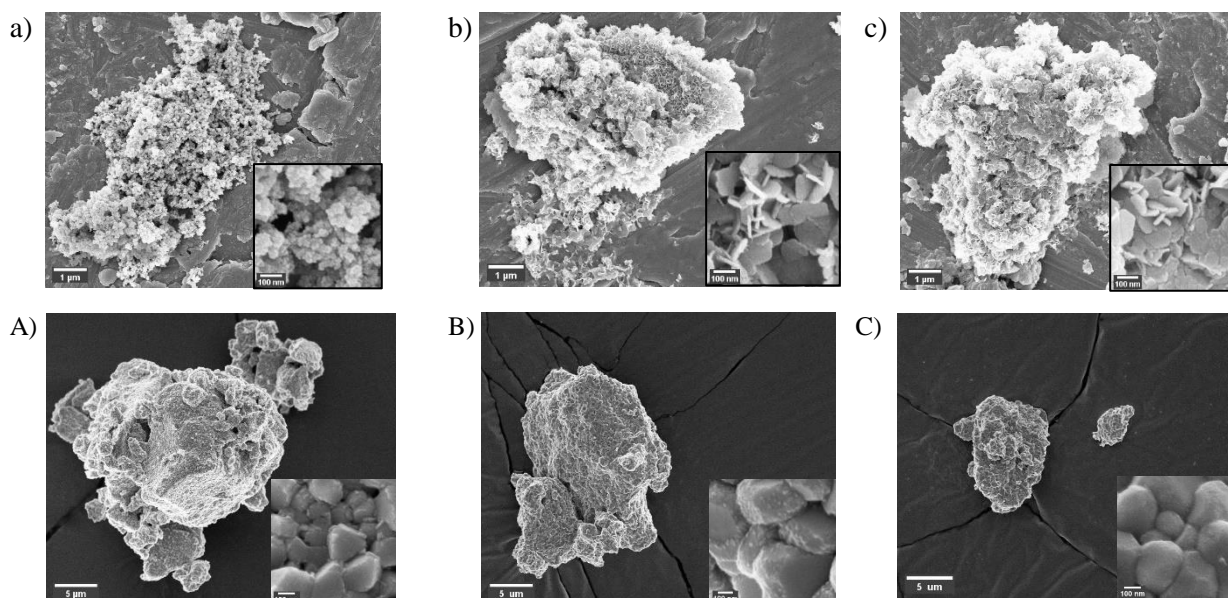


Figure 2. SEM images of $\text{Ni}_{0.8}\text{Mn}_{0.1}\text{Co}_{0.1}(\text{OH})_2$ (a, b, c) and of $\text{LiNi}_{0.8}\text{Mn}_{0.1}\text{Co}_{0.1}\text{O}_2$ (A, B, C) for different aging times, t_{mix} (a, A), 3 hs (b, B) and t_{ON} (c, C).

4. Conclusions

Throughout this study it is analyzed the electrochemical capacity of the NMC synthesized from precursors obtained under different synthesis conditions. The higher specific capacities are obtained when the precursor particles are smaller and more compact. This meaning that the best synthesis condition to synthesize the precursor is at high flow rates to obtained smaller particles and more monodisperse, and age the suspensions to promote a lamellar shape of the primary particles and more compact secondary particles.

Acknowledgment

The research reported in this paper was funded by European Union, Horizon 2020 Programme, SimDOME Project, Grant Agreement No 814492. The views and opinions expressed in this publication are the sole

responsibility of the author(s) and do not necessarily reflect the views of the European Commission/Research Executive Agency

References

- [1] M. Armand, P. Axmann, D. Bresser, M. Copley, K. Edström, C. Ekberg, D. Guyomard, B. Lestriez, P. Novák, M. Petranikova, W. Porcher, S. Trabesinger, M. Wohlfahrt-Mehrens, H. Zhang, J. Power Sources. 479 (2020) 228708.
- [2] A. van Bommel, J.R. Dahn, Chem. Mater. 21 (2009) 1500–1503.

Engineering the Electrochemical CO₂ Conversion to Chemicals and Fuels by using Metal-oxide-based Catalysts and Optimized Cell Configurations

Simelys Hernández*, Hilmar Guzmán, Samir Bensaid, Nunzio Russo
*CREST group, Department of applied science and technology (DISAT), Politecnico di Torino
C.so Duca degli Abruzzi, 24, 1019, Turin, Italy
e-mail: simelys.hernandez@polito.it

1. Introduction

Anthropogenic activities have impacted the planet's carbon cycle by the emissions of large amounts of greenhouse gases (GHGs), shifting the equilibrium of human history since the industrial revolution. CO₂ is the key contributor to global climate change in the atmosphere. For this reason, the synthesis of high added-value products CO₂ conversion is a promising approach to mitigate climate change.[1] However, it represents a major challenge because CO₂ is a thermodynamically stable molecule. It entails multi-electron transfer reactions and parallel reaction mechanisms, the main causes of low selectivity and productivity.

Among the different alternatives, exploiting CO₂ via electrochemical reduction under mild conditions (ambient pressure and temperature) represents an opportunity to support a low carbon economy.[2,3] The electrocatalytic (EC) CO₂ reduction (CO₂R) driven by renewable energy can be exploited for the future energy transition, for the carbon storage into valuable products like syngas (H₂/CO mixtures), organic acids (formic acid) and chemicals/fuels (C₁₊ alcohols).[4] Although this option is very attractive for scientists, many challenges still remain, namely to achieve low overpotentials, high production rates at high current densities, as well as stable and long term operations.[3,5] A big challenge for the industrialization of this technology is to find low-cost electrocatalyst, efficient reactors and process conditions. Regarding the electrocatalysts, noble metals like Ag and Au are the most used ones for syngas production.[6] On the other hand, the performance of Cu-based electrocatalysts is among the best ones that have ever been achieved to transform CO₂ into C₁₊ products.[1,7,8]

In the efforts to reduce the catalyst cost, we have developed electrodes made of Ag nanoparticles (NPs) on TiO₂ nanotubes (NTs),[9] showing a higher electrochemical surface area and electrons transport than a bare Ag. Titania was used as an efficient support, for enhancing the stability of key CO₂⁻ radical intermediate and decreasing the EC CO₂R overpotential. We also have exploiting the current knowledge of the thermocatalytic CO₂ hydrogenation to develop noble-metal-free CO₂R electrocatalysts.[10–12] For instance, Cu/Zn/Al-based catalysts producing methanol and CO from the CO₂ thermocatalytic (TC) hydrogenation (at H₂ pressure (P) of 30 bar and temperature (T) > 200 °C) generates H₂, CO and other C₁ to C₃ liquid products during the EC CO₂R in a gas-diffusion-electrode system; while operating in the liquid phase, the same catalyst produces syngas with a tunable composition (depending on the applied potential) and other liquid C₂₊ products (in both cases at ambient T,P).[10,13] On the other hand, Cu/ZnO electrocatalyst also have been tested at industrially relevant current densities in liquid phase configuration.[14] We demonstrated through ex-situ characterisations that the presence of ZnO nanoparticles in the mixed Cu/ZnO catalyst plays an important role in the formation and stabilisation of mixed oxidation states of copper and Cu¹⁺/Cu⁰ interfaces in the electrocatalyst (in bulk and surface). These interfaces seem to promote the C₂₊ products formation. Our results open a promising path for the prospective implementation of metal-oxides nanostructures for the CO₂ conversion to the chemicals and fuels of the future.

2. Methods

The TiO₂ nanotubes (NTs) were prepared as follows: i) Titanium foil was sandblasted and etched by the solution of HF to remove the native oxide layer, and then the TiO₂ nanotubes were synthesized by anodization method in a 0,5 wt% NH₄F and 2,5 wt% H₂O in ethylene glycol electrolyte at 60 V.[15] After some minutes, the synthesized NTs are removed by sonication in H₂O₂ (40%) solution. The anodization procedure was

repeated. In this way, well organized TiO₂ nanotubes can be grown in the footprint of previously removed ones; ii) After cleaning the NTs arrays with DI-Water and ethanol to remove the residual of electrolyte, they were calcined at 450 °C for 1 h in ambient pressure; iii) for the deposition of Ag nanoparticles (NPs) a sputter coater equipped with an Ag target has been used to prepare a set of catalyst samples with different Ag NPs loadings, which depend on the sputtering conditions (current and time).

The Cu/Zn/Al-based catalysts were synthesised by a precipitation method with a procedure analogous to that proposed by Schüth et al.[16] The procedure started with preparing a solution of hydrated copper nitrate as a precursor. A solution of sodium carbonate was used as the precipitating agent. The setup consists of a beaker with an initial volume of distilled water of 200 mL kept at 70°C. It is important to mention that the pH was maintained at a constant value during the precipitation process. The synthesis begins with pumping the nitrate solution at a constant flow rate by using a peristaltic pump. The system is left ageing for one hour, then the precipitate is filtered and later left drying overnight in an oven. Finally, the calcination was performed at 350°C in a muffle for 3 hours with a heating ramp of 2°C min⁻¹. [13]

The Cu/ZnO mixture catalysts were prepared by using commercial copper and zinc oxide nanoparticles (NPs). The copper nanoparticles were selected with a size range of 40-60 nm (Cu), while the zinc oxide was around 20-25 nm. The samples were prepared by pre-oxidation of the Cu NPs at 150°C for 2 hours in static air (Cu calc) and then manually mixing it with the ZnO (CZ calc). The molar ratio between Cu and ZnO is equal to 65/35.

These electrocatalysts have been tested in a conventional 3-electrode system and in a more complex setup based on a gas diffusion electrode (GDE), where a continuous flow configuration also has been adopted (see **Figure 1**). On the other hand, the catalyst materials have been characterised by different physico-chemical methods to determine the features that make these materials perform for the CO₂-to-added value products conversion.

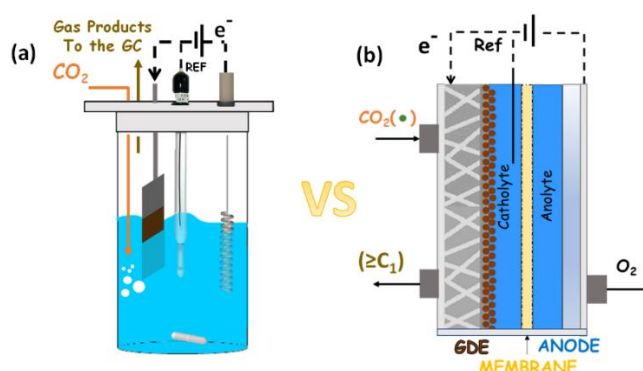


Figure 1. Simplified conceptual schemes of the electrochemical CO₂ reduction setups: (a) single-chamber configuration with CO₂ dissolved in the liquid electrolyte; (b) three-chambers gas diffusion electrode (GDE) cell configuration with gaseous CO₂ feed to the cathode back side, and anolyte and catholyte are separated by an ion exchange membrane.

3. Results and discussion

We found that the quasi-one-dimensional arrangement of the TiO₂ NTs provide higher surface area for Ag adhesion and superior electron transport properties than other Ti substrates (e.g., Ti foil and TiO₂ nanoparticles), as confirmed by different electrochemical techniques, like electrochemical active surface area, and physico-chemical analysis, like FESEM, TEM and EDS. These characteristics and the role of the TiO₂ NTs to enhance the stability of CO₂⁻ intermediate formed due to titania redox couple (Ti^{IV}/Ti^{III}) lead to an improvement of the CO production in the Ag/TiO₂ NTs electrodes.[9]

Inspired by the knowledge of the thermocatalytic CO₂ reduction process, metal oxides like ZnO and Al₂O₃ were proposed as promoters and support structures for copper catalysts. The electrocatalytic activity of the CuZnAl-oxide materials was dependent on both the intrinsic properties of the electrocatalyst and the cell configuration used for the tests. These are factors controlling the CO₂ availability at the active electrode surface. When moving from CO₂-saturated systems to a gas diffusion layer-type catalytic electrode

configuration, the selectivity of the catalysts changed from syngas production (95% of FE at the most positive applied potential) to the generation of liquid products (e.g. methanol or propanol), respectively, as shown in **Figure 2**. In this sense, the Cu/Zn/Al-based commercial catalyst was able to achieve ~25% of FE to propanol. In contrast, the co-precipitated Cu/Zn/Al-based material promoted the formation of methanol (~32% of FE). However, the thermodynamically preferred hydrogen was the main product in most cases due to mass-transfer limitations issues. It must be pointed out that the formation and stabilization of different oxidation states of copper (during the catalyst synthesis and/or during testing) and the local pH play an essential role in the selectivity of the reaction. From an environmental and techno-economic analysis applied to the case of study of the scaled-up methanol production, including downstream purification processes, we determined that optimized EC process conditions could lead to a practical implementation of this technology; that is, recirculation of the not reacted CO₂, achievement of current densities in the range of 100-200 mA/cm² with faradaic efficiencies (> 90%), and use of renewable electricity sources (*i.e.* 30% of the total energy).[10] Hence, considering the effective allocation of methanol on a real market scenario, the EC process results to be economically advantageous over the TC one at a productivity scales as low as 19.1 kg/h, and could lead to a carbon footprint that is comparable to that of current industrial technologies for methanol production (climate change impact of 2.72 kg_{CO2}/kg_{CH3OH}). Moreover, in a scenario with a 100% renewable energy such as photovoltaic, it is possible to reach savings in that carbon footprint of up to 62%.[10]

Cu/ZnO and bare Cu catalysts enriched with Cu⁺ species were also studied to convert CO₂ via the EC pathway. Integrating Cu with ZnO (a CO-generation catalyst) is a strategy explored to reduce the kinetic barrier and enhance C-C coupling to produce C₂₊ chemicals and energy carriers. Herein, ethanol was produced with the Cu/ZnO catalyst up to a FE of 8%, reaching ethanol productivity of about 5.3 mmol·g_{cat}⁻¹·h⁻¹ in a liquid-phase configuration at ambient conditions. In contrast, bare copper preferentially produced C₁ products like formate and methanol.[14]

Our results confirm that a well-performing catalyst for the TC CO₂ hydrogenation can also be encouraging for the EC CO₂ conversion to added-value products. Hence, the strategies developed in the TC technology to improve the catalytic activity and selectivity of the materials can also be exploited in the less energy-demanding EC CO₂ conversion technology. Otherwise, the current knowledge on CO₂R electrocatalyst reconstruction could be of helpful for developing new TC systems, leading to the production of more reduced C₂₊ products.

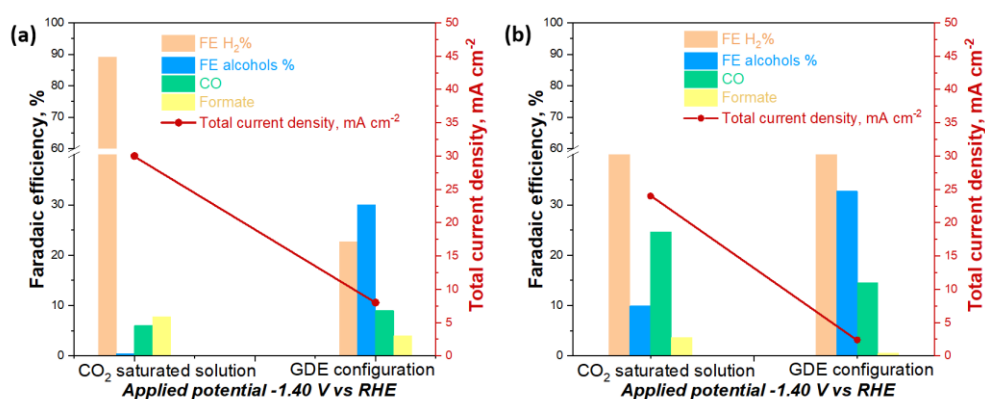


Figure 2. FE for the different products formed after 60 min of EC CO₂R to a constant potential of -1.4 V vs RHE for the electrocatalyst: (a) Commercial Cu/Zn/Al (CZA CC) and (b) Cu/Zn/Al synthesized (CuZA-06-03-01).

4. Conclusions

- Titania enhance the stability of key CO₂⁻ intermediate decreasing the CO₂ electroreduction overpotential,
- Cu based catalysts were synthesized by standardized and scalable co-precipitation method and demonstrate their ability to produce of C₁ to C₃ oxygenates,

- Pyramidal CuZnAl-based catalysts with enhanced catalytic activity and stability have been developed for the CO₂ conversion to Syngas in a liquid-based cell configuration,
- Different cell configurations led to a different reconstruction of Cu superficial states and catalyst selectivity; in a GDE cell, our synthesised CuZnAl catalyst produced methanol thanks to the stabilization of superficial Cu⁺² & Cu⁺¹ species,
- ZnO plays a role in stabilizing Cu⁺¹ and promoting the CO dimerization to ethanol and C₂₊ products,
- By a techno-economic analysis, optimized process conditions that could lead to a practical implementation of the electrocatalytic CO₂ reduction technology were identified: i.e., recirculation of the not reacted CO₂, operation at current densities of 100-200 mA/cm², achievement of FE > 90% and use of >30% of renewable electricity sources to power the EC system.

Acknowledgements

This work has received financial support by the EU H2020 Projects SunCOChem, CELBICON and RECODE (grant agreements: 862192, 679050, 768583).

References

- [1] H. Guzmán, N. Russo, S. Hernández, CO₂ valorisation towards alcohols by Cu-based electrocatalysts: challenges and perspectives, *Green Chem.* 23 (2021) 1896–1920. <https://doi.org/10.1039/D0GC03334K>.
- [2] N.S. Romero Cuellar, K. Wiesner-Fleischer, M. Fleischer, A. Rucki, O. Hinrichsen, Advantages of CO over CO₂ as reactant for electrochemical reduction to ethylene, ethanol and n-propanol on gas diffusion electrodes at high current densities, *Electrochim. Acta.* 307 (2019) 164–175. <https://doi.org/10.1016/j.electacta.2019.03.142>.
- [3] R.M. Cuéllar-Franca, A. Azapagic, Carbon capture, storage and utilisation technologies: A critical analysis and comparison of their life cycle environmental impacts, *J. CO₂ Util.* 9 (2015) 82–102. <https://doi.org/10.1016/j.jcou.2014.12.001>.
- [4] H. Guzmán, M.A. Farkhondehfal, K. Rodolfo Tolod, N. Russo, S. Hernández, Photo/electrocatalytic hydrogen exploitation for CO₂ reduction toward solar fuels production, in: *Sol. Hydrog. Prod. Process. Syst. Technol.*, Elsevier Inc., 2019: p. 560. <https://doi.org/10.1016/C2017-0-02289-9>.
- [5] H. Guzmán, F. Zammillo, D. Roldán, C. Galletti, N. Russo, S. Hernández, Investigation of gas diffusion electrode systems for the electrochemical CO₂ conversion, *Catalysts.* 11 (2021). <https://doi.org/10.3390/catal11040482>.
- [6] S. Hernández, M.A. Farkhondehfal, S. Francesc, M. Makkee, G. Saracco, N. Russo, Syngas production from electrochemical reduction of CO₂: Current status and prospective implementation, *Green Chem.* 19 (2017) 2326–2346. <https://doi.org/10.1039/c7gc00398f>.
- [7] Y. Liu, F. Li, X. Zhang, X. Ji, Recent progress on electrochemical reduction of CO₂ to methanol, *Curr. Opin. Green Sustain. Chem.* 23 (2020) 10–17. <https://doi.org/10.1016/j.cogsc.2020.03.009>.
- [8] T.K. Todorova, M.W. Schreiber, M. Fontecave, Mechanistic Understanding of CO₂ Reduction Reaction (CO₂RR) Toward Multicarbon Products by Heterogeneous Copper-Based Catalysts, *ACS Catal.* 10 (2020) 1754–1768. <https://doi.org/10.1021/acscatal.9b04746>.
- [9] M.A. Farkhondehfal, S. Hernández, M. Rattalino, M. Makkee, A. Lamberti, A. Chiodoni, K. Bejtka, A. Sacco, F.C. Pirri, N. Russo, Syngas production by electrocatalytic reduction of CO₂ using Ag-decorated TiO₂ nanotubes, *Int. J. Hydrogen Energy.* 45 (2020) 26458–26471. <https://doi.org/10.1016/j.ijhydene.2019.04.180>.
- [10] H. Guzmán, F. Salomone, E. Batuecas, T. Tommasi, N. Russo, S. Bensaid, S. Hernández, How to make sustainable CO₂ conversion to Methanol: Thermocatalytic versus electrocatalytic technology, *Chem. Eng. J.* (2020) 127973. <https://doi.org/10.1016/j.cej.2020.127973>.
- [11] K. Bejtka, J. Zeng, A. Sacco, M. Castellino, S. Hernández, M.A. Farkhondehfal, U. Savino, S. Ansaloni, C.F. Pirri, A. Chiodoni, Chainlike Mesoporous SnO₂ as a Well-Performing Catalyst for Electrochemical CO₂ Reduction, *ACS Appl. Energy Mater.* 2 (2019) 3081–3091. <https://doi.org/10.1021/acsaem.8b02048>.
- [12] H. Guzmán, N. Russo, S. Hernandez, CO₂ valorisation towards alcohols by Cu-based electrocatalysts: Challenges and perspectives, *Green Chem.* in press (2021). <https://doi.org/10.1039/D0GC03334K>.
- [13] H. Guzmán, D. Roldán, A. Sacco, M. Castellino, M. Fontana, N. Russo, S. Hernández, CuZnAl-Oxide Nanopyramidal Mesoporous Materials for the Electrocatalytic CO₂ Reduction to Syngas: Tuning of H₂/CO Ratio, 11 (2021) 3052.
- [14] H. Guzmán, F. Salomone, S. Bensaid, M. Castellino, N. Russo, S. Hernández, CO₂ Conversion to Alcohols over Cu/ZnO Catalysts: Prospective Synergies between Electrocatalytic and Thermocatalytic Routes, *ACS Appl. Mater. Interfaces.* 14 (2021) 517–530. <https://doi.org/10.1021/acsaami.1c15871>.
- [15] M.A. Farkhondehfal, S. Hernández, M. Rattalino, M. Makkee, A. Lamberti, A. Chiodoni, K. Bejtka, A. Sacco, F.C. Pirri, N. Russo, Syngas production by electrocatalytic reduction of CO₂ using Ag-decorated TiO₂ nanotubes, *Int. J. Hydrogen Energy.* 45 (2020) 26458–26471. <https://doi.org/10.1016/j.ijhydene.2019.04.180>.
- [16] C. Baltes, S. Vukojević, F. Schüth, Correlations between synthesis, precursor, and catalyst structure and activity of a large set of CuO/ZnO/Al₂O₃ catalysts for methanol synthesis, *J. Catal.* 258 (2008) 334–344. <https://doi.org/10.1016/j.jcat.2008.07.004>.

Computational Modelling of the Solid Electrolyte Interface (SEI) in Lithium-ion Batteries and Its Impact on Long-Term Battery Aging

Luca Banetta¹, Graziano Frungieri², Agnese Marcato¹, Gianluca Boccardo¹,
 Silvia Bodoardo¹, Daniele Marchisio¹

¹ Dipartimento di Scienza Applicata e Tecnologia, Politecnico di Torino, Corso Duca degli Abruzzi 24, 10129 Torino(TO);

² Lehrstuhl für Systemverfahrenstechnik, TUM School of Life Sciences, Technische Universität München, Gregor-Mendel-Straße 4, 85354 Freising, Germany.

*Corresponding author E-Mail: luca.banetta@polito.it

1.Introduction

During the last three decades, lithium-ion batteries have become the choice of power source for most portable electronic devices [1].

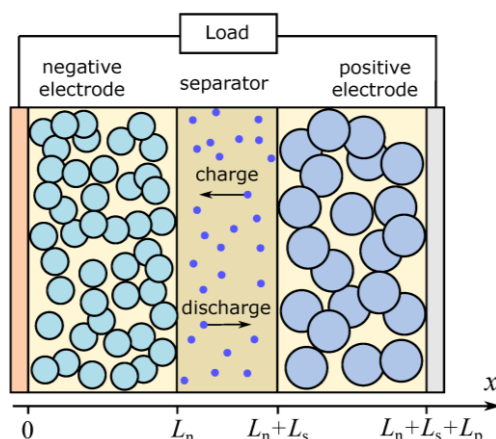


Figure 1: Simplified representation of a Li-ion battery: the small blue dots represent the lithium ions Li^+ moving in the electrolyte (image taken from [2]).

A simplified representation of a Li-ion battery is shown in Figure 1. What follows is a brief explanation on the basic functioning of this category of energy storage devices during discharge cycle under galvanostatic conditions, where a constant current i_{tot} is drained from the system. The lithium ions, which are initially stored in the anode, deintercalate, diffuse out in the electrolyte, reach the cathode/electrolyte interface, and intercalate into the cathodic material. At the same time, electrons will be taken from the anodic current collector thanks to the oxidation of the anodic material, and travel through the load to the cathodic current collector, where they will reduce the cathodic material.

On the other hand, during a galvanostatic charge cycle, the application of an external work will reverse the motion of Li^+ , which will deintercalate from the cathode and intercalate into the anode, and of the electrons as well.

Despite the remarkable scientific advancement of the last years, the degradation phenomena occurring in lithium ion batteries are unfortunately still far from being well understood: one of the main problem affecting battery life is, in fact, the continuous growth of a passivation layer known as the Solid Electrolyte Interface (SEI) at the Anode/Electrolyte Interface (AEI) during charge cycles: this event takes place if the anodic potential $\phi_{s,a}$ is located outside the stability window of the electrolyte (typically $1 \text{ V} < \phi_e < 4.5 \text{ V}$) [3]. This scenario is inevitable for graphite, the most frequent choice for the anodic material due to its reliability when it comes to safety, which will be used in the current work.

As mentioned earlier, Li^+ will move from the cathode towards the anode into the electrolyte during charge cycles: when the lithium ions approach the AEI, a portion of them will not intercalate, but undergo interfacial reduction reactions together with high dielectric components dissolved into the electrolyte. This reactive path

will allow the passivation layer to grow, which causes a progressive degradation of the battery performance, as a result of the loss of cyclable lithium ions (*capacity fade*) and of the increased resistance to their motion (*impedance rise*).

In this work the authors will analyse the impact of the growth dynamics of the Solid Electrolyte Interface (SEI) on the performance of a lithium-ion battery over a short series of charge/discharge cycles by using a 3D- time resolved (4D) electrochemical model. Across the project, we have adopted different geometries of increasing complexity to represent the morphology of a battery, which is featured by a graphitic anode (Li_xC) and a NCAO ($\text{Li}_x\text{Ni}_y\text{Co}_z\text{Al}_{1-y-z}\text{O}_2$) cathode.

2. Methods

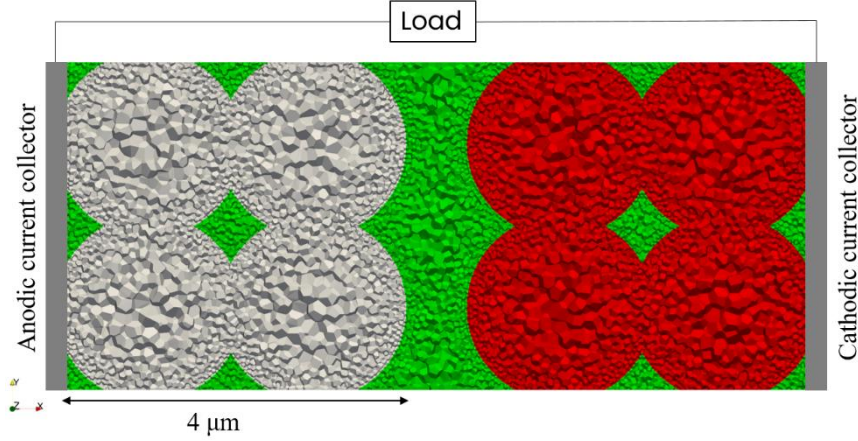


Figure 2: Slice of the computational grid representing one of the considered systems. Different colours represent the two electrodes and the electrolyte, in particular the anodic (grey) and cathodic structures (red), and the surrounding electrolyte (green).

The 4D model is based on Fluent (Ansys-CFD) lithium-ion electrochemical model: the simulation domain has been decomposed through a polyhedral computational grid; an example of a slice of one of the geometries adopted in this work is presented in Figure 2. The mass and charge conservation equations associated to the transport lithium ions across the electrodes and the electrolyte are numerically solved for each cell by adopting a finite-volume methodology. All the transport equations must be naturally closed by adopting the proper boundary conditions. First, the current collectors will be impermeable to any flux of Li^+ coming from either the fluid or the solid phase. Afterwards, at every electrode/electrolyte interface the flux of Li^+ j_{tot} exchanged between the different phases will be modelled by adopting the well-known Butler-Volmer kinetics:

$$j_{tot} = \frac{i_0}{F} \left[\exp\left(\frac{F\eta}{2RT}\right) - \exp\left(-\frac{F\eta}{2RT}\right) \right], \quad (1)$$

where i_0 is the exchange current density and F the Faraday constant. Finally, η is the overpotential which allows the transition of Li^+ from one phase to the other, which is defined as:

$$\eta = \phi_s - \phi_e - U. \quad (2)$$

In Eq. (2) ϕ_s and ϕ_e are the electrode and electrolyte potentials, respectively, while U is the open circuit potential of the anodic or cathodic half-cell reaction.

Finally, ϕ_s will be constrained to zero at the anode/anodic current collector interface ($\phi_{s,a} = 0 \text{ V}$), meanwhile a constant current density i_{tot} is allowed to cross the cathode/cathodic current collector interface to represent the galvanostatic conditions: it will assume a negative value during discharge cycles and a positive one during charge ones.

The novelty of this approach relies on the description of the local growth dynamics of the SEI at the Anode-Electrolyte Interface during each charge cycle: every cell composing the AEI is coupled with a user-defined-function which describes the temporal increase of the SEI growth as a function j_s , the fraction of j_{tot} which undergoes the interfacial reduction kinetics:

$$\frac{d\delta(\mathbf{x})}{dt} = - \frac{j_s}{\rho_{SEI}/M_{SEI}}, \quad (3)$$

where ρ_{SEI} and M_{SEI} represent the average density and molecular weight of the SEI; here j_s is supposed to be the 5% of the overall Li^+ flux approaching the AEI.

The impact of the passivation layer on the impedance rise is, instead, described by a local contact resistance $R_F(\mathbf{x})$, which depends on the local thickness $\delta(\mathbf{x})$ of the SEI and its thermal conductivity κ_{SEI} :

$$R_F(\mathbf{x}) = R_{SEI} + \frac{\delta(\mathbf{x})}{\kappa_{SEI}}, \quad (4)$$

which will impact the anodic overpotential in the Butler-Vomer kinetic equation related to the trespassing of the AEI by Li:

$$\eta = \phi_s - \phi_e - U - R_F F j_{tot}. \quad (5)$$

3. Results and discussion

Here, we briefly propose the main results obtained in the project. As mentioned in the introduction, a series of geometries with increasing complexity have been adopted, which are proposed in the Supporting Images. In Figure S1 we propose a 2D domain, where the electrodes are composed of 3 circles of radius $R_p = 1 \mu m$ and they are located $1 \mu m$ away from each other. In Figure S2 it is showed a simplified 3D geometry, in which each electrode is now composed of 8 compenetrating spheres with $R_p = 1 \mu m$ $1 \mu m$ apart from each other as well. Finally, we have adopted a realistic 3D battery morphology, which is showed in Figure S3: here, the electrodes have been reconstructed by using experimental information on the Particle Size Distribution and porosity of commercial electrodes: in this case the particles assume an average particle size $R_{p,av} = 5 \mu m$ and separated by $10 \mu m$.

A series of simulations has been conducted to make sure that the model reliably describes the functioning of a battery during a series of galvanostatic charge/discharge cycles with different values of current density. In particular, i_{tot} is expressed as a C-rate: given the total capacity of the battery $C_{tot}[Ah]$, a C-rate equal to X C is the value of i_{tot} , which is necessary to complete a full discharge/charge of the system in $1/X$ hours.

In Figure 4, we present the different concentration profiles of Li^+ obtained at 2C during different stages of a discharge cycle.

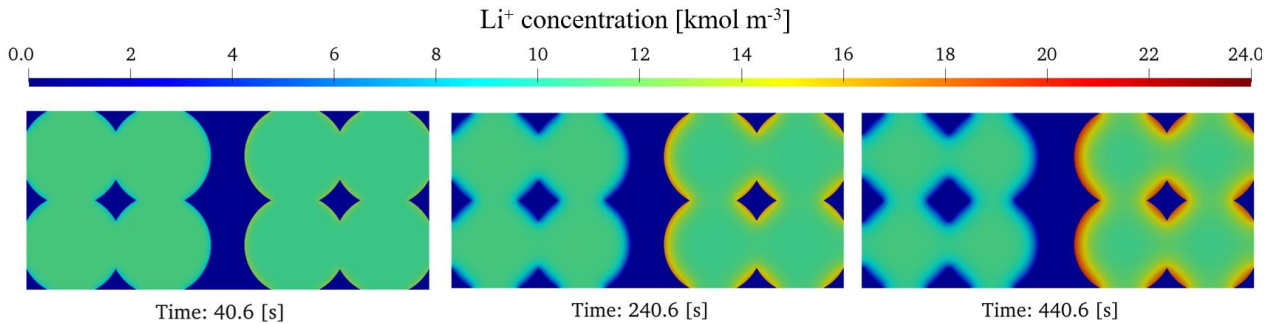


Figure 4: Temporal variation of the Li^+ concentration across a slice of the 3D simplified geometry at different stages of a discharge cycle at 2C.

It can be appreciated the depletion of Li^+ from the anode on the left side of each image: this phenomenon naturally starts at the surface of the electrodes and keeps propagating towards the core of each anodic particle. At the same time, the intercalation of the Li^+ on the cathode at the right end of the images can be observed, where the Li^+ starts accumulating at the surface of this electrode and starts diffusing into the particles.

In Figure 5, we instead propose the charge/discharge curves computed at two different C rates. They show the temporal trend of the cell voltage V , formally defined as the difference between the cathodic $\phi_{s,c}$ and the anodic electric potential $\phi_{s,a}$

$$V = \phi_{s,c} - \phi_{s,a}, \quad (6)$$

V can be interpreted as the driving force for the motion of Li^+ from the anode to the cathode during the discharge, allowing the battery to provide energy to the load.

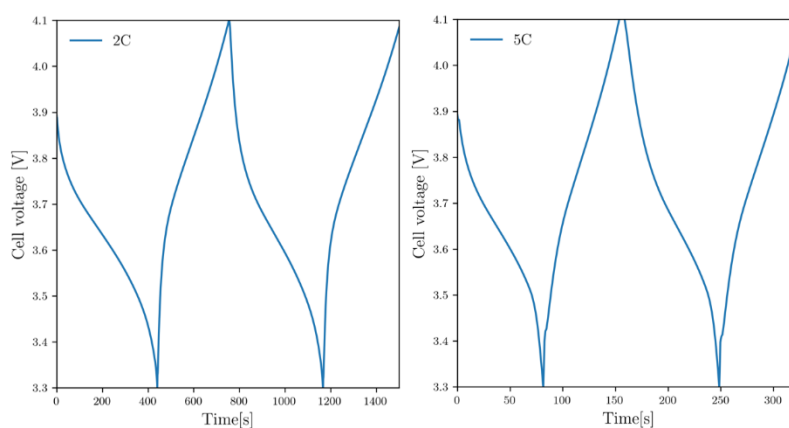


Figure 5: Charge/discharge curves for a simplified 3D geometry at the considered C-rates.

Overall, during the discharge energy is taken from the system and electrons are flowing through the external load, with parallel motion of Li^+ from the anode and their subsequent intercalation of Li^+ in the cathode, as previously showed in Figure 4. During the discharge the cell voltage keeps decreasing due to increasing mass transport limitations: since the diffusion of Li^+ in the particles is slow, these cations start accumulating on the most external areas of the cathodic material, getting closer and closer to the Li^+ solubility limit. This phenomenon translates into an increasing resistance to the intercalation of new Li^+ , which ultimately causes V to decrease in a non-linear way until a cut-off voltage of 3.3 V is reached: the decision to stop the discharge at this specific value derive from the fact that reaching lower voltages can lead to structural collapses of the electrodes.

At this point, the current within the system is reversed and a charge is begun, where the cell voltage is allowed to increase thanks to the application of an external work until an upper limit of $V_{\text{lim}} = 4.1$ V is achieved; it is not recommended to charge to higher values than V_{lim} because an overcharge of the system can cause unstable conditions, which ultimately lead to dangerous phenomena, including thermal runaway reactions.

It can be noticed that the temporal scale at which the cell voltage varies from the cut-off voltage to the upper limit depends on the C-rate: increasing its value leads to a much quicker decrease of the cell voltage during discharges. This happens because a higher discharge current causes the surface of the particles to saturate quicker with respect to lower C-rates, so the internal resistance to the intercalations of new Li^+ increases over a smaller time-span. This ultimately causes the battery to release a much smaller amount of energy per cycle under higher C-rates.

Figure 4 and 5 indicates that the 4D model correctly represents the behaviour of the cell voltage during a series of discharges and charges as widely reported in the literature [4]; the natural next step will be the description of the impact of the local SEI growth dynamics on the overall cell performance.

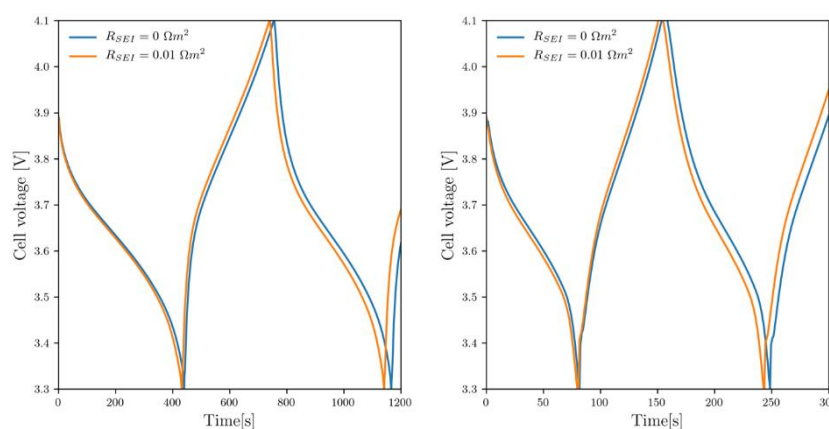


Figure 6: Charge/Discharge curves for a simplified 3D geometry with C-rates of 2C (left) and 5C (right) considering and neglecting the impedance rise provided by the SEI.

In Figure 6 we propose the impact of the impedance rise provided by the SEI growth dynamics on the temporal trends of the cell voltage at the aforementioned C-rates: an initial value of $R_{\text{SEI}} = 0.01 \Omega \text{ m}^2$ has

been chosen. To the authors' knowledge, this is the first time that a rigorous 4D model describes the impact of local SEI growth dynamics on the performance of a lithium-ion battery instead of considering uniform average values as previously done in the literature [4].

We can clearly see that the presence of the passivation layer causes the cell voltage of the lithium-ion battery to decrease: this happens because the growing SEI offers an ulterior resistance to the motion of Li^+ inside the system described by the resistivity R_F , which affects the flux of Li^+ at the AEI by modifying the anodic overpotential in Eq.(5), which subsequently affects j_{tot} according to Eq.(1): basically, the de-intercalation from the anode will be hindered during a discharge, which leads to a degradation of the battery performance since the cut-off cell voltage is reached at an earlier time with respect to a system which neglects the presence of the SEI.

Moreover, it can be noticed that the time difference between the reach of the cut-off voltage between the systems with $R_{\text{SEI}} = 0 \Omega \text{ m}^2$ and $R_{\text{SEI}} = 0.01 \Omega \text{ m}^2$ gets wider as the cycles progress. This happens because the thickness of the SEI increases at every charge cycle according to Eq.(3): the increase of $\delta(\mathbf{x})$ leads to an increase of $R_F(\mathbf{x})$ according to Eq.(4), which magnifies the impedance rise provided by the SEI for every subsequent discharge, with the ultimate effect of a progressive loss of battery performance between one discharge cycle and the other.

4. Conclusions

In this work, the authors have proposed preliminary results of a rigorous 4D model, among them the Li^+ concentration profiles inside the electrodes during a complete discharge cycle at 2C. Next, two different charge/discharge curves at 2C and 5C have been proposed, highlighting the reliability of the model to reproduce the fundamental functioning of a lithium-ion battery, in particular the inverse proportion between the C-rate and the amount of energy that can be provided by the battery. Finally, it has been highlighted for the first time the impact of the local SEI growth dynamics on the battery performance by comparing the temporal trend of the cell voltage of a series of charge/discharge cycles at different C-rates including and excluding the impact of the SEI: the presence and continuous growth of the passivation layer causes the time the cell voltage takes to reach the cut-off limit from fully charged conditions to be shorter as we progress from one discharge cycle to the other. This is a clear sign of a gradual loss of battery performance due to the increasing impedance rise provided by the passivation layer.

The main issue of this 4D model is its high computational cost, so the authors are also exploring other options to describe long term battery aging. A future alternative is the development of a surrogate model based on the use of a Convolutional Neural Networks (CNN). The authors will follow the same workflow adopted in a previous project focused on the prediction of colloidal filtration in porous media [5]. The idea is based on the launch of several simulations of the 4D model under different operating conditions for both the anode and the cathode. Their outputs, which will be the temporal profiles of Li^+ concentration across the battery and of R_F at the AEI, will be used to create a dataset, which will subsequently be used to train the CNN. The goal is to reproduce, and subsequently predict, the long-term battery aging as it is described by the 4D model but without the necessity of extreme computational efforts.

Acknowledgements

The authors acknowledge support from the European Union's Horizon 2020 research and innovation programme under Grant Agreement No. 957189.

References

- [1] W. Aiping, K. Sanket, L. Hong, S.Siqi, Q. Yue, Review on modeling of the anode solid electrolyte interphase (SEI) for lithium-ion batteries, *npj Computational Materials* 15 (2018) 1-26. G.F. Froment, K.B. Bishoff, *Chemical Reactor Analysis and Design*, second ed., Wiley, New York, 1990.
- [2] R. T. Sibatov, V.V. Svetukhin, E.P. Kitsyuk, A.A. Pavlov, Fractional Differential Generalization of the Single Particle Model of a Lithium-ion Cell, *Electronics* 8 (2019) 650.
- [3] B. Horstmann, F. Single, A. Latz, Review on multi-scale models of solid-electrolyte interface formation, *Current opinion in Electrochemistry*, The Electronic Technology, E-Publishing Inc., New York, 2009, pp. 181–304.
- [4] A. Lamorgese, R. Mauri, B. Tellini, Electrochemical-thermal P2D aging model of a $\text{LiCoO}_2/\text{graphite}$ cell: Capacity fade simulations, *Journal of Energy Storage* 20 (2018) 289-297.
- [5] A. Marcato, G. Boccoardo, D.L. Marchisio, A computational workflow to study particle transport and filtration in

porous media: Coupling CFD and deep learning, Chemical Engineering Journal **417** (2021) 128936.

Supporting Images

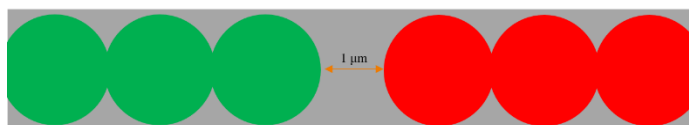


Figure S1: Simplified 2D geometry, where the different colours represent the anode (green), electrolyte (grey) and cathode (red).

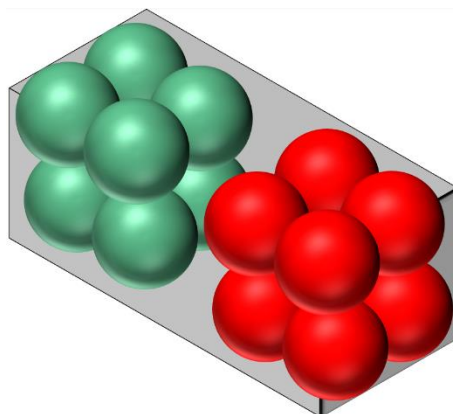


Figure S2: Simplified 3D geometry, where the different colours represent the anode (green), electrolyte (grey) and cathode (red).

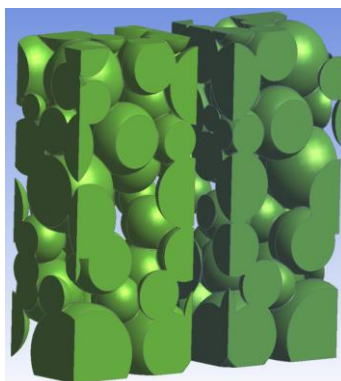


Figure S3: Visualization of the realistic 3D geometry: the electrodes are composed of particles with an average $R_{p,av} = 5 \mu\text{m}$ located $10\mu\text{m}$ away from each other.

Hemp fibers modified with graphite oxide as a sustainable system for removal of cationic dyes from wastewaters

Elena Lamberti^{1*}, Gianluca Viscusi¹, Giuliana Gorrasi¹

¹Department of Industrial Engineering, University of Salerno, Via Giovanni Paolo II, 132, 84084, Fisciano (SA), Italy

*Corresponding author E-Mail: ellamberti@unisa.it

1. Introduction

Nowadays, the presence of synthetic dyes in industrial effluents is leading to environmental concerns due to the impact of such contaminants on ecosystems and human health [1,2]. Dyes are substances used in many industrial fields [3]. Among all, methylene blue is a cationic dye with high water solubility. Many methods have already been applied to remove synthetic dyes from industrial wastewaters [4]. Adsorption process is the most used one since its technological simplicity, low cost and wide availability of adsorbents [5]. The use of common sorbents and their regeneration could noticeably increase the cost of the adsorption process [6]. In our case, in an effort to address the need to develop more sustainable biomaterial-based sorbents, modified and engineered hemp fibers are fabricated to be a versatile class of sorbents. The use of hemp fiberboards will allow to easily handle the adsorbent facilitating the desorption and reusability processes and limiting, in this way, the operating costs.

2. Methods

Low density hemp fiberboards (HF) were supplied by Nafco Company (Naples). (3-Aminopropyl)triethoxysilane (APTES), NaOH in pellet form, HCl solution 37% v/v, graphite oxide (GO) and methylene blue (MB) were used as reagents.

Scanning electron microscopy (SEM) was adopted to investigate the hemp fibers morphology. Before the analysis, hemp fabric samples (0.25*0.25 cm²) were covered with a thin film of gold by sputtering. Images were acquired by a Quanta 200 F microscope, working in high-vacuum mode.

Fourier transform infrared (FTIR) analysis was performed using a Bruker spectrometer model Vertex 70 (average of 64 scans, resolution of 4 cm⁻¹). The spectra were normalized taking as reference the peak absorbance at 1054 cm⁻¹ (=C–CO/C–C stretching vibration) [7].

Point of zero charge (pH_{PZC}) was evaluated as reported hereinafter. The point of zero charge (PZC) is the pH of the solution at which the net surface charge is zero. An initial solution of NaNO₃ (0.1 M) was prepared. An aliquot of 40 mL of NaNO₃ solution (0.1 M) was collected in ten flasks. The pH was set from 3 to 12 by using HCl (1 M) and NaOH (1 M) solutions. Then, a fixed amount of adsorbent was placed inside the flasks, shaken for 24 h, at room T and 350 rpm. After that, the solid adsorbent was removed and the final pH (pH_f) was evaluated by using a pH-meter (Crison-pH-Burette 24 1S). The change in pH was calculated and a plot of ΔpH versus the initial pH (pH_i) was obtained from the experimental data. The pH_{PZC} was easily estimated by the intercept on x-axis of the curve.

Adsorption tests, in batch process, were carried out. Dye solutions were prepared by dissolving MB in distilled water, in order to obtain three solutions at concentrations of 5 mg/L, 20 mg/L and 35 mg/L. Then, a pre-weighed amount of adsorbent was immersed in MB solution. The adsorption dosage was fixed at 10 g/L. The pH of the MB solutions was adjusted by adding NaOH (1 M) or HCl (1 M) solutions. The adsorption tests were carried out in batch conditions by shaking the samples at set temperature for 24 h. The concentration of MB in the solution was then calculated through UV–Vis technique by taking the absorbance at 664 nm which refers to the maximum absorption wavelength of methylene blue.

Desorption studies were carried out by agitating the used HF/GO adsorbent with ethanol (40 mL) for 4 h at 350 rpm. The adsorbent was then dried at 100 °C for 8 h. After that, the regenerated adsorbent was ready to be further used for adsorption tests.

For examining the probability of leaching out of GO from adsorbent surface, 0.04 g were immersed in 50 mL of distillate water at pH = 7 and room temperature. The release of GO into the solution was measured after 1 h, 5 h, 10 h, 24 h and 5 days through UV–Vis technique by taking the absorbance at 230 nm.

3. Results and discussion

The use of hemp fibers modified with graphite oxide for the removal of methylene blue from aqueous solutions was investigated. SEM micrographs of untreated HF and HF modified with GO. After GO treatment, hemp fiber surface still keeps its morphology.

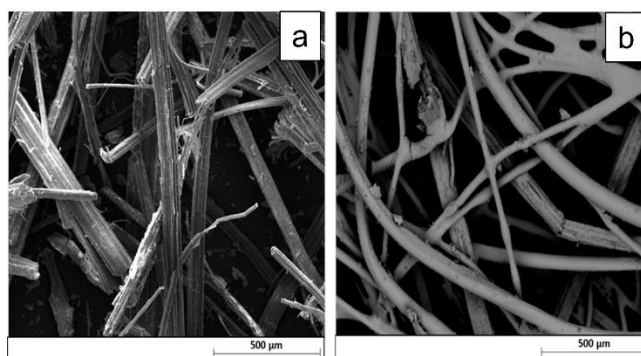


Figure 1. SEM micrographs of a) HF and b) HF/GO

Figure 2a reports the FTIR spectra of untreated hemp fiberboards and GO treated ones. Regarding the not modified HF, the IR region 3000 cm^{-1} - 3600 cm^{-1} is indicative of hydroxyl groups (OH) in polysaccharides. In the HF/GO IR-spectrum, the C=O carbonyl stretching at 1728 cm^{-1} and the C–O epoxide group stretching at 1229 and 1061, 1036 cm^{-1} are observed. Finally, the peak at 1625 cm^{-1} can be associated to the sp^2 character of C=C functional groups. The results mentioned above indicated the effective deposition of GO onto the surface of hemp fibers. To further prove that, the peaks belonging to OH broad band (3600 - 3000 cm^{-1}) are analyzed by applying a deconvolution algorithm followed by a curve fitting procedure (Figure 2b and 2c).

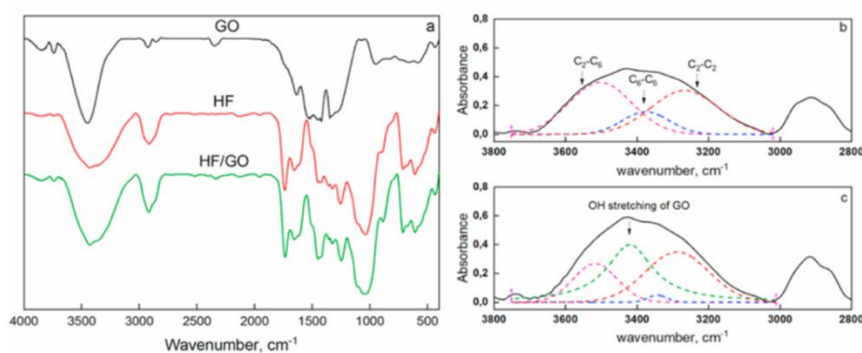


Figure 2. FTIR spectra of untreated and GO treated hemp fiberboards; b and c) FTIR deconvoluted spectra of untreated and GO treated hemp fiberboards.

Parameters such as contact time, pH, temperature and initial concentration of dye were varied and their effects on the adsorption recovery were evaluated.

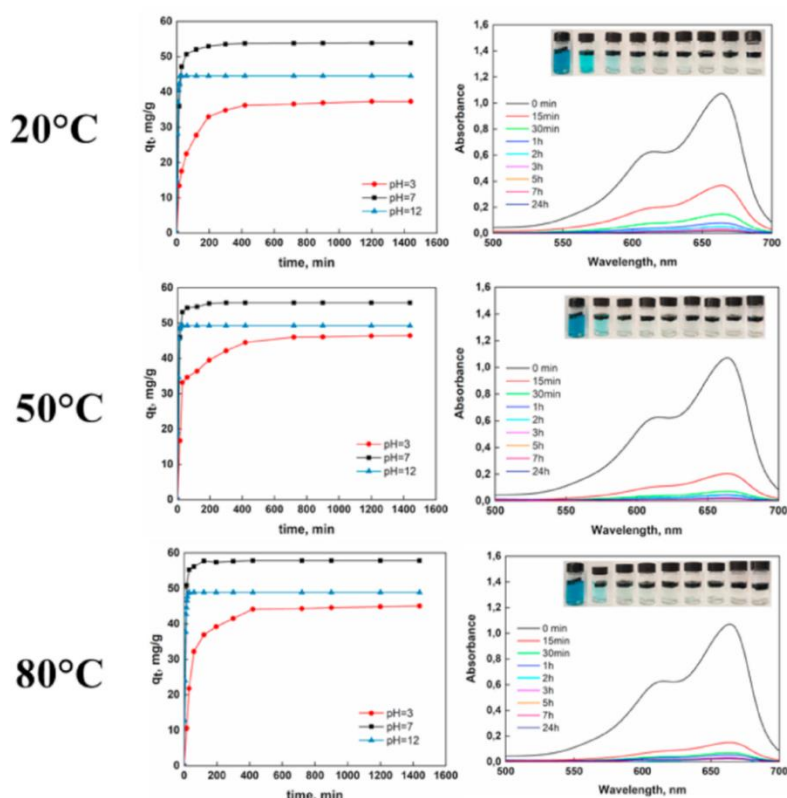


Figure 3. q_t versus t for adsorption of MB at different temperatures and different pH. On the right side, UV-Vis spectra variations as function of contact time are present

The adsorption process attained the equilibrium within 30 minutes while the adsorption capacity was found to increase with increasing contact time. Maximum adsorption capacity slightly increases with temperature indicating that the process is slightly endothermic ($\Delta H=3.43$ KJ/mol). The amount of dye was found to be highly dependent on pH regime, initial concentration of dye and slightly dependent on temperature. The pH level has important bearing on adsorption content indicating that weak electrostatic interactions could exist between cationic dye and electron rich sites of surface. Regeneration studies showed 5% drop in adsorption capacity after 7 cycles. A mathematical algorithm was applied to individuate the optimal set of process parameters (pH=9.25, $T=53.8^\circ\text{C}$ and $C_0=13.2$ mg/L) which maximizes the removal capacity.

4. Conclusions

The present study concerns the use of an agro-based waste material, such as hemp fibers, modified with graphite oxide as an innovative and sustainable adsorbent for the removal of organic dye from aqueous solutions. Effect of temperature, sorbate concentration and pH on adsorption was investigated. The produced adsorbent is chemically stable, showing no noticeable leaching of GO. It follows that hemp fibers modified with carbons could be used as an easily available adsorbent. So, it is raising up as an alternative for costlier adsorbent materials used in wastewater treatment processes.

References

Bibliography

- [1] Guo R, Wilson LD. Synthetically engineered chitosan-based materials and their sorption properties with methylene blue in aqueous solution. *J Colloid Interface Sci* 2012;388:225–34. <https://doi.org/10.1016/j.jcis.2012.08.010>.
- [2] Renita AA, Vardhan KH, Kumar PS, Ngueagni PT, Abilarasu A, Nath S, et al. Effective removal of malachite green dye from aqueous solution in hybrid system utilizing agricultural waste as particle electrodes. *Chemosphere* 2021;273:129634. <https://doi.org/10.1016/j.chemosphere.2021.129634>.

- [3] Crini G, Torri G, Lichtfouse E, Kyzas GZ, Wilson LD, Morin-Crini N. Dye removal by biosorption using cross-linked chitosan-based hydrogels. *Environ Chem Lett* 2019;17:1645–66. <https://doi.org/10.1007/s10311-019-00903-y>.
- [4] Forgacs E, Cserháti T, Oros G. Removal of synthetic dyes from wastewaters: A review. *Environ Int* 2004;30:953–71. <https://doi.org/10.1016/j.envint.2004.02.001>.
- [5] Bhattacharya KG, Sharma A. Kinetics and thermodynamics of Methylene Blue adsorption on Neem (*Azadirachta indica*) leaf powder. *Dye Pigment* 2005;65:51–9. <https://doi.org/10.1016/j.dyepig.2004.06.016>.
- [6] Sarioglu M, Atay ÜA, Sarioglu M, Atay UA. Removal of methylene blue by using biosolid. vol. 8. 2006.
- [7] Das M, Chakraborty D. Influence of alkali treatment on the fine structure and morphology of bamboo fibers. *J Appl Polym Sci* 2006;102:5050–6. <https://doi.org/10.1002/app.25105>.

Understanding the role of imidazolium-based ionic liquids in the electrochemical CO₂ reduction reaction: an experimental and theoretical study

Alessia Fortunati¹, María José Rubio¹, Boyan Iliev², Thomas J.S. Schubert², Francesca Risplendi¹, Michele Re Fiorentin¹, Giancarlo Cicero¹, Nunzio Russo¹, Simelys Hernández^{1*}

¹ Department of Applied Science and Technology, Politecnico di Torino, Corso Duca degli Abruzzi 24, 10129, Turin, Italy

² Iolitec Ionic Liquids technologies GmbH, Im Zukunftspark 9, 74076 Heilbronn, German

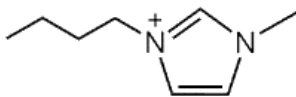

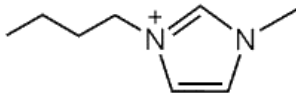
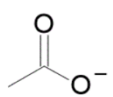
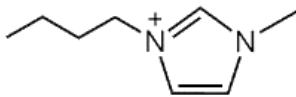
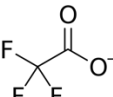
*Simelys Hernández (simelys.hernandez@polito.it); Alessia Fortunati (alessia.fortunati@polito.it)

1. Introduction

The exponential increase in the concentration of greenhouse gases in the atmosphere is considered as one of the most important reasons for climate change. Carbon dioxide is the most significant anthropogenic gas that contributes to global warming. CO₂ capture and storage (CCS) has been proposed as one of the most important strategies to mitigate CO₂ emissions. Moreover, conversion of carbon dioxide into energy-rich chemicals is a viable approach to reduce the global carbon footprint. The most common techniques to remove CO₂ from industrial gas streams are the chemical and physical absorption by liquid solvents. Traditionally, aqueous amine solutions have been used as chemical solvents because of their high selectivity, high reactivity and low price. Unfortunately, they also present many disadvantages associated with the high energy demand required for the solvent regeneration, corrosion issues and loss of solvent because of their high volatility. Hence, in the need to find more efficient solvents for CO₂ capture and conversion, Ionic Liquids (ILs) have been highlighted as very good alternatives to the common amine solutions.[1] Within this field lies this research, which in turn is part of a much broader European project called SunCoChem. For this project we are testing the stability and performance of various ionic liquids, provided by Iolitec Ionic Liquids technologies GMBH, and, in particular, their ability to capture and favor the electrochemical conversion of a pure CO₂ stream to CO with high efficiencies.

2. Methods

The electrochemical (EC) studies were performed by using ionic liquids made of imidazolium salts. The ILs listed in Table 1 were supplied by IOLITEC GmbH (high purity grade, >99%) and used without any further purification.

Ionic Liquid	Abbreviation	Cation	Anion
1-Butyl-3-Methylimidazolium Tetrafluoroborate	[BMIM][BF ₄]		
1-Butyl-3-Methylimidazolium Acetate	[BMIM][CO ₂ CH ₃]		
1-Butyl-3-Methylimidazolium Triflate	[BMIM][SO ₃ CF ₃]		

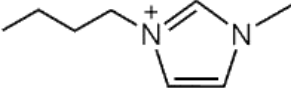
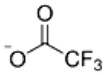
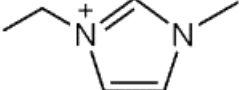
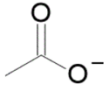
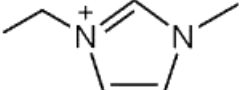
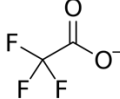
1-Butyl-3-Methylimidazolium Trifluoroacetate	[BMIM][CO ₂ CF ₃]		
1-Ethyl-3-Methylimidazolium Acetate	[EMIM][CO ₂ CH ₃]		
1-Ethyl-3-Methylimidazolium Triflate	[EMIM][SO ₃ CF ₃]		

Table 1: Ionic liquids investigated.

The experimental setup is described in Figure 1. The EC CO₂ reduction tests with each IL-based electrolyte were done in a two-compartment H-type cell. The cell used for the experiment and all other glassware were cleaned by several rinsing ultrasonicated cycles with Milli-Q water ($R > 18.2 \text{ M}\Omega$, 25°C) and dried with nitrogen stream. The cathodic chamber contained the working (Ag Foil, active area of 3 cm^2) and reference (Ag/AgCl) electrodes, which were immersed in a solution of the ionic liquids in an organic solvent ([IL]=0.3M in Acetonitrile, ACN). Due to their high viscosity, ionic liquids are often mixed with organic solvents or water.[2] Because of the low CO₂ solubility and the competitive hydrogen evolution reaction (HER), aqueous solutions are not favorable for the CO₂ conversion. It has been reported in the literature that ACN is a highly suitable organic solvent for the electro-reduction of CO₂ since, in addition to increasing the conductivity and decreasing the viscosity of the imidazole salts, the CO₂ solubility in it is eight times greater than in water. [3] In the anodic chamber there was a platinum mesh, used as counter electrode, immersed in a solution of strong electrolyte, such as KOH 0.1M. A very conductive aqueous solution helps an effective passage of current. [4],[5] A solution of potassium hydroxide was chosen as anodic electrolyte because of its properties such as high conductivity, that affect the total current density of the system. The cell chambers were separated by a commercial bipolar membrane (BM) (Fumasep FBM - Bipolar Membrane by Fumatech). The BM consists of an anion exchange layer (AEL), and a cation exchange layer (CEL) facing the anode and cathode compartments of the cell, respectively. At the interface between the AEL and CEL, water dissociates into OH⁻ and H⁺ ions. This configuration prevents the mixing of the chamber contents and avoids further oxidation of the formed CO₂ reduction products.

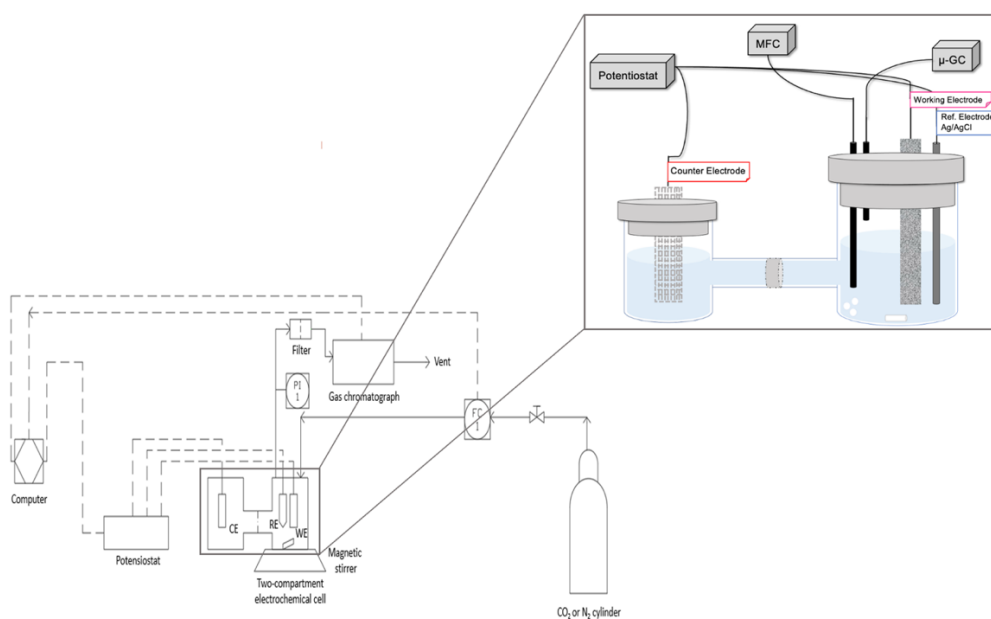


Figure 1: Set-up scheme for the EC CO₂RR with IL-based electrolytes.

3. Results and discussion

The ILs tested so far have a cationic part based on imidazole, which is expected to stabilize and lower the activation energy for the reduction of CO₂, namely [BMIM][BF₄], [BMIM][CH₃CO₂], [BMIM][CF₃CO₂] and [BMIM][CF₃SO₃]. This trend was confirmed by a shift to more positive potentials of the onset for the CO₂ reduction reaction in the presence of these Ionic Liquids. Our results evidence relevant current density values, a good stability during chronopotentiometry (CP) tests and a high selectivity towards the target product: CO, which however changes depending on the used IL.

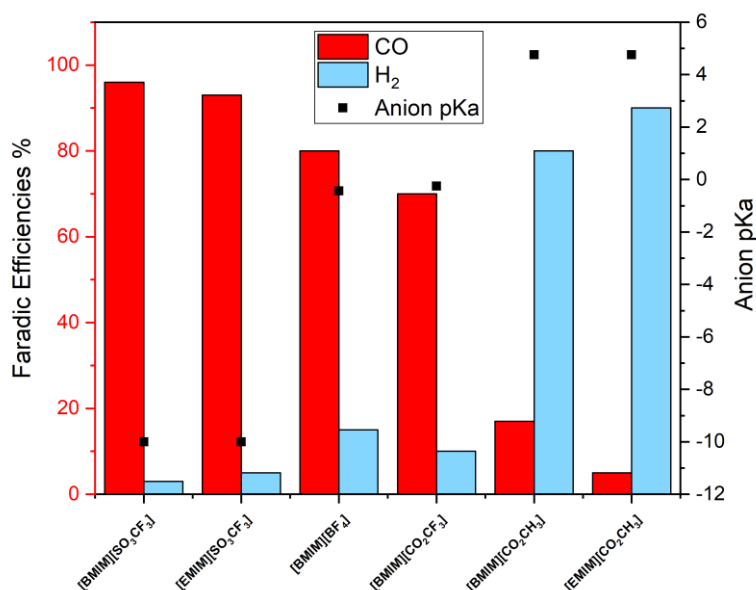


Figure 2: Bar graph summarizing faradic efficiency values of the gaseous products of CO₂ ECR for six different ionic liquid. The faradic efficiencies are also compared with the pKa IL anion. The pKa values refer to the respective acid of the conjugate base, which in this work is assumed to be the anion of the IL.

In fact, by analyzing the faradic efficiencies an interesting CO production was verified, mostly considering [SO₃CF₃] salts. In that case, a high amount of carbon monoxide (FE% ~ 90%) and a low amount of hydrogen (FE% ~ 5%) were evidenced. In the case of the acetate anion, a very low amount of CO was collected. Moreover, a correlation between the CO or H₂ productions and the pKb values of the anions was found. Acetate salts have the highest pKb value and the highest H₂ selective production, while triflate salts have the lowest pKb value and the highest CO selective production.

A more in-depth study by means of Density Functional Theory (DFT) allowed to confirm the experimental hypotheses. Deprotonated EMIM and BMIM in presence of acetate, are found to strongly chemisorb on the Ag electrode surface and to spontaneously capture the CO₂ molecule, thus hindering its reduction. The reaction mechanisms of CO₂ reduction in presence of the cation of the ionic liquid have been investigated and a dependence on the length of the alkyl chain linked to the imidazole ring and on the type of counterion present in the ionic liquid has been observed.

4. Conclusions

Different imidazolium salts were tested as electrolytes for the electrocatalytic CO₂ conversion to CO: 0.3M solutions of ILs in acetonitrile were used to reduce the viscosity of the pure compounds. Acetonitrile was chosen as solvent thanks to its ability to solubilize ILs, its lower molecular weight than most organic solvents that guarantees high conductivity and low viscosity. Moreover, non-aqueous solutions were used as catholyte

to limit the hydrolysis of hydrolytically unstable fluorinated-based anion and the consequent HF production. The anionic part of imidazolium salts influences the CO₂ solubility, and the cationic part plays mainly a role in stabilizing the reaction intermediates and determines a lowering of the activation energy for CO₂RR. Imidazolium salts of acetate are more selective towards the production of H₂ given their large binding energy with the electrode surface and the ability to form a carboxylated species. [SO₃CF₃] salts promote CO₂RR better than the commonly used [BMIM][BF₄] in terms of onset potential and FE% to CO. Acetate salts are more selective towards the production of H₂ than CO, which supports the fact that the CO₂ reduction reaction depends also on the type of anion in ionic liquids.

5. Acknowledgment

The research leading to these results has received funding from the European Union's Horizon 2020 Research and Innovation Action programme under the SunCoChem project (Grant Agreement No 862192).

References

- [1] S. Sarmad, J. P. Mikkola, and X. Ji, "Carbon Dioxide Capture with Ionic Liquids and Deep Eutectic Solvents: A New Generation of Sorbents," *ChemSusChem*, vol. 10, no. 2, 2017, doi: 10.1002/cssc.201600987.
- [2] T. R. Anderson, E. Hawkins, and P. D. Jones, "CO₂, the greenhouse effect and global warming: from the pioneering work of Arrhenius and Callendar to today's Earth System Models," *Endeavour*, vol. 40, no. 3, pp. 178–187, 2016, doi: 10.1016/j.endeavour.2016.07.002.
- [3] I. Ganesh, "BMIM-BF₄ Mediated Electrochemical CO₂ Reduction to CO Is a Reverse Reaction of CO Oxidation in Air - Experimental Evidence," *J. Phys. Chem. C*, vol. 123, no. 50, pp. 30198–30212, 2019, doi: 10.1021/acs.jpcc.9b09819.
- [4] J. Feng, S. Zeng, J. Feng, H. Dong, and X. Zhang, "CO₂ Electroreduction in Ionic Liquids: A Review," *Chinese J. Chem.*, vol. 36, no. 10, pp. 961–970, 2018, doi: 10.1002/cjoc.201800252.
- [5] N. J. Firet and W. A. Smith, "Probing the Reaction Mechanism of CO₂ Electroreduction over Ag Films via Operando Infrared Spectroscopy," *ACS Catal.*, vol. 7, no. 1, pp. 606–612, 2017, doi: 10.1021/acscatal.6b02382.

Production of acidic and alkaline solutions via Electrodialysis with bipolar membranes from synthetic and real brines from saltworks

Antonia Filingeri¹, Andrea Culcasi¹, Andrea Cipollina^{1*}, Alessandro Tamburini^{1,2}, Giorgio Micale¹

¹ Dipartimento di Ingegneria, Università degli Studi di Palermo - viale delle Scienze Ed.6, 90128 Palermo, Italy;

² ResourSEAs SrL, viale delle Scienze Ed.16, 90128 Palermo

*Corresponding author E-Mail: andrea.cipollina@unipa.it

1. Introduction

In recent decades, there has been a great deal of interest at both the industrial and academic levels in identifying unconventional sources for chemical production and raw material recovery. In this context, brine disposal, which was previously addressed as a priority to reduce environmental problems, is now seen as an opportunity to apply new or existing technologies in circular processes that allow for the valorization of previously considered waste solutions [1]. In this regard, Electrodialysis with bipolar membranes (EDBM) can be used to produce acidic and alkaline solutions from salty solutions. EDBM is an electro-membrane process distinguished by the alternated position of Ion Exchange Membranes (IEMs) for selective ion separation and the use of bipolar membranes that allow water dissociation [2]. In this work, a novel application of EDBM was proposed to valorize the remaining brine provided by the saltworks, which is typically returned to the sea despite being a highly concentrated solution (i.e., 20–40 times more concentrated than seawater). In more detail, an EDBM unit was tested for the first time with (i) synthetic and (ii) real brines from Trapani's saltworks (Italy), which had previously been treated for mineral recovery.

2. Methods

A laboratory-scale EDBM unit, supplied by SUEZ-WTS France®, was equipped with 5 triplets of commercial IEMs (0.028 m² of membrane active area). Closed-loop tests (see Figure 1) were carried out at constant current (typically 100-300 A m⁻²) and for a time duration sufficient to achieve a target NaOH concentration of 1M in the base compartment. Tests with various compositions were carried out in the salt compartment: (i) a reference case with pure NaCl solutions, (ii) synthetic brines containing NaCl, Na₂SO₄, and KCl, and (iii) real bitterns, containing traces of other minor elements. The initial composition of the feeds was assumed to be variable between several scenarios in the ranges reported in Table 1 in order to analyze the effect of different feeds in the process performance and acid and base solutions purities. Specific energy consumption, current efficiency, yield, and products purities were evaluated as performance indicators.

Table 1. Initial composition of the feeds for closed-loop experiments.

	Salt compartment			Base compartment	Acid compartment
	Pure NaCl solutions	Synthetic brines	Real brines		
NaCl	1-3 M	0.5-4 M	0.5-4 M	0-4 M	0-4 M
Na ₂ SO ₄	-	0.1-1.2 M	0.1-1.2 M	0.1-1.2	0.1-1.2
KCl	-	0.1-0.7 M	0.1-0.7 M	0.1-0.7 M	0.1-0.7 M
HCl	-	-	-	-	0-0.05 M
NaOH	-	-	-	0-0.05 M	-
Other elements	-	-	traces	-	-

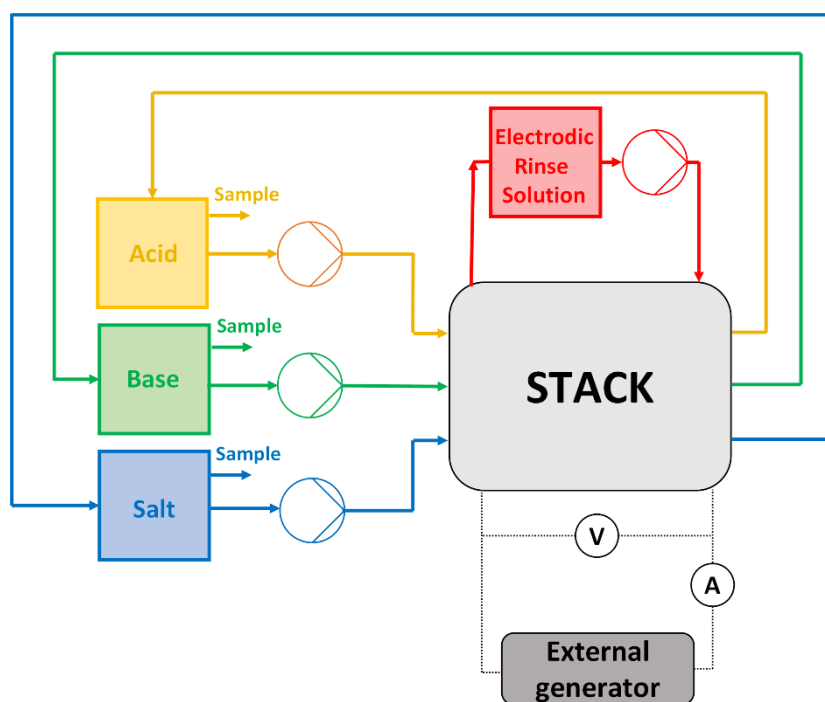


Figure 1. Closed-loop (batch) experimental configuration (adapted from [2]).

3. Results and discussion

For tests performed at the highest current density, the target concentration of 1M of NaOH for the alkaline solution was reached after ~45 minutes. Specific energy consumptions (SEC) of $\sim 2.4 \text{ kWh kg}^{-1}_{\text{NaOH}}$ were obtained at the target condition with pure NaCl solutions in the salt compartment at an initial concentration of 2M, whereas the use of a more concentrated synthetic brine reduced SECs to values less than $2 \text{ kWh kg}^{-1}_{\text{NaOH}}$. Current efficiency as a function of time showed a decreasing trend, but it remained relatively high (in the ~70-80% range) at the end of the test. In the case of ion mixtures, purities of ~90% were obtained in acid and base compartments, respectively.

4. Conclusions

A new application of EDBM for the valorization of highly concentrated brines from the saltworks process was proposed. The results obtained at laboratory-scale unit demonstrated the feasibility of the process for producing chemicals, specifically HCl and NaOH solutions, as an alternative to brine disposal. The process could then be tested at the pilot scale with long-run tests to determine its scalability at the industrial level.

Acknowledgements

This project has received funding from the European Union's Horizon 2020 research and innovation programme under Grant Agreement No. 869467 (SEArCularMINE). This output reflects only the author's view. The European Health and Digital Executive Agency (HaDEA) and the European Commission cannot be held responsible for any use that may be made of the information contained therein.

References

- [1] A. Panagopoulos, K.J. Haralambous, M. Loizidou, Desalination brine disposal methods and treatment technologies - A review, *Sci. Total Environ.* 693 (2019) 133545. <https://doi.org/10.1016/j.scitotenv.2019.07.351>.
- [2] Culcasi, A., Gurreri, L., Cipollina, A., Tamburini, A., & Micale, G. (2022). A comprehensive multi-scale model for bipolar membrane electrodialysis (BMED). *Chemical Engineering Journal*, 437(P1), 135317. <https://doi.org/10.1016/j.cej.2022.135317>

An application of Reverse ElectroDialysis: energy production from produced water.

Giovanni Campisi¹, Alessandro Cosenza¹, Andrea Cipollina¹, Alessandro Tamburini^{1*}, Giorgio Micale¹.

¹ Dipartimento di Ingegneria, Università degli Studi di Palermo, Viale delle Scienze ed.6, 90128 Palermo, Italy

*Corresponding author E-Mail: alessandro.tamburini@unipa.it

1. Introduction

Produced water (PW) is extracted from crude oil and represents the main waste in oil industry. The volumes of water extracted are prominent: approximately, for each barrel of crude oil drilled, 3-4 barrels of produced water come up on average [1]. With the continuous increasing demand of fuel, these volumes are going to increase and it is everyday more relevant to find a way to valorize or at least treat them in an efficient and sustainable way. These wastewaters are characterized by a large concentration of dissolved salts, up to 300.000 ppm [1] and by a high level of contamination especially with dangerous organic compounds, like hydrocarbons (included BTEX, PAHs and phenols, harmful for the environment). For the first time, Reverse ElectroDialysis (RED), an emerging salinity gradient power technology, is proposed, as method to harvest energy from these wastewaters, thus valorizing them. Furthermore, since the RED technology converts the salinity gradient in electrical energy by mixing two solutions with different salinity, the reduction of concentration in the PW could ease a subsequent treatment process.

2. Methods

A RED unit (stack) is constituted by the repetitions of ionic exchange membranes (IEMs) separated by spacers (that create the diluted and concentrated compartments) [2]. These repetitive units (cell-pairs) are stacked between two end electrode plates (situ of redox reactions), which are externally connected to an electric circuit. Electrode compartments and red-ox reactions are used to convert the ionic flux generated in the unit into electrons flux flowing in the external circuit when an external load is connected. In the present experimental campaign, a real PW (filtered through a 5 μm cartridge filter), with a conductivity of 104.5 mS/cm (corresponding to a total salinity of 74g/l) was used as concentrated feed solution (H). Conversely, the diluted solution (L) is a synthetic solution of 0.73 g/l of NaCl and demineralized water. A *Feed and Bleed* system was used in order to keep the concentration of both solutions constant. According to this operation mode, the lab scale unit can be considered as representative of a small section of an industrial scale unit fed always with the same feed. The features of the investigated system are presented in *Table 1* a simplified layout of the experimental set-up is shown in *Figure 1*.

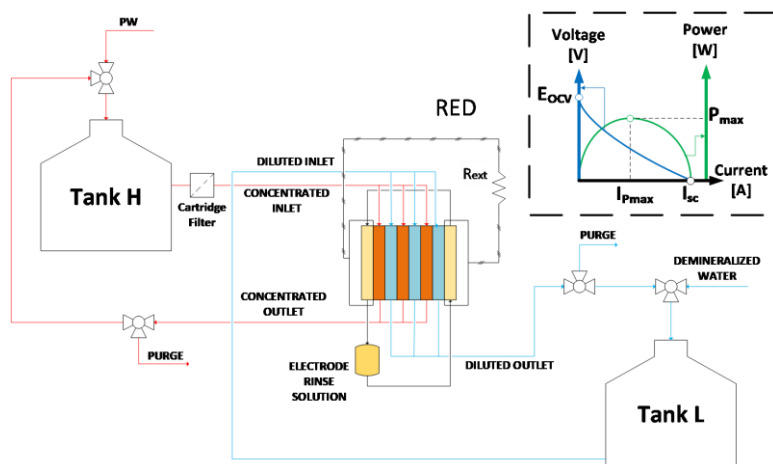


Figure 1. Block flow diagram of the experimental set-up.

Features	
Membrane	Fujifilm Type10
N_{cp} no. cell pair	10
A_m active membrane area	100 cm ²
δ_{sp} spacers width	300 μm
v_H, v_L feed velocity	0.5 cm/s
σ_{Hin} concentrated initial conductivity	104.4 mS/cm
σ_{Lin} diluted initial conductivity	1.49 mS/cm
R_{load} external load	6.8 Ω

Table 1. Reverse ElectroDialysis data.

The experimental test lasted 15 days during which solution conductivities, pressure drops, voltage and current were recorded. The characteristic quantities as power density [3] and specific energy provided by RED can be calculated as shown by equations (1), (2) and (3):

Gross power density $P_d = \frac{E_{stack} \cdot I_{stack}}{N_{cp} \cdot A_m}$ (1)

Specific Energy $E_{sp} = \frac{1}{H_{treated}} \int_{t=0}^t E_{stack} \cdot I_{stack} dt$ (2)

Net power density $P_{d,net} = P_d - P_{d,loss} = P_d - \frac{H \cdot \Delta P_H - L \cdot \Delta P_L}{N_{cp} \cdot A_m}$ (3)

where E_{stack} and I_{stack} are the voltage and current experimentally measured in the stack, H and L are the volumetric flow rate of concentrated and diluted solutions, ΔP is the pressure drop inside the unit channels and $H_{treated}$ is the total volume of PW treated during the entire duration (t) of the test. During the test, in order to counteract the effects of fouling, a maintenance operation was carried out, consisting of a physical and a chemical wash of the unit. In fact, the physical wash is expected to remove the particles that could obstruct the unit channels, meanwhile a treatment with acid and alkaline (pH 3 and pH 11 respectively) solutions can act on scaling or on a deeper fouling as the biofouling.

3. Results and discussion

During the first 3 days, a transitory is observed, due to the dilution of the PW from 104.4 to 74.4 mS/cm and to the conditioning of the membranes to the feed conditions. As shown in *figure 2*, taking off the first 3 days, the gross power density is mostly constant for the entire test, presenting a pick of about 1.02 W/m². Fouling phenomena occurred during the test, caused an increase of the pressure drops inside the RED unit, for this reason the net power density decreased with time. After the 15th day, the test was interrupted because the net power density became negative and no more energy would have been produced. The main fouling phenomenon observed was a physical clogging of the channel unit probably caused by the bacteria colonies growth inside the manifold.

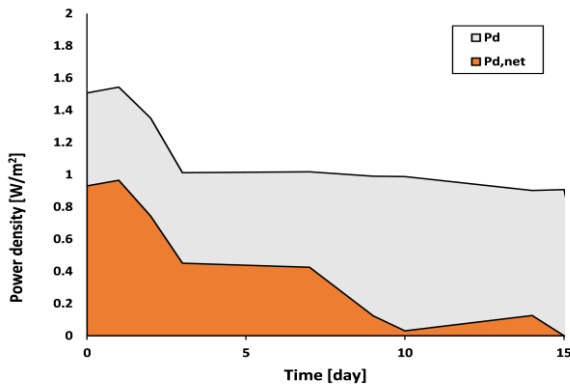


Figure 2. Power gross density (grey) and net power density (orange) trend during the test.

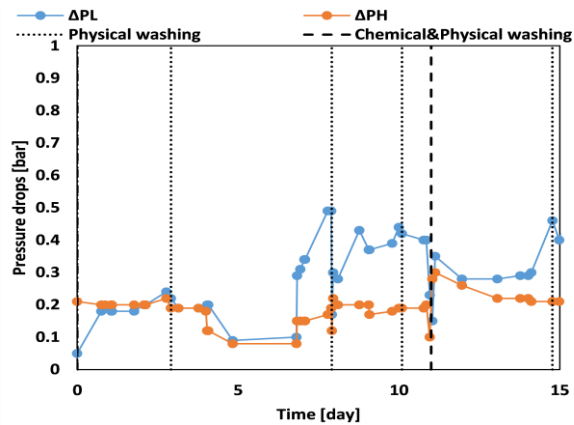


Figure 3. Pressure drops trend of diluted (L) and concentrated (H) compartments.

The area under the curve of *figure 2* represents the energy generated by the stack during the entire test. A specific energy (2) of 0.36 kWh/m³ was generated during the test, although the net specific energy (i.e. subtracting the pump energy requirement) is about 0.11 kWh/m³.

The vertical dashed lines in the graphs of *figure 3* indicate the moments when physical and chemical washings were performed. As it is possible to observe in the figure, the washings reduced the pressure drops and, once optimized, might have a positive effect on the system, allowing to increase the test duration.

4. Conclusions

PWs are an enormous problem in oil industry, but they might represent a resource for power production thanks to the RED technology. The preliminary results collected suggest that there is room for improvements and that suitable antifouling strategies should be set-up in order to allow a long operation at industrial scale.

References

- [1] Y. Liua, Hao Lu, Yudong Li, Hong Xu, Zhicheng Pan, Pinyi Dai, Hualin Wang, Qiang Yang, "A review of treatment technologies for produced water in offshore oil and gas fields" *Science of the Total Environment*, 775 (2021) 145485
- [2] J. Veerman, D.A. Vermaas, "Reverse electro dialysis: Fundamentals" in *Sustainable Energy from Salinity Gradients*; A. Cipollina.; G. Micale, Eds.; Woodhead Publishing, (2016) 77-134.

Simulation-based design of a bipolar membranes electro dialysis unit for chemicals production from brines.

Giovanni Virruso¹, Andrea Culcasi¹, Andrea Cipollina¹, Alessandro Tamburini^{1*}, Giorgio Micale¹

1 Dipartimento di Ingegneria, Università degli studi di Palermo (UNIPA) – Viale delle Scienze, Ed 6, 90128 Palermo, Italy;

**Corresponding author E-Mail: alessandro.tamburini@unipa.it*

1. Introduction

Nowadays environmental concerns are modifying the production and consumption patterns used so far. An important objective to improve our society is the use of sustainable processes that can reduce industrial waste streams. Bipolar membranes electro dialysis (EDBM) is an emerging environmentally friendly process that could be easily integrated into a circular economy approach to valorize waste brines. It is an electro-membrane process that allows the production of chemicals using only water, electrical energy and a salty solution. When electric current is applied to the electrodes of the EDBM stack, water dissociation takes place in the bipolar membranes. Therefore, the ions from water are combined with those coming from the salt generating acid and base. The increasing interest in the EDBM process requires appropriate design procedures. This study proposed a simulation-based design of a EDBM unit for the production of hydrochloric acid and sodium hydroxide from sodium chloride solution. The design was performed in terms of configuration and operational conditions. A model, realized by Culcasi et al. [1], was used to describe the EDBM process's behaviour. This model was validated with experimental data so that a high quality design could be achieved. This procedure was used to design a EDBM unit that will be part of the demo-plant of the Horizon 2020 Water-Mining project.

2. Methods

To properly design the EDBM unit it is important to define the initial conditions of the process, in terms of concentrations and volumes of the of the three solutions (acid, base, salt) fed to the EDBM unit and the target concentration at which stops the process. Then, it is important to select a specific type of membranes and spacers with dimensions appropriate to the scale of the process. To take into account the resistance of the electrode compartments, the Blank resistance is needed; this could be calculated in the laboratory or taken from literature. It is also necessary to define some configurations that will be investigated to find out which is the most appropriate. The procedure uses only three performance parameters: process time, Specific Energy Consumption (SEC) and Specific Production (SP). These three parameters will be monitored in the simulations of the selected configurations and then used to select which is the best. The SEC is the energy consumed to produce 1 kg of the target product and it is expressed in kWh/kg . The SP is the flowrate of target product produced by one triplet with a unit membrane area and it is expressed in $kg/(h m^2_{triplet})$.

The EDBM unit of the Water-Mining will be operated in closed-loop (batch way) in order to reach high concentration of electrolyte solutions. The initial conditions of the three solutions fed to EDBM unit and the target that we want to reach at the end of the process are reported in Table 1.

Table 1. Initial conditions of the three solutions fed to the EDBM unit and target that we want to reach at the end of the process.

<i>Solution</i>	V_0 [m ³]	$C_{0,NaCl}$ [mol/l]	$C_{0,NaOH}$ [mol/l]	$C_{0,HCl}$ [mol/l]	$Target_{NaOH}$ [mol/l]
<i>Acid</i>	0,5	0,01	-	0,02	-
<i>Salt</i>	0,5	2	-	0,01	-
<i>Base</i>	0,5	0,01	0,02	-	1

The membranes selected for this EDBM unit are fumasep® FAB, FKB, FBM as anionic, cationic and bipolar membrane respectively. Six different configurations were selected with a total number of triplets that ranges from 20 to 60 that could be disposed in one or two different stacks arranged in a parallel way. The configurations were simulated at three different current densities, 200, 400, 600 A/m².

3. Results and discussion

The results of the simulations are reported in Figure 1. With the same total number of triplets, the time reduces if two stacks in parallel are used. The SEC, plotted as a function of the number of triplets in one stack, shows a trend with a minimum. The minimum always lies between 20 and 30 triplets in one stack. There is also an increase in the SEC with the increase of the current density. Focusing on the SEC, it is convenient to use a number of triplets that range between 20 and 30 in one stack and a low current densities. The SP shows a monotonous decreasing trend as the number of triplets in one stack increases; it also increases linearly with the current density. From the point of view of the SP, it is convenient to use a low number of triplets in one stack and a high current densities. Taking into account all these parameters, in order to minimize the time and the SEC and maximize the SP, the best configuration is that with a total number of triplets equal to 40, arranged in two stacks in parallel. This configuration needs to be operate at moderate current density (400 A/m²).

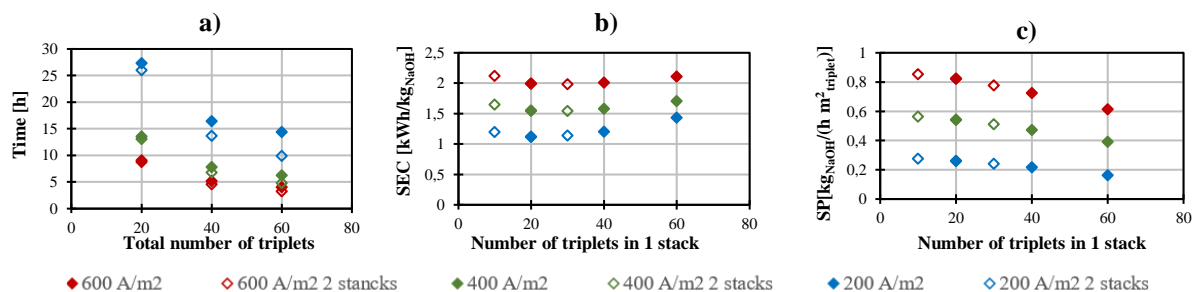


Figure 1. a) Process time, b) Specific energy consumption and c) Specific production for the configurations analyzed at three different current densities.

The procedure's results were compared to those obtained from a cost-of-production analysis of sodium hydroxide. The cost was calculated as the sum of CAPEX and OPEX. The analysis demonstrates which values of triplets number and current density minimize production cost. It was found that a number of triplets of 44 and a current density of 300 A/m² are the values that minimize the cost of sodium hydroxide production. It can be seen that those values are very similar to those obtained with the proposed procedure.

4. Conclusion

This work presented a procedure for designing an EDBM unit. The unit was simulated with a model that was validated with experimental data. Three important performance parameters, that take into account the main aspects of these units, were used to carry out the design. The results of the procedure were compared with those from a cost-of-production analysis, thus demonstrating the design's efficacy.

5. Acknowledgement

This project has received funding from the European Union's Horizon 2020 research and innovation program under Grant Agreement no. 869474 (WATER-MINING – Next generation water-smart management systems: large scale demonstrations for a circular economy and society). www.watermining.eu

References

- [1] A. Culcasi, L. Gurreri, A. Zaffora, A. Cosenza, A. Tamburini, G. Micale, On the modelling of an Acid/Base Flow Battery: An innovative electrical energy storage device based on pH and salinity gradients, *Applied Energy*. 277 (2020) 115576. <https://doi.org/10.1016/j.apenergy.2020.115576>.

Comprehensive steady state behavior modeling of polyelectrolyte hydrogels

Raffaella De Piano^{1*}, Diego Caccavo^{1,2}, Anna Angela Barba^{2,3}, Gaetano Lamberti^{1,2}

1 Department of Industrial Engineering, University of Salerno, Via Giovanni Paolo II, 132, 84084 Fisciano (SA), Italy; 2 EST Srl, University spin-off, <https://est.srl>, 83100 Avellino, Italy; 3 Department of Pharmacy, University of Salerno, Via Giovanni Paolo II, 132, 84084 Fisciano (SA), Italy

**Corresponding author E-Mail: rdepiano@unisa.it*

1. Introduction

Hydrogels are a class of polymeric material whose main characteristic is to absorb a large quantity of water and swell due to presence on their chains of hydrophilic groups such as -OH, -CONH, -CONH₂ [1, 2]. The huge family of hydrogels comprehends a particular category of them called smart hydrogels which are sensible to variation of the external stimuli such as mechanical forces, temperature, light or electric fields. In this class, particularly interesting are the so-called polyelectrolytes, long chained polymers characterized by the presence, on their chain, of ionizable groups. These groups lead the hydrogel to be sensible to variation of pH of the external surrounding since, changing the external conditions, they dissociate in a fixed part that remain on the chain and in a mobile part that goes in solution. These hydrogels are important in different fields from pharmaceutical to medical and polymeric applications. To fully understand the behavior relates to the hydrogel swelling, during years several mathematical models have been studied. Starting from the work of Caccavo et al. on the PoroViscoElastic behavior of neutral hydrogel[3-5], aim of this work is to extend the model to a polyelectrolyte in a steady state condition. In addition, to tune the model, a first series of experimental data has been obtained monitoring the swelling behavior of an anionic copolymer gel of Acrylamide in aqueous solution at different pH [6].

2. Methods

As regard the modeling part a monophasic approach, which relies on a strong thermodynamic basis, has been used. Starting from the dissipation inequality and using the Helmholtz Free Energy for polyelectrolytes the constitutive equations have been derived. The Helmholtz Free Energy in this case is formed by four terms: the one related to the elastic part, the one related to the mixing, and the terms related to the ionization and the dissociation of the charges. The system is formed by six variables (the deformation and the concentrations of the species together with the pressure) and so six equations are needed. The deformation and the pressure are calculated using the linear momentum balance and the volumetric constraint, while the concentrations are calculated considering the thermodynamic criterion for the phase equilibrium according to which when two phases are in equilibrium the chemical potential are equal. These equations are solved numerically through the software MATLAB R2020b.

To observe swelling phenomena under experimental point of view, an anionic copolymer gel of Acrylamide was prepared. In particular, a solution of Acrylamide (632 mM), N,N'-MethylenBis (Acrylamide) (8.6 mM), Sodium Acrylate (71.2 mM) were dispersed in 50 mL of solution, then Ammonium Persulfate (1.75 mM) and Sodium Betafisulfite (2.1 mM) were added as initiator and accelerator respectively. The solution was transferred into cylinders molds for 24 hours and then the original mass M_0 of each sample was determined. The degree of swelling was measured by soaking a sample of gel in 100 mL of solution of known pH. After equilibration for 48 h, the swollen gel was removed from the solution, drained and weighed. The swelling ratio was defined as the ratio of swollen mass, M , to the original mass M_0 . The measurements of each sample were performed in triplicate.

3. Results and discussion

The system is mainly based on five parameters: salt concentration, acidic dissociation constant, elastic modulus, number of ionizable groups and enthalpic Flory Huggins parameter. With the aim of understanding the mechanism of swelling of anionic hydrogels, a first parametric study, assuming a free swelling experiment, has been done. The general behavior of an anionic hydrogel is well described by the model in a range of pH from 1 to 7 together with the degree of ionization as depicted in the figure below:

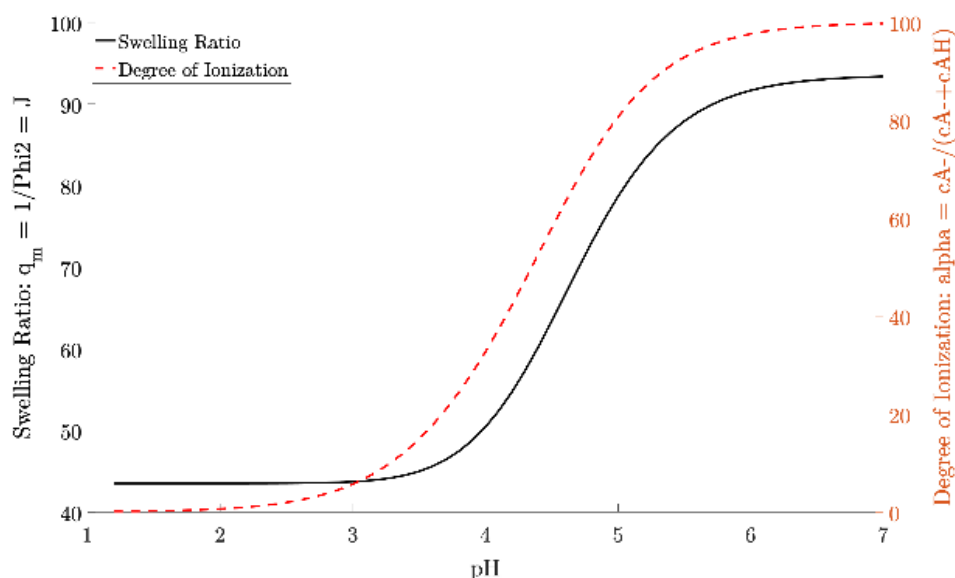


Figure 1. Swelling ratio and degree of ionization as a function of pH

As it can be seen from the Figure 1 the model describes a completely association of the charges and a lower swelling for lower pH, and a completely dissociation increasing the swelling of the matrix for higher pH, as also reported in literature.

Figure 2 shows the experimental data of the anionic gel at equilibrium in aqueous solutions at different pH, while the solid line represents the swelling curve obtained from the model fitting the parameters for the examined system.

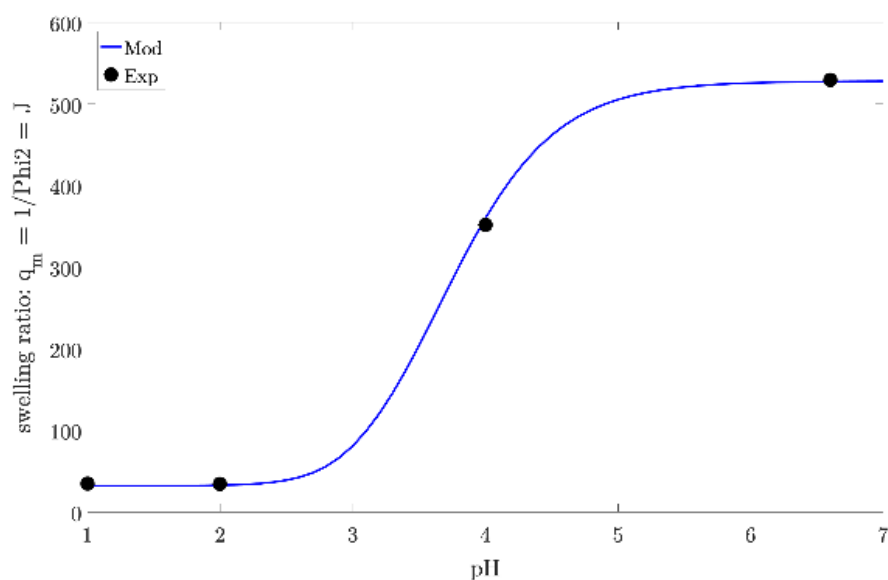


Figure 2. Comparison of model and experimental swelling data

4. Conclusions

Using a monophasic modeling approach the steady state behavior of polyelectrolyte was modeled. It was shown that, for a simple experiment, the system of equations to be solved is constituted by six equations. These equations were used to perform a study to understand the general behavior of the hydrogel. Furthermore, a first set of experimental data was obtained soaking hydrogels of known initial mass in solution at different pH and the behavior of the system is well described by the model. The proposed model can describe the general behavior of the hydrogel in a steady state condition and it could be seen as an important tool to develop a transient model, extending the description to unsteady state problems.

References

1. Peppas, N.A. and A.R. Khare, *Preparation, structure and diffusional behavior of hydrogels in controlled release*. *Advanced drug delivery reviews*, 1993. **11**(1-2): p. 1-35.
2. Flory, P.J., *Principles of polymer chemistry*. 1953: Cornell University Press.
3. Caccavo, D. and G. Lamberti, *PoroviscoElastic model to describe hydrogels' behavior*. *Materials Science and Engineering: C*, 2017. **76**: p. 102-113.
4. Caccavo, D., et al., *Modeling the modified drug release from curved shape drug delivery systems - Dome Matrix®*. *Eur J Pharm Biopharm*, 2017. **121**: p. 24-31.
5. De Piano, R., et al., *Drug release from hydrogel-based matrix systems partially coated: experiments and modeling*. *Journal of Drug Delivery Science and Technology*, 2021. **61**: p. 102146.
6. Vasheghani-Farahani, E., et al., *Swelling of ionic gels in electrolyte solutions*. *Industrial & engineering chemistry research*, 1990. **29**(4): p. 554-560.

Improved Electrochemical CO₂ reduction to C₂₊ Products on B-doped CuO catalysts

Hilmar Guzmán*, Daniela Roldán, Federica Zammillo, Nunzio Russo, Simelys Hernández*

Department of applied science and technology (DISAT), Politecnico di Torino

C.so Duca degli Abruzzi, 24, 1019, Turin, Italy

**e-mail: hilmar.guzman@polito.it; simelys.hernandez@polito.it*

1. Introduction

Greenhouse gas emissions from natural systems and human activities have caused an alteration in climate patterns. CO₂ is the key contributor to global climate change in the atmosphere. Climate change occurs because the Earth does not have enough capacity to neutralise all the emitted CO₂, meaning that humanity demands more than the Earth can offer. Therefore, strategies are requested to implement renewable energy sources and prevent the consequences of climate change.[1] Among the different alternatives, exploiting the hydrogenation of CO₂ via electrocatalytic reaction represents an opportunity to store renewable energy in the form of chemicals and fuels and consequently to support a low carbon economy. The inert nature of CO₂ makes its conversion into any other product difficult. Therefore, the catalyst material plays a crucial role in disrupting the stability of the CO₂ molecule and breaking the C-O bond, allowing the molecule to be electro-reduced to multi-carbon products. In this regard, copper-based material has an appealing ability to promote C-C coupling toward C₂₊ products, which are among the most generally desired chemicals.[2–5]

The dimerisation reactions (namely, *CO–*CO or *CH_x–*CO) are considered the crucial selectivity determining step towards C₂₊ products. The polarised Cu^{δ+} sites induced under reaction conditions, for instance, are believed to be responsible for inducing that step of C-C coupling.[6] However, the stable presence of the above-mentioned active species is a matter of common concern. To date, researchers have focused on observing the effects of surface modification (e.g., nano-structuring and surface tailoring) on catalysts selectivity and activity to produce C₂₊ products. Nonetheless, it remains an ongoing challenge due to high C-C coupling barriers. Among these studies, incorporating light heteroatoms into the Cu catalyst has been reported to induce the formation and stabilisation of Cu⁺¹/Cu⁰ interfaces and reduce the *CO dimerisation barrier, promoting a high activity for the electrochemical CO₂ reduction (EC CO₂R) towards C₂ products.[7] In particular, the boron-doped Cu catalysts have shown boosted CO₂ reduction performance, most likely resulting from the electron-donating ability of copper in the presence of B element and hence from a stable and positively charged Cu oxidation state.[7–9] Zhou and co-workers in their work[9] have obtained a high selectivity towards C₂ products on a B-doped copper catalyst, with a Faradaic efficiency of about 80% (ethylene and ethanol) and a current density of 70 mA cm⁻². Likewise, the incorporation of nitrogen into the catalytic matrix has been explored by many. Dongare et al. have reported N-doped graphene supported Cu nanoparticles as a promising material for forming multi-carbon alcohol [10]. A highly selective copper nanoparticles/N-doped graphene-based electrode has been used by Song et al., enabling an FE of 63% toward ethanol at -1.2 V vs RHE.[11]

In the efforts to achieve 100% of C₂₊ products (e.g., alcohols) selectivity, incorporating heteroatoms has been investigated as a strategy for obtaining selective electrocatalysts. It is shown that by identifying the optimal conditions, a single product may be targeted. Herein, copper-based materials are employed as platforms for introducing boron and/or nitrogen elements. These electrocatalysts have been tested in a conventional rotating disk electrode (RDE) system and in a more complex setup based on a gas diffusion electrode (GDE), where a continuous flow configuration also has been adopted. We have recently demonstrated how every single factor can affect both the activity and the selectivity of the system under investigation[12]. Consequently, by exploring the impact of the catalyst loading and the binder content on the electrode performance, the best conditions for the catalytic ink composition have been found in the GDE-based device.

2. Methods

The catalysts were synthesised by assisting the precipitation method with ultrasonic irradiation. The catalysts were prepared with a procedure analogous to that proposed by Schüth et al.[13,14] The procedure started with preparing a solution of hydrated copper nitrate as a precursor. As the precipitating agent, a solution of sodium carbonate was used. It is important to mention that the pH and temperature were maintained at a constant value during the precipitation process. The synthesis begins with pumping the nitrate solution at a constant flow rate by using a peristaltic pump. The system is left ageing for one hour, then the precipitate is filtered and later left drying overnight in an oven. The solution was irradiated with a constant amplitude/intensity. The ultrasound effect was evaluated during the ageing process.

The prepared copper hydroxy carbonate powder (Cu-06-%30-A) obtained from the US-assisted co-precipitation synthesis was impregnated, as shown schematically in **Figure 1**. The B-doped CuO catalysts were prepared according to an adapted synthetic procedure from the literature.[7] The impregnation was carried out with different volumes of B₂O₃ solution in a mixed solvent of ethanol and water. Four different volumes of a B₂O₃ solution were prepared. The prepared B₂O₃ solution was then mixed with the US-prepared powder catalyst, and the dispersions were kept under stirring. Subsequently, the impregnated CuO powders were dried overnight. The obtained B₂O₃-copper hydroxy carbonate was calcined in a muffle furnace, resulting in the following oxide catalysts: Cu-06-%30-A-#% wt B. The # in the name of the catalyst corresponds to the content of B. Thus, four different contents of B were obtained. It is worth mentioning that the obtained B₂O₃- and copper hydroxy carbonate powders were also calcined under nitrogen. The thermal treatment was carried out in a tubular furnace under nitrogen flow. The prepared samples were denoted as Cu-06-%30-A -2.4% wt B-N and Cu-06-%30-A-N, where N stands for flowing nitrogen used as a gas atmosphere.

The catalyst materials have been characterised by different physico-chemical methods like X-ray diffraction, BET, porosimetry, and field-emission scanning electron microscopy (FESEM) to determine the features that make these materials perform for the CO₂-to-alcohols conversion.

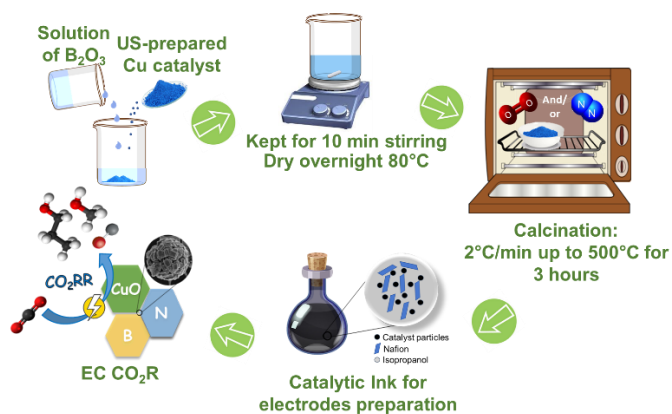


Figure 1. Schematic of procedure for developing electrocatalysts for CO₂ reduction to C₂₊ products.

3. Results and discussion

As shown in **Figure 2**, incorporating both B heteroatom and the controlled atmosphere calcination of N₂ led to greater selectivity for reducing CO₂ to products of interest like alcohols, formate, and CO. This behaviour is attributed to the fact that these elements belong to the p-block of the periodic table, which stabilise the carboxyl group by promoting the dimerisation of the *CO intermediate. On the other hand, incorporating both heteroatoms (B and N) increases formate desorption and enhances the *CO dimerisation towards more reduced products. It led to even better performance, as a higher conversion of CO₂ towards the products of interest was observed than in the other cases, with a total FE of 64% to CO₂ reduction products with ~50% of liquid products (i.e., 77% selectivity towards formate and alcohols) at a total current density of 23 mA cm⁻².

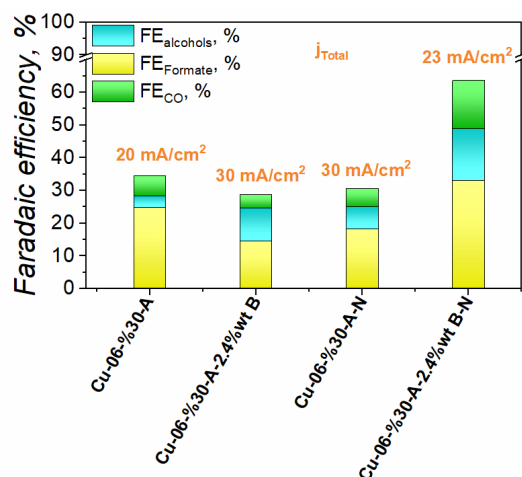


Figure 2. Faradaic efficiencies towards the main high-value products (alcohols, formate and CO) obtained from EC CO₂R on ultrasonic-synthesised CuO base catalysts (Cu-06-% 30-A). Effect of B content (2.4wt%) and calcination in N₂.

Besides, a correlation between the productivity towards CO and the productivity towards ethanol on the studied catalysts was found. It was also demonstrated that the porosity of the as-synthesised catalysts plays a role in the selectivity of the reaction. Based on this, a possible reason for the high activity of the as-synthesised CuO is proposed. Then, the catalyst must increase the adsorption of *COOH intermediate, which is the 1° uphill reaction formed through CO₂ activation and hydrogenation, and then conducts to the production of *CO. The results revealed that in addition to a suitable *CO bond strength in the catalyst surface, there should be an appropriate diffusion of CO₂ and key intermediates like *CO to generate more reduced products.

4. Conclusions

- All the catalysts were synthesised through a fully standardised method of synthesis, allowing the control of the intrinsic properties of the materials (porosity, crystalline structure, morphology) and the future scalability of the synthesis process,
- Materials with mean pores size between 15 nm and 25 nm were formed, with a crystallite size between 14 and 15 nm, which induced better CO₂ adsorption and diffusion,
- B atom and N₂ calcination improved the selectivity for CO₂ reduction reaction: FE of ~50% (formate + alcohols),
- The synthesised catalysts have reduced the energy barrier to producing C₂ oxygenate products.

Acknowledgements

This work has been performed with the financial support of Eni SpA: R&D Program Energy Transition (Cattura e Utilizzo CO₂).

References

- [1] F. Adedoyin, I. Ozturk, I. Abubakar, T. Kumeka, O. Folarin, F.V. Bekun, Structural breaks in CO₂ emissions: Are they caused by climate change protests or other factors?, *J. Environ. Manage.* 266 (2020) 110628. <https://doi.org/10.1016/j.jenvman.2020.110628>.
- [2] Y.C. Li, Z. Wang, T. Yuan, D.H. Nam, M. Luo, J. Wicks, B. Chen, J. Li, F. Li, F.P.G. De Arquer, Y. Wang, C.T. Dinh, O. Voznyy, D. Sinton, E.H. Sargent, Binding Site Diversity Promotes CO₂ Electroreduction to Ethanol, *J. Am. Chem. Soc.* 141 (2019) 8584–8591. <https://doi.org/10.1021/jacs.9b02945>.
- [3] H. Guzmán, F. Salomone, S. Bensaid, M. Castellino, N. Russo, S. Hernández, CO₂ Conversion to Alcohols over Cu/ZnO Catalysts: Prospective Synergies between Electrocatalytic and Thermocatalytic Routes, *ACS Appl. Mater. Interfaces.* 14 (2021) 517–530. <https://doi.org/10.1021/acsami.1c15871>.
- [4] H. Guzmán, F. Zammillo, D. Roldán, C. Galletti, N. Russo, S. Hernández, Investigation of Gas Diffusion Electrode Systems for the Electrochemical CO₂ Conversion, *Catalysts.* 11 (2021) 482. <https://doi.org/10.3390/catal11040482>.
- [5] J.J. Lv, M. Jouny, W. Luc, W. Zhu, J.J. Zhu, F. Jiao, A Highly Porous Copper Electrocatalyst for Carbon Dioxide Reduction, *Adv. Mater.* 30 (2018) 1–8. <https://doi.org/10.1002/adma.201803111>.
- [6] F. Dattila, R. Garclá-Muelas, N. López, Active and Selective Ensembles in Oxide-Derived Copper Catalysts for CO₂

- Reduction, *ACS Energy Lett.* 5 (2020) 3176–3184. <https://doi.org/10.1021/acsendergylett.0c01777>.
- [7] C. Chen, X. Sun, L. Lu, D. Yang, J. Ma, Q. Zhu, Q. Qian, B. Han, Efficient electroreduction of CO₂ to C₂ products over B-doped oxide-derived copper, *Green Chem.* 20 (2018) 4579–4583. <https://doi.org/10.1039/c8gc02389a>.
- [8] Q. Wan, J. Zhang, B. Zhang, D. Tan, L. Yao, L. Zheng, F. Zhang, L. Liu, X. Cheng, B. Han, Boron-doped CuO nanobundles for electroreduction of carbon dioxide to ethylene, *Green Chem.* 22 (2020) 2750–2754. <https://doi.org/10.1039/d0gc00730g>.
- [9] Y. Zhou, F. Che, M. Liu, C. Zou, Z. Liang, P. De Luna, H. Yuan, J. Li, Z. Wang, H. Xie, H. Li, P. Chen, E. Bladt, R. Quintero-Bermudez, T.K. Sham, S. Bals, J. Hofkens, D. Sinton, G. Chen, E.H. Sargent, Dopant-induced electron localisation drives CO₂ reduction to C₂ hydrocarbons, *Nat. Chem.* 10 (2018) 974–980. <https://doi.org/10.1038/s41557-018-0092-x>.
- [10] S. Dongare, N. Singh, H. Bhunia, Nitrogen-doped graphene supported copper nanoparticles for electrochemical reduction of CO₂, *J. CO₂ Util.* 44 (2021) 101382. <https://doi.org/10.1016/j.jcou.2020.101382>.
- [11] Y. Song, R. Peng, D.K. Hensley, P. V. Bonnesen, L. Liang, Z. Wu, H.M. Meyer, M. Chi, C. Ma, B.G. Sumpter, A.J. Rondinone, High-Selectivity Electrochemical Conversion of CO₂ to Ethanol using a Copper Nanoparticle/N-Doped Graphene Electrode, *ChemistrySelect.* 1 (2016) 6055–6061. <https://doi.org/10.1002/slct.201601169>.
- [12] H. Guzmán, F. Zammillo, D. Roldán, C. Galletti, N. Russo, S. Hernández, Investigation of gas diffusion electrode systems for the electrochemical CO₂ conversion, *Catalysts.* 11 (2021) 482. <https://doi.org/10.3390/catal11040482>.
- [13] C. Baltes, S. Vukojević, F. Schüth, Correlations between synthesis, precursor, and catalyst structure and activity of a large set of CuO/ZnO/Al₂O₃ catalysts for methanol synthesis, *J. Catal.* 258 (2008) 334–344. <https://doi.org/10.1016/j.jcat.2008.07.004>.
- [14] H. Guzmán, D. Roldán, A. Sacco, M. Castellino, M. Fontana, N. Russo, S. Hernández, CuZnAl-Oxide Nanopyramidal Mesoporous Materials for the Electrocatalytic CO₂ Reduction to Syngas: Tuning of H₂/CO Ratio, 11 (2021) 3052.

Insight into the practical challenges of membrane-electrode assembly for the CO₂ electrochemical reduction and its advantages

Federica Zammillo¹, Hilmar Guzmán¹, Simelys Hernández^{1*}

¹ Department of applied science and technology (DISAT), Politecnico di Torino

C.so Duca degli Abruzzi, 24, 10129, Turin, Italy

*Corresponding author E-Mail: simelys.hernandez@polito.it

1. Introduction

The heat-trapping nature of carbon dioxide (CO₂) makes its ever-increasing concentration in the atmosphere a growing threat to global security. The International Energy Agency (IEA) recently found that the CO₂ emissions rose by over two billion tons in 2021, that is after the pandemic impacted the world economy, reaching their highest ever level[1]. Then, efforts are needed to counteract this trend and to avoid the irreversible consequences of climate change. In this context, several alternatives have been proposed to convert CO₂ to valuable products: the electrochemical reduction of CO₂ (ECR-CO₂) represents one of the most promising routes, allowing to employ renewable resources and to obtain a wide spectrum of gaseous and liquid products, in accordance with sustainable development and circular economy. In this work, the ECR-CO₂ has been carried out in gas diffusion electrodes (GDE)-based systems, where the limitations of mass transport associated with the CO₂ diffusion in electrolyte solutions can be overcome by directly feeding CO₂ in gaseous form to the electrode surface[2]. Copper (Cu)-based catalysts[3] have been employed in our alkaline continuous flow cell, in which a potassium hydroxide solution has been selected as electrolyte both in the cathodic and the anodic chambers. Moreover, the two liquid chambers have been separated by an anion exchange membrane (AEM). In view of an industrial deployment, CO₂ electrolyzers must provide modest cell voltages during operations as well as they must selectively produce concentrated target products at high rates[4]. This challenge is being currently met by researchers moving from a so-called three chambers configuration towards a membrane-electrode assembly (**Figure 1**). The purpose of this work is therefore to demonstrate the benefits of reducing the distance between the electrode surface and the membrane to reach a zero-gap system, analyzing also the critical issues which might have to be addressed.



Figure 1. Schematic layouts of the GDE (left) and MEA (right) configurations.

2. Methods

A porous and conductive support was employed for the manufacturing process of the GDEs, where the Cu-based catalyst was deposited by means of a spray coater (automated technique). In the case of MEA, the electrode was successively hot-pressed to the AEM according to our own optimized procedure[5]. The characterization of the electrodes was performed by X-Ray Diffraction (XRD) and Field Emission Scanning Electron Microscopy (FESEM) analytical techniques. On the other hand, the electrochemical behavior of the electrodes was assessed by conducting cyclic and linear sweep voltammetry measurements (CV, LSV).

Furthermore, two hours-chronopotentiometry (CP) tests were carried out to investigate on the stability and the CO₂ reduction performance of the GDEs. With reference to the latter aspect, the gaseous products were monitored continuously during the CP, while the liquid products analysis was conducted at a later time by means of high-performance liquid chromatography (HPLC) and gas chromatography-mass spectrometry (GC-MS) methods.

3. Results and discussion

The findings highlight a general suppression of the hydrogen evolution, the main competitor for the electrochemical CO₂ reduction in aqueous electrolytes, when migrating from GDE to MEA configuration. In addition, the formation of C₂₊ products was enhanced (with an increase in FE towards C₂₊ of about 13%), leading to a more efficient process in energy terms. Moreover, the MEAs required lower applied cell potentials for sustaining two-hours experiments than GDEs, under the same operating conditions (i.e., current density, catalyst loading, electrolyte solutions, gas and liquid(s) flow rates, etc.). However, the process of getting a well-made MEA is not a straightforward task as well as finding the most suitable working conditions: going by order, one first need to identify the temperature and pressure conditions of the hot-pressing step which on the one hand allow the complete transfer of the catalytic layer onto the membrane, and on the other hand do not cause unwanted breakage/cracks of either the carbon support or the membrane itself; subsequently, the proper moisture content of the CO₂ feed gas must be found in order to optimize the water balance in the components of the MEA (herein, we obtained a humid stream by sending CO₂ in a water source at 80°C); ultimately, the operating conditions and the cell design aspects need to be deeply studied to avoid delamination and, thus, the worsening of the performance during operation.

4. Conclusions

The challenging need to move towards low-carbon emitting technologies has pushed researchers in the last period to focus not only on the catalyst development but also on the overall system design, with the aim to minimize the potential losses while keeping high selectivities at sustained rates. Accordingly, due to the low solubility of CO₂ in aqueous solutions and to mass transfer limitations, the attention is currently being drawn towards GDE-based systems, where shorter diffusion pathways and higher CO₂ concentration than in traditional devices can lead to commercially-relevant current densities. The intent of the present work is to prove the advantages that result from the use of a membrane-electrode assembly, i.e., reducing the gap between membrane and electrode up until reaching a distance equal to zero, not neglecting but rather discussing the experimental challenges that the worker potentially has to deal with. In particular, we observed that switching from GDE to MEA is possible to promote the CO₂ reduction reactions at the expense of hydrogen production and with lower energy consumption.

The financial support of ENI SpA: R&D Program Energy Transition (Cattura e Utilizzo CO₂) is acknowledged.

References

- [1] IEA, Global Energy Review: CO₂ Emissions in 2021, 2021.
- [2] H. Guzmán, F. Zammillo, D. Roldán, C. Galletti, N. Russo, S. Hernández, Investigation of gas diffusion electrode systems for the electrochemical CO₂ conversion, *Catalysts*. 11 (2021). <https://doi.org/10.3390/catal11040482>.
- [3] H. Guzmán, N. Russo, S. Hernandez, CO₂ valorisation towards alcohols by Cu-based electrocatalysts: Challenges and perspectives, *Green Chemistry*. (2021). <https://doi.org/10.1039/d0gc03334k>.
- [4] C.M. Gabardo, C.P. O'Brien, J.P. Edwards, C. McCallum, Y. Xu, C.T. Dinh, J. Li, E.H. Sargent, D. Sinton, Continuous Carbon Dioxide Electroreduction to Concentrated Multi-carbon Products Using a Membrane Electrode Assembly, *Joule*. 3 (2019) 2777–2791. <https://doi.org/10.1016/j.joule.2019.07.021>.
- [5] I. Merino-Garcia, J. Albo, A. Irabien, Productivity and Selectivity of Gas-Phase CO₂ Electroreduction to Methane at Copper Nanoparticle-Based Electrodes, *Energy Technology*. 5 (2017) 922–928. <https://doi.org/10.1002/ente.201600616>.

Electrochemical sensor for H₂O₂ released from human THP-1 macrophages

Astrid Sofia Fiorentino^{1*}, Bernardo Patella¹, Maria Rita Giuffrè², Chiara Cipollina², Serena Di Vincenzo^{3,4}, Maria Ferraro^{3,4}, Elisabetta Pace⁴, Giuseppe Aiello¹, Michele Russo⁵, Rosalinda Inguanta¹

¹Engineering Department, Università degli Studi di Palermo, Viale delle Scienze, 90128 Palermo, Italy

²Ri.MED Foundation, 90133 Palermo, Italy

³Institute of Biomedical Research and Innovation, National Research Council, 90146 Palermo, Italy

⁴Institute of Translational Pharmacology, National Research Council, 90146 Palermo, Italy

⁵Dipietro Group, Siracusa, Italy

*Corresponding author E-Mail: astridsofia.fiorentino@unipa.it

1. Introduction

Reactive oxygen species (ROS) are by-products of aerobic metabolism. The superoxide anion (O₂⁻), hydrogen peroxide (H₂O₂) and hydroxyl radicals (OH⁻) are part of the ROS. ROS are usually indicative of oxidative stress, and high ROS concentration induces disease by damaging lipids, proteins and DNA[1][2][3][4].

Among ROS species, hydrogen peroxide is of interest due to its unique physiological property. H₂O₂ can cross biological membranes and is therefore more damaging to DNA than hydroxyl radicals[5]. For this reason, it is very important to measure and estimate oxidative stress, especially H₂O₂ levels. Current methods to measure ROS in cell cultures use fluorescent probes, colorimetric/fluorometric biochemical assays, or liquid chromatography coupled with mass spectrometry-based approaches[6][7]. These methods have limitations, such as the need to stain cells. In addition, fluorescence methods are not specific for a particular ROS, so they do not allow absolute quantification[8]. Recently, the electrochemical detection of H₂O₂ has been of great interest due to its many advantages, such as ease of use, low-cost instrumentation, suitability, high sensitivity and selectivity, rapid response and low cost chemical instruments[9][10][11][12][13]. Several electrode materials have been tested [14][8][15][16][17] and in particular, graphene oxide (GO) modified with metal nanoparticles (NPs) has been widely studied as active material for H₂O₂ detection[18][19]. In the present study, we show the fabrication and calibration of a nanostructured electrochemical sensor, based on rGO and Au-NPs, to measure H₂O₂ released from human THP-1 macrophages exposed to different treatments.

2. Methods

The fabrication of the rGO/Au-NPs-based electrode is realized by the method detailed in a previous study[20]. In particular, Indium tin oxide coated PET (ITO-PET) sheet was used as a substrate for sensor fabrication. ITO-PET was ultrasonically washed in pure isopropanol and deionized water for 10 min each. ITO-PET was used as working in an electrochemical cell manufactured by a stereolithography 3D printer (3D Form 3+ Low Force Stereolithography (LFS)TM). The 3D printed cell is equipped with two channels with a diameter of 1 mm that allow the connection with a peristaltic pump which recirculates the electrolyte with a speed of 50 ml/min. All electrochemical measurements were carried out using a potentiostat/galvanostat (Solartron CellTest® System). The electrochemical co-deposition of rGO and Au-NPs was carried out in acetate buffer solution (ABS), containing 0.5 mg/ml GOx and 0.5 mM KAuCl₄. A constant cathodic potential of 0.8 V vs. SCE was applied for 200 s. The electrodes were characterized using scanning electron microscopy (SEM, FEG-ESEM, FEI QUANTA 200), energy dispersive spectroscopy (EDS), X-ray diffraction and Raman spectroscopy. For the electrochemical detection a three-electrode cell was used where the working is the ITO-PET/rGO-Au-NPs electrode, the counter is a platinum wire and the reference is an SCE. The sensor was tested and calibrated using cell growth medium mixed with PBS as a blank in a 1:1 ratio.

3. Results and discussion

The co-electrodeposition of rGO and Au-NPs from an aqueous solution containing GO and HClAu_4 as precursors, occurs following the reactions proposed in previous studies[21][22].

Figure 1 shows the SEM image of the rGO/Au-NPs-based electrode. The co-electrodeposition led to the formation of Au-NPs of about 33 nm that uniformly covered the electrode surface. The presence of rGO and Au NPs was confirmed by Raman spectroscopy and X-ray diffraction.

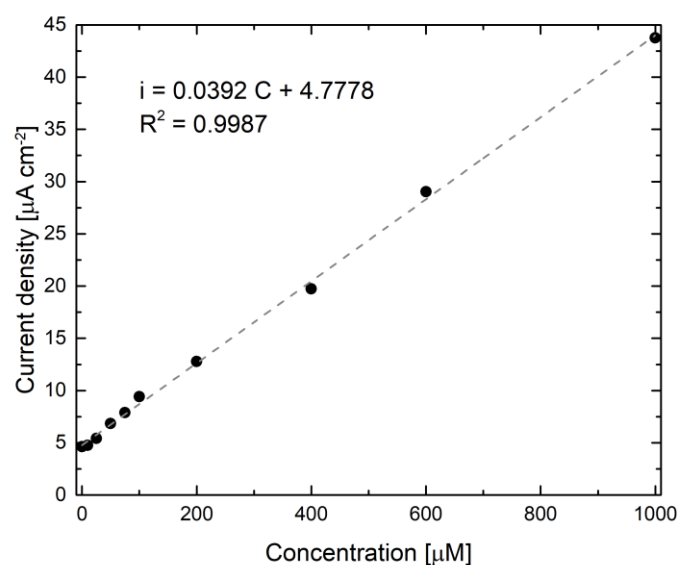
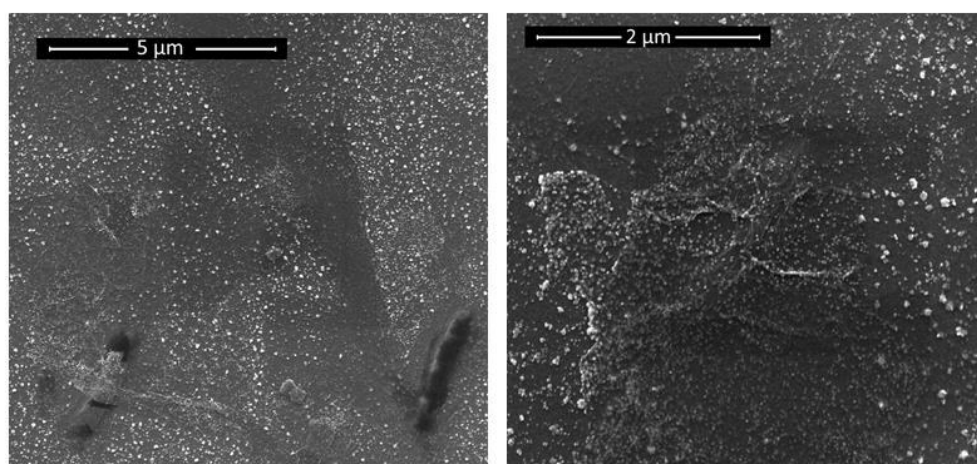


Figure 1. A) SEM images of the rGO/Au-NPs-based electrode; B) calibration curve of sensor for H_2O_2 detection.

Calibration was performed in blank solution where different concentration of H_2O_2 were inserted. The detection was carried out by chronoamperometric test at -0.8 V vs SCE. For each investigated H_2O_2 concentration three different tests were performed. Figure 1B shows the calibration curve of the electrode. A linear range from 10 to 1000 μM was obtained with a LOD and a sensitivity of 3.3S/b and $0.0392 \mu\text{A} \mu\text{M}^{-1} \text{cm}^{-2}$, respectively. Sensor was also validated to measure H_2O_2 released from human THP-1 macrophages exposed to different treatments.

4. Conclusions

In this work an electrochemical sensor based on rGO and Au-NPs were used for the to detect H₂O₂ released from human THP-1 macrophages. The results are significant because they support the possibility of direct quantification of extracellular H₂O₂ release in order to monitor intracellular ROS levels with a fast, easy, reproducible and low-cost electrochemical method. This electrochemical sensor may have an easy use to implement in research laboratories where direct measurement of H₂O₂ in cell supernatants can replace current expensive and time-consuming biochemical and flow cytometry-based approaches. In addition, the future development of a sensor based on gold nanowires or nanotubes is envisaged in order to develop a sensor with a larger surface area and hypothetical higher sensitivity.

References

- [1] C. E. Cross *et al.*, “Oxygen radicals and human disease. Davis conference,” *Ann. Intern. Med.*, vol. 107, no. 4, pp. 526–545, 1987, doi: 10.7326/0003-4819-107-4-526.
- [2] M. Schieber and N. S. Chandel, “ROS function in redox signaling and oxidative stress,” *Curr. Biol.*, vol. 24, no. 10, pp. R453–R462, 2014, doi: 10.1016/j.cub.2014.03.034.
- [3] Z. A. Wood, L. B. Poole, and P. A. Karplus, “Peroxiredoxin evolution and the regulation of hydrogen peroxide signaling,” *Science (80-.)*, vol. 300, no. 5619, pp. 650–653, 2003, doi: 10.1126/science.1080405.
- [4] T. Finkel, “Signal transduction by reactive oxygen species,” *J. Cell Biol.*, vol. 194, no. 1, pp. 7–15, 2011, doi: 10.1083/jcb.201102095.
- [5] “P r o t e c t i v e e f f e c t o f e r d o s t e i n e m e t a b o l i t e I a g a i n s t h y d r o g e n p e r o x i d e - i n d u c e d o x i d a t i v e DNA - d a m a g e i n l u n g e p i t h e l i a l c e l l s,” vol. 1, pp. 700–706.
- [6] Y. Zhang, M. Dai, and Z. Yuan, “Methods for the detection of reactive oxygen species,” *Anal. Methods*, vol. 10, no. 38, pp. 4625–4638, 2018, doi: 10.1039/c8ay01339j.
- [7] M. Katerji, M. Filippova, and P. Duerksen-Hughes, “Approaches and methods to measure oxidative stress in clinical samples: Research applications in the cancer field,” *Oxid. Med. Cell. Longev.*, vol. 2019, 2019, doi: 10.1155/2019/1279250.
- [8] A. Depeursinge *et al.*, “Fusing Visual and Clinical Information for Lung Tissue Classification in HRCT Data,” *Artif. Intell. Med.*, vol. 229, p. ARTMED1118, 2010, doi: 10.1016/j.
- [9] B. Patella, C. Sunseri, and R. Inguanta, “Nanostructured Based Electrochemical Sensors,” *J. Nanosci. Nanotechnol.*, vol. 19, no. 6, pp. 3459–3470, 2019, doi: 10.1166/jnn.2019.16110.
- [10] K. Dhara and D. R. Mahapatra, “Recent advances in electrochemical nonenzymatic hydrogen peroxide sensors based on nanomaterials: a review,” *J. Mater. Sci.*, vol. 54, no. 19, pp. 12319–12357, 2019, doi: 10.1007/s10853-019-03750-y.
- [11] E. Anastasiou, K. O. Lorentz, G. J. Stein, and P. D. Mitchell, “Prehistoric schistosomiasis parasite found in the Middle East,” *Lancet Infect. Dis.*, vol. 14, no. 7, pp. 553–554, 2014, doi: 10.1016/S1473-3099(14)70794-7.
- [12] H. Uğuz *et al.*, “ce pte d M us pt,” *J. Phys. Energy*, vol. 2, no. 1, pp. 0–31, 2020.
- [13] J. Huang *et al.*, “High-Linearity Hydrogen Peroxide Sensor Based on Nanoporous Gold Electrode,” *J. Electrochem. Soc.*, vol. 166, no. 10, pp. B814–B820, 2019, doi: 10.1149/2.1241910jes.
- [14] N. Aydemir, J. Malmström, and J. Travas-Sejdic, “Conducting polymer based electrochemical biosensors,” *Phys. Chem. Chem. Phys.*, vol. 18, no. 12, pp. 8264–8277, 2016, doi: 10.1039/c5cp06830d.
- [15] Y. H. Wang, K. J. Huang, and X. Wu, “Recent advances in transition-metal dichalcogenides based electrochemical biosensors: A review,” *Biosens. Bioelectron.*, vol. 97, pp. 305–316, 2017, doi: 10.1016/j.bios.2017.06.011.
- [16] R. Zhang and W. Chen, “Recent advances in graphene-based nanomaterials for fabricating electrochemical hydrogen peroxide sensors,” *Biosens. Bioelectron.*, vol. 89, pp. 249–268, 2017, doi: 10.1016/j.bios.2016.01.080.
- [17] Y. Wang *et al.*, “Electrochemistry and biosensing activity of cytochrome c immobilized in macroporous materials,” *Microchim. Acta*, vol. 175, no. 1–2, pp. 87–95, 2011, doi: 10.1007/s00604-011-0638-8.
- [18] Y. Song, Y. Luo, C. Zhu, H. Li, D. Du, and Y. Lin, “Recent advances in electrochemical biosensors based on graphene two-dimensional nanomaterials,” *Biosens. Bioelectron.*, vol. 76, pp. 195–212, 2016, doi: 10.1016/j.bios.2015.07.002.
- [19] K. Dhara, T. Ramachandran, B. G. Nair, and T. G. Satheesh Babu, “Au nanoparticles decorated reduced graphene oxide for the fabrication of disposable nonenzymatic hydrogen peroxide sensor,” *J. Electroanal. Chem.*, vol. 764, pp. 64–70, 2016, doi: 10.1016/j.jelechem.2016.01.011.

- [20] B. Patella, A. Sortino, G. Aiello, C. Sunseri, and R. Inguanta, "Reduced graphene oxide decorated with metals nanoparticles electrode as electrochemical sensor for dopamine," *FLEPS 2019 - IEEE Int. Conf. Flex. Printable Sensors Syst. Proc.*, pp. 1–3, 2019, doi: 10.1109/FLEPS.2019.8792267.
- [21] M. Zhou *et al.*, "Controlled synthesis of large-area and patterned electrochemically reduced graphene oxide films," *Chem. - A Eur. J.*, vol. 15, no. 25, pp. 6116–6120, 2009, doi: 10.1002/chem.200900596.
- [22] G. Gotti, K. Fajerweg, D. Evrard, and P. Gros, "Electrodeposited gold nanoparticles on glassy carbon: Correlation between nanoparticles characteristics and oxygen reduction kinetics in neutral media," *Electrochim. Acta*, vol. 128, pp. 412–419, 2014, doi: 10.1016/j.electacta.2013.10.172.
- [23] B. Patella *et al.*, "Electrochemical sensor based on rGO/Au nanoparticles for monitoring H₂O₂ released by human macrophages," *Sensors Actuators, B Chem.*, vol. 327, no. April 2020, p. 128901, 2021, doi: 10.1016/j.snb.2020.128901.

Technical and economic analysis of most promising electrochemical routes for the conversion of CO₂ to formic acid

Federica Proietto, Alessandro Galia, Onofrio Scialdone^{1*}

1 Dipartimento di Ingegneria, Università degli studi di Palermo, Viale delle Scienze, 90128, Palermo, Italy.

**Corresponding author E-Mail: onofrio.scialdone@unipa.it*

1. Introduction

In the last decade, the electrochemical conversion of CO₂ (ERCO₂) to formic acid (FA) using Sn-based cathodes, was widely investigated *i*) to valorise waste-CO₂ as a feedstock to produce value-added chemicals, *ii*) from the industrial standpoint, to cope with the stringent environmental regulations on greenhouse gas (GHG) emissions and *iii*) to potentially store the excess electric energy from intermittent renewable sources as chemical energy. Among the ERCO₂ products, FA is a valuable building block with a mature market and a relatively high value, which is used in food technologies, agriculture and pharmaceutical industry [1]. Currently, the synthesis of FA is a fossil fuels-based process, which is not straightforward neither environmentally friendly [2]. Extensive studies have shown that ERCO₂ using Sn-based cathodes can lead to the production of FA/formate with high selectivity. Appealing results were reported by using both Sn gas diffusion electrodes (GDEs) and high CO₂ pressures (HPs); however, to date, the real potential of ERCO₂ on an industrial scale is still uncertain [3] In this work, the technical feasibility and economic viability of this process were evaluated considering the most promising electrochemical routes reported in the literature. Five case studies were examined. The cost for producing FA by the electrochemical route was compared with that of the conventional chemical route. Several scenarios were envisioned finding the target figures of merit, the potential bottlenecks (including low FA concentration, GDE cost and high energy consumption) of each technology and the challenges that need to be faced.

2. Methods

Analysis of the main costs. The technical-economic analysis reported in this work includes the main costs related to the stages of *i*) CO₂ capture and recycling (C&R), *ii*) ERCO₂ and, *iii*) FA concentration and separation (C&S). The total cost for the conversion of CO₂ into FA at 85% wt. was estimated by eq. (1).

$$C_{EP} = C_{C\&R} + C_E + C_{C\&S} \quad (1)$$

where $C_{C\&R}$ are the costs due to the carbon capture and recycling; C_E are the total costs of the electrolysis, including the capital investment (C_{E-I}) and energetic costs (C_{E-O}) and $C_{C\&S}$ are the costs related to the C&S of the FA solution up to 85% wt. The main figures used for the estimation of the costs as described in detail in Proietto et al. [3].

3. Results and discussion

A simplified supply chain was envisioned, which includes the stage of *i*) CO₂ C&R, *ii*) ERCO₂ and, *iii*) FA C&S. For the ERCO₂ stage, five case studies (CSs) including the utilisation of GDE-based technologies at atmospheric pressure (CS I [4], CS II [5], CS III [6]) and of pressurised systems equipped with simple Sn plate cathodes (CS IV [7], CS V [8]), were investigated in detail.

Figure 1 reports an estimation of the overall costs for the electrochemical conversion of CO₂ to FA at 85% wt., C_{EP} , for each CSs. CS I presents the highest C_{EP} followed by CS V, CS II, CS IV and CS III. To show their market competitiveness, C_{EP} was compared with the sum of the costs for producing FA by the conventional chemical route (C_{CP}) and the Carbon Tax (CT) value, that would be saved by converting CO₂ into FA, $C_{CP}+CT$, and the FA market price (P_{FA}) (Fig.1). It was shown that, to date, the electrochemical route is not more cost-

effective than the commercial chemical one. The C&S stage presents the highest costs (Fig.1) due to the low final concentrations of FA obtained in the electrolysis stage (<10% wt.). Overall, CS III and IV presented the lowest C_{EP} since these processes presented the highest final [FA]. In addition, the technological improvements necessary to achieve a process sustainable from an economic point of view were identified and discussed for the future steps of research. Hence, several scenarios, characterized by some potential target technological improvements, were envisioned aiming to find the bottlenecks of each technology, to reduce the C_{EP} and to highlight the challenges that need to be faced for the implementation on a large-scale.

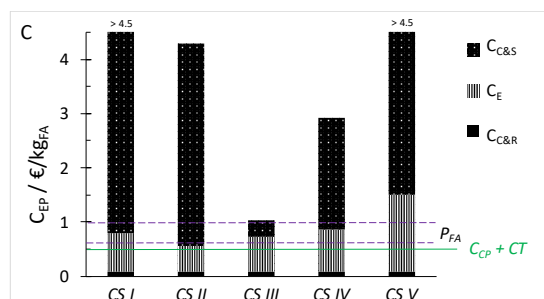


Figure 1. Comparison of the C_{EP} for each CS with the FA market price, P_{FA} (0.6–1 €/kg_{FA}), and the sum of conventional production process cost and the Carbon tax ($C_{CP} = 0.475$ €/kg_{FA} and $CT = 0.025$ €/kg_{FA}) [3].

4. Conclusions

In this work, a technical-economic analysis of ERCO₂ to FA/formate in aqueous electrolyte using Sn-based cathodes was performed considering the most promising routes reported in the literature. Five CSs based on the utilisation of GDE- (CS I–III) and HP- (CS IV–V) technologies were analysed. Under the hypotheses of this study, it was found that the FA electrochemical production process based on both GDE- and HP-technologies is not able yet to compete with the conventional FA production process. Economic viability is significantly limited by the low [FA] obtained in the electrolysis stage, due to the expensive costs for the C&S for FA diluted solution. In addition, it was shown that the successful implementation of different technological improvements for both electrochemical routes would make the ERCO₂ process economically suitable. Indeed, to be suitable for the commercialization, the ERCO₂ to FA using Sn-based electrodes should reach simultaneously high $j \sim 120$ mA cm⁻², FE $\sim 95\%$, [FA] > 30% wt., and low EC as well as long term stability. For GDE-based technologies, several efforts must focus on GDE optimisation decreasing its cost and enhancing the long-term stability. For HP-based technologies, the main technological challenge is to strongly improve the productivity of the process. Furthermore, it was shown that the potential use of excess electric energy generated by renewable sources to feed the electrolyser could significantly reduce the cost of energy.

References

- [1] A.S. Agarwal, Y. Zhai, D. Hill, N. Sridhar, *ChemSusChem* 4 (2011) 1301– 1310.
- [2] H.R.M. Jhong, S. Ma, P.J.A. Kenis, *Curr. Opin. Chem. Eng.* 2 (2013) 191– 199.
- [3] F. Proietto, A. Galia, O. Scialdone, *ChemElectroChem* 8 (2021) 2169–2179.
- [4] A. Del Castillo, M. Alvarez-Guerra, J. Solla-Gullón, A. Sáez, V. Montiel, A. Irabien, *Appl. Energy* 157 (2015) 165– 173
- [5] D. Kopljar, N. Wagner, E. Klemm, *Chem. Eng. Technol.* 39 (2016) 2042– 2050.
- [6] H. Yang, J.J. Kaczur, S.D. Sajjad, R.I. Masel, *ECS Trans.* 77 (2017) 1425– 1431.
- [7] F. Proietto, B. Schiavo, A. Galia, O. Scialdone, *Electrochim. Acta* 277 (2018) 30–40.
- [8] M. Ramdin, A.R.T. Morrison, M. e Groen, R. van Haperen, R. de Kler, E. Irttem, A.T. Laitinen, L.J. P. van den Broeke, T. Breugelmans, J.P.M. Trusler, W. de Jong, T.J.H. Vlught, *Ind. Eng. Chem. Res.* 58 (2019) 22718– 22740.

Functionalized Cathodic Porous Transport Layers for Alkaline Water Electrolyzer

Andrea Zaffora*¹, Francesco Di Franco¹, Davide Pupillo^{1,2}, Barbara Seminara¹, Giada Tranchida¹,
Monica Santamaria¹

¹Dipartimento di Ingegneria, Università degli Studi di Palermo, Viale delle Scienze, 90128 Palermo

²Dipartimento Scienza Applicata e Tecnologia, Politecnico di Torino, Corso Duca degli Abruzzi, 24, 10129 Torino

*Corresponding author E-Mail: andrea.zaffora@unipa.it

1. Introduction

Green H₂ production can be carried out through water electrolysis (WE). Currently, among the available technologies the best one is potentially the Anion Exchange Membrane electrolyzer that can exploit the advantages to operate in alkaline environment with the use of an ion exchange membrane as separator [1]. A crucial component of electrolyzers is the Porous Transport Layer (PTL) that is needed to have an efficient mass transport of both reagents and products (in liquid and gaseous phase), to connect the catalyst layer with the bipolar plate and to support the membrane that can operate with high differential pressure.

In alkaline environment Platinum Group Metal (PGM) free catalysts can be used. Especially at the cathode of the electrolyzers, where oxidating conditions are not present, Ni foams are typically used as PTLs. However, even unexpensive stainless steel mesh (cost < 10 €/m²) can be used as PTL but they need a functionalization process to have suitable catalyst layer for efficient H₂ evolution reaction (HER).

In this work we present functionalized stainless steel mesh as suitable and reliable PTL for alkaline electrolyzer. Functionalization process was carried out by electrodeposition in a suitable electrolyte to make a Ni, Cu and Mo-containing catalyst layer [2]. Electrodeposition operating parameters, such as electrolyte composition, cell potential and operating time were optimized to minimize the applied overpotential for the HER reaction.

2. Methods

Stainless steel AISI 304 mesh were used as PTLs. Mesh samples were polished in 0.5 M H₂SO₄ with an ultrasonic bath. Then, they were functionalized through an electrodeposition process where they were polarized at different potentials (ranging between -1 and -2 V) for different times (ranging between 3 and 10 min) in a three electrode setup with a Pt mesh as counter electrode and a Ag/AgCl/3.5 M KCl electrode as reference electrode. Electrodeposition bath was an aqueous solution containing NiSO₄, CuSO₄, H₃BO₃ and (NH₄)₆Mo₇O₂₄. Electrolyte pH was corrected with H₂SO₄ to maintain pH values under 3.

Characterization was carried out in 1 M KOH by using the same three electrode setup used for the functionalization process. Electrochemical Impedance Spectroscopy and Differential capacitance measurements were carried out in the same electrolyte.

3. Results and discussion

Overpotential vs current density curves, as a function of Mo content in electrodeposition bath, are reported in Figure 1.

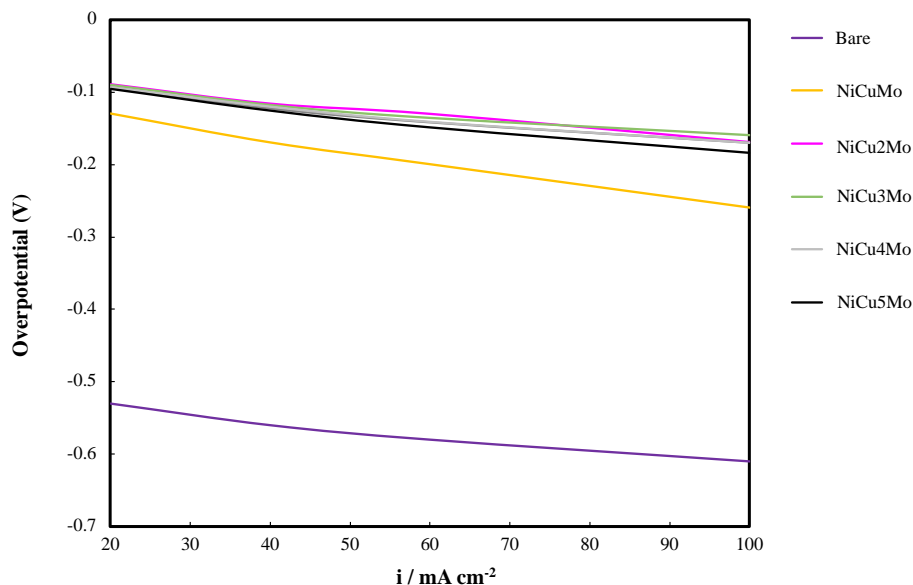


Figure 1. Overpotential vs current density curves as a function of Mo content in electrodeposition bath.

In the case of bare stainless steel mesh, overpotential at 100 mA cm^{-2} is about -610 mV . It is noteworthy to mention that the operating typical current density value for electrolyzers is 100 mA cm^{-2} . After the functionalization process, the overpotential is reduced to -260 mV . This result can be explained by taking into account the effect of Ni presence, in terms of higher catalytic activity (i.e. higher exchange current density), and the effect of Cu presence, in terms of weakening of H-adsorption on catalyst layer. Differential capacitance measurements confirmed that there is also an effect in terms of higher electrochemical surface active area. By optimizing the content of Mo in the electrodeposition bath, we further minimized the overpotential, reaching -160 mV . In order to study the kinetics of HER reaction, we also performed Electrochemical Impedance Spectroscopy measurements. Impedance spectra were modeled with a suitable equivalent electrical circuit obtaining the exchange current density value for each sample. Stability tests were carried out, reaching 6 hours without any sign of degradation of catalytic performances.

4. Conclusions

In this work we have prepared PTLs for H_2 production in alkaline environment by electrodeposition process on stainless steel mesh. Overpotential was reduced by optimizing operating parameters of the functionalization process, such as applied voltage, operating time and electrodeposition bath composition. Results are promising to take into account the cheapness of the stainless steel mesh with respect to typical Ni foams that are used as PTLs in electrolyzers. Further investigation are needed in order to test the PTLs in a flow through cell configuration.

References

- [1] C. Santoro et al, ChemSusChem (2022), <https://doi.org/10.1002/cssc.202200027>.
- [2] Y. Li et al., Nat. Communications 11:2720 (2020).

Experimental findings on the application of electric fields to enhance the deposition rate of Carbon Nanoparticle films in flame-synthesis

Arianna Parisi^{1*}, Gianluigi De Falco¹, Mariano Sirignano¹, Patrizia Minutolo², Mario Commodo², Claudia Carotenuto³, Francesco Di Natale¹

1 Dipartimento di Ingegneria Chimica, dei Materiali e della Produzione Industriale, Università degli Studi di Napoli Federico II, 80125 Napoli, Italy; 2 Istituto di Scienze e Tecnologie per l'Energia e la Mobilità Sostenibili, STIMS-CNR, 80125 Napoli, Italy; 3 Dipartimento di Ingegneria, Università della Campania "L. Vanvitelli", 81031 Aversa (CE), Italy

*Corresponding author E-Mail: arianna.parisi@unina.it

1. Introduction

Flame generated Carbon NanoParticles (CNPs) are recognized as hazardous materials [1], but their fascinating properties turn them into potential candidates for diverse applications in the fields of bioimaging, nanomedicine, photo/electro-catalysis and bio/chemical sensing [2]. CNPs are simply collected in a flame by thermophoretic forces generated after the rapid insertion of a cold substrate into the flame. Different film properties can be achieved by changing the position and the duration of substrate insertion and by varying combustion parameters [3]. This paper, which is part of the PRIN 2017PJ5XXX: MAGIC DUST project, provides first experimental results on the use electric fields to improve the harvesting process. The substrate has been kept at a fixed negative potential and the burner is grounded in order to generate an electric field directing toward the substrate and ignite electrophoretic deposition phenomena of CNP [4] that are influenced due to the presence of positively and negatively charged particles, whose dynamics are highly impacted by the presence of additional electrostatic forces [5]. Recently, a dedicated CNPs deposition model has been developed through COMSOL Multiphysics software [6]. It simulates the flame environment in terms of temperature, fluid-dynamics and space charge condition using the momentum balance equations over CNPs particles to sample their trajectories close to an electrified collector. The model matching the trend of experimental data predicts an increase in the harvesting rate up to six times combining electro and thermophoretic effects respect to the sole thermophoresis by applying a -3kV potential to the substrate. Preliminary experimental results on the electrophoretic-enhanced CNP film synthesis onto the cold substrate used for CNP harvesting in flame are also reported. To this aim, a controlled flame reactor has been equipped with a CNPs collector unit which is pneumatically driven to provide a given number of temporary insertions of a substrate in the flame, at a given height above the burner (HAB), with controlled residence time and speed of insertion. The substrate has been connected to a high voltage DC generator and kept at a constant potential up to -3kV. CNPs deposited on electrified substrates have been analyzed by Atomic Force Microscopy (AFM) and UV-visible light absorption. Overall the results show the possibility to tune film features in terms of morphology and optical properties just by changing the electric field.

2. Methods

A flat laminar premixed ethylene-air flame stabilized on a water-cooled McKenna burner to generate CNPs. The carbon-to-oxygen ratio (C/O) was adjusted at 0.67, which corresponds to a slightly sooting flame, and the cold gas velocity was 9.8 cm/s. During the last decade, these flame conditions have been thoroughly described [3,7], revealing a typical bimodal particle size distribution (PSD) at distances from the burner surface (HAB) greater than 10 mm, with a first mode about 2-3 nm and a second made up of particles bigger than 10 nm. Furthermore, prior studies [8,9] have revealed particle charge distributions. Accordingly, it is possible to

assume an even distribution of positively and negatively charged particles sampled from flames at atmospheric pressure and that all the particles with sizes up to 20 nm carry on at most a single electric charge [10]. CNPs are deposited on glass circular substrates. The insertion time t_{ins} is of 100 ms, and the HAB is 15 mm. The probe containing the substrate is kept at a fixed electric potential by connection with a controlled high voltage DC generator (Bertrand 230-20R), while the burner is grounded. The electric potential on the substrate is varied from 0 kV up to -3kV, below the onset of corona discharge [11]. AFM images were acquired over freshly cleaved mica substrates with a single insertion in flame in order to obtain a morphological characterization of CNPs. AFM measurements were performed with Scanning Probe Microscope NTEGRA Prima from NT-MDT, operated in semi-contact mode in air and equipped with NANOSENSORSTM SSS-NCHR super-sharp silicon probes with nominal tip radius of 2 nm. AFM images were postprocessed in order to obtain information about the fraction of substrate that is covered with CNPs (degree of coverage) at different applied voltages. Chemical/structural characterization of the thin films obtained with different electric potential was performed by UV-vis absorption spectroscopy via an Agilent UV-vis 8453 spectrophotometer. From the light absorbance, it is possible to estimate the film thickness, δ_{Abs} , under the assumption of absence of voids, using the classical Lambert-Beer expression [3]:

$$\frac{Abs(\lambda)}{\ln 10} = \frac{4\pi k(\lambda)\delta_{Abs}}{\lambda} \quad (1)$$

For the refractive index of CNP, $k(\lambda)$, a typical value found for soot particles of $k=0.56$ at $\lambda=532$ nm has been used [12].

3. Results and discussion

Figure 1 shows the AFM degree of coverage obtained with a single insertion in flame varying the electric potential from 0kV to -3kV and representative AFM images.

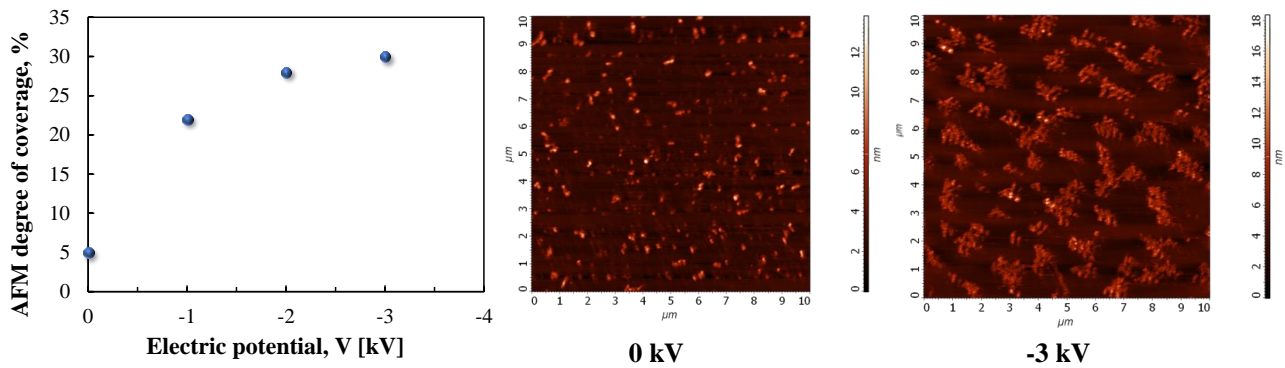


Figure 1. From left to right: AFM degree of coverage, % as a function of electric potential and AFM images at 0 kV and -3 kV ($C/O=0.67$, $HAB=15\text{mm}$, $t_{ins}=100\text{ms}$; $N_{ins}=1$).

Deposited CNPs increase as the absolute values of the electric potential increase. In particular, the estimated degree of coverage increases from 5% at 0kV to 30% at -3kV. Interestingly, these experimental results are consistent with the model predictions [6], showing both a six-fold increase. Moreover, in the case of pure thermophoresis at 0 kV, CNPs are distributed uniformly on the substrate and appear mostly as single spherical entities following a ballistic deposition mechanism, whereas in presence of -3kV applied to the deposition substrate, CNPs are organized as fractal petal-like structures. These morphological results are consistent with literature [13,14] and can be explained through a polarization model [11]: positively charged CNPs are

deposited on the negatively charged substrate as a result of Coulomb interactions. CNPs reach the negative charge at equilibrium with the substrate. The neutral CNPs in the flame - the majority - can be polarized by the applied field determining faster deposition that takes place preferentially over the already deposited particles due to the higher chemical affinity [8,9].

Figure 2 shows the UV-vis absorption spectra of CNPs films deposited on glass substrates after 100 insertions, varying the electric voltage from 0 to -3kV and the film thickness $\delta_{\text{Abs}(\lambda=532\text{nm})}$, obtained using the Lambert-Beer expression [3].

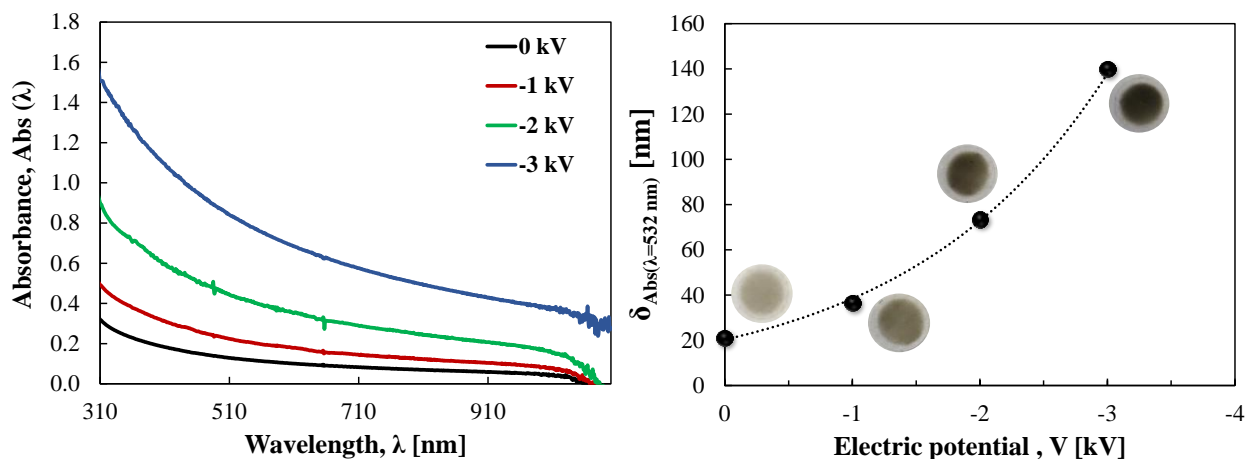


Figure 2. From right to left: UV-Vis spectra of CNP as a function of wavelength varying the electric potential (0,-1,-2;-3) kV applied to the glass substrate; film thickness $\delta_{\text{Abs}(\lambda=532\text{nm})}$ against the electric potential V (kV). (C/O=0.67, HAB=15mm, $t_{\text{ins}}=100\text{ms}$; $N_{\text{ins}}=100$). Images of real samples are showed.

Figure 2 shows an increase of absorption, and consequently of the film thickness, as the electric voltage increases. The trend of the thickness increases with the electric potential more than the AFM degree of coverage. This could be explained by considering that during film formation CNPs are deposited over carbon layers to which they are more chemical affine, so that nanoparticle aggregation, also favoured by the lower substrate temperature, may take place.

4. Conclusions

This paper presents results on the application of electric field to the flame synthesis of CNPs over electrically charged collectors. An ethylene/air premixed laminar flame with C/O=0.67 at atmospheric pressure stabilized on a McKenna burner and a collector device consisting of a probe alternatively inserted inside the flame have been used. The probe is kept at a fixed electric potential (from 0kV to -3kV) while the burner is grounded. CNPs have been firstly deposited on a mica substrate after a single insertion in the flame and analyzed with Atomic Force Microscopy. Additionally, CNPs films have been obtained with 100 insertions over glass substrates in flame varying the electric potential from 0 to -3 kV. Both AFM degree of coverage and film thickness show the enhancement in CNPs deposition up to six times. This paper findings indicate that the production of a film of a required thickness can be achieved with a much faster rate than those used in thermophoretic deposition, by using electric fields at medium potential (up to -3 kV in this work). This enhancement makes also reliable the production of films of CNPs from flames at low C/O values, producing films with properties different from those generated by more sooting flames. Further studies will be conducted to assess the morphological properties of deposited films in the presence of electric fields.

Acknowledgements

This work was financially supported by the PRIN project 2017PJ5XXX: “MAGIC DUST”.

References

- [1] De Falco G, Terlizzi M, Sirignano M, Commodo M, D’Anna A, Aquino RP, et al. Human peripheral blood mononuclear cells (PBMCs) from smokers release higher levels of IL-1-like cytokines after exposure to combustion-generated ultrafine particles. *Scientific Reports* 2017;7:1–11.
- [2] Mulay MR, Chauhan A, Patel S, Balakrishnan V. Candle soot : Journey from a pollutant to a functional material. *Carbon* 2019;144:684–712.
- [3] De Falco G, Commodo M, Barra M, Chiarella F, D’Anna A, Aloisio A, et al. Electrical characterization of flame-soot nanoparticle thin films. *Synthetic Metals* 2017;229:89–99.
- [4] Di Natale F, Carotenuto C. Particulate matter in marine diesel engines exhausts: Emissions and control strategies. *Transportation Research Part D: Transport and Environment* 2015;40:166–91.
- [5] Sardari PT, Rahimzadeh H, Ahmadi G, Giddings D. Nano-particle deposition in the presence of electric field. *Journal of Aerosol Science* 2018;126:169–79.
- [6] Formisano M, Parisi A, Di Natale F. Deposition of Carbon Nanoparticles using electric fields in flame. Master Thesis. 2021.
- [7] De Falco G, Picca F, Commodo M, Minutolo P. Probing soot structure and electronic properties by optical spectroscopy. *Fuel* 2020;259:116244.
- [8] Sgro LA, D’Anna A, Minutolo P. Charge fraction distribution of nucleation mode particles: New insight on the particle formation mechanism. *Combustion and Flame* 2011;158:1418–25.
- [9] Sgro LA, D’Anna A, Minutolo P. Charge distribution of incipient flame-generated particles. *Aerosol Science and Technology* 2010;44:651–62.
- [10] Maricq MM. A comparison of soot size and charge distributions from ethane, ethylene, acetylene, and benzene/ethylene premixed flames. *Combustion and Flame* 2006;144:730–43.
- [11] Olevanov MA, Mankelevich YuA, Rakhimova TV. Coagulation And Growth Mechanisms for dust particles in a low-temperature plasma. *Technical Physics* 2014;48:1270–9.
- [12] Smyth KC, Shaddix CR. The Elusive History of $\rho = 1.57-0.56i$ for the Refractive Index of Soot. *Combustion and Flame* 1996;197.
- [13] Nie MSM. Growth and morphology evolution of semiconducting oxides and sulfides prepared by magnetron sputtering. 2014.
- [14] Liu BG, Wu J, Wang EG, Zhang Z. Two-dimensional pattern formation in surfactant-mediated epitaxial growth. *Physical Review Letters* 1999;83:1195–8.

2D modelling of a molten carbonate cell for steam electrolysis

Maria Anna Murmura^{1*}, Silvia Lo Conte¹, Luca Turchetti², Stefano Cerbelli¹, Maria Cristina Annesini¹

1 Department of Chemical Engineering Materials and Environment, University of Rome "La Sapienza", Via Eudossiana 18, 00184, Roma; 2 ENEA, Italian National Agency for New Technologies, Energy and Sustainable Economic Development, Via Anguillarese 301, Rome, 00123, Italy

**Corresponding author E-Mail: mariaanna.murmura@uniroma1.it*

1. Introduction

It is well known that one of the biggest issues with the use of renewable sources consists in their inherent intermittency. In this context, processes that can convert electrical energy into chemical energy represent a viable solution to reduce the imbalance between the rates of production and demand of electricity. These processes are generally referred to as Power-to-Gas (PtG) or Power-to-Liquid (PtL), depending on the physical state of the components used to store the chemical energy. Steam electrolysis falls under the first category, as it allows the production of hydrogen. Compared to water electrolysis, in the steam-based process part of the required energy is provided as heat, thereby allowing a reduction in the amount of electrical energy to be provided. Naturally, the increase in operating temperature of any process is accompanied by water-related problems. In this context, steam electrolysis based on the use of a molten carbonate electrolyte is interesting because it operates at temperatures around 600°C, which is about 200°C lower than steam electrolysis in solid oxide cells. The lower temperature level is advantageous not only because of the lower strain on the materials, but also because it allows coupling the electrolysis process with mid-scale solar concentrating systems.

The net electrolysis reaction is



and, in molten carbonate cells, it is the result of reduction reaction at the cathode



and an oxidation reaction at the anode



Although molten carbonate cells for the electrolysis of water or carbon dioxide have been receiving significant attention in the past years, a literature review has highlighted a complete lack of modelling studies that go beyond so-called "lumped parameter" models capable of describing the correlation between current density and applied voltage without entering into the detail of the cell geometry or operating conditions.

In the present work a 1D model accounting for activation and ohmic overpotentials was developed for a preliminary analysis of experimental data available in the literature [1]. The model was then extended to cells operating at temperatures lower than 550°C. The main difference between the two models (high and mid-temperature) lies in the fact that, while at temperatures higher than 550°C it is possible to work with binary mixtures of Li, Na, or K carbonates, operating below 550°C requires the use of a specific carbonate mixture whose melting temperature is lower than 400°C. The use of a eutectic ternary mixture of Li, Na and K was proposed [2]. Such a mixture is characterized by a different dependence of the ionic conductivity on temperature, which needs to be accounted for when describing ohmic losses. Subsequently, a 2D model,

accounting for chemical, electrochemical, and heat transport phenomena was developed. The results have highlighted the importance of ohmic losses in the performance of the cell and have indicated that activation overpotentials at the cathode are negligible.

2. Methods

The model was developed for a planar cell made up of porous electrodes separated by a molten carbonate electrolytic matrix. A schematic representation of the cell is shown in Figure 1. A 1D model accounting for ohmic and activation losses was initially developed to analyze experimental data available in the literature [REF]. The 2D model also accounts for gas flow in the square gas channels running parallel to the electrodes. The cathodic gas was considered to be an equimolar mixture of H_2O , CO_2 , H_2 , and N_2 ; the gas fed to the anode channel was instead a mixture containing 50% N_2 , 25% O_2 , and 25% CO_2 .

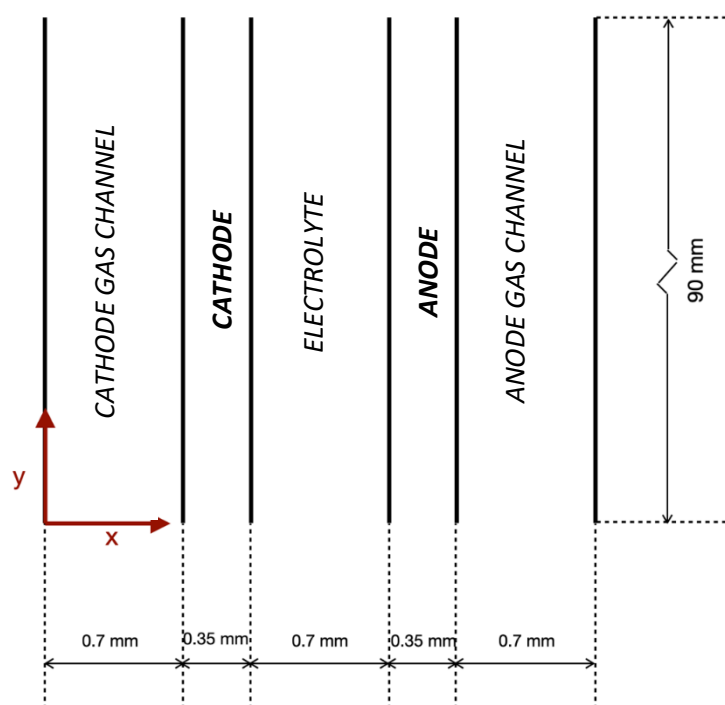


Figure 1. Schematic representation of the modeled electrolysis cell

The 2D model accounted for

- heat transport
- mass transport
- electrochemical reactions (2) and (3) at the cathode and anode, respectively
- reverse water-gas shift reaction in the cathode channel
- heat effects due to the electrochemical and chemical reactions, as well as Joule heating

It is worth noting that the rate of the electrochemical oxidation semi-reaction taking place at the anode was modelled using the Butler-Volmer rate expression with a reference exchange current density evaluated from the 1D model. On the other hand, the analysis of the experimental data showed that the cathodic reaction was very fast, and therefore offered no significant resistance (infinite exchange current density at the cathode).

3. Results and discussion

Figure 2 shows an example of current-potential curves evaluated from the 1D model at different temperatures and considering the exchange current density at the cathode to be sufficiently high as to not have any effect on the performance of the cell. The exchange current density at the anode, on the other hand, was fitted from the

experimental data [1]. The agreement of the experimental (points) and numerical results confirms the validity of assuming negligible activation overpotentials at the cathode. In addition, the shape of the curves suggests that polarization losses are negligible under the entire range of operating conditions investigated, as highlighted by the fact that the slope of the curves does not increase at high current densities.

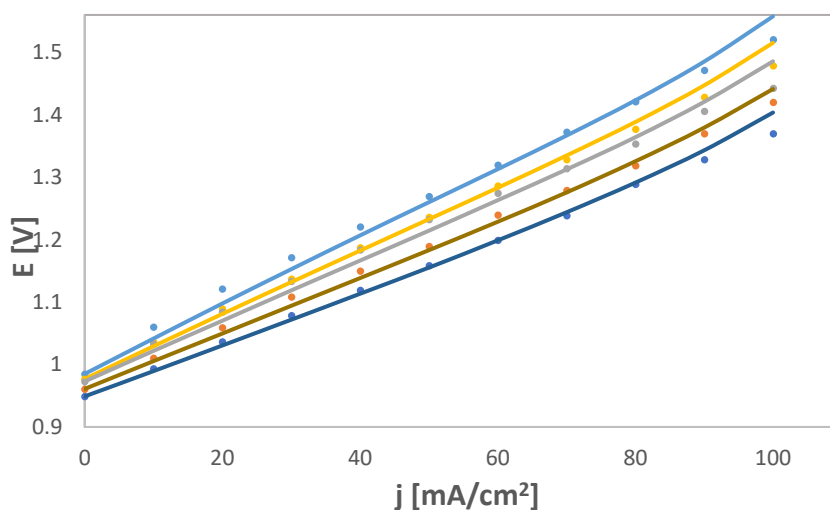


Figure 2. Current-potential curves evaluated from the 1D model at temperatures ranging from 843 (light blue) to 923 K (dark blue) and comparison with experimental data (points) available in [1].

Extending the model to the lower temperature range allowed to carry a sensitivity analysis on the main process parameters, in order to gain insight on this novel process. Figures 3-5 show the effect of varying the effective ionic conductivity of the electrolyte matrix, the thickness of the electrolyte layer, and the exchange current density at the anode, respectively. The base case values of these parameters, determined from the analysis of experimental data, were 2.82 S/m for the effective ionic conductivity, 0.7 mm for the matrix thickness and 2×10^{-2} mA/cm² for the anodic exchange current density. It is interesting to note that the Ohmic resistances seem to have a stronger effect on the overall performance of the cell, suggesting that the correct choice of electrolyte and of its supporting matrix is crucial.

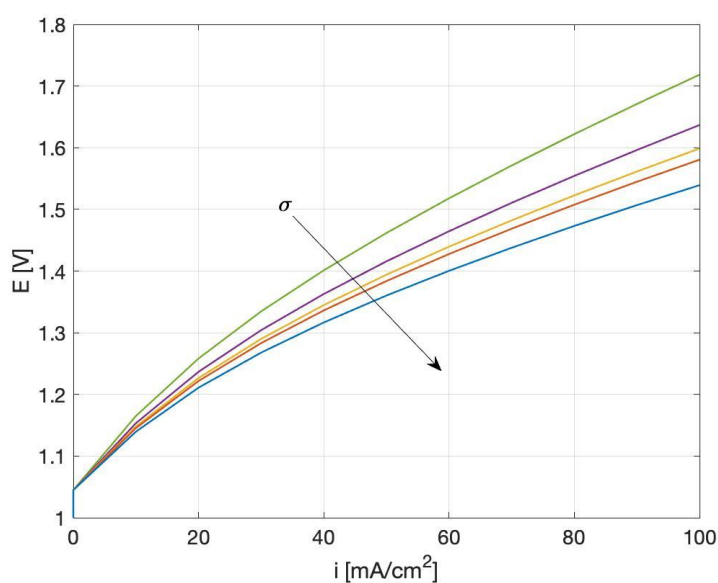


Figure 3. Current-potential curves evaluated from the 1D model at 763 K and effective ionic conductivities of the electrolyte of 2, 2.5, 2.82, 3 e 3.5 S/m.

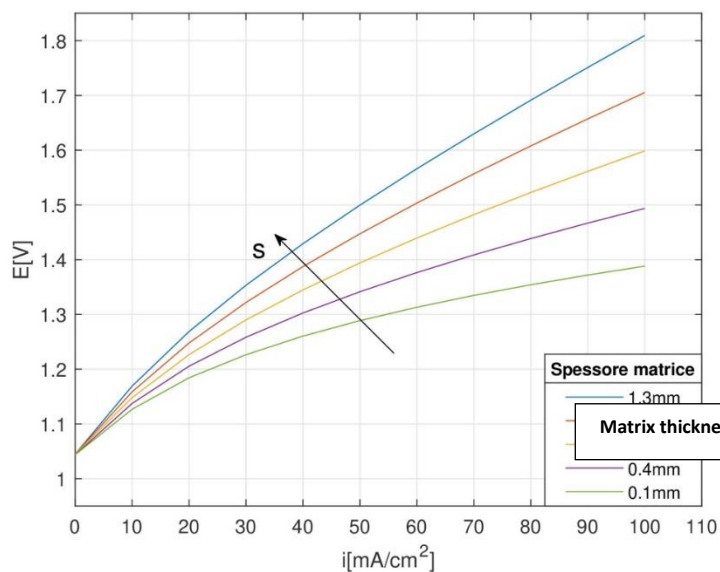


Figure 4. Current-potential curves evaluated from the 1D model at 763 K and thicknesses of the electrolyte layer ranging from 0.1 to 1.3 mm.

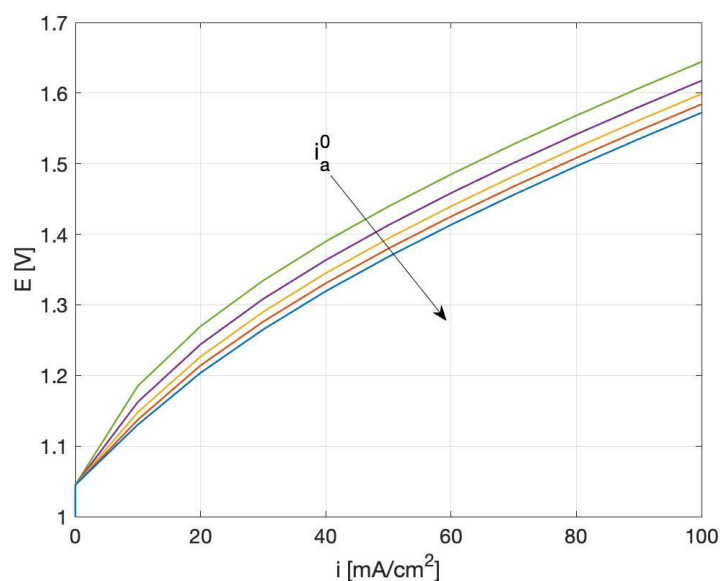


Figure 5. Current-potential curves evaluated from the 1D model at 763 K and exchange current densities at the anode of 1×10^{-2} , 1.5×10^{-2} , 2×10^{-2} , 2.5×10^{-2} , e 3×10^{-2} mA/cm².

The 2D model allowed to determine temperature profiles within the cell and concentration profiles in the gas channels running parallel to the electrode. The temperature was found to be virtually uniform throughout the cell. Typical concentration profiles of hydrogen and water in the cathodic gas channels are reported in Figures 5-8 for a cell operating at 883 K and with an applied potential of 1.5 V and 1.29 V. It is clear that the increase in applied potential favors hydrogen production. The negligible gradients in the direction transversal to that of the main gas flow confirm the finding made with the 1D model that concentration overpotentials are negligible.

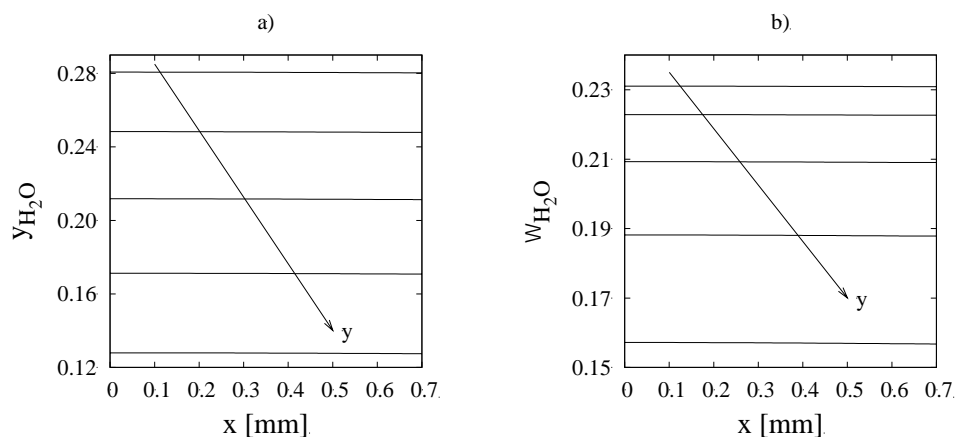


Figure 5. Water concentration profiles in terms of molar (a) and mass (b) fractions a 5, 25, 65, and 85 mm from the inlet section at 883 K and applied voltage of 1.5 V.

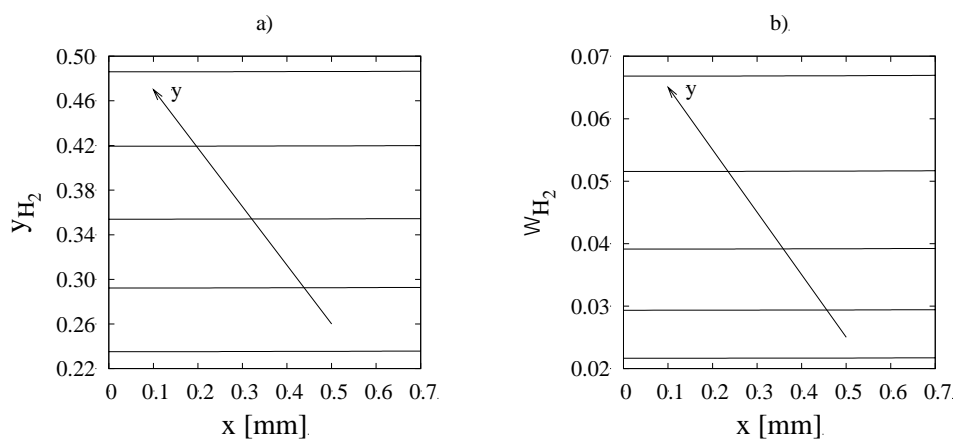


Figure 6. Hydrogen concentration profiles in terms of molar (a) and mass (b) fractions a 5, 25, 65, and 85 mm from the inlet section at 883 K and applied voltage of 1.5 V.

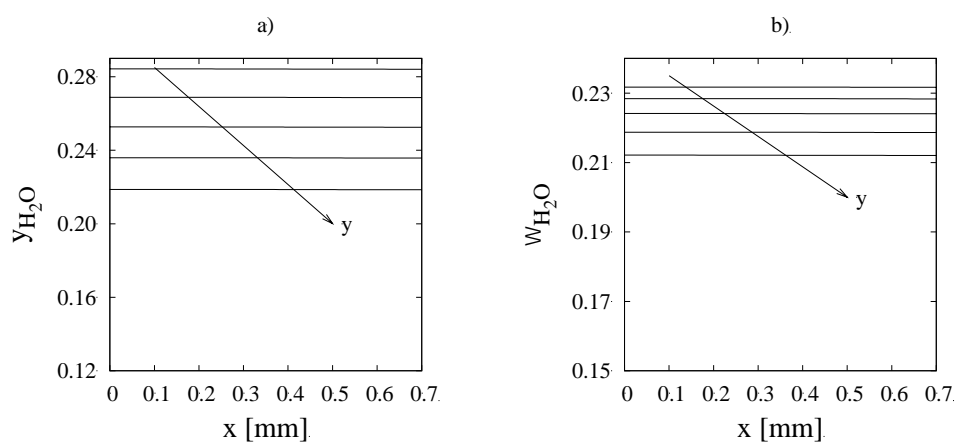


Figure 7. Water concentration profiles in terms of molar (a) and mass (b) fractions a 5, 25, 65, and 85 mm from the inlet section at 883 K and applied voltage of 1.29 V.

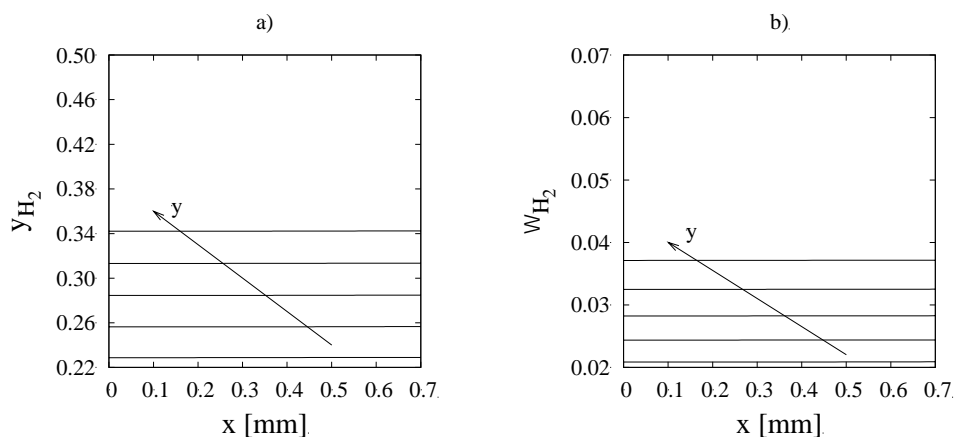


Figure 8. Hydrogen concentration profiles in terms of molar (a) and mass (b) fractions a 5, 25, 65, and 85 mm from the inlet section at 883 K and applied voltage of 1.29 V.

4. Conclusions

1D and 2D models were developed to describe the behavior of electrolysis cells operating with different mixtures of molten carbonates. It was found that the cathodic activation overpotential is negligible, whereas Ohmic losses in the electrolyte matrix have a significant effect on the performance of the cell. The 2D model allows to account for different mass transport and electrochemical phenomena occurring within the cell, thereby allowing to gain more insight on the mechanisms causing the observed overpotentials. More specifically, the 2D model confirmed that concentration overpotentials are not significant under the range of operating conditions investigated and that temperature gradients may also be neglected.

Acknowledgments

The work has been carried out in the framework of the Piano Triennale di Realizzazione ENEA 19-21 per la Ricerca di Sistema Elettrico Nazionale (RdS). Progetto 1.2 “Sistemi di accumulo e relative interfacce con le reti”.

References

- [1] S. Frangini, C. Felici, P. Tarquini, A novel process for solar hydrogen production based on water electrolysis in alkali molten carbonates. *ECS Transactions*, 61(22):13, 2013.
- [2] J.P. Perez-Trujillo, F. Elizalde-Blancas, M. Della Pietra, S.J. McPhail, A numerical and experimental comparison of a single reversible molten carbonate cell operating in fuel cell mode and electrolysis mode, *Applied Energy*, 226:1037-1055, 2018.

One year of surgical mask testing at the University of Bologna labs

C. Boi,^{1,2,5,*} M. Cappelletti,^{2,3} M. G. De Angelis,¹ T. Fabiani,^{1,5} G. Foli,^{5,6} D. Ghezzi,^{3,9} E. Lalli,^{1,5} N. Mehrabi,⁹ M. Minelli,¹ L. Morelli,^{3,5} A. Paglianti,⁴ K. Papchenko,¹ N. F. Parisi,⁹ R. Onesti,^{1,5} M. Roselli,^{1,9} V. Signorini,¹ A. Storione¹, M. Torsello,^{5,7} E. Tugnoli,⁹ F. S. Violante^{2,9}

1. *Department of Civil, Chemical, Environmental and Materials Engineering (DICAM), Alma Mater Studiorum - University of Bologna, Italy*
2. *Interdepartmental Centre for Industrial Research in Health Sciences and Technologies (CIRI-SDV). Alma Mater Studiorum - University of Bologna, Italy*
3. *Department of Pharmacy and Biotechnology (FaBit), Alma Mater Studiorum - University of Bologna, Italy*
4. *Department of Industrial Chemistry "Toso Montanari" (CHIMIND), Alma Mater Studiorum - University of Bologna, Italy*
5. *General Hospital Sant'Orsola Foundation, Bologna, Italy*
6. *Institute of Organic Synthesis and Photoreactivity (ISOF) – National Research Council (CNR), Bologna, Italy*
7. *Department of Chemistry "Giacomo Ciamician", Alma Mater Studiorum - University of Bologna, Italy*
8. *Laboratory of NanoBiotechnology, IRCCS Istituto Ortopedico Rizzoli, Bologna, 40136, Italy*
9. *Division of Occupational Medicine, IRCCS Azienda Ospedaliero-Universitaria di Bologna. Occupational Medicine Unit, Department of Medical and Surgical Sciences, Alma Mater Studiorum - University of Bologna, Italy*

The outbreak of SARS-CoV-2 pandemic highlighted the worldwide lack of surgical masks and personal protective equipment, which represent the main defense available against respiratory diseases as COVID-19. At the time, masks shortage was dramatic in Italy, the first European country seriously hit by the pandemic: aiming to address the emergency and to support the Italian industrial reconversion to the production of surgical masks, a multidisciplinary team of the University of Bologna organized a laboratory to test surgical masks according to European regulations. The group, driven by the expertise of chemical engineers, microbiologists, and occupational physicians, set-up the test lines to perform all the functional tests required. In Europe, surgical masks must be labeled with the CE mark and must meet the requirements defined in EN 14683:2019 and in EN ISO 10993-1. Four test lines were assembled to perform the required tests, namely breathability, bacterial filtration efficiency (BFE), microbial cleanliness (bioburden), and splash test (for IIR type masks). According to the standard, the experimental workflow included first a breathability test that was used to exclude non-suitable materials on the basis of the air permeability. Suitable masks were then tested for BFE, which provides the indication on the filtration capabilities towards droplets with size within the range of the breathing aerosol. Eventually, the microbial cleanliness of the masks was also assayed as an additional parameter of user safety. For masks of Type IIR, the resistance to blood penetration was determined by means of the splash test using synthetic blood. The laboratory started its activity on late March 2020, and as of the end of December of the same year, more than 600 surgical mask prototypes were tested, with nearly 1200 tests performed in total. Here, a critical analysis of the results is presented, with correlations between results for breathability and BFE on surgical mask prototypes. Finally, the protocols for mask testing and validation indicated in the EN standard are discussed, revealing some critical aspects and possible room for improvement. Such analysis aims to optimize the characterization methods for what concern the reliability and the accuracy, as well as the duration, of the surgical masks' standard tests.

*Corresponding author

Email address: cristiana.boi@unibo.it

An electronic nose for COVID-19 detection by means of exhaled breath analysis

Stefano Robbiani², Carmen Bax^{1*}, Emanuela Zannin², Christian Ratti¹, Simone Bonetti³, Luca Novelli³, Federico Raimondi³, Fabiano Di Marco^{3,4}, Raffaele Dellacà², Laura Capelli¹

1 Politecnico di Milano, Department of Chemistry, Materials and Chemical Engineering, piazza Leonardo da Vinci 32, 20133 Milano

2 Politecnico di Milano, Department of Electronics Information and Bioengineering (DEIB), via Colombo 40, 20133 Milano

3 Azienda Ospedaliera Socio Sanitaria Territoriale Papa Giovanni XXIII, Unit of Pneumology, 24127 Bergamo

4 Università degli Studi di Milano, Department of Health Sciences, 20142 Milano

**Corresponding author E-Mail: carmen.bax@polimi.it*

1. Introduction

The COVID-19 has revolutionized our lives, and imposed extraordinary and new challenges on the scientific community worldwide ¹. In this context, chemical engineering has offered methods and technologies to face with the emergency. More in detail, chemical engineers around the world have focused on various aspects associated to the COVID-19 pandemic, such as the study of the nature and physiological mechanisms of the virus ², transport mechanisms in the atmosphere ³, virus stability on materials (e.g., plastic, steel, glass, paper) constituting everyday objects, the production and testing of face masks ⁴, and the research on vaccines, drugs and novel chemicals or technologies for disinfections ⁵⁻⁷.

Many efforts were also devoted to diagnosis. The SARS-CoV-2 can cause fever, cough and even respiratory failure, which is a severe condition that requires prompt intervention ⁸. Nevertheless, those symptoms are not specific for SARS-CoV-2 but can be also related to other infections caused by other viruses or bacteria. For this reason, the research in this field aimed at investigating potentialities and drawbacks of different diagnostic tests (e.g., reverse transcription-polymerase chain reaction (RT-PCR), serological test and antigenic test) or developing alternative approaches, is particularly active.

The analysis of endogenous Volatile Organic Compounds (VOC) of exhaled breath represents an interesting tool to early identify COVID-19 and improve personalizing treatments. Those VOC, resulting from metabolic processes potentially altered by the presence of the disease, can, in fact, provide information on the conditions of subjects, and guide the choice of treatment ⁹.

Electronic noses (ENs), instruments designed for mimicking human olfaction by means of the combination of an array of non-specific gas sensors with machine learning tools ¹⁰, could be considered as a novel, non-invasive and fast diagnostic technique for the rapid identification of COVID-19 patients ⁹.

Several research studies proved the applicability of this technology to exhaled breath analysis to support non-invasive diagnosis of various diseases ¹¹⁻¹⁴, and recent preliminary studies also evaluated the use of ENs for diagnosing SARS-CoV-2 infection ¹⁵⁻¹⁶.

Even though exhaled breath analysis by EN might enable identifying treatable traits in patients with different respiratory disorders, its application to patients with respiratory failure, as it is the case of COVID-19 patients, remains a challenge. Diagnostic systems for the study of VOCs in the exhaled breath should filter out or compensate for ambient VOCs altering the composition of exhaled breath and affecting the diagnosis. In general, systems proposed in the scientific literature obtain lung wash-out by making the subject inhale through a charcoal filter, which adds respiratory load ¹⁷. Therefore, this approach is not suitable for respiratory failure patients.

The present study proposes an experimental set-up for exhaled breath sampling, specifically designed for patients with acute respiratory failure. The set-up was tested with a feasibility study carried out at the hospital

ASST Papa Giovanni XXIII, Bergamo, Italy, involving 1) patients with COVID-19 respiratory failure, 2) asymptomatic patients with SARS-CoV-2 infection and 3) controls.

2. Materials and Methods

2.1. Set-up for exhaled breath collection

The experimental set-up comprises a T-piece to allow a bias flow through the breathing circuit, a non-rebreathing valve (BB089YBPV, Burke & Burke Spa, Milan, Italy), and an antiviral filter to avoid patients cross-contamination (Figure 1). The system is connected to the hospital medical gasses pipeline system to provide clean gasses to prevent sample contamination due to ambient air VOCs influencing the composition of exhaled breath and potentially affecting the results. The connection to the medical gasses pipeline system also allows regulating, according to the patient's needs, the fraction of inspired oxygen (FiO_2). The FiO_2 is an estimation of the oxygen content a person inhales and it is, thus, involved in gas exchange at the alveolar level.

The bias flow of medical gasses passing through the breathing circuit and the FiO_2 can be adjusted using two rotameters on the air and oxygen lines. In the present study, we used a bias flow of 45 L/min and a FiO_2 of 0.21. A 10 cm-long tube at the outlet of the T-piece guarantees that the subject inhales only the gas from the pipeline system and not the environment air.

A Nalophan bag with a capacity of 5L was connected to the expiratory outlet of the non-rebreathing valve to collect exhaled gas.

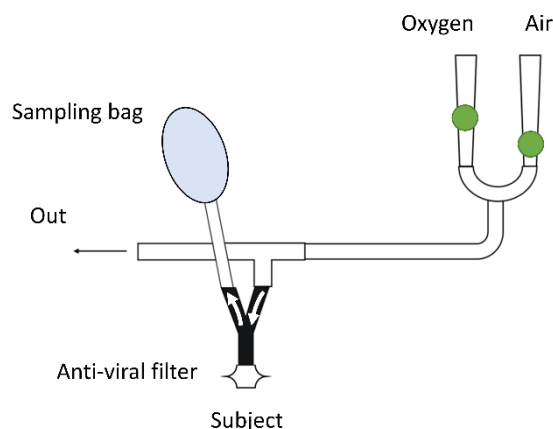


Figure 1. Proposed breath sampling apparatus a) wash-out phase b) exhaled breath sampling.

2.2. Population

The feasibility study carried out at the hospital ASST Papa Giovanni XXIII, Bergamo, Italy (ethical committee approval number 223/20) involved 55 subjects: 1) 25 patients with respiratory failure positive to SARS-CoV-2; 2) 8 asymptomatic subjects positive to SARS-CoV-2; 3) 22 healthy controls. Table 1 summarizes the characteristics of study participants.

Infection with SARS-CoV-2 was determined by PCR test on oropharyngeal swabs. Controls were age-matched subjects with a negative molecular swab to SARS-CoV-2 without chronic respiratory disorders who did not present any respiratory tract infection in the last 90 days.

Table 1. Characteristics of study participants.

	SARS-CoV-2 and respiratory failure	SARS-CoV-2 and asymptomatic	Controls	p-value
N	25	8	22	
Male sex, n	17	3	14	0.295
Age (years), median [IQR]	50 [18.46]	50 [24.15]	50 [23.76]	0.403
Smokers, n	2	2	1	0.219
Ex-smokers, n	5	2	5	0.948
Subjects with other comorbidities, n	10	5	3	0.425

2.3. Experimental protocol

Subjects were asked not to eat, drink, or smoke in the two hours before the study. The sampling protocol consisted of two phases:

- 1) Wash out phase: The subject breathed for 3 minutes through the set-up with the exhalation line of the non-rebreathing valve open, which allowed inhalation of a mixture of medical gasses from the hospital pipeline system and exhalation into the ambient. The subject wore a nose clip to avoid nasal respiration and breathed through a mouthpiece.
- 2) Exhaled breath sampling: At the end of the wash-out phase, patients hold their breath while the operator connects a Nalophan bag to the expiratory line of the non-rebreathing valve to collect exhaled gas. Approximately five breaths were sampled, and the whole procedure lasted less than 5 min.

The bags with exhaled breath samples were stored for 2 to 24 hours after collection in the same room where the EN was installed to reduce the moisture content of samples¹⁸. This sample conditioning phase, exploiting the Nalophan permeability to humidity, allowed preventing the potential interference of moisture on EN responses, thereby ensuring good stability and reproducibility of the measurements¹⁹**Errore. L'origine riferimento non è stata trovata.**

After conditioning, exhaled breath samples were analysed by a commercial e-nose (EOS-AROMA, SACMI s.c) equipped with 4 Metal Oxide (MOX) Sensors. The sampled exhaled gas were sucked at a constant flow rate of 50 mL/min for 20 min into the sensor chamber using a vacuum pump. Then, room reference air was sucked into the sensor chamber at 50 mL/min for 20 min to restore the sensors' baseline. Each sample was analyzed once.

2.4. Data processing

The data processing procedure developed for this study comprises three steps: features extraction, features selection, and pattern recognition. A total of 112 features representative of both steady-state and transient conditions were extracted from sensor time responses, as reported by¹⁹. Then, a feature selection model based on Boruta algorithm²⁰ was implemented to identify the features that better discriminated between respiratory failure patients with SARS-CoV-2 and controls. Selected features were processed by Principal Component Analysis (PCA)²⁰**Errore. L'origine riferimento non è stata trovata.**, and PCA scores were used as inputs of a Support Vector Machine (SVM) classifier²¹.

A 10-fold cross-validation approach was used to optimize features selection and pattern recognition and estimate the classification performances of the proposed model. The diagnostic accuracy of the model was evaluated using the Area Under the Receiving Operating Characteristic (ROC)²² and expressed both as Area Under the ROC curve (AUC), sensitivity, and specificity.

3. Results and discussion

The breath sampling set-up proved suitable clinical setting and well tolerated by the patients. All measurements were completed successfully.

Concerning the EN capability to differentiate odour fingerprints of breath samples from respiratory failure patients with SARS-CoV-2 and controls, Figure 2 illustrates the score plot of the PCA built on the training dataset. Respiratory failure patients with SARS-CoV-2 and controls clustered in different plot regions: samples from controls clustered in the upper right part of the plot, while samples from respiratory failure patients with SARS-CoV-2 clustered in the lower left portion. This evidence suggests that EN has the potential to identify the specific odour fingerprint associated with respiratory failure due to COVID-19.

We superimposed data from asymptomatic SARS-CoV-2 patients as an exploratory analysis on the PCA model. Interestingly, the asymptomatic SARS-CoV-2 infected subjects fell between the two clusters, i.e., respiratory failure patients with COVID-19 and controls. This result, also confirmed by the analysis of the 2-Norm of PCA scores (Figure 3), suggested that the EN may provide information about the presence of the infection and the severity of the disease.

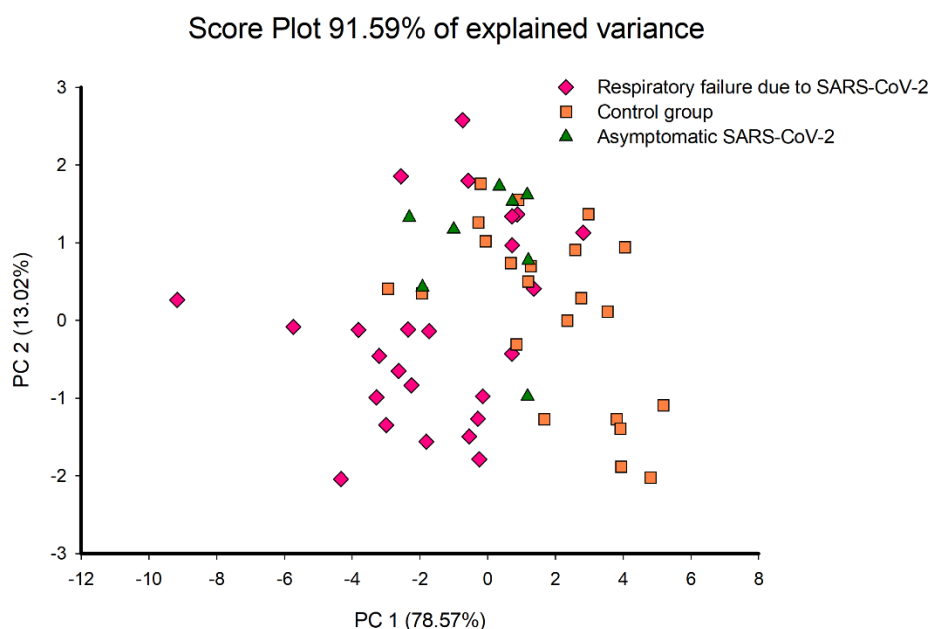


Figure 2. Principal components of selected features in asymptomatic SARS-CoV-2 infected patients (red circles), respiratory failure patients with COVID-19 (blue circles), and control subjects (green circles).

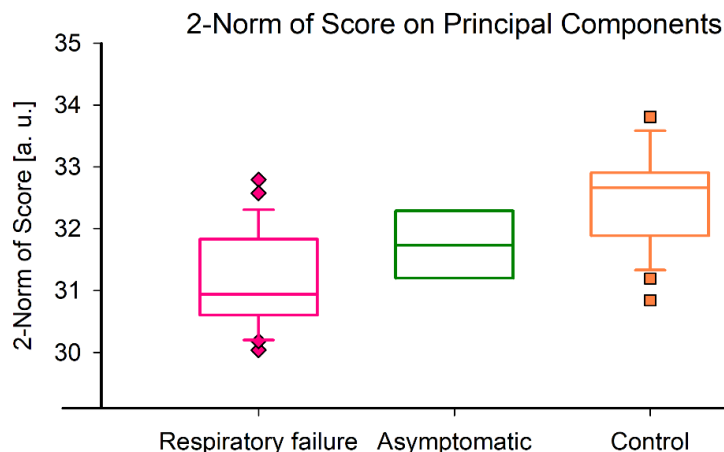


Figure 3. 2-Norm of scores of all the Principal Component of COVID-19 patients with respiratory failure, asymptomatic SARS-CoV-2 infected patients, and healthy controls. The boundaries of the boxes indicate the 25th and 75th percentiles, the lines within the boxes mark the median values. Whiskers indicate the 90th and 10th percentiles. Closed circles are considered outliers.

The classification model achieved a sensitivity of 92% (CI_{95%} 87 - 99), a specificity of 68% (CI_{95%} 54 - 78), and an AUC of 81% (CI_{95%} 54 – 78).

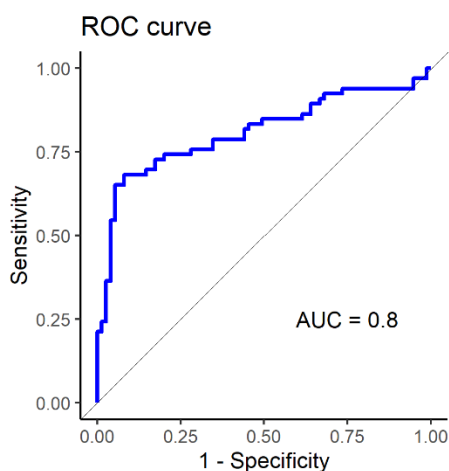


Figure 8. Receiving Operating Characteristic (ROC) curve.

4. Conclusions

The feasibility study here described proved the potentialities of EN technologies for the exhaled breath analysis aimed at diagnostic purposes. It can provide an alternative to traditional clinical tests to ease the identification of respiratory failure causes' and improve patients' management. However, this type of analysis in patients with respiratory failure is challenging because of patients' unstable conditions and VOCs contains in the environment that can affect the EN analysis (e.g., VOCs associated with cleaning chemicals, drugs, other diseases, etc).

This study introduces an innovative breath sampling system specifically designed for respiratory failure patients, overcoming the issues associated with using charcoal filters to compensate for ambient VOCs, which add respiratory load and are usually not certified to be used with oxygen-enriched mixtures. The proposed set-up uses medical gasses available from the hospital pipeline system to wash out the lungs from ambient VOCs and collect uncontaminated exhaled breath without increasing the patient's work of breathing. Such a solution also allows the investigator to provide oxygen-enriched air with fine control of the FiO_2 , as commonly required by patients with respiratory failure.

This system was evaluated on stable patients with and without respiratory failure due to SARS-CoV-2 infection and on healthy controls and proved feasible for the critical care setting. At first, a classification model to investigate whether the device can detect differences in the odour fingerprints of patients with respiratory failure compared with controls was developed. Sensitivity and specificity of 92% and 69%, respectively, were achieved within this feasibility study. Those results proved EN's potentialities in discriminating between SARS-CoV-2 patients with respiratory failure and the control group.

An exploratory analysis included asymptomatic subjects who tested positive for SARS-CoV-2. Asymptomatic patients distinguished from the control group, suggesting that the proposed method can identify subjects positive to SARS-CoV-2 even if they do not present symptoms. Moreover, our preliminary results show that they present an intermediate response between patients with COVID-19 and respiratory failure and the control group. Such finding is very interesting because it suggests that the proposed method is sensitive both to the presence of an infection and the severity of the disease. Further studies are warranted to investigate whether the proposed method can be used to identify the treatable traits of respiratory failure or to monitor the progression of disease severity.

References

- [1] Sohrabi, C.; Mathew, G.; Franchi, T.; Kerwan, A.; Griffin, M.; Soleil C Del Mundo, J.; Ali, S. A.; Agha, M.; Agha, R., Impact of the coronavirus (COVID-19) pandemic on scientific research and implications for clinical academic training – A review. *International Journal of Surgery* 2021, 86, 57-63.
- [2] Mittal, A.; Manjunath, K.; Ranjan, R. K.; Kaushik, S.; Kumar, S.; Verma, V., COVID-19 pandemic: Insights into structure, function, and hACE2 receptor recognition by SARS-CoV-2. *PLOS Pathogens* 2020, 16 (8), e1008762.
- [3] Setti, L.; Passarini, F.; De Gennaro, G.; Barbieri, P.; Perrone, M. G.; Piazzalunga, A.; Borelli, M.; Palmisani, J.; Di Gilio, A.; Piscitelli, P.; Miani, A., The Potential role of Particulate Matter in the Spreading of COVID-19 in Northern Italy: First Evidence-based Research Hypotheses. *medRxiv* 2020, 2020.04.11.20061713
- [4] Chua, M. H.; Cheng, W.; Goh, S. S.; Kong, J.; Li, B.; Lim, J. Y. C.; Mao, L.; Wang, S.; Xue, K.; Yang, L.; Ye, E.; Zhang, K.; Cheong, W. C. D.; Tan, B. H.; Li, Z.; Tan, B. H.; Loh, X. J., Face Masks in the New COVID-19 Normal: Materials, Testing, and Perspectives. *Research* 2020, 2020, 7286735.
- [5] Wang, J.; Shen, J.; Ye, D.; Yan, X.; Zhang, Y.; Yang, W.; Li, X.; Wang, J.; Zhang, L.; Pan, L., Disinfection technology of hospital wastes and wastewater: Suggestions for disinfection strategy during coronavirus Disease 2019 (COVID-19) pandemic in China. *Environmental Pollution* 2020, 262, 114665.
- [6] Kotecha, P.; Light, A.; Checcucci, E.; Amparore, D.; Fiori, C.; Porpiglia, F.; Dasgupta, P.; Elhage, O., Repurposing of drugs for Covid-19: a systematic review and meta-analysis. *medRxiv* 2020, 2020.06.07.20124677.
- [7] Silveira, M. M.; Moreira, G. M. S. G.; Mendonça, M., DNA vaccines against COVID-19: Perspectives and challenges. *Life Sciences* 2021, 267, 118919.
- [8] Papazian, L.; Calfee, C. S.; Chiumello, D.; Luyt, C.-E.; Meyer, N. J.; Sekiguchi, H.; Matthay, M. A.; Meduri, G. U., Diagnostic workup for ARDS patients. *Intensive Care Medicine* 2016, 42 (5), 674-685.
- [9] Dragonieri, S.; Pennazza, G.; Carratu, P.; Resta, O., Electronic Nose Technology in Respiratory Diseases. *Lung* 2017, 195 (2), 157-165.
- [10] Covington, J. A.; Marco, S.; Persaud, K. C.; Schiffman, S. S.; Nagle, H. T., Artificial Olfaction in the 21st Century. *IEEE Sensors Journal* 2021, 21 (11), 12969-12990.
- [11] Fens, N.; van der Schee, M. P.; Brinkman, P.; Sterk, P. J., Exhaled breath analysis by electronic nose in airways

- disease. Established issues and key questions. *Clinical & Experimental Allergy* 2013, 43 (7), 705-715.
- [12] Turner, A. P. F.; Magan, N., Electronic noses and disease diagnostics. *Nature Reviews Microbiology* 2004, 2 (2), 161-166.
- [13] Behera, B.; Joshi, R.; Anil Vishnu, G. K.; Bhalerao, S.; Pandya, H. J., Electronic nose: a non-invasive technology for breath analysis of diabetes and lung cancer patients. *Journal of Breath Research* 2019, 13 (2), 024001.
- [14] Wilson, A. D., Advances in electronic-nose technologies for the detection of volatile biomarker metabolites in the human breath. *Metabolites* 2015, 5 (1), 140-63.
- [15] Wintjens, A.; Hintzen, K. F. H.; Engelen, S. M. E.; Lubbers, T.; Savelkoul, P. H. M.; Wesseling, G.; van der Palen, J. A. M.; Bouvy, N. D., Applying the electronic nose for pre-operative SARS-CoV-2 screening. *Surgical endoscopy* 2021, 35 (12), 6671-6678.
- [16] Kurstjens, S.; García-Tardón, N.; Fokkert, M.; van Geffen, W. H.; Slingerland, R.; Van Der Palen, J.; Kusters, R., Identifying COVID-19-infected healthcare workers using an electronic 'nose'. *European Respiratory Journal* 2021, 58 (suppl 65), PA3869.
- [17] Krauss, E.; Zoelitz, J.; Wagner, J.; Barretto, G.; Degen, M.; Seeger, W.; Guenther, A., The use of electronic nose technology for the detection of Lung Cancer (LC): analysis of exhaled volatile compounds by Aeonose®. *European Respiratory Journal* 2018, 52 (suppl 62), PA1758.
- [18] Guillot, J.M.; Beghi, S. (2008). Permeability to water vapour and hydrogen sulphide of some sampling bags recommended by EN 13725. 15.
- [19] Capelli, L.; Bax, C.; Grizzi, F.; Taverna, G. Optimization of training and measurement protocol for eNose analysis of urine headspace aimed at prostate cancer diagnosis. *Sci. Reports | 123AD*, 11, 20898, doi:10.1038/s41598-021-00033-y.
- [20] Kursa, M.B.; Jankowski, A.; Rudnicki, W.R. Boruta - A system for feature selection. *Fundam. Informaticae* 2010, 101, doi:10.3233/FI-2010-288.
- [21] Kasemsap, K., Artificial Intelligence: Current Issues and Applications. In *Handbook of Research on Manufacturing Process Modeling and Optimization Strategies*, Das, R.; Pradhan, M., Eds. IGI Global: Hershey, PA, USA, 2017; pp 454-474.
- [22] Fan, J.; Upadhye, S.; Worster, A., Understanding receiver operating characteristic (ROC) curves. *Canadian Journal of Emergency Medicine* 2006, 8 (1), 19-20.

From Reaction Safety Modelling towards COVID-19 Pandemic Risk Early Detection

Chiara Vianello¹, Fernanda Strozzi², Paolo Mocellin¹, Bruno Fabiano³,
Flavio Manenti⁴, Giuseppe Maschio^{1*}

1 Università degli Studi di Padova, Dipartimento di Ingegneria Industriale. Via Marzolo 9, 35131, Padova, Italy

2 Università Carlo Cattaneo e LIUC. Corso Matteotti 22, 21053, Castellanza (Varese), Italy

3 Università di Genova, Dipartimento di Ingegneria Civile, Chimica e Ambientale. Via Montallegro 1, 15145, Genova, Italy

4 Politecnico di Milano. CMIC Dept. "Giulio Natta", Piazza Leonardo da Vinci 32, 20133, Milano, Italy

* Corresponding author Giuseppe Maschio: giuseppe.maschio@unipd.it

1. Introduction

The ongoing COVID-19 epidemic highlights the need for effective tools to predict the onset of infection outbreaks at their early stages. The tracing of confirmed cases and the prediction of the local dynamics of contagion through early indicators are crucial measures to a successful fight against emerging infectious diseases (EID).

The proposed framework is model-free and applies Early Warning Detection Systems (EWDS) techniques to detect changes in the territorial spread of infections in the very early stages of onset. This study uses publicly available raw data on the spread of SARS-CoV-2, mainly sourced from the Italian Civil Protection Department database.

Two distinct EWDS approaches, the Hub-Jones (H&J) and Strozzi-Zaldivar (S&Z), are adapted and applied to the current SARS-CoV-2 outbreak. They promptly generate warning signals and detect the onset of an epidemic at early surveillance stages even if working on the limited daily available, open-source data.

The EWDS S&Z criterion is theoretically validated based on the epidemiological SIR.

Discussed EWDS successfully analyze self-accelerating systems, like the SARS-CoV-2 scenario, to identify an epidemic spread by calculating onset parameters precociously. This approach can also facilitate early clustering detection, further supporting common fight strategies against the spread of EIDs. Overall, we are presenting an effective tool based on solid scientific and methodological foundations to be used to complement medical actions to contrast the spread of infections such as COVID-19.

2. Methods

This paper proposes a contribution to analysing and interpreting real data on the spread of SARS-CoV-2.

This study is based on the processing of publicly available raw data of which the main source is the database of the Italian Civil Protection Department [1] [2].

The proposed methodology is inspired by the previous experience developed in chemical engineering for the early analysis of the onset of runaway reactions in chemical processes that have been the cause in the past of industrial accidents such as that of Seveso and Bhopal, only to name a few. The approach used is devoid of mathematical models for describing the phenomenon and applies Early Warning Detection Systems (EWDS) techniques to detect changes in the territorial spread of infections in the very early stages of onset.

The study discusses the applicability and adaptability of two EWDS criteria to the pandemic in order to monitor viral spread: the approaches used are those of Hub-Jones (H&J) [3] and Strozzi-Zaldivar (S&Z) [4].

They can process the SARS-CoV-2 data available, in real-time and open-source at the different stages of the development of the pandemic, to promptly generate warning signals and detect the onset or resumption of a potential epidemic and monitor the effects of contrast measures adopted such as social distancing and the classification in coloured zones of our regions [5].

The Hub & Jones criterion states that the runaway occurs when the first and second mathematical derivatives of a system variable s (usually the temperature, T) concerning time t are simultaneously positive.

In a typical reaction system, when the temperature of a reactor increases such that $dT/dt > 0$, the runaway occurs if the second condition is also met.

The boundary between stable and unstable behaviour (runaway) is represented by the temperature trajectory concerning the time when the value of d^2T / dt is greater than zero while the reactor temperature is increasing $dT / dt > 0$

The Strozzi & Zaldivar criterion is based on chaos theory. The method was born from the study of the sensitivity to initial conditions of complex chaotic systems through the Lyapunov exponents (Benettin et al., 1980), i.e. the average increase in the lengths of the axes of an ellipsoid in the state space defined using a single variable of the system (the temperature $T(t)$ in the case of chemical reactors).

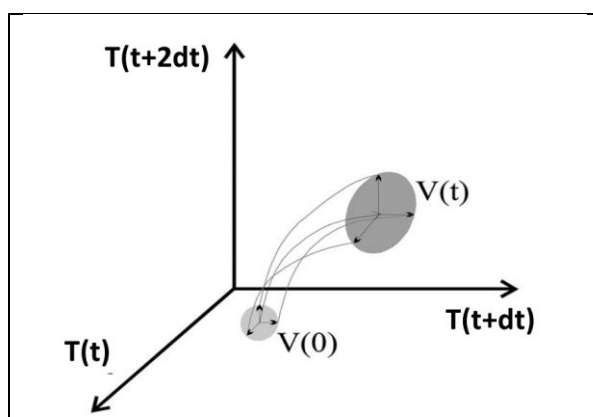


Figure 2. S&Z methodology

The increase in volume is measured by the divergence that allows you to quickly detect a runaway reaction in order to intervene in advance thus putting the system in safety. Furthermore, the EWDS S&Z criterion is theoretically validated based on the epidemiological SIR [7].

The EWDS discussed are suitable for analyzing self-accelerating systems, such as the SARS-CoV-2 scenario, to identify an epidemic spread early through onset parameters. This innovative approach can promote cluster detection and identify the early spread of emerging infectious diseases to support common control strategies. This method and the related results represent a proactive tool based on solid scientific and methodological foundations that can be used as a complementary system of medical and social distancing actions to combat the viral spread of COVID-19.

3. Results and discussion

The characteristics of the Covid-19 epidemic, combined with the high population density and intense movements on the territory in the North Italian area, has required and still requires an intense scientific and technological effort to support the control and prevention of the virus spread.

An effective fight against similar future scenarios must be a rapid, integrated, and proactive intervention based on the ability to aggregate large datasets from different sources by tracing confirmed cases and predicting the local dynamics of contagion through early indicators.

These elements are part of a “quick learn” strategy, where rapid interpretation of evolving data is crucial to identify the best actions to prevent and contain infection outbreaks, thus enabling Governments to implement timely mitigating strategies. Additionally, the rapid enforcement of preventive measures may avoid resorting to drastic and prolonged lockdowns, which carry dramatic financial implications [6].

To support this strategy, we proved that EWDS algorithms developed and tested on the basis of ongoing epidemic dynamics, can be validly used to monitor the evolution of EIDs. This approach can be useful even if an EID is latent for medium to long periods in a specified area, giving early warnings to detect the onset of new outbreaks or the disease spread resumption.

Both discussed and adopted EWDS systems allow robust monitoring of the development status of the epidemic, and to predict early on-set peaks even in case of overlapping outbreaks. The main advantage of the

EWDS is the fact of being Model Free, thus simply requiring series of data and not consolidated mathematical models, thus greatly reducing the sources of error and increasing their versatility.

The results of the two methodologies show that the H&J method can predict well in advance the set point of the exponential growth of the epidemic. The S&Z method relying on the divergence, highlights in advance the impact of the effects due to the mitigation decrees. The measures adopted in March in Italy influenced the trend of the divergence, by decreasing it. On the contrary, when the epidemic restarts the divergence again increases becoming higher than zero and it can be used as an early warning system.

The results achieved with the combination of the two developed EWDS systems, can represent an early alerting tool for tracking the epidemic. This combined approach can robustly support decision makers to best define switches between phases (tightening and/or untightening of restriction measures), also differentiated in the national territory, and it can mainly be used as an early warning tool for future epidemic outbreaks to be rapidly detected, confined and recovered.

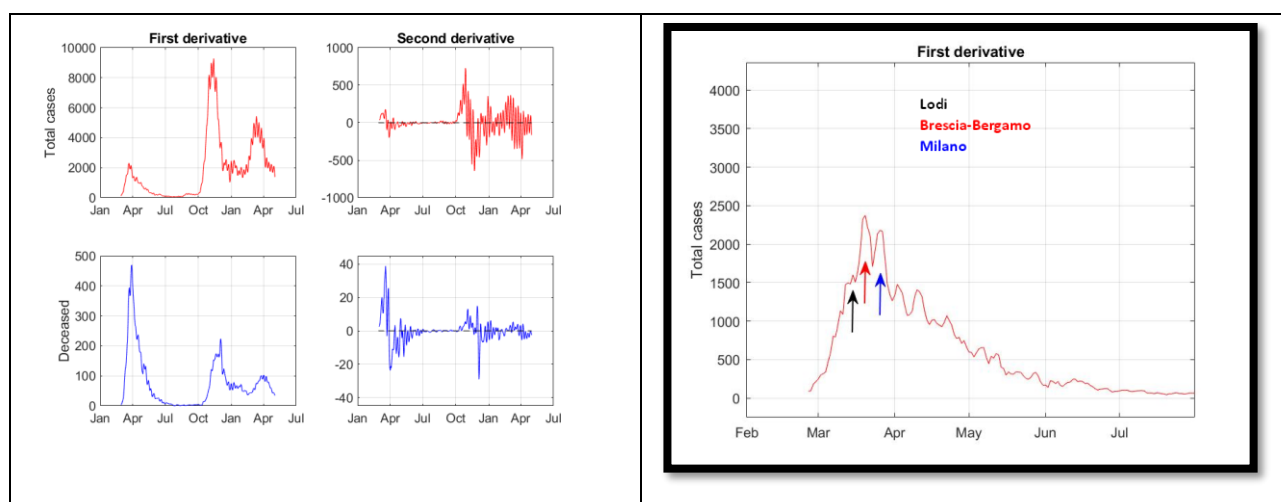


Figure 2. H&J criterion, first and second derivatives calculated from raw data for Lombardy

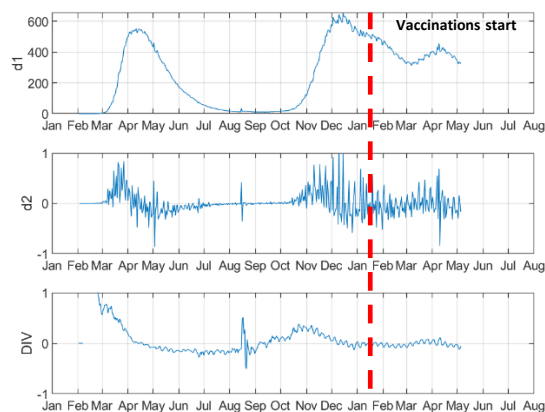


Figure 3. S&Z criterion, divergence during the whole evolution of the contagion

In perspective, the EWDS criteria may also be coupled with the monitoring of other relevant data that will be identified by decision makers on the basis of the fundamental scientific contribution of the medical community. Even considering the limitations of the combined approach, as commented by Thomas “the knowledge about the main modes of the epidemic’s behaviour and the orders of magnitude of the numbers of people affected under the various options can regarded as good enough to guide policy decisions”.

The proposed framework therefore lends itself easily to being extended and applied to an increasingly evolved, exhaustive and accurate context of available information. In this way, upon proper refinement and possible connection with advanced epidemiological data, a predictive tool based on solid scientific and methodological foundations will be made available to decision makers which, coupled with medical and epidemiological

studies suitable for understanding the mechanisms of replication and spread of the virus, can provide an integrated method for contrasting its spread.

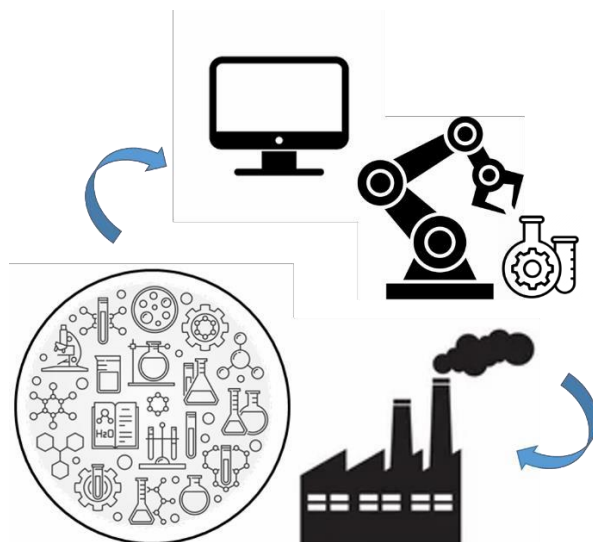
References

- [1] Johns Hopkins Resource Center, COVID-19 Map, Johns Hopkins Coronavirus Resour. Cent, 2020.
- [2] Dipartimento della Protezione Civile. COVID-19 Monitoring Italy Database (2020). <https://github.com/pcm-dpc/COVID-19>
- [3] L. Hub, J.D. Jones. Early on-line detection of exothermic reactions *Plant/Operations Prog.*, 5 (1986), pp. 221-224, 10.1002/prsb.720050408
- [4] F. Strozzi, J.M. Zaldívar, A.E. Kronberg, K.R. Westerterp. On-Line runaway detection in batch reactors using chaos theory techniques. *AIChE J*, 45 (1999), pp. 2429-2443.
- [5] World Health Organization, WHO Coronavirus Disease (COVID-19) Dashboard, World Heal. Organ., 2020.
- [6] Vianello et als., A perspective on early detection systems models for COVID-19 spreading in *Biochemical and Biophysical Research Communications* 2020 DOI: 10.1016/j.bbrc.2020.12.010
- [7] S. Zhao, H. Chen. Modeling the epidemic dynamics and control of COVID-19 outbreak in China. *Quant. Biol.* (2020), 10.1007/s40484-020-0199-0
- [8] K. Sasaki. COVID-19 Dynamics with SIR Model (2020). <https://www.lewuathe.com/covid-19-dynamics-with-sir-model.html>

Automation and Machine Learning in Chemical Engineering

D. Russo*

*Dipartimento di Ingegneria Chimica, dei Materiali e della Produzione Industriale, Università degli Studi di Napoli, Federico II.



Chemical Engineering has a central role in our ever-changing world, offering promising pathways to an energetic paradigm change and new sustainable processes and products. In such a scenario, it is clear that traditional teaching, research, and applicative paradigms of chemical engineering need to be integrated in a wider framework, including a large number of disciplines and professional skills. Automation and Machine Learning are not new to fundamental research and technological development. However, in the last decade we have assisted to an exceptionally growing number of applications of such techniques to science and engineering both in the academia and industry. This shift from the traditional fields of social media, search indexing, and information management from webpages, to applied sciences, and in particular to chemical engineering, poses a large number of new challenges.

In this talk, I will provide an overview of the state-of-art of automation and machine learning techniques in the chemical engineering fields of product design and process optimization, also discussing the open problems of computer-aided product discovery, scale-up, and multistage design. The topics will be discussed from an academic research point of view, giving an insight into the possibility of integrating and/or deriving fundamental physical knowledge from automated experiments, and highlighting the fundamental differences between the traditional applications of machine-learning-aided robotics and the new challenges in the field of chemical engineering.

The Role of Safety for the Implementation of Cryogenic Systems

Gianmaria Pio

Dipartimento di Ingegneria Civile, Chimica, Ambientale e dei Materiali dell'Università di Bologna

gianmaria.pio@unibo.it

The need for sustainable and environmentally friendly raw materials, together with the geopolitical instability, pushed toward the development of alternative technologies in several industrial fields. A clear example of this tendency is the energy supply chain, where several molecules showing the potentiality to be alternative fuels have been produced and deeply investigated. The novelty in the chemical structure, leading to different physical properties, has required the adaption of the existing combustion and storage conditions, together with process layout. Besides, the utilization of low-temperature conditions has been largely suggested because of the possible lean solutions and the subsequent reduction in the production of the most harmful pollutants. Moreover, also storage and transportation systems are facing an era of great changes. Indeed, cryogenic transportation has promoted the exploration and exploitation of remote reservoirs, with obvious implications for the differentiation of possible sources. One of the main actors involved in this mutation is liquefied natural gas (LNG), as testified by the increasing number of research projects investigating this topic. The knowledge and know-how required for the realization of infrastructures and processes suitable for LNG production, transportation, and utilization have positive spill-over toward the development of technological solutions promoting the hydrogen economy. Indeed, liquid hydrogen (LH₂) has been considered one of the most promising fuels, especially for the civil and industrial transportation fields, mainly because of its carbon-free nature and elevated energy density. However, the shift toward cryogenic conditions has posed new challenges, especially from the safety perspective, requiring the development and validation of dedicated sub-models for the evaluation of the source terms and physical-chemical phenomena.

Dedicated research projects have unravelled some of the most peculiar phenomena occurring at extremely low temperatures (e.g., mist condensation, non-equilibrium evaporation, and the ortho-to-para transformation). It is also worth mentioning that the initial conditions strongly influence the chemical aspects too, making some empirical correlations developed for temperatures above atmospheric ones unreliable. In this sense, the development and implementation of detailed kinetic mechanisms deriving from automated approaches are strongly suggested. Besides, the increasing availability of computational power has opened the integration of these mechanisms, in a reduced form, in computational fluid dynamic (CFD) models for the evaluation of physical-chemical interactions in a wide range of operative conditions and 3-dimensional domains. On the other hand, the main drawbacks are represented by the increase in complexity of the analyses, requiring specific expertise and engineering tools. The numerical root of the described approaches suggests the realization of a validation procedure. However, practical limitations in producing a robust experimental database exist, requiring additional considerations in the design of experiments (e.g., the ineffectiveness of traditional emergency response strategies and material embrittlement).

In this view, this lecture outlines and presents the most relevant phenomena and available techniques for the experimental and numerical characterization of the safety aspects determining the behaviour at low temperatures relevant for applications related to chemical engineering and process plants.

Acknowledgements

The author gratefully acknowledges the financial support of the Adriatic-Ionian Programme INTERREG V-B Transnational 2014-2020. Project #118: SUPER-LNG - "Sustainability PERFORMANCE of LNG-based maritime mobility"

Ottimizzazione delle condizioni operative di processi di produzione di microalghe in continuo attraverso modelli matematici

Elena Barbera

Dipartimento di Ingegneria Industriale DII,

Università di Padova,.

elena.barbera@unipd.it

Microalghe e cianobatteri hanno recentemente suscitato l'interesse della comunità scientifica e industriale, grazie alle loro potenzialità di applicazione in diversi settori quali nutraceutica, agricoltura, trattamento di acque reflue, ecc., favorendo lo sviluppo di un'industria bio-based. Rispetto ai convenzionali sistemi di coltivazione batch, la produzione di questi microrganismi in sistemi operanti in continuo appare vantaggiosa, in quanto garantisce un miglior controllo delle condizioni operative e, in condizioni di stato stazionario, una maggiore stabilità della produzione, in termini di quantità e qualità (i.e. composizione) della biomassa prodotta. In questo contesto, la disponibilità di modelli matematici che descrivano l'andamento delle performance del processo in funzione delle principali variabili (intensità e qualità della luce, temperatura, concentrazione di nutrienti e di ossigeno disciolti, tempo di residenza) è fondamentale per ottimizzare le condizioni operative relativamente all'applicazione di interesse. In questa lecture verrà descritto lo sviluppo di modelli cinetici per la crescita microalgale in relazione a diverse applicazioni, la determinazione e validazione dei relativi parametri sulla base del confronto con dati sperimentali, e la loro applicazione a diversi casi studio, quali la produzione di biomassa in diverse tipologie di fotobioreattori, la rimozione di azoto e fosforo da acque reflue, e la produzione di uno specifico composto di interesse. L'approccio adottato ha permesso di evidenziare come, attraverso l'applicazione di un metodo sistematico e dei principi dell'ingegneria chimica e di processo, sia possibile migliorare significativamente la produttività, in quanto, nel caso di microrganismi fotosintetici, uno scostamento anche lieve dalle condizioni operative ottimali (in particolare in riferimento al tempo di residenza) ne diminuisce sensibilmente le prestazioni.

Single-Atom Catalysts for a New Generation of Industrial Chemical Processes

Gianvito Vilé

Laboratory of Applied Physical
Chemistry

Department of Chemistry, Materials and Chemical Engineering “Giulio Natta” Politecnico di Milano

New catalytic processes are urgently needed to drive the transition to a cleaner and more sustainable future, and the European Commission has identified that this is an asset to fulfill the Paris Agreement.

Single-atom catalysts are the new frontier of chemical reaction engineering and can accelerate the shift to a greener future due to their groundbreaking reactivity and ability to economize the amount of critical raw materials.

This lecture will present my groundbreaking contribution in this emerging field, from discovering these new catalysts, to the possibility of studying their reactivity under continuous-flow conditions. Specifically, by focusing on the cycloaddition reactions, which are widely applied in the pharmaceutical sector, I will demonstrate that single-atom catalysts can provide unprecedented activities and selectivities compared to state-of-the-art catalysts. With the help of density functional theory calculations and operando characterization studies, I will elucidate the active sites and propose a plausible reaction mechanism for the flow reaction. Finally, I will demonstrate how the nanomaterials can be nanostructured in flow microreactors to obtain novel structured thin films and foams with integrated single-atom functionalities for intensified chemical processes. This will close the gap on challenges related to catalyst-device integration, going beyond traditional packed-bed and structured reactors, building new bridges between physical chemistry and unit operation.

FROM WASTE TO NEW PRODUCTS: RECOVERY AND APPLICATIONS OF BIOACTIVE COMPOUNDS FROM AGRI-FOOD INDUSTRY BY-PRODUCTS

ABSTRACT

Waste valorization is one of the most important challenges to improve circular economy and to approach the zero-waste goal. Agri-food industry produces huge amount of by-products, often containing several bioactive molecules, like antioxidants, whose recovery can provide valuable compounds for applications in pharmaceutical, cosmetic, and food industries. This solution is able also to respond to the increasing demand of the market towards naturally-derived compounds, due to consumers who are more aware and pay a lot of attention to their lifestyle. The complex chemical composition of biomasses deriving from the agri-food sector led to many proposals reported in literature for their reuse and their valorization. Albeit several strategies are valuable, a higher impact on the economic sustainability of the processes involving agri-food industry by-products could be identified firstly in the recovery of high-added value compounds, and then the solid residue of the extraction could be further exploited for biofuels and chemicals production, in agreement with the hierarchical approach proposed by biorefineries. In this context, the extraction step plays a pivotal role, due to the nature of target compounds. Innovative techniques like microwave-assisted extraction, ultrasound-assisted extraction and high-pressure and temperature extraction can increase the performance of process allowing to protect the activity of recovered compounds. Indeed, antioxidants, like polyphenols and carotenoids are able to prevent oxidative stress in our body, counteracting aging and the development of several chronic diseases such as cancer, stroke and type 2 diabetes, and can exert antimicrobial action. Their bioactivity makes them suitable for producing innovative products like nutraceuticals and active food packaging enhanced with antioxidant properties to prolong food shelf life. Nevertheless, thermosensitivity of such compounds requires innovative strategies for their recovery and for products formulation.

This talk aims to discuss the role of non-conventional extraction techniques, the optimization of process variables and post-processing methods in the recovery of bioactive compounds from agri-food waste and to explore new potential applications of the extract in the food sector.

ANALYSIS OF TECHNOLOGIES FOR CO₂ CAPTURE FROM THE AIR

The increase of CO₂ concentration in the atmosphere urges the research community to find other solutions to solve this environmental problem, causing climate change and global warming. The removal of CO₂ through the use of negative emission technologies could lead the global emission level to be net negative towards the end of the century. Among these negative emissions technologies, direct air capture (DAC), capturing CO₂ directly from the atmosphere, could play an important and significant role. The captured CO₂ can be removed in the long term with its storage as well as it can be used for chemical processes, allowing to have closed carbon cycles in the short term. For DAC, different technologies have been suggested in the literature and an overview of these is proposed. Absorption and adsorption are the most studied and mature but others are under investigation. An analysis of the main key performance indicators is also reported suggesting how more efforts should be done to develop DAC at a large scale by reducing costs and improving efficiency.

Municipal solid waste and circular economy: alternative resource for the production of energy vectors and green fine chemicals

Giorgio Vilardi

La Sapienza Università di Roma

giorgio.vilardi@uniroma1.it

La lecture tratta la tematica del riutilizzo circolare degli RSU per la produzione accoppiata di energia, vettori energetici (idrogeno, metano e combustibili liquidi) e fine chemicals partendo dalla gassificazione degli RSU/CSS/plasmix. Il focus è su tecnologie promettenti di gassificazione a basso impatto ambientale (melting-gasification, slagging-gasification, moving injection horizontal gasification, chemical looping gasification) e su processi di produzione circolare (ad esempio da plasmix a syngas a olefine e quindi nuovamente a LDPE, o da RSU a syngas e biodiesel, ad ammoniaca e acroleina e infine a piridina).

Composite materials based on self-assembly strategies and FDM techniques: versatile tools to realize innovative hybrid materials for energetic, environmental and biomedical applications

Massimiliano Gaeta

Dipartimento di Scienze Chimiche dell'Università degli Studi di Catania.

massimiliano.gaeta@unict.it

Scientists have been fascinated by the challenging syntheses of nature-inspired materials. In this regard, over the last decades, a fascinating development in material science is the construction of engineered nanomaterials by self-assembly of small molecular building blocks [1]. Among them, porphyrinoid molecules can be employed as interesting molecular synthons. However, these molecules hide manifold trouble; even if the peripheral charged groups make these macrocycles water-soluble, nevertheless, porphyrins remain mainly hydrophobic molecules, preserving the well-known tendency to aggregate. This “dichotomy” is worthy of special attention because (i) it plays a central role in the non-covalent syntheses and, interestingly, (ii) in conjunction with inorganic -or polymeric- structures to arrange quite complex hybrid composite materials for energetic and environmental applications.

Therefore, in this keynote, I intend to describe the guiding principles about that and some interesting cases of engineered composite materials based on the self-assembly approach which we have realized [2-4]. In addition, new bio-composite suitable for Fused Deposition Modelling (FDM) methods will be also discussed [5-6].

For instance, from an energetic point of view, polyaromatic membranes, such as sulphonated polyetheretherketone (sPEEK), can be considered as a low-cost alternative to PFSA (i.e., Nafion™) based membranes for portable fuel cell applications. However, sPEEK membranes do not own sufficient performance to tackle the Nafion™ [2].

Thus, in order to improve the characteristics of such sPEEK membranes, we succeed in synthesizing new composite membranes by adding meso-tetrakis(4-sulfonatophenyl) porphyrin, TPPS [2]. In particular, we obtained hybrid TPPS/sPEEK materials with peculiar behavior in terms of good proton conductivity, chemical stability, and fuel cells performance. To get better insight into the specific interaction responsible for the improved quality of the materials, we have conducted a detailed spectroscopic investigation and physical-chemical characterizations of the composite membranes.

Furthermore, the electrochemical accelerated degradation test on PEFC single cell, simulating the typical operative conditions for portable applications, highlighted the improved stability of the composite membrane compared to that of the pristine sPEEK [2].

From another point of view, antibiotics represent essential drugs to contrast the insurgence of bacterial infections in humans and animals. However, their overuse can implicate a risk of water pollution and related antimicrobial resistance. As a consequence, innovative strategies for successfully removing antibiotic contaminants have to be advanced to protect human health. In this respect, a growing interest is arising in the degradation of antibiotics by heterogeneous photocatalysis using suspended TiO₂ nanoparticles. With the attempt to increase the photocatalytic efficiency of TiO₂, we decided to functionalize it with porphyrins [3]. Thus, we tested the photocatalytic efficiency of our hybrid organic/inorganic porphyrin@TiO₂ materials to degrade, in water, oxolinic acid (OXA) and oxytetracycline (OTC), two of the most extensively used antibiotics in aquaculture [3]. Accordingly, our porphyrin functionalized TiO₂ nanomaterials can represent an innovative tool for depuration of water and wastewater by OTC contamination, aimed to improve the reduction of bacterial resistance to antibiotics and, finally, to reduce the health outcomes related to the inefficacy of current pharmacological therapies against these diseases [3].

Concerning the safe water matter, another challenging problem of public health is the pollution due to dye-contaminants. Inspired by adhesive proteins secreted by mussels for attachment to wet surfaces, melanin-like materials result in efficient adsorbents for entrapping organic water-pollutants via synergic non-covalent interactions [4]. So, in order to enhance the adsorption performance, the strategy is to form melanin-coated nanomaterials having a higher specific surface area. Consequently, we employed a synthetic porphyrin–spermine derivative, namely H₂TCPPspm₄, to realize a new functionalized DOPA-melanin film, self-assembled film onto a commercial glass substrate, through a viable synthesis in aqueous medium at room temperature [4]. Our H₂TCPPspm₄/L-DOPA-melanin@glass device displayed an increased adsorption capacity against aqueous solutions of methylene blue dye. Furthermore, the possibility to reuse our prototype for continuous adsorption/desorption cycles enable us to have a smart device for water remediation technology on a larger scale [4].

Finally, from a different perspective, by exploiting the Fused Deposition Modelling (FDM) methods, we have recently realized novel bio-composites useful for biomedical prototypes [5,6]. In fact, FDM techniques have promoted the

extension of 3D printing technologies to new applications ranging from the biomedical, aerospace, and submarine fields, to some specific applications in manufacturing and civil fields. The expansion of the fields of application, generally, entails considering peculiar characteristics, such as complex geometries or requirements as low density. Furthermore, the breathability, the pleasantness to the touch, aesthetic appearance and a strong visual identity, that can be achieved by means of 3D printing, are especially requested for some applications such as biomedical. Thus, the development of purpose-dedicated filaments can be considered a key factor to successfully meet all these requirements.

In this respect, we fabricated and analyzed five new thermoplastic materials with fillers [5,6]: they are organic bio-plastic compounds made of polylactic acid (PLA) and organic by-products.

We preliminarily studied the main properties of these materials with a major emphasis on their strength, lightweight, and surface finish. In addition, experimental tests were performed in order to assess the suitability for FDM printing. The interesting final properties make these materials suitable for biomedical and, indeed, we reported the production of two different biomedical devices with one of the analyzed thermoplastic materials. In addition, such innovative bio-composite materials allow reducing the cost of environmental impact as well as the production management costs.

References

- [1] J.A.A.W. Elemans, R. van Hameren, R.J.M. Nolte, A.E. Rowan, *Adv. Mater.* 18 (2006) 1251-1266; C.J. Medforth Z. Wang, K.E. Martin, Y. Song, J.L. Jacobsenc, J.A. Shelnut, *Chem. Commun.* (2009) 7261-7277.
- [2] A. Carbone, M. Gaeta, A. Romeo, G. Portale, R. Pedicini, I. Gatto, M.A. Castriciano, *ACS Appl. Energy Mater.* 1 (2018) 1664-1673.
- [3] M. Gaeta, G. Sanfilippo, A. Fraix, G. Sortino, M. Barcellona, G. Oliveri Conti, M.E. Fragalà, M. Ferrante, R Purrello, A. D'Urso, *Int. J. Mol. Sci.* 21 (2020) 3775.
- [4] M. Gaeta, M. Barcellona, R. Purrello, M.E. Fragalà, A. D'Urso, *Chemical Engineering Journal* 433 (2022) 133262.
- [5] M. Cali, G. Pascoletti, M. Gaeta, G. Milazzo, R. Ambu, *Procedia Manufacturing* 51 (2020) 698-703.
- [6] M. Cali, G. Pascoletti, M. Gaeta, G. Milazzo, R. Ambu, *Appl. Sci.* 10 (2020) 5852.